REPORT DOCUMENTATION PAGE

AFRL-SR-AR-TR-03-

0146

1. AGENCY USE ONLY (Leave Blank)	2. REPORT DATE 02/28/03	3. REPORT TYPE AND DATES COVERED FINAL 01-01-2002 - 12-31-2002

4. TITLE AND SUBTITLE
~~Organization of the 2002 Photonic Science Topical Meetings~~

5. FUNDING NUMBERS
F49620-02-1-0065

6. AUTHOR(S)
Optical Society of America

7. PERFORMING ORGANIZATION NAME(S) AND ADDRESS(ES)
Optical Society of America
2010 Massachusetts Ave., NW
Washington, DC 20036

8. PERFORMING ORGANIZATION REPORT NUMBER

9. SPONSORING / MONITORING AGENCY NAME(S) AND ADDRESS(ES)

U. S. Air Force Office of Scientific Research
4015 Wilson Blvd. Rm. 713
Arlington, VA 22203

10. SPONSORING / MONITORING AGENCY REPORT NUMBER

11. SUPPLEMENTARY NOTES
The views, opinions and/or findings contained in this report are those of the author(s) and should not be construed as an official US AFOSR position, policy or decision, unless so designated by other documentation.

12 a. DISTRIBUTION / AVAILABILITY STATEMENT
Approved for public release; distribution unlimited.

12 b. DISTRIBUTION CODE

13. ABSTRACT (Maximum 200 words)

The OSA topical meetings that received support under this grant provided a forum for researchers in various specialty areas to meet and share ideas and technology in their fields. Following are the meetings that were supported by this grant:

- Advanced Solid State Lasers -- This meeting provided a forum for leading edge results in the fields of solid state lasers, laser materials, nonlinear optical materials and high power diode lasers.
- Laser Applications to Chemical and Environmental Analysis – This meeting presented and discussed advances in the use of lasers for chemical analysis and environmental monitoring.
- Biomedical Optics – This meeting was composed of three meetings that offered a unique venue to present and discuss recent research activities and developments in the field of lasers and optics in biomedicine.
- Ultrafast Phenomena - This meeting brought together a multidisciplinary group sharing a common interest in the generation of ultrashort pulses in the picosecond, femtosecond, and attosecond regimes and their application to studies of ultrafast phenomena in physics, chemistry, biology, material sciences and electronics.
- Nonlinear Optics – This meeting provided and international forum for discussion of all aspects of nonlinear optics, including new phenomena, novel devices, advanced materials and applications.
- Nonlinear Guided Waves and their Applications – This meeting emphasized on development of new ideas and novel techniques in the areas of materials, fabrication, devices , applications and nonlinear theory.
- Laser Induced Plasma Spectroscopy and Applications – This Meetings focused on major advances in LIBS fundamentals, instrumentation and applications and featured new commercial laboratory LIBS systems and advanced components, as well as field portable systems.

14. SUBJECT TERMS

15. NUMBER OF PAGES

16. PRICE CODE

17. SECURITY CLASSIFICATION OR REPORT UNCLASSIFIED	18. SECURITY CLASSIFICATION ON THIS PAGE UNCLASSIFIED	19. SECURITY CLASSIFICATION OF ABSTRACT UNCLASSIFIED	20. LIMITATION OF ABSTRACT UL

NSN 7540-01-280-5500

Standard Form 298 (Rev.2-89)
rescribed by ANSI Std. 239-18
298-102

20030513 108

2002

Nonlinear Guided Waves and their Applications

Technical Digest

September 1--4, 2002

Stresa Congress Centre
Stresa, Italy

OSA®
Optical Society of America

Sponsored by
Optical Society of America

Nonlinear Guided Waves and Their Applications

Technical Digest

September 1–4, 2002

Stresa Congress Centre
Stresa, Italy

OSA®
Optical Society of America

Articles in this publication may be cited in other publications. To facilitate access to the original publication source, the following form for the citation is suggested:

Name of Author(s), "Title of Paper," in OSA *Trends in Optics and Photonics (TOPS) Vol. 80, Nonlinear Guided Waves and Their Applications*, OSA Technical Digest, Postconference Edition (Optical Society of America, Washington DC, 2001), pp. xx-xx.

Technical Digest (meeting edition)

TOPS Vol. 80: NLGW Technical Digest–Postconference Ed.

Technical Program Committee

General Chairs

Alain Barthelemy, *Univ. de Limoges, France*
Yuri Kivshar, *Australian Natl. Univ, Canberra Australia*

Program Chairs

Marc Haelterman, *Univ. Libre de Bruxelles, Belgium*
Luigi A. Lugiato, *Univ. dell' Insubria a Como, Italy*
Richart Slusher, *Lucent Tech., USA*

Category 1: Nonlinear Fiber Effects and Temporal Solitons

Stefan Wabnitz, *Alcatel CIT, France*, Subcommittee Chair
Govind P. Agrawal, *Univ. of Rochester, USA*
Nail N. Akhmediev, *Australian Natl. Univ., Australia*
Peter A. Andrekson, *Cenix, USA*
Guy Millot, *Univ. de Bourgogne, France*

Category 2: Spatial Solitons and Transverse Effects

Demetrios N Christodoulides, *Lehigh Univ., USA*, Subcommittee Chair
Gaetano Assanto, *Univ. degli Studi Roma, Italy*
Allan Boardman, *Univ. of Salford, UK*
Paolo Di Trapani, *Univ. dell' Insubria a Como, Italy*
Lluis Torner, *Polytechnic Univ. of Catalonia, Spain*

Category 3: Nonlinear Periodic Structures and Frequency Conversion

Neil G. R. Broderick, *Univ. of Southampton, UK*, Subcommittee Chair
Ole Bang, *Univ. of Denmark, Denmark*
Martijn de Sterke, *Univ. of Sydney, Australia*
Benjamin J. Eggleton, *Lucent Tech., Bell Labs., USA*

Category 4: Solitons and Self-organized Spatial Structures in Cavities and Feedback Systems

William J. Firth, *Strathclyde Univ., UK*, Subcommittee Chair
Thorsten Ackemann, *Univ. Munster, Germany*
Nikolay Rosanov, *S.I Vavilov State Opt. Inst., Russia*
Mark Staffman, *Univ. of Wisconsin-Madison, USA*

Category 5: Materials and Fabrication

Joseph Zyss, *Ecole Normale Superieure de Cachan, France*, Subcommittee Chair
Alfred Driessen, *Univ. of Twente, The Netherlands*
James Grote, *Air Force Research Lab., USA*
Peter Van Daele, *Optoelectronics/Optoelectronic Tech., Belgium*
Shlomo Ruschin, *Tel Aviv Univ., Israel*

Daniel Gauthier, *Duke Univ., USA**

*OSA Technical Council Representative

Agenda

■ **Monday**
■ **September 2, 2002**

Room: Auditorium

8:00am–10:00am
NLMA ■ Temporal Fiber Solitons
Stefan Wabnitz, Xtera Communications, Inc.,
United States, Presider **Presider**

NLMA1   8:00am   Invited
Is soliton communications really beneficial in presence of polarization mode dispersion? *M. Karlsson, C. Xie, H. Sunnerud, P. A. Andrekson, Chalmers Univ. of Tech., Sweden.*
We discuss and review the impairments from random birefringence and PMD on soliton systems, including timing jitter coming from PMD and WDM-collision-induced polarization scattering.

NLMA2   8:30am
Phase-locked soliton pairs in a fiber ring laser, *Ph. Grelu, F.Belhache, F.Gutty, Univ. de Bourgogne, France; J. M. Soto-Crespo,Instituto de Optica, Spain.*
We have experimentally observed the formation of stable pulse pairs with a π/2 phase difference in a passively mode-locked stretched-pulse fiber ring laser. We have developed a simplified theoretical model that, keeping the essential features of the experiment, reduces greatly the number of free parameters and solved it numerically. The agreement with the experimental results is excellent.

NLMA3   8:45am
Observation of soliton explosions, *Steven T. Cundiff, Natl. Inst. of Standards and Tech. and Univ. of Colorado-Boulder, USA; J. M. Soto-Crespo,C.S.I.C., Spain; Nail Akhmediev, Australian Natl. Univ., Australia.*
We show, experimentally and numerically, that Ti:sapphire mode-locked lasers can operate in a regime in which they produce exploding solitons. In stable conditions of operation all explosions have similar features, but are not identical.

NLMA4   9:00am
Temporal soliton compression in beta-barium borate, *S. Ashihara, T. Shimura, K. Kuroda, Univ. of Tokyo, Japan.*
We present the temporal soliton compression of femtosecond pulses in quadratic media, where cascade quadratic nonlinearity and normal dispersion contribute for compression. Compression factor of 3 is achieved by using ~30 mm long beta-barium borate.

NLMA5   9:15am
Nonrecursive multiple shock formation via four-wave mixing: Theory and experiment, *S. Trillo, Univ. of Ferrara, Italy; F. Gutty, G. Millot, Univ. de Bourgogne, France.*
We show theoretically and experimentally that a beat signal propagating along a normally dispersive fiber can trigger the formation of multiple shocks. This phenomenon critically depends on the input frequency separation and power of the beat signal.

NLMA6   9:30am
Importance sampling for noise-induced amplitude and timing jitter in soliton transmission systems, *R. O. Moore, Brown Univ., USA; G. Biondini, Ohio State Univ., USA; W. L. Kath, Northwestern Univ., USA.*
We apply importance sampling to the Monte-Carlo simulation of low-probability amplitude and timing jitter events produced by amplified spontaneous emission noise in a soliton-based lightwave transmission system.

NLMA7   9:45am
Complete characterization of milliwatt peak power picosecond pulses at 10 GHz propagating over 300 km in a fiber recirculation-loop, *Marc Hanna, Pierre-Ambroise Lacourt, GTL-CNRS Telecom, France; John M. Dudley, Jean-Pierre Goedgebuer, Univ. de Franche-Comté, France.*
Frequency resolved optical gating using a novel fiber-based wavelength conversion geometry is used to characterize the intensity and phase evolution of milliwatt peak power pulses propagating over 300 km in an optical fiber recirculation loop.

10:30am–12:30pm
NLMB ▪ Spatial Solitons and Spatio-Temporal Effects

*Mordechai Segev, Technion Israel Inst. of Tech.,
Israel, Presider*

`Presider`

NLMB1   10:30am   (Invited)
Nonlinear X-waves: A new perspective for space-time localization, *S. Trillo, INFM and Univ. of Ferrara, Italy; C. Conti, INFM, Italy; P. Di Trapani, O. Jedrkiewicz, J. Trull, INFM and Univ. of Insubria, Italy; G. Valiulis, Vilnius Univ., Lithuania.*
Nonlinear and normally dispersive media support a novel form of space and time 3D localization of light in the form of so-called X-waves. We discuss their properties and their evidence in second-harmonic generation experiments.

NLMB2   11:00am
Induced Group-Velocity Dispersion in Second-Harmonic Generation: a Route to Light Bullets, *K. Beckwitt, Y.-F. Chen, F. W. Wise, Cornell Univ.,USA; T. Wang, H. Zhu, L. Qian,Fudan Univ., China.*
We show that in phase-mismatched second-harmonic generation, an effective group-velocity dispersion is induced at the second-harmonic frequency. In quasi-phase-matched structures this allows for temporal soliton formation and therefore facilitates the formation of 3-D spatiotemporal solitons.

NLMB3   11:15am
Snake instability of the 2+1D spatio-temporal bright soliton stripe, *N. Roig, S.-P. Gorza, Ph. Emplit, M. Haelterman, Univ. Libre de Bruxelles, Belgium.*
We demonstrate experimentally the snake instability of the bright soliton stripe in the 2+1D hyperbolic nonlinear Schroedinger equation. The instability is observed on a spatially extended femtosecond pulse propagating in a normally dispersive self-defocusing semiconductor planar waveguide.

NLMB4   11:30am
Observation of self-similar nonlinear wave collapse, *K.D. Moll, Alexander, L. Gaeta, Cornell Univ., USA; Gadi Fibich, Tel Aviv Univ., Israel.*
We show that during self-focusing induced collapse of a laser beam, the spatial profile evolves into the same cylindrically symmetric shape, known as the Townes soliton, regardless of the shape of the input beam profile.

NLMB5   11:45am
3D mapping of self-focussed light pulses, *Stefano Minardi, Giovanni Blasi, Paolo Di Trapani, INFM and Univ. degli Studi dell'Insubria, Italy; Arunas Varanavicius, Gintaras Valiulis, Algis Piskarskas; Vilnius Univ.,Lithuania.*
By exploiting a cross-correlation technique, we were able to investigate the space-time structure of the parametric spatial solitons excited by picosecond light pulses. Temporal effects that a simple 2D model cannot explain are discussed.

NLMB6   12:00pm
Symmetry-breaking instability of multimode vector solitons in Kerr media, *C. Cambournac, Thibaut Sylvestre, Hervé Maillote, Université de Franche-Comté, France; Bruno Vanderlinden, Pascal Kockaert, Philippe Emplit,Marc Haelterman, Univ. Libre de Bruxelles, Belgium.*
We show experimentally that the two-component two-hump vector soliton exhibits a sharp left-right symmetry-breaking instability in Kerr media. The experiment is performed using molecular re-orientation in CS_2 and the opposite circular polarization states of light as the two components of the vector soliton.

NLMB7   12:15pm
Skewed coherence along space-time trajectories in parametric generation processes, *Antonio Picozzi,Univ. de Nice-Sophia Antipolis, France; Marc Haelterman,Univ. Libre de Bruxelles,France.*
Considering the spatio-temporal problem of the parametric generation process, we show theoretically that the down-converted fields exhibit, as a general rule, a hidden coherence characterized by skewed coherence lines along specific space-time trajectories.

Room: Auditorium

2:00pm–4:00pm
NLMC ▪ Nonlinear Fiber Optics and Pulse Propagation

*Marc Haelterman, Univ. Libre de Bruxelles,
Belgium, Presider*

`Presider`

NLMC1   2:00pm   (Invited)
What is the role of modulational instability in ultra-high repetition rate pulse generators based on passive and active fiber cavities? *Stephane Coen, Univ. Libre de Bruxelles, Belgium.*
We study experimentally the role of modulational instability in two classes of devices that are commonly called "modulational instability lasers". For one of them, this denomination is found to be misleading.

NLMC2   2:30pm
Temporal modulational instability controlled by pulse envelope dynamics, *Domenico Salerno, Univ. of Milano, Italy; Jose Trull, Paolo Di Trapani, INFM and Univ. degli Studi dell'Insubria, Italy; Gintaras Valiulis, Vilnius Univ., Lithuania; S. Trillo, C. Conti, INFM, Italy.*
In second harmonic generation, temporal splitting into a train of solitons is observed owing to modulational instability seeded by a self-induced pulse-envelope modulation.

NLMC3 2:45pm
Generation of entanglement between frequency bands via a nonlinear fiber propagation and a spectral pulse shaping, *F. Kannari, D. Fujishima, K. Ohno, M. Sakurama, Keio Univ., Japan; M. Sasaki, M. Takeoka, Comm. Res. Lab., Japan.*
A novel fiber-based scheme for generating quadrature entanglement between a desired pair of frequency bands is proposed. The scheme is based on a nonlinear fiber, a spectral pulse shaper, and an adaptive feedback loop.

NLMC4 3:00pm
Experimental observation of modal attraction in optical fibers, *Stéphane Pitois, Guy Millot, Univ. de Bourgogne,France; Marc Haelterman, Univ. Libre de Bruxelles, Belgium.*
We investigate experimentally nonlinear optical attractors based on four-photon mixing interaction of counterpropagating waves in optical fibers.

NLMC5 3:15pm
Nonlinear optical properties of As-Se fiber, *R.E. Slusher, Lucent Tech., USA; J.S. Sanghera, L.B. Shaw, I.D. Aggarwal, NRL, USA.*
Large optical Kerr nonlinearities in low linear loss As-Se glass fibers are shown to have potential for ultra-fast, low power, all-optical processing applications. Nonlinear phase shifts near pi radians are demonstrated in fibers only 60 cm long.

NLMC6 3:30pm **Invited**
Slow light, fast light, and optical solitons in structured optical waveguides, *Robert W. Boyd, John E. Heebner, Univ. of Rochester, USA.*
We describe the exotic optical properties of a device consisting of a sequence of optical microresonators coupled to an optical waveguide. This device can display slow or fast group voelocities of propagation, large tailored dispersion, and the propagation of optical solitons.

Room: Lower Level Foyer

4:00pm–6:00pm
NLMD ∎ Poster Session: 1

NLMD1
Nonlinear transmission in photonic crystal waveguides: Optical switchers and diodes, *Sergei F. Mingaleev, The Australian Natl. Univ., Australia and Bogolyubov Institute for Theoretical Physics,Ukraine; Yuri S. Kivshar, The Australian Natl. Univ., Australia.*
We derive effective discrete equations with long-range interaction which accurately describe light transmission in photonic crystal waveguides with embedded nonlinear defects and demonstrate the possibility of a bistable (all-optical switcher) and unidirectional (optical diode) transmission.

NLMD2
Modulational instability of Bose-Einstein condensates in two- and three-dimensional optical lattices, *B.B. Baizakov, M. Salerno, Univ. of Salerno, Italy; V.V. Konotop, Univ. of Lisboa, Portugal.*
We show that the phenomenon of modulational instability gives rise to coherent spatial structures in arrays of Bose-Einstein condensates confined to optical lattices. A simple way to retain these spatial structures is proposed, which may be of interest for applications.

NLMD3
Optimized 2-dimensional poling pattern for fourth harmonic generation, *Andrew H. Norton, C. Martijn de Sterke, Univ. of Sydney, Australia.*
The efficiency of a recently proposed fourth harmonic generation scheme depends on two Fourier coefficients of a 2-dimensional periodic poling pattern. We describe a poling pattern responding to a local maximum of this efficiency.

NLMD4
Negative group velocities in quasi-phase-matched second-order nonlinear optical interactions, *S. Longhi, P. Laporta, M. Marano; Istituto Nazionale per la Fisica della Materia, Dipartimento di Fisica, Politecnico di Milano, Italy.*
Cascading effects can lead to anomalous group velocities for pulse propagation in quasi-phase-matched parametric amplifiers. This phenomenon permits to observe negative transit times in a photonic devices, simulating resonant propagation through a gain-doublet atomic system

NLMD5
Novel type nonlinear semiconductor waveguide crystal for efficient frequency up/down conversion, *E. U. Rafailov, P. Loza-Alvarez,Univ. of St. Andrews, UK; D. Artigas,Univ. Politecnica de Catalunya, Spain; M. B. Flynn, W. Sibbett,Univ.of St Andrews, UK.*
We demonstrate SHG at 980 nm from a novel first-order QPM semiconductor GaAs/AlGaAs waveguide crystal. Our calculations show that the SHG conversion efficiency from the crystal significantly exceeds that from PPLN for wavelengths exceeding 3.4 µm for both femtosecond and CW pump beams

NLMD6
Semiconductor optical amplifier Mach-Zehnder interferometers with feedback, *R. Van Dommelen, M. Cada, Dalhousie Univ.,Canada.*
We present new results on numerical simulations carried out on semiconductor optical amplifier Mach-Zehnder interferometers with feedback. We show that these devices can exhibit bistability, with the potential for high speed all-optical switching applications.

NLMD7
Shaping the optical components of solitary three-wave weakly coupled states in a two-mode crystalline waveguide, *Alexandre S. Shcherbakov, Natl. Inst. for Astrophysics, Mexico.*
Bragg solitons, representing collinear three-wave weakly coupled states, are investigated both theoretically and experimentally. The dynamics of shaping their optical components is studied, and the roles of localizing pulse width and phase mismatch are revealed.

NLMD8
Instability of gap 2π-pulses, *B.I.Mantsyzov,R.A.Silnikov, Moscow State Univ., Russia.*
Different regimes of the gap 2π-pulse dynamics in the one-dimensional resonantly absorbing Bragg grating are studied. A new family of stable oscillating and excited unstable gap 2π-pulses is analytically and numerically described by transition from the two-wave Maxwell-Bloch equation to the modified sine-Gordon equation and by direct integration of the Maxwell-Bloch equation.

NLMD9
All-optical AND gate using Kerr nonlinear microresonators, *Suresh Pereira, Philip Chak, J. E. Sipe, Univ. of Toronto, Canada.*
We demonstrate numerically that two channel waveguides, coupled by Kerr nonlinear microresonators, can operate as an all-optical AND gate. The device is about 100mm long, and intensity thresholds are lower than in similar Bragg systems.

NLMD10
Triply resonant integrated optical parametric oscillator, *B. Naveh, S. Ruschin, Tel-Aviv Univ., Israel; Z. Weissman, Tel-Hai Academic Coll., Israel.*
We report the modeling of a triply resonant, quasi phase matched, one chip, integrated optical parametric oscillator. Using a novel iterative calculation scheme, we predict threshold levels, conversion efficiency, passive and active tuning behavior and bistability.

NLMD11
Complete description of all modulational instability gain bands generated by nonlinear QPM gratings, *Ole Bang, Tech. Univ. of Denmark, Denmark; Joel F. Corney, Univ. of Queensland, Australia.*
We consider plane waves propagating in quadratic nonlinear slab waveguides with nonlinear quasi-phase-matching gratings. We predict analytically and verify numerically the complete gain spectrum for transverse modulational instability, including hitherto undescribed higher order gain bands.

NLMD12
Temporal compression of self-focusing femtosecond pulses in silica glasses, *Helene Ward, Luc Berge, CEA-DAM, France.*
Compression of femtosecond pulses to a few optical-cycles duration by coupling with an electron plasma in solids is shown. Nonlinear dissipation induced by multiphoton-absorption, and fast temporal modulations induced shock-terms can, however, maintain self-guided propagation.

NLMD13
Mode coupling by photorefractive grating in multiple quantum well slab waveguide, *Ewa Weinert-Raczka, Marek Wichtowski, Tech. Univ. of Szczecin, Poland.*
Photorefractive grating in slab waveguide based on semi-insulating AlGaAs/GaAs multiple quantum well structure with electric field applied along the quantum well planes as an externally controlled, frequency selective mode coupling element with memory is analysed.

NLMD14
Measurement of optical frequency ratios using a spectrally broadened frequency comb, *Nils Haverkamp, Joern Stenger, Harald Schnatz, Christian Tamm, Harald R. Telle, Phys.-Tech. Bundesanstalt, Germany.*
Due to nonlinear effects, fsec-pulses from a mode-locked laser are spectrally broadened in a photonic crystal fiber to span an octave in the visible wavelength region. Using this comb, we measured frequency ratios.

NLMD15
Nonlinear interactions in slow-wave structures, *A. Melloni, M. Martinelli, S. M. Pietralunga, DEI, Italy; F. Morichetti, CoreCom, Italy.*
Nonlinear interactions in coupled resonator slow-wave structures are investigated. Kerr based phase modulation and wavelength conversion by four-wave-mixing result strongly enhanced thanks to both the increase of the intra-cavity mean power and the interaction time between propagating fields.

NLMD16
Peakons - a novel type of robust pulses in photonic crystals, *U.Peschel, F.Lederer, Friedrich-Schiller-Univ. Jena, Germany; B.A.Malomed, Tel Aviv Univ., Israel.*
We demonstrate that near resonances, e.g. around the band gaps of Bragg gratings, non-solitonic pulses can propagate undistorted. These so-called peakons are stabilized by nonlinearly induced self-phase modulation, which shifts their frequency out of resonance.

NLMD17
Canonical Hamiltonian formulation for nonlinear pulse propagation in 3D photonic bandgap structures, *Suresh Pereira, Philip Chak, J. E. Sipe, Univ. of Toronto, Canada.*
We present a canonical Hamiltonian formulation for pulse propagation in a Kerr nonlinear 3D photonic bandgap material (PBG). The formulation is amenable to bulk crystals and to patterned waveguides in PBGs.

NLMD18
Depositing light in a photonic stop gap using Kerr nonlinear microresonators, *Philip Chak, J. E. Sipe, Suresh Pereira, Univ. of Toronto, Canada.*
We numerically simulate the trapping of light, via four-wave mixing, in a photonic stop gap using Kerr nonlinear microresonators. We also present a scheme, based on cross-phase modulation, to retrieve the trapped light.

NLMD19
Efficient integrated Ti:PPLN MIR-optical parametric generator, *Marc C. Huebner, D. Hofmann, W. Sohler, Univ. of Paderborn, Germany.*
Efficient tunable MIR-optical parametric fluorescence was demonstrated for the first time in a 80mm long single mode Ti:PPLN channel guide of 31 μm domain periodicity. Up to several μW of MIR-power were generated using a modelocked fiber laser as pump source.

NLMD20
Faraday patterns in Bose-Einstein condensates,
Kestutis Staliunas, PTB Braunschweig, Germany; Stefano Longhi, Politech. di Milano, Italy; German J. de Valcarcel, Univ. de València, Spain.
Temporal periodic modulation of the scattering length in Bose-Einstein condensates is shown to excite subharmonic patterns of atomic density through a parametric resonance. The patterns are analogous to the Faraday waves excited in vertically vibrated liquids.

NLMD21
Stability of spiralling solitary waves in Hamiltonian systems, *D.V. Skryabin, Univ. of Bath, UK; J.M. McSloy, W.J. Firth, Univ. of Strathclyde, UK.*
We present a rigorous criterion for stability of spiralling solitary structures in Hamiltonian systems incorporating the angular momentum integral and demonstrate its applicability to the spiralling of two mutually incoherent optical beams propagating in photorefractive material.

NLMD22
Dynamics of an optical beam in parabolic waveguide with periodic and random nonlinear refractive index,
F.Kh. Abdullaev, Physical-Tech. Inst. of the Uzbek Acad. of Sciences, Uzbekistan; J.C.Bronski, Univ. of Illinois-Urbana-Champaign, USA; R.M. Galimzyanov, Physical-Tech. Inst. of the Uzbek Acad. of Sciences, Uzbekistan.
Oscillations and associated resonance of an 2D optical beam under periodic and random modulations of nonlinear refractive index. For random oscillations the mean growth rate for the beam width is calculated. Analytical results are compared with the numerical simulations of the full 2D NLS equation.

NLMD23
Non-paraxial dark solitons, *P. Chamorro-Posada, Univ. de Oviedo, Spain; G.S. McDonald, Univ. of Salford, UK; G.H.C. New, Imperial Coll., UK.*
We present an analysis of the properties of dark spatial solitons when the paraxial restriction is removed. The results reveal modifications in the soliton phase period, width and transverse velocity.

NLMD24
Lossless planar X-junctions induced by vector solitons,
Andrey A. Sukhorukov, Nail N. Akhmediev, Australian Natl. Univ., Australia.
We propose a new design for planar X-junctions based on vector soliton theory. Transmission coefficients for such device can vary from zero to a maximun value for any fixed angle between the waveguide channels.

NLMD25
Optical vortices of parametrically coupled waves,
Anatoly P. Sukhorukov, Alexey A. Kalinovich, Moscow State Univ., Russia; Gabriel Molina-Terriza, Lluis Torner, Univ. Politech. da Catalunya, Spain.
We demonstrate two-component generation of one or three dislocations by equally charged input vortices, and two or four ones by oppositely charged singularities. The vortex 3D trajectories are calculated when the beams interact due to frequency conversion.

NLMD27
Collapse of optical vacuum pulses due to QED nonlinearities, *D. Anderson, M. Lisak, M. Marklund, P. Johannisson ,Chalmers Univ. of Tech., Sweden; G. Brodin, L. Stenflo, Umea Univ., Sweden.*
Due to quantum electrodynamical (QED) effects there are nonlinear corrections to Maxwell's equations in vacuum. We show that stationary two-dimensional light bullets can form, which are unstable and exhibit the possibility of self-focusing collapse.

NLMD28
Self-pumped phase conjugation in a BaTiO$_3$:Rh waveguide, *P.A. Márquez Aguilar, Univ. Autónoma del Estado de Morelos, México; P. Mathey, Univ. de Bourgogne, France; P. Moretti, Univ. Claude, France; D. Rytz, GmbH, Germany.*
We present a self-pumped phase conjugator originated by self-bending of the incident beam at λ = 515 nm in a BaTiO$_3$:Rh waveguide elaborated by three successive He$^+$ ion implantations. Phase conjugate reflectivity reached is 28 %.

NLMD29
Reflection of excited vector spatial solitons from an interface between two photorefractive media, *Ilya Shadrivov, The Australian Natl. Univ. Canberra, Australia; Alexander A. Zharov, Russian Acad. of Sciences, Russia*
Momentum method towards a study of multi-component spatial solitons dynamics in photorefractive media was developed. It describes both an excitation of the soliton intrinsic degrees of freedom associated with the oscillations of centres of gravity of the beams making up the soliton and soliton interaction with nonlinear interface.

NLMD30
Analysis of fields of nonlinear-cladding optical waveguides with butt-coupled linear waveguides: Effects of the film index, *Kiyoshi Tsutsumi, Kyoto Inst. of Tech., Japan.*
Effects of the film index of nonlinear-cladding optical waveguides are investigated numerically. The path of a beam winds between tbe film and the nonlinear cladding for larger film index, whereas soliton-like emission occurs for smaller film index.

NLMD31
Interaction of incoherently coupled transversely asymmetric beams, *P. Papagiannis, K. Hizanidis, Natl. Tech. Univ. of Athens, Greece.*
The stationary evolution of two incoherently coupled beams of bi-Gaussian intensity profile propagating in a bulk Kerr or saturable medium is studied variationally. The stability is investigated on the basis of the Vakhitov-Kolokolov criterion and comparisons are made with numerical integration of the (2+1)D coupled NLS equations involved.

NLMD32
Spatial solitons in nematic liquid crystals: A new model, *Claudio Conti, Marco Peccianti, Gaetano Assanto, Natl. Inst. for the Physics of Matter, Univ. "Roma Tre", Italy.*
We derive a model describing 3D spatial solitons in nematic liquid crystals. These solitary waves are governed by the same equations of parametric simultons, with nonlocality being the dominant stability mechanism.

NLMD33
Exact soliton solutions of the quintic complex Swift-Hohenberg equation of the quintic complex Swift-Hohenberg equation, *Adrian Ankiewicz, The Australian Natl. Univ., Australia; Kenichi Maruno, Kyushu Univ.,Japan; Nail Akhmediev,Australian Natl.Univ.,Australia.*
Several soliton solutions of the complex quintic generalized complex Swift-Hohenberg equation (CSHE) are found analytically. These solutions exist for certain relations between the parameters of CSHE which are also presented analytically.

NLMD34
Spatial solitons and Anderson localisation, *Kestutis Staliunas, PTB Braunschweig,Germany.*
Anderson localization is the spatial localization of the wavefunction of electrons in random media. We suggest, that analogous phenomenon can stabilize the spatial solitons in optical resonators: the spatial solitons in resonators with randomly distorted mirrors are more stable, than in perfect mirror resonators.

NLMD35
Discrete solitons in nonlinear zigzag optical waveguide arrays with tailored diffraction properties, *Nikos K. Efremidis, Jared Hudock, Demetrios N. Christodoulides, CREOL, USA.*
We show that the discrete diffraction properties of a nonlinear optical zigzag waveguide array can be signifigantly modified by exploiting the topological arrangement of the lattice itself. This introduces extended interactions (beyond nearest-neighbors), which, in turn, affect the lattice dispersion relation within the Brillouin zone. As a result, we demonstrate that new families of discrete soliton solutions are possible which are stable over a wide range of parameters. Our method opens new opportunities for diffraction management that can be employed to generate low power spatial discrete optical solitons.

NLMD36
Engineering the nonlinear phase shift, *Yan Chen, Benjamin Yang, Geeta Pasrija, Steve Blair, Univ. of Utah, USA.*
Large nonlinear phase shifts can be achieved using cascaded and coupled microresonator systems even if the constituent material has large linear and two-photon absorption. Proper design can maintain nearly constant intensity transmittance.

NLMD37
Characterisation and process evolution of quasi-phase-matched semiconductor superlattice waveguides using intermixing, *K. Zeaiter, T. C. Kleckner, J. S. Aitchison, D. C. Hutchings, Univ. of Glasgow, UK.*
We characterise the intermixing fabrication process by examining the photoluminescence spectra. Subsequently we adapt the process, which was initially developed for optoelectronic integration, to be optimised for the production of semiconductor superlattice waveguides for quasi-phase-matched frequency conversion.

NLMD38
Symmetry properties of χ^3 in semiconductor heterostructure waveguides, *D. C. Hutchings, Univ. of Glasgow, UK.*
The symmetry of the third-order susceptibility tensor elements is addressed for semiconductor heterostructures. 8 independent elements are found for the normal sample geometry and coefficients for nonlinear refractive phenomena are derived. The change in dimensionality with intermixing is discussed.

NLMD39
Self-bending of the light in a photorefractive planar waveguide fabricated with He^+ implanted $BaTiO_3$:Rh, *Pierre Mathey,Univ. de Bourgogne,France; Pedro Marquez, Univ. Autonoma del Estado de Morelos, Mexico; Paul Moretti, Univ. Claude Bernard Lyon 1, France; Daniel Rytz, Edelmetalle GmbH, Germany.*
The self-bending of a beam caused by the photorefractive non-linearity is observed in a $BaTiO_3$:Rh waveguide. The response time in function of the intensity is compared with the results in the bulk.

NLMD40
Diffraction effects in copper-doped helium-implanted LiNbO₃ waveguide, *Yury M. Larionov, Marina N. Frolova, Stanislav M. Shandarov, State Univ. of Control Systems and Radioelectronics, Russia; Sergey M. Kostritski, Kemerovo State Univ., Russia.*

We report an experimental observation of leaky substrate TM modes diffraction on a grating-like periodical structure formed by defects of waveguide layer. Appearance of such defects we explain by features of copper-doped helium-implanted optical $LiNbO_3$ waveguide fabrication process.

NLMD41
Femtosecond measurement of nonlinear refraction in periodically poled lithium tantalate, *S. Ashihara, J. Nishina, T. Shimura, K. Kuroda, Univ. of Tokyo, Japan.*

We present femtosecond measurements of nonlinear refraction in periodically poled lithium tantalate by using spectrally resolved two-beam coupling. The sign and magnitude of nonlinear phase shifts induced by cascade quadratic nonlinearity and intrinsic Kerr nonlinearity are measured.

NLMD42
Towards an optical parametric oscillator in a GaAs-based waveguide, *A. De Rossi, M. Calligaro, V. Ortiz, THALES Res. and Tech., France; V. Berger, Univ. Denis Diderot Paris VII, France.*

We will discuss the feasibility of an integrated parametric oscillator based on GaAs. Results on parametric fluorescence will be presented. Minimization of losses and mirror deposition are the crucial points for obtaining parametric oscillation. A threshold around 100 mW is expected

NLMD43
Photorefractive solitons and light induced resonance control in semiconductor CdZnTe, *Tal Schwartz, Yaniv Ganor, Tal Carmon, Raam Uzdin, Sharon Shwartz, Mordechai Segev, Technion - Israel Inst. of Tech., Israel; Uri El-Hanany, Imarad Imaging Systems LTD., Israel.*

We experimentally demonstrate the formation of (1+1)D and (2+1)D solitons in photorefractive CdZnTe:V, exploiting the intensity-resonant behavior of the space charge field. We show that the resonance intensity is tunable, allowing soliton formation times as low as 10μ sec scales with very low optical power.

NLMD44
Efficient parallel algorithm for Simulating wavelength-division-multiplexed dispersion-managed optical fiber systems, *P.M. Lushnikov, Los Alamos Natl. Lab., USA.*

An efficient numerical algorithm is presented for massively parallel computation of dispersion-managed wavelength-division-multiplexed optical fiber systems. The algorithm is based on a weak nonlinearity approximation and independent parallel calculation of fast Fourier transforms.

NLMD45
Nonclassical statistics of intracavity coupled quadratic nonlinear waveguides: The quantum optical dimmer, *M. Bache, Yu. B. Gaididei, P. L. Christiansen, Tech. Univ. of Denmark, Denmark.*

Two quadratic nonlinear waveguides are immersed in a cavity suited for second-harmonic generation. The quantum equations are derived to calculate intensity correlation spectra and strong quantum violations of the classical limit is observed.

NLMD46
Dark-ring cavity solitons in lasers with bichromatic injected signal, *German J. de Valcarcel, Univ. de Valencia, Spain; Kestutis Staliunas, Physikalisch Tech. Bundesanstalt, Germany.*

We show theoretically that broad area lasers driven by a nearly resonant bichromatic field may support dark-ring cavity solitons as well as domain walls and labyrinthine patterns.

NLMD47
Localized structures formation and control in second-harmonic, intra-cavity generation, *E. Toniolo, M. Giltrelli, M. Santagiustina, INFM and Univ. of Padova, Italy.*

A regime in which spontaneous formation of localized structures occurs is found for intra cavity second harmonic generation. Independent writing, erasing and moving of structures are numerically demonstrated.

NLMD48
Two-dimensional clusters of solitary structures in driven optical cavities, *J. M. McSloy, W. J. Firth, Univ. of Strathclyde, UK; A. G. Vladimirov, St. Petersburg State Univ., Russia; D. V. Skryabin, Univ. of Bath, UK; N. N. Rosanov, Res. Inst. for Laser Physics, Russia.*

Interaction between localized structures in the transverse plane of a passive optical cavity containing a saturable medium is studied analytically and numerically. Stability properties of clusters of localized structures and their spontaneous motion are described.

NLMD49
Optical parametric oscillator in waveguides induced by photorefractive spatial solitons, *Song Lan, Princeton Univ., USA; J.A. Giordmaine, Princeton Univ., USA and NEC Res. Inst., USA; Mordechai Segev, Technion – Israel Inst. of Tech., Israel and Princeton Univ., USA; Daniel Rytz, FEE GmbH, Germany.*

We demonstrate experimentally an optical parametric oscillator constructed in the waveguide induced by photorefractive spatial solitons, and show that the pumping threshold is reduced considerably.

NLMD50
Frequency up-conversion of 770 nm ultra-short pulses by two-photon absorption in doped PMMA fibers, *Grace Jordan, Takeyuki Kobayashi, Werner J. Blau, Trinity Coll.,Ireland; Hartwig Tillmann, Hans-Heinrich Hörhold, Friedrich-Schiller-Univ., Germany.*

We report on the up-converted emission of blue light from a novel organic stilbenoid compound (1,4-bis(diphenylamino-styryl)-benzene) dopant in a PMMA fiber due to the two-photon absorption of 770 nm pulses from a Tittanium Sapphire laser.

NLMD51
Long-wavelength continuum generation about the second dispersion zero of a tapered fiber, *J. M. Harbold, F. O. Ilday, F. W. Wise,Cornell Univ., USA; T. A. Birks,W. J. Wadsworth, Univ. of Bath, UK;Z. Chen, Univ.of California-Irvine, USA.*

We demonstrate continuum generation at wavelengths longer than the zero-dispersion wavelength of ordinary fiber for the first time using a narrow-diameter tapered fiber.

NLMD52
Origin of supercontinuum generation in microstructured fibers, *Alexander L. Gaeta, Cornell Univ., USA;Xun Gu, Lin Xu, Mark Kimmel, Erik Zeek, Patrick O'Shea, Aparna P. Shreenath, Rick Trebino, Georgia Inst. of Tech., USA;Robert S. Windeler, OFS Fitel Lab., USA.*

We investigate the propagation of femtosecond pulses in microstructured fibers under conditions in which a supercontinuum is generated. We find that higher-order dispersion primarily determines the spectral envelope and that it contains a highly complicated underlying sub-structure which is highly sensitive to input fluctuations.

NLMD53
Exact solitary wave solutions of the nonlinear Schrodinger equation with distributed gain, *V.I. Kruglov,J.D. Harvey, Univ. of Auckland, New Zealand.*

We present new exact analytical solutions to the NLSE with gain in the anomalous dispersion regime corresponding to a compressing or spreading solitary pulses. These solutions have application in high gain nonlinear fiber amplifiers.

NLMD54
Timing and amplitude jitter due to intra-channel dispersion-managed pulse interactions, *Toshihiko Hirooka, Mark J. Ablowitz, Univ. of Colorado, USA.*

Analytical expressions to estimate timing and amplitude jitter due to intra-channel pulse interactions in dispersion-managed systems are provided. Results are compared to direct numerical simulation. Distributed amplification reduces timing and amplitude jitter with fixed path-average power.

NLMD55
Design considerations of all-optical header processing circuit for a novel packet forwarding scheme in optical networks, *W. M. Wong, K. J. Blow,Aston Univ., UK.*

Design of an all-optical circuit that performs modulo-N operation for packet forwarding without header modification in optical networks is presented. Design considerations such as gain modulation effects and bit rate and pattern depen-dence are investigated.

NLMD56
Traveling-wave model of semiconductor optical amplifier based nonlinear loop mirror with feedback, *W. M. Wong, K. J. Blow, Aston Univ., UK.*

A traveling-wave model of an all-optical switching device with feedback is developed to identify important dynamical effects for better prediction of device behavior. Using a constant lifetime approximation, an efficient heuristic model is also developed.

NLMD57
Wavelength-division-multiplexed bi-soliton transmis-sion in dispersion-managed system, *Takashi Inoue, Yasuhiro Yoshika, Akihiro Maruta, Osaka Univ., Japan.*

Bi-soliton transmission in dispersion-managed WDM system is studied. It is numerically confirmed that anti-phase bi-soliton is more robust for the collision than in-phase one. The XPM effects induced by the collision can be analyzed by using the variational method.

NLMD58
Towards nonlinear waveguide devices from conjugated polymers: Tuning of the materials properties and structuring, *A. Bahtiar, K. Koynov, C. Bubeck, Max-Planck-Inst. for Polymer Res., Germany; M. A. Bader, U. Wachsmuth, G. Marowsky, Laser-Lab. Göttingen e.V., Germany.*

We prepared slab waveguides of the conjugated polymer MEH-PPV and demonstrate that fine-tuning of refractive index is feasible by control of molecular weight. Grating waveguide structures are fabricated by UV-laser ablation.

Room: Auditorium

8:00am–10:00am
NLTuA ■ Discrete Solitons and Waveguide Arrays

George I. Stegeman, Univ. of Central Florida, United States, Presider

Presider

NLTuA1   8:00am
Discrete solitons in quadratic nonlinear waveguide arrays, *T. Pertsch, U. Peschel, F. Lederer, Friedrich-Schiller-Univ. Jena, Germany; J. Meier, Roland Schiek, Robert Iwanow, George Stegeman, CREOL, USA; Yoo Hong Min, Wolfgang Sohler, Univ. Paderborn, Germany.*

We observed the formation of discrete solitons in periodically poled Lithium Niobate (PPLN) waveguide arrays. Strongly localized dichromatic nonlinear beams were excited with fundamental wave pulses at a wavelength of 1572 nm.

NLTuA2   8:15am
Discrete gap solitons in modulated waveguide arrays, *Andrey A. Sukhorukov, Yuri S. Kivshar, Australian Natl. Univ., Australia.*

We demonstrate that the discrete gap solitons can be efficiently generated in arrays of optical waveguides with alternating widths. Depending on the light intensity, these solitons display the properties of both conventional and Bragg grating solitons.

NLTuA3   8:30am
Discrete vector Kerr spatial solitons in AlGaAs array waveguides, *Joachim Meier, George Stegeman, CREOL, USA; H.S. Eisenberg, Y. Silberberg, The Weizmann Institute of Science, Israel; R. Morandotti, J.S. Aitchison, Univ. of Toronto, Canada.*

We report the first observation of discrete vector solitons in arrays of AlGaAs waveguides. By changing the phase between the TE and TM soliton components, we were able to control their relative amplitude.

NLTuA4   8:45am
Discrete solitons in photorefractive optically-induced photonic lattices, *Nikos K. Efremidis, Jared Hudock, Demetrios N. Christodoulides, CREOL, USA; Jason Fleischer, Suzanne Sears, Mordechai Segev, Princeton Univ., USA.*

We demonstrate that optical discrete solitons are possible in appropriately oriented biased photorefractive crystals. This can be accomplished in optically-induced periodic waveguide lattices that are created via plane wave interference. Our method paves the way towards the observation of entirely new families of discrete solitons.

NLTuA5   9:00am
The action of linear modes on the evolution and on the decay of discrete solitons, *U.Peschel, F.Lederer, Friedrich-Schiller-Univ. Jena, Germany; R. Morandotti, J. S. Aitchison, Univ. of Toronto, Canada; H. S. Eisenberg, Y. Silberberg, The Weizmann Inst. of Science, Israel.*

We experimentally investigate how linear modes evolve around the soliton state. In the presence of nonlinear absorption they induce collapse and subsequent splitting of the soliton, or a transverse motion opposite to initial beam tilts.

NLTuA6   9:15am
Strong spatiotemporal localization in an array of silica waveguides, *D. Cheskis, S. Bar-Ad, Tel Aviv Univ., Israel; R. Morandotti, J. S. Aitchison, Univ. of Toronto,Canada;D. Ross, Univ. of Glasgow,UK; H.S Eisenberg, Y. Silberberg, Weizmann Inst. of Science, Israel.*

We experimentally investigated beam propagation in an array of silica waveguides, under a regime of anomalous dispersion and for different input conditions. In all the cases, we succeeded in compressing most of the energy in a single waveguide.

NLTuA7   9:30am
Optically-controlled photorefractive solitons arrays, *Jürgen Petter, Inst.of Applied Physics, Germany; Denis Träger, Cornelia Denz,Wilhelms-Univ. Münster, Germany.*

We present an optically-controlled array of photorefractive spatial screening solitons. Each channel of the array is found to guide a probe beam independently. Furthermore a Y-coupler within the array is realized by combining two channels with an additional control beam.

NLTuA8   9:45am
Discrete solitons in optically-induced real-time waveguide arrays, *J. W. Fleischer, M. Segev, Technion - Israel Inst. of Tech., Israel and Princeton Univ., USA; T. Carmon, Technion - Israel Inst. of Tech., Israel; N. K. Efremidis, D. N. Christodoulides, CREOL, USA.*

We report the first experimental observation of discrete solitons in an array of optically-induced waveguides. The waveguide arrays are induced in photorefractives by interfering pairs of plane waves, and the solitons form when the screening nonlinearity is employed. We demonstrate both in-phase and staggered bright solitons in 1-D arrays and discuss recent experiments in 2D waveguide lattices.

Room: Auditorium

10:30am–12:30pm
NLTuB ■ Dissipative Spatial Structures
Luigi Alberto Lugiato, Univ. Degli Studi Dell'Insubria, Italy, Presider **Presider**

NLTuB1   10:30am   **Invited**
Interaction of dissipative localized structures in nonlinear optics, *Dmitry V. Skryabin, Univ. of Bath, UK.*
Recent theoretical results on existence and stability of static, moving and rotating clusters of bright spatially localized structures of light in passive and active optical cavities will be reported.

NLTuB2   11:00am
Cavity pattern formation with incoherent light, *Tal Carmon, Mordechai Segev, Technion, Israel; Marin Soljacic, MIT, USA.*
We present the first observation of cavity modulation instability and pattern formation with incoherent light. In addition, we also study, theoretically and experimentally, the evolution of patterns in a nonlinear cavity without resonant frequencies: a passive cavity for which beams from different cycles are mutually-incoherent with one another.

NLTuB3   11:15am
Self-propelled solitons and moving patterns in a nonlinear resonator, *Andrew J. Scroggie, John M. McSloy, William J. Firth, Univ. of Strathclyde, UK.*
Spontaneously moving bright and dark spatial solitons and patterns are shown to exist in a nonlinear resonator. The motion is caused by thermal effects and arises through an instability of the stationary soliton.

NLTuB4   11:30am
Cavity solitons work as pixels in semiconductors, *S. Barland, M. Giudici, J. R. Tredicce,Inst. Non Lineaire de Nice, France; S. Balle, IMEDEA, Spain; M. Brambilla, T. Maggipinto, Univ. di Bari, Italy; L. A. Lugiato, L. Spinelli, G. Tissoni, Univ. dell'Insubria, Italy;T. Knödl, M. Miller, R. Jäger, Univ. of Ulm, Germany.*
By using a vertical cavity semiconductor amplifier with a large Fresnel number, driven by a coherent field, we provide the first proof of the generation of cavity solitons in semiconductors, written and erased independently of each other and of the boundary.

NLTuB5   11:45am
The origin of motion of solitary waves near Hopf bifurcations, *D. Michaelis, Fraunhofer Inst. für Angewandte Optik und Feinmechanik, Germany; U. Peschel, F. Lederer, Friedrich Schiller-Univ. Jena, Germany; D.V. Skraybin, Univ. of Bath, UK; W.J. Firth, Univ. of Strathclyde, UK..*
We show that the coupling between oscillating eigenstates and the translational mode causes solitary waves to move steadily, oscillatory or with irregular jumps. Theoretical results are compared with numerical simulations for different dissipative systems.

NLTuB6   12:00pm
Effects of nonlinear guiding on spontaneous pattern formation: Formation of spirals and target patterns, *F. Huneus, T. Ackemann, B. Schaepers, W. Lange, Univ. Muenster, Germany.*
Nonlinear guiding induced by gradients of the pump beam intensity can drastically affect optical pattern formation. A specific example is the emergence of spiral and target patterns in a single-mirror scheme with sodium vapor.

NLTuB7   12:15pm
Dark ring cavity solitons and stable droplets in models of nonlinear optical cavities, *Damià Gomila, Pere Colet, Maxi San Miguel,IMEDEA (CSIC-UIB), Spain;Gian-Luca Oppo,Andrew Scroggie, Univ. of Strathclyde, UK.*
Two kinds of localized structures are found in different regimes in nonlinear Kerr cavities and optical parametric oscillators. Its dynamics is closely related to the growth rate of spatial domains of different phases.

Room: Auditorium

2:00pm–4:00pm
NLTuC ■ Fiber Nonlinearity Applications
Nail N. Akhmediev, Australian National University, Australia, Presider **Presider**

NLTuC1   2:00pm   **Invited**
Ultrafast optical TDM transmission with the use of novel nonlinear optical fiber devices, *Masataka Nakazawa, Tohoku Univ., Japan.*
We have recently succeeded in transmitting an ultrafast OTDM signal which exceeds 1 Tbit/s over 70 km with the adoption of nonlinear optical fiber devices such as soliton compressor, DI-NOLM for pulse shaping, and NOLM for Terabit/s demultiplexing. In this talk, key technologies for ultrahigh-speed OTDM transmission are described.

NLTuC2   2:30pm
Raman gain efficiencies of modern terrestrial transmission fibers in S-, C- and L-band, *D. Grot, L. Bathany, S. Gosselin, M. Joindot, France Telecom R&D, France; S. Bordais, Y. Jaouen, J.M. Delavaux, Keopsys, France.*
We report the most complete measurements presented to date of Raman gain efficiency and noise figure for current G.652 and G.655 fibers in all three transmission windows (S-, C- and L-band). Such fiber characterization is paramount to the engineering and deployment of future terrestrial 40 Gbit/s-based WDM transmission systems.

NLTuC3   2:45pm
160-GHz picosecond pulse train generation through multiwave mixing compression of a dual frequency beat signal, *Julien Fatome, Stéphane Pitois, Guy Millot, Univ. de Bourgogne,France.*
We report the experimental generation and characterization of a 160-GHz picosecond pulse train using multiple four-wave mixing temporal compression of an initial dual frequency beat signal in the anomalous-dispersion regime of a non-zero dispersion shifted fiber.

NLTuC4　3:00pm
Cross correlation frequency-resolved optical gating characterization of supercontinuum generation in microstructure fiber: Simulation and experiment, *John M. Dudley, Univ. de Franche-Comté, France; Xun Gu, Lin Xu, Mark Kimmel, Erik Zeek, Patrick O'Shea, Aparna P. Shreenath, Rick Trebino, Georgia Inst. of Tech., USA; Stéphane Coen, Univ. Libre de Bruxelles, Belgium.*

Cross-correlation frequency resolved optical gating (XFROG) characterization of supercontinuum generation in microstructure fiber is studied using numerical simulations and experiments. The XFROG trace clearly reveals the signatures of dispersive wave and Raman soliton generation.

NLTuC5　3:15pm
Broadband 60% energy conversion of a two-pump fiber optical parametric amplifier, *Jose Manuel Chavez Boggio, Hugo Luis Fragnito, IFGW-UNICAMP, Brazil; Walter Margulis, ACREO, Sweden.*

We demonstrate over 60% energy conversion on 20 nm bandwidth centered at 1568 nm in a two-pump fiber optical parametric amplifier.

NLTuC6　3:30pm
Spectral phase fluctuations and coherence degradation in supercontinuum generation in photonic crystal fibers, *John M. Dudley, Remo Giust, Univ. de Franche-Comté, France; Stéphane Coen, Univ. Libre de Bruxelles, Belgium.*
Numerical simulations are used to study spectral phase fluctuations and coherence degradation in supercontinuum generation in photonic crystal fibers. The spectral coherence is shown to depend strongly on the input pulse duration and wavelength.

NLTuC7　3:45pm
Single-mode supercontinuum generation in a standard dispersion-shifted fiber using a nanosecond microchip laser, *A. Mussot, L. Provino, T. Sylvestre, H. Maillotte, UMR CNRS/Univ. de Franche Comté, France.*
We have generated a single-mode supercontinuum of more than 1100-nm simply using a nanosecond microchip laser and an usual dispersion-shifted fiber in a regime in which both self-phase modulation and parametric generation near the zero dispersion wavelength cannot be involved in the continuum formation.

Room: Lower Level Foyer

4:00pm–6:00pm
NLTuD ■ Poster Session: 2

NLTuD1
Thermal effects and spontaneous motion of cavity solitons in semiconductor microcavities, *T. Maggipinto, I. M. Perrini, M.Brambilla, INFM and Univ. di Bari, Italy; L. Spinelli, G. Tissoni, L.A. Lugiato, INFM and Univ. dell'Insubria, Italy.*
We formulate a model to describe the spatio-temporal dynamics of a semiconductor microcavity driven by an external field including the thermal field. A new kind of modulational instability is found, leading to travelling cavity solitons and patterns.

NLTuD2
Image processing with cavity type-II second harmonic generation, *Pierre Scotto, Pere Colet, Maxi San Miguel, Campus Univ. Illes Balears, Spain.*
Injecting in a Type II intracavity second harmonic generation an image in one polarization and a homogeneous field in the other, we can perform either a frequency and polarization transfer or a contrast enhancement.

NLTuD3
Noise-induced growth of arrays of spatial solitons in optical parametric oscillator, *Ivan Rabbiosi, Andrew Scroggie, Gian-Luca Oppo, Univ. of Strathclyde, UK.*
Domain walls with oscillatory tails can lock and form spatially irregular stable states in models of nonlinear optical devices. Their stochastic dynamics lead instead to the formation of periodic arrays of solitons.

NLTuD4
Unconditional instability of the degenerate backward optical parametric oscillator, *C. Montes,A. Picozzi, Univ. de Nice-Sophia Antipolis, France; C. Durniak, M. Taki,Univ. de Sciences et Tech. de Lille,France.*
Stability analysis of the degenerate backward optical parametric oscillator in the quasi-phase-matching decay interaction, between a cw-pump and a counter-propagating signal, proves that the inhomogeneous stationary solutions are always unstable whatever the cavity length and pump power.

NLTuD5
Spatial solitons in an optically pumped semiconductor microresonator, *V. B. Taranenko, C. O. Weiss, Physikalisch-Tech. Bundesanstalt, Germany.*
We show experimentally and numerically the existence of stable spatial solitons in an optically pumped semiconductor microresonator. We demonstrate that the pump substantially reduces the light intensity necessary to sustain the solitons.

NLTuD6

Spectral control of solitons under periodical dispersion-slope compensation, *Joji Maeda, Ichiro Matsuda, Tokyo Univ. of Science, Japan.*

Effects of guiding filters on solitons in fiber links with periodical dispersion slope-compensation are numerically studied. The optimum filter bandwidth and the optimum transmission power are discussed in comparison with slope-free fiber links.

NLTuD7

Stability criterion for solitons in passively mode-locked fiber lasers, *J. M. Soto-Crespo, C.S.I.C., Spain, Nail Akhmediev, Australian Natl. Univ., Australia, Graham Town, Univ. of Sydney, Australia.*

The complex cubic-quintic Ginzburg-Landau equation has multiplicity of soliton solutions for the same set of parameters. Based on their analysis, we propose a conjecture for a stability criterion for solitons in dissipative systems.

NLTuD8

Compound state of dark and bright solitons in dispersion-managed fibers, *M. Stratmann, F. Mitschke, Univ. Rostock, Germany.*

We report of a bright-dark-bright soliton compound state in dispersion managed fibers with either sign of path-average dispersion.

NLTuD9

Cross-phase-modulation induced modulation instability in Raman fiber amplifiers, *I. Velchev, R. Pattnaik, J. Toulouse, Lehigh Univ., USA.*

Modulation instability in forward-pumped Raman amplifiers is investigated in detail. The frequency dependence of the instability is explained in terms of a two-beam coupling process due to a finite relaxation time of the Kerr nonlinearity.

NLTuD10

Numerical study of parabolic pulse generation in microstructured fibre Raman amplifiers, *A.C. Peacock, N.G.R. Broderick, T.M. Monro, Univ. of Southampton, UK.*

Numerical simulations are used to demonstrate parabolic pulse generation in a highly nonlinear, normally dispersive microstructrured fibre Raman amplifier. The results show that the output pulse shape depends on the sign of the third order dispersion.

NLTuD11

Improving eficiency of supercontinuum generation in photonic crystal fibers by direct degenerate four-wave-mixing, *N. I. Nikolov, Univ. of Denmark, Denmark; O. Bang, A. Bjarklev, Tech. Univ. of Denmark, Denmark.*

The efficiency of supercontinuum generation in photonic crystal fibers is significantly improved by designing the dispersion to allow widely separated spectral lines generated by degenerate four-wave-mixing directly from the pump to broaden and merge.

NLTuD12

Carrier frequency hopping for optical pulse transmission in dispersion-managed fiber links, *Alessandro Tonello, Istituto Nazionale per la Fisica della Materia, italy; Fabrizio Carbone, Luciano Socci, Marco Romagnoli, Pirelli Labs., Italy.*

We propose a chirped return-to-zero transmission format, combining wavelength conversion with dispersion management. Periodically varying the pulse's carrier frequency at optimal points, we reduce the impairments of third-order dispersion and we mitigate the timing jitter.

NLTuD13

Eigenvalues of the Zakharov-Shabat scattering problem for real symmetric pulses, *M. Desaix, Univ. Coll. of Boras, Sweden; D. Anderson, L. Helczynski, M. Lisak, Chalmers Univ. of Tech., Sweden.*

The problem of determining the solitons generated from symmetric real initial conditions in the Nonlinear Schrödinger equation is revisited. The corresponding Zakharov-Shabat scattering problem is solved for an example of a real double-humped rectangular initial pulse form. It is found that this real symmetric pulse generates moving soliton pulse pairs corresponding to eigenvalues with non-zero real parts.

NLTuD14

Interaction of pulses in optical fibers, *E. N. Tsoy, F. Kh. Abdullaev, Uzbek Acad. of Sciences, Uzbekistan.*

Interaction of pulses in optical fibers is analyzed by solving the scattering problem associated with the nonlinear Schroedinger equation. It is shown that two pulses without initial phase modulation can generate moving daughter solitons.

NLTuD15

Suppression of soliton self-frequency shift by up-shifted filtering, *P. Tchofo Dinda, A. Labruyere, Univ. de Bourgogne, France; K. Nakkeeran, Hong Kong Polytech. Univ., Hong Kong.*

We propose an efficient method for suppressing the soliton self-frequency shift in high-speed transmission lines by means of up-shifted filters.

NLTuD16

Analytical design of dispersion-managed fiber systems with S≈1.65, *K. Nakkeeran, Hong Kong Polytech. Univ., Hong Kong; A. B. Moubissi, P. Tchofo Dinda, Univ. de Bourgogne, France.*

We present an easy analytical method for designing dispersion-managed fiber systems with map strength of 1.65, where the transmission lines have minimal pulse-pulse interactions.

NLTuD17
Suppression of nonlinear effects by phase alternation in strongly dispersion-managed optical transmission, *P. Johannisson, D. Anderson, M. Marklund ,Chalmers Univ. of Tech., Sweden; A. Berntson, M. Forzati, J. Martensson, Ericsson Telecom AB, Sweden.*
The nonlinear effects amplitude jitter and ghost pulse generation can be suppressed by alternating the phase of the bits. This is due to destructive interference between different contributions to the total nonlinear effect.

NLTuD18
Optical solitons in the femtosecond regime, *J. Wyller, Agricultural Univ. of Norway, Norway; Jan S. Hesthaven, Brown Univ., USA; Jens Juul Rasmussen, Risø Natl. Lab., Denmark.*
The evolution of optical solitons in the presence of amplification effects and nonlocal Raman response is investigated using perturbational analysis. The analysis reveals the existence of a soliton which acts as a global attractor in certain regimes of the amplification parameters.

NLTuD19
Stability of dissipative solitons in transmission lines beyond the average concept, *C.Knoell, D. Michaelis, Z. Bakonyi, G. Onishchukov, F. Lederer, Friedrich Schiller Univ. Jena, Germany.*
We investigate existence and stability of dissipative solitons in a transmission line with lumped amplification/absorption introducing a matrix algorithm. Parts of the domain in parameter space where the background is stable exhibit Hopf instabilities.

NLTuD20
Dynamical evolution of weak perturbations superposed to dispersion-managed soliton transmission, *Alessandro Tonello, Antonio-D. Capobianco, Gianfranco Nalesso, Costantino De Angelis, Francesco Consolandi, INFM, Italy.*
We analyze numerically and analytically the evolution of weak perturbations in fiber systems with dispersion management. Linearizing the governing equation around a dispersion-managed soliton, we discuss the role of average dispersion and of nearby pulses.

NLTuD21
Dependence of spectral width and gain of stimulated Brillouin scattering on numerical aperture in optical fibre, *Valeri I. Kovalev, Heriot-Watt Univ., UK and Russian Acad. of Sciences, Russia; Robert G. Harrison, Heriot-Watt University, UK.*
We give theoretical interpretation for the recently observed phenomenon of inhomogeneous spectral broadening of Brillouin scattering in optical fibres. SBS spectral width and gain dependencies on numerical aperture and are shown to be in good agreement with experiments for both single- and multi-mode fibres.

NLTuD22
Pulse broadening in dispersion-managed optical fiber links with random dispersion, *Tobias B. Schaefer, Richard O. Moore, Christopher K. R. T. Jones, Brown Univ., USA.*
Random dispersion variations lead to pulse degradation in fiber lines. We discuss the validity of a finite-dimensional reduction of the nonlinear Schroedinger equation and derive an analytical formula describing pulse broadening induced by randomness.

NLTuD23
The role of dispersion of nonlinearity in supercontinuum generation with photonic crystal fibers, *Rumen Iliew, Falk Lederer, Friedrich-Schiller-Univ. Jena, Germany.*
We derive field equations in frequency domain for describing spectrally broad pulses in nonlinear waveguides. Applying this model to supercontinuum generation in photonic-crystal fibers we investigate the influence of a frequency-dependent nonlinear term for realistic fibers.

NLTuD24
Pulse train dynamics in actively modelocked lasers, *J. Nathan Kutz, Jennifer J. O'Neil, Univ. of Washington, USA.*
A new model for the active modulation of a modelocked laser cavity shows pulsetrains can be stabilized only if adjacent pulses are out-of-phase, whereas instabilities destroy the pulsetrain or give Q-switching.

NLTuD25
On the theory of self-similar parabolic optical solitary waves, *S. Boscolo, S.K. Turitsyn, Aston Univ., UK; V. Yu. Novokshenov, Inst. of Mathematics RAS, Russia; J.H.B. Nijhof, Marconi Solstis, UK.*
Solutions of the nonlinear Schrodinger equation with gain, describing optical pulse propagation in an amplifying medium, are examined. A self-similar parabolic solution in the energy-containing core of the pulse is matched to the linear low-amplitude tails. The theoretical analysis reproduces accurately the numerically calculated solution.

NLTuD26
Error preventable line-coding schemes using bi-soliton to suppress intra-channel interactions in dispersion-managed system, *Akihiro Maruta, Yasumichi Nonaka, Takashi Inoue, Osaka Univ., Japan.*
Bi-soliton is a periodically stationary pulse propagating in a dispersion-managed (DM) transmission system. We propose novel transmission line coding schemes in which binary data are assigned to single DM solitons and bi-solitons to reduce impairments arising from intra-channel interactions.

NLTuD27

Experimental investigations and theoretical description of the spectral broadening of a femtosecond pulse train in tapered fiber, *S.N.Bagayev, S.V.Chepurov, V.I.Denisov, A.K. Dmitriyev, A.S. Dychkov, V.M.Klementyev, D.B.Kolker, I.I.Korel, S.A.Kuznetsov, Yu.A.Matyugin, M.V. Okhapkin, V.S.Pivtsov, M.N. Skvortsov, V.F.Zakharyash, Inst. of Laser Physics, Russia; T.A.Birks, W.J.Wadsworth, P.St.J.Russell, Univ. of Bath, UK.*

Experimental investigations and theoretical description of the tapered fiber influence on the spectral characteristics of the passed continuous femtosecond pulse train were made with the use of high stable Ti:S laser. Study of the input and output broadened spectrum envelope and intermode beats noise pedestal for various experimental conditions are presented.

NLTuD28

Wavelength conversion of femtosecond pulses by cross phase modulation in single mode fibers, *Gilbert Boyer, Ecole Polytech. -ENSTA, France.*

Efficient wavelength conversion of a femtosecond probe pulse in a single-mode fiber is performed by collision with a pump pulse. The background-free auto-correlation of the blue- and red-shifted probe is presented and discussed.

NLTuD29

Anti-guide assisted spatial soliton logic gate, *Balakishore Yellampalle, Kelvin Wagner, Univ. of Colorado-Boulder, USA; Steve Blair, Univ. of Utah, USA.*

An anti-guiding structure is shown to assist spatial soliton dragging logic gate. A weak beam easily breaks the balanced symmetry of a pump propagating in an anti-guide, allowing very efficient optical switching. More than an order of magnitude improvement over previous spatial dragging gates is possible.

NLTuD30

Competition of gain—guided modes in stimulated Raman scattering with Bessel beams, *T. Manz, J. Baier, J. Zeitler, U. T. Schwarz, Max Maier,Univ. Regensburg, Germany.*

Stimulated Raman scattering with a Bessel pump beam in hydrogen gas shows conical or axial Stokes emission. Selection of the gain—guided Stokes modes is due to gain suppression in phase—matched Stokes—anti—Stokes coupling.

NLTuD31

Spatial trapping in PPLN waveguides with picosecond pulsed excitation at 1548nm, *Fabio Baronio, Costantino De Angelis, Univ. di Brescia, Italy; Paul Pioger, Vincent Couderc, Laurent Lefort, Alain Barthelemy, I.R.C.O.M., Univ. de Limoges/CNRS, France; Yoohong Min, Victor Quiring, Wolfgang Sohler, Univ.-GH Paderborn, Germany.*

Numerical simulations and experiments have shown the possibility of exciting spatially trapped beams in PPLN slab waveguides with pulses significantly shorter than the temporal walk off between FF and SH, with only FF at input.

NLTuD32

Ultrafast temporal reshaping of picosecond pulses based on quadratic spatial soliton generation, *C. Simos, V. Couderc, A. Barthélémy, IRCOM, France.*

We propose and demonstrate the use of quadratic spatial soliton generation together with a spatial filtering of the optical beam, as an efficient mean for the realization of ultrafast temporal reshaping of optical pulses.

NLTuD33

Collisions between optical spatial Solitons, *Oren Cohen, Raam Uzdin, Tal Carmon, Technion, Israel; Jason W. Fleischer, Mordechai Segev, Technion, Israel and Princeton University, USA; Serguey Odouov, Inst. of Physics, Ukraine.*

We theoretically study interactions between spatial solitons that propagate in opposite directions. Coherent collisions in this setting give rise to interference-induced focusing, are insensitive to the relative phase between the beams, and are accompanied by radiation even in the ideal Kerr case.

NLTuD34

High-order vortices and multi-hump rotating laser solitons, *Sergey V. Fedorov, Nikolay N. Rosanov, Anatoliy N. Shatsev, Res. Inst. for Laser Physics, Russia; Nikolay A. Veretenov, Andrei G. Vladimirov, St. Petersburg State Univ., Russia.*

We present results of semianalytical and numerical study of transversely two-dimensional spatial and spatio-temporal solitons in a laser with a saturable absorber. We demonstrate axially symmetric and asymmetric rotating solitons with wavefront dislocations of different order.

NLTuD35

Blocking and routing discrete solitons in two-dimensional networks of nonlinear waveguide arrays, *Nikos K. Efremidis, Jared Hudock, Demetrios N. Christodoulides, CREOL, USA; Eugenia D. Eugenieva, Intel Corp., USA.*

We show that discrete solitons can be navigated in two-dimensional nonlinear waveguide arrays. This can be accomplished by using vector interactions between two classes of solitons – signals and blockers. Disrete solitons in such two dimensional array networks exhibit a rich variety of functional operations, e.g. blocking, routing, logic functions, and time-gating.

NLTuD36

Minimizing bending losses in two-dimensional discrete soliton networks, *Jared Hudock, Nikos K. Efremidis, Demetrios N. Christodoulides, CREOL, USA; Eugenia D. Eugenieva, Intel Corp., USA.*

We show that reflection losses suffered by discrete solitons along sharp bends in two-dimensional waveguide-array networks can be almost eliminated. Analysis indicates that this can be accomplished by appropriately engineering the corner site of the bend. Our analytical results are verified using numerical simulations.

NLTuD37

Self-focusing of light mediated by cubic nonlinearities in potassium titanyl phosphate, *Silvia Carrasco, Hongki Kim, George Stegeman, CREOL, USA; Lluis Torner, Univ. Politecnica de Catalunya, Spain.*
We report our observations of the self-narrowing of light beams mediated by dominant dissipative Kerr nonlinearities in a bulk KTP crystal. Observations agree with comprehensive numerical investigations. Drastic differences between up and down-conversion processes are uncovered.

NLTuD38

Inverse transverse modulational instability, *C. McCormick, R. Y. Chiao, Univ. of California–Berkeley, USA; J. M. Hickmann, Univ. Federal de Alagoas, Brazil.*
We investigate the inverse of a spatial modulational instability process resulting from a cross-phase modulation mediated four-wave interaction between two noncolinear beams crossing a self-defocusing Kerr media.

NLTuD39

Dielectric nonlinearity in photorefractive spatial soliton formation, *Eugenio DelRe, Univ. dell'Aquila and INFM, Italy; Aharon J. Agranat, Hebrew Univ. of Jerusalem, Israel.*
We find that anomalous behavior of spatial screening solitons observed in the paraelectric phase is a consequence of nonlinear dielectric effects. These change the effective optical nonlinearity even far from the phase-transition regime.

NLTuD40

Nonlocal mean-field theory in N-body quantum mechanics for Bose-Einstein condensation, *J. Nathan Kutz, Univ. of Washington, USA; Bernard Deconinck, Colorado State Univ., USA.*
Nonlocal interactions in the mean-field theory for Bose-Einstein condensation can destabilize nonlinear wavetrain solutions for a condensate trapped in standing light waves. The dynamics and stability are considered for arbitrary interaction potential.

NLTuD41

All-optical AND & XOR logic gates in a single device, *Marco A. Magaña Cervantes, J. Stewart Aitchison, Univ. of Glasgow; UK.*
We simulate an all-optical device which performs the AND and XOR logic operations. The device is based on the Kerr-like nonlinear effect present in AlGaAs optimised to operate at 1.55 micrometers.

NLTuD42

Nonlinear beam shaping in an ensemble of cold rubidium atoms, *T. Ackemann, M. Pesch, Univ. Muenster, Germany; G. L. Lippi, Inst. Non Lineaire de Nice, France; G. Labeyrie, B. Klappauf, R. Kaiser, Lab. Ondes et Desordre, France.*
Nonlinear beam shaping is observed in the far field of an intense resonant beam traversing a sample of cold rubidium atoms. Numerical simulations indicate the significance of the dispersive action of neighboring lines.

NLTuD43

Soliton interaction in weakly nonlocal nonlinear media, *N.I. Nikolov, O. Bang, P.L. Christiansen, Tech. Univ. of Denmark, Denmark; J.J. Rasmussen, Risø Natl. Lab., Denmark; Wieslaw Krolikowski, The Australian Natl. Univ., Australia.*
A new way to reduce the Kerr type soliton interaction due to nonlocality of the nonlinear responce function is reported. This effect may lead to stabilization of the two soliton propagation.

NLTuD44

Dark spatial solitons in photorefractive planar waveguide LiNbO$_3$:Ti:Fe, *Marina N. Frolova, Maxim V. Borodin, Stanislav M. Shandarov, Vladimir M. Shandarov, State Univ. of Control Systems and Radioelectronics, Russia.*
We study the processes of formation of dark photovoltaic spatial soliton in photorefractive LiNbO$_3$:Ti:Fe waveguide. The 2-D distribution of the optical field is considered to define the nonlinear change of the refractive index.

NLTuD45

Thermally induced spatial soliton in dye doped nematic liquid crystal, *J.F. Henninot, F. Derrien, M. Debailleul, M. Warenghem, Univ. d'Artois, France.*
We have observed the self-trapping of a laser beam in a liquid crystal thick sample. This propagation mode, which can be assimilated to a spatial soliton, is due to a thermally induced index change, especially strong for nematics. We show here that the non-locality of the thermal effect insures the stability of the soliton.

NLTuD46

Instabilities of multicomponent spatial solitons in photorefractive media, *Kristian Motzek, Friedemann Kaiser, Darmstadt Univ. of Tech., Germany; Wieslaw Krolikowski, Glen McCarthy, Anton Desyatnikov, Yuri S. Kivshar, The Australian Natl. Univ., Australia; Carsten Weilnau, Cornelia Denz, Univ.Muenster; Germany.*
We investigate numerically the dynamics associated with the instabilities of multicomponent spatial solitons in photorefractive media. The instabilities can lead to the formation of swinging structures, giving evidence of the oscillatory nature of the instabilities.

NLTuD47

Distortion and improvement of the formation of quadratic spatial solitons by temporal walk-off and wave-vector-mismatch non-uniformities, *Roland Schiek, Univ. of Applied Sciences Regensburg, Germany; Robert Iwanow, George I. Stegeman, CREOL, USA; Gerhard Schreiber, Wolfgang Sohler, Univ. of Paderborn, Germany.*
The influence of temporal walk-off and wave-vector mismatch non-uniformities on the formation of quadratic spatial solitons in lithium niobate film waveguides with a specially engineered non-uniform QPM grating is experimentally investigated.

NLTuD48

Internal oscillations of (2+1) dimensional solitons in a saturable nonlinear medium, *Jianke Yang, Univ. of Vermont, USA.*

Internal oscillations of (2+1) dimensional fundamental solitons in a saturable medium is studied. Internal modes both with and without angular dependence are discovered. The effect of angle-dependent internal modes on the soliton visually appears as a rotation of the perturbed soliton.

NLTuD49

Single-component higher-order mode solitons in liquid crystals, *X. Hutsebaut, M. Haelterman, Univ. Libre de Bruxelles, Belgium; A. Adamski, K. Neyts, Ghent Univ., Belgium.*

We demonstrate experimentally the existence of single-component multihump spatial solitons in a dye-doped nematic liquid crystal planar cell. The low absorption obtained at the working wavelength of 890 nm allows us to observe soliton propagation over lengths in the centimeter range.

NLTuD50

Optical solitons in twisted nematics, *Miroslaw A. Karpierz, Katarzyna Brzdakiewicz, Quang V. Nguyen, Warsaw Univ. of Tech., Poland.*

Light beam propagation in twisted nematic liquid crystal layer is analyzed theoretically. Reorientation nonlinearity induces self-focusing and moreover changes the direction of light beam propagation. This behavior requires milliwats of light power.

NLTuD51

Formation of photorefractive solitons in barium-calcium titanate: From dark and bright solitons to self-trapped bright rings, *Detlef Kip, Monika Wesner, Univ. of Osnabrück, Germany; Vladymir M. Shandarov, State Univ. of Control Systems and Radioelectronics, Russia; Jingjun Xu, Nankai Univ., China.*

We investigate photorefractive spatial soliton formation in iron-doped barium-calcium titanate. In this material with both photovoltaic and screening nonlinearity, we observe bright and dark spatial solitons, as well as the propagation of self-trapped bright rings.

Room: Auditorium

8:00am–10:00am
NLWA ■ New Materials and New Directions
Alain J. Barthelemy, UER Des Science, France,
Presider   Presider

NLWA1   8:00am   Invited)
Nonlinear phenomena in Bose-Einstein condensates,
Luis Santos, Univ. at Hannover, Germany.
We present a brief overview of the research on Bose-Einstein condensation, discussing some of the most recent developments in the field, with particular enphasis in the links between condensate physics and nonlinear physics.

NLWA2   8:30am   Invited
Single-photon and two-photon photopolymerization for micro-nano fabrication, *Satoshi Kawata, Satoru Shoji, Hong-Bo Sun, Osaka Univ., Japan.*
Self-growth of micro-fiber structures and spatial optical soliton propagation based on single- photon photopolymerization, and nonlinear property of two-photon photopolymerizaiton which gives rise to three-dimensional microfabrication with sub-diffraction limit spatial resolution are introduced.

NLWA3   9:00am
Ultrahigh-speed all-optical wavelength conversion, *B. S. Ham, ETRI, Korea; P. R. Hemmer, Texax A&M Univ., USA.*
Ultrahigh-speed all-optical wavelength conversion has been demonstrated using a rare-earth doped crystal as a proof of principle. The observed switching time is two orders of magnitude shorter than the carrier lifetime for on-resonance transitions. This demonstration shows a breakthrough in the T_1 limitation of current switching technologies.

NLWA4   9:15am   Invited
Waveguiding by optically induced dipolar clusters at the ferroelectric-paraelectric phase transition region, *Aharon Agranat, The Hebrew Univ., Israel.*
Abstract not available at this time.

Room: Auditorium

10:30am–12:30pm
NLWB ■ Spatial Solitons
Demetrios N. Christodoulides, Univ. of Central Florida, United States, Presider   Presider

NLWB1   10:30am
Spatial solitons and their interactions via nonlocality and reorientation in nematic liquid crystals, *Marco Peccianti, Claudio Conti, Gaetano Assanto, Terza Univ. of Rome, Italy.*
A reorientational nonlocal nonlinearity governs 3D-spatial solitons in undoped nematic liquid crystals. We demonstrate solitons, their attraction and interlacing, outlining the role of nonlocality in time and in space, in agreement with a simple model.

NLWB2   10:45am
Experimental observation of phase controlled three-dimensional interactions between two quadratic spatial solitons: Scattering, fusion and spiraling, *Christos Simos, Vincent Couderc, Alain Barthelemy, Inst. de Recherche en Comm. Optiques et Microondes, France.*
We experimentally investigated the non-planar interaction of two quadratic spatial solitons in a bulk crystal. We obtained repulsion, fusion and spiraling by controlling the phase difference between the input fields and/or their direction.

NLWB3   11:00am
Collisions of (2+1)D Dipole-mode vector solitons in an anisotropic nonlinear medium, *Carsten Weilnau, Cornelia Denz, Westfälische Wilhelms-Univ., Germany;Marcus Ahles, Kristian Motzek, Friedemann Kaiser, Darmstadt Tech. Univ., Germany;Wieslaw Krôlikowski, Glen McCarthy, The Australian Natl. Univ.,Australia.*
We investigate the specific influence of anisotropy on generation, stability and dynamics of dipole-mode vector solitons in a photorefractive medium, experimentally and numerically. Further, we demonstrate collision-induced transformation of transverse to angular momentum.

NLWB4   11:15am
Multicomponent vector solitons: Theory and experiment, *Glen McCarthy,Wieslaw Krolikowski,Barry Luther-Davies, Australian Natl. Univ.,Australia; Anton Desyatnikov,Yuri S. Kivshar ,Australian Natl. Univ., Australia; Kristian Motzek, Friedemann Kaiser, Darmstadt Univ.of Tech., Germany; Carsten Weilnau,Cornelia Denz, Westfalische Wilhelms-Univ. Muenster,Germany.*
We study, theoretically and experimentally, multicomponent spatial solitons in nonlinear saturable (isotropic and anisotropic photorefractive) bulk media. We find numerically a family of the three-component dipole-mode solitons and demonstrate their stability in a wide range of the input parameters. We also observe the formation and stability of these spatial solitons in experiment with photorefractive strontium barium niobate (SBN) crystals.

NLWB5   11:30am
Propagation of spatially and temporally incoherent light and modulation instability in non-instantaneous nonlinear media, *Hrvoje Buljan, Univ. of Zagreb, Croatia; Antonio Siber, Inst. of Physics, Croatia; Marin Soljacic, MIT, USA; Mordechai Segev, Technion - Israel Inst. of Tech., Israel.*
We present a theory describing propagation of spatially and temporally incoherent light in non-instantaneous nonlinear media, and demonstrate the existence of modulation instability of "white" light. We find that modulation instability of "white" light is fundamentally a collective effect, where all the temporal frequencies participate in the formation of a pattern, and self-adjust their respective contributions.

NLWB6   11:45am
A solitonic all-optical switch based on the fractional Talbot effect, *Stefano Minardi, Gianluca Arrighi, Paolo Di Trapani, INFM and Univ. degli Studi dell'Insubria, Italy; Arunas Varanavicius, Algis Piskarskas, Vilnius Univ., Lithuania.*
In a parametric down-conversion scheme, a weak seeding can shift a periodic array of optical beams by half of its transverse period as the result of the spatial solitons excitation and the fractional Talbot effect.

NLWB7   12:00pm
The final state of evolution of incoherent light patterns in nonlinear media, *Mordechai Segev, Raam Uzdin, Technion, Israel.*
By using a new coherence measure which can be measured without interferometry, we find that a pattern of weakly correlated light evolves into a state characterized by [pattern's feature size]/[correlation distance]. A new relation between intensity profile and coherence is presented.

NLWB8   12:15pm
Nonlinear beam dynamics in χ^2 waveguides, *G. Stegeman, R. Malendevich, R. Schiek, R. Iwanow, L. Jankovic, H. Fang, CREOL, USA; G. Schreiber, W. Sohler, Univ. GH Paderborn, Germany; L. Torner, Un. Polit. de Catalunya, Spain.*
The evolution from diffraction, to single and then multiple quadratic soliton generation, and finally the onset of modulational instability were observed for wide fundamental beams in both birefringence and quasi-phase matched $LiNbO_3$ slab waveguides.

Room: Auditorium

2:00pm–4:00pm
NLWC ■ Nonlinear Periodic Structures
Neil G. Broderick, Univ. of Southampton, United Kingdom, Presider   ●Presider

NLWC1   2:00pm   ⬤Invited
Microstructured photonic crystal optical fiber device structures, *Benjamin J. Eggleton, OFS Fitel Lab., USA.*
We review several applications of microstructured photonic crystal optical fibers that incorporate active materials infused into the air-holes. The tunable optical characteristics of the materials combined with the unique structure of the fiber enable a number of functionalities including reconfigurability, tunability and enhanced nonlinearities for various fiber device applications.

NLWC2   2:30pm
Discrete temporal solitons along a chain of nonlinear coupled microcavities embedded in photonic crystals, *Demetrios N. Christodoulides, Nikos K. Efremidis, Jared Hudock, Univ. of Central Florida, USA.*
We demonstrate that spatiotemporal discrete solitons are possible in nonlinear photonic crystal structures. Analysis indicates that these states can propagate undistorted along a series of coupled resonators or defects by balancing the effects of discrete lattice dispersion with material nonlinearity.

NLWC3   2:45pm
Soliton engineering with two-period QPM gratings, *Steffen Kjaer Johansen, Univ. Politecnica de Catalunya, Spain and Tech. Univ. of Denmark, Denmark; Silvia Carrasco, Lluis Torner, Univ. Politecnica de Catalunya, Spain; Ole Bang, Tech. Univ. of Denmark, Denmark.*
Two-period quasi-phase-matching schemes might make it practically possible to engineer the averaged effective competing nonlinearities governing beams in quadratic materials. We show that the bandwidth for soliton generation is broader than in homogeneous structures.

NLWC4   3:00pm
Quasi-phase-matched second harmonic generation in polymer rib waveguides, *Jung-Jin Ju, Suntak Park, Seung Koo Park, Jung Yun Do, Myung-Hyun Lee, Electronics and Telecommunications Research Institute (ETRI), Korea.*
Single-mode rib waveguides at both pump and second harmonic wavelengths were fabricated with low-loss polymers. We investigated the quasi-phase matching characteristics, and the second harmonic generation properties for wavelength conversions at the optical communication band.

NLWC5 3:15pm

Quadratic interactions in an hexagonally poled lithium niobate buried waveguide, *K. Gallo, R. T. Bratfalean, A. C. Peacock, N. G. R. Broderick, C. B. E. Gawith, L. Ming, P. G. R. Smith, D. J. Richardson, Univ. of Southampton, UK.*

We demonstrate for the first time second harmonic generation from 1.536 um in a buried planar waveguide fabricated by an annealed and reverse proton exchange in a two-dimensional (2D) nonlinear photonic LiNbO$_3$ crystal.

NLWC6 3:30pm **Invited**

Bistability in photonic crystal defects, *Marin Soljacic, Mihai Ibanescu, Steven G. Johnson, Chiyan Luo, Yoel Fink, J.D. Joannopoulos, MIT, USA; Shanhui Fan, Stanford Univ., USA.*

We present an analytical theory and computational experiments to demonstrate optical bistability in a class of non-linear photonic crystal devices. Lengths of our devices are smaller than the wavelength of light, they can operate with only a few mW of power, and can be faster than 1ps.

Nonlinear Guided Waves

Temporal Fiber Solitons

Monday, September 2, 2002

Stefan Wabnitz, Xtera Communications, Inc., USA
Presider

NLMA
8:00am – 10:00am
Auditorium

Is soliton communications really beneficial in presence of polarization mode dispersion?

M. Karlsson, C. Xie*, H. Sunnerud, P. A. Andrekson**

Photonics Laboratory, Department of Microelectronics, Chalmers University of Technology, SE-412 96 Gothenburg, Sweden
* now with Lucent Technologies, Bell Labs, 101 Crawfords Corner Road Holmdel, NJ 07733, USA
** also with CENiX Inc., 7360 Windsor Drive, Allentown Pennsylvania 18106, USA
Email: magnus@elm.chalmers.se

Abstract: We discuss and review the impairments from random birefringence and PMD on soliton systems, including timing jitter coming from PMD and WDM-collision-induced polarization scattering.

1. Introduction

The fact that soliton pulses are robust to the broadening effects associated with random birefringence and polarization mode dispersion (PMD) in optical fibers is was demonstrated by simulation work in 1989 [1]. However, in communication systems, there are some other effects in sequences of pulses, such as pulse interaction and timing jitter, which might be affected by PMD as well. In this paper we discuss and review the complete system performance of solitons affected by PMD, including the effects of timing jitter, and we also introduce a novel timing jitter effect arising in soliton WDM systems.
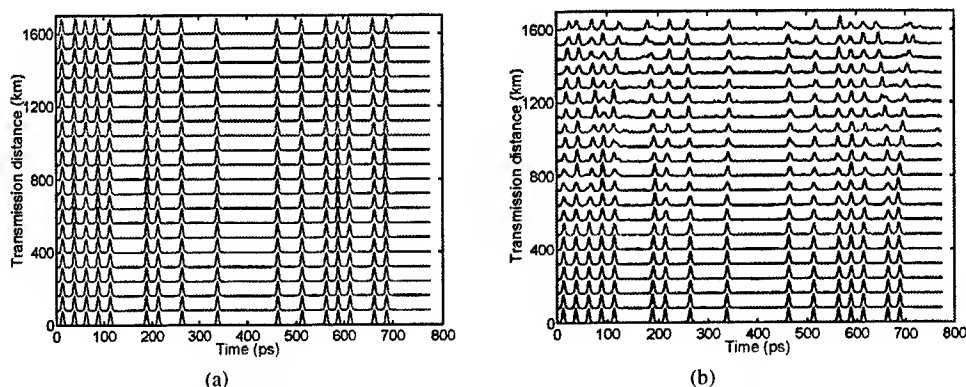
Fig.1. Evolution of soliton pulse PRBS data with transmission length. The GVD is 0.5 ps/km.nm, and the initial pulse width 5 ps. (a) Without PMD. (b) With PMD, PMD coefficient 0.15 $ps/\sqrt{km}$.

2. PMD-induced distorsions

Already in the early work it was found that the soliton perturbed by PMD radiated [1]. This radiation causes the data to be distorted in mainly two ways; direct pulse broadening and intersymbol interference, and also (which is much less known and investigated) an increased interaction originating from the interaction between the solitons and the radiation. The pulse broadening have been investigated in an number of papers, both for conventional [1-6] and DM [7-9] solitons, and to put the amount of broadening for conventional solitons in perspective, it is on average of the same order as the average broadening of linear pulses for which the first-order PMD have been compensated away [10]. For DM solitons [7-9], the performance is improved since the radiation is maintained in the vicinity of the pulses [7]. However, the radiation that is lost from the solitons will, in addition to the pulse broadening, also give rise to an increased soliton interaction that significantly will degrade the soliton system performance. This effect can be seen in

Fig. 1, comparing the transmission of a soliton data sequence without (a) and with (b) PMD. Note that in (b) a single pulse remains stable, but a pulse sequence (i.e. data) is distorted. This will reduce the system robustness to PMD so that conventional soliton systems will always be worse than linear systems in terms of bit error rates (neglecting the influence of amplified spontaneous emission (ASE) noise in long systems, and the fact that solitons have better OSNR due to their higher power). However, if the radiation is removed, via e.g. soliton control methods, or reduced by the use of DM solitons, the performance of solitons can be much better than that of the linear systems [11-12]. For DM solitons, the performance is improved with increasing map strength and decreasing average dispersion. In terms of outage probability (the probability the system bit error rate is larger than 10^{-12}), the average differential group delay (DGD) allowed for the outage probability to be below 10^{-3} is 17% of the bit slot for linear transmission. For conventional solitons with sliding filters we found that this value could increase to approximately 30 %, and with amplitude modulation 65% of the bit slot. For DM solitons the corresponding figure is 25 % of the bit slot, but those values will of course depend on the details of th receiver, te amount of noise and power margins of the systems etc.

3. WDM soliton systems

3.1 XPM-induced timing jitter

One problem that arises for conventional solitons used in WDM configurations is that collisions between pulses of different wavelengths may, if they occur asymmetrically around an amplifier, give rise to a frequency shift induced by cross-phase modulation (XPM), and this frequency shift will, via the dispersion, transform into a subsequent timing jitter. This collision-induced timing jitter puts strict design demands on the wavelength separation and the dispersion of conventional WDM-soliton systems [2]. However, for DM solitons the average dispersion can be kept low which means that the resulting timing jitter will be reduced. Moreover, if the local dispersion is high, the collisions will occur rapidly and give rise to smaller frequency shift than for the conventional systems. The result is that the collision-induced timing jitter is more or less negligible for DM solitons, and this is an important reason for the good WDM compatibility of DM solitons.

3.2 PMD-and-XPM-induced timing jitter

When PMD and birefringence effects are present there are two additional sources of timing jitter. One is the birefringence-mediated timing jitter [13], which originates in the fact that the presence ASE noise will scatter the polarization state of each soliton, and this will via the PMD be transformed in to a random transit time. The second timing jitter source is the PMD-XPM-induced timing jitter, which originates from the polarization scattering when WDM solitons with different polarizations collide[14]. Due to XPM the polarization will be scattered, as shown by the simulations in fig 2. Via the PMD this polarization scattering will transform into a timing jitter (as shown in fig 3). The figures correspond to are a DM-system with map strength S=2 and length 600 km at 40 Gb/s.
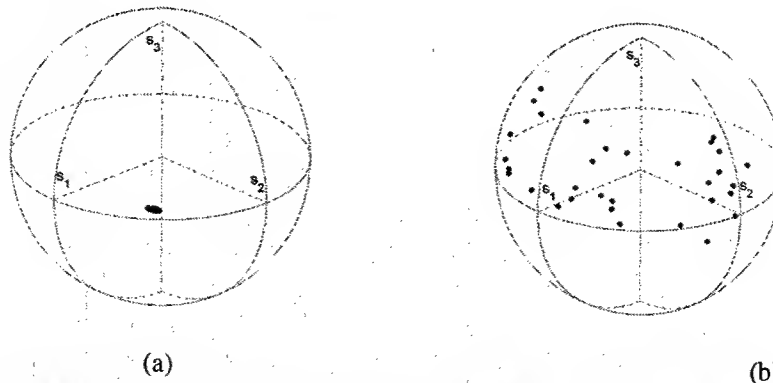

(a)   (b)

Fig.2. Distribution of polarization states at the center of mark bits on Poincare sphere. The PMD coefficient 0.20 $ps/\sqrt{km}$. (a) Single channel, (b) Three channels with 200 GHz channel spacing.
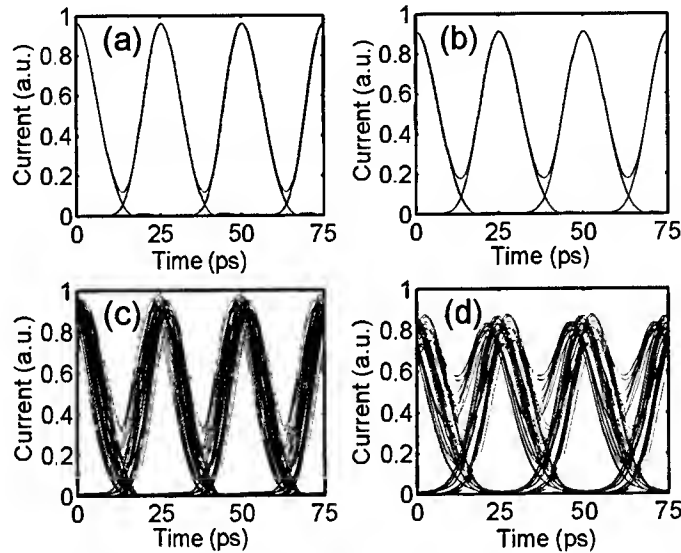
Fig.3. Electrical Eye-diagram at 600 km for DM soliton systems with S=2.0 and Dav = 0.05 ps/km.nm. (a) Single channel without PMD, (b) Single channel with PMD coefficient 0.20 $ps/\sqrt{km}$, (c) Three channels with 200 GHz channel spacing and without PMD, (d) Three channels with 200 GHz channel spacing and PMD coefficient 0.20 $ps/\sqrt{km}$.

The variance of this timing jitter can be simply estimated (assuming first-order PMD and completely random polarization scattering over the Poincare sphere) as $<\delta t^2> = DGD^2/12$. The effect is closely related to the birefringence mediated timing jitter [13] and the XPM-induced timing jitter for conventional solitons, and can probably be reduced by proper system design. It should be stressed, however that such a timing jitter may arise in any WDM system with significant XPM between the channels, since the same polarization scatter have been observed also in such systems [15].

4. Conclusions

We have discussed and reviewed the performance of soliton systems in presence of PMD. We have found that conventional soliton systems are significantly impaired by the radiation-mediated interaction, but DM solitons can show improved performance due to the lower radiation from DM solitons. For WDM soliton systems we have discussed a novel source of timing jitter [16].

References
[1] L. F. Mollenauer, K. Smith, J. P. Gordon, and C. R. Menyuk, Opt. Lett., vol. 14, p. 1219 (1989).
[2] L. F. Mollenauer, J. P. Gordon, and P. V. Mamyshev, Optical Fiber Telecommunications IIIA, I. P. Kaminow and T. L. Koch, eds. Chap. 12, (Academic Press, San-Diego, 1997).
[3] M. Matsumoto, Y. Akagi, and A. Hasegawa, J. Lightwave Technol., vol. 15, no. 4, p. 584 (1997).
[4] P. K. A. Wai, C. R. Menyuk, and H. H. Chen, Opt. Lett., vol. 16, no. 16, p. 1231, (1991).
[5] B. Bakhshi, et al., Electron. Lett., vol. 35, p. 65 (1999).
[6] C. Xie, M. Karlsson, P. A. Andrekson, IEEE Photon. Technol. Lett., vol. 12, no. 7, p.801 (2000).
[7] T. I. Lakoba, Opt. Lett., vol. 25, no. 24, p. 1789, (2000).
[8] C. Xie, M. Karlsson, P. A. Andrekson, and H. Sunnerud, IEEE Photon. Technol. Lett., vol. 13, no. 2, p. 121, (2001).
[9] Y. Chen and H. A. Haus, Opt. Lett., vol. 25, no. 5, p.290, (2000).
[10] C. Xie, M. Karlsson, H. Sunnerud, and P. A. Andrekson, Opt Lett., vol. 26, no. 10, p. 672 (2001).
[11] C. Xie, H. Sunnerud, M. Karlsson, P. A. Andrekson, IEEE Photon. Technol. Lett., vol. 13, no. 10, p. 1079 (2001).
[12] C. Xie, H. Sunnerud, M. Karlsson, P. A. Andrekson, Electron. Lett., vo. 37, no. 24, p. 1472 (2001).
[13] L. F. Mollenauer and J. P. Gordon , Opt. Lett., vol. 19, no. 6, p. 375, (1994).
[14] L. F. Mollenauer, J. P. Gordon, and F. Heismann, Opt. Lett., vol. 20, no. 20, p. 2060, (1995).
[15] B. C. Collings and L. Boivin, IEEE Phot. Technol. Lett., vol. 12, p. 1582 (2000).
[16] C. Xie, , M. Karlsson, P. A. Andrekson, H. Sunnerud and J. Li, to appear in IEEE J. Sel. Top. Quant. El. (2002).

phase-locked soliton pairs in a fiber ring laser

Ph. Grelu, F. Belhache and F. Gutty

Laboratoire de Physique de l'Université de Bourgogne, UMR 5027, B.P. 47870,
21078 Dijon, France
Tf.:333.80.39.60.15, Fax : 333.80.39.59.71, E-mail: Philippe.Grelu@u-bourgogne.fr

J. M. Soto-Crespo

Instituto de Óptica, C.S.I.C., Serrano 121, 28006 Madrid, Spain
Tf.:34915616800, Fax: 34915645557 E-mail:iodsc09@io.cfmac.csic.es

Abstract: We have experimentally observed the formation of stable pulse pairs with a $\pi/2$ phase difference in a passively mode-locked stretched-pulse fiber ring laser. We have developed a simplified theoretical model that, keeping the essential features of the experiment, reduces greatly the number of free parameters and solved it numerically. The agreement with the experimental results is excellent.
© 2002 Optical Society of America

OCIS codes: (060.5530) Pulse propagation and solitons; (140.3510) Lasers, fiber

Fiber lasers have been a field of intense research activity for more than a decade [1]. They are sought as compact high repetition rate sources for telecommunications. The field confinement in doped optical fiber provides both large optical gain and Kerr nonlinearity, key ingredients for passive mode-locking. Anomalous dispersion favors the existence of multiple pulses inside the cavity when the pump power is increased. Pulses may spread equally along the cavity, but are more likely to agglutinate into a more or less compact bunch. Under certain conditions these bunches of pulses are very stable [2].

Soliton-soliton interaction has also been deeply studied from a theoretical point of view. In the frame of the nonlinear Schrödinger equation, soliton-soliton interaction does not produce any stable bunch of solitons. However, the increase of complexity of the physical system, when taking into account gain and losses, or higher order dispersion terms, allows for stable bound states of pulse pairs to be found. In the first case, which is the relevant here, modeling distributed gain and losses leads to the complex cubic-quintic Ginzburg-Landau equation (CGLE) in which stable two-soliton bound states were predicted [3, 4]. An important feature of the stable bound states found in Ref.[4] is the $\pm\pi/2$ phase difference between the two pulses.

Very recently, the observation of a closely interacting pair of pulses that formed a soliton bound state in an anomalous fiber ring was reported. The bound state formation required the injection of an intense CW field, and the phase relationship between pulses seemed to be around π [5]. In the present work we report that a pulse pair is formed with a $\pi/2$ phase difference as predicted in the frame of the CGLE analysis [4]. Nevertheless, as the pulse experiences strong changes in one roundtrip, the analysis based in the CGLE cannot be strictly applied to model our laser. We here develop a more accurate model and find, indeed, the existence of $\pi/2$ phase locked pair of solitons.

The fiber laser setup is illustrated in Fig.1(a). The optical gain is provided by a 1.6 m. long 1400 ppm Erbium doped fiber (EDF) with normal dispersion (D=-40 ps/nm/km). The EDF is followed by a polarization-insensitive coupler-isolator (WDM-IS), into which the 980 nm pumping light is injected. A 4.8 m. length of SMF-28 fiber provides anomalous dispersion (D=+17 ps/nm/km). Nonlinear polarization evolution that takes place along the propagation in both fibers makes transmission through polarizer P1 intensity dependent, allowing for passive mode locking to be triggered by an appropriate adjustment of the preceding waveplates. The transmission through P1 is then higher for pulse operation than for continuous wave operation. Auto-correlation traces and spectra of the output pulses are used for characterization.

The laser self-mode-locks for a pumping power above 35 mW. We observe low-pedestal sech-profiled pulses, whose FWHM varies between 400 fs and 650 fs. Stable bunches of pulses are easily obtained when the pump power is increased above 80 mW, as described in Ref.[2]. The procedure to obtain a pair of interacting pulses is the following. We start from a bunch of regularly spaced pulses whose separation is around 20 ps, as it is the easiest stable configuration to be obtained in our setup. The pump power is then reduced to keep only two interacting pulses of the same amplitude, with 20 ps separation. We notice the presence of interference fringes in the spectrum, indicating that the two pulses are phase-locked. However, the precise phase difference
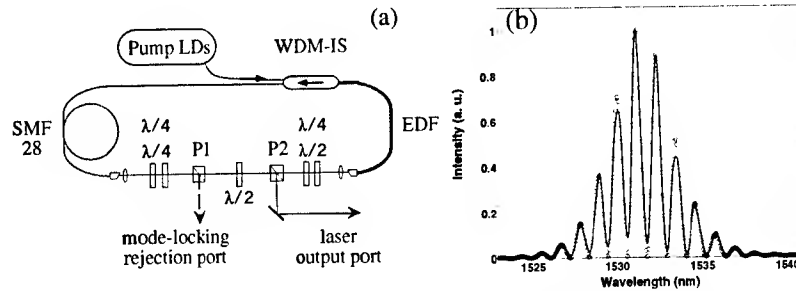
Fig. 1. (a) Experimental setup (b) Spectrum of the laser output port (solid line). It is fitted (open circles) by the spectrum of two unchirped 610-fs sech-profiled pulses separated by 6.8 ps. and having a $\pi/2$ phase difference

is difficult to measure, due to the large pulse separation. When the pair separation is below 10 ps ($\approx$ 18 pulsewidths), this phase relationship can be inferred with good precision from the position of fringes in the pair spectrum. The spectrum in fig.1(b) is well fitted (open circles) by the spectrum resulting from two 610 fs FWHM sech-profiled pulses separated by 6.8 ps, and having a phase difference of $\pi/2$ [6].

The theoretical model is illustrated in Fig2(a). It basically consists of three different parts which represent, I) the Erbium doped fiber, assumed to be nonbirefringent; II) the SMF fiber where we put all the birefringence of the cavity and III) a polarizer whose axis form a certain angle θ with respect to the fast axis of the birefringent SMF fiber. Between the different parts, at points a),b),c) and d) lumped linear losses are assumed, representing the different losses (coupling losses and rejected energy) of the real cavity. The field propagation in the Erbium doped fiber is governed by the following equation:

$$iU_z - \frac{D}{2}U_{tt} + \Gamma|U|^2 U+ = ig(Q)U + i\beta U_{tt}, \tag{1}$$

where, $D = \beta_2^{Er}/\beta_2^{SMF}$ (β_2 being the corresponding dispersion coefficients), $\Gamma = A_{eff}^{SMF}/A_{eff}^{Er}$ (A_{eff} being the effective area in each type of fiber), β is the strength of spectral filtering, due to the gain limited bandwidth and optical components ($\beta > 0$). $g(Q)$ is the gain in the cavity, it describes an active medium with a recovery time much longer than the round-trip time of the cavity and therefore does not depend explicitly on t. It can be modeled through:

$$g(Q) = \frac{g_0(z)}{1 + Q/E_L}, \qquad g_0(z) = g_{0i} + \frac{(g_{0f} - g_{0i})}{L_{Er}}z, \quad where \quad Q = \int_{-\infty}^{\infty} (|U|^2)\, dt,$$

E_L is the saturation energy and $g_0(z)$ is the small signal gain and depends on z to take into account pump depletion, L_{Er} is the total length of the Erbium doped fiber, and g_{0i} and g_{0f} are the corresponding small signal gains at both ends of the fiber as indicated in the figure.

The output field at the end of the Er fiber is considered to be circularly polarized[7]. Therefore its components along the principal axes of the linearly birefringent SMF fiber at its input are: $(\phi, \psi) = \frac{1}{\sqrt{2}}(1, i)U$. The pulse evolution is then governed by the following two coupled nonlinear equations:[7]

$$i\phi_z + \gamma\phi - \tfrac{1}{2}\phi_{tt} + |\phi|^2\phi + \tfrac{2}{3}|\psi|^2\phi + \tfrac{1}{3}\psi^2\phi^* = 0,$$
$$i\psi_z - \gamma\psi - \tfrac{1}{2}\psi_{tt} + |\psi|^2\psi + \tfrac{2}{3}|\phi|^2\psi + \tfrac{1}{3}\phi^2\psi^* = 0, \tag{2}$$

where ψ and ϕ are the normalized envelopes of the two optical field components, and γ is the half-difference between the propagation constants of the two components of the field. After the polarizer the field becomes $U = \phi cos(\theta) + \psi sin(\theta)$, and the process repeats until finding some stationary solutions.

Taking as initial condition any arbitrary input, fixing the rest of the cavity parameters and by properly choosing the angle of the polarizer θ, we obtain after many roundtrips a stationary solution consisting of one or several pulses, depending of the pump power, determined by the saturation energy E_L and the small signal gain g_o. When two pulses appear its relative phase(α) and distance (ρ) evolves converging to a fixed
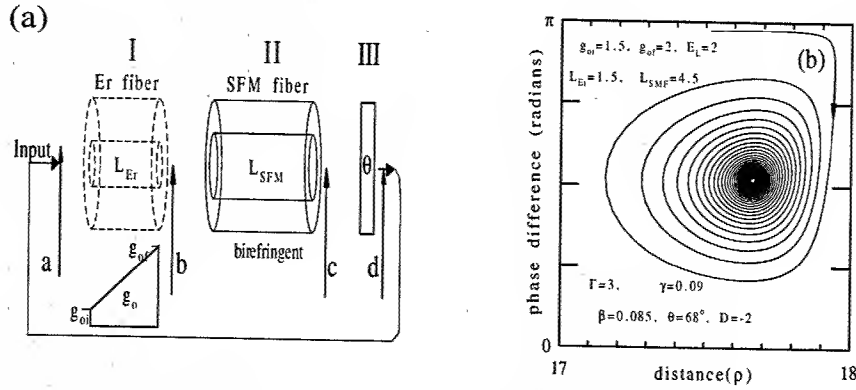
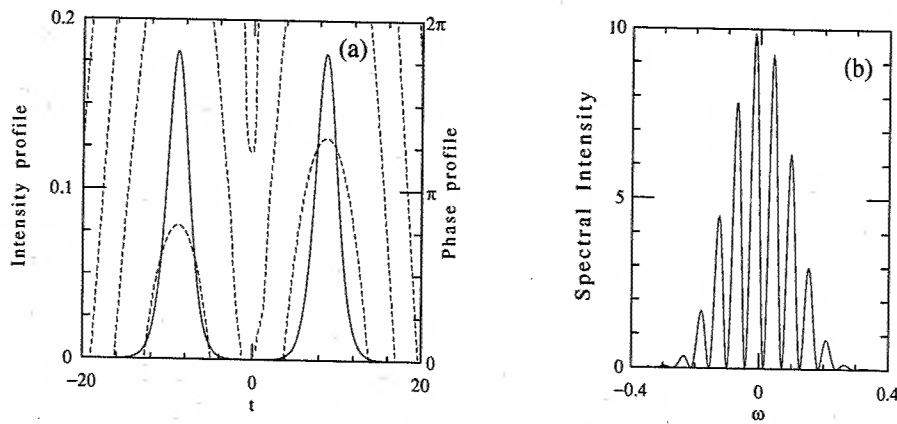Fig. 2. a)Scheme of the theoretical model. b)Trajectory in the (ρ, α) plane of two interacting pulses

Fig. 3. a) Intensity profile (solid line) and phase profile (dotted line) of one stationary solution. b)Spectrum. Parameters are the same as in Fig.2(b)

value as shown in Fig.2(b). Fig.3(a) shows the corresponding stationary solution obtained in this way. Both intensity and phase profiles are plotted showing clearly two identical pulses with a $\pi/2$ phase difference. The corresponding spectrum is shown in Fig3(b); it resembles very much the experimental one sown in Fig.1(b).

The relation between the adimensional magnitudes: $z, t, U(\psi, \phi)$ used above and the real ones: $Z, T, E(E_x, E_y)$ is the following:

$$z = Z/Z_o, \quad Z_o = \frac{T_o^2}{|\beta_2^{SMF}|}, \quad t = (T - \frac{Z}{v_g})/T_o, \quad U = E\sqrt{RT_o^2/|\beta_2^{SMF}|}, \quad R = \frac{2\pi n_2}{\lambda A_{eff}^{SMF}}$$

Taking, $Z_o = 1.07m$, gives us as time unit in Fig.3a) $T_o = 150fs$.

References

1. "Rare-Earth-Doped Fiber Lasers and Amplifiers", edited by M.J.F. Digonnet, 2nd edition, M.Dekker, New York (2001).
2. F.Gutty, Ph.Grelu, N.Huot, G.Vienne and G.Millot, Electron.Lett. **37**, 745 (2001).
3. B.A.Malomed, Phys.Rev.A **44**, 6954 (1991).
4. N.N.Akhmediev, A.Ankiewicz and J.M.Soto-Crespo, J.Opt.Soc.Am. B **15**, 515 (1998).
5. D.Y.Tang, W.S. Man, H.Y.Tam and P.D. Drummond, Phys Rev. A **64**, 33814 (2001)
6. Ph.Grelu, F.Belhache, F.Gutty and J.M.Soto-Crespo To appear in Opt.Lett. (2002).
7. J.M. Soto-Crespo et al., J.Opt.Soc.Am. B **17**, 366 (2000).

Observation of soliton explosions

Steven T. Cundiff

*JILA, National Instute of Standards and Technology and University of Colorado,
Boulder, CO 80309-0440 USA
fax: 1 303 735 0101, E-mail: cundiffs@jila.colorado.edu*

J. M. Soto-Crespo

*Instituto de Óptica, C.S.I.C., Serrano 121, 28006 Madrid, Spain
Tf.:34915616800, Fax: 34915645557 E-mail:iodsc09@io.cfmac.csic.es*

Nail Akhmediev

*Optical Sciences Centre, RSPhysSE, IAS, Australian National University,
Australian Capital Territory 0200, Australia
phone: (+612) 61250191, fax: (+612) 61255184. e-mail:
nna124@rsphysse.anu.edu.au*

Abstract: We show, experimentally and numerically, that Ti:sapphire mode-locked lasers can operate in a regime in which they produce exploding solitons. In stable conditions of operation all explosions have similar features, but are not identical.
© 2002 Optical Society of America
OCIS codes: (060.5530) Pulse propagation and solitons; (140.3510) Lasers, fiber

Mode-locked lasers provide an excellent test bed for soliton dynamics because they represent an essentially infinite propagation distance system with identical conditions for each period. For example, polarization locked vector solitons were first observed in a modelocked fiber laser [1]. The concept of soliton dispersion management yielded important new insight into mode-locked laser dynamics [2]. From a practical point of view, scientists were mostly interested in stable ultra-short pulses. Dissipative systems admit stable pulses in a certain range of parameters. Beyond this range, pulses might change on propagation regularly or chaotically [3]. There can be periodic pulsations or more complicated dynamics [4]. Experimentally, changes of the short pulses in shape or in length from one round trip to another is often present in laser dynamics but usually is avoided. Careful study of this complicated behavior can be useful both for understanding of conditions of stability as well as for creating more versatile systems.

One of the most striking forms of pulsations are pulse explosions that happen for certain values of the laser parameters. These were predicted theoretically [5] for dissipative systems and have been observed in [6]. In this work, we, report soliton explosions in a mode-locked laser and give explicit numerical results taking into account third order dispersion. We have experimentally observed unstable "exploding" solitons in a Kerr lens modelocked (KLM) Ti:sapphire laser [7]. To experimentally detect soliton explosions, we temporally record the output spectrum of the laser as well as the integrated energy of the generated pulse.

Experimental setup is shown in Fig.1. The laser has a "stretched" cavity that is 4 times longer than typical (40 ns roundtrip time). The laser spectrum shows very strong "Kelly" sidebands from phase matching of the dispersive waves shed as the 50 fs soliton undergoes periodic perturbation [8]. These are stronger than typically observed in a KLM laser due to the long cavity and lack of spectral filtering. The gain bandwidth is broader than the pulse spectrum and mainly limited by the mirror reflectivity. The output of the laser is spectrally dispersed by a diffraction grating across an array of 6 detectors. The spectral dispersion is adjusted so that each channel has a spectral width of approximately 12 nm (full width half maximum). The data from all of the channels is synchronously recorded with a bandwidth corresponding to averaging over 5 successive pulses.

The spectrally integrated intensity (i.e. total pulse energy) is also synchronously recorded on a separate channel. The optical spectrum analyzer is used to record the steady state spectrum. The 6 channels are positioned on the short wavelength side of the steady state spectrum because the spectral transients occur in that direction. This was verified by running the optical spectrum analyzer in "peak hold" mode during a large number of explosions. This captures the highest spectral intensity at a given wavelength. The long wavelength side of the captured spectrum was identical to the steady state spectrum. A typical steady state spectrum and the spectral response of the individual channels are shown in 1. Typical measured intracavity dispersion is also shown. Measurements were performed *in situ* by measuring the repetition rate as a function of wavelength [9].
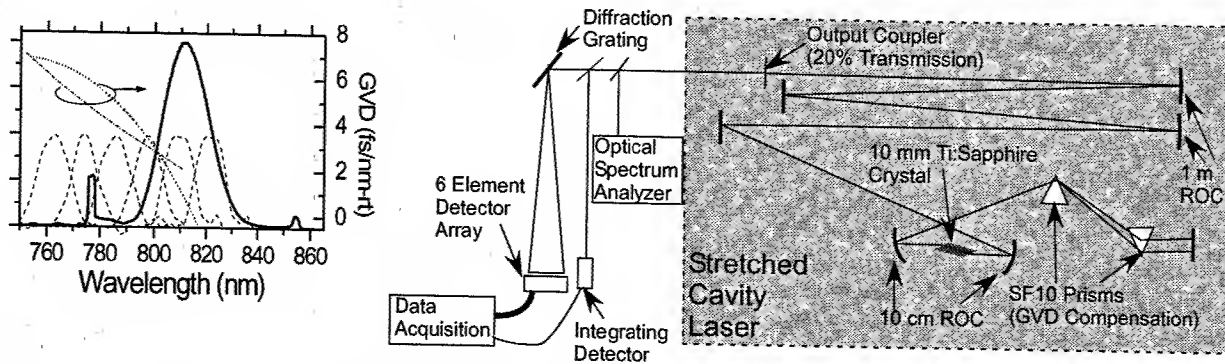
Fig. 1. Experimental setup. The graph in the left shows a typical steady state spectrum, the spectral response of the individual channels and the dispersion as a function of wavelength.

Data exhibiting a typical soliton explosion are shown in Fig.2. The bulk of the integrated spectrum is concentrated around the central frequency 812 nm. When an explosion occurs, the spectrum becomes asymmetric and abruptly shifts to shorter wavelength. It subsequently returns to the original position. Small oscillations that slowly increase in amplitude precede an explosion. The oscillations appear in the spectrally integrated intensity. They slowly die out after the explosion. If explicit spectral filtering is imposed on the laser, explosions do not occur, instead strong oscillations eventually break out at pump powers lower than those characteristic of the occurrence of explosions. We attribute these oscillations to relaxation phenomena because the damping time of relaxation oscillations increases as the pump power is lowered towards the lasing threshold [10].

We observe the following characteristics of the explosions: explosions occur intermittently; the time interval between the explosions depends on various conditions and strongly depends on system parameters; different explosions are similar but not identical; the explosions occur when the laser is close to a critical point of unstable operation; the frequency depends on pulse energy; explosions happen spontaneously, but external perturbations can trigger them. All these features are similar to those predicted theoretically in the continuous model [5]. However, the real system is not continuous. The discreteness of the laser must be taken into account to verify that the predictions still hold.

Numerical analysis has been done using a periodic system, similar to the experiment. Mode-locked lasers are typically modeled using the complex cubic-quintic Ginzburg-Landau (CGL) equation [11].

$$i\psi_z + \frac{D}{2}\psi_{tt} + |\psi|^2\psi = i\delta\psi + i\epsilon|\psi|^2\psi + i\beta\psi_{tt} + \frac{i}{6}\beta_3\psi_{ttt} + i\mu|\psi|^4\psi - \nu|\psi|^4\psi, \tag{1}$$

where t is retarded time (proportional to the the number of round trips), z is the propagation distance, ψ is the complex envelope of the electric field, D is the dispersion coefficient, δ accounts for the linear gain, β describes spectral filtering, ϵ and μ account for nonlinear gain/absorption processes, ν is a higher order correction term to the intensity-dependent refractive index and β_3 accounts for the third order dispersion.

We model the laser with the above CGL equation but periodically vary the parameters D, δ, β, ϵ, μ, ν and β_3 with z, the period corresponding to a cavity round trip. The goal of this is to capture the essential effects of periodicity and abrupt changes of parameters inside the cavity, not to model the laser in detail. The map of the parameters is shown in the inset of Fig.3. Dispersion, nonlinearity and linear and nonlinear gain act for a certain propagation length, L_1 (modeling the evolution in the gain crystal). The output coupler is modeled by concentrating losses at the end of each round trip. For the bulk of the cavity, the pulse propagates a distance L_2 under the sole effect of the dispersion term, D_2, the only important parameter in this stage being then the product $L_2 D_2$. This accounts for the prisms induced dispersion.

As illustrated in the inset in Fig.3, the sequence during a roundtrip is the following: i) propagation inside the active medium a certain distance L_1 governed by Eq.(1) with constant parameters ϵ, δ, β, μ, β_3 and ν, all of them different of zero. ii) Purely dispersive propagation a distance L_2. iii) Same as step i) (backward propagation in the active medium) iv) Instantaneous linear coupling losses. This model differs from the earlier work [5], which had distributed parameters and from the model in [6] which had no third order dispersion.
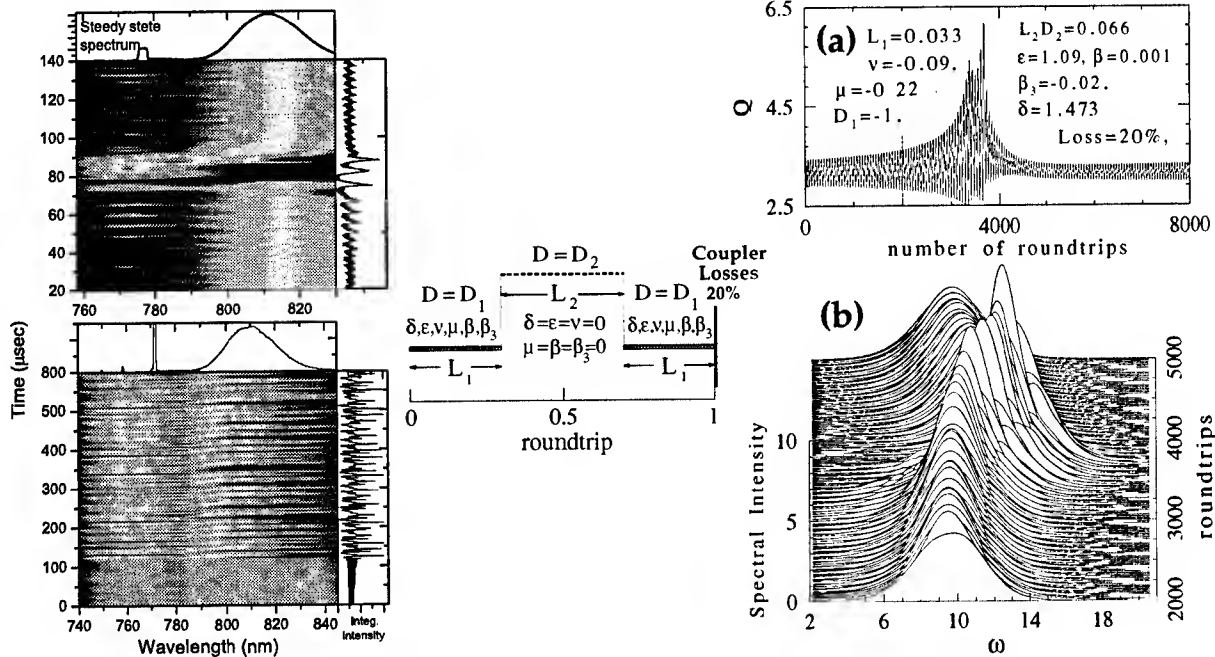
Fig. 2. (Left) Typical data showing solitons explosions. In the upper panel the dispersion is adjusted to yield solitary explosions, while in the lower one it is adjusted to yield burst of explosions. The resolution and position of spectral channels has been optimized in the lower panel.

Fig. 3. (Right) Soliton explosion in numerical simulations. (a) The soliton energy Q is plotted versus the number of round trips. Q corresponds to the experimental integrated intensity. Parameters of the simulation are shown in the figure. (b) The spectral evolution of the pulse at the time of explosion. The inset in the middle shows the map of the parameters of the CGLE for a single round trip in the laser as used in our numerical simulations.

However, explosions exist even in the current model, which is closer to the experimental conditions.

Fig.3 illustrates the soliton explosions observed in the above model. Here we calculated the spectral evolution of the pulse at the time of explosion. As initial condition, we use a pulse of Gaussian shape with the amplitude and width as initial parameters. This initial condition converges to a soliton with the shape which depends on the equation parameters. The soliton evolves and now and then explodes. Explosions happen irregularly but each of them have similar features. The number of explosions is indefinite. The spectra are symmetric in the quiet regime of soliton propagation. They become chaotic and asymmetric at the time of explosion. The 3rd order dispersion produces spectrally asymmetric explosions, just as occurs in the experiment.

References

1. S. T. Cundiff, B. C. Collings, N. N. Akhmediev, J. M. Soto-Crespo, K. Bergman, and W. H. Knox, Phys. Rev. Lett. **82**, 3988-3991 (1999).
2. Y. Chen, F. X. Kartner, U. Morgner, S. H. Cho, H. A. Haus, E. P. Ippen, J. G. Fujimoto, J. Opt. Soc. Am. B **16**, 1999 (1999).
3. S.R. Bolton and M.R. Acton, Phys. Rev. A **62**, 063803 (2000).
4. N. Akhmediev, J. M. Soto-Crespo, G. Town, *Phys. Rev. E* **63**, 56602 (2001).
5. J. M. Soto-Crespo, N. Akhmediev and A. Ankiewicz. *Phys. Rev. Lett.* **85**, 2937 (2000).
6. S. T. Cundiff, J. M. Soto-Crespo and N. Akhmediev, Phys. Rev. Lett., **88**, No 7, 073903 (2002).
7. For a review of passive modelocking see for example, E. P. Ippen, Appl. Phys. B **58**, 159 (1994).
8. S. M. J. Kelly, Electron. Lett. **28**, 806 (1992); J.P. Gordon. J. Opt. Soc. Am. B **9**, 91 (1992).
9. W. H. Knox, Opt. Lett. **17**, 514 (1992).
10. A.E. Siegman, Lasers (University Science Books, Mill Valley, 1986) pp.962-964.
11. N. N. Akhmediev and A. Ankiewicz. *Solitons: Nonlinear Pulses and beams*, (Chapman & Hall, London), 1997.

Temporal soliton compression in beta-barium borate

S. Ashihara, T. Shimura, and K. Kuroda

Institute of Industrial Science, University of Tokyo, 4-6-1, Komaba, Meguro-ku, Tokyo,153-8505 Japan

TEL: +81-3-5452-6137 FAX: +81-3-5452-6159 E-mail: ashihara@iis.u-tokyo.ac.jp

Abstract: We present the temporal soliton compression of femtosecond pulses in quadratic media, where cascade quadratic nonlinearity and normal dispersion contribute for compression. Compression factor of 3 is achieved by using ~30 mm long beta-barium borate.

OCIS codes: (320.5520) Pulse compression; (190.5530) Pulse propagation and solitons; (320.7110) Ultrafast nonlinear optics

Introduction

Pulse compression is a useful technique to shorten pulse durations from those generated by oscillators or amplifiers. The most popular pulse compression technique utilizes self-phase modulation due to the Kerr nonlinearity in an optical fiber and successive dispersion compensation by grating pairs [1]. Another type of compression system, called the soliton compressor, has also been demonstrated [2]. Although the soliton compression technique is attractive because of its small loss and its simplicity, the use of this technique with Kerr nonlinearity is limited in the spectral region of anomalous dispersion.

Here we report the numerical and experimental study on soliton propagation and compression in quadratic media of β-BaB$_2$O$_4$ (BBO), where the negative phase shift due to cascade quadratic nonlinearity (CQN) [3] and normal dispersion in the identical material contribute for soliton formation. This soliton compression scheme is an extended technique of the work of Liu et al. [4], who demonstrated the pulse compression by using negative phase shifts induced by CQN and successive material, such as glass prisms, for dispersion compensation.

Soliton propagation and compression in BBO

We consider femtosecond pulse propagation along z-axis in a nonlinear and dispersive material. Within the slowly varying amplitude approximation, pulse propagation under type I phase mismatched second harmonic generation is described by the coupled-wave equations as [5]

$$\begin{cases} \dfrac{\partial A_1}{\partial z} = i\xi_1 \dfrac{\partial^2 A_1}{\partial \eta^2} - i\rho_1 A_1^* A_2 \exp(-i\Delta kz) - i\sigma_1 \left(|A_1|^2 A_1 + 2|A_2|^2 A_1 \right), \\ \dfrac{\partial A_2}{\partial z} = -\zeta \dfrac{\partial A_2}{\partial \eta} + i\xi_2 \dfrac{\partial^2 A_2}{\partial \eta^2} - \dfrac{1}{2}i\rho_2 A_1^2 \exp(+i\Delta kz) - i\sigma_2 \left(|A_2|^2 A_2 + 2|A_1|^2 A_2 \right), \end{cases} \quad (1)$$

where $\Delta k = k_2 - 2k_1$ denotes the wave-vector mismatch, η, the new temporal coordinate propagating with the group velocity of the fundamental pulse, ζ, the GVM parameter, and ξ, the group-velocity dispersion (GVD) parameter. ρ

and σ denotes the quadratic and cubic nonlinearity, respectively. Under the conditions of large phase mismatch, these equations can be reduced into the nonlinear Schrodinger equation [6].

$$i\frac{\partial A_1}{\partial z}+\xi_1\frac{\partial^2 A_1}{\partial \eta^2}-\left(\frac{\rho_1\rho_2}{2\Delta k}-\sigma_1\right)|A_1|^2 A_1 = 0. \quad (2)$$

Soliton-like propagations are implied by this equation. The difference between CQN solitons in BBO at 800 nm and the fiber solitons is the signs of nonlinearity. Solitons we present here are supported by the cascade nonlinearity of negative sign and normal dispersion of the material itself, whereas fiber solitons are supported by Kerr nonlinearity and anomalous dispersion. Figure 1 shows critical peak intensity for supporting fundamental solitons as a function of the wave-vector mismatch Δk, for various pulse durations. We can predict that the soliton compression should occur by pumping the higher-order soliton with peak intensity higher than the critical intensity [2].
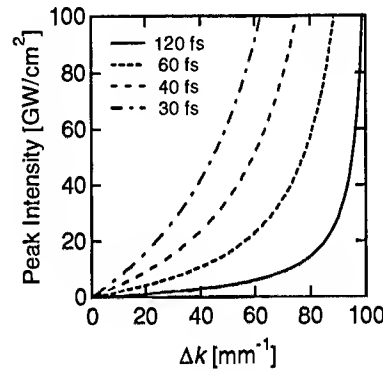
Fig. 1 Critical peak intensity for supporting fundamental solitons as a function of Δk for various pulse durations.

We performed soliton compression experiments by using BBO crystals cut for type I phase matching, of totally 32 mm length. Linearly polarized pulses of ~130 fs duration, 800 nm center wavelength, and of 1 kHz repetition rate are generated by a mode-locked Ti: sapphire laser and a regenerative amplifier. The pulses are input to the crystal with an appropriate intensity and phase-mismatched angle. The transmitted pulses are characterized by using the frequency-resolved optical gating (FROG) method.

When considering the CQN interaction of femtosecond pulses, the GVM effect should be taken into account. We choose here relatively large wave-vector mismatch condition, $\Delta k \sim 60$ mm^{-1}, to avoid nonlinear chirp induced by
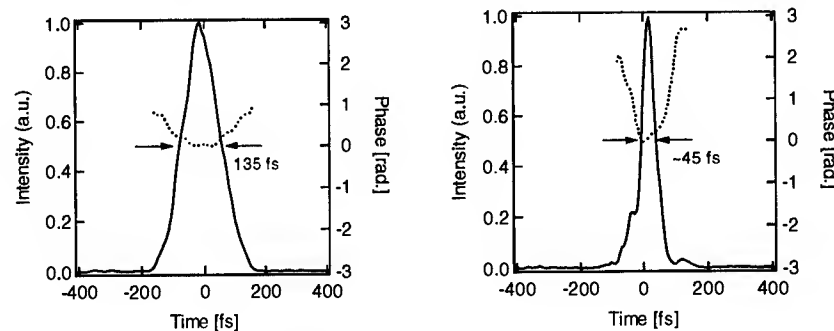
Fig. 2 Retrieved intensity and phase profiles of (a) the input and (b) the transmitted pulses.

GVM [4]. Figure 2 shows the retrieved pulse profiles of (a) the incident and (b) the transmitted pulses after the 32 mm propagation, when the input peak intensity is 50 GW/cm^2 and Δk = 60mm^{-1}. The pulse duration is successfully compressed down to ~45 fs, by a factor of 3. We also measured the compressed pulse duration at the length of 15 mm and 32 mm. Figure 3 shows the compressed pulse duration as a function of propagation length. The theoretical results obtained by numerically solving the equation (1) under the condition of 30 GW/cm^2 and Δk = 60 mm^{-1} are also shown as a dashed line. The measured data showed similar behavior as that obtained by calculations.
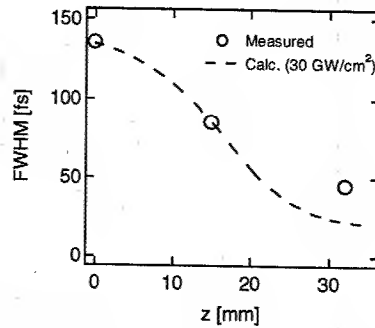
Fig. 3 The measured (markers) and calculated (dashed line) pulse durations as a function of propagation length.

Conclusions

In conclusion, we have demonstrated efficient soliton compression of femtosecond pulses in quadratic nonlinear media. 3-times compression was achieved by use of 32 mm BBO crystal. This compressor proved useful for high-energy pulse compression because of its efficient compression ratio and small loss, as well as its extreme simplicity.

References

[1] C. V. Shank, R. L. Fork, R. Yen, R. H. Stolen, and W. J. Tomlinson, "Compression of femtosecond optical pulses," Appl. Phys. Lett. **40**, pp.761-763 (1982).

[2] L. F. Mollenauer, R. H. Stolen, J. P. Gordon, and W. J. Tomlinson, "Extreme picosecond pulse narrowing by means of soliton effect in single-mode optical fibers," Opt. Lett. **8** pp. 289-291 (1983).

[3] R. DeSalvo, D. J. Hagan, M. Sheik-Bahae, G. 1. Stegeman, E. W. Van Stryland, and H. Vanherzeele, "Self-focusing and self-defocusing by cascaded second-order effects in KTP," Opt. Lett. **17**, pp.28-30 (1992).

[4] X. Liu, L. J. Qian, and F. Wise, "High-energy pulse compression by use of negative phase shifts produced by the cascade $\chi^{(2)}$:$\chi^{(2)}$ nonlinearity," Opt. Lett. **24**, pp. 1777-1779 (1999).

[5] E. Sidick, A. Knosen, and A. Dienes, "Ultrashort-pulse second-harmonic generation. I. Transform-limited fundamental pulses," J. Opt. Soc. Am B 12, pp. 1704-1712 (1995).

[6] C. R. Menyk, R. Shiek and L. Torner, "Solitary waves due to $\chi^{(2)}$:$\chi^{(2)}$ cascading," J. Opt. Soc. Am B 11, pp. 2434-2443 (1994).

Nonrecursive multiple shock formation via four-wave mixing: theory and experiment

F. Gutty, G. Millot

Laboratoire de Physique, Université de Bourgogne,
9, Avenue A. Savary, B.P. 47870, 21078 Dijon, France
phone: 33-380-395981, fax: 33-380-395971, email: guy.millot@u-bourgogne.fr

S. Trillo

Dept. of Engineering, University of Ferrara,
Via Saragat 1, 44100 Ferrara, Italy

Also with INFM-RM3, Via della Vasca Navale 84, 00146 Roma, Italy
phone: +39-0532-293838, fax: +39-0532-768602, email: strillo@ing.unife.it

Abstract: We show theoretically and experimentally that a beat signal propagating along a normally dispersive fiber can trigger the formation of multiple shocks. This phenomenon critically depends on the input frequency separation and power of the beat signal.

The propagation along a normally dispersive optical fiber is described by the one-dimensional nonlinear Schrödinger equation (NLSE) in the so-called *defocusing* case. This is a universal equation which describes several different phenomena such as propagation in shallow water,[1] the mean-field evolution of a Bose-Einstein condensate in large aspect ratio traps,[2] or diffraction in planar waveguides with negative Kerr coefficient.[3] It is well-known that the defocusing NLSE support the propagation of dark solitons, which have been widely studied in the recent past.[3] On the other hand the periodic problem (i.e., how a periodic input condition evolves) is not equally well understood, though it can be easily accessed experimentally by injecting a two-frequency beat signal along the fiber. It is known that a sinusoidal input signal (i.e., two symmetric frequencies $\omega_0 \pm \Delta\omega/2$) gives rise to generation of four-wave mixing (FWM) sidebands $\omega_0 \pm n\Delta\omega/2$, n odd integer,[4] in such a way that the input condition is eventually restored at some propagation distance.[4,5] In time domain the counterpart of the FWM phenomenon is the formation of a train (at rep rate $\propto \Delta\omega^{-1}$) of dark solitons, which is formed in a recursive way along the fiber.[6] Except for the fact that efficient frequency conversion requires two or more finite-amplitude waves, this recursive phenomenon is qualitatively similar to its counterpart in the anamalous dispersion regime, where modulational instability permits the recursive amplification or arbitrarily weak waves.[7,8]

The aim of this work is to show that a new regime sets in the modulationally stable, normally dispersive case, when the frequency separation of the two input frequencies $\Delta\omega$ is small enough, (or equivalently the power of the beat signal is high enough). In this regime the dynamics is ruled by the collision of multiple shocks and is intrinsically nonrecursive. The evolutions might be so complicated to look disordered in spite of the fact that the propagation can be still described analytically, being governed by the integrable NLSE. To show this let us consider the following dimensionless form of the defocusing NLSE

$$i\frac{\partial u}{\partial z} - \frac{1}{2}\frac{\partial^2 u}{\partial t^2} + |u|^2 u = 0,\qquad(1)$$

subject to the following initial condition $u_0 = u(z = 0, t)$, describing a two-color input (possibly asymmetrical with power fractions p_0 and $1 - p_0$)

$$u_0 = \sqrt{p_0}\exp\left[-i(\Omega/2)t\right] + \sqrt{1 - p_0}\exp\left[i(\Omega/2)t\right].\qquad(2)$$

In Eq. (1) z is the distance measured in units of the nonlinear length $Z_{nl} = (\chi P)^{-1}$, $\chi = k_0 n_{2I}/A_{eff}$ being the standard fiber nonlinear coefficient, and P the real-world total power of the input, t is a retarded time measured in units of $T_0 = (k'' Z_{nl})^{1/2}$. The use of these dimensionless variables permits to characterize the dynamics in term of the single parameter $\Omega = \Delta\omega T_0$, which can be independently controlled by means of changing the physical frequency separation $\Delta\omega$ or the power P. Different regimes are found for $\Omega >$
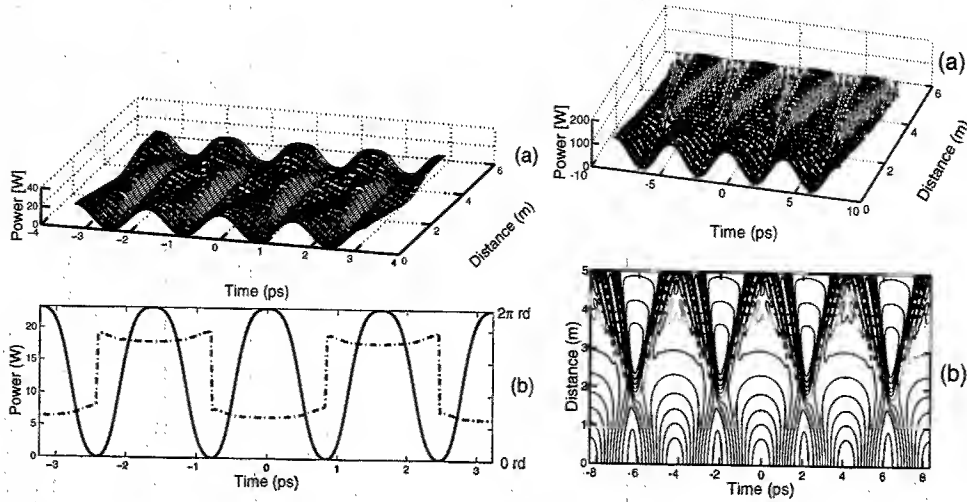
Fig. 1. Evolution of the field u ruled by the defocusing NLSE. Left: Recursive behavior corresponding to a symmetric ($p_0 = 0.5$) input beat signal with $\Delta f = 616$ GHz, and $P = 13$ W. (a) Intensity evolution; (b) snapshot of the intensity and phase at the output. Right: Nonrecursive dynamics obtained with $\Delta f = 239$ GHz, and $P = 75$ W. (a) Intensity evolution; (b) Contour plot of the intensity.

1 (recursive behavior) and $\Omega < 0.3$ (nonrecursive behavior), with the intermediate values marking the transition between the two regimes. In Fig. 1 we display examples of the dynamical evolutions obtained from numerical integration of Eq. (1). The left panel is relative to the recursive case. The input experiences compression forming a train of dark solitons (corresponding in frequency domain to moderate generation of FWM sidebands) and eventually the input is restored at the output. The right panel shows that the dynamics change qualitatively at lower frequency and higher power (in order to show that this regime is not necessarily related to the symmetry of the input, we display a result obtained in the asymmetric case $p_0 = 1/5$). Several shocks or grey solitons characterized by different velocity are emitted and collide along the fiber, leading to a strongly nonrecursive dynamics. In the time domain, the output exhibits handfuls of closely spaced dips (grey solitons, characterized by phase jumps between adjacent solitons) repeated with half the period of the beat signal, whereas the signature of this phenomenon in the frequency domain is the appearence of shoulders in the spectrum corresponding to high-order FWM sidebands. Without entering the details here, it is however important to point out that we have been able to explain this phenomenon, in spite of its complexity, in the framework of the inverse scattering theory for the periodic problem.[9]

To investigate this phenomenon experimentally we have performed measurements in a short sample ($L = 5$ m in order to avoid the onset of Raman scattering) of a high-birefringence fiber, aligned in such a way to ensure scalar propagation. We have used a laser source capable of producing a two-color tunable beat signal at visible wavelengths. The use of nanosecond pulses ensures relatively high peak powers, while the envelope is still quasi-cw compared with the time scale associated with the frequency separation $\Delta f = \Delta \omega / 2\pi$ of the two colors. We have performed a first series of experiments by recording the output spectrum against changes of the frequency separation Δf at fixed power, or versus variations of the power at fixed frequency detuning. Typical peak powers are in the range of few tens of watts, while the detuning changes in the range from 150 GHz to 700 GHz. Figure 2 shows the output spectra obtained at fixed detuning $\Delta f = 239$ GHz, and power of one beam (say the pump) while increasing the power of the weaker component (say the signal) of the two beams. As shown, characteristic spectra with shoulders corresponding to high order FWM sidebands appear above 1 W of signal power. A similar phenomenon is observed when Δf is decreased at constant power levels.

In order to have a more direct proof of the fact that what is really forming at the fiber output is a handful of grey solitons with rep rate higher than the modulation period, one has to resort to techniques that permit to resolve the field in modulus and phase on the picosecond time scale. To this purpose the FROG technique seems particularly well suited.[10] We have used a FROG scheme based on SHG, and have adapted the retrieval algorithm, which permits to obtain the modulus and phase of the field from the SHG trace, to deal with the (nsec) pulsed nature of our experiment.[11] The retrieved field is displayed in Fig. 3 in modulus (b) and phase (a) for a typical value of the frequency separation and power such to yield a spectrum with
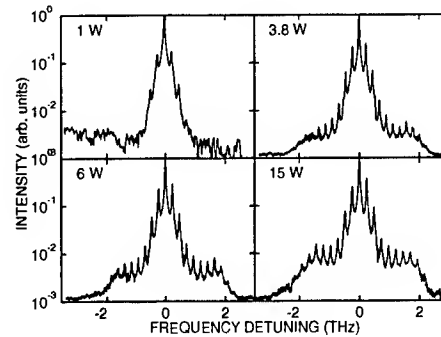
Fig. 2. Sequence of experimental spectra obtained with a fixed 60 W pump beam and a frequency detuned ($\Delta f = 239$ GHz) signal with power ranging from 1 W to 15 W. The high-frequency sidebands appear for signal powers above ≈ 1 W.
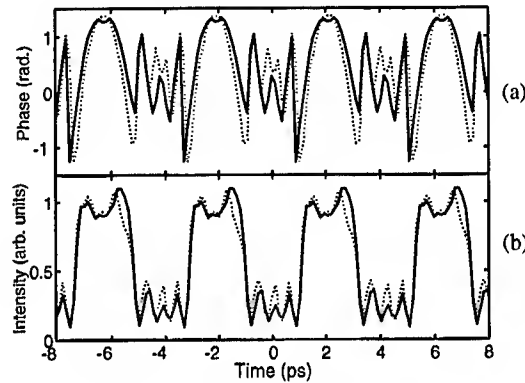

Fig. 3. Retrieved phase (a) and intensity (b) obtained from the measured FROG trace (solid lines), compared with the expected results from NLSE simulations with a pulsed input (dotted lines).

pronounced shoulders (see Fig. 2). As shown in Fig. 3(b) the intensity pattern exhibits a series of dips, though the contrast between adjacent dips is substantially lower than that expected from the cw theory based on Eqs. (1-2). This, however, should be ascribed to the pulsed nature of the beam. In fact, once the latter is accounted for in the calculation based on the NLSE (1), the agreement becomes satisfactory (compare the solid and dotted line in Fig. 3b). On the other hand also the phase pattern shown in Fig. 3(a) is in very good agreement with that obtained from NLSE calculations. Finally, to be sure that the FROG and spectral measurement are consistent, we have calculated the intensity spectrum from the FROG retrieved field, and have found excellent agreement with the measured spectra.

In summary we have shown that FWM in a normally dispersive fiber pumped by (symmetric or asymmetric) beams with small frequency separation or high powers leads to the nonrecursive formation of multiple shocks.

References

[1] V.E. Zakharov and E.A. Kuznetsov, Physica D **18**, 455 (1986).
[2] Th. Bush, and J.R. Anglin, Phys. Rev. Lett. **84**, 2298 (2000); T. Tsuzuki, J. Low Temp. Phys. **4**, 441 (1971).
[3] Y.S. Kivshar, and B. Luther-Davies, Phys. Rep. **298**, 81 (1998).
[4] J. R. Thompson, and R. Roy, Phys. Rev. A **43**, 4987 (1991); S. Trillo, S. Wabnitz, and T.A.B. Kennedy, Phys. Rev. A **50**, 1732 (1994); D.L. Hart, A.F. Judy, R. Roy, and J.W. Beletic, Phys. Rev. E **57**, 4757 (1998).
[5] C. S. West, and T. A. B. Kennedy, Phys. Rev. A **47**, 1252 (1993).
[6] P. V. Mamyshev, P.G. Wigley, J. Wilson, C. Bosshard, and G.I. Stegeman, Appl. Phys. Lett. **64**, 3374 (1994). P. V. Mamyshev, C. Bosshard, and G.I. Stegeman, J. Opt. Soc. Am. B **11**, 1254 (1994).
[7] S. Trillo, and S. Wabnitz, Opt. Lett. **16**, 986 (1991).
[8] G. Van Simaeys, Ph. Emplit, and M. Haelterman, Phys. Rev. Lett. **87**, 033902 (2001).
[9] A.R. Osborne, Phys. Lett. A **176**, 75 (1993).
[10] R. Trebino, and D.J. Kane, J. Opt. Soc. Am. A **10**, 1101 (1993); D.J. Kane, IEEE J. Quantum Electron. **35**, 421 (1999).
[11] F. Gutty, S. Pitois, P. Grelu, G. Millot, M. D. Thomson, and J. M. Dudley, Opt. Lett. **24**, 1389 (1999).

Importance sampling for noise-induced amplitude and timing jitter in soliton transmission systems

R. O. Moore[1], G. Biondini[2] and W. L. Kath[3]

[1]*Division of Applied Mathematics, Box F,*
Brown University, Providence, RI, 02912, USA

[2]*Department of Mathematics, Ohio State University,*
231 W. 18th Ave., Columbus, OH 43210, USA

[3]*Department of Engineering Sciences and Applied Mathematics,*
Northwestern University, 2145 Sheridan Road, Evanston, IL 60208-3125, USA

Introduction. One common source of transmission impairments in lightwave systems comes from pulse amplitude and/or timing jitter induced by amplified spontaneous emission (ASE) noise [1, 2]. Since ASE noise is a stochastic phenomenon, Monte Carlo simulations can be used to determine its effects on a system. The direct calculation of bit error rates through standard Monte Carlo simulations is impossible, however, because error rates are required to be very small, e.g., one error per trillion bits or smaller. As a result, an exceedingly large number of realizations would be needed to observe even a single transmission error, and even more would be required to obtain reliable error estimates. To overcome this limitation, a common approximation is to numerically calculate the relevant variances and then extrapolate into the tails by assuming a Gaussian probability distribution function (pdf). It is clear, however, that nonlinearity and pulse interactions both contribute to make the resulting distributions non-Gaussian [3-5].

Recently we have successfully applied a technique known as importance sampling (IS) [6] to the direct simulation of transmission impairments produced by polarization-mode dispersion [7]. In general, IS works by concentrating Monte-Carlo trials on those configurations that are most likely to lead to transmission errors, thus significantly speeding up the simulations. Here we show how importance sampling can be applied to numerical simulations of ASE-induced transmission impairments. For simplicity, we consider the case of a simple soliton-based transmission system (because in the absence of noise the pulse shape remains fixed), but it is anticipated that the technique can be extended to systems employing more general transmission formats. The advantages of the method will be shown to be substantial, allowing a speedup of several orders of magnitude over standard Monte Carlo simulations.

Solitons and amplifier noise. After averaging out the periodic power variations due to fiber loss and amplification, an optical pulse's slowly varying envelope propagates between amplifiers according to the nonlinear Schrödinger equation [8]

$$i\frac{\partial u}{\partial z} + \frac{1}{2}\frac{\partial^2 u}{\partial t^2} + |u|^2 u = 0\,, \tag{1}$$

where z and t are dimensionless distance and time, $z = \hat{z}/L$ and $t = \hat{t}/T_0$, where $\hat{z}$ and $\hat{t}$ are the dimensional quantities, $T_0 = T_{\text{FWHM}}/1.76$ and $L = T^2/|k''|$ (here T_{FWHM} is the pulse FWHM and k'' is the fiber dispersion coefficient in ps^2/km); furthermore, $|u|^2 = L\gamma|q|^2$, where $|q|^2$ is the electric field photon flux intensity in 1/ps and γ is the fiber nonlinear coefficient in ps/km [9]. Equation (1) admits the well-known soliton solution

$$u_s(z,t) = A\,\text{sech}[A(t - T - \Omega z)]\exp i[\Omega t + \Phi]\,, \tag{2}$$

where A, Ω and T are constant, and $\Phi(z) = \Phi_0 + (A^2 - \Omega^2)z/2$. When the pulse reaches an amplifier at $z = nz_a$ (where z_a is the dimensionless amplifier spacing and $n = 1, 2\ldots, N$, with N being the total number of amplifiers in the transmission line), a small amount of noise $\Delta u_n(t)$ is added to u: $u(nz_a^+, t) = u(nz_a^-, t) + \Delta u_n(t)$. Part of the noise is absorbed by the soliton, where it produces small changes of the soliton parameters [8, 9]. This process is repeated at each amplifier, resulting in a random walk of A, Ω, T and Φ_0 [2]. The rest of the noise propagates along with the perturbed soliton.

The ASE noise $\Delta u_n(t)$ is modelled as classical zero-mean white noise: $\langle\Delta u_n(t)\rangle = 0$ and $\langle\Delta u_m(t)\Delta u_n^\dagger(t')\rangle = \sigma^2\delta_{m,n}\delta(t-t')$, where $\sigma^2 = [(G-1)^2/G\ln G]\,(\gamma T/|k''|)\,\eta_{\text{sp}}$; here G is the amplifier gain and η_{sp} is the excess spontaneous emission factor [9]. For typical system configurations, the noise amplitude at each amplifier is small, and thus the noise-induced changes of the soliton parameters per amplifier are also usually small. In

rare cases, however, the individual noise contributions combine to produce large deviations, thus resulting in potential transmission errors.

Importance sampling for amplitude and timing jitter. The main idea of importance sampling is to bias the probability distributions used to select the random Monte-Carlo trials so that errors occur more frequently than otherwise would be the case [6]. Generally, the difficulty is in determining how to bias the distributions in the ways most likely to generate errors (which in this case means determining the particular noise instantiations at each amplifier which produce large variations in pulse amplitude or position). Fortunately, much is known about solutions of the NLS equation, and this knowledge can be used to guide the biasing process. The key information comes from the soliton solution Eq. (2), and in particular, its dependence upon the parameters A, Ω, T and Φ_0. Because any values of these parameters are allowed, this means that there is no resistance encountered if the noise at an amplifier changes one of them slightly. This lack of resistance to variations allows large fluctuations to build up after many amplifiers.

The goal is to use this knowledge to selectively bias the noise at each amplifier to induce larger-than-normal changes in A, Ω and T (we will ignore the phase since it does not lead to amplitude or position fluctuations). Soliton perturbation theory [8, 9] shows that at a given amplifier, the changes in these parameters are given to first order by

$$\Delta A_n = \operatorname{Re} \int \underline{u}_A^\dagger(z,t)\Delta u_n(t)\,dt\,, \quad \Delta\Omega_n = \operatorname{Re} \int \underline{u}_\Omega^\dagger(z,t)\Delta u_n(t)\,dt\,, \quad \Delta T_n = \operatorname{Re} \int \underline{u}_T^\dagger(z,t)\Delta u_n(t)\,dt\,, \quad (3)$$

where the integrals are from $-\infty$ to ∞ and the functions $\underline{u}_A^\dagger$, $\underline{u}_\Omega^\dagger$ and $\underline{u}_T^\dagger$ are the modes of the *adjoint* linearized NLS operator [9]. Note our intent is not the same as soliton perturbation theory: we will not use it to approximate the solution over the entire transmission distance, but rather only to show how to modify the noise at each amplifier to preferentially bias the Monte-Carlo simulations toward large amplitude and timing jitter. As long as the noise added per amplifier is small, this is valid.

To make these ideas definite, suppose we are numerically solving a discretized version of the NLS equation, Eq. (1), using a split-step or other technique. At each amplifier, we first have to determine the soliton parameters associated with the solution to that point. We do this either by solving the Zakharov-Shabat eigenvalue problem [8], or by using the moment integrals for the soliton parameters [9]. Next, we add random noise Δu_n; we can also represent this noise by a vector $\mathbf{x} = (x_1,\ldots,x_{2K})^T$ giving the real and imaginary components at each discretized time point in the computational interval (here the total number of time points, or equivalently, the total number of Fourier modes, is taken to be K). In the unbiased case, the x_k are independent, identically distributed normal random variables with mean zero and variance $\sigma_a^2 = \sigma^2/(2\Delta t)$; explicitly, $p_{\mathbf{x}}(\mathbf{x}) = \exp[-\mathbf{x}^T\mathbf{x}/2\sigma_a^2]/(2\pi\sigma_a^2)^K$.

The procedure is to first select an unbiased instantiation of the random noise Δu_n; this produces parameter changes that can be evaluated using Eq. 3. Then the actual biasing is done by modifying the noise to further change the pulse parameters A, Ω or T in the desired direction. If, for example, we are biasing the amplitude A toward larger values, we first determine the amplitude shift $\Delta A_n = \operatorname{Re} \int \underline{u}_A^\dagger(z,t)\Delta u_n(t)\,dt$ associated with the unbiased noise, and then add an additional deterministic variation to Δu to further increase it. (The result for position shifts is similar, but slightly more complicated, since frequency shifts couple to position shifts.) It is easy to show that the most likely perturbation Δu to further shift the amplitude is the one that minimizes $\mathbf{x}^T\mathbf{x} \propto \int |\Delta u|^2\,dt$ subject to the constraint $\Delta u = $ constant; the result shows that we should shift Δu proportional to $\underline{u}_A^\dagger$. This produces a biased perturbation Δu^*, or $\mathbf{x}^*$; we then also calculate the IS likelihood ratio $p_{\mathbf{x}}(\mathbf{x}^*)/p_{\mathbf{x}^*}(\mathbf{x}^*)$ needed to correct the results for the effect of the biasing [6].

Finally, to determine the probability P that the amplitude A falls in a given range, we calculate importance-sampled Monte Carlo estimate [6]

$$P = \frac{1}{M}\sum_{m=1}^{M} I(A_m)r(x_m)\,, \qquad (4)$$

where the m indicates the trial number, M is the total number of trials, and $I(A)$ is an indicator function equal to 1 if A falls in the prescribed range and is 0 otherwise. In addition, $r(x)$ is the product of the likelihood ratios calculated at each individual amplifier.
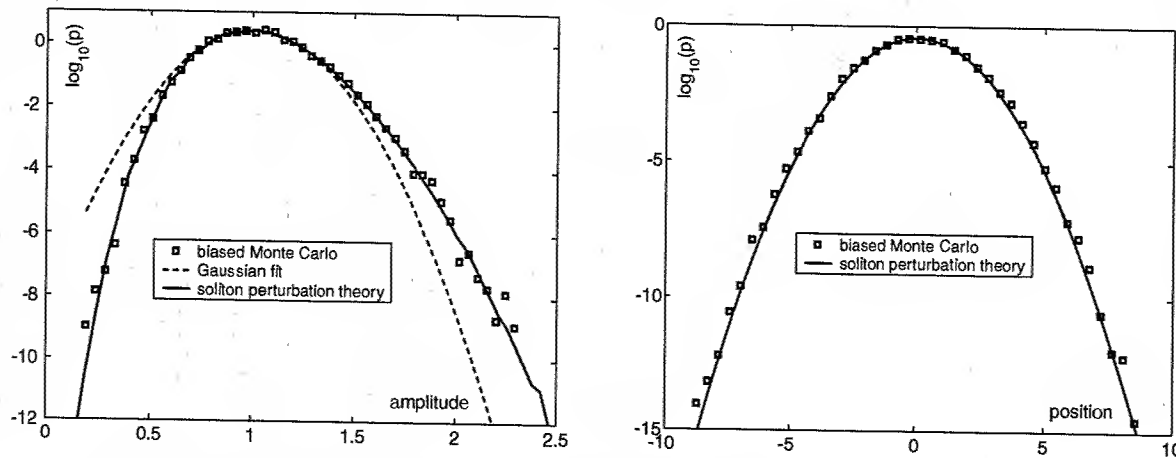
Fig. 1. Results of importance-sampled Monte-Carlo simulations for amplitude and timing jitter in a soliton-based transmission system. The simulations assume a pulse FWHM of 17.6 ps, an amplifier spacing of 50 km and a fiber loss of 0.2 dB/km, a spontaneous emission factor of η_{sp} of 1.5, a fiber dispersion $k''=-0.2\,\mathrm{ps}^2/\mathrm{km}$, and a total transmission distance of 10,000 km. In dimensionless units, this gives an amplifier spacing of 0.1, a power gain $G=10$, and a total propagation distance of 20. Furthermore, we take the nonlinear coefficient of the fiber to be 4.8×10^{-7} ps/km, which means that the dimensionless noise variance $\sigma^2=1.3\times10^{-4}$. At total of 5,000 Monte-Carlo trials were used. In addition to the results of the Monte-Carlo simulations, the results of a simple model using soliton perturbation theory (explained in the text) are also shown. A Gaussian fit is also given for the case of amplitude jitter.

Results. Figure 1 shows the results of importance-sampled Monte-Carlo simulations for one set of parameters (given in the caption). In the simulations, different biasings were employed and combined using a weighting scheme known as *balance heuristics* [10]. Note that although only a relatively small number of Monte-Carlo trials (5,000) is used, the method produces amplitude and timing jitter far down into the tails of the probability distributions. For comparison, the results from simple models obtained via soliton perturbation are also shown. For amplitude jitter, the model is [9]

$$A_{n+1} = A_n + \sigma^2\sqrt{A_n}\,z_n \qquad (5)$$

where the z_n are independent standard normal RVs. The simple model and the full simulations are in good agreement. Full unbiased Monte-Carlo simulations also agree well with these results (for as far down in probability as such simulations go). Thus, we have provided a proof-of-concept demonstration that importance sampling is an effective tool for simulating rare events in lightwave systems due to ASE noise.

References

1. D. Marcuse, "Calculation of bit-error probability for lightwave system with optical amplifiers and post-detection Gaussian noise", *J. Lightwave Tech.* **9**, 505–513 (1991)
2. J. P. Gordon and H. A. Haus, "Random walk of coherently amplified solitons in optical fiber transmission", *Opt. Lett.* **11**, 665–667 (1986)
3. C. R. Menyuk, "Non-Gaussian corrections to the Gordon-Haus distribution resulting from soliton interactions", *Opt. Lett.* **20**, 270–272 (1995)
4. T. Georges, "Study of the non-Gaussian timing jitter statistics induced by soliton interaction and filtering", *Opt. Commun.* **123**, 617–623 (1996)
5. R. Holzlöhner, V. S. Grigoryan, C. R. Menyuk, and W. L. Kath, "Accurate calculation of eye diagrams and bit error rates in optical transmission systems using linearization", *J. Lightwave Tech.* **20**, 389–400 (2002)
6. P. J. Smith and M. Shafi and H. Gao, "Quick simulation: a review of importance sampling techniques in communications systems", *IEEE J. Select. Areas Commun.* **15**, 597–613 (1997)
7. G. Biondini, W. L. Kath and C. R. Menyuk, "Importance sampling for polarization-mode dispersion", *Photon. Technol. Lett.* **14**, 310–312 (2002)
8. A. Hasegawa and Y. Kodama, *Solitons in Optical Communications* (Oxford University Press, Oxford, 1995)
9. E. Iannone, F. Matera, A. Mecozzi and M. Settembre, *Nonlinear Optical Communication Newtorks* (Wiley, New York, 1998)
10. E. Veach, *Robust Monte Carlo Methods for Light Transport Simulation*, Ph.D. thesis, Stanford University, 1997.

Complete characterization of milliwatt peak power picosecond pulses at 10 GHz propagating over 300 km in a fiber recirculation-loop

Marc Hanna, Pierre-Ambroise Lacourt
GTL-CNRS Telecom, UMR CNRS 6603, 2-3 rue Marconi, 57070 Metz FRANCE

John M. Dudley, Jean-Pierre Goedgebuer
Laboratoire d'Optique P. M. Duffieux, Universite de Franche-Comte, 25030 Besançon Cedex, FRANCE
Tel: +33 3 81 66 64 16, Fax: +33 3 81 66 64 23, Email: john.dudley@univ-fcomte,fr

Abstract: Frequency resolved optical gating using a novel fiber-based wavelength conversion geometry is used to characterize the intensity and phase evolution of milliwatt peak power pulses propagating over 300 km in an optical fiber recirculation loop.
©2002 Optical Society of America
OCIS codes: (320.7100) Ultrafast measurements, (060.5530) Pulse propagation and solitons

1. Introduction

Driven by the demands of high capacity optical communications systems, there has been much recent activity to develop sensitive intensity and phase characterization methods for pulses around 1.55 μm. As well as techniques such as second harmonic generation frequency-resolved optical gating (SHG-FROG) [1], methods using sonogram analysis [2], time-resolved optical gating [3] and pulse spectral analysis have also been reported [4]. Recently, a novel variant of FROG using wavelength conversion has been reported, and has demonstrated mW peak power sensitivity, sufficient to characterize the intensity and phase of unamplified pulses from gain-switched semiconductor lasers [5]. In this paper, we report the use of this ultrasensitive FROG geometry to perform the complete intensity and chirp characterization of mW peak power picosecond pulse propagation over a distance of more than 300 km in an optical fiber recirculation loop. Although intensity and chirp evolution in fibers has been the subject of previous studies using either indirect measurement techniques with recirculation loops [6] or using FROG for sub–km fiber lengths [7-9], the results described here are the first to report direct intensity and chirp characterization at peak power levels and over propagation distances corresponding to realistic parameters of optical fiber telecommunications systems.

2. Experiment

When applied to demultiplexing and optical sampling, wavelength conversion typically uses four-wave mixing (FWM) between a CW pump at frequency v_p and a pulsed signal at frequency v_s in order to generate an idler at frequency $v_i = 2v_p - v_s$ whose amplitude is directly proportional to that of the signal to be demultiplexed or sampled. In our experiments, however, we use a novel configuration where the idler field is generated from a pulsed pump E_p mixed with a CW signal E_s. The idler amplitude $E_i \propto E_s^* E_p^2$ thus depends quadratically on the pump pulse amplitude so that the spectral resolution of the idler as a function of delay yields a FROG trace equivalent to that obtained via SHG. This allows existing FROG deconvolution algorithms to be readily used. The FWM process is efficiently phasematched for pump wavelengths near the zero dispersion wavelength (ZDW) of an optical fiber, and the use of kilometer lengths of commercially-available dispersion shifted fiber (DSF) permits measurements of milliwatt peak power pulses in the 1–10 ps range [5]. Fig. 1(a) shows the setup used in our experiments. Here, the pulses to be characterized (around 1557 nm) are injected into a Michelson interferometer to yield a pulsed pump $E_p(t) + E_p(t-\tau)$. This is mixed with a CW signal at 1560.15 nm and launched into a ~20 km length of DSF with a ZDW of (1557 ± 1) nm to generate the nonlinear idler signal. Fig 1(b) shows the DSF input and output at zero delay (τ=0) to illustrate the generation of the idler via FWM. The ready availability of high dynamic range spectrum analyzers round 1.55 μm means that the idler spectral resolution can be carried out with excellent signal to noise ratio, and deconvolution from the resulting "FWM-FROG" trace yields accurate intensity and phase profiles with typical FROG retrieval errors around 0.3%.

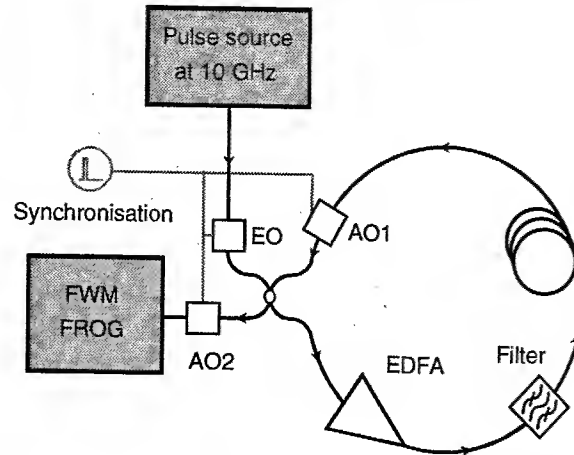## (a) FROG CHARACTERIZATION BY FWM
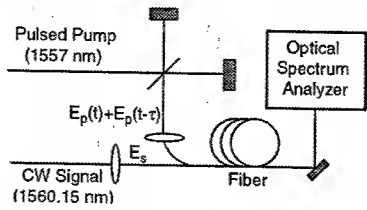
(b) RECIRCULATION LOOP

Fig. 1 (a) The top figure shows the experimental FWM-FROG setup, whilst the bottom figure shows typical input and output spectra of the fiber to illustrate the generation of the nonlinear idler field. (b) The details of the recirculation loop.

FWM-FROG was used to characterize pulse evolution in the recirculation loop shown in Fig. 1(b). The primary pulse source is a 10 GHz gain-switched distributed feedback laser which generates negatively-chirped pulses of 10–20 ps duration at 1557 nm. The pulses are injected into the loop via a LiNbO$_3$ electro-optic (EO) modulator. The recirculation loop consists of a 22-km span of Corning DSF (ZDW $\approx$ 1551 nm, dispersion slope $\approx$ 0.085 ps/nm^2 km), an EDFA, a 2 nm bandwidth optical filter, and an acousto-optic switch (AO1). The average power in the loop (measured at the DSF input) was 1.7 mW. An external acousto-optic switch AO2 was synchronized with AO1 and the EO to permit pulses to be switched out of the loop for FWM-FROG characterization after an integral number of between 1 and 14 loop round trips, corresponding to a maximum propagation distance in the loop of 308 km. Fig. 2(a) shows the intensity and chirp retrieved from these FWM-FROG measurements, plotted at 44 km intervals (every 2 loop roundtrips). The retrieved chirp is plotted at the loop input and after propagation distances of 132 km and 308 km, and clearly shows progressive compensation and flattening with propagation. The physical origin of this chirp evolution is the compensation of the input pulse negative chirp by the positive chirp introduced by nonlinear self-phase modulation (SPM) in the DSF. Previous studies of this phenomenon using kW-peak power femtosecond pulses have shown how this is associated with spectral compression and a decrease in the pulse bandwidth during propagation [10–12]. This effect was also seen in our experiments, and is shown in Fig. 2(b). We stress that this nonlinear spectral compression is a result of the interaction between the incident negative pulse chirp and the fiber SPM, and is not a result of spectral filtering during propagation. In particular, we note that the response of the spectral filter in the loop was measured to be flat across the < 0.5 nm propagating pulse bandwidth.
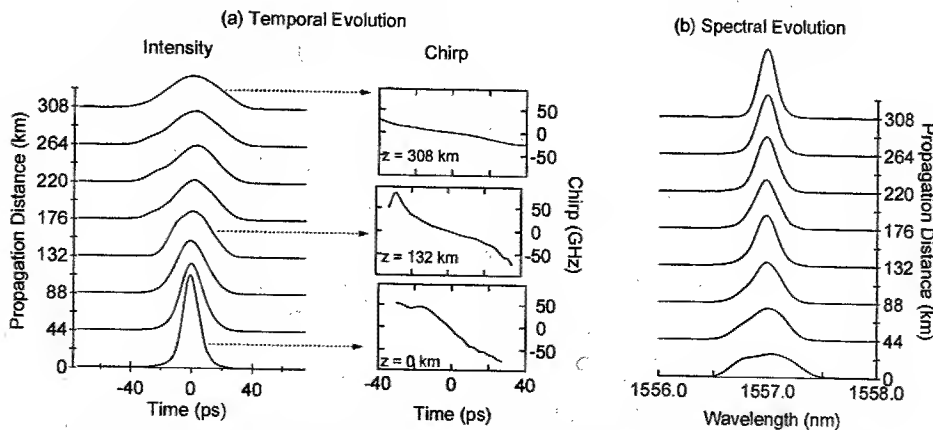
Fig. 2 Measured pulse evolution along 308 km, showing (a) the retrieved intensity and chirp obtained from the FWM-FROG measurements at the distances shown. (b) shows the corresponding spectral compression.

The complete intensity and chirp characterization using FWM-FROG allows the quantitative comparison between experiment and the results of numerical simulations of the recirculating loop based on the scalar nonlinear Schrödinger equation. Although the loop modelling included the EDFA and the spectral filter, these elements were found to have negligible effect on the pulse properties, and the dominant effects on the intensity and phase evolution in the loop were identified as SPM and residual dispersion in the DSF segment. Fig. 3 plots the results of experiment (open circles) and simulation (solid line), with Fig. 3(a) comparing the mean slope of the chirp calculated across the pulse full width at half maximum (FWHM) and Fig. 3(b) comparing the intensity FWHM of the pulse temporal profile. These results confirm the validity of our numerical model of the fiber recirculating loop, and clearly illustrate the progressive flattening of the temporal chirp with propagation.
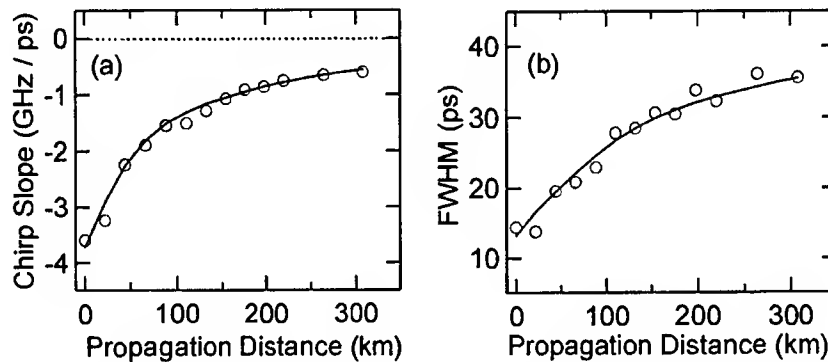
Fig. 3   Comparison of results from experiment (circles) and numerical simulations for (a) the chirp slope and (b) the intensity full width at half maximum (FWHM), plotted as a function of propagation distance.

3. Conclusion

We have demonstrated the complete intensity and chirp characterization of telecommunications-compatible pulses over 300 km in a recirculation loop by use of an ultrasensitive, FWM-based FROG geometry. Our results represent the first direct measurements of SPM-induced spectral compression and chirp compensation on initially negatively chirped pulses in a realistic telecommunications context. We anticipate that this FWM-FROG geometry will find widespread use in the design and optimization of optical links based on chirped return-to-zero and dispersion-managed soliton technologies.

References:

1.   R. Trebino, K. W. DeLong, D. N. Fittinghoff, J. N. Sweetser, M. A. Krumbügel, and D. J. Kane, Rev. Sci. Instrum., **68**, 3277 (1997).
2.   D. T. Reid, B. C. Thomsen, J. M. Dudley, J. D. Harvey, Electron. Lett. **36**, 1141 (2000).
3.   R. G. M. P. Koumans and A. Yariv, IEEE Photon.Tech. Lett. **12**, 666 (2000).
4.   P. Kockaert, M. Peeters, S. Coen, Ph. Emplit, M. Haelterman and O. Deparis, IEEE Photon. Tech. Lett. **12**, 187 (2000).
5.   P.A. Lacourt, J. M. Dudley, J-M Merolla, H. Porte, J-P Goedgebuer, W. T. Rhodes, *accepted for publication*, Opt. Lett. **27**, 863-865 (2002).
6.   F. Favre, D. Le Guen, and T. Georges, J. Lightwave Technol., **17**, 1032-1036 (1999).
7.   L. P. Barry, J. M. Dudley, P. G. Bollond, J. D. Harvey, R. Leonhardt, Electron. Lett. 32, 2339-2340 (1996).
8.   J. M. Dudley, L. P. Barry, P. G. Bollond, J. D. Harvey, R. Leonhardt, Opt. Fiber. Tech. **4**, 237-265 (1998).
9.   F. G. Omenetto, B. Luce, D. Yarotsky, and A. J. Taylor, Opt. Lett., **24**, 13 92 (1999).
10.   M. Oberthaler and R. A. Höpfel, Appl. Phys. Lett. **63**, 1017-1019 (1993).
11.   B. R. Washburn, J. A. Buck, S. E. Ralph, Opt. Lett. **25**, 445-447 (2000).
12.   J. Limpert, T. Gabler, A. Liem, H. Zellmer, A. Tünnermann, Appl. Phys. B **74**, 191-195 (2002).

Nonlinear Guided Waves

Spatial Solitons and Spatio-Temporal Effects

Monday, September 2, 2002

Mordechai Segev, Technion Inst. of Tech., Israel
Presider

NLMB
10:30am – 12:30pm
Auditorium

Nonlinear X-waves: a new perspective for space-time localization

S. Trillo,[1] C. Conti

Istituto Nazionale di Fisica della Materia, INFM-RM3,
Via della Vasca Navale 84, 00146 Roma, Italy

[1] *Also with Dept. of Engineering, University of Ferrara, Italy*
phone: +39-0532-293838, fax: +39-0532-768602, email: strillo@ing.unife.it

P. Di Trapani, O. Jedrkiewicz, J. Trull

INFM and Dept. of Chemical, Physical and Mathematical Sciences,
University of Insubria, Via Valleggio 11, 22100 Como, Italy

G. Valiulis

Department of Quantum Electronics, Vilnius University,
Building 3 Sauletekio Avenue 9, 2040, Vilnius, Lithuania

Abstract: Nonlinear and normally dispersive media support a novel form of space and time 3D localization of light in the form of so-called X-waves. We discuss their properties and their evidence in second-harmonic generation experiments.
OCIS codes: (190.5530) Pulse propagation and solitons; (190.4420) Nonlinear optics, transverse effects in

The dynamics of self-focusing driven by ultrashort intense pulses have been widely investigated recently.[1-6] The coupling of space and time, occurring in the high-intensity regime, leads to qualitatively different dynamical evolutions depending on the sign of group-velocity dispersion (GVD). For instance, in focusing Kerr media which exhibit anomalous GVD, light bullets (combined soliton trapping in space and time[7]) can be formed. Although mechanisms as different as a saturable intensity-dependent index and second-harmonic generation (SHG) support the existence of stable bullet-type solitons, their observation have proven difficult for several different reasons. On the other hand, when the GVD is normal, such trapping is not allowed and the temporal dynamics is ruled by pulse splitting and wave breaking phenomena.[1,2] In this work we show, against the common belief that space-time localization is not allowed in the normally dispersive regime, that a novel type of localized wavepackets can play a key role in the dynamics of ultrashort tightly focused beams. We introduce the concept of nonlinear X-waves (NLXWs), spatio-temporal wavepackets with characteristic X-shape, which play the role of general eigenmodes of nonlinear paraxial wave propagation models in the normal dispersion regime. In particular NLXWs exist both in cubic media, e.g. in ideal Kerr media where the propagation is governed by the scalar 1+3 nonlinear Schrödinger (NLS) equation,

$$i\partial_z u_1 + \nabla^2_\perp u_1 - \partial_{tt} u_1 + \Gamma|u_1|^2 u_1 = 0, \tag{1}$$

and in quadratic media, e.g. described by the following standard model for SHG

$$
\begin{aligned}
(i\partial_z + \nabla^2_\perp - \partial_{tt})u_1 + \Gamma u_2 u_1^* e^{i\delta k z} &= 0, \\
(i\partial_z + \sigma\nabla^2_\perp + iv\partial_t - d\partial_{tt})u_2 + \Gamma\frac{u_1^2}{2}e^{-i\delta k z} &= 0.
\end{aligned}
\tag{2}
$$

In Eqs. (1-2) we have adopted suitably normalized dimensionless quantities, leaving Γ as a coefficient that quantifies the impact of nonlinearity. Also, in Eqs. (2) v measures the group-velocity mismatch (GVM), δk is the wavevector mismatch, and σ and d are second-harmonic diffraction and dispersion coefficients, respectively. Radially symmetric NLXW solutions of Eq. (1) $u_1 = f_1(r,t)\exp(-i\beta z)$ and $u_m = f_m(r,t)\exp[-i(m\beta + (m-1)\delta k)z]$, $m = 1,2$, of Eqs. (2) can be searched by integrating the resulting equations for f_m by pseudo-spectral methods. Typical results for the Kerr case are reported in Fig. 1, which shows the existence of ground-state NLXW (Fig. 1a) as well as higher-order NLXWs with oscillatory decay (Fig. 1b). In GVM-matched (i.e., $v = 0$) SHG, we find two-color coupled NLXWs of similar type. Along the same lines also walking NLXW solutions can be found, even in the presence of strong GVM. NLXWs have distinguished features which makes them qualitatively different from bullet-type solitons. For instance, NLXWs have slow decay ($\sim 1/r$), exist in different domains, and infinitely many solutions coexist
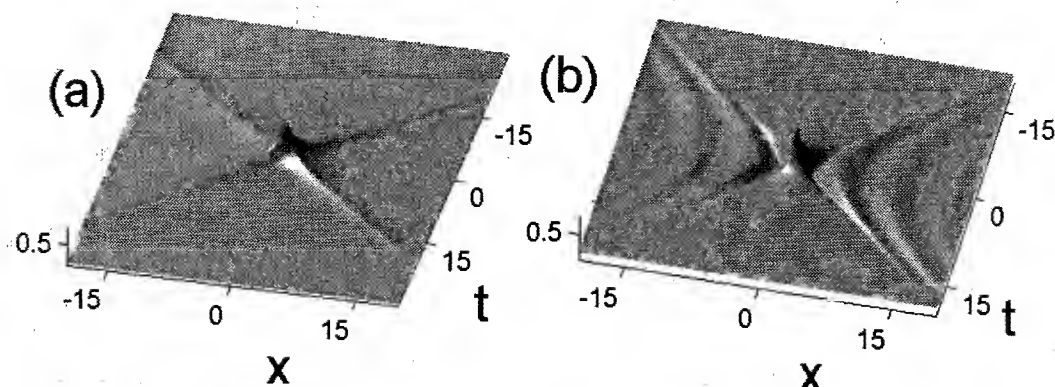
Fig. 1. Space-time field profiles ($y = 0$ cut of $u_1(r, t)$, $r = (x^2 + y^2)^{1/2}$ being the radial coordinate) of NLXW solutions in normally-dispersive Kerr media, as obtained from Eq. (1): (a) $\beta = 0$, $\Gamma = 1$; (b) $\beta = 1$, $\Gamma = 10$.
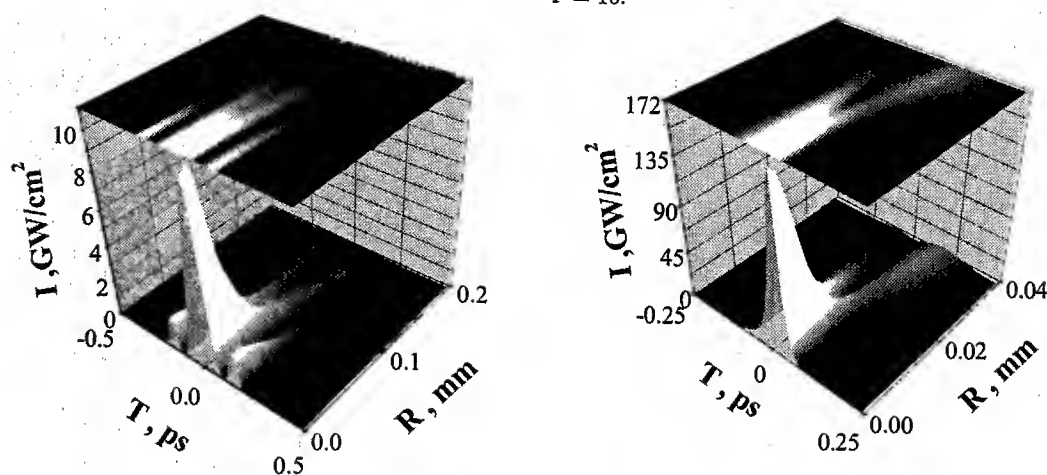

Fig. 2. Spatio-temporal intensity $|u_1(r, t)|^2$ as obtained in SHG from Eqs. (2) with gaussian input. left panel: output intensity in a 4 cm sample of LBO, GVM-matched ($v = 0$) configuration. right panel: intensity pattern after 1.5 cm propagation in the presence of strong GVM.

for a given β. Importantly, in the low intensity limit, NLXWs do not vanish, reducing instead to *linear* X waves (or so-called focus-wave modes), which are known to be the polichromatic generalization of conical Bessel J_0 (or Durnin) beams.[8] Linear X-waves have been observed in optics,[9] and acoustics,[10] and share with Durnin beams the requirements of special input conditions. Conversely, in the nonlinear regime, we conjecture that the formation of NLXWs occurs spontaneously from conventinal (chirp-free, bell-shaped in space and time) beams, via a universal mechanism of conical emission, well known in Kerr media[11]. This entails amplification of perturbations constituted by conical waves with aperture angles proportional to their frequency detunings. In SHG our linear stability analysis, carried out for cw plane-wave pump beams, predicts the amplification of conical waves around both central pump frequencies. In order to understand the dynamics of ultrashort focused beams, however, it is necessary to resort to numerical simulation of Eqs. (2). We have mainly addressed the case of large negative wavevector mismatch $\Delta k = k_2 - 2k_1$, where SHG mimics an effective Kerr effect led by the beam at fundamental frequency with lesser impact from higher-orded effects (Raman, steepening,...). Our numerical results suggest that the formation of NLXWs play an important role. For instance we show in Fig. 2 the spatio-temporal profiles obtained from an input gaussian beam with $65\mu m$ (FWHM) width and 170 fsec (FWHM) duration, as obtained after propagation in a LBO crystal operating in the normal GVD regime, either in the GVM-matched configuration (left panel), or in the case of GVM-dominated dynamics (right panel).

Remarkable evidence for these phenomena has been obtained in SHG experiments, where a 22 mm LBO crystal, operating around $\Delta k = -30$ cm^{-1} is pumped by a pulse/beam at fundamental frequency. First, at high fluences, strong pulse compression from 170 down to 25-30 fsec have been observed, which cannot
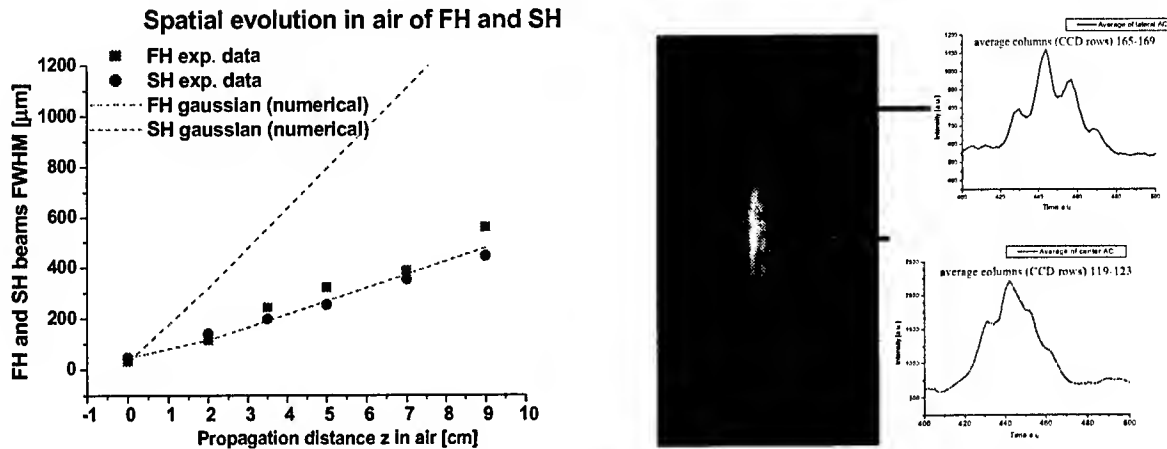
Fig. 3. Experimental data obtained in a LBO crystal. Left panel: FWHM beam sizes reported against the distance from the output face ($z = 0$) of the crystal, and compared with gaussian diffraction (upper curve for the FH beam); Right panel: radially resolved (vertical axis) autocorrelation trace of the output field.

be expected on the basis of a pure temporal phenomenon, since the interplay of (focusing) nonlinearity and (normal) GVD would lead to temporal broadening. Moreover, at the same intensity, also nonlinear compensation of walk-off due to GVM is observed. These considerations have motivated us to investigate the role of spatio-temporal coupling mediated by localized wavepackets of the X-wave type. To this end, the temporal diagnostic of the output beams (mainly based on noncollinear autocorrelation measurements) was enriched by measurements of the near-field and far-field profiles. The collected data indicates that the temporal compression is associated with a reshaping of the beam. For instance Fig. 3 (left panel) shows that the leading (fundamental) component of beam experience subgaussian diffraction in air after the crystal, i.e. it diffracts considerably less than a gaussian beam of the same spot-size. This is also consistent with the observation of rings in the far-field measurements. As far as the temporal dynamics is concerned, the autocorrelation traces show that a dramatic pulse compression occurs as the intensity is increased. However, the spatially resolved autocorrelation trace (see Fig. 3, right panel), shows that the beam has a nonuniform temporal structure, with pulse splitting becoming clear in the outer portion of the beam.

Finally, measurements performed in the spectral domain (in time and space, i.e., λ and transverse angle) at the same intensity levels clearly show the presence of angular dispersion. This, in turn, affects the effective GVD leading to an anomalous contribution which counteract the material normal GVD. Therefore, we believe to be in the presence of a genuine effect of spatio-temporal coupling where diffraction and dispersion (at least GVM and GVD orders) can be counterbalanced by the nonlinearity via a complex mechanism that involves the spontaneous reshaping of the beam/pulse into wavepackets that are reminiscent of X-waves.

In summary we have shown that X-waves constitute novel solutions of Maxwell wave equations in normally dispersive media with nonlinear response, which introduces a new perspective for the interpretation of real-world and numerical experiments. Experiments carried out in SHG support this picture.

References

[1] J.K. Ranka, R.W. Schirmer, and A.L. Gaeta Phys. Rev. Lett. **77**, 3783 (1996).

[2] A. A. Zozulya, S.A. Diddams, A.G. Van Engen, and T.C. Clement, Phys. Rev. Lett. **82**, 1430 (1999).

[3] X. Liu, L.J. Qian, and F.W. Wise, Phys. Rev. Lett. **82**, 4631 (1999).

[4] I.G. Koprinkov, A. Suda, P. Wang, and K. Midorikawa, Phys. Rev. Lett. **84**, 3847 (2000); A.L. Gaeta and F. Wise, Phys. Rev. Lett. **87**, 229401 (2001).

[5] H.S. Eisenberg, R. Morandotti, Y. Silberberg, S. Bar-Ad, D. Ross, and J.S. Aitchison, Phys. Rev. Lett. **87**, 043902 (2001).

[6] S. Tzortazis, L. Sudrie, M. Franco, B. Prade, A. Mysyrowicz, A. Couairon, and L. Berge, Phys. Rev. Lett. **87**, 213902 (2001).

[7] Y. Silberberg, Opt. Lett. **15**, 1282 (1990).

[8] J. Durnin, J.J. Miceli, and J.H. Eberly, Phys. Rev. Lett. **58**, 1499 (1987);

[9] P. Saari and K. Reivelt, Phys. Rev. Lett. **79**, 4135 (1997); H. Sönajalg, M. Rtsep, and P. Saari, Opt. Lett. **22**, 310 (1997).

[10] J. Lu and J.F. Greenleaf, IEEE Trans. Ultrason. Ferrelec. Freq. contr. **39**, 441-446 (1992).

[11] L.W. Liou, X.D. Cao, C.J. McKinstrie, and G.P. Agrawal, Phys. Rev. A **46** 4202-4208 (1992); G.G. Luther, A.C. Newell, J.V. Moloney, and E.M. Wright, Opt. Lett. **19** 789-791 (1994).

Induced Group-Velocity Dispersion in Second-Harmonic Generation: a Route to Light Bullets

K. Beckwitt, Y.-F. Chen, and F. W. Wise
Department of Applied Physics, 212 Clark Hall, Cornell University, Ithaca, NY 14853,
tel: (607) 255-9956, fax: (607) 255-7658, email: kb77@.cornell.edu

T. Wang, H. Zhu, and L. Qian
Fudan University, Shanghai 200433, China

Abstract: We show that in phase-mismatched second-harmonic generation, an effective group-velocity dispersion is induced at the second-harmonic frequency. In quasi-phase-matched structures this allows for temporal soliton formation and therefore facilitates the formation of 3-D spatiotemporal solitons.
©2002 Optical Society of America
OCIS codes: (190.5530) Pulse propagation and solitons; (190.4420) Nonlinear optics, transverse effects in

It is well known that quadratic nonlinear media can support spatiotemporal solitons (STS) [1, 2]. Phase-mismatched second-harmonic generation (SHG) produces an effective saturable self-focusing nonlinearity, which balances diffraction and group-velocity dispersion (GVD) to produce the soliton. The formation of multidimensional solitons requires anomalous GVD at both fundamental (FH) and second-harmonie (SH) frequencies, and this presents a significant obstacle to their experimental observation. A survey of available SHG crystals reveals no materials with anomalous GVD (and insignificant absorption) at any pair of fundamental and harmonic frequencies. To achieve eharacteristic lengths much shorter than available SHG crystals, anomalous GVD an order of magnitude greater than typical values in transparent materials is needed. To date, this has been produced by the use of tilted pulses [3, 4]. This technique consumes one transverse dimension and thus cannot be used to make 3-dimensional STS.

Here we show theoretically that an effective GVD is induced at the SH in the SHG process. The magnitude of the induced GVD is particularly large when the process is quasi-phase-matched (QPM). Initial experimental results are consistent with the theoretical predictions. The induced GVD allows the formation of temporal solitons in quadratic media with normal GVD at the SH frequency, and provides a promising path to the generation of 3-D STS.

An indication of the induced GVD can be obtained analytically if we neglect the group-velocity mismatch (GVM) between the fields and assume negligible depletion of the FH field. Under those conditions the SH field is

$$E_{2\omega} \approx \frac{1}{i\Delta k} e^{i\Delta kz} \exp(-(\frac{\omega\tau_p}{2\sqrt{2}})^2 + i\frac{\beta_1}{2}\omega^2 z) - \frac{1}{i\Delta k} \exp(-(\frac{\omega\tau_p}{2\sqrt{2}})^2), \qquad (1)$$

where β_1 is the GVD at the FH frequency and half that value ís induced at the SH frequency. (Space-time duality implies that diffraction will be similarly induced.) Numerical simulations of pulse propagation performed without simplifying approximations clearly exhibit the effects of the induced GVD. Figure 1 shows the FH and SH pulses produced in a QPM process at large phase mismatch, with zero GVD at the SH frequency.
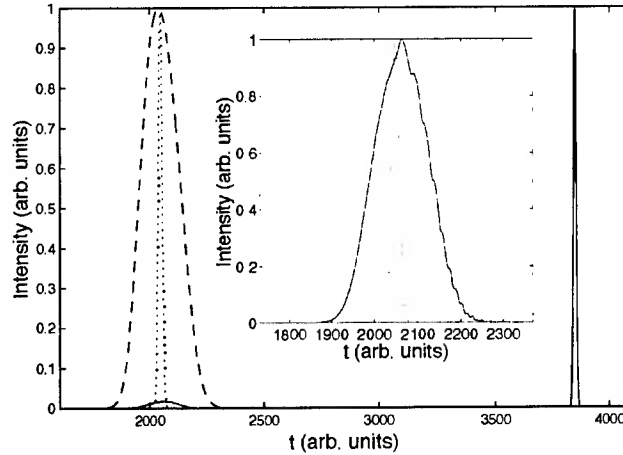
Fig. 1. Second harmonic (solid line) and fundamental (dashed) intensity profiles after propagation through 6 dispersion lengths (for the FH). There is no material dispersion at the SH. Dotted line is the launched fundamental. Inset: broadening of the SH with respect to the launched FH.

To observe the induced GVD experimentally we used SHG in barium metaborate with birefringent phase-matching. Femtosecond pulses at 2.4 μm wavelength generated SH pulses at 1.2 μm, and the temporal profile of the SH pulses was measured. The SH pulse calculated under conditions of large phase mismatch ($\Delta kL = 100\pi$) is shown in Figure 2(a). Experimental results obtained under the corresponding conditions (Figure 2(b)) agree reasonably well with the calculations. Detailed quantitative verification of the magnitude of the induced GVD is not possible from these data because the SH field produced with such large phase mismatch is weak. Measurements in QPM media will rectify this and are currently in progress.
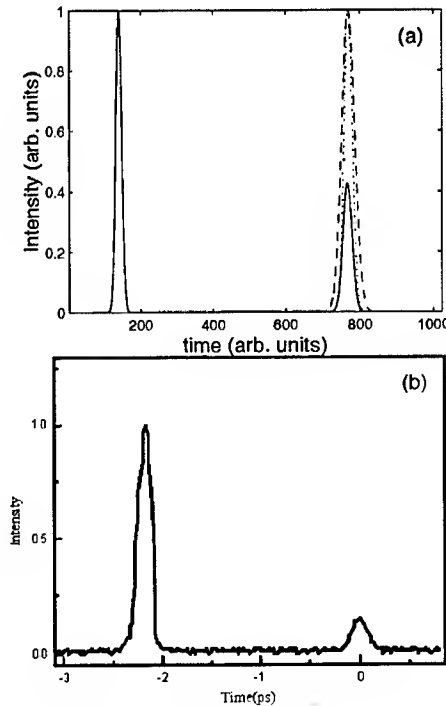
Fig. 2. Calculated (a) and measured (b) SH pulses. The dashed line in (a) is the output at the FH wavelength and dots indicate the launched fundamental.

The induced GVD can be exploited to obtain net anomalous GVD at the SH frequency if the GVD at the FH frequency is large and anomalous. As an example, the GVD of lithium niobate goes from normal to anomalous near

1.6 μm, and is large and anomalous at wavelengths beyond ~2.5 μm. For SH wavelengths near 1.6 μm, small normal GVD will combine with anomalous induced GVD to produce net anomalous GVD that can support solitons. This is illustrated in the numerical simulations of Figure 3. The top panel shows (plane-wave) pulse propagation at low intensity: the pulse decays owing to GVD. At higher intensity (bottom panel) the pulse evolves to a form that is stable over at least 5 dispersion lengths. At higher intensities, the periodic evolution characteristic of quadratic solitons is observed. These simulations further demonstrate the significance of the induced GVD. The observation of temporal solitons in quadratic media without the use of tilted pulses is clearly possible, and this should remove the primary obstacle to the production of spatiotemporal solitons.
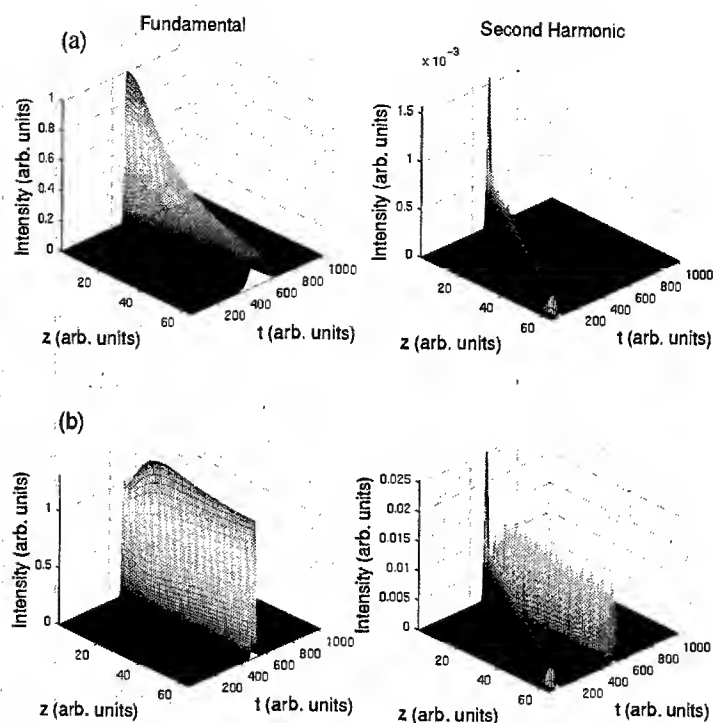
Fig. 3. Propagation of FH and SH waves in QPM SHG. Parameters correspond to lithium niobate, and the FH wavelength is 3 μm. Top panel: low intensity. Bottom panel: a temporal soliton forms. The "ragged" appearance of the SH field in the bottom panel is a consequence of coarse sampling.

In conclusion, we have shown theoretically that an effective GVD is induced at the second-harmonic wavelength in the SHG process, and this effect is pronounced in QPM media. Initial experiments agree reasonably well with theoretical expectations. Numerical simulations show that this effect can be exploited to generate temporal solitons in quadratic media, which is a crucial step toward the generation of light bullets. Numerical and experimental studies of light bullets produced this way are in progress.

1. Y. N. Karamzin and A. P. Sukhorukov, *Sov. Phys. JETP* **41**, 414 (1975).
2. B. A. Malomed *et al.*, *Phys. Rev. E* **56**, 4725 (1997).
3. P. DiTrapani *et al.*, *Phys. Rev. Lett.* **81**, 570 (1998).
4. X. Liu, L. J. Qian, and F. W. Wise, *Phys. Rev. Lett.* **82**, 4631 (1999).

Snake instability of the 2+1D spatio-temporal bright soliton stripe

N. Roig, S.-P. Gorza, Ph. Emplit and M. Haelterman

Service d'Optique et d'Acoustique, Universit' Libre de Bruxelles, CP 194/5
Av. F. D. Roosevelt 50, B-1050 Brussels, Belgium
Tel : +32-2-650.44.94, Fax : +32-2-650.44.96, e-mail : Marc.Haelterman@ulb.ac.be

Abstract: We demonstrate experimentally the snake instability of the bright soliton stripe in the 2+1D hyperbolic nonlinear Schrödinger equation. The instability is observed on a spatially extended femtosecond pulse propagating in a normally dispersive self-defocusing semiconductor planar waveguide.

Zakharov and Rubenchik have made an early major theoretical breakthrough by showing that the bright soliton solutions of the canonical 1+1D Nonlinear Schrödinger (NLS) equation are unstable when propagating under the form of rectilinear stripes in 2+1 dimensions [1]. In that early work, the additional dimension was introduced to take into account the effect of chromatic dispersion on spatial soliton laser beams propagating in nonlinear optical media with one transverse dimension (planar waveguide structure). Considering both signs of dispersion, Zakharov and Rubenchik implicitly dealt with both the elliptic and the hyperbolic 2+1D NLS equations. Indeed, when chromatic dispersion is negative (positive) the associated second order derivative terms representing dispersion and diffraction have the same (opposite) signs, and the NLS equation is elliptic (hyperbolic). Zakharov and Rubenchik showed that the bright soliton stripe is always unstable in 2+1 dimensions regardless of the dispersion regime. However, they showed that the scenario strongly differs from one regime to the other. Indeed, they predicted that in the elliptic NLS equation (negative dispersion), the bright soliton stripe undergoes a neck-type instability (formation of a rectilinear periodic row of spots evolving to catastrophic self-focusing), while in the hyperbolic NLS equation (positive dispersion) it exhibits a snake-type instability (appearance of a zig-zag-shaped distortion of the stripe followed by its radiative decay).

Theory was also developed for the dark soliton the NLS equation [2, 3]. The dark soliton was shown to be unstable through the exponential growth of an unstable symmetric mode, as for the case of the bright soliton stripe in the elliptic NLS equation. However, due to the antisymmetric nature of the dark soliton, this unstable symmetric mode constitutes a translational mode and thus naturally leads to the snake instability.

Experimental observation of the breakup of a bright spatial soliton stripe due to the transverse neck-type instability was performed by Mamaev *et al.* in a photorefractive crystal [4]. The snake instability of the dark NLS soliton was observed experimentally in the two-dimensional transverse profile of laser beams in Rubidium vapor [5] and in photorefractive crystals [6]. However, all experimental demonstrations of bright and dark soliton stripe instabilities were performed in systems ruled by the elliptic NLS equations. And, to our knowledge, experimental studies of the stability of soliton stripes in the 2+1D hyperbolic NLS equation have never been reported despite the importance of this equation in physics.

We present in our communication an experimental study of the stability of the bright soliton stripe ruled by the 2+1D hyperbolic NLS equation. From a mathematical viewpoint, the originality of our demonstration is to provide evidence for the existence of an antisymmetric unstable mode in the bright soliton stripe of the hyperbolic NLS equation [1]. Since this unstable mode constitutes a translational mode of the bright soliton, it leads to the snake instability of the bright soliton stripe.

Our experiment has been performed with femtosecond laser pulses propagating in a planar AlGaAs waveguide that exhibits a self-defocusing Kerr nonlinearity at photon energies just below the energy bandgap, which is the situation considered in our experiment [7]. Because the chromatic dispersion of AlGaAs is positive (normal dispersion) close to the bandgap energy [8], the spatio-temporal propagation equation must include a second-order derivative with a sign opposite to that of diffraction. As a result, our system is ruled by the 2+1D hyperbolic NLS equation. A soliton stripe can be formed by considering ultrashort pulses in a broad laser beam so that the sech-shaped soliton envelope is generated in the temporal domain while the spatial transverse coordinate constitutes the homogeneous coordinate of the stripe.
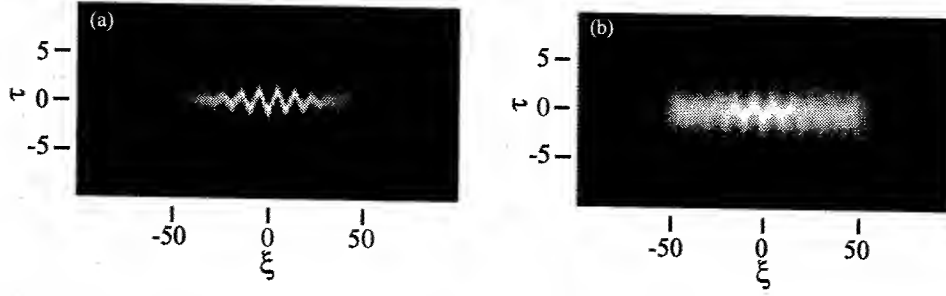
Fig. 1. Density plots of the spatio-temporal intensity distributions obtained by numerical simulation of Eq. 1, (a) without TPA ($\kappa = 0$) at $\zeta = 11$, and (b) with TPA ($\kappa = 4 \cdot 10^{-2}$) at $\zeta = 18$.

As regards the temporal aspects, our experimental conditions are in fact similar to those considered by Belanger *et al.* in the study of the (1+1)-dimensional temporal bright NLS soliton in normally dispersive cylindrical (channel) waveguide with negative Kerr nonlinearity [9]. Having one additional dimension in our problem, we focus our attention on the transverse spatial features of the beam in order to provide evidence for the snake instability of the temporal bright NLS soliton stripe. Because we use femtosecond laser pulses we are unable to observe the two-dimensional spatio-temporal patterns generated by the snake instability, contrary to what has been performed in the spatial domain for the bright and dark soliton stripes instabilities of the elliptic NLS. Our observations are thus limited to the time-averaged spatial spectrum obtained at the waveguide output. However, as we shall see, the spectral signature is very specific to the snake instability and constitutes a genuine experimental proof of the theoretical predictions of Zakharov and Rubenchik.

The soliton stripe is obtained by launching a broad laser beam made of ultrashort pulses into a 5 mm long planar waveguide made of a 1.5 μm thick guiding layer of $Al_{0.04}Ga_{0.96}As$ surrounded by 3 μm thick upper and lower claddings of $Al_{0.06}Ga_{0.94}As$. The gaussian beam of a mode-locked Ti:sapphire laser producing 80 fs (FWHM) pulses at 82 MHz and tunable around 850 nm is shaped by a set of cylindrical lenses to be end-fire coupled into the waveguide with a 150 μm width. The input power is tuned by means of a half-wave plate combined to a polarizer as well as a series of neutral filters.

We fixed the wavelength to $\lambda = 870$ nm so as to have a negative nonlinear index coefficient $n_2 = -5.35 \cdot 10^{-17}$ m^2/W and a dispersion $\beta'' = 3.39 \cdot 10^{-23}$ s^2/m, as calculated from Refs. [7] and [8], respectively. Note that this value of dispersion combined to the pulse duration of 80 fs, corresponds to a dispersion length of $6.1 \cdot 10^{-5}$ m. The waveguide is thus about 80 times longer than the dispersion length. The two-photon absorption (TPA) coefficient has been evaluated from transmission measurements. The inverse waveguide transmission versus input power exhibits a linear slope that provides the value $\alpha_2 = 3.09 \cdot 10^{-11}$ m/W in good agreement with theory [7].

For the sake of simplicity of the presentation, we introduce a convenient scaling that leads to the canonical form of the hyperbolic NLS equation plus the two-photon absorption term.

$$A_\zeta = i\frac{1}{2}A_{\xi\xi} - i\frac{1}{2}A_{\tau\tau} - i|A|^2A - \kappa|A|^2A \ , \tag{1}$$

where $\kappa = \lambda\alpha_2/(4\pi n_2) = 4 \cdot 10^{-2}$ is the normalized two-photon absorption coefficient. With this scaling, the normalized soliton stripe $E(\zeta, \xi, \tau) = sech(\tau)exp(i\zeta/2)$ is characterized by a dispersion length L_D and a nonlinear length L_{NL} both equal to unity, while the characteristic TPA length is $L_{TPA} = 1/\kappa \approx 25$. Zakharov and Rubenchik showed that the gain of the snake instability scales as self-phase modulation [1], i.e., the characteristic length of the snake instability is equal to unity, which is much shorter than the TPA length $L_{TPA} \approx 25$. One can therefore reasonably expect the development of the snake instability in our system.

This conclusion is confirmed by our numerical simulations of the generalized NLS Eq. (1). The density plots of Figs. 1(a) and (b) show the spatio-temporal intensity distributions resulting from the propagation, respectively, without and with TPA, of the initial field distribution $A(\xi, \tau) = sech(\tau) * exp[-(\xi/\xi_0)^2]$, with $\xi_0 = 78$. As can be seen, the snake instability occurs on finite-beam width and in the presence of TPA, which reveals that it does not require a perfect soliton propagation regime. The resulting spatio-temporal zigzag patterns can of course not be observed directly but its characteristic associated spatial spectrum (integrated over the time variable) can be easily obtained. Fig. 2(a) shows a typical example of time-averaged spectrum calculated by numerical simulation of our experiment in real-units. This spectrum is obtained at the waveguide output, i.e., $z = 5$ mm, in the presence of TPA and taking
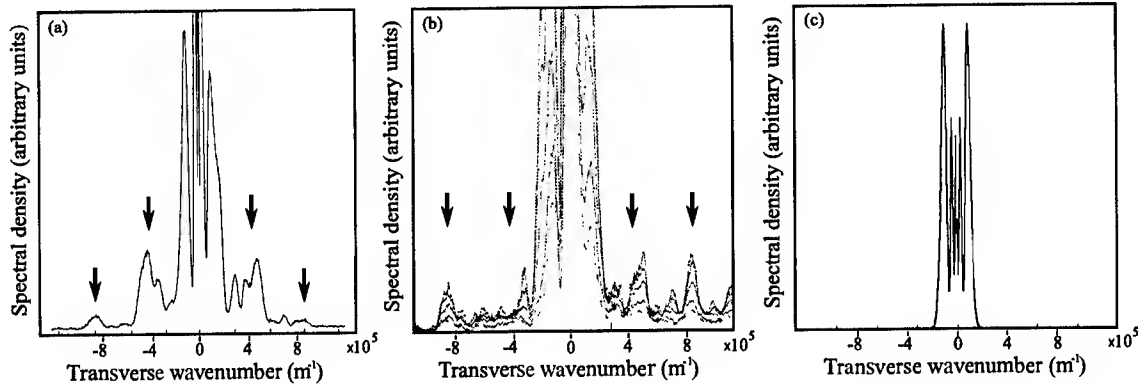
Fig. 2. Time-averaged spatial spectra at the waveguide output obtained from (a) numerical simulation at the power of 30 MW/m , (b) experiment at various input powers in the range 2.5-34 MW/m, and (c) numerical simulation at zero dispersion.

$E = E_0 sech(t/t_0)exp[-(x/x_0)^2]$ (plus a random spatio-temporal noise) as initial conditions, where $t_0 = 45$ fs and $x_0 = 127$ μm, the peak power being 4kW. Fig. 2(a) reveals that, at high input powers, the averaged spatial spectra exhibit (besides the broad central modulated lobe characteristic of self-phase modulation of the gaussian beam) lateral peaks characteristic of modulational instability. On the basis of these observations, we established a very simple experimental procedure to identify the snake instability of the bright NLS temporal soliton stripe. We progressively increase the power at the waveguide input until we approach the soliton regime. With the calculated and measured parameters of the waveguide we estimate a soliton peak power of $1.86 \ 10^7$ W/m, in the absence of TPA. Our power range goes slightly above this value to compensate for TPA. Of course the snake instability does not only occur in the exact soliton regime and its characteristic spectral signature appears progressively. We thus simply measure, for a series of input power levels, the averaged spatial spectra by means of a CCD camera located in the Fourier plane of a lens at the waveguide output. The result is shown in Fig. 2(b) that reveals the formation of four lateral peaks at the location predicted by theory. An asymmetry appears on the first harmonic on the left hand side but this can be attributed to the sensitivity of the spectral signature to perturbations in the initial condition, as observed numerically. Let us notice that the amplitudes of the second harmonic peaks appear larger in the experiment, a feature that we have not been able to explain up to now. It is important to note that, in the absence of dispersion (i.e., in the absence of spatio-temporal coupling) our numerical simulations do not show these peaks because no spatial modulational instability occurs in self-defocusing Kerr media in the absence of space-time coupling, which is illustrated in Fig. 2(c). Comparison of Figs. 2(a) and (b) reveals a reasonable agreement between theory and experiment and allows us to conclude that the snake instability does occur in our system.

In summary, through the experimental study of the propagation of a spatially extended ultrashort pulse in a self-defocusing and normally dispersive semiconductor planar waveguide excited close to the bandgap, we have provided the first confirmation of the existence of the bright soliton snake instability predicted three decades ago by Zakharov and Rubenchik. This observation proves the existence and the essential role of the soliton antisymmetric unstable mode pertaining to the hyperbolic nature of the NLS equation considered in the present study. Owing to the universality of the NLS equations in physics, our results have potential ramifications in other fields of research including plasma physics, fluid dynamics or nonlinear matter waves.

References

1. V. E. Zakharov and A. M. Rubenchik, Sov. Phys. JETP **38**, 494 (1973).
2. E. A. Kuznetsov and S. K. Turitsyn, Sov. Phys. JETP **67**, 1583 (1988).
3. D. E. Pelinovsky, Yu. A. Stepanyants, and Yu. S. Kivshar, Phys. Rev. E **51**, 5016 (1995).
4. A. V. Mamaev, M. Saffman, D. Z. Anderson, and A. A. Zozulya, Phys. Rev. A **54**, 870 (1996).
5. V. Tikhonenko, J. Christou, B. Luther-Davies, and Yu. S. Kivshar, Opt. Lett. **21**, 1129 (1996).
6. A. V. Mamaev, M. Saffman, and A. A. Zozulya, Phys. Rev. Lett. **76**, 2262 (1996).
7. M. Sheik-Bahae *et al.*, IEEE J. Quantum Electron. **27**, 1296 (1991).
8. M. Sheik-Bahae, J. Wang and E. W. Van Stryland. IEEE J. Quantum Electron. **30**, 249 (1994).
9. N. Belanger, A. Villeneuve, and J. S. Aitchison. J. Opt. Soc. Am. **B14**, 3003 (1997).

Observation of self-similar nonlinear wave collapse

K.D. Moll and Alexander L. Gaeta
School of Applied and Engineering Physics, Cornell University, Ithaca, NY 14853
Tel: (607) 255-0657, fax: (607) 255-7658, email: kdm14@cornell.edu

Gadi Fibich
School of Mathematical Sciences, Tel Aviv University, Tel Aviv 69978, Israel

Abstract: We show that during self-focusing induced collapse of a laser beam, the spatial profile evolves into the same cylindrically symmetric shape, known as the Townes soliton, regardless of the shape of the input beam profile.
©2002 Optical Society of America

Nonlinear wave collapse is a phenomenon that occurs in many different areas of physics. In nonlinear optics, wave collapse can transpire via the process of self-focusing. Mathematically, this corresponds to the appearance of a singularity in the 3-D nonlinear Schrodinger equation (NLSE), which is used to model the propagation of light under self-focusing conditions, when the power P of the input beam is greater than a certain critical power P_{cr}. For the case in which P is equal to P_{cr}, the NLSE possesses a cylindrical symmetric waveguide solution known as the Townes soliton which represents the profile that exactly balances diffraction and the nonlinearity associated with the intensity-dependent refractive index. The Townes profile cannot be represented in terms of elementary functions and must be numerically calculated as shown in Fig. 1(a); a gaussian is also plotted for comparison. However, this solution is unstable to arbitrarily small perturbations which results in either catastrophic collapse or the eventual diffraction of the beam. Catastrophic collapse associated with self-focusing of elliptical beams has been the subject of many theoretical studies which have utilized a variety of techniques such as the variational principle [1], modulation theory [2], and numerical simulations [2,3]. One of the remarkable predictions of the modulation theory, which is supported by numerical simulations, is that as the beam collapses, its shape evolves into a profile that is self-similar to the cylindrically symmetric Townes soliton regardless of the shape of the input beam profile. Furthermore, the power contained in the collapsing portion of the beam will always be exactly equal to the critical power for self-focusing.
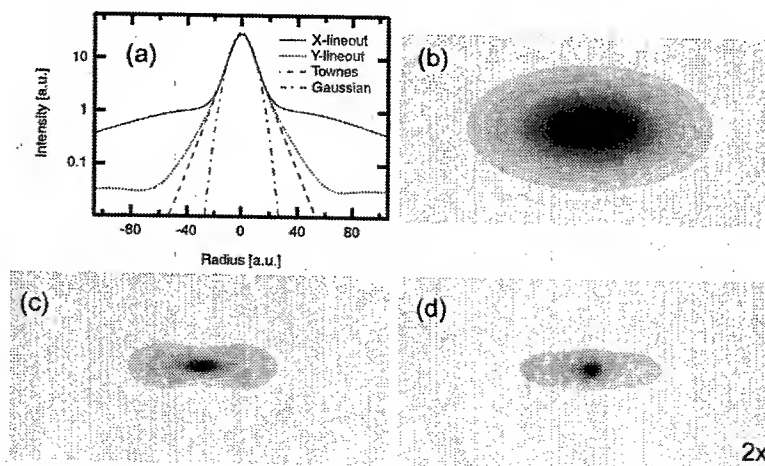
Fig. 1. (a) The Townes profile is numerically calculated and compared to a gaussian profile. (b) An elliptically shaped input beam is numerically simulated. As it collapses (c-d), a circularly symmetric on axis component emerges. Lineouts of the output beam along both dimensions (a) match precisely with the Townes soliton on-axis. Part (d) has been magnified two times to show more detail of the collapsing beam.

In this report, we present experimental evidence that confirms the prediction that the collapsing portion of the beam approaches the Townes soliton profile for a variety of input beam profiles including those that are elliptically-shaped. To illustrate the process of Townes-soliton formation, we numerically simulate the propagation of a beam with a noisy profile and an elliptically-shaped beam for input powers above the critical power for self-focusing. Figure 1 illustrates the robust nature of the collapse for the case of an elliptically-shaped input beam. As collapse occurs [depicted in Fig. 1(b)-(d)], the on-axis portion of the beam becomes circularly symmetric. Lineouts of the output beam along both axes [Fig. 1(a)] confirm that the on-axis profile is both circularly symmetric and precisely matches the calculated Townes profile. However, it is important to note that only the on-axis portion of the beam will approach the Townes profile, and the power contained in the collapsing portion of the beam is equal to the critical power; the residual input power remains in the wings.

We have experimentally reproduced the results simulated above. The beam from an amplified femtosecond Ti:sapphire laser propagates through a 30-cm-long block of BK7 glass at powers close to the critical power for self-focusing. To study the effects of ellipticity, a pair of cylindrical lenses is inserted into the beam to reduce one dimension with respect to the other. For the case of a beam with random perturbations, a roughened microscope slide was inserted into the beam. The beam is further telescoped to a diameter of ~0.5 mm and collimated. The output beam is imaged by a CCD camera or, alternatively, is allowed to strike a thin slit which is then imaged onto a linear photodiode array to yield a lineout through the center of the output beam. Figure 2 is representative of the data acquired as the input power is increased. The solid line shows a center slice of the beam profile for the low-power beam after propagating through the block of glass. As the power is increased, an intense, symmetric on-axis component suddenly appears (dotted line). The numerically calculated Townes profile is then fit to the resulting peak (dashed/dotted line) and is found to be in excellent agreement with the experimentally observed feature. We believe this to be the first experimental observation of the Townes soliton.
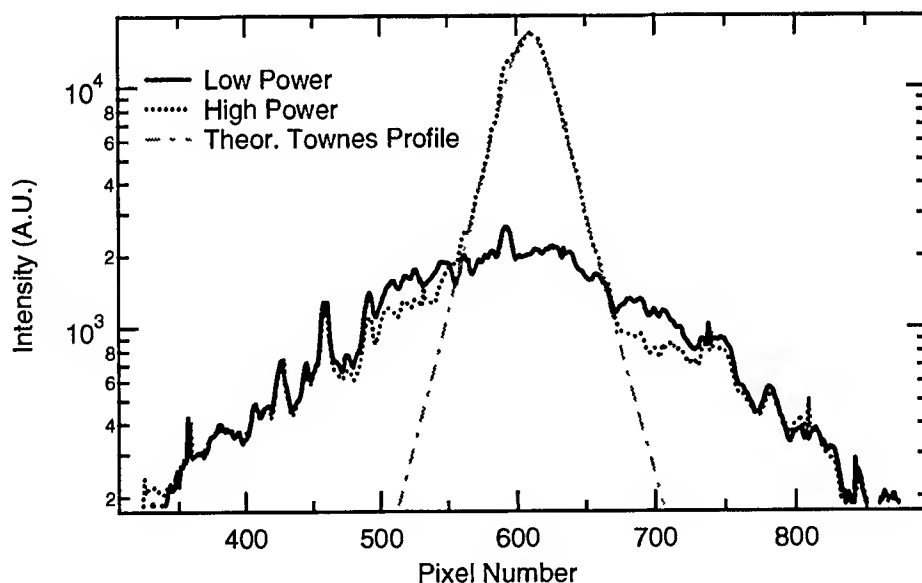
Fig. 2. Experimental observation of the Townes soliton. Lineouts are taken through the center of the beam at two different powers. At sufficiently high powers, a strong on-axis component is observed which matches with the Townes profile predicted by numerical simulations. The low-power profile has been scaled by a constant factor to account for different input powers.

While a singularity is predicted by the model equation for powers above the critical power, the field intensity is limited by higher-order processes that are not included in the model. A commonly observed result of the collapse of femtosecond pulses is the extreme spectral broadening known as supercontinuum generation (SCG) [4]. Thus, the spatial shape of the emitted SCG gives an indication of the shape of the beam as it undergoes collapse. Figure 3 depicts results for an elliptically shaped input beam with a 3:1 ratio of the axes after propagation through the sample. Whereas the relatively clean input beam shown in Fig. 2 clearly shows the Townes-soliton formation, the collapse dynamics of the elliptically-shaped beam
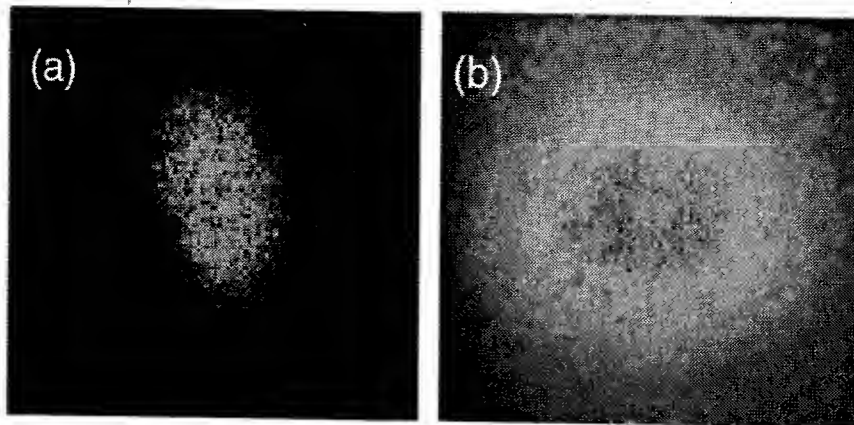
Fig. 3. (a) An elliptically shaped input beam propagates through a 30-cm sample and (b) forms circularly symmetric continuum generation.

was always accompanied by SCG. We believe this is due to the fact that as the shape of the input profile deviates further from the Townes-soliton shape, it is necessary for the beam to propagate closer to the collapse point in order for the beam to evolve into the Townes profile. As a result, the shape of the continuum was always generated in a nearly perfectly circularly symmetric profile. This observation substantiates that even with highly irregular input beam geometries, the evolution to the circularly symmetric beam Townes profile persists. This behavior holds even for the case in which the beam is made highly elliptical by only using one cylindrical lens which focuses the beam within the sample. However, substantial power remains in the wings at the input wavelength because of the extreme departure from the Townes profile.

In conclusion, we have experimentally observed the Townes soliton in agreement with numerical simulations. We believe these results will lead to an improved understanding of the propagation of high-power laser beams where self-focusing effects are important such as in the filamentation of femtosecond pulses in air [5,6].

1. M. Desaix, D. Anderson, and M. Lisak, "Variational approach to collapse of optical pulses," J. Opt. Soc. Am. B **8**, 2082-2086 (1991)
2. G. Fibich and B Ilan, "Self-focusing of elliptic beams: an example of the failure of the aberrationless approximation," J. Opt. Soc. Am. B **17**, 1749-1758 (2000).
3. B. Gross and J. T. Manassah, "Numerical solution for the propagation of an elliptic Gaussian beam in a Kerr medium," Phys. Lett. A **169**, 371-378 (1992).
4. A. L. Gaeta, "Catastrophic collapse of ultrashort pulses," Phys. Rev. Lett. **84**, 3582-3585 (2000).
5. A. Braun, et al., "Self-channeling of high-peak-power femtosecond laser-pulses in air," Opt. Lett. **20**, 73-75 (1995).
6. M. Mlejnek, E.M. Wright, J.V. Moloney, "Dynamic spatial replenishment of femtosecond pulses propagating in air," Opt. Lett. **23**, 382-384 (1998).

3D mapping of self-focussed light pulses

Stefano Minardi, Giovanni Blasi, Paolo Di Trapani

*INFM and Dipartimento di Scienze CC.FF.MM. –Università degli Studi dell'Insubria –Via Valleggio, 11 –I 22100 COMO –Italy
Tel. +39 031 238 6257 Fax. +39 031 238 6209 e-mail: sminardi@fis.unico.it*

Arunas Varanavičius, Gintaras Valiulis, Algis Piskarskas

*Department of Quantum Electronics –Vilnius University –Sauletekio g . 9 –r. III –LT 2040 VILNIUS -Lithuania
Tel. +370 2 366050 Fax. +370 2 366006 e-mail: arunas.varanavicius@ff.vu.lt*

Abstract: By exploiting a cross-correlation technique, we were able to investigate the space-time structure of the parametric spatial solitons excited by picosecond light pulses. Temporal effects that a simple 2D model cannot explain are discussed.
©2002 Optical Society of America

OCIS Codes: 190.4410, 190.5530, 190.1900

Self-focussing of light beams due to parametric interaction is a well known phenomenon [1-3], which has been successfully described in the frame of the parametric spatial soliton theory [4]. However, since short light pulses (1-100ps) were used to achieve simultaneously the high intensities of the self-focusing threshold and prevent the non-linear material damage, the time domain dynamics may affect the ideal self-focussing effect. Departure form the ideal behavior of the parametric 1D spatial soliton has been already shown theoretically in the case of strong group velocity mismatch between the interacting pulses [5]. Furthermore, relying upon modulational instability analysis, it appears that the group velocity dispersion is responsible for the instability of 1D spatial solitons, even in the regime of continuos wave [6]. With the exception of the characterization of the 1+1+1 spatio-temporal solitons [7], to date no extended experimental investigation on the impact of the time evolution on self-focusing in parametric interaction has been performed.

In this work, we study the time-resolved self-focussing dynamics of the pump beam in the regime of parametric amplification of the quantum noise. To achieve this goal, we exploited a spatially resolved second-harmonic cross-correlation technique, which allows to reconstruct the temporal evolution of the pump-beam profile by mixing it with a probe of much smaller duration. This technique is a generalization of the so-called second-harmonic holography [8]. The recovered 3D maps of the pump field exiting the nonlinear crystal support the understanding of some counterintuitive features of the self-focussing process as it appears in usual time-integrated images.

In our setting, the self-focussed beam is generated by propagating a 1 ps, 1-2 µJ, 527nm, 25µm FWHM diameter (at the input) wave-packet inside a 15 mm long LBO crystal, cut and oriented for optical parametric generation in the condition of non-critical type I phase-matching ($\phi=0°$, $\theta=90°$). The crystal temperature was initially set to 110°C, which ensures the generation of a signal centered around 750 nm, an operating condition whose small group velocity mismatch (GVM) was proven to be optimum for spatial solitons formation from quantum noise amplification [9]. The 527nm pump field exiting the crystal is reconstructed (by a M=2.5x telescope) onto a thin SGH crystal, where it is mixed with a quasi-plane-wave 200fs probe pulse, of the same wavelength, in slightly non-collinear geometry (external angle of 16°). The probe pulse is generated by means of a non-linear pulse compressor [10], starting from the same initial laser pulse. For a given delay, the non-collinearily generated radiation at 264nm provides a snapshot of the self-focussed pump-beam profile integrated over the 200 fs time-slice. The whole pulse space-time profile is then easily recovered, with 200 fs resolution, by scanning the delay between the two pulses. Note that the non-collinear angle and the beam size were small enough to make negligible the broadening effect due to the time delay accumulated across the beam.
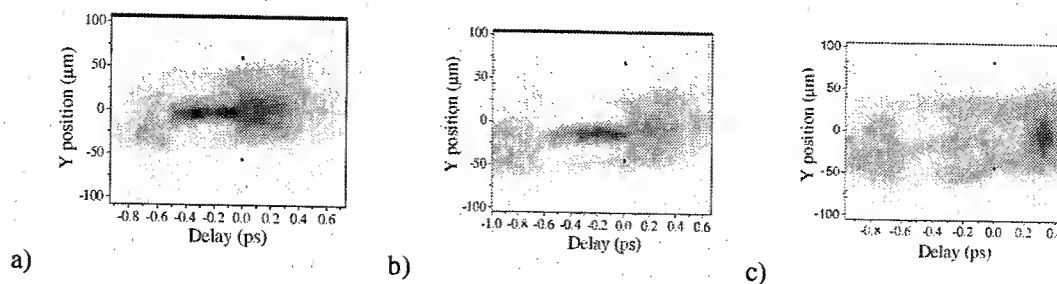
Fig.1: Space-time intensity sections of the self-focussed pump beam. a) and b), crystal temperature 110°C ($\lambda_S = 715$ nm), input pump energy 1.5 µJ and 1.9 µJ respectively. c) Crystal temperature 125°C ($\lambda_S = 815$ nm), input pump energy 1.5 µJ. Negative delay values correspond to the leading edge of the pulse.

Contour plots of the time-resolved pump-beam profile are depicted in fig. 1.a and 1.b, for the case of two different input-pulse energies. The data reveal that the self-focusing process is more effective in the leading edge of the pulse. Even if the focused region increases its duration at increasing the input energy, the results show that a relevant portion of the pump remains always unfocused. The reason, as clarified by numerical experiments, is due to GVM between the interacting pulses, which prevents any effective interaction to occur in the pulse trailing edge. Note that this effect should causes the appearance of a pedestal to the spatial-soliton beam profile, when the temporal-integrated images are taken.

The important and quite unexpected result is that the temporal dynamics of the parametric process dramatically affects the determination of the threshold for the soliton formation from time-integrated profiles. Evaluating the pump level at which the pump beam gets self-focussed, we have found dramatic disagreement between the prediction of a pure spatial model and the reality. By integrating a purely spatial (2D+1) code, we calculated the expected output beam widths for the pump field as a function of its input intensity for different phase-matching conditions. The results are plotted in Fig. 2.a which show that the threshold for stable self-focusing is decreasing as the signal wavelength is approaching the degeneracy. This effect is a clear signature of the idler wave diffraction parameter, which is obviusly more important for wavelengths which are far form the degeneracy. However, if one tries to measure this effect by exciting the solitons with short pulses and using a not time-resolved imaging system, he measures exactly the opposite effect. For the sake of comparison, the results of the radially symmetric space-time (2D+1) simulation are shown in Fig. 2.b, but experimental data are extremely similar. The output beam diameters are here calculated after an integration over the time coordinate. A dramatic increase of the threshold for stable self-focusing as the signal wavelength approaces the degeneracy is now evident.
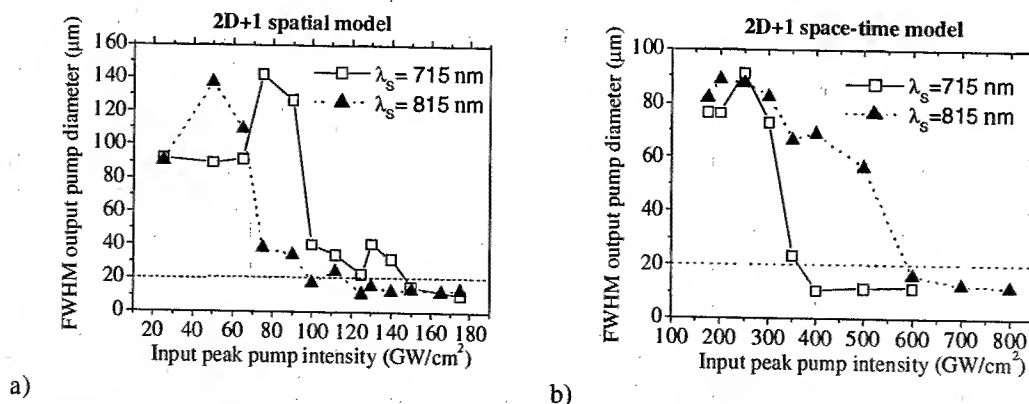

Fig.2 Pump beam output diameter as a function of input intensity, for two different phase-matching conditions of the parameric interaction. a) As resulting form the 2D+1 spatial model integration. b) As resulting form the 2D+1 space-time radial symmetric model.

The solution of this puzzle comes if one considers that the ratio between the energy content in the focussed and not-focussed portions of the pump pulse decreases dramatically moving towards the degenerate phase matching condition. This is evident in the experimental space-time map depicted in Fig. 1.c. The input intensity of the pump is the same as in fig. 1.a, but here the crystal temperature was raised up to 125°C to achieve phase-matching with a signal wavelength closer to degeneracy (815nm). In a time-integrated spatial profile it would be difficult to recognize the self-foussed part except if the pump intensity is so high that all the pulse gets completely self-focussed, this leading to an apparent increase of the self-focussing threshold on time-integrated profiles.

Our measurements show that the same effect does not occur at the signal mode, where the self-focussed energy content dominates over the background across the whole tuning range (data not shown). This leads to the situation in which the time-integrated signal (idler) field exhibits a well contrasted focussed profile, while the focussed part is barely visihle in the background dominated pump-beam profile. The space-time numerical simulation shows that the time integrated signal (idler) profile exhibits diffraction free-properties as well.

In summary, what we have here shown that time-resolved measurements provide the explanation for two quite puzzling phenomena that we have often observed with time-integrated measurements. (i) The apparent increases of the soliton-formation threshold on moving from tuning edge to degeneracy, when only the pump-beam profile is monitored, in contrast with what one will get from a purely cw-model. (ii) The occurrence (close to degeneracy) of a diffraction-free regime in the signal (or idler) mode only, whilst the pump beam seems to experience just linear diffraction. Work is in progress to provide simultaneous spatio-temporal reconstruction of both the pump and signal wave packets, and so afford a more complete physical interpretation of the entire process.

[1] W.E.Toruellas, Z.Wang, D.J.Hagan, E.W. Van Stryland, G.I. Stegeman, L. Torner, and C.R. Menyuk, Phys.Rev.Lett. 74, 5036 (1995)

[2] R.A. Fuerst, M.T.G. Canva, G.I. Stegeman, G.Leo, and G. Assanto, Opt.Lett. 22, 1683 (1997); errata, 26, 105 (2001)

[3] P.Di Trapani, G.Valiulis, W.Chinaglia, and A.Andreoni, Phys.Rev.Lett. 80, 265 (1998)

[4] Yu.N. Karamazin, and A.P. Sukorukov, JETP Lett. 20, 339 (1974)

[5] S. Carrasco, J.P. Torres, D. Artigas, and L. Torner, Opt. Comm. 192, 347 (2001)

[6] A. De Rossi, S. Trillo, A.V. Buryak, and Y.S. Kivshar Opt.Lett. 22, 868 (1997)

[7] X. Liu, L.J. Qian, and F. Wise Phys.Rev.Lett. 82, 4631 (1999)

[8] Y.N.Denisyuk, A.Andreoni, M.Bondani, M.A.C.Potenza, Opt.Lett. 25, 890 (2000)

[9] P.Di Trapani, W.Chinaglia, Opt.Lett. 23, 1653 (1998)

[10] A.Stabinis, G.Valiulis, E.A Ibragimov Opt.Comm. 86, 301 (1991)

Symmetry-breaking instability of multimode vector solitons in Kerr media

C. Cambournac,[1] T. Sylvestre,[1] H. Maillotte,[1]
B. Vanderlinden,[2] P. Kockaert,[2] Ph. Emplit,[2] and
M. Haelterman[2]

[1] *Laboratoire d'Optique P.M. Duffieux,*
Unité mixte CNRS/Université de Franche-Comté 6603
16, route de Gray, 25030 Besançon cedex, France
[2] *Service d'Optique et d'Acoustique, Université Libre de Bruxelles,*
50, avenue F.D. Roosevelt, B-1050 Brussels, Belgium

Abstract: We show experimentally that the two-component two-hump vector soliton exhibits a sharp left-right symmetry-breaking instability in Kerr media. The experiment is performed using molecular re-orientation in CS_2 and the opposite circular polarization states of light as the two components of the vector soliton.
© 2002 Optical Society of America
OCIS codes: (190.3100) Instabilities and chaos; (190.5530) Pulse propagation and solitons (190.4420) Nonlinear optics, transverse effects in

The complex and intriguing dynamics induced by the vector nature of nonlinear physical phenomena have recently witnessed a renewed interest because of their experimental realization in emerging areas of physics. The concept of multicomponent soliton (or *vector soliton*) is such an important example of current interest. It has been introduced in optics by Christodoulides *et al.* [1] in a theoretical study of nonlinear optical wave coupling in birefringent Kerr media, where stationary solitary waves consisting of a bound state of two distinct orthogonally polarized field envelopes were found. Later, Haelterman *et al.* showed that bound states of solitons can also exist without birefringence and four-wave mixing (i.e., coherent nonlinear coupling) simply on the basis of the mutual trapping induced by cross-phase modulation (i.e., incoherent coupling) between the circular polarization components of light in Kerr media [2]. In the spatial domain, incoherent coupling between the field components allows one to simply interpret these solitons as a superposition of the fundamental and the first-order (or higher) modes of the waveguide they induce themselves through self- and cross-phase modulations. That is why they can be regarded as being *multimode vector solitons* [3]. By exploiting the concept of multimode spatial soliton, impressive experiments were then performed in photorefractive materials [4], including incoherent light self-trapping [5] and observation of the dipole-mode vector soliton [6]. The latter two-dimensional two-hump multimode soliton has a fundamental nature, in the sense that it constitutes a "self-generated robust basic composite structure of incoherently coupled fields" [7]. For the completeness of such studies however, the question of stability is a crucial issue to investigate for fundamental as well as applied purposes. Unlike saturable Kerr-like media [8], pure Kerr media were theoretically shown to give rise to unstable propagation of multimode vector solitons [9, 10, 11]. Furthermore, in addition to the nonlinearity saturation, the nonlinear systems considered so far in experiments have the particularity of exhibiting self- and cross-phase modulations of identical strengths. When cross-phase modulation is stronger than self-phase modulation, the multimode soliton undergoes a symmetry-breaking instability [11], an interesting phenomenon that could apply to all-optical switching without threshold. The present work is aimed at presenting the experimental demonstration of this instability.

To obtain cross-phase modulation (CPM) stronger than self-phase modulation (SPM) we consider, for the two components of the vector soliton, the circular polarization states of light propagating in a Kerr medium with a nonlinearity induced by molecular re-orientation, such as in carbon disulfide (CS_2). Hence, the CPM/SPM ratio attains the value of 7 [12], strongly favoring the symmetry-breaking instability of the multimode vector soliton, as explained in Ref. [11]. The experiment is performed in a planar waveguide (to avoid catastrophic beam breakup) and propagation of both circular polarization components is ruled by the two following incoherently coupled nonlinear Schrödinger equations

$$\frac{\partial U}{\partial z} = i\frac{1}{2k}\frac{\partial^2 U}{\partial x^2} + i\gamma(|U|^2\,U + 7|V|^2\,U), \tag{1a}$$

$$\frac{\partial V}{\partial z} = i\frac{1}{2k}\frac{\partial^2 V}{\partial x^2} + i\gamma(|V|^2\,V + 7|U|^2\,V), \tag{1b}$$

where $U(x,z)$ and $V(x,z)$ are the transverse beam envelopes of the circular polarization components of the electromagnetic field (x and z being the transverse and longitudinal coordinates, respectively), k is the wavevector modulus in the waveguide and γ is the nonlinear coefficient. These equations possess a one-parameter family of steady-state (or soliton) solutions consisting of a superposition of an envelope of even parity (say U) with an envelope of odd parity (say V) [10]. An example of such a solution is given in Fig. 1(a) in dimensionless units u and v. U and V can be interpreted physically as being, respectively, the fundamental and the first-order modes of the bimodal waveguide they induce together through the Kerr nonlinearity (here analogous to a two-core waveguide-induced directional coupler). Similarly to the odd-mode of the nonlinear directional coupler (fast mode instability) [13], one can very easily check that the bimodal vector soliton undergoes a symmetry-breaking instability by solving numerically Eqs.(1) with the solution of Fig. 1(a) as initial condition. A typical result is shown in Fig. 1(b). As can be seen, the energy that is initially evenly distributed goes abruptly from one hump towards the other resulting in the destruction of the initial two-core induced waveguide. Interestingly, as was noticed in Ref. [11], after the transient regime the field remains confined in a steady-state single-hump distribution (i.e., both U and V exhibit even parity) corresponding to the fundamental elliptically polarized vector soliton [14].
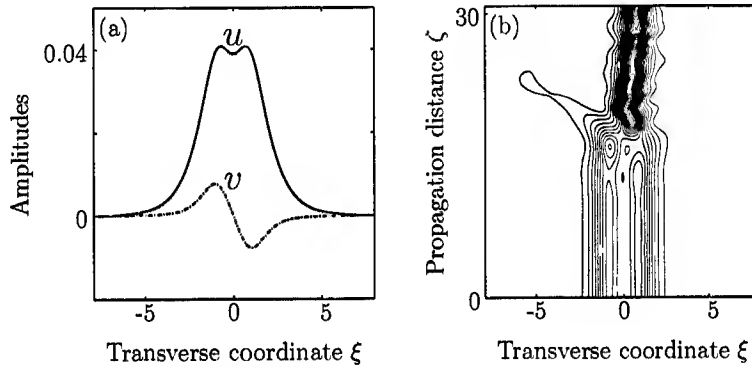
Fig. 1: (a) Envelopes u and v of the circular polarization components of the bimodal vector soliton. (b) Contour plot showing the evolution of the vector soliton in (a) when sightly perturbed by random noise.

The observation of the left-right symmetry breaking of the bimodal vector soliton has been performed in a 3 cm-long planar waveguide made of a 10 μm-thick CS_2 layer sandwiched between two SK5 glass plates corresponding to a refractive index step of $\Delta n = 0.04$ [15]. The difference between the propagation constants (wavevector moduli) of the TE and TM fundamental modes of this waveguide is small enough to be neglected over the propagation distance considered in the experiment, which allows us to consider that the nonlinear medium is isotropic as assumed in the theory [2]. The experimental setup is sketched in Fig.2. A gaussian laser beam coming from a 10 Hz Q-switched, mode-locked and frequency-doubled YAG laser is split into two orthogonally polarized beams by a polarizing beam splitter (PBS). A Michelson interferometer adjusted to a zero relative phase difference is used to shape the U and V components. In one arm, a $\lambda/4$ phase-step mirror (PSM) introduces the π phase-shift necessary to shape the V component of odd symmetry. In both arms, quarter-wave plates ensure transmission of both beams at the output of the PBS after reflection on each mirror. Then, a quarter-wave plate provides the required left- and right-handed circular polarization of both beams. Finally, a combination of lenses images the plane of the mirrors at the input of the waveguide. The output beams then go through a quarter-wave plate and a Wollaston prism (WP) in order to measure the U- and V-wave intensity profiles separately by means of a CCD camera. Fig. 2(a) shows the input beam intensity profiles for both polarization components. The V-wave is characterized by a zero intensity (node) at the origin. Fig. 2(b) shows the same beams at the waveguide output at low intensity (linear regime). According to our experimental parameters, both beams diffract significantly over slightly more than one diffraction length. Fig. 2(c) shows the output U- and V-beam profiles obtained when the power is raised until diffraction broadening is canceled by the nonlinearity, i.e., when the bimodal vector soliton is formed. This condition is characterized by powers of 2.9 kW and 0.9 kW for the U- and V-waves, respectively. As can be seen in Fig. 2(c), although we observe a clear reshaping of wave U that now exhibits two humps (in agreement with Fig. 1(a)), both the output U- and V-waves exhibit the same width as the input waves, confirming in this way, for the first time, the existence of the bimodal vector soliton in pure Kerr media. However, as mentioned above, this soliton is not stable. Indeed, the intensity profiles of Fig. 2(c) are obtained only for 38% of the laser shots. The other 62% of the shots are characterized by a strongly asymmetric

output in which the beam is randomly displaced either on the left or on the right of the initial beam axis. A typical example of asymmetric output is shown in Fig. 2(d) where the V-wave envelope has lost its node due to the energy transfer from one core to the other of the initial self-induced two-core waveguide. Apart from some residual energy in the wings of the beam profile, the resulting beam has the characteristics of the fundamental elliptically polarized soliton [9, 14] in agreement with the numerical simulations [11]. Importantly, these asymmetric outputs appear to be almost evenly distributed between left (53%) and right (47%), which indicates that they are induced by the random noise of the laser. The 38% of symmetric shots correspond to situations in which the noise asymmetry is too small to induce the symmetry breaking over one diffraction length.

Fig. 2: LEFT: Schematic of the experimental setup. RIGHT: Intensity profiles of the circular polarization components measured with the CCD camera (the insets show the corresponding total intensity profiles): (a) Input profiles, (b) output profiles at low intensity, (c) output profiles in the soliton regime, (d) right-oriented asymmetric output profile resulting from the symmetry breaking of the soliton.

In summary, we have demonstrated experimentally the existence and the symmetry-breaking instability of the bimodal vector soliton in optical Kerr media. Because the mechanism that underlies this instability has a universal nature, the present study has potential ramifications in other contexts. In particular, our results suggest that symmetry breaking can be observed in a binary mixture of miscible Bose-Einstein condensates (BECs) set in the bimodal vector soliton configuration, i.e., a configuration in which one BEC has a symmetric bell-shaped envelope that confines another BEC exhibiting an antisymmetric envelope. Finally, besides the fundamental interest of the present study, we can also expect interesting application to all-optical "thresholdless" switching since the symmetry breaking can, in principle, be triggered by an arbitrarily small perturbation.

References

1. D. N. Christodoulides and R. I. Joseph, Opt. Lett. **13**, 53 (1988).
2. M. Haelterman, A. P. Sheppard, and A. W. Snyder, Opt. Lett. **18**, 1406 (1993).
3. A. W. Snyder, S. J. Hewlett, and D. J. Mitchell, Phys. Rev. Lett. **72**, 1012 (1994).
4. See e.g. M. Segev and D. N. Christodoulides, Opt. Photon. News **72**, 71 (2002);
   A. S. Desyatnikov *et al.*, J. Opt. Soc. Am. B **19**, 586 (2002) and references therein.
5. M. Mitchell, M. Segev, T. H. Coskun, and D. Christodoulides, Phys. Rev. Lett. **79**, 4990 (1997).
6. T. Carmon *et al.*, Opt. Lett. **25**, 1113 (2000); W. Krowlikowski *et al.*, Phys. Rev. Lett. **85**, 1424 (2000).
7. D. Neshev, W. Krolikowski, D. E. Pelinovsky, G. McCarthy, and Yu. Kivshar, Phys. Rev. Lett. **87**, 103903 (2001).
8. E. A. Ostrovskaya, Yu. Kivshar, D. V. Skryabin, and W. J. Firth, Phys. Rev. Lett. **83**, 296 (1999).
9. Y. Silberberg and Y. Barad, Opt. Lett. **20**, 246 (1995).
10. M. Haelterman and A. P. Sheppard, Phys. Rev. E **49**, 3376 (1994).
11. P. Kockaert and M. Haelterman, J. Opt. Soc. Am B **16**, 732 (1999).
12. P. D. Maker and R. W. Terhune, Phys. Rev. A **137**, 801 (1965).
13. S. Trillo, S. Wabnitz, E. M. Wright, and G. I. Stegeman, Opt. Lett. **13**, 672 (1988).
14. M. Haelterman and A. P. Sheppard, Phys. Lett. A **194**, 191 (1994).
15. C. Cambournac, H. Maillotte, E. Lantz, J. M. Dudley, and M. Chauvet, J. Opt. Soc. Am B **19**, 574 (2002).

Skewed coherence along space-time trajectories in parametric generation processes

Antonio Picozzi,[1] and Marc Haelterman[2]

[1] C.N.R.S., L.P.M.C., Université de Nice –Sophia Antipolis, Parc Valrose, 06108 Nice cedex,
picozzi@unice.fr

[2] 50 Avenue F. D. Roosevelt, Université Libre de Bruxelles, C.P. 194/5, B-1050 Bruxelles

Abstract: Considering the spatio-temporal problem of the parametric generation process, we show theoretically that the down-converted fields exhibit, as a general rule, a hidden coherence characterized by skewed coherence lines along specific space-time trajectories.
©2002 Optical Society of America
OCIS codes: 190.4410, 190.4970, 030.1640

1. Introduction

The achievement of efficient parametric amplification of broadband spectral light has been the object of particular interest these last few years. In this perspective, several recent experiments investigated the properties of coherence of the parametric down-converted fields generated from quantum noise fluctuations [1]. However, so far the spatial and temporal coherence properties of the down-converted fields have not been analyzed into a general framework.

We analyze theoretically and numerically the spatial and temporal coherence of the generated waves and show that they evolve, as a rule, to a specific state that contains a hidden coherence [2], i.e., a coherent state that can not be identified by means of the standard concepts of coherence theory. Indeed, one usually deals with two distinct concepts of optical coherence [3]: Temporal coherence refers to the ability of a field to interfere with a delayed (but not spatially shifted) version of itself, whereas spatial coherence refers to the ability of the field to interfere with a spatially shifted (but not delayed) version of itself. As we shall see, this dichotomous picture of optical coherence fails to describe the novel state of coherence revealed by our study of the parametric generation process. Indeed, our analysis reveals that the parametric interaction generates fields that are self-correlated along specific spatio-temporal trajectories. In other words, the coherence of the fields is neither spatial nor temporal, but skewed in the space-time reference frame.

2. Spatial and temporal properties of coherence

We consider the parametric process in its linear regime of interaction where the depletion of the pump wave may be neglected. The propagation of the two down-converted fields (i.e., the signal and the idler) is studied through their slowly varying envelopes $A_{1,2}$ that obey the usual linear coupled evolution equations

$$(\partial_z + w\partial_t + \rho\partial_y + i\eta_1\partial_{yy})A_1 = \kappa A_2^*, \qquad (\partial_z - w\partial_t - \rho\partial_y + i\eta_2\partial_{yy})A_2 = \kappa A_1^*. \qquad (1)$$

The parameters $w = (v_1^{-1}-v_2^{-1})/2$ and $\rho = (\rho_1-\rho_2)/(v_1+v_2)$ represent, respectively, the temporal and spatial walk-off between the daughter waves $A_{1,2}$ along the longitudinal z and transverse y axes, where $v_{1,2} = (v_{1,2}, \rho_{1,2})$ are the longitudinal and transverse components of the group-velocities of $A_{1,2}$. The parameters $\eta_{1,2} = 1/(2k_{1,2})$ are the diffraction coefficients of both waves and the parameter $\kappa = \sigma e_0$ accounts for the nonlinear $\chi^{(2)}$ efficiency σ, and the constant pump amplitude $A_3 = e_0$. The symmetric form of Eqs.(1) with respect to these velocities is obtained by writing the equations in the reference frame traveling at the average velocity of the fields $A_{1,2}$.

To investigate the coherence properties of the daughter waves $A_{1,2}$ during the generation process, we determine the spatio-temporal autocorrelation functions $C_i(z;t,y) = <A_i(z,t'+t,y'+y) A_i^*(z,t',y')>$ ($i=1,2$), that may be calculated following the Green's function approach (see Ref.[2] for details). Let us first discuss the coherence properties of $A_{1,2}$ in the limit of zero diffraction parameter, i.e., $s = \eta/w \rightarrow 0$, where the function $C_i(z;t,y)$ takes the following form [2]:

$$C_{1,2}(z;t,y) \propto \exp\left[-t^2/(2\tau_c^2)\right] \delta(y - rt), \qquad (2)$$

where δ denotes the Dirac distribution. The first factor of $C_{1,2}$ is a gaussian whose temporal width increases with z according to $\tau_c = w(2z/\kappa)^{1/2}$, which corresponds to an increase of temporal coherence. This increase of coherence is well known since the pioneering works on parametric fluorescence [4]. It is due to the temporal walk-off between

the daughter waves, w, that smoothes down the initial noisy fields. However, the second factor that appears in Eq.(2) reveals a previously unrecognized fundamental aspect of parametric generation processes: The factor $\delta(y - r\,t)$ clearly limits the extension of the correlation function to the region surrounding the line $y = r\,t$. This means that the waves $A_{1,2}$ become coherent along specific spatio-temporal trajectories parallel to the line $y = r\,t$, whereas the initial incoherence remains unchanged between points that do not belong to such trajectories.

This unexpected finding has been checked by numerical simulations of Eqs.(1). As shown in Fig. 1a, the fields evolve to a peculiar state of coherence characterized by the presence of skewed spatio-temporal lines of correlation, in complete agreement with theory [Eq.(2)]. To interpret physically this phenomenon, we must consider the fact that the coherence of the fields appears thanks to the feedback action caused by the walk-off between the daughter waves [5]. In the framework of the present spatio-temporal analysis, the concept of walk-off is generalized to two dimensions and hence has a vector nature. The feedback action thus takes place between points belonging to lines that are parallel to the walk-off vector (i.e., in the direction of the velocity difference v_1-v_2, as illustrated in Fig. 1b), which explains why coherence develops only along such lines.

In the particular limit where the parameter $r = \rho/w$ tends to zero (or infinity), the interaction takes place in the absence of spatial ρ (temporal w) walk-off and the trajectory of spatio-temporal coherence becomes parallel to the temporal (spatial) axis. It is only in these two particular cases that the coherence properties of the generated fields can be correctly described by the usual concepts of spatial and temporal coherence [3]. In the general case of skewed coherence, the use of these usual concepts would lead to the conclusion that the field exhibits no coherence since it is neither spatial nor temporal but hidden along spatio-temporal trajectories.
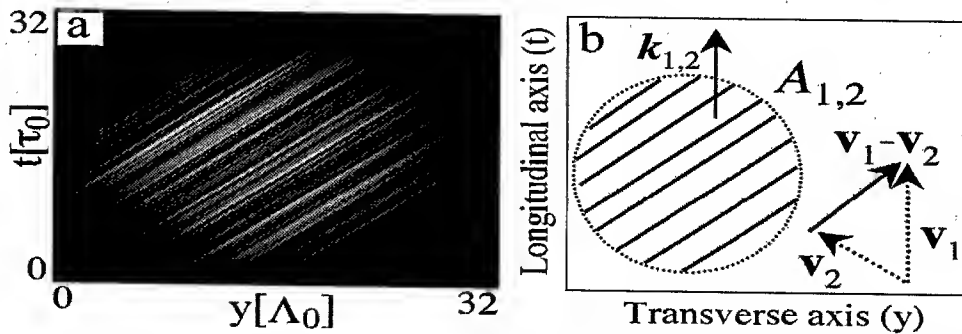
Fig. 1. Skewed spatio-temporal coherence: (a) space-time intensity distribution of $|A_1\,(t,y)|$ at $z = 11\ \kappa^{-1}$ in the absence of diffraction ($s = 0$) for $\kappa^{-1} = 1.88$mm ($\tau_0 = 0.35$ps, $\Lambda_0 = 68\ \mu$m). (b) Schematic representation of the group-velocities $v_{1,2}$: Coherence emerges along lines parallel to v_1-v_2 (the collinear type II configuration is considered here).

Let us consider the influence of diffraction ($s \neq 0$) on the coherence of the generated waves. As illustrated in Fig. 2a, the diffraction causes the lines of coherence to cross each other, whereas they were simply juxtaposed side by side in the diffractionless case (Fig. 1a). This observation is in agreement with the analytical expression of the autocorrelation function that may be easily calculated for $s \neq 0$ [2]:

$$C_{1,2}^s(z;t,y) \propto \frac{\exp\left[-t^2/(2\tau_c^2)\right]}{\sqrt{l_0^2 - 4ist}}\ \exp\left(-\frac{(y - rt)^2}{l_0^2 - 4ist}\right) \tag{3}$$

where l_0 represents the initial correlation length of the down-converted fields. Fig. 2b shows that this autocorrelation function exhibits an aperture around the direction $y = r\,t$, a feature that naturally reflects the appearance of coherence lines of different slopes in the presence of diffraction, as revealed in Fig. 2a. For higher values of the diffraction parameter the aperture of the autocorrelation results in a drastic reduction of coherence characterized by speckle-like patterns. This effect is naturally due to the random interferences between the intersecting uncorrelated spatio-temporal lines whose slopes span the larger aperture of $|C_{1,2}^s(z;t,y)|$. Note that this theoretical analysis explains in simple terms the experimental observation reported in Ref.[1a] where it is shown that diffraction yields a coherent parametric amplification only for very narrow injected pump beams and thus far from the quasi-plane-wave configuration considered in our analysis. Conversely, as the beam size of the pump increases, the amplification process becomes incoherent in agreement with our theory.

3. Young's interference experiment

The previous discussion reveals that the usual technique that consists in measuring the spectral properties of a field to determine its coherence can not be used to characterize the hidden coherence of the generated waves. It is

therefore important to propose alternative techniques. We show that the classic Young's interference experiment is able to demonstrate the phenomenon of skewed coherence (Fig. 2c). Indeed, we calculated the visibility V of the fringe pattern generated when making one of the daughter waves, say A_1, pass through the two Young's pinholes. The visibility is determined by $V(\tau) = |\Gamma_{1,2}(\tau)| / [\Gamma_{1,1}(0) \Gamma_{2,2}(0)]^{1/2}$ where $\Gamma_{1,2}(\tau) = \langle A_1(t'+\tau,y_1) A_1^*(t',y_2) \rangle$ is the mutual coherence function [3], which can be calculated explicitly by means of the Green's function approach [2]:

$$V = \frac{\exp[-\tau^2/(2\tau_c^2)]}{(1+16s^2\tau^2/l_0^2)^{1/4}} \exp\left[-\frac{l_0^2(a+r\tau)^2}{l_0^2+16s^2\tau^2}\right] \tag{4}$$

where $a = y_2-y_1$ is the distance between the two pinholes and τ is the time delay between the two beams coming from the two pinholes [3]. In contrast with the usual symmetric fringe patterns encountered in Young's experiments, $V(\tau)$ displays an asymmetric shape characterized by a hump localized in $\tau \sim -a/r$ (see Fig. 2d). This asymmetry is actually the signature of the presence of skewed lines of spatio-temporal coherence: It merely reflects the ability of the daughter wave to interfere with the spatially shifted version of itself provided it is delayed by an appropriate quantity determined by the slope r of the spatio-temporal lines of coherence, i.e., $\tau \sim -a/r$, as indicated in Eq.(4). According to Eq.(4) and the numerical simulation reported in Fig. 2a, the phenomenon of skewed coherence could be easily demonstrated in Young's experiment with a bulk BBO crystal in the collinear type II configuration.
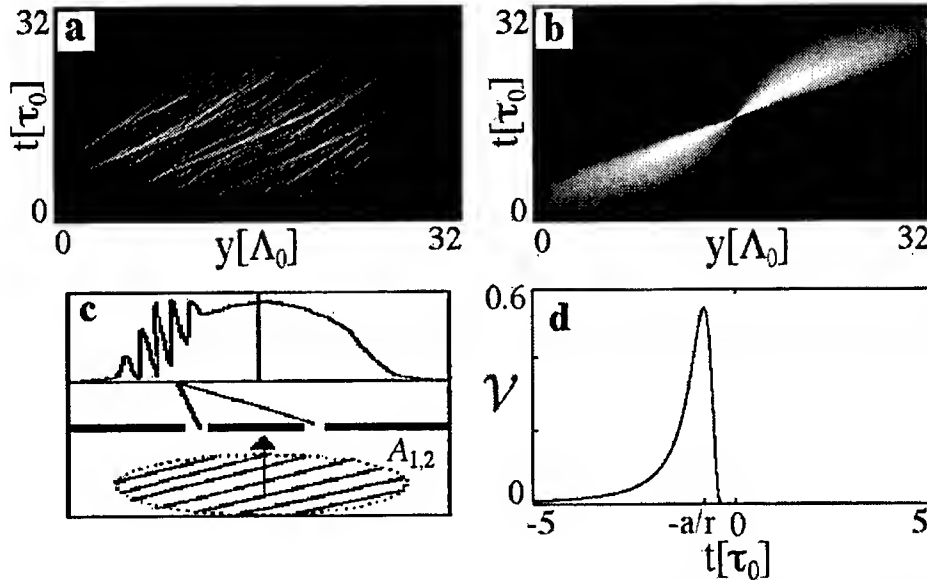
Fig. 2. (a) Same as in Fig.1a, except that diffraction is included (s = 210m²s⁻¹). (b) Respective autocorrelation function $|C_{1,2}(z;t,y)|$ [Eq.(3)] that illustrate the aperture of a cone of spatio-temporal coherence along the trajectory $y = r t$. (c) Schematic representation of the Young's interference experiment. and (d) repective asymmetric pattern of the fringe visibility $V(\tau)$ [Eq.(4)] demonstrating the skewed coherence phenomenon ($\tau_0 = w/\kappa = 0.35$ps, $\Lambda_0 = \rho/\kappa = 68$ μm).

4. Conclusion

In summary, we analyzed the coherence properties of the parametric generation process and showed that the generated waves exhibit a hidden coherence under the form of skewed spatio-temporal coherence lines. We showed that despite the fact that these new coherent states cannot be identified through the standard concepts of spatial and temporal coherence, they can be demonstrated by means of simple methods such as the Young's interference experiment. The experimental verifications of our predictions would be of great interest, on the one hand, for the fundamental study of this previously unrecognized form of optical coherence, and, on the other hand, for a better knowledge and control of broadband practical traveling-wave optical parametric generators [6].

References

[1] See, e.g., P. Di Trapani et al., Phys. Rev. Lett. 81, 5133 (1998); J. Arlt et al., Phys. Rev. A 59, 3950 (1999).

[2] A. Picozzi and M. Haelterman, Phys. Rev. Lett. 88, 083901 (2002).

[3] See e.g., L. Mandel and E. Wolf, Optical Coherence and Quantum Optics (Cambridge University Press, New York, 1995), Chap. 4.

[4] R. L. Byer and S. E. Harris, Phys. Rev. 168, 1064 (1968).

[5] A. Picozzi and M. Haelterman, Phys. Rev. E 63, 056611 (2001).

[6] See, e.g., P. Di Trapani et al., J. Opt. Soc. Am. B 14, 1245 (1997).

Nonlinear Guided Waves

Nonlinear Fiber Optics and Pulse Propagation

Monday, September 2, 2002

Marc Haelterman, Univ. Libre de Bruxelles, Belgium
Presider

NLMC
2:00pm – 4:00pm
Auditorium

What is the role of modulational instability in ultra-high repetition rate pulse generators based on passive and active fiber cavities ?

Stéphane Coen

Service d'Optique et d'Acoustique, Université Libre de Bruxelles, CP 194/5
Av. F. D. Roosevelt 50, B-1050 Brussels, Belgium
Tel : +32-2-650.28.01, Fax : +32-2-650.44.96, e-mail : Stephane.Coen@ulb.ac.be

Abstract: We study experimentally the role of modulational instability in two classes of devices that are commonly called "modulational instability lasers". For one of them, this denomination is found to be misleading.

For both its fundamental and applied interests, modulational instability (MI) in fibers has attracted growing attention over the last two decades (see e.g., [1]). As regards applications, MI provides a natural means of generating ultra-short pulses at ultra-high repetition rates and is thus potentially useful for the development of future high capacity optical communication systems. MI in an optical fiber leads to the spontaneous break-up of continuous wave (cw) excitation into a periodic train of ultra-short pulses, provided that the dispersion of the fiber is anomalous and the cw input power sufficiently high [2, 3]. Owing to the simplicity of this ultra-short pulse formation process, the exploitation of MI has been considered in many theoretical and experimental studies for the realization of laser sources adapted to ultra-high bit-rate optical transmissions. However, despite its simplicity, the MI process in fibers is difficult to control and presents, in this respect, some important drawbacks. For instance : - The required cw power level is relatively high and is, in general, much larger than the power threshold for stimulated Brillouin scattering so that, in practice, cw operation cannot be performed. - The pulses generated by MI are supcrimposed on a complex background field, which is detrimental to their subsequent propagation in fiber.

To circumvent the difficulties inherent in the control of the MI process, many configurations have been studied. In particular, Nakazawa *et al* have suggested the use of a coherently driven passive fiber cavity [4]. In this configuration [see Fig. 1(a)], a cw beam is injected into a ring cavity made of a fiber with anomalous dispersion. During the first round-trips in the cavity, sideband waves grow from noise due to MI gain. If the MI gain is larger than the cavity loss, oscillation of the MI sidebands can be sustained and steady-state pulse trains are generated. Owing to this principle of operation, this simple device has been called MI laser [4]. Considering a high-finesse cavity, we note that the strong field-confinement effect that occurs at resonance leads to a substantial decrease of the cw pump power necessary to obtain MI. Moreover, one can easily avoid SBS by incorporating an optical isolator into the cavity to prevent the buildup of the backscattered Brillouin Stokes wave. Additionally, the cw background field superimposed on the generated pulses can be suppressed by destructive interference with the residual pump beam at the cavity output [5].

Tough the initial experimental demonstration of the MI laser has been made with a pulsed pump beam [4], we have recently successfully operated this device in the cw regime thanks to the help of an interferometrically-stabilized high finesse all-fiber cavity. In our first experiment, the laser cavity was made up of 100 m of standard single-mode fiber, which has led to the generation of a 52 GHz repetition-rate pulse train with a pump power of 100 mW [6]. Later, we have been able to increase the repetition rate of our MI laser up to 150 GHz (see Fig. 2) by decreasing the intracavity dispersion through the use of a dispersion-shifted fiber. It is even possible to increase the repetition rate of the laser while decreasing the required pump power through intracavity dispersion management. In this way, the overall cavity
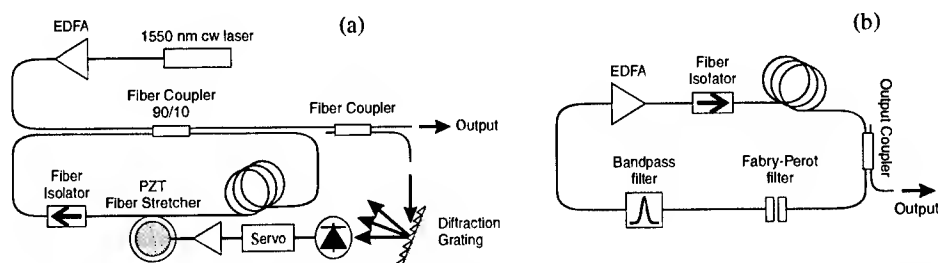

Fig. 1. Schematic setup of the passive (a) and active (b) MI laser cavity configurations

NLMC1-2

Stéphane Coen, What is the role of modulational instability in ultra-high repetition rate pulse generators based on ... ?   NLGW/2002 Page 2
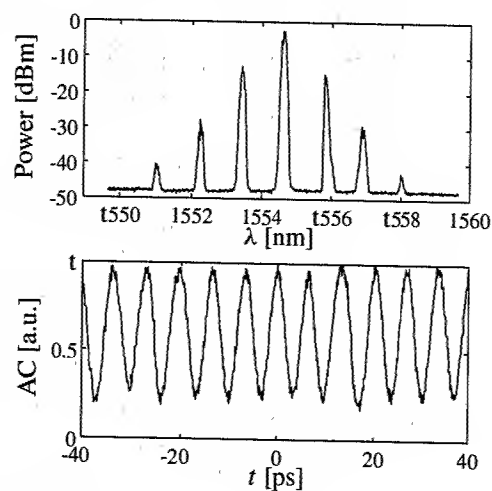
Fig. 2. Optical spectrum (top) and intensity autocorrelation (bottom) of the 150 GHz pulse train generated by the passive-cavity MI laser with a dispersion shifted fiber and 110 mW input power.
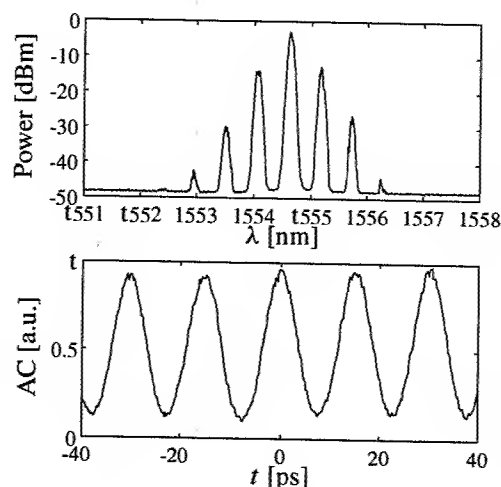
Fig. 3. Optical spectrum (top) and intensity autocorrelation (bottom) of the 70 GHz pulse train generated by the passive-cavity MI laser with a dispersion managed cavity and 70 mW input power.

dispersion can be reduced while the cavity length is simultaneously increased. The low average dispersion leads to the generation of a high-repetition-rate pulse train while the long cavity length increases the effective nonlinearity of the device, therefore reducing the required input power. The successful operation of a dispersion-managed passive-cavity MI laser is demonstrated in Fig. 3. Here, we have combined 100 m of standard fiber and 100 m of dispersion-shifted fiber so as to generate 70 GHz pulse trains with only 70 mW of pump power, which constitutes a significant improvement in comparison with a cavity made of standard fiber alone. Additionally, the fact that we are able to predict the laser repetition rate with a simple average-dispersion model indicates that the cavity dynamics is averaged over many round-trips and that it can be accurately described with a simple mean-field equation.

In parallel with the experiments performed in coherently driven passive cavities, several authors have investigated the generation of pulse trains in active fiber devices such as erbium-doped fiber lasers. In this context, passive mode-locking techniques that take advantage of the fiber nonlinearity to create an effective ultra-fast saturable absorber appear as simple solutions to obtain all-optically ultra-high repetition rates. Interestingly, several authors have reported in the last few years the spontaneous generation of pulse trains with repetition rates in excess of 100 GHz from passively mode-locked fiber ring lasers [7, 8]. As initially demonstrated [7], this phenomenon can occur in very simple laser cavities incorporating only an optical amplifier, a bandpass (BP) filter, and an anomalously dispersive fiber [see Fig. 1(b)]. Mode-locking was interpreted as resulting from a MI of the cw field resonating in the laser cavity. MI explains naturally the occurrence of ultra-high repetition rate pulse trains [1], and this interpretation is consistent with the observed linear dependence between the intracavity power and the square of the laser repetition rate [7]. This so-called self-induced MI laser has later been improved by introducing a Fabry-Perot (FP) filter inside the laser cavity [8]. The role of the FP filter is to select the modes that grow in the pulse formation process in order to stabilize the laser repetition rate on the FP free spectral range. Also, by selectively confining the intracavity energy in the longitudinal modes of the FP filter, the power threshold for the generation of pulses is drastically reduced, which allows cw operation of the laser with a relatively low pump power.

In view of its potential interest for ultrafast technologies, we have revisited this so-called self-induced MI laser. As a matter of fact, we have verified that its principle of operation is not intrinsically linked to MI in contrast with the passive cavity device discussed in the previous paragraphs. To offer a conclusive proof of this assertion, we have performed both numerical simulations and experiments of the laser operating with an overall normal dispersion instead of the anomalous dispersion necessary to get MI [9]. The result is clear: The laser still generates pulses, which means that pulse formation and mode-locking does not rely on MI. The mode-locking mechanism is in fact a rather complex process that has been described theoretically by Quiroga-Teixeiro et al [10] It can be identified as resulting from a dissipative four-wave mixing (DFWM) process in which only the two central frequencies selected by the BP and FP filters experience net positive gain and transmit their energy by four-wave mixing to their higher-order harmonics that
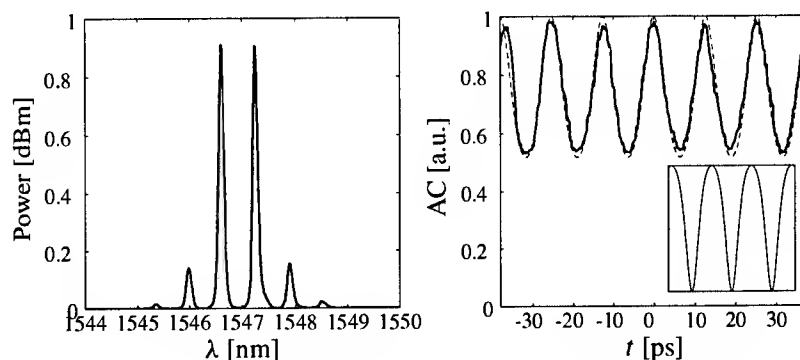
Fig. 4. Optical spectrum (left) and intensity autocorrelation (right) of the 80 GHz pulse train obtained with a DFWM mode-locked laser operated in the normal dispersion regime. The inset shows the theoretical pulse profile whose autocorrelation (dashed curve) is found to match the experimental measurement.

undergo linear losses due to the band-pass nature of the filter. As a result of the parametric wave mixing, the phase of the longitudinal modes are locked and pulses are formed.

Our experimental results are presented in Fig. 4 which shows the autocorrelation and the optical spectrum of the 80 GHz repetition rate pulse train generated by our normally dispersive laser. In inset, we also present a theoretical temporal profile of a dark pulse train whose autocorrelation is found to match the experimental observations. The fact that our laser generates dark soliton-like pulses is confirmed by the spectrum that exhibits an even number of lines with two central peaks of identical amplitude, and by the high level of background that is seen in the autocorrelation. The measure of the average intracavity power (62 mW) and of the temporal width of the generated pulses (5 ps) is also consistent with the characteristics of fundamental dark solitons. We must stress that the generation of dark pulses in our laser is not accounted for by a model based on MI but is correctly predicted by the DFWM mode-locking theory [10]. We note that we can interpret pulse formation through DFWM mode-locking in the temporal domain as resulting from the nonlinear conversion of the high-frequency beat signal selected by the combined action of the FP and BP filters into a soliton train. As a matter of fact, this process is well known to lead to the generation of dark pulse trains in the normal dispersion regime without the need for MI [11].

In summary, we have studied two different devices that are commonly referred to in the literature as "modulational instability lasers". In both cases, we were able to obtain cw pulse trains with repetition rates in the 100 GHz domain. However, our observations indicate that only in the passive cavity configuration can pulse formation be attributed to MI. In the active cavity configuration, a description in terms of MI appears misleading as it cannot account for the generation of dark pulse trains in the normal dispersion regime. Rather, we demonstrate that the pulse formation at play in this device relies on DFWM mode-locking as proposed in Ref. [10]. Our experiments show that the physics of this so-called self-induced MI laser is not as simple as what is commonly admitted. In fact, reference to MI in the literature is only justified by the simple linear relation that exists between the generated signal power and the square of its repetition frequency. Such a relation is, however, the result of the simplicity of the phenomenology inherent to dispersive Kerr media and can, in fact, be obtained from a simple dimensional analysis of the model. One of the natural issues of our paper is therefore to show that one should not draw conclusions too quickly from the observation of a simple mathematical law.

1. G. P. Agrawal, *Nonlinear Fiber Optics, Optics and Photonics Series*, 3rd ed. (Academic Press, San Diego, 2001).
2. A. Hasegawa and W. F. Brinkman, IEEE J. Quantum Electron. **16**, 694 (1980).
3. K. Tai, A. Hasegawa, and A. Tomita, Phys. Rev. Lett. **56**, 135 (1986).
4. M. Nakazawa, K. Suzuki, and H. A. Haus, Phys. Rev. A **38**, 5193 (1988).
5. S. Coen and M. Haelterman, Opt. Commun. **146**, 339 (1998).
6. S. Coen and M. Haelterman, Opt. Lett. **26**, 39 (2001).
7. P. Franco, F. Fontana, I. Cristiani, M. Midrio, and M. Romagnoli, Opt. Lett. **20**, 2009 (1995).
8. E. Yoshida and M. Nakazawa, Opt. Lett. **22**, 1409 (1997).
9. T. Sylvestre, S. Coen, Ph. Emplit, and M. Haelterman, Opt. Lett. **27**, 482 (2002).
10. M. Quiroga-Teixeiro, C. Balslev Clausen, M. P. Sørensen, P. L. Christiansen, and P. A. Andrekson, J. Opt. Soc. Am. B **15**, 1315 (1998).
11. D. J. Richardson, R. P. Chamberlin, L. Dong, and D. N. Payne, Electron. Lett. **30**, 1326 (1994).

Temporal Modulational Instability Controlled by Pulse-Envelope Dynamics

Domenico Salerno[1], Jose Trull[2], Gintaras Valiulis[3], S. Trillo[4], C. Conti[4], and Paolo Di Trapani[2]

[1] Faculty of Sciences, University of Milano, 20100 Milano, Italy
[2] INFM and Dipartimento di Scienze CC.FF.MM. –Università degli Studi dell'Insubria –Via Valleggio, 11 –22100 COMO –Italy
[3] Department of Quantum Electronics –Vilnius University –Sauletekio g . 9 –r. III - LT 2040 VILNIUS –Lithuania
[4] Istituto Nazionale di Fisica della Materia (INFM)-RM3, Via della Vasca Navale 84, 00146 Roma, Italy

Abstract: In second harmonic generation, temporal splitting into a train of solitons is observed owing to modulational instability seeded by a self-induced pulse-envelope modulation.

The modulational instability (MI) is a fundamental process in quadratic nonlinear interaction, leading to soliton formation, wave-packet break-up and spatio-temporal coupling [1]. Up to date, the experimental analysis has characterized the MI-induced beam spatial break up; the main attempt has been that of recovering the intensity dependence expected from noise-induced dynamics in the 2-D spatial domain, with the single exception of [2] where corrections due to temporal pulse compression were considered too. The resulting scenario leaves opened two important questions: (i) since the noise lives naturally in 3-D, which are the operating conditions that might eventually force the dynamics in a lower dimensional space? (ii) Which is the process, competing with the noise-induced one, capable of leading in some case to the spontaneous occurrence of pattern with a good regularity [3]?.

An indirect indication of the natural 3-D nature of the MI process comes from ref [2], in which it was shown that the threshold for the spatio-temporal solitons (STS) formation is quite close to that of their MI-induced spatial break-up, in the non-localized dimension. In support to this claim, it is worth noting how the best agreement between the experiment and the spatial-model predictions was obtained when the MI process was "forced" in the pure spatial domain by seeding it with a spatial modulation that largely overcome the 3-D noise [4].

In this work we have proceeded in a somewhat similar way as in ref. [4], forcing here the MI process to take place in the pure temporal domain. Here the forcing temporal modulation, however, was not provided externally as in ref [4], via the interference of two waves, but raised spontaneously due to a peculiar pulse-envelope control (PEC), which we will describe here below in the numerical section of the paper. The spatial analogous of this effect, we believe, has to be considered as the source of regular pattern formation in ref [3].

Figure 1 shows the experimental result concerning the multiple-shot intensity autocorrelation of the first harmonic (FH) pulse exiting the nonlinear crystal. The operating conditions (see figure caption) are equivalent to those used for the temporal-soliton formation in second-harmonic (SH) generation with tilted pulses [5], the only difference being that here the crystal was operated in phase-matching regime. Note that the tilted-pulse configuration is essential for the process in exam since it cancels the dominant group-velocity mismatch (GVM) and provides a large, negative, group-velocity dispersion (GVD), thus allowing MI process to occur at intensities low enough to prevent dominance of higher-order nonlinear effects. Note that the presence of a numher of well distinguishahle peaks in the autocorrelation proves that the input pulse experienced a temporal break-up in a sequence of pulses

with rather constant separation in time. In fact, a chaotic breakup would lead to a single central pcak in the autocorrelation.
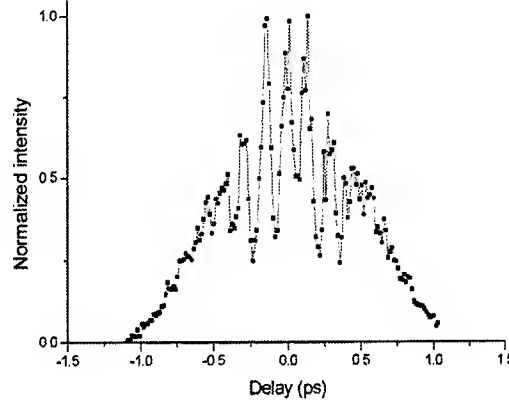

Figure 1 Experimental output pulse autocorrelation of FH pulse at phase matching. Crystal: 7 mm type I BBO. $I_{inp}=13$ GW/cm^2, $\tau_{pulse}=200$ fs. Tilted pulse configuration as in ref [5].

In order to clarify the underlying mechanism that controls the breakup we performed numerical simulation of the process adopting a pure temporal (1-D) model, in which thc pulse tilt was accounted for *via* effective GVD and GVM valucs. The contribution of the real and imaginary cubic nonlinearity was also accounted for in the model. The analysis brought us to the following conclusions:

(i)   In the absence of noise, a long pulse with an initially gaussian-type profile brcaks up into a regular train due to the alternance of pump depletion and back conversion across the pulse. In phase matching, both FH and SH pulscs exhibit a high-contrast modulation, initially with opposite phase, whose frequency increases with the pulse propagation inside the crystal. When the frequency becomes large enough to lead to dominant GVD effects then self-trapping between FH and SH occurs and a train of temporal solitons appcars. Figure 2a shows the calculated intensity autocorrelation in case of a fairly long (5ps) input pulse. In this case the propagation is by far too short to let any GVD effect (*e. g.* self trapping) to occur. The modulation is entirely due to a GVD-free pulse envelope effect.

(ii)   In the presence of noise, the same (long) pulse exhibits completely different dynamics, since the GVD effect starts immediately and causes a chaotic breakup of the pulse. The resulting autocorrelation, shown in Figure 2b, exhibits a single, thin, spike at 0 delay, whilst a trace of the previous effect is barely visible in the weak modulations of its profile. The long-pulse dynamics is therefore virtually noise dominated.

(iii)   On shortening the input pulse, the two effects start to compete and finally the first dominate over the second, in the regime in which our experiment was done. Figure 3 report the intensity autocorrelation for the same operating conditions as in Fig. 1. In this case, the calculations gave identical results in the presence and in the absence of noise, proving that the breakup is here fully controlled by the pulse-envelope effect (PEC regime). The FH and SH are here self-trapped after few mm in the crystal, leading to a short sequence of solitons to appear.

(iv)   We note that the two-photon absorption is relevant in our regime (due to large SH content in phase matching), affecting quantitatively (but not qualitatively) our results.
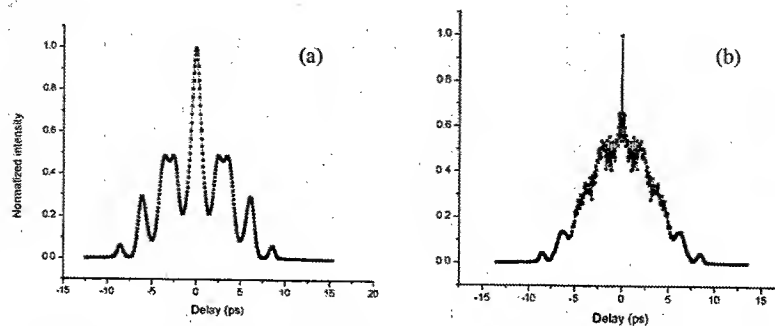
Figure 2 Numerical pulse autocorrelation corresponding to the fundamental pulse with (a) and without (b) presence of noise for the case of incident 5 ps pulse. Crystal: 10 mm type I BBO. I_{inp}=13 GW/cm^2. Tilted puse configuation
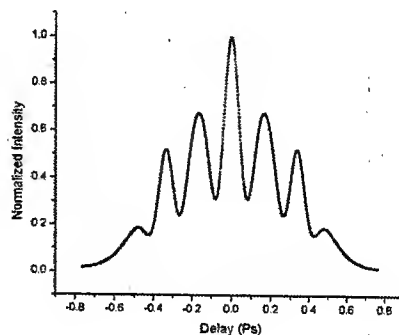

Figure 3 Numerical pulse autocorrelation corresponding to the fundamental pulse with presence of noise for the case of incident 200 fs pulse. Crystal: 7 mm type I BBO. I_{inp}=13 GW/cm^2. Tilted pulse configuration.

In summary we have shown that the pulse envelope modulation due to periodic pulse evolution plays a fundamental role in the dynamics of the instability leading to temporal pulse splitting of ultrashort pulses in bulk quadratic media. The performed simulations in the 1-D temporal are in good agreement with the experimental data, indicating that the observed dynamics actually takes place in the pure temporal domain. We like to stress that in the long-pulse case one should not necessarily expect the dynamics presented in Figure 2(b), whose features are limited to the adopted 1D temporal model. On the contrary, the 3D nature of noise might lead to spatio-temporal nonlinear effects [6,7].

References

[1] Alexander V. Buryak, Paolo Di Trapani, Dmitry V. Skyrabin and Stefano Trillo, "Optical solitons due to quadratic nonlinearities: from basic principles to futuristic applications", Phys.Rep. (accepted for publication)

[2] Xiang Liu, Kale Beckwitt and Frank Wise, "Transverse instability of optical spatiotemporal solitons in quadratic media", Phys.Rev.Lett. **85**, 1871-1874 (2000)

[3] R.A. Fuerst, D-M. Baboiu, B. Lawrence, W.E. Torruellas, G.I. Stegeman, S. Trillo and Stefan Wabnitz. "Spatial modulational instability and multisolitonlike generation in a quadratically nonlinear optical medium", Phys.Rev.Lett. **78**, 2756-2759 (1997)

[4] R. Schiek, H. Fang, R. Malendevich and G.I. Stegeman, "Measurement of modulational instability of second-order nonlinear optical eigenmodes in a one-dimensional system", Phys.Rev.Lett. **86**, 4528-4531 (2001).

[5] P. Di Trapani, D. Caironi, G. Valiulis, A. Dubietis, R. Danielius and A. Piskarskas, "Observation of temporal solitons in second-harmonic generation with tilted pulses", Phys.Rev.Lett. **81**,570-573 (1998)

[6] S.Trillo, C. Conti, P. Di Trapani, O. Jedrkiewicz, J. Trull, G. Valiulis and G. Bellanca "Coloured conical emission via second harmonic generation" Opt. Lett. (submitted)

[7] C.Conti, S. Trillo, P. Di Trapani, O. Jedrkiewicz, G. Valiulis and J. Trull. Electromagnetic nonlinear X waves Phys.Rev.Lett (submitted)

Generation of entanglement between frequency bands via a nonlinear fiber propagation and a spectral pulse shaping

F. Kannari, D. Fujishima, M. Takeoka*, K. Ohno, M. Sakurama and M. Sasaki*

Department of Electronics and Electrical Engineering, Keio University, 3-14-1, Hiyoshi, Kohoku-ku, Yokohama 223-8522, Japan
*Communications Research Laboratory, 4-2-1 Nukui-kitamachi, Koganei-city, Tokyo 184-8795, Japan
Tel/FAX: +81-45-566-1535, e-mail: kannari@elec.keio.ac.jp

Abstract: A novel fiber-based scheme for generating quadrature entanglement between a desired pair of frequency bands is proposed. The scheme is based on a nonlinear fiber, a spectral pulse shaper, and an adaptive feedback loop.
©2000 Optical Society of America
OCIS codes: (270.6570, 320.5540, 060.5530) General

In the new emerging field of quantum information technology, the nonlocal correlation in a quantum entity, *i.e.* entanglement, plays a central role. Entanglement in photonic domain is of particular importance in order to realize a practical quantum information network. Common types of entangled state of light are a twin photon pair with the polarization entanglement[1] and a twin single-mode vacuum with the quadrature entanglement[2], that are both created from $\chi^{(2)}$ materials. The former is based on a spontaneous parametric downconversion and the latter, called a two-mode squeezed state, is made by superposing two squeezed states generated from an optical parametric oscillator. These two types have been expermimentally used as a source of entanglement for quantum teleportation[3]. Alternative schemes have been brought up recently, such as entanglement of the orbital angular momentum of photons [4], the quadrature entanglement of optical solitons created from the Kerr nonlinearity in an optical fiber[5], and several theoretical and experimental studies on fiber-based systems[6-8].

We present a novel fiber-based scheme for generating quadrature entanglement between a desired pair of frequency bands. This scheme may have two potential advantages at least. One is that the scheme is based on a fiber system, which is relatively simple and easily integrable into present fiber-optic communication systems. The other is the possibility of the broadband generation of entanglement, which enables us to access the vast resource in optical frequency domain for quantum communications. Our proposal is based on the spectral filtering of an ultrashort optical pulse after propagating through a nonlinear fiber, which was used for generating the photon-number squeezing[9]. It is confirmed theoretically and experimentally that a major contribution to squeezing in this method is interpreted as the interference of the correlated frequency modes at the filtering process [10,11]. For efficient squeezing, the mode-mode coupling needs to be controlled appropriately. The mode-mode coupling depends not only on the physical parameters of a fiber, but also strongly on the envelope of the pulse itself.

Therefore, it was theoretically shown that, by controlling the phase spectrum of the input pulse, the photon-number squeezing can be optimized [12]. The idea is similarly applied to generate the quadrature squeezing in two selected frequency bands and to entangle them each other simultaneously. We numerically show that the quadrature entanglement is generated between two selected frequency bands inside the pulse (the inset of Fig.~1) due to the nonlinear fiber propagation, which is directly observable by the present technology.

Schematic of our proposal is illustrated in Fig. 1.An ultrashort pulse is directed into a programmable pulse shaper in which the pulse is spectrally manipulated [13]. We assume a phase only modulator as a pulse shaper for the sake of simplicity. Then the shaped pulse is sent to an anomalous dispersion fiber to generate entanglement.

Adopting the Gaussian state approximation which is reasonable in a practical situation, the condition for the amplitude and phase quadratures entanglement is defined by the following inequality [14];

$$\left\langle \left(\Delta\hat{X}_1 \pm \Delta\hat{X}_2\right)^2\right\rangle, \quad \left\langle \left(\Delta\hat{Y}_1 \pm \Delta\hat{Y}_2\right)^2\right\rangle \le \frac{1}{4} \le \left\langle \left(\Delta\hat{X}_1 \mp \Delta\hat{X}_2\right)^2\right\rangle, \quad \left\langle \left(\Delta\hat{Y}_1 \pm \Delta\hat{Y}_2\right)^2\right\rangle, \quad (1)$$

where $\Delta\hat{X}_{1,2}$ and $\Delta\hat{Y}_{1,2}$ are the linearized fluctuation operators for the quadratures $\hat{X}_{1,2} = \left(\hat{a}_{1,2}^* + \hat{a}_{1,2}\right)/\sqrt{2}$ and $\hat{Y}_{1,2} = i\left(\hat{a}_{1,2}^* - \hat{a}_{1,2}\right)/\sqrt{2}$, respectively. The suffices 1 and 2 represent the

selected two frequency bands of the pulse (the inset of Fig.~1). $\hat{a}_{1,2} = \int_{1,2} d\omega \hat{a}(\omega)$ and $\hat{a}_{1,2}^* = \int_{1,2} d\omega \hat{a}^*(\omega)$ are the anihilation and creation operators, respectively, for the two selected bands. These variances can be detected by the spectrally filtered homodyne detection with a 50/50 beam splitter as in Fig. 1. We here assumed that the
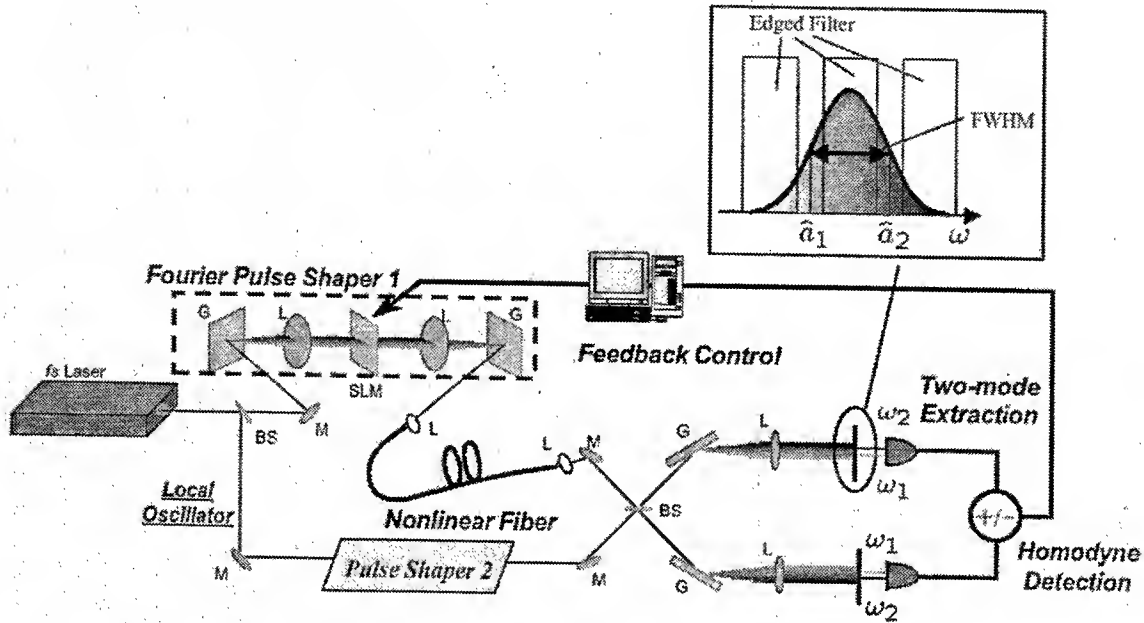

Fig. 1 Schematic of the adaptive coherent control system for generation, detection and optimization of the intrapulse frequency entanglement

spectrum of the local oscillator pulse is arbitrarily prepared. It is worthy to note that more sophisticated or practical multimode quantum detection schemes have been studied recently [15]. The observed entanglement is fed back to the phase mask of the pulse shaper to optimize the mask pattern. The simulated annealing (SA) method is utilized as an optimization algorithm [12].

Propagation of the pulse in a nonlinear fiber and the spectrally filtered homdyne detection are simulated by means of the back propagation method [10,16] which calculates the variances of quantum fluctuations with the linearization approximation. The pulse propagation in a fiber is described by the quantum nonlinear Schrodinger equation. We consider the normalized optical field and neglect linear losses and the stimulated Raman scattering.

In our simulation, the initial pulse is assumed to be in a coherent state with a classical envelope of sech(t). The phase mask of a pulse shaper supports all of the pulse spectrum with 128 pixels and 64 gray levels and is set to be zero modulation for all pixels at the beginning of the calculation. The SA algorithm is programmed to minimize the product of the squeezed variance $\left\langle \left(\Delta\hat{X}_1 + \Delta\hat{X}_2\right)^2 \right\rangle \left\langle \left(\Delta\hat{Y}_1 - \Delta\hat{Y}_2\right)^2 \right\rangle$.
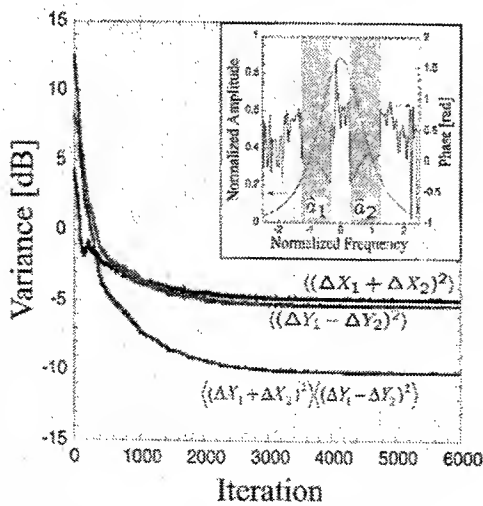
Fig. 2 Optimization of the quadrature entanglement by the SA iteration.

Figure 2 shows the result of iteration calculation for 4.7 normalized dispersion lengths of the fiber length L. It is

shown that the variances $\left\langle \left(\Delta \hat{X}_1 + \Delta \hat{X}_2 \right)^2 \right\rangle$ and $\left\langle \left(\Delta \hat{Y}_1 - \Delta \hat{Y}_2 \right)^2 \right\rangle$, that are 4.16 dB and 8.21 dB above the shot noise limit (SNL) initially, are clearly squeezed to -4.86 dB and -5.33 dB, respectively.

In conclusion, we have proposed and numerically evaluated an alternative scheme for the generation of the frequency-band entanglement inside an ultrashort pulse by using a nonlinear fiber, a pulse shaper and an adaptive feedback loop. Once the optimal phase mask is obtained, the entangled pulse is automatically generated from a fiber. It provides a greatly simplified system for entanglement generation compared to the other systems that utilize cavities or interferometers with severe requirements for mode or phase lockings [2,5].

References

[1] P. G. Kwiat, E. Waks, A. G. White, I. Appelbaum, and P. H. Eberhard, "Ultrabright source of polarization-entangled photons," Phys. Rev. A **60**, R773 (1999).

[2] Z. Y. Ou, S. F. Pereira, and H. J. Kimble, "Realization of the Einstein-Podolsky-Rosen paradox for continuous variables in nondegenerate parametric amplification," Appl. Phys. **55**, 265 (1992).

[3] D. Bouwmeester, J.-W. Pan, K. Mattle, M. Eibl, H. Weinfurther, and A. Zeilinger, "Experimental quantum teleportation," Nature **390**, 575 (1997), A. Furusawa, J. L. Sorensen, S. L. Braunstein, C. A. Fuchs, H. J. Kimble, and E. S. Polzik, "Unconditional quantum teleportation," Science **282**, 706 (1998), Y.-H. Kim, S. P. Kulik, and Y. Shih, "Quantum teleportation of a polarization state with a complete Bell state measurement," Phys. Rev. Lett. **86**, 1370 (2001).

[4] A. Mair, A. Vazirl, G. Welhs, and A. Zeilinger, "Entanglement of the orbital angular momentum states of photons," Nature **412**, 313 (2001).

[5] Ch. Silberhorn, P. K. Lam, O. Weiβ, F. Konig, N. Korolkova, and G. Leuchs, "Generation of continuous variable Einstein-Podolsky-Rosen entanglement via the Kerr nonlinearity in an optical fibre," Phys. Rev. Lett. **86**, 4267 (2001).

[6] E. Schmidt, L. Kn\"{o}ll, D.-G. Welsch, "Partitioning optical solitons for generating entangled light beams," Opt. Commun. **194**, 393 (2001).

[7] L. J. Wang, C. K. Hong, and S. R. Fribcrg, "Generation of correlated photons via four-wave mixing in optical fibers" J. Opt. B **3**, 346 (2001).

[8] J. E. Sharping, M. Fiorentino, and P. Kumar, "Observation of twin-beam-type quantum correlation in optical fiber," Opt. Lett. **26**, 367 (2001).

[9] S. R. Friberg, S. Machida, M. J. Werner, A. Levanon, and T. Mukai, "Observation of optical soliton photon-number squeezing," Phys. Rev. Lett. **77**, 3775 (1996).

[10] A. Mecozzi, and P. Kumar, "Linearized quantum-fluctuation theory of spectrally filtered optical solitons" Opt. Lett. **22**, 1232 (1997).

[11] S. Spa}lter, N. Korolkova, F. Konig, A. Sizmann, and G. Leuchs, "Observation of multimode quantum correlations in fiber optical solitons," Phys. Rev. Lett. **81**, 786 (1998).

[12] M. Takeoka, D. Fujishima, and F. Kannari, "Optimization of ultrashort-pulse squeezing by spectral filtering with the Fourier pulse-shaping technique," Opt. Lett. **26**, 1592 (2001).

[13] A. M. Weiner, "Femtosecond optical pulse shaping and processing," Prog. Quant. Electr. **19**, 161 (1995).

[14] U. Leonhardt, *Measuring the quantum state of light* (Cambridge University Press, Cambridge, 1997).

[15] M. Beck, C. Dorrer, and I. A. Walmsley, "Joint quantum measurement using unbalanced array detection" Phys. Rev. Lett. **87**, 253601 (2001) and references therein.

[16] Y. Lai and S.-S. Yu, "General quantum theory of nonlinear optical-pulse propagation," Phys. Rev. A **51**, 817 (1995).

Experimental observation of modal attraction in optical fibers

S. Pitois, G. Millot and M. Haelterman*

Laboratoire de Physique de l'Université de Bourgogne, UMR CNRS 5027
9 avenue A. Savary, BP 47870, 21078 Dijon, France
* Service d'Optique et Acoustique, Université Libre de Bruxelles,
50 Av. Roosevelt, CP 194/5, B-1050 Bruxelles, Belgium
email : spitois@u-bourgogne.fr

Abstract: We investigate experimentally nonlinear optical attractors based on four-photon mixing interaction of counterpropagating waves in optical fibers.
© 2002 Optical Society of America
OCIS codes: (060.4370) Nonlinear optics, fibers ; (190.4360) Nonlinear optics, devices

Repolarization of an unpolarized signal laser heam hy a pump polarized wave in a nonlinear optical medium is a fascinating effect of both fundamental and applicative interests. In ref. [1] Heebner et al. have presented the design of such a nonlinear polarizer that can transform unpolarized light into polarized light with unit efficiency by means of a photorefractive two-beam coupling scheme. This device constitutes what could be called a polarization funnel, or a polarization attractor, in the sense that all input polarization states are transformed into a unique well-defined polarization state. In previous works, we have shown that this particuliar feature can be also observed by using pure nonlinear interaction between two waves propagating in an isotropic fiber with a high group-velocity mismatch [2,3]. In this paper, we show that the phenomenology that plays a role in refs. [2,3] can appear in numerous optical fiber systems such as high birefrigent fibers or bimodal fibers. We report two experimental observations of this remarkable effect of modal attraction.

Let us consider two counter-propagating waves of equal frequencies, a pump beam and a signal beam, that propagate in an optical fiber. We assume that each wave propagates along two guided modes of the fiber, for example two orthogonal states of polarization (SOP) in a Hi-Bi fiber or two linearly polarized (LP_{mn}) modes with different transverse field distribution in a bimodal fiber. The time-dependent interaction of these counter-propagating waves in a Kerr medium is described by the following equations :

$$\frac{\partial E_1}{\partial z} + \frac{1}{v_1}\frac{\partial E_1}{\partial t} = i\gamma\left[\left(\mid E_1\mid^2 +2\mid E_2\mid^2 +C\mid \bar{E}_1\mid^2 +C\mid \bar{E}_2\mid^2\right)E_1 + C\bar{E}_2\bar{E}_1^*E_2\right],\tag{1}$$

$$\frac{\partial E_2}{\partial z} + \frac{1}{v_2}\frac{\partial E_2}{\partial t} = i\gamma\left[\left(\mid E_2\mid^2 +2\mid E_1\mid^2 +C\mid \bar{E}_1\mid^2 +C\mid \bar{E}_2\mid^2\right)E_2 + C\bar{E}_2^*\bar{E}_1E_1\right],\tag{2}$$

$$-\frac{\partial \bar{E}_1}{\partial z} + \frac{1}{\bar{v}_1}\frac{\partial \bar{E}_1}{\partial t} = i\gamma\left[\left(\mid \bar{E}_1\mid^2 +2\mid \bar{E}_2\mid^2 +C\mid E_1\mid^2 +C\mid E_2\mid^2\right)\bar{E}_1 + CE_2E_1^*\bar{E}_2\right],\tag{3}$$

$$-\frac{\partial \bar{E}_2}{\partial z} + \frac{1}{\bar{v}_2}\frac{\partial \bar{E}_2}{\partial t} = i\gamma\left[\left(\mid \bar{E}_2\mid^2 +2\mid \bar{E}_1\mid^2 +C\mid E_1\mid^2 +C\mid E_2\mid^2\right)\bar{E}_2 + CE_2^*E_1\bar{E}_1\right],\tag{4}$$

where E_1 ($\bar{E}_1$) and E_2 ($\bar{E}_2$) are the slowly varying field amplitudes of the first and second components of the signal (pump) beam respectively, whereas v_1 ($\bar{v}_1$) and v_2 ($\bar{v}_2$) are the associated group-velocities. γ is the usual nonlinear coefficient and C represents the cross-phase modulation coefficient ($C = 2/3$ for two orthogonal SOP and $C \simeq 2$ for two spatial modes). The last term on the right-hand side of each equation describes a fully-degenerate phase-matched four-wave mixing process which is responsible for energy exchange between the waves. We assume now that the pump beam is launched into the fiber along only one mode of propagation, whereas the signal wave is injected into any comhination of the two modes. Numerical simulations show that this situation is quite interesting since it may lead to an unilateral transfer of energy between the two signal components. This unidirectional exchange of energy is a consequence of both the nonlinear interaction and the high-group velocity mismatch between the forward (signal) and the backward (pump) waves. For sufficient interaction length, almost all the power of the signal heam can be transfered onto its second component whatever its initial input state. This remarkable feature is illustrated in Fig. 1 where Eqs. (1-4) have been solved numerically.
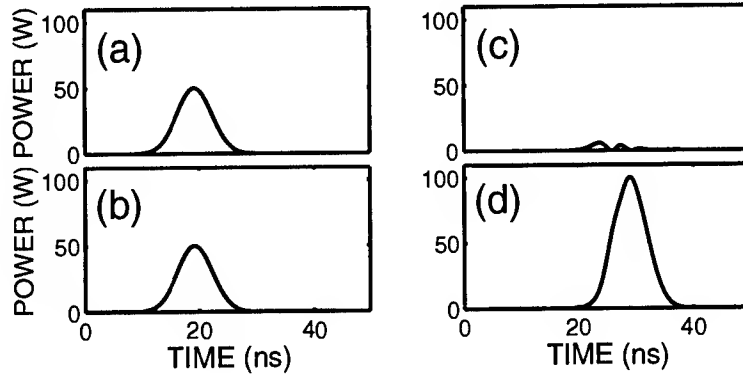
Fig. 1. Numerical evolution of the signal components. (a) and (b) : first and second components at the fiber input (z=0), (c) and (d) : first and second components at the fiber output (z = 2 m). The pump beam is a 6.5-ns FWHM, 100 W peak power pulse injected along the first mode of the fiber. The cross-phase modulation coefficient is $C = 2$ and the nonlinear coefficient is $\gamma = 0.025$ m^{-1}W^{-1}.

We confirm this property experimentally by means of two different optical fiber systems in which the propagation of the waves can be described by Eqs. (1-4). The setup used in both cases is shown in Fig. 2. The 6.5-ns FWHM pulses were obtained from a Q-switched frequency-doubled Nd:YAG laser emitting at λ=532 nm with a repetition rate of 25 Hz. The laser was used in the multimode regime to increase the threshold for Brillouin scattering well above the power levels involved in the experiment. A beam splitter was used to split the laser beam into two equal intensity beams. Each beam was first polarized and then injected into the fiber by means of microscope objectives. Half-wave plates were inserted after each polarizer to control the orientation of the two wave polarizations with respect to the fiber axis. A portion of the signal output beam was removed and analysed.
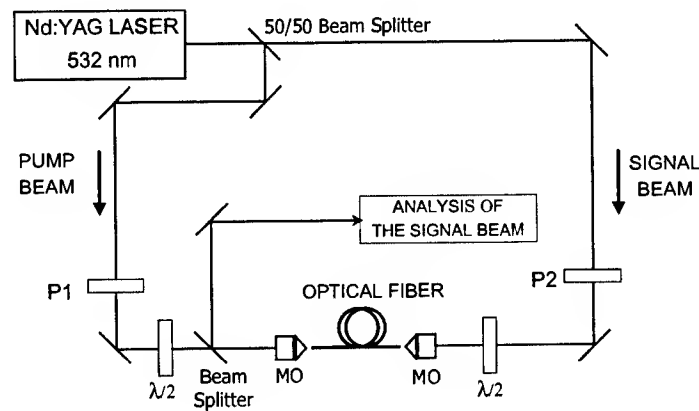
Fig. 2. Schematic of experimental setup. P's, polarizer, λ/2's, half-wave plates, MO's, microscope objectives

In the first example, we consider counter-propagating waves polarized collinearly in a two meters-long bimodal fiber which sustains two guided LP_{01} and LP_{11} modes. Far-field radiation ouput patterns of the pump and the signal beams are shown in Fig. 3. Peak powers of both laser beams were fixed to 100 W. The launching conditions were first adjusted so that the pump wave propagates only along the LP_{01} mode (Fig. 3a) whereas

the signal beam was injected into the fiber to give equal excitations of the two spatial modes (Fig. 3c). When both waves counter-propagate, almost all the signal power is transfered onto the LP_{11} mode (Fig. 3e), in complete agreement with the previous numerical simulations (see Fig. 1). Similar results were obtained when injecting the pump beam into the LP_{11} mode (see Figs. 3b,d,f).
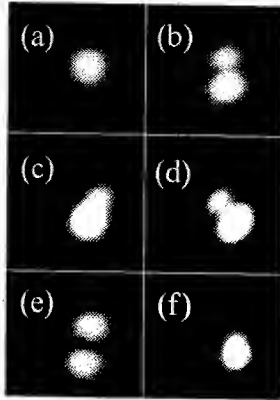
Fig. 3. *Far-field radiation output patterns from the bimodal fiber for (a) the pump beam propagating alone in the LP_{01} mode, (c) the signal beam propagating alone into the LP_{01} and LP_{11} modes and (e) the signal beam when both waves are counter-propagating into the fiber. Similar results are obtained when the pump beam is launched along the LP_{11} mode (see (b), (d) and (f)).*
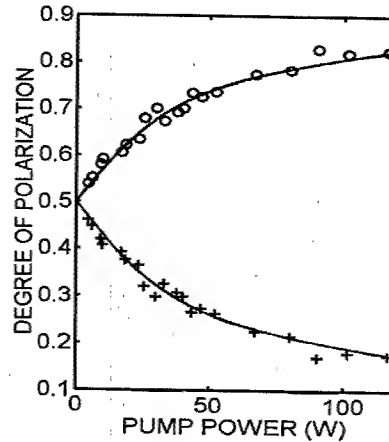
Fig. 4. *Experimental degree of polarization of the output signal beam along the x- (circles) and y- (crosses) axis of the Hi-Bi fiber as a function of the pump power. The pump beam is launched along the y-axis of the fiber. Solid curves are obtained by numerical integration of Eqs.(1-4).*

The second experimental observation was performed in a high-birefringent two meters-long optical fiber. The pump beam was injected along the y-axis of the fiber whereas the signal beam was polarized at 45 degrees with respect to this axis. We define the degree of polarization of the output signal wave along each axis by :

$$d_i = I_i/I_{tot}, \quad i = x, y \tag{5}$$

where I_x (I_y) is the part of the total energy polarized along the x- (y-) axis and $I_{tot} = I_x + I_y$ is the total energy of the signal laser beam. The signal peak power was fixed to 60 W. Experimental measurements of the degree of polarization of the signal beam as a function of the pump peak power are shown in Fig. 4. The attraction of the signal SOP towards the x-axis as the pump power increases is clearly observed. Attraction towards the y-axis can also be obtained by injecting the pump wave along the x-axis.

In summary, we have studied the modal attraction of a signal wave that travels in an optical fiber in the presence of a counter-propagating pump wave. Experimental results are in excellent agreement with numerical simulations describing this effect. We believe that this effect may find important applications for optical signal processing.

References

1. John E. Heebner, Ryan S. Bennink, Robert W. Boyd and R.A. Fisher "Conversion of unpolarized light to polarized light with greater than 50 % efficiency by photorefractive two-beam coupling," Opt. Lett. **25**, 257 (2000).
2. S. Pitois, G. Millot and S. Wabnitz, "Nonlinear polarization dynamics of counterpropagating waves in an isotropic optical fiber: theory and experiments", J. Opt. Soc. Am. B, **18**, 432 (2001).
3. S. Pitois and M. Haelterman, "Optical fiber polarization funnel," NLWG 2001 MCF79-1, (2001)

Nonlinear optical properties of As-Se fiber

R.E. Slusher

Lucent Technologies, Bell Labs, 600 Mountain Ave.,Murray Hill, NJ 07974, USA

TEL: (908)582-4094, FAX: (908)582-3260, email: res@lucent.com

J.S. Sanghera, L.B. Shaw and I.D. Aggarwal

Naval Research Laboratory, Code 5606
Washington, DC 20375

Abstract: Large optical Kerr nonlinearities in low linear loss As-Se glass fibers are shown to have potential for ultra-fast, low power, all-optical processing applications. Nonlinear phase shifts near π radians are demonstrated in fibers only 60 cm long.
©2000 Optical Society of America
OCIS codes: (060.2290) Fiber materials, (190.4370) Nonlinear optics, fibers

Summary

Fiber based optical processing devices are interesting for optical communication systems because of their low insertion loss and long fiber mode interaction lengths that allow low power operation. High nonlinearity fibers are being used at present to demonstrate optical regeneration[1] and parametric amplification[2]. At present these devices require high powers because they use silica based fibers that have very small Kerr nonlinearities at infrared communication wavelengths resulting from the very large ratio of the optical bandgap to operating photon energy. This paper reports new results for chalcogenide fibers based on As_2Se_3 where the optical bandgap is approximately twice the communication photon energies resulting in Kerr nonlinearities 500 times[3] the nonlinearity of silica. These very high nonlinearity fibers could provide a new generation of nonlinear optical devices.

Chalcogenide fibers used in our experiment are formed from very high purity materials in order to achieve multimode and single mode fibers with relatively low losses of about 0.1 dB/m and 0.8 dB/m, respectively. We are also interested in the effect of low impurity content in our materials has on the nonlinear losses and hysteretic photon induced losses that often limit device applications of chalcogenide materials.

All-optical processing devices typically require a nonlinear phase shift $\Delta\phi = \gamma PL = \pi$ radians for an optical pulse propagating with a peak power P through a fiber length L. The nonlinear fiber response is measured by $\gamma = 2\pi n_2/\lambda A_{eff}$, where n_2 is the nonlinear Kerr coefficient, λ is the wavelength and A_{eff} is the effective core area. Some typical values are $\gamma = 2$ $W^{-1}km^{-1}$ for silica fiber with $50\mu m^2$ core areas, $\gamma = 10$ $W^{-1}km^{-1}$ for "high nonlinearity" silica based fiber with core areas near 15 μm^2, and $\gamma = 100$ $W^{-1}km^{-1}$ for As_2S_3 fibers with 50 μm^2 cores[4]. Our experiments demonstrate $\gamma = 1000$ $W^{-1}km^{-1}$ for core areas of 50 μm^2. For micro-structured fibers[5] with 5 μm^2 core areas, the gamma values for fibers similar to those studied here could reach 10,000 $W^{-1}km^{-1}$. These very high γ values would allow fabrication of very compact devices with fiber lengths of only 10 cm and power levels near one watt.

We measure strong self-phase modulation in As-Se fibers formed from high purity materials. The double crucible process was used to draw single mode fiber with a cladding composed of $As_{38.25}Se_{61.75}$ and a slightly higher index core of $As_{39}Se_{61}$. The core diameter is approximately 10μm and a numerical aperture of about 0.25 resulting in nearly single mode propagation at 1.55 μm wavelengths. The fiber is 60 cm in length and has cleaved faces on both ends. The total loss through the fiber, including mode coupling losses for the microscope objective lens used at the input and reflection looses at the fiber faces was 65%. This

loss is consistent with less than 1db loss in the fiber material. The exciting light source is a mode-locked Er doped fiber laser and amplifier that emits 2.2 ps duration pulses at a 10 Gb/s rate at peak powers near 50W. The input pulse width is measured using an autocorrelator. Fiber coupling losses in the present experiments reduce the maximum peak power levels in the fiber to approximately 5W. The mode pattern at the fiber output was a well-formed Gaussian shaped pattern indicating single mode propagation.

The optical spectrum of the pulses propagating through the fiber for three values of the input intensity are shown in Figure 1, (a) experimentally as measured using an optical spectrum analyzer and (b) numerical simulations using the experimentally measured power levels, 60 cm fiber length, $n_2 = 500$ times the silica value, $A_{eff} = 50 \, \mu m^2$ and a dispersion value of 3000 ps/nm/km. The frequency spectrum broadens as the intensity increases and there is reasonably good agreement between the experiment and simulation. At the highest intensity the dip in the central region of the spectrum is characteristic of a nonlinear phase shift equal to π.

The dispersion value of 3000 ps/nm/km, required for agreement between the experimental spectra and the simulations, indicates that in the linear intensity regime a broadening of the 2.2 ps input pulse to approximately 2.9 ps is expected for our 60 cm long fiber. A streak camera measurement of the output pulse broadening is consistent with this expectation.

The experimental output power as a function of input power is sub-linear as shown in Figure 2, indicating two-photon losses of near 50% at the power level required for a π phase shift. This is only marginally acceptable for device applications and indicates that a slightly larger chalcogenide energy gap is optimal. The bandgap of our fiber material was chosen to be close to the optimum for maximum enhancement of the nonlinearity while the operating light field energies at wavelengths near 1.5 μm are below half of the bandgap energy where they will not induce large two-photon absorption. Clearly we need to increase the bandgap in order to further reduce the two-photon absorption. A larger gap can be obtained by adding a small fraction of Ge or S to the binary As-Se material. A 10 to 20% decrease in the output intensity is seen in Figure 2 as the intensity is reduced after being at the maximum value. This unwanted hysteretic loss effect remained for from minutes to hours, but eventually the fiber reverted to its initial transmission value. Increasing the bandgap to reduce two-photon absorption as well as using lower power levels and increasing the fiber length to a few meters should help to reduce this hysteretic loss. The persistence of these hysteretic effects in the high purity fiber points toward an intrinsic mechanism for the photon induced losses in As-Se materials.
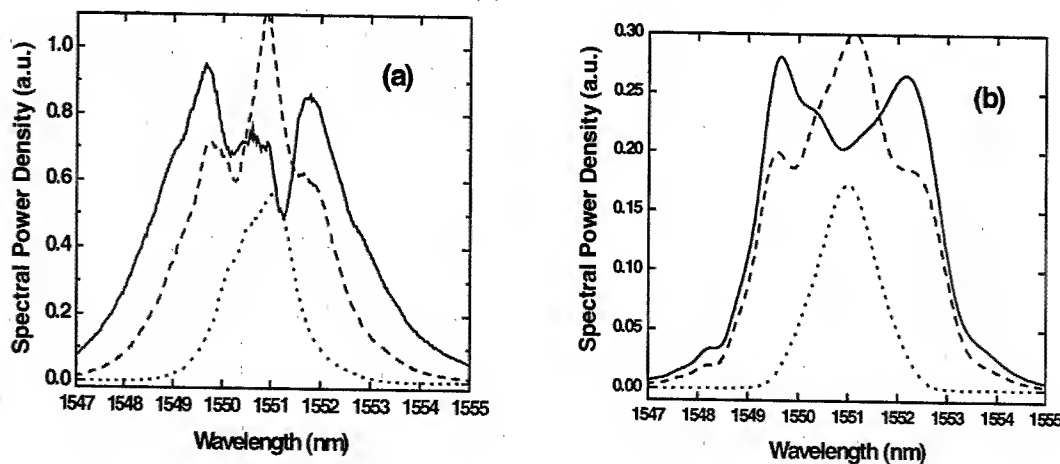
Figure 1 Experimental (a) and numerically simulated (b) spectra for peak power levels of 200mW in the linear propagation regime (dotted curve, the data are multiplied by a factor of 10 for comparison with nonlinear results), 4W (dashed curve) and 5W (solid curve).
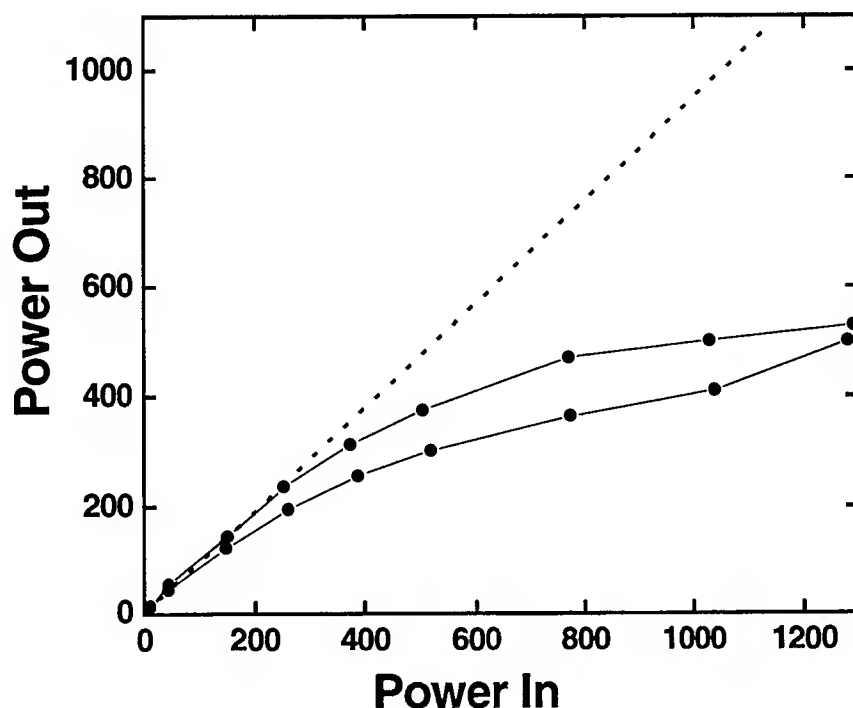
Figure 2 Power out of the fiber as a function of the input power up to the power level required for a π phase shift. The units on both axes are arbitrary with linear scales. The dashed line is an extrapolation of the initial linear slope to higher powers. The solid circles are the data points and the line is a guide for the eye. The upper solid curve corresponds to power increase and the lower to power decrease after remaining at the maximum power for 5 minutes.

Applications of these fibers to parametric amplifiers and optical processing devices will be discussed. Fibers several meters long with losses less than a few dB could be used for optical regenerators based on self-phase modulation[1]. Microstructured fibers[5] with efficient tapered fiber couplers could reduce the device length to tens of centimeters while maintaining the low power levels. Broadband parametric amplifiers present the problem of phase matching the signals and pump over an extended spectrum. This may be difficult in the chalcogenide fibers since the material dispersion and dispersion slope are both large. However multi-section microstructured fibers[2] might offer tailoring of the dispersion values that could achieve broadband, low power amplifiers.

[1] G. Raybon, Y. Su, J. Leuthold, R. Essiambre, T. Her, P. Steinvurzel, K. Dreyer, K. Feder, and C. Joergensen, "40 Gbit/s pseudo-linear transmission over one million kilometers", OFC Anaheim , March 17-22 (2002), PD FD 10.

[2] L. Provino, A. Mussot, E. Lantz, T. Sylvestre, and H. Maillotte, "Broadband and flat parametric gain with a single low-power pump in a multi-section fiber arrangement", OFC Anaheim , March 17-22 , 125 (2002).

[3] G. Lenz, J. Zimmermann, T. Katsufuji, M. E. Lines, H. Y. Hwang, S. Spalter, R. E. Slusher, S.-W. Cheong, J. S. Sanghera, and I. D. Aggrawal, "Large Kerr effect in Se-based chalcogenide glasses", Opt. Lett. 25, 254 (2000).

[4] M. Asobe, "Nonlinear optical properties of chalcogenide glass fibers and their applications in all-optical switching", Opt. Fiber Tech. 3, 142-148, (1997).

[5] T. M. Monro, K. M. Kiang, J. H. Lee, K. Frampton, Z. Yusoff, R. Monroe, J. Tucknott, D. W. Hewak, H. N. Rutt, and D. J. Richardson, "High nonlinearity extruded single-mode holey optical fibers", OFC Anaheim , March 17-22 (2002), PD FA1-1.

Slow Light, Fast light, and Optical Solitons in Structured Optical Waveguides

Robert W. Boyd and John E. Heebner
The Institute of Optics, University of Rochester, Rochester, NY 14627
585-275-2329; boyd@optics.rochester.edu

Abstract: We describe the exotic optical properties of a device consisting of a sequence of optical microresonators coupled to an optical waveguide. This device can display slow or fast group voelocities of propagation, large tailored dispersion, and the propagation of optical solitons.

The goal of our research effort is to design materials and structures with optical properties fundamentally unlike those of naturally occurring materials. Some of the exotic characteristics these devices are expected to display include ultra-slow and superluminal group velocities of propagation, enhanced optical nonlinearities, and large dispersion with a controllable magnitude and sign. Previous related work includes the development of photonic bandgap (PBG) structures [1] and structures consisting of waveguides coupled to arrays of optical resonators [2, 3]. One of the structures we are presently investigating is shown in part (a) of Fig. 1. It consists of an optical waveguide coupled to a series of optical resonators. The resonators can be of arbitrary design, although in our experimental work we are concentrating on resonators in the form of a ring waveguide or a whispering gallery mode [4,5] of a disk. A pulse of light is shown propagating through this structure. Evanescent coupling between the waveguide and each resonator injects light into each resonator where it circulates many times (on resonance, 2π times the finesse F of the resonator) before being coupled back into the waveguide. For a densely packed collection of high-finesse resonators, a light wave spends much more time circulating within each resonator than in propagating between resonators. Thus the group velocity of propagation can become very low. Because the time delay acquired in interacting with each resonator depends critically on the detuning of the optical wave from the resonance frequency, this device displays tailorable dispersion with a magnitude very much larger than that of conventional materials. Also, because of the build-up of intensity within each resonator, the nonlinear response of this structure is greatly enhanced with respect to propagation through a bulk nonlinear material. We have shown [3] that the enhancement scales as the square of the resonator finesse. Under appropriate conditions, these dispersive and nonlinear effects can precisely balance one another, leading to the propagation of optical solitary waves. Some examples of the predicted behavior are shown in Fig. 2.

(a)

(b)
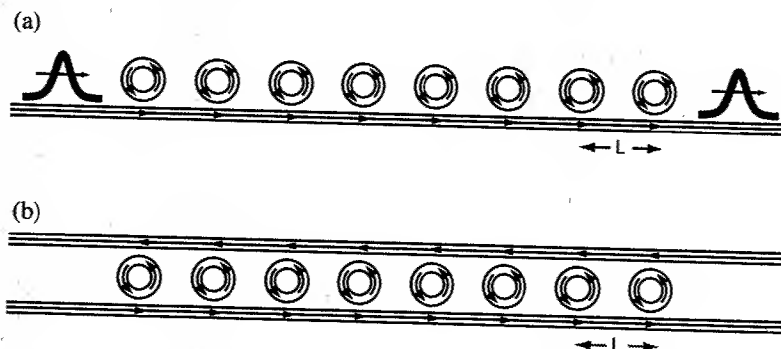
Fig. 1. Structured waveguides which display slow or fast light propagation, large controllable dispersion, and large controllable nonlinearity. (a) Single-guide structure amd (b) double-guide structure.

A related structure is shown in the Fig. 1(b). It consists of an upper and lower waveguide coupled to the same sequence of resonators. The optical properties of such a device differ in fundamental ways from those of the single-guide structure. Because forward and backward going waves are coupled in the two-guide structure, it possesses a photonic bandgap, which is not present in the single-guide structure. Both structure are expected to possess useful photonic properties, which however differ in their detailed behavior. We expect either of these sorts of devices to have important implications for applications such as soliton propagation, controllable optical delay lines, and photonic switching.

Our work is related to recent research on the development of nanocomposite materials. Such materials display useful optical properties that can be qualitatively dissimilar [6] from those of their underlying constituents. Nanocomposite materials are especially well suited for photonics applications, because they can be constructed in such a manner as to produce enhanced nonlinear optical response. Some such materials are formed by a random association of the underlying constituents [7, 8], whereas other are formed with deterministic properties through various fabrication methods [9,10]. Nanofabrication techniques are capable of forming structures with specially tailored optical properties. One approach leads to the creation of structures such as photonic crystals [11, 12] and related [13] materials. In these materials, the refractive index is modulated periodically on the distance scale of an optical wavelength. Such structures necessarily produce a strong coupling between counterpropagating optical waves; for a sufficiently strong index modulation such structures produce a photonic bandgap, that is, a range of frequencies over which light cannot propagate.

Moreover, our work has been motivated in part by recent work on slow and fast light propagation. This work is aimed at the development of techniques that can lead to a significant modification of the group velocity of propagation of a light pulse through a material medium. Proposed applications of these procedures include the development of optical delay lines and the "storage" of light pulses [14, 15] with perhaps implications to the field of quantum information. Most of this research has made use of the response of resonant media [16] and much of it has made use of the concept of electromagnetically induced transparency [17]. Our research pursue an alternative procedure for the generation of slow light based on inducing large dispersive effects in optical waveguides by coupling the waveguide to an array of optical resonators.
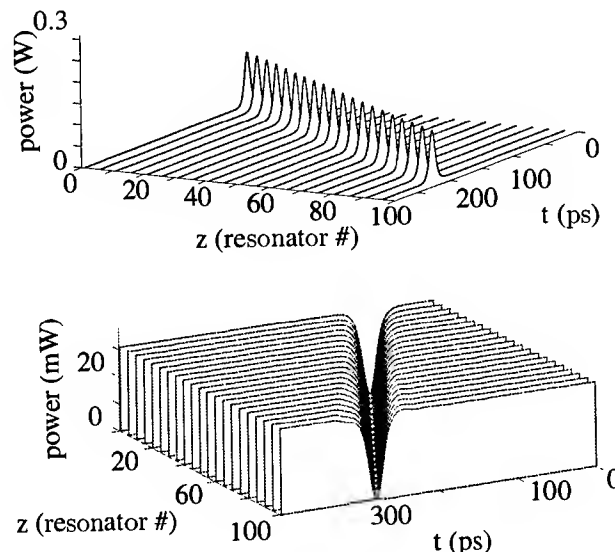
Fig. 2. Because the sign of the group-velocity dispersion parameter can be controlled by the optical frequency, both bright and dark solitons can propagate through a given photonic device.

References

[1] E. Yablonovitch, J. Opt. Soc. Am, B10, 283 (1993).

[2] A. Yariv, Y. Xu, R. K. Lee, and A. Scherer, Opt. Lett. 24, 711, 1999.

[3] J. E. Heebner and R. W. Boyd, Opt. Lett. 24, 847, 1999; R. W. Boyd and J. E. Heebner, Applied Optics, 40, 5742-7, 2001. J. E. Heebner, R. W. Boyd, and Q-H. Park, Phys. Rev. E, 65, 036619, 2002; J. E. Heebner, R. W. Boyd, and Q-H. Park, J. Opt. Soc. Am., B. 19, 722 2002.

[4] V. B. Braginsky and V. S. Ilchenko, Sov. Phys. Dokl., 32 306 (1987).

[5] S. L. McCall, A. F. J. Levi, R. E. Slusher, S. J. Pearton, and R. A. Logan, Appl. Phys. Lett. 60, 289 (1992).

[6] J. C. Maxwell Garnett, Philos. Trans. R. Soc. London 203, 385 (1904); 205, 237 (1906).

[7] F. Hache, D. Ricard, C. Flytzanis, and U. Kreibig, Appl. Phys. A, 47, 347, (1988).

[8] W. Kim, V. P. Safonov, V. P. Drachev, V. A. Podolskiy, V. M. Shalaev, and R. L. Armstrong, in Optical properties of nanostructured random media, ed. by V. M. Shalaev, Springer Verlag, Topics in applied physics, Berlin (2001).

[9] G. L. Fischer, R. W. Boyd, R. J. Gehr, S. A. Jenekhe, J. A. Osaheni, J. E. Sipe, and L. A Weller-Brophy, Phys. Rev. Lett., 74, 1871, (1995).

[10] R. L. Nelson and R. W. Boyd, Appl. Phys. Lett., 74, 2417, (1999).

[11] E. Yablonovitch, J. Opt. Soc. Am. B, **10,** 283 (1993).

[12] S. John, and T. Quang, Phys. Rev. Lett., **76,** 2484, (1996).

[13] A. Yariv, Y. Xu, R. K. Lee, and A. Scherer, Opt. Lett., 24, 711 (1999).

[14] C. Liu, Z. Dutton, C. H. Behroozi, and L. V. Hau, Nature 409, 490, 2001.

[15] D. F. Phillips, M. Fleischhauer, A. Mair, R. L. Walsworth, and M. D. Lukin, Phys. Rev. Lett. 86, 783, 2001.

[16] S. Chu and S. Wong, Phys. Rev. Lett. **48,** 738, 1982.

[17] L. V. Hau, Harris, S. E., Dutton, Z., and Behroozi, C. H., Nature 397 594, 1999.

Notes

Nonlinear Guided Waves

Poster Session: 1

Monday, September 2, 2002

NLMD
4:00pm – 6:00pm
Lower Level Foyer

Nonlinear transmission in photonic crystal waveguides: Optical switchers and diodes

Sergei F. Mingaleev [1,2] **and Yuri S. Kivshar** [1]

[1] *Nonlinear Physics Group, Research School of Physical Sciences and Engineering*
Australian National University, Canberra ACT 0200, Australia

[2] *Bogolyubov Institute for Theoretical Physics, 14-B Metrologichna Street*
Kiev 03143, Ukraine
sfm124@rsphysse.anu.edu.au and ysk124@rsphysse.anu.edu.au
http://wwwrsphysse.anu.edu.au/nonlinear/

Abstract: We derive effective discrete equations with long-range interaction which accurately describe light transmission in photonic crystal waveguides with embedded nonlinear defects and demonstrate the possibility of a bistable (all-optical switcher) and unidirectional (optical diode) transmission.
© 2002 Optical Society of America
OCIS codes: (230.7370) Waveguides; (130.2790) Guided waves; (130.3120) Integrated optics devices

One of the most promising applications of photonic crystals is a possibility to create compact integrated optical devices, which would be analogous to the integrated circuits in electronics, but operating entirely with light. To accomplish this, it is crucially important to achieve a dynamical tunability of the properties of photonic crystals, and one of the most promising approaches is based on the idea to employ *nonlinear photonic crystals*, i.e. photonic crystals made from dielectric materials whose refractive index depends on the light intensity. This opens a broad range of novel applications of photonic crystals for all-optical signal processing and switching.

The properties of the photonic crystals and photonic crystal waveguides are usually studied by solving Maxwell's equations numerically, and such calculations are, generally speaking, time consuming. Moreover, the numerical solutions do not always provide a good physical insight. Recently we have shown [1] that many of the properties of the photonic-crystal waveguides and circuits, including the transmission spectra of sharp waveguide bends, can be accurately described by the effective discrete equations which are somewhat analogous to the Kirchhoff equations for the electric circuits. However, in contrast to electronics, in photonic crystals both diffraction and interference become important, and thus the resulting equations involve the long-range interaction effects.
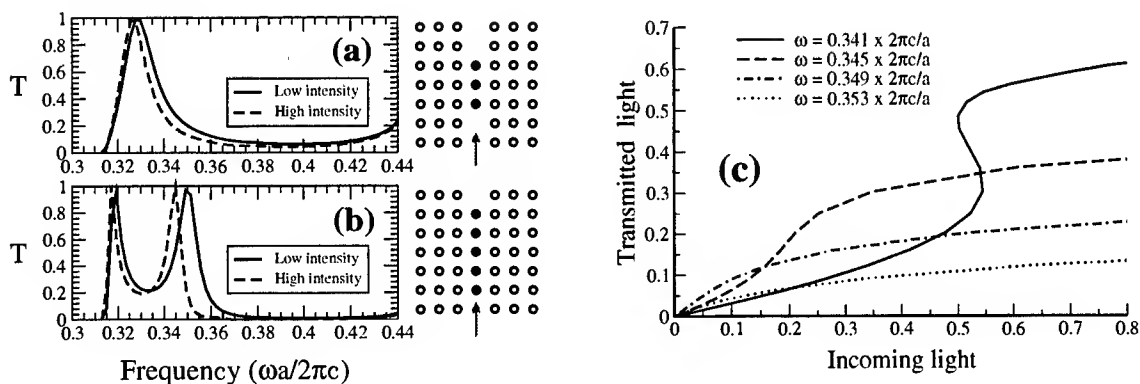
Fig. 1. Transmission coefficients for (a) three and (b) five nonlinear defect rods embedded into straight photonic crystal waveguide, calculated from Eqs. (1)–(2) for low-intensity and high-intensity output light. The nonlinear defect rods with the dielectric constant $\varepsilon_d = 7$ are marked by black circles. (c) Bistability in the nonlinear transmission of an array of five nonlinear defect rods shown in Fig. 1(b).

Let us introduce our approach for a 2D photonic crystal consisting of infinitely long dielectric rods arranged in the form of a square lattice with the lattice spacing a. We study the light propagation in the plane normal to the rods, assuming that the rods have the radius $r = 0.18a$ and the dielectric constant $\varepsilon = 11.56$. For the electric field $E(\vec{x}, t) = e^{-i\omega t} E(\vec{x} \,|\, \omega)$ polarized parallel to the rods, such a photonic crystal possesses a large

TM band gap in the frequency interval from $\omega = 0.303 \times 2\pi c/a$ to $\omega = 0.444 \times 2\pi c/a$. To create a waveguide circuit, we introduce a system of defect rods characterized by the radiuses r_n, dielectric constants ε_n, and located at the points $\vec{x}_n$, where n is the index number of the defect rods. Assuming that the radiuses $r_n \leq r$ are small, and thus the defects support only *localized eigenmodes of a monopole symmetry*, one can obtain rather accurate results in the approximation that the electric field remains constant inside the defect rods [2]. In this case, averaging the electric field over the cross-section of the defect rods, we obtain approximate discrete equations for the amplitudes of the electric fields $E_n(\omega) \equiv E(\vec{x}_n \,|\, \omega)$ of the eigenmodes excited at the defect sites in the following matrix form:

$$\sum_m M_{n,m}(\omega) E_m(\omega) = 0 , \qquad \text{where} \qquad M_{n,m}(\omega) = \varepsilon_m(E_m)\, J_{n,m}(\omega) - \delta_{n,m} , \tag{1}$$

and

$$J_{n,m}(\omega) = \left(\frac{\omega}{c}\right)^2 \int_{r_m} d^2\vec{y}\ G(\vec{x}_n, \vec{x}_m + \vec{y}\,|\,\omega) \tag{2}$$

are coupling constants determined by the Green function $G(\vec{x}, \vec{y}\,|\,\omega)$ of a perfect 2D photonic crystal (see details in Refs. [2, 3]). As described in Refs. [1, 4], Eqs. (1)–(2) can be used for accurate describing both linear and nonlinear properties of the photonic crystal circuits, including their transmission.
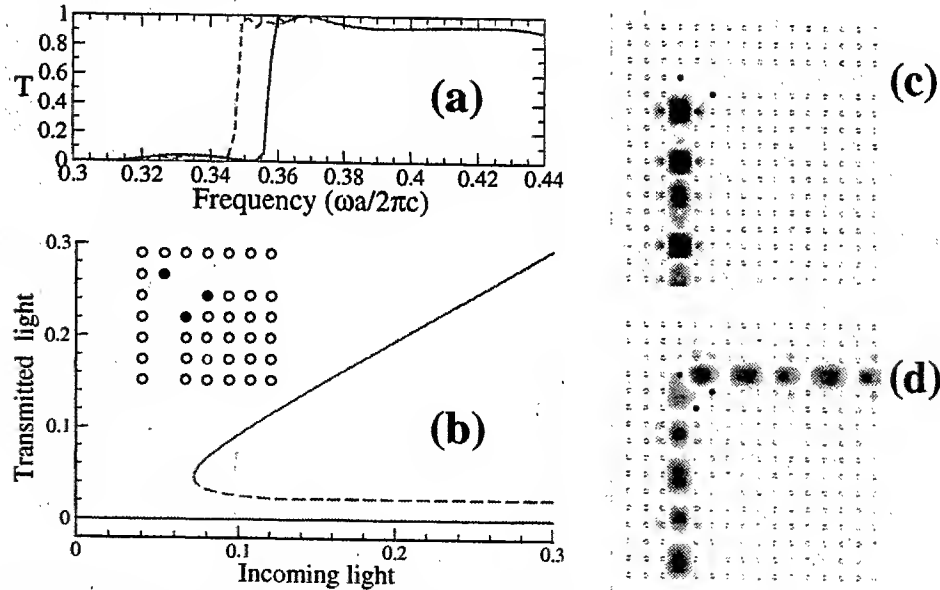
Fig. 2. (a) Transmission of a waveguide bend with three embedded nonlinear defect rods for low-intensity (solid curve) and high-intensity (dashed curve) output light. Nonlinear defect rods with the dielectric constant $\varepsilon_d = 7$ are marked by black circles. (b) Bistable nonlinear transmission through the waveguide bend shown in Fig. 2(a), for the light frequency $\omega = 0.351 \times 2\pi c/a$. (c)–(d) Electric field distribution for the waveguide bend in its "closed" and "open" states.

As the first example, in Fig. 1(a)–(b), we present our results for the transmission spectra of the straight waveguides (created by a row of removed rods) with an array of embedded nonlinear defects. We assume throughout the paper that all nonlinear defect rods are identical, with the radius $r_n = r = 0.18a$ and the dielectric constant, $\varepsilon_n = \varepsilon_d + |E_n|^2$ (with $\varepsilon_d = 7$), which grows linearly with the light intensity (the so-called Kerr effect). In the linear limit (low-intensity light), the embedded defects behave like an effective resonant filter, and only the waves with some specific resonance frequencies can be effectively transmitted through the defect section. The resonances appear due to the excitation of cavity modes inside the defect region. When the intensity of the input wave grows, the resonant frequencies found in the linear limit get shifted to lower values. The sensitivity of different resonances to the change of the light intensity is quite different and may be tuned by matching of the defect parameters. The nonlinear transmission of such a waveguide is found to possess *bistability*, which occurs for the frequencies smaller then the resonant, in a linear limit, frequency [see Fig. 1(c)]. This bistability phenomenon can be exploited for creating all-optical switching devices. However,

such a simple switcher is not very efficient, because it has non-zero transmission in its "closed" state and non-zero reflection in its "open" state.
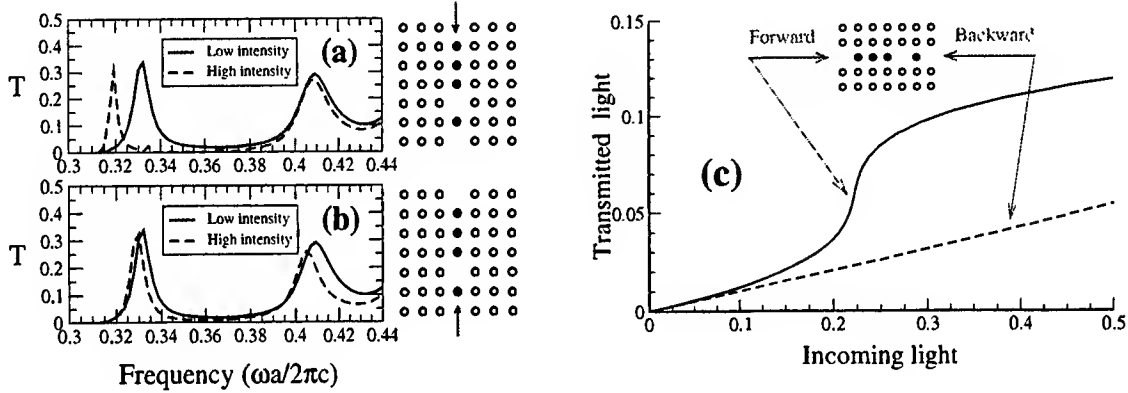

Fig. 3. Transmission coefficients of an asymmetric array of nonlinear defect rods in the (a) forward and (b) backward directions, calculated for the same parameters as in Fig. 1. (c) Nonlinear transmission of the optical diode for both directions at the light frequency $\omega = 0.326 \times 2\pi c/a$.

The performance of an all-optical switcher can be drastically improved by harnessing more elaborated waveguide structures. To illustrate such a possibility, we consider the waveguide bend with three embedded nonlinear defects, as is depicted in Fig. 2. In the linear regime, such a sharp bend with defects behaves as an optical threshold device that efficiently transmits the guided waves with frequencies above the threshold one, but completely reflects the waves with the lower frequencies. The transmission coefficient of this waveguide bend in the linear limit is shown in Fig. 2(a) by a solid curve. When the input intensity increases, the threshold frequency decreases, extending the transmission region [see a dashed curve in Fig. 2(a)]. The resulting transmission as a function of the input intensity [see Fig. 2(b)] demonstrates a sharp nonlinear threshold character with an extremely low transmission of the waves below a certain (rather small) threshold intensity, see Fig. 2(c), and possibility to switch to nearly 100% transmission above this intensity, see Fig. 2(d).

Another idea is to take advantage of a spatially nonreciprocal waveguide structure for creating an all-optical "diode" which allows unidirectional propagation of a signal at a given wavelength. In the ideal case, the diode transmission is 100% in the "forward" propagation, while it is much smaller or vanishes for "backward" (opposite) propagation. To implement this concept, let us consider the asymmetric structure made of four nonlinear defect rods embedded into the straight waveguide, as shown in Fig. 3. Figure 3(a)–(b) shows the transmission spectra of such an asymmetric structure in the opposite directions indicated by two arrows in the right insets. As is seen, in the linear limit the transmission is characterized by two resonant frequencies and does not depend on the propagation direction. However, since the sensitivity of both resonant frequencies to the change of the light intensity is different for the "forward" and "backward" propagation directions, the transmission becomes, in the vicinity of resonant frequencies, highly asymmetric for large input intensities. This results into nearly unidirectional waveguide transmission, as shown in Fig. 3(c). Similar to the all-optical switcher, we expect that the optical diode effect with much better efficiency can be found in other types of waveguide geometry, and a unitary contrast can be achieved by a proper optimization of the waveguide and defect parameters, that can be carried out by employing our method and the effective discrete equations derived above.

References

1. S.F. Mingaleev and Yu.S. Kivshar, *"Effective equations for photonic crystal waveguides and circuits"*, Opt. Lett. **27**, 231-233 (2002).
2. S.F. Mingaleev, Yu.S. Kivshar, and R.A. Sammut, *"Long-range interaction and nonlinear localized modes in photonic crystal waveguides"*, Phys. Rev. E **62**, 5777-5782 (2000).
3. S.F. Mingaleev and Yu.S. Kivshar, *"Self-trapping and stable localized modes in nonlinear photonic crystals"*, Phys. Rev. Lett. **86**, 5474-5477 (2001).
4. S.F. Mingaleev and Yu.S. Kivshar, *"Nonlinear transmission and light localization in photonic crystal waveguides"*, J. Opt. Soc. Am. B (September 2002 Focus Issue): Preprint: arXiv:cond-mat/0201266.

Modulational instability of Bose-Einstein condensates in two- and three-dimensional optical lattices

B. B. Baizakov, M. Salerno
Dipartimento di Fisica "E.R. Caianiello" and Istituto Nazionale di Fisica della Materia (INFM), Università di Salerno, I-84081 Baronissi (SA), Italy

V. V. Konotop
Departmento de Física and Centro de Física da Materia Condensada, Universidade de Lisboa, Complexo Interdisciplinar, Av. Prof. Gama Pinto 2, Lisboa 1649-003, Portugal
Tel: +39-089-965397, Fax. +39-089-965275, e-mail: salerno@sa.infn.it

Abstract: We show that the phenomenon of modulational instability gives rise to coherent spatial structures in arrays of Bose-Einstein condensates confined to optical lattices. A simple way to retain these spatial structures is proposed, which may be of interest for applications.
© 2002 Optical Society of America
OCIS codes: (020.0020) Atomic and molecular physics; (270.3100) Instabilities and chaos

Optical lattices formed by laser waves are the media where Bose-Einstein condensates (BEC) exhibit remarkable properties. In this paper we consider the evolution of the atomic distribution over the optical lattice, guided by the modulational instability. The phenomenon of modulational instability is well known in different areas of nonlinear science (hydrodynamics, plasma physics, nonlinear fiber optics) for its relevance to formation of solitons.

The origin and dynamics of solitons in BEC are the subjects which attract considerable interest. In view of the fact that a continuous BEC with repulsive interatomic forces doesn't support localized humps of atomic concentration (for review see e.g. [1]), the possibility of employing optical lattices for creation of solitons appears to be most promising. A stimulating discovery here was the proof of the existence of bright solitons in arrays of BECs with repulsive interaction between atoms [2]. The physical mechanism by which this possibility arises is similar to that of electrons in a periodic potential, in specific cases acquiring negative effective mass. The presence of the optical lattice can invert the sign of the dispersive term, which then balances the action of the nonlinearity. Therefore, bright solitons in BEC arrays with repulsive interaction between atoms are possible only in the presence of the periodic potential of the optical lattice.

Out of existing studies on the properties of solitons in arrays of BEC, little attention has been devoted to methods of creation of solitons, so far. It has recently been suggested to employ the phenomenon of modulational instability in order to create solitons in effectively 1D optical lattice [3]. It was demonstrated that particular initial waveforms (Bloch states) for the atomic distribution over the optical lattice give rise to formation of solitons. In Ref. [4] a variety of localized solutions are found to the one-dimensional nonlinear Schrödinger equation with a periodic potential, describing the dynamics of BEC in the optical lattice.

The extension of the above considerations [3, 4] to 2D and 3D optical lattices seems to be interesting both from the viewpoints of the physics and applications of BEC. The major difference here is that, contrary to 1D case, the nonlinear Schrödinger equation which governs the dynamics of localized excitations in 2D and 3D optical lattices doesn't have stable solitonic solutions. Nevertheless, as the modulational instability results in formation of spatially localized soliton-like excitations in 2D and 3D optical lattices, they could be stabilized by external means, e.g. changing the parameters of the periodic trap potential. In what follows we demonstrate the possibility to create regularly spaced localized excitations in arrays of BEC, which present narrow tubes in 2D and small hollows in 3D cases, filled in with BEC atoms of much greater density compared to surrounding array sites.

To develop the model we consider a dimensionless 3D Gross-Pitaevskii (GP) equation

$$i\frac{\partial \psi}{\partial t} = -\Delta \psi + V(\mathbf{r})\psi + \chi|\psi|^2\psi, \tag{1}$$

where the potential $V(\mathbf{r})$ is assumed, for the sake of simplicity, to be separable, i.e. of the form $V(\mathbf{r}) = \sum_j V_j(r_j)$, $j = x, y, z$ and periodic in each of the spatial directions: $V_j(r_j) = V_j(r_j + a_j)$, with a_j the

period in the direction r_j. For convenience Eq. (1) is considered subject to periodic boundary conditions $\psi(\mathbf{r}) = \psi(r_x + L_x, r_y, r_z)$, etc., where $L_j = N_j a_j$ with N_j and L_j respectively, the number of primitive cells and the length of the system in the direction r_j. The theory is developed for the small amplitude limit, when the multiscale analysis is applicable. This means that we are looking for a solution of Eq. (1) in the form $\psi = \epsilon\psi_1 + \epsilon^2\psi_2 + \epsilon^3\psi_3 + \cdots$, where the ψ_j are functions of the scaled independent variables $\tau_p = \epsilon^p t$, $\xi_p = \epsilon^p \mathbf{r}$, $p = 0, 1, 2, ...$, with ϵ a small parameter. Further, denoting with $\omega_{\alpha_j}(q_j)$, and $\Phi_{\alpha_j}(r_j) \equiv |\alpha_j, q_j\rangle$, the eigenvalues and eigenfunctions of the periodic operators $\mathcal{L}_{r_j} = -\partial_{r_j}^2 + V_j(r_j)$, and applying the arguments which are similar to those of Ref.[3], one arrives at the following 3D nonlinear Schrödinger equation for the slowly varying envelope

$$i\frac{\partial \mathcal{A}}{\partial \tau_2} + \frac{1}{2}\sum_{j=x,y,z} \mathbf{M}_{\alpha_j,jj}^{-1}\frac{\partial^2 \mathcal{A}}{\partial R_j^2} - \tilde{\chi}|\mathcal{A}|^2\mathcal{A} = 0, \tag{2}$$

where $\mathcal{A} = \mathcal{A}(\mathbf{R}; \xi_2...; \tau_2, ...)$ with $\mathbf{R} = \xi_1 - \mathbf{v}\tau_1$ and $\mathbf{v} = -\langle\alpha_{0x}\alpha_{0y}\alpha_{0z}|2i\nabla|\alpha_{0x}\alpha_{0y}\alpha_{0z}\rangle$ is the group velocity of the carrier wave. We also introduced the inverse of the effective mass tensor and the effective nonlinearity

$$\frac{1}{2}\mathbf{M}_{\alpha,jj}^{-1} = 1 + \sum_{\alpha_x} \frac{|\Gamma_{\alpha_x\alpha_{0,x}}^{(y,z)}|^2}{\omega_{\alpha_x}(q_{0,x}) - \omega_{\alpha_{0,x}}(q_{0,x})} = \frac{1}{2}\partial_{q_j}^2\omega_{\alpha_j}(\mathbf{q}), \qquad \tilde{\chi} = \chi\prod_{j=x,y,z}\int_0^{L_j}|\Phi_{m_{0j}}|^4\, dr_j.$$

To analyze the stability problem within the framework of Eq. (2), we look for a solution of the form $\mathcal{A} = (\rho + ae^{i(\Omega\tau_2 - \mathbf{K}\mathbf{R})} + be^{-i(\Omega t_2 - \mathbf{K}\mathbf{R})})e^{-i\rho^2\tau_2}$, where $|a|, |b| \ll \rho$. This solution is unstable if

$$Z(Z + 4\tilde{\chi}\rho^2) < 0, \qquad Z = \sum_{j=x,y,z} \mathbf{M}_{jj}^{-1}K_j^2. \tag{3}$$

For the numerical study we have used the potential $V_j(r_j) = 2\Lambda\cos(kr_j)$ for $j = x, y, z$. Numerical solution of Eq.(1) has been performed by the operator splitting procedure using multi-dimensional fast Fourier transform [5]. The spatial domain $x, y, z \in [-\frac{L}{2}..\frac{L}{2}]$ (i.e. $L_x = L_y = L_z = L$) was represented by an array of 128 x 128 x 128 points and the time step was $\delta t = 0.001$. Below we present the results for a box $L = 12\pi$, restricting consideration to lowest two bands of the Brillouin zone (BZ).

First we outline results for the 2D case, specifying parameter values as $\chi = 1.0$, $k = 2.0$, (i.e. $a_x = a_y = \pi$) $\rho = 0.5$. Then considering particular Bloch states, e.g. corresponding to points $\bar{q}_0 = (\pm 1, \pm 1)$ at the boundary of the BZ one can distinguish the following three different cases. *Case 1.* Both eigenfunctions $\Phi_{m_{0,x}}$ and $\Phi_{m_{0,y}}$ belong to the first lowest zone: $m_{0,x} = m_{0,y} = (1, \pm 1)$. Then $\mathbf{M}_{1,xx}^{-1} = \mathbf{M}_{1,yy}^{-1} = \mathbf{M}_1^{-1} < 0$ and the wave is unstable. BEC dynamics in this case is presented in Fig. 1. The most interesting feature of
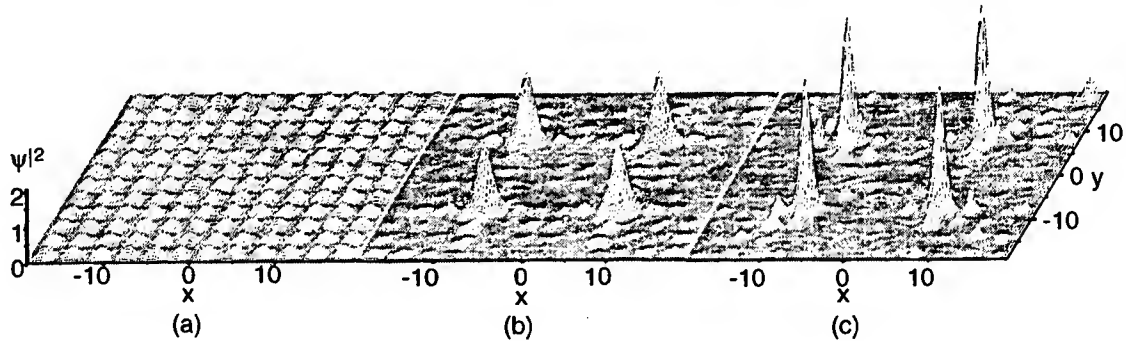

Fig. 1.   Evolution of BEC atomic distribution in a 2D optical lattice according to Eq. (2) with $\Lambda = 0.5$, $k = 2.0$, $\chi = 1.0$, $L = 12\pi$. (a) The initial waveform $\psi(x, y, 0) = 0.5\sin(x)\sin(y)$ at $t = 0$. (b) Formation of soliton-like excitations due to modulational instability at t=50. (c) The distribution (b) remains stable for long times when the strength of the trap potential is adiabatically increased up to $\Lambda = 1.5$ during $50 < t < 55$. The snapshot (c) is shown at $t = 100$ (stability is verified up to t=1000).
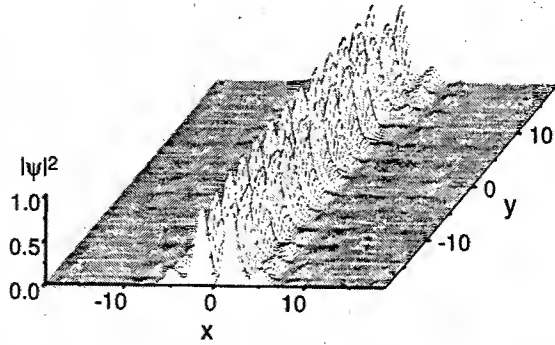
Fig 2.   Distribution of a BEC in the 2D periodic potential with $\Lambda = 0.5$ subject to the initial condition $\psi(x, y, 0) = 0.5 \sin(x) \cos(y)$. Regular pattern of soliton-like excitations are formed at t =32.
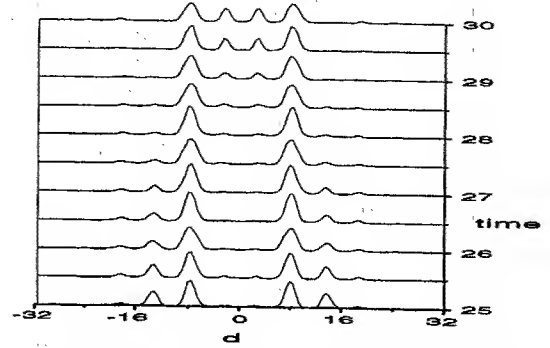

Fig 3.   Formation of soliton-like excitations by $t \sim$ 28 in 3D BEC array. d is the distance along the main diagonal of the cubic domain with $L = 12\pi$. The initial condition is $\psi(x, y, z, 0) = 0.5 \sin(x) \sin(y) \sin(z)$.

the modulational instability developed is that it evolves in a *regular* structure which represents symmetrically spaced localized in space (we call them soliton-like) distributions (see Fig. 1b). Each of the humps shown in the figure represents a tightly confined tube along z-direction. The number of the tubes is proportional to the size of the box. However, these structures eventually decay in accordance with Eq.(2), which does not support stable solitonic solutions in 2D and 3D. A simple way to retain these excitations would be the increasing of the strength of the periodic trap potential, when excitations are formed. High potential barrier between lattice sites then suppresses the atomic tunneling, providing strong confinement (see Fig. 1c).

Case 2. The eigenfunctions $\Phi_{m_{0,x}}$ and $\Phi_{m_{0,y}}$ belong to different zones, say $\Phi_{m_{0,x}}$ belongs to the first lowest zone: $m_{0,x} = (1, \pm 1)$ and $\Phi_{m_{0,y}}$ belongs to the second lowest zone: $m_{0,y} = (2, \pm 1)$. Then $M_{1,xx}^{-1} < 0$ and $M_{1,yy}^{-1} > 0$, and the condensate is unstable. In this case the instability condition takes the form $0 < M_{2,yy}^{-1} K_y^2 - |M_{1,xx}^{-1}| K_x^2 < 4\tilde{\chi}\rho^2$, and the most unstable excitations have $K_x^2 < \frac{M_{2,yy}^{-1}}{|M_{2,xx}^{-1}|} K_y^2$ (which is related to the fact that an eigenfunction $\Phi_{m_{0,x}}$ belongs to the "unstable" branch). That is why the main instability results in a pattern having different symmetry: it develops in the x-direction. Along this direction the pattern is rapidly split in a sequence of solitary waves. The instability develops also along y-direction, but at much larger time scales (see Fig. 2.).

Case 3. Both eigenfunctions $\Phi_{m_{0,x}}$ and $\Phi_{m_{0,y}}$ belong to the second lowest zone: $m_{0,x} = m_{0,y} = (2, \pm 1)$. Then $M_{2,xx}^{-1} = M_{2,yy}^{-1} > 0$ and the wave is stable, which was confirmed numerically using the initial conditions $\psi(x, y, 0) = 0.5 \cos(x) \cos(y)$.

Qualitatively similar behaviour of the modulational instability with respect to formation of soliton-like excitations was observed in 3D case. Fig. 3 illustrates the emergence of spatial structures with high atomic concentration in a 3D BEC array, shown as a section along the main diagonal of the cubic domain with $L = 12\pi$. The time interval is selected to display the emergence of soliton-like excitations at $t = 28$, and their subsequent decay. Long-term evolution exhibits the recurrence phenomenon.

In conclusion, we have illustrated the possibility to create and preserve regularly spaced soliton-like excitations in 2D and 3D BEC arrays employing the phenomenon of modulational instability. Main features of their spatial arrangement are described by the theory based on the multiple scale expansion.

References

1. F. Dalfovo, S. Giorgini, L. P. Pitaevskii, and S. Stringari, Rev. Mod. Phys. **71**, 463 (1999).
2. S. Pötting, P. Meystre, and E. M. Wright, cond-mat/0009289.
3. V. V. Konotop and M. Salerno, Phys. Rev. A **65**, 021602 (2002).
4. G. L. Alfimov, V. V. Konotop, and M. Salerno, Europhys. Lett. **58**, 7 (2002).
5. W. H. Press, S. A. Teukolsky, W. T. Vetterling, and B. P. Flannery, *Numerical Recipes. The Art of Scientific Computing.* (Cambridge University Press, 1996).

Optimized 2-dimensional poling pattern for fourth harmonic generation

Andrew H. Norton and C. Martijn de Sterke

School of Physics, University of Sydney, 2006 Australia
Phone: 61 2 9351 3849, Fax: 61 2 9351 7726
Email: andrewn@physics.usyd.edu.au, desterke@physics.usyd.edu.au

Abstract: The efficiency of a recently proposed fourth harmonic generation scheme depends on two Fourier coefficients of a 2-dimensional periodic poling pattern. We describe a poling pattern corresponding to a local maximum of this efficiency.
© 2002 Optical Society of America
OCIS codes: (190.2620) Frequency conversion; (190.4400) Nonlinear optics, materials

1 The collinear 2-channel FHG scheme

Quadratically nonlinear optical materials with a 2-dimensional periodic poling pattern were recently shown to support a variety of frequency generation processes [1]. These structures, referred to here as nonlinear photonic crystals (NPCs), can be fabricated from materials such as lithium niobate ($LiNbO_3$) and lithium tantalate ($LiNbO_3$) by 2-dimensional periodic poling of the nonlinear quadratic susceptibility ($\chi^{(2)}$). One possible application for NPCs is collinear fourth harmonic generation (FHG). The FHG scheme proposed in [2] is a 2-channel quasi-phase matched process in which a pair of second harmonic (SH) waves mix to generate a fourth harmonic (FH) wave collinear with the fundamental.

The FHG scheme is described in Figure 1(a). Three reciprocal lattice vectors G_1, G_2 and G_3 are needed for phase matching,

$$\mathbf{k}_{21} = 2\mathbf{k}_1 + \mathbf{G}_1, \qquad \mathbf{k}_{22} = 2\mathbf{k}_1 + \mathbf{G}_2, \qquad \mathbf{k}_4 = \mathbf{k}_{21} + \mathbf{k}_{22} + \mathbf{G}_3. \tag{1}$$

The wave vectors are: $\mathbf{k}_1$ for the fundamental; $\mathbf{k}_{21}$, $\mathbf{k}_{22}$ for the pair of SH waves; and $\mathbf{k}_4$ for the FH wave.
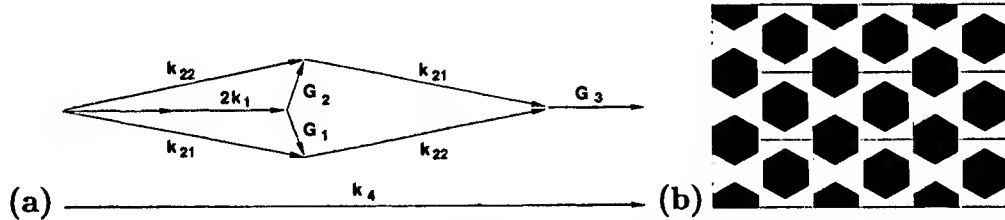
Fig. 1. (a) Phase matching diagram for the FHG scheme. The G_i are reciprocal lattice vectors of the NPC and the k_i are discussed in the text. (b) Simple hexagonal poling pattern considered in [2]. The poling lattice is such that the phase matching conditions (1) are satisfied for $LiTaO_3$ at 150 °C at a fundamental wavelength of $\lambda = 1.53\,\mu$m. The hexagon edge length is 5.12 μm, corresponding to a maximum of FHG efficiency with respect to hexagon size.

A 2-dimensional NPC lattice can always be found so that phase matching conditions (1) are satisfied by three reciprocal lattice vectors. The equation given in [2] fixes the lattice vectors (eg., dimensions of the rectangles in Fig. 1(b)) in terms of the refractive index of the material at the fundamental, SH and FH. So the NPC lattice is fixed by the frequency of the fundamental, the material and the operating temperature. Relations (1) say nothing about about the poling pattern within a fundamental domain of the NPC lattice, other than to suggest that it has a reflection symmetry. On the other hand, the efficiency of the FHG scheme does depend on the poling pattern. Thus some effort must be put into choosing a good pattern.

Figure 1(b) shows a poling pattern considered in [2]. Hexagonal regions are poled so that the $\chi^{(2)}_{333}$ component of the second order susceptibility tensor changes sign across hexagon boundaries. The hexagonal poling pattern is simple but not very efficient, despite being optimized with respect to hexagon size and orientation. Here more general polygonal poling patterns are considered.

2   FHG efficiency and optimization constraints

Using standard perturbation methods [3] one can derive evolution equations for the slowly varying amplitudes of the waves involved in the FHG scheme. Let A_1, A_{21}, A_{22}, A_4 be amplitudes for the fundamental, pair of SH and FH waves respectively. Then,

$$\frac{\partial A_1}{\partial x^1} = \frac{i}{n_1}\sigma_1^* A_1^* (A_{21} + A_{22}) , \tag{2}$$

$$\frac{\partial A_{2j}}{\partial x^1} = \frac{i}{n_2 \cos\theta}\left(\sigma_1(A_1)^2 + \sigma_2^* A_4 A_{2(3-j)}^*\right) , \tag{3}$$

$$\frac{\partial A_4}{\partial x^1} = \frac{i}{n_4}2\sigma_2 A_{21} A_{22} . \tag{4}$$

Here n_1, n_2, n_4 are the extraordinary refractive indices at the fundamental, SH and FH respectively, and θ is the angle between the fundamental and SH wave vectors. The coefficients σ_1,σ_2 are proportional to the relevant Fourier coefficients of the poling function $f(x^1, x^2) = \pm 1$. With respect to an orthogonal reciprocal lattice basis $\{\mathbf{K}_1, \mathbf{K}_2\}$, with $\mathbf{K}_1$ in the direction of $\mathbf{k}_1$, these coefficients are given by,

$$\sigma_1 = \hat{f}_{N_1 N_2} |\mathcal{X}^{(2)}_{333}|\omega/c, \qquad \sigma_2 = 2\hat{f}_{M0} |\mathcal{X}^{(2)}_{333}|\omega/c, \tag{5}$$

where ω is the frequency of the fundamental. The indices N_1, N_2, M are fixed when the NPC lattice is fixed (see [2] for details). For the lattice shown in Fig 1(b), $N_1 = N_2 = 1$ and $M = 8$. Although the methodology in the following applies quite generally, it is this particular case which is considered here.

A convenient measure of FHG efficiency can be defined by considering the initial growth of the FH energy flux for standard initial data, $A_1 = 1$, $A_{21} = A_{22} = A_4 = 0$ at $x = 0$. The first non-zero coefficient in the Taylor series solution for $A_4^* A_4$ is easily found to be $[\partial^6 A_4^* A_4/\partial x^6]_{x=0} = (n_4 n_2^2 \cos^2\theta/4)^{-2} \sigma_2^* \sigma_2 (\sigma_1^* \sigma_1)^2$. Thus, for the purpose of comparing FHG efficiency, one can define a poling pattern merit functional,

$$\alpha[f] = 4 \hat{f}_{M0}^* \hat{f}_{M0} \left(\hat{f}_{N_1 N_2}^* \hat{f}_{N_1 N_2}\right)^2 . \tag{6}$$

For the following, $\alpha[f] = 4 |\hat{f}_{80}|^2 |\hat{f}_{11}|^4$. The poling pattern shown in Fig 1(b) has $\alpha[\text{Hexagonal}] = 2.04 \times 10^{-4}$.

The optimization of $\alpha[f]$ with respect to poling function f is subject to several constraints:
(1) The poling function can only take the values $f(x^1, x^2) = \pm 1$.
(2) The poling function periodicity is $f(x^1, x^2) = f(x^1 + n_1 d_1, x^2 + n_2 d_2)$ for $n_1, n_2 \in \mathbf{Z}$. The NPC lattice parameters d_1 and d_2 are fixed once the frequency, material and operating temperature have been specified.
(3) The poling function is polygonal. All discontinuities in f must coincide with crystal planes of the material. For LiNbO$_3$ and LiTaO$_3$ this means poling boundaries are parallel to the sides of some hexagon.
(4) The poling function has reflection symmetry, $f(x^1, -x^2) = f(x^1, x^2)$. This is suggested by the phase matching diagram, and is in fact assumed in deriving the evolution equations (and therefore $\alpha[f]$).
(5) Fabrication constraints. Roughly speaking, f should not have features that are too small. In particular, poling boundaries that are parallel should be separated by at least $1\,\mu$m.

3   On Fourier transforms of polygons

The feasibility of numerically optimizing $\alpha[f]$ depends on being able to efficiently calculate the Fourier coefficients of an arbitrary polygonal poling function. The following result gives a simple expression for these coefficients in terms of polygon vertex coordinates.

Proposition. Let $\{l_1, l_2\}$ be a basis for the lattice L and let $D = \{t^1 l_1 + t^2 l_2 \; : \; t^1, t^2 \in [0, 1)\}$ be a fundamental domain of L. Let $P \subset D$ be a polygonal region, and denote by $L(P)$ the union of its lattice images. Let the characteristic function $h(x)$ of the set $L(P)$ have Fourier series expansion,

$$h(x) = \sum_{a_1=-\infty}^{\infty} \sum_{a_2=-\infty}^{\infty} \hat{h}_{a_1 a_2} e^{i(a_1 k^1 + a_2 k^2)\cdot x} = \begin{cases} 1 & \text{for } x \in L(P), \\ 0 & \text{elsewhere,} \end{cases}$$

where $\{k^1, k^2\}$ is the reciprocal basis satisfying $k^i \cdot l_j = 2\pi\delta^i_j$. Finally, let the N vertices of P be labeled anticlockwise as $x_{(q)}$, $q = 0, \ldots, N-1$, $(x_{(N)} = x_{(0)})$. Then for $(a_1, a_2) \neq (0, 0)$ the following formula holds,

$$\hat{h}_{a_1 a_2} = \frac{-1}{A \cdot K \, \mathrm{Vol}(D)} \sum_{q=0}^{N-1} \mathcal{E}_{(q)}, \quad \text{where} \quad \mathcal{E}_{(q)} = \begin{cases} \frac{A \cdot \nu_{(q)}}{K \cdot \Delta_{(q)}} \left(e^{-iK \cdot x_{(q+1)}} - e^{-iK \cdot x_{(q)}} \right) & \text{for } K \cdot \Delta_{(q)} \neq 0, \\ -iA \cdot \nu_{(q)} e^{-iK \cdot x_{(q)}} & \text{otherwise}. \end{cases}$$

Here $A = a_1 l_1 + a_2 l_2$, $K = a_1 k^1 + a_2 k^2$, $A \cdot K = 2\pi \left((a_1)^2 + (a_2)^2 \right)$, $\Delta^j_{(q)} = x^j_{(q+1)} - x^j_{(q)}$ and $\nu_{i(q)} = \varepsilon_{ij} \Delta^j_{(q)}$.

Proof. An application of Stokes theorem to $\int_P d(A^1 e^{-iK \cdot x} dx^2 - A^2 e^{-iK \cdot x} dx^1)$, where $A = A^i \partial/\partial x^i$.

Remark. For the case $(a_1, a_2) = (0, 0)$ one has, $\hat{h}_{00} = \frac{1}{2\mathrm{Vol}(D)} \sum_{q=0}^{N-1} \left(x^1_{(q)} x^2_{(q+1)} - x^1_{(q+1)} x^2_{(q)} \right)$.

4 Optimal poling pattern for FHG

The numerical search for a poling function that optimizes $\alpha[f] = 4 |\hat{f}_{80}|^2 |\hat{f}_{11}|^4$ requires a good initial guess as to what such a pattern may look like. Figure 2 outlines the general approach taken. Figure 3 shows the optimized Escher-like poling pattern, having $\alpha[\text{Escher}] = 5.00 \times 10^{-3} = 24.5 \times \alpha[\text{Hexagonal}]$. Let us assume that similar design improvements can be achieved for other wavelengths and operating temperatures. Then, based on a scaling of the results in Fig 3(b) in [2], one can expect roughly 40% of the incident power to be converted to the FH frequency using a 1 cm long sample and a few $\mathrm{MW/cm}^2$ of incident fundamental light in $\mathrm{LiNbO_3}$, or less than $10\,\mathrm{MW/cm}^2$ in $\mathrm{LiTaO_3}$. The optimization code used here is limited in that vertices can not automatically appear or vanish. More general procedures are currently being considered.
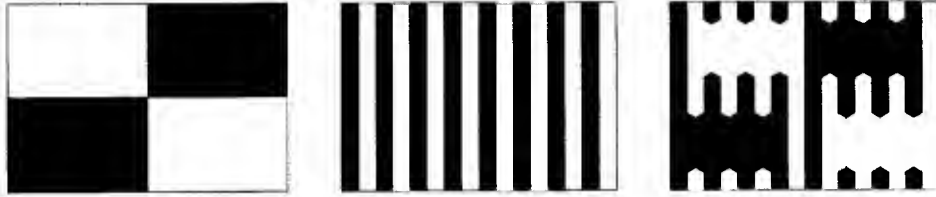
Fig. 2. A qualitative design approach. *Left:* Poling pattern with large (1,1) Fourier component. *Center:* Poling pattern with large (8,0) Fourier component. *Right:* Compromise between the (1,1) and (8,0) patterns, used as the initial configuration in a numerical optimization of $\alpha[f] = 4 |\hat{f}_{80}|^2 |\hat{f}_{11}|^4$.
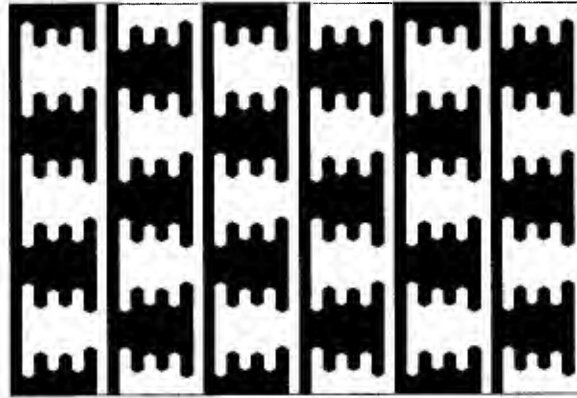
Fig. 3. Numerically generated optimal Escher-like poling pattern, $\alpha[\text{Escher}] = 5.00 \times 10^{-3}$.

References

1. N.G.R. Broderick, G.W. Ross, H.L. Offerhaus, D.J. Richardson and D.C. Hanna, Phys. Rev. Lett. **84**, 4345 (2000).
2. M. de Sterke, S.M Saltiel and Y.S. Kivshar, Optics Lett. **26**, 539 (2001).
3. J. Kevorkian, J.D. Cole, *Perturbation methods in Applied Mathematics* (Springer-Verlag, New York, 1981).

Negative group velocities in quasi-phase-matched second-order nonlinear optical interactions

S. Longhi, P. Laporta, M. Marano

Istituto Nazionale per la Fisica della Materia, Dipartimento di Fisica and IFN-CNR, Politecnico di Milano, Piazza L. da Vinci 32, I-20133 Milano (Italy)

Phone: +30 02 2399 6156; Fax: +39 02 2399 6126, E.mail address: longhi@fisi.polimi.it

The existence of anomalous, i.e. superluminal or negative, group velocities [1] provides one of the most amazing phenomenon of wave propagation which is compatible with, and even a consequence of, causality [2]. Anomalous wave propagation generally relies on the *resonant* interaction of light with an atomic medium, i.e. it exploits the dispersive properties of absorptive [3] or inverted [4,5] atomic media near resonances. Evanescent wave propagation across photonic barriers [1] provides the other wide framework where anomalous group velocities have been observed, however in such cases the achievement of a *negative* group velocity seems unlikely. By exploiting the dispersive properties of a gain doublet, a narrow spectral region of *transparent* anomalous dispersion around the dip center of two Lorentzian gain lines, leading to negative transit times and no pulse attenuation, can be created [4]. A recent demonstration thereof has been indeed reported in an experiment by Wang and coworkers using Cs vapor [5].
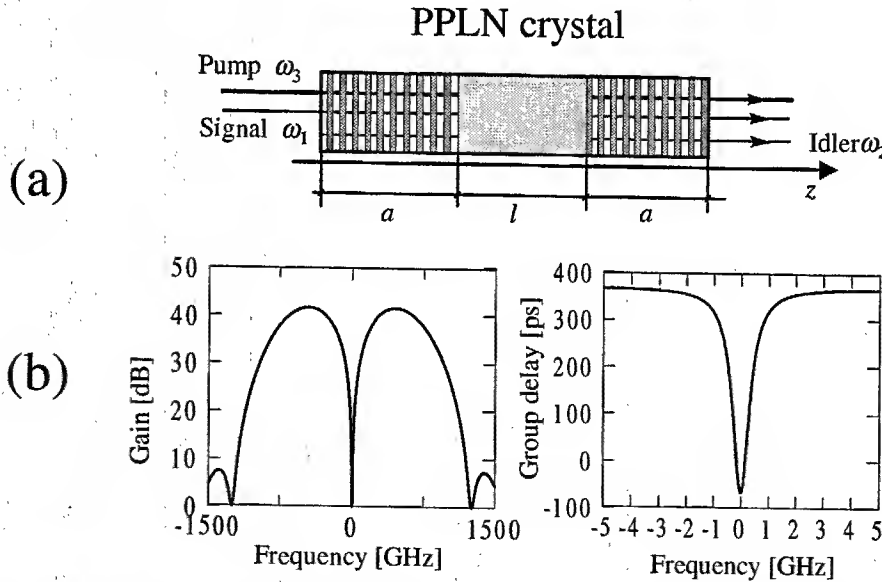
Fig.1 (a) Schematic of the QPM parametric amplifier, composed by the cascading of two uniform QPM grating sections. (b) Spectral power gain curve and group delay curve of the amplifier for: a=3 mm, l=2 mm, and I_3=135 MW/cm^2.

In this work we show that negative group velocities, corresponding to negative transit times for propagation of spectrally-narrow optical pulses, can be achieved exploiting the *nonresonant* interaction of light with a nonlinear quadratic medium, with the possibility of controlling the transit time by means of a control pump beam. In particular, we show that a proper design of the quasi-phase-matching (QPM) grating structure of quadratic nonlinearity can reproduce the experimental conditions of the gain-assisted superluminal experiment by Wang et al. [5].

We consider the propagation of a weak signal wave at frequency ω_1 through a QPM nondegenerate optical parametric amplifier, pumped by a strong continuous-wave (CW), or quasi-CW, pump beam at frequency ω_3 [see Fig.1(a)]. Under the plane wave and undepleted pump approximations and neglecting group velocity dispersion, the coupled equations for the amplitudes A_1 and A_2 of signal and idler waves are:

$$\partial_z A_1 + (1/v_{g1})\partial_t A_1 = i\frac{\omega_1 d_{eff}(z)}{n_1 c_0}\sqrt{\frac{2I_3}{\varepsilon_0 c_0 n_3}}A_2^* \qquad (1a)$$

$$\partial_z A_2 + (1/v_{g2})\partial_t A_2 = i\frac{\omega_2 d_{eff}(z)}{n_2 c_0}\sqrt{\frac{2I_3}{\varepsilon_0 c_0 n_3}}A_1^* \qquad (1b)$$

where $v_{g1,2}= 1/k'(\omega_{1,2})$ are group velocities of signal and idler fields, I_3 is the intensity of the pump wave, $d_{eff}(z)= (1/2) <\chi^{(2)}(z)\exp(i\Delta kz)>$ is the effective nonlinear interaction coefficient that depends on the QPM grating design, Δk is the wave vector mismatch, and the bracket denotes a spatial average over the short coherence length $\Lambda=2\pi/\Delta k$. The properties underlying the propagation of a spectrally-narrow signal pulse across the parametric amplifier can be derived by determining the complex-valued spectral gain curve $g(\Omega)$ of the amplifier, where Ω is the frequency offset from the reference frequency ω_1 at the signal wavelength. The determination of the spectral gain curve involves the analysis of coupled-mode equations usually encountered in the study of inverse scattering problems and wave propagation through periodic media. The modulus $G(\Omega)=|g(\Omega)|^2$ provides the spectral power gain curve, whereas the group delay $\tau_g= Im[\partial (\ln g)/\partial\Omega]$ gives the transit time for a spectrally-narrow pulse. As a consequence of causality, one can show that the group delay τ_g is univocally determined by the power spectral gain curve $G(\Omega)$ through a Hilbert-like transform [6]. For $v_{g1}>v_{g2}$, this may imply the existence of anomalous transit times near *local minima* of the spectral power gain curve. As an example, we considered a PPLN crystal pumped at the wavelength $\lambda_3=532$ nm with a signal field at $\lambda_1=1.55$ μm, ($d=d_{33} \approx 27$ pm/V for extraordinary wave propagation, $v_{g1} \cong 0.4815$ c_0, and $v_{g1} \cong 0.44220$ c_0). The QPM grating [Fig.1(a)] consists of a sequence of two +/- square-wave uniform gratings, each of length a and period $\Lambda=2\pi/\Delta k \cong 7.39$ μm (first-order QPM), separated by a distance l; a sign reversal of d_{eff} in the two grating sections is assumed. For such a QPM structure, a gain dip at $\Omega=0$, corresponding to superluminal and even negative transit times, is obtained at sufficiently high pump intensities [see Fig.1(b)]. The transit time can be pushed from subluminal to superluminal and further to negative values by increasing the pump intensity. An example of control of pulse transit time by pump intensity for picosecond Gaussian pulses is shown in Fig2. Assuming a $\cong 200$ μm spot-size, $\cong 5$ ns duration Gaussian pump pulse, about twenty times longer than the probing pulses, a pump pulse energy of $\cong 0.90$ mJ is required to observe negative transit times. Such power levels can be obtained using, e.g., a frequency-doubled Q-switched Nd-based laser system as a pump source. We checked that the occurrence of superluminal and negative group velocities persists also when a more realistic model, in which imperfections of the QPM grating as well as higher-order dispersion effects, is considered. This is a consequence of the causality (Kramers-Krönig) relation between $G(\Omega)$ and $\tau_g(\Omega)$, so that local minima in the spectral gain curve usually yield anomalous dispersive properties, regardless of the exact shape of $G(\Omega)$, which may be indeed quite sensitive to fabrication imperfections. The basic physics underlying anomalous propagation with no appreciable
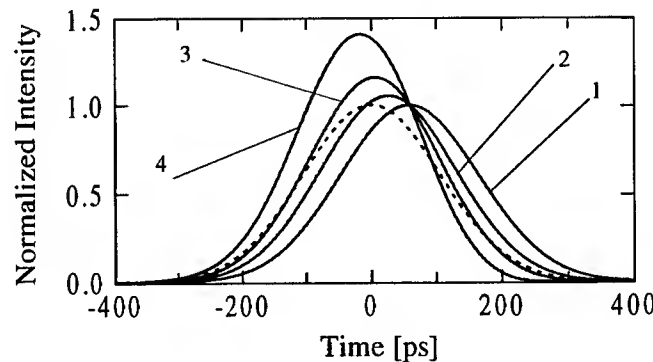

Fig.2. Traces of the intensity of transmitted signal pulse at the exit of the crystal ($z=L$) for a few values of pump intensities (curve 1: $I_3=0$; curve 2: $I_3=108$ MW/cm²; curve 3: $I_3=135$ MW/cm²; curve 4: $I_3=162$ MW/cm²). The dashed curve is the Gaussian signal pulse trace at the input plane $z=0$ (250 ps FWHM duration). Notice that, for curves 3 and 4, the peak pulse leaves the amplifier before the peak of incident pulse has entered into the crystal. The pulse intensities are normlazide to the peak intensity of incident pulse.

pulse amplification and distortion can be understood as follows. In the fist section of the QPM grating the signal pulse is amplified, with the generation of the idler wave ($\omega_3 \rightarrow \omega_1 + \omega_2$); however, owing to the phase reversal in the second QPM grating, a back conversion process ($\omega_1 + \omega_2 \rightarrow \omega_3$) occurs in the second grating section. The result of such a cascading process is that the signal pulse is basically not amplified at the output of the crystal, however the phase delays suffered by its spectral components produce a temporal advancement with no appreciable pulse distortion.

In conclusion, we have theoretically shown that QPM parametric amplifiers can simulate dispersive properties of resonant pulse propagation in inverted atomic media. The possibility of observing and controlling superluminal and negative group velocities of picosecond optical pulses seems feasible with current QPM technology using a PPLN-based optical parametric amplifier.

[1] R.Y. Chiao and A.M. Steinberg, Prog. Opt. **37**, 345 (1997).

[2] E.L. Bolda, R.Y. Chiao, and J.C. Garrison, Phys. Rev. A **48**, 3890 (1993).

[3] S. Chu and S. Wong, Phys. Rev. Lett. **48**, 738 (1982).

[4] A.M. Steinberg and R.Y. Chiao, Phys. Rev. A **49**, 2071 (1994).

[5] L.J. Wang, A. Kuzmich, and A. Dogariu, Nature **406**, 277 (2000).

[6] S. Longhi, M. Marano, and P. Laporta, "Dispersive properties of quasi-phase-matched optical parametric amplifiers", Lanl Archives #physics/0204059 (submitted for publication).

Novel Type Nonlinear Semiconductor Waveguide Crystal For Efficient Frequency Up/Down Conversion.

E. U. Rafailov, P. Loza-Alvarez, D. Artigas[*], M. B. Flynn, W. Sibbett.

School of Physics and Astronomy, University of St Andrews, North Haugh, St. Andrews, Fife KY16 9SS, UK.
Phone +44 (0) 1334 463124, Fax +44 (0) 1334 463104, er8@st-andrews.ac.uk

*Laboratory of Photonics,Department of Signal Theory and Communication, Universitat Politecnica de Catalunya, Gran Capitan D3, 08034 Barcelona, Spain

Abstract:

We demonstrate SHG at 980 nm from a novel first-order QPM semiconductor GaAs/AlGaAs waveguide crystal. Our calculations show that the SHG conversion efficiency from the crystal significantly exceeds that from PPLN for wavelengths exceeding 3.4 μm for both femtosecond and CW pump beams.

Recent progress in the development of electric-field poling techniques for the patterning of the domain structure of ferroelectric materials has enabled the implementation of distinctive quasi-phase-matched (QPM) structures for efficient nonlinear optical interactions [1]. Such QPM devices have been fabricated in $LiNbO_3$, $LiTaO_3$ and in the KTP-family crystals. Semiconductor materials which have larger nonlinear coefficients ($\chi^{(2)}$), are also promising candidates for efficient frequency up/down conversion. However, the technology employed at present to fabricate semiconductor QPM devices suffers from limitations such as the difficulty in producing and stacking thin plates for first-order QPM.

We report here a first-order quasi-phase matched semiconductor device based on a novel methodology that involves a "periodically-switched-nonlinearity (PSN)" [2]. In these PSN-structures, the $\chi^{(2)}$-coefficient in the material is changed periodically using a re-growth process. To achieve this change in $\chi^{(2)}$ we have engineered a GaAs/Al_xGa_{1-x}As structure, where $\chi^{(2)}_{GaAs} >> \chi^{(2)}_{AlGaAs}$ [3]. The PSN-design is described in [2].

The coherence lengths in the original and re-grown material (l_c and l'_s, respectively) are different due to their unequal refractive indices. The period Λ of the PSN gratings is given by $\Lambda = l_c + l'_s$.

The semiconductor structure was fabricated by growing three different layers on a GaAs <100> substrate: 2 μm of $Al_{0.6}Ga_{0.4}$As, ~0.2 μm of $Al_{0.4}Ga_{0.6}$As, and 1.15 μm of undoped GaAs. The wafer was then processed by etching a 1.1 μm deep grating with a period of $\Lambda = 2.97 + 4.73$ μm into the GaAs layer. This was followed by re-growing two new layers over the grating: 2 μm of $Al_{0.4}Ga_{0.6}$As and 0.2 μm of $Al_{0.6}Ga_{0.4}$As, terminating with a 10 nm GaAs protective cap. Finally, waveguide ridges of 3, 5, 8 and 15 μm widths were etched perpendicular to the grating, and the sample was cleaved into ~0.3 and 1.1 mm long devices. The SHG intensity as a function of the fundamental wavelength power (from a PPLN-based femtosecond (<150 fs) OPO) launched into the 15 μm wide waveguide is plotted in **Fig. 1** (squares). These data are in good agreement with a linear fit having a slope of 1.97, as expected for a QPM quadratic process. We also observed that the SHG signal disappeared when the polarisation at the fundamental wavelength was rotated by 90 degrees, which is consistent with the behaviour expected. The spectra of the fundamental wavelengths measured with and without the sample are reproduced in Fig.2 (a). The spectra of SHG wavelengths for two different crystal lengths, measured from behind the samples are shown in Fig.2 (b).

To further investigate this technique, a detailed numerical analysis was undertaken. This model was based on the slowly varying envelope approximation that describes pulse evolution in a collinear SHG configuration [4]. The model includes group-velocity mismatch, second-order and third-order group-velocity dispersion and the nonlinear coefficient. All concerned coefficients change periodically depending on the material in each domain and were calculated using the Sellmeier equations from [5]. The model does not take into account waves propagating in the

negative z direction, therefore the reflection at the interfaces between domains was included by considering the Fresnel transmission coefficients.
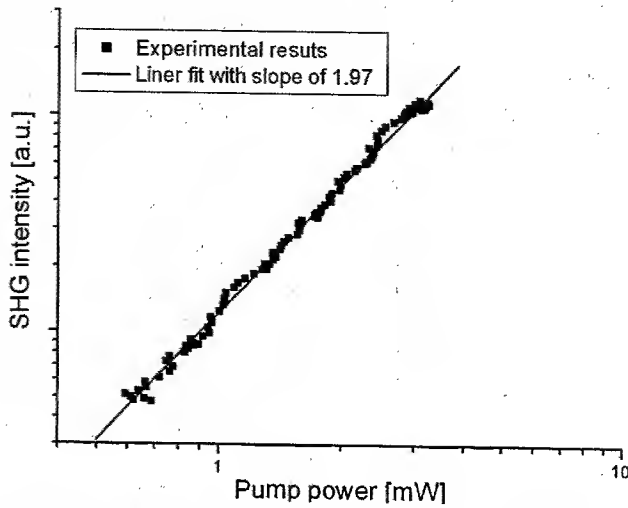

Figure 1. The SHG intensity as a function of fundamental power launched into the waveguide (squares).
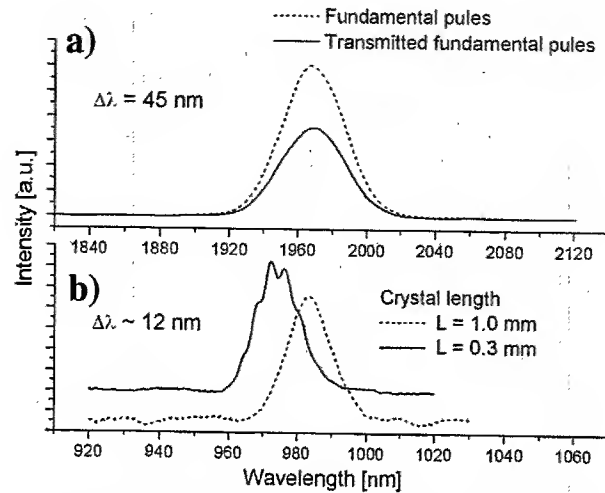

Figure 2 The spectra of the fundamental (a) and SHG (b) pulses.

Our numerical results showed that efficient SHG conversion in PSN device is limited mainly by the large group velocity mismatching at wavelengths shorter than 4.2 µm (femtosecond regime) and interface reflection losses (in both femtosecond and CW regimes). **Fig.3.** shows the change of SHG output power for optimal crystal length as a function of fundamental wavelength for (a) the femtosecond and (b) CW regimes and its comparison with conventional PPLN crystal. In the femtosecond regime our calculations showed that the wavelength range longer than 4.2 µm becomes better when compared with a PPLN crystal. For the CW case **Fig.3** (b) the conversion efficiency from PSN device increased significantly in the wavelength range beyond 3.4 µm. **Fig.3** also shows that semiconductor PSN device may cover the wavelength range from 6 to 12 µm which can not be reached with conventional periodically-poled nonlinear crystal such as PPLN.
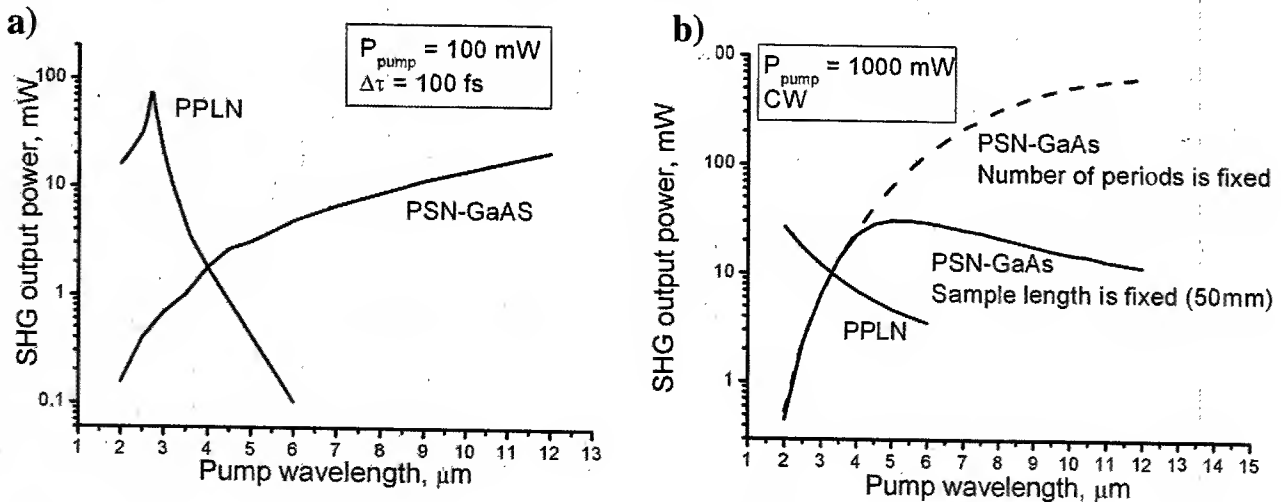
Figure 3. Calculated output SHG power versus pump wavelength for optimal crystal length with (a) a femtosecond pump beam and (b) a CW pump beam.

The conversion efficiency for our power levels was predicted as ~0.1 % at 2.0 µm pump wavelength and this agrees with the experimentally obtained conversion efficiency for examined crystals with an input pump average power of ~3 mW.

Further experimental investigations will include the use of sources having narrower spectral bandwidths and the implementation of this technique in OPO-related applications where it has particular potential for efficient light generation in the mid-infrared (>3.4 μm) region.

In conclusion, we have reported a successful demonstration of first-order QPM devices that utilise a periodically-switched-nonlinearity in a novel design of a GaAs/AlGaAs structure, which is based on a re-growth procedure. Our calculations have good agreement with our experimental results for the 2 μm wavelength range. These calculations also show that SHG conversion efficiencies from such devices at wavelengths beyond ~4 μm are significantly higher than those in the 1-3 μm range.

References
1 M. M. Fejer, G. A. Magel, D. H. Jundt, R. L. Byer, IEEE J. Quantum Electron., **28**, 2631 (1992).
2 E.U.Rafailov, P.Loza-Alvarez, C.T.A. Brown, W.Sibbett, R.M.DeLaRue, P.Millar, D.A.Yanson, J.S.Roberts, P.A.Houston, Opt. Lett., **26,** 1984 (2001).
3 M.Ohashi, T.Kondo, R.Ito, S.Fukatsu, Y.Shiraki, K.Kumata, S.S.Kano, J. of Appl. Phys. **74**, 596 (1993).
4 P. Loza-Alvarez, M. Ebrahimzadeh, W Sibbett, D. Reid, D. Artigas, M. Missey, J.Opt.Soc.Am., 18, 1212 (2001).
5 R. J. Deri and M. A. Emanuel, J. Appl. Phys. **77**, 4667 (1995).

Semiconductor optical amplifier Mach-Zehnder interferometers with feedback

R. Van Dommelen and M. Cada

Department of Electrical and Computer Engineering, Dalhousie University, P.O. Box 1000, Halifax, NS. Canada
Tel: (902) 494-3258 Fax: (902) 494-6154 Email: dommelen@is2.dal.ca
Tel: (902) 494-6074 Fax: (902) 494-6154 Email: michael.cada@dal.ca

Abstract: We present new results on numerical simulations carried out on semiconductor optical amplifier Mach-Zehnder interferometers with feedback. We show that these devices can exhibit bistability, with the potential for high speed all-optical switching applications.
©2000 Optical Society of America
OCIS codes: (190.1450) Bistability; (230.4320) Nonlinear optical devices

Semiconductor optical amplifiers (SOAs) arranged in a Mach-Zehnder interferometer (MZI) and employing cross-phase modulation, have been well studied for use as all-optical wavelength converters. The same device can also be used for performing all-optical logical operations [1]. By applying feedback to the device, its transfer function is modified. Sufficient feedback results in bistability, which has applications in high speed all-optical switching.

The device under investigation is shown in Figure 1. The structure was proposed for use as a latch, however no results on its operation were reported [2]. In our simulations, it is assumed that the two optical inputs, P_{IN3} and P_{IN4}, do not interference as they are independent sources.
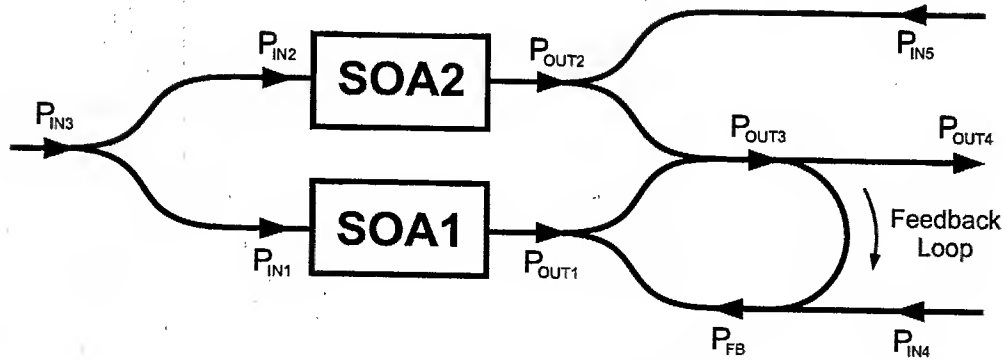
Fig. 1. Device under study; MZI interferometer with feedback.

The SOAs were studied using a numerical model based on a wave and a carrier rate equation [3,4]; however amplified spontaneous emission noise was neglected for simplicity. The wave and rate equations for a given SOA are

$$\frac{dP_i}{dz} = \Gamma g_{i,N} P_i \tag{1}$$

and

$$\frac{dN}{dt} = \frac{J}{qV} - \frac{N}{\tau_N} - \sum \frac{\Gamma g_{i,N} P_i}{h v_i S}, \tag{2}$$

where i represents each wave in the SOA. P is the optical power of a given wave, z is the axis along the length of the SOA, is the waveguide confinement factor, g is the gain per unit length, N is the carrier density, t is time, J is

the injection current density, q is the charge of an electron, V is the volume of the active region, hv is the photon energy, and S is the area of the waveguide. For each SOA we use a cubic gain described by

$$g = a(N - N_0) - \gamma_1(\lambda - \lambda_N)^2 + \gamma_2(\lambda - \lambda_N)^3$$ where a, $_1$, and $_2$ are gain constants and N_0 is the carrier density at transparency. The spectral shift and carrier lifetime dependence on carrier density are described by

$$\lambda_N = \lambda_0 - \kappa_0(N - N_0)$$ and $\tau_N = (A + B N + C N^2)^{-1}$, respectively, where $_0$ is the wavelength of peak material gain at transparency and $_0$ is the peak material gain shift constant. A, B, and C are the nonradiative, bimolecular, and Auger material recombination constants respectively. The dependence of the phase shift imparted by the SOA on the carrier density is given by [5]

$$\Delta\phi = -\frac{2\pi L \Gamma (N - N_0)}{\lambda_{r_1}} \frac{dn}{dN}. \tag{3}$$

where L is the length of the SOA and dn/dN is the differential refractive index. A modifying term can be also added to the phase shift equation [6]; however, for simplicity it is not included here.

Equations 1 and 2 are integrated over the length of the SOA and the resulting equation is solved numerically to produce a transfer function of the device [7]. The results are shown in Figure 2 for various values of feedback gain, u. These new results show that sufficient gain results in bistability, while the width of the bistability is controlled by the strength of the feedback. In these simulations the feedback gain is calculated as the increase in feedback optical power relative to the case where the exiting waveguide splitter, at P_{OUT3}, yields a 50:50 power division. Thus the required feedback gain can be achieved by designing the exiting splitter to be asymmetrical, thereby directing more power through the feedback loop. Alternatively, a short active waveguide section in the feedback arm could be used to provide an adjustable power gain.
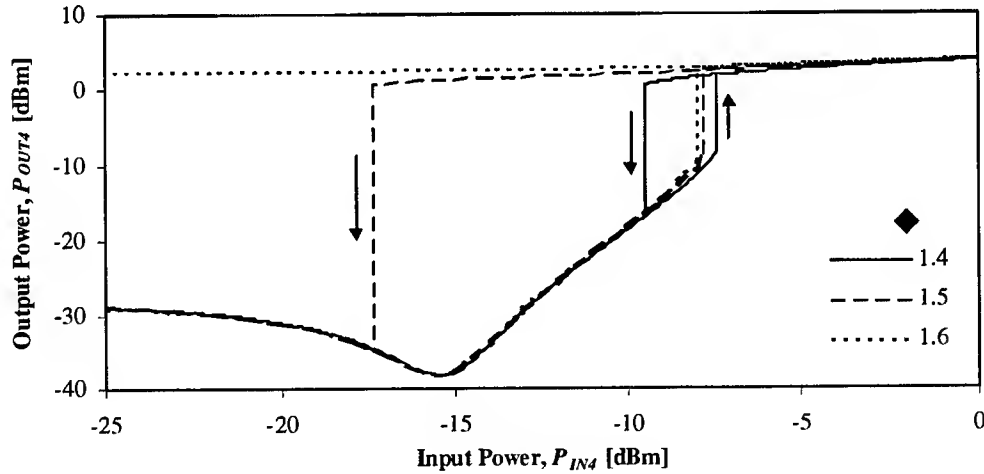
Fig. 2. Transfer function for various values of feedback gain.

Dynamic simulations were also carried out to study the transient behavior of the bistable switching. The device is latched, or switched on by increasing the input power temporarily. Figure 3 shows the switch-on behavior for $u = 1.5$ and for two different control signals. If the control signal increases to -7.5dBm, just slightly more power than the switch-on threshold, the turn on time is very long. This is described as critical slowing down [8]. When the control signal contains more power, the switching time improves. The overall switching speed is controlled by the speed of the SOA, the delay time of the feedback loop, and the bistability itself.
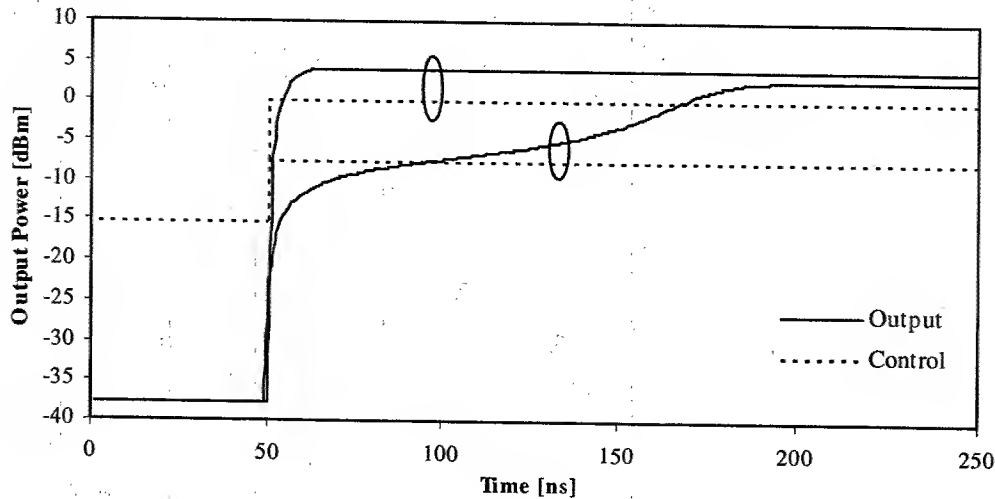
Fig. 3. Switch-on transient behavior.

The device can be reset or turned off optically by one of several methods. The first is by decreasing the control signal power to below the switch-off threshold. However, in this case the feedback power is still quite large and the turn-off time is limited by critical slowing down. In some cases, such as when $u = 1.6$, the control signal cannot be lowered to below the switch-off threshold. Thus the device may alternatively be reset through the use of a reset pulse at P_{IN5} [2]. The pulse nulls the output of the interferometer by matching the phase shifts in the two arms. We have shown that in this case timing is critical to prevent the device from entering an oscillating state. For proper operation, the duration of the reset pulse must be equal to the delay time of the feedback loop. To satisfy this condition is difficult in a practical application. We therefore propose a third method of resetting the device that involves blocking the feedback power. This might be achieved with another active device in the feedback waveguide using cross-gain modulation or cross-phase modulation. The reset pulse is fed into the new active device which nulls the feedback power. In this way the strict timing requirements on the reset pulse are avoided.

The new results obtained so far include numerically determining the transfer function of an SOA-MZI with feedback and showing that a bistability results when the appropriate feedback is supplied. Also, the transient switching behavior of the bistability was investigated including the effects of critical slowing down. We have proposed a new method of resetting the device that overcomes the critical slowing down, as well as timing issues associated with other reset methods that lead to undesirable and unacceptable instabilities. Work is continuing in an effort to have more control over the shape of the bistable transfer functions and to improve switching times.

References

[1] R. Van Dommelen and M. Cada, *Canadian Institute for Photonic Innovation (CIPI) Progress Report: All-optical logic using SOA wavelength converters*, (2000).

[2] K.B. Roberts, J.E.A. Whiteaway, and M. Tait, *Optical Logic Devices and Methods*, United States Patent 5,999,284 (1999).

[3] D. Marcenac and A. Mecozzi, "Switches and frequency converters based on cross-gain modulation in semiconductor optical amplifiers," IEEE Photon. Tech. Lett., **9**, 749-751 (1997).

[4] A.E. Willner and W. Shieh, "Optimal spectral and power parameters for all-optical wavelength shifting: single stage, fanout, and cascadability," IEEE J. Light. Tech., **13**, 771-781 (1995).

[5] M. Asghari, I.H. White, and R.V. Plenty, "Wavelength conversion using semiconductor optical amplifiers," IEEE J. Light. Tech., **15**, 1181-1190 (1997).

[6] S.-C. Cao, J. Cartledge, and E. Berolo, "Theoretical model of gain-saturated semiconductor optical amplifiers in cross-phase modulation wavelength converters," in Lasers and Electro-Optics Society 2000 Annual Meeting, (Institute of Electrical and Electronics Engineers, New York, 2000), pp. 778-779.

[7] R. Van Dommelen and M. Cada, *Canadian Institute for Photonic Innovation (CIPI) Progress Report: Cross-gain and cross-phase modulation in semiconductor optical amplifier wavelength converters*, (2001).

[8] J.-Y. Wang, M. Cada, R. Van Dommelen, and T. Makino, "Bistable characteristics of bistable laser diodes," IEEE J. Select. Topics in Quan. Electron., **3**, 1271-1279 (1997).

Shaping the optical components of solitary three-wave weakly coupled states in a two-mode crystalline waveguide

Alexandre S. Shcherbakov

National Institute for Astrophysics, Optics & Electronics, A.P. 51 y 216, 72000, Puebla, Pue., Mexico
Fax/Phone + 52 (222) 2472940. E-mail: alex@inaoep.mx .

Abstract: Bragg solitons, representing collinear three-wave weakly coupled states, are investigated both theoretically and experimentally. The dynamics of shaping their optical components is studied, and the roles of localizing pulse width and phase mismatch are revealed.
©2002 Optical Society of America
OCIS codes: (190.5530) Pulse propagation and solitons. (190.4410) Nonlinear optics, parametric processes

1. Introduction

In a number of cases the analysis of three-wave processes leads to finding various solitary waves in the form of coupled states, where waves of the same or even different nature become to be mutually trapped and propagate together [1,2]. Under certain condition it is also possible to find the coupled states with the Bragg acousto-optical interaction in a two-mode optical waveguide [3], because nonlinear scattering of light by acoustic wave in photoelastic medium represents a three-wave parametric process exhibiting itself as a mechanism of stabilizing self-action in a system with square-law nonlinearity. The study of weakly coupled states, originating with scattering the light by relatively slow non-optical wave, and the development of quasi-stationary model for describing a phenomenon are the subjects of this work. In the main, the dynamics of localizing just optical components of coupled states is studied and the parts of their major parameters are analytically estimated. A correlation between the results of computer simulation and the data of experiments with a crystalline waveguide substantiates the model present.

2. Originating the weakly coupled states in a two-mode waveguide; the localization conditions

A three-wave co-directional collinear interaction with the mismatched wave numbers in anisotropic medium is described by a set of three nonlinear partial differential equations [4]. Here, we consider a regime of weak coupling, when two light modes are scattered from a pulse of relatively slow wave, being non-optical by its nature, and essentially effective Bragg scattering of light can be achieved without any observable influence of the scattering process on that non-optical wave, because the number of interacting photons is several orders less than the number of scattering quanta injected into a medium. Then, the velocities of light modes can be approximated by the same value c, because the length of a crystalline waveguide does not exceed of 10 cm. In this regime, the above-mentioned set of equations falls into a homogeneous wave equation for a slow wave, which possesses the traveling-wave solution $U(x-vt)$, v is the velocity of this wave, and the pair of combined equations for light wave amplitudes. The complex amplitudes $C_0(x,t)$ and $C_1(x,t)$, corresponding to the incident light wave and scattered one, are governed by

$$\frac{\partial C_0}{\partial x} = -q_1 C_1 U^*(x-vt)\exp(2i\eta x) , \qquad \frac{\partial C_1}{\partial x} = q_0 C_0 U(x-vt)\exp(-2i\eta x). \qquad (1)$$

Here $q_{0,1}$ are the constants of interaction; k_0, k_1, and K are the wave numbers for both the light waves and non-optical wave; $2\eta = |k_0 - k_1 - K|$ is the mismatch of wave numbers. On the assumption that non-optical pulse $U(x-vt) = u(x-vt)\exp(i\varphi)$ has the constant phase φ, Eqs.(1) can be converted into a pair of equations

$$\frac{\partial^2 C_{0,1}}{\partial x^2} - \left(\frac{1}{u}\frac{\partial u}{\partial x} \pm i\eta\right)\frac{\partial C_{0,1}}{\partial x} + q_0 q_1 u^2 C_{0,1} = 0 \qquad (2)$$

We put $C_{0,1} = a_{0,1}(x,t)\exp(i\Phi_{0,1}[x,t])$, $\gamma_{0,1} = \partial\Phi_{0,1}/\partial x$ and divide real and imaginary parts in Eqs.(2) as

$$\frac{\partial^2 a_{0,1}}{\partial x^2} - \left(\frac{1}{u}\frac{\partial u}{\partial x}\right)\frac{\partial a_{0,1}}{\partial x} + \left(q_0 q_1 u^2 - \gamma_{0,1}^2 \pm 2\eta\gamma_{0,1}\right)a_{0,1} = 0 , \qquad (3)$$

$$2\left(\gamma_{0,1} \mp \eta\right)\frac{\partial a_{0,1}}{\partial x} + \left(\frac{\partial \gamma_{0,1}}{\partial x} - \frac{\gamma_{0,1}}{u}\frac{\partial u}{\partial x}\right)a_{0,1} = 0, \tag{4}$$

It follows from Eqs.(4) that $\gamma_{0,1} = \pm\eta\left(u/a_{0,1}^2\right)\int u^{-1}\left(\partial a_{0,1}^2/\partial x\right)dx + \Gamma_{0,1}u/a_{0,1}^2$, but here our consideration will be restricted by the simplest choice of $\Gamma_{0,1} = 0$. Now, we focus on the process of localization in the case, when first, two facets of waveguide at $x = 0$ and $x = L_0$ bound the area of interaction and the spatial length x_0 of non-optical pulse is much less than L_0; and second, the non-optical pulse $u(x,t) = U_0\left(\theta\left[z - vt\right] - \theta\left[x - x_0 - vt\right]\right)$ has a rectangular shape with the amplitude U_0. We analyze Eqs.(3) and (4) with the fixed magnitude of η and the natural boundary conditions $a_0(x = 0,t) = 1$, $a_1(x = 0,t) = 0$ and trace the dynamics of phenomenon as far as the localizing pulse of non-optical wave is incoming through the facet $x = 0$, passing in a waveguide, and issuing through the facet $x = L_0$ with the constant velocity v. There are two possibilities. The first of them is connected with a quasi-stationary description of this effect in the assumption that $v \ll c$, while the second one presupposes a weak inequality $v < c$. With a quasi-stationary approach, we may put that $\partial u/\partial x \approx 0$ in Eqs.(3), (4) everywhere, excluding the points $x = \{0, x_0\}$, and yield $\gamma_{0,1} = \pm\eta$. Then, we follow three stages in the localization processes.

Stage 1: Localizing pulse is incoming through the facet $x = 0$: Applying the values of $\gamma_{0,1} = \pm\eta$, Eqs.(3) can be solved exactly. The intensities of light waves on $x \in (0, x_0)$ with $q_0 q_1 U_0^2 = \sigma^2$ are given by

$$\left|?_0\right|^2 = \frac{\eta^2}{\sigma^2 + \eta^2} + \frac{\sigma^2}{\sigma^2 + \eta^2}\cos^2\left(x\sqrt{\sigma^2 + \eta^2}\right), \qquad \left|?_1\right|^2 = \frac{q_0}{q_1}\frac{\sigma^2}{\sigma^2 + \eta^2}\sin^2\left(x\sqrt{\sigma^2 + \eta^2}\right). \tag{5}$$

To find the coefficients in Eqs.(5) and (6) we use the conservation law $q_0 a_0^2 + q_1 a_1^2 = q_0$, resulting from Eqs.(1).

Stage 2: Localizing pulse is passing in a medium. In this regime the rectangular pulse as the whole is in a waveguide, so $\partial u/\partial x = 0$ exactly and one has to put simply $x = x_0$ in Eqs.(5) and (6) in the region $(x_0, L_0 - x_0)$.

Stage 3: Localizing pulse is issuing through the facet $x = L_0$. This stage is symmetrical to the stage 1, whose solutions, i.e. the above-mentioned Eqs.(5), can be inverted and related to the spatial interval of $x \in (L_0 - x_0, L_0)$.

The obtained solutions include contributions of two types. The first summand in $\left|?_0\right|^2$ exhibits the contribution of a background, whose level is determined by the mismatch η; the second one represents the oscillating portion of solution, i.e. the localized part of incident light imposed on a background. The scattered light contains the only oscillating portion of field that gives the localization condition $x_C^2\left(q_0 q_1 U^2 + \eta^2\right) = \pi^2 N^2$, where $N = 0, 1, 2, \ldots$

On the second possibility ($v < c$), it is reasonable to put $u = \alpha U_0 x$ (α is to be found), when the localizing pulse is incoming through the facet $x = 0$. In so doing, we have to take into account the fact that solutions to Eqs.(3) are known if only the last coefficients are proportional to u^2 [5], i.e. $\gamma_{0,1}^2 \mp 2\eta\gamma_{0,1} = \eta^2\zeta^2 x^2$ with $\zeta = const$. That is why we are forced to exploit the smallness of mismatch, believing that $\eta \ll 1$, and to find approximate solutions to Eqs.(3), (4) at this stage. Resolving this algebraic equation relative to $\gamma_{0,1}$, we yield $\gamma_{0,1} = \pm\eta\left(1 \pm\sqrt{1 + \zeta^2 x^2}\right)$.

In terms of these values for $\gamma_{0,1}$, Eqs.(4) can be satisfied with an accuracy of η^2, while Eqs.(3) can be solved exactly. The intensities of light waves with $\alpha = \zeta$ on the interval of $x \in (0, x_0)$ are given by

$$\left|?_0\right|^2 = \frac{\eta^2}{\sigma^2 + \eta^2} + \frac{\sigma^2}{\sigma^2 + \eta^2}\cos^2\left(\frac{\alpha x^2}{2}\sqrt{\sigma^2 + \eta^2}\right), \qquad \left|?_1\right|^2 = \frac{q_0}{q_1}\frac{\sigma^2}{\sigma^2 + \eta^2}\sin^2\left(\frac{\alpha x^2}{2}\sqrt{\sigma^2 + \eta^2}\right). \tag{6}$$

To find the coefficients in Eqs.(6) we approximate $\gamma_{0,1}$ as $\gamma_0 = -\eta x\zeta$ and $\gamma_1 = -\eta\left[(4/3) + x\zeta\right]$ on the interval of $x \in (0, x_0)$ and then use the conservation law. The stage 2 with $v < c$ is governed by Eqs.(5) as well, because again $\partial u/\partial x = 0$; finally, we can invert and apply Eqs.(6) at the stage 3. The parameter α makes it possible to join Eqs.(5) and (6) at the point x_0, therefore the localization condition takes the form $\alpha^2 x_S^4\left(q_0 q_1 U^2 + \eta^2\right) = 4\pi^2 N^2$.

3. Computer simulation and experimental verification in the quasi-stationary case.

Shaping the optical components of solitary three-wave weakly coupled states was simulated using Eqs.(5). As an example, Fig.1 shows a set of plots for the scattered light intensity $|C_1|^2$, when both the amplitude U_0 and the mismatch η are fixed, while its width $\tau_0 = x_0/v$ is increasing plot by plot in the temporal scale of $\tau_C = x_C/v$. Figures 1b and 1d illustrate shaping the scattered optical components of one- and two-pulse weakly coupled states.
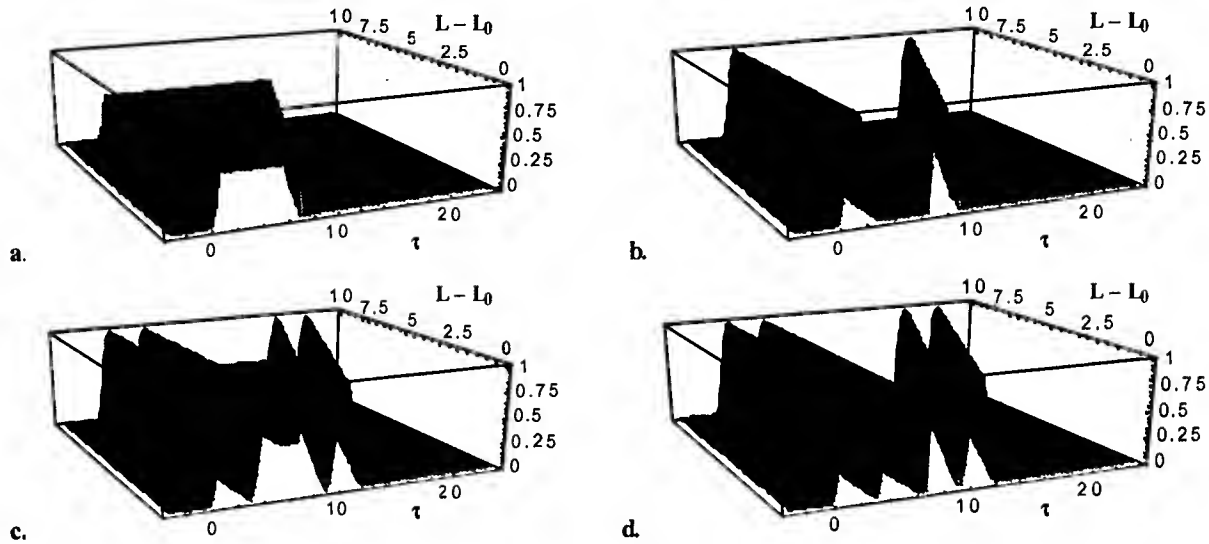
Fig.1. Intensity of the scattered optical component, normalized by the ratio q_1/q_1, in a weakly coupled state (vertical axis) versus the temporal coordinate $\tau = x/v$ and the waveguide length $L-L_0$: a. $\tau_0 < \tau_C/2$; b. $\tau_0 = \tau_C$; c. $3\tau_C/4 < \tau_0 < 2\tau_C$; d. $\tau_0 = 2\tau_C$.

Verification has been carried out due to acousto-optical experiments in a two-mode crystalline waveguide based on calcium molybdate (exact synchronism acoustic frequency 43.7 MHz, L_0= 3 cm, v = 2.95 mm/μs) on an optical wavelength of 0.633 nm. During the experiments rather effective (> 10%) Bragg scattering of the light has been observed without any effect on the acoustic wave, since the number of interacting photons was 10^5 times less then the number of phonons injected into a waveguide, when their powers were approximately equal to 100 mW each, so the regime of weak coupling had taken place. The intensity distributions in both incident and scattered optical components of coupled states as the functions of the acoustic power density, the localizing pulse width τ_0, and the frequency mismatch $\Delta f = \eta v/\pi$ has been measured. The oscilloscope traces in Fig.2 illustrate the particular case, when the only localizing pulse width τ_0 is varied. One can see 4 sequential steps in shaping the optical components of weakly coupled states in a waveguide, which are in agreement with the analysis performed, see Eqs.(5) and Fig.1.
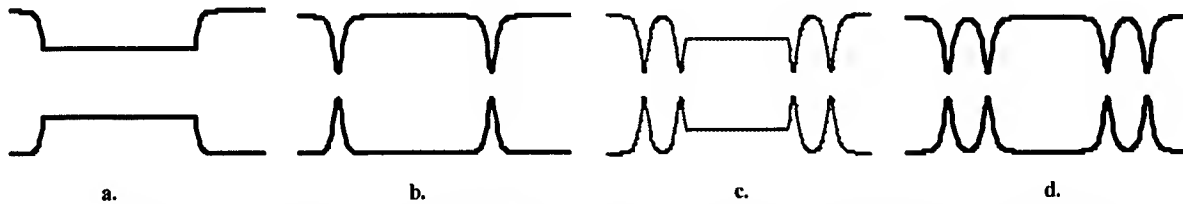
Fig.2. Temporal traces of the incident (upper lines) and scattered (bottom lines) light intensities with Δf = 0.4 MHz in a two-mode calcium molybdate waveguide: a. τ_0 = 0.8 μs; b. $\tau_0 = \tau_C$ = 2.5 μs; c. τ_0 = 4.2 μs; d. $\tau_0 = 2\tau_C$ = 5.0 μs.

References

1. A.P.Sukhorukov. *Nonlinear Wave Interactions in Optics and Radiophysics.* (Nauka Press, Moscow. 1988).
2. A.S.Shcherbakov. *A three-wave interaction. Stationary coupled states.* (St.Petersburg State Technical University Press, St.Petersburg. 1998).
3. A.S.Shcherbakov. "Properties of solitary three-wave coupled states in a two-mode optical waveguide." in *Nonlinear Guided Waves and Their Applications,* OSA Technical Digest (Optical Society of America, Washington DC. 2001), pp. 100-102.
4. R.K.Dodd, J.C. Eilbeck, J.D.Gibbon, and H.C.Morris. *Solitons and Nonlinear Wave Equations.* (Academic Press, Orlando, FL. 1984).
5. E.Kamke. *Differentialgleichungen. Losungmethoden und Losungen.* Part 1: Gewohnliche Differentialgleichingen. (Chelsea Co. NY. 1974).

Instability of Gap 2π-pulses

B.I.Mantsyzov and R.A.Silnikov

Department of Physics, M.V.Lomonosov Moscow State University,
Moscow 119899, Russia ; e-mail address: mants@genphys.phys.msu.su

In recent years, there has been vast interest in nonlinear pulse propagation in photonic band gap structures, or photonic crystals [1]. It has been shown [2,3], that due to nonlinear light-matter interaction, intensive laser pulse can propagate at frequency within the linear forbidden Bragg gap band through the structure with different types of nonlinearity, so called gap soliton. The steady gap soliton moves in periodical structure like optical soliton in homogeneous medium keeping its shape and constant velocity. However, the existence of photonic band gap gives rise to specific features of the gap soliton dynamics, for instance, the pulse can stand with zero velocity [2,3] or oscillate periodically changing its amplitude and sign of velocity [4,5]. These oscillations have been investigated in the framework of the generalized massive Thirring model for gap solitons in periodic cubic materials [5]. However, the oscillations of gap 2π-pulse of self-induced transparency in a resonant periodic structure were only numerically demonstrated in the case of complicated set of equations in complex functions [4], and the physical nature of the oscillations has not been described. Physically, it is clear that a reason of the oscillations is in photonic band gap. If an optical soliton is formed by arbitrary pulse in homogeneous medium, then the part of energy, which has not been trapped by the soliton, leaves fast the space region of the slow soliton as free linear radiation. In the case of gap soliton, this untrapped energy is fixed in excited atoms and in weak field that can not propagate through the structure because of linear photonic band gap. As a result, if the initial soliton velocity is slow enough, the gap soliton, interacting with the perturbation, cannot leave the region of interaction because its kinetic energy is smaller than the potential energy of the interaction. This gives rise to gap soliton oscillations. In the present paper, we study the instability of gap 2π-pulse of self-induced transparency in a resonantly absorbing Bragg grating. It is shown that initial problem for simple two-wave Maxwell-Bloch equations in real functions are reduced to modified sine-Gordon equation. This allows one to obtain an equation of motion to describe the evolution of stable oscillating gap 2π-pulse and unstable excited gap 2π-pulse, which decays to a steady soliton and perturbation. The oscillating pulse is physically stable because it does not decay, and is unsteady because this solution is within a region of oscillatory instability on phase-plane of equation of motion. Solving a boundary problem, we explain the physical nature of delayed reflection and delayed transmission of gap 2π-pulse, when an incident pulse forms the gap 2π-pulse at low velocity near the boundary.

Let us consider the coherent interaction of light with one-dimensional resonantly absorbing Bragg grating consisting of periodically distributed thin layers of two-level oscillators. This model closely corresponds to a real structure of periodically arranged quantum wells with resonant excitons in semiconductor. Under exact Bragg condition, the problem of light-matter interaction in semiclassical approximation is described by coupled-mode two-wave Maxwell-Bloch (TWMB) equations [2] for the slowly varying envelope of electric-field amplitudes of the forward and backward waves $E^{\pm}$, the dimensionless polarization P, and the population difference density of two-level oscillators n:

$$\Omega_t^+ + \Omega_x^+ = P, \quad \Omega_t^- - \Omega_x^- = P, \quad P_t = n(\Omega^+ + \Omega^-), \quad n_t = -P(\Omega^+ + \Omega^-), \qquad (1)$$

where $\Omega^{\pm} = 2\tau_c(\mu/\hbar)E^{\pm}$; τ_c is the cooperative time characterizing the mean photon lifetime in the medium preceding resonant absorption, μ is the matrix element of the transition dipole moment; $x = x'/c\tau_c$, $t = t'/\tau_c$ are dimensionless space and time coordinates.

Using the solution of the Bloch equation $P = -\sin\theta$, where θ is the Bloch angle, the Eqs. (1) are reduced to the form:

$$\widetilde{\Omega}_x + \Omega_t = -2\sin\theta, \quad \Omega_x + \widetilde{\Omega}_t = 0, \quad \theta_t = \Omega, \qquad (2)$$

where $\Omega \equiv \Omega^+ + \Omega^-$, $\widetilde{\Omega} \equiv \Omega^+ - \Omega^-$. The second equation of Eqs. (2) yields

$$\widetilde{\Omega}(x,t) = -\theta_x(x,t) + f(x). \qquad (3)$$

Then Eqs.(2) gives the following equation for the Bloch angle :

$$\theta_{xx} - \theta_{tt} = 2\sin\theta + f_x(x) \qquad (4)$$

This is the modified sine-Gordon equation, the function $f(x)$ is determined by the initial condition (3):

$$f(x) = \widetilde{\Omega}(x,0) + \theta_x(x,0).$$ (5)

Thus, if the fields and population inversion are absent in a medium at $t=0$, i.e., $\widetilde{\Omega}(x,0) = 0$ and $\theta(x,0) = 0$, or if the steady 2π-pulse propagates through the structure and $\widetilde{\Omega}(x,t) = -\theta_x(x,t)$ [2], then $f(x) = 0$ and Eq.(4) is reduced to the exact sine-Gordon equation describing steady gap 2π-pulse. In general case of $f(x) \neq 0$, the gap soliton dynamics becomes more complicated. The second term in right-hand side of Eq.(4) describes the interaction of soliton of exact sine-Gordon equation with a localized perturbation and determines the dynamics of gap 2π-pulse oscillations and instability.

In order to solve the Eq.(4), we use a simple "energetic" method, which allows one to obtain an equation of motion for soliton of modified sine-Gordon equation in the case where its shape is close to the shape of exact sine-Gordon equation solution, i.e., the function $f(x)$ is assumed to be small. Rewriting Eq. (4) in variables $\eta = \sqrt{2}\,x$, $\tau = \sqrt{2}\,t$, $f' = f/\sqrt{2}$ we get the equation in traditional form

$$\theta_{\eta\eta} - \theta_{\tau\tau} = \sin\theta + f'_\eta(\eta).$$ (6)

The corresponding Hamiltonial density function for Eq. (6) is the following $H = \theta_\tau^2/2 + \theta_\eta^2/2 - f'\theta_\eta + f'^2/2 + (1-\cos\theta)$. Assuming the shape of unsteady solution of Eq. (6) to be close to soliton of the exact sine-Gordon equation, we write the desired solution for a 2π-pulse as

$$\theta = 4\tan^{-1}\{\exp[(-\eta + \xi(\tau))/\sqrt{1 - u^2(\tau)}]\},$$ (7)

where $u(\tau)$ is the time-depending soliton velocity, $\xi(\tau) = \int_0^\tau u(\tau')d\tau'$ is the coordinate of soliton center.

Since the system is conservative, the total energy of the localized solutions is integral of motion, $d(\int_{-\infty}^\infty H\,d\eta)/dt = 0$, then assuming u^2 to be small we find the following Newton equation of motion:

$$\xi_{\tau\tau} = -\frac{1}{4}\frac{\partial}{\partial\xi}\int_{-\infty}^\infty \operatorname{sech}(\eta - \xi)f'(\eta)d\eta.$$ (8)

Overlap integral in right-hand side of Eq. (8) fixes potential energy of interaction of the kink-solution (7) with the perturbation.

Let us take the perturbation in a simple form $f'(\eta) = f_0\operatorname{sech}(\eta)$, which coincides with the shape of exact 2π-pulse solution. Then Eq. (8) gives the following equation of motion of the pulse:

$$\xi_{\tau\tau} = -U_\xi,\ U = (f_0/2)(\xi/\operatorname{sh}\xi).$$ (9)

Equation (9) describes the motion of a unit mass quasi-particle in potential U under action of potential force $-U_\xi$. Total energy of the particle (9) is $u^2/2 + U = const$, therefore finite motion is possible if the potential is attractive, $f_0 < 0$, and the pulse velocity have to be sufficiently small on the

Fig.1. Phase-plane of Eq.(9) for attractive potential U at $f_0 = -0.1$ (a), and repulsive potential at $f_0 = 0.1$ (b).

potential well bottom $|u(\xi = 0)| < \sqrt{-f_0}$ (Fig.1(a)). The gap 2π-pulse can oscillate but does not decay, it is unsteady but stable. An increase in the initial velocity leads to escape of the pulse from the potential well. If the initial condition (5) corresponds to positive $f_0 > 0$, the potential of interaction U is positive and the pulse is repelled from the potential (Fig.1(b)). It means that the pulse is unstable and can be described as excited gap 2π-pulse, since it decays to perturbation and steady soliton whose kinetic energy equals to the energy of excitation (potential energy of interaction). If displacement of the soliton is small compared to the width of
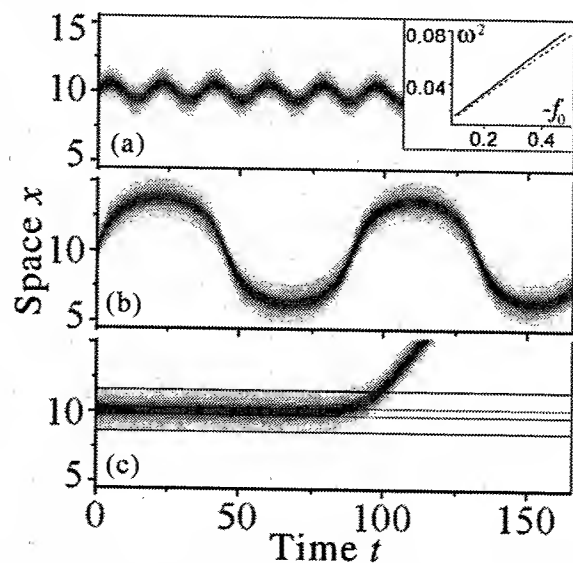
Fig.2. Evolution of inversion n of initial gap 2π-pulse (the gray scale is proportional to n). The initial conditions are chosen such that (a) $f_0 = -0.4$, the initial pulse velocity $u_0 = 0.2$; (b) $f_0 = -0.4$, $u_0 = 0.55$; (c) $f_0 = 0.07$, $u_0 \approx 0$. The contour lines correspond to perturbation $f(x,t)$ (3). The inset shows the analytically (10)(solid line) and numerically (dashed line) calculated frequency of harmonic oscillations.
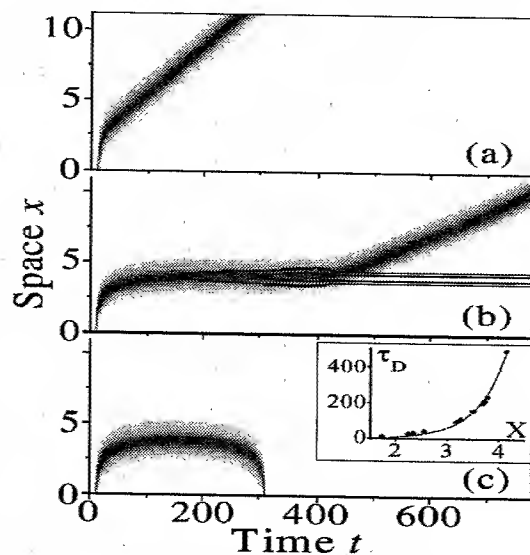

Fig.3. Evolution of inversion n of the incident pulse in the structure. The incident pulse amplitudes are 2.701 (a), 2.70063 (b), and 2.70062 (c). The contour lines in (c) show the perturbation $f(x,t)$ (3). The inset shows the dependence of time delay τ_D on the depth of pulse penetration X.

potential $\xi \ll 1$ and $f_0 < 0$, then the soliton executes harmonic motion:

$$\xi = \xi_0 \sin \omega\tau, \quad \omega^2 = -f_0 / 6. \qquad (10)$$

The "energetic" method, we used above, is very convenient but approximate, because one does not take into account a change of kink shape. Thus, it is important to check our analytical results by numerical integration of Eq. (1) directly. Figures 2 illustrate the dynamics of gap 2π-pulse for attractive (a,b) and repulsive (c) potentials U. We see a good agreement with analytical results although the taken values f_0 and ξ are not too small.

The analytical description of gap 2π-pulse instability in an initial problem allows one to explain dynamics of formation of gap 2π-pulse near the structure boundary, which is a realistic physical process. In Fig.3 results of the numerical simulation for different values of incident field amplitudes Ω_0 are presented. If the incident field is large, the steady moving gap 2π-pulse is formed after nonlinear reflection of some part of incident field (Fig.3(a)). Figure 3(b) demonstrates the delayed transmission of incident pulse. The corresponding unstable initial state is marked by circle on phase-plane in Fig.1(b). After time of delay, the excited gap 2π-pulse decays to moving steady gap 2π-pulse and residual perturbation, i.e. small standing waves and inversion. If amplitude of incident pulse is chosen smaller, the influence of the boundary on the process of gap 2π-pulse formation is very important. Due to the attraction, the pulse can not propagate into the structure and is reflected (Fig.3(c)). The value of time delay τ_D of the incident pulse, in this delayed reflection process, exponentially depends on depth of the pulse penetration and may be in two order of magnitude greater than the incident pulse duration.

In summary, it has been shown that besides traditional moving and standing gap 2π-pulses, which are steady soliton solutions of TWMB equations, there is a class of stable oscillating and unstable excited gap 2π-pulses. The oscillations and instability arise because of interaction of slow gap 2π-pulse with localized weakly excited two-level oscillators and small standing waves within photonic band gap.

1. "Linear and Nonlinear Nanoscale Optics", Ed. by C. M. Bowden, M. Bertolotti, and C. Sibilia (AIP, 2001).
2. B. I. Mantsyzov and R. N. Kuzmin, Sov. Phys. JETP **64**, 37 (1986).
3. W. Chen and D. L. Mills, Phys. Rev. Lett. **58**, 160 (1987); C. Conti, S. Trillo, and G. Assanto, Phys. Rev. Lett. **78**, 2341 (1997).
4. B. I. Mantsyzov, Phys. Rev. A **51**, 4939 (1995).
5. F. De Rossi, C. Conti, and S. Trillo, Phys. Rev. Lett. **81**, 1, 85-88 (1998).

All-optical AND gate using Kerr nonlinear microresonators

Suresh Pereira, Philip Chak and J. E. Sipe,
University of Toronto, Toronto, ON, M5S 1A7, Canada
phone: 416-978-5444; fax: 416-978-2537
email: pereira@physics.utoronto.ca

We consider all-optical switching in the device shown in Figure 1a, which consists of two channel waveguides coupled by microresonators, all of which are Kerr nonlinear. We present numerical simulations that show that it is possible to use the channels as input ports, hence creating an optical AND gate based on a scheme similar to coupled gap soliton formation, even in the presence of linear and nonlinear loss mechanisms. The advantage of our AND gate scheme over earlier proposed schemes based on Bragg gaps is twofold[1,2]: First, our gate is much shorter than those based on Bragg gaps; second, the threshold energy required for operation is much smaller than in a Bragg gap system. The basic operation of the gate is as follows. Forward travelling light in the bottom (top) channel guide can couple, *via* the resonators, to backward travelling light in the top (bottom) guide[3,4]. For simplicity we assume that light propagation is governed by the effective index n_{eff}, common to both channel guides and the resonator. We define the resonant frequency, $\omega_r = c/(n_{eff}R)$ – the frequency at which one round-trip through the resonator corresponds to the accumulation of 2π of phase. Light with frequency at or near an integer multiple of ω_r is highly reflected, because the coupling of light from one channel guide to the other is resonantly enhanced. In the presence of nonlinearity, light of high intensity will experience nonlinear phase accumulation through self phase modulation (SPM) and cross phase modulation (CPM). We consider the situation where one pulse of high intensity injected into either the top or bottom channel is reflected, despite its SPM. However, when pulses are injected into the top and bottom channels *simultaneously*, then the added phase accumulation due to CPM will be sufficient to switch off the resonance, so that the structure becomes highly transmitting. For our system, the coefficient describing CPM is twice as large as that describing SPM, whereas in schemes based on orthogonal polarization the CPM coefficient is only two-thirds of the SPM coefficient[1]; this makes our scheme more efficient than one based on polarization.

Figure 1: (a) Schematic of the AND gate. (b) One unit cell of the AND gate.

To simulate device operation, we generalize a numerical technique used to investigate structures similar to the AND gate, but with only one channel guide[5]. In Figure 1b we show one cell of the device. We assume that light can couple between the channel guides and the resonators only at the two large dots indicated in Figure 1b, which we call the coupling points[4,5]. We describe the coupling of the electric field using the self-coupling coefficient σ and the cross-coupling coefficient κ; thus, for example $A_3 = \sigma A_4 + i\kappa A_1$ and $A_2 = \sigma A_1 + i\kappa A_4$. For simplicity we assume the that σ and κ are real so that to conserve energy we require $\sigma^2 + \kappa^2 = 1$. Away from the

coupling points optical propagation is described by the familiar nonlinear Schrödinger equation[6], modified to include the effects of SPM and CPM, quantified by the nonlinear index of refraction coefficient, n_2, and the effects of linear loss, two-photon absorption (2PA) and three-photon absorption (3PA), quantified by α_1, α_2 and α_3 respectively[7]. In the presence of a positive (negative) nonlinearity, we expect the frequency associated with resonance to be slightly lower (higher) than ω_r, since ω_r was defined assuming linear intensity.

We first consider CW illumination of the structure in the absence of nonlinearity or loss. We use $n_{eff}=3.0$, $2\pi R=26\mu m$ and $d=16\mu m$, and consider structures with 1 and 5 units cells, apodized such that the first and last cells have $\sigma=0.99$, and the middle cells have $\sigma=0.98$ (the 1 cell structure has $\sigma=0.98$). This apodization helps to remove oscillations in the CW transmission spectrum of the device[8]. In Figure 2 we show CW transmission spectra for the 1 cell (straight) and 5 cell (dash) structures, using vacuum wavelengths in the vicinity of $\lambda=1.529412\mu m$, which corresponds to the 51st resonance of the microresonators. Although the 1 cell structure is, indeed,
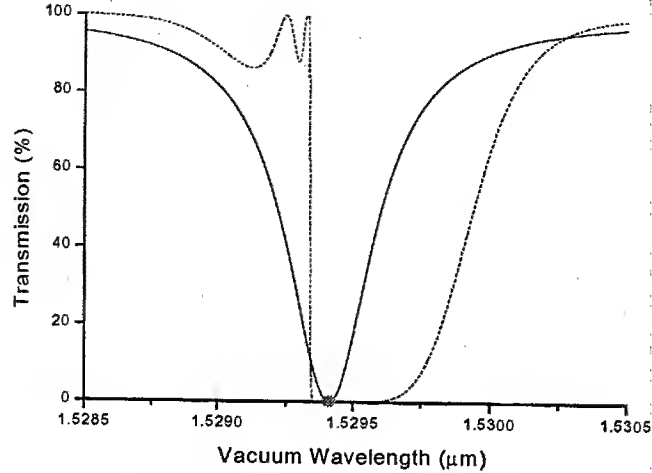
Figure 2: CW transmission spectrum for device with 1 cell (solid line) and 5 cells (dashed line). The small dot indicates the resonant wavelength. The oscillations in the 5 cell spectrum are due to imperfect apodization.

0% transmitting at the resonant frequency, the range over which the transmission is $\cong 0\%$ is quite small. By contrast, the 5 cell structure has a relatively large region of $\cong 0\%$ transmission, and a sharp edge at which the transmission switches to $\cong 100\%$. Because of this sharp edge, longer structures are more effective AND gates, although loss is a limiting factor.

We now simulate Gaussian pulses of 100ps full width at half-maximum intensity (FWHM), carried at $\lambda=1.529412\mu m$. We assume that the structure is fabricated using $Al_{0.18}Ga_{0.82}As$, a material used in nonlinear waveguiding applications for its low loss, for which $n_2 = 0.00011cm^2/GW$, $\alpha_2 = 0.05cm/GW$ and $\alpha_3 = 0.08cm^3/GW^2$ are the appropriate nonlinear parameters[7]. We use an intensity loss of 1dB/cm ($\alpha_1=0.23cm^{-1}$) in our simulations, which is consistent with the observed loss in straight-waveguides fabricated using $Al_{0.18}Ga_{0.82}As$. Losses in resonator structures have typically been much higher than this, but they are primarily scattering losses, and are due to fabrication problems rather than the fundamental limit imposed by bending loss[9]. The value of 1dB/cm is significantly higher than the fundamental bending loss[9].

We simulate propagation in finite structures apodized as discussed above. To characterize device operation we introduce $\gamma(I_p)$, where I_p is the peak intensity of the input pulse: This is the ratio between the energy transmitted by the device for a Gaussian pulse of peak intensity I_p in the presence of a sister pulse of the same form in the neighbouring channel, to the corresponding transmission of the same pulse in the absence of a sister pulse. Put another way, $\gamma(I_p)$ gives the contrast between the "1" and "0" at the output of the structure for a given I_p. In Figure 3 we plot

$\gamma(I_p)$ for a 5 cell (straight), 10 cell (dot) and 20 cell (dash-dot) structure; the maximum value of $\gamma(I_p)$, γ_{max}, increases as the number of unit cells increases, but in all cases it occurs at $I_p \cong$ 20MW/cm^2. The value of γ_{max} is largest for the 20 cell structure, but at γ_{max} the 20 cell structure has only 12% energy transmission while for the 5 and 10 cell structure the energy transmission is 30%. This attenuation of the output is chiefly due to linear loss. Inset in Figure 3 we plot the input (solid) and output pulses (dash) associated with γ_{max} for the 20 cell structure. Although the peak intensity of the output pulse is attenuated, its shape is relatively undistorted. The pulse has experienced nonlinear compression to 35ps FWHM. The time separation between the input and
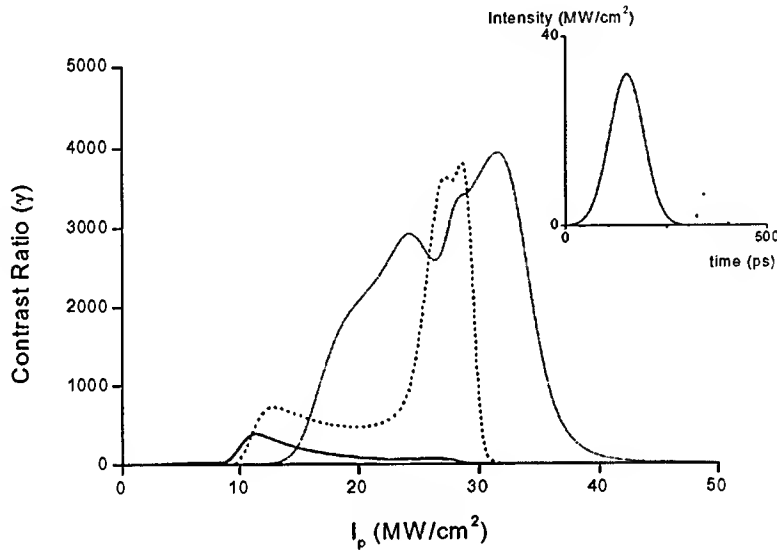
Figure 3: Constrast ratio, γ, for 5 (solid), 10 (dot) and 20 (dash-dot) cell structures. Inset are the input (solid) and output (dot) pulses for the 20 cell structure with input intensity corresponding to the maximum value of γ.

output peaks is 188ps, which, since the structure is only 320μm long, suggests a group velocity of 1.7μm/ps, which is 1.7% the delay expected in the absence of the resonators. This enhanced group delay occurs because the light was trapped in the resonators for a long time, so that the local intensity in the resonators was enhanced, and the effect of the nonlinearity was increased. This partly explains the low switching threshold required for the device[5].

1. Sangjae Lee and Seng-Tiong Ho, Opt. Lett. **18**, 962 (1993).
2. D. Taverner et. al., Opt. Lett. **23**, 259 (1998).
3. A. Melloni, Opt. Lett. **26**, 917 (2001).
4. Suresh Pereira, J. E. Sipe, John E. Heebner and R. W. Boyd, Opt. Lett **27**, 536 (2002).
5. John E. Heebner, Robert W. Boyd and Q-Han Park, JOSA B **19**, 722 (2002).
6. G. P. Agrawal, *Nonlinear Fiber Optics*, (Academic, San Diego, 1989).
7. A. Villeneuve et. al Appl. Phys. Lett. **61**, 147 (1992).
8. Suresh Pereira, Philip Chak and J. E. Sipe, accepted for publication in JOSA B, Sept. 2002.
9. V. Van, Philippe P. Absil, J. V. Hryniewicz and P. –T. Ho, J. Lightwave Tech. **19** (2001).

Triply resonant integrated optical parametric oscillator

B. Naveh and S. Ruschin

Department of Physical Electronics, Faculty of Engineering, Tel-Aviv University, Tel-Aviv 69978 ISRAEL
Tel: +972 3 6408529 Fax: +972 3 6423508 E-Mail: ruschin@eng.tau.ac.il

Z. Weissman
Tel-Hai Academic College, Upper Galilee, ISRAEL

Abstract: We report the modeling of a triply resonant, quasi phase matched, one chip, integrated optical parametric oscillator. Using a novel iterative calculation scheme, we predict threshold levels, conversion efficiency, passive and active tuning behavior and bistability.
©2000 Optical Society of America
OCIS codes: (130.130) (190.190) (190.4410)

1. Introduction

This work focuses on the modeling of a proposed, triply resonant optical parametric oscillator in a quasi phase matched waveguide device, incorporating several components integrated on a single chip. This device can serve as a compact, rugged, widely tunable source of coherent IR radiation for a variety of applications ranging from communications to spectroscopy. Through the confinement of the optical field, non-linear devices based on waveguided designs [1]-[3] offer high field intensities over greater interaction lengths than possible in other schemes. Furthermore, non-linear ferroelectric crystals like KTP or LiNbO$_3$ enjoy of both high second-order conversion coefficients and efficient electro-optic modulation properties, since both these effect originate basically on a common $\chi^{(2)}$ susceptibility tensor. This fact allows the incorporation of functions like parametric amplification and phase modulation in the same chip device.
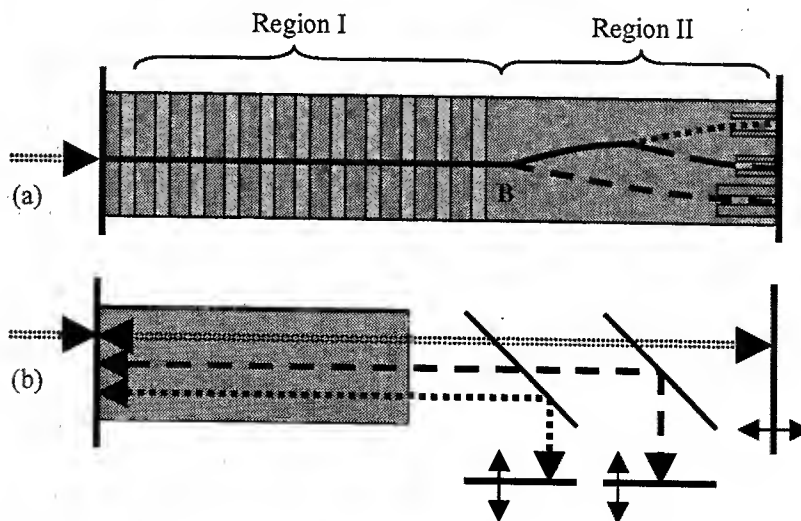
Fig. 1. Schematic layout of a waveguided monolithic and independently tunable Quasi-Phase-Matched TRO (a), and its free-space propagating counterpart (b).

By far, most work on OPOs as for nowadays has been concentrated in the Singly Resonant Oscillator (SRO) scheme. Doubly and Triply Resonant schemes (DRO and TRO) though attractive in terms of lowering pump thresholds, have been readily found to suffer some serious stability and control problems. As shown in this study the integrated waveguided and multi-path scheme proposed here can overcome most of these problems, since it allows independent and fast phase control of the light path of each individual field involved in the interaction. Another physical effect playing crucial role in the overall function and stabilization of the device is the intensity dependent phase shift phenomenon typical of second order $\chi^{(2)}$ interaction. This phenomenon has recently received attention as responsible for "self locking effects" [4] in OPOs. In this work we contribute a novel modeling approach aimed to achieve what one may call "pathway to stable solution". This approach is somewhat similar to that pioneered by Fox

and Li in the context of maser resonators. Similarly to that approach, the fields are tracked during each round-trip taking account for the diverse physical interactions taking place at each one of the device's components. In contradistinction to the method of Fox and Li, the method introduced here is based on *active tuning of the resonator between round trips*, so that the interacting waves will eventually settle to a stable steady state. The method's justification is not only based on its success to furnish the desired stable solutions but also is motivated by the fact that the device actually posses the physical mechanisms of phase tuning needed to reach those stable states. Within the algorithm we introduce the notion of *interaction continuity* as an alternative to round-trip self-consistency used in static resonators.

2. Overview of the model.

Figure 1 denotes schematically the waveguided device under discussion together with its free-space propagating counterpart. Analogies should be clear. The dicroic mirrors in the later case are replaced by wavelength dividing junctions [5], and both types are assumed to possess low losses. Electro-optic phase modulators in the monolithic case have the same role as adjustable mirrors etc. A central distinction however resides in the fact that in the guided case, propagation will induce different phase delays between the three interacting waves due to material and waveguide dispersion. The model accurately tracks the complex amplitude at different sections in the Integrated Optic device. Transition over the QPM amplifier section is accomplished by direct numerical integration of the three coupled non-linear differential equations, adapted to the waveguided case. Waveguide modes and propagation constants were numerically solved by finite difference method. QPM curves were thus produced taking into account both waveguide and material dispersion. Material parameters were chosen to correspond to Rb exchanged waveguides in KTP substrate. The mechanism for actively tuning the OPO was chosen as the tuning the pump laser in a range of about 5nm around 752nm.

At first glance the three degrees of freedom (DOFs) in control, seems not to be sufficient to furnish stable CW operation over a continuous range of wavelengths. The three interacting waves are required to fulfill energy conservation (ω(sign)+ω(idler)=ω(pump)), three round-trip self-consistent conditions (standing waves) and QPM condition in a narrow range for each given pump intensity and wavelength value. In addition, the bi-directional amplification implies the demand that phase synchronization needed for efficient amplification should not be spoiled in the non-amplifying section (Region II) due to non-equal paths, dispersion etc. A condition of identical phases differences for the right and left propagating waves at the interface between Regions I and II (phase continuity) surely would ensure that the amplification process will continue for the returning wave as if the fields never left the QPM region I. Multiple choices exist thus for the utilization of the DOFs and we have evidenced that different choices would lead to solutions of different character and eventually to no stable solutions at all. Our choice for DOFs utilization, lead mainly by physical intuition was the following:

1. The phase modulator of the pump was tuned to attain self-consistency (standing wave).
2. The phase of idler and signal were adjusted for phase difference continuity with the pump at interface B.

Changing phases at the boundary between Regions II and I for the left propagating field, resulted in varying the initial conditions for the QPM amplification. This implied varying the efficiency of energy transfer between the fields and thus the phase variation at section I is modified by the non-linear process. The external phase adjustment process is thus repeated for each round-trip until steady-state was attained. At steady-state the standing-wave condition was *automatically fulfilled* by both the signal and idler waves in all cases via the intensity dependent phase mechanism described above (self phase locking effect). A last remark concerns equalization of wave amplitudes for both wave directions at the boundary point **B**. Strict field continuity would require zero losses al Region II for all three waves. Simulations show that steady state is reached even if this condition is not strictly fulfilled. Generally however low and balanced losses are very desirable for efficient operation. This condition is imposed on device fabrication.

3. Results

The device studied provides a vast choice of results with interesting physical implications. They will be presented at the Conference site or published elsewhere. Here we show two examples of practical significance. Figure 2 depicts the output powers of the three interacting waves as a function of the pump wavelength for two cases. In the first the cavity was tuned according to the algorithm described above for each point at the graph. In the second case, the process was carried out only once, i.e. only one (central) cavity resonance point was set according to the tuning procedure, then the pump wavelength was changed without modifying the phase modulators' voltages. In the first

case, the signal and idler spanned 185nm and 245nm respectively at the 1500nm region. Next we show the effects of threshold and slope efficiency for two cases (Figure 3). First the device was tuned with pump power at 500mW, and then the power was gradually decreased to zero and increased again. The phase delay parameters remained constant throughout the simulation. P_{th} was found at about 300mW. Mostly, the output powers are the same when scanning the power up or down. In the second graph the device was tuned using all three DOFs for each power value.
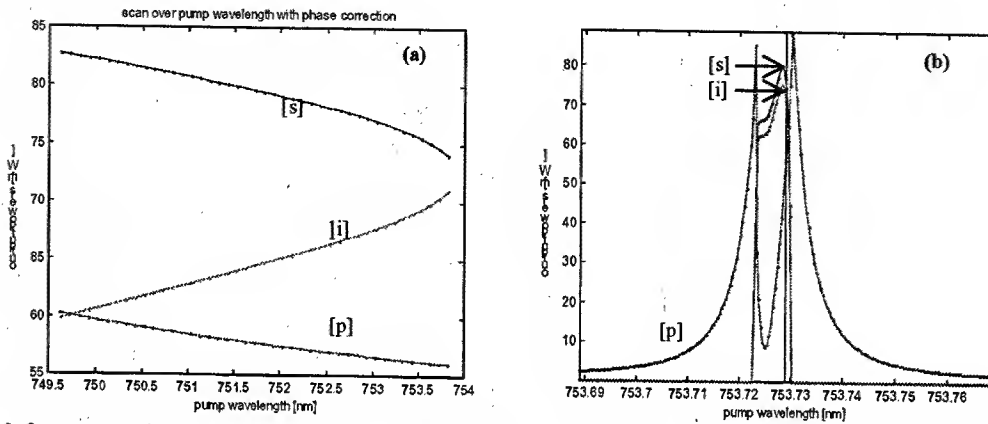
Fig. 2 Output power for the different waves; pump [p] signal [s] and idler [i]. (a) re-tuning the device at each point. (b) no re-tuning.
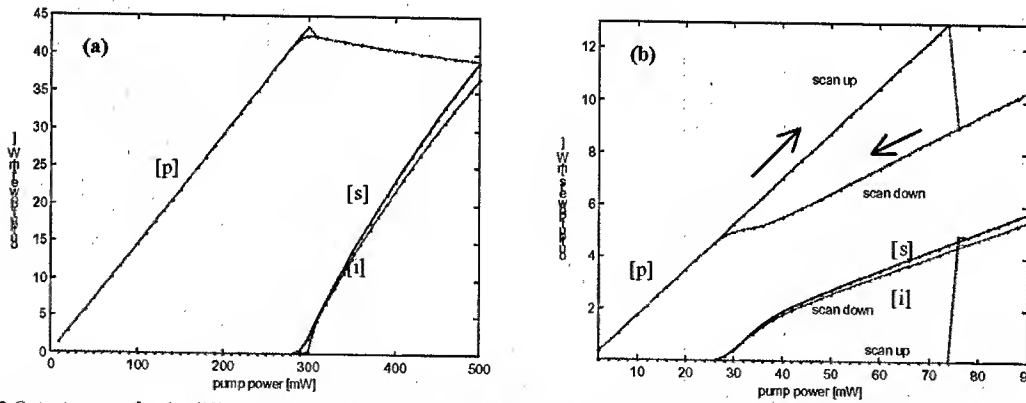
Fig. 3 Output power for the different waves as a function of pump power; (a) without re-tuning the device at each point. (b) with re-tuning.

The differences in behavior for the two cases are drastic. The retuning process lowers the threshold pump power by one order of magnitude (from 300mW to 30mW). In addition a bistability effect is apparent.

4.Conclusion
This study asserts the possibility of attaining stable steady-state operation in an Integrated Optic TRO. This possibility is strongly dependent on the choice and utilization of the available DOFs. We have also introduced a simulation method able to predict many of the complex phenomena observed in TROs. The method should be applicable to other types of waveguided optical parametric generators.

5. References
1. M.A. Arbore and M.M. Fejer. Optics Letters 22 ,151-153 (1997
2. G. P. Bava, 1. Montrosset, W. Sohler and H. Suche. IEEE J.Q.E. QE-23 ,42-51 (1987)
3. P. Baldi, S. Nouh, K. El Hadi, M. de Micheli and D.B. Ostrowsky, JOSA B. 14, 3197-3203 (1997)
4. C. Fabre, E.J. Mason and N.C. Wong. Opt. Commun. 170, 299-307 (1999)
5. Z. Weissman, D. Nir, S. Ruschin and A. Hardy, Appl. Phys. Lett., 67, 302-304 (1995).

Complete description of all modulational instability gain bands generated by nonlinear QPM gratings

Ole Bang

Department of Informatics and Mathematical Modelling, Technical University of Denmark, DK-2800 Kongens Lyngby, Denmark
Tel: +45 4525 3108, fax: +45 4593 1235, email: ob@imm.dtu.dk

Joel F. Corney

Department of Physics, University of Queensland, St. Lucia Qld 4072, Australia
Tel: +61 7 3346 9398, Fax: +61 7 3365 1242, email: corney@physics.uq.edu.au

Abstract: We consider plane waves propagating in quadratic nonlinear slab waveguides with nonlinear quasi-phase-matching gratings. We predict analytically and verify numerically the complete gain spectrum for transverse modulational instability, including hitherto undescribed higher order gain bands.

OCIS codes: (190.4410) Nonlinear optics, parametric processes; (190.4420) Nonlinear optics, transverse effects

With the maturing of the quasi-phase-matching (QPM) technique, in particular by electric-field poling of ferro-electric materials, such as $LiNbO_3$ [1], and by poling of polymers [2] and quantum-well disordering in semiconductors [3], the number of applications of quadratic nonlinear (or $\chi^{(2)}$) materials has increased significantly. Thus even complicated QPM grating structures are now commercially available in periodically poled $LiNbO_3$ (PPLN). It is therefore more important than ever to have complete knowledge of the effects a QPM grating has on the properties of $\chi^{(2)}$ materials. The most fundamental effect of a QPM grating, with a certain spectrum of spatial wave-vectors, is of course to allow noncritical phase-matching at all wavelength for which the wave-vector mismatch Δk between the interacting waves matches a component of the grating spectrum. Thus QPM gratings allow for efficient multiple wavelength second harmonic generation (SHG) [4], which may, e.g., be used for multiple-channel wavelength conversion [5].

In addition to providing effective phase-matching, QPM gratings have the basic effect that they induce an artificial asymmetric cubic nonlinearity (ACN) in the equations for the average field in the form of self- and cross-phase modulation terms [6]. This cubic nonlinearity appears in linear and/or nonlinear periodic QPM gratings of arbitrary shape [7], it can be focusing or defocusing, depending on the sign of the phase-mismatch [7], and its strength can be significantly increased (e.g., dominating the Kerr nonlinearity) by modulating the grating [8]. In continuous-wave operation the ACN induces an intensity-dependent phase mismatch, just as the inherent Kerr nonlinearity, with potential use in switching applications [9]. The ACN further explains a wide spectrum of novel fundamental properties of solitons [6, 7, 10] and modulational instability (MI) [11]. Importantly the ACN is a general effect of non-phase-matched wave interaction and as such appear also in homogeneous $\chi^{(2)}$ materials in the cascading limit. In fact, in this case the asymmetric signature of the ACN may be measured as the difference between the properties in upconversion and downconversion, since there is no effective $\chi^{(2)}$ nonlinearity with which the ACN must compete, as in QPM gratings. Such an experiment was just reported [12] and thus the ACN has now been confirmed both numerically and experimentally.

The MI gain spectrum in general QPM gratings has a multipeaked structure of up to three fundamental bands with accompanying overtones [11]. The fundamental (long-wave instability) bands at low transverse wavenumbers is due to MI of the averaged field. For QPM with a simultaneous linear and nonlinear grating and/or with a nonlinear grating with a dc-value (as with QPM in multilayered poled polymers [2] and quantum-well disordered semiconductors [3]), the ACN is necessary to describe how these fundamental bands may disappear, making plane wave modulationally stable over hundreds of diffraction lengths [11]. The gain bands in the first overtone were surmised to be related to the inherent instability in homogeneous (non-phase-matched) $\chi^{(2)}$ media [11]. However, an accurate description of the first overtone bands has not been found and the higher overtone bands have not been discussed at all.

Here we study MI in 1+1D $\chi^{(2)}$ media with a purely nonlinear QPM grating with no dc-component, such as in PPLN slab waveguides. With this simple QPM grating the ACN is not necessary to take into account for an accurate description of MI [11]. We present the first analytical and numerical description of the

complete MI spectrum with all overtones. We show explicitly that the overtone series are caused by MI in the rapidly varying components of the propagating fields, which are in turn induced by the grating. We derive approximate analytic expressions for the positions of the gain bands and compare them with exact Floquet results and direct numerical simulation, to find good agreement.

We consider a linearly polarized electric field propagating in a lossless $\chi^{(2)}$ slab waveguide with a QPM grating under conditions for (the most efficient) first-order QPM and type I SHG. The normalized dynamical equations for the slowly varying envelopes of the fundamental $E_1(x,z)$ and SH $E_2(x,z)$ take the form

$$i\frac{\partial E_1}{\partial z} + \frac{1}{2}\frac{\partial^2 E_1}{\partial x^2} + \chi(z)E_1^* E_2 e^{i\beta z} = 0, \quad i\frac{\partial E_2}{\partial z} + \frac{1}{4}\frac{\partial^2 E_2}{\partial x^2} + \chi(z)E_1^2 e^{-i\beta z} = 0, \tag{1}$$

where the x and z scales have been normalised by X_0 and $Z_0 = k_1 X_0^2$, respectively. The normalized wavevector mismatch is given by $\beta = (k_2 - 2k_1)Z_0$. The nonlinearity is periodic in z with Fourier expansion $\chi(z) = \sum_n d_n \exp(in\kappa z)$, where $d_n = d_{-n}^*$ (χ is real) and the grating wave number κ is defined to be positive. The periodic QPM grating will force the same periodicity in the propagating fields. We therefore expand these in Fourier series also: $E_1(x,z) = \sum_n w_n(x,z) \exp(in\kappa z)$, $E_2(x,z) = \sum_n v_n(x,z) \exp(in\kappa z - i\tilde{\beta}z)$, allowing the amplitudes w_n and v_n to vary slowly compared to $\exp(i\kappa z)$. The residual mismatch is defined as $\tilde{\beta} = \beta - s\kappa$, where $s = \text{sign}(\beta)$ for first-order QPM. Substituting all Fourier series into Eqs. (1) gives

$$(\hat{L}_1 - n\kappa)w_n + \sum_{l,m} d_{n+m-l-s}w_m^* v_l = 0, \quad (\hat{L}_2 - n\kappa)v_n + \sum_{l,m} d_{n-m-l+s}w_m w_l = 0, \tag{2}$$

where $\hat{L}_j = i\partial_z + \partial_x^2/(2j) + (j-1)\tilde{\beta}$. This set of equations has plane-wave solutions of the form $w_n = \bar{w}_n \exp(i\Lambda z)$, $v_n = \bar{v}_n \exp(2i\Lambda z)$ [11]. To study MI we consider small perturbations of the plane-wave solutions: $w_n = [\bar{w}_n + \Delta w_n(x,z)]\exp(i\Lambda z)$, $v_n = [\bar{v}_n + \Delta v_n(x,z)]\exp(2i\Lambda z)$. Substitution into Eq. (2) gives

$$(\hat{L}_1' - n\kappa)\Delta w_n + \sum_{l,m} d_{n+m-l-s}(\bar{w}_m^* \Delta v_l + \bar{v}_l \Delta w_m^*) = 0, \quad (\hat{L}_2' - n\kappa)\Delta v_n + 2\sum_{l,m} d_{n-m-l+s}\bar{w}_m \Delta w_l = 0, \tag{3}$$

where $\hat{L}_j' = \hat{L}_j - j\Lambda$. Writing the perturbations in the form $\Delta w_n(x,z) = \delta_n^{(1)}(z)\exp(i\nu x) + \delta_n^{(2)*}(z)\exp(-i\nu x)$, and $\Delta v_n(x,z) = \delta_n^{(3)}(z)\exp(i\nu x) + \delta_n^{(4)*}(z)\exp(-i\nu x)$, one obtains finally a complicated linear matrix equation for the transverse perturbations $\vec{\delta}_n = (\delta_n^{(1)}, \delta_n^{(2)}, \delta_n^{(3)}, \delta_n^{(4)})^T$, which couples all Fourier components.

To derive a simple result we consider nearly phase matched interaction with $|\kappa| \sim |\beta| \gg 1$ in the for PPLN typical square QPM grating, for which $d_n = 0$ for n even and $d_n = 2/(i\pi n)$ for n odd. The assumption $|\kappa| \sim |\beta| \gg 1$ is essential, since then $|\bar{w}_0|, |\bar{v}_0| \gg |\bar{w}_{n\neq 0}|, |\bar{v}_{n\neq 0}|$. In this case the evolution of the perturbation in each component is to a good approximation decoupled from the other components and described by

$$\frac{\partial}{\partial z}\vec{\delta}_n = i\begin{bmatrix} a_n & b_n & c & 0 \\ -b_n^* & -a_n & 0 & -c^* \\ 2c^* & 0 & e_n & 0 \\ 0 & -2c & 0 & -e_n \end{bmatrix}\vec{\delta}_n = M_n\vec{\delta}_n, \tag{4}$$

where $a_n = -\nu^2/2 - \Lambda - n\kappa$, $b_n = d_{2n-s}\bar{v}_0$, $c = d_{-s}\bar{w}_0^*$, and $e_n = -\nu^2/4 + \tilde{\beta} - 2\Lambda - n\kappa$. Inspecting the diagonal terms of the MI matrix leads to the conclusion that gain bands in adjacent overtones (or n's) approximately differ in spatial frequency by $\sqrt{2\kappa} \sim \sqrt{4\kappa}$. The four eigenvalues of M_n are given by

$$\lambda_n^2 = A_n \pm \sqrt{A_n^2 - B_n}, \quad A_n = (|b_n|^2 - 4|c|^2 - a_n^2 - e_n^2)/2, \quad B_n = (a_n e_n - 2|c|^2)^2 - e_n^2|b_n|^2, \tag{5}$$

where $|c|^2 = \Lambda(2\Lambda - \tilde{\beta})$ and $|b_n|^2 = \Lambda^2/(2n - s)^2$. Any positive real part of an eigenvalue corresponds to MI with the gain $g_n(\nu) = \Re(\lambda_n)$. Analysing the gain versus a_n and e_n reveals two gain bands around (1) $a_n = -e_n$ and (2) $a_n = 0$. For $|b_n| = 0$ the extrema of these branches lie at (1) $a_n + e_n = 0$ (the diagonal branch) and (2) $a_n e_n = 2|c|^2$ (the hyperbolic branch). For $|b_n| \neq 0$ the extrema remain close to these lines. On the diagonal branch, corresponding to $\nu^2 = -8/3n\kappa - 4\Lambda + 4\beta/3$, the gain is largest near $a_n = 0$, which corresponds to the fundamental $n = 0$ Fourier component, or average field. The gain bands in the higher order Fourier
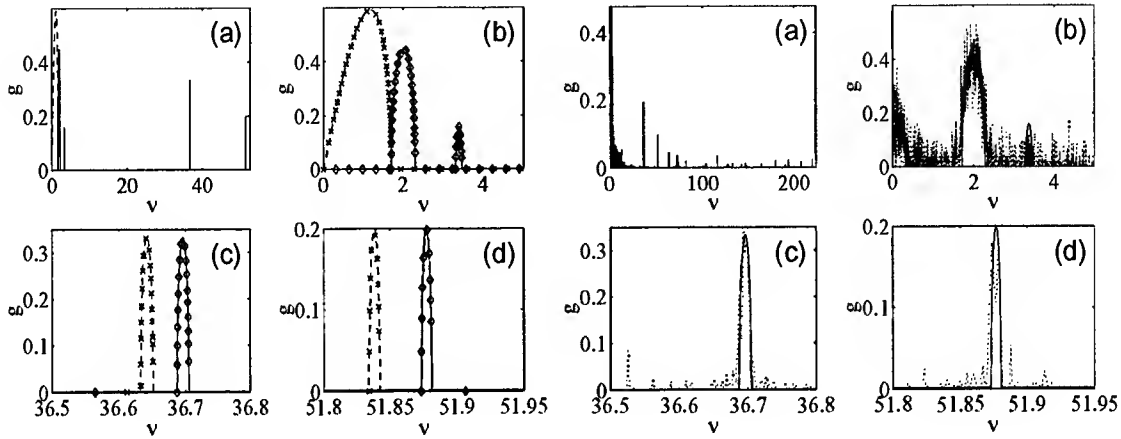
Fig. 1. Left (a-d). MI gain for $\Lambda = 1$ (dashed) and $\Lambda = -1$ (solid) calculated exactly by use of Floquet theory. The crosses and diamonds give the results of the approximate theory, Eq. (5) for (b) the $n = 0$ bands, (c) the largest of the $|n| = 1$ bands and (d) the largest of the $|n| = 2$ bands. We have chosen $\kappa = \beta = 672.31$. Fig. 2. Right (a-d). Gain calculated by numerical simulation [(a) and dotted line in (b-d)] and by use of Floquet theory [solid line in (b-d)]. We have chosen $\kappa = \beta = 672.31$ and $\Lambda = -1$.

components (higher n or overtones) will thus be small. On the hyperbolic branch $\nu^2 = -3n\kappa - 5\Lambda + 2\beta \pm [(n\kappa + 3\Lambda - 2\tilde{\beta})^2 + 16|c|^2]^{1/2}$. For $n \neq 0$ the gain bands appear at $\nu^2 \simeq -2\Lambda - 2\kappa n$ (corresponding to $a_n=0$) and $\nu^2 \simeq -8\Lambda - 4\kappa n + 4\beta$ (corresponding to $e_n=0$). Thus we have the structure of up to 3 gain bands in the average field ($n=0$), each with a set of equally spaced weak overtone gain bands ($n \neq 0$).

The results can be compared with exact Floquet calculations [11]. For example consider $\kappa=672.31$, $\Lambda = \pm1$ and $\tilde{\beta}=0$, corresponding to a particular PPLN crystal at exact phase-matching. Our analytic results give $n = 0$ bands at $\nu=1.18$ ($\Lambda=1$), and $\nu=2$ and 3.38 ($\Lambda=-1$), which agree with Fig. 1(b). In the first overtone, bands appear at $\nu \simeq \sqrt{-2n\kappa - 2\Lambda}$, which for $n = -1$ gives $\nu=36.64$ ($\Lambda=1$) and $\nu=36.70$ ($\Lambda=-1$), both agreeing with Fig. 1(c). Similar results appear for $|n|=2$ [Fig. 1(d)] and higher. In Fig. 1 we also show the gain profiles predicted by Eq. (5), which shows a very good match with the exact Floquet results. Direct numerical simulation [11] of Eqs. (1) with MI seeded by noise confirmed again our results (see Fig. 2). This research is supported by the Danish Technical Research Council (Grant No. 26-00-0355).

References

1. M.M. Fejer, in *Beam Shaping and Control with Nonlinear Optics*, eds. F. Kajzar and R. Reinisch, 375-406 (Plenum, New York, 1998).
2. V. Ricci, G.I. Stegeman, and K.P. Chan, "Poling of multilayer polymer films for modal dispersion phase matching of second-harmonic generation: effects in glass-transition temperature imatching in different layers", J. Opt. Soc. Am. B. **17**, 1349 (2000).
3. A. Saber Helmy *et al.*, "Quasi-phase-matching in GAAS-ALAS superlattice waveguides via bandgap tuning using quantum well intermixing", Opt. Lett. **25**, 1370-1372 (2000).
4. P. Baldi *et al.*, "Simultaneous generation of red, green and blue light in room temperature periodically poled lithium niobate waveguides using single source", Electron. Lett. **31**, 1350-1351 (1995).
5. M.H. Chou, K.R. Parameswaran, M.M. Fejer, and I. Brener, "Multiple-channel wavelength conversion by use of engineered quasi-phase-matching structures in LiNbO$_3$ waveguides", Opt. Lett. **24**, 1157-1159 (1999).
6. C. Balslev Clausen, O. Bang, and Y.S. Kivshar, "Spatial solitons and induced Kerr effects in quasi-phase-matched quadratic media", Phys. Rev. Lett. **78**, 4749-4752 (1997) 4749.
7. J.F. Corney and O. Bang, "Solitons in quadratic nonlinear photonic crystals", Phys. Rev. E **64**, 047601 (2001).
8. O. Bang, C. Balslev Clausen, P.L. Christiansen, and L. Torner, "Engineering competing nonlinearities", Opt. Lett. **24**, 1413 (1999).
9. O. Bang, T.W. Graversen, and J.F. Corney, "Accurate switching intensities and optimal length scales in quasi-phase-matched materials", Opt. Lett. **26**, 1007-1009 (2001).
10. S.K. Johansen, S. Carrasco, L. Torner, and O. Bang, "Engineering of spatial solitons in two-period QPM structures", Opt. Commun. **203**, 393-402 (2002).
11. J.F. Corney and O. Bang, "Modulational instability in periodic quadratic nonlinear materials", Phys. Rev. Lett. **87**, 133901 (2001); "Plane waves in periodic, quadratically nonlinear slab waveguides: stability and exact Fourier structure", J. Opt. Soc. Am. B **19**, 812-821 (2002).
12. P. Di Trapani, A. Bramati, S. Minardi, W. Chinaglia, C. Conti, S. Trillo, J. Kilius, and G. Valiulis, "Focusing versus defocusing nonlinearities due to parametric wave mixing" Phys. Rev. Lett. **87**, 183902 (2001).

NLMD12-1

Hélène Ward and Luc Bergé
Département de Physique Théorique et Appliquée,
CEA-DAM/Ile de France, B.P. n° 12, F-91680 Bruyères-le-Châtel, France.
Tel.: (+33) 169 26 48 92, Fax: (+33) 169 26 71 06, e-mail: helene.ward@cea.fr

Compression of femtosecond pulses to a few optical-cycles duration by coupling with an electron plasma in solids is shown. Nonlinear dissipation induced by multiphoton-absorption, and fast temporal modulations induced shock-terms can, however, maintain self-guided propagation.

Propagation of ultra-short laser pulses in gases as well as in solids has recently become a very active research field. Laser beams with a duration of about 100 fs and a maximum intensity less than 10^{14} W/cm^2 have indeed the amazing property of covering several Rayleigh lengths in transparent media, opening potential LIDAR applications for, e.g., atmospheric propagation [1–4]. In glass, experimental observation of light channels was recently reported for an input laser of 160 fs duration and maximum peak intensity of 10^{13} W/cm^2, for which the pulse is shortened to a two peak temporal profile [5]. From the nonlinear Kerr response of the medium, a light pulse with input power above the critical threshold for self-focusing (SF), first focuses at a finite distance. Beam collapse predicted in an idealized Kerr medium is then arrested by the formation of a defocusing electron plasma excited by the laser through multiphoton-ionization (MPI). At high enough powers, a dynamic balance between Kerr SF and MPI maintains the light channel through several focusing/defocusing cycles. In contrast, at powers close to critical, the dynamic interplay between SF and MPI can be stabilized along the propagation axis. In this situation, plasma defocusing depletes the temporal profile of the light channel to a time slice having exactly the critical power for SF [6]. It has been numerically shown, that, in silica glass, a robust filament can indeed be captured within one sharp leading peak [7]. However this structure was discovered in the scope of weak, even zero dissipative processes.

Here, we wish to go one step beyond. First, we show that the formation of narrow solitary pulses is possible in solids. Second, we discuss the influence of multiphoton-absorption (MPA) on the propagation of such pulses. We display evidence that MPA may help in maintaining the self-guiding of temporally-compressed pulses. Since their leading peak results from a stringent pulse shortening to a few fs duration, we finally investigate the action of self-steepening terms used in previous models [6–8]. Theoretical arguments based on a self-similar modeling enables us to get a deeper insight in the dynamics of these fs pulses.

We consider a linearly-polarized beam propagating in fused silica with central frequency ω_0, wavenumber

$k = n_0 k_0$ ($k_0 = \omega_0/c$), and laser wavelength $\lambda_0 =$790 nm. At the entrance face of the glass sample, the input beam profile is $\sqrt{2P_{in}/\pi\omega_0^2} \exp\left(-r^2/w_0^2\right) \exp\left(-t^2/t_p^2\right)$ with input power $P_{in} = 1.5P_{cr}$, beam waist $w_0 = 15\mu$m, and temporal FWHM diameter $\tau = \sqrt{2\ln 2}\, t_p =$160fs. The critical power for self-focusing is $P_{cr} = \lambda_0^2/2\pi n_0 n_2 \simeq 2.2$ MW with $n_2 = 3.2$ x 10^{16} cm^2/W ($n_0 = 1.4$) corresponding to the nonlinear (linear) refraction index of fused silica. Following standard models [2, 3, 7], the complex envelope $\mathcal{E}(r,\,t,\,z)$ of the electric field and the electron density ρ of the excited plasma evolve as:

$$i\partial_z \mathcal{E} + \frac{1}{2k}\, T^{-1}\, \nabla_\perp^2 \mathcal{E} - \frac{k''}{2}\partial_t^2 \mathcal{E} + k_0 n_2\, T\left(|\mathcal{E}|^2 \mathcal{E}\right)$$
$$- \frac{k_0}{2\rho_c}\, T^{-1}\left(\rho\mathcal{E}\right) + i\frac{\beta^{(K)}}{2}|\mathcal{E}|^{2K-2}\mathcal{E} = 0 \qquad (1)$$

$$\partial_t \rho = \sigma_K\, \rho_{at}\, |\mathcal{E}|^{2K}\left(1 - \rho/\rho_{at}\right), \quad \rho \ll \rho_{at} \qquad (2)$$

where z is the propagation direction and t the retarded time $(t - z/v_g)$ with group velocity v_g. The transverse Laplacian ($\nabla_\perp^2$) term accounts for diffraction of axis-symmetric beams and $k'' = [\partial^2\omega/\partial k^2]^{-1}|_{\omega_0} = 340$ fs^2/cm is the group velocity dispersion (GVD) coefficient. The following terms of Eq. (1) are the Kerr response of the material, the defocusing from the plasma density ρ excited by MPI, and multiphoton-absorption (MPA) with $\beta^{(K)} = K\hbar\omega_0\sigma_K\rho_{at}$. The critical plasma density is denoted by ρ_c and the background atom density by $\rho_{at} = 2.1$ x 10^{22} atoms/cm$^{-3} = 11.75\rho_c$. Band-to-band transitions are induced in silica from the gap potential $U_i = 7.8$ eV [7], yielding the number of photons $K = 5$ required for ionization. The MPI coefficient in Eq. (2) reads as $\sigma_K = 1.3$ x 10^{-55} s^{-1} cm^{2K}/W^K. In addition we included deviations from the slowly-varying envelope approximation (SVEA) through the operator $T \equiv 1 + (i/\omega_0)\partial_t$ as proposed in [9, 10]. These temporally-dispersive effects refer to self-steepening for the operator T in front of the cubic nonlinearity and to space-time focusing for T^{-1} in front of the transverse Laplacian.

Eq. (1) is solved by means of a split-step Fourier in time and Cranck-Nicholson in space scheme, and Eq. (2) by a variable-step Runge-Kutta scheme [3]. To

with no MPA, and within the slowly varying envelope approximation (*i.e.* $T = 1$). We observe that the beam first self-focuses, then triggers an electron plasma. As expected for powers close to critical, SF is almost exactly balanced by MPI, so that the beam slowly relaxes to a waveform with intensity clamped around threshold $I_{max} \sim \rho^{max}/2\rho_c n_2$, where $\rho^{max} \sim \Delta t \, \sigma_K \, \rho_{at} I_{max}^K$ is fixed by the pulse time scale Δt. Inspection of the numerics confirms that the peak electron density forms a plateau which remains coupled with the beam along z. This equilibrium remains "stable" over two Rayleigh lengths, $z_0 = \pi \omega_0 n_0/\lambda_0 = 1.25$ mm. An attractor is promoted by a quasi-static balance between MPI, diffraction, and the Kerr response of the material, keeping the spatial size of the beam unchanged. The corresponding temporal profiles are depicted in Fig. 1(b). The coupling between light and electrons strongly shortens the pulse duration and only one leading peak survives at the time slice located near $t \simeq -\left[\ln \sqrt{P_{in}/P_{cr}}\right]^{1/2} t_p$, which contains the critical power for the self-focusing of Gaussian beams.

In Figs. 1(c-d), addition of MPA leads to dissipate the leading peak formed by MPI. However, it is clearly seen that MPA does not necessarily reduce the propagation range. Instead, dissipation of the first leading peak does not prevent the emergence of a trailing peak with comparable intensity, which maintains the propagation. Because MPI-induced temporal compression produces pulse durations which become of the order of a few optical cycles, it is natural to investigate the action of the operator T. Assuming a SF regime along which the cubic nonlinearity in Eq. (1) dominates over diffraction, we present here numerical simulations describing self-steepening only. In Figs. 1(e-f), the pulse undergoing self-steepening and no MPA is shifted in time. This results into an optical shock that allows the pulse to self-focus again, which, on the whole, maintains the propagation range to some extent. Inclusion of space-time focusing, i.e., T^{-1} in front of the diffraction term of Eq. (1), also contributes to the establishment of an optical shock regime (not shown here).

These dynamical aspects are now discussed through analytical arguments. For notational convenience, we use the rescalings $r \to \omega_0 r$, $t \to t_p t$, $z \to 4z_0 z$, and $\mathcal{E} \to \sqrt{P_{cr}/4\pi\omega_0^2}\psi$. Eqs. (1) and (2) then take, at leading order, the dimensionless form

$$i\partial_z \psi \; + \; \nabla_\perp^2 \psi + \left(|\psi|^2 - \rho\right) \psi + i\nu \, |\psi|^{2K-2}\psi$$
$$+ \; \frac{i}{t_p\omega_0}\partial_t \left[|\psi|^2\psi - \nabla_\perp^2 \psi\right] = 0 \qquad (3)$$

after a straightforward expansion of the T operator for an envelope frequency assumed smaller than ω_0. Here
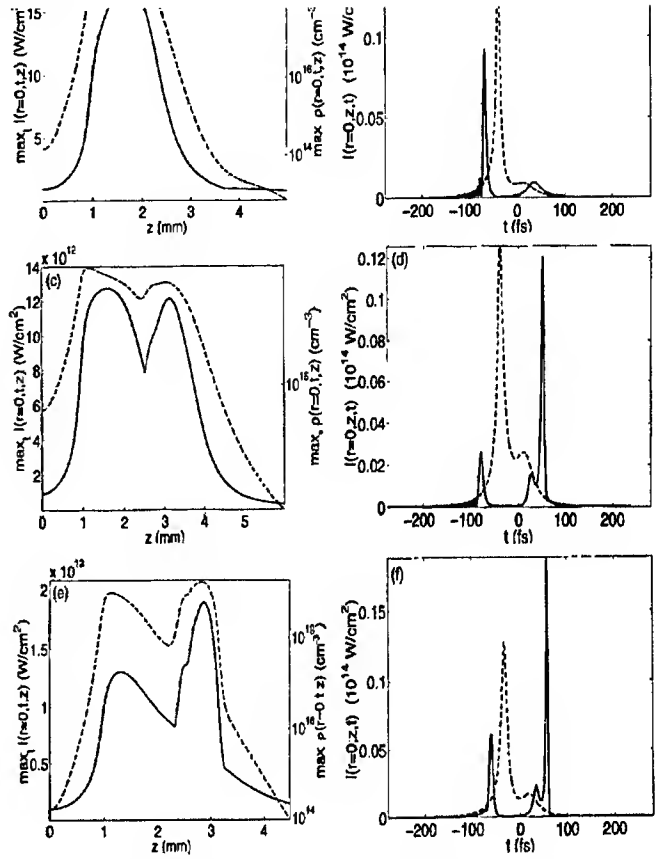
FIG. 1: Numerical simulations of 160 fs pulses with moderate input powers $P_{in} = 1.5 P_{cr}$ in silica glass. (a) maximum-in-time intensity I (solid curve) and electron density ρ (dashed curve) for Eqs. (1) and (2) with no absorption and $T = 1$. (b) Temporal profiles displaying evidence of pulse temporal shortening at $z = 1.4$mm $\simeq z_0$ (dashed line) and $z = 2.4$mm $\simeq 2z_0$ (solid line). (c) Peak intensity and electron density of the same pulse undergoing MPA. (d) Related temporal profiles at $z = 1.4$mm (dashed line) and $z = 3.2$mm (solid line). (e) Same plots with MPA = 0 and self-steepening. (f) Related temporal profiles at $z = 1.45$mm (dashed line) and $z = 2.91$mm (solid line).

the electron density ρ obeys $\partial_t \rho = \Gamma \, |\psi|^{2K}$ with $\Gamma = 1.71$ x 10^{-8}. The MPA normalized coefficient is $\nu = 3.24$ x 10^{-8}. The rescaled GVD coefficient $\delta = 2z_0 k''/t_p^2 = 4.6$ x 10^{-3} is so small, that action of GVD is not meaningful for the present parameters. We therefore omit it.

(i) *MPI saturation:* Let us first discuss the case with no dissipation and $T = 1$. In the SF stage, the beam envelope tends to collapse at a finite distance z_c, with a self-similar distribution $\psi \to \sqrt{I(z,t)} \, \phi(\xi) \, e^{iS}/R(z,t)$ and phase $S = \int_0^z du/R^2(u,t) + R_z R \, \xi^2/4$. Here ϕ is chosen as the real stationary wave solution of Eq. (3) with power equal to 11.7, $\xi = r/R(z,t)$, and $R(z,t) = R[z_c(t) - z]$ denotes the wave radius that self-contracts as $z \to z_c$.

section of the pulse ("time slice") and thus moves in time as $z_c(t) \simeq Z_0 \left[\alpha P_{in}/P_{cr} \, e^{-2t^2} - 1\right]^{-\beta}$ with $\alpha = 4\pi/11.7$ and $\beta \simeq 0.63$ [11, 12]. The central time slice is located at $t = 0$ and focuses at the minimum distance $z_c(0)$ with $\dot{z}(0) = 0$ and $\ddot{z}(0) > 0$. Importantly, $\dot{z}(t)$ reaches infinity as $t \to \pm t^*$, where $t^* \equiv -\left[\ln \sqrt{\alpha P_{in}/P_{cr}}\right]^{1/2}$. Because the time slices self-focus inside the narrow range $|t| < |t^*| < 1$ only, we emphasize that, except in the vicinity of caustics located near $\pm t^*$, the temporal variations in the beam radius are relatively flat in the inner domain $t^2 \ll 1$ compared with e^{-2Kt^2}. The electron density thus behaves as

$$\rho(r, t, z) \simeq \sqrt{\frac{\pi}{8K}} \, \Gamma\left(\alpha \frac{P_{in}}{P_{cr}} \phi^2\right)^K \frac{\mathrm{Erf}\left(\sqrt{2K}t\right) + 1}{R^{2K}\left[z_c(t) - z\right]}. \quad (4)$$

At positive times, the slices neighboring $t = 0$ are defocused by the density front becoming maximum in this range. In contrast, at negative times, the leading edge of the central slice continues to self-focus. The self-similarity assumption holds, which we can repeat at each time slice unaffected by the electron density. Plasma defocusing then develops step by step until $t \simeq t^*$ where $\dot{z}_c$ reaches infinity. Near this instant, a local equilibrium results from the balance between SF and MPI.

(ii) *MPA dissipation:* Multiphoton-absorption introduces pulse dissipation as $\partial_z P = -2\nu \int |\psi|^{2K} d\vec{r}$. It acts at the instant when the pulse reaches its maximum intensity. At this time slice, dissipation decreases the beam power P_{in} to below critical over the physical propagation interval $\Delta z \simeq \ln\left[P_{in}/P_{cr}\right]/\beta^K I_{max}^{K-1} \simeq 0.44$ mm. However, the power lost by the leading peak is here transferred from the front to the rear of the pulse. So, whereas MPA could be believed to shorten the propagation length of the self-trapped beam, it actually enhances it by exciting a trailing peak, which keeps the intensity clamped to its maximum $|\mathcal{E}|^2_{max}$, before being dissipated in turn.

(iii) *Deviations from the SVEA:* Contributions affected by the operators T and T^{-1} in Eq. (3) lead to power variations of the form

$$\partial_z P = -\frac{\partial_t}{t_p \omega_0} \int \left(\frac{3}{2} |\psi|^4 + |\nabla_\perp \psi|^2\right) d\vec{r}, \quad (5)$$

where the two integrals tend to diverge around z_c. In

erences therein). Considering for instance a bell-shaped pulse centered on $t = 0$, we easily infer that power will be transferred into the time region where $\partial_t |\psi|^2$ is negative and thus create a leading spike emerging in the time domain $t > 0$. In the present scope, the narrow structure created as a leading peak located at $t = t^*$ is shifted to positive times, under the shape of a shock profile. The shape of this shock can be evaluated analytically. Self-steepening and space-time focusing thus distort the temporal profile of the pulse by creating a strong enhancement of the trailing peak, which was earlier experimentally reported in [13] without MPI and clears up our numerical results. It is important to observe that these terms do not kill plasma generation. Instead, they move the pulse along time and enhance its intensity through a shock dynamics, which locally preserves MPI active.

In summary, we have shown that ultra-short solitary pulses resulting from a quasi-static balance between MPI and SF can form in silica samples at input powers moderately above critical. While MPA and temporal deviations from the SVEA could be thought to dissipate the pulse energy and shorten the propagation range, they actually enhance it by exciting other temporal slices through shock structures emerging along propagation.

[1] A. Braun, G. Korn, X. Liu, D. Du, J. Squier, and G. Mourou, *Op. Lett.* **20**, 73 (1995); E.T.J. Nibbering *et al.*, *Opt. Lett.* **21**, 62 (1996); B. LaFontaine *et al.*, *Phys. Plasmas* **6**, 1615 (1999).

[2] M. Mlejneck, E.M. Wright, and J.V. Moloney, *Opt. Lett.* **23**, 382 (1998).

[3] A. Couairon and L. Bergé, *Phys. Plasmas* **7**, 193 (2000); L. Bergé and A. Couairon, *Phys. Plasmas* **7**, 210 (2000).

[4] H.R. Lange *et al.*, *Opt. Lett.* **23**, 120 (1998); A. Chiron *et al.*, *Euro. Phys. J. D* **6**, 383 (1999).

[5] S. Tzortzakis *et al.*, *Phys. Rev. Lett.* **87**, 213902-4 (2001).

[6] L. Bergé and A. Couairon, *Physica D* **152-153**, 752 (2001).

[7] S. Henz and J. Herrmann, *Phys. Rev. A* **59**, 2528 (1999).

[8] P. Chernev and V. Petrov, *Opt. Lett* **17**, 172 (1992); J.E. Rothenberg, *ibidem*, 583 (1992).

[9] T. Brabec and F. Krausz, *Phys. Rev. Lett.* **78**, 3282 (1997).

[10] A.L. Gaeta, *Phys. Rev. Lett.* **84**, 3582 (2000).

[11] G. Fibich and G. Papanicolaou, *Opt. Lett.* **22**, 1379 (1997); *ibidem*, *SIAM J. Appl. Math.* **60**, 183 (1999).

[12] A. Brodeur *et al.*, *Opt. Lett* **22**, 304 (1997).

[13] J.K. Ranka and A.L. Gaeta, *Opt. Lett.* **23**, 534 (1998).

Mode Coupling by Photorefractive Grating in Multiple Quantum Well Slab Waveguide

Ewa Weinert-Rączka and Marek Wichtowski

Institute of Electronics, Informatics and Telecommunication, Technical University of Szczecin
Al.Piastów 17, 70-310 Szczecin, Poland, Tel +(48)-91-4495113, Fax +(48)-91-4340926
e-mail: ewa.raczka@ps.pl

1. Introduction

Diffraction gratings are commonly used in integrated optics systems as frequency filters, Bragg reflectors, couplers, elements of multiplexing and demultiplexing devices and distributed feedback lasers. Traditional waveguide gratings have constant parameters and are sensitive for any production imperfections. Optically induced gratings are adjustable and therefore independent on fabrication errors and on the influence of external conditions. The grating created by two mutually coherent external waves interfering in a nonlinear material can be used for the same purposes as stable grating but obtained elements can be tuned in real-time by varying external waves parameters [1]. The grating created in photorefractive material does not require permanent illumination. It can be created by a short pulse of the external waves and last until the arrival of the next pulse which can renew or erase it [2].

The grating analysed here is induced in a single-mode planar waveguide made from semi-insulating multiple quantum well (MQW) structure operated with an external electric field applied along the quantum well planes (Fig.1). The grating is created by two beams forming an interference pattern in the MQW structure. The light intensity is

$$I = I_0(x,z,t) \, exp(-\alpha x) \, [1 + m \, cos(Kz)], \quad (1)$$

where I_0 denotes the intensity of the external beams at the boundary of the slab, α describes the absorption coefficient, m is the modulation depth and K is the grating constant. A high frequency light cause an interband excitation of electrons and holes. Free carriers move due to the drift and diffusion and recombine to the

donor traps. The resulting space-charge electric field causes the change of the refractive index due to the electro-optic effect. The refractive index grating can be used for frequency selective reflection, deflection or out-coupling of modes guided in the structure. Signals guided in the structure have frequencies below the absorption threshold and their influence on the grating can be neglected.
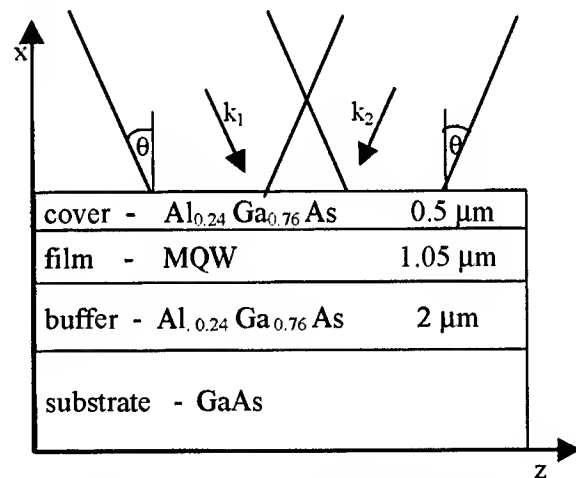
Figure. 1 Cross-section of the waveguide.

2. Dynamics of the grating

The dynamics of the carriers can be described by equations based on a classical Kukhtarev-Vinetskii model [3], where transverse carrier mobility is neglected due to the high difference between longitudinal and transverse carrier mobilities characteristic for MQW structure. If thermal excitation of the carriers is not included, the equations for MQW planes perpendicular to the x axis and the electric field applied along the z axis take the form:

$$\frac{\partial n_e}{\partial t} = \frac{\alpha}{h\nu} I - \gamma_e n_e N_D^+ + \frac{1}{e}\frac{\partial j_e}{\partial z},$$

$$\frac{\partial n_h}{\partial t} = \frac{\alpha}{h\nu} I - \gamma_h n_h (N_D - N_D^+) - \frac{1}{e}\frac{\partial j_h}{\partial z}$$

$$j_e = e\mu_e n_e E + \mu_e k_B T \frac{\partial n_e}{\partial z},$$

$$j_h = e\mu_h n_h E - \mu_h k_B T \frac{\partial n_h}{\partial z} \qquad (2)$$

$$\frac{\partial N_D^+}{\partial t} = \gamma_h n_h (N_D - N_D^+) - \gamma_e n_e N_D^+,$$

$$\frac{\partial E}{\partial z} = \frac{e}{\varepsilon\varepsilon_0}(N_D^+ + n_h - n_e - N_A)$$

where n_e denotes the free electron and n_h - the free hole concentration, N_D - donor, N_D^+ - ionized donor, N_A - acceptor concentrations, j_e - the electronic and j_h - the hole current densities, E - the total electric field ($E = E_0 + E_{sc}$, where E_{sc} is a space-charge field and E_0 is an external field), I - the light intensity, γ_e and γ_h - electron and hole recombination constants, μ_e - electron and μ_h - hole mobilities along the quantum wells, ε_0 - the vacuum permittivity, ε - the effective dielectric constant of MQW structure, e - the elementary charge value, k_B - the Boltzmann constant and T - the absolute temperature.

Time evolution of the space charge electric field in MQW structure is described in our former paper [2]. The final value of the field is independent on light intensity and growing time of the grating is inversely proportional to the intensity. For example continuos external waves with intensity of 0.1 W/cm^2 need about 0.2 µs to create 90% of the final space charge field. The grating life-time after switching off the external illumination depends mainly on the material dark conductivity and in the absence of free carriers can be very long.

3. Steady state grating
Under the steady state conditions electric field can be presented as a sum of harmonic elements

$$E(z) = E_0 + mE_1 \exp(iKz) + m^2 E_2 \exp(2iKz) + \dots$$

where $E_1 = (A - iB)/(C + iD)$

$A = E_D(E_{Mh} - E_{Me})$, $\quad B = E_0(E_{Mh} + E_{Me})$,

$C = E_0/E_q(E_{Mh} - E_{Me})$,

$D = [E_D^2 + E_0^2 + E_D(E_{Mh} + E_{Me})$

$+ E_q(E_{Mh} + E_{Me} + E_D)]/E_q$,

$E_{Me} = \gamma N/(4\mu_e K)$, $\quad E_{Mh} = \gamma N/(4\mu_h K)$,

$E_q = eN/(2K\varepsilon)$, $\quad E_D = (k_B T/e)K$, $\quad \gamma_e = \gamma_h = \gamma$.

The amplitude of the first order element have real and imaginary part describing an arbitrary phase shift between the space charge field and the intensity pattern. The dependence of the real part of space charge field amplitude on the grating space period, $\Lambda = 2\pi/K$, for different trap concentrations is presented in Fig.2. Higher order terms as well as phase shifted part of the field can be neglected [2]. The refractive index changes are given by $\Delta n(E) = (-1/2) n_0^3 s E^2$, where s is a quadratic electrooptic coefficient [4] and E the total electric field.
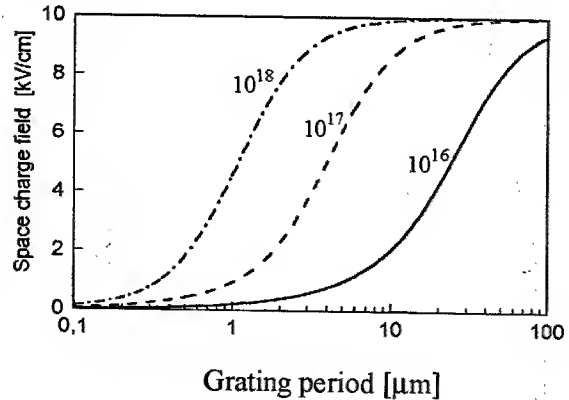
Figure 2 Amplitude of the first order space-charge field in the steady state in dependence on the grating period Λ for applied electric field intensity $E_0 = 10$ kV/cm and trap densities: $N_D = 10^{16}$ cm^{-3}, 10^{17} cm^{-3} and 10^{18} cm^{-3}.

Gratings with different space periods can be used for different purposes like frequency selective reflection, deflection or out-coupling of modes guided in the structure.

4. Example
A waveguide with photorefractive layer consisting of 7.5 nm GaAs wells and 10 nm Al$_{0.3}$Ga$_{0.7}$As barriers was considered as an

example. Wavelengths of external waves writing the grating (λ_{ex}=630nm) and guided modes reading it (λ_g=845nm) were chosen on the basis of the spectral dependence of the absorption and electro-refraction [2] presented in Fig.3.
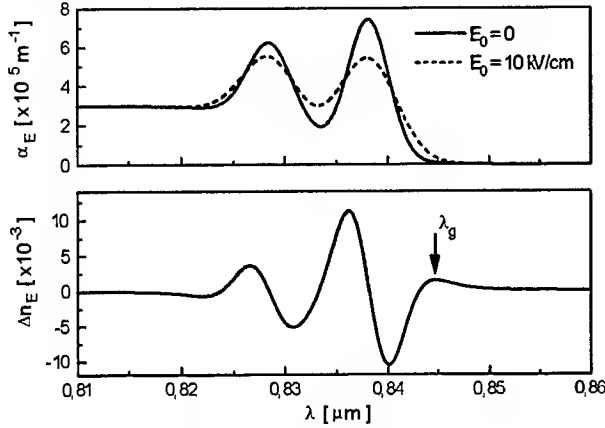
Figure 3. Spectral dependence of absorption and electro-refraction.

Absorption curves consist from Gaussian peaks for light hole and heavy hole absorption and continuum contribution from absorption to free electron-hole pairs (parameters taken from [6]). The refractive index change due to the electric field, $\Delta n_E(\lambda)$, was calculated using Kramers-Krönig relations. The obtained value of the quadratic electrooptic coefficient, s, for λ_g = 845 nm is in the range of 7×10^{-13} cm^2/V^2.

The grating constant, necessary to obtain reflection preserving polarisation type of the mode (TE or TM) is given by

$$K = 2\beta \cos\phi,$$

where β is a propagation constant and ϕ is the incidence angle of the guided mode at the periodic structure. The dependence of the refractive index grating amplitude on the external electric field E_0 for the grating space period necessary for backward reflection (Λ = 123 nm) and for reflection at 60 deg angle (Λ = 245 nm) is presented in Fig.4

5. Conclusions

The results of calculations show, that a photorefractive grating in semi-insulating MQW single mode waveguide can be used as an optically controlled mode coupler with memory. The wavelength of coupled signals

depends on the grating constant and can be varied during the work of the device. The grating does not require a permanent presence of the external waves. Pump pulses are necessary only for writing, refreshing or erasing of the grating. Because signal waves with low frequency do not destroy the grating the system may have an application as all-optical switching element with memory.
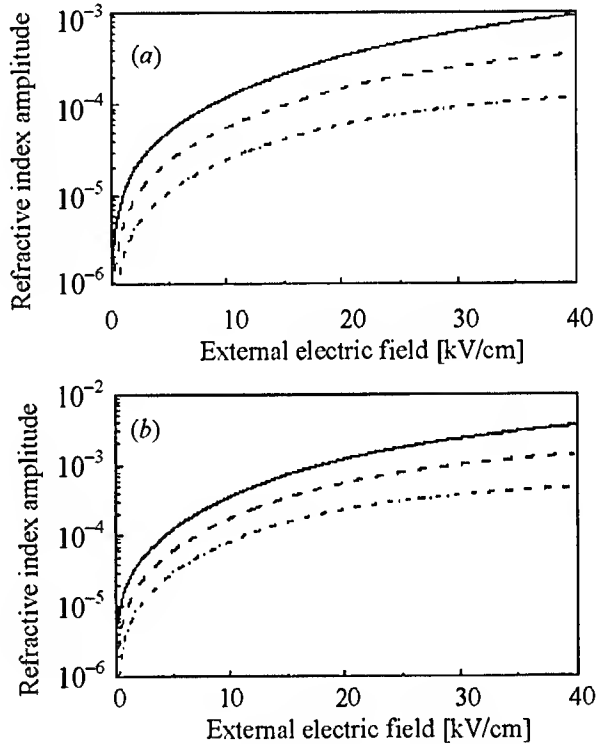
Figure 4. Refractive index changes amplitude in the steady state in dependence on the applied electric field intensity E_0 for different values of N_D: $0,5 \cdot 10^{18}$ cm^{-1}, $1 \cdot 10^{18}$ cm^{-1}, $2 \cdot 10^{18}$ cm^{-1}. Grating constants are Λ=123 nm (a) and Λ=246 nm (b).

REFERENCES

[1] E. Weinert - Rączka, *J. Opt. Soc.* Am. **B11**, 2340 (1994).

[2] E.Weinert-Rączka and R.Iwanow, *Acta Physica Polonica A*, **99**, 175 (2001).

[3] L. F. Magaña, F. Agulló-López, M. Carrascosa, *J. Opt. Soc. Am.* **B 11**, 1651 (1994).

[4] A.M.Glass, D.D.Nolte, H.D.Olson, G.E.Doran, D.S.Chemla, W.H.Knox, *Opt.Lett.*15, 264 (1990).

[5] M. Aguilar, M. Carrascosa and F. Agulló-López, *J. Opt. Soc. Am.* **B 13**, 2630 (1996).

[6] Q. Wang, R. M. Brubaker, D. D. Nolte and M. R. Melloch, *J. Opt. Soc. Am.* **B 9**, 1626 (1992).

Nils Haverkamp, Jorn Stenger, Harald Schnatz, Christian Tamm and Harald R. Telle
Physikalisch-Technische Bundesanstalt, Bundesallee 100, 38116 Braunschweig, Germany
phone: +49-531-592-4425, fax: +49-531-4423, email: nils.haverkamp@ptb.de
(April 22, 2002)

Stimulated by the development of optical frequency comb generators based on Kerr-lens modelocked femtosecond lasers [1,2], the absolute frequencies of several narrow transition lines in cold atoms or single stored ions, such as H, Ca, Yb$^+$ were recently measured by phase-coherently linking optical signals to a cesium-clock controlled hydrogen maser [3–6]. This phase-coherent link is established via a frequency-comb generated by a femtosecond laser. In the frequency domain the femtosecond laser's pulse train corresponds to a comb spectrum. This comb is spectrally broadened to extend over the whole visible wavelength region and into the near infrared. In our experiment this was achieved in a micro-structure/photonic crystal fiber from Lucent Technologies. This fiber has core diameter of 1.7 μm and its GVD ist zero at 780 nm [7], which is the center wavelength of the spectrum emitted by our Ti:Sa-laser similar to that described in ref. [8]. Its spectrum of some 170 nm width around 780 nm is broadened to extend from 500 nm to about 1100 nm, by passing approximately 30 mW through a 10 cm piece of the micro-structure fiber. During the propagation in the fiber, the comb nature of the spectrum is not altered, only its spectral width is extended. The result is an evenly spaced comb spectrum over almost the whole visible wavelength range and into the near infrared, where the individual comb mode m_i has the frequency $\nu_i = m_i \times f_{rep} + \nu_{ceo}$. The last term, the so called carrier envelope offset frequency is due to different group and phase velocity delay in the laser cavity. It results in a collective shift of all comb modes with respect to the frequency origin. Any external optical frequency ν_i is measured by detecting a beat note Δ_i with a suitable comb mode with the order number m_i:

$$\nu_i(t) = \nu_{ceo}(t) + m_i \times f_{rep}(t) + \Delta_i(t). \tag{1}$$

Absolute frequency measurements therefore necessitate determination of three radio frequencies and the knowledge of the order number m_i of the comb mode the signal to be measured beats with. However, a frequency comb can also be used to phase-coherently link two optical frequencies, i.e. measure optical frequency ratios rather than absolute frequencies. A schematic of the setup is shown in fig. 1. Three frequencies are measured: Δ_1, Δ_2, and ν_{ceo}, thus

$$\nu_1(t) = \nu_{ceo}(t) + m_1 \times f_{rep}(t) + \Delta_1(t) \tag{2}$$

$$\nu_2(t) = \nu_{ceo}(t) + m_2 \times f_{rep}(t) + \Delta_2(t) \tag{3}$$
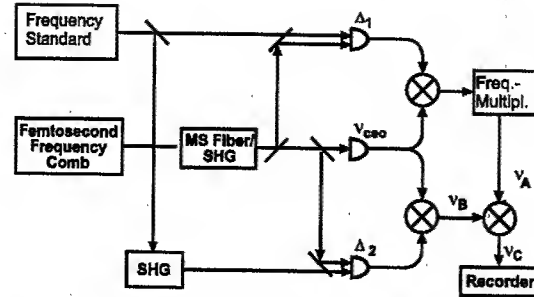
FIG. 1. Linking two optical frequencies with a femtosecond frequency comb: real-time signal processing scheme.

Two mixers remove the detected carrier envelope offset frequency in real time. Therefore the frequency-ratio between the signals from these mixers, reflects the ratio of the order numbers of the comb modes the two standards were beaten against, plus a residual arising from different Δ_i's.

In our experiment a special choice of frequencies was used to test the limits of the comb generator: Two frequencies differing exactly by a factor of two where chosen, so all deviations from this known factor recorded during the measurement can be attributed to the measurement device. Such a set of frequencies is the fundamental of Nd:YAG (1064 nm) and its second harmonic (532 nm), which is generated from the same laser by frequency doubling in a nonlinear crystal. Both frequencies lie within the span of the comb, after it was broadened in the photonic crystal fiber.

An analysis of the difference signal $\nu_C = \nu_A - \nu_B$ generated in a last mixer before the recorder gives the following result:

$$\frac{\nu_{SH}}{\nu_0} = 2.000\,000\,000\,000\,000\,001 \times (1 \pm 7 \times 10^{-19}).$$

The Allan standard deviation, showing how the instability of the measurement decreases with averaging time, is shown in fig.2. (Additionally it includes the data of a measurement of the ratio of the subharmonic of the output of a single-ytterbium-ion frequency standard [9]. Here the observed instabilities are much greater, because unlike in the experiment described above, the frequency noise of both independent standards enter the measurement.)
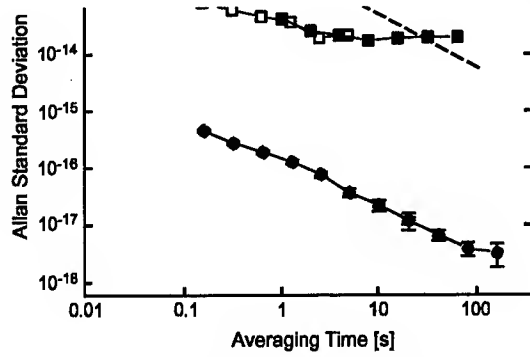
FIG. 2. Measured Allan standard deviation of two frequency-ratio measurements using the Yb$^+$ and Nd:YAG reference frequencies (squares) and the second harmonic and fundamental of a Nd:YAG laser (circles). The frequency instability of a typical microwave reference (hydrogen maser) is included for comparison (dashed line).

The observed deviation from the exact value of 2 can be considered as an upper limit of the uncertainty of the measurement principle, since technical noise contributions, for example fluctuating path length differences of the optical signals, could possibly be suppressed.
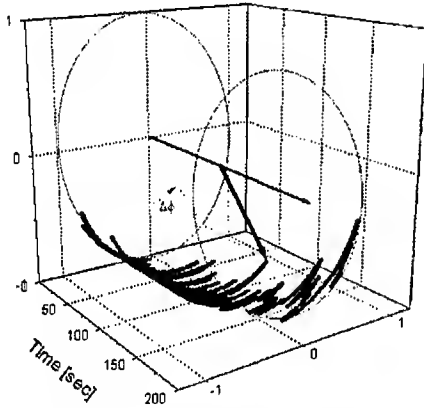
FIG. 3. Phase deviation $\Delta\Phi$ of the recorded signal as function of time

A typical phase record derived from the signal ν_C is shown in fig.3. It shows phase deviations between ν_A and ν_B as an angle in a polar plot, while the third axis is used to show its evolution in time. The phase slope of roughly 1 rad per second corresponds to a frequency shift as low as 170 mHz at 563 212 670 MHz.

In conclusion, we have demonstrated, that a spectrally broadened comb behind a micro-structure fiber can be used to measure frequency ratios with an accuracy of 10^{-18} within 100 sec. This may be of interest in future experiments searching for drifts of the finestructure constant α, where two different frequency standards with different scaling in α will have to be compared.

[1] T. Udem, J. Reichert, R. Holzwarth, and T. W. Hänsch, Opt. Lett. **24**, 881 (1999).
[2] S. A. Diddams, D. J. Jones, J. Ye, S. T. Cundiff, J. L. Hall, J. K. Ranka, R. S. Windeler, R. Holtzwarth, T. Udem, and T. W. Hänsch; Phys. Rev. Lett. **84**, 5102 (2000).
[3] M. Niering, R. Holzwarth, J. Reichert, P. Pokasov, Th. Udem, M. Weitz, T. W. Hänsch, P. Lemonde, G. Santarelli, M. Abgrall, P. Laurant, C. Salomon, and A. Clairon; Phys. Rev. Lett. **84**, 5496 (2000).
[4] J. Stenger, T. Binnewies, G. Wilpers, F. Riehle, H. R. Telle, J. K. Ranka, R. S. Windeler, A. J. Stentz; Phys. Rev. A. **63**, 021802(R) (2001).
[5] T. Udem, S. A. Diddams, K. R. Vogel, C. W. Oates, E. A. Curtis, W. D. Lee, W. M. Itano, R. E. Drullinger, J. C. Bergquist, and L. Hollberg; Phys. Rev. Lett. **86**, 4996 (2001).
[6] J. Stenger, Chr. Tamm, N. Haverkamp, S. Weyers, and H. R. Telle; Opt. Lett. **26**, 1589 (2001).
   S. A. Diddams, Th. Udem, J. C. Bergquist, E. A. Curtis, R. E. Drullinger, L. Hollberg, W. M. Itano, W. D. Lee, C. W. Oates, K. R. Vogel, and D. J. Wineland; Science **293**, 825 (2001).
[7] J. K. Ranka, R. S. Windeler, and A. J. Stentz; Opt. Lett. **25**, 25 (2000).
[8] D. H. Sutter, G. Steinmeyer, L. Gallmann, N. Matuschek, F. Morier-Genoud, U. Keller, V. Scheuer, G. Angelow, and T. Tschudi; Opt. Lett. **24**, 631 (1999).
[9] Chr. Tamm, D. Engelke, V. Bühner; Phys. Rev. **A61**, 053405 (2000).

Nonlinear interactions in slow-wave structures

A. Melloni and M. Martinelli
DEI, Politecnico di Milano, via Ponzio 34/5, Milano 20133, Italy
melloni, martinelli @elet.polimi.it

F. Morichetti and S. M. Pietralunga
CoreCom, via Ampere 30, Milano 20131, Italy
morichetti, pietralunga @corecom.it

Abstract: Nonlinear interactions in coupled resonator slow-wave structures are investigated. Kerr based phase modulation and wavelength conversion by four-wave-mixing result strongly enhanced thanks to both the increase of the intra-cavity mean power and the interaction time between propagating fields.
©2002 Optical Society of America

OCIS codes: (230.7370) Waveguides, (230.5750) Resonators, (050.2230) Fabry Perot, (130.3120) Integrated optics Devices, (070.4340) Nonlinear optical signal processing.

Generally the efficiency of nonlinear processes in typical nonlinear materials is extremely low. In order to obtain appreciable performances in passive nonlinear optical components, long devices (hundreds of metres for silica fiber or several centimetres for semiconductors) or high pump powers (several watts) are often needed. It is also known that nonlinear interactions, such as Kerr-induced phase shift [1] and frequency mixing [2], are greatly enhanced inside an optical cavity. However, the price to be paid is bandwidth reduction whenever a single resonator is used; therefore, such resonating devices may not efficiently operate on optical communication signals, typically modulated up to several Gbit/s rates. On the contrary multiresonator structures, already known as filtering and dispersion compensating devices [3,4], do not suffer from this band-gain trade-off and recently some applications have been proposed, such as tunable delay lines [5] and slow-wave electro-optic phase modulators [6].

In this work we investigate the main nonlinear properties of Slow-Wave Structures (SWS) based on passive coupled optical resonators. We show as the efficiency of nonlinear phenomena may be substantially increased by slow-wave propagation, leading to wide-band, low power devices for all-optical processing, such as switching, routing and wavelength conversion.

Optical slow-wave structures may be realized in different ways (Fig.1), for example by cascading partially reflecting mirrors inside an optical waveguide, by directly cascading a sequence of microring resonators or by introducing proper defects in a photonic bandgap waveguide. All these structures possess a periodic passband-stopband spectral response and support waves with group velocity much lower than phase velocity. Input-output impedance matching sections, consisting of resonators at suitably lower finesse, are required to avoid detrimental ripples within the passband [3].
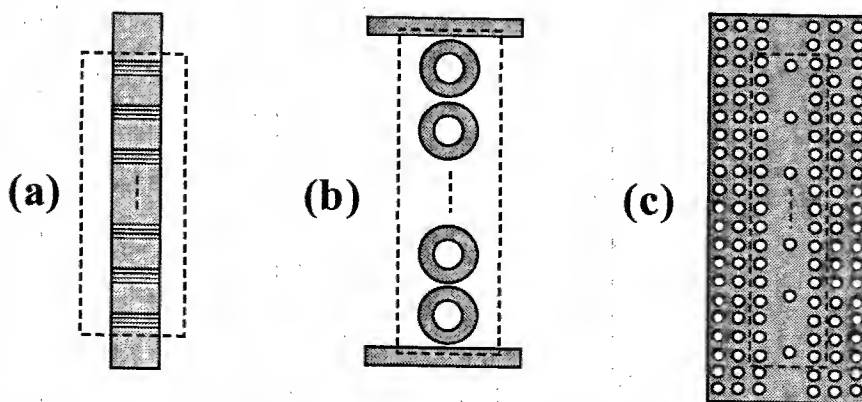
Fig. 1. Some examples of direct-coupled optical resonator SWS: direct coupled Fabry-Perot SWS (a), direct coupled microring SWS (b) and photonic band gap SWS (c).

If a sufficiently large number of equal resonators are cascaded, an optical pulse propagates through the SWS as in a periodic system. From the Floquet-Bloch theory we derived the width of each frequency bandpass of the periodic structure

$$B = \frac{2FSR}{\pi} \sin^{-1}(t),$$ (1)

where the *Free Spectral Range*, FSR= $c/2n_0 d$, is the distance between two consecutive resonant modes, n_0 is the group waveguide linear effective index, $2d$ is the round trip of each resonator and t is the wavelength independent field coupling ratio between two consecutive resonators. An optical pulse well propagates through the structure only if its spectrum lies inside one of these frequency bands, otherwise it is strongly backward reflected. High spectral selectivity, required by modern WDM optical filters, is reachable by cascading only few coupled resonators [3].

Inside each bandpass the group velocity v_{sw} is substantially reduced with respect to the group velocity $v_g = c/n_0$ in an unloaded waveguide. The slowing ratio $S = v_g/v_{sw}$ is defined as

$$S = \frac{v_g}{v_{sw}} = \frac{\cos(kd)}{\sqrt{t^2 - \sin^2(kd)}},$$ (2)

where $k = \omega n_0/c$ is the wavevector in the absence of resonating structure . The group velocity assumes its maximum value $v_{sw} = c/n_0 \, t$ exactly at resonances, where the group velocity dispersion (GVD), mainly due to β_3, is minimum. Moving towards the band edges v_{sw} ideally drops to zero, while GVD increases due to β_2. An optical pulse is differently delayed when either the coupling ratio t or the detuning from resonance are varied, thus adjustable delay lines based on SWS may be realized [5]. Moreover, thanks to the group velocity dependence on detuning, SWS may also be employed in dispersion compensating devices.

As a consequence of multiple round trips, the effective phase shift ϕ_{eff} experienced by a propagating wave is increased from the single-pass phase shift ϕ by a factor $d\phi_{eff}/d\phi = S$. Therefore, the efficiency of (electro)optic phase modulators may be strongly increased, since the same phase shift results from a lower index modulation. If such index modulation is induced by optical nonlinearities, the effective phase shift is further increased by the intra-cavity enhancement of the mean power P_m with respect to the input value P_o by a factor $dP_m/dP_o = S$. Therefore a gain factor proportional to S^2 is expected for both self-phase modulation (SPM) and cross-phase modulation (XPM) inside a SWS.

When the input signal is tuned at the lower frequency side of the bandpass (anomalous dispersion), if SPM exactly balances the negative β_2, an input pulse having the shape of the fundamental soliton may propagate undistorted. Fig. 2 shows two examples of pulse propagation obtained by using a time-domain numerical simulator we developed in order to accurately analyse linear and nonlinear pulse propagation in SWS. Because of the combined effects of second and third order dispersion, a weak gaussian pulse (Fig. 2a) detuned from resonance of $-B/4$ is strongly corrupted after few tenth of resonators, even though no reflected power is observed at the front end. On the contrary, a solitary wave may propagate undistorted along a large number of resonator of the same SWS, in spite of the presence of a residual β_3.
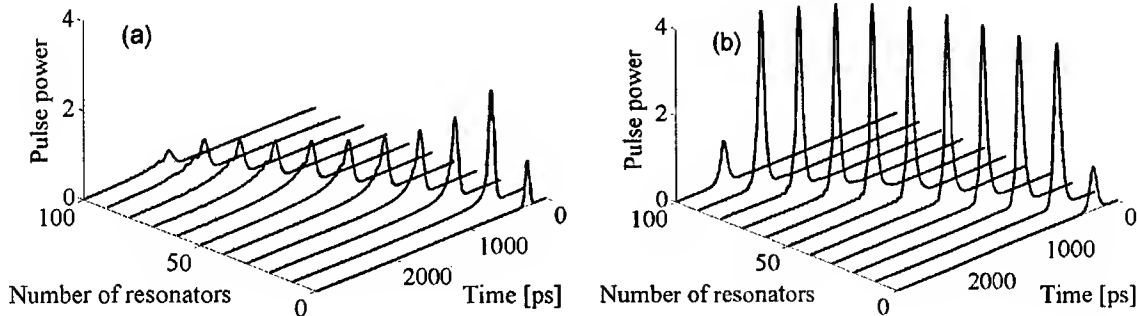
Fig.2. Propagation of a weak gaussian optical pulse (a) and a solitary wave (b) through the same SWS when the detuning from resonance is –B/4 (anomalous regime). Pulse power is normalised to input power.

When a strong pump and a weak signal are tuned at two different resonances, the frequency generation of an idler wave by four-wave-mixing (FWM) is observed at a third SWS resonance. The converted power depends on the

pump power P_p, the signal power P_s and on the nonlinear constant $\gamma = \omega n_2 / cA_{eff}$, n_2 being the nonlinear refractive index and A_{eff} the waveguide effective area. Thanks to the above discussed enhancement of both the interaction time and the intra-cavity mean power, the converted power $P_{c,sw}$ for wavelength conversion in SWS is given by

$$P_{c,sw} = \gamma^2 P_p^2 P_s z^2 sinc^2\left(\frac{\Delta\beta\,z}{2}\right)\frac{S^4}{4}, \tag{3}$$

where $\Delta\beta = \Delta k/S$ is the intra-cavity phase mismatch and $\Delta k = 2k_p - k_s - k_c$ takes into account the phase mismatch between interacting fields. As a result, the conversion gain due to slow-wave propagation is proportional to S^4. Since the bandwidth decreases versus S, an accurate design of the device must be carried out in order to obtain a wide-band, high efficiency wavelength converter.

The maximum length of the device is limited by the phase mismatch $\Delta\beta$, which generally includes material dispersion, waveguide dispersion, SPM and XPM contributions. Since highly nonlinear materials are often highly dispersive, material dispersion generally dominates. Despite the maximum number of resonators is limited by $\Delta\beta$, converted power can be increased by cascading more than one nonlinear SWS interleaved by linear rephasing devices, in order to perform a *quasi-phase-matched* multistage structure. Fig. 3 shows the performances of a quasi-phase-matched SWS having B=20GHz, FSR=200GHz and operating a wavelength conversion over 4THz. The pump and signal powers are respectively 100mW and 10mW. A more than 26dB conversion gain ($S^4/4$) with respect to an unloaded waveguide of the same physical length is confirmed by numerical time-domain simulations. Dotted lines indicate the inversion of the power transfer from the converted wave to the pump wave in absence of rephasing at the end of the first stage. Rephasing elements are required every 11 resonators for AlGaAs and 237 resonators for SiO$_2$.

In conclusion, coupled resonator SWS offer a way to realize extremely efficient nonlinear devices without introducing severe bandwith penalties. The detrimental effects of dispersion on pulse propagation are overcome by soliton-like propagation supported by SWS. Gain factors proportional to higher-orders powers of the slowing ratio, are found for both Kerr-based modulation and FMW wavelength conversion inside SWS. Therefore SWS-based nonlinear devices are supposed to play a key role in future all-optical processing.
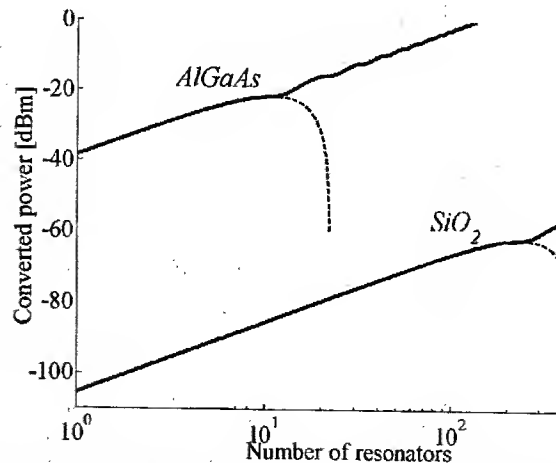
Fig.3. Performances of a quasi-phase-matched slow-wave wavelength converter (B=20GHz, FSR=200GHz) for two different nonlinear materials (AlGaAs and SiO$_2$). A 100mW pump power and 10mW signal power are used.

References

[1] J.E.Heebner and R.W. Boyd, "Enhanced all-optical switching by use of a nonlinear fiber ring resonator", Opt. Lett. **12**, 847-849 (1999).

[2] P.P.Absil, J.H.Hryniewicz, B.E. Little, P.S.Cho, R.A.Wilson, L.G.Joneckis and P.-T. Ho, "Wavelength conversion in GaAs micro-ring resonators", Opt. Lett. **25**, 554-556 (2000).

[3] A. Melloni and M.Martinelli, "Synthesis of direct-coupled resonators bandpass filters for WDM systems", IEEE J. Lightwave Technol. **20**, 296-303 (2002).

[4] G. Lenz, B. J. Eggleton, C. K. Madsen and R. E. Slusher, "Optical delay lines based on optical filters", IEEE J. Quantum Electron. **37**, 525-532 (2001).

[5] Y. Xu, A. Yariv, G. Gunn, R.K. Lee and A. Scherer, "Tunable group velocity reduction in coupled-resonator optical waveguide", Quantum Electronics and Laser Science Conference (QELS) 2000, Technical Digest , 93 -94.

[6] N. Shaw, W. J. Stewart, J. Heaton and D. R. Wight, "Optical slow-wave resonant modulation in electro-optic GaAs/AlGaAs modulators", Electron. Lett. **35**, 1557-1558 (1999).

Peakons - a novel type of robust pulses in photonic crystals

U.Peschel and F.Lederer

Friedrich-Schiller-Universität Jena, Max-Wien-Platz 1, 07743 Jena
phone: +(49) 3641 947176, fax: +(49) 3641 94717, e-mail: p6peul@rz.uni-jena.de

B.A.Malomed

Tel Aviv University, Tel Aviv 69978, Israel

Abstract: We demonstrate that near resonances, e.g. around the band gaps of Bragg gratings, non-solitonic pulses can propagate undistorted. These so-called peakons are stabilized by nonlinearly induced self-phase modulation, which shifts their frequency out of resonance.

Integrability has largely determined our understanding of field evolution under the influence of nonlinearity. Every excitation of an integrable system finally decomposes into a number of solitons and into quasi-linear radiation. Unfortunately, integrability is a rare exception. However, it is common belief that also in non-integrable systems solitary waves mark the only fixed-points of an often-complicated field dynamics. Here we demonstrate that there is a third way for an initial excitation to evolve towards a stable object being neither a stationary solitary wave nor linear radiation.

The basic prerequisite for our considerations is a conservative system with the following properties. First, dispersive broadening is due to the action of single resonances, which are well localized in frequency space. Strictly speaking, this is the more general case, because dispersion always originates from resonances. Secondly, we assume a nondispersive nonlinearity. It might also be generated by remote resonances, but not by those, which are the origin of the group velocity dispersion. These requirements are met in many optical systems. Here we restrict ourselves to an one-dimensional photonic crystal (Bragg grating), where resonant back-reflection occurs for frequencies in the band-gap. The nonlinearity is represented in its simplest form as a Kerr-like one. The scaled evolution equations for the forward u_+ and backward u_- propagating field envelopes read as [1]

$$i\left(\frac{\partial}{\partial t} \pm \frac{\partial}{\partial x}\right)u_\pm + \left(\left|u_\pm\right|^2 + 2\left|u_\mp\right|^2\right)u_\pm + u_\mp = 0.\qquad(1)$$

The system (1) is known to be not integrable. However, there is a close relative – the massive Thirring model – where integrability is ensured by vanishing self-phase modulation.

It is easy to show that linear wave propagation is prohibited in Eq.(1) for the so-called gap $\left|\omega\right| < 1$. Despite of the lack of integrability stationary bright solitary waves of Eq.(1) are analytically known as so-called gap- or Bragg-solitons [1]. They have two independent parameters, namely velocity v and frequency ω. Because bright solitons require evanescent tails to exist, the soliton parameters are bound within a circle $v^2 + \omega^2 < 1$. Consequently the energy of a solitary pulse is limited, in our case to a value below π. Also the width of a Bragg-soliton cannot be less than a critical value of ≈ 1.3. Hence, it is rather likely that an initial pulse does not fit to a soliton of this family, e.g., if it has a large amplitude or steep edges. We therefore launched a strong Gaussian-shaped pulse with energy of about π, a width of 0.2 and a carrier frequency just in the gap ($\omega=0$). The first result is the apparent stability of the field distribution (see Fig.1).

It moves almost with the velocity of the forward propagating wave and the amount of backward propagating field is negligible. But most important, it maintains its overall shape. Only around its peak signatures of decay are observed. It seems that high gradients as they appear on the wings of the pulse promote stability. We follow this concept and launch a triangularly shaped pulse, which we call peakon, (see Fig.2a) like

$$u_0(t) = A_{\text{peakon}}\left[1 - \left|\frac{t-t_0}{W_{\text{peakon}}}\right|\right] \text{ for } \left|t-t_0\right| < W_{\text{peakon}} \text{ and } u_0(t) = 0 \text{ otherwise.}\qquad(2)$$

Note that Eq.(1) only requires a finite first derivative, but not necessarily a continuous one.

Because a flat top is absent almost no decay is observed. The peak amplitude even oscillates around a final state (see Fig.2c) similar as stable solitary waves do. The outflow from the pulse rapidly decays to zero (see Fig.2d).

However, this pulse cannot be a solitary wave, because Bragg-solitons have completely different shapes [1]. Looking at the phase evolution we find that only the intensity is stationary, while the internal frequency d/dx $\varphi(x)$ grows linearly with distance (see Fig.2b). This is the key point to understand, why these pulses are so robust. Due to the action of self phase modulation every intensity gradient within the pulse causes a frequency shift. Consequently the pulse is shifted out of resonance and the coupling to the backward propagating field is diminished. Hence, the stabilization of the pulse is obtained in a completely different way. Whereas in conventional systems the nonlinearity balances the dispersion here it allows the pulse to escapes from the linear back-reflection regime of the grating, while shifting its internal frequency. Outside the resonance the group velocity dispersion vanishes and no spreading can occur. Therefore the frequency within the pulse keeps on growing, while its shape remains stationary. Provided that internal gradients are large enough, every pulse shape can be stabilized in this way. The internal frequency of the pulse increases linearly with the propagation distance, therefore providing a kind of internal clock.

However, the coupling to the backward propagating wave permanently sustains. This is important, because all the light, which is transferred to the backward direction, is lost. Even if these losses are weak they can finally destroy
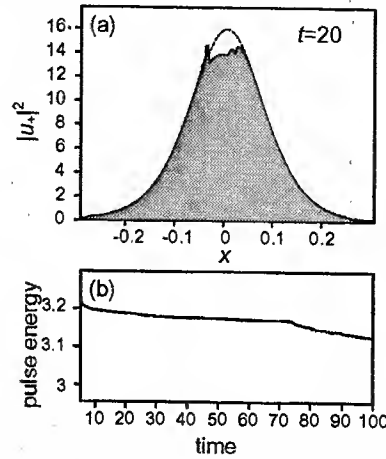
Fig.1 Evolution of a short and intense Gaussian pulse, a) field profile at $t=20$ (dashed line: input profile), b) evolution of the pulse energy during propagation

the pulse. Therefore we are going to estimate the strength of the backward radiation. In the lowest order approximation the forward propagating pulse is almost only influenced by self-phase modulation. It results in a stationary field shape, but in a varying phase as

$$u_+(x,t) \cong u_0(t-x)\exp\left[\frac{i}{2}|u_0(t-x)|^2(x+t)\right],\tag{3}$$

where $u_0(t)$ is the field incident at $x=0$. Inserting Eq.(3) into the evolution for the backward propagating field yields

$$u_-(x,t) = \frac{i}{2}\int_{-\infty}^{t-x}d\eta\, u_0(\eta)\exp\left[\frac{i}{2}|u_0(\eta)|^2(x+t) - i\int_{-\infty}^{\eta}d\eta'\,|u_0(\eta')|^2\right]\exp\left[i\int_{-\infty}^{t-x}d\eta\,|u_0(\eta)|^2\right].\tag{4}$$

The total loss of the pulse is given by

$$Q(t) = \lim_{x\to-\infty}|u_-(x,t-x)|^2\tag{5}$$

Approximate solutions show that the outflow from a peakon, as it is defined in Eq.(2), behaves like

$$Q_{\text{peakon}}(t) \approx \frac{A^2_{\text{peakon}}W^2_{\text{peakon}}}{2}\text{sinc}^2\left[\frac{A^2_{\text{peakon}}}{2}(t-t_0)\right].\tag{6}$$

Hence it oscillates and decays like $1/t^2$, a fact that is well reproduced by numerical simulations (see Fig.2d). Integrating Eq.(6) yields a finite value, which defines a critical energy E_{crit}. Depending on its width the energy of the peakon should by far exceed a value of

$$E_{crit} = \frac{\pi}{2} W_{peakon}^2 \cdot \qquad (7)$$

Peakons with energies much higher than that critical value will leave the resonance and will propagate forever. Note that according to Eq.(7) there is no lower threshold for the excitation of a peakon. In fact the peakon reproduced in Fig.2 has a total energy of 0.27, which is well within the energy domain of Bragg solitons. This is because its stabilization is based on its shape rather than on its total power. Hence also weak pulses can propagate undistorted, provided that they are short enough.
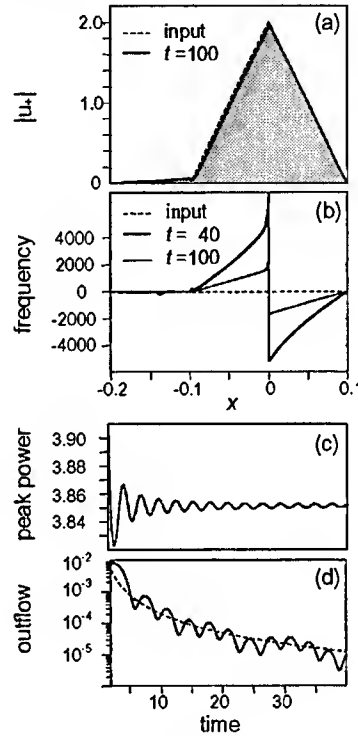
Fig.2 Evolution of a peakon during propagation through a Bragg-grating, a) amplitude distribution at t=100 (dashed line: input profiel), b) distribution of the local frequency d/dx $\varphi(x)$ for different times ($\varphi(x)$: phase of the forward propagating wave), c) Evolution of the peak power during propagation, d) evolution of the outflow from the pulse in a logarithmic plot

Arbitrary initial excitations can therefore decay into Bragg-solitons, linear radiation and some steep field distributions similar to the peakons. The higher the initial gradients the more energy is converted into these "peakon-like" structures. Even if the field distribution is flat as on the top of a smooth pulse the field tries to adapt to a peakon-like shape, while increasing local gradients (see Fig.1). This scenario should change for an integrable system. In fact if self-phase modulation vanishes and we approach the integrable massive Thirring model the peakon disappears. However, this is by far a surprise, because the stabilization of the peakon entirely relies on self-phase modulation. Because the backward propagating wave is orders of magnitude weaker, cross-phase modulation cannot induce the required frequency shift. This gives us a quite intuitive explanation, why only the massive Thirring model is integrable.

Up to now we have only studied pulses, which were launched with a frequency inside the band gap. They immediately leave the resonance due to the nonlinearly induced frequency shift. However, the local frequency shift growths monotonously, even if the pulse is launched outside the resonance. In this case a certain part of the pulse will always cross the resonance, while causing an outburst of radiation. Hence, while choosing a respective center frequency of the initial pulse, we can control outbursts of radiation within the sample.

In conclusion we have shown that field distributions with high gradients can pass nonlinear 1D photonic crystals almost undistorted. This result should apply to other physical systems with sharp resonances as well.

[1] A.B.Aceves and S.Wabnitz "Self-induced transparency solitons in nonlinear refractive periodic media," Physics Letters A **141**, 37 (1989)

Canonical Hamiltonian formulation of nonlinear pulse propagation in 3D photonic bandgap structures

Suresh Pereira, Philip Chak and J. E. Sipe
University of Toronto, Toronto, ON, M5S 1A7, Canada
phone: 416-978-5444; fax: 416-978-2537
email: pereira@physics.utoronto.ca

We present a canonical Hamiltonian formulation of Maxwell's equations in the presence of a nonlinear polarization. We then use this formulation to derive pulse propagation equations in a three-dimensional photonic bandgap (PBG) material with a Kerr nonlinearity. We start by writing a Hamiltonian that is equal to the energy in the electromagnetic field[1]

$$H = \frac{1}{2\mu_0} \int B^i(\mathbf{r},t) B^i(\mathbf{r},t) d\mathbf{r} + \frac{1}{2\varepsilon_0} \int D^i(\mathbf{r},t) D^i(\mathbf{r},t) d\mathbf{r}$$

$$- \frac{1}{2\varepsilon_0} \int D^i(\mathbf{r},t) \Gamma_1^{ij}(\mathbf{r}) D^j(\mathbf{r},t) d\mathbf{r} - \frac{1}{3\varepsilon_0} \int D^i(\mathbf{r},t) \Gamma_2^{ijm}(\mathbf{r}) D^j(\mathbf{r},t) D^m(\mathbf{r},t) d\mathbf{r} \quad (1)$$

$$- \frac{1}{4\varepsilon_0} \int D^i(\mathbf{r},t) \Gamma_3^{ijmn}(\mathbf{r}) D^j(\mathbf{r},t) D^m(\mathbf{r},t) D^n(\mathbf{r},t) d\mathbf{r}$$

where $\mathbf{r}=(x,y,z)$, B^i and D^i are the components of the $\mathbf{B}$ and $\mathbf{D}$ fields respectively, and repeated indices are summed over; we have ignored magnetic effects in (1). The Γ's are defined *via* $D(\mathbf{r},t) = \varepsilon_0 E(\mathbf{r},t) + P(\mathbf{r},t)$, where the full polarization is given by[1]

$$P^i(\mathbf{r},t) = \Gamma_1^{ij}(\mathbf{r}) D^j(\mathbf{r},t) + \Gamma_2^{ijm}(\mathbf{r}) D^j(\mathbf{r},t) D^m(\mathbf{r},t) + \Gamma_3^{ijmn}(\mathbf{r}) D^j(\mathbf{r},t) D^m(\mathbf{r},t) D^n(\mathbf{r},t) + ... (2)$$

with $\Gamma_n^{ij\cdots}$ characterizing the nth order nonlinear effects. Usually the constitutive relationship gives $\mathbf{P}$ terms of the electric field, $\mathbf{E}$, but for a canonical formulation in the presence of nonlinearity, (2) is more advantageous. By allowing the Γ's to depend on position we allow for an inhomogeneous dielectric, but the response is taken to be local in both space and time, which implies that any frequencies of interest are well below any resonant frequencies of the medium[2]. In this limit the Γ's are invariant under a permutation of their Cartesian components. We recover the field dynamics with the equal-time commutation relations

$$\left[D^i(\mathbf{r},t), D^j(\mathbf{r}',t) \right] = \left[B^i(\mathbf{r},t), B^j(\mathbf{r}',t) \right] = 0,$$

$$\left[D^i(\mathbf{r},t), B^j(\mathbf{r}',t) \right] = i\hbar \in^{ilj} \frac{\partial}{\partial r'^l} (\delta(\mathbf{r}-\mathbf{r}')), \quad (3)$$

and the Heisenberg equations of motion,

$$i\hbar \frac{\partial D}{\partial t} = [D, H]; \quad i\hbar \frac{\partial B}{\partial t} = [B, H]. \quad (4)$$

We now specialize this formulation to consider a medium in which both the linear index of refraction and the nonlinear susceptibility are periodic: $n(\mathbf{r})=n(\mathbf{r}+\mathbf{R})$ and $\chi^{(3)}(\mathbf{r})=\chi^{(3)}(\mathbf{r}+\mathbf{R})$, for any lattice vector $\mathbf{R}$. We adopt periodic boundary conditions, characterized by a volume V, and solve the nonlinear problem in terms of the Bloch solutions to the linear problem[3], characterized by a band index, m, and a reduced wave vector, $\mathbf{k}$. We expand a general $\mathbf{B}$ or $\mathbf{D}$ field as

$$\mathbf{D}(\mathbf{r},t) = \sum_{m\mathbf{k}} a_{m\mathbf{k}}(t)\mathbf{D}_{m\mathbf{k}}(\mathbf{r}) + a^{\dagger}_{m\mathbf{k}}(t)\mathbf{D}^{*}_{m\mathbf{k}}(\mathbf{r}),$$

$$\mathbf{B}(\mathbf{r},t) = \sum_{m\mathbf{k}} a_{m\mathbf{k}}(t)\mathbf{B}_{m\mathbf{k}}(\mathbf{r}) + a^{\dagger}_{m\mathbf{k}}(t)\mathbf{B}^{*}_{m\mathbf{k}}(\mathbf{r}),$$

(5)

where $\mathbf{B}_{m\mathbf{k}}$ and $\mathbf{D}_{m\mathbf{k}}$ are the Bloch functions of the medium, and where the $a_{m\mathbf{k}}(t)$ are mode amplitudes. The Bloch functions are normalized such that

$$\int_V \mathbf{B}^{*}_{m\mathbf{k}}(\mathbf{r}) \cdot \mathbf{B}_{m\mathbf{k}'}(\mathbf{r}) = \frac{1}{2}\mu_0 \hbar \omega_{m\mathbf{k}} \delta_{mm'}\delta_{\mathbf{k}\mathbf{k}'},$$

$$\int_V \frac{\mathbf{D}^{*}_{m\mathbf{k}}(\mathbf{r}) \cdot \mathbf{D}_{m\mathbf{k}'}(\mathbf{r})}{n^2(\mathbf{r})} = \frac{1}{2}\varepsilon_0 \hbar \omega_{m\mathbf{k}} \delta_{mm'}\delta_{\mathbf{k}\mathbf{k}'},$$

(6)

where $\omega_{m\mathbf{k}}$ is the frequency associated a given $m,\mathbf{k}$. In principal a solution (5) can include all $m,\mathbf{k}$, but in pulse propagation experiments, values of $\mathbf{k}$ will typically be centred around a value $\bar{\mathbf{k}}$. We construct effective fields as Fourier superpositons of the mode amplitudes[4]

$$g_m(\mathbf{r},t) = \frac{1}{\sqrt{V}} \sum_{\mathbf{k}} a_{m\mathbf{k}}(t)e^{i(\mathbf{k}-\bar{\mathbf{k}})\cdot\mathbf{r}},$$

(7)

which, using (5) and (4), can be shown to have commutation relations

$$[g_m(\mathbf{r},t), g^{\dagger}_{m'}(\mathbf{r}',t)] = \delta_{mm'}\delta(\mathbf{r}-\mathbf{r}'),$$

(8)

where, strictly speaking, the Dirac delta-function holds only in the limit where $V\to\infty$.

We can now rewrite the the Hamiltonian (1) and the Heisenberg equations of motion (4) in terms of these g's, which would constitute an exact, canonical formulation of Maxwell's equations. To give an example of the usefulness of such a formulation, we consider the situation when the frequency content of a pulse contained entirely within one band ($\bar{m}$) of the system, is well away from a photonic band gap of the system, and is sufficiently narrowly concentrated about $\bar{\mathbf{k}}$ that it is reasonable to expand the frequencies in the pulse in a Taylor series, truncated after the 2nd derivative[5]. These approximations lead to an effective Hamiltonian[4]

$$H_{eff} = \hbar \int_V \left\{ \omega_{\bar{m}\mathbf{k}}|g_{\bar{m}}|^2 - \frac{\partial \omega_{\bar{m}\mathbf{k}}}{\partial k^i}\frac{\partial g_{\bar{m}}}{\partial r^i}g^{\dagger}_{\bar{m}} - \frac{1}{2}\frac{\partial^2 \omega_{\bar{m}\mathbf{k}}}{\partial k^i \partial k^j}\frac{\partial^2 g_{\bar{m}}}{\partial r^i \partial r^j}g^{\dagger}_{\bar{m}} \right\}d\mathbf{r}$$

$$-\frac{6\beta_0}{4\varepsilon_0}\int_V |g_{\bar{m}}|^2 d\mathbf{r} + \frac{12i}{4\varepsilon_0}\left\{ \bar{\beta}_0 \cdot \int_V (\nabla g_{\bar{m}})|g_{\bar{m}}|^2 g^{\dagger}_{\bar{m}} d\mathbf{r} - c.c. \right\},$$

(9)

where the nonlinear coefficients are

$$\beta_0 \equiv \int_{cell} \frac{d\mathbf{r}}{\Omega_{cell}} \Gamma_3^{j_1 j_2 j_3 j_4} d^{j_1}_{\bar{m}\mathbf{k}} d^{j_2}_{\bar{m}\mathbf{k}} d^{j_3}_{\bar{m}\mathbf{k}} d^{j_4}_{\bar{m}\mathbf{k}}; \quad \bar{\beta}_0^p \equiv \int_{cell} \frac{d\mathbf{r}}{\Omega_{cell}} \Gamma_3^{j_1 j_2 j_3 j_4} \left(\frac{\partial d^{j_1}_{\bar{m}\mathbf{k}}}{\partial k} \right)^p d^{j_2}_{\bar{m}\mathbf{k}} d^{j_3}_{\bar{m}\mathbf{k}} d^{j_4}_{\bar{m}\mathbf{k}},$$

(10)

where $d_{m\mathbf{k}}(\mathbf{r})$ is the portion of the Bloch function, $\mathbf{D}_{m\mathbf{k}}(\mathbf{r})$, that is periodic with the lattice[3], and where the derivatives with respect to $\mathbf{k}$ in (9) and (10) are evaluated at $\mathbf{k}=\bar{\mathbf{k}}$. We note that $\bar{\beta}_0$ is a vector quantity, while β_0 is a scalar. Using H_{eff} with the commutation relations (8), and the equations of motion $i\hbar \partial g_m/\partial t = [g_m, H_{eff}]$, we find

$$\frac{\partial g_{\bar{m}}}{\partial t} = -i\omega_{\bar{m}\mathbf{k}}g_{\bar{m}} - \frac{\partial \omega_{\bar{m}\mathbf{k}}}{\partial k^i}\frac{\partial g_{\bar{m}}}{\partial r^i} + \frac{i}{2}\frac{\partial^2 \omega_{\bar{m}\mathbf{k}}}{\partial k^i \partial k^j}\frac{\partial^2 g_{\bar{m}}}{\partial r^i \partial r^j} + \frac{12i}{4\hbar\varepsilon_0}|g_{\bar{m}}|^2\{\beta_0 - 2i\operatorname{Re}(\bar{\beta}_0)\cdot\nabla\}g_{\bar{m}}. \quad (11)$$

This is a nonlinear Schrödinger equation (NLSE) with a shock term added, which extends previously analyses of nonlinear pulse dynamics in 3D PBGs[5]. The form of this shock term is slightly different that the shock term often discussed in the literature[6], because we are working with effective fields that are Fourier superpositions of the mode amplitudes $a_{mk}(t)$. Were we to work with fields that were related directly to the Bloch functions of the medium, then those fields would give the familiar shock term; however, it is difficult to use such fields to construct a canonical formulation of Maxwell's equations[4]. In our formulation, the interpretation of the shock term is directly analogous to that of the familiar self phase modulation (SPM) term: The SPM term describes an intensity-dependent phase shift; the shock term describes an intensity-dependent shift in the local group velocity of the pulse. This shock term will prove useful in the analysis of structures such as coupled microresonators[7]. In these systems light can experience a very low group velocity dispersion, but a very high nonlinearity, so that shock effects should be visible experimentally, and relatively straightforward to separate from other propagation effects.

In addition to deriving the shock term, we have used our method to develop a set of coupled mode equations that can describe PBG materials into which waveguiding layers have been grown. In such materials, light has been experimentally observed to have an extremely low group velocity[8], which, consequently, means that if the material is Kerr nonlinear, then the effect of that nonlinearity will be enhanced[9].

Finally, we note that our technique allows for a straightforward interpretation of the conserved quantities of the system. For example, for a system described by H_{eff} (9) we find two more conserved quantites: a momentum-like quantity, P, associated with the space translation invariance that obtains at the level of the effect fields, and a conserved charge, Q, associated with phase invariance[4]:

$$P = i\frac{\hbar}{c}\frac{\partial \omega_{\overline{mk}}}{\partial \mathbf{k}^i} \cdot \int_V \left\{ g_{\overline{m}} \frac{\partial g_{\overline{m}}^\dagger}{\partial r^i} - g_{\overline{m}}^\dagger \frac{\partial g_{\overline{m}}}{\partial r^i} \right\} d\mathbf{r},$$

$$Q = \hbar \omega_{\overline{mk}} \int_V \left| g_{\overline{m}} \right|^2 d\mathbf{r}.$$

(12)

The quantity Q looks like the energy in the electromagnetic field, but comparing (12) to the effective Hamiltonian (9) shows that it is only equal to the lowest order portion of the full energy[4]. These definitions avoid the introduction of a free energy, or other interpretational issues that have arisen in the study of conserved quantities of nonlinear systems[10].

1. M. Hillery and L. D. Mlodinow, Phys. Rev. **30**, 1860 (1984).
2. R. W. Boyd, *Nonlinear Optics* (Academic, San Diego, 1991).
3. See, eg, N. W. Ashcroft and N. D. Mermin, *Solid State Physics* (Saunders College, Philadelphia, 1976).
4. Suresh Pereira and J. E. Sipe, Phys. Rev. E **65**, 046601 (2002)
5. N. A. R. Bhat and J. E. Sipe, Phys. Rev. E **64**, 056604 (2001).
6. H. A. Haus and E. P. Ippen, Opt. Lett. **26** 1654 (2001).
7. John E. Heebner, Robert W. Boyd and Q-Han Park, JOSA B **19**, 722 (2002).
8. M. Notomi *et. al*, Phys. Rev. Lett. **87**, 253902 (2001).
9. C. M. de Sterke and J. E. Sipe, in *Progress in Optics*, edited by E. Wolf (North-Holland, Amsterdam, 1994), Vol. **33**, pp. 203-260.
10. C. Pask, D. R. Rowland and W. Samir, J. Opt. Soc. Am. B **15**, 1871 (1998).

Depositing light in a photonic stop gap using Kerr nonlinear microresonators

Philip Chak, J. E. Sipe and Suresh Pereira
University of Toronto, Toronto, ON, M5S 1A7, Canada
phone: 416-978-5444; fax: 416-978-2537
email: pereira@physics.utoronto.ca

We demonstrate numerically that it is possible to trap light in the structure shown in Figure 1a using four-wave mixing. We define two resonant frequencies associated with the structure: $\omega_{\{o,i\}} = c/(n_{eff}R_{\{o,i\}})$, where "i" and "o" refer to the inner resonators (not shaded) and the outer resonators (shaded) respectively, and R_i and R_o are the radii of the inner and outer resonators. The quantity n_{eff} is a linear effective index of refraction, assumed to be common to all the resonators and the channel guides, furthermore the frequency dependence of n_{eff} is ignored; these assumptions simplify the presentation of the effect. The outer microresonators couple the channel waveguides, so that forward travelling light in the bottom (top) channel is coupled to backward travelling light in the top (bottom) channel[1,2]. If light has frequency at or near $N\omega_o$, where N is an integer, then the coupling is resonant, and a stop gap opens in the transmission spectrum of the structure[1,2]. These gaps lead to the dips in the transmission spectrum of the structure shown by the solid line in Figure 1b; the dotted lines in Figure 1b show some resonances of the inner microresonators (which do not lead to gaps). Material parameters, used throughout this paper, are n_{eff}=3.0, $2\pi R_i$=25µm, $2\pi R_o$=30µm and σ=0.98 for all resonators.
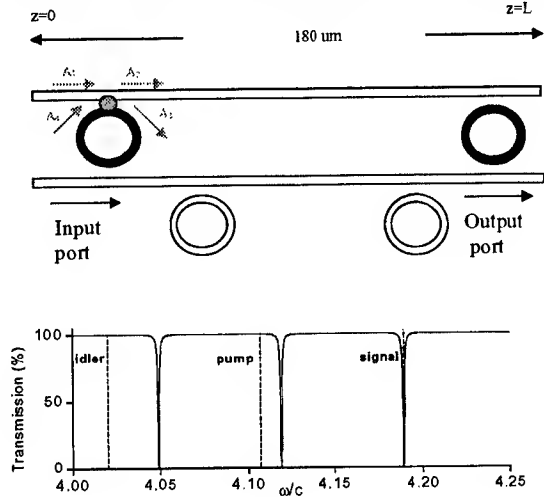
Figure 1: (a) Schematic of the system. All pulses are injected along the bottom channel. (b) Transmission spectrum (solid line) of the structure, the dips correspond to resonances of the outer resonators. The dotted lines correspond to resonances of the inner resonators. In units of wavelength, the signal corresponds to roughly 1.5µm.

To trap light in the structure, we inject a strong pump, and a weak idler beam with frequencies ω_p and ω_i into the bottom channel of the structure. Neither pump nor idler corresponds to a resonance of the outer resonators, so that essentially all of their energy propagates through the bottom channel. However, we choose ω_p and ω_i such that they correspond to resonances of the inner resonators (Figure 1b); this leads to a large build-up of pump and idler intensity in the inner resonators. Since the resonators are Kerr nonlinear, the build-up of intensity enhances four-wave mixing[3,4]. This nonlinear process will produce light at $2\omega_p - \omega_i$ and $2\omega_i - \omega_p$. We choose our parameters such that $\omega_s = 2\omega_p - \omega_i$ corresponds to a resonance of *both* the inner and the outer resonators, and hence any light generated at frequency ω_s will be trapped in the structure by the outer resonators.

To simulate this effect we generalize a numerical technique previously applied to a structure consisting of *one* channel guide coupled to microresonators[5]. We divide the problem into two distinct parts: coupling between the

resonators and guides, which we assume happens only at discrete 'coupling points', and propagation of light. To describe the coupling, we introduce a self-coupling coefficient σ, and a cross-coupling coefficient κ. For simplicity we assume that these coefficients are the same for all of the resonators. On the leftmost resonator of Figure 1a we show a schematic of coupling between the channel and the resonators. The large dot indicates the coupling point. The fields are coupled[2,5] such that $A_3 = \sigma A_4 + i\kappa A_1$ and $A_2 = \sigma A_1 + i\kappa A_4$. To describe pulse propagation we first define a set of fields, $A_{(p,i,s)}(z,t)$, where the subscript indicates the pump, idler or signal, that are normalized such that their square modulus represents the intensity in the pulse. We describe the evolution of these fields using a set of coupled nonlinear equations[3,6],

$$\frac{\partial A_p}{\partial z} + \frac{1}{v_g}\frac{\partial A_p}{\partial t} = i\gamma_p \left\{ |A_p|^2 A_p + 2A_s A_i A_p^* \right\} - \frac{1}{2}\left\{ \alpha_1 + \alpha_2 |A_p|^2 + \alpha_3 |A_p|^4 \right\} A_p,$$

$$\frac{\partial A_i}{\partial z} + \frac{1}{v_g}\frac{\partial A_i}{\partial t} = i\gamma_i \left\{ 2|A_p|^2 A_i + A_p^2 A_s^* \right\} - \frac{1}{2}\left\{ \alpha_1 + 2\alpha_2 |A_p|^2 + 3\alpha_3 |A_p|^4 \right\} A_i, \qquad (1)$$

$$\frac{\partial A_s}{\partial z} + \frac{1}{v_g}\frac{\partial A_s}{\partial t} = i\gamma_s \left\{ 2|A_p|^2 A_s + A_p^2 A_i^* \right\} - \frac{1}{2}\left\{ \alpha_1 + 2\alpha_2 |A_p|^2 + 3\alpha_3 |A_p|^4 \right\} A_s,$$

where, $v_g = c/n_{eff}$, $\gamma_{(p,i,s)} = \omega_{(p,i,s)} n_2/c$, n_2 is the nonlinear index of refraction coefficient, and where α_1, α_2 and α_3 account for linear loss, two-photon absorption (2PA) and three-photon absorption (3PA) respectively. In Equations (1) we have assumed that $I_p \gg I_i$ and $I_p \gg I_s$, where $I_{(p,i,s)}$ is the peak intensity in the pump, idler and signal respectively. As boundary conditions we set $A_p(z=0,t)$ and $A_i(z=0,t)$ at the bottom channel to be our input pulses of interest, and we assume no energy enters the system through the top channel, or through the bottom channel at z=L.

We choose nonlinear parameters consistent with $Al_{0.18}Ga_{0.82}As$, a material used in nonlinear waveguiding applications for its low loss[6], for which $n_2 = 0.00011 cm^2/GW$, $\alpha_2 = 0.05 cm/GW$ and $\alpha_3 = 0.08 cm^3/GW^2$ are the appropriate nonlinear parameters. We vary the value of intensity loss from 0 to 2dB/cm ($\alpha_1 = 0.46 cm^{-1}$), which is consistent with the observed loss in straight-waveguides fabricated using $Al_{0.18}Ga_{0.82}As$. Losses in resonator structures have typically been much higher than this, but they are primarily scattering losses, and are due to fabrication problems rather than the fundamental limit imposed by bending loss[7]. The value of 0.7dB/cm is significantly higher than the fundamental bending loss[7]. We set the input pump and idler pulses to be Gaussian with 20ps full-width at half maximum

Figure 2: Energy trapped in structure for linear loss 0dB/cm (solid), 0.7dB/cm (dot) and 2dB/cm (dash-dot).

intensity (FWHM), with $I_p = 50 MW/cm^2$ and $I_i = 0.5 MW/cm^2$. In Figure 2 we plot the signal energy in the structure as a function of time, using linear losses 0dB/cm (solid line), 0.7dB/cm (dotted line), 2dB/cm (dash-dot). The initial transient, lasting until about 100ps, is due to the fact that not all of the frequencies of the signal light are reflected by the resonators, so some energy immediately escapes. Disregarding the transient, about 90fJ of energy is trapped; the half-life of the trapped light is 100ps when the loss is 2dB/cm, and 500ps with a loss of 0.7dB/cm.

To remove the trapped signal light from the structure, we send a 20ps flush pulse, with $I_f = 500 MW/cm^2$, and with $\omega_f = \omega_p$. We again use equations (1), but replace A_p with A_f. It is

well-known[3] that because of cross phase modulation (CPM), the frequency of the signal light will shift; this shift is proportional to $n_2(\partial I_f/\partial t)$. The shifted frequencies will no longer be matched to the resonance of the outer resonators, and will leave the structure. In Figure 3 we demonstrate the efficacy of this technique when the linear loss is 0.7dB/cm. The solid line shows the signal energy in the system, building up exactly the same way as in Figure 2. At
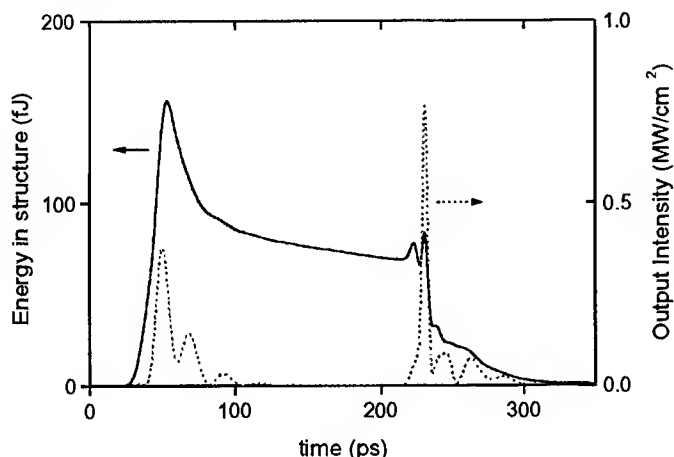

Figure 3: **Energy in the structure (solid) and output signal intensity (dotted). The energy is flushed out at about 200ps. Prior to that point it decays due to linear loss.**

t=200ps we inject the flush pulse, which has two effects. Initially there is a transient, because the flush and signal light create light at the idler frequency, which can then be used to create *more* light at the signal frequency. However, after the transient, the signal light is flushed from the system in two stages. These two stages are as follows. The dotted line in Figure 3 shows the intensity of the signal light that leaves the structure from the bottom channel at z=L. There is initially a sharp output peak, which consists of signal light that has been blue shifted by the CPM induced by the leading edge of the flush pulse[3]. After the sharp peak there is a small trailing signal pulse, which consists of light that has been red shifted by the CPM induced by the trailing edge of the flush pulse.

Our scheme is similar to one presented earlier using fiber gratings[8], but has two main benefits: first, our structure is about 50 times smaller, but can trap similar amounts of energy; second, we have presented a method based on cross phase modulation (CPM) for removing the energy.

1. A. Melloni, Opt. Lett. **23**, 259 (1998).
2. Suresh Pereira, J. E. Sipe, John E. Heebner and R. W. Boyd, Opt. Lett. **27**, 536 (2002).
3. G. P. Agrawal, *Nonlinear Fiber Optics*, (Academic, San Diego, 1989).
4. P. P. Absil *et. al*, Opt. Lett. **25**, 554 (2000).
5. John E. Heebner, Robert W. Boyd and Q-Han Park, JOSA B **19**, 722 (2002).
6. A. Villeneuve *et. al* Appl. Phys. Lett. **61**, 147 (1992).
7. V. Van, Philippe P. Absil, J. V. Hryniewicz and P. –T. Ho, J. Lightwave Tech. **19**, 1734 (2001).
8. C. Martijn de Sterke, E. N. Tsoy and J. E. Sipe, Opt. Lett. **27**, 485 (2002).

Efficient integrated Ti:PPLN MIR-optical parametric generator

M. C. Hübner, D. Hofmann and W. Sohler

Universität Paderborn, Angewandte Physik,
Warburger Straße 100, D-33098 Paderborn, Germany
Tel.: +49 5251 60-2295, Fax: +49 5251 60-3882, EMail: sol_mh@physik.upb.de

Abstract: Efficient tunable MIR-optical parametric fluorescence was demonstrated for the first time in a 80 mm long single mode Ti:PPLN channel guide of 31 µm domain periodicity. Up to several µW of MIR-power were generated using a modelocked fiber laser as pump source.
© 2002 Optical Society of America
OCIS codes: (130.3120) Integrated optics devices; (130.3730) Lithium niobate; (190.2620) Frequency conversion; (190.4410) Nonlinear optics, parametric processes

Introduction

The generation of optical parametric fluorescence (OPF) in bulk nonlinear crystals is a well-known method for frequency down-conversion of coherent laser radiation [1]. It is mainly used for spectroscopy in the near (NIR) and mid (MIR) infrared. However, high conversion efficiencies can only be obtained in a pulsed mode of operation with very high peak power levels.

Contrary to bulk configurations nonlinear integrated optical waveguides promise conversion efficiencies, which can exceed those of bulk optical approaches by several orders of magnitude. Moreover, if quasi phase matching is used in periodically poled $LiNbO_3$ (PPLN) waveguides, the largest nonlinear coefficient d_{33} can be exploited and the spectral range of the OPF-emission can be adjusted by a corresponding periodicity of the ferroelectric grating.

In this contribution we report the first investigation of quasi phase matched tunable MIR-OPF around 3 µm wavelength in long Ti:PPLN waveguides.

Waveguide fabrication and experimental setup

Single-mode channel waveguides for the 3 µm wavelength range were fabricated on a 86 mm long, 10 mm wide and 0.5 mm thick Z-cut optical grade LN substrate. The guides were prepared by the indiffusion of photolithographically delineated 160 nm thick Ti-stripes of 18, 20 and 22 µm width oriented parallel to the crystallographic X-axis. Subsequently, the periodic domain inversion was performed over a length of 80 mm using the electric field induced poling technique described in more detail in [2]. The periodicity of the domains ranges from 31.06 to 31.48 µm with duty cycles close to 1. The losses of these waveguides were investigated at $\lambda=3391.3$ nm with TM polarized light using the low-finesse resonator method [3]. Loss coefficients in the range 0.05–0.12 dB cm^{-1} were measured. Afterwards, the end faces of the sample were anti-reflection coated for the pump wavelength to suppress Fabry-Perot-resonances.

The experimental setup consists of a pump laser, followed by a high power EDFA (33 dBm), a mechanical chopper, a coupling optics, the Ti:PPLN waveguide parametric generator, a collimating lens, a Ge- and a dielectric filter to suppress the transmitted pump radiation and an HgCdZnTe-' or an InSb-detector. The pump laser is either an external cavity laser (ECL), tunable from 1520 to 1580 nm, or an actively modelocked fiber laser emitting pulses of 5.4 ps halfwidth and 20 mW average power at 10 GHz repetition rate; it is tunable from 1541 to 1564.5 nm. The amplified pump radiation of an average power of up to 2 W is chopped and coupled in TM-polarization into a Ti:PPLN waveguide. The generated signal and idler radiations were measured using a lock-in technique. A power calibration was obtained by comparing the response of the InSb-diode with a commercial power meter at $\lambda=1550$ nm and a subsequent extrapolation to the MIR wavelength range by the documented spectral response. The HgCdZnTe-detector was then calibrated by a comparison of its response at $\lambda=3391.3$ nm with the signal obtained from the InSb-diode. For spectral investigations of the fluorescence radiation a standard monochromator was used.
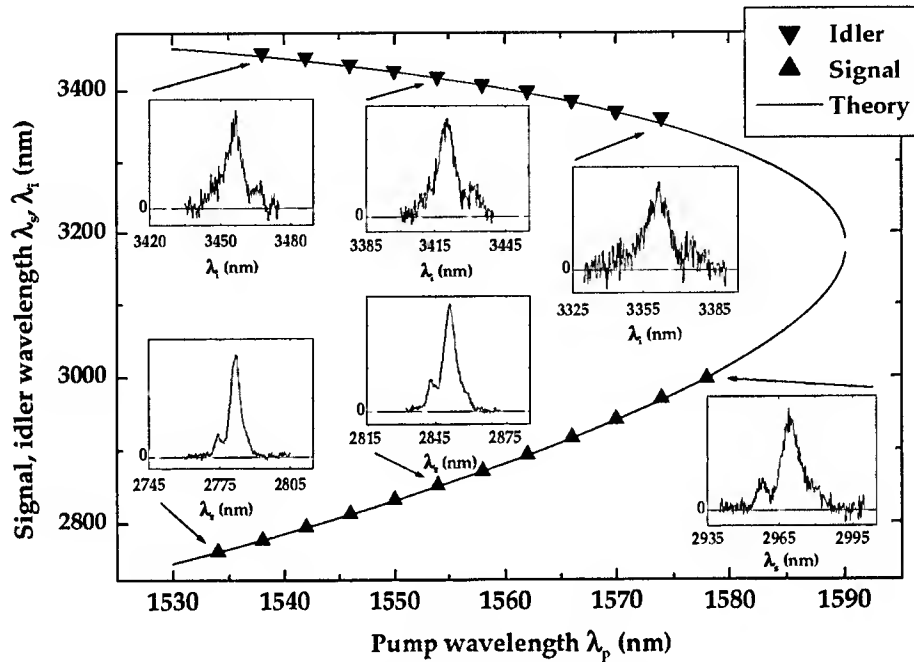
Fig. 1. Measured (▼▲) and calculated (—) tuning characteristics of OPF from an 18 µm wide waveguide with a domain period of 31.36 µm as signal and idler wavelengths versus the pump wavelength in cw-operation. Selected spectral characteristics of the fluorescence are shown in the insets.

Results

Fig. 1 shows as an example the tuning characteristics of the signal and idler waves generated in an 18 µm wide waveguide of 31.36 µm domain periodicity. The coupled (cw) pump power was approximately 300 mW. The MIR-OPF was continuously tunable from 2760 to 3000 nm (signal) and from 3360 to 3450 nm (idler). A gap remained near degeneracy due to the limited tuning range of the pump source. Moreover, selected spectral characteristics are given as insets; they all have one pronounced sidelobe, probably due to waveguide inhomogeneities. The longer the wavelength, the noisier the spectrum is arising from the weaker efficiencies of monochromator and detector. All peaks become broader with increasing pump wavelength in good agreement with theoretical considerations [4]. A calculated phase matching curve shows excellent accordance with the measured results. In waveguides of larger domain periodicity the tuning characteristics shifts as a whole to the left reducing the gap near degeneracy. The same happens, if broader waveguides or higher temperatures are used.

Experimental room temperature data for the total OPF output power (signal and idler) from the same waveguide are shown in Fig. 2 as function of the pump power (λ_p=1550 nm, λ_s=2835 nm, λ_i=3420 nm) (Note, that the given figures for OPF and pump correspond to the power levels at open chopper, averaged during the opening intervals in the pulsed mode of operation with the modelocked pump laser). The chopper duty cycle was changed from 1:1 to 1:9 to reduce OPF power fluctuations at high pump power levels probably caused by photorefractive effects. The OPF output power is a nearly linear function of the pump power in the quasi-cw-case; it rises up to 7.5 nW at 1725 mW of coupled pump power. In the pulsed operation with pulses of a peak power of 31 W the average OPF power shows an exponential rise up to 32.5 nW at an average pump power of 1676 mW. The maximum conversion efficiencies can thus be determined as $4.3 \cdot 10^{-9}$ and $1.9 \cdot 10^{-8}$ for the pulsed operation, respectively.

These figures are much smaller than expected from theory, which assumes excitation of the lowest order pump mode alone. However, selective coupling to the fundamental mode of the guide, which is multimode at the pump wavelength, is hard to achieve experimentally. Moreover, slight photorefractive effects can modify the spatial pump spectrum reducing the efficiency of OPF generation as well.
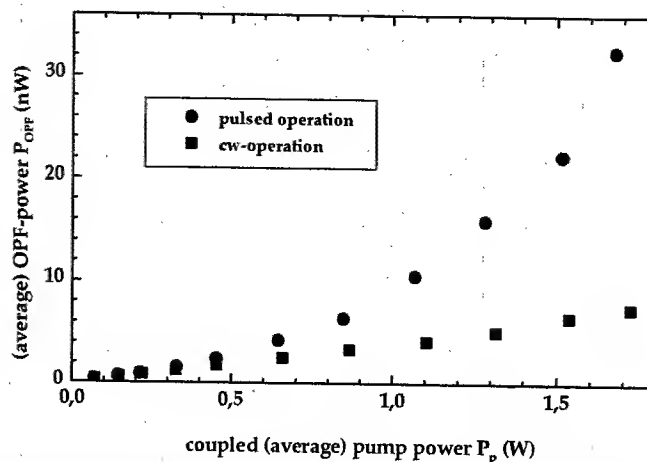
Fig. 2. OPF output power for pulsed and quasi-cw-operation as function of the coupled pump power, averaged during shutter openings (λ_p=1550 nm, λ_s=2835 nm, λ_i=3420 nm)

In another channel of the same sample an average OPF power of up to 2.4 μW was obtained at 1.75 W average pump power, resulting in a conversion efficiency of $1.4 \cdot 10^{-6}$. However, the strong (stimulated) fluorescence was not stable and decreased rapidly with time. During 140 s the output signal dropped by 73% and the whole sample shimmered in an intense green light. A spectral characterization of this radiation showed two strong peaks at 775 nm and 517 nm, respectively. They are due to non phasematched second harmonic generation (SHG) of the pump and sum-frequency generation (SFG) of the pump with its second harmonic, resulting in third harmonic generation. Photorefractive effects induced by these shorter wavelength radiations could be the origin of the strong decrease of the MIR-fluorescence power; they could be minimized by higher sample temperatures.

Conclusions

For the first time MIR-OPF, generated in a Ti:PPLN single mode waveguide, has been studied in detail. A large tuning range of 2760 nm < λ_s, λ_i < 3450 nm could be demonstrated with a small gap around degeneracy. In a quasi cw-mode of operation up to 7.5 nW of OPF power was obtained with about 1.7 W pump power. In a pulsed mode of operation the average OPF-power increased to 33 nW, corresponding to a peak power of ∼0.6 μW. Even 2.4 μW average output (∼44 μW peak power) was demonstrated in another channel; however, the emission decreased rapidly with time probably due to photorefractive effects. We are confident that operation at elevated temperatures will reduce these effects and improve in this way the performance of the device. Moreover, a tapered coupling section for the pump will guarantee the selective excitation of the fundamental pump mode alone; this means will also contribute to increase the OPF output. A stronger stimulation (amplification) of the guided MIR-fluorescence will also result in a spectral narrowing attractive for spectroscopic applications.

References

1. J.-Y. Zhang, J. Y. Huang, J. F. Hong and N. B. Ming, "Optical parametric generation and amplification" vol. 19 of *Laser Science and Technology, An international handbook*, (Harwood Academic Publishers 1985).
2. D. Hofmann, G. Schreiber, C. Haase, H. Hermann, W. Grundkötter, R. Ricken and W. Sohler, "Quasi-phase-matched difference-frequency generation in periodically poled Ti:LiNbO$_3$ channel waveguides," Opt. Lett. **24**, 896–898 (1999).
3. R. Regener and W. Sohler, "Loss in low-finesse Ti:LiNbO$_3$ optical waveguide resonators," Appl. Phys. B **36**, 143–147 (1985).
4. H. Suche and W. Sohler, "Integrated optical parametric oscillators," Optoelectronics – Devices and Technologies **4**, 1–20 (1989).

Faraday Patterns in Bose-Einstein Condensates

Kestutis Staliunas
PTB Braunschweig, Bundesallee 100, 38116 Braunschweig, Germany
kestutis.staliunas@ptb.de

Stefano Longhi
INFM and Dipartimento di Fisica, Politecnico di Milano, Piazza L. da Vinci 32, I-20133 Milano, Italy
longhi@fisi.polimi.it

Germán J. de Valcárcel
Departament d'Òptica, Universitat de València, Dr. Moliner 50, E-46100 Burjassot, Spain
german.valcarcel@uv.es

Abstract: Temporal periodic modulation of the scattering length in Bose-Einstein condensates is shown to excite subharmonic patterns of atomic density through a parametric resonance. The patterns are analogous to the Faraday waves excited in vertically vibrated liquids.
©2000 Optical Society of America
OCIS codes: (190.4420) Nonlinear optics, transverse effects

1. Introduction

Spontaneous formation of spatial patterns occurs in many natural systems as well in laboratory experiments. The very essence of spontaneous pattern formation is that a uniform state loses its stability against spatially modulated states when an external control parameter is varied. The character of the instability, e.g. dominant wavelength and symmetries of the selected patterns, is purely an intrinsic property of the system, independent of- (or only weakly dependent on-) initial or boundary conditions.

So far, no mechanism for spontaneous pattern formation has been suggested for the most recently created state of the matter, the Bose-Einstein Condensates (BECs). Although vortices and vortex ensembles were predicted and observed in BECs [1], such structures can not be referred to as spontaneous patterns, since they occur due to particular initial or particular boundary conditions (e.g. due to stirring of the condensate). In this sense vortex ensembles are reproduced from one state of the matter into another, but do not appear spontaneously, like the spontaneously occurring patterns in biological morphogenesis, Rayleigh-Benard convection, etc.

We suggest that parametric excitation of a BEC can lead to spontaneous breaking of the space symmetry, and to the appearance of spatial patterns and quasipatterns. The parametric excitation can be obtained by a periodic modulation in time of the scattering length of the condensed atoms. Experimentally this can be achieved via the Feshbach resonance, where the variation of a magnetic field modifies the s-wave interatomic scattering length. The nonlinear coefficient of low dimensional (1D or 2D) condensates can also be varied by modulation of the trapping potential along a spatial coordinate normal to the "working" space.

In the framework of the mean-field model of BECs (usually described by Gross-Pitaevskii equation), the modulation of the scattering length of atoms leads to a time-dependent nonlinear coefficient. We show both by analytical and numerical calculations that the dominant wavenumber of the patterns arising from the parametric instability are selected by the excitation frequency through a dispersion-induced mechanism, and that the resulting patterns are of square, rhombic, and of eightfold symmetry, resembling the taxonomy of patterns observed in the Faraday instability on a free surface of a fluid undergoing oscillatory vertical acceleration.

2. Model

We investigate the parametric excitation of patterns in condensates by considering the mean-field Gross-Pitaevskii equation for the single-particle wave function $\psi(\mathbf{r},t)$ in an external trapping potential $V_{\text{trap}}(\mathbf{r})$ assuming a two-body repulsive interaction periodically modulated in time:

$$i\frac{\partial \psi}{\partial t} = \left[-\nabla^2 + V_{\text{trap}}(\mathbf{r}) + C(t)|\psi|^2\right]\psi \tag{1}$$

where $C(t) = 1 + 2\alpha\cos(2\omega t)$ is the nonlinearity harmonically modulated in time. We mainly study 2D ("pancake") BECs, in which a strong trap confinement occurs in the z direction while in the transverse directions (x,y) weak confinement is realized by, e.g., a harmonic trap $V_{trap}(x,y) = -1 + \frac{1}{2}\omega_{trap}^2(x^2 + y^2)$ with $\omega_{trap} \ll \omega$. Since we are interested on the occurrence of pattern forming instabilities on a spatial scale much smaller than the size of the condensate, we consider the limiting case of a flat potential and choose arbitrarily $V_{trap}(r) = -1$. We also shown by numerical simulations that the pattern forming instability found in the flat trapping potential limit persists under a more realistic weakly-trapping harmonic potential.

2. Patterns

The linear Floquet analysis of (1) yields that for given driving frequency 2ω the spatial modulation of particular wavenumbers grow. The most unstable wavenumbers are located around:

$$k = k_n \equiv \sqrt{-1 + \sqrt{1 + (n\omega)^2}} \qquad (2)$$

Here the integer n = 1 (n > 1) represents the main (the higher order) parametric resonances.

Numerical simulations in the flat potential limit were performed to check the onset and evolution of the parametric instability of the homogeneous BEC state. Fig.1 indicates the growth of modulation: In the early stage the formation of a main resonant ring in momentum space is apparent, which corresponds to transient quasipatterns in physical space. In the further evolution higher-order resonance rings appear in momentum space, which correspond to the higher-order resonances. On a long time scale one observes heating and eventual destruction of the condensate.
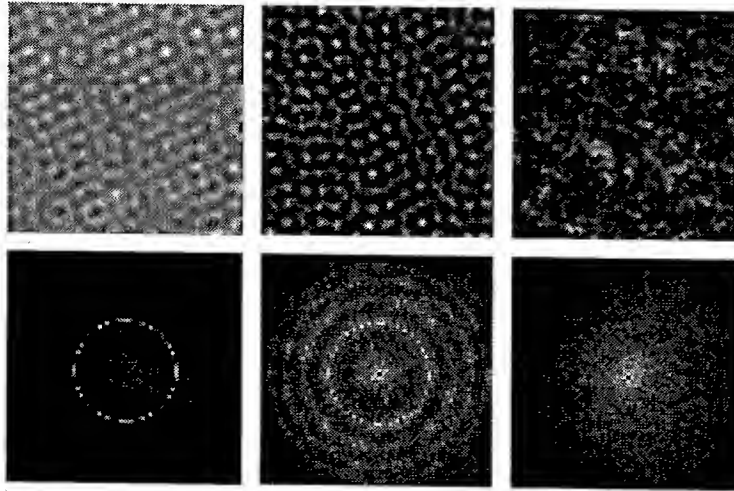
Fig. 1. Transient patterns as obtained by numerical integration of (1) in a flat potential with periodic boundary conditions, with the intensity of the order parameter (particle density of condensate in physical space) in the upper row, and the spatial Fourier power spectrum (particle density of condensate in momentum space) in the lower row. Time increases from left to right

3. Dissipative patterns

In order to determine the intrinsic symmetries of parametric patterns, we investigated weakly dissipative BECs, since the inclusion of dissipative terms in the equation, capable of describing damping mechanisms of trapped BECs, can lead to the final selection of patterns with a well-defined symmetry:

$$i\frac{\partial\psi}{\partial t} = (1 - i\gamma)\left(-\nabla^2 - 1 + |\psi|^2\right)\psi + 2\alpha\cos(2\omega t)|\psi|^2\psi \qquad (3)$$

The damping γ, ensures an evolution towards an equilibrium state in the absence of parametric driving. Numerical integration of (3) with small dissipation indicates that the formation of stationary spatial patterns with different symmetries is possible (Fig.2). For large frequencies of forcing, typical patterns are squares, or quasiperiodic patterns with eightfold symmetry, for moderate frequencies rhombic patterns are favored. The mechanism of symmetry selection is related with the matching conditions between the first and second order resonant wavevectors, and will be discussed.
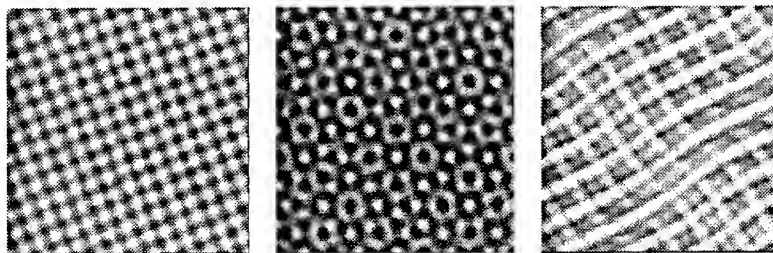
Fig. 2. Stationary patterns in dissipative BECs, as obtained by numerical integration of (3) in a flat potential with periodic boundary conditions. The driving frequency is $\omega = 1.5 \cdot \pi$ for the left and middle pattern, and $\omega = 0.5 \cdot \pi$ for the right pattern.

4. Nonlinear resonance

Whereas the linear analysis of (1) and (3) yields a dispersion relation for standing waves of small amplitudes (2), the weakly nonlinear analysis shows that the resonant wavenumber depends also on the amplitude of modulation:

$$k = k_n \equiv \sqrt{-|\psi_0|^2 + \sqrt{|\psi_0|^4 + (n\omega)^2}} \qquad (4)$$

where $|\psi_0|^2$ is the occupation of the spatially homogeneous (zero) mode. The zero mode depletes for increasing spatial modulation in both cases: because of the conservation of the number of particles in conservative case (1): $|\psi_0|^2 = 1 - |\psi_{mod}|^2$; because of the conservation of energy in dissipative case (3): $|\psi_0(t)|^2 = 1 - 2|\psi_{mod}(t)|^2$. In both cases the resonant wavenumber increases with growing spatial modulation, therefore the nonlinear resonance is of "focussing" type. Since the spatial nonlinear resonance of focussing type may be at the root for spatial solitons [2], we expect to demonstrate such spatial solitons in parametrically driven BECs too. We note, that the spatially localized patterns, so called oscillons are known in periodically shaken granular materials [3], the systems related to the Faraday systems, and consequently related to the parametrically driven BECs studied here.

5. Conclusions

In conclusion, we have shown that spontaneous formation of patterns, a very general phenomenon studied in different fields of nonlinear science, is possible also for the newly created state of matter, the BECs. Pattern formation can be achieved by modulation of the scattering length of atoms in the condensate, a mechanism that bears a close connection with the formation of spatial patterns on the surface of a vibrating fluid. We have been concerned up to now with 2D condensates, in which the dynamics occurs in the plane transverse to the tight confinement direction, and found squares, rhombi and octagons as typical patterns; patterns with more complex symmetries are expected to occur in 3D condensates.

A nonlinear spatial resonance is also found, which gives hope of observing spatial localized structures in BECs.

6. References

1. M. Mathews, B. P. Anderson, P. C. Haljan, D. C. Hall. C. E. Wieman, and E. A. Cornell, Vortices in a Bose-Einstein Condensate, Phys. Rev. Lett. **83**, 2498 (1999)
2. K.Staliunas, and V.J.Sanchez-Morcillo, Spatial Localized Structures in Degenerate Optical Parametric Oscillators, Phys.Rev.A57 1454 (1998)
3. P.B.Umbanhowar, F.Melo, and H.L. Swinney, Localized excitations in a vertically vibrated granular layer, Nature 382, 373 (1996).

Stability of spiralling solitary waves in Hamiltonian systems

Dmitry V. Skryabin[1], John M. McSloy[2], and William J. Firth[2]

[1] *Department of Physics, University of Bath, Bath BA2 7AY, United Kingdom*
d.v.skryabin@bath.ac.uk; fax: 44 (1225) 386110
[2] *Department of Physics and Applied Physics, University of Strathclyde, Glasgow G4 0NG, United Kingdom*
jmc@phys.strath.ac.uk; fax: 44 (141) 5522891

Abstract: We present a rigorous criterion for stability of spiralling solitary structures in Hamiltonian systems incorporating the angular momentum integral and demonstrate its applicability to the spiralling of two mutually incoherent optical beams propagating in photorefractive material.
©2002 Optical Society of America

Stability of spiralling solitary waves in Hamiltonian systems

Dmitry V. Skryabin[1], John M. McSloy[2], and William J. Firth[2]

[1]*Department of Physics, University of Bath, Bath BA2 7AY, United Kingdom*
d.v.skryabin@bath.ac.uk; fax: 44 (1225) 386110

[2]*Department of Physics and Applied Physics, University of Strathclyde, Glasgow G4 0NG, United Kingdom*
jmc@phys.strath.ac.uk; fax: 44 (141) 5522891

The richness of spatio-temporal dynamics of light in nonlinear media has attracted much attention over the last decade. One of the many recent areas of interest is spiralling of self-localized beams of light, which has been stimulated largely by a series of experiments demonstrating spiralling of a pair of mutually incoherent light beams propagating in photorefractive materials [1–3], and in concomitant numerical modelling [2–5] broadly supporting these experiments. Later developments have also shown seemingly stable spiralling structures resulting from azimuthal instability of a vortex beam within the potential created by a strong soliton field incoherent with the vortex [4,5]. These structures have been termed *propeller solitons* [4] or *rotating dipole-mode vector solitons* [5].

Obtaining a rigorous and general analytical criterion for the stability of spiralling solutions in Hamiltonian models has, however, remained an open and important problem, which we approach and solve in this work. Results presented below are rather general, but we derive them in the context of two coupled nonlinear Schrödinger equations (NLS) with saturable nonlinearity, which have well established spiralling solutions [3–5], and are believed to provide a reasonable approximation to the nonlinear interaction of incoherent beams in photorefractives [1,3,4]:

$$(i\partial_z + \partial_x^2 + \partial_y^2)E_{1,2} - f(I)E_{1,2} = 0, \qquad (1)$$

where $f(I) = 1/(1 + I)$, $I = |E_1|^2 + |E_2|^2$, and z and x,y are, respectively, dimensionless longitudinal and transverse coordinates. We consider solutions which rotate with constant angular frequency ω in propagation along z and change to a rotating coordinate system: $E_{1,2}(x,y,z) = F_{1,2}(X,Y,z)e^{i\kappa_{1,2}z}$ with $X = x\cos(\omega z) + y\sin(\omega z)$, $Y = -x\sin(\omega z)+y\cos(\omega z)$. The wave-number corrections $\kappa_{1,2}$, together with ω, parametrize the solutions of interest. Now Eqs. (1) read as

$$[i\partial_z + \omega\widehat{L} + \partial_X^2 + \partial_Y^2]F_{1,2} - [\kappa_{1,2} + f(I)]F_{1,2} = 0, \quad (2)$$

where $\widehat{L} = -i(X\partial_Y - Y\partial_X) = i\partial_\theta$ is the z component of the angular momentum operator, familiar in quantum mechanics, and $\theta = arg(X + iY)$.

By analogy with stability thresholds known for other multiparameter solitary waves [11], which in their turn stem form the seminal Vakhitov-Kolokolov criterion [12], we can already guess the expression for the stability

threshold for such a solution ($F_{1,2}$ localized in X,Y and independent of z). This condition is

$$D_0 = det \begin{pmatrix} \frac{\partial P_1}{\partial \kappa_1} & \frac{\partial P_1}{\partial \kappa_2} & \frac{\partial P_1}{\partial \omega} \\ \frac{\partial P_2}{\partial \kappa_1} & \frac{\partial P_2}{\partial \kappa_2} & \frac{\partial P_2}{\partial \omega} \\ \frac{\partial L}{\partial \kappa_1} & \frac{\partial L}{\partial \kappa_2} & \frac{\partial L}{\partial \omega} \end{pmatrix} = 0, \qquad (3)$$

where $P_{1,2} = \int dX\, dY |F_{1,2}|^2$ are the independently conserved power flows of the two interacting fields and $L = \vec{i}_z \cdot \int \int dX\, dY \vec{r} \times \vec{j} = \sum_{n=1,2} \int \int r\, dr\, d\theta\, Im(F_n^* \partial_\theta F_n)$ is the orbital angular momentum integral. Here $\vec{r} = \vec{i}_X X + \vec{i}_Y Y$, $\vec{j} = \sum_{n=1,2}[F_n^*(\vec{i}_X \partial_X + \vec{i}_Y \partial_Y)F_n - c.c.]/(2i)$. $\vec{i}_X, \vec{i}_Y, \vec{i}_z$ are the unit vectors along X,Y and z axes. The conservation laws $\partial_z L = \partial_z P_{1,2} = 0$ follow directly from the Hamiltonian nature of our model combined with invariance of Eqs. (2) with respect to rotations in the (X,Y)-plane and to the two phase shifts $(F_1, F_2) \rightarrow (F_1 e^{i\phi_1}, F_2 e^{i\phi_2})$.

To formally derive Eq. (3) and verify its applicability to the stability of spiralling solutions of Eqs. (1), we adopt the following approach: first, we prove, both analytically and numerically, that stationary, $\omega = 0$, dipole-mode soliton solutions of Eqs. (2) can be smoothly continued along ω; second, we derive an expression for the eigenvalues governing stability of this solution and numerically verify change of stability at $D_0 = 0$; third, we discuss applicability and generalization of our results for other cases and models.
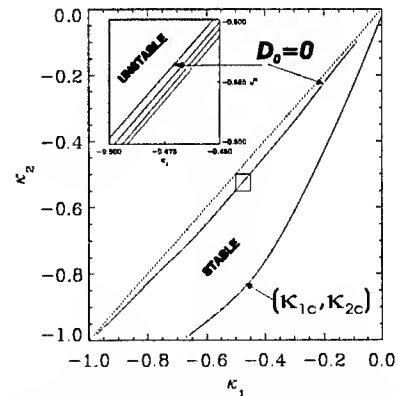

FIG. 1. Diagram showing region of existence and stability of the spiralling solutions in the (κ_1, κ_2) plane, for different values of ω. Interchanging E_1 and E_2, one can plot a symmetric diagram in the region $\kappa_2 > \kappa_1$. Inset shows $D_0 = 0$ lines corresponding to $\omega = 0$, 0.02, 0.03 and 0.04, which are plotted from left to right respectively. $D_0 = 0$ lines marked by arrows correspond to $\omega = 0$.

It has been previously established that stationary dipole-mode solitons and rotating dipoles [4,5], bifurcate from the scalar fundamental soliton solution, $F_1 = A_0(r = \sqrt{X^2 + Y^2})$, $F_2 = 0$, for certain values of (κ_1, κ_2). Linearization of Eqs. (2) near this soliton leads to a factorizable eigenvalue problem. The modes of the excitations of the F_2 component are related to the eigenstates of the operator $\partial_X^2 + \partial_Y^2 - \kappa_2 - 1/(1 + A_0^2)$, which has eigenfunctions of the form $f_m(r)e^{\pm im\theta}$, $m = 0, 1, 2, \ldots$. Scanning the (κ_1, κ_2)-plane, one can show that the scalar soliton always remains stable, but that there are special lines, where eigenvalues corresponding to F_2 eigenstates with a particular value of m cross zero. That corresponding to $m = 1$ marks the boundary line, $(\kappa_{1c}, \kappa_{2c})$, where dipole-mode solitons bifurcate from the scalar soliton, see Fig. 1. Thus the weak F_2 component of the emerging two-component solutions can be seen as a field guided by the strong F_1 component. To obtain expressions for the bifurcating solutions we use asymptotic expansions $F_1 = A_0(r) + O(\epsilon^2)$, $F_2 = \epsilon B_1(z, r, \theta) + O(\epsilon^3)$, where $\epsilon \ll 1$ measures distance from the bifurcation line. Assuming $\omega \sim \epsilon^2$ one can show that $\epsilon B_1 = f(r)(a_+(z)e^{i\theta} + a_-(z)e^{-i\theta})$, where $f(r)$ vanishes at zero and infinity and $a_\pm$ obey

$$i\partial_z a_\pm = a_\pm(\alpha|a_\pm|^2 + \beta|a_\mp|^2) \pm \omega a_\pm. \tag{4}$$

The self- and cross-phase modulation constants α, β can be found only numerically. The term in ω originates from $\hat{L}$ in Eqs. (2).

The solution of interest to Eqs. (4) is:

$$a_\pm = \tilde{a}_\pm e^{i\tilde{\kappa}_2 z}, \quad |\tilde{a}_\pm|^2 = \frac{\tilde{\kappa}_2(\beta - \alpha) \mp \omega(\alpha + \beta)}{\alpha^2 - \beta^2}, \tag{5}$$

where $\tilde{\kappa}_2 = (\kappa_2 - \kappa_{2c}) \sim \epsilon^2$. This solution exists for $\tilde{\kappa}_2 > 0$ and in the ω-interval

$$\frac{\tilde{\kappa}_2(\beta - \alpha)}{\beta + \alpha} < \omega < \frac{\tilde{\kappa}_2(\alpha - \beta)}{\beta + \alpha}, \tag{6}$$

where $0 < (\alpha - \beta)/(\alpha + \beta) < 1$. For $\omega = 0$ it describes stationary, and, for $\omega \neq 0$, rotating or spiralling dipoles. At the boundaries of its existence (6) this solution is a vortex solution, with either a_+ or a_- equal zero.

Thus we have demonstrated analytically that a spiralling solution is parameterized by its frequency ω and, therefore, derivatives $\partial_\omega P_{1,2}$, $\partial_\omega L$ indeed exist. Note that equations analogous to (4) have been also derived in [4], but this link between the stationary and rotating dipoles following from them was not discussed. Several other new and important consequences of these equations are presented below.

To find spiralling solutions arbitrary far from the bifurcation boundary we have solved Eqs. (2) with $\partial_z = 0$ using a quasi-exact numerical technique based on a Newton method. We obtained such solutions throughout the region bounded by the lines $\kappa_{1,2} = \kappa_{1c,2c}$ and $\kappa_1 = \kappa_2$ in the (κ_1, κ_2) plane, see Fig. 1. By symmetry, corresponding solutions with E_1 and E_2 interchanged exist in the mirror-image domain $\kappa_2 > \kappa_1$.

For $\kappa_{1,2}$ values far enough from $\kappa_{1c,2c}$, the F_1 field develops two strong intensity peaks overlapping with those of the F_2 dipole. In this region a spiralling structure can be interpreted as a dynamical bound state of two weakly overlapping single-hump vector solitons [3]. Thus our results indicate that the spiralling solitons found in [3] and the rotating dipole (or propeller) solitons [4,5] belong to the same soliton family.

Having established existence of stationary solutions of Eqs. (2) parameterized by ω and $\kappa_{1,2}$ we now consider their stability. Eqs. (4) predict that both spiralling dipoles and vortex solutions are stable. However, these equations do not capture possible instabilities due to angular harmonics with $|m| \neq 1$ and are only valid close to $(\kappa_{1c}, \kappa_{2c})$. The straightforward method to study stability of the spiralling solution $F_{1,2} = F_{1s,2s}$ found from Eqs. (2), is to set $F_{1,2} = F_{1s,2s}(X, Y) + (u_{1,2}(X, Y)e^{\lambda z} + iw_{1,2}(X, Y)e^{\lambda z} + c.c.)$ and linearize Eqs. (2) assuming that $u_{1,2}, w_{1,2}$ are small. The next step is to find the spectrum of the resulting eigenvalue problem $\hat{\mathcal{J}}\vec{u} = \lambda \vec{u}$, where $\vec{u} = (u_1, u_2, w_1, w_2)^T$. The explicit form of of the operator $\hat{\mathcal{J}}$ is too cumbersome to be presented here, and reliable numerical analysis of its spectrum is a formidable computational problem in its own right. Therefore we will rely in what follows on a combination of analytical techniques and direct numerical modelling of Eqs. (1).

We have undertaken extensive numerical modelling of Eqs. (1), initialized with our computed spiralling solutions with small added noise. For various values of $\kappa_{1,2}$ and ω, we observe unstable behavior in the vicinity of the line $\kappa_1 = \kappa_2$. The unstable dynamics was monitored by plotting the z-evolution of the powers $P_{1,2}$ and angular momentum L, see Fig. 2. Any instability resulting in the radiation of energy leads to the decay of these quantities, because we used absorbing boundary conditions on the perimeter of the computational window, where the solitonic field is negligible. Fig. 2 shows several such plots for $\kappa_2 = -0.7$ and several values of κ_1. $P_{1,2}$, L are conserved for $\kappa_1 > \sim -0.65$, but, closer to the line $\kappa_1 = \kappa_2$, their evolution indicates shedding of radiation with subsequent stabilization at new stationary levels. Corresponding volume plots are shown in Fig. 3.

We interpret this as an intrinsic instability of the spiralling solutions. Because $\kappa_{1,2}$ and ω parameterize a particular solution, not the system as a whole, they can change during the evolution of an unstable solution. Therefore, as Figs. 2,3 illustrate, unstable spiralling solutions with given values of $P_{1,2}$ and L can evolve into stable spiralling solutions carrying different powers and angular momentum, plus some non-solitonic radiation.
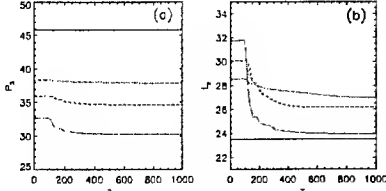
FIG. 2. z evolution of P_2 and L. $\kappa_2 = -0.7$. Solid, dotted, dashed and dash-dotted lines respectively denote, $\kappa_1 = -0.63$, -0.670, -0.675 and -0.680.
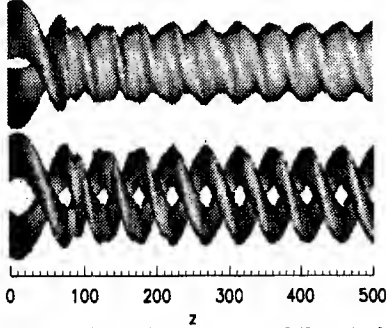

FIG. 3. Volume plots showing instability induced dynamics of $|E_1|$ (top) and $|E_2|$ (bottom) for initial condition corresponding to $\kappa_1 = -0.68$, $\kappa_2 = -0.7$, $\omega = 0.04$. One can observe an instability induced increase of the frequency to $\omega \simeq 0.065$. Surfaces plotted correspond to $|E_{1,2}| = 0.5$.

By numerically computing the properties of whole families of spiralling solutions we have been able to evaluate the determinant D_0 given by Eq. (3). We find that it does indeed change sign at the onset of instability. D_0 is positive in the region where numerical modelling of Eqs. (1) indicates stable spiralling, and negative in the region where unstable dynamics is observed. We now prove that change of sign of D_0 is a sufficient condition for the existence of instability. To derive this criterion formally we solve the eigenvalue problem $\widehat{\mathcal{J}}\vec{u} = \lambda \vec{u}$, assuming that $|\lambda|$ is a small parameter, and taking $\vec{u}$ as a superposition of the neutral (or Goldstone) eigenmodes of $\widehat{\mathcal{J}}$ [11]. These neutral modes can be found by applying infinitesimal symmetry transformations to the soliton solution. In our case the two phase symmetries generate the neutral modes $\vec{u}_{\phi_1} = (-ImF_{1s}, 0, ReF_{1s}, 0)^T$, $\vec{u}_{\phi_2} = (0, -ImF_{2s}, 0, ReF_{2s})^T$, while the rotation symmetry in the (X,Y)-plane generates $\vec{u}_\theta = \partial_\theta (ReF_{1s}, ReF_{2s}, ImF_{1s}, ImF_{2s})^T$. Thus we set $\vec{u} = \vec{u}_{cr} = C_1\vec{u}_{\phi_1} + C_2\vec{u}_{\phi_2} + C_3\vec{u}_\theta + O(|\lambda|)$, where $C_{1,2,3} = O(1)$ are some constants which can be found at higher order. Developing perturbation theory up to the fourth order in $|\lambda|$, (analogous to the theory described in [11]) we have found that eigenvalues corresponding to $\vec{u}_{cr}$ are given by $\lambda_{cr}^2 = -D_0/D_1 + O(|\lambda_{cr}|^4)$. The expression for D_1 is quite cumbersome, but can be deduced from the corresponding two-parameter formulae given in [11]. Provided D_1 is finite, our expression for λ_{cr}^2 formally demonstrates that spiralling solutions always have at least one unstable

mode in any neighborhood of $D_0 = 0$. Direct modelling of Eqs. (1) indicates that $D_0 = 0$ marks the *first* instability threshold met as spiralling solutions are tracked in parameter space (see Fig. 1) from the bifurcation line $(\kappa_{1c}, \kappa_{2c})$, where they emerge towards the line $\kappa_1 = \kappa_2$.

Our expression (3) for D_0 is in fact a new generalized form of the Vakhitov-Kolokolov criterion [11,12], incorporating the angular momentum integral. This is a direct consequence of the need to include the rotational mode $\vec{u}_\theta$ in the derivation of D_0. The relevance of this neutral mode in our case can be seen by noting that Eqs. (4) are invariant with respect to the two phase shifts $(a_+, a_-) \rightarrow (a_+ e^{i\phi_2 + i\psi}, a_- e^{i\phi_2 - i\psi})$. The phase ϕ_2 is the same as previously introduced for Eqs. (2), but the physical meaning of ψ is an angle of rotation in the (X,Y)-plane. The solution $\tilde{a}_\pm = 0$, corresponding to the scalar soliton, is itself rotationally invariant. For the pure vortex solitons any change of ψ can be mimicked by a shift of ϕ_2. Thus for these two classes of solution rotational symmetry is not broken and so the corresponding neutral mode is absent from their spectra. This can be easily verified by direct linearization of Eqs. (4). The dipole solution with both $\tilde{a}_\pm \neq 0$, however, breaks rotational symmetry and therefore acquires an extra neutral eigenmode, which in turn implies an additional dimension in the determinant D_0.

In conclusion, we have presented and proved a new form of the Vakhitov-Kolokolov criterion which incorporates the angular momentum integral and is generally applicable in Hamiltonian systems exhibiting breaking of the rotational symmetry. We have demonstrated that this criterion correctly predicts instability thresholds for spiralling solutions of the saturable vector Kerr model, which describes recent experimental observations in photorefractive media.

[1] M. Shih, M. Segev, and G. Salamo, Phys. Rev. Lett. **78**, 2551 (1997).
[2] A. Stepken *et al.*, Phys. Rev. Lett. **82**, 540 (1999).
[3] A.V. Buryak *et al.*, Phys. Rev. Lett. **82**, 81 (1999).
[4] T. Carmon *et al.*, Phys. Rev. Lett. **87**, 143901 (2001).
[5] J.J. Garcia-Ripoll *et al.*, Phys. Rev. Lett. **85**, 82 (2000).
[6] A.S. Desyatnikov and A.I. Maimistov, J. Exp. Teor. Fiz. **86**, 1101 (1998).
[7] J. Schjodt-Eriksen *et al.*, Phys. Lett. A **246**, 423 (1998).
[8] B. A. Malomed and R. S. Tasgal, Phys. Rev. E **58**, 2564 (1998).
[9] A.S. Desyatnikov and Y.S. Kivshar, Phys. Rev. Lett. **88**, 053901 (2002).
[10] B.A. Malomed, Phys. Rev. E **58**, 7928 (1998).
[11] D.V. Skryabin, Physica D **139**, 186 (2000) and refs. therein.
[12] M.G. Vakhitov and A.A. Kolokolov, Izv. Vyssh. Uchebn. Zaved. Radiofiz. 16, 1020 (1973).

Dynamics of an optical beam in parabolic waveguide with periodic and random nonlinear refractive index

F.Kh. Abdullaev
Physical-Technical Institute of the Uzbek Academy of Sciences,
G. Mavlyanov str. 2-b, 700084, Tashkent, Uzbekistan
Tel: 998 (712) 35-43-38, Fax: 998 (712) 35-42-91, e-mail: fatkh@physic.uzsci.net

J.C. Bronski
Department of Mathematics, University of Illinois at Urbana-Champaign, 1409,
West Green St. IL, 61801, USA

R.M. Galimzyanov
Physical-Technical Inastitute of the Uzbek Academy of Sciences,
G. Mavlyanov str. 2-b, 700084, Tashkent, Uzbekistan

Abstract: We consider the oscillations and associated resonance of an 2D optical beam under periodic and random modulations of nonlinear refractive index. For random oscillations we calculate the mean growth rate for the beam width. Analytical results are compared with the numerical simulations of the full 2D NLS equation with modulated in space coefficients.
©2002 Optical Society of America
OCIS codes: (190.0190) Nonlinear optics

Recently propagation of 2D optical beams in the layered in longitudinal direction and homogeneous in transverse direction nonlinear media has been studied [1]. For rapid periodical variations of the nonlinearity of medium it was shown the possibility of stationary propagation of the beam. This is the analogue of the existence of DM solitons in the dispersion-managed fibers.

The purpose of this communication is to analyze the propagation of 2D beams in periodic and random nonlinear media with a parabolic-index. This problem is also interesting for the analysis of dynamics of a 2D Bose-Einstein condensate in harmonic trap potential with oscillating in time atomic scattering length [2].

The equation governing the evolution of the slowly varying envelope of the optical field in the waveguide with quadratic transverse profile of the linear part of the refractive index and periodic modulations of the nonlinear part of index is in the dimensionless form

$$iE_z + \Delta E + V(x,y)E + n(z)|E|^2 E = 0, \tag{1}$$

where $V(x,y) = -(x^2 + y^2), n(z) = 1 + \epsilon(z)$; and for periodic variations $\epsilon(z) = \epsilon_0 \sin(\Omega z)$, for the random modulations the mean zero white noise model is assumed i.e. $< \epsilon > = 0, < \epsilon(z)\epsilon(z') > = 2\sigma^2 \delta(z - z')$.

A number of methods can be employed to investigate the dynamics of a 2D optical beam under variations of the nonlinearity of medium. One of the simplest to apply is the averaged Lagrangian approach. According to this method we take the Gaussian anzatz for the field [3].

$$u(r,z) = A(z)\exp(-\frac{r^2}{2a(z)^2} + \frac{ib(z)r^2}{2} + i\phi(z)), \tag{2}$$

To derive the equations for the beam parameters $A(z), a(z), b(z), \phi(z)$ one should calculate the averaged Lagrangian $\bar{L}$. The Euler-Lagrange equations for the functional $\bar{L}(z)$ lead to the following equation for a:

$$a_{zz} + a = \frac{Q(z)}{a^3}, \tag{3}$$

where $Q(z) = Q(1 + \epsilon(z)), Q = 2 - N, \epsilon = N\epsilon_0/(2 - N)$ and $z \rightarrow \sqrt{2}z$. For the focusing nonlinearity $n(z) = 1$ the variational approach predicts the critical threshold for the collapse $N_c = 2, N = \int |u|^2 dx dy/(2\pi)$, compared with the exact value $N_c = 1.862$.

We comment that, if the initial condition is close to that of the ground state (Townes) soliton, $|N - N_c| \sim \epsilon \ll 1$, then the modulation theory of [4] leads naturally to a modulation equation of the same form as the above, where again the constant 2 is replaced by the critical value 1.862. The qualitative types of behavior

exhibited by the above equation do not, of course, depend on the exact values of the constants, since all such constants can be scaled out.

We begin our analysis of the Eq.(3) by constructing the action-angle variables. Of course any two dimensional Hamiltonian system can always be reduced to quadrature, but the above system is particularly nice because the action-angle variables can be expressed in terms of elementary functions. First we note that Eq.(3) is Hamiltonian:

$$H_0(a_z, a) = \frac{a_z^2}{2} + U(a), U(a) = \frac{a^2}{2} + \frac{Q}{2a^2}. \tag{4}$$

For $N < 2, Q > 0$ the motion of the effective particle is bounded, and bounded away from 0 due to the "angular momentum" barrier $\frac{Q}{2a^2}$. If the energy is E then the width oscillates between $a_{min} = \sqrt{E - \sqrt{E^2 - Q}}$ and $a_{max} = \sqrt{E + \sqrt{E^2 - Q}}$. The minimum of the potential U occurs at $a_c = Q^{1/4}$, with a minimum energy of $E = U_c = \sqrt{Q}$. When $N > 2, Q < 0$ there is no local minimum, and there exist solutions for which $a \to 0$, corresponding to collapse of a beam. The solution for $Q > 0$ is

$$a(z) = \sqrt{E + \sqrt{E^2 - Q} \sin(2z + \psi_0)}. \tag{5}$$

The action variable J is equal to: $J = \frac{1}{2}(E - \sqrt{Q})$. The bottom of the potential well, $E = \sqrt{Q}$, corresponds to $J = 0$. Since the energy is linear in the action, $E = 2J + \sqrt{Q}$, the frequency of the unperturbed oscillations is constant $\omega = dE/dJ = 2$. This can, of course, also be seen directly from the solution given in Eq. (5). The Hamiltonian for the perturbed problem is given by $H = H_0 + \epsilon(z)V, V(a) = Q/(2a^2)$.

The perturbed equations of motion are given by $dJ/dz = -\epsilon(z)\partial V/\partial\theta, d\theta/dz = 2 + \epsilon(z)\partial V/\partial J$.

Let us consider perturbations $\epsilon(z)$ which are **periodic** in space. For simplicity we discuss the case $\epsilon(z) = \sin(\Omega z)$, though this can easily be generalized. To analyze the resonances of the beam under such perturbations we use the multiscale expansion method. We introduce the slow space $Z = \epsilon z$ and assume a multiple-scales ansatz of the form $\theta = \theta^{(0)}(z, Z) + \epsilon\theta^{(1)}(z, Z) + ..., J = J^{(0)}(z, Z) + \epsilon J^{(1)} + \epsilon J^{(1)}(z, Z) + ...$ The solution to the evolution on the fast scale is obviously $\theta^{(0)} = 2z + \Phi, J = $ constant. At the next order we find the slow Hamiltonian,

$$\bar{H}(J, \Phi) = \frac{1}{2\pi} \int_0^\pi \frac{\sin(\Omega z)dz}{(2J + Q^{1/2} + 2J^{1/2}(J + Q^{1/2})^{1/2}\sin(2z + \Phi))}.$$

It is clear that we have a resonant response whenever $\Omega = 2n$, and the period of the perturbation is commensurate with the natural period of the waveguide. Note that, even though this is a nonlinear oscillator the period is *independent* of the amplitude. The effect of this is that there is no "detuning" from the resonant frequency as the amplitude increases. Of course when J becomes large and the width oscillations become significant we no longer expect the averaged Lagrangian ODE's to provide an accurate description of the dynamics of the beam width. The first (nontrivial) resonance occurs for $\Omega = 2$. In this case the slow Hamiltonian is given by

$$\bar{H}(J, \Phi) = -\frac{\cos(\Phi)J^{1/2}}{2(J + Q^{1/2})^{1/2}Q^{1/2}}. \tag{6}$$

Note that the line $\Phi = -\pi/2$ in a phase plane is invariant under the dynamics, and along this line J evolves according to

$$\frac{dJ}{dz} = \frac{J^{1/2}}{2(J + Q^{1/2})^{1/2}Q^{1/2}}. \tag{7}$$

This solution corresponds to a resonant driving, where the variations in the scattering length reinforce the width oscillations. It is clear that for large z the action grows linearly, $J \propto t/2Q^{1/2}$ and thus amplitude of oscillations grows like $a \sim \sqrt{z}$. It is also clear from the phase portrait that all orbits for which $\Phi \neq \pi/2$ are asymptotic to the invariant manifold $\Phi = -\pi/2$, so for generic initial conditions one expects that the width will grow like $a \sim \sqrt{z}$. There is, of course, also the solution $\Phi = \pi/2$ in which the variations in the scattering length are anti-resonant with variations in the width of the beam, and act to *damp* the width oscillations. It
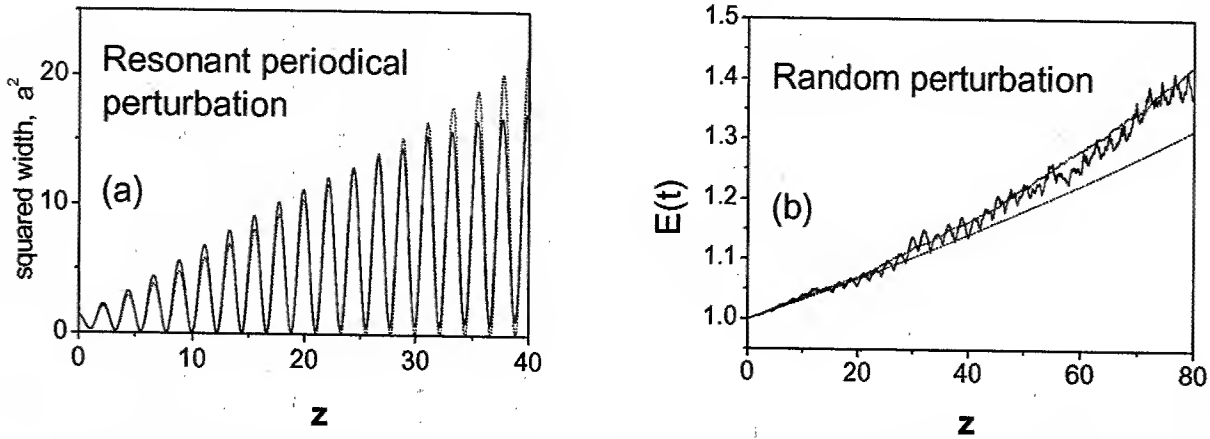
Fig. 1. (a) - Oscillations of the beam squared width at the resonant point; (b) - the energy of the beam width oscillations under random perturbation versus propagation distance z for $\sigma = 0.04$ and $N = 1$.

is easy to see that when $\Phi = \pi/2$ the action J goes to zero in finite distance. Since generic initial conditions are asymptotic to $\Phi = -\pi/2$ the $\Phi = \pi/2$ solutions are unlikely to be observed experimentally, though it is possible that they could be realized with some kind of control. The graph in Fig.1a depicts the beam squared width versus propagation distance for the ODE (dotted line) and PDE (solid line) simulations at the resonance point $\Omega = 2, N = 1$. The agreement between simulations of the full PDE and ODE is very good for distances less than 30 or so, though for distances between 30 and 40 the oscillations in the energy of the PDE are smaller than the analogous oscillations of the ODE, probably due to radiative damping. Next resonance occurs at $\Omega = 4$. Again it is easy to see that the line $\Phi = \pi/2$ is invariant under the dynamics.

For the investigation of the beam evolution under **random** modulations of the nonlinear refractive index, an interesting quantity which can be calculated is the mean distance to achieve a given distortion. From the ODE point of view this problem is equivalent to the problem of the mean distance to achieve the given level of the oscillations amplitude in the effective potential. We obtain for the distance to pass from the bottom of the potential well where the action $J_0 = 0$ to the state with the action J

$$J = \frac{\sqrt{Q}(e^y - 1)}{2 - e^y} \qquad y = \frac{\sigma^2 z}{2},$$ (8)

or in the terms of the total energy

$$E = \frac{\sqrt{Q}e^y}{2 - e^y}.$$ (9)

From the above it is easy to see that the expected distance for the width of the beam to grow to infinity - the mean distance for the beam to break up - is given by $z^* = 2\ln 2/\sigma^2$. In Fig. 1b we compare the theoretical expression Eq.(9) (dash line) with numerical simulations of the full stochastic NLS equation (solid line) and ODE (dot line) with fluctuating scattering length in the case where $\sigma = 0.04$ and $N = 1.0$. The energy has been numerically calculated for the localized part of the beam wavefunction. We observe good agreement between the theory and numerical simulations for $z \leq 80$.

Thus we have shown that the optical beam width in periodic nonlinear media with parabolic transverse profile of the refractive index has resonant oscillation and the growth rate of the beam distortion is found. This result can be also applied to evolution of 2D BEC under oscillating atomic scattering length.

References

1. L. Berge, V.K. Mezentsev, J.J. Rasmussen, P.L. Christiansen, and Yu.B. Gaididei, Opt.Lett. **25**, 1037 (2000).
2. P.O. Fedichev, Yu. Kagan, G.V. Shlyapnikov, and J. Walraven, Phys.Rev.Lett. **77**, 2913 (1996).
3. D. Anderson, M. Lisak, and T. Reichel, JOSA **B5**, 207 (1988).
4. G. Fibich, G. Papanicolaou, SIAM J.Appl.Math. **60**, 183 (1999).
5. F.Kh. Abdullaev, J.C. Bronski, and G.Papanicolaou, Physica D **135**, 369 (2000).

Non-paraxial dark solitons

P. Chamorro-Posada

*Área de Teoría de la Señal y Comunicaciones, DIEECS,Universidad de Oviedo,
Edificio Departamental 4, Campus de Viesques,33204 Gijón, Spain*

*Permanent address: Departamento de Teoría de la Señal y Comunicaciones e
Ingeniería Telemática, Universidad de Valladolid, ETSI Telecomunicación,
Campus Miguel Delibes s/n, 47011, Valladolid, Spain
Tel.: +34 985 182212, fax.: +34 985 182068,e-mail: pedro@tsc.uniovi.es*

G.S. McDonald

*Photonics and Nonlinear Science Group, Joule Physics Laboratory, School of
Sciences, University of Salford, Salford M5 4WT, UK
Tel.: +44 161 295 5079, fax.: +44 161 295 5147,e-mail:
g.s.mcdonald@salford.ac.uk*

G.H.C. New

*Quantum Optics and Laser Science, The Blackett Laboratory, Imperial College of
Science Technology and Medicine, Prince Consort Road, London SW7 2BW, UK
Tel.: +44 20 7594 7791, fax.: +44 20 7594 7714, e-mail: g.new@ic.ac.uk*

Abstract: We present an analysis of the properties of dark spatial solitons when the paraxial restriction is removed. The results reveal modifications in the soliton phase period, width and transverse velocity.

Non-paraxial effects play a fundamental role in the dynamics of optical solitons in nonlinear media. In previous work, the effects of non-paraxiality on beam propagation in self-focusing media have been addressed using a scalar approach based on the non-paraxial nonlinear Scrhödinger equation (NNSE) [1, 2, 3]

$$\kappa \frac{\partial^2 u}{\partial \zeta^2} + i \frac{\partial u}{\partial \zeta} + \frac{1}{2} \frac{\partial^2 u}{\partial \xi^2} \pm |u|^2 u = 0, \tag{1}$$

where ξ, ζ and u are the transverse and propagation coordinates and the field amplitude, respectively, obtained from their unscaled counterparts x, y and E through

$$\zeta = \frac{z}{L_D}, \qquad \xi = \frac{\sqrt{2}x}{w_0}, \qquad u(\xi,\zeta) = \sqrt{\frac{kn_2 L_D}{n_0}} E(\xi,\zeta). \tag{2}$$

w_0 is the waist of a reference Gaussian beam with diffraction length $L_D = kw_0^2/2$, $k = n_0\omega/c$, n_0 is the linear refractive index and n_2 is the Kerr coefficient. $\kappa = 1/(kw_0)^2$ is a measure of non-paraxiality and the plus (minus) sign corresponds to the focusing (defocusing) case. Earlier studies uncovered the exact non-paraxial bright soliton solution, its detailed physical interpretation[1] and general analytical properties of the solutions of the NNSE[2]. This proved fundamental in the development and testing of new non-paraxial numerical techniques[3]. A full equivalence with the nonlinear Helmholtz equation has also been noted[4]. In this work, we present an extension of previous results to defocusing nonlinear media.

Highly non-paraxial situations, defined in terms of the breadth of the angular spectrum, can arise in two distinct contexts[2]: (a) the intrinsic spatial bandwidth of a single axial beam and (b) in non-axial configurations where one or several narrow-band components propagate or interact at modest angles relative to the reference direction, or to each other. The first kind of non-paraxial scenario described is normally attributed to large field gradients and, for example, introduces a fundamental limitation to high order soliton solutions of the NSE[2]. It can also off-set the paraxial collapse of self-focusing beams in (2+1)D propagation[3, 6, 7, 5]. However, it has been shown that other mechanisms, such as polarization effects[5], can play a fundamental role and make it more difficult to isolate effects due only to non-paraxiality. The second context of non-paraxial effects presents an, arguably more important, intrinsic limitation in the paraxial description of beams. Off-axis NNSE solitons have been shown to possess invariance under rotational transformation given by:

$$\xi = \frac{\xi' + V\zeta'}{\sqrt{1 + 2\kappa V'^2}} \quad , \quad \zeta = \frac{-2\kappa V\xi' + \zeta'}{\sqrt{1 + 2\kappa V'^2}} \tag{3}$$

and

$$u(\xi,\zeta) = \exp\left[i\left(\frac{V\xi'}{\sqrt{1+2\kappa V^2}} + \frac{1}{2\kappa}\left(1 - \frac{1}{\sqrt{1+2\kappa V^2}}\right)\zeta'\right)\right]u'(\xi',\zeta'), \tag{4}$$

where the rotation angle in the original (unscaled) coordinate system is given by $\sec\theta = \sqrt{1+2\kappa V^2}$. In the appropriate paraxial limit, $\kappa V^2 \to 0$, the well known Galilean transformation invariance of the NSE is recovered. These results, in conjunction with analytical paraxial techniques[8], have been used to predict the asymptotic behavior of non-paraxial solitons[2].

We report here the exact non-paraxial dark soliton solution of the NNSE:

$$u(\xi,\zeta) = u_0\left\{A\tanh\left[u_0 A\sqrt{1 - \frac{2\kappa u_0^2 F^2}{1-4\kappa u_0^2}}\left(\xi - \frac{u_0 F}{\sqrt{1-4\kappa u_0^2 - 2\kappa u_0^2 F^2}}\zeta\right)\right] + iF\right\}$$
$$\times \exp\left[-i\frac{1}{2\kappa}\left(1 - \sqrt{1-4\kappa u_0^2}\right)\zeta\right], \tag{5}$$

where u_0 is the background amplitude and F and A are real constants with $A^2 + F^2 = 1$. The case $A = 1$ corresponds to the black soliton solution, whereas for $0 < A < 1$ grey soliton solutions are obtained from (5). In the limit $\kappa \to 0$ the general dark soliton solution of the NSE is obtained

$$u(\xi,\zeta) = u_0\left\{A\tanh\left[u_0 A\left(\xi - u_0 F\zeta\right)\right] + iF\right\}\exp\left[-iu_0^2\zeta\right]. \tag{6}$$

By comparing the paraxial and non-paraxial solutions, equations (6) and (5), one finds that for the black soliton case $F = 0$, a correction in the nonlinear phase variation is introduced in the non-paraxial solution as $4\kappa u_0^2$ is increased, which proves to be a general result when non-paraxial effects are included [1]. For grey solitons, both the soliton width and the transverse velocity are modified when the effect of non-paraxiality is included in the analysis. Whereas the soliton width is given by $u_0 A$ in the paraxial case, its actual value in the full non-paraxial framework is found to be

$$\xi_0 = u_0 A\sqrt{1 - \frac{2\kappa u_0^2 F^2}{1-4\kappa u_0^2}}. \tag{7}$$

Moreover, the transverse velocity of the grey soliton is modified from its paraxial value $u_0 F$ to

$$V = \frac{u_0 F}{\sqrt{1-4\kappa u_0^2 - 2\kappa u_0^2 F^2}}. \tag{8}$$

In the paraxial case, dark soliton solutions of the type described in (6) exist for arbitrary values of the background intensity u_0^2. This is not the case when non-paraxial effects are included in the analysis. From equation (5), one finds that propagating solutions only exist for $4\kappa u_0^2 < 1$. Using the transformations (2), this condition can be written as $2n_2 I < n_0$, where $I = |E_0|^2$ is the unscaled background intensity. Thus, dark solitons can only be found when the nonlinear phase shift is slower than the linear phase term $\exp(-jkz)$. In the defocusing case, the nonlinear phase is of opposite sign to that of the linear phase shift; this result can be interpreted as dark solitons only existing on top of travelling wave type background. Grey paraxial solitons exist for any real value of the parameter F provided that $A^2 + F^2 = 1$. When non-paraxiality is accounted for, the value of $|F|$ is limited by the condition $|F| < |F|_{max}$ when $4\kappa u_0^2 > 2/3$, where

$$|F|_{max} = \sqrt{\frac{1-4\kappa u_0^2}{2\kappa u_0^2}}, \tag{9}$$

which reveals the physical limit imposed on the fastest possible transverse variation on the moving background.

The generation, propagation and interaction of dark spatial solitons in the non-paraxial framework can be studied by using recently developed numerical techniques [3]. Figure 1 shows the propagation of two dark
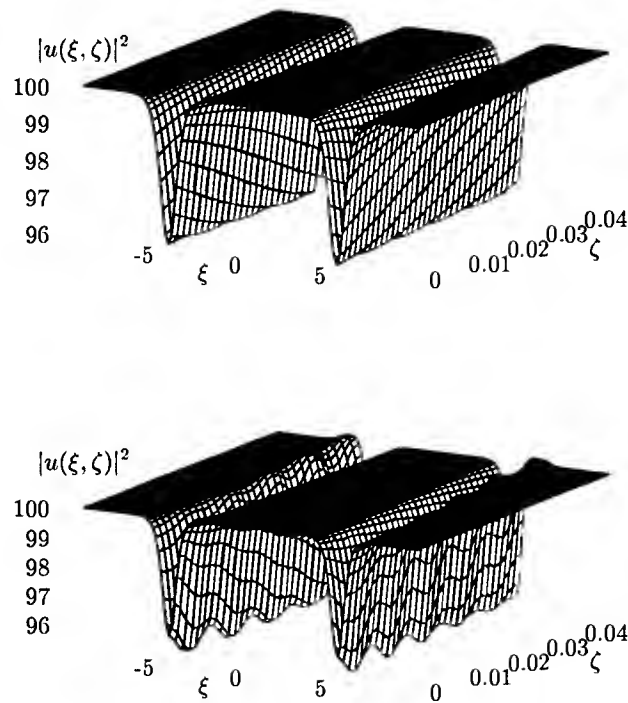
Fig. 1. Evolution of a pair of dark solitons with $A = 0.2$, $u_0 = 10$ and $\kappa = 0.001$ under the NNSE assuming initial conditions corresponding to the exact non-paraxial dark soliton (top) and its paraxial counterpart (bottom).

solitons with parameters $A = 0.2$, $u_0 = 10$, $\kappa = 0.001$ and an initial (normalized) separation of 10 under the nonparaxial evolution equation (1). The top subfigure shows the field evolution when an initial condition corresponding to the exact nonparaxial soliton (5) is assumed, whereas the bottom subfigure shows the evolution from an initial condition corresponding to the paraxial soliton (6). In this latter case, the solitons evolve to the actual shape given by (5) in a fashion similar to that found for bright solitons [2].

References

1. P. Chamorro-Posada, G.S. McDonald and G.H.C. New, "Non-paraxial solitons," J. Mod. Opt. **45**, 1111-1121 (1998).
2. P. Chamorro-Posada, G.S. McDonald and G.H.C. New, "Propagation properties of non-paraxial spatial solitons," J. Mod. Opt. **47**, 1877 (2000).
3. P. Chamorro-Posada, G.S. McDonald and G.H.C. New, "Non-paraxial beam propagation methods," Opt. Commun. **19**, 1-12 (2001).
4. P. Chamorro-Posada, G.S. McDonald and G.H.C. New, "Exact soliton solutions of the nonlinear Helmholtz equation", J. Opt. Soc. Am. B (to be published).
5. S. Chi and Q. Guo, "Vector theory of self-focusing of an optical beam in Kerr media" Opt. Lett. **20**, 1598-1600 (1995).
6. M.D. Feit and J.A. Fleck Jr., "Beam nonparaxiality, filament formation, and beam breakup in the self-focusing of optical beams", J. Opt. Soc. Am. B **5**, 633-640 (1988).
7. J.M. Soto-Crespo and N. Akhmediev, "Description of the self-focusing and collapse effects by a modified Nonlinear Schrodinger Equation," Opt. Commun. **101**, 223-230 (1993).
8. J. Satsuma and N. Yajima,"Initial value problems of one-dimensional self-modulation of nonlinear waves in dispersive media," Progr. Theor. Phys., Osasha, Supplement **55**, 284-306 (1974).
9. Y.S. Kivshar and B. Luther-Davies, "Dark optical solitons: physics and applications," Phys. Reports **298**, 81-197 (1998).

Lossless planar X-junctions induced by vector solitons

Andrey A. Sukhorukov
Nonlinear Physics Group,
Research School of Physical Sciences and Engineering,
Australian National University,
Canberra, ACT 0200, Australia
Email: ans124@rsphysse.anu.edu.au; Home page: http://www.rsphysse.anu.edu.au/nonlinear/ans
Tel: +61-2-6125-8276; Fax: +61-2-6125-8588

Nail N. Akhmediev
Optical Sciences Centre,
Research School of Physical Sciences and Engineering,
Australian National University,
Canberra, ACT 0200, Australia
Email: nna124@rsphysse.anu.edu.au; Home page: http://www.rsphysse.anu.edu.au/~nna124/
Tel: +61-2-6125-0191; Fax: +61-2-6125-5184

We propose new planar X-junctions and multi-port devices written by spatial vector solitons, which are composed of two (or more) nonlinearly coupled components in Kerr-type media. Such devices have no radiation losses at a given wavelength. We demonstrate that, for the same relative angle between the channels of the X-junctions, one can *vary the transmission coefficients* into the output channels by adjusting the *polarizations of vector solitons*. We determine analytically the transmission properties of the proposed devices.

Optical X-junctions and couplers are devices that have two waveguide channels with a weak interaction between them, so that they can swap signals after some distance[1]. In more general terms an X-junction or a coupler is a four-port device with two inputs and two outputs arranged so that the output signals depend on the parameters of the input signals (e.g., wavelength) and some internal controlling parameters (e.g., coupling coefficients).

It was suggested that two colliding spatial solitons, that are formed in a nonlinear Kerr-type medium, induce a change of refractive index, and this can be viewed as a linear X-junction or coupler[2] (see Fig. 1). Such a waveguide device can be permanently set after its creation in a photorefractive medium[3]. The transmission characteristics of the coupler depend on the soliton intensities, and on the angle of incidence between solitons[4]. On the other hand, the radiation losses are completely absent at a given wavelength. In this work, we extend the analysis of soliton-written devices to the case of vectorial, or multi-component, interactions. This extension allows us to increase significantly the flexibility of the device as the transmission coefficients become multi-parameter functions of the angle between the channels and the two polarization angles. In previous works, only one of these parameters has been used.

We consider the interaction dynamics of "vector solitons", which are composed of two or more incoherently coupled components in a medium with Kerr-type self-focusing nonlinearity. Such solitons can be observed, for example, in photorefractive crystals[5]. The soliton evolution along the propagation direction can be modeled, in the parabolic approximation, by a system of nonlinear Schrödinger equations for the set of modes, which are coupled through the change of refractive index. In the case of (1+1)-D spatial geometry, the normalized equations are
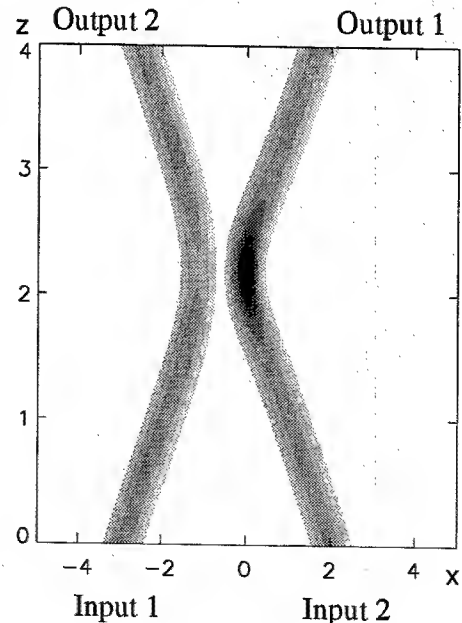
FIG. 1: Spatial distribution of refractive index created by two colliding vector solitons with amplitudes $r_1 = r_2 = 2$, velocities $\mu_1 = -\mu_2 = 1$, and relative polarization angle $\tan^{-1}(1/\rho_1^-) = \pi/3$.

$$i\frac{\partial \psi_m}{\partial z} + \frac{1}{2}\frac{\partial^2 \psi_m}{\partial x^2} + I(x,z)\psi_m = 0, \tag{1}$$

where ψ_m is the normalized amplitude of the m-th component ($1 \leq m \leq M$), M is the number of components, z is the coordinate along the direction of propagation, and x is the transverse coordinate. We assume that the change of refractive index is proportional to the total intensity,

$$I(x,z) = \sum_{m=1}^{M} |\psi_m(x,z)|^2. \tag{2}$$

Such an approximation is valid, in particular, for the description of photorefractive screening solitons in the low-saturation regime.

It was demonstrated that Eqs. (1) are *completely integrable* by means of the inverse scattering technique (IST)[6,7] and, therefore, any localized solution can be represented as a nonlinear superposition of solitary waves. Specifically, the solution for N interacting bright solitons can be found by solving a set of auxiliary linear equations[8], which we present in the following form,

$$\sum_{n'=1}^{N} \sum_{m'=1}^{M} u_{n'm'} \frac{\delta_{m'm} + (\chi_{nm} e_n)(\chi_{n'm'} e_n')^*}{k_n + k_{n'}^*} = -\chi_{nm} e_n. \tag{3}$$

Here $e_n = \exp(\beta_n + i\gamma_n)$, $\beta_n = r_n(x - \mu_n z)$, $\gamma_n = \mu_n x + (r_n^2 - \mu_n^2)z/2$, $k_n = r_n + i\mu_n$ are the complex soliton wavenumbers ($r_n > 0$ with no loss of generality), and the complex numbers χ_{nm} are arbitrary constants. The N-soliton solution of the original Eq. (1) is then obtained by adding up of all the u_{nm} functions corresponding to a given component number m,

$$\psi_m(x,z) = \sum_{n=1}^{N} u_{nm}(x,z). \tag{4}$$

Finally, a linear soliton-written device is characterized by the refractive index profile that is fixed according to Eqs. (2) and (4). As a matter of fact, the functions u_{nm} form *a full set of localized modes* of the corresponding linear Eq. (1), if the laser frequency is not changed. Below, we use this property to calculate the transmission properties of soliton-written devices.

We consider the situation when the input and output coupler channels are formed by well separated solitons. Then, solutions of Eqs. (3) can be expressed as decompositions over the profiles of individual, non-interacting, solitons,

$$u_{nm}^{\pm} = \sum_{j=1}^{N} U_{nmj}^{\pm} \mathrm{sech}\left\{ r_j[x - x_j^{\pm} - \mu_j(z - z^{\pm})] \right\} e^{i\gamma_j}, \tag{5}$$

where the signs $-$ and $+$ correspond to the input (at $z = z^-$) and output (at $z = z^+$) channels, respectively, and $x_n^{\pm}$ define the soliton positions.

In order to find the complex coefficients $U_{nmj}^{\pm}$, we analyse the properties of original Eqs. (3), . First, we note that only N modes are linearly independent, since

$$\chi_{nm_2} \sum_{n'=1}^{N} \frac{u_{n'm_1}}{k_n + k_{n'}^*} = \chi_{nm_1} \sum_{n'=1}^{N} \frac{u_{n'm_2}}{k_n + k_{n'}^*}, \tag{6}$$

for arbitrary n, m_1, and m_2. Second, we use the fact that for well separated solitons $|e_n| \gg |e_{n'}|$, if $x_n \ll x_{n'}$, and obtain the following relations:

$$S_\chi(n,j) \equiv \sum_{m'=1}^{M} U_{nm'j}^{\pm}(\chi_{nm'})^* = 0, \; x_n^{\pm} \ll x_j^{\pm}, \qquad S_k^{\pm}(n,m,j) \equiv \sum_{n'=1}^{N} \frac{U_{n'mj}^{\pm}}{k_n + k_{n'}^*} = 0, \; x_n^{\pm} \gg x_j^{\pm},$$

$$x_j^{\pm} = \mu z^{\pm} + \ln(C_j^{\pm})/r_j, \qquad C_j^{\pm} = \sqrt{\frac{S_k^{\pm}(j,m,j)}{\chi_{jm} S_A^{\pm}(j,j) S_\chi^{\pm}(j,j)}}, \qquad 2S_k^{\pm}(j,m,j) + C_j^{\pm}\left[1 + S_B^{\pm}(j,j)\right] = 0, \tag{7}$$

where

$$S_A^{\pm}(n,j) \equiv \sum_{n'=1}^{N} \frac{A_{n'j}^{\pm}}{k_n + k_{n'}^*} = 0, \; x_n^{\pm} \ll x_j^{\pm}, \qquad S_B^{\pm}(n,j) \equiv \sum_{n'=1}^{N} \frac{B_{n'j}^{\pm}}{k_n + k_{n'}^*} = -1, \; x_n^{\pm} \ll x_j^{\pm},$$

$$A_{nj}^{\pm} = B_{nj}^{\pm} = 0, \; x_n^{\pm} \gg x_j^{\pm}, \qquad A_{jj}^{\pm} = 1, \; B_{jj}^{\pm} = 0. \tag{8}$$

Using these equations, one can calculate all the complex amplitudes $U^{\pm}_{nmj}$, and the soliton shifts that are expressed through the constants $C^{\pm}_j$. Additionally, the input and output polarizations of vector solitons, can be found with the help of Eqs. (4) and (5). We note that in earlier studies the polarization rotation was only calculated for two-soliton collisions[9,10].

A multi-port linear device can be conveniently characterized by the complex transmission matrix **T**. By definition,

$$V^+_j = \sum_{j'=1}^N \mathbf{T}_{jj'} V^-_{j'}, \tag{9}$$

where $V^{\pm}_j$ are the mode amplitudes at the input $(-)$ and output $(+)$ channels created by the soliton number j. On the other hand, according to Eq. (5), $A^{\pm}_j = U^{\pm}_{nmj}$ should satisfy the relation (9) for arbitrary n and m, and these conditions can be used to uniquely determine the transmission matrix coefficients.

We now apply the above general analytical results to the description of an X-junction, which is created by two colliding vector solitons ($N = M = 2$). An example of refractive index distribution in such planar device is shown in Fig. 1. When only the first input channel is illuminated, i.e. $V^-_2 = 0$, then the power in the output channels can be found in a simple analytical form,

FIG. 2: Power splitting between the two output channels vs. the relative polarization angle $\tan^{-1}(1/\rho^-_1)$ of two vector solitons, with the wavenumbers being the same as in Fig. 1.

$$\frac{P^+_1}{P^-_1} \equiv |T_{11}|^2 = \frac{1+|\rho^-_1|^2}{1+|\rho^+_1|^2}, \quad \frac{P^+_2}{P^-_1} \equiv \frac{r_2}{r_1}|T_{21}|^2 = \frac{r_2}{r_1}\frac{1+|\rho^-_1|^2}{1+|\rho^+_2|^2}, \tag{10}$$

where

$$\rho^-_1 = \frac{\eta_2\eta_1+1}{\eta_2-\eta_1}, \quad \rho^+_1 = \rho^-_1\frac{k_1+k^*_2}{k_1-k_2}, \quad \rho^+_2 = \frac{1}{(\rho^-_1)^*}\left[(k_1+k^*_2)\frac{1+|\rho^-_1|^2}{2r_1}-1\right], \tag{11}$$

and η_j characterize the input polarizations of vector solitons, for which $|\psi_1/\psi_2| = \eta_j$, where $j = 1,2$ is the soliton number. It follows from Eqs. (10) and (11) that the *power splitting can be tuned by changing the relative polarizations* of vector solitons at the input, while the soliton amplitudes and propagation angles remain the same, as illustrated in Fig. 2. The *maximum cross-talk* is observed in the case of scalar solitons. On the other hand, solitons with orthogonal polarizations create *zero cross-talk* intersections. By tuning the relative soliton polarization, it is possible to obtain any desired power splitting in between the two extremes. For example, the junction shown in Fig. 1 has a 1:1 splitting ratio, despite the fact that the spatial distribution of the refractive index is asymmetric.

In conclusion, we have demonstrated that the X-junctions formed by colliding vector solitons in Kerr-type media can be used as ideal single-level optical integrated circuits, that can share the signal in any desired proportion between output channels. We also found that it is possible to construct zero cross-talk waveguide intersections. Such devices can be designed to have no radiation losses at any given wavelength. The parameters of arbitrary soliton induced multi-port devices can be optimized using solutions of coupled algebraic equations. The latter can readily be obtained numerically using our analytic results. NA acknowledges support from the US Army Research Office - FE.

References

[1] A. W. Snyder and J. D. Love, *Optical Waveguide Theory* (Chapman and Hall, London, 1983).
[2] N. Akhmediev and A. Ankiewicz, Opt. Commun. **100**, 186 (1993).
[3] A. Guo, M. Henry, G. J. Salamo, M. Segev, and G. L. Wood, Opt. Lett. **26**, 1274 (2001).
[4] P. D. Miller and N. N. Akhmediev, Phys. Rev. E **53**, 4098 (1996).
[5] E. DelRe, B. Crosignani, and P. Di Porto, "Photorefractive spatial solitons," in *Spatial Optical Solitons*, Vol. 82 of *Springer series in optical sciences*, S. Trillo and W. E. Torruellas, eds., (Springer-Verlag, New York, 2001), pp. 61–85.
[6] S. V. Manakov, Zh. Éksp. Teor. Fiz. **65**, 505 (1973) (in Russian) [JETP **38**, 248 (1974)].
[7] V. G. Makhan'kov and O. K. Pashaev, Teor. Matem. Fiz. **53**, 55 (1982) [Theor. Math. Phys. **53**, 979 (1982)].
[8] Y. Nogami and C. S. Warke, Phys. Lett. A **59**, 251 (1976).
[9] R. Radhakrishnan, M. Lakshmanan, and J. Hietarinta, Phys. Rev. E **56**, 2213 (1997).
[10] T. Kanna and M. Lakshmanan, Phys. Rev. Lett. **86**, 5043 (2001).
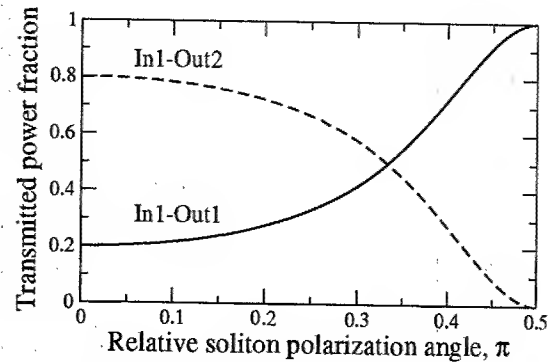
Optical vortices of parametrically coupled waves

Anatoly P. Sukhorukov and Alexey A. Kalinovich
Laboratory of Nonlinear Waves, Radiophysics Department, Physics Faculty,
Moscow State University, Leninskie Gory Moscow 119992, Russia, email aps@nls.phys.msu.su

Gabriel Molina-Terriza and Lluis Torner
Laboratory of Photonics, Department of Signal Theory and Communications,
Universitat Politecnica da Catalunya, Gran Capitan UPC-D3 Barcelona ES 08034, Spain, email torner@tsc.upc.es

We demonstrate two-component generation of one or three dislocations by equally charged input vortices, and two or four ones by oppositely charged singularities. The vortex 3D trajectories are calculated when the beams interact due to frequency conversion.

Attention of many researches is attracted to optical vortex creation, interaction and propagation in media with different nonlinear properties[1,2]. The number and position of created dislocations depend on the phase difference, amplitude ratio, and distance between the initial singularities. In quadratic media, dislocations can be transformed from one frequency to another. In particular, they can be converted to the second optical harmonic[3-5] and to the sum frequency wave[6]. Recently, dynamics of dislocations created by a linear superposition of two equally charged spatially separated vortices was investigated[7].

We consider a more general case of three-wave vortex generation by two separated dislocations. In the presence of parametric coupling, each wave has its own vortex, and the one which is transferred from another component. As a result, new dislocations appear in the beam profiles. Depending on the amplitude ratio and phase difference between the input vortices, a different number of dislocations can be created. Necessary conditions for generation of the fixed number of new vortices are specified.

In particular, a superposition of two equally charged vortices creates either one or three singularities, Fig. 1. On the other hand, either two or four singularities are generated by oppositely charged vortices, and these dislocations are located on hyperbolic curves. In case of parametric interaction between the input beams, the number of generated dislocations and their coordinates change along the propagation direction. We analyze the 3D dynamics of such dislocations in the cases of perfect phase matching, or large phase mismatch. The original analytical theory of coupled singularities is developed using a weak diffraction model. Numerical simulations of parabolic equations for the slowly varying beam envelopes are also performed. The excellent agreement with the analytical predictions is obtained.

We study a three-wave interaction of diffracting optical beams with the carrier frequencies $\omega_3 = \omega_1 + \omega_2$. At the input, vortex dislocations are superimposed on top of Gaussian beams,

$$A_{j0} = E_j \left[x - x_j + i sign(m_j)y \right]^{|m_j|} e^{-\frac{(x-x_j)^2+y^2}{w_j^2}}, \quad (1)$$

where A_j are the slowly varying amplitudes, x_j are the initial coordinates of field singularities, m_j are the vortex charges, and w_j are the beam widths.

In the following, we study parametric interactions between the vortices nested in the sum-frequency (ω_3) and difference-frequency (ω_2) components under the presence of high-intensity pump wave with the frequency ω_1 and amplitude $E_1 \gg E_{2,3}$. It should be noted that this amplitude relation is preserved at arbitrary distances in the nonlinear medium, as follows from the Manley-Rowe relations [8].

(a) (b) (c) (d) (e)

FIG. 1: The interferograms of vortices generated by plus-plus dislocations nested in the two-component beams at different propagation distance: (a) the input, (b) buildup of two new dislocations, (c) three singularities, (d) two vortex disappearance, (e) again single dislocation. Data of numerical simulation.

In order to reveal the characteristic features appearing due to the superposition of vortices in the sum- and difference-frequency waves, we consider the case of a very wide pump beam without dislocations, when $m_1 = 0$, $w_1 \gg 1$, and therefore $A_1 \simeq E_1$. If the propagation distance is smaller than the diffraction lengths of all the interacting waves, $z \ll l_{d_j} = k_j w_j^2/2$, the diffraction terms can be omitted from the dynamic equations.

Then, the vortex dynamics can be approximately modelled by only two coupled equations

$$\frac{\partial A_2}{\partial z} = -i\gamma_2 A_3 E_1^* e^{-i\Delta kz}, \quad \frac{\partial A_3}{\partial z} = -i\gamma_3 E_1 A_2 e^{i\Delta kz},$$

(2)

where γ_j are the nonlinear coefficients, and $\Delta k = k_1 + k_2 - k_3$ is the phase mismatch. Similar equations with $\Delta k = 0$ also describe two-wave interactions in gyrotropic media and photonic crystals. In gyrotropic media two orthogonal linearly polarized components are coupled [9]. In photonic crystals two one-way propagating beams can be coupled due to Laue diffraction [10]. Therefore, vortices transform from one component to the other one, and complicated dynamics occurs.

Eqs. (2) have an exact analytical solution for any component $|A_2| = |A_{20}\cos(\Gamma z) + i(\Delta k A_{20} - 2\gamma_2 E_1 A_{30})\sin(\Gamma z)/(2\Gamma)|$, where $\Gamma_0 = \sqrt{\gamma_2\gamma_3}E_1$, $\Gamma = [\Gamma_0^2 + (\Delta k/2)^2]^{1/2} = 1/L_{nl}$ is the inverse beating length. Positions of new vortex dislocations (x,y) can be determined as zeros of the amplitude profile A_2, where we assume, with no loss of generality, that $x_2 = -x_3 = x_0$, and $\beta_c = \beta\exp(i\varphi)$ is the Gaussian amplitude ratio. We compliment approximate analytical theory by direct numerical simulations of three-wave (2+1)D parabolic equations for the slowly varying beam envelopes [11]:

$$\frac{\partial A_1}{\partial z} + iD_1\Delta_\perp A_1 = -i\gamma_1 A_3 A_2^* e^{-i\Delta kz}, \quad \frac{\partial A_2}{\partial z} + iD_2\Delta_\perp A_2 = -i\gamma_2 A_3 A_1^* e^{-i\Delta kz}, \quad \frac{\partial A_3}{\partial z} + iD_3\Delta_\perp A_3 = -i\gamma_3 A_1 A_2 e^{i\Delta kz}.$$

(3)

Let us first consider the superposition of equally charged vortices, $m_2 = m_3 = 1$. Then, the generated dislocation coordinates should satisfy the relation

$$x\cosh(4xx_0 - \ln\beta) + x\cos\varphi = x_0\sinh(4xx_0 - \ln\beta).$$

(4)

New vortices are placed on the circle $x^2 + (y - x_0\cot\varphi)^2 = x_0^2\sin^{-2}\varphi$, which passes through the points $(x_0, 0)$ and $(-x_0, 0)$. Either one or three vortices are created, depending on the beam separation at the input x_0, the amplitude ratio β, and the phase difference φ. For a fixed beam separation, we use Eq. (4) to find the domains in the $(\beta, \cos\varphi)$ parameter space where three vortices are generated, and present these results in Fig. 2(left plot). Inside the domain the topological charges of three vortices alternate as plus, minus, and plus. The domain has the extreme point of a beak type at $\cos\varphi_{ex} = 4x_0^2 - 1$ on the straight line $\beta = 1$. The domain is invariant with respect to a symmetry transformation $\beta \to 1/\beta$.

In the case of $\Delta k = 0$, the amplitude ratio and phase difference are $\beta = \beta_m\tan(\Gamma_0 z)$, $\varphi = \varphi_0 - \pi/2$, where $\beta_m = (\gamma_2/\gamma_3)^{1/2}E_3/E_2$. The typical dynamics of vortex generation is presented in Fig. 3, left panel. If the beam separation is supercritical, three dislocations can be generated simultaneously [Fig. 1 and Fig. 3(a)]. Vortex dynamics is modified for out-of-phase beams [Fig. 3(b)]. A middle dislocation appears because of the diffraction-induced phase mismatch $\varphi_d = 8z[(D_3/w_3^2) - (D_2/w_2^2) - (D_1/w_1^2)] \simeq 0.056z$. We note that the analytical results are in good agreement with the results of numerical simulations.

It should be noted that a behavior of dislocations at sum and difference frequencies differ one from another. For example, if $\beta_{m32} > \beta_{m23}$, then three-vortex generation starts earlier and stops later in the difference frequency component. Thus, three-vortex region is wider for
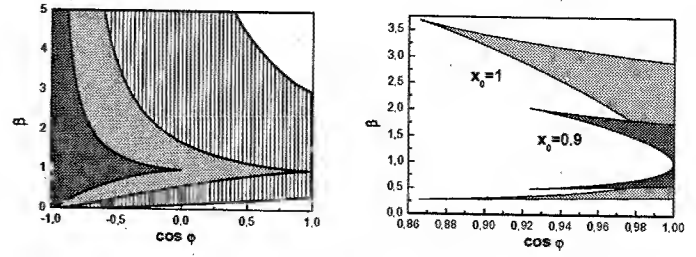
FIG. 2: Left: parameter domains for generation of three vortices by plus-plus screw dislocations at $x_0 = 0.5$ (dark gray area), $1/\sqrt{2}$ (gray), and 1 (crosshatched). Right: parameter domains for generation of four vortices by plus-minus screw dislocations at $x_0 = 0.9$ (dark gray) and 1.0 (gray).
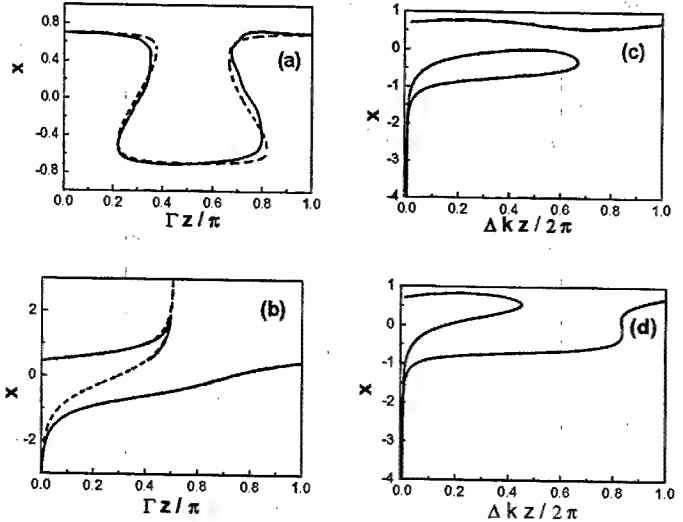
FIG. 3: Spatial dynamics of the vortices under phase matching with $\beta_m = 1$ for (a) $\varphi = \pi/2$, $x_0 = 0.7$, (b) $\varphi = \pi$, $x_0 = 0.45$, and under phase mismatch $\Delta k = 10$ with (c) $\varphi_0 = \pi/2$, $x_0 = 0.7$ for $\beta_{mm} = 1$, (d) $\beta_{mm} = 2$. Solid line corresponds to numerical simulation Eqs. (3), and dashed line to analytical solution Eq. (4).

initially weaker beam. In the degenerate case $\beta_{m32} = \beta_{m23} = 1$, the behavior of coupled vortices is same in both components.

In the phase mismatched configuration, the phase difference φ varies along the propagation distance, and spatial dynamics becomes more complicated. If the phase mismatch is large, $|\Delta k| \gg \Gamma_0$, the amplitude ratio and phase difference become $\beta(z) = \beta_{mm}|\sin(\Delta k z/2)|$, $\varphi(z) = \varphi_0 - \pi/2 - \Delta k z/2$, where $\beta_{mm} = (2\gamma_2 E_1/|\Delta k|)(E_3/E_2)$ is the maximum achievable amplitude ratio along the propagation distance z. Strong penetration of the guest dislocation occurs if β_{mm} is large. The vortex dynamics for $\Delta k = 10$ is shown in Fig. 3, right panel, for the superposition of out-of-phase beams, when three vortices are excited at the input. If β_{mm} is small, two generated vortices move towards the central region, then merge and disappear [see Fig. 3(c)]. However, when β_{mm} is large, the middle vortex moves towards the host one, and they meet and disappear [see Fig. 3(d)].

FIG. 4: 3D dynamics of plus-minus vortex superposition in the difference-frequency wave with $x_0 = 1$, $\Delta k = 0$, $\beta_m = 1$, and the phase difference (a) $\varphi = \pi/2$, (b) $\varphi = 0.2$.

Let us now turn to the case of two input vortices with opposite charges, $m_2 = 1$ and $m_3 = -1$. The coordinates of created dislocations in weak diffraction model can be found from the following equations:

$$x_0 \cosh(4xx_0 - \ln\beta) - x_0 \cos\varphi = x \sinh(4xx_0 - \ln\beta). \tag{5}$$

The plus-minus dislocations excite either two or four vortices, which are placed on hyperbolas $y^2 + 2xy \cot\varphi - x^2 + x_0^2 = 0$. We derive the analytical expressions for the boundaries for domain in the parameter space, when four vortices are generated, and present examples in Fig. 2 (right plot). Such domains consist of two parts with $\beta > 1$ and $\beta < 1$, and an extreme beak-type point appears at at $\cos\varphi_{ex} = (4x_0^2 - 1)^{1/2}/(2x_0^2)$. The four-vortex domain completely disappears for $x_0 < x_{cr} = 1/\sqrt{2}$. When $\cos\varphi < 0$, only two vortices are excited for any beam distance and amplitude ratio. In the four-vortex domain the topological charges alternate as plus, minus, plus, minus.

The typical examples of analytical theory are presented in Fig. 4. In the event that $\cos\varphi = 0$ at the input two dislocations always appear [Fig. 4 (a)]. On conditions that $\cos\varphi = 0.99$ four-vortex generation occurs [Fig. 4 (b)]. As cosine of phase difference change sign at the distance $z_{ph} = \pi/(2\Gamma)$, only two vortices are created at larger propagation distance. Contrary to plus-plus superposition (see Fig. 3) the vortex trajectories do not cross anywhere in Fig. 4.

In conclusion, we have analyzed vortex interaction in the coupled wave beams. Under the conditions of weak diffraction, we have developed an analytical description of parametrically coupled vortices in the field of wide low-frequency pump beam. The theory was applied to analyze vortex generation by the separated screw singularities with either equal or opposite charges. We have found that either one or three, or two or four vortices can be generated in these cases, respectively, and calculated the corresponding parameter domains. We have determined the trajectories of coupled vortices along the propagation direction under the conditions of phase matching, and large phase mismatch, when the input vortices are positively charged. In this case, periodic transformation between one and three vortices can occur. We have performed numerical simulations, which confirmed analytical predictions. Our results can also be applied to the description of vortex interaction due to coupling between (i) the orthogonally polarized components in gyrotropic media, and (iii) the resonantly scattered waves in photonic crystals under Bragg-resonance conditions. In all these cases, each wave can contain its own vortex, and the other vortex which is transferred from another component.

References

[1] M. S. Soskin, V. N. Gorshkov, M. V. Vasnetsov, J. T. Malos, and N. R. Heckenberg, Phys. Rev. A **56**, 4064 (1997).

[2] Yu. S. Kivshar and E. A. Ostrovskaya, Opt. Photon. News **12**(4), 24 (2001).

[3] M. Brambilla, F. Battipede, L. A. Lugiato, V. Penna, F. Prati, C. Tamm, and C. O. Weiss, Phys. Rev. A **43**, 5090 (1996).

[4] N. R. Heckenberg, M. Vaupell, J. T. Malos, and C. O. Weiss, Phys. Rev. A **54**, 2369 (1996).

[5] G. Molina-Terriza, L. Torner, and D. V. Petrov, Opt. Lett. **24**, 899 (1999).

[6] A. A. Kalinovich and A. P. Sukhorukov, Izv. Akad. Nauk Ser. Fiz. **63**, 2411 (1999) [Bull. Russ. Acad. Sci. Phys. **63**, 1866 (1999)].

[7] G. Molina-Terriza, J. Recolons, and L. Torner, Opt. Lett. **25**, 1135 (2000).

[8] Y. R. Shen, *The Principles of Nonlinear Optics* (John Wiley and Sons, New York, 1984).

[9] M. Born and E. Wolf, *Principles of Optics* (Pergamon Press, London, 1959).

[10] M. Notomi, Phys. Rev. B **62**, 10696 (2000).

[11] Yu. N. Karamzin and A. P. Sukhorukov, Zh. Eksp. Teor. Fiz. **68**, 834 (1975) [Sov. Phys. JETP **41**, 414 (1975)].
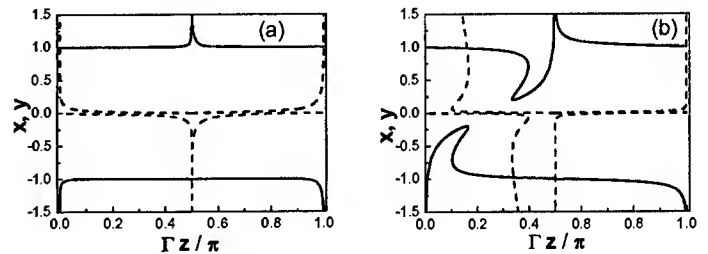
Collapse of optical vacuum pulses due to QED nonlinearities

D. Anderson, M. Lisak, M. Marklund, P. Johannisson

Dept. of Electromagnetics, Chalmers University of Technology, SE–412 96 Göteborg, Sweden
Tel.: +46 31 772 50 59, Fax: +46 31 772 15 73, E-mail: mattias.marklund@elmagn.chalmers.se

G. Brodin, L. Stenflo

Department of Plasma Physics, Umeå University, SE–901 87 Umeå, Sweden

Abstract: Due to quantum electrodynamical (QED) effects there are nonlinear corrections to Maxwell's equations in vacuum. We show that stationary two-dimensional light bullets can form, which are unstable and exhibit the possibility of self-focusing collapse.

Introduction

According to quantum electrodynamics (QED), the non-classical phenomenon of photon–photon scattering can take place due to the exchange of virtual electron–positron pairs. This is a second order effect (in terms of the fine structure constant $\alpha \equiv e^2/4\pi\varepsilon_0\hbar c \approx 1/137$), which in standard notation can be formulated in terms of the Euler–Heisenberg Lagrangian density [1, 2]

$$\mathscr{L}_{\mathrm{EH}} = \varepsilon_0\mathscr{F} + \xi(4\mathscr{F}^2 + 7\mathscr{G}^2), \tag{1}$$

where $\xi \equiv 20\alpha^2\varepsilon_0^2\hbar^3/45m_e^4c^5$, $\mathscr{F} \equiv \frac{1}{2}(E^2 - c^2B^2)$, $\mathscr{G} \equiv c\mathbf{E}\cdot\mathbf{B}$, e is the electron charge, c the velocity of light, $2\pi\hbar$ the Planck constant and m_e the electron mass.

From the Lagrangian (1), we derive the general wave equations for $\mathbf{E}$ and $\mathbf{B}$ [3]

$$\frac{1}{c^2}\frac{\partial^2\mathbf{E}}{\partial t^2} - \nabla^2\mathbf{E} = -\mu_0\left[\frac{\partial^2\mathbf{P}}{\partial t^2} + c^2\nabla(\nabla\cdot\mathbf{P}) + \frac{\partial}{\partial t}(\nabla\times\mathbf{M})\right] \tag{2}$$

and

$$\frac{1}{c^2}\frac{\partial^2\mathbf{B}}{\partial t^2} - \nabla^2\mathbf{B} = \mu_0\left[\nabla\times(\nabla\times\mathbf{M}) + \frac{\partial}{\partial t}(\nabla\times\mathbf{P})\right], \tag{3}$$

where the effective polarisation and magnetisation in vacuum due to photon–photon scattering induced by the exchange of virtual electron–positron pairs are given by (see, e.g., Ref. [4])

$$\mathbf{P} = 2\xi\left[2(E^2 - c^2B^2)\mathbf{E} + 7c^2(\mathbf{E}\cdot\mathbf{B})\mathbf{B}\right] \tag{4}$$

and

$$\mathbf{M} = -2c^2\xi\left[2(E^2 - c^2B^2)\mathbf{B} + 7(\mathbf{E}\cdot\mathbf{B})\mathbf{E}\right], \tag{5}$$

respectively.

Light bullet solutions and optical collapse

We consider propagation between two parallel conducting planes with spacing x_0 (i.e., the region $0 \leq x \leq x_0$ is vacuum surrounded by the plates that, as a starting point, are assumed to be perfectly conducting). We assume that only one TE$_{n0}$ mode ($n = 1, 2, ...$) is present. To linear order, this gives the fields

$$B_z = \frac{\pi}{x_0}\tilde{A}\cos\left(\frac{n\pi x}{x_0}\right)\exp[\mathrm{i}(kz - \omega t)] + \text{c.c.}, \tag{6}$$

$$B_x = -\mathrm{i}k\tilde{A}\sin\left(\frac{n\pi x}{x_0}\right)\exp[\mathrm{i}(kz - \omega t)] + \text{c.c.}, \tag{7}$$

$$E_y = \mathrm{i}\omega\tilde{A}\sin\left(\frac{n\pi x}{x_0}\right)\exp[\mathrm{i}(kz - \omega t)] + \text{c.c.}, \tag{8}$$

together with $0 \approx \omega^2/c^2 - k^2 - n^2\pi^2/x_0^2$. Here c.c. stands for complex conjugate, and we have expressed the fields in terms of the vector potential amplitude $\tilde{A}$, given by $\mathbf{A} = (0, A, 0)$, where

$$A = \tilde{A}\sin\left(\frac{n\pi x}{x_0}\right)\exp[\mathrm{i}(kz - \omega t)] + \text{c.c.} \tag{9}$$

using the radiation gauge ($\phi = 0$). A nonlinear dispersion relation can be derived by inserting the linear expression for the fields into the right hand side of Eq. (3), taking the z-component of the resulting equation, and separating into orthogonal trigonometric functions. From that equation the coefficients in the NLSE can be found.

Assuming that the amplitude $\tilde{A} = \tilde{A}(t, y, z)$ is weakly modulated, dropping the tilde, we obtain

$$2\mathrm{i}\omega\left(\frac{\partial}{\partial t} + v_g\frac{\partial}{\partial z}\right)A + c^2\frac{\partial^2 A}{\partial y^2} + \omega v_g'\frac{\partial^2 A}{\partial z^2} + \frac{6n^4c^4\pi^4\xi}{\varepsilon_0 x_0^4}|A|^2 A = 0, \tag{10}$$

where v_g is the group velocity and v_g' the group dispersion that follows from the linear dispersion relation. The equations can be put in a more compact by changing to a system moving with the group velocity while rescaling the coordinates and the amplitude according to

$$\tau = \omega t/2 , \quad v = \omega y/c , \quad \xi = \sqrt{\omega/v_g'}\,(z - v_g t) , \quad a = \sqrt{\frac{6n^4c^4\pi^4\xi}{\omega\varepsilon_0 x_0^4}}\,A. \tag{11}$$

Equation (10) then reads

$$\mathrm{i}\frac{\partial a}{\partial \tau} + \frac{\partial^2 a}{\partial v^2} + \frac{\partial^2 a}{\partial \xi^2} + |a|^2 a = 0. \tag{12}$$

Restricting our analysis to the cylindrically symmetric case, such that $a = a(t, \rho)$, where $\rho^2 = v^2 + \xi^2$, we see that Eq. (12) becomes

$$\mathrm{i}\frac{\partial a}{\partial \tau} + \frac{1}{\rho}\frac{\partial}{\partial \rho}\left(\rho\frac{\partial a}{\partial \rho}\right) + |a|^2 a = 0. \tag{13}$$

There are no known exact solutions to Eq. (13), but approximate solutions can be found by means of variational methods. Using as trial function [5]

$$a_T(\tau, \rho) = F(\tau)\operatorname{sech}\left[\frac{\rho}{f(\tau)}\right]\exp\left[\mathrm{i}b(\tau)\rho^2\right], \tag{14}$$

where the amplitude F is complex. Using Rayleigh–Ritz optimisation, we find that F, F^* and b can be written as explicit functions of the width $f(\tau)$, which satisfies the equation

$$\frac{d^2 f}{d\tau^2} = \gamma\left(1 - \frac{I}{I_c}\right)\frac{1}{f^3} \tag{15}$$

where $\gamma = 4(\ln 4 + 1)/(27\zeta(3)) \simeq 0.29$, $I(\tau) = f^2(\tau)|F(\tau)|^2 = f^2(0)|F(0)|^2 = I_0$, and $I_c = (2\ln 2 + 1)/(4\ln 2 - 1) \simeq 1.35$, with the solution

$$f(\tau) = f(0)\sqrt{1 + \frac{\gamma}{f^2(0)}\left(1 - \frac{I_0}{I_c}\right)\tau^2} . \tag{16}$$

Thus, Eq. (16) shows that the stationary solution is unstable and collapses to zero width in a finite time when $I_0 > I_c$. Naturally this unbounded self-focusing will eventually be saturated by some kind of higher order nonlinear mechanism. However, this will not occur before an electric field level of order $E \sim E_{\text{crit}} \equiv \varepsilon_0/\xi$ is reached, which is the field strength when both our perturbative nonlinear calculation scheme and our starting expression, the Euler–Heisenberg Lagrangian (1), breaks down. For such extreme energy densities, higher order Feynman diagrams must be included in the QED description, and possibly the corresponding physical

effects may then counteract the collapse scenario, resulting in a saturated beam radius $r_{sat} \sim r_{init} E_{init}/E_{crit}$, where E_{init} and r_{init} are the initial electric field and beam radius.

A very interesting question from a principal point of view, would be whether it is possible to have fully three-dimensional QED-structures which do not require any guiding support. However, it seems that this issue cannot be addressed within a perturbational approach, and further research is thus required.

References

1. Heisenberg W. and Euler H., Z. Physik **98**,714 (1936).
2. Schwinger J., Phys. Rev. **82**, 664 (1951).
3. Brodin G., Marklund M. and Stenflo L., Phys. Rev. Lett. **87** 171801 (2001).
4. Soljacic M. and Segev M., Phys. Rev. A **62**, 043817 (2000).
5. Desaix M., Anderson D. and Lisak M., J. Opt. Soc. Am. B **8** 2082 (1991).

Self-pumped phase conjugation in a BaTiO$_3$:Rh waveguide.

P.A. Márquez Aguilar

Facultad de Ciencias Químicas e Ingenierios; Centro de Investigaciones en Ingeniería y Ciencias Aplicadas de la Universidad Antónoma del Estado de Morelos. Av. Universidad No. 1001, Col. Chamilpa. Cuernavaca, Morelos, México. Phone/fax:(52-7) 3297084 .
pmorquez@uaem.mx

P. Mathey

Laboratoire de Physique de l'Université de Bourgogne, UMR CNRS 5027, 9 Avenue Alain Savary, 21078 Dijon Cedex France.
pmathey@n-baurgogne.fr.

P. Moretti

Laboratoire de Physico Chimie des Matériaux Luminescents, UMR CNRS 5620, Université Claude Bernard Lyon 1, 43 boulevard du 11 Novembre 1918, 69622 Villeurbanne, France.

D. Rytz

Forschunginstitut für mineralische und metallischeWerkstoffe, Edelsteine/Edelmetalle GmbH, Struthstrasse 2, Wackenmühle,55743 Idar-Oberstein, Germany.

Abstract: We present a self-pumped phase conjugator originated by self-bending of the incident beam at $\lambda = 515$ nm in a BaTiO$_3$:Rh waveguide elaborated by three successive He^+ ion implantations. Phase conjugate reflectivity reached is 28 %.
©2002 Optical Society of America.
OCIS codes: 190.5040, 190.5330, 130.2790.

Self-pumped phase conjugation in a BaTiO$_3$:Rh waveguide.

P.A. Márquez Aguilar

Facultad de Ciencias Químicas e Ingenierías; Centro de Investigaciones en Ingeniería y Ciencias Aplicadas de la Universidad Autónoma del Estado de Morelos, Av. Universidad No. 1001, Col. Chamilpa. Cuernavaca, Morelos, México, Phone/fax: (52-7) 3297084.
pmarquez@uaem.mx

P. Mathey

Laboratoire de Physique de l'Université de Bourgogne, UMR CNRS 5027, 9 Avenue Alain Savary, 21078 Dijon Cedex France.
pmathey@u-bourgogne.fr.

P. Moretti

Laboratoire de Physico Chimie des Matériaux Luminescents, UMR CNRS 5620, Université Claude Bernard Lyon 1, 43 boulevard du 11 Novembre 1918, 69622 Villeurbanne, France.

D. Rytz

Forschunginstitut für mineralische und metallischeWerkstoffe, Edelsteine/Edelmetalle GmbH, Struthstrasse 2, Wackenmühle,55743 Idar-Oberstein, Germany.

1.- Introduction

The generation of the self-pumped phase conjugation (SPPC) with photorefractive crystal is a very active research topic since its first discovery by Feinberg [1]. SPPC is easy to be used for versatile applications because it requires no external beam or optics. Ligth paths inside the crystal in this conjugator form closed loops by total internal reflections at a corner of the crystal. Then by four wave mixing, the conjugate waves are generated. Barium titanate (BaTiO$_3$) crystal is the first and the most often used material for self-pumped phase conjugation because of its high electrooptical coefficient $r_{42} \sqcup 1600$ pm/V.

In some of these papers two beams are injected to perform mutually pumped phase conjugator. The phase conjugate reflectivy of $\sqcup 20\%$ at 488 nm has been obtained in a BaTiO$_3$ waveguide implanted with H$^+$ ions using this method [2,3].

In the present study we report the SPPC in a BaTiO$_3$:Rh waveguide. One beam is injected perpendicularly to the face of the sample and we use the self-pumped configuration for producing the phase conjugate.

2. Main Results and Conclusion:

The generation of self-pumped phase conjugate beam in our waveguide results from the coupling between the self bending beam and its reflection. The observation of self bending is carried in the setup shown in Fig. 1. An Argon laser beam ($\lambda = 515$ nm) is focused to a size of nearly 10 µm by a cylindrical lens onto the front face of the waveguide. The substrate used to realize the waveguide is a rhodium doped (1000 parts in 10^6 in the melt) BaTiO$_3$ crystal grown at FEE by the top seeded solution growth technique. The planar waveguide involved in the present study has been achieved using three successive He^+ ion implantations with the energies of 2 MeV, 1.9 MeV, 1.8 MeV at respectively the doses of 5 x 10^{15}, 4 x 10^{15}, 4 x 10^{15} ions/cm^2.
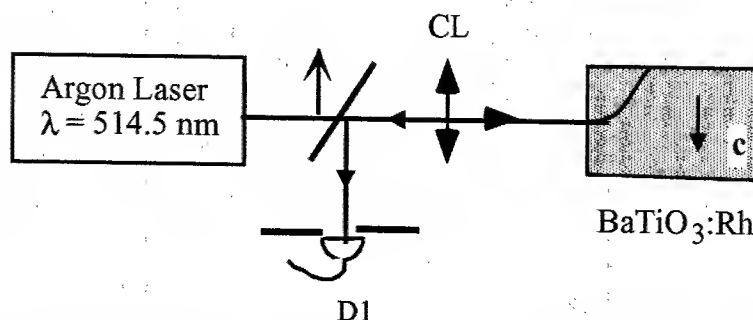
Fig. 1.- Experimental Setup. The light is injected to the waveguide by a Cylindrical lens. an the coupling efficiency is 85%.

The self-pumped phase conjugated beam is turned aside by a beam splitter and sent to a detector D1. A diaphragm is placed in front of D1 in order to select only the phase conjugate beam. As is expected when the beam is ordinary polarized we observe just the reflected beam (Fig 2a) and no phase conjugate beam. For an extraordinary polarized beam, the conjugate beam is created (Fig. 2b) via four wave mixing process [1].

It is important to remark that in our experimental configuration:
- ➤ A single input beam is injected perpendicularly to the c axis unlike as was done by W. Stephen et al. [3].
- ➤ The counter propagation beam comes from the reflection of the bending beam, with the lateral surface. This means that there exists some area where the four wave mixing acts.

(a)   (b)
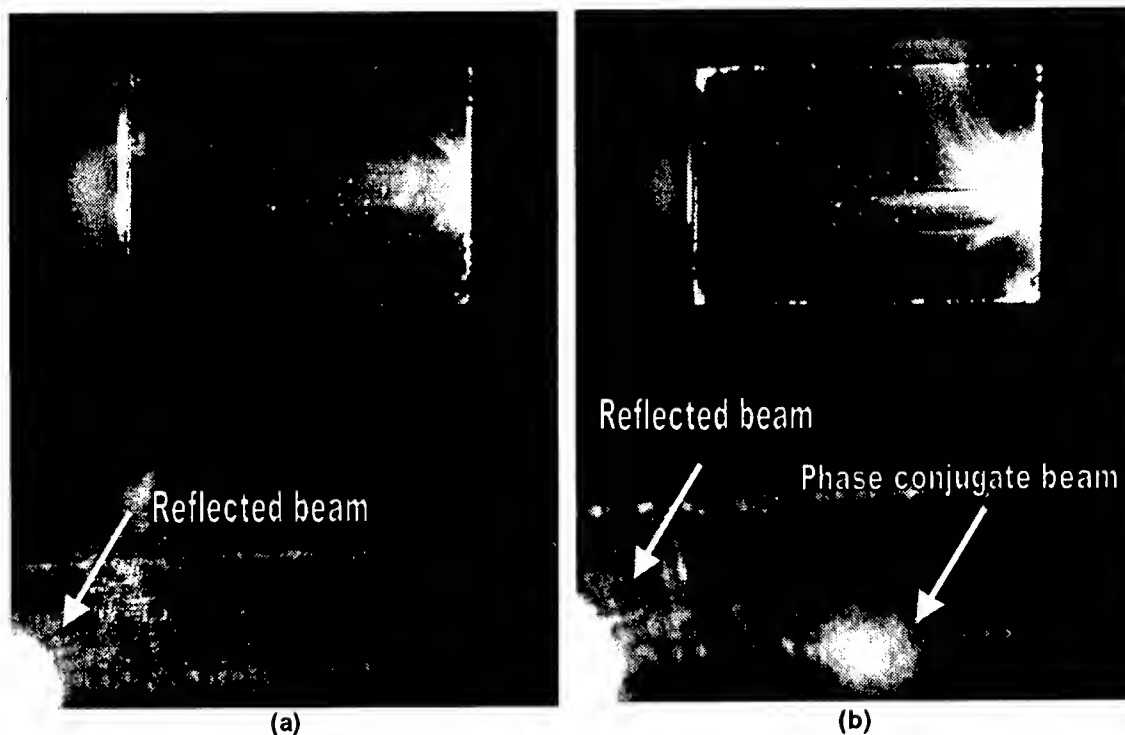
Fig. 2. Images of the beam propagation through the waveguide and the self-phase conjugate beam observed on a screen in the plane of detector D1 (see Fig. 1). a) Incident beam ordinary polarized, b) Incident beam extraordinary polarized.

The kinetics of the phase conjugate beam can be adjusted with single exponential laws by this way we obtain the response time τ. Its dependence in function of the injected intensity I is fitted according to the law I^{-x} and gives us the exponents x = 0.89 for the waveguide and x= 1.05 for the bulk. The maximum phase conjugate reflectivity observed in the waveguide is 28% (Fig. 3) approximatly 4 times higher than the value was reported by W. Stephen et al. [3]. For the bulk the phase conjugate reflectivity obtained is 10.3 %. This last value seems low in comparison with reflectivity usually obtained with $BaTiO_3$. But in our experiment, just one pump is incident on the crystal and the second pump beam is generated via the internal reflections inside the crystal. So that we can not adjust the ratio of the pump intensity to optimize the reflectivity. Nevertheless, since the experimental conditions are identical for the waveguide and the crystal we can compare our results.
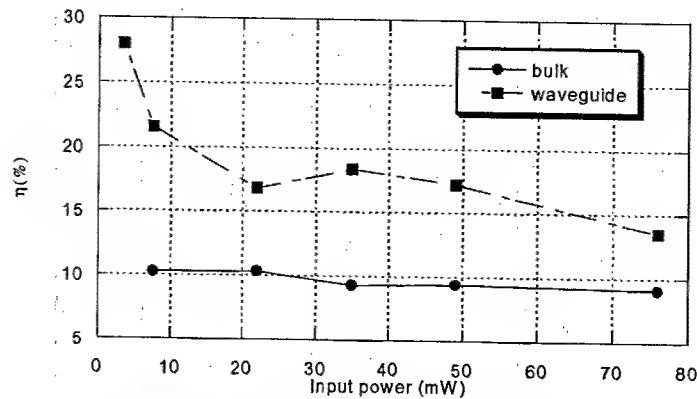
Fig. 3.- Dependence of the PC reflectivities on the input beam power.

In conclusion we present a self-pumped phase conjugator in a $BaTiO_3$:Rh waveguide, obtaining a phase conjugate reflectivity of 28%. Under the same experimental conditions at a given input intensity, the response time in the guide is approximatly 7 times shorter than in the bulk and the reflectivity obtained in the waveguide is higher. These first results are promising to realise with this guide phase conjugation at the near infrared wavelengths.

3.- References

1.- J. Feinberg, *Self-pumped, continuous-wave phase conjugator using internal reflection*, *Opt. Lett.* 7 (1982), p. 486.
2.- Stephen W. James, Katharine E. Youden, Philip M. Jeffrey, Robert W. Eason, Peter J. Chandler, Ling Zhang, and Peter D. Townsend, *BaTiO 3 waveguide self-pumped phase conjugator*", Opt. Lett. 18 (1993), p. 1138-1140.
3.- Stephen W. James, Katharine E. Youden, Philip M. Jeffrey, Robert W. Eason, Peter J. Chandler, Ling Zhang, and Peter D. Townsend, *Waveguide mutually pumped phase conjugators*", Appl. Opt. 32, (1993). 5299.

Reflection of excited vector spatial solitons from an interface between two photorefractive media.

I.V.Shadrivov

Research School of Physical Sciences and Engineering,, The Australian National University,
Canberra, ACT 0200 Australia. Email: ivsl11@yandex.ru

A.A.Zharov

Institute for Physics of Microstructures, Russian Academy of Sciences, GSP-105, Nizhny Novgorod, 603950 Russia
Tel: +7-831-2- 675-037, Fax: +7-831-2- 609-111, e-mail: zharov@ipm.sci-nnov.ru

Abstract: Momentum method towards a study of multi-component spatial solitons dynamics in photorefractive media was developed. It describes both an excitation of the soliton intrinsic degrees of freedom associated with the oscillations of centres of gravity of the beams making up the soliton and soliton interaction with nonlinear interface.

1. Introduction

In the present paper we consider vector spatial solitons in photorefractive medium in which nonlinear correction to dielectric permittivity is:

$$\varepsilon_{NL} = \frac{I}{1+sI},$$ (1)

where s is the saturation parameter, I is the distribution of the total intensity in the beam. Further we shall suppose incoherent components of vector soliton. It means that the total intensity equals to the sum of intensities of each component: $I = I_1 + I_2 + ... + I_n$, $I_j = |\Psi_j|^2$. In this case equations describing soliton components can be written in the form [1]:

$$i\frac{\partial \Psi_j}{\partial x} + \frac{\partial^2 \Psi_j}{\partial z^2} - \lambda_j \Psi_j + \varepsilon_{NL}(I)\Psi_j = 0, \ j=1,2 ...n,$$ (2)

where λ_j is relative phase mismatch parameter. In a stationary case $\partial/\partial x = 0$ and $\Psi_j = \Psi_j^{(0)}(z - z_j)$, where z_j is solitons centre of gravity. Distinctive feature of this state is that the centres of gravity of each component coincide with centre of gravity of the whole complex. In nonstationary case multi-component beam can form a bound state when amplitude of each component oscillates. One can guess that a similar excited state can appear when centres of gravity of components oscillate in the transversal direction.

2. Description of excited states of vector solitons by momentum method.

Momentum method describes electromagnetic beams in terms of average field characteristics — momenta [2]. First and second momenta are

$$P_j = \int_{-\infty}^{\infty} I_j dz, \ \bar{z}_j = \int_{-\infty}^{\infty} z I_j dz$$ (3)

P_j has a physical sense of the energy flux in the component j. $z_j = \bar{z}_j / P_j$ has the sense of the centre of gravity of corresponding beam component. Equations describing these momenta are:

$$\frac{dP_j}{dx} = 0 \ ; \ P_j \frac{d^2 z_j}{dx^2} = \int_{-\infty}^{\infty} I_j \frac{\partial \varepsilon_{NL}(I)}{\partial z} dz$$ (4)

From the set of equations (4) one can obtain that the common centre of gravity moves along a straight line:

$$\frac{d^2 z_c}{dx^2} = \frac{d^2}{dx^2} \left(\frac{z_1 P_1 + z_2 P_2 + ... + z_n P_n}{P_1 + P_2 + ... + P_n} \right) = 0.$$ (5)

To derive a closed system of equations we substitute in (5) some trial functions instead of Ψ_j. Since these functions are in the integrand, the result of integration is not sensitive to small variations of transversal soliton structure. It is natural to choose the trial function in the form of stationary solution $\Psi_j^{(0)}$. Let us consider a

particular case of two-component solitons. Transversal shift between components $\Delta = z_2 - z_1$, according to (5) is governed by the equation:

$$\overline{P}\frac{d^2\Delta}{dx^2} = -\frac{d}{d\Delta}V,$$ (6)

$$V(\Delta) = -\int_0^\Delta d\Delta' \int_{-\infty}^\infty dz I_2(z+\Delta')\frac{\partial \varepsilon_{NL}(I_1(z)+I_2(z+\Delta'))}{\partial z}$$ (7)

and $\overline{P} = \dfrac{P_1 P_2}{P_1 + P_2}$ is the effective reduced mass of the soliton. One can see that (6) allows us to use a simple

mechanical interpretation: the same equation describes relative shift between two interacting particles with masses P_1 and P_2 with potential of interaction $V(\Delta)$. Fig.1 shows effective potential profile (b) for numerically calculated one-hump soliton with two identical components (a). The minimum of potential corresponds to lowest energy state of the soliton (ground state).
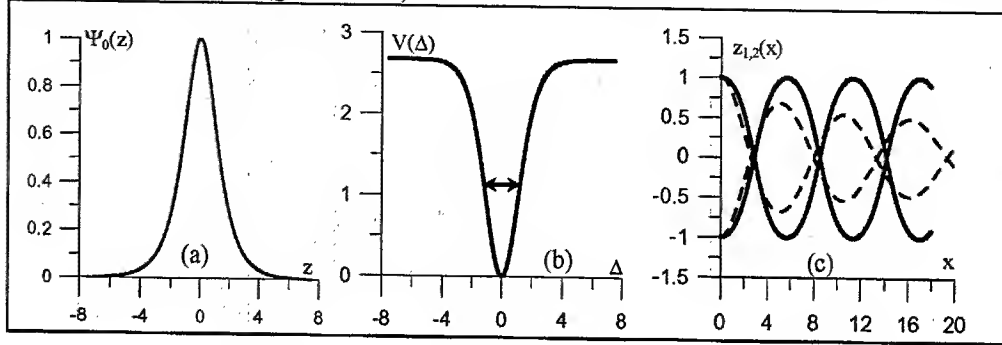
Figure 1

If transversal kinetic energy of the components is nonzero, the oscillations of the components take place (Fig.1c, solid line). Dashed lines represent numerically calculated trajectories of beams by means of Eqs.(2). One can see that we have a good agreement as far as the period of oscillations is concerned. But decreasing of the oscillations is not described by momentum method since it does not take into account radiation processes. Fig. 2 demonstrates potential profiles (b,d) for two-hump solitons, transversal structure of which is shown on fig. 2 a,c. One can see that coaxial state of the components is unstable (fig. 2b) when the amplitude of the two-hump component is essentially smaller then the amplitude of the one-hump one and it becomes stable when the amplitudes are commensurate (fig. 2d).
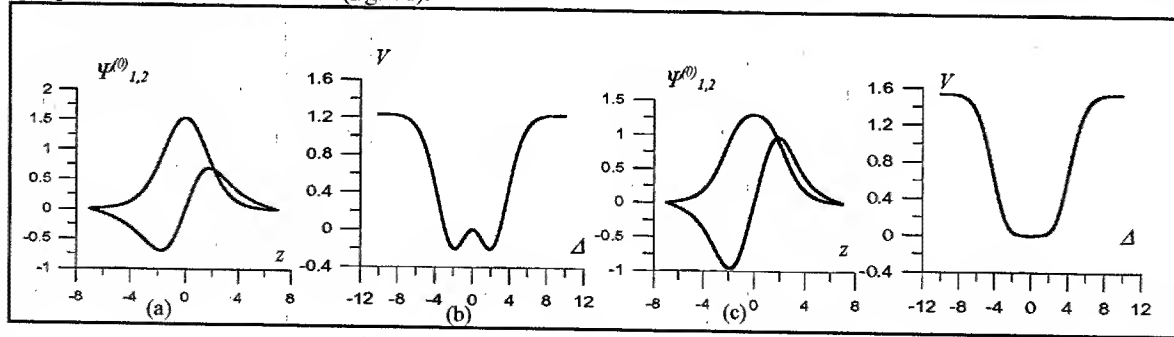
Figure 2

3. Description of excited soliton interaction with an interface.

Momentum method looks perspective in the problems of soliton dynamics in inhomogeneous media. To demonstrate it we consider two-component beams interaction with an interface (one-component beams interaction with interface was done in [3]) when linear and nonlinear properties of the medium have jumps:

$$\begin{aligned}\lambda_{1,2}(z) &= \lambda_{1,2} + \delta\lambda_{1,2}\cdot 1(z)\\ \varepsilon_{NL}(z) &= \varepsilon_{NL}(I)\cdot(1+\delta\varepsilon_{NL}\cdot 1(z))\end{aligned}, \quad 1(z) = \begin{cases}1, z \geq 0\\ 0, z < 0\end{cases}$$ (8)

It can be shown that energy flux in both beams is conserved quantity. For the centres of gravity we have:

$$P_1 \frac{\partial^2 z_1}{\partial x^2} = \int_{-\infty}^{\infty} (1 + \delta\varepsilon_{NL} \cdot 1(z)) I_1 \frac{\partial\varepsilon_{NL}(I)}{\partial z} dz - \delta\varepsilon_{NL} \cdot I_1(-z_1) + \delta\lambda_1 I_1(-z_1) \cdot \varepsilon_{NL}(I_1(-z_1) + I_2(-z_2)),$$

$$P_2 \frac{\partial^2 z_2}{\partial x^2} = \int_{-\infty}^{\infty} (1 + \delta\varepsilon_{NL} \cdot 1(z)) I_2 \frac{\partial\varepsilon_{NL}(I)}{\partial z} dz - \delta\varepsilon_{NL} \cdot I_2(-z_2) + \delta\lambda_1 I_2(-z_2) \cdot \varepsilon_{NL}(I_1(-z_1) + I_2(-z_2)). \quad (9)$$

The further result we present are obtained using one-hump soliton structure shown on fig. 3a. Parameters of the interface are as follows: $\delta\lambda_{1,2} = -0,15$; $\delta\varepsilon_{NL} = 0,2$, $s = 0$. Using ordinary differential equations (9) we have got the following remarkable results:

a) We have shown that excitation of the internal oscillations in the soliton takes place after soliton reflection from the interface (Fig. 3b) when the beam components have different masses.

b) Soliton dynamics near the interface strongly depends on the energy of internal oscillations of the beam components. On Fig. 3.c soliton components was launched to the interface at the same angle ($dz_{1,2}/dx = -0,18$) and from the same position of the common centre of gravity. The difference is in initial relative shift between components Δ: $(1) - \Delta = 0,532$; $(2) - \Delta = 0,5$; $(3) - \Delta = 0,528$; $(4) - \Delta = 0,12$. In dependence on the value of the shift reflection (1,2), transmission (4), stable (3) and unstable (1,2) surface waves excitation take place.

c) We found separation of the beams (fig. 4b) at the angle close to the angle of the total internal reflection and at a large enough values of initial transversal shift of the components ($\Delta = 2,5$; $dz_1/dx = -0,18$; $dz_2/dx = -0,33$).
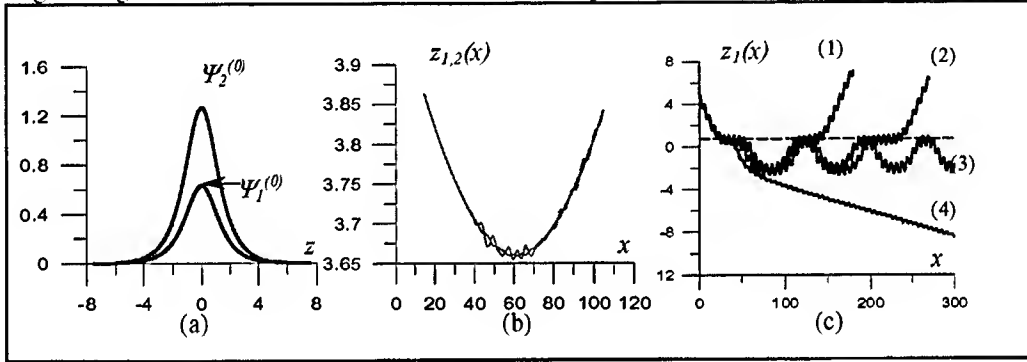
Figure 3
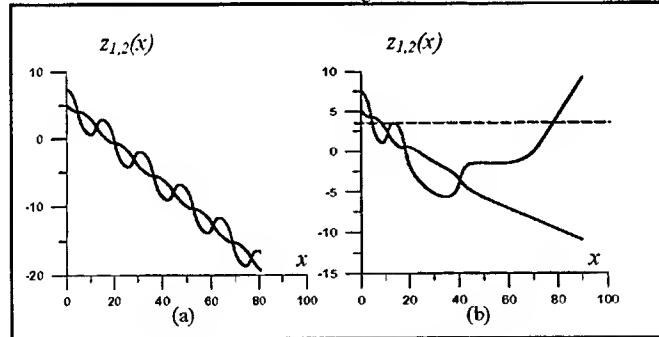
Figure 4

((a) – trajectories of the beams without interface (bound state), (a) – the same with interface (beam separation)

4. Conclusions

We presented momentum method for the problems of multi-component solitons dynamics in photorefractive medium. This method makes possible the analytical description of internal degrees of freedom of vector solitons. Also it allows us to describe soliton dynamics in inhomogeneous media. As an example, the problem of the soliton interaction with an interface was solved. It is shown, that the beam dynamics depend on the intrinsic energy state of the soliton. In dependence on the internal energy, the soliton can be reflected by the interface, can pass through, can be captured and, eventually, soliton components can be separated by the interface.

5. References

[1] E.A.Ostrovskaya and Yu.S.Kivshar, Opt. Lett. 23, 1268 (1998).
[2] S.N.Vlasov, V.A.Petrishchev and V.I.Talanov, Sov. Radiophys. 14, 1353 (1971).
[3] A.D.Boardman. P.Bontemps, W.Ilecki and A.A.Zharov, J. Mod. Opt., 47, 1941-1957 (2000)

Analysis of fields of nonlinear-cladding optical waveguides with butt-coupled linear waveguides: effects of the film index

Kiyoshi Tsutsumi

Department of Electronics and Information Science, Faculty of Engineering and Design, Kyoto Institute of Technology, Matsugasaki, Sakyo-ku, Kyoto 606-8585, Japan.

phone +81-75-724-7450, fax +81-75-724-7400, e-mail address tsutsumi@dj.kit.ac.jp

Abstract: Effects of the film index of nonlinear-cladding optical waveguides are investigated numerically. The path of a beam winds between the film and the nonlinear cladding for larger film index, whereas soliton-like emission occurs for smaller film index.
© 2002 Optical Society of America
OCIS codes: (130.2790) Guided waves; (130.4310) Nonlinear; (190.4390) Nonlinear optics, integrated optics

Optical waveguides with third-order nonlinear dielectric media are attractive for their use of various signal processing applications such as switches, power dividers, limiters, scanners, and logic elements[1 − 4]. In design of nonlinear waveguide devices, to know excited guided waves is essential. In most practical nonlinear waveguide systems, a section of nonlinear waveguides is fabricated on linear films. Consequently nonlinear waveguides are butt-coupled to linear waveguides made up of the same film. Guided mode fields of the linear waveguide are input fields to the nonlinear waveguide.

Launching of Gaussian beams or linear waveguide modes to nonlinear waveguides was analyzed numerically[5−9]. It was reported that high power guided waves generate solitons whose angles of emission depend on the input power[6−8]. Angular scanning elements based on the emission of spatial solitons were proposed[6, 10−11]. Moreover, the exchange of energy between adjacent waveguides by the transfer of spatial solitons was investigated[6, 12 − 13]. Soliton emission by launching of Gaussian beams or linear waveguide modes has been treated as a standard problem to check the accuracy of various numerical methods[14 − 16].

However, effects of the waveguide structure such as the index difference between the film and the linear part of the index of the nonlinear cladding on the the evolution of excited fields have not been reported to the best of our knowledge. The index difference and the film thickness of nonlinear waveguides may cause interesting effects on propagating fields that are not brought about in the case of linear waveguides. In this paper, effects of the index difference of nonlinear waveguides are analyzed numerically. The evolution of the profile of propagating fields is shown. The input power from butt-coupled linear waveguides is assumed to be not so high. The effect of lateral shift of a butt-coupled linear waveguide is also analyzed numerically. In addition, the effects of saturation of the dielectric permittivity and linear absorption are analyzed.

We consider fields of nonlinear-cladding planar waveguides at an optical wavelength of $0.515\mu m$. The TE_0 modal fields of a linear waveguide are incident on the end surface of a nonlinear waveguide. The refractive indices of film and substrate and the film thickness of a nonlinear waveguide are assumed to be identical with those of a linear waveguide. The nonlinear cladding shows self-focusing Kerr-type nonlinearities of index $n = n_0 + n_{2I}I$ with the local intensity I, where the linear part of index n_0 is 1.55 and the nonlinear coefficient n_{2I} is $10^{-9}m^2/W$. We assume a $1\mu m$ thick film with a index of 1.56 as the standard case. The values of the film index and the film thickness are varied from these standard values, whereas the substrate index is 1.55. The index of a linear waveguide cladding is also 1.55. The standard nonlinear waveguide and the linear waveguide support a single mode. We assume an input power of $23W/m$, in which soliton-like channels are not formed for the standard case.

The method of numerical analysis is based on the expansion of local normal modes [9, 16 − 18]. Refractive index profiles in a nonlinear cladding vary with fields intensity distributions. The nonlinear waveguide is replaced by a discrete succession of linear waveguide segments of length Δz in the propagation direction. The modes of a linear waveguide with a graded index cladding are used as local normal modes. The index profile of a nonlinear cladding approximated as multiple layers is determined by the intensity distribution
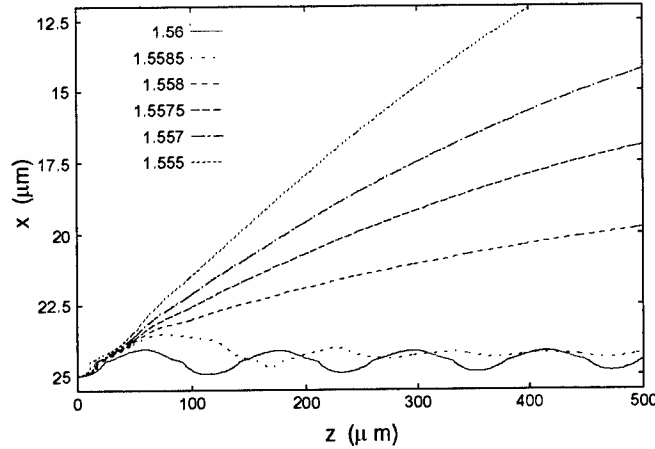
Fig. 1. Position of the peak of the E_y field as a function of z in the cases of various film indices. Film indices are 1.555, 1.557, 1.5575, 1.558, 1.5585, and 1.56.

of incident fields on the end surface of the segment [9]. Local normal modes consist of slow modes and fast modes of bounded waveguides corresponding to radiation modes and guided modes [17]. Amplitudes of local normal modes are obtained by mode matching at the interface of Δz waveguide segments. It is expected that accurate numerical results can be obtained by the superposition of local normal modes, whereas solutions of local normal modes are required.

The length of a segment is $\Delta z = 0.05 \mu m$, which is several thousandths of the segment length in the analysis of linear waveguide y-junctions. The nonlinear cladding was divided into stepwise layers of a thickness of $0.1 \mu m$. To reduce the number of the stepwise layers of a nonlinear cladding, a thickness of a nonlinear cladding was assumed to be from $5 \mu m$ to $15 \mu m$ as occasion demands. These thicknesses are more than thick enough to approximate the nonlinear cladding. A linear layer with a 1.55 index, which is the index of the nonlinear cladding of zero intensity, was assumed as the upper part of the nonlinear cladding. At each Δz segment, 30 local normal modes were calculated. The separation of bounds is $50 \mu m$ with the bounds at $x = 0$ and $x = 50 \mu m$.

The values of the film index were varied from 1.555 to 1.565. The variation of the film index means changing the difference between the film index and the linear part of index n_0 of the nonlinear cladding. In Fig.1, the position of the peak of the E_y field is plotted as a function of z for various film indices. The evolution of propagating fields for some film indices is shown in Fig.2. In Fig.2, we plot the peak values of the input field as the same value. The ratio of the peak value to the case of 1.56 is 0.923 for 1.557. The maximum index increase in the nonlinear cladding is 0.025 for a film index of 1.56. For other film indices, the maximum index increase is 0.022 for 1.555, 0.025 for 1.557, 0.027 for 1.558, 0.025 for 1.559, 0.020 for 1.562, 0.015 for 1.565. Although these values of the maximum index increase are almost same, drastically different paths of beams are caused.

For the film index greater than 1.558, the path of the beam winds. In the waveguide with a film of a 1.565 index, fields are almost confined to the linear film including the peak of the E_y field. For a film index less than 1.563 ($1.558 < n_f < 1.563$), beams penetrate into the nonlinear cladding, after which the beams return to the linear film. This movement of beams is iterative. In the nonlinear cladding, a change of the x coordinate with respect to an increase of the z coordinate is slower than in the linear film. For a film with lower index, a beam penetrate deeper into the nonlinear cladding. Moreover, damping of the oscillation of path is faster for the lower film index. The winding path of a beam depends on the input power level as well as the difference in location between the input beam and the nonlinear modal field (NMF) [18]. Although waveguides are excited at a fixed input power level, similar effects to waveguides excited at a higher input power are caused by waveguides with lower film index.

For the film index less than 1.5583, a beam is emitted to the nonlinear cladding. The lower film index in Fig. 1 causes the larger angle of emission. The angle of emission depends on the film index. The increase of the angle is decreased as the film index is decreased. For the waveguides with fixed film index, the higher input
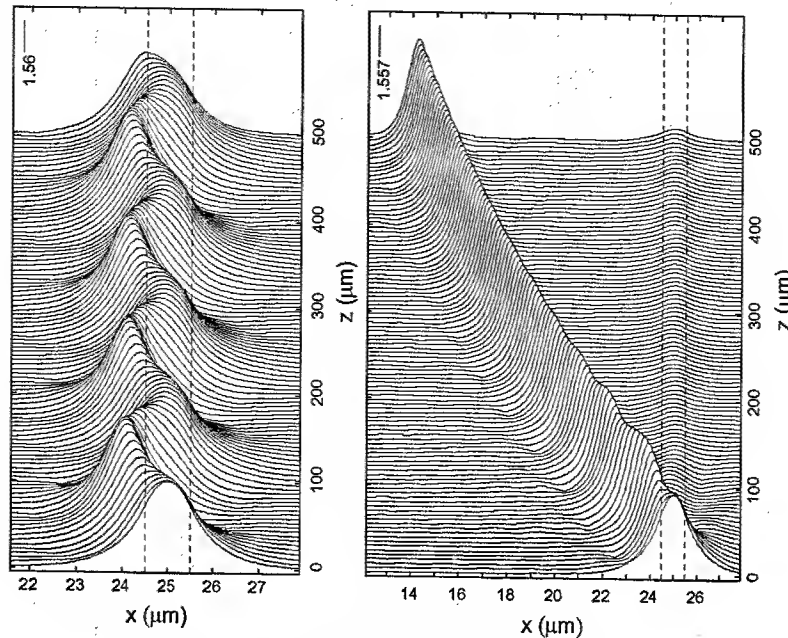
Fig. 2. Evolution of the E_y field in the cases of various film indices. The interface of a film and a nonlinear cladding ($x = 24.5\mu m$) and the film-substrate interface ($x = 25.5\mu m$) are shown in dashed lines. Film indices are 1.56 (left) and 1.557 (right).

power causes the greater angle of emission. We have possibilities that beam characteristics with high input power are obtained at medium power levels by lowering the film index.

In the case of a large index difference between the film and the linear part of the index of the nonlinear cladding, the path of a beam winds between the film and the nonlinear cladding or in the film. For the small index difference, a beam of the same power is emitted to the nonlinear cladding. On the other hand, the change of the film thickness does not lead to drastic change in propagating fields. The lateral shift of a butt-coupled linear waveguide affects the path of a beam. In the case in which the path is winding for zero lateral shift, the emission to the nonlinear cladding is caused by shifting the butt-coupled linear waveguide toward the substrate. The input beam travels toward the location of the NMF. After passing the location, the beam is forced to turn back or emitted into the nonlinear cladding with an angle. The saturation of the permittivity of nonlinear media decreases the amplitudes of oscillation of a winding path or the angles of emission. The angle of emission as well as the oscillation of a winding path decays owing to the linear absorption of nonlinear media.

References

1. C. T. Seaton, X. Mai, G. I. Stegeman, and H. G. Winful, Opt. Eng., **24**, 593-599 (1985).
2. G. I. Stegeman, E. M. Wright, N. Finlayson, R. Zanoni, and C. T. Seaton, J. Lightwave Technol., **6**, 953-970 (1988).
3. D. Mihalache, M. Bertolotti, and C. Sibilia, in *Progress in Optics XXVII*, E. Wolf, ed. (Elsevier, 1989), pp.227-313.
4. M. Bertolotti, in *Advances in Integrated Optics*, S. Martellucci, et al. eds. (Plenum Press, 1994), pp.21-55.
5. E. M. Wright, G. I. Stegeman, C. T. Seaton, and J. V. Moloney, Appl. Phys. Lett. , **49**, 435-436 (1986).
6. E. M. Wright, G. I. Stegeman, C. T. Seaton, J. V. Moloney, and A. D. Boardman, Phys. Rev. A , **34**, 4442-4444 (1986).
7. M. A. Gubbels, E. M. Wright, G. I. Stegeman, C. T. Seaton, and J. V. Moloney, J. Opt. Soc. Am. B , **4**, 1837-1842 (1987).
8. L. Leine, C. Wächter, U. Langbein, and F. Lederer, J. Opt. Soc. Am. B , **5**, 547-558 (1988).
9. S. Ohke, T. Umeda, and Y. Cho, Trans. IEICE C-I, **J73-C-I**, 573-579 (1990). (in Japanese)
10. P. Varatharajah, A. B. Aceves, and J. V. Moloney, Appl. Phys. Lett. , **54**, 2631-2633 (1989).
11. F. Farjady, M. G. F. Wilson, and P. M. Radmore, IEEE Photon. Technol. Lett., **8**, 1047-1048 (1996).
12. D. P. Heatley, E. M. Wright, and G. I. Stegeman, Appl. Phys. Lett. , **53**, 172-174 (1988).
13. H.E. Hernández-Figueroa, F. Di Pasquale, R.D. Ettinger, F.A. Fernández, and J.B. Davies, Opt. Lett. ,**19**,326-328(1994).
14. M. Bertolotti, P. Masciulli and C. Sibilia, J. Lightwave Technol., **12**, 784-789 (1994).
15. H. Yokota, M. Hira, and S. Kurazono, Trans. IEICE C-I, **J77-C-I**, 529-535 (1994). (in Japanese)
16. T. Rozzi, and L. Zappelli, J. Lightwave Technol., **14**, 229-235 (1996).
17. K. Tsutsumi, Y. Imada, H. Hirai, and Y. Yuba, J. Lightwave Technol., **6**, 590-600 (1988).
18. K. Tsutsumi, and E. Aoki, Appl. Opt. , **39**, 3644-3648 (2000).

Interaction of Incoherently Coupled Transversely Asymmetric Beams

P. Papagiannis (__panospan@central.ntua.gr__) and
K. Hizanidis (__kyriakos@central.ntua.gr__)

Department of Electrical and Computer Engineering,
National Technical University of Athens
9 Iroon Polytechniou Str. 157 73, Athens, GREECE
Tel.: 30 10 772 3685, 2470
Fax: 30 10 772 3513

Abstract: The stationary evolution of two incoherently coupled beams of bi-Gaussian intensity profile propagating in a bulk Kerr or saturable medium is studied variationally. The stability is investigated on the basis of the Vakhitov-Kolokolov criterion and comparisons are made with numerical integration of the (2+1)D coupled NLS equations involved.

SUMMARY

The model which describes the evolution of two incoherently coupled beams propagating in a bulk Kerr or saturable medium is the following [the function $f(|E_1|, |E_2|, \omega_1, \omega_2)$ refers to the case of a saturable medium] [1]:

$$i\frac{\partial E_1}{\partial z} + \Delta_\perp E_1 - E_1 \left\{ \frac{(\eta^{-1}|E_1| + \sigma|E_2|)}{f(|E_1|, |E_2|, \omega_1, \omega_2)} \right\} = 0 \tag{1}$$

$$i\kappa\frac{\partial E_1}{\partial z} + \Delta_\perp E_1 - E_2 \left\{ \frac{\gamma(\eta|E_2| + \sigma|E_1|)}{f(|E_2|, |E_1|, \omega_2, \omega_1)} \right\} = 0, \tag{2}$$

where E_1, E_2 are the slowing varying beam envelopes, $\Delta_\perp = \partial^2_x + \partial^2_y$, η and κ are the squared frequency wave-number ratios respectively. Finally, the parameter σ ($\sigma > 0$) refers to the polarization of the interacting fields while $\gamma = 1$ ($\gamma = -1$) corresponds to a focusing (defocusing) nonlinearity.

The variational method is applied with the following bi-Gaussian ansatz for the field envelope functions:

$$E_i(x, y, z) = \alpha_i(z)\exp\left(-\frac{\chi^2}{X_i^2(z)} - \frac{y^2}{Y_i^2(z)}\right)\exp(i\phi_i(z)) \quad i = 1, 2, \tag{3}$$

where,

$$\chi = (x - x_{0i}(z))\cos(\theta_i(z)) + (y - y_{0i}(z))\sin(\theta_i(z))$$
$$y = -(x - x_{0i}(z))\sin(\theta_i(z)) + (y - y_{0i})\cos(\theta_i(z)) \quad i = 1, 2 \tag{4}$$

Thus, we consider beams of elliptical cross sections with evolving semi-axes and centers as well as rotating, while colliding, with respect to a fixed reference system.

For $\gamma = 1$ the Lagrangian is real while $\gamma = -1$ acquires an imaginary part as well. However, one in general can split the Lagrangian into a functional L_C corresponding to the

"conservative" part of the dynamical system in hand and a non-conservative part L_{NC} [2-5]. Integration over the cross section easily yields the following averaged conservative part of the Lagrangian:

$$\langle L_C \rangle = -\frac{\pi}{2} a_1^2 X_1 Y_1 \sec(2\theta_1)\phi_1' - \frac{\pi}{2} a_2^2 X_2 Y_2 \sec(2\theta_2)\phi_2' +$$

$$-\frac{\pi}{8\eta} a_1^4 X_1 Y_1 \sec(2\theta_1) - \frac{\pi\eta}{8} a_2^4 X_2 Y_2 \sec(2\theta_2)$$

$$\sum_{i=1}^{2} \left(2a_i^2 \left(\pi X_i Y_i \sec(2\theta_i) - 4\right)\right)$$

$$\times\left(\frac{1}{X_i^2}\left(x_{0i}\cos(\theta_i) + y_{0i}\sin(\theta_i)\right)^2 + \frac{1}{Y_i^2}\left(y_{0i}\cos(\theta_i) - x_{0i}\sin(\theta_i)\right)^2\right) -$$

$$\frac{\pi\alpha_i^2}{2X_i Y_i}\sec^2(2\theta_i)\left(X_i^2 Y_i^2 \sec(2\theta_i) + X_i^4 \cos^2(\theta_i)\left(2\sec(2\theta_i) - 1\right) -\right.$$

$$\left. Y_i^2 \sin^2(2\theta_i)\right) +$$

$$\frac{8\pi\sigma}{X_1 X_2 Y_1 Y_2} \alpha_1^2 \alpha_2^2 \exp(\Omega)$$

$$\left(\frac{X_1^2\left((y_{01} - y_{02})\cos(2\theta_1) + (x_{01} - x_{02})\sin(2\theta_1)\right)^2 + X_2^2\left((y_{01} - y_{02})\cos(2\theta_2) + (x_{01} - x_{02})\sin(2\theta_2)\right)^2}{\sqrt{X_1^2 Y_1^2 + X_2^2 Y_1^2 + \left(X_2^2 Y_1^2 + X_1^2 Y_2^2\right)\cos^2(\theta_1 - \theta_1) + \left(X_1^2 X_2^2 + Y_1^2 Y_2^2\right)\sin^2(\theta_1 - \theta_1)}} +\right.$$

$$\left.\frac{X_1^2\left((y_{01} - y_{02})\cos(2\theta_1) + (x_{01} - x_{02})\sin(2\theta_1)\right)^2 + X_2^2\left((y_{01} - y_{02})\cos(2\theta_2) + (x_{01} - x_{02})\sin(2\theta_2)\right)^2}{\sqrt{X_1^2 Y_1^2 + X_2^2 Y_1^2 + \left(X_2^2 Y_1^2 + X_1^2 Y_2^2\right)\cos^2(\theta_1 - \theta_1) + \left(X_1^2 X_2^2 + Y_1^2 Y_2^2\right)\sin^2(\theta_1 - \theta_1)}}\right)$$

(5)

The variational equations yield a set of equations which represent a dynamical system evolving in z. The form of this complicated system for the case $\gamma = 1$ is as follows:

$$f_j\left(\phi_1'; b_i, c_i, \theta_1 - \theta_2\right) = 0 \quad j = 1,..,4$$
$$f_k\left(\alpha_1, b_i, c_i, \theta_1 - \theta_2\right) = 0 \quad k = 1,2$$
$$f\left(\alpha_1', X_1', Y_1', \theta_1'\right) = 0$$

and

$$g_j\left(\phi_2'; b_i, c_i, \theta_1 - \theta_2\right) = 0 \quad j = 1,..,4$$
$$g_k\left(b_i, c_i, \theta_1 - \theta_2\right) = 0 \quad k = 1,2$$
$$g\left(\alpha_2', X_2', Y_2', \theta_2'\right) = 0$$

where $\{b_i\} = \{\alpha_1, x_{01}, y_{01}, X_1, Y_1, \theta_1, \varphi_1\}$ and $\{c_i\} = \{\alpha_2, x_{02}, y_{02}, X_2, Y_2, \theta_2, \varphi_2\}$

As far as the case $\gamma = -1$ is concerned additional terms enter in Eq. (5) due to the presence of the non-conservative force $Q_{NC} = 2\sigma |E_1|^2 E_2$, namely the term

$$2\,\mathrm{Re}\int dx \int dy Q_{NC} \frac{\partial E_2^*}{\partial c_i}$$

The dynamical systems in hand are investigated and the issue of the stability of the proposed ansatz is addressed in the framework of Vakhitov-Kolokolov criterion. Comparisons of the results thus obtained are made with direct numerical integration of the sysyem(s) given by Eq. (1).

References

1. J.N.Malmberg, A.H.Carlsson, D.Aderson, M.Lisak, E.A.Ostovskaya, Y.S Kivshar, *"Vector solitons in (2+1) dimensions"*, (preprint)arXiv:patt-sol/9912001 v1, A.H.Carlsson *et all 'Linear and nonlinear waveguides induced by optical vortex solitons"* , (preprint) arXiv:patt-sol/9909009 v2.

2. P.M. Morse, H.Fesbach *Methods of theoretical physics* ,NY, Mc Graw-Hill, 1953.

3. D.Anderson *'Variational approach to nonlinear pulse propagation in optical fibers"* , Phys. Rev .A 27 (1983.) 3135.

3. Y. S. Kivshar,W. Krolikowski *'Lagrangian approach for dark solitons"* , Opt. Com. 114 (1995) 353.

4. F. Kh. Abdullaev, J. G. Caputo *'Validation of the variational approach for chirped pulses in fibers with periodic dispersion"*, Phys. Rev. E 58 (1998) 6637.

5. S.C.Cerda, S.B.Cavalicanti, J.M. Hickmann *'A variational approach of nonlinear dissipative pulse propagation"*, Eur. Phys. J. D 1 (1998) 313.

Spatial Solitons in nematic liquid crystals: a new model

Claudio Conti, Marco Peccianti and Gaetano Assanto

National Institute for the Physics of Matter, University "Roma Tre"
Via della Vasca Navale, 84, 00146 Rome, Italy
Tel. (+39)0655177028, Fax (+39)065579078, assanto@ele.uniroma3.it

In a linear medium the simplest physically realizable spatial wave-packet is the gaussian beam, which spreads during propagation. Surprisingly enough, in nonlinear media it is replaced by an even simpler entity: the spatial soliton. The latter is the basic concept for understanding the interplay between diffraction and nonlinearity, and its universality is confirmed by the several and diversified media where it has been theoretically predicted and experimentally observed. [1] We propose a novel model describing spatial solitons in nematic liquid crystals, and supporting the recent experimental investigations carried out on 3D solitons due to a re-orientational nonlinearity. Our approach immediately sets this new family of nonlinear waves in the framework of the recent results obtained for quadratic solitary waves, as well as for nonlocal media, and it permits to understand the basic mechanism of energy trapping and stabilization in the phenomena observed in undoped nematics. The model described hereby catches the underlying physics and generalizes in a substantial way previous approaches, limited to an equivalent Kerr response [2], or neglecting the effects of an external bias [3].

For the sake of concreteness, we will refer to the geometry of the experiments reported in [4], where an external electric field determines a rest value θ_0 of the tilt angle of the molecular director in the bulk of the planar cell (see figure 1). Our approach, however, also holds when such a distribution is obtained otherwise, for example in the presence of a magnetic field [5].

The spatial distribution of the tilt angle in the cell $\hat{\theta}(Z)$, determined by the X-directed static (or low frequency) electric field E (rms value), is given by

$$K\frac{d^2\hat{\theta}}{dZ^2} + \frac{\varepsilon_{RF}E^2}{2}\sin(2\hat{\theta}) = 0$$

where K is the Frank's elastic constant (taken equal for splay, bend and twist), ε_{RF} is the low-frequency dielectric anisotropy and, for planar alignment, $\hat{\theta}$ vanishes at the cell boundaries (top and bottom along X, see figure 1). In the presence of an X-directed optical field of amplitude A, neglecting vectorial effects, the tilt distribution is altered due to a field-dipole torque. Taking $\hat{\theta}$ as a slowly varying function and writing $\theta(X,Y,Z) = \hat{\theta}(X) + \frac{1}{2}\Psi(X,Y,Z)$ for the whole angle distribution, in the limit of a large (thick) cell we obtain the following equation (1st- order in Ψ):

$$K\Delta\Psi - \varepsilon_{RF}E^2\frac{\sin(2\theta_0)}{2\theta_0}\Psi + \frac{\varepsilon_0 n_a^2|A|^2}{2}\sin(2\theta_0) = 0 \tag{1}$$

with n_a^2 the optical dielectric birefringence [6]. In deriving (1) we made the additional hypothesis that $\theta_0 \cong \pi/4$. The latter is realized by an appropriate value of E, and provides the highest nonlinear response.

With regards to the Z-propagating optical field in the paraxial approximation, for a cell much wider than the beam waist, we get the corresponding Foch-Leontovich equation

$$2ik\frac{\partial A}{\partial Z}+\nabla_{XY}^2 A+\frac{k_0 n_a^2}{2}\sin(2\theta_0)\Psi A = 0 \qquad (2)$$

where $k=k_0\sqrt{n_\perp^2+n_a^2\sin(\theta_0)^2}$, k_0 the vacuum wavenumber and $n_\perp$ the refractive index "seen" by the X-polarized beam when $\theta_0 = 0$. Equations (1) and (2) constitute the basic model for our analysis, and show the nonlinear interaction between the material response and the light field. After a suitable normalization, we can recast them in a dimensionless format:

$$i\frac{\partial a}{\partial z}+\nabla_{xy}^2 a - a + \psi a = 0$$

$$\epsilon\frac{\partial^2\psi}{\partial z^2}+\nabla_{xy}^2\psi-\alpha\psi+\frac{1}{2}|a|^2 = 0. \qquad (3)$$

The two parameters introduced in (3) are defined as

$$\alpha = \frac{\varepsilon_{RF}E^2}{2kK\beta}\frac{\sin(2\theta_0)}{2\theta_0}$$

$$\epsilon = \frac{\beta}{2k},$$

with β the nonlinear correction to the wavevector k. As discussed below, α determines the degree of nonlocality of the medium, and ϵ is expected to be small.

Solitary-wave solutions are obtained from eqs. (3) by setting $\partial_z = 0$. For a a real amplitude, the soliton profile is determined by the system

$$\nabla_{xy}^2 a - a + \psi a = 0$$

$$\nabla_{xy}^2\psi-\alpha\psi+\frac{1}{2}a^2 = 0. \qquad (4)$$

Equations (4) are the very same describing (1D and) 2D spatial solitons in quadratic media, with ψ playing the role of the optical second harmonic. Thus we establish for the first time an important connection between two rather different physical systems which, in the limit of the adopted approximations, turn out to support the same solitary solutions.

With emphasis to 2D self-trapped beams, it is natural to wonder which mechanism inhibits collapse and filamentation. The question naturally arises when dealing with the stability of the spatial solitons, and can be initially addressed assuming for simplicity $\epsilon = 0$. By letting $a = \sqrt{2\alpha}\varphi\, e^{iz}$ and rewriting eqs. (3) as

$$i\varphi_z+\nabla_{xy}^2\varphi = -\frac{|\varphi|^2}{1-\nabla^2/\alpha}\varphi \cong -(|\varphi|^2+\frac{1}{\alpha}\nabla_{xy}^2|\varphi|^2)\varphi, \qquad (5)$$

with the last equality holding for large α (a condition satisfied when Ψ is small). It is immediate to recognize the spatial nonlocality as the stabilizing effect. Indeed, when the beam shrinks, the term with spatial derivatives of the intensity counterbalances the Kerr-like term. As anticipated, α identifies the degree of nonlocality in the medium. When the smallness condition on Ψ fails, the saturable nature of the nonlinearity does contribute. A rigourous analysis of these issues will be presented.

In conclusion, in this Communication we discuss a theoretical model of spatial solitons in undoped nematic liquid crystals, underlining the link with parametric simultons and nonlocal nonlinearities. The general properties of this new type of self-trapped beams will be discussed, including their stability and the comparison with the recent experiments performed in our laboratory.
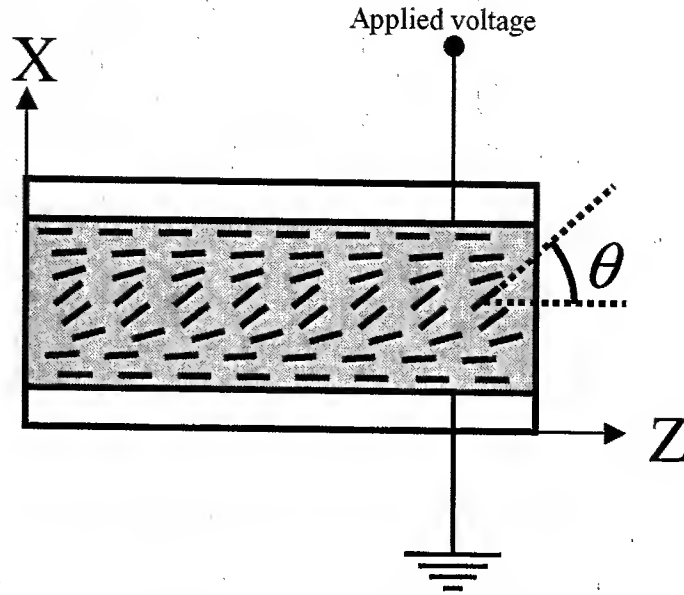
Figure 1. Reference geometry, as employed for the experiments reported in [4]. The liquid crystal cell and the spatial distribution of the directors and are sketched.

References

[1] *Spatial Solitons*, S. Trillo and W. E. Torruellas eds., Springer-Verlag, Berlin (2001)

[2] M. A. Karpierz, M. Sierakowski, M. Swillo and T. Wolinski, Mol. Cryst. Liq. Cryst. **320**, 157 (1998)

[3] D. W. McLaughlin, D. J. Muraki, M. J. Shelley, and X. Wang, Physica D **88**, 55 (1995)

[4] M. Peccianti, A. De Rossi, G. Assanto, A. De Luca, C. Umeton, and I. C. Khoo, Appl. Phys. Lett. **77**, 7 (2000)

[5] N. V. Tabiryan, A. V. Sukhov, and B. Ya. Zel'dovich, Mol. Cryst. Liq. Cryst. **136**, 1 (1986)

[6] I. C. Khoo, *Liquid Crystals*, John Wiley & Sons, New York (1995).

Exact soliton solutions of the quintic complex Swift-Hohenberg equation

Adrian Ankiewicz

Applied Photonics Group, Research School of Physical Sciences and Engineering,
The Australian National University, Canberra ACT 0200, Australia
phone: (+612) 61253423, fax: (+612) 61255184, e-mail:
ana124@rsphysse.anu.edu.au

Kenichi Maruno

Research Institute for Applied Mechanics, Kyushu University, Kasuga Koen,
Kasuga, Fukuoka, 816-8580, Japan
phone: (+81)92-583-7684, e-mail: maruno@riam.kyushu-u.ac.jp

Nail Akhmediev

Optical Sciences Centre, Research School of Physical Sciences and Engineering,
IAS, Australian National University, ACT 0200, Australia
ph: (+612) 61250191, fax: (+612) 61255184, e-mail:
nna124@rsphysse.anu.edu.au

Abstract: Several soliton solutions of the complex quintic generalised complex Swift-Hohenberg equation (CSHE) are found analytically. These solutions exist for certain relations between the parameters of CSHE which are also presented analytically.
© 2002 Optical Society of America
OCIS codes: 190.4420 Nonlinear optics, transverse effects; 140.3430 Laser theory

1. Introduction. Complicated pattern-forming dissipative systems can be described by the Swift Hohenberg (S-H) equation [1]. A classic example is the Rayleigh-Benard problem or convection in a horizontal fluid layer in the gravitational field [2]. Examples in optics include synchronously-pumped optical parametric oscillators [3], three-level broad-area cascade lasers [4] and large aspect ratio lasers [5, 6]. The latter admit the existence of transverse localized structures and phase domains [7]. Localized structures and their stability are of great interest for the study of any pattern-forming system. However, the equation used in optics, the generalized quintic complex S-H equation, has additional terms in comparison to the standard one. The main difference between the S-H equation [8] and the previously-studied complex Ginzburg-Landau equation [9] lies in its more involved diffraction term. Furthermore, these complications prevent us from analyzing the solutions easily. In fact, it was not clear that such solutions could exist at all [3]-[6]. In this work, we study the quintic complex S-H equation in 1D and report various new exact solutions.

The normalized (1+1)-dimensional generalized quintic complex S-H equation is:

$$i\psi_z + \frac{D}{2}\psi_{tt} + |\psi|^2\psi + (h+is)\psi_{tttt} + (\nu - i\mu)|\psi|^4\psi = i\delta\psi + i\beta\psi_{tt} + i\epsilon|\psi|^2\psi.$$

In mode-locked laser applications, z is the propagation distance or the cavity round-trip number (treated as a continuous variable), t is the retarded time, $D\,(=\pm 1)$ gives the sign of the 2nd order dispersion, h is the 4th order dispersion, ϵ is a nonlinear gain (or 2-photon absorption if negative) and δ (usu. negative) represents a constant gain or loss. The band-limited gain (e.g. due to an EDFA, where the gain band may be about 30 nm around 1.5 microns) is represented by β (parabolic spectrum shape) and s (4th order correction). We find exact forms for a range of solitons, including bright and dark cases, and both chirped and unchirped forms. They have various features which differentiate them from solitons of the complex Ginzburg-Landau equation [10]. These first solutions can give some clues for analysing more involved solutions.

2. Analysis. Let $\psi = f(t)\,exp[-i\,\Omega\,z]$. This reduces the S-H equation to an ordinary differential eqn. in f:

$$\Omega f + (\frac{D}{2} - i\beta)f''(t) + (1 - i\epsilon)|f|^2 f - i\delta f + (h + is)f''''(t) + (\nu - i\mu)|f|^4 f = 0. \tag{1}$$

We will show that basic [unchirped] bright and dark solitons exist, and that there are also chirped bright and dark solitons.

3.1 Bright soliton If we take

$$f = c\,\gamma\,sech(\gamma t),$$ (2)

then we note that $f''(t)/[\gamma^2 f(t)] = 2\,T^2 - 1$ and that $f''''(t)/[\gamma^4 f(t)] = 5 - 28\,T^2 + 24\,T^4$, where $T \equiv tanh(\gamma t)$. On dividing through by f, it is clear that the coefficients of $T^n \equiv tanh^n(\gamma t)$ for $n = 0, 2, 4$ can be set to zero to reduce the problem to an algebraic one and obtain the solution. From the $n = 4$ term , we find a consistency condition on the equation parameters: $\nu = -h\,\mu\,/s$. Thus $c^4 = 24s/\mu\ (= -24h/\nu)$. From the other terms we find γ, c, etc and conditions we need to impose as constraints on the equation parameters. Thence we can easily find β, δ, γ and Ω. Note that , if $\epsilon = 0$ then we have $\gamma^2 = \frac{\beta}{10s}$, and so the solution simplifies to

$$f = \sqrt{\frac{\beta}{5}}\,(\frac{6}{s\,\mu})^{\frac{1}{4}}\,sech[\sqrt{\frac{\beta}{10s}}\,t].$$

3.2 Black soliton.

If we take $f = c\,\gamma\,tanh(\gamma t)$, then we see that

$$f''(t)/[\gamma^2 f(t)] = 2\,[T^2 - 1],$$

and that

$$f''''(t)/[\gamma^4 f(t)] = 8\,[T^2 - 1]\,[3\,T^2 - 2].$$

Again, on dividing by f, it is clear that the coefficients of T^n for $n = 0, 2, 4$ can be set to zero to reduce the problem, and we then determine all the solution parameters. From the other terms we find the conditions we need to impose as constraints on the equation parameters. Thus γ and c are the same as above, and

$$\beta\,h = -(s + h\,\epsilon)\,\sqrt{6s/\mu} - s\,D/2,$$

while

$$\gamma^2 = \frac{D + 2\,\sqrt{6\,s/\mu}}{40\,h}\,(> 0).$$

4.1. Chirped bright soliton.

This involves the function

$$f = a(t)\,exp[id\,log\,a(t)],$$

where $a(t) = \gamma\,c\,sech(\gamma\,t)$. With this form, the derivatives can still be written in a convenient way. For example,

$$f''(t)/[\gamma^2 f(t)] = -(d - i)\,[i + (d - 2i)\,T^2].$$

We need to find the roots of a 4th order polynomial in d:

$$(\mu\,h + s\,\nu)(d^4 - 35d^2 + 24) + 10d(\nu\,h - s\,\mu)(5 - d^2) = 0.$$ (3)

Thus d depends on a balance of the highest order derivative (4th) and strongest nonlinearity and is quite different from that of the CGLE [10] or CGLE with an integral term [11] where d is determined by β and ϵ. Eqn(3) provides insight into the chirpless ($d = 0$) case, as we see that $d = 0$ is a root of eqn.(3) when $\mu\,h + s\,\nu = 0$.

4.2 Chirped black soliton

Here $f(t) = a(t)\,exp[id\,log\,b(t)]$, where $a(t) = r\,\gamma\,tanh(\gamma t)$ and $b(t) = \gamma\,sech(\gamma t)$, and we proceed as above to find the solution.

With this form, the derivatives are as follows:

$$f''(t)/[\gamma^2 f(t)] = -(d - i)\,(d - 2i)\,T^2 - (2 + 3\,id).$$ (4)

and that

$$f''''(t)/[\gamma^4 f(t)] = 16 + 30\,id - 15\,d^2 + 10(1 + id)\,(d - 2i)^2\,T^2 + (d - i)\,(d - 2i)\,(d - 3i)\,(d - 4i)\,T^4.$$ (5)

Again, we equate the coefficients of T^n for $n = 0, 2, 4$ to zero. The quartic eqn. for d is the same as eqn.(3) above.

5. Energy and momentum balance. As any other equation describing dissipative systems, the S-H equation does not have any conserved quantities. Instead, we can write balance equations for the energy and momentum. A study of the S-H eqn., using the energy balance approach ([10],[11]) leads to the evolution equation for the energy, Q:

$$Q = \int_{-\infty}^{\infty} |\psi|^2 dt$$

$$\frac{dQ}{d\xi} = 2 \int_{-\infty}^{\infty} \left[\delta|\psi|^2 - \beta \left| \frac{\partial \psi}{\partial t} \right|^2 - s\, |\psi_{tt}|^2 + \epsilon|\psi|^4 + \mu|\psi|^6 \right] dt. \tag{6}$$

By definition, the right hand side of this equation is the rate of change of the energy. The term with s here is new in comparison with similar equation for CGLE [10]. The form of this term reflects its role as a higher-order band-limited gain. For any stationary exact solution, we need the r.h.s. of eqn.(6), and also the rate of change of the momentum, to be zero. This provides a way of finding or checking solutions. Hence, using one of the exact solutions, we can find the result for the evolution of the pulse amplitude. For example, for the form of the bright unchirped soliton eq.(2), the energy balance condition is

$$15\delta + 5\gamma^2 \left(2\epsilon c^2 - \beta \right) + \gamma^4 \left(8\mu c^4 - 7s \right) = 0.$$

It is easy to verify that the soliton given by eq.(2) satisfies this identity. Similarly, we can find the rate of change of the momentum, and thus constrain other possible solutions. The momentum is defined in ch.2 of [10]. The balance equation is also an important tool in studying the interaction between the pulses [10].

Conclusion. The solutions presented here are novel examples of exact solutions which exist for the S-H equation. As with the Ginzburg -Landau equation [10], they certainly do not cover the whole set of possible solutions. In fact, they only represent a small subset of the range of soliton-like solutions. Other solutions have to be studied numerically, and this may require a considerable number of simulations. However, finding the exact solutions is an important step in analysing the laser systems with involved spectral properties which can be described by the S-H equation.

References

1. J. Biceta, K. Lindenberg, and J. M. R. Parrondo, *Phys. Rev. Lett.*, **88**, 024103 (2002).
2. M. I. Tribelskii, Short-wavelength instability and transition to chaos in distributed systems with additional symmetry, Physics-Uspekhi **40**, 159-180 (1997).
3. V. J. Sanchez-Morcillo and K. Staliunas, Generalized complex Swift-Hohenberg equation for optical parametric oscillators, *Phys. Rev. A* ,**56**,3237 (1997) .
4. J. Garcia-Ojalvo, R. Vilaseca and M. C. Torrent, Coupled pattern formation near threshold in a broad-area cascade laser, *Phys. Rev. A*, **56**, 5111 (1997).
5. J. Lega, J. V. Moloney and A. C. Newell, Swift-Hohenberg equation for lasers, *Phys. Rev. Lett.*, **73**, 2978 (1994).
6. C. O. Weiss et al., Spatial solitons in nonlinear resonators, In *Soltion-driven photonics (eds. A. D. Boardman and A. P. Sukhorukov), Kluwer, 2001*, pp.169-210.
7. V. J. Sanchez-Morcillo and K. Staliunas, Stability of localized structures in the Swift-Hohenberg equation, *Phys. Rev. E*, **60**, 6153 (1999).
8. H. Sakaguchi and H. R. Brand, Localized patterns for the quintic complex Swift-Hohenberg equation, *Physica D*, **117**, 95 (1998).
9. K. Staliunas, Laser Ginzburg-Landau equation and laser hydrodynamics, *Phys. Rev. A*, **48**, 1573 (1993).
10. N. Akhmediev and A. Ankiewicz, *'Solitons, nonlinear pulses and beams'*, Chapman & Hall, London (1997) 336 pp.
11. A. Ankiewicz, N. Akhmediev and P.Winternitz, Singularity analysis, balance equations and soliton solution of the nonlocal complex Ginzburg-Landau equation, *Jnl. of Enrg. Maths* **36**,(1999) 11-24.

Spatial Solitons and Anderson Localization

Kestutis Staliunas

PTB Braunschweig, Bundesallee 100, 38116 Braunschweig, Germany
tel: +49-531-5924482, fax: +49-531-5924423, e-mail: kestutis.staliunas@ptb.de

Abstract: Anderson localization is the spatial localization of the wavefunction of electrons in random media. We suggest, that analogous phenomenon can stabilize the spatial solitons in optical resonators: the spatial solitons in resonators with randomly distorted mirrors are more stable, than in perfect mirror resonators.
©2000 Optical Society of America
OCIS codes: (190.4420) Nonlinear optics, transverse effects

1. Introduction

The phenomenon of Anderson localization is well known in quantum mechanics, and in solid state physics. It states, that whereas the wavefunction of a quantum particle (e.g. of an electron) is delocalized (extended) for a homogeneous potential, then it can be spatially localized for a random potential. In particular the Anderson localization is believed to be responsible for the metal-insulator transitions in semiconductors with impurities.

The Anderson localization is usually investigated by solving the linear Schrödinger equation. Although some controversy still exists it is now generally accepted, that: 1) in 1-dimensional system the localization is absolute (i.e. occurs for infinitesimal dispersion of the random potential), and the wave-function decays exponentially in space; 1) in 2-dimensional system the localization is weak (i.e. occurs only for sufficiently strong dispersion of the random potential), and the wave-function decay in space follows a power law; 3) in 3- and more-dimensional systems the localization due to a random potential is absent.

We apply the concept of Anderson localization to bistable spatial solitons in dissipative nonlinear optical resonators (cavitons). There are different pictures for the formation of such spatial solitons in resonators: in one interpretation the soliton is a single spot of the stripe solution (in 1D) or of hexagonal solution (in 2D) embedded in the trivial zero solution, serving as a background [1]. A bistability between the modulated state and the zero (dark) state is necessary for this interpretation. In another interpretation the soliton is a small island of homogeneous nonzero solution embedded in the trivial zero solution [2]. The bistability between the homogeneous bright and the dark states of the radiation is necessary for this interpretation. In both cases the dissipative soliton is stabilized in some parameter range (stability balloon) due to the balance between the gain, saturation, focussing, diffraction, and resonator detuning.

The idea is that if the Anderson localization tends to localize spatially the solutions in the linear systems due to a random potential, then perhaps random potentials could provide additional stabilization of the spatial solitons in nonlinear optical systems. Also, if the solitons are weakly unstable for homogeneous potential (outside of the stability balloon in the parameter space, but close to its boundary), then perhaps the random potential could stabilize the soliton. In the first case – due to the randomness of potential, the negative real parts of the stability exponent becomes more negative. In the second case – the small positive real parts of stability exponents cross the zero and become negative.

We show such localization on a particular example of solitons in lasers with saturable absorber [1]. The numerical integration of corresponding equations shows an increase of stability of the soliton due to the random potentials. We also derive the deterministic (mean field) equations, perturbatively accounting for the randomness of the potential. Also we seek for a general solution of the problem: we attempt to show, that generally the real part of the eigenvalue in a stability analysis of solitons is shifting towards negative values due to random potentials.

2. Equations

The linear Schrödinger equation, as used to analyze theoretically the Anderson localization is:

$$\frac{\partial A(\vec{r},t)}{\partial t} = i\nabla^2 A(\vec{r},t) + iV(\vec{r})A(\vec{r},t) \qquad (1)$$

where the potential $V(\vec{r})$ is a random function the stationary in time and delta-correlated in space: $\langle V(\vec{r}_1)V(\vec{r}_2)\rangle = \sigma\delta(\vec{r}_1 - \vec{r}_2)$, with the dispersion σ.

The nonlinear optical resonators in paraxial approximation are generally described by a dissipative generalization of the Schrödinger equation:

$$\frac{\partial A(\vec{r},t)}{\partial t} = i\nabla^2 A(\vec{r},t) + iV(\vec{r})A(\vec{r},t) + \hat{N}(A,\nabla^2 A) \tag{2}$$

the operator $\hat{N}(A,\nabla^2 A)$ corresponds to the gain, saturation, spatial frequency filtering and other possible dissipative effects occurring in nonlinear resonators. The first r.h.s term corresponds to the diffraction, and the second r.h.s term correspond to the mirrors of the resonator: the spherical mirrors result in a parabolic form of potential $V(\vec{r})$, and the rough (scattering) flat mirrors correspond to the random potential.

In particular we show here the Anderson localization of solitons for lasers with saturable absorber, where the dissipative part of (2) is given by:

$$\hat{N}(A,\nabla^2 A) = \left(\frac{D_0}{1+|A|^2} - 1 - \frac{\alpha_0}{1+|A|^2/I_\alpha}\right)A \tag{3}$$

i.e. consisting of saturating gain, of linear losses, and of saturating losses respectively.

3. Numerics

We performed a numerical analysis in order to investigate the influence of the random potential on the stability of spatial solitons in 2D case. Fig.1 shows the energy of the soliton depending on the gain parameter for the random and for homogeneous potential. Evident is a significant increase of the soliton stability area due to the random potential. The corresponding spatial distributions of the intensity of the light for random and for homogeneous spatial dimensions are given in Fig.1. Evident is the decrease of the overall size of solitons.

Fig. 1. Energy of a soliton for homogeneous (open circles) and for random (filled circles) potential as obtained by numerical integration of the equations (2) (3), for laser with saturable absorber in 2 spatial dimensions. Note a significant increase of the stability range of the solitons due to the random potential. For comparison the intensity of the extended (delocalized) solution is shown both for homogeneous (small open circles) and for random (small filled circles) potential, corresponding to the stable upper branches. The zero solution branch is also stable up to D_0=3.02 for the parameters used.
The inset a) shows the stable spatial solitons for homogeneous potential ($\sigma = 0$) for D_0=1.96, and the inset b) shows the stable solitons for random potential ($\sigma \neq 0$) for D_0=2.01. Note the spatial distortion, and overall decrease of the size of the solitons due to random potential.
The parameters of saturable absorber are:
$I_\alpha = 0.29$, $\alpha = 2$.
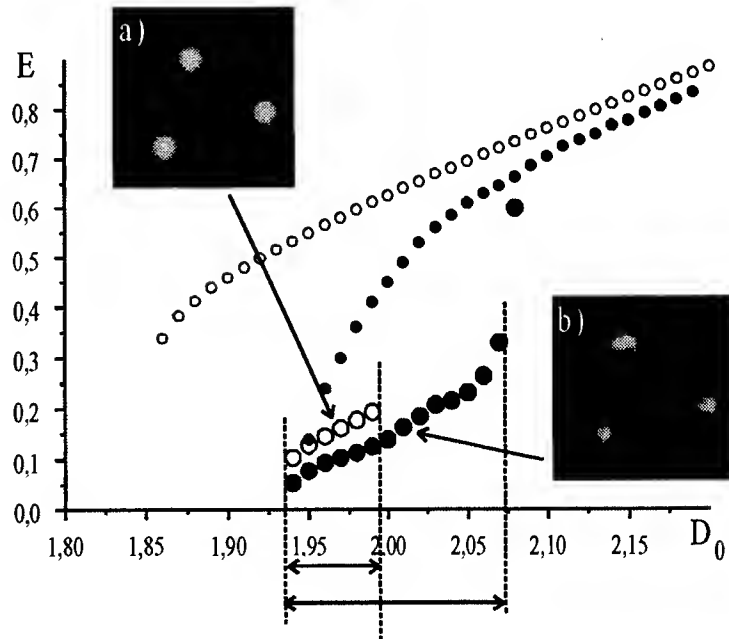
4. Analytics

We use the general equation (2) with the general form of the nonlinear operator, and assume, that its localized solution in the presence of a random potential is: $A(\vec{r},t) = A_0(\vec{R},t) + a(\vec{r},\vec{R},t)$. $\vec{R}$ is a large scale coordinate (corresponding to the soliton width), and $\vec{r}$ is a small scale coordinate (much smaller compared to the soliton width). We linearize (2) with respect to small $a(\vec{r},\vec{R},t)$; we introduce an incoherent part of the soliton: $b(\vec{R},t) = \int V(\vec{r}) \cdot a(\vec{R},\vec{r},t)d\vec{r}$ in addition to the coherent part of the soliton $A_0(\vec{R},t)$; we eliminate the small scale coordinate, and we obtain a closed system of equation for $A_0(\vec{R},t)$ and $b(\vec{R},t)$:

$$\frac{\partial A_0}{\partial t} = \hat{N}(A_0) + i\nabla^2 A_0 + i \cdot b \qquad\qquad (4.a)$$

$$\frac{\partial b}{\partial t} = \hat{L}_0 \cdot b + i\nabla^2 b + i\sigma \cdot A_0 \qquad\qquad (4.b)$$

where $\hat{L}_0 = D\hat{N}(A)/DA$ is the linear stability matrix of the soliton for homogeneous potential.

(4) is a deterministic (mean field) equation system, accounting in a perturbative way for the randomness of the potential through its dispersion σ. We integrate (4) numerically for particular soliton supporting systems, and investigate the σ-dependence of the soliton stability range. We also perform the linear stability analysis of (4) by linearizing it around soliton solution, and investigate the dependence of eigenvalues on σ.

In all investigated cases (including the laser with saturable absorber) the real parts of the eigenvalues decrease with increasing σ. This proves the role of the Anderson localisation for the particular systems. However, we hope to demonstrate the corresponding shift of the eigenvalues, thus the Anderson localization also for a more general class of the soliton supporting systems.

5. Conclusions

Our numerical and analytical investigations lead to a somewhat counterintuitive result, that the spatial solitons in resonators with randomly distorted (randomly scratched) mirrors and randomly scattering optical elements should be more stable than the solitons in the resonators with the perfect mirrors and perfect optical elements.

6. References

1. N.N. Rosanov, Transverse patterns in wide-aperture nonlinear optical systems, in Progress in Optics XXXV (E.Wolf ed.), North-Holland, Amsterdam, 1996).
2. S. Fauve and O.Thual, Solitary waves generated by subcritical instabilities in dissipative systems, Phys. Rev. Lett. 64, 282 (1990).

Discrete solitons in nonlinear zigzag optical waveguide arrays with tailored diffraction properties

Nikos K. Efremidis, Jared Hudock, and Demetrios N. Christodoulides

School of Optics/CREOL, University of Central Florida,
Florida, 32816-2700

Abstract: We show that the discrete diffraction properties of a nonlinear optical zigzag waveguide array can be significantly modified, by exploiting the topological arrangement of the lattice itself. This introduces extended interactions (beyond nearest-neighbors), which, in turn, affect the lattice dispersion relation within the Brillouin zone. As a result, we demonstrate that new families of discrete soliton solutions are possible which are stable over a wide range of parameters. Our method opens new opportunities for diffraction management that can be employed to generate low power spatial discrete optical solitons.

Discrete solitons (DS) in nonlinear lattices are, by nature, self-localized modes that own their existence to the interplay between coupling and nonlinear effects. Solitary waves of the discrete nonlinear Schröedinger (DNLS) equation have been suggested in many diverse areas of science, such as, for example, in biology, in nonlinear optics, in solid state, as well as in dilute Bose-Einstein condensates. In optics, discrete solitons in nonlinear waveguide arrays have been suggested in 1988 [1] and have experimentally verified a decade later [2]. Several other issues, such as, DS dynamics [3] and their interactions [4] have been investigated. Regarding applications, it was recently shown that DS in two-dimensional networks of nonlinear waveguide arrays can be used to realize intelligent functional operations, such as, blocking, routing, logic functions time gating, etc. [5].

In this paper we investigate the properties of a zigzag array of coupled optical waveguides [Fig. 1]. We show that the discrete diffraction properties of such a nonlinear optical waveguide array can be significantly modified by exploiting the topological arrangement of the lattice. As a result of this band alteration, we demonstrate that new families of DS solutions are possible, which are stable over a wide range of parameters. These include π-out-of-phase bright DS in self-focusing media and π-out-of-phase dark staggered DS in self-defocusing media.

Figure 1 depicts an array of optical waveguides in a zigzag configuration. In this array, D is the distance between "nearest" neighbors and θ is the angle between the lines connecting the nth element of the array with its neighbors $(n \pm 1)$. Because of this new topological configuration, it is also essential that one also considers linear coupling effects between the nth site and its second-order neighbors $(n \pm 2)$. From Fig. 1, these latter elements are separated by a distance $D_2 = 2D\sin(\theta/2)$. In normalized units the equation describing the field evolution in such as array is given by

$$i\frac{du_n}{d\zeta} + \Delta_1 u_n + \alpha\Delta_2 u_n + |u_n|^2 u_n = 0, \tag{1}$$

where the operators Δ_j, $(j = 1, 2)$ are defined by the relations $\Delta_1 u_n = u_{n+1} + u_{n-1} - 2u_n$, $\Delta_2 u_n = u_{n+2} + u_{n-2} - 2u_n$. $u_n = E_n/G$ is the dimensionless field amplitude, E_n represents the modal field amplitude, ζ is a normalized propagation distance with respect to the coupling length $z_0 = 1/c_1$, $G = \sqrt{2c_1/k_0 n_2}$ is a characteristic electric field amplitude, and α signifies the relative strength between the first and the second neighbor couplings, i.e.,

$$\alpha = K_0(WD_2/\rho)/K_0(WD/\rho) \tag{2}$$
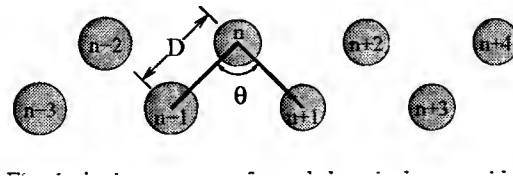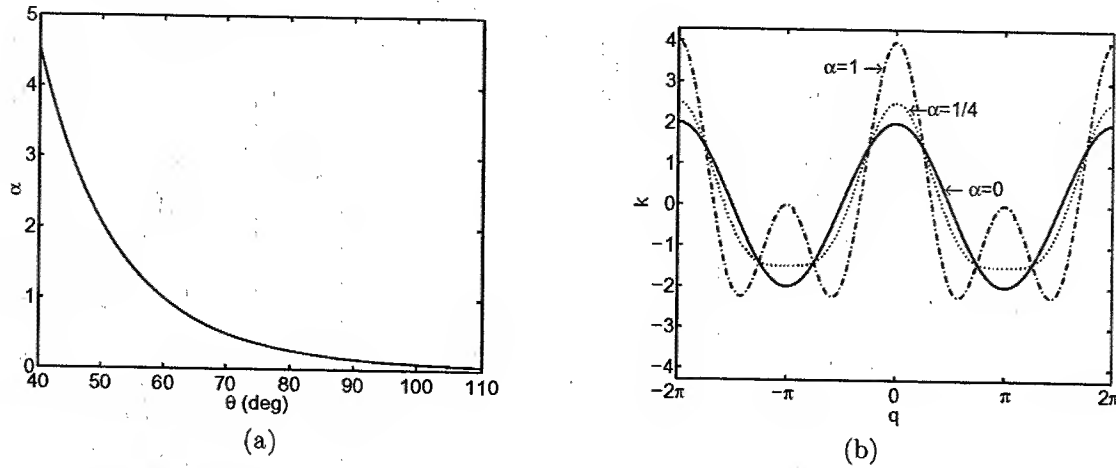
Fig. 2. (a) The variation of α as a function of θ for a zigzag optical waveguide array, and (b) the linear part of the dispersion relation for $\alpha = 1, 1/4, 1$.

for step index waveguides. In Eq. (2), ρ is the core radius, $W = \rho(\beta^2 - k_0^2 n_s^2)^{(1/2)}$, β is the propagation constant, and n_s, n_c are the core ant the cladding refractive indices, respectively. For demonstration, let us assume that $\lambda_0 = 1.5$ μm, $n_c = 1.5$, $\Delta = 2 \times 10^{-3}$, $\rho = 5.3$ μm, $D = 15.9$ μm so that $D_2 = 31.8 \sin(\theta/2)$ (in μm), $V = 2.1$, $U = 1.561$, and $W = 1.405$. For this set of values Fig. 2(a) depicts the variation of α as a function of θ as it can be obtained from Eq. (2).

To obtain the dispersion relation of this zigzag nonlinear lattice we use the "plane wave" solution $u_n = Ae^{i(kz+qn)}$, where the wavenumber, k, satisfies

$$k = 2\cos q + 2\alpha \cos 2q + A^2 - 2(1 + \alpha), \tag{3}$$

and q represents the phase shift among successive sites and plays the role of "particle momentum". The shifted [by $2(1 + \alpha)$] linear part of the dispersion relation, $2(\cos q + \alpha \cos 2q)$, is depicted in Fig. 2(b) for three different values of α, namely $\alpha = 0, 1/4, 1$. Note that the first Brillouin zone is defined in the domain $-\pi \leq q \leq \pi$. First, we would like to discuss the properties of this linear dispersion curve. The curvature of the dispersion relation characterizes the diffraction properties of the array. More specifically, when the curvature of the dispersion relation [$k''(q)$] is positive (negative) the effective diffraction of the array is anomalous (normal), respectively. As we can see from Fig. 2(b), the dispersion curve attains a maximum at $q = 0$, and, as a matter of fact, bright soliton solutions reside at this point with eigenvalues that lie above this curve (in the bandgap). Each member of this family of bright solitons is characterized by the separation distance between the eigenvalue of the solution and the edge of the band. Furthermore, these solutions have altogether different properties depending on their position inside the bandgap. When the eigenvalue is relatively close to the edge of the band, the bright soliton solutions are broad (occupying many lattice sites), they possess a narrow spatial frequency spectrum, and, as a result, the long wavelength approximation of the dispersion relation is valid. The soliton solutions with wavenumbers positioned very deep inside the bandgap represent highly nonlinear "defect" states occupying, in essence, $1 - 3$ lattice sites.

However, as clearly seen in Fig. 2(b), the properties of the dispersion diagram at the edge of the Brillouin zone ($q = \pi$) can be drastically altered for appreciable values of the second-order-coupling strength α. In particular, for α's located inside the region $[0, 1/4)$ the second derivative of the dispersion curve, $k''(\pi)$, is always positive and, therefore, the lattice dispersion is normal. As a result, dark π-out-of-phase DS solutions reside at the edge of the Brillouin zone for these values of α. In the case $\alpha = 1/4$ the second-order dispersion is zero and the first nonzero contribution comes from the fourth-order dispersion which happens to be positive. When α is above $1/4$, the value of $k''(\pi)$ becomes negative, and as we will show a new family of bright staggered solitons in self-focusing arrays exists. We were able to identify two different types of staggered bright solitons: (a) a symmetric mode, and (b) an antisymmetric mode. Figure 3 depicts a highly confined, symmetric and antisymmetric DS solution as was obtained numerically using relaxation methods. Between these two possible staggered solutions, the Hamiltonian of the symmetric mode is always greater than the corresponding value for the antisymmetric mode (for a fixed value of the power and appreciable
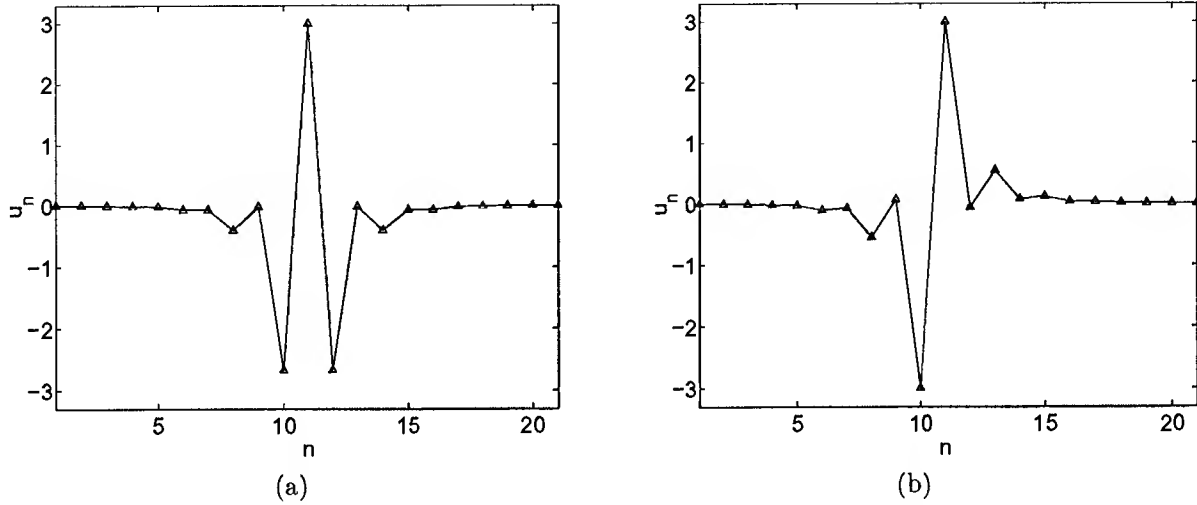
Fig. 3. (a) symmetric and (b) antisymmetric π-out-of-phase bright soliton.
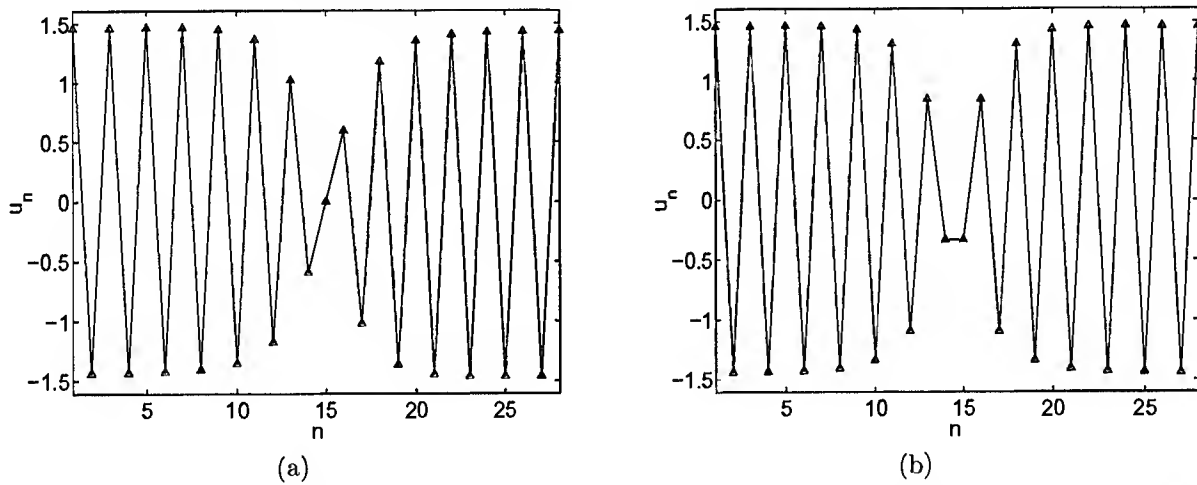
Fig. 4. A staggered dark soliton at the edge of the Brillouin zone (a) centered on a site and (b) centered between two sites.

values of α). As a result, the symmetric mode is transversely unstable. To study the stability properties of the antisymmetric solution, we numerically solved the associated eigenvalue problem. Our numerical investigation shows that above a certain threshold of the maximum amplitude these solutions are stable.

The leading diffraction term of a staggered DS will be given by $d_2 = \cos q + 4\alpha \cos 2q$. Interestingly enough, by appropriately selecting α the diffraction properties of the array can be significantly modified. For $\alpha = 1/4$ the second order diffraction is zero, while d_2 increases linearly with α. Thus, staggered discrete solitons can exist even in media with relatively small values of the nonlinearity. Following similar arguments, we anticipate that for values of α less than $1/4$ staggered bright soliton solutions should exist. Again, two different types of dark solitons can be obtained; one centered on a site [Fig. 4(a)] and one centered between two consecutive sites [Fig. 4(b)].

References

1. D. N. Christodoulides and R. I. Joseph, Opt. Let. **13**, 794 (1988).
2. H. Eisenberg, Y. Silberbeg, R. Morandotti, A. Boyd and J. Aitchison, Phys. Rev. Lett. **81**, 3381 (1998).
3. R. Morandotti, U. Peschel, J. S. Aitchison, H. S. Eisenberg, and Y. Silberberg, Phys. Rev. Lett. **83**, 2726 (1999).
4. A.B. Aceves, C. De. Angelis, T. Peschel, R. Muschall, F. Lederer, S. Trillo, and S. Wabnitz, Phys. Rev. E **53**, 1172 (1996).
5. D. N. Christodoulides and E. D. Eugenieva, Phys. Rev. Lett. **87**, 233901 (2001).

Engineering the nonlinear phase shift

Yan Chen, Benjamin Yang, Geeta Pasrija and Steve Blair

Dept. of Electrical and Computer Engineering, University of Utah, 50 S. Central Campus Drive, Rm 3280, Salt Lake City, UT 84112
ph: (801) 585-6157 fax: (801) 581-5281 e-mail: blair@ece.utah.edu

ABSTRACT

Large nonlinear phase shifts can be achieved using cascaded and coupled microresonator systems even if the constituent material has large linear and two-photon absorption. Proper design can maintain nearly constant intensity transmittance.

Engineering the nonlinear phase shift

Yan Chen, Benjamin Yang, Geeta Pasrija and Steve Blair

Dept. of Electrical and Computer Engineering, University of Utah, 50 S. Central Campus Drive, Rm 3280, Salt Lake City, UT 84112
ph: (801) 585-6157 fax: (801) 581-5281 e-mail: blair@ece.utah.edu

Materials with strong nonlinearity and high, constant transmittance are desirable for a variety of nonlinear optical processes and devices. Recent research shows that a single resonator can be used in a nonlinear Mach-Zehnder interferometer to significantly reduce the switching power [1] by increasing the nonlinear phase sensitivity. When taking material absorption into account, a ring resonator can facilitate a larger nonlinear phase shift and greater figure of merit than the constituent bulk material [2]. However, this arrangement produces a magnitude response that is non-ideal for a general-purpose phase shifting element. Multiple resonators can be used in a serial cascade [3,4] or lattice arrangement [5] to further improve the nonlinear sensitivity while providing degrees of freedom to control the magnitude and phase response.

As a first embodiment, we examine a simple modification to the serial-cascaded microring (CMRR) configuration - adding an extra output port on the top of the last ring. This modification facilitates an enhanced nonlinear sensitivity, a large saturating phase shift, and nearly ideal intensity transmittance characteristics even if the material itself has large linear and two-photon absorption. This structure is shown in Figure 1, using five ring resonators in series [4], as an example. We assume that all the rings are perfectly optically isolated from one another.

Fig.1 *Five coupled microring resonators in a series cascade configuration (CMRR), shown on the left. Linear square magnitude and phase response as a function of number of resonators (right). The nonlinear phase shift at the output is the result of intensity-dependent detuning of the resonance. The flat-top square magnitude response results in a nearly constant intensity transmittance under detuning.*

We can consider the overall structure as a two-port device, with one input and one output, as shown. The electric field ratio and phase shift of the output relative to the input are

$$\frac{E_{out}}{E_{in}} = \left[\frac{t - a\exp(+i\phi)}{1 - ta\exp(+i\phi)}\right]^{N-1}\left[\frac{-r^2\sqrt{a\exp(+i\phi)}}{1 - t^2a\exp(+i\phi)}\right] \qquad \Delta\phi = (N-1)(\Delta\Phi_t) + \left\{\pi + \frac{\phi}{2} + \arctan\left[\frac{t^2a\sin(\phi)}{1 - t^2a\cos(\phi)}\right]\right\} \qquad (1)$$

In the above equations, N is the number of the rings, r and t are the coupling coefficients between the channel waveguide and resonator related by $r^2 + t^2 = 1$; α is the attenuation, and $a = \exp(-\alpha L/2)$; $\Delta\Phi_t$ is the transmission phase shift after the light passes through a single side-coupled ring resonator, which can be expressed as

$$\Delta\Phi_t = \pi + \phi + \arctan\left[\frac{t\sin(\phi)}{a - t\cos(\phi)}\right] + \arctan\left[\frac{ta\sin(\phi)}{1 - ta\cos(\phi)}\right] \qquad \phi = \phi^L + \phi^{NL} = \beta L + \frac{1}{2K}\ln\left(1 + 2\beta\frac{n_2}{n}KI_{in}L_{eff}\right) \qquad (2)$$

where ϕ is the total single-pass phase shift accumulated in one ring which is the sum of the linear phase shift due to propagation and nonlinear phase shift due the optical Kerr effect, including linear and two-photon absorption loss [2], $\phi^L = \beta L$ and ϕ^{NL} are the single-pass linear and nonlinear phase shift respectively; $\beta = 2\pi n/\lambda_0$ is the propagation constant in the material, n is the refractive index, and λ_0 is the wavelength in free space; $K = n\beta_2/2n_2\beta$ is the normalized TPA coefficient, β_2 is the TPA coefficient, n2 is the nonlinear refractive index; $L_{eff} = (1 - e^{-\alpha L})/\alpha$ is the effective interaction length due to linear absorption and L=50 µm is the circumference, which is the same for each ring.

The ideal nonlinear phase shifting element will have a region of input intensity over which a phase change of at least π can be obtained while maintaining constant intensity transmittance. In order for any switching device based upon this element to be practical, the phase shift must occur under low input intensity. Based on these requirements, we determine the magnitude and phase response of the resonator system as a function of input intensity for different coupling coefficients. We also use the figure-of-merit (FOM) [2] as a criterion for comparison, where FOM>1 is desired. Figure 2 and fig. 3 are for absorption α of 1 cm^{-1} and 5 cm^{-1} respectively. The TPA coefficient K=1 and the coupling coefficient r^2 varies from 0.1 to 0.25 in fig. 2. By comparing fig.2 (a) with fig.3 (a), it is evident that the intensity transmittance is highly dependent on the single-pass ring loss. Also, with increasing r^2, I_{out}/I_{in} increases (because over coupling into the ring occurs) but the phase shift decreases. An input intensity $n_2 I_{in}$ less than 10^{-5} produces a π phase shift for most cases.

(a)   (b)
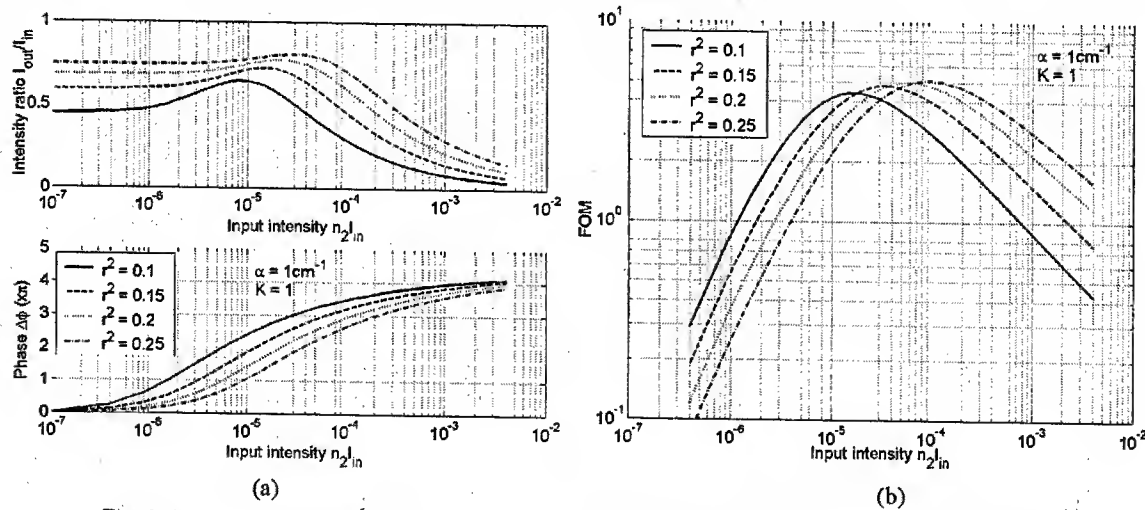
Fig. 2 *Attenuation $\alpha = 1cm^{-1}$, (a) Intensity ratio and total phase shift of CMRR; (b) FOM of CMRR.*

It is important to compare the nonlinear resonator response to that of bulk, as shown in fig. 3 using $\alpha = 5$cm^{-1} for both, and $r^2 = 0.2$ for the rings. The bulk material is taken to have a length of 120 µm, which is about the same length as the CMRR device. We calculated the intensity ratio I_{out}/I_{in}, phase shift, and FOM for different TPA coefficients: K=0, 0.1, 1, 10. The figure shows that the bulk material is much more sensitive to K: with increasing K, I_{out}/I_{in} decreases and the phase shift decreases at high input intensity. On the contrary, TPA has no significant effect on the CMRR if K is less than 1. The phase shift and FOM given by CMRR are both much larger than the bulk material.

The second embodiment consists of coupled microresonators in a one-dimensional photonic bandgap lattice [5], as shown in fig. 4. The nonlinear response of this structure is shown in fig. 5 in comparison to a bulk material indicating again that nonlinear sensitivity enhancement by more than an order of magnitude is feasible. Unlike the ring resonator structures, this photonic bandgap microcavity array structure is suitable for the study of transverse nonlinear propagation effects. Preliminary studies show that the 1-D self-focusing threshold can be reduced by nearly an order of magnitude even though the symmetry of the structure demands that the rate of diffraction is enhanced over bulk.

(a)

(b)
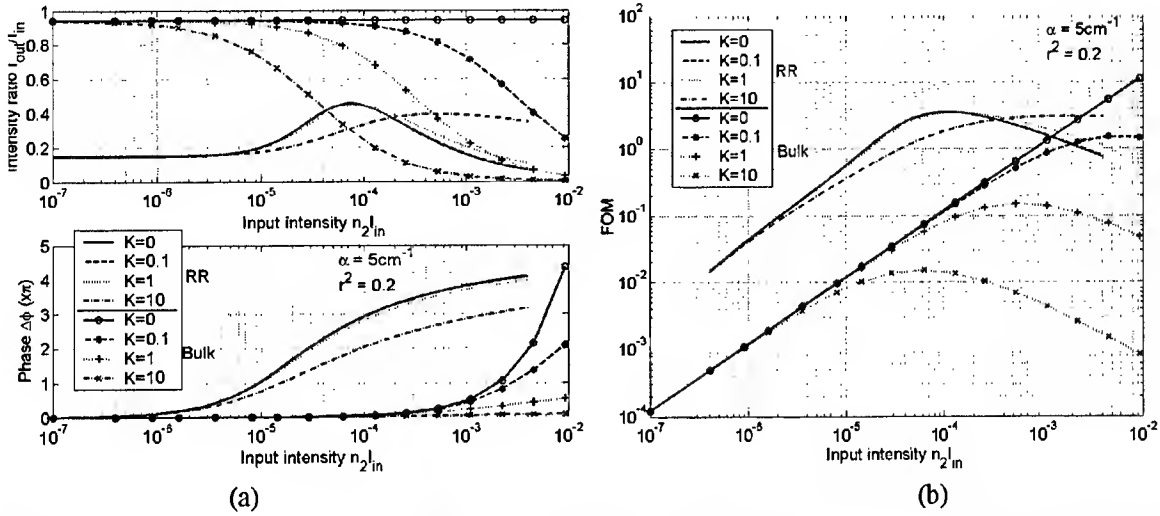
Fig. 3 *Attenuation* $\alpha=5cm^{-1}$, $r^2 = 0.2$, *(a) Intensity ratio and total phase shift of CMRR and bulk material; (b) FOM of CMRR and bulk material for different TPA coefficienst K.*
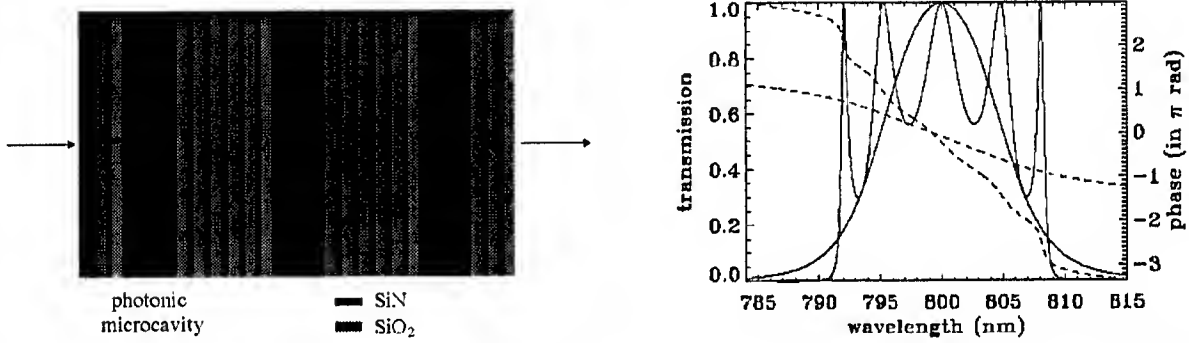
Fig. 4. 1-D photonic microcavity array structure (left) and linear square magnitude (solid lines) and phase(dashed lines) response (right) for an array of three and seven (thick linestyles) microcavities.
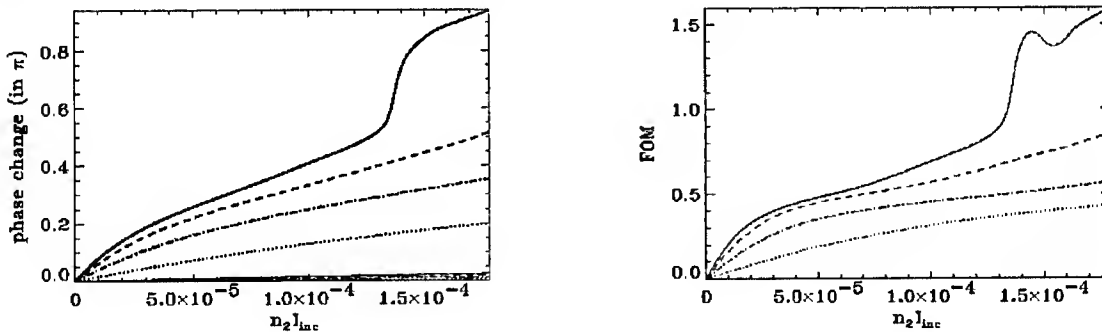
Fig. 5. Nonlinear phase shift (left) and figure of merit (right) for a 3 (dotted), 5, 7, and 11 (solid) photonic microcavity array. The corresponding response of a bulk material of the same length is also shown in the figures using a thinner linestyle.

1. J. Heebner and R. W. Boyd "Enhanced all-optical switching by use of a nonlinear fiber ring resonator," Opt. Lett. **24**, 847 (1999)
2. S. Blair, J. Heebner and R. W. Boyd "Beyond the absorption-limited nonlinear phase shift with micro-ring resonators" Opt. Lett. **27**, 357 (2002)
3. J. Heebner, R. W. Boyd, and Q-Han Park, "SCISSOR solitons and other novel propagation effects in microresonator-modified waveguides," Journal of the Optical Society of America B **19**, 722 (2002)
4. Y. Chen and S. Blair "Towards a better nonlinear phase-shifting element with microring resonators," submit. to Opt. Lett. (2002)
5. S. Blair, "Nonlinear sensitivity enhancement of one-dimensional photonic bandgap microcavity arrays,"Opt. Lett. **27**, 613 (2002)

Characterisation and Process Evolution of Quasi-Phase-Matched Semiconductor Superlattice Waveguides using Intermixing

K. Zeaiter, T. C. Kleckner, J. S. Aitchison[*] and D. C. Hutchings

Department of Electronics and Electrical Engineering, University of Glasgow, Glasgow G12 8QQ, Scotland, UK
Tel: +44-141-330-6026, Fax: +44-141-330-6002, Email: D.Hutchings@elec.gla.ac.uk

Abstract: We characterise the intermixing fabrication process by examining the photoluminescence spectra. Subsequently we adapt the process, which was initially developed for optoelectronic integration, to be optimised for the production of semiconductor superlattice waveguides for quasi-phase-matched frequency conversion.
©2002 Optical Society of America
OCIS codes: (190.5970) Semiconductor nonlinear optics; (190.2620) Frequency conversion; (160.4330) Nonlinear optical materials

There is an emergence of semiconductors as nonlinear optical elements for wavelength conversion as techniques for phase-matching are developed. III-V semiconductors have intrinsically large second-order optical susceptibilities in comparison to conventional ferroelectric crystals. However, of potentially greater advantage is the mature fabrication technology in GaAs and the possibility of direct integration with semiconductor diode laser sources. This could ultimately lead to compact devices for flexible wavelength sources and amplifiers (where the peak gain wavelength is determined by the post-growth fabrication rather than being specific to each material system) and for channel conversion in WDM using difference frequency generation.[1]

A novel method of using quasi-phase-matching was recently demonstrated for second-harmonic generation (SHG) using spatially resolved intermixing to periodically modulate the second-order susceptibility.[2] This recent development in quasi-phase-matching using intermixing exploits the larger absolute modulation in the second-order susceptibility based on the bulk-like coefficients $\chi_{xyz}^{(2)}$ and $\chi_{zxy}^{(2)}$ rather than the far smaller induced coefficients in asymmetric heterostructures. The QPM grating is defined in the post-growth processing of a wafer grown using standard methods and hence this phase-matching technique is compatible with integration of laser diode pumps. With careful process optimisation, it has been shown that the impurity-free vacancy disordering (IFVD) quantum well intermixing does not significantly increase optical losses. However, the SHG output power levels in this initial demonstration were rather low and hence further characterisation and process optimisation is required.

A theoretical optimisation study has been performed on this quasi-phase-matching technique.[3] It was concluded that (1) the 14:14 monolayer symmetric GaAs/AlAs superlattice used initially is close to optimal for maximising the modulation in the second-order susceptibility for applications in the telecommunications 1.55 μm window, (2) the spatial resolution of the disordering must be less than a coherence length regardless of the order of the QPM process and (3) coupling efficiencies can be improved without compromising the nonlinear overlap integral by padding out the waveguide core with additional AlGaAs alloy layers. Furthermore, preliminary spatially resolved photoluminescence measurements seem to indicate that in the initial SHG experiment the intermixing was only partial in terms of depth and extent.

We report here a reassessment of the IFVD technique for producing QPM gratings. The structure used comprised of 0.6 μm of a symmetric superlattice waveguide core made of 14:14 monolayers of GaAs/AlAs respectively. The lower and upper cladding were bulk $Al_{0.6}Ga_{0.4}As$ of 4 μm and 0.8 μm width respectively. A 100 nm GaAs cap was used to cover the upper cladding. By adding 0.3 μm layer of bulk $Al_{0.56}Ga_{0.44}As$ on each side of the superlattice layer, the coupling efficiency was observed to increase by over an order of magnitude. The structure was nominally undoped grown by molecular beam epitaxy (MBE) on a semi-insulating GaAs substrate. The standard process developed at the University of Glasgow for fabricating low-loss regions for integrated optoelectronic applications uses lithography based on the lift-off technique with a PMMA mask to deposit a pattern of PECVD and sputtered silica.[4] As the initiation temperature for intermixing is dependent on the silica deposition

---

[*] Current affiliation: Edward S. Rogers Sr. Department of Electrical and Computer Engineering, University of Toronto, Toronto, ON M5S 3G4, Canada.

method, a rapid thermal anneal at the appropriate temperature results in a patterned bandgap shift in the semiconductor heterostructure. However, at the micron-scale feature size necessary for QPM, this fabrication process resulted in a contamination of the sample surface with PMMA deposits after the lithography processes were completed with a resulting detrimental affect on the photoluminescence efficiency after the rapid thermal anneal. Therefore we have adopted an alternate fabrication process of using UV3 as a mask to etch windows into the PECVD silica layer followed by sputtered silica deposition.
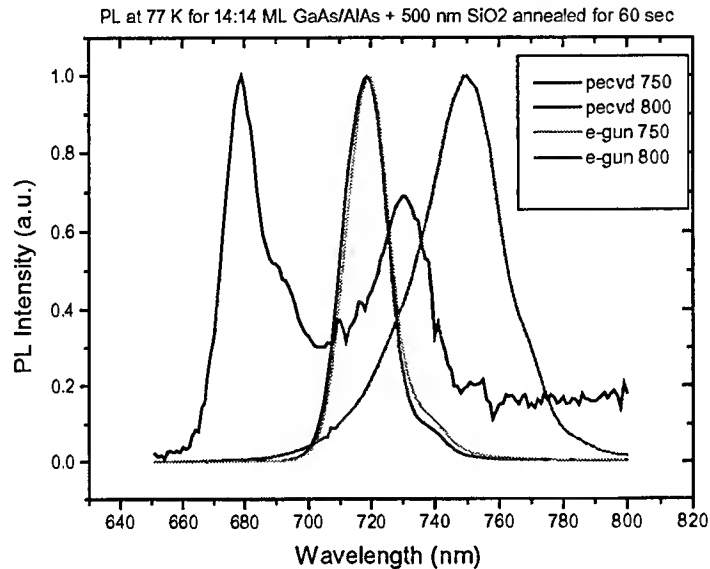
Fig. 1. PL spectra from superlattice under PECVD and e-gun deposited silica caps following a rapid thermal anneal for 60s at the temperature shown.

We examine the silica deposition process for the intermixing suppressed region, particularly at higher anneal temperatures where we aim to fully intermix the regions capped by the sputtered silica. Figure 1 shows the photoluminescence spectra after a rapid thermal anneal from portions of the superlattice wafer, which have been completely covered with silica deposited using the PECVD and electron-gun processes. It can be seen that at these temperatures used, the shift in the photoluminenscence peak is inconsistent on the PECVD samples, with a red shift at 750°C and a blue-shift of the major feature at 800°C. In contrast the e-gun silica deposition samples show a photoluminescence spectrum essentially identical to the as-grown material.

We also investigate the dependence of the bandgap shift on the thickness of the sputtered silica layer. Figure 2(a) shows the photoluminescence spectra from superlattice with the given thickness of sputtered silica cap following a rapid thermal anneal at 650°C for 60s and figure 2(b) shows the blue-shift of photoluminescence peak for RTA temperatures of 650°C and 700°C. It can be seen that the spectra are inconsistent for the thinnest sputtered silica layers but for layer thicknesses ≥100 nm, the spectra obtained are uniform. It is therefore recommended that the sputtered silica thickness should be at least 100 nm. Currently, the recommended anneal conditions are 800°C for 60s, which is sufficient to complete the intermixing process under the sputtered silica cap, but such that there is minimal change under the e-gun deposited silica cap.

In figure 3 we show a scanning electron microscope photograph of a rib waveguide fabricated by reactive ion etch in a QPM grating using the current recipe. Only segments which are aligned with the rib waveguide have been exposed to the sputtered silica, which requires precise alignment of the masks for each etching process. The processing associated with the intermixing leads to slightly different etch rates in the semiconductor wafer which is visible on top of the waveguide rib.

In conclusion, by using photoluminescence as a characterisation tool we have re-examined the fabrication recipe for producing QPM gratings in semiconductor waveguides by intermixing. We have found that the demands of maximising the modulation of the second-order susceptibility and the micron-scale resolution requirements are

not satisfied by the standard IFVD recipe. It is found that the requirements can be met by (1) using a UV3 etch process in the lithography, (2) using e-gun silica as an intermixing suppression mask and (3) ensuring that the sputtered silica thickness is at least 100 nm.
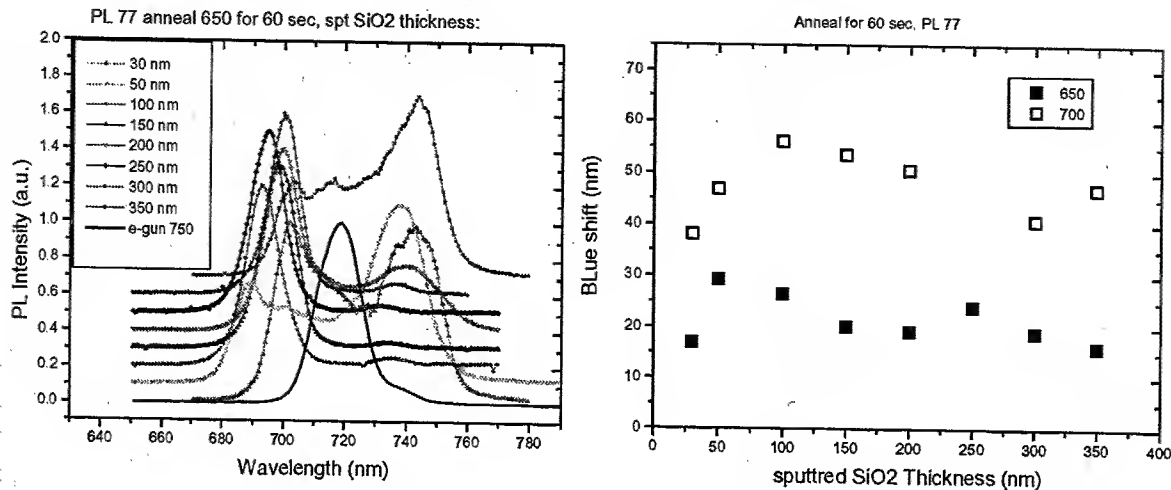
Fig. 2 (a) Photoluminescence spectra from superlattice with the given thickness of sputtered silica cap following a rapid thermal anneal at 650°C for 60s. The photoluminescence spectra for e-gun deposited silica is shown for comparison which is essentially identical to the as-grown spectra. (b) Blue-shift of the photoluminescence peak as a function of silica thickness for the 650°C anneal data presented in (a) and also for an RTA temperature of 700°C.
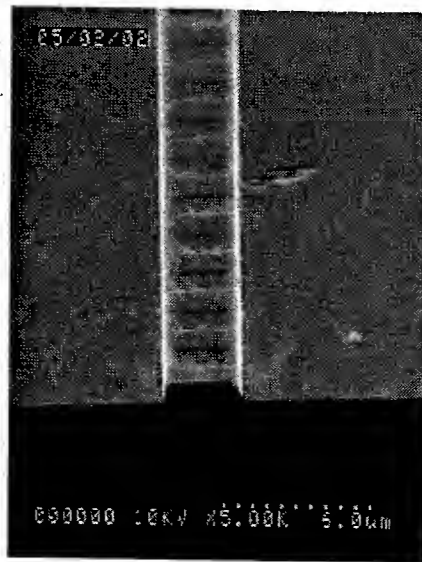
Fig. 3 SEM picture of QPM waveguide after the intermixing processing and reactive ion etching of a rib waveguide. The intermixing-suppressed regions experience a slight additional etching in comparison to the intermixed regions.

[1] S. J. B. Yoo, C. Caneau, R. Bhat, M. A. Koza, A. Rajhel and N. Antoniades, Appl. Phys. Lett. **68**, 2609 (1996).
[2] A. Saher Helmy, D. C. Hutchings, T. C. Kleckner, J. H. Marsh, A. C. Bryce, J. M. Arnold, C. R. Stanley, J. S. Aitchison, C. T. A. Brown, K. Moutzouris and M. Ebrahimzadeh, Optics Lett. **25**, 1370 (2000).
[3] D. C. Hutchings and T. C. Kleckner, J. Opt. Soc. Am B (2002).
[4] O. P. Kowalski, C. J. Hamilton, S. D. McDougall, J. H. Marsh, A. C. Bryce, R. M. De La Rue, B. Vogele, and C. R. Stanley, C. C. Button and J. S. Roberts, Appl. Phys. Lett. **72**, 581 (1997).

Symmetry Properties of $\chi^{(3)}$ in Semiconductor Heterostructure Waveguides

D. C. Hutchings

Department of Electronics and Electrical Engineering, University of Glasgow,
Glasgow G12 8QQ, Scotland, U.K.
Tel: +44-141-330-6026, Fax: +44-141-330-6002, e-mail: dch@elec.gla.ac.uk

Abstract: The symmetry of the third-order susceptibility tensor elements is addressed for semiconductor heterostructures. 8 independent elements are found for the normal sample geometry and coefficients for nonlinear refractive phenomena are derived. The change in dimensionality with intermixing is discussed.

There is an emergence of direct-gap semiconductors as nonlinear optical elements. In particular, the ultrafast Kerr-type nonlinear refractive coefficient n_2 at 1.55 μm (half-gap nonlinearity) in AlGaAs is around 10^3 times larger than in silica. The mature fabrication technology allows low-loss waveguides and complex device structures to be fabricated on centimetre-scale chips. Experiments have used this nonlinearity to demonstrate all-optical switching in directional couplers[1], Mach-Zehnder interferometers and X-junctions, spatial and temporal soliton propagation[2], polarisation coupling and laser mode-locking.

The symmetry properties of $\chi^{(3)}$ in bulk semiconductors with a zinc-blende structures are now well-understood. As the photon energies employed are a sizeable fraction of the fundamental bandgap, Kleinmann symmetry cannot be utilised, as it does in silica fibre. The cubic structure of the semiconductor also gives rise to an anisotropy of the nonlinear susceptibilities not evident in the linear susceptibility. Essentially for degenerate wavelengths there are 3 independent $\chi^{(3)}$ tensor elements and hence 3 numbers are sufficient to completely characterise Re$\chi^{(3)}$ at a particular wavelength including its polarisation dependence. Similarly another 3 numbers are sufficient to completely characterise Im$\chi^{(3)}$ (e.g. two-photon absorption) at a particular wavelength. Bandstructure calculations of nonlinear refraction in GaAs, with the inclusion of higher conduction bands which provide an anisotropy[3], are found to describe well the observed polarisation dependence of nonlinear refraction through the measurement of self- and cross-phase modulation in AlGaAs waveguides[4]. Propagation equations have been derived to describe the nonlinear phase-shift and polarisation coupling for an arbitrary propagation direction[5].

In heterostructures there is an additional breaking of symmetry which leads to an increase in the number of independent $\chi^{(3)}$ tensor elements. The substrate orientation will determine the symmetry group of the resulting structure and hence which independent susceptibility tensor elements result. In table 1 the 8 independent $\chi^{(3)}$ tensor elements are listed for the usual case of a [001]-grown heterostructure in a semiconductor with a zinc-blende structure.

$xxxx$	$zzzz$	$xxzz$	$zzxx$	$xzxz$	$zxzx$	$xxyy$	$xyxy$

Table 1. The indices $ijkl$ corresponding to the 8 independent $\chi^{(3)}_{ijkl}(-\omega,\omega,\omega)$ tensor elements for a [001]-grown heterostructure in a zinc-blende structure.

For weakly-guided waveguide propagation along an axis of high symmetry, the third-order susceptibility produces the phenomena of self-phase-modulation, cross-phase-modulation and four-wave-mixing between the two polarisation components (here we neglect third harmonic generation which requires phase-matching). The nonlinear polarisation terms corresponding to these are dependent on the waveguide orientation. The usual configuration for a [001]-grown heterostructure is determined by the [110] cleaved facets and results in the nonlinear polarisation contributions listed in table 2 for monochromatic light of frequency ω_0.

$$\mathcal{E}(\omega) = \frac{1}{2}\left[E_{TE}\delta(\omega-\omega_0) + E^*_{TE}\delta(\omega+\omega_0)\right] + \frac{1}{2}\left[E_{TM}\delta(\omega-\omega_0) + E^*_{TM}\delta(\omega+\omega_0)\right]$$

This table can also be used to provide the polarisation terms for bulk semiconductors by taking the equivalence between the direction indices x, y and z.

	$\mathcal{P}^{(3)}(\omega)$
TM: SPM	$\frac{3}{8}\epsilon_0\chi^{(3)}_{zzzz}|E_{TM}|^2 E_{TM}\delta(\omega-\omega_0) + c.c.$
TM: XPM	$\frac{3}{4}\epsilon_0\chi^{(3)}_{zxzx}|E_{TE}|^2 E_{TM}\delta(\omega-\omega_0) + c.c.$
TM: 4WM	$\frac{3}{8}\epsilon_0\chi^{(3)}_{zzxx}E_{TE}^2 E_{TM}^*\delta(\omega-\omega_0) + c.c.$
TE: SPM	$\frac{3}{16}\epsilon_0\left(\chi^{(3)}_{xxxx} + 2\chi^{(3)}_{xyxy} + \chi^{(3)}_{xxyy}\right)|E_{TE}|^2 E_{TE}\delta(\omega-\omega_0) + c.c.$
TE: XPM	$\frac{3}{4}\epsilon_0\chi^{(3)}_{xzxz}|E_{TM}|^2 E_{TE}\delta(\omega-\omega_0) + c.c.$
TE: 4WM	$\frac{3}{8}\epsilon_0\chi^{(3)}_{xxzz}E_{TM}^2 E_{TE}^*\delta(\omega-\omega_0) + c.c.$

Table 2. The third order polarisation contributions for a [001]-grown heterostructure with cleaved facets. The frequency ordering in the third-order susceptibilities is again taken to be $(-\omega, \omega, \omega)$.
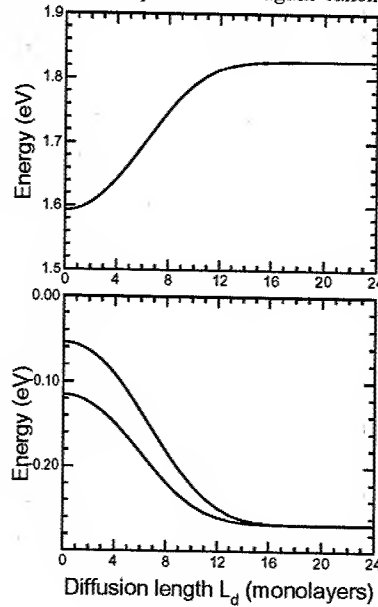
Fig. 1. Calculated shift of the lowest conduction and highest valence bands with disordering for a 14/14 monolayer GaAs/AlAs superlattice.

It can be seen that measuring these phenomena alone provides 6 values and another two measurements are necessary, including an out-of-plane propagatiuon geometry, if $\chi^{(3)}$ is required to be completely characterised.

The post-growth process of quantum well intermixing can be used to modify the bandgap. The resulting modification to $\chi^{(1)}$ has been employed in the fabrication of low-loss regions in semiconductor integrated optoelectronics, and to $\chi^{(2)}$ for quasi-phase-matching in frequency conversion. Similarly $\chi^{(3)}$ can be modified[6] and used to produce regions on a semiconductor chip with different nonlinear refraction coefficients which have, for example, been proposed for soliton emission. We also note here the increase in symmetry, where the structure reverts to the bulk average alloy. This is illustrated in figure 1 where the bandstructure calculations based on a 14 band $\mathbf{k}\cdot\mathbf{p}$ model incorporating intermixing[7] are used to determine the the conduction band edge and the heavy- and light-hole valence band edges with increasing intermixing diffusion length demonstrating the restoration of the (bulk) valence band degeneracy.

The reduction in the number of independent $\chi^{(3)}$ tensor elements provides a method to explore the increase in symmetry upon intermixing. For example the cross-phase-modulation coefficients between the two polarisation components will have their degeneracy restored as the heterostructure reverts to bulk material.

The superlattice bandstructure model, incorporating anisotropy and intermixing and described in Ref. [7], provides the band energies and optical matrix elements to enable the nonlinear susceptibility tensor elements to be computed. We have previously performed this type of calculation for the second-order susceptibility to demonstrate the feasibility of using selective area intermixing for quasi-phase-matching.[8] Extended calculations for the third-order susceptibility tensor elements in superlattices will be addressed.

NLMD38-3

References

1. J. S. Aitchison, A. Villeneuve, G. I. Stegeman, J. Nonlinear Opt. Phys. **4** 871 (1995).
2. J. S. Aitchison, *et al*, Electron. Lett. **28** 1879 (1992).
3. D. C. Hutchings and B. S. Wherrett, Phys. Rev. B **52**, 8150 (1995).
4. D. C. Hutchings, J. S. Aitchison, B. S. Wherrett, G. T. Kennedy and W. Sibbett, Optics Lett. **20**, 911 (1995).
5. D. C. Hutchings, J. S. Aitchison and J. M. Arnold, J. Opt. Soc. Am. B **14**, 869 (1997).
6. C. J. Hamilton, J. H. Marsh, D. C. Hutchings, J. S. Aitchison, G. T. Kennedy and W. Sibbett, Appl. Phys. Lett. **68**, 3078 (1996).
7. D. C. Hutchings, Superlattices and Microstructures **26**, 195 (1999).
8. D. C. Hutchings, Appl. Phys. Lett. **76**, 1362 (2000).

Self-bending of the light in a photorefractive planar waveguide fabricated with He$^+$ implanted BaTiO$_3$:Rh

Pierre Mathey

Laboratoire de Physique de l'Université de Bourgogne, Matériaux Photoréfractifs et Applications,
UMR CNRS 5027, 9 Avenue Alain Savary, BP 47870, 21078 Dijon Cedex, France
E-mail : pmathey@u-bourgogne.fr   Fax number : 33 3 80 39 59 61

Pedro Marquez

Centro de Investigaciones en Ingeniera y Ciencas Aplicadas de la Universidad Autonoma del Estado de Morelos,
Av. Universidad No. 1001, Col. Chamilpa, Cuernavaca, Morelos Mexico

Paul Moretti

Laboratoire de Physico Chimie des Matériaux Luminescents, UMR CNRS 5620, Université Claude Bernard Lyon 1,
43 boulevard du 11 Novembre 1918, 69622 Villeurbanne, France

Daniel Rytz

Forschunginstitut für mineralische und metallische Werkstoffe, Edelsteine/Edelmetalle GmbH,
Struthstrasse 2, Wackenmühle, 55743 Idar-Oberstein, Germany

Abstract: The self-bending of a beam caused by the photorefractive non-linearity is observed in a BaTiO$_3$:Rh waveguide. The response time in function of the intensity is compared with the results in the bulk.

OCIS codes: (130.2790) Guided waves; (160.5320) Photorefractive materials; (190.5330) Photorefractive nonlinear optics

Self-bending of the light in a photorefractive planar waveguide fabricated with He$^+$ implanted BaTiO$_3$:Rh

Pierre Mathey

Laboratoire de Physique de l'Université de Bourgogne, Matériaux Photoréfractifs et Applications,
UMR CNRS 5027, 9 Avenue Alain Savary, BP 47870, 21078 Dijon Cedex, France
E-mail : pmathey@u-bourgogne.fr   Fax number : 33 3 80 39 59 61

Pedro Marquez

Centro de Investigaciones en Ingeniera y Ciencas Aplicadas de la Universidad Autonoma del Estado de Morelos, Av. Universidad No. 1001, Col.
Chamilpa, Cuernavaca, Morelos Mexico

Paul Moretti

Laboratoire de Physico Chimie des Matériaux Luminescents, UMR CNRS 5620, Université Claude Bernard Lyon 1,
43 boulevard du 11 Novembre 1918, 69622 Villeurbanne, France

Daniel Rytz

Forschunginstitut für mineralische und metallische Werkstoffe, Edelsteine/Edelmetalle GmbH,
Struthstrasse 2, Wackenmühle, 55743 Idar-Oberstein, Germany

Abstract: Original observations obtained in a BaTiO$_3$:Rh waveguide are presented. The self-bending of a guided beam caused by the strong photorefractive non-linearity is observed. The response time of the phenomenon is studied in function of the injected intensity. A comparison with the results obtained in the bulk material is conducted.
©2002 Optical Society of America
OCIS codes: (130.2790) Guided waves; (160.5320) Photorefractive materials; (190.5330) Photorefractive nonlinear optics

1. Introduction

Barium titanate is famous for its significant photorefractive properties coming from its high electrooptical coefficient $r_{42} = 1600$ pm/V. In particular, this one confers to this material an excellent capacity to transfer energy from a beam towards another [1]. For a single beam propagating in the crystal, a small portion of the incident beam is scattered from inhomogeneities and impurities in the crystal. The remaining part of the incident beam interacts with these beamlets via multi-wave mixing. This leads to an amplification of the scattered light in the direction of the energy transfer [2]. For the first time to our knowledge, we observe this phenomenon in the configuration of guided optics.

2. Experimental Setup

The observations are carried out with the wavelength of an argon laser ($\lambda = 514.5$ nm). The light is extraordinarily polarized to obtain significant amplifications. The beam is injected into the guiding layer by a cylindrical lens (F = 6 mm), the coupling efficiency is about $\eta \sim 85\%$. The substrate used to realize the waveguide is a Rhodium doped (1000 parts in 10^6 in the melt) BaTiO$_3$ crystal grown at FEE by the top seeded solution growth method. It is cut along its crytallographic axis with a size of $a_1 \times a_2 \times c = 6 \times 2 \times 5$ mm. All the faces are optically polished. The planar waveguide involved in the present study has been achieved using three successive He ions implantations with the energies of 2 MeV, 1.9 MeV, 1.8 MeV at respectively the doses of $5\ 10^{15}$, $4\ 10^{15}$, $4\ 10^{15}$ ions/cm^2. The light from the output of guide is collected by a microscope objective and sent to a detector. A diaphragm is placed in front of the detector in order to select only the guided part of the output beam, the bending light is detected by another detector. The two detectors are connected to the computer. A CCD camera placed above the sample allows the observation of the beam paths in the guiding zone or in the crystal if the light is injected in the bulk.

3. Observations and measurements

Fig. 1 illustrates some of our observations. In the waveguide as in the crystal, the curvature of the incident beam appears clearly when the light is extraordinarily polarized, it does not appear in ordinary polarization. The direction of the beam deviation depends on the direction of the c axis. These observations are in accordance with the usual properties of photorefractivity.
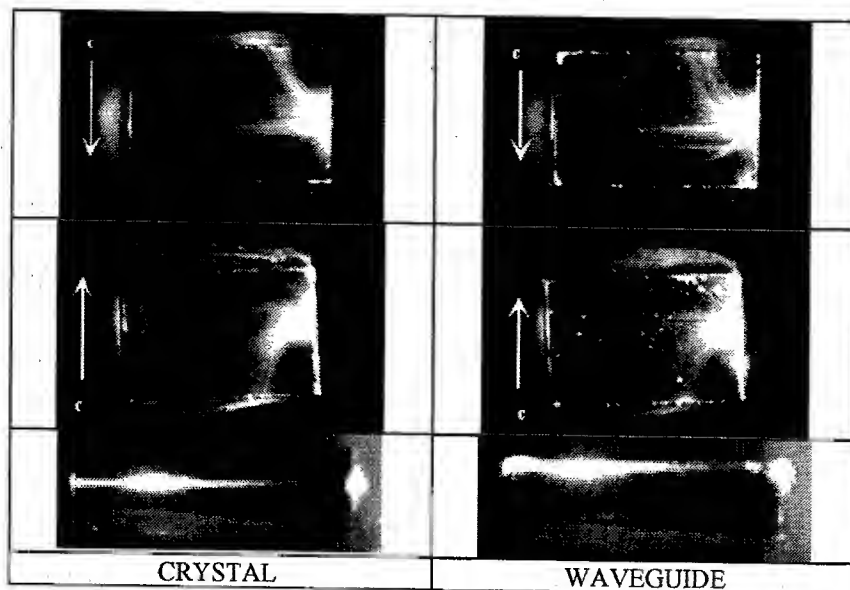
Fig. 1 . Observations of the self-bending in the bulk crystal and in the waveguide.

An example of dynamics of the directly transmitted and the deviated beams is shown in Fig.2. The kinetics of the transmitted beam can be adjusted by exponential laws to deduce the response time. Its dependence in function of the injected intensity according to a law I^{-x} gives the exponents $x = 0.76$ for the guide and $x = 0.8$ for the crystal. These coefficients are in close agreement with our preceding studies undertaken in this same sample at $\lambda = 854$ nm [3]. However, at the time of this preceding study, we had not observed the beam-fanning in the guiding layer because the injection of the light was carried out in a less effective way by prism coupling ($\eta \sim 15\%$). Let us underline that with the injection with the cylindrical lens, the same bending effect is observed in the same sample at $\lambda = 854$ nm.
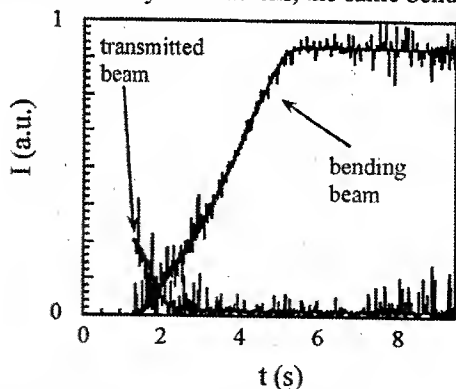
Fig.2. Dynamics of the transmitted output beam and bending beam in the guide
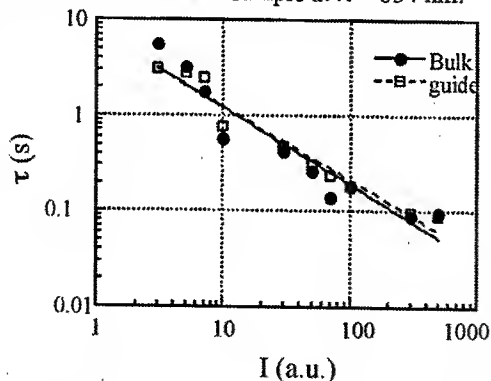
Fig. 3. Response time versus the light intensity in the guide (squares) and inside the bulk (squares). The straight lines are numerical adjustments according to laws I^{-x}.

4. Conclusion

The self-bending of the light is observed at $\lambda = 514.5$ nm and at $\lambda = 854$ nm for the first time in a planar monomode waveguide BaTiO$_3$:Rh fabricated by the technique of ion beam implantation. The photorefractive origin of the phenomenon is identified and characterized. This offers the possibility to achieve phase conjugation in the guide.

References

[1] P. Mathey, P. Jullien, B. Mazu , D. Rytz, Dynamics of novelty filtering and edge enhancement in cobalt-doped barium titanate, J. Opt. Soc. Am. B 15, 135-1361 (1998).
[2] J. Feinberg, Asymmetric self-defocusing of an optical beam from the photorefractive effect, J. Opt. Soc. Am. 72,46 (1982).
[3] P. Mathey, A. Dazzi, P. Jullien,, D. Rytz, P. Moretti, Guiding properties and nonlinear wave mixing at 854 nm in a rhodium-doped BaTiO$_3$ waveguide implanted with He$^+$ ions, J. Opt. Soc. Am. B 18, 344-347 (2001).

Diffraction effects in copper-doped helium-implanted LiNbO₃ waveguide

Yury M. Larionov, Marina N. Frolova, Stanislav M. Shandarov
Department of Electronic Devices, State University of Control Systems and Radioelectronics, 40 Lenin Avenue, Tomsk 634050, Russia
yular@ed.rk.tusur.ru

Sergey M. Kostritski
Department of Physics, Kemerovo State University, Krasnaya St. 6, Kemerovo 650043, Russia

Abstract: We report an experimental observation of leaky substrate TM modes diffraction on a grating-like periodical structure formed by defects of waveguide layer. Appearance of such defects we explain by features of copper-doped helium-implanted optical LiNbO₃ waveguide fabrication process.
©2002 Optical Society of America
OCIS codes: (050.1940) Diffraction; (130.3730) Lithium niobate; (230.7370) Waveguides

1. Introduction

It is known that in photorefractive LiNbO₃ waveguides fabricated by proton and helium implantation the surface damage can take place [1,2]. The cracks are the results of the mismatch of lattice constant between a strongly proton-exchanged (or helium-implanted) region near the surface of the waveguide and regions deeper in the waveguide where less exchange has taken place. Thus the long exchange and oxidation times lead to the change of crystal structure. In turn the defects induced by He⁺ implantation have a non-point nature and might be assigned to large-dimension clusters, having a new crystalline structure with a very specific lattice vibration spectrum, and in case of H⁺ implantation the lattice defects of point nature, inducing weak crystal disorder only, predominate[1].

It was also shown [2] that nascent cracks can form precisely oriented, stress-induced grating-like structures with irregular periods. As a result, the light of an excited mode can be diffracted into other modes and mode spectrum can be anomalously side-shifted out of the expected geometrical plane.

Other experiments show influence of annealing processes on a waveguide surface destruction. It was found that long-time annealing of LiNbO₃ layer after the process of H⁺ or He⁺ implantation results in the formation of the lithium triniobate phase in the samples and, with time, to destruction of their surface. Depending on crystal orientation the damages have linear or tessellated structure [3].

2. Experimental results and discussion

In our experiments we used a sample that was formed on Y-cut wafer by three-sequential He-implantation and following Cu-doping by ion exchange at a temperature of 230°C for a 20 min. To increase the efficiency of helium-implanted waveguide it was annealed at 215°C for a 30 min.

For investigation of waveguides properties of the sample the standard one-prism coupling method was used. Scheme of experiment is shown in Fig. 1. The focused TE or TM-polarized beam of He-Ne laser with wavelength λ = 0.633 μm is coupled into the waveguide throw the rutile prism. The direction of light beam propagation is a X-axis of crystal.

On a screen 1 we have observed dark and bright m-lines of waveguide modes. Experimental investigation have shown simultaneously excitation of TE and TM modes on both TE and TM input polarization of light beam. Such an effect can be explained by an existence of described above grating-like structure in waveguide layer that may lead to diffraction of wavegide mode into other modes. On screen 2 we have observed leaky substrate modes. 4 substrate modes (always TM-polarized) are excited simultaneously with excitation of waveguide modes. This modes have appeared due to non-diagonal components of dielectric permittivity tensor of birefringent negative crystal. Part of energy of TE or TM polarized waveguide modes are transmitted to the ordinary wave arising in substrate.

For all modes the excitation angles α_m^{in} and outlet angles of substrate modes related to the flatness of waveguide Θ_m^{out} were detected (Fig. 1) and converted into effective refractive indices,

$$n_m^* = n_p \sin\left[A + \arcsin\left(\frac{\sin\left(\alpha_m^{in}\right)}{n_p}\right)\right],$$ (1)

where n_p is the refractive index of the used rutile prism, m is order number of mode, and A the relevant prism angle. Using Eq.1 we have calculated the spectrum of effective refractive indices for TM modes: $n_0^* = 2.243$, $n_1^* = 2.2262$, $n_2^* = 2.1923$, $n_3^* = 2.1803$, and refractive indices of wafer: $n_o = 2.25$ and $n_e = 2.18$.

For input TM polarization the set of angles Θ_m^{out} is following: $\Theta_0^{out} = 20.29°$, $\Theta_1^{out} = 28.16°$, $\Theta_2^{out} = 40.38°$, $\Theta_3^{out} = 43.44°$. This outlet angles are related with the light propagation angles in crystal by equation

$$n_o \sin\Theta_m = \sin\Theta_m^{out}.$$ (2)

From here $\Theta_0 = 8.65°$, $\Theta_1 = 12.02°$, $\Theta_2 = 16.73°$, $\Theta_3 = 17.84°$.
The effect of TM-polarized wave beaming from waveguide take place for modes with effective refractive indices satisfying to following proportion

$$n_m^* = n_o \cos\Theta_m,$$ (3)

where n_o is refractive index of ordinary light wave.
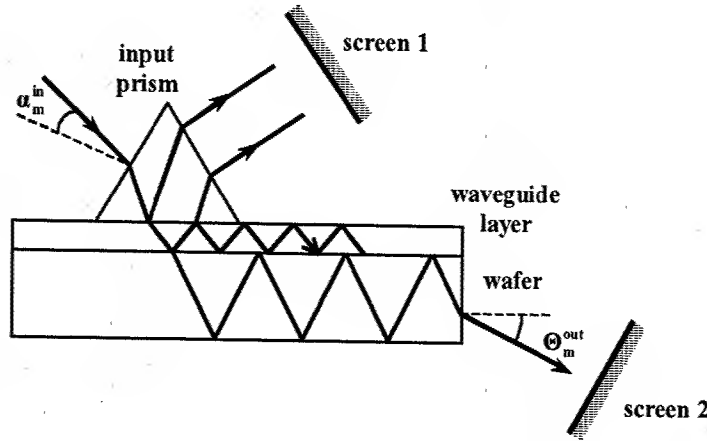
Fig. 1. Scheme of prism-coupling method and experimental observation of leaky substrate modes.

Furthermore among the ordinary leaky modes described above the substrate modes looking like diffraction pattern were observed on a screen 2 (Fig. 1). Such type of diffraction can take place only in a case of existence of periodical structure in the waveguide layer. Periodical structure deflect part of energy of waveguide radiation from the angle of total reflection. As a result the substrate mode appear. Adding of wave vectors of periodical grating-like structure to the wave vector of waveguide mode leads to arising of additional substrate modes closely located to each other (Fig. 2). This modes were situated before or between the lines of leaky modes over the range of outlet angles α_i^{out} from 5° to 28°. For the zero-order TM-mode outlet angles α_i^{out} for 22 fringes were measured: 21.75°, 21.23°, 20.72°, 20.13°, 19.54°, 19.09°, 18.50°, 17.97°, 17.44°, 16.83°, 16.16°, 15.48°, 14.73°, 14.04°, 13.58°, 12.36°, 11.52°, 10.53°, 9.53°, 8.46°, 6.94°, 5.44°.
An equation binding effective refractive indexes of waveguide modes and period of structure can be obtained from the vector diagram (Fig. 2):

$$k_0 n_m^* + \frac{2\pi}{L_s}i = k_0 n_o \cos\alpha_i,$$ (4)

where n_m^* is an effective refractive index for waveguide mode of m order, i is a order number of grating vector, L_s is a grating period, k_0 is a wave number, $\alpha_i = \arcsin\left(\sin\left(\alpha_i^{out}\right)/n_o\right)$ is an angle of substrate mode propagation, and n_o is a refractive index of wafer (refractive index of ordinary light wave).
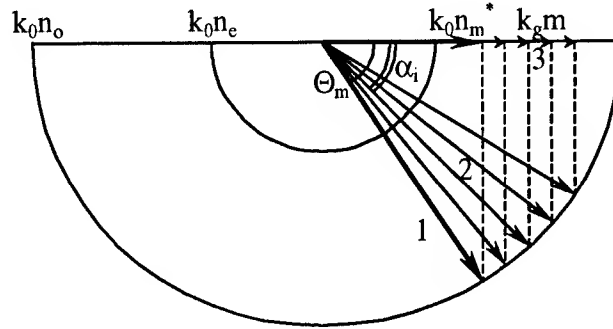
Fig. 2. Vector diagram. 1 - leaky substrate TM mode, 2 – leaky substrate TM modes forming a diffraction pattern, 3 – grating vector formed by periodical structure of waveguide layer.

Using the measured spectrum of angles α_i and set of equations (4) for $n_0^* = 2.243$, we calculated the value of grating period $L_x \approx 400$ μm. Leaky substrate modes in addition had a periodical structure in transverse direction. We measured spacing between the diffraction maximums and evaluated the period of structure as $L_z \approx 100$ μm. Changing of plate orientation by rotating it to 90 degrees (light beam propagate along the Z-axis) is leaded to generation of interference pattern along the m-line of leaky substrate mode. The period of diffraction grating in this case also equal $L_x \approx 400$ μm. Congruence of periods L_x at orthogonal orientations of waveguide allow us to make an assumption about linear character of grating-like structure with orientation of grating in the line of Z-axis. An existence of similar defect structure acquired in a process of H:LiNbO₃ waveguides, with the same orientation of crystal, annealing was observed [3].

3. Conclusion

The conducted observations and measurements show an existence of grating-like periodical structure in waveguide layer of investigated sample. To all appearance the grating have a complex structure, but the linear character of structure (with a period $L = 400$ μm) predominates. However, presence of orthogonal to described above linear structure interference pattern, corresponding to a periodical structure with another period (100 μm), bring us to make a conclusion about an existence of some kind of periodical substructures in a waveguide layer. Probably on a formation of such kind of grating-like structure different stages of technological process of waveguide fabrication (including He⁺ implantation, Cu-doping and annealing) were able to affect. Further investigation may help to determine relations between parameters of waveguide fabrication process and structure of waveguide layer damages.

1. S.M. Kostritskii and P. Moretti "Comparative study of defects induced by proton and helium implantation in LiNbO₃ crystal," Radiat. Eff. 150, 151-156 (1998)
2. F. Richerman, D. Kip, B. Gather, and E. Krätzig "Characterization of photorefractive LiNbO₃ waveguides fabricated by combined proton and copper evchange," Phis. Stat. Sol. A 150, 763-772 (1995)
3. V.A. Ganshin and Yu.N. Korkishko "H:LiNbO₃ waveguides: effects of annealing," Optic Comm. 86, 523-530 (1991)

Femtosecond measurement of nonlinear refraction in periodically poled lithium tantalate

S. Ashihara, J. Nishina, T. Shimura, and K. Kuroda

Institute of Industrial Science, University of Tokyo, 4-6-1, Komaba, Meguro-ku, Tokyo,153-8505 Japan

TEL: +81-3-5452-6137 FAX: +81-3-5452-6159 E-mail: ashihara@iis.u-tokyo.ac.jp

Abstract: We present femtosecond measurements of nonlinear refraction in periodically poled lithium tantalate by using spectrally resolved two-beam coupling. The sign and magnitude of nonlinear phase shifts induced by cascade quadratic nonlinearity and intrinsic Kerr nonlinearity are measured.

OCIS codes: (190.7110) Ultrafast nonlinear optics; (190.3270) Kerr effect; (320.7100) Ultrafast measurement

Introduction

Cascade quadratic nonlinearity (CQN) generates large phase shifts of controllable sign [1]. Due to its non-resonant nature, its application for ultrashort pulse evolution is promising [2]. The temporal dynamics of CQN phase shifts in type I phase mismatched conditions have been measured in femtosecond domain so far [3]. CQN with quasi-phase matched structure is attractive because of its large nonlinearity and possibility of domain engineering. However the measurements of cascade phase shifts or their applications in femtosecond domain have not yet been reported.

The intrinsic nonlinear index, n_2, plays an important role in the spatial, spectral and temporal pulse evolution in many quadratic nonlinear wave-mixing processes with ultrashort or high-energy optical pulses. Accurate knowledge of n_2 is particularly useful for designing ultrashort frequency converters and pulse shapers based on quadratic media. M. Sheik-Bahae et al. [4] has measured the nonlinear indices of important quadratic nonlinear materials by using the Kerr-lens autocorrelation technique. However n_2 of lithium tantalate (LT), which is an important nonlinear material for quasi-phase matching (QPM) devices, have not been reported so far. It has large second-order nonlinear coefficient (15.1 pm/V), deep transparency into the wavelength of 280 nm, and high photorefractive resistance.

Here we report the femtosecond measurement of intrinsic Kerr nonlinearity and cascade phase shifts in periodically poled lithium tantalate (PPLT) by use of spectrally-resolved two-beam coupling (SRTBC) technique [5].

Experiments and discussions

SRTBC is a sensitive method for determining the sign and magnitude of the real and imaginary parts of $\chi^{(3)}$. It is also useful for measuring the temporal dynamics of various kinds of Kerr-like nonlinearity, including cascading nonlinearity. This technique is based on the well-known pump-probe arrangement, followed by the spectrally filtered

transmittance measurement. Assuming that the electric field of the pulse is $E(t) \sim \exp(-t^2/t_0^2)$, the nonlinear transmittance as a function of delay τ and detuning $\delta = \omega - \omega_0$ (ω_0 is the center frequency of the spectrum) is [5]

$$\frac{\Delta T}{T}(\tau,\delta) = \frac{2}{\sqrt{3}}\exp(\delta^2 t_0^2/6)\exp(-2\tau^2/3t_0^2)\times[2\Delta\Phi\sin(2\delta\tau/3) - q\cos(2\delta\tau/3)] \quad (1)$$

Here $\Delta\Phi = k\gamma I_{pu}L$ ($\gamma = 4\pi n_2/cn$) is the nonlinear phase shift, $q = \beta I_{pu}L$, the effect of two-photon absorption, I_{pu}, the pump intensity and L, the interaction length. We can obtain β and γ by fitting the measured transient signal.

The mode-locked Ti: sapphire laser supplied 5 nJ pulses of 80 fs duration and center wavelength around 800 nm. The probe beam power was made 10 times smaller than the pump beam by use of 10/90 beam splitter. The pump and the probe beams were noncollinear, and the polarizations of the two beams were linear and parallel. The incident pump pulse is set to be 3.7 nJ, which corresponds to the peak intensity of 3.1 GW/cm^2. While scanning the delay line, the transmitted probe pulse was analyzed spectrally with a spectrometer and a photo-diodes array.

Intrinsic nonlinear refractions of BBO and bulk LT are measured for first. The samples are 1 mm thick BBO cut for type I phase matching at 800 nm ($\theta = 29$ deg.) and 1 mm thick bulk LT cut perpendicular to c-axis. The pump and probe beams propagates as ordinary waves. Figure 1(a) shows the measured SRTBC signals for LT (circles) and for BBO (squares) at the detuning of $\Delta\lambda = +1.13\sigma$ (σ is FWHM of the probe spectrum). The fitting curves obtained by using Eqn.(1) are also shown as dashed lines. We measured the SRTBC traces at several positive and negative detuning points. Figure 1(b) shows the phase shifts obtained by fitting the traces for various detunings. From these results, we estimated the nonlinear index of LT to be relatively large, n_2 (LT) $\sim 4 \times n_2$ (BBO). By using the previously reported value of n_2 (BBO) = 3.65 x 10^{-16} [cm^2/W] [5], we obtain n_2 (LT) $\sim 14.6 \times 10^{-16}$ [cm^2/W].
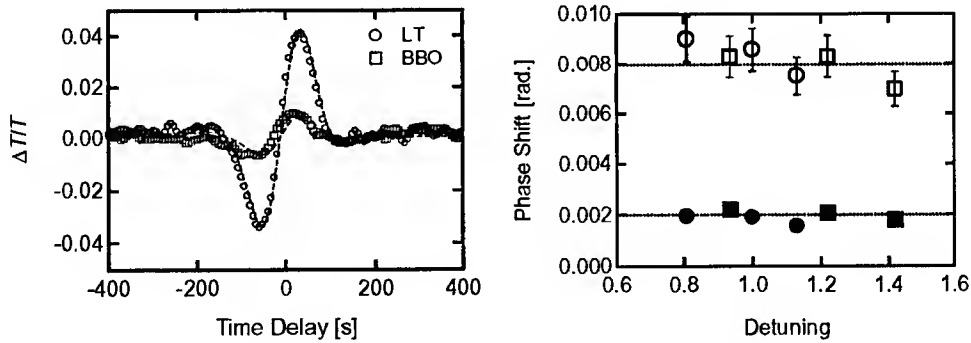
Fig. 1 (a) SRTBC signals of intrinsic n_2 in bulk LT and in BBO. (b) Measured phase shift as a function of detuning for LT (blank) and for BBO (filled). Points represented by squares (circles) were measured with positive (negative) detuning.

Next we measured the nonlinear phase shifts due to cascade nonlinearity in PPLT. The PPLT sample is fabricated by the usual lithography technique followed by the electric field application (~21kV/mm). The sample has thickness of 0.3 mm, interaction length (along x-axis) of 0.8 mm, and the domain inversion period of 3.1 μm. The device is kept to be 180 ^{0}C to reduce photorefractive effects. The pulses are polarized as extraordinary waves. We measured SRTBC signals for various phase mismatches by varying the center wavelength from 800 nm to 840 nm. Figure 2 shows the measured SRTBC traces both for positive and negative phase mismatch conditions. In our definition, the

positive phase shift $\Delta\Phi\,(>0)$ is generated for negative wave-vector mismatch ($\Delta k < 0$), and vice versa. The signals showed apparent dependence on Δk, which confirms that the measured signals originate from CQN. The measured phase shift of positive sign for $\Delta k < 0$ is larger than those of negative sign for $\Delta k > 0$. This should be due to the competition with intrinsic Kerr-nonlinearity. These measurements showed that CQN phase shift have clear dependence on Δk even in femtosecond domain and its magnitude is comparable with the intrinsic Kerr-nonlinearity. Because the CQN phase shift is degraded by the relatively large GVM at this wavelength, the CQN should be much more prominent under smaller GVM conditions, for example, at longer wavelength.
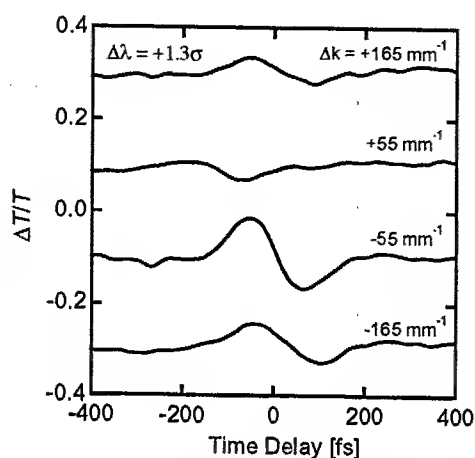
Fig. 2 Measured SRTBC signals in PPLT under positive and negative phase mismatch conditions.

Conclusions

In conclusion, we have measured, for the first time to our knowledge, nonlinear refraction in periodically-poled lithium tantalate in femtosecond domain. Nonlinear phase shifts due to cascade quadratic nonlinearity and intrinsic Kerr-nonlinearity have been measured by use of SRTBC technique. The results give important insight for designing ultrafast frequency converters, mode-lockers, and pulse compressors based on QPM devices.

References

[1] R. DeSalvo, D. J. Hagan, M. Sheik-Bahae, G. Stegeman, E. W. Van Stryland, and H. Vanherzeele, "Self-focusing and self-defocusing by cascaded second-order effects in KTP," Opt. Lett. **17**, pp.28-30 (1992).

[2] L. J. Qian, X. Liu, and F. W. Wise, "Femtosecond Kerr-lens mode locking with negative nonlinear phase shifts," Opt. Lett. 24, pp.166-168 (1999).

[3] O. Albert and J. Etchepare, "Femtosecond temporal behavior measurement of Kerr-like cascaded second-order non-linearities," Opt. Commun. 154, pp. 345-349 (1998).

[4] M. Sheik-Bahae and M. Ebrahimzadeh, "Measurements of nonlinear refraction in the second-order $\chi^{(2)}$ materials KTiOPO$_4$, KNbO$_3$, β-BaB$_2$O$_4$, and LiB$_3$O$_5$," Opt. Commun. 142, pp. 294-298 (1997).

[5] I. Kang, T. Krauss, and F. Wise, "Sensitive measurement of nonlinear refraction and two-photon absorption by spectrally resolved two-beam coupling," Opt. Lett. 22, pp. 1077-1079 (1997).

Towards an Optical Parametric Oscillator in a GaAs-based waveguide

A. De Rossi, M. Calligaro, V. Ortiz
*THALES Research and Technology, Domaine de Corbeville, 91400 ORSAY France
Tel. (+33)1.6933.9387, Fax (+33)1.6933.0740. alfredo.derossi@thalesgroup.com*

V. Berger
*Pôle "Matériaux et Phénomènes Quantiques", Fédération de Recherche CNRS 2437, Université Denis
Diderot Paris VII, case 7021, 2 Place Jussieu, 75251 PARIS, vberger@ccr.jussieu.fr*

Abstract: We will discuss the feasibility of an integrated parametric oscillator based on GaAs. Results on parametric fluorescence will be presented. Minimization of losses and mirror deposition are the crucial points for obtaining parametric oscillation. A threshold around 100 mW is expected.
© 2002 Optical Society of America
OCIS Codes: (190.4410) Nonlinear optics, parametric processes; (230.7370) Waveguides; (260.1440) Birefringence

Efficient low-power compact sources of tunable coherent near and mid-infrared wavelength radiation are necessary for many applications, including communications, spectroscopy, and process monitoring. Optical parametric oscillators (OPOs) offer extremely wide tunability intrinsically limited only by material transparency. OPOs require only a single pump laser, and offer an energy conversion efficiency much larger than that of single-pass nonlinear interactions such as difference-frequency generation. Singly and doubly resonant integrated OPO's have been demonstrated in LiNbO$_3$ waveguides [1-2].
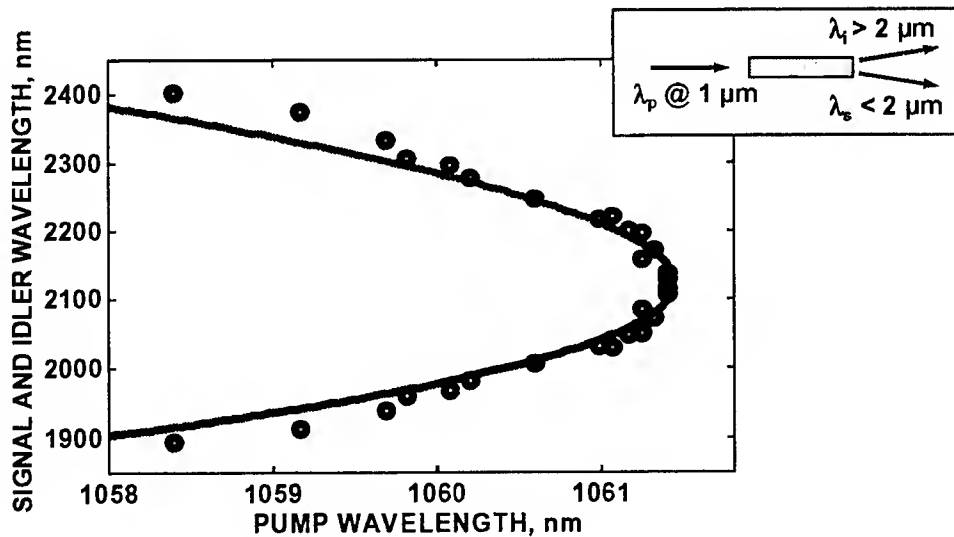
Fig. 1. Measured parametric fluorescence signal vs. pump wavelength and fit with theory (dashed). Inset: PF signal vs. pump power at degeneracy.

Gallium Arsenide has a very high second-order susceptibility (d_{eff} is in the range of 100–200 pm/V). This advantage, together with the possibility of integration with laser sources, makes this material very attractive for integrated nonlinear optics. GaAs, however, is not birefringent nor ferroelectric and thus the standard phase-matching or quasi-phase-matching techniques cannot be applied in a straightforward way. This had prevented the use of GaAs in quadratic nonlinear optics.

In order to circumvent this limitation, the concept of form-birefringence was implemented in oxidized GaAs/AlAs waveguides. The critical step is the selective oxidation of AlAs, which is carried out at 400°-500°C in a water vapour atmosphere. The resulting refractive index contrast is strong enough to compensate the dispersion and phase-match the parametric interaction. Due to this technique, phase-matched difference frequency generation and second harmonic generation have been observed [3-4].
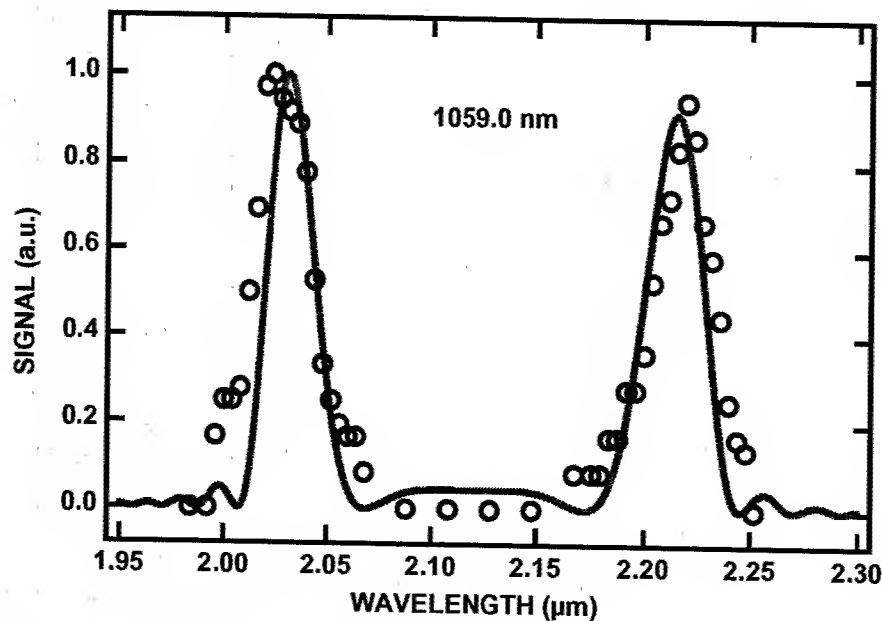
Fig. 2. Measured PF spectra (markers) compared with calculated spectra. The pump wavelength is 1059.0 nm, 0.6 nm off degeneracy. The sample length is 5 mm.

One of the most exciting possibilities with this new type of nonlinear material is the realization of an OPO on a GaAs chip. To this aim, we investigated the parametric fluorescence (PF) generated in such waveguides [5]. The PF yield, however, was limited severely by the high optical losses. This motivated a systematic effort in improving the sample processing, which recently lead to orders of magnitude increase in the yield. The parametric fluorescence has been analyzed quantitatively, the tuning curve has been measured (Fig. 1) and the "selection rules" on pump and signal polarization have been verified. A parametric fluorescence efficiency as high as 6×10^{-7} W/W has been measured in a 3-mm long waveguide [6]. This is comparable with what is obtained with periodically poled $LiNbO_3$ waveguides, that are much longer, typically [7].

From the analysis of the emitted PF spectra (Fig. 2) we have deduced some important parameters such as the normalized conversion efficiency, scaled with the waveguide length, which is approximately 1000% $cm^{-2}W^{-1}$. We could also estimate the effective interaction length, which was slightly shorter than the physical waveguide length, thus indicating reduced waveguide inhomogenity.

In wide, multimode, waveguides, different transverse modes can be phase-matched and generate PF, provided that the additional selection rules associated with mode symmetry are respected. We observed up to 3 peaks, associated to 3 different combinations of the modes TM_{00}, TM_{01}, TE_{00}, TE_{01} (Fig. 3).

Optical losses have been measured at different wavelengths using Fabry-Perot method and the scattered light method [8]. The results (~0.5cm^{-1}, at 1.32 and 2 μm) are encouraging. The estimated pump power threshold is about 100 mW, using high reflecting coating at the waveguide end facets. Work is now focussed on deposing high quality dielectric mirrors.
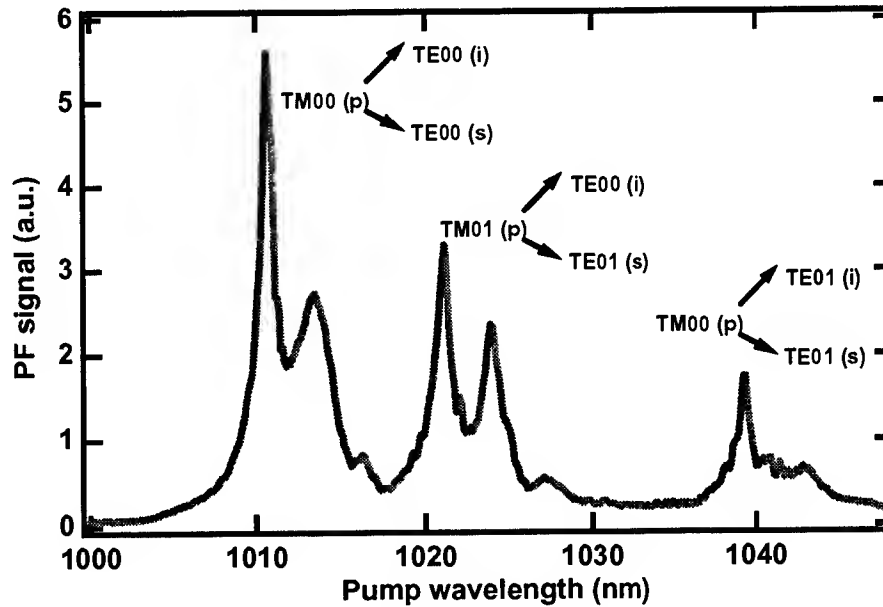
Fig. 3. Multimode parametric fluorescence involving TM_{00}, TM_{01} (pump) and TE_{00}, TE_{01} (signal).

References

[1]. H. Suche, W. Sohler, in *Integrated and Guided Wave Optics*, Vol. 5 of OSA Technical Digest Series (Optical Society of America, Washington D.C., 1988), p. 176.

[2]. M. A. Arbore, and M. M. Fejer, Opt. Lett. **22**, 151 (1997)

[3]. A. Fiore, V. Berger, E. Rosencher, P. Bravetti, and J. Nagle, Nature **391**, 463-466 (1998);

[4]. A. Fiore, S. Janz, L. Delobel, P. van der Meer, P. Bravetti, V. Berger, E. Rosencher, and J. Nagle, Appl. Phys. Lett. **72**, 2942 (1998)

[5]. G. Leo, V. Berger, C. OwYang, J. Nagle, J. Opt. Soc. Am. B, **16**, 1597 (1999)

[6]. A. De Rossi, V. Berger, M. Calligaro, G. Leo, V. Ortiz, X. Marcadet, Appl. Phys. Lett. **79**, 3758 (2001)

[7] S. Tanzilli, H. De Riedmatten, W. Tittel, H. Zbinden, P. Baldi, M. De Micheli, D.B. Ostrowsky and N. Gisin, Electron. Lett. **37**, 26 (2001)

[8] S. Venugopal Rao, K. Moutzouris, M. Ebrahimzadeh, A. De Rossi, M.Calligaro, V. Ortiz, G. Ginitz, and V. Berger, submitted to Appl. Phys. Lett.

Photorefractive Solitons and Light-Induced Resonance Control in Semiconductor CdZnTe

Tal Schwartz, Yaniv Ganor, Tal Carmon,

Raam Uzdin, Sharon Shwartz and Mordechai Segev

Physics Department and Solid state Institute,

Technion - Israel Institute of Technology, Haifa 32000, Israel

Uri El-Hanany

Imarad Imaging Systems LTD., Rehovot 76124, Israel,

We experimentally demonstrate the formation of (1+1)D and (2+1)D solitons in photorefractive CdZnTe:V, exploiting the intensity-resonant behavior of the space charge field. We show that the resonance intensity is tunable, allowing soliton formation times as low as 10μsec scales with very low optical power.

Photorefractive Solitons and Light-Induced Resonance Control in Semiconductor CdZnTe

Tal Schwartz, Yaniv Ganor, Tal Carmon,
Raam Uzdin, Sharon Shwartz and Mordechai Segev
Solid state Institute, Technion - Israel Institute of Technology, Haifa 32000, Israel

Uri El-Hanany
Imarad Imaging Systems LTD., Rehovot 76124, Israel,

Optical spatial solitons and self trapping of beams have been investigated for almost four decades. Much of the progress in this field was made in the last 10 years, partly following the discovery of photorefractive solitons [1], which enabled solitons with very low power levels, as well as soliton experiments in bulk media. Photorefractive solitons, and the waveguides they induce, combine properties that suggest interesting applications, many of them are in optical communication. In general, however, the formation time of solitons in most photorefractive materials is rather long, determined by the dielectric relaxation time, i.e., inversely proportional to the product of the mobility and the optical intensity, and the mobility in photorefractive oxides is low (~1 [cm^2/Vsec]). In principle, photorefractive semiconductors, (e.g., InP), have a high mobility and could offer formation times 1000 faster than in the other photorefractives. However, the electrooptic coefficient in these semiconductors is tiny, which implies that solitons that are as narrow as ~20 optical wavelengths necessitate very large applied fields, making solitons in them almost impossible [2]. But, in some of these materials (e.g. InP and CdZnTe) a unique resonance mechanism enhances the space charge field by as much as 10 times the applied electric field, enough to support the self-trapping of a narrow beam. The resonant enhancement of the space charge field in soliton formation was previously observed in InP [3] and recently theoretically explained [4].

The resonant enhancement of the space charge field occurs in materials with both types of charge carriers, both being excited from a common trap level: one excited optically and the other excited by temperature. When a focused beam illuminates a biased crystal of this kind, and the beam intensity is such that the photo-excitation and thermal excitation rates comparable, the local electric field is highly enhanced. It is a **resonant enhancement,** although it is an intensity-resonance and not an atomic resonance. The enhanced electric field compensates for the smallness of the electrooptic coefficient and enables a sufficiently large change in the refractive index to support narrow solitons. Self focusing and solitons based on the resonance enhancement in photorefractive semiconductors was thus far demonstrated experimentally only in InP:Fe. This mechanism could facilitate narrow and fast solitons in photorefractives, but unfortunately, a new problem arises: the electron excitation rate is determined by temperature, so the value of the resonance intensity is prefixed and is very low (~30mWatt/cm^2 at T=300°K), which inhibits the exploitation of the ability for short formation times. Increasing the temperature could offer some improvement as it shifts the resonant intensity to higher values, but most applications cannot afford temperatures much higher than room temperature. Furthermore, it is difficult to control the resonance through temperature because of its high sensitivity. All-optical control of the resonance is desirable because it is fast, easy, and very accurate.

Here we demonstrate the formation of (1+1)D and of (2+1)D solitons in another photorefractive semiconductor material: CdZnTe:V, and show optical control over the resonance intensity, facilitating formation times of 10μsec with very low optical power.

CdZnTe:V has a similar intensity-resonant mechanism as InP:Fe, with an important difference: the electrons and the holes exchange roles [5]. Electrons are optically excited by a 1.3μm (or shorter)

wavelength, whereas holes are thermally excited. But, the holes can also be excited optically, by a ~1.5μm wavelength beam [6]. We use this to increase (and control) the hole excitation rate considerably by uniformly illuminating the crystal with a 1.48μm wavelength beam ("background beam"). The background beam sets the resonance intensity to much higher values than temperature-driven resonance, thereby substantially shortening their formation time.

Our experimental setup resembles that of Refs. [3]. The CdZnTe:V crystal is situated on a temperature control device, stabilizing the crystal temperature to 21°C. The soliton-forming beam comes from a CW 936nm wavelength Ti:Sapphire laser. We carry out two sets of experiments, demonstrating (1+1)D and (2+1)D solitons. In both cases the beam is linearly polarized along the (110) direction and is propagating in the ($1\bar{1}0$) direction. In the absence of applied field, the beam diffracts to ~3 times its input FWHM after 5 mm propagation. For the background beam, we use a 1.48μm wavelength beam from a diode laser, which illuminates the crystal uniformly. The external bias field is applied along the (001) direction.

Figure 1: Observation of (1+1)D and (2+1)D self trapping in CZT. A 17µm FWHM (1+1)D input beam (a) is self trapped with E_0=1.8 kV/cm (b). The peak intensity at the input face of the crystal is 1.5mw/cm². When E_0=0, this beam diffracts (c) to 40µm FWHM. A circular 15µm FWHM input beam (d) is self trapped (e) with E_0=9.4 kV/cm. The peak intensity at the input face is 3.4mw/cm². When E_0=0, this beam diffracts (f) to 50µm FWHM.

Typical results with (1+1)D and with (2+1)D solitons are shown in the upper and lower rows of Fig. 1, respectively. Shown are photographs and beam profiles of the input beams [(a),(d)], output soliton beams [(b),(e)] when the intensity and applied fields are adjusted to the appropriate values, and linear diffraction [(c),(f)] in the absence of applied field. The 1D soliton [Fig. 1(b)] is at an applied field E_0 =1.8 kV/cm, and the 2D soliton of Fig. 1(e) is at E_0 = 9.4 kV/cm, both with no background illumination. In both cases, the data clearly shows very nice undistorted narrow beams that are as narrow as the input beam.

To illustrate the resonant self-focusing behavior, we perform a set of experiments with all parameters kept constant and varying only the intensity. Typical results are shown in Fig. 2, showing photographs and beam profiles taken at the output face of the crystal. All the data in this figure is without background illumination, so the "natural" (thermal) resonance intensity is ~1.5mW/cm². Figure 2 (a-e) shows experiments with the input beam of Fig. 1(a) and E_0 = 6 kV/cm. The output beam in (a) is far below resonance and it shows some fanning-like features (the intensity spread to the right). At higher intensities it self-focuses (b), until it forms a soliton (c) when the peak intensity is in the range 0.45-1.5 mW/cm².

The reason for this somewhat wider range of intensities is the presence of fairly high absorption (2.2 cm⁻¹), which means that the ratio between the resonance intensity and the intensity of the beam is varying throughout propagation. At the resonance intensity and slightly above it, the beam breaks up in two (Fig. 2d), as explained

Figure 2: Observation of the self-focusing dynamics for (1+1)D (left) and (2+1)D (right) beams, as a function of input intensity. Keeping the beams width and resonance intensity fixed, the beams intensities are successively increased. The focusing effect increases with the intensity [(a-c) and (f-h)] until it reaches its maximum strength (c,h). Then, at higher intensities, the self-focusing effects decrease (d,i) until they are non-apparent (e,j).

theoretically in [4]. The reason is that in this range the beam induces a waveguide that is shifted away from the beam center. As the intensity is further increased (Fig. 2e), the induced waveguide moves further away from the beam, until it no longer affects the beam. The trend with a 2D beam is very similar: the beam displays fanning-like features at intensities far below resonance (Fig. 2f), solitons form at the proper intensity range (2h), and the beam is distorted at higher intensities (2i), until, at high enough intensities (2j) the nonlinearity no longer affects the beam.
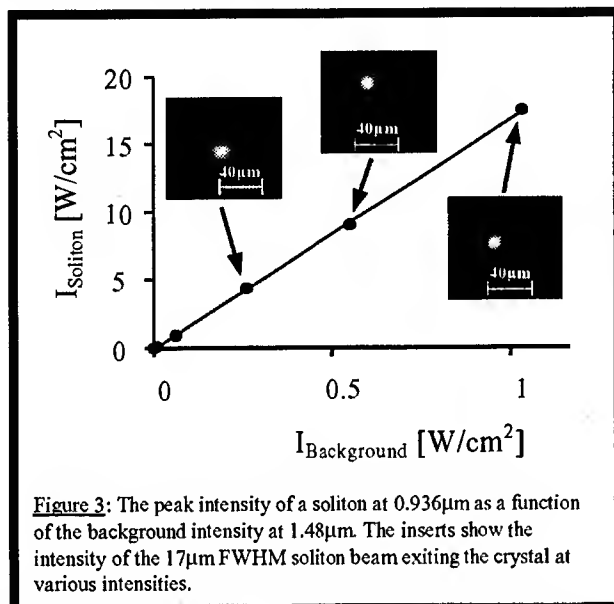
Figure 3: The peak intensity of a soliton at 0.936μm as a function of the background intensity at 1.48μm. The inserts show the intensity of the 17μm FWHM soliton beam exiting the crystal at various intensities.

Finally, we show how the background intensity determines the resonance. We carry out a set of experiments with the input beam of Fig. 1a, $E_0 = 6kV/cm$, and vary the value of the background intensity from zero to as high as 54 mW/cm^2. To isolate the control over the resonance, we vary the background intensity while keeping the input (soliton-forming) beam shape and the applied field fixed, and adjust the intensity of the input beam until a soliton forms. Figure 3 shows typical results with 2D solitons for various resonant intensities that are induced via the background beam. At the highest intensity point the resonance intensity is ~1000 times higher than the thermal resonance intensity. This shows we can generate solitons in a wide range of intensities, by optically controlling the resonance accurately. We carry out similar experiments with a 1D beam and the trend is very similar. The response time at the point of the highest resonance intensity is 10 μsec for a 17μm FWHM circular beam ~46 $\mu Watt$ power (peak intensity ~17 Watt/cm^2). This response time is 1000 times faster than the response time of solitons of the same intensity in SBN, as expected from the 1000-fold higher mobility in CdTe. Yet we emphasize that to form solitons at this speed in CdTe, one must increase the resonance intensity from its natural (thermal) level by 10^3 times, which is exactly what we did. We envision that in the near future, light emerging from ordinary optical fibers carrying (temporal) data will be used to form spatial solitons. The average optical power emerging from such fibers is a few mWatts, which when distributed across a 10μm FWHM circular soliton beam, can lead to formation times as low as 100 nanoseconds.

In conclusion, we reported the observation of (1+1)D and (2+1)D solitons in CdZnTe:V which has a resonant photorefractive nonlinearity. We have shown how to control the resonance intensity of the nonlinearity by applying background illumination at wavelength different than that of the soliton. This enabled narrow solitons in intensities much higher than those inspired by the thermal excitation alone. Optical regulation of the resonance is a crucial step towards CZT-based applications, because it enables short response times, and because the system becomes temperature independent. We estimate that by using light beams emerging from ordinary optical fibers used for data transmission, we can form photorefractive solitons in CZT in within 100 nanoseconds.

References

1. M. Segev, B. Crosignani, A. Yariv, and B. Fischer, Phys. Rev. Lett. **68**, 923 (1992).
2. M. Segev, M. Shih and G. C. Valley, JOSA B **13**, 706 (1996).
3. M. Chauvet et. al., Opt. Lett. **21**, 1333 (1996); Appl. Phys. Lett. **70**, 2499 (1997).
4. R. Uzdin, M. Segev and G.J. Salamo, Opt. Lett. **26**, 1547 (2001).
5. J. Y. Moisan et. al, J. Opt. Soc. Am. B **11**, 1655 (1994).
6. P. Pogany, H. J. Eichler and M. Hage Ali, J. Opt. Soc. B **15**, 2716 (1998).

Efficient parallel algorithm for simulating wavelength-division-multiplexed dispersion-managed optical fiber systems

P. M. Lushnikov

Theoretical Division, Los Alamos National Laboratory, MS-B284, Los Alamos,
New Mexico, 87545, USA
Phone: 505 667 8715
Fax: 505 665 5757
lushnikov@lanl.gov

A wavelength-division-multiplexed (WDM) dispersion-managed (DM) optical fiber system is one of the key components of current development of ultrafast high-bit-rate optical communication lines. High capacity of optical transmission is achieved using both wavelength multiplexing and dispersion management (see e.g. Ref. [1, 2]). A dispersion-managed [3, 4, 5, 6] optical system is designed to create a low (or even zero) path-averaged dispersion by periodically alternating dispersion sign along an optical fiber that dramatically reduces pulse broadening. Second-order GVD (dispersion slope) effects and path-averaged GVD effects cause optical pulses in distinct WDM channels to move with different group velocities. Consequently modeling of WDM systems requires simulating a long time interval. Enormous computation resources are necessary to capture accurately the nonlinear interactions between channels which deteriorates bit-rate capacity. Here an efficient numerical algorithm is developed for massive parallel computation of WDM systems. The required computational time is inversely proportional to the number of parallel processors used. This makes feasible a full scale numerical simulation of WDM systems on a workstation cluster with a few hundred processors.

Neglecting polarization effects and stimulated Raman scattering and Brillouin scattering, the propagation of WDM optical pulses in a DM fiber is described by a scalar nonlinear Schrödinger equation (NLS):

$$iA_z - \frac{1}{2}\beta_2(z)A_{tt} - \frac{i}{6}\beta_3(z)A_{ttt} + \sigma(z)|A|^2A = i\Big(-\gamma + [\exp{(z_a\gamma)} - 1]\Sigma_{k=1}^{N}\delta(z-z_k)\Big)A$$
$$\equiv iG(z)A, \qquad (1)$$

where z is the propagation distance along an optical fiber, A is a slow amplitude, β_2, β_3 are first and second order group-velocity dispersions respectively which are periodic function of z, $\sigma = (2\pi n_2)/(\lambda_0 A_{eff})$ is the nonlinear coefficient, n_2 is the nonlinear refractive index, $\lambda_0 = 1.55\mu m$ is the carrier wavelength, A_{eff} is the effective fiber area, $z_k = kz_a$ $(k=1,\ldots,N)$ are amplifier locations, z_a is the amplifier spacing and γ is the loss coefficient.

Change of variables $u = Ae^{-\int_0^z G(z')dz'}$ results in NLS with z-dependent nonlinear coefficient $c(z) \equiv \sigma(z)\exp\Big(2\int_0^z G(z')dz'\Big)$:

$$iu_z - \frac{1}{2}\beta_2(z)u_{tt} - \frac{i}{6}\beta_3(z)u_{ttt} + c(z)|u|^2u = 0, \qquad (2)$$

Assuming that the nonlinearity is small $z_{nl} \equiv 1/|p|^2 \gg L$, where L is a dispersion map period and p is a typical pulse amplitude, one can express u in Fourier domain as a product of an exact solution of linear part of the Eq. (2) on a slow function $\hat{\psi}(\omega, z)$: $\hat{u}(\omega, z) \equiv \hat{\psi}(\omega, z)\exp\Big(\frac{i}{2}\omega^2\int_0^z\beta_2(z')dz' + \frac{i}{6}\omega^3\int_0^z\beta_3(z')dz'\Big)$, where $\hat{u}(\omega, z) = \int_{-\infty}^{\infty} u(t,z)e^{i\omega t}dt$. $\hat{\psi}$ is a slow function of z on a scale L (see reference [7, 8, 9]) which allows to integrate the Eq. (1) over the period L neglecting the slow dependence of $\hat{\psi}$ on z and get:

$$\hat{\psi}(\omega, (m+1)L) = \hat{\psi}(\omega, mL) + iR(\hat{\psi}, \omega), \qquad (3)$$

where

$$R(\hat{\psi}, \omega) = \frac{1}{(2\pi)^2}\int \hat{\psi}(\omega_1, mL)\hat{\psi}(\omega_2, mL)\hat{\psi}^*(\omega_3, mL)K(\triangle, \triangle_3)\delta(\omega_1 + \omega_2 - \omega - \omega_3)d\omega_1 d\omega_2 d\omega_3,$$
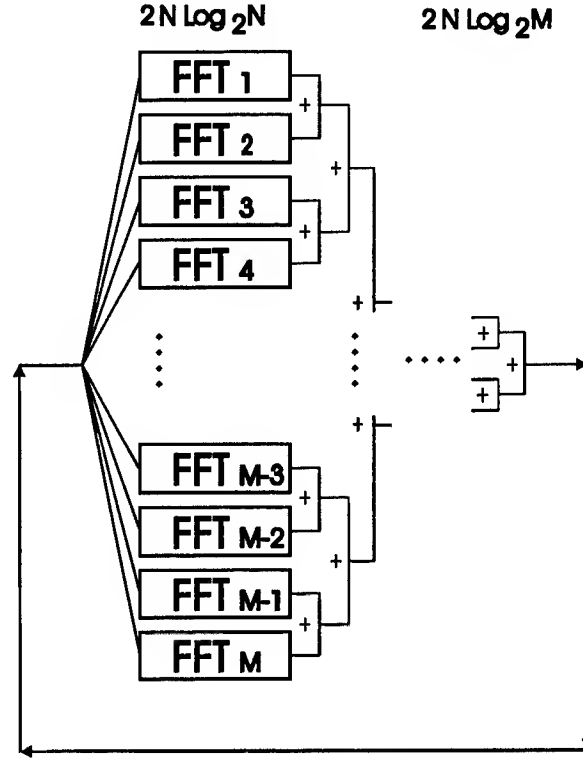
Fig. 1. A schematic of parallel computation algorithm. FFT_1, FFT_2, ... represent FFT in first CPU, second CPU, etc., respectively. $+$ sign means summation of the results of FFT in different processors.

$$K(\triangle, \triangle_3) = \int_{mL}^{(m+1)L} dz\, c(z) \exp\left(\frac{i}{2}\triangle \int_0^z \beta_2(z')dz' + \frac{i}{6}\triangle_3 \int_0^z \beta_3(z')dz'\right), \qquad (4)$$

$\triangle \equiv \omega_1^2 + \omega_2^2 - \omega^2 - \omega_3^2$, $\triangle_3 \equiv \omega_1^3 + \omega_2^3 - \omega^3 - \omega_3^3$, m is an arbitrary integer number.

Eq. (3) allows to find $\hat{\psi}(\omega, (m+1)L)$ from given $\hat{\psi}(\omega, mL)$ and thus to recover $u(t, z)$ using definition of ψ. The main obstacle in numerical integration of Eq. (3) is the computation of integral term $R(\hat{\psi}, \omega)$ which generally require N^3 operations for each iteration, where N is a number of grid points in ω or t-space. Here we introduce much more efficient numerical algorithm for calculation of $R(\hat{\psi}, \omega)$.

Using definition of $\triangle$, $\triangle_3$ one gets from (4) :

$$R(\hat{\psi}, \omega) = \frac{1}{(2\pi)^2} \int_{mL}^{(m+1)L} dz\, c(z) \exp\left(-\frac{i}{2}\omega^2 \int_0^z \beta_2(z')dz' - \frac{i}{6}\omega^3 \int_0^z \beta_3(z')dz'\right) \int \hat{\psi}^{(z)}(\omega_1, mL)$$

$$\times \hat{\psi}^{(z)}(\omega_2, mL)\hat{\psi}^{(z)*}(\omega_3, mL)\delta(\omega_1 + \omega_2 - \omega_3 - \omega)d\omega_1 d\omega_2 d\omega_3, \qquad (5)$$

where $\hat{\psi}^{(z)}(\omega, mL) \equiv \hat{\psi}(\omega, mL) \exp\left(\frac{i}{2}\omega^2 \int_0^z \beta_2(z')dz' + \frac{i}{6}\omega^3 \int_0^z \beta_3(z')dz'\right)$. In t-space this expression takes the form

$$\hat{F}^{-1}\left(R(\hat{\psi}, \omega)\right) = \int_{mL}^{(m+1)L} dz\, c(z)\mathbf{G}^{(z)}\left(\Psi^{(z)}(t)\right), \qquad (6)$$

where $\Psi^{(z)}(t, mL) \equiv |\psi^{(z)}(t, mL)|^2 \psi^{(z)}(t, mL)$ and $\mathbf{G}^{(z)}$ is an integral operator corresponding to a multiplication operator $\hat{\mathbf{G}}^{(z)}\left(\hat{\Psi}^{(z)}(\omega, mL)\right) \equiv \exp\left(-\frac{i}{2}\omega^2 \int_0^z \beta_2(z')dz' - \frac{i}{6}\omega^3 \int_0^z \beta_3(z')dz'\right)\hat{\Psi}^{(z)}(\omega, mL)$ in ω-space. It follows from the Eqs. (5), (6) that numerical procedure for calculation of $R(\hat{A}, \omega)$ includes four steps:

(i) The Backward Fourier Transform of $\hat{\psi}^{(s')}(\omega, mL) = \hat{\psi}(\omega, mL) \exp\left(\frac{i}{2}\omega^2 \int_0^z \beta_2(z')dz' + \frac{i}{6}\omega^3 \int_0^z \beta_3(z')dz'\right)$ for every value of z $(mL < z \le (m+1)L)$.

(ii) A calculation of $\Psi^{(z)}(t, mL)$ from $\psi^{(z)}(t, mL)$.

(iii) The Forward Fourier Transform of $\Psi^{(z)}(t, mL)$.

(iv) A numerical integration (summation) of $c(z) \exp\left(-\frac{i}{2}\omega^2 \int_0^z \beta_2(z')dz' - \frac{i}{6}\omega^3 \int_0^z \beta_3(z')dz'\right)\hat{\Psi}^{(s')}(\omega)$ over z for every value of ω.

The forward and backward Fourier transforms can be performed with the fast Fourier transform (FFT) which requires $NLog_2(N)$ operations. The steps (i)-(iii) need only a value of $\psi(t, mL)$ and these steps can be performed simultaneously in M processors (see Fig. 1), where M is a number of grid points for integration over z. Thus the total computational time equals to time necessary to perform $2NLog_2(N)$ operations in one processor. The step (iv) assume summation of the results of calculation in M processors. This summation can be effectively implemented by simultaneous summation in $M/2$ pairs of processors, then by summation of the results in $M/4$ pairs of processors etc. what totally requires a time which is equivalent to $2NLog_2(M)$ operation in one processor (see Fig. 1).

Numerical simulations of the WDM system were performed using both the split-step method for NLS (2) and using the numerical algorithm given by Eqs. (3) and (5) to demonstrate the accuracy of the proposed numerical scheme. Simulations were performed for 5 WDM channels (20 Gb/s per channel) over a typical transoceanic distance of $10^4\,km$. The channel spacing was $0.6\,nm$. The GVD periodically alternates between spans of standard monomode fiber ($\beta_2^{(1)} = -20.0\,ps^2/km$, $\beta_3^{(1)} = 0.1\,ps^3/km$, $\sigma_1 = 0.0013\,(km\,mW)^{-1}$, length $L_1 = 40\,km$) and dispersion compensating fiber ($\beta_2^{(2)} = 103.9\,ps^2/km$, $\beta_3^{(2)} = -0.3\,ps^3/km$, $\sigma_2 = 0.00405\,(km\,mW)^{-1}$, length $L_2 = -\beta_2^{(1)}L_1/\beta_2^{(2)}\,km$) so that the average GVD is zero. Fiber losses and amplifiers were not considered. However they can be easily included in the coefficient $c(z)$. A pseudo-random binary sequence of length 20 was used for every WDM channel. The boundary conditions are periodic in time. Each binary "1" was represented by an initially zero-chirp Gaussian pulse (return to zero format) of $10ps$ width and peak power $|u|^2 = 1\,mW$ at the beginning ($z = 0$) of the fiber line which is taken at the middle of standard monomode fiber span. The integration length L (see Eqs. (3) and (5)) is set to be equal to $(L_1 + L_2)/4$; $M = 2^9$; and $N = 2^{11}$. The resulting power distributions after propagating $10^4 km$ obtained from both the split-step and the proposed parallel algorithm differ in about 1% so the proposed numerical algorithm gives good numerical accuracy. Numerical simulations were performed on usual workstation without use of parallel computations. The objective of this numerical example is to demonstrate the relative accuracy of numerical algorithm. Hardware implementation of the parallel simulation for numerical algorithm (3) and (5) is beyond the scope of this paper.

One can conclude that the proposed efficient numerical algorithm allows to implement a numerical simulation of Eq. (1) in about M times faster than a direct numerical simulation of that Eq. by a split-step method (which requires $2MNLog_2(N)$ steps for the same numerical steps along z and the same numerical accuracy). The absence of communications between parallel processors during computation of FFT allows to implement proposed massive parallel computation algorithm on workstation clusters. One can estimate that using of about 1000 parallel processors would allow a full scale numerical simulation of WDM transmission in optical fiber on transoceanic distance (this estimate is made for 27×10 Gb WDM transmission given in Ref. [2]).

References

1. D. LeGuen, S. Del Burgo, L. Moulinard, D. Grot, M. Henry, F. Favre, T. Georges, OFC/IOOC'99, 21-26 Feb. 1999, San Diego, CA, USA
2. L.F. Mollenauer, P.V. Mamyshev, J. Gripp, M.J. Neubelt, N. Mamysheva, L. Grüner-Nielsen and T. Veng, Optics Letters, **25**, 704 (2000).
3. C. Lin, H. Kogelnik and L.G. Cohen, Opt. Lett., **5**, 476 (1980).
4. C. Kurtzke, IEEE Phot. Tech. Lett., **5**, 1250 (1993).
5. A.R. Chraplyvy, A.H. Gnauck, R.W. Tkach and R.M. Derosier, IEEE Phot. Tech. Lett., **5**, 1233 (1993).
6. N.J. Smith, F.M.Knox, N.J. Doran, K.J. Blow and I. Bennion, Electron. Lett., **32**, 54 (1996).
7. I. Gabitov and S.K. Turitsyn, Opt. Lett., **21**, 327 (1996).
8. I. Gabitov and S.K. Turitsyn, JETP Lett., **63**, 861 (1996).
9. P.M. Lushnikov, Opt. Lett. **26**, 1535 (2001).

Nonclassical statistics of intracavity coupled quadratic nonlinear waveguides: the quantum optical dimer

M. Bache, Yu. B. Gaididei and P. L. Christiansen

Informatics and Mathematical Modelling, Technical University of Denmark,
DK-2800 Lyngby, Denmark.
Tel:+45 4525 3095, fax: +45 4593 1235, email: mba@imm.dtu.dk

Abstract: Two quadratic nonlinear waveguides are immersed in a cavity suited for second-harmonic generation. The quantum equations are derived to calculate intensity correlation spectra and strong quantum violations of the classical limit is observed.
© 2002 Optical Society of America

The $\chi^{(2)}$-nonlinear materials have been the subject of various investigations in recent years. Using a cavity setup the weak nonlinearities can be resonantly amplified, and complex spatiotemporal behaviour has been predicted from a classical point of view [1]. Moreover, due the the quantum fluctuations of light many interesting non-classical behaviours have been reported, such as squeezed light and sub-Poissonian light [2], both theoretically and experimentally. The interplay between the classical spatial instabilities and the quantum fluctuations in the system has been investigated intensively lately [3], a study devoted to characterizing the mode interaction on a quantum level.

We will focus on the case of second-harmonic generation (SHG), where the photons of the pump field (fundamental, FH) are upconverted in pairs to photons of the double frequency (second-harmonic, SH). The model we consider here consists of two quadratically nonlinear waveguides resonated in a cavity, taking a linear coupling between the waveguides into account. The question is how the coupling between the fields affect the cavity dynamics, and especially we will focus on the nonclassical behaviour of the system. It has been shown that in single waveguide SHG excellent squeezing is possible [4] and in the presence of diffraction strong correlations exist between different spatial modes in the presence of a spatial instability [5]. This includes correlations between the FH and the SH, as well as quantum violations of the classical coherent limit. In the present model the simple linear coupling across the waveguides also turns out to give strong nonclassical correlations, and since it is closely related to the dynamics of coupled atomic and molecular Bose-Einstein condensates [6] the results presented here should have widespread importance.
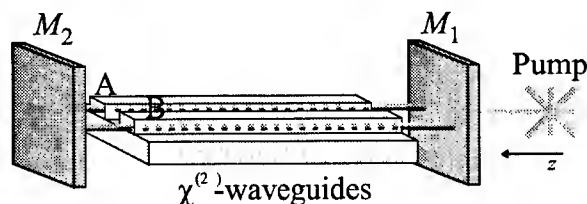
Fig. 1. Model setup: two waveguides A and B inside a cavity pumped by a classical field.

We consider the setup shown in Fig. 1. Two $\chi^{(2)}$-nonlinear waveguides immersed in a cavity with a high reflection input mirror M_1 and a fully reflecting mirror M_2 at the other end. The cavity is pumped with a classical field at the frequency ω_1 and SHG is ocurring through the nonlinear interaction in the waveguides by generating photons of frequency $\omega_2 = 2\omega_1$. The coupling between the waveguides is assumed linear. The system is now described using boson operators $\hat{A}_1$ and $\hat{B}_1$ ($\hat{A}_2$ and $\hat{B}_2$) of the FH (SH) intracavity photons of waveguide A and B, respectively. Using the mean field approach a Hamiltonian is set up describing the operator interaction in the system including coupling of fluctuations into the cavity from external modes, and this Hamiltonian is the basis for deriving the master equation. Using the quantum-to-classical correspondence an equivalent equation is derived describing the time evolution of a quasi-probability distribution, where the quantum mechanical operators are replaced by classical c-numbers. In some cases this equation may be modelled by a set of Langevin stochastic differential equations, which in normalized form read for the positive P quasi-probability distribution

$$\dot{A}_1 = -\tilde{\gamma}_1 A_1 + A_1^\dagger A_2 - iJ_1 B_1 + \sqrt{2\tilde{\gamma}_1} A_{1,\text{in}}, \qquad \dot{A}_1^\dagger = -\tilde{\gamma}_1 A_1^\dagger + A_1 A_2^\dagger + iJ_1 B_1^\dagger + \sqrt{2\tilde{\gamma}_1} A_{1,\text{in}}^\dagger \qquad (1)$$

$$\dot{A}_2 = -\tilde{\gamma}_2 A_2 - \tfrac{1}{2}A_1^2 - iJ_2 B_2, \qquad \dot{A}_2^\dagger = -\tilde{\gamma}_2 A_2^\dagger - \frac{1}{2}(A_1^\dagger)^2 + iJ_2 B_2^\dagger \tag{2}$$

$$\dot{B}_1 = -\tilde{\gamma}_1 B_1 + B_1^\dagger B_2 - iJ_1 A_1 + \sqrt{2\tilde{\gamma}_1}B_{1,\mathrm{in}}, \qquad \dot{B}_1^\dagger = -\tilde{\gamma}_1 B_1^\dagger + B_1 B_2^\dagger + iJ_1 A_1^\dagger + \sqrt{2\tilde{\gamma}_1}B_{1,\mathrm{in}}^\dagger \tag{3}$$

$$\dot{B}_2 = -\tilde{\gamma}_2 B_2 - \tfrac{1}{2}B_1^2 - iJ_2 A_2, \qquad \dot{B}_2^\dagger = -\tilde{\gamma}_2 B_2^\dagger - \frac{1}{2}(B_1^\dagger)^2 + iJ_2 A_2^\dagger \tag{4}$$

with the input fields consisting of both the external pump E and noise terms ξ

$$F_{1,\mathrm{in}} = \frac{E}{\sqrt{2\tilde{\gamma}_1}} + \xi_{F_1}(t), \quad F_{1,\mathrm{in}}^\dagger = \frac{E}{\sqrt{2\tilde{\gamma}_1}} + \xi_{F_1}^\dagger(t), \quad F = A, B \tag{5}$$

$$\langle \xi_{F_1}(t)\xi_{F_1}(t')\rangle = \frac{F_2\delta(t-t')}{2n_s}, \quad \langle \xi_{F_1}^\dagger(t)\xi_{F_1}^\dagger(t')\rangle = \frac{F_2^\dagger\delta(t-t')}{2n_s} \tag{6}$$

The equivalent intracavity c-numbers to the boson operators are $\hat{A}_j \leftrightarrow A_j$, $\hat{A}_j^\dagger \leftrightarrow A_j^\dagger$ and $\hat{B}_j \leftrightarrow B_j$, $\hat{B}_j^\dagger \leftrightarrow B_j^\dagger$. γ_1 and γ_2 are the FH and SH loss rates of M_1 and $\tilde{\gamma}_j = \gamma_j/\gamma_1$, and the FH and SH coupling between the waveguides are J_1 and J_2, respectively. n_s is a dimensionless parameter determining the strength of the quantum fluctuations.

Using a linearized stability analysis the bifurcation scenario of the system is analyzed starting from the symmetric steady state. The symmetric state means that both waveguides have the same steady state solution, and the system may now become self-pulsing (Hopf) unstable, bistable or destabilize in favor of an asymmetric steady state. An example is shown in Fig. 2 which shows that self-pulsing solutions exist in a large area of the (J_1, J_2) phase space, and also bistable solutions exist for large enough coupling strengths.
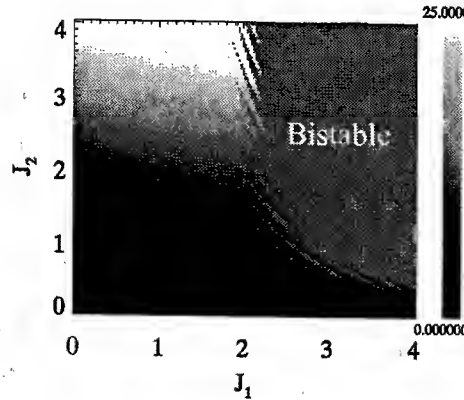
Fig. 2. Gray scale plot showing the threshold for self pulsing for $\tilde{\gamma}_2 = 0.1$. The grey area is bistable in the steady states.

The input fields $\hat{O}_{j,\mathrm{in}}$ coupled into the cavity through the input mirror are posing instantaneous boundary conditions for the output fields

$$\hat{O}_{j,\mathrm{out}}(t) = \sqrt{2\gamma_j}\hat{O}_j(t) - \hat{O}_{j,\mathrm{in}}(t), \quad \hat{O} = \hat{A}, \hat{B}, \quad j = 1, 2. \tag{7}$$

The fields outside the cavity obey the standard free field commutator relations

$$[\hat{O}_{j,\mathrm{out}}(t), \hat{O}_{k,\mathrm{out}}^\dagger(t')] = \delta_{jk}\delta(t-t'), \quad [\hat{O}_{j,\mathrm{in}}(t), \hat{O}_{k,\mathrm{in}}^\dagger(t')] = \delta_{jk}\delta(t-t') \tag{8}$$

Using these relations we can now calculate the two-time correlations of the output field intensities $\hat{N}_{j,\mathrm{out}}^A \equiv \hat{A}_{j,\mathrm{out}}^\dagger \hat{A}_{j,\mathrm{out}}$ from the intracavity c-number fields governed by the Langevin equations as follows

$$\begin{aligned} C_{A_j B_k}^{(\pm)}(\tau) &\equiv \langle \hat{N}_{j,\mathrm{out}}^A(0) \pm \hat{N}_{k,\mathrm{out}}^B(0), \hat{N}_{j,\mathrm{out}}^A(\tau) \pm \hat{N}_{k,\mathrm{out}}^B(\tau)\rangle \\ &= 2(\gamma_j\langle I_j^A\rangle_P + \gamma_k\langle I_k^B\rangle_P)\delta(\tau) + 4\langle \tilde{\gamma}_j I_j^A(0) \pm \tilde{\gamma}_k I_k^B(0), \tilde{\gamma}_j I_j^A(\tau) \pm \tilde{\gamma}_k I_k^B(\tau)\rangle_P \end{aligned} \tag{9}$$

using $\langle X, Y\rangle = \langle XY\rangle - \langle X\rangle\langle Y\rangle$. Both the intracavity intensities $I_j^A = A_j^\dagger A_j$ and the averages $\langle \cdot\rangle_P$ are calculated from the positive P Langevin equations. Fourier transforming the correlations (9) gives

$$V_{A_j B_k}^{(\pm)}(\omega) = 2(\tilde{\gamma}_j\langle I_j^A\rangle_P + \tilde{\gamma}_k\langle I_k^B\rangle_P) + 4\int_{-\infty}^{\infty}d\tau e^{i\omega\tau}\langle \tilde{\gamma}_j I_j^A(0) \pm \tilde{\gamma}_k I_k^B(0), \tilde{\gamma}_j I_j^A(\tau) \pm \tilde{\gamma}_k I_k^B(\tau)\rangle_P \tag{10}$$

$$\tilde{\gamma}_2=0.1, J_1=2, J_2=1 \qquad \tilde{\gamma}_2=1.0, J_1=4, J_2=1 \qquad \tilde{\gamma}_2=10, J_1=6, J_2=6$$
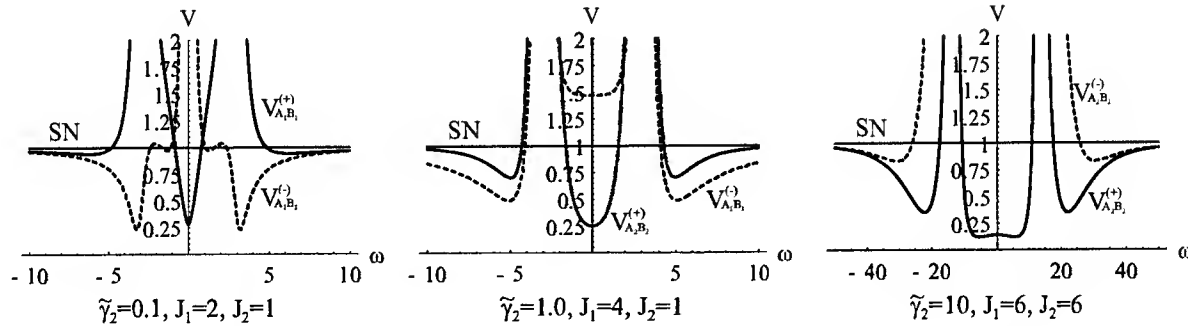
Fig. 3. Photon number spectra calculated in the linearized regime normalized to shot noise level (indicated by "SN").

The first term represents the shot noise of the measurement, *i.e.* the classical limit corresponding to the system being described by coherent states. The second part may now become negative, which can only happen for a quantum state that cannot be described by classical equations. Here, a quantum violation of the classical limit results in anti-bunching of the time statistics of the photons being measured, *i.e.* sub-Poissonian behaviour.

Using a linearized approach the correlation spectra may be calculated from the Langevin equations, assuming that the fluctuations are small compared with the steady state solutions. The spectra (10) are in the following normalized to the shot noise level so $V(\omega) = 1$ is the classical limit.

For $\tilde{\gamma}_2 = 0.1$ strong violations of the quantum limit originate both from the self-pulsing instability and from the presence of a bistable turning point. The left plot in Fig. 3 shows that the difference of the FH in the two waveguides have strong noise suppression for nonzero ω, and this originates from a self-pulsing instability. Also the sum shows strong noise suppression now at $\omega = 0$, caused by the presence of the bistability; as can bee seen from Fig. 2 the parameters discussed here are very close to the bistable area. Almost complete anti-bunching has been observed just before a bistable transition. Setting $\tilde{\gamma}_2 = 1$ the self-pulsing instability gives rise to strong violations of the shot noise limit. Moreover, the nonclassical behaviour persists all the way up to the self-pulsing transition, cf. the middle spectra in Fig. 3 which is set very close to the transition. The sum of the SH fields from each waveguide displays strong correlations at $\omega = 0$. Also strong correlations are displayed by the difference of the FH fields from each waveguide for nonzero ω. When $\tilde{\gamma}_2 = 10$ mostly self-pulsing instabilities are observed, and here the sum of the SH fields from each waveguide shows strong nonclassical correlations, while the difference displays excess noise, cf. the right spectra in Fig. 3.

The results show that strong anti-bunching effects can be observed originating from a linear coupling across the waveguides. We will present numerical simulations to back up the analytical results, and discuss the possible applications of these observations.

References

1. L. A. Lugiato and R. Lefever, "Spatial dissipative structures in passive optical systems," Phys. Rev. Lett. **58**, 2209 (1987).
2. L. Davidovich, "Sub-poissonian processes in quantum optics," Rev. Mod. Phys. **68**, 127 (1996).
3. L. A. Lugiato, M. Brambilla, and A. Gatti, "Optical pattern formation" in *Advances in atomic, molecular and optical physics* 40, 229, B. Bederson and H. Walther, ed. (Academic, Boston, 1999).
4. M. J. Collett and D. F. Walls, "Squeezing spectra for nonlinear optical systems," Phys. Rev. A **32**, 2887 (1985).
5. M. Bache, P. Scotto, R. Zambrini, M. San Miguel, and M. Saffman, "Quantum properties of transverse pattern formation in second-harmonic generation," (to be published).
6. R. Wynar, R.S. Freeland, D. J. Han, C. Ryu, and D. J. Heinzen. "Molecules in a Bose-Einstein condensate," Science **287**, 1016 (2000).

Dark-ring cavity solitons
in lasers with bichromatic injected signal

Germán J. de Valcárcel
Departament d'Òptica, Universitat de València, Dr. Moliner 50, 46100-Burjassot, Spain
Telephone: +34 963 864 766 (ext. 16), fax: +34 963 864 715, e-mail address: german.valcarcel@uv.es

Kestutis Staliunas
Physikalisch Technische Bundesanstalt, Bundesallee 100, 38116 Braunschweig, Germany
Telephone:+49 531 592 4482, fax: +49 531 592 4423, e-mail address: kestutis.staliunas@ptb.de

Abstract: We show theoretically that broad area lasers driven by a nearly resonant bichromatic field may support dark-ring cavity solitons as well as domain walls and labyrinthine patterns.
©2002 Optical Society of America
OCIS codes: (190.4420) Nonlinear optics, transverse effects in; (210.0210) Optical data storage

1. Introduction

Many nonlinear optical cavities have been shown to support transverse patterns with different symmetries (rolls, hexagons, and also quasi-patterns) as well as cavity solitons (CS) [1]. The latter are particularly interesting objects because of their potential use as memory bits in optical information processing systems [2]. However usual lasers do not fall into the category of CS-supporting systems since, usually, such systems are either phase-sensitive and/or exhibit a bistability. Up to now two ways have been proposed for exciting CSs in lasers: the use of saturable absorbers [3], or the injection of a monochromatic signal [4]. Also very recently two-photon lasers have been predicted to support CS [5].

Here we demonstrate theoretically an alternative way for exciting CSs in lasers based on the injection of a resonant bichromatic signal into the laser cavity. Differently from the previously suggested laser CSs, the ones we present here are based on the development of two dynamically equivalent laser field phases differing by π. Hence the reported CSs belong to the class of dark-ring cavity solitons, in which a bright spot with a definite phase is surrounded by an oppositely phased, spatially uniform light distribution, both phases being separated by a dark ring. These phases appear when the laser emission frequency locks halfway between the two injected signal components, which can be understood as a result of the competition between a (phase sensitive) resonant, degenerate four-wave mixing process –in which two injected photons (one of each signal component) are converted into two equal laser photons– and the usual (phase insensitive) stimulated emission process of free running lasers.

Apart from CSs other phase patterns (e.g. domain walls or labyrinths) are shown to form in the laser transverse plane. We find two generic types of phase patterns, which differ in the way the light phase varies between two oppositely phased regions. In the first type the phase abruptly changes by π along the line separating both regions; in these patterns the referred lines are dark and we speak of Ising-like patterns, in analogy with the Ising walls of ferromagnets [6]. In the second type the phase varies continuously and smoothly across the line, still accumulating π between both sides; in these patterns the referred lines are gray and we speak of Bloch-like patterns [6].

As we show below the detuning between the central injection frequency and the free-running laser frequency selects the geometry of the observed patterns (domain walls, labyrinths, or dark-ring CSs), as well as the injected signal strength controls their Ising or Bloch character.

2. Model

We consider the standard Maxwell-Bloch equations [7] that model pattern formation in a single longitudinal mode, two-level laser with injected signal, inside a plane mirrors resonator, which can be written in dimensionless form as

$$\partial_t E = \sigma[-(1+i\Delta)E + P] + i\nabla^2 E + E_{\text{in}}, \tag{1}$$

$$\partial_t P = -(1-i\Delta)P + (r-N)E, \tag{2}$$

$$\partial_t N = b[-N + \text{Re}(E^*P)] \tag{3}$$

The complex fields E and P are the scaled envelopes of the electric field and medium polarization, $-N$ is proportional to the difference between the population inversion and its steady value in the absence of lasing, and E_{in} is the scaled complex envelope of the injected signal. $\sigma = \kappa/\gamma_\perp$, and $b = \gamma_\parallel/\gamma_\perp$, being $\kappa = cT/L$ the cavity

linewidth (c is the effective light velocity within the resonator, L is the cavity length, and T is the mirrors' transmissivity), and $\gamma_\perp$, and $\gamma_\parallel$ the decay rates of P, and N, respectively. The transverse Laplacian $\nabla^2 = \partial_x^2 + \partial_y^2$, where the spatial coordinates $\mathbf{r} = (x, y)$ are measured in units of $(\gamma_\perp \omega_L)^{-1/2} c$, being ω_L the laser emission frequency; t is time measured in units of $1/\gamma_\perp$. Finally r is the usual laser pump parameter and the detuning $\Delta = (\omega_C - \omega_A)/(\gamma_\perp + \kappa)$, being $\omega_C (\omega_A)$ the cavity (atomic) frequency.

Eqs. (1)–(3) have been written in the frequency frame $\omega_0 = (\gamma_\perp \omega_C + \kappa \omega_A)/(\gamma_\perp + \kappa)$ of the on-axis, or plane wave $(\partial_x E = \partial_y E = 0)$, steady lasing solution in the absence of injected signal. Previous studies have considered pattern formation in model (1)–(3) when the injected signal is monochromatic, either as $E_{in} = E_0 \exp(-i\theta t)$ [7,8], or as $E_{in} = E_0 \exp(ikx - i\theta t)$ [9], with E_0 constant. These represent an on-axis, resp. a tilted, injected signal whose frequency detuning from ω_0 is $\gamma_\perp \theta$. Here we consider the case

$$E_{in} = E_0 \cos(\omega t)\exp(-i\theta t), \tag{4}$$

which represents an amplitude modulated field of carrier frequency $\omega_0 + \gamma_\perp \theta$, and modulation frequency $\gamma_\perp \omega$. Alternatively (4) represents a bichromatic injection formed by the superposition of two coherent light beams of frequencies $\omega_0 + \gamma_\perp \theta \pm \gamma_\perp \omega$, and equal amplitudes. In order that (4) be consistent with the uniform field and single longitudinal mode approximations that lead to Eqs. (1)–(3), both the carrier frequency offset $\gamma_\perp \theta$ and the modulation frequency $\gamma_\perp \omega$ must be much smaller than the cavity free spectral range $\alpha = 2\pi c/L = 2\pi \kappa/T$. Hence we must impose $|\theta|, |\omega| \ll 2\pi\sigma/T$. Note however that the rhs of the inequality is much larger than σ since $T \ll 1$ is assumed in the uniform field limit, hence in fact there is almost no practical limitation to the values of θ and ω.

In all this work we shall consider the positive detuning case $\Delta > 0$ for which, in the absence of injected signal, the laser is off for $r < r_0 \equiv 1 + \Delta^2$, and switches on at $r = r_0$ giving rise to the on-axis lasing solution [10,11].

3. Reduction of the Maxwell-Bloch equations to a driven, complex Ginzburg-Landau equation

In order to gain insight into the basic pattern forming properties of the system, we undergo next a reduction of Eqs. (1)–(3) to a compact form that allows a simplified treatment of the problem. The reduction will be done, as usual [8-12], in the close to threshold regime $r = r_0 + \varepsilon^2 r_2$, being $0 < \varepsilon \ll 1$ an auxiliary smallness parameter. We consider $\Delta = O(\varepsilon^0)$, where a complex Ginzburg-Landau (CGL) equation describes the laser in the absence of injection [10,11]. For smaller detunings, say $\Delta = O(\varepsilon)$, the nature of the bifurcation changes and a complex Swift-Hohenberg equation is obtained [12]. As for the injected signal we consider $F = O(\varepsilon^3)$ and $\omega, \theta = O(\varepsilon^2)$, which correspond to a weak field almost resonant with the free running laser emission frequency. Finally, we introduce slow spatial scales $(X = \varepsilon x, Y = \varepsilon y)$, and multiple slow time scales $(T_k = \varepsilon^k t, k = 1, 2, ...)$, and assume that the laser variables admit the expansion $G(x, y, t) = \sum_{n=1}^{\infty} \varepsilon^n G_n(X, Y, T_1, T_2, ...)$, $G = E, P, N$ [10,11]. Upon substituting all previous scalings into Eqs. (1)–(3) and equating equal powers in ε, an infinite hierarchy of equations is obtained which must be solved up to $O(\varepsilon^3)$. As usual, at this order a solvability condition must be imposed (in order to avoid unbounded solutions) which yields the searched equation. By undoing all the scalings the equation can be written as

$$s\, \partial_t U = i\theta U + \sigma(1 - i\Delta)^{-1}(r - r_0 - |U|^2)U + i\nabla^2 U + E_0 \cos(\omega t), \tag{5}$$

where $s = 1 + \sigma(1 + i\Delta)/(1 - i\Delta)$, and $U(\mathbf{r}, t) = \exp(i\theta t)E(\mathbf{r}, t)$. Eq. (5) is a CGL equation with direct ac-driving which, for $E_0 = 0$, reduces to the laser CGL equation derived in [10]. Interesting, although cumbersome, analytical information can be obtained from Eq. (5). Hence we consider for simplicity the case $\sigma = 1$ which, according to our numerics, represents most of the basic features of Eqs. (1)–(3). In this case the CGL eq. (5) can be written as

$$\partial_\tau U = (\mu + i\nu)U + (1 + i\alpha)\nabla^2 U - |U|^2 U + f \cos(2\omega\tau) \tag{6}$$

where $\tau = t/2$, $\mu = (r - r_0)$, $\nu = 2\theta$, $\alpha = \Delta^{-1}$, $f = (1 - i\Delta)E_0$, and space has been normalized to $\sqrt{\Delta}$. In the following we choose, without loss of generality, f as a positive real number since the phase of F has not been fixed.

4. Ising and Bloch domain walls

Let us consider now the limit of "strong" and "fast" modulation $f, \omega \gg 1$ in Eq. (6). By no means this limit is ess-

ential, but it allows a clear understanding of the role played by the bichromatic injection. In fact, the numerics we show in Sec. 5 do not verify that limit, eventhough they are qualitatively described by the features we describe next.

In the limit $f = \eta^{-1} F$, $\omega = \eta^{-1} \Omega/2$, being $0 < \eta \ll 1$ a smallness parameter, one can search for solutions to Eq. (6) in the form $U(\mathbf{r}, \tau) = u_0(\mathbf{r}, T, \tau) + \eta u_1(\mathbf{r}, T, \tau) + O(\eta^2)$, where $T = \eta^{-1} \tau$. At order η^{-1} the solution reads $u_0(\mathbf{r}, T, \tau) = (F/\Omega) \sin(\Omega T) + iU(\mathbf{r}, \tau)$. The evolution equation for U is found as a solvability condition, which must be imposed at order η^0. The searched equation reads:

$$\partial_\tau U = [(\mu - 2\gamma) + iv]U + (1 + i\alpha)\nabla^2 U - |U|^2 U + \gamma U^* , \qquad (7)$$

where $\gamma = \frac{1}{2}(F/\Omega)^2 = \frac{1}{2}(f/\omega)^2$ is a parameter capturing the effect of driving. The effect of driving is evidenced via the last, phase symmetry breaking term, which allows *stable* domain wall solutions. Outstandingly, for $\alpha = v = 0$ Eq. (7) such solutions are analytical in one spatial dimension, and are known as Ising (I) and Bloch (B) walls [10]:

$$U_I(x) = \pm\sqrt{\mu - \gamma}\tanh\left(\sqrt{\mu - \gamma}\,x/\sqrt{2}\right),$$
$$U_B(x) = \pm\sqrt{\mu - \gamma}\tanh\left(\sqrt{2\gamma}\,x\right) \pm i\sqrt{\mu - 5\gamma}\operatorname{sech}\left(\sqrt{2\gamma}\,x\right). \qquad (8)$$

The Ising wall (a dark line where $U = 0$) is stable for $\mu/5 < \gamma < \mu$, and the Bloch wall (a gray line) is stable for $0 < \gamma < \mu/5$. At $\gamma = \mu/5$ an Ising-Bloch transition occurs.

5. Numerics: Phase domains, labyrinths, and dar-ring cavity solitons

Regarding the pattern forming properties of the system, a linear sability analysis of the spatially homogeneous solutions to Eq. (7) reveals that extended patterns arise with wavenumber k given by $\alpha k^2 = v - \gamma/\sqrt{1 + \alpha^2}$ or $\alpha k^2 = v - \sqrt{(\mu - 2\gamma)^2 + v^2}/\sqrt{1 + \alpha^2}$, depending on whether the trivial or the nontrivial solutions is considered.

All previous analytical predictions were tested against the numerical integration of Eq. (6), and also of the full Maxwell-Bloch equations (1)–(3). A split-step integration technique was used on a two-dimensional grid of 128×128 points with periodic boundary conditions. Numerics started from a spatially random distribution of the electric field U. In the absence of injection vortex ensembles spontaneously developed, Fig. (a). For negative or null detunings θ Ising and Bloch domain walls were found as transient states, as usual in two-dimensional systems, Fig. (b). Also labyrinthine patterns, Fig. (c), were found for positive values of v and α. Finally, for detuning values between those for domain walls and labyrinths, dark-ring cavity solitons were found, Fig. (d).

(a) (b) (c) (d)
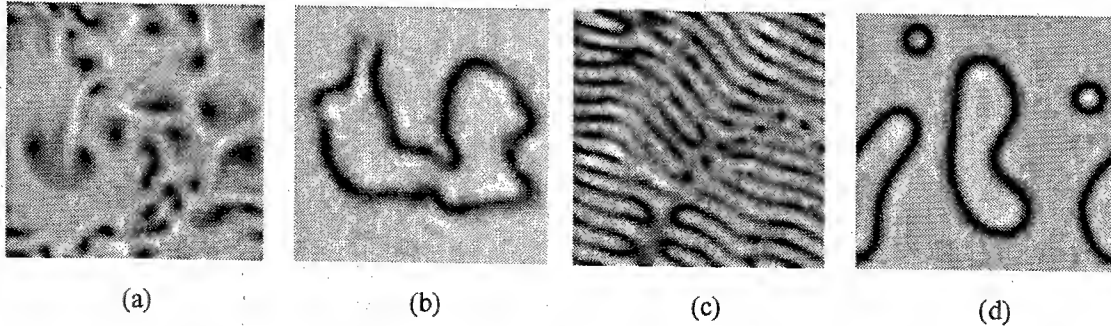
Figure. Laser intensity distribution according to the ac-driven complex Ginzburg-Landau equation (6). Parameters are $\mu = 1$, $\omega = 2\pi$, $\alpha = 10$. Rest of parameters are $f = 0$ (a); $f = 7$, $v = 0$ (b); $f = 7.5$, $v = 0.6$ (c), $f = 10$, $v = 0.27$ (d).

[1] L.A. Lugiato, M. Brambilla, and A. Gatti, Adv. At. Mol. Opt. Phys. **40**, 229 (1998).
[2] W.J. Firth and C.O. Weiss, Opt. Photon. News **13**(2) 54 (2002).
[3] N.N. Rosanov and G.V. Khodova, J. Opt. Soc. Am. B **7**, 1065 (1990).
[4] M. Brambilla, L.A. Lugiato, F. Prati, L. Spinelli, and W.J. Firth, Phys. Rev. Lett. **79**, 2042 (1997).
[5] R. Vilaseca, M.C. Torrent, J. García-Ojalvo, M. Brambilla, and M. San Miguel, Phys. Rev. Lett. **87**, 083902 (2001).
[6] P. Coullet, J. Lega, B. Houchmanzadeh, and J. Lajzerowicz, Phys. Rev. Lett. **65**, 1352 (1990).
[7] L.A. Lugiato, C. Oldano, and L.M. Narducci, J. Opt. Soc. Am. B **5**, 879 (1988).
[8] M. Tlidi, M. Georgiou, and P. Mandel, Phys. Rev. A **48**, 4605 (1993).
[9] S. Longhi, Phys. Rev. A **56**, 2397 (1997).
[10] P. Coullet, L. Gil, and F. Rocca, Opt. Commun **73**, 403 (1989).
[11] A.C. Newell and J.V. Moloney, *Nonlinear Optics* (Addison Wesley, Redwood City, CA, 1992).
[12] G.J. de Valcárcel, K. Staliunas, E. Roldán, and V.J. Sánchez-Morcillo, Phys. Rev. A **54**, 1609-1624 (1996)
[13] J. Lega, J.V. Moloney, and A.C. Newell, Phys. Rev. Lett. **73**, 2978 (1994).

Localized structures formation and control in second-harmonic, intra-cavity generation

E. Toniolo, M. Giltrelli, M. Santagiustina

INFM, Dipartimento di Elettronica e Informatica, via Gradenigo 6/a, University of Padova, 35131 Padova, Italy
tel: +39 049 827 7717, fax: +39 049 827 7699, email: marco.santagiustina@unipd.it

Abstract: A regime in which spontaneous formation of localized structures occurs is found for intra cavity second harmonic generation. Independent writing, erasing and moving of structures are numerically demonstrated.
©2002 Optical Society of America
OCIS codes: 190.4420 Nonlinear optics, transverse effects in; 210.4680 Optical memories

1. Introduction

Formation of localized structures (LS's) has been predicted and experimentally observed in many nonlinear optical systems [1]. Such structures, that are also termed cavity solitons, can form due to the interplay between nonlinearity and diffraction in driven-damped systems. Their search, beyond the scope of scientific investigation, is pursued because of their possible applications as all-optical storage elements, opening the way to all-optical signal processing and all-optical computing. Intra-cavity second harmonic generation (SHG) is one among the most interesting systems where LS's are expected. This stems from the fact that new materials (e.g. periodically poled crystals) have lowered the pump power necessary to reach SHG threshold to few mW and novel structures (e.g. monolithic micro-cavities) have been developed. LS's have been found under very different conditions, e.g. the existence of a bistability range between a homogeneous and a patterned solution [2] or between equivalent homogeneous solutions [3,4], however an exhausting study of possible conditions sufficient to observe LS has not been performed. Spontaneous structure generation in intra-cavity SHG has been the object of previous studies: in those papers [5] LS's have been found in the bistability parameter range between an hexagonal pattern and a homogeneous solution. LS's have been also predicted in the stability analysis of type II SHG but their properties have not been investigated [6]. In this contribution, a regime where spontaneous generation of LS's is identified; in such a regime control of one and more LS's is numerically demonstrated. Type II SHG has been also considered; this case is particularly interesting because the additional degree of freedom represented by light polarization should allow for independent setting and resetting operations, leading to parallel control of spatially distributed flip-flops [7]. In this work numerical evidence of polarization patterns and LS's has been searched for.

2. Equations and stability analysis

The equations governing the time evolution of intra-cavity fields (A_1, A_2) in type I SHG can be found in [5]. They read:

$$\frac{\partial A_1}{\partial t} = \gamma_1 \left[-(1 + i\Delta_1)A_1 + ia_1\nabla^2 A_1 + A_2 A_1^* + E \right]$$

$$\frac{\partial A_2}{\partial t} = \gamma_2 \left[-(1 + i\Delta_2)A_2 + ia_2\nabla^2 A_2 + A_1^2 \right]$$

(1)

where $\gamma_{1,2}$ are the cavity decay rates, $\Delta_{1,2}$ the cavity detunings, $a_{1,2}$ the diffraction coefficients respectively for the first harmonic (FH, A_1) and the second harmonic (SH, A_2) fields. All coefficients, including the external pump uniform amplitude E (that can be considered real without loss of generality) and variables (time and transverse space) can be scaled in order to become dimensionless quantities. The trivial, homogeneous steady-state for this equation is given by the solutions of the equations $A_1[|A_1|^2/(1+i\Delta_2)-(1+i\Delta_1)]+E=0$, $A_2=A_1^2/(1+i\Delta_2)$. The complete stability analysis of this homogeneous solution can be found in ref. [5]. Here we just recall only some results necessary for the purpose of explaining the observations presented here. In fig. 1 the stability diagrams, as a function of the SH detuning, for two particular values of FH detuning are given. The main difference between the parameter region of fig. 1 (left and center) is that in the latter the homogeneous steady-state is a multivalued function. In both cases the bifurcation (Re(λ)>0), at threshold, occurs for plane waves $\delta A_{1,2} \approx \exp\left[i\left(\vec{k}_c \cdot \vec{r}\right) + \lambda t \right]$, whose transverse

spatial wave vector is such that $k_c = \left| \vec{k}_c \right| \neq 0$ and $\text{Im}(\lambda)=0$. These conditions means that spatially dependent and time independent (Hopf bifurcation has a larger threshold as shown in fig. 1) structure formation can be expected.
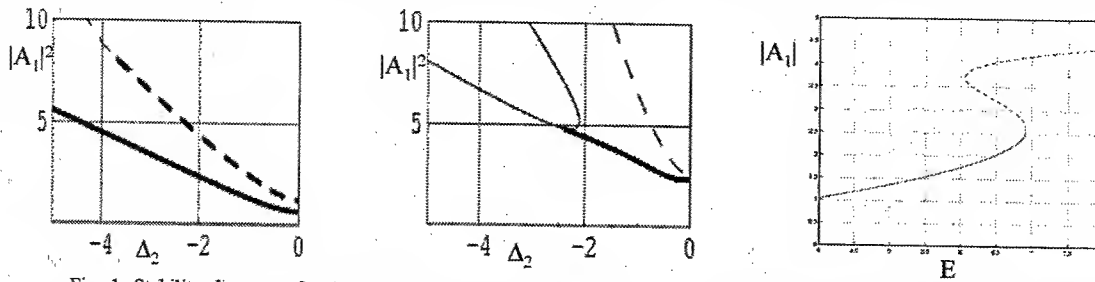
Fig. 1. Stability diagrams for $\Delta_1=2$ (left) and $\Delta_1=-4$ (center). Solid curve is the cavity field threshold of the homogeneous steady-state. Dashed curve is the threshold of Hopf instability. In the figure on the left the input-output curve for the homogeneous steady-state solution is shown for $\Delta_1=-4$.

3. Patterns and localized structures

Numerical integrations of eqs. (1), starting from a weakly perturbed homogeneous steady-state, presented in fig. 2, show different results as for the formation of LS's, depending on FH detuning. For the case $\Delta_1=2$ the fields ($|A_1|^2$ is shown because the SH pattern is similar) evolves toward the formation of a stable hexagonal pattern [5]; however, for $\Delta_1=-4$, the resulting self-organized structure is not regular but rather made of single spots, randomly distributed in the transverse section.
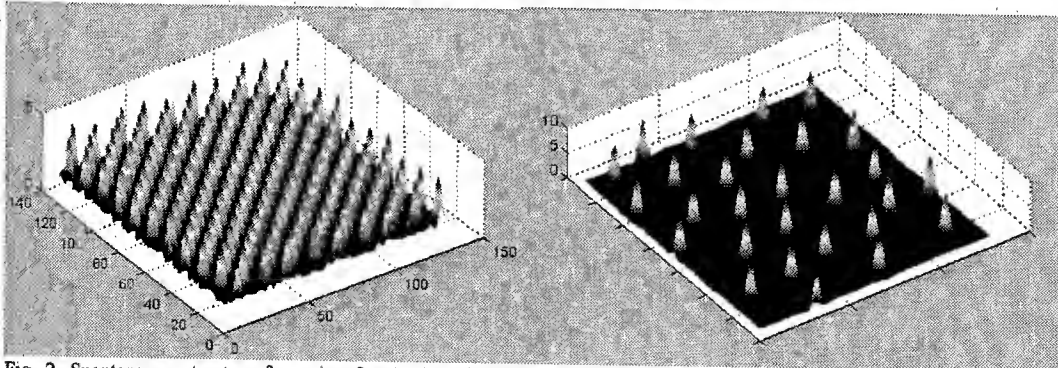
Fig. 2. Spontaneous structure formation for $\Delta_1=2$ (left) and $\Delta_1=-4$ (right). $|A_1|^2$ is shown as a function of the transverse spatial coordinates. All other parameters are the same.

This seems a clear example of spontaneous formation of LS's; such a regime is different either from optical bistability [4] or from LS formation due to the existence of robust fronts between patterns and homogeneous solutions. In fact, the parameter range is not close to any of those situations. This interesting behaviour has not been predicted before for intra cavity SHG and to our knowledge, there is not a clear explication. The results presented here seem to indicate that it might be related with the presence of the homogeneous multivalued solution, since this is the main difference between the two regimes as it results from fig. 1. Intuition suggests that this parameter range and system are very suitable for LS formation. To explore more in detail the properties of such LS's, additional numerical simulations have been performed; the scope is to demonstrate that LS's in this regime can be easily controlled. Fig. 3 shows that single LS can be switched on and off independently, by simply shining the homogeneous solution with in-phase or out-of-phase, time and space limited pulses. In the figure the spacing between structures has been chosen close to the critical distance value $2\pi/k_c$; this value proved to be the minimum in order to guarantee the stable writing of LS's; lower distances may result in LS annihilation. Data of fig. 3 refer to a possible experiment, with a LiNbO$_3$ crystal ($\chi^{(2)}_{\text{eff}} \approx 5$pm/V) and a micro cavity (10µm long); a single LS occupies about 90X90 µm^2, the writing time (from excitation to steady-state) is about 100ps, the writing beam power (for switching on and off the LS) is about 100mW, while the holding beam is about 10W. Lower powers could be attained by using poled crystals or semiconductors.
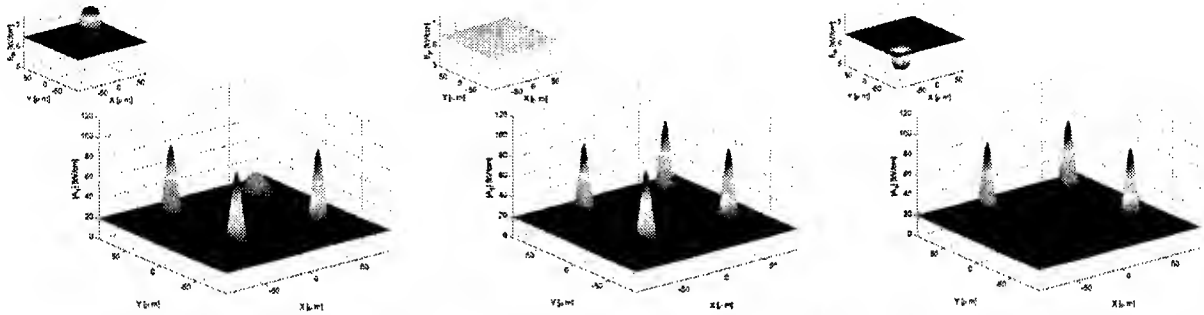
Fig. 3. Snapshots of $|A_1|^2$, at different times demonstrating independent switching on and off of LS's. On the top left the external pump (writing plus holding beam) is represented.

Motion of LS's occurs when the pump field is not homogeneous [8], e.g. a Gaussian beam. If the intensity gradient is large enough, collisions between LS's at the beam center result into annihilation. This effect seemingly hampers the real observation of LS's and their exploitation for the purpose of optical memories. Nonetheless the control and the localization of LS's could be attained by counterbalancing intensity motion with a phase potential of the external pump field E. In fig. 4 the effects, on a single LS, of the presence of a Gaussian phase variation of the input pump E are shown.
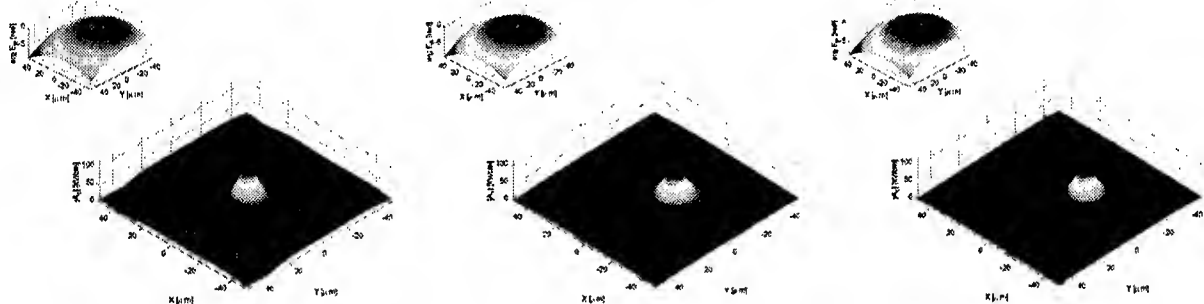
Fig. 4. LS motion due to the phase gradient of the holding beam E, whose phase is shown on the left top.

The LS tends to move at a velocity dictated by the phase gradient and to settle at the point of maximum phase. This runs demonstrate that LS can be controlled and moved through phase variations of the external beam. This is very easily attained by means of phase masks. Besides the fact that this behaviour could be exploited for making shift registers, the phase control also allows for a denser and better allocation of structures. Numerical simulations confirmed that LS's can be written and erased independently on top of a square lattice of pump phase maxima.

4. Type II, localized structures

Some numerical simulations have been performed for the case of type II SHG. Here, the instability of the homogeneous state can be of an asymmetric type, i.e. causes polarization symmetry breaking [9]. Such a bifurcation allows for the observation of different types of regular patterns (squares, hexagons etc.) as shown in the same reference. Search of LS, that has been predicted in ref. [6] is undergoing and will be reported later.

5. Conclusions

In conclusion LS formation in intra-cavity, type I SHG has been studied. An interesting regime where LS's are spontaneously generated has been found. In such regime LS can be easily written, erased and moved. Experimental parameters for their observation have been evaluated. Polarization structures have been also observed for the case of type II SHG

6. References

[1] Nonlinear optical structures, patterns, chaos, ed. L.A. Lugiato special issue of, Chaos, solitons and fractals 10, 617 (1999).
[2] W. Firth, A.J. Scroggie, Phys. Rev. Lett. 76, 1623 (1996).
[3] R. Gallego, M. San Miguel, R. Toral, Phys. Rev. E 61, 2241 (2000).
[4] M. Tlidi, P. Mandel, R. Lefever, Phys. Rev. Lett. 73, 640 (1994).
[5] C. Etrich, U. Peschel, F. Lederer, Phys. Rev. Lett. 79, 2454 (1997); C. Etrich, U. Peschel, and F. Lederer, Phys. Rev. E 56, 4803 (1997)
[6] S. Longhi , Optics Letters 23, 346 (1998).
[7] U. Peschel, C. Etrich, F. Lederer, Optics Letters 23, 500 (1998).
[8] S. Fedorov, D. Michaelis, U. Peschel, C. Etrich, D. V. Skryabin, N. Rosanov, and F. Lederer, Phys. Rev. E 64, 036610 (2001).
[9] S. Longhi, Phys. Rev. E 59, R24 (1999).

Two-dimensional clusters of solitary structures in driven optical cavities

J. M. McSloy[1], A. G. Vladimirov[2], D. V. Skryabin[3], W. J. Firth[1], and N. N. Rosanov[4]

[1]*Department of Physics and Applied Physics, University of Strathclyde, Glasgow G4 0NG, Scotland*

[2]*St. Petersburg State University, Physics Faculty, 1 Ulianovskaya st, 198904 St. Petersburg, Russia*

[3]*Department of Physics, University of Bath, Bath BA2 7AY, England*

[4]*Research Institute for Laser Physics, Theoretical Department, 199034 St. Petersburg, Russia*

Abstract: Interaction between localized structures in the transverse plane of a passive optical cavity containing a saturable medium is studied analytically and numerically. Stability properties of clusters of localized structures and their spontaneous motion are described.
©2002 Optical Society of America
OCIS codes: (190.4420) Nonlinear optics, transverse effects in: (140.3440) Laser theory

Potential applications of localized structures of light excited in externally driven optical cavities (cavity solitons) in technology are of interest [1]. One such application is the exploitation of individually addressable and steerable localized spots of light in externally pumped optical cavities [2,3]. These structures have been proposed as pixel elements for an all optical memory, parallel and image processing [4-6], with additional applications emerging for use in optical buffering, solitonic CCDs, and for confinement and manipulation of small particles [7]. This applicational interest has been renewed recently due to the observation of cavity solitons in semiconductor microcavities (see [2] and references therein) which have diameters of approximately 10 μm, evolve on pico-nanosecond time scales, and have the ability to move transversely at speeds in excees of 1000m.s^{-1} [8]. As forces between such structures must be controlled in the afore mentioned schemes, we provide a basis for assessing and controlling cavity soliton interactions through both analytical and numerical approaches. In a two-level saturable absorbing ring cavity [9,10], we analyze in detail stability and instability properties of clusters of two, three and four structures. We develop a modified Bessel function technique for analytical calculation of the expression for the interaction potential between such structures and their response to external perturbations. This method has applicability going beyond the model under consideration. Qualitative differences between stability properties of triangular and square clusters formed by localized structures are found which emphasize the role of diagonal interactions in the latter. Localized structures in such clusters are shown to interact through forces obeying a linear superposition principle. Separation distances obtained for equilateral triangular cluster are in very good agreement with cracked patches of hexagonal patterns [11]. Clusters with sufficiently low symmetry may exhibit spontaneous motion. Analysis of this interesting phenomena, and simulation results, are presented.

References

[1] G. I. A. Stegman, D. N. Christodoulides and M. Segev, "Optical Spatial Solitons: Historical Perspectives", IEEE Journal on Selected Topics in Quantum Electronics **6**, 1419-1427 (2000).

[2] W. J. Firth and C. O. Weiss, "Cavity and Feedback Solitons", Optics and Photonics News **26**, 54-58 (2002).

[3] N.N. Rosanov, *Spatial hysteresis and optical patterns* (Springer, Berlin, 2002).

[4] W. J. Firth and A. J. Scroggie, "Optical Bullet Holes: Robust Controllable Localized States of a Nonlinear Cavity", Phys. Rev. Lett. **76**, 1623-1626 (1996).

[5] Processing of Information by Arrays of Nonlinear Optical Solitons Homepage, "www.pianos-int.org".

[6] B. A. Samson and M. A. Vorontsov, "Localized states in a nonlinear optical system with binary-phase slice and a feedback mirror", Phys. Rev. A **56**, 1621-1626 (1997).

[7] A. J. Scroggie and G.-L. Oppo, "Optical Sprinklers", to be published.

[8] T. Maggipinto, M. Brambilla, G. K. Harkness and W. J. Firth, "Cavity Solitons in Semiconductor Microresonators: Existence stability and dynamical properties", Phys. Rev. E **62**, 8726-8739 (2000).

[9] L. A. Lugiato and C. Oldano, "Stationary spatial patterns in passive optical systems: Two-level atoms", Phys. Rev. A **37**, 3896-3908 (1988).

[10] A. G. Vladimirov, J. M. McSloy, D. V. Skryabin and W. J. Firth, "2D Clusters of Solitary Structures in Driven Optical Cavities", Phys. Rev. E **65**, 046606 (2002).

[11] G. K. Harkness, W. J. Firth, G.-L. Oppo and J. M. McSloy, "Computationally Determined Existence and Stability of Transverse Structures: 1. Periodic Optical Patterns", Phys. Rev. E , Submitted (2002).
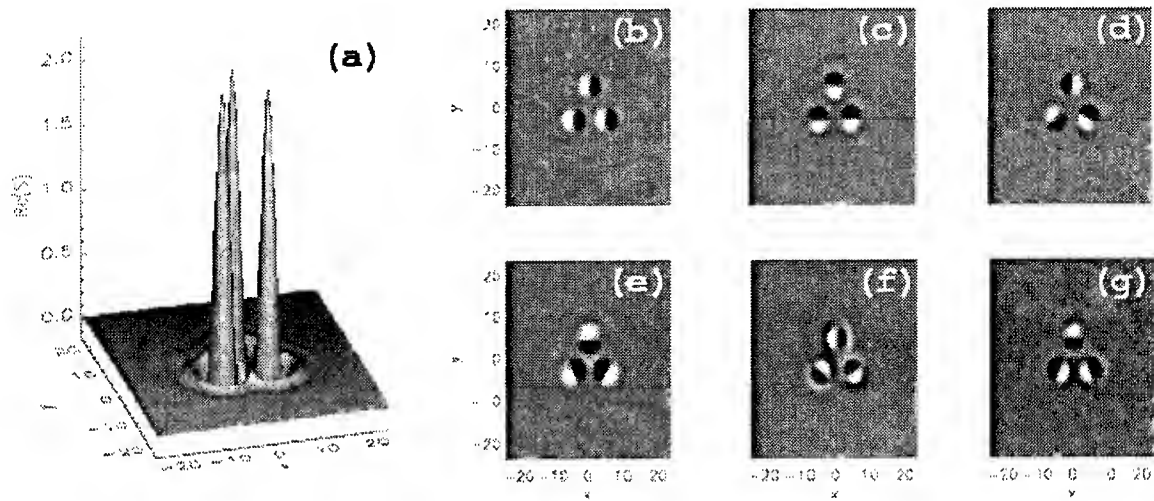
Fig. 1. An unstable tri-soliton cluster (a) with respective neutral (b), (c) and unstable eigenmodes (d)-(f).
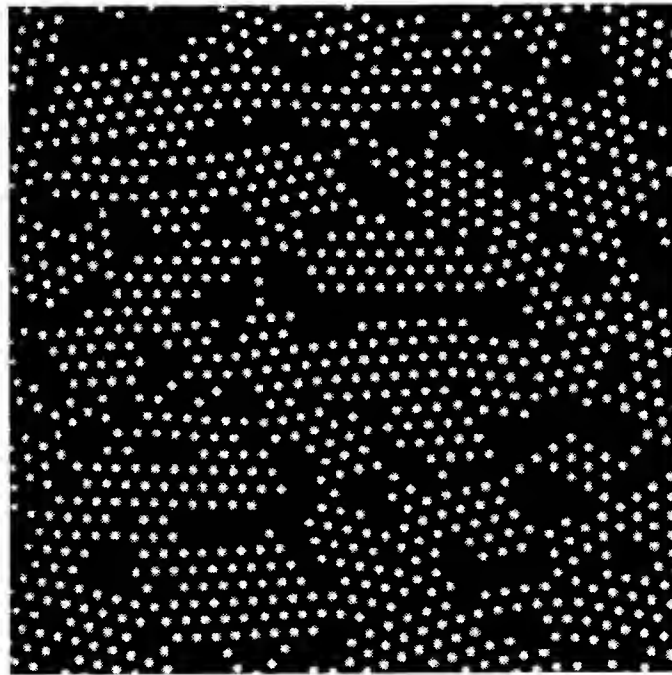
Fig. 2. Our asymptotic equation for cluster speparations and stability shows very good agreement with that of islands of a "cracked" pattern.

Optical parametric oscillator in waveguides induced by photorefractive spatial solitons

Song Lan,[1] J.A. Giordmaine,[1,2] Mordechai Segev,[1,3] and Daniel Rytz[4]

1. *Department of Electrical Engineering, Princeton University, New Jersey 08544*
2. *NEC Research Institute, Princeton, New Jersey 08540*
3. *Department of Electrical Engineering, Princeton University, Princeton, New Jersey 08544*
4. *FEE GmbH, Struthstr. 2, D-55743 Idar-Oberstein, Germany*

Photorefractive spatial solitons and their induced waveguides[1] have been of great interest in recent years because of their dimensionality, wavelength sensitivity, and fixability. With these properties, they offer potential applications, some of which are truly unique[2,3]: reconfigurable near-field optical interconnects, three-dimensional optical circuitry[4], directional coupling[5,6], beam steering,[7] and frequency conversion[8,9]. The most promising one is nonlinear frequency conversion. Since the conversion efficiency in $\chi^{(2)}$ processes is proportional to the intensity of the pump beam, one easy way is to use a focused beam. However, in bulk, diffraction reduces the conversion efficiency, because as the beam diffracts, (1) the intensity decreases, and (2) the beams acquire quardratic phases thus the phase-matching condition cannot be satisfied across the entire beam. Therefore, using waveguides for frequency conversion can largely improve the conversion efficiency. Employing waveguides induced by photorefractive solitons not only increases the conversion efficiency but also offers flexibility, because the waveguide structure can be modified at will. For example, waveguides induced by photorefractive solitons offer much tunability: wavelength tunability in frequency conversion is achieved by rotating the crystal and launching a soliton in the new direction, or by changing the propagation constants of the guided modes by varying the intensity ratio and external voltage (without mechanical movements).

In our earlier work[8,9] we demonstrated second-harmonic generation in waveguides induced by photorefractive solitons with improved conversion efficiency and tunability. Here we are interested in optical parametric oscillators (OPOs). In an OPO, the threshold pump power is dependent on the signal gain per pass through the crystal. Here we demonstrate OPOs in waveguides induced by photorefractive solitons, and show that by using waveguiding, the gain in increased for the same cavity loss, leading to a greatly reduced threshold pump power.
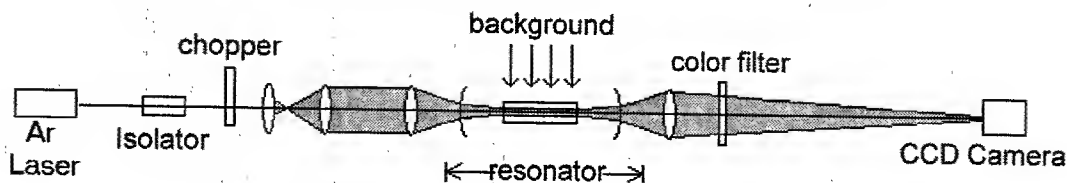
Fig. 1 Experimental setup

Our setup is shown as Fig. 1. We build a doubly-resonant oscillator, in which the oscillation occurs at both the signal and the idler wavelengths. The oscillator consists of two concave mirrors with 2.5 cm radius and a nonlinear crystal. The mirrors are coated to obtain almost 100% transmission for the pump light, and high reflectivities for the signal and the idler beams. A 488nm laser beam acts as the pump and also generates the soliton. The beam is adjusted to match the fundamental mode of the cavity, with the minimum beam waist located at the input surface of the crystal. A chopper is put into the path of the pump to "chop" the CW pump beam into 150 μs pulses with repetition rate of 67 Hz. The duration of the pulses is much longer than the response time of the nonlinear polarization excited by the pump beam, so for the parametric process it is essentially CW pumping, and the gain is related to the peak power of the pump pulses. On the other hand, the pulse duration is much shorter than the response time of the photorefractivity so the formation of the soliton is dependent only on the average power of the pump beam. Therefore, with the chopper we control the parametric process and the spatial soliton structure independently. The nonlinear crystal is a 5mm×15.8mm×5mm (a×b×c) KNbO$_3$ crystal. All beams propagate along b-axis, and the external voltage is applied along c-axis. The pump is polarized along c-axis, while the signal and the idler are both polarized along a-axis. The crystal is also illuminated uniformly by a white light beam as necessary for the photorefractive screening nonlinearity.
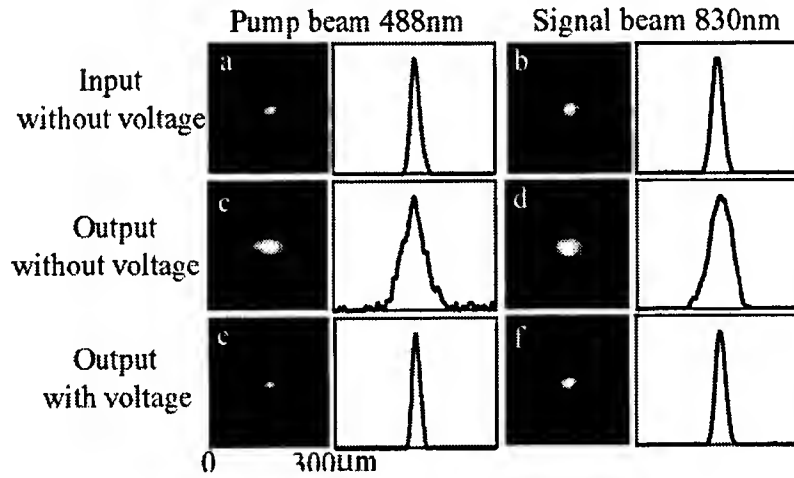
Fig. 2 Beam cross-sections profiles at input and output surfaces

First we investigate the operation of the OPO without the waveguiding induced by the solitons, and obtain oscillation at threshold pump power of 84mW. Fig. 2 shows the cross-sections of the pump and the signal beams. The 488nm beam is focused at the input surface of the crystal with a FWHM of 21 μm as shown in Fig. 2a. It diffracts to 54 μm at the output surface (Fig. 2c). The minimum beam waist of the signal beam is also located at the input surface of the crystal with a FWHM of 28 μm (Fig. 2b). At the output the signal beam size is 69 μm, (Fig. 2d). The signal and the idler wavelengths are 830.2 nm and 1186.4 nm at temperature of 40°C. The output signal peak power as a function of pump power is shown as Fig. 3. Then, we move the output mirror further away from the crystal a distance of L/n, (n is the crystal refractive index) and generate the soliton (turning the applied field on). We obtain oscillation, optimize the voltage and the intensity ratio, and

find the maximum output signal power. The beam profiles are shown in Fig. 2. The soliton at the output is shown in Fig. 2e, and the guided signal beam in Fig. 2f. Comparing Fig. 2f and 2d, we can see the oscillator is operated with the guidance of the induced waveguide. The output signal power as a function of pump power is shown in Fig. 3. The oscillator with the soliton actually works with a threshold of 56mW, 33% lower than that of the oscillator without the soliton. We note that at the highest pump power, the output signal is slightly weaker than without the soliton. This is because on the reverse direction the signal and the idler transfer energy back to the pump beam, and the soliton waveguiding improves the efficiency of this reverse process as too. But this issue can be readily resolved by use of a singly-resonant oscillator or by a ring oscillator.
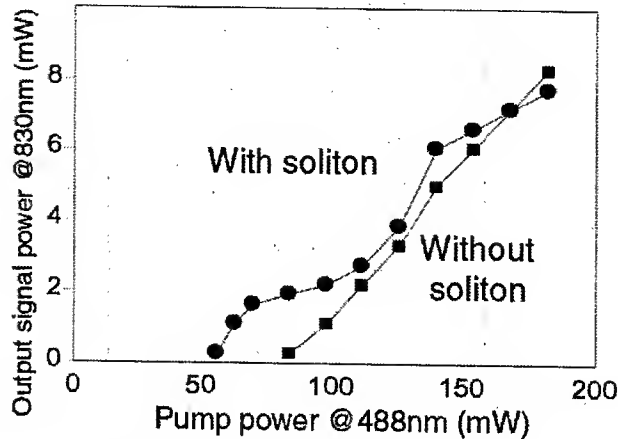
Fig. 3 Output signal power vs. input pump power

In conclusion, we have demonstrated an optical parametric oscillator in a waveguide induced by a photorefractive soliton, and have shown that the threshold pump power is significantly reduced. This technique should work even better with singly resonant OPOs and it can substantially reduce the threshold pump power when very narrow solitons are employed. For example, if we use a soliton beam with a beam waist of 8 μm and a 15 mm crystal, we can reduce the threshold pump to only 3.5% of that for an OPO in the same nonlinear medium, using the same mirrors but without the soliton.

Reference:

1. M. Segev, B. Crosignani, A. Yariv, and B. Fischer, *Phys. Rev. Lett.* **68**, 923 (1992)
2. M. Segev, M. Shih, and G. Valley, *J. Opt. Soc. Am. B* **13**, 706 (1996)
3. M. Shih, Z. Chen, M. Mitchell, M. Segev, H. Lee, R.S. Feigelson, and J.P. Wilde, *J. Opt. Soc. Am. B* **14**, 3091 (1997)
4. M. Klotz, H. Meng, G.J. Salamo, M. Segev and S.R. Montgomery, *Opt. Lett.* **24**, 77 (1999)
5. S. Lan, E. DelRe, Z. Chen, M. Shih, and M. Segev, *Opt. Lett.* **24**, 475 (1999)
6. J. Petter, and C. Denz, *Opt. Communications*, **188**, 55 (2001)
7. E. DelRe, M. Tamburrini, and A.J. Agranat, *Opt. Lett.* **25**, 963 (2000)
8. S. Lan, M. Shih, G. Mizell, J.A. Giordmaine, Z. Chen, C. Anastassiou, J. Martin, and M. Segev, *Opt. Lett.* **24**, 1145 (1999)
9. S. Lan, C. Anastassiou, M. Shih, J.A. Giordmaine, G. Mizell, and M. Segev, *Appl. Phys. Lett.* **77**, 2101 (2000)

Frequency up-conversion of 770 nm ultra-short pulses by two-photon absorption in doped PMMA fibers

Grace Jordan, Takeyuki Kobayashi, Werner J. Blau

Department of Physics, Trinity College Dublin, Dublin 2

Ireland.

Tel: 353 1 6081675, Fax: 353 1 6711759

Email: wblau@tcd.ie

Hartwig Tillmann, Hans-Heinrich Hörhold

Institut für Organische Chemie und Makromolekulare Chemie, Friedrich-Schiller-Universität Jena,

Humboldtstraße 10, D-07743, Jena,

Germany

Email: hoerhold@rz.uni-jena.de

Abstract: We report on the up-converted emission of blue light from a novel organic stilbenoid compound (1, 4-bis(diphenylamino-styryl)-benzene) dopant in a PMMA fiber due to the two-photon absorption of 770 nm pulses from a Tittanium Sapphire laser.

Summary: Considerable research is continually underway into materials and devices, which convert light from the IR to the visible and UV regions of the spectrum. Lasing by frequency up-conversion has advantages over other techniques such as harmonic generation or frequency mixing as no phase matching is required and thus waveguides and fibers can be used. We report on an all polymer fiber system, which has the added advantage of flexibility and low cost making it appealing for the construction of an up-converting blue laser. The fibers used were made from PMMA doped with 1% wt 1, 4-bis(diphenylamino-styryl)-benzene. They have a core diameter of 175μm, an outer diameter of 350μm. The novel compound is specifically designed and synthesized for the blue spectral region and has a high quantum yield.

The high intensity necessary to induce non-linear absorption was achieved using ~180 fs pulses from a mode-locked Titanium-Sapphire tunable laser. This pump was tuned to the relatively low loss region of PMMA at 770 nm to achieve maximum peak power in the fiber. In our experimental setup, the pump beam and induced fluorescence co-propagate in the fiber. The pump pulse duration and spectral width were 180fs and 10nm, respectively. The beam was launched through an f=10cm lens into the cleaved fiber end. An IR filter was used to remove the remnant pump beam prior to detection with an Oriel grating spectrograph and Andor Technology CCD camera. The pump beam input power was measured using a photo-diode and the induced fluorescence intensity and pump transmission were measured as a function of peak power in the fiber. At optimum coupling the two-photon induced fluorescence was readily observed at ~500nm. The spectrum for the fluorescence is shown in Fig 1. along with the absorption and emission spectra of the dopant in dioxane. There is a noticeable red shift evident in the two-photon induced emission peak, which may be attributed to re-absorption in the fiber. Our study will open the door to the development of a compact blue polymer fiber source that can be pumped with a single chip of an inexpensive InGaAs laser diode.
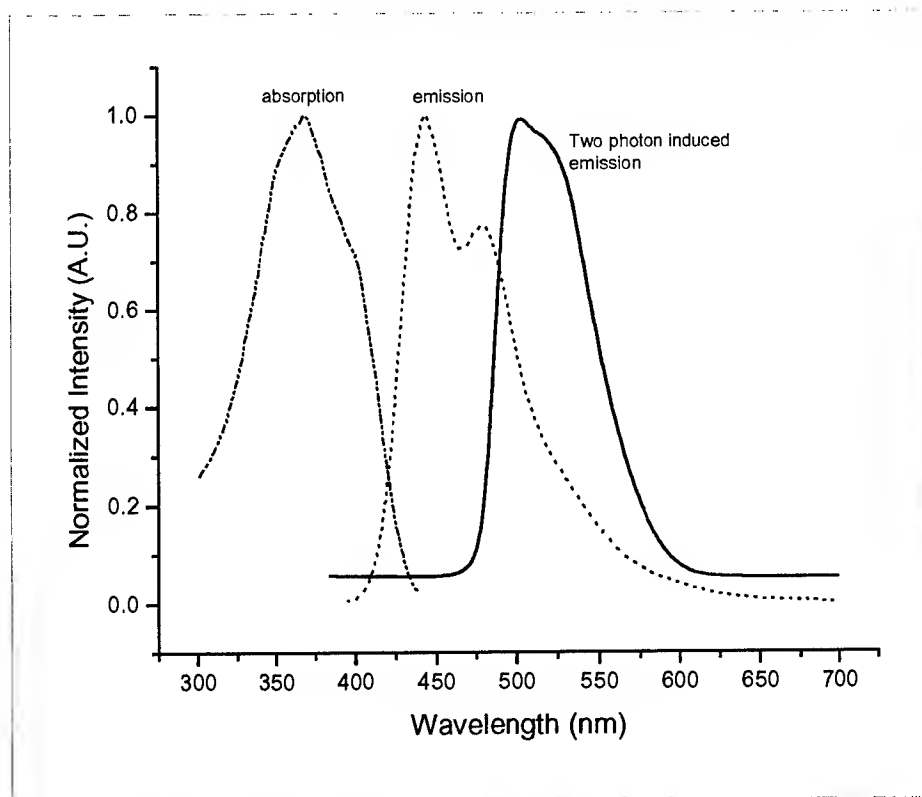
Figure 1

Spectra for absorption, spontaneous emission and up-converted emission.

Long-wavelength continuum generation about the second dispersion zero of a tapered fiber

J. M. Harbold, F. Ö. Ilday, and F. W. Wise
Department of Applied Physics, 212 Clark Hall, Cornell University, Ithaca, NY 14853,
tel: (607) 255-9956, fax: (607) 255-7658, email: *jeffh@ccmr.cornell.edu*

T. A. Birks and W. J. Wadsworth
Department of Physics, University of Bath, Claverton Down, Bath BA2 7AY, United Kingdom

Z. Chen
Beckmann Laser Institute and Center for Biomedical Engineering, University of California, Irvine, CA 92612

Abstract: We demonstrate continuum generation at wavelengths longer than the zero-dispersion wavelength of ordinary fiber for the first time using a narrow-diameter tapered fiber.
©2002 Optical Society of America
OCIS codes: (190.4370) Nonlinear optics, fibers; (060.7140) Ultrafast processes in fibers

Much attention has been paid to the spectral broadening of femtosecond pulses that occurs in microstructured and tapered fibers [1]-[3]. To date, experiments in this area have been performed at pump wavelengths around 800 nm; however, applications such as optical Doppler tomography (ODT) [4] and optical frequency metrology [5] motivate the development of broadband light sources at longer wavelengths. A requirement for the generation of broadband
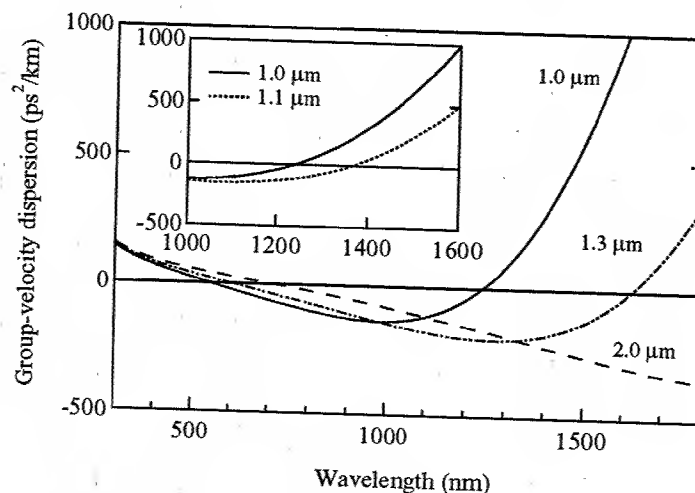
Fig. 1. Calculated group-velocity dispersion for (top to bottom) 1.0, 1.3, and 2.0 μm-diameter waist tapered fibers. The inset shows the GVD of the 1.0 and 1.1 μm waist tapers in proximity to their second ZDWs.

continua is small group-velocity dispersion (GVD) at the propagating wavelengths. In addition to reducing dispersive spreading of the input pulse, propagation near the zero-dispersion wavelength (ZDW) allows phase-matching and group-velocity matching of four-wave mixing (FWM) processes. It is known that higher-order dispersion produces a second ZDW at longer wavelengths in both microstructured and tapered fibers. In this work we show that this second ZDW can be exploited to generate continua centered on ~ 1300 nm.

Calculations indicate that tapered fibers with waist diameters between 1.0 and 1.1 μm should have the second ZDW at 1240 nm and 1370 nm, respectively (Figure 1). Therefore, a tapered fiber was prepared with a targeted diameter within this range [2]. The resulting structure consists of a 20-mm-long taper waist with a diameter of ~ 1 μm, connected to untapered fiber on each side by 35-mm-long transition regions. We numerically model the

propagation of intense femtosecond pulses through the tapered fiber with an extended nonlinear Schrödinger equation including Kerr nonlinearity, self-frequency shift through Raman scattering, and up to fifth-order dispersion [6]. Propagation of 80-fs pulses centered near 1260 nm with varying energy content is considered in the simulations (Figure 2, top).
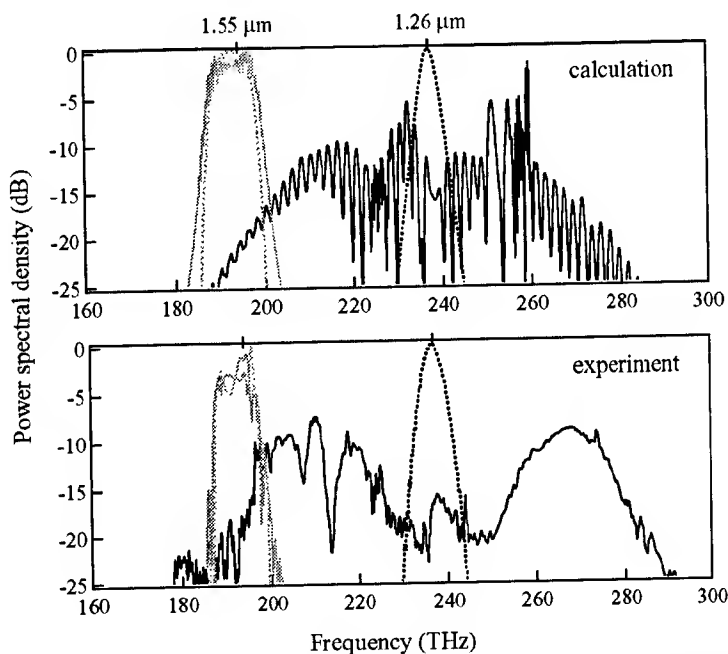
Fig. 2. Comparison of numerical simulations (top) and experimental results (bottom) for: 750-pJ, 80-fs pulses at 1.26 μm (black) and 350-pJ, 100-fs pulses at 1.55 μm (gray). The input spectra are shown as dotted lines.

A mode-locked Cr:forsterite laser provided 1.5-nJ, transform-limited, 80-fs pulses centered at 1.26 μm [7]. Approximately 50% of the available energy was coupled into the taper's input fiber, which was kept as short as possible to minimize the initial pulse broadening. The evolution of the continuum observed in the experiment with launched pulse energy varying between 7 pJ and 750 pJ is presented in Figure 3. As the pulse energy is increased, the spectrum splits and most of the energy is shifted to higher and lower frequencies, which leaves the center of the spectrum largely depleted (Figure 3, 375 pJ – 750 pJ). The observed features agree qualitatively and semi-quantitatively with the numerical simulations, and are consistent with nonlinear pulse propagation at the second ZDW. The experimental spectrum corresponding to 750 pJ pulse energy is plotted in Figure 2 (bottom) for comparison with the numerical results (Figure 2, top). The spectrum spans 700 nm at the points 20-dB from the peak of the continuum. As a control experiment, 100-fs pulses at 1550 nm from an Er-doped fiber laser were coupled into the same tapered fiber. We observed no significant spectral broadening of the pulses at the highest coupled pulse energy of about 350 pJ, in accordance with the numerical simulations (Figure 2).
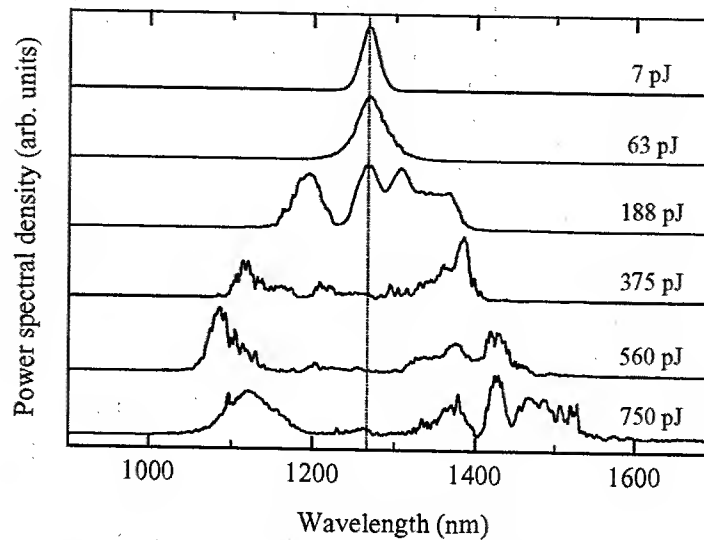
Fig. 3. Experimentally observed evolution of the continuum with pulse energy. The dotted line indicates the center of the input spectrum.

In conclusion, we have demonstrated that a tapered fiber is an effective medium for generating broadband light in the near-infrared by the use of its second ZDW. Unamplified femtosecond pulses from a Cr:forsterite laser were spectrally-broadened to cover 700 nm from 1000 to 1700 nm. By changing the diameter of the tapered fiber's waist, this method for continuum generation about the second ZDW should be easily adapted to other wavelengths. We expect continua generated this way to find application in high-resolution biological imaging systems as well as in frequency metrology for telecommunications.

J. K. Ranka, R. Windeler, and A. J Stentz, *Opt. Lett.* **25**, 25-27 (2000).
T. A. Birks, W. J. Wadsworth, and P. St.J. Russell, *Opt. Lett.* **25**, 1415-1417 (2000).
I. Hartl, X. D. Li, C. Chudoba, R. K. Hganta, T. H. Ko, J. G. Fujimoto, J. K. Ranka, R. S. Windeler, *Opt. Lett.* **26**, 608-610 (2001).
Y. Zhao, Z. Chen, C. Saxer, Q. Shen, S. Xiang, J F. de Boer, and J. S. Nelson, *Opt. Lett.* **25**, 1358-1360 (2000).
D. J. Jones, S. A. Diddams, J. K. Ranka, A. Stentz, R. S. Windeler, J. L. Hall, and S. T. Cundiff, *Science* **288**, 635-639 (2000).
A. Gaeta, *2001 Conference on Lasers and Electro-Optics*, Baltimore, MD, Talk CMK3.
V. Yanovsky, Y. Pang, and F. Wise, *Opt. Lett.* **18**, 1541-1543 (1993).

Origin of supercontinuum generation in microstructured fibers

Alexander L. Gaeta

School of Applied and Engineering Physics, Cornell University, Ithaca, NY 14853
Tel: (607) 255-9983 fax: (607) 255-7658 e-mail: a.gaeta@cornell.edu

Xun Gu, Lin Xu, Mark Kimmel, Erik Zeek, Patrick O'Shea, Aparna P. Shreenath, and Rick Trebino

School of Physics, Georgia Institute of Technology, Atlanta, GA 30332-0430, USA
Tel: (404) 894-1690 fax: (404) 385-0830 e-mail: rick.trebino@physics.gatech.edu

Robert S. Windeler

OFS Fitel Laboratories, 700 Mountain Ave., Murray Hill, NJ 07974, USA

Abstract: We investigate the propagation of femtosecond pulses in microstructured fibers under conditions in which a supercontinuum is generated. We find that higher-order dispersion primarily determines the spectral envelope and that the spectrum contains a highly complicated underlying sub-structure which is highly sensitive to input fluctuations.

OCIS codes: (320.7140) Ultrafast processes in fibers; (320.7110) Ultrafast nonlinear optics

1. Introduction

Small-core microstructured fibers (MF's) have drawn great interest due to their large effective nonlinearity and to their ability to shift the zero-dispersion point of the waveguide to wavelengths at which femtosecond Ti:sapphire lasers operate. Such fibers allow for strong nonlinear interactions, as illustrated by recent experiments in which an extremely broad spectral continuum spanning from 400 nm to 1600 nm has been generated [1] at the output of the fiber. Such a coherent white-light source has proven useful for various applications including optical coherence tomography [2] and frequency metrology [3]. Although there have been numerous experimental and theoretical investigations [4] of nonlinear propagation near the zero-group-velocity dispersion (GVD) point of optical fibers, none of these studies have considered the operating conditions of these recent experiments in which the combination of relatively high-energy femtosecond pulses and tight mode confinement produces such a highly nonlinear interaction.

We present a theoretical and experimental investigation of the nonlinear propagation of femtosecond pulses tuned near the zero-dispersion point of a microstructured fiber. We find that the spectral envelope of the generated continuum is determined primarily by the higher-order dispersion of the fiber. Specifically, we find that the interplay between third-order dispersion (TOD) and self-phase modulation (SPM) dominates the propagation dynamics and largely determines the extent of the blue edge of the spectrum and the relative lack of broadening to the red edge. In addition, we find that the spectrum exhibits a highly complicated sub-structure that is extremely
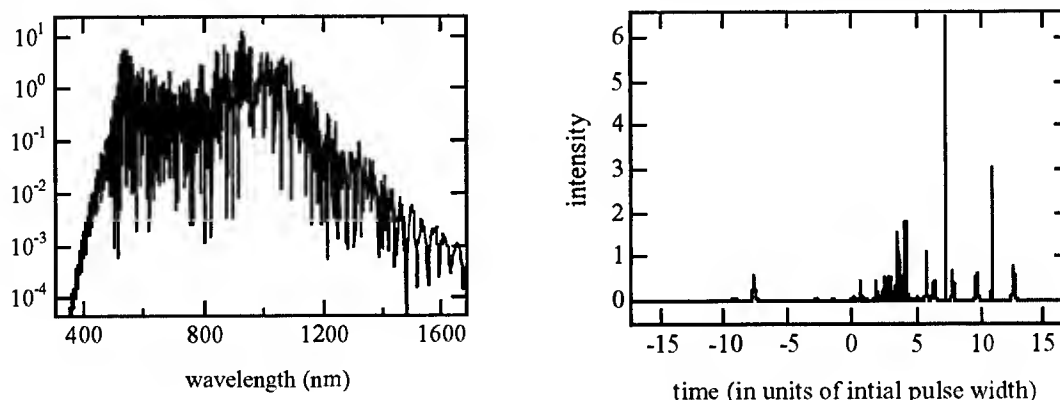
Fig. 1. Predicted spectrum (a) and corresponding temporal profile (b) of the transmitted light after propagating through a microstructure fiber near the zero-dispersion point.
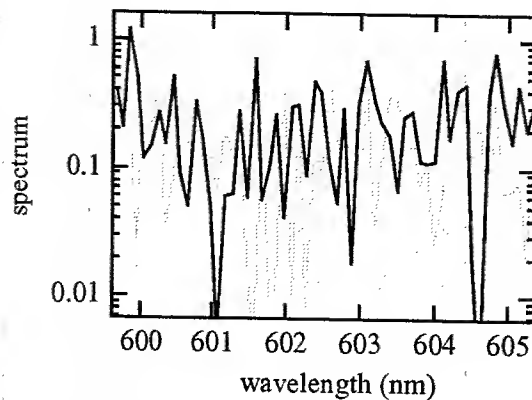
Fig. 2. High resolution spectra for the same conditions (solid curve) as in Fig. 1 and for the same conditions but with an 0.1% higher input pulse energy (dotted curve).

sensitive to input pulse energy. As discussed below, these predictions are confirmed via single-pulse measurements.

In our theoretical model, we employ the nonlinear envelope equation [5,6], which is valid for pulses as short as a single optical cycle, or alternatively, for spectral bandwidths that are comparable to the central frequency of the input pulse. we include all the relevant processes for such an interaction, such as Raman scattering and self-steepening, we find that the spectral envelope of the generated continuum is primarily determined by the higher-order dispersion of the fiber. An example of the generated continuum spectrum under conditions similar to the experiments is shown in Fig. 1(a). The spectral envelope is very similar to that observed in experiments in which there is a sharp edge at the blue side of the initial pulse at 800 nm and relatively long sloping tail to the red side. We find that the amount of TOD determines the position of the blue edge of the spectrum, whereas the shape of the red side is governed by the third- and fourth-order dispersion. The input pulse undergoes significant pulse break-up as it propagates down the fiber [see Fig. 1(b)], resulting in the creation of soliton-like pulses out of the red-shifted part of the spectrum. In our simulations, we find that both Raman and self-steepening play relatively minor roles in determining the observed spectral envelope. As the amount of third-order dispersion is decreased, the blue edge moves to shorter wavelengths. However, above a certain input intensity, we find that the resulting blue edge of the spectrum does not shift significantly to shorter wavelengths, and thus we conclude that only by decreasing the third-order dispersion is it possible to increase the continuum bandwidth. The predicted spectrum is also found to exhibit substantial sub-structure which is very sensitive to the input pulse energy [See Fig. 2] and thus could play an
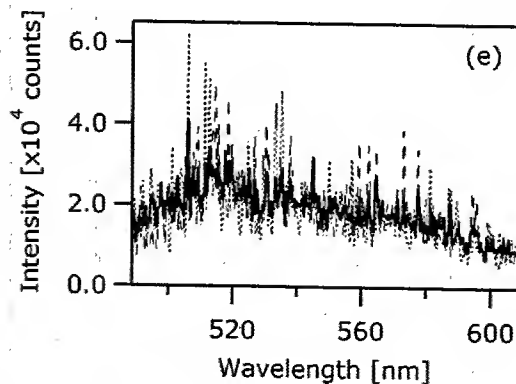
Fig. 3. Numerical average of single-shot measurements taken successively, where the dashed and dotted lines are two single-shot spectra taken seconds apart, and the solid line is the average of four single-shot spectra.

important role in frequency metrology experiments. We believe that this sub-structure and these large fluctuations have not been observed in most of the measured spectra either due to insufficient spectral resolution or as a result of the spectra being an average of many laser pulses.

This hypothesis was verified with series of measurements in which single-shot spectral measurements of the microstructured-fiber continuum were taken [7]. The output pulse from a Ti-Sapphire oscillator was amplified by an adjustable-rep-rate regenerative amplifier to ~100 µJ per pulse, which was then attenuated to ~1 nJ for injection into 152 cm of a 2-µm-diameter microstructure fiber from OFS Fitel Laboratories. Using different amplifier repetition rates and camera exposure times, we could vary the number of shots in a measurement (see Fig. 3). Single-shot spectra were observed to exhibit significant substructure which was on the scale of 1 nm. Spectra acquired for different shots resulted in spectra that were completely distinct, although the spectral envelopes were similar. As multiple shots were averaged the spectrum evolved into a shape that did not change over time.

Since third-order dispersion (TOD) primarily determines the dynamics that leads to the supercontinuum, manipulation of its magnitude and sign will play a crucial role in optimizing the shape and width of the spectrum for particular applications. For example, by changing the sign of the TOD, but keeping all other parameters the same, the red edge of the spectrum can be substantially extended whereas the extent of the blue edge is reduced. Generation of supercontinuum further into the infrared could thus be achieved by operating at the long-wavelength second zero-GVD point [8] of these fibers. We believe that suitable designs of microstructured fibers offer the possibility of further increases in the total spectral bandwidth by reducing the air-filling fraction of the MF's and thus decreasing the TOD and flattening the dispersion profile.

[1]   J. K. Ranka, R. Windeler and A. J. Stentz, *Opt. Lett.* **25**, 25 (2000).

[2]   I. Hartl, X.D. Li, C. Chudoba, R. K. Ghanta, T. H. Ko, J.G. Fujimoto, J.K. Ranka, and R.S. Windeler, *Opt. Lett.* **26**, 608 (2001).

[3]   D. J. Jones, S. A. Diddams, J. K. Ranka, A. Stentz, R. S. Windeler, J. L. Hall, and S. T. Cundiff, *Science* **288**, 635, 2000.

[4]   See, For example, G. Boyer, *Opt. Lett.* **24**, 945 (1999).

[5]   T. Brabec and F. Krausz, *Phys. Rev. Lett.* **78**, 3283 (1997).

[6]   A. Gaeta, to be published in *Opt. Lett.* (2002).

[7]   X. Gu, M. W. Kimmel, A. Shreenath, R. Trebino, R. S. Windeler, C. Kerbage, and B. J. Eggleton, to be published in *Opt. Lett.* (2002).

[8]   J. C. Knight, J. Arriga, T. A. Birks, A. Ortigosa-Blanch, W. J. Wadsworth, and P. St. J. Russell, *IEEE Photon. Tech. Lett.* **12**, 807 (2000).

Exact Solitary Wave Solutions of the Nonlinear Schrödinger Equation with Distributed Gain

V.I. Kruglov and J.D. Harvey

Physics Department, The University of Auckland, Private Bag 92019, Auckland, New Zealand
Tel +64-9-3737999, Fax +64-9-3737445, e-mail j.harvey@auckland.ac.nz

Abstract

We present new exact analytical solutions to the NLSE with gain in the anomalous dispersion regime corresponding to a compressing or spreading solitary pulses. These solutions have application in high gain nonlinear fiber amplifiers.

Exact Solitary Wave Solutions of the Nonlinear Schrödinger Equation with Distributed Gain

V.I. Kruglov and J.D. Harvey

Physics Department, The University of Auckland, Private Bag 92019, Auckland, New Zealand
Tel +64-9-3737999, Fax +64-9-3737445, e-mail j.harvey@auckland.ac.nz

1.   Introduction

The one-dimensional nonlinear Schrödinger equation (NLSE) with gain, and its complex generalization the Ginzburg-Landau equation have a wide range of applications in nonlinear optics[1] and laser physics[2]. In contrast to the NLSE without gain, these equations are not integrable by the inverse scattering method and therefore they do not have soliton solutions in a strict mathematical sense. They do, however have solitary wave solutions which often have been called solitons. In this paper we present solutions to the NLSE with gain in the anomalous dispersion regime. These solutions propagate self similarly under the influence of nonlinearity, dispersion and distributed gain or loss, and constitute a new class of analytic solitary solutions which are appropriate for the description of pulse evolution in single mode fiber amplifiers, and describe a pulse which continuously spreads or compresses during propagation, but which maintains its shape. This solitary propagating regime has also been investigated numerically and has been found to be stable against small perturbations of the chirp and the amplitude, leading to the expectation that this solution will find application in high gain amplifier systems. In the limit when the gain approaches zero, the amplitude reduces to the familiar hyperbolic secant fundamental soliton solution of the NLSE without gain, and the chirp tends to zero.

2.   Self Similar Solutions

Recently, quite general results for the analytic solution of the NLSE with an arbitrary gain distribution for *normal* dispersion have been found using self similarity techniques [3,4]. In these papers asymptotically exact self-similar parabolic solutions for an arbitrary initial solitary wave profile have been found in high-power limit. We note that in the particular case of the NLSE without gain and the normal group velocity dispersion the asymptotic parabolic solution was first given in [5].

In this work we present the discovery of exact self-similar solitary solutions of the NLSE with distributed gain in the case of *anomalous* group velocity dispersion.

The nonlinear Schrödinger equation with gain in the form used to describe nonlinear pulse propagation in optical fibres is given by:

$$i\frac{\partial\psi}{\partial z} = \frac{\beta}{2}\frac{\partial^2\psi}{\partial\tau^2} - \gamma|\psi|^2\psi + i\frac{g(z)}{2}\psi, \tag{1}$$

where $\psi(z,\tau)$ is the complex amplitude of the electric field in a co-moving frame, z is the propagation distance, τ is the retarded time, β is the group velocity dispersion (GVD) parameter, γ is the nonlinearity parameter and $g(z)$ the distributed gain function. The function $\psi(z,\tau)$ can always be written as :

$$\psi(z,\tau) = U(z,\tau)\exp(i\Phi(z,\tau)), \tag{2}$$

where U and Φ are real functions of z and τ. We look for self similar solutions of the NLSE assuming that the phase has a quadratic form:

$$\Phi(z,\tau) = a(z) + b(z)\tau + c(z)\tau^2. \tag{3}$$

This ansatz follows from analysis of the existence of self-similarity, and the value of this approach has been confirmed for any gain function in the case when $\beta\gamma > 0$ [3,4]. The necessary and sufficient conditions for the existence of a self similar solution in this case are as follows:

$$a(z) = a_0 + \left(\frac{\tau_c^2}{2\beta} - \frac{\lambda\beta}{2\sigma^2}\right)\frac{\sigma}{1-\sigma z}, \quad b(z) = -\frac{\sigma\tau_c}{\beta(1-\sigma z)}, \quad c(z) = \frac{\sigma}{2\beta(1-\sigma z)}, \quad (4)$$

and

$$g(z) = \frac{\sigma}{1-\sigma z} = \frac{1}{z_c - z}. \quad (5)$$

All results below are applicable to both positive and negative σ but we note that when $\sigma > 0$, the solutions remain finite only in the interval $0 \le z < z_c$. When $\sigma = 0$, the equation reduces to the NLSE without gain which can be solved by the inverse scattering method[6]. Using the results in equations 4 and 5, we find 15 non trivial solutions of the NLSE with distributed gain where nine are bounded (six of them periodic) and six are unbounded periodic solutions. We concentrate here on the most interesting exact solutions corresponding to $\beta\gamma < 0$ which have a quadratic phase and an amplitude with the solitary wave form:

$$U(z,\tau) = \frac{|\beta|^{1/2}|\gamma|^{-1/2}}{\tau_0(1-\sigma z)}\mathrm{sech}\left(\frac{(\tau-\tau_c)}{\tau_0(1-\sigma z)}\right), \quad (6)$$

where $\lambda = \tau_0^{-2}$ in Eq 4.

These solitary wave solutions correspond to the self similar evolution of a fundamental solitary pulse under the influence of distributed gain.

There are two cases: (i) $\sigma > 0$, which corresponds to positive gain and the solution then represents a self compressing and amplifying pulse of particular relevance to high gain nonlinear amplifier systems; and (ii) $\sigma < 0$, which corresponds to loss and the solution then represents a spreading solitary wave. Evidently the shape of this self similar solution does not change on propagation but the width and amplitude of the pulse scale as functions of the propagation distance z. This solution has two important integrals of motion which show that the self compressing pulse shape tends to a delta function at z_c and that the energy of the pulse as a function of distance can be written:

$$E(z) = 2|\beta||\gamma|^{-1}\tau_0^{-1}(1-\sigma z)^{-1} = 2|\beta|/(|\gamma|w(z)),$$

where $w(z)$ is the width of the propagating pulse.

It is also possible to show that propagation in a dispersion decreasing fibre $\beta(z) = \beta\exp(-\sigma z)$ is formally equivalent to propagation in a distributed gain amplifier, and this corresponds to the fact that solitary self similar propagation also occurs in such a fibre, although in this case the energy of the pulse is constant and the pulse either collapses towards a delta function or spreads continuously depending on the sign of σ.

3. Discussion

The self similar solitary wave solutions derived here correspond to hyperbolic secant pulses with a linear chirp which propagate without change in shape, only a scaling of their width and amplitude, whilst the pulses are amplified through the distributed gain. These self similar pulses maintain their linear chirp, although this chirp intensifies during amplification. These features are shown in Figure 1 where the analytical solution is compared with the results of numerical propagation of a hyperbolic secant pulse with the correct initial amplitude and chirp though an amplifier with the distributed gain given in Eq 5. In these simulations, the input pulse has an initial width of 7ps and energy of 0.5pJ, the critical length of the amplifier is 10m ($\sigma = 0.1$), and the pulse shapes are shown for propagation to z=2m and z=8m. The numerical simulations are in agreement with the analytical predictions, indeed the agreement is excellent even at 99% of the critical propagation distance z_c where the pulse has been compressed by a factor of about 150 in a 20dB power amplifier, although it must be emphasized that before this level of compression

and amplification is reached in a real amplifier, the pulse evolution would be affected by higher order terms in the NLSE which are neglected in this analysis.

We have also performed numerical simulations to determine the stability of the evolution of these solitary pulses in the presence of perturbations and non ideal amplifier gain profiles. The evolution is more sensitive to the initial chirp than the peak amplitude, but in both cases the addition of small amounts of random noise to the input pulse amplitude and phase did not significantly affect the evolution. Indeed in both cases the pulses evolved towards the ideal form, indicating the stability of the solution.

Previous attempts to investigate the nonlinear amplification of pulses in the anomalous dispersion regime using constant gain by numerical simulation have shown that the pulse tends to break up into a series of pulses due to the combined effects of self phase modulation and dispersion. This is in contrast to the situation in the normal dispersion regime where numerical simulations indicated that all pulses tended to evolve to a parabolic shape. Subsequent application of the techniques of self similar analysis explained this behaviour, and indeed the parabolic profile is obtained in the high intensity limit no matter what the gain profile.
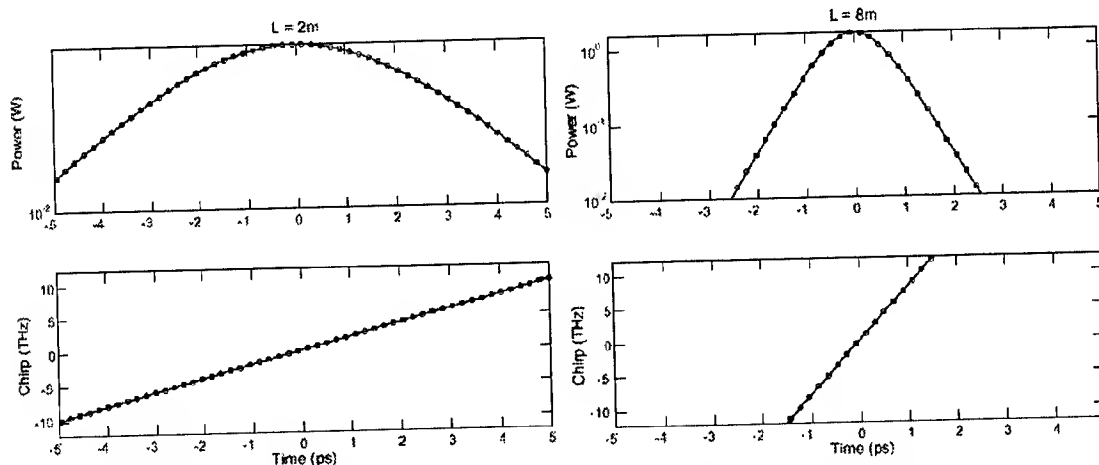
Fig. 1 Comparison of analytical solution (circles) with numerical simulation (solid line) for propagating solitary pulse in a distributed gain amplifier ($\sigma > 0$) having a critical length of 10m.

The situation in the anomalous dispersion regime is quite different. If the gain is constant we do indeed find by simulations that the pulse evolution is very complex leading to multiple pulses and significant pulse distortion. In the presence of the particular gain profile given in Eq 5 however, exact self similar solutions exist which correspond to the propagation of hyperbolic secant pulses with a linear chirp. Since linearly chirped pulses can readily be generated and compensated, these distributed amplifier systems may find significant application in high gain guided wave amplifiers.

4.   References

1. A. Mecozzi, J.D. Moores, H.A. Haus, and Y. Lai, Opt. Lett. **16**, 1841 (1991).
2. Y. Kodama and A. Hosegawa, Opt. Lett. **17**, 31 (1992).
3. M. E. Fermann, V. I. Kruglov, B. C. Tomsen, J. M. Dudley, and J. D. Harvey, Phys. Rev. Lett. **84**, 6010 (2000).
4. V. I. Kruglov, A. C. Peacock, J. M. Dudley, and J. D. Harvey, Opt. Lett. **25**, 1753 (2000).
5. D. Anderson, M. Desaix, M. Karlsson, M. Lisak, and M.L. Quirogs-Teixeiro, J. Opt. Soc. Am. B **10**, 1185 (1993).
6. V.E. Zakharov and A.B. Shabat, Sov. Phys. JETP **34**, 62 (1972)

Timing and amplitude jitter due to intra-channel dispersion-managed pulse interactions

Toshihiko Hirooka and Mark J. Ablowitz

Department of Applied Mathematics, University of Colorado, Boulder, CO 80309-0526
Phone: 303-492-4543, Fax: 303-492-4066, E-mail: hirooka@colorado.edu

Abstract: Analytical expressions to estimate timing and amplitude jitter due to intra-channel pulse interactions in dispersion-managed systems are provided. Results are compared to direct numerical simulation. Distributed amplification reduces timing and amplitude jitter with fixed path-average power.
© 2002 Optical Society of America
OCIS codes: (060.5530) Pulse propagation and solitons: (060.4370) Nonlinear optics, fibers

Introduction Nonlinear intra-channel crosstalk imposes a major limitation to system performance in dispersion-managed RZ pulse transmission with channel bit rates over 40 Gbit/s and beyond because of strong overlap of neighboring pulses associated with large pulse width broadening [1, 2]. Intra-channel XPM causes a mean frequency shift of a signal resulting in timing jitter through fiber dispersion [3,4], whereas intra-channel FWM brings about amplitude fluctuations via energy transfer and generation of ghost pulses in zero bit slots [5, 6].

In this paper, we provide analytical formulae to estimate timing and amplitude jitter induced by intra-channel pulse interactions in a transmission system with strong periodic dispersion management. The analytical model developed here is used to evaluate system performance for a wide range of dispersion map strengths. Analytical results are compared to direct numerical simulation. We also find that distributed Raman amplification provides a reduction of timing and amplitude jitter as compared with lumped amplification for the same value of path-average signal power.

Analysis Propagation of optical pulses in dispersion-managed fibers in the presence of loss and amplification is described by the perturbed nonlinear Schrödinger equation. We introduce dimensionless variables $t = t_{\rm ret}/t_*$, $z = z_{\rm lab}/z_*$, $u = E/\sqrt{gP_*}$, $D = k''/k_*''$ with the characteristic parameters denoted by the subscript $*$, where $t_{\rm ret}$ and $z_{\rm lab}$ are the retarded time and the propagation distance, respectively, and E denotes the slowly varying envelope of the optical field. With a particular choice of t_*, P_*, and $z_* = z_{\rm NL} \equiv 1/\nu P_*$ where ν is the nonlinear coefficient (which yields $k_*'' = -t_*^2/z_{\rm NL}$), we have

$$i\frac{\partial u}{\partial z} + \frac{D(z)}{2}\frac{\partial^2 u}{\partial t^2} + g(z)|u|^2 u = 0. \tag{1}$$

The functions $D(z)$ and $g(z)$ describe the dispersion variation of the fiber and the variation of power due to loss and amplification, respectively, which are both periodic with period z_a.

The timing shift and energy change of a signal centered at $t = 0$ due to nonlinear intra-channel interactions with adjacent pulses u_l, u_m and u_n can be analyzed by writing $u = u_0 + u_l + u_m + u_n$ in (1), where u_k denotes a pulse centered at $t = kT$ with $k = l$, m, n integers, and T the bit interval. It is convenient to introduce the following integrals in order to calculate the timing shifts and energy change of u_0: the energy $W_0 = \int_{-\infty}^{\infty} |u_0|^2 dt$ and the mean temporal position $t_0 = \int_{-\infty}^{\infty} t|u_0|^2 dt/W_0$. Explicit formulae to compute the timing shift at the chirp-free points (Δt_0) and the energy change (ΔW_0) are obtained by assuming that average disperion is negligible and a signal u_k is periodic in z. When u_k is written as a Gaussian pulse of the form

$$u_k(z,t) = \frac{\alpha}{\sqrt{2\pi\xi(z)}}\exp\left[-\frac{(t-kT)^2}{2\xi(z)}\right], \quad \xi(z) = \beta + iC(z), \tag{2}$$

where β is constant and $C(z) = \int_0^z D(z')dz'$, we find the timing shifts and energy change satisfy [4, 7]

$$\Delta t_0(z) = \sum_{n=-N/2}^{N/2} b_n \bar{P}_n z, \quad \bar{P}_n = -\frac{\alpha^2 \beta nT}{\sqrt{2\pi}z_a}\int_0^{z_a}\frac{C(z)g(z)}{|\xi(z)|^3}\exp\left(-\frac{\beta n^2 T^2}{2|\xi(z)|^2}\right)dz, \tag{3}$$

$$\Delta W_0(z) = \sum_{n=-N/2}^{N/2}\sum_{m=-N/2}^{N/2} b_{m+n}b_m b_n \bar{Q}_{m,n} z,$$

$$\bar{Q}_{m,n} = -\frac{\alpha^4}{2\pi^2 z_a}\sqrt{\frac{\pi}{2\beta}}\int_0^{z_a} \mathrm{Im}\left[\frac{g(z)}{|\xi(z)|}\exp\left(-\frac{(m^2+n^2)\beta + 2imnC(z)}{2|\xi(z)|^2}T^2\right)\right]dz. \tag{4}$$

where b_k represents encoded binary data of the bit at $t = kT$ which takes either 1 or 0, and N is the total number of the interacting pulses. Because of a random sequence of bits b_k, Δt_0 and ΔW_0 are random variables and thus Eq. (3) and (4) allow us to compute the mean value and the variance of Δt_0 and ΔW_0, which yields timing and amplitude jitter. Timing and amplitude jitter are given by the variance of the mean temporal position of pulses and the normalized energy variance respectively: $\sigma_t^2 = \langle t_0^2\rangle - \langle t_0\rangle^2 = \langle(\Delta t_0)^2\rangle - \langle\Delta t_0\rangle^2$, $\rho^2 \equiv \sigma_W^2/W_0^2 = (\langle W_0^2\rangle - \langle W_0\rangle^2)/W_0^2 = [\langle(\Delta W_0)^2\rangle - \langle\Delta W_0\rangle^2]/W_0^2$. Since b_k takes the value 1 and 0 with probability 1/2, from (3) and (4) we have

$$\sigma_t^2 = \frac{z^2}{4}\sum_n \bar{P}_n^2, \tag{5}$$

$$\rho^2 = \frac{z^2}{W_0^2}\left[\frac{3}{16}\sum_n\left(\bar{Q}_{n,n}^2 + \bar{Q}_{n,n}\bar{Q}_{2n,2n}\right) + \frac{7}{64}\sum_{\substack{m,n\\m\neq n}}\bar{Q}_{m,n}^2 + \sum_{\substack{n_1,m_2,n_2\\m_2\neq n_2}}p_1\bar{Q}_{n_1,n_1}\bar{Q}_{m_2,n_2} + \sum_{\substack{m_1,n_1,m_2,n_2\\m_1\neq n_1,m_2\neq n_2}}p_2\bar{Q}_{m_1,n_1}\bar{Q}_{m_2,n_2}\right], \tag{6}$$

where all sums are taken from $-N/2$ to $N/2$, and $p_1 = 3/16$ or $1/16$ if for each combination (n_1,m_2,n_2) there are 3 or 4 distinct elements respectively among the sequence $\{n_1, 2n_1, m_2, n_2, m_2 + n_2\}$, and $p_2 = 3/64$ or $1/64$ if for each (m_1,n_1,m_2,n_2) there are 4 or 5 distinct elements respectively among $\{m_1, n_1, m_1 + n_1, m_2, n_2, m_2 + n_2\}$.

As a model of a dispersion map, we consider a symmetric two-step profile composed of fibers having positive and negative dispersion ($\pm\Delta$) with equal length $z_a/2$. The dimensionless map strength for this profile is defined as $s = \Delta z_a/4$. In this profile, when $g(z) = 1$ (i.e. lossless), we find $\bar{P}_n = \bar{Q}_{m,n} = 0$. This indicates that distributed amplification can be effective in reducing the intra-channel crosstalk since it can provide a more nearly lossless transmission line by compensating loss uniformly. Lumped amplification based on EDFA and distributed amplification based on backward Raman amplifiers can be modeled in the following way. The nonlinear coefficient $g(z)$ for EDFA is given by

$$g(z) = g_e \exp[-2\Gamma(z - nz_a)], \quad nz_a \le z < (n+1)z_a, \tag{7}$$

where $g_e = 2\Gamma z_a/[1 - \exp(-2\Gamma z_a)]$ so that $\langle g\rangle = 1$, and Γ is the dimensionless loss coefficient. For Raman amplifier, we have

$$g(z) = g_r \exp\left\{-2\Gamma(z - nz_a) + g_1[\exp(2\Gamma_p(z - nz_a)) - 1]\right\}, \quad nz_a \le z < (n+1)z_a, \tag{8}$$

where $g_1 = 2\Gamma z_a \exp(-2\Gamma_p z_a)/[1 - \exp(-2\Gamma_p z_a)]$, Γ_p represents fiber loss at the pump wavelength, and g_r is determined so that $\langle g\rangle = 1$.

Numerical results   In order to verify the analysis above, we compare the obtained analytical result with direct numerical simulation of (1). The parameters used in the calculations are as follows: $\alpha = \sqrt{2\pi}$, $\beta = 1.0$, $T = 8.3$, and $z_a = 0.125$. With the choice of $t_* = 3$ ps, $\nu = 2.5$ W^{-1}km^{-1} and $P_* = 1$ mW (i.e. $z_{NL} = 400$ km and $k_*'' = -2.25 \times 10^{-2}$ ps^2/km), they correspond to the full-width at half maximum (FWHM) $\tau_{FWHM} = 5$ ps (minimum), the path-average peak power 1 mW, the bit interval $t_{bit} = 25$ ps (i.e. the bit rate 40 Gbit/s) and period 50 km. The number of interacting pulses are estimated as $N = (2/M)\sqrt{1 + (s/\beta)^2}$ where $M = t_{bit}/\tau_{FWHM} = 5$ [5].

Figure 1 shows plots of timing jitter σ_t and amplitude jitter ρ versus transmission distance in an EDFA and a Raman system when $s = 30$, corresponding to $k'' = \pm21.6$ ps^2/km. The initial peak power is 2.72 mW for an EDFA system and 1.7 mW for a Raman system. Note that the comparison is made with the same value of path-average power (1 mW) in both systems. The fiber loss at the signal and pump wavelength is 0.22 dB/km and 0.28 dB/km, namely $\Gamma = 10$ and $\Gamma_p = 12.5$ respectively. As predicted from the model, both timing and amplitude jitter grow linearly with respect to distance in an EDFA system. A Raman system is especially effective in suppressing timing jitter. As a simple estimate, in order to achieve the bit-error rate $< 10^{-9}$, σ_t and ρ must satisfy the condition $\sigma_t < 0.06t_{bit} = 1.5$ ps and $\rho < 1/6 = 0.167$ by assuming that t_0 and W_0 follow Gaussian statistics [8]. The threshold required for error-free transmission is also plotted in this figure.

The analytical model allows us to study how system performance is limited by intra-channel pulse interactions depending on the value of map strength. Figure 2 shows the normalized growth rate of timing and amplitude jitter for various values of map strength obtained from Eq. (5) and (6) with Eq. (3) and (4). Timing jitter takes the largest value for moderate values of s ($\sim 15 - 20$). For larger s, timing jitter decreases whereas amplitude jitter still remains to be a potential dominant cause of transmission penalty.

Conclusion   We have studied system impact of nonlinear intra-channel interactions on high-speed dispersion-managed RZ pulse transmission. Explicit formulae to estimate timing and amplitude jitter caused by intra-channel crosstalk have been presented. Timing and amplitude jitter grows linearly with respect to distance. Based on the analytical model, we found that timing jitter is a major limitation in system performance for smaller values of map strength, whereas for larger map strength amplitude jitter can cause significant transmission impairments. Timing and amplitude jitter are found to be reduced by employing distributed Raman amplification with the same value of path-average power. Since Raman amplifiers provide lower noise accumulation and allow a large margin to the input power than EDFA's, further reduction of intra-channel crosstalk is expected by lowering path-average power without sacrificing SN ratio.
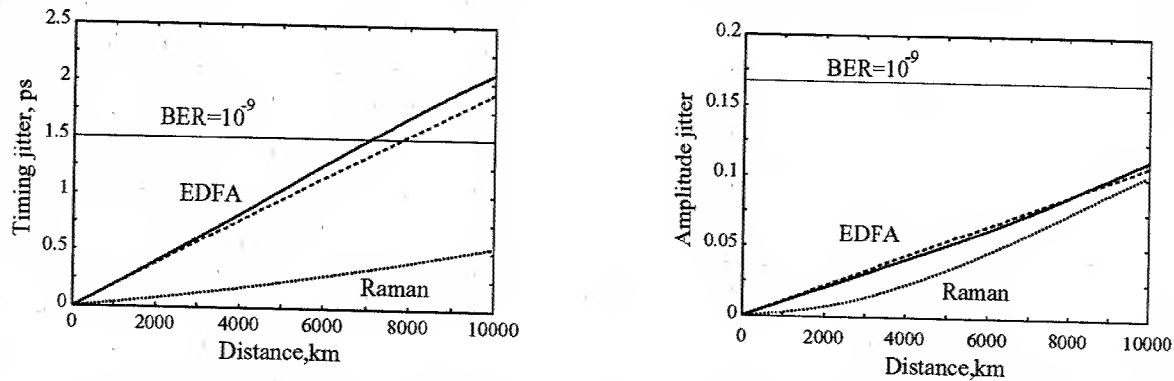
Fig. 1. Timing jitter σ_t (left) and amplitude jitter ρ (right) versus transmission distance for $s = 30$. The solid and dotted lines are results of direct numerical simulation of Eq. (1) with $2^8 - 1$ PRBS bit pattern in an EDFA and Raman system respectively, and the dashed lines are the analytical results for an EDFA system obtained from Eq. (5) and (6) with Eq. (3) and (4).
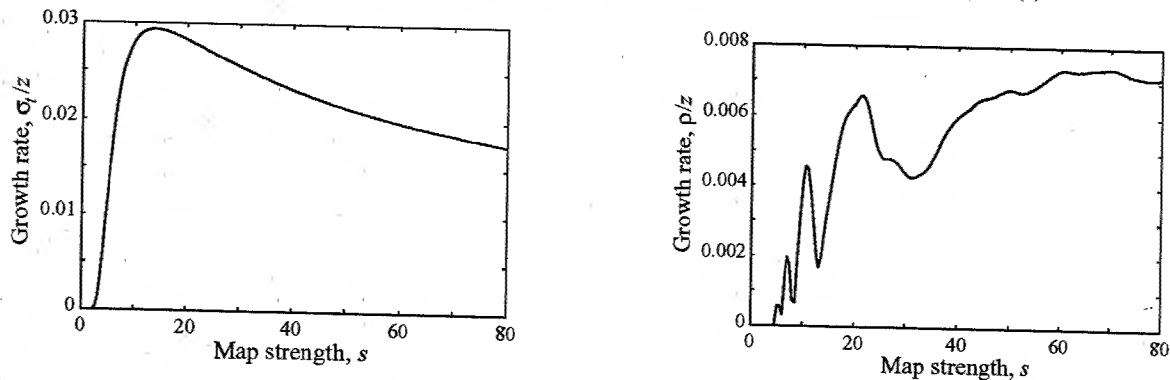
Fig. 2. Normalized growth rate of timing jitter σ_t/z (left) and amplitude jitter ρ/z (right) versus map strength s, obtained from Eq. (5) and (6) with Eq. (3) and (4) calculated numerically.

References

1. R. J. Essiambre, B. Mikkelsen, and G. Raybon, 'Intra-channel cross-phase modulation and four-wave mixing in high-speed TDM systems,' *Electron. Lett.*, vol. 35, pp. 1576-1578, 1999.
2. P. V. Mamyshev and N. A. Mamysheva, 'Pulse-overlapped dispersion-managed data transmission and intrachannel four-wave mixing,' *Opt. Lett.*, vol. 24, pp. 1454-1456, 1999.
3. J. Martensson, A. Berntson, M. Westlund, A. Danielsson, P. Johannisson, D. Anderson, and M. Lisak, "Timing jitter owing to intrachannel pulse interactions in dispersion-managed transmission systems," *Opt. Lett.*, vol. 26, pp. 55-57, 2001.
4. M. J. Ablowitz and T. Hirooka, "Intra-channel pulse interactions in dispersion-managed systems: timing shifts," *Opt. Lett.*, vol. 26, pp. 1846-1848, 2001.
5. M. J. Ablowitz and T. Hirooka, 'Resonant nonlinear intrachannel interactions in strongly dispersion-managed transmission systems,' *Opt. Lett.*, vol. 25, pp. 1750-1752, 2000.
6. S. Kumar, "Intrachannel four-wave mixing in dispersion managed RZ systems," *IEEE Photon. Technol. Lett.*, vol. 13, pp. 800-802, 2001.
7. M. J. Ablowitz and T. Hirooka, "Intra-channel pulse interactions in dispersion-managed systems: energy transfer," *Opt. Lett.*, vol. 27, pp. 203-205, 2002.
8. E. Iannone, F. Matera, A. Mecozzi, and M. Settembre, *Nonlinear Optical Communication Networks*. John Wiley & Sons, 1998.

Design Considerations of All-optical Header Processing Circuit for a Novel Packet Forwarding Scheme in Optical Networks

W. M. Wong and K. J. Blow
Photonics Research Group, Aston University,
Aston Triangle, Birmingham B4 7ET, U.K.
email:w.m.wong@aston.ac.uk

Abstract: Design of an all-optical circuit that performs modulo-N operation for packet forwarding without header modification in optical networks is presented. Design considerations such as gain modulation effects and bit rate and pattern dependence are investigated.
OCIS codes: (200.4660) Optical logic (200.4740) Optical processing

I. INTRODUCTION

The rapid growth of the Internet is putting a strain on the bandwidth handling capability of electronic routers. The future Internet will rely on optical routers without the need for any optoelectronic conversion. Although optical technologies are playing increasingly important roles in wide and local area networks, current optical network elements still offer limited functionality compared to their electronic counterparts. Recently, a packet forwarding scheme without header modification for optical networks known as the *key identification scheme* (KIS) has been proposed [1]. In KIS, the path through the network could be chosen by computing a *label* (*L*) at the ingress node, which is then used to make routing decisions. The computation of the label involves modular arithmetic which could be performed electronically at the edge nodes. The KIS simplifies processing in the optical core nodes by eliminating the need for header modifications. In KIS, by performing a modulo-N operation on the same label in the network using different *node-specific keys* (*N*), the packets could be directed to the correct output ports of the traversed nodes. In this work, the design of a modulo-N optical processing circuit is presented. The performance of the bit serial processing circuit is optimized in the presence of differential gain modulation (DGM) and pulse-to-pulse interactions.

II. THE OPTICAL CIRCUIT DESIGN

A simple method to calculate the modulo-N result is by repeatedly subtracting the label by N until the smallest positive number (remainder) is obtained. The most significant bit (MSB) is initially set as '0' so that an overflow could be detected when it becomes '1'. The mod-N result is then given by the subtracted answer (SUB) in the previous round before the SUB bits become overflow. By using TOADs [2] as logic gates, optical circuits could be constructed that perform logic operations and regenerative memory [3-5]. To perform subtraction, a bit serial full subtractor is realized by adding an inverting gate (NOT) in the full adder circuit [3]. In the subtractor circuit shown in Figure 1(a), the XOR gate produces the SUB bits, the NOT gate is used to invert the SUB bits, while the AND gate produces the CARRY bits. The circuit elements DELAYn are optical delay lines, INPUT is the serial m-bit input, CLK is a clock source (continuous train of 1's), and the SUMn combine optical signals.

(a)   (b)
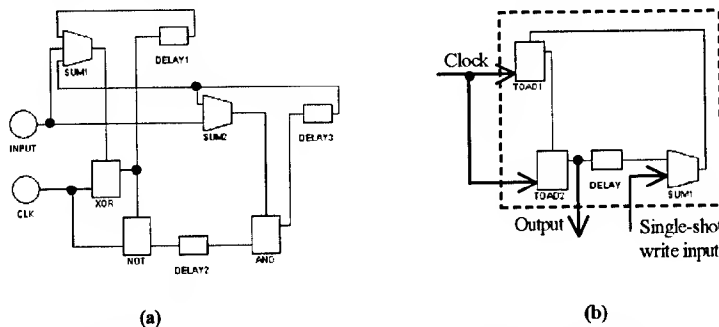
Figure 1 (a) Bit serial full subtractor circuit (b) Regenerative memory module with single-shot write capability.

In the XOR gate, we could either have 0, 1 or 2 pulses present at the control port. Since the phase shift ($\Delta\phi$) is proportional to the control pulse energy, this should generate phase shifts of 0, π, and 2π, respectively. Looking at the transmission function (T) of the TOAD,

$$T = \frac{1}{2}[1 - cos(\Delta\phi)] \qquad (1)$$

we see that for a phase shift of 2π the transmission returns to zero and hence the device would be logically equivalent to an XOR operation (0+0=0, 0+1=1, 1+1=0). The regenerative memory module [4] in Figure 1(b) is used to store the final mod-N result. It consists of two TOAD gates with an optical delay line of length equal to m

bits. The complete modulo-N operation circuit is shown in Figure 2. The input LABEL contains the routing information (m bits long) that gives the output port number after (L mod N) is computed. The function of the each TOAD gate is summarized in the following. The SUB RESULT gate gives the intermediate mod-N results (e.g. 10 mod 3 gives 7, then 4, then 1). The FIND ANS gate scans for the first overflow and activates the WRITE ANS gate, which then writes the final mod-N result into the regenerative memory circuit. The SELECT bit pattern and FEEDBACK gate selectively feedback the SUB bits to the starting point of the circuit for the next *subtraction cycle*. Each subtraction cycle requires a maximum of *m rounds* to obtain an answer but 2 extra rounds are used in each cycle so that any amplitude modulation settles down before the next cycle begins. The CLEAR bit pattern together with the CLEAR SUB and CLEAR CARRY gates clear the SUB and CARRY bits before the next subtraction cycle. The SCAN MSB bit pattern and the OVERFLOW gate monitor the MSB in the SUB bits for an overflow. The FLIP-FLOP gate operates in the following manner. If the MSB in the SUB bits is initially '0' (not overflow), its transmitted output follows the SELECT bit pattern. When an '1' in the MSB (overflow) is detected, the output becomes inverted. The SUBTRACT-BY-N bit pattern periodically contains the binary N that is repeatedly subtracted from LABEL until the final mod-N result is obtained. The CONTINUE gate initially follows the SUBTRACT-BY-N bit pattern but then becomes a continuous train of '0's when overflow is detected, which subsequently stops all subtraction. The amplifiers (AMPn) are used to cancel the DGM effect, which will be discussed in the next section.
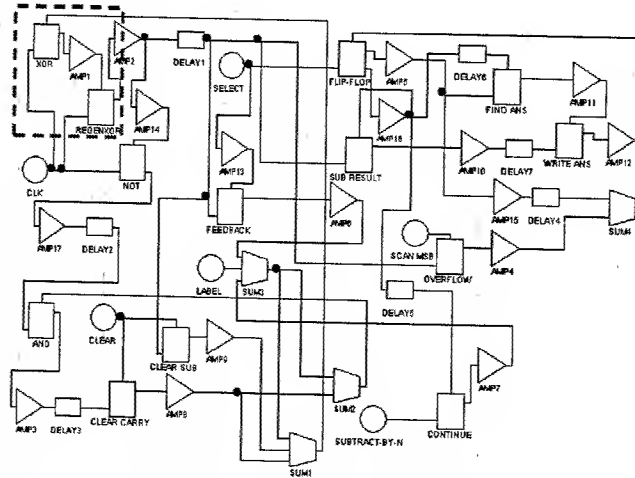
Figure 2 The modulo-N optical processing circuit.

III. OPTIMIZATION

A custom-written CAD simulator, which implements a simple analytic model of the TOAD [6], was used to test the mod-N optical circuit design. Neglecting DGM, the best extinction ratio is obtained when the XOR gate is biased at 178mA while the other gates are biased at 173mA. The control pulses (LABEL, CLEAR and SCAN MSB) are assumed to be 400fJ while the input pulses (CLK, SELECT, and SUBTRACT-BY-N) are 10fJ. The bit rate should be kept below 3.3GHz, corresponding to a SOA recovery lifetime of 300ps, to minimize pulse-to-pulse interactions. We found that the gain difference (DGM) of the counter-propagating pulses in the TOAD could have a significant effect on device performance. To consider the DGM effect, assuming a coupler ratio of 50:50, the normalized transmission(T) and reflection(R) of the TOAD are given by:

$$T\ (or\ R) = \frac{gI}{g_0}\left(\frac{1}{2}\left(1+\frac{1}{g}\right) \mp \frac{1}{\sqrt{g}}cos(\Delta\phi)\right) \tag{3}$$

where I is the normalized optical intensity and g_0 is the unsaturated gain. Eqn.(3) assumes that the clockwise pulse in the TOAD sees the unsaturated gain (g) while the counter clockwise pulse passes through a fully saturated SOA ($g=1$). In this worst-case scenario, notice that when the gain difference is very large, no switching occurs ($T:R=$ 50:50). However, the SOAs in the loop mirrors are usually operated below full saturation. We show that even when the SOAs are operated in full saturation, where DGM effects are significant, mod-N operation could still be achieved by using amplifiers around the circuit to re-adjust the pulse energy levels. In addition, a regenerative gate could be used to stabilize the signal of the XOR gate (shown by dashed lines in Figure 2). When maximum DGM is present, it was found impossible to achieve good switching performance with a SOA nonlinearity index (n_{eh}) of only 2×10^{-26} m^3. Therefore, we have used $n_{eh} = 8 \times 10^{-26}$ m^3 to increase the nonlinearity for better switching. The

XOR gate is now biased at 133mA and other gates are biased at 130mA. Initially, there are 17 amplifiers used to compensate for signal attenuation and the DGM effect, with the required gain of each amplifier given in Table 1. In Figure 3, the mod-N circuit failed to work when DGM is present but is rectified when the amplifiers are used. The maximum operating bit rate allowed was 2GHz for the original circuit without DGM. However, the optimized circuit with DGM present could operate up to 4GHz because of its higher nonlinear index. We also achieved mod-N operation in a more realistic case with smaller gain difference (10%) between the counter-propagating signal pulses by using SOAs with a nonlinear index of 2×10^{-26} m^3. The circuit could further be optimized by reducing the number of amplifiers along the flow of the signal pulses, hence eliminating amplifiers 2, 3, 5, 10, and 17.

Table 1 Gain requirement of each amplifier.

Amplifier number	Gain
1,4,6,7,8,9,11,12,16	52
2,3,5,10,17	1.3
13,14,15	40

(a) (b) (c)
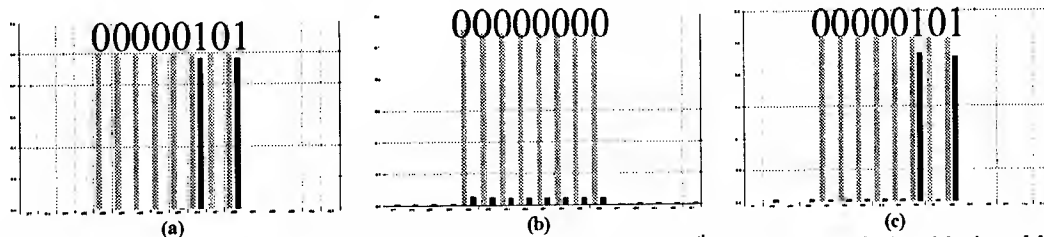
Figure 3 Simulation results of the operation 0100 0001$_2$ mod 0000 1100$_2$ for bits 496-513 (5th subtraction cycle). Differential gain modulation is: (a) not present (b) present (circuit not optimized) (c) present (circuit optimized). Both control pulses (light) and transmitted pulses (dark) from the SUB RESULT gate are shown.

Although the maximum operating speed of the optimized circuit is 4GHz, which actually exceeds the SOA recovery rate, the regenerative memory module limits the overall speed to only 3GHz. Above 3GHz, the amplitude modulation grows with every circulation in the regenerative memory module until a stable but wrong answer is stored (Figure 4). Note that the degree of pulse-to-pulse interaction also depends on the *bit pattern*. For example, 0000 1001$_2$ will have less pulse-to-pulse interaction than 0000 0101$_2$ or 0000 0111$_2$.

(a) (b) (c)
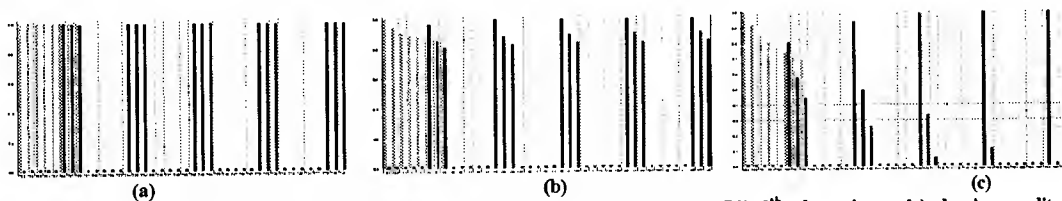
Figure 4 Bit rate dependence of the operation 0110 0111$_2$ mod 0000 1100$_2$ during bits 720-760 (9th subtraction cycle) showing amplitude modulation of the answer 0000 0111$_2$ (dark) in the regenerative memory module at (a) 1GHz (b) 3GHz and (c) 4GHz. The control pulses (light) used to write the mod-N result into memory are also shown.

IV. CONCLUSION

In optimum switching conditions where differential gain modulation is negligible and pulse-to-pulse interactions do not occur, a modulo-N optical circuit could be realized that gives excellent extinction ratio. We have also studied the operation of the circuit under the worst case condition of complete SOA saturation and shown that amplifiers could be used in the optical circuit to compensate for the DGM effects. The problem of DGM could also be solved in a fundamental approach by using SOAs with large nonlinear index, which would also allow higher operating bit rates.

REFERENCES

[1] H. Wessing, H. Christiansen, T. Fjelde, and L. Dittman. "Novel Scheme for Packet Forwarding without Header Modifications in Optical Networks," *IEEE J. Lightwave Tech.*, to be published.

[2] J. P. Sokoloff, P. R. Prucnal, I. Glesk, and M. Kane, "A Terahertz Optical Aymmetric Demultiplexer (TOAD)," *IEEE Photon. Tech. Lett.*, vol. 5, no. 7, pp. 787-790, 1993.

[3] A. J. Poustie, K. J. Blow, A. E. Kelly, and R. J. Manning, "All-optical full adder with bit-differential delay," *Opt. Comm.*, vol. 168, pp. 89-93, 1999.

[4] A. J. Poustie, A. E. Kelly, R. J. Manning, and K. J. Blow, "All-optical regenerative memory with full write/read capability," *Opt. Comm.*, vol. 154, pp. 277-281, 1998.

[5] A. J. Poustie, K. J. Blow, A. E. Kelly, and R. J. Manning, "All-optical parity checker with bit-differential delay," *Opt. Comm.*, vol. 162, pp. 37-43, 1999.

[6] K. J. Blow, R. J. Manning, and A. J. Poustie, "Model of longitudinal effects in semiconductor optical amplifiers in a nonlinear loop mirror configuration," *Opt. Comm.*, vol. 148, pp. 31-35, 1998.

Traveling-wave model of semiconductor optical amplifier based nonlinear loop mirror with feedback

W. M. Wong and K. J. Blow

Photonics Research Group, Aston University,
Aston Triangle, Birmingham B4 7ET, U.K.
email:w.m.wong@aston.ac.uk

Abstract: A traveling-wave model of an all-optical switching device with feedback is developed to identify important dynamical effects for better prediction of device behavior. Using a constant lifetime approximation, an efficient heuristic model is also developed.

OCIS codes: (250.5980) Semiconductor Optical Amplifier (200.4740) Optical processing

I. INTRODUCTION

Substantial work has been reported in semiconductor optical amplifier (SOA) based nonlinear loop mirrors known as TOADs [1] for all-optical processing such as demultiplexing, logic operations, and regenerative memory. The strong nonlinearity of the SOA compared to silica fiber allows shorter loops, thereby improving stability, minimizing latency, and enabling bit-serial processing.

In the feedback TOAD configuration [2] (Figure 1), input signal pulses (1's) are injected into the loop, and amplified reflected pulses are fed back into the loop as control pulses. The feedback device has two stable modes of operation [3] – *block mode*, where alternating blocks of 1's and 0's are observed, and spontaneous *clock division* mode, where halving of the input repetition rate is achieved. In block mode, the device acts as an inverted circulating shift register. The clock division phenomenon arises from the combination of incomplete SOA gain recovery and memory of the startup sequence that is provided by the feedback.

In this work, a traveling-wave (TW) model has been developed to identify important dynamical effects that have significant influence on the feedback device behavior. The computational efficiency of the TW model could be improved by using the integrated carrier traveling-wave (ICTW) model. Finally, the major dynamical effects were incorporated into an efficient heuristic model for performance study and device optimization. Simulation results from the ICTW model compare favorably with the heuristic model.
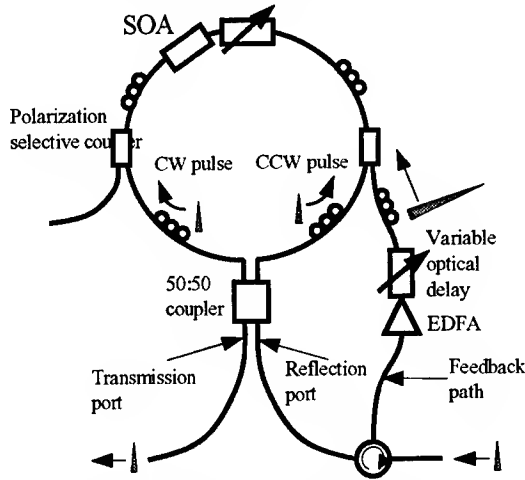
Figure 1 The TOAD with a feedback configuration.

II. TRAVELING-WAVE MODEL

In the traveling-wave (TW) model, the optical pulse shape is modeled as Gaussian. Usually, the signal pulses have substantially low energies so that it is reasonable to assume that only the high-energy control pulse causes any saturation in the SOA. Since only the control pulse influences the carrier dynamics, to save computation time delayed versions of the carrier dynamics could be re-used to solve the traveling-wave equations for the signal pulses. By solving the traveling-wave equations [4] along the SOA, the *inhomogeneous carrier distribution* in the SOA could be taken into account. It is important to use enough sections in the SOA model to accurately simulate the correct amount of differential phase shift per unit differential gain. Simulations show that using less than 10 sections in the SOA model results in the gain being overestimated while the phase shift is underestimated. Therefore, *clock division* could not be achieved because it requires a substantial amount of differential phase shift per unit differential gain.

One of the main advantages of using the TW model is that the *carrier dependence* of the recovery rate could be taken into account. Strictly speaking, the instantaneous recovery lifetime (τ) is carrier dependent in the form of,

$$\tau(N(z,t)) = \frac{1}{A_{nr} + B_{rad}N(z,t) + C_{aug}N(z,t)^2} \qquad (1)$$

where $N(z,t)$ is the time and space-dependent carrier density while A_{nr}, B_{rad}, and C_{aug} are the SOA recombination constants. We found it possible to obtain an accurate fit between the constant effective lifetime model and the carrier dependent lifetime model by using two different SOA bias current levels so that the initial equilibrium carrier levels are the same. The carrier recovery depends on the control pulse energy – at very low pulse energies, the carrier recovery is

fastest while at very high pulse energies, the recovery is slowest. When the SOA is fully saturated ($E \gg E_{sat}$), the carrier recovery is set to 80ps [3], where E is the control pulse energy and E_{sat} is the SOA saturation energy. At $E \ll E_{sat}$, the effective lifetime (τ_{eff}) that gives the best fit is 72ps (Figure 2). Therefore, the effective lifetime changed by only 10% for a wide range of pulse energy levels. The efficient heuristic model in this work is based on the effective lifetime model.

The behavior of the feedback TOAD is highly sensitive to its phase dynamics compared to the case when it is simply used as a demultiplexer. Simulations showed that when a long SOA (1000μm) is used, there is a gradual phase change in a clockwise (CW) traveling continuous-wave signal immediately after the arrival of the control pulse. If the clockwise signal pulse sees this slow transition during the start-up phase dynamics, this may give a completely different device behavior from the case of a short SOA. This slope exists because the clockwise pulse has finite *propagation delay time* down the SOA in the opposite direction to the control pulse. To better predict the feedback device behavior, this effect is included in the TW model.

In the TW model, *differential gain modulation* (DGM) between the counter-propagating signal pulses is taken into account. Since the clockwise and counter clockwise (CCW) pulses are delayed in time from each another, the pulses see different levels of gain, which leads to poorer switching. In the presence of DGM, the TOAD transmission response is plotted against the normalized differential phase shift ($\Delta\phi/\pi$) in Figure 2. We assumed the worst-case scenario where the control pulse fully saturates the SOA so that the CCW pulse sees unity gain. By observing the following equation,

$$T \text{ or } R = gI\left(\frac{1}{2}\left(1+\frac{1}{g}\right) \mp \frac{1}{\sqrt{g}}cos(\Delta\phi)\right) \qquad (2)$$

we can easily see that devices with high differential gain constants quickly lead to poor switching (approaching $T:R = 50:50$) as it operates further away from $|\Delta\phi| = \pi$. The terms T and R are the transmitted and reflected pulse intensities, respectively, and I is the input intensity.
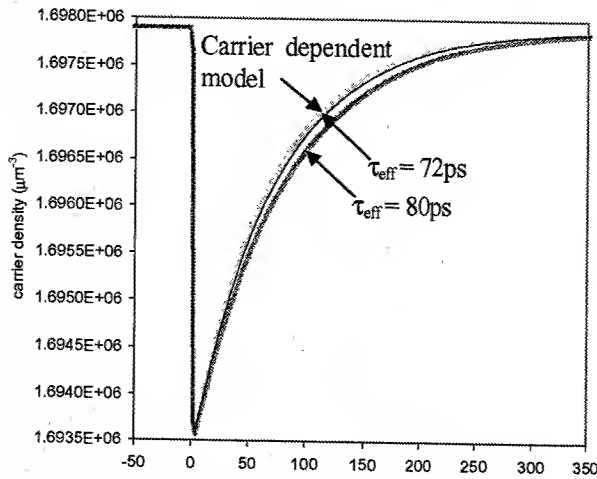
Figure 2 SOA carrier recovery: Comparison between effective lifetime and carrier dependent lifetime models.
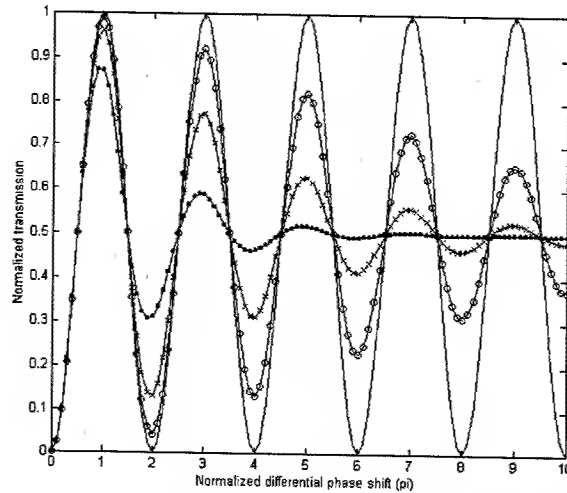
Figure 3 The effect of differential gain modulation on switching. Definition of symbols: (–) g = 0 (no gain modulation); (x) g= 8.4 × 10⁻²¹ m²; (o) g= 4.2 × 10⁻²⁰ m² (•) g= 8.4 × 10⁻²⁰ m²

III. INTEGRATED CARRIER TRAVELING-WAVE MODEL

Simulations showed that adequate accuracy could only be achieved if we use 10 sections or above in the TW model. In addition, at low repetition rates and long feedback paths, very large number of pulses must be simulated before the stable mode of behavior could be reached. These conditions require excessive simulation time making the TW model impractical for device optimization purposes. To overcome this problem, the integrated carrier traveling-wave model (ICTW) model has been developed. This is similar to the approach in [4] but instead of the single-pass gain, the spatially-integrated carrier (N_{avg}) is used, defined as $N_{avg} = \int_0^L N(z,t)dz$, so that the carrier-dependent lifetime could be included. Furthermore, the SOA internal loss (α_{int}), which was neglected in [4], is included here in the ICTW

model. For a given level of gain, it is found that smaller operating pulse energies could lead to clock division mode when internal loss is present [5]. The carrier rate equation of the ICTW model is given as,

$$\frac{dN_{avg}}{dt} = \frac{J\Delta z}{qd} - \frac{N_{avg}}{\tau} - \left(1 + \frac{\alpha_{int}}{\Gamma a(N_{avg}/\Delta z - N_0) - \alpha_{int}}\right)\left\{exp(\Gamma a(N_{avg} - N_0\Delta z) - \alpha_{int}\Delta z) - 1\right\}\frac{I_{in}(t)}{\Gamma h\nu} \quad (3)$$

where J is the current density, q is the electronic charge, Γ is the optical confinement factor, a is the differential gain coefficient, h is Planck's constant, v is the operating frequency, $I_{in}(t)$ is the optical intensity, Δz is the unit section length, N_0 is the transparency carrier density, and τ is the carrier dependent recovery lifetime. By using the ICTW model, only 3 sections are required to give the same converged result that is obtained from a 20-section TW model as shown in Figure 3.
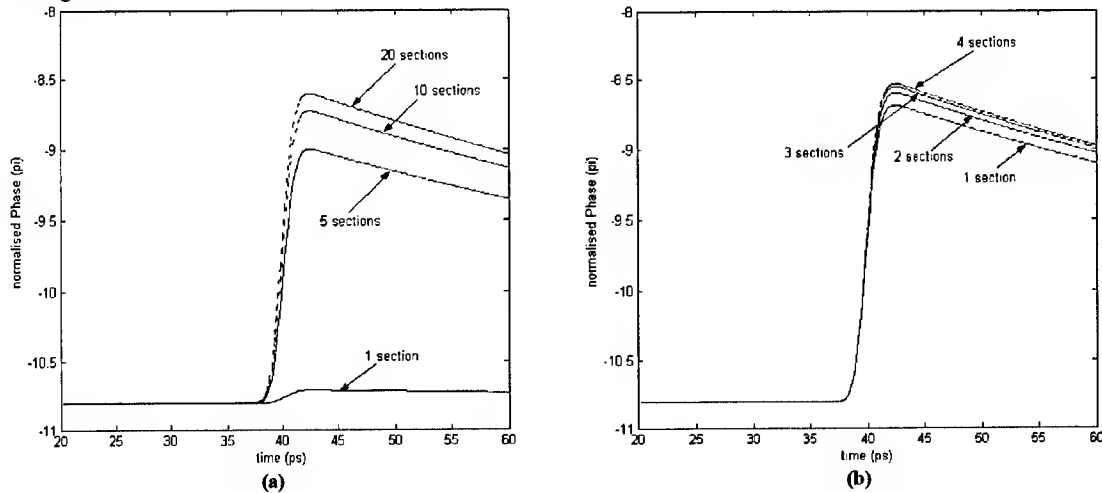
Figure 1 Comparison between the (a) TW model (slow convergence) and ICTW model (fast convergence).

Although the ICTW model is more efficient than the TW model, both models still required long simulation time. To perform device optimization, a more efficient model is required. The simple model in [2,6] has been refined by incorporating the major dynamical effects in a heuristic approach. The efficient heuristic model is based on the constant effective lifetime approximation, which was justified in section II. Simulation results show that the startup sequences leading to stable clock division for the ICTW and heuristic models are in good agreement. We also compared the block mode operation and results from the two models agree favorably.

IV. CONCLUSION

The feedback TOAD has two stable modes of operation that are sensitive to its startup dynamics. In this work, detailed models are developed that include traveling-wave effects and gain/phase dynamics. The traveling-wave models could be used for an in-depth investigation of the device at a given operating condition while the efficient heuristic model is used for performance study and device optimization.

REFERENCES

[1]   J. P. Sokoloff, P. R. Prucnal, I. Glesk, and M. Kane, "A Terahertz Optical Aymmetric Demultiplexer (TOAD)," *IEEE Photon. Tech. Lett.*, vol. 5, no. 7, pp. 787-790, 1993.

[2]   K. J. Blow, R. J. Manning, and A. J. Poustie, "Nonlinear optical loop mirrors with feedback and a slow nonlinearity," *Opt. Comm.*, vol. 134, pp. 43-48, 1997.

[3]   R. J. Manning, A. E. Kelly, K. J. Blow, A. J. Poustie, and D. Nesset, "Semiconductor optical amplifier based nonlinear optical loop mirror with feedback: two modes of operation at high switching rates," *Opt. Comm.*, vol. 157, pp. 45-51, 1998.

[4]   G. P. Agrawal and N. A. Olsson, "Self-Phase Modulation and Spectral Broadening of Optical Pulses in Semiconductor Laser Amplifiers," *IEEE J. Quant. Electron.*, vol. QE-25, no. 11, pp. 2297-2306, 1989.

[5]   W. M. Wong and K. J. Blow, "Semiconductor optical amplifier based nonlinear optical loop mirror with feedback", paper OE-4653-20, Photonics West 2002.

[6]   K. J. Blow, R. J. Manning. and A. J. Poustie, "Model of longitudinal effects in semiconductor optical amplifiers in a nonlinear loop mirror configuration," *Opt. Comm.*, vol. 148, pp. 31-35, 1998.

Wavelength-division-multiplexed bi-soliton transmission in dispersion-managed system

Takashi Inoue, Yasuhiro Yoshika, and Akihiro Maruta

Graduate School of Engineering, Osaka University,
2-1 Yamada-oka, Suita, Osaka, 565-0871 Japan
TEL: +81-6-6879-7728, FAX: +81-6-6879-7688,
e-mail: maruta@comm.eng.osaka-u.ac.jp

Abstract: Bi-soliton transmission in dispersion-managed WDM system is studied. It is numerically confirmed that anti-phase bi-soliton is more robust for the collision than in-phase one. The XPM effects induced by the collision can be analyzed by using the variational method.
© 2002 Optical Society of America
OCIS codes: (060.5530) Pulse propagation and solitons; (060.4230) Multiplexing

Dispersion-managed (DM) soliton is a periodically stationary solution of the nonlinear Shrödinger (NLS) equation having periodic coefficients of fiber's dispersion and nonlinearity, and owing to its various advantages it is a promising candidate for achieving a transoceanic high speed optical transmission system over 10000km with more than 40Gbit/s/ch.[1] The compatibility of DM soliton with wave-length-division-multiplexed (WDM) transmission has been widely studied and admitted.[2] On the other hand, intra-channel interactions between neighboring DM solitons induce fatal time position shifts,[3,4] resulting in degradation of bit-error-rate. Bi-soliton which consists of a couple of gaussian-like pulses is also a periodically stationary solution of the NLS equation.[5] Therefore, it can propagate for long distance without any distortion of its waveform due to intrachannel nonlinear interactions unlike a couple of conventional DM solitons. From the fact, it is expected that intrachannel interactions can be completely suppressed by employing novel coding schemes using bi-soliton.[6] In this paper, we study interchannel interactions of bi-solitons in a WDM transmission system, based on direct numerical calculation of the NLS equation and the variational analysis with which a couple of gaussian pulses are used as a test function.

We briefly summarize bi-soliton solutions. The fundamental equation which governs behavior of an optical pulse propagating in DM transmission line is given by:[5]

$$i\frac{\partial u}{\partial z} - \frac{\beta(z)}{2}\frac{\partial^2 u}{\partial t^2} + |u|^2 u = 0, \qquad (1)$$

where $u(z,t)$, z, and t are the complex amplitude of pulse envelope, propagation distance, and time, respectively. $\beta(z)$ is effective fiber dispersion and contains fiber dispersion, fiber nonlinearity, and effects of loss and amplification, all of which are periodic functions of DM period L_p. Equation (1) permits us to describe the effects of periodical variations of dispersion, nonlinearity, and damping loss by a single variable $\beta(z)$ on the distance z which is measured with the accumulation of nonlinearity. We assume $\beta(z)$ has locally fixed values, i.e. $\beta(z) = \beta_1 \, (< 0)$ for $0 \le z < L_1/2$ and $L_1/2 + L_2 \le z < L_p$, and $\beta(z) = \beta_2 \, (> 0)$ for $L_1/2 \le z < L_1/2 + L_2$, where L_1 and L_2 are the lengths of anomalous and normal dispersion fibers within a DM period L_p, respectively. We define

the following parameters to characterize a DM system: map strength $S = (|\beta_1|L_1 + |\beta_2|L_2)/\tau_m^2$, accumulated dispersion $B = (\beta_1 L_1 + \beta_2 L_2)/\tau_m^2$, and the ratio of the length of anomalous dispersion fiber to DM period $R = L_1/L_p = L_1/(L_1 + L_2)$. τ_m is the minimum full width at half maximum (FWHM) of a single DM soliton. S, B, and R completely characterize a DM soliton in the transmission line. To find a bi-soliton solution, a couple of gaussian pulses whose amplitude is adjusted to a value with which a DM soliton is formed is launched into a DM line. In the specific parameter region where a couple of pulses propagate with slightly few time position shift, we apply the numerical averaging method[7,8] to dig up the waveform of bi-soliton. For example, while an in-phase bi-soliton solution whose peak-to-peak spacing is three times of the FWHM of a single DM soliton is found at $S = 2.3$, $B = -0.1$, and $R = 0.8$,[5] an anti-phase bi-soliton with which the peak-to-peak spacing is two times of the FWHM is found at $S = 1.9$, $B = -0.1$, and $R = 0.8$. We will use these parameters in the rest of this paper.

(a)

(b)
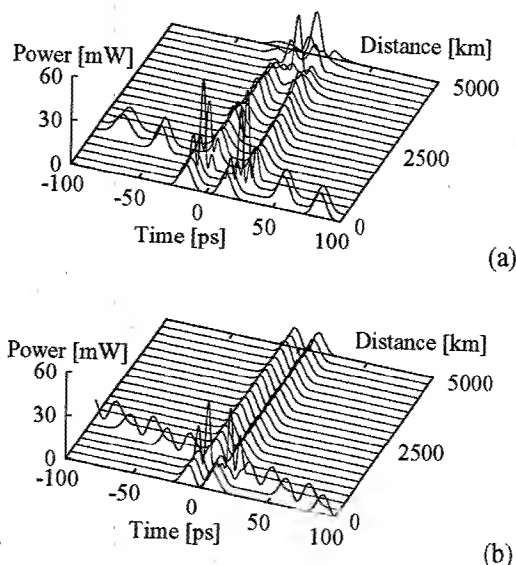
Fig. 1. Collisions of (a) in-phase and (b) anti-phase bi-solitons in a 2-channels WDM transmission system. The channel spacing is $\Delta f = 100$[GHz]. While the in-phase bi-soliton collapses at distance of 4000km due to the collision, anti-phase bi-soliton completely remains its waveform throughout 5000km propagation.

DM solitons in different channels in a WDM system have different group velocities and collide with each other while they propagate in a fiber. DM solitons are so stable against the collision that they continue to propagate with neither exhibiting instability nor waveform distortion, except small perturbation induced by cross-phase modulation (XPM). We here discuss the stability of bi-solitons against the collision in a 2-channels WDM system by solving Eq. (1) numerically. To carry out the simulation, we set DM period L_p to 50km, path-averaged dispersion to 0.156ps/nm/km, and fiber nonlinearity to $0.3 \times 10^{-9} \text{W}^{-1}$. The minimum pulse width (FWHM) τ_m of a single DM soliton is fixed to 10ps and optimal peak power is calculated by the variational method[8] under given conditions. Fiber's loss is neglected for simplicity. With such parameters, $(S, B, R) = (2.3, -0.1, 0.8)$ with which in-phase bi-soliton is found leads to dispersion map as $d_1 = 2.34$ [ps/nm/km] for $0 \le z < 20$ and $30 \le z < 50$ [km], and $d_2 = -8.59$ [ps/nm/km] for $20 \le z < 30$ [km], and similarly $S = 1.9$ leads to $d_1 = 1.95$ [ps/nm/km] and $d_2 = -7.03$ [ps/nm/km] for anti-phase bi-soliton. A pulse u_1 in channel 1 has the central frequency $f_1 = f_0$ [GHz], which is corresponding to wavelength of $\lambda_0 = 1.55$ [μm] and is initially positioned at $t_1 = 0$ [ps], while a pulse u_2 in channel 2 has the central frequency $f_2 = f_0 + \Delta f$ [GHz], where Δf is the channel spacing. Figure 1 shows (a) in-phase and (b) anti-phase bi-solitons' propagations, where the channel spacing is $\Delta f = 100$ [GHz] and the bi-solitons in channel 2 is initially positioned at $t_2 = 100$ [ps]. From Fig. 1, one can see that anti-phase bi-soliton is stable throughout long distance propagation after the collision, while in-phase bi-soliton collapses after propagating a certain distance. We note that anti-phase bi-soliton is also more tolerant to perturbation as ASE noise than in-phase one. Confirmation of the stability encourages us to employ anti-phase bi-soliton for high-speed WDM transmission systems.

The XPM due to fiber nonlinearity causes residual frequency and time position shifts after the collision of DM solitons in different channels.[2] It is known that the variational method with gaussian ansatz considering only the XPM effect between different channels as a perturbation term is available to analyze DM soliton's dynamics. We here apply the method to the case of bi-soliton assuming that a bi-soliton consists of a couple of gaussian pulses and they behave independently each other without suffering from intrachannel effects. Then a bi-soliton $u_n(z, t)$ in channel n ($n = 1, 2$) can be written as follows:

$$u_n(z, t) = u_{nL}(z, t) + u_{nR}(z, t) \qquad (2)$$

with

$$
\left.
\begin{aligned}
u_{nX}(z, t) &= A(z) \exp\left[-\frac{\tau_{nX}^2}{2} + i\varphi_{nX}\right] \\
\tau_{nX}(z, t) &= p(z)\{t - T_{nX}(z)\} \\
\varphi_{nX}(z, t) &= \frac{C(z)}{2}\tau_{nX}^2 - \frac{\kappa_{nX}(z)}{p(z)}\tau_{nX} + \theta_{nX}(z),
\end{aligned}
\right\}
$$
$$(3)$$

where u_{nX} ($X = L, R$) represents one of gaussian components of the bi-soliton in channel n, and $A(z)$, $p(z)$, $C(z)$ are the amplitude, the inverse of the pulse width, and the chirp of each gaussian component, respectively, and they are common to any gaussian components. On the other hand, $\kappa_{nX}(z)$, $T_{nX}(z)$, and $\theta_{nX}(z)$ are the central frequency, the central time position, and the phase of u_{nX}, respectively, and we define the bi-soliton u_n's central frequency as $\kappa_n(z) = (\kappa_{nL} + \kappa_{nR})/2$ and the central time position as $T_n(z) = (T_{nL} + T_{nR})/2$. Considering propagation of u_{nX}, we neglect intrachannel interactions between u_{nL} and u_{nR} and adopt interchannel XPM effect induced by $u_{(3-n)L}$ and $u_{(3-n)R}$ independently. Then Eq. (1) reduces to

$$
i\frac{\partial u_{nX}}{\partial z} - \frac{\beta(z)}{2}\frac{\partial^2 u_{nX}}{\partial t^2} + |u_{nX}|^2 u_{nX}
$$
$$
= -2\left\{|u_{(3-n)L}|^2 + |u_{(3-n)R}|^2\right\} u_{nX}. \qquad (4)
$$

Applying the variational method[2,4] to Eq. (4), we obtain a set of ordinary differential equations for the parameters $p(z)$, $C(z)$, $\kappa_{nX}(z)$, and $T_{nX}(z)$ as

$$
\left.
\begin{aligned}
\frac{\mathrm{d}p}{\mathrm{d}z} &= \beta p^3 C \\
\frac{\mathrm{d}C}{\mathrm{d}z} &= -\beta p^2(1 + C^2) - \frac{E_0 p}{\sqrt{2\pi}} \\
\frac{\mathrm{d}\kappa_{nX}}{\mathrm{d}z} &= \sqrt{\frac{2}{\pi}}E_0 p^2 \{F(p\Delta T_L) + F(p\Delta T_R)\} \\
\frac{\mathrm{d}T_{nX}}{\mathrm{d}z} &= \beta\kappa_{nX}
\end{aligned}
\right\}
$$
$$(5)$$

where $\Delta T_Y = T_{nX} - T_{(3-n)Y}$, $F(x) = x\exp(-x^2/2)$ and $E_0 = \sqrt{\pi}A^2/p$ is the constant energy of a single gaussian pulse u_{nX}. By solving Eqs. (5) numerically, evolution of the central frequency and the time position of the bi-solitons for propagation distance can be analyzed. Figure 2 shows variations of the central frequency f_1 [GHz] and central time position T_1 [ps] of the anti-phase bi-soliton u_1 in channel 1 which appears in Fig. 1 (b). Solid curves are calculated by the variational method, and dotted curves by direct numerical calculations of Eq. (1). In both figures, the results from the variational method agree with numerical results, and therefore the variational method is available for analyzing interchannel XPM effect not only between conventional DM solitons but also in case of bi-solitons. We can also see from Fig. 2 that residual frequency shift is very small since map strength S is so large, but residual time position shift δT_1 is large and it is a serious obstacle which might induce bit error.

When we introduce bi-soliton to a WDM transmission system, the bit stream in a channel is a mixture of bi-solitons and conventional DM solitons.[6] So we have to consider all kinds of collisions, that is, collisions between (i) bi-soliton and bi-soliton, (ii) DM soliton and bi-soliton, (iii) bi-soliton and DM soliton, and (iv) DM soliton and DM soliton for u_1 and u_2, respectively. Figure 3 shows the relation between channel spacing Δf [GHz] and time
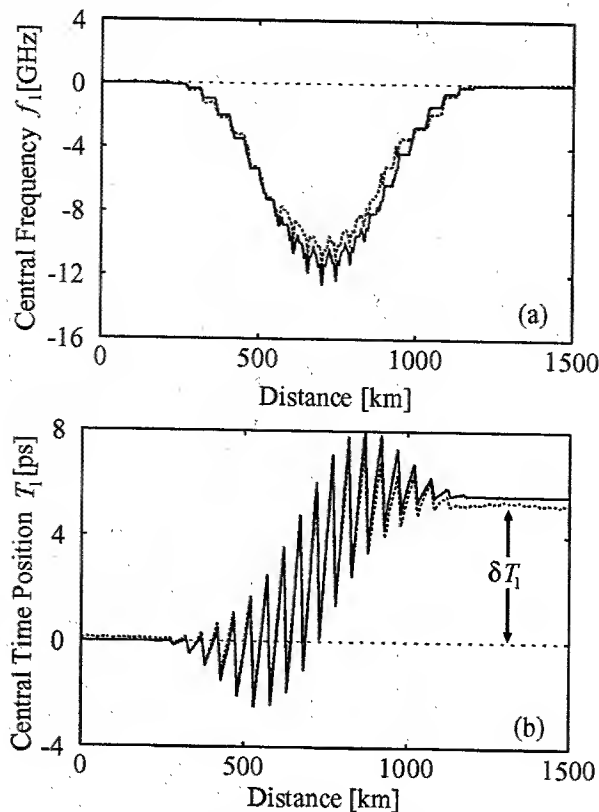
Fig. 2. The XPM-induced (a) central frequency and (b) central time position shifts of an anti-phase bi-soliton which appears in Fig. 1 (b). The solid curves and dotted curves are obtained by the variational method and direct numerical calculation of the NLS equation, respectively.
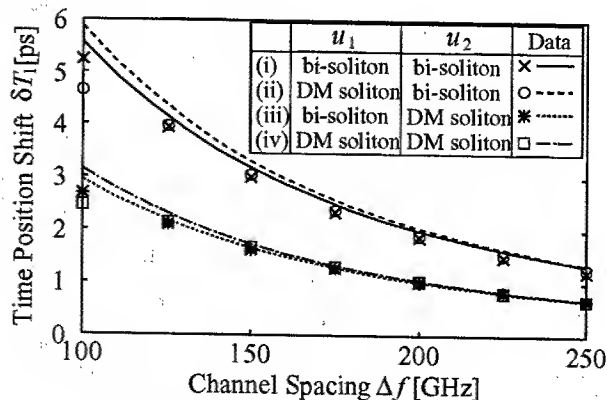
Fig. 3. Channel spacing Δf versus residual central time position shift δT_1 of u_1 after a collision with u_2. Four cases should be considered as combination of signal formats in channel 1 and 2. The curves and symbols are obtained by variational method and numerical calculation, respectively.

position shift δT_1 [ps] of u_1 after a collision with u_2 for each case. The curves and symbols are obtained by the variational method and direct numerical simulation, respectively. As can be seen in Fig. 3, larger Δf results in smaller δT_1 for any cases, because the propagation distance in which u_1 and u_2 are overlapping becomes shorter for larger channel spacing. A remarkable feature in Fig. 3 is that cases (i) and (ii), (iii) and (iv) show almost the same results for time position shift δT_1, respectively. So we can conclude that residual time position shift of a pulse in channel 1 depends only on the signal format of a pulse in channel 2. It is directly recognized from Eq. (4) because u_{nR} doesn't suffer from u_{nL} and vice versa. For the channel spacing Δf larger than 200GHz, the time position shift δT_1 is less than 2ps in any case and WDM bi-soliton transmission system is then feasible with using a properly chosen channel spacing.

We have studied bi-soliton transmission in dispersion-managed WDM systems. We discussed robustness of bi-soliton against the collision with a pulse in different channel and showed that anti-phase bi-soliton is so stable that it could be applicable to WDM systems. We also obtained some results about frequency and time position shifts caused by the XPM effect due to the collision. Direct numerical calculation of the NLS equation supported that the variational method is available for the analysis of the modulated central frequency and the time position shifts. We have also shown a remarkable feature in which the time position shift of a pulse in a channel depends only on the signal format of a pulse in the other channel.

References

1. N. J. Smith, F. M. Knox, N. J Doran, K. J. Blow, and I. Bennion, "Enhanced power solitons in optical fibres with periodic dispersion management," Electron. Lett., **32**, 54–55 (1996).

2. H. Sugahara, H. Kato, T. Inoue, A. Maruta, and Y. Kodama, "Optimal dispersion management for a wavelength division multiplexed optical soliton transmission system," IEEE/OSA J. Lightwave Technol., **17**, 1547–1559 (1999).

3. T. Yu, E. A. Golovchenko, A. N. Pilipetskii, and C. R. Menyuk, "Dispersion-managed soliton interactions in optical fibers," Opt. Lett., **22**, 793–795 (1997).

4. T. Inoue, H. Sugahara, A. Maruta, and Y. Kodama, "Interactions between dispersion managed solitons in optical-time-division-multiplexed system," IEEE Photon. Technol. Lett., **12**, 299–301 (2000).

5. A. Maruta, Y. Nonaka, and T. Inoue, "Symmetric bi-soliton solution in a dispersion-managed system", Topical Meeting on Nonlinear Guided Waves and Their Applications 2001 (NLGW2001), Clearwater, Florida, Paper PD4 (2001), and Electron. Lett., **37**, 1357–1358 (2001).

6. A. Maruta, Y. Nonaka, and T. Inoue, "Novel coding schemes using bi-soliton to suppress intrachannel interactions in dispersion-managed system," submitted to IEEE Photon. Technol. Lett.

7. J. H. B. Nijhof, W. Forysiak, and N. J. Doran, "The averaging method for finding exactly periodic dispersion-managed solitons," IEEE J. Selected Topics in Quantum Electron., **6**, 330–336 (2000).

8. V. Cautaerts, A. Maruta, and Y. Kodama, "On the dispersion-managed soliton," Chaos, **10**, 515–528 (2000).

Towards nonlinear waveguide devices from conjugated polymers: Tuning of the materials properties and structuring

A. Bahtiar, K. Koynov, C. Bubeck
Max-Planck-Institute for Polymer Research, Ackermannweg 10, D-55128, Mainz, Germany
Tel +49 6131 379 316, Fax +49 6131 379 100, email: bahtiar@mpip-mainz.mpg.de

M. A. Bader, U. Wachsmuth, G. Marowsky
Laser-Laboratorium Göttingen e.V., Hans-Adolf-Krebs-Weg 1, 37077 Göttingen, Germany

Abstract: We prepared slab waveguides of the conjugated polymer MEH-PPV and demonstrate that fine-tuning of refractive index is feasible by control of molecular weight. Grating waveguide structures are fabricated by UV-laser ablation.
© 2002 Optical Society of America
OCIS codes: 190.4710 Optical nonlinearities in organic materials, 310.6860 Thin films, optical properties

Conjugated polymers have been considered the most promising organic material candidates for high-speed photonic switching and all-optical signal processing due to their high third-order nonlinearity, fast response times and relative ease of waveguide preparation [1-3]. Materials such as polydiacetylenes and DANS have been investigated in detail with respect to their application in integrated optics [4, 5]. In particular poly(p-phenylenevinylene), PPV, and its derivatives have found considerable interest because of their large third-order nonlinearities and superior waveguide properties [6-10]. Recently, we have carried out a detailed study of several new PPV derivatives and have found out that derivatives like MEH-PPV are particularly promising solution processable photonic materials [9].

Materials properties like linear refractive index, low waveguide losses and possibility for sub-micron structuring are getting primary importance for the realization of nonlinear waveguide devices. We will show at the example of MEH-PPV that the synthesis parameters such as molecular weight M_w of the polymer have impact on important optical properties like refractive index and linear waveguide losses. Furthermore we will demonstrate structuring of the waveguides by laser ablation applying direct illumination of a phase mask [11].

Three different compounds of MEH-PPV provided by Prof. Hoerhold, Jena [9] (M_w=40000) and ADS, Canada (M_w=260000 and M_w=420000) have been studied. Ultrathin films (thickness around 50 nm) as well as waveguides (thickness around 1 µm) have been deposited onto quartz substrates by spin coating of toluene solutions of these compounds as described in detail recently [10].

In Fig. 1 the dispersions of the refractive index for TE (full symbols) and TM (open symbols) polarizations are plotted as measured by prism coupling in the MEH-PPV waveguides [8]. Obviously the birefringence is dependent strongly on the molecular weight. For comparison we have measured the TE refractive indices (solid lines) for the same compounds but in ultrathin film configuration by means of reflectometry [9]. The good agreement between the results of optical waveguides and ultrathin films shows that the origin of the birefringence is caused primarily by molecular weight. In Fig. 2a we have plotted the TE and TM refractive indices at λ=1064nm versus molecular weight M_w of the polymer. The observed increase of the refractive index for TE and respective decrease for TM with the molecular weight can be explained by the degree of orientation of the polymer chains in the plane of the film. Evidently at large M_w the number of polymer chains parallel to the substrate surface increases (n(TE) increases) while the number of polymer segments perpendicular to this plane decreases (n(TM) decreases). In Fig. 2b we show the dependence of the waveguide attenuation loss coefficient α_{gw} on the molecular weight. This coefficient was determined for TE0 and TM0 propagation modes by imaging of the scattered light from the waveguide onto a diode array as described earlier [12]. The increase of α_{gw}(TE0) for high molecular weight polymers is quite remarkable. Preliminary FTIR studies confirm that the preferred orientation of polymer chains parallel to the plane of the film increases with M_w.

The dependencies shown in Figs. 1 and 2 suggest an easy way of fine-tuning of both the refractive index and attenuation loss coefficients by proper choice of the molecular weight M_w.
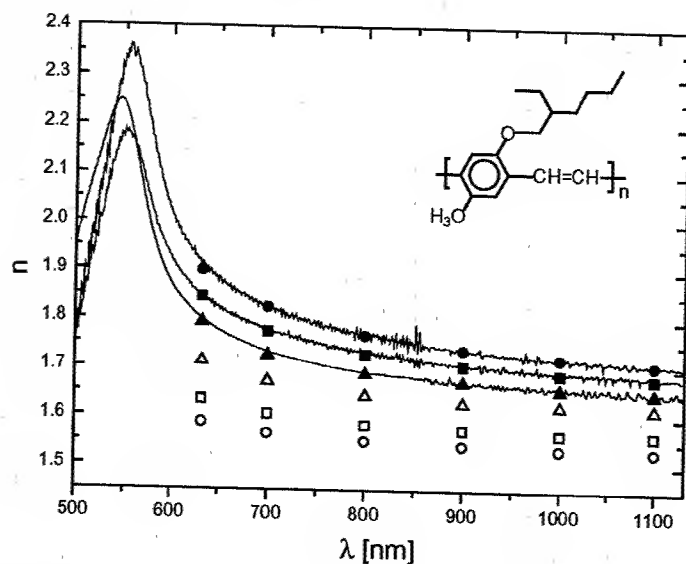
Fig.1. Chemical structure of MEH-PPV and dispersions of the refractive index for TE (full symbols) and TM (open symbols) polarizations of the waveguides made from compounds with different molecular weight M_w: 40000 – triangles, 260000 – squares and 420000 – circles respectively. The solid lines represent the TE refractive index measured in ultrathin (50nm) films for the same compounds by means of reflectometry.
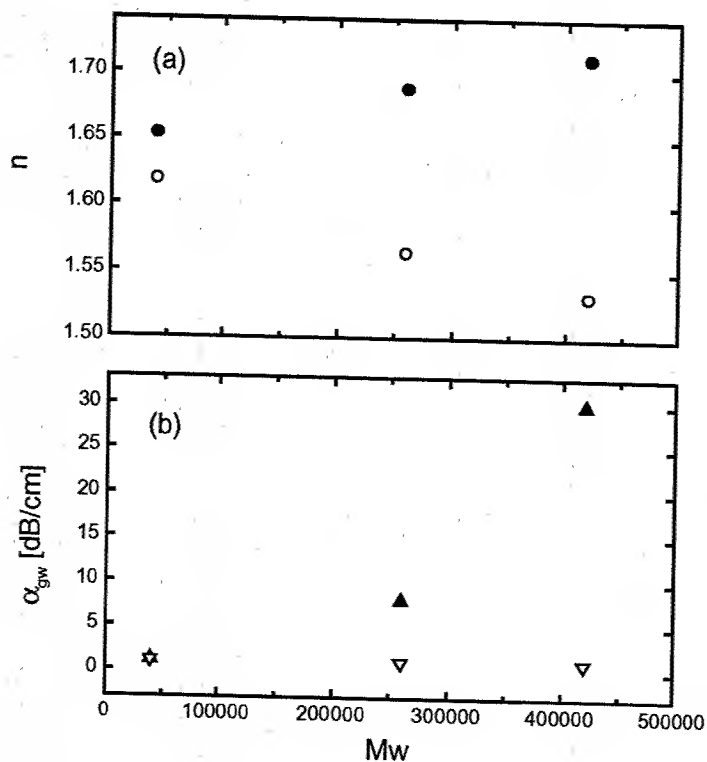
Fig. 2. Refractive index (a) and linear waveguide loss (b) versus molecular weight of the polymers measured at λ=1064nm. The full symbols correspond to TE polarization and open symbols correspond to TM polarization respectively.

Sub-micrometer gratings have been fabricated in thin films of MEH-PPV on quartz substrates by UV photo ablation. A 248 nm KrF excimer laser with a pulse duration of 20 ns was used to illuminate a phase mask positioned directly in front of the polymer film. Self-interference between the orders of diffraction of the phase mask created an interference pattern on the polymer film surface with a period equal to the phase mask period of 720 nm. Different grating thicknesses of up to several tens of nanometers have been generated applying fluences in the range of 10 mJ/cm^2 to 30 mJ/cm^2. The number of pulses was varied from 30 to 140 to achieve homogeneous gratings.

In Fig. 3 a typical example of one of the generated gratings is given. In the left hand panel an AFM picture of a 720 nm period grating in a MEH-PPV thin film of a thickness of 570 nm is shown. It has been generated using 40 pulses of a 20 ns KrF excimer laser at a wavelength of 248 nm and a fluence of 19.5 mJ/cm^2. The grating area is of the size 1 mm × 1 mm. The right hand panel of Fig. 3 shows the surface trace of the grating structure measured with the AFM. Evaluation of the grating thickness gives a value of 40.2 nm, the grating period of 720 nm equal to the grating period of the phase mask and a homogneous grating structure are confirmed by the measurement.
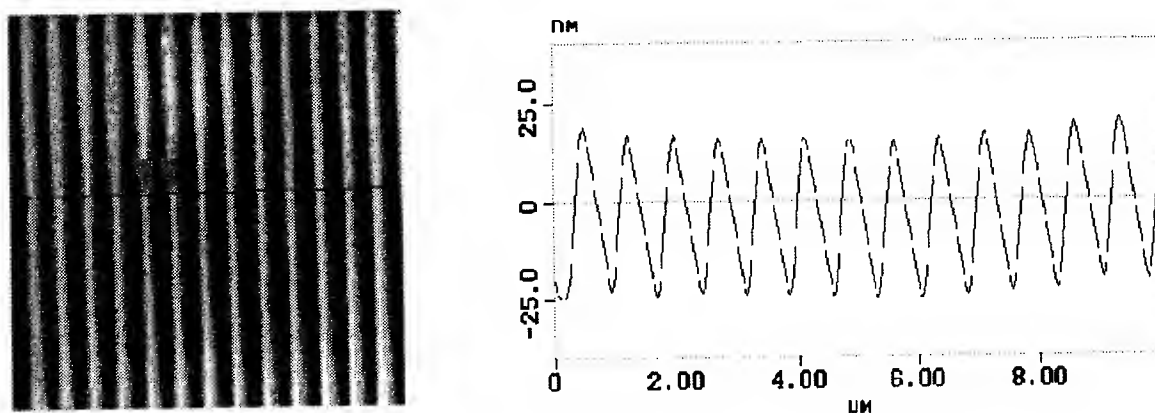
Figure 3. AFM image and surface measurement of a typical grating fabricated in MEH-PPV by UV laser ablation.

Our results suggest that MEH-PPV is suitable for the generation of well defined grating structures by UV laser ablation applying direct phase mask imaging. The sub-micrometer gratings shown here can be used for applications in integrated optics based on periodic structures in planar polymer waveguides.

In conclusion, we demonstrate that fine-tuning of the refractive index of polymer waveguides can be accomplished by control of the molecular weight. Structuring of the MEH-PPV waveguides in order to fabricate gratings, is feasible by means of UV-laser ablation. This allows easy control of relevant device properties of nonlinear waveguide devices in MEH-PPV, e.g. for all-optical switching based on Bragg reflectors.

References

[1]   J. Messier, F. Kajzar, P. N. Prasad, and D. Ulrich, eds., *Nonlinear Optical Effects in Organic Polymers*, (Kluwer, Dordrecht, 1989).

[2]   F. Kajzar and J. D. Swalen, eds., *Organic Thin Films for Waveguiding Nonlinear Optics* (Gordon and Breach Publ. Amsterdam, 1996).

[3]   G. I. Stegeman, in: H. S. Nalwa, S. Miyata (Eds.), *"Nonlinear Optics of Organic Molecules and Polymers"* (CRC Press, Boca Raton, 1997), pp. 799-812.

[4]   D. S. Chemla, J. Zyss (Eds.) *"Nonlinear Optical Properties of Organic Molecules and Crystals"*, Vol. 2 (Academic Press, Orlando, 1987)

[5]   S. Aramaki, G. Assanto, G. I. Stegeman, W. H. G. Horstuis, G. R. Möhlman, *Optics Commun.* 94, 326-330 (1992).

[6]   A. Mathy, K. Ueberhofen, R. Schenk, H. Gregorius, R. Garay, K. Muellen, C. Bubeck, *Phys. Rev. B* 53, 4367-4376 (1996).

[7]   K. Ueberhofen, A. Deutesfeld, K. Koynov, and C. Bubeck, *J. Opt. Soc. Am. B*, 16, 1921-1935 (1999).

[8]   K. Koynov, N. Goutev, F. Fitrilawati, A. Bahtiar, A. Best, C. Bubeck, H.-H. Hörhold. *J. Opt. Soc. Am. B*, 19, 895-901, (2002).

[9]   M. A. Bader, G. Marowsky, A. Bahtiar, K. Koynov, C. Bubeck. H. Tillmann, H.-H. Hörhold, *J. Opt. Soc. Am. B* (acepted 2002).

[10]   F. Fitrilawati, M. O. Tjia, S. Pfeiffer, H. Tillmann, H.-H. Hoerhold, A. Deutesfeld, H. Eichner. C. Bubeck, *Opt. Mater.*, (submitted).

[11]   P. E. Dyer, R. J. Farley, R Giedl, D. M. Karnakis, *Appl. Surf. Sci.* 96-98, 537-549 (1996)

[12]   A. Mathy, H.-U. Simmrock, and C. Bubeck, *J. Phys. D: Appl. Phys.* 24, 1003-1008 (1991).

Nonlinear Guided Waves

Discrete Solitons and Waveguide Arrays

Tuesday, September 3, 2002

George I. Stegeman, Univ. of Central Florida, USA
Presider

NLTuA
8:00am – 10:00am
Auditorium

Discrete Solitons in Quadratic Nonlinear Waveguide Arrays

Thomas Pertsch, Ulf Peschel, and Falk Lederer

Institut für Festkörpertheorie und Theoretische Optik, Friedrich-Schiller-Universität, Max-Wien-Platz1, 07743 Jena, Germany
phone +49 3641 947176, fax +49 3641 947177, pertsch@pinet.uni-jena.de

Joachim Meier, Roland Schiek, Robert Iwanow, and George Stegeman

School of Optics/CREOL, UCF, 4000 Central Florida Blvd, Orlando Florida, 32816, USA

Yoo Hong Min and Wolfgang Sohler

Universität Paderborn, Fachbereich Physik, Angewandte Physik, 33095 Paderborn, Germany

Abstract: We observed the formation of discrete solitons in periodically poled Lithium Niobate (PPLN) waveguide arrays. Strongly localized dichromatic nonlinear beams were excited with fundamental wave pulses at a wavelength of 1572 nm.

©2002 Optical Society of America

OCIS codes: (190.4420) transverse effects in nonlinear optics, (190.5530) pulse propagation and solitons

The nonlinear dynamics of discrete systems is a theoretically well investigated field because of its relevance in many areas of natural sciences. Recent experimental progress in linear and nonlinear waveguide arrays established a new convenient laboratory for the observation of such discrete dynamics on a macroscopic scale. This should allow for the experimental verification of numerous theoretical predictions in the near future (for a recent review, see [1]).

The nonlinear dynamics of a particular system is always characterized by an interplay of its linear and nonlinear properties. While the first experimental investigation of the linear properties of waveguide arrays dates back to the early 70's [2] only very recently this field was revisited and a broader understanding of discrete diffraction and refraction phenomena was established [3-7]. At the same time the experimental investigation of nonlinear effects started with the observation of discrete solitons in AlGaAs waveguide arrays exhibiting a Kerr nonlinearity [8-11].

Simultaneously, the experimental investigation of spatial soliton formation, a prominent intrinsic localization effect in nonlinear dynamics, in different nonlinear environments progressed. Among them, especially second-order ($\chi^{(2)}$-) processes provide a variety of interesting effects with a promising potential for practical applications [12]. Furthermore, the maturity of technological processes, like periodical poling to achieve quasi-phase-matching (QPM) upon quadratic interaction, has provided the experimentalists with the necessary materials for engineering applications [13].

It is therefore quite natural to focus attention on discrete soliton formation in $\chi^{(2)}$ - waveguide arrays where there is already a history regarding theoretical studies. In particular, various kinds of discrete solitons with complicated stability properties have been predicted [1, 14]. Here we present the first experimental evidence of discrete soliton formation in $\chi^{(2)}$ - waveguide arrays.

Sample fabrication and characterization

The experiments were performed in PPLN waveguide arrays consisting of 101 waveguides. Arrays with different coupling strength have been fabricated on 0.5 mm thick 4" diameter Z-cut LiNbO$_3$ substrates. The waveguides were defined by in-diffusion of 7 µm wide and 98 nm thick Titanium stripes. Thereafter, the microdomain structure with a period of 16.8 µm was obtained by electric field poling with a structured photoresist on the +Z-side. The wafers were cut into samples of 74 mm length and anti-reflection coated on the polished coupling facets.

The final waveguides were single-mode in the spectral region of the TM-polarized fundamental harmonic wave (FH, λ~1550 nm) but multi-mode for the TM-polarized second harmonic wave (SH, λ~775 nm). The typical loss of the FH TM-polarized mode was determined as 0.2 dB/cm. The waveguide modes are coupled in the array due to the partial overlap of their evanescent FH fields. By producing arrays with a channel pitch of 14.0, 15.0, and 16.0 µm the strength of the coupling was varied. In order to measure the characteristic coupling length, a single waveguide of each array was excited with a weak FH beam and the measured characteristic output patterns were fit to the theoretical Green's function of the array (see Figs. 1). To investi-
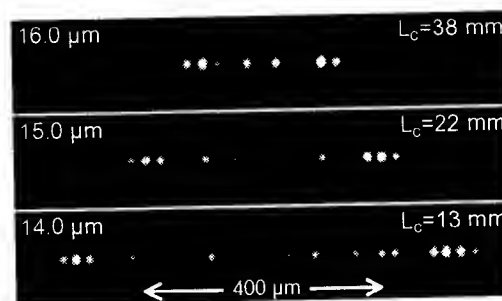
FIG. 1. FH output intensity distribution for low power single waveguide excitation (Green's function) for different waveguide pitch and resulting coupling length (half-beat).
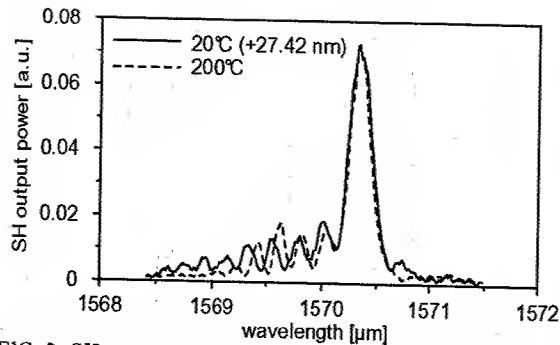
FIG. 2. SH generation tuning curve at low and high temperature in a PPLN test waveguide. The low temperature curve is shifted by 27.42 nm.

gate the nonlinear properties of the waveguides, single-pass SHG measurements have been performed in separate test waveguides on the sample using a wavelength-tunable external cavity diode laser. At room temperature (20°C), phase matching with the lowest order SH TM-mode was achieved for λ=1542.95nm. To prevent photo-refractive effects in the material the high power soliton experiments were performed at an elevated temperature of ~200°C, where phase matching was achieved for λ=1570.37 nm (see Fig. 2).

Experimental setup

For the soliton experiments a tunable ultra-short pulse laser source (Spectra Physics) was used. The source consisted of a mode-locked Ti-Sapphire laser (Tsunami) which was amplified by a stretched-pulse regenerative amplifier (Spitfire) and subsequently converted to the desired operation wavelength in a two stage OPG/OPA system (OPA-800C). This system provided Gaussian pulses of 1.1 ps FWHM with a spectral width of 4 nm (FWHM) at a repetition rate of 1 kHz. The wavelength was set to 1574 nm. The input pulse energy was measured in front of the coated 10x objective by which the beam was focused into a single waveguide. The coupling efficiency is estimated as 20%. The output near field intensity distribution of the FH and the SH were recorded separately on a vidicon camera (Hamamatsu). The sample was temperature controlled at 200°C in an oven enclosing the whole sample. It was therefore impossible to monitor the propagating light along the sample.

Experimental results

When increasing the input pulse energy the measured output intensity distributions show for all arrays a self-focusing process where the output narrowed for increasing input energy, see Fig. 3. Beyond a well-defined input pulse energy the output is essentially localized in a single channel, which corresponds to the shape of the input field, and can therefore be regarded as the formation of a most strongly localized discrete soliton.
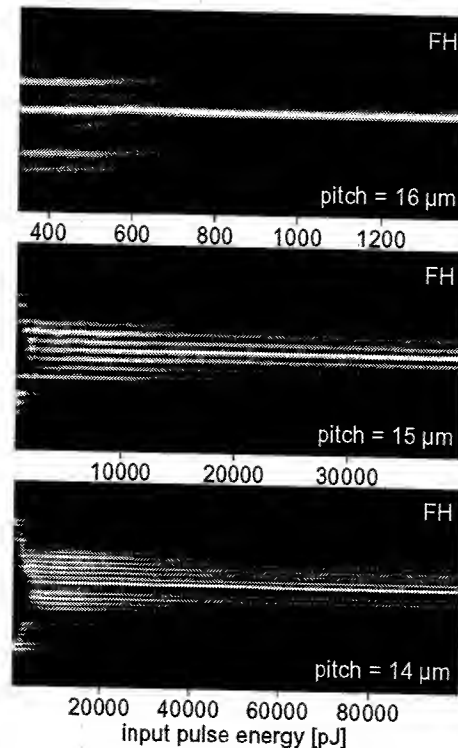
FIG. 3. FH output intensity distribution vs. input pulse energy for arrays with different waveguide pitch.

The narrowing of the output field intensity distribution for an increasing input power is not a smooth process. The output narrows in a rather stepwise manner (see Figs. 3, 4 and 5). For the weakly coupled array (pitch: 16 μm) an increase in power results in a sudden collapse of the output to the final single channel soliton. For an increased coupling strength (pitch: 15 μm) we observed an intermediate stage where a rectangular output pattern is formed over a wide range of input energies. If this is just some transient behavior or if it is a sign of the theoretically predicted rectangular soliton [15] is not yet clear. For the strongest coupling
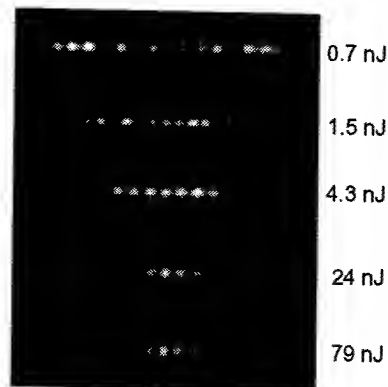
FIG. 4 FH output intensity distribution vs. input pulse energy. The rectangular output state persist over a wide input pulse energy range from 2.5 to 8.5 nJ (pitch = 15 μm).
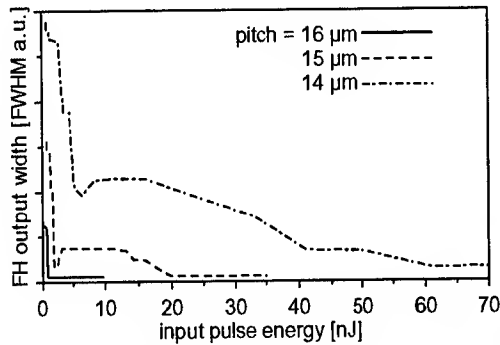
FIG. 5. FH output width vs. input pulse energy for arrays with different waveguide pitch.

(pitch: 14 μm) the stepwise decreases of the output width for increasing input energy is even more pronounced. As expected the necessary power for the excitation of the solitons increased with the strength of the coupling (see Fig. 5).

The SH output field distribution in Fig. 6 is much narrower than the FH output for all input pulse energies. This was expected from the theory, since for low powers the SH is most effectively generated at the input where the FH is still localized to a small number of waveguides. After its generation at the input the SH couples only weakly to the other waveguides because it is more strongly guided by the diffusion profile. Therefore already for moderate power levels we observe a collapse of the SH output to the single waveguide of the FH input.

The measured pulse energies imply peak powers (power [W] ≈ pulse energy [pJ] * 0.47) that are much higher than expected for cw-experiments. This discrepancy is due to the spectral width of the short pulses (~4 nm) used which is much wider then the phase matching bandwidth of the 74 mm long samples (~0.3 nm). This effect compares to the previously reported short pulse experiments in nonlinear directional couplers [16].

In conclusion we reported for the first time the formation of discrete solitons in waveguide arrays with a second-order nonlinearity. The authors gratefully acknowledge support by the European Community (IST-2000-26005) and in the US by an ARO MURI and the National Science Foundation.

FIG. 6 SH output intensity distribution vs. input pulse energy for arrays with different waveguide pitch.

1. F. Lederer, S. Darmanyan, and A. Kobyakov, 'Discrete solitons', in: Spatial Solitons, eds.: S. Trillo and W. Torruellas, Springer Series on Optical Sciences, Vol. 82, Springer, Berlin, New York, 2001.

2. S. Somekh, E. Garmire, A. Yariv, H. Garvin, and R. Hunsperger, Appl. Phys. Lett. 22, 46 (1973).

3. T. Pertsch, P. Dannberg, W. Elflein, A. Bräuer, and F. Lederer, Phys. Rev. Lett. 83, 4752 (1999).

4. R. Morandotti, U. Peschel, J. S. Aitchison. H. S. Eisenberg, and Y. Silberberg, Phys. Rev. Lett. 83, 4756 (1999).

5. H. S. Eisenberg, Y. Silberberg, R. Morandotti, and J. S. Aitchison, Phys. Rev. Lett. 85, 1863 (2000).
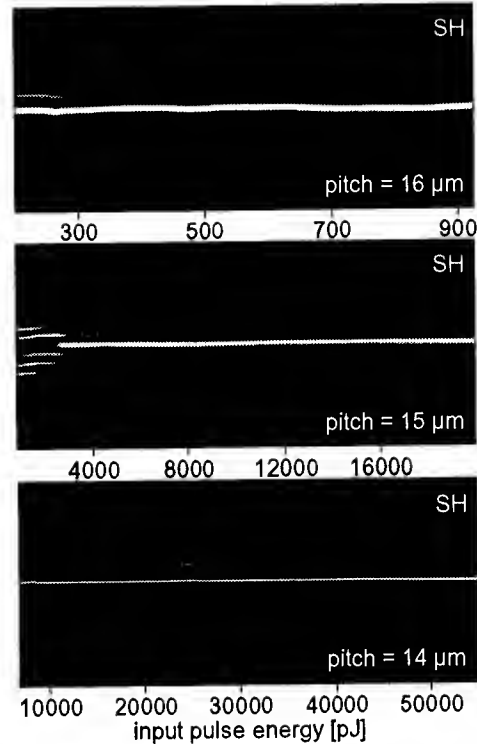
6. T. Pertsch, T. Zentgraf, U. Peschel, A. Bräuer, and F. Lederer, Phys. Rev. Lett. 88, 093901 (2002).

7. T. Pertsch, T. Zentgraf, U. Peschel, A. Bräuer, and F. Lederer, Appl. Phys. Lett. (to appear in May 2002).

8. H. S. Eisenberg, Y. Silberberg. R. Morandotti, A. Boyd, and J. S. Aitchison. Phys. Rev. Lett. 81, 3383 (1998).

9. U. Peschel, R. Morandotti, J. S. Aitchison, H. S. Eisenberg, and Y. Silberberg, Appl. Phys. Lett. 75, 1348 (1999).

10. R. Morandotti, U. Peschel, J. S. Aitchison, H. S. Eisenberg, and Y. Silberberg, Phys. Rev. Lett. 83, 2726 (1999).

11. R. Morandotti, H. S. Eisenberg, Y. Silberberg, M. Sorel, and J. S. Aitchison, Phys. Rev. Lett. 86, 3296 (2001).

12. W. Torruellas, Y. S. Kivshar, and G. Stegeman, 'Quadratic solitons', in: Spatial Solitons, eds.: S. Trillo and W. Torruellas, Springer Series on Optical Sciences, Vol. 82, Springer, Berlin, New York, 2001.

13. G. Schreiber, H. Suche, Y. L. Lee, W. Grundkötter, V. Quiring, R. Ricken, and W. Sohler, Appl. Phys. B 73, 501 (2001).

14. T. Peschel, U. Peschel, and F. Lederer, Phys. Rev. E 57, 1127 (1998); S. Darmanyan. A. Kobyakov, and F. Lederer, Phys. Rev. E 57, 2344 (1998).

15. A. Kobyakov, S. Darmanyan, T. Pertsch, F. Lederer, J. Opt. Soc. Am. B 16, 1737 (1999).

16. R. Schiek, W. Elflein, T. Pertsch, A. Tünnermann, K. R. Parameswaran, and M. M. Fejer: in Nonlinear Optics: Materials, Fundamentals and Applications. OSA Technical Digest (Optical Society of America, Washington DC, 2000) pp. 171-173).

Discrete gap solitons in modulated waveguide arrays

Andrey A. Sukhorukov and Yuri S. Kivshar

Nonlinear Physics Group,
Research School of Physical Sciences and Engineering,
Australian National University,
Canberra, ACT 0200, Australia;
Home page: http://www.rsphysse.anu.edu.au/nonlinear
Tel: +61-2-6125-3423; Fax: +61-2-6125-8588

We analyze the beam propagation in modulated waveguide arrays, which consist of two types of alternating waveguides with different widths. Using effective discrete equations, we identify the presence of the so-called Rowland ghost gap in the linear transmission spectrum, and consider the effect of Kerr-type nonlinear self-action, describing two distinct classes of discrete solitons: (i) conventional discrete solitons, and (ii) *discrete gap solitons*. We demonstrate that the gap solitons can be efficiently generated by Gaussian input beams; both the soliton velocity and its propagation direction can be controlled by varying the input light intensity.

Photonic structures with a periodic modulation of the refractive index can be used to precisely control propagation of optical pulses and beams. Wave localization is possible inside the *band gaps* of the linear frequency spectrum, whereas dispersion characteristics are strongly modified near the band edges. Recent papers[1,2] reported fabrication of one-dimensional structures consisting of a periodic array of planar optical waveguides, where the effective diffraction coefficient can be reduced to zero, and even made negative, being controlled by the input conditions and the array parameters.

In comparison with homogeneous media, efficiency of nonlinear processes can be greatly enhanced in properly designed periodic structures. For waveguide arrays, where waves are primarily localized in weakly coupled waveguides, the effective diffraction can be reduced, further lowering the threshold for spatial beam self-focusing. It was predicted that diffractional spreading is suppressed for the special beams in the form of *discrete solitons*[3], and these nonlinear localized waves possess many remarkable properties[4]. For example, unlike their continuous counterparts, discrete solitons can propagate across an array at low powers, while at high powers they become trapped by the discreteness to a single waveguide[5,6], and this behavior is readily observed in experiment[7]. It was also demonstrated that discrete solitons can be efficiently routed through two-dimensional networks of coupled waveguides[8]. Similar concepts were also developed for coupled-resonator optical waveguides, which are created by arrays of defects embedded in photonic crystals[9].

In a number of recent publications[10,11], it was suggested that the properties of discrete solitons can be modified by a periodic

FIG. 1: Schematic of a binary array of waveguides with alternating widths.

modulation of waveguides along the propagation direction. In this paper, we introduce another idea of the array engineering and consider *a binary waveguide array* composed of alternating "thick" and "thin" waveguides, as illustrated in Fig. 1. In such a structure, the effective refractive index experiences additional modulation, and therefore a "Rowland ghost gap" appears in the linear spectrum[12]. Formation of solitons in such gaps was earlier studied in the context of superstructure fiber Bragg gratings[13], where the analysis was based on the coupled-mode equations. Below, we demonstrate the existence of *discrete gap solitons* that display the properties of both conventional discrete and Bragg grating solitons and resemble nonlinear localized modes in diatomic lattices[14].

Propagation of waves in an array of weakly coupled single-mode waveguides can be approximately described[3] by the discrete nonlinear Schrödinger equation (DNLS) for the normalized amplitude of the electric field E_n localized at the waveguide with the index n,

$$i\frac{dE_n}{dz} + \lambda_n E_n + (E_{n-1} + E_{n+1}) + \gamma_n |E_n|^2 E_n = 0, \tag{1}$$

where λ_n characterizes the linear propagation constant of the mode guided by the n–th waveguide (which depends on its width), and γ_n is the effective nonlinear coefficient. For the analysis of the structure shown in Fig. 1, it is convenient to introduce the notation $a_n = E_{2n}$, $b_n = E_{2n+1}$, $\lambda_{2n+1} \equiv -\rho$, and $\lambda_{2n} \equiv 0$, where the appropriate normalization of Eq. (1) is implied. In order to simplify the analysis, we neglect absorption and also assume that the nonlinear coefficients are identical, $\gamma_n \equiv \gamma$. However, we have verified that the main conclusions of our study remain valid if γ_n are weakly modulated. With no loss of generality, we have $\rho > 0$, so that a_n and b_n are the field amplitudes at the thick and thin waveguides, respectively.

First we analyze the properties of *linear waves* characterized by the Bloch wave number K_b,

$$a_n = A e^{i\beta z + i K_b n}, \quad b_n = B e^{i\beta z + i K_b n}, \qquad (2)$$

where β is the mode propagation constant. We substitute Eq. (2) into the linearized Eq. (1) (with $\gamma = 0$), and obtain the *linear dispersion relation* that couples the propagation constant and the Bloch wave number, and yields the corresponding relation between the amplitudes at the thin and thick waveguides,

$$K_b = \cos^{-1}(\eta/2), \quad A = B e^{-iK_b/2}\sqrt{2-\eta}/\beta, \qquad (3)$$

where $\eta = 2 - \beta(\beta + \rho)$. It follows that transmission bands, corresponding to real K_b, appear when $\beta_- \leq \beta \leq -\rho$ or $0 \leq \beta \leq \beta_+$, where $\beta_\pm = -(\rho/2) \pm \sqrt{(\rho/2)^2 + 4}$. On the other hand, the Rowland ghost gap appears for $-\rho < \beta < 0$, and it increases for a larger difference between the widths of the neighboring waveguides. A characteristic dispersion relation and the corresponding band-gap structure are presented in Fig. 2(a). This dependence is calculated for $\rho = 2$, since this value can be realized in experiments. For example, for a thin defect layer in a fabricated structure, which was studied in Ref.[15], the normalized detuning parameter was $\rho \simeq 1.5$.

Using the dispersion relation (3), we calculate the *group velocity*, $v_g = -2(\partial\beta/\partial K_b)$, and the effective *diffraction coefficient*, $D = -4(\partial^2\beta/\partial K_b^2)$. Characteristic dependencies of these parameters on the propagation constant β are shown in Figs. 2(b,c). In both transmission bands, there exist regions with effective normal and anomalous diffraction and a zero-diffraction point between them.

FIG. 2: Characteristic dependencies of the Bloch wave number (K_b), group velocity (v_g), and the effective diffraction coefficient (D) on the propagation constant β. Gray shadings mark the transmission bands. The normalized detuning between the thick and thin waveguides is $\rho = 2$.

Assuming that the medium has a self-focusing nonlinearity, bright discrete solitons can form when the effective diffraction coefficient is positive. We consider excitation of such solitons by an input Gaussian beam,

$$E_n(z = 0) = C \exp\left[-(n - n_0)^2/\nu^2 + i\kappa(n - n_0)\right], \qquad (4)$$

where n_0 is the position of the beam center, ν is the beam width, and κ characterizes the inclination angle. Such input beam can be represented as a superposition of two modulated linear eigenmodes, whose eigenvalues $\beta_{1,2}$ correspond to the Bloch number $K_b = \cos^{-1}[\cos(2\kappa)]$,

$$E_{2n}(0) = (A_1 + A_2)\exp\left[-(2n - n_0)^2/\nu^2 + iK_b n\right], \quad E_{2n+1}(0) = (B_1 + B_2)\exp\left[-(2n + 1 - n_0)^2/\nu^2 + iK_b n\right],$$

where the amplitudes A_j and B_j ($j = 1, 2$) satisfy Eq. (3) at $\beta = \beta_j$ (with no loss of generality, we choose $\beta_1 > \beta_2$). For a wide input beam ($\nu \geq 4$), a ratio of the powers of two excited Bloch modes can be presented in a simple form,

$$p = \frac{P_2}{P_1} \simeq \left(\frac{1 - \delta}{1 + \delta}\right)^2, \qquad (5)$$

where $\delta = \sqrt{1 + \rho/\beta_1}$. It is important to note that the two modes always have opposite group velocities and diffraction coefficients (see Fig. 2).

Let as first discuss the excitation of gap solitons with a beam which is incident at a normal angle, so that $\kappa = K_b = 0$, and $\beta_{1,2} = \beta_{+,-}$. In this case, $p < 1$, i.e. the first ($j = 1$) mode is always dominant (for example, $p \simeq 0.15$ for $\rho = 2$). As demonstrated in Fig. 2, at $\beta = \beta_+$ the effective diffraction coefficient is positive and, therefore, discrete solitons can be formed in self-focusing media. The properties of such solitons are similar to those existing in homogeneous waveguide arrays.

In order to excite the stationary gap solitons in a self-focusing medium, one might attempt to use an input beam with $\kappa = \pi/2$, so that $K_b = \pi$, $\beta_1 = 0$, $\beta_2 = -\rho$. In this case, the two Bloch modes have equal powers ($p = 1$), however one of them experiences self-focusing and another — self-defocusing, and in this situation an efficient generation of gap solitons is not possible.

The optimum conditions for generating discrete gap solitons can be realized when $\pi/2 < \kappa < \pi$, and $D(\beta_2) > 0$. Indeed, under such conditions $p > 1$, i.e. the second mode, which experiences self-focusing, is dominant. Moreover, the Bloch wave envelopes have opposite group velocities, so that they move apart in the opposite directions. In Fig. 3(a), we show that two beams are indeed generated at the input. The beam which moves to the right is localized at odd (i.e. thin) waveguides, and it transforms into a gap soliton. On the contrary, the other beam moves to the left, and experiences self-defocusing and broadens.

Stationary gap solitons can be generated at higher input intensities. In this case, the soliton is not able to overcome the Peierls-Nabarro potential of the periodic structure, and it becomes trapped. At such high intensities, the two Bloch

FIG. 3: Excitation of discrete gap solitons in a self-focusing medium ($\gamma = +1$) by input beams with $\kappa = 0.6\pi$, $n_0 = 1$, $\nu = 4$, and normalized peak intensities (a) $|C|^2 = 0.3$, (b) 0.7, (c) 0.8, (d) 5. The waveguide array parameters correspond to Fig. 2.

modes are initially trapped together, resulting in a periodic beating that can strongly affect the soliton formation process. Examples shown in Figs. 3(b,c) demonstrate that, depending on the input intensity, the gap soliton can remain in the center, or even can shift to the left, in the direction opposite to the propagation direction of the input beam. If the intensity is increased even further, then the gap soliton becomes oscillatory unstable, similar to gap solitons in fiber Bragg gratings[16]. We illustrate the instability development in Fig. 3(d).

In conclusion, we have studied the diffraction properties and nonlinear wave propagation in binary waveguide arrays with alternating waveguide widths. We have predicted the existence of discrete gap solitons and demonstrated their intriguing dynamics controlled by varying the input intensity.

References

[1] R. Morandotti, H. S. Eisenberg, Y. Silberberg, M. Sorel, and J. S. Aitchison, Phys. Rev. Lett. **86**, 3296 (2001).
[2] T. Pertsch, T. Zentgraf, U. Peschel, A. Brauer, and F. Lederer, Phys. Rev. Lett. **88**, 093901 (2002).
[3] D. N. Christodoulides and R. I. Joseph, Opt. Lett. **13**, 794 (1988).
[4] F. Lederer, S. Darmanyan, and A. Kobyakov, "Discrete solitons," in *Spatial Optical Solitons*, Vol. 82 of *Springer series in optical sciences*, S. Trillo and W. E. Torruellas, eds., (Springer-Verlag, New York, 2001), pp. 269–292.
[5] C. Claude, Yu. S. Kivshar, O. Kluth, and K. H. Spatschek, Phys. Rev. B **47**, 14228 (1993).
[6] A. B. Aceves, C. De Angelis, T. Peschel, R. Muschall, F. Lederer, S. Trillo, and S. Wabnitz, Phys. Rev. E **53**, 1172 (1996).
[7] R. Morandotti, U. Peschel, J. S. Aitchison, H. S. Eisenberg, and Y. Silberberg, Phys. Rev. Lett. **83**, 2726 (1999).
[8] D. N. Christodoulides and E. D. Eugenieva, Phys. Rev. Lett. **87**, 233901 (2001).
[9] D. N. Christodoulides and N. K. Efremidis, Opt. Lett. **27**, 568 (2002).
[10] M. J. Ablowitz and Z. H. Musslimani, Phys. Rev. Lett. **87**, 254102 (2001).
[11] U. Peschel and F. Lederer, J. Opt. Soc. Am. B **19**, 544 (2002).
[12] P. St. J. Russell, Phys. Rev. Lett. **56**, 596 (1986).
[13] N. G. R. Broderick, C. M. de Sterke, and B. J. Eggleton, Phys. Rev. E **52**, R5788 (1995).
[14] O. A. Chubykalo and Yu. S. Kivshar, Phys. Rev. E **48**, 4128 (1993); Erratum: Phys. Rev. E **49**, 5906 (1994).
[15] U. Peschel, R. Morandotti, J. S. Aitchison, H. S. Eisenberg, and Y. Silberberg, Appl. Phys. Lett. **75**, 1348 (1999).
[16] I. V. Barashenkov, D. E. Pelinovsky, and E. V. Zemlyanaya, Phys. Rev. Lett. **80**, 5117 (1998).

Discrete Vector Kerr Spatial Solitons in AlGaAs Array Waveguides

Joachim Meier and George Stegeman
CREOL/School of Optics. University of Central Florida, Orlando, Florida, 32816
joachim@steglab.creol.ucf.edu

H.S. Eisenberg and Y. Silberberg
Department of Physics of Complex Systems. The Weizmann Institute of Science, 76100 Rehovot, Israel

R. Morandotti and J.S. Aitchison
Department of Electrical and Computer Eng., University of Toronto, Toronto, Ontario, Canada M5S 3G4

Abstract: We report the first observation of discrete vector solitons in arrays of AlGaAs waveguides. By changing the phase between the TE and TM soliton components, we were able to control their relative amplitude.

©2002 Optical Society of America
OCIS codes: (190.5530) Nonlinear optics, Pulse propagation and solitons

Address : CREOL, P.O. Box 162700,
4000 Central Florida Blvd.
Orlando, FL 32816-2700
Tel. 407-823-6267; Fax. 407-823-6955
E-mail : **joachim@steglab.creol.ucf.edu**

Discrete Vector Kerr Spatial Solitons in AlGaAs Array Waveguides

Joachim Meier and George Stegeman
CREOL/School of Optics, University of Central Florida, Orlando, Florida, 32816
joachim@steglab.creol.ucf.edu

H.S. Eisenberg and Y. Silberberg
Department of Physics of Complex Systems, The Weizmann Institute of Science, 76100 Rehovot, Israel

R. Morandotti and J.S. Aitchison
Department of Electrical and Computer Eng., University of Toronto, Toronto, Ontario, Canada M5S 3G4

1. Introduction

The equivalent of diffraction occurs in arrays of weakly coupled waveguides. Similar to continuous systems, discrete arrays can support stable solitons, which are formed when an intensity-dependent, self-focusing mechanism is present to counteract discrete diffraction [1]. These discrete solitons form a non-integrable system and are expected to have many different properties when compared to their continuous counterparts. Their properties have been studied in Kerr and quadratically nonlinear materials and they have been observed experimentally in AlGaAs waveguide arrays [2-4]. It has also been shown that the unique dispersion properties of such arrays should allow the observation of dark solitons in such system [5]. Although the case of vector solitons with two orthogonal and mutually incoherent polarizations has been investigated theoretically, only the scalar version (single polarization) has been observed to date [6]. In this paper we report on the excitation of a dual polarization vector soliton, and on the ability of controlling the relative amplitudes of the polarization components by changing the relative input phase.

2. Experimental Conditions

In order to perform our experiment, we used an array of 2D AlGaAs waveguides. The sample (whose geometry is presented in Fig. 1), was 13.9mm long and had losses of about 1.5dB/cm. The light source was a Spectra Physics OPA-800CP which produced 1.1ps FWHM pulses at a 1 kHz rep rate, with a maximum pulse energy of 65 nJ. The 1550 nm pulses were attenuated and split into two orthogonal polarizations. Their relative phase was adjusted with a precision delay line and measured interferometrically. Subsequently the beams were recombined and focused into the sample in order to excite only a single waveguide. The output was detected by a camera and the energies of the input and output beams were measured by germanium detectors.
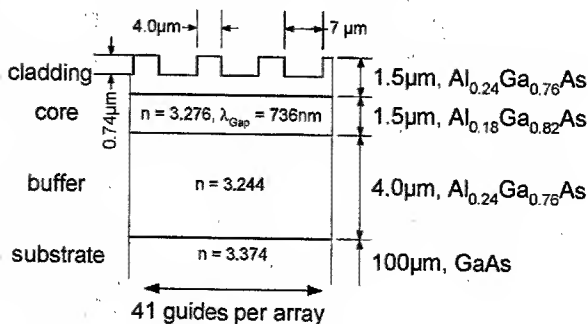
Fig. 1. The sample geometry
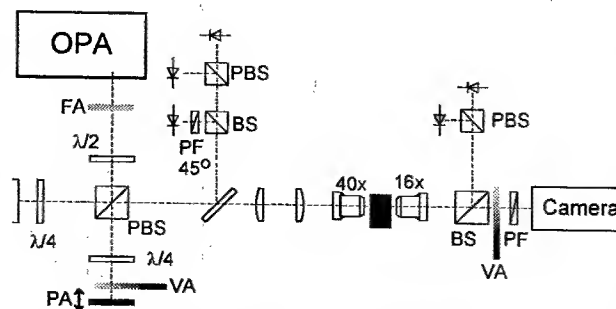
Fig. 2. Experimental Set-up (BS: 50/50 beamsplitter, PBS: polarizing BS, PF: polarizing filter, FA;VA: fixed; variable attenuator, PA: piezo-electric actuator)

3. Theoretical Considerations

The equations in reference [6] can be modified as follows to describe radiation fields in the array:

$$i\frac{da_n}{dz} + c_{TE}\left(a_{n+1} + a_{n-1}\right) + (\lambda_{a\parallel} \mid a_n \mid^2 + \lambda_{a\perp} \mid b_n \mid^2)a_n + \lambda_{ab}b_n^2 a_n^* \exp[2i(\Delta\beta z + \phi_{TE} - \phi_{TM})] = 0$$

$$i\frac{db_n}{dz} + c_{TM}\left(b_{n+1} + b_{n-1}\right) + (\lambda_{b\parallel} \mid b_n \mid^2 + \lambda_{b\perp} \mid a_n \mid^2)b_n + \lambda_{ba}a_n^2 b_n^* \exp[-2i(\Delta\beta z + \phi_{TE} - \phi_{TM})] = 0$$

Here a_n and b_n are the field envelopes of the TE and TM polarized fields, β_{TE} and β_{TM} are the respective propagation wavevectors with $\Delta\beta = \beta_{TE} - \beta_{TM}$, c_{TE} and c_{TM} are the coupling coefficients, and $\phi_{TE} - \phi_{TM}$ is the initial phase difference between the TE and TM polarizations. The other terms $\lambda_{\parallel}$, $\lambda_{\perp}$ and $\lambda_{ab,ba}$ are the self-phase-, cross-phase and four-wave-mixing nonlinear coefficients, respectively. For the case of AlGaAs the self- and cross-phase coefficients are almost equal and the TE and TM field distributions are quite similar. Hence, the coupling coefficients are approximately the same and $\Delta\beta$ is small [7].

Although we are not aware of any theoretical work in the literature on soliton solutions to these equations, we expect localized solitons to exist. Because of the four-wave mixing term, energy is exchanged periodically with propagation distance between the two polarizations, possibly accompanied by a periodic change in the soliton's width. However, as the self- and cross-phase coefficients are almost equal for the two polarizations, only a small variation of the soliton widths is expected during propagation. It is not known to date whether the system will bifurcate into truly stationary spatial solitons at high powers as in the homogeneous medium case [8].

4. Results and Discussion

The first experiments were performed in order to verify the existence of strongly localized vector solitons in our sample. In Figure 3 we show the intensity profiles recorded at the output facet of the waveguide array for a TE excitation alone, for a TM excitation alone and for the two combined excitations. The TE and TM powers were set to have the same value. The combined output shows a strongly confined soliton, almost entirely localized into a single waveguide.

	TE: 650nW	TM: 650nW
alone		
together		
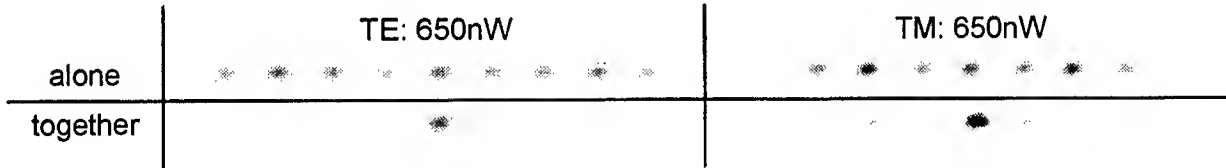
Fig. 3. The TE and TM polarized outputs from the waveguide array for single channel excitation of both the TE polarization and TM polarization individually, and then combined together at the input. The power given is the average power.

Figure 4 shows the collapse of both a strong TM polarized component and a weak TE component as a function of the input TM power. The monotonic beam narrowing of the strong TM component as a function of the input power is similar to the case of a homogenous slab waveguide. However, in contrast to the homogeneous case, the weak probe beam sharply collapses into a strongly localized soliton just over a small range of intensity values. We also note that before the soliton is fully formed, the weak TE probe beam remains highly delocalized, instead of smoothly narrowing as in the homogeneous case. This may be due to the discrete nature of the system and merits further theoretical consideration.

For these vector solitons the two polarizations are coherently coupled through the four-wave mixing term. As discussed above, there is a periodic exchange of energy between the two polarizations which will depend on the initial phase difference between the two fields. In Fig. 5 we show the dependence of the TE output polarization as a function of the relative phase between the TE and TM components at the input. The TE average power was fixed at 350 nW and the TM power was increased. We changed the initial phase difference $\phi_{TE}-\phi_{TM}$ from 0 to 4 π using a piezo-electric actuator for each TM power level. Note that the changes ("drift") with increasing TM power in the position of the peak output TE energy relative to the phase difference axis in Fig. 5 is probably due to the hysteresis of our piezo-electric actuator. We observed for high powers periodic gain and loss for the TE output power with an

oscillation period twice that associated with the input phase difference because of the four-wave mixing term which varies as $\exp[2i(\phi_{TE}-\phi_{TM})]$.
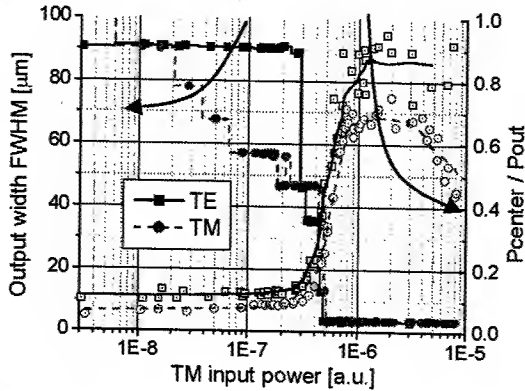
Fig. 4. Evolution of TE and TM output beam width (FWHM) and the ratio of power in the excited guide to the total output power.
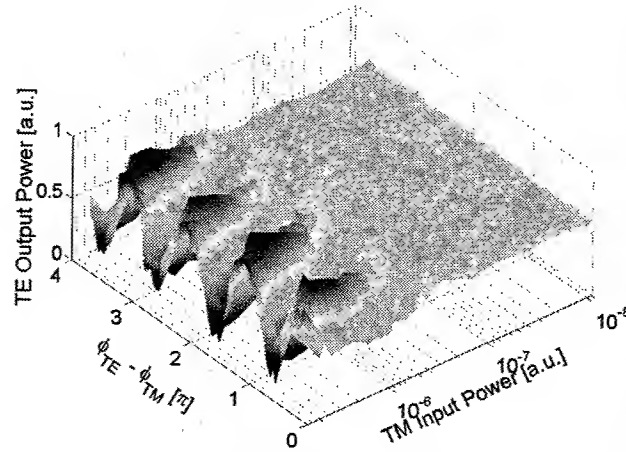
Fig. 5. Evolution of TE output power vs. TM input power and input TE/TM phase difference $\phi_{TE}-\phi_{TM}$.

In summary, we observed for the first time highly localized, discrete vector solitons, consisting of two orthogonal polarizations. Due to the coherent coupling between the two components, a periodic exchange of energy with twice the period of the relative phase at the input was observed, in good agreement with the prediction of four-wave-mixing in the sample.

This research was supported by an ARO MURI grant on "Solitonic Gateless Computing" in the US. The collaboration between the American and the Israeli partners was supported by the Bi-National Science Foundation.

5. References

[1] D.N. Christodoulides and R.1. Joseph, Opt. Lett., 13, 794 (1988)
[2] A.B. Aceves, C. DeAngelis, T. Peschel, R. Muschall, F. Lederer, S. Trillo and S. Wabnitz, Phys. Rev. E, 53, 1172 (1996)
[3] H. S. Eisenberg, Y. Silberberg, R. Morandotti, A.R. Boyd and J.S. Aitchison, Phys. Rev. Lett., 81, 3383 (1998)
[4] T. Peschel, U. Peschel and F. Lederer, Phys. Rev. E, 57, 1127 (1998)
[5] R. Morandotti, H.S. Eisenberg, Y. Silberberg, M. Sorel and J.S. Aitchison, Phys. Rev. Lett., 86, 3296 (2001)
[6] S. Darmanyan, A. Kobyakov, E. Schmidt and F. Lederer, Phys. Rev. E, 57, 3520 (1998).
[7] J. U. Kang, G. I. Stegeman, D. C. Hutchings, J. S. Aitchison and A. Villeneuve, IEEE J. Quant. Electron., 33, 341 (1997).
[8] E.A. Ostrovskaya, N.N. Akhmediev, G.1. Stegeman, J.U. Kang and J.S. Aitchison, JOSA B, 14, 880 (1997).

Discrete Solitons in Photorefractive Optically-Induced Photonic Lattices

Nikos K. Efremidis, Jared Hudock, and Demetrios N. Christodoulides
School of Optics/CREOL, University of Central Florida,
Florida, 32816-2700

Jason W. Fleischer, Suzanne Sears, and Mordechai Segev
Physics Department, Technion-Israel Institute of Technology, Haifa 32000, Israel
Electrical Engineering Department, Princeton University,
Princeton, New Jersey 08544

Abstract: We demonstrate that optical discrete solitons are possible in appropriately oriented biased photorefractive crystals. This can be accomplished in optically-induced periodic waveguide lattices that are created via plane wave interference. Our method paves the way towards the observation of entirely new families of discrete solitons.
© 2002 Optical Society of America
OCIS codes: 190.4390, 190.5530, 130.4310

Wave propagation in nonlinear periodic lattices is associated with a host of exciting phenomena that have no counterpart whatsoever in bulk media. Perhaps, the most intriguing entities that can exist in such systems are self-localized states-better known as discrete solitons (DS) [1-4]. Over the years, DS have been a topic of intense investigation in several branches of science such as biological physics [1], nonlinear optics [2], Bose-Einstein condensates [3], and solid state physics [4]. In optics, DS have been predicted [2] and experimentally verified [5] in nonlinear waveguide arrays and most recently they were also shown to exist in chains of coupled microcavities embedded in photonic crystals [6]. Furthermore, it has recently been shown that DS are promising in terms of realizing intelligent functional operations such as blocking, routing, logic functions, and time gating in two-dimensional DS array optical networks [7]. Yet, to date, only a small subset of the plethora of interesting theoretical predictions has actually been demonstrated at the experimental level. This is partly due to the fact that such arrays have only been implemented in single-row topologies (on the surface of a wafer) using a particular self-focusing material system. Establishing two-dimensional waveguide array lattices in the bulk is an even more complicated task, since no technology is currently available to fabricate such structures. It is therefore important to identify highly versatile nonlinear lattice systems where such DS entities can be observed, especially at low power levels.

In this paper, we show that optical DS are possible in appropriately oriented biased photorefractive crystals. This can be accomplished through the screening nonlinearity [8] in optically-induced waveguide periodic lattices that are established via plane wave interference. To do so, we exploit the large electrooptic anisotropy that is possible in certain families of crystals that, in turn, allows invariant propagation of 1-D and 2-D periodic intensity patterns. Our method offers exciting possibilities towards the observation of entirely new families of DS at mW power levels. Moreover we note, that our scheme offers considerable flexibility in the sense that the same photorefractive waveguide array (1-D or 2-D) can be of the self-focusing or defocusing type (depending on the polarity of the external bias [8]) with adjustable lattice parameters.
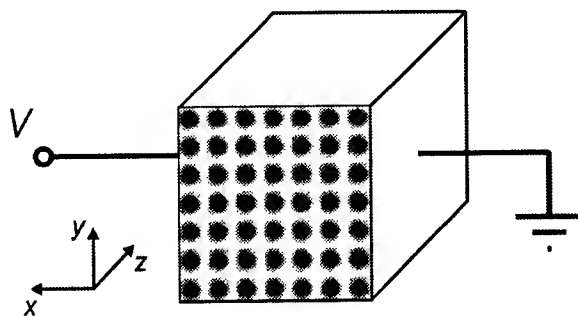
Fig. 1. A biased photorefractive crystal illuminated by a periodic intensity pattern created through the interference of plain wave pairs.
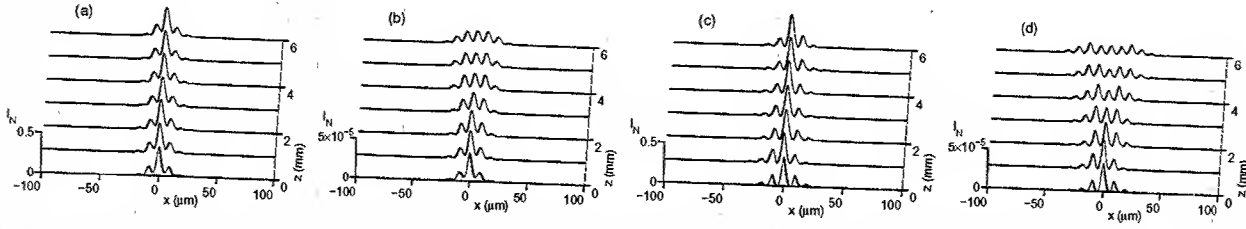
Fig. 2. Invariant propagation of (a) an in-phase DS and (c) a staggered DS in a 1-D photorefractive optically induced potential; (b) and (d) depict the diffraction dynamics of the field patterns shown in (a) and (c), respectively, when their intensities are considerably lowered.

We begin our analysis by considering a biased photorefractive crystal as shown in Fig. 1. For demonstration purposes, let the crystal be of the Strontium Barium Niobate type (SBN:75) having length L and width W in both transverse dimensions. The SBN sample is externally biased along its extraordinary x-axis (crystalline c-axis) with voltage V. The refractive index along the extraordinary axis is $n_e = 2.299$ whereas that along the ordinary (y-axis) is $n_0 = 2.312$. The relevant electro-optic coefficients of this crystal are $r_{33} = 1340$ pm/V and $r_{13} = 67$ pm/V and the wavelength of the lightwaves used is taken here to be $\lambda_0 = 0.5$ μm. In this case an x-polarized wave will see a refractive index $n_e'^2 = n_e^2 - n_e^4 r_{33} E_{sc}$ while the corresponding n_0' for a y-polarized wavefront is given by $n_0'^2 = n_0^2 - n_0^4 r_{13} E_{sc}$, where $E_{sc}\hat{x}$ is the external space-charge field under external bias.

Next, we identify methods to establish optically induced waveguide lattices in the bulk of the photorefractive crystal where DS are expected to occur. Such stationary 1-D or 2-D array lattices can be photo-induced by periodic diffraction-free intensity patterns that result from plane-wave superposition (provided that the system is linear for the interfering waves). In the suggested configuration of Fig. 1, this is accomplished by linearly polarizing these plane waves along the ordinary y-axis (since $r_{13} \ll r_{33}$) and, therefore, propagation along z is *essentially linear*. On the other hand, it is important to note that these same induced waveguides are *highly nonlinear* for extraordinary polarized waves because of the large value of r_{33}. For example, a one-dimensional periodic intensity pattern $I = I_0 \cos^2[k_2 \sin(\theta)x]$ can be generated from the interference of two plane waves $\hat{y}E_0 \exp[\pm ik_2 \sin(\theta)x] \exp[ik_2 \cos(\theta)z]$, where $k_2 = k_0 n_0$, $k_0 = 2\pi/\lambda_0$, and $\pm\theta$ is the angle at which these two plane waves propagate with respect to the z-axis. The spatial period of this array lattice is $D = \lambda_0/(2n_0 \sin\theta)$. Using two orthogonal mutually incoherent plane wave pairs 2-D "crystals" can be established from a diffraction-free intensity pattern $I = I_0\{\cos^2[k_2 \sin(\theta_1)x] + \cos^2[k_2 \sin(\theta_2)y]\}$. In addition, such 2-D (rectangular or square) structures can also be created by coherent superposition of four plane waves in which case $I = I_0 \cos^2[k_2 \sin(\theta_1)x] \cos^2[k_2 \sin(\theta_2)y]$. More complicated (hexagonal, etc.) nonlinear lattices can be generated by superimposing two or more mutually incoherent plane wave pairs at different angles.

We first consider a one-dimensional array configuration. In this case one can show that the evolution dynamics of both the DS and the optically induced lattice fields in a biased photorefractive SBN crystal is governed by the following set of equations [9]

$$iu_z + \frac{1}{2k_1}u_{xx} - \frac{k_0 n_e^3 r_{33}}{2}E_{sc}u = 0, \quad iv_z + \frac{1}{2k_2}v_{xx} - \frac{k_0 n_0^3 r_{13}}{2}E_{sc}v = 0, \tag{1}$$

where $k_1 = k_0 n_e$, E_{sc} is the space-charge field given by [8], $E_{sc} = E_0/(1+I(x)) - (K_B T/e)(\partial I/\partial x)/(1+I(x))$, and $I = |u|^2 + |v|^2$ is the normalized total intensity with respect to the dark irradiance of the crystal I_d [8]. K_B is the Boltzmann constant, T is the temperature, and e is the electron charge. u represents the x-polarized DS field that is affected by the strong r_{33} nonlinearity, and v is the y-polarized periodic field (evolving almost linearly) responsible for setting up the waveguide lattice. In addition, under a constant bias V, the following constraint holds true along z, $V = \int_0^W E_{sc}dx$.

Using numerical relaxation methods, we obtained DS solutions in this system. The dynamical evolution of these states is then examined by exactly solving Eqs. (1)) under a constant bias V. As an example, let the dimensions of the SBN crystal be $L = W = 6$ mm. Let also the normalized v field at the input be $v = v_0 \cos(\pi x/D)$, where here $|v_0|^2 = 2.56$ and $D = 9$ μm. The periodic v field is assumed to cover the entire
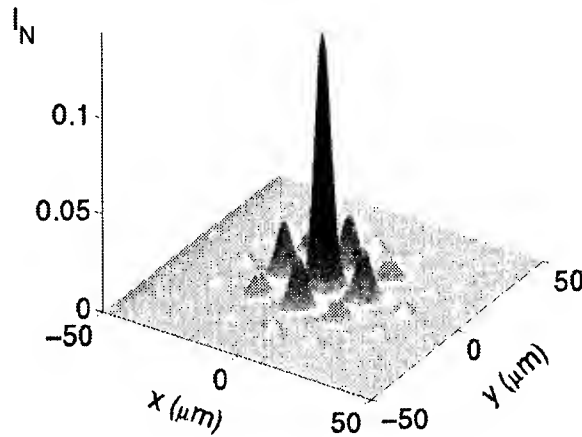
Fig. 3. A 2-D in-phase DS in a biased photorefractive crystal.

$W \times W$ input face of the crystal. The applied voltage across W is taken to be 325 V which corresponds to an $E_0 \simeq (V/W)\sqrt{1+v_0^2} = 102$ V/mm and leads to a self-focusing nonlinearity. Figure 2(a) depicts the invariant propagation of a well confined in-phase DS when its normalized peak intensity $|u_0|^2 = 0.36$. In addition, our simulations indicate that the 1-D waveguide lattice, as induced by the v field, remains essentially undistorted over the length of this crystal. This discrete soliton entity is possible through the combined effects of nonlinearity and lattice periodicity. The diffraction dynamics of this same field pattern when its peak intensity has been appreciably lowered is also depicted in Fig. 2(b). Evidently, the beam expands considerably after 6 mm of propagation, thus reaffirming the soliton nature of the state shown in Fig. 2(a). In addition to in-phase bright DS staggered dark solitons are also possible in this self-focusing system provided that the phase shift among sites is π. By reversing the polarity of the applied voltage, the nonlinearity of the lattice becomes defocusing. In this regime, the induced waveguide sites are located on the dark regions of the $|v|^2$ periodic intensity pattern. In such defocusing lattices, two families of DS exist. These are in-phase dark solitons (at the center of the Brillouin zone) and staggered (π out of phase) bright solitons at the edge of the Brillouin zone [10]. As an example we will discuss here only the latter DS family. Figure 2(c) depicts the propagation dynamics of a staggered bright soliton. This DS solution was obtained numerically for $|u_0|^2 = 0.36$, $|v_0|^2 = 4$, $D = 9$ μm, and by assuming again that the v field covers the entire crystal. The applied voltage in this case is -182 V. As Fig. 2(c) demonstrates, the staggered soliton can propagate in an invariant fashion over the length of the crystal. Note that this particular type of DS solution cannot exist in the bulk and is purely the outcome of discreteness. At much lower intensities, this field pattern diffracts considerably as shown in Fig. 4(d) since the nonlinearity is not enough to compensate for linear coupling effects.

Similarly two-dimensional DS are also possible in optically induced photonic lattices in biased photorefractive crystals. As previously mentioned, such lattices can be established in the bulk by coherently superimposing two plane wave pairs. Figure 3 shows an in-phase two-dimensional bright DS in a square lattice with $D = 15$ μm, $|u_0|^2 = 0.13$, and $|v_0|^2 = 3$ as obtained using relaxation methods.

References

1. A.S. Davydov, J. Theor. Biol. **38**, 559 (1973).
2. D. N. Christodoulides and R. I. Joseph, Opt. Let. **13**, 794 (1988).
3. A. Trombettoni and A. Smerzi, Phys. Rev. Lett. **86**, 2353 (2001).
4. W. P. Su, J. R. Schieffer, and A. J. Heeger, Phys. Rev. Lett. **42**, 1698 (1979); A. J. Sievers and S. Takeno, Phys. Rev. Lett. **61**, 970 (1988).
5. H. Eisenberg, Y. Silberbeg, R. Morandotti, A. Boyd and J. Aitchison, Phys. Rev. Lett. **81**, 3381 (1998).
6. D. N. Christodoulides and N. K. Efremidis, Opt. Lett. **27**, 565 (2002).
7. D. N. Christodoulides and E. D. Eugenieva, Phys. Rev. Lett. **87**, 233901 (2001).
8. M. Segev, G. C. Valley, B. Crosignani, P. D. Porto, and A. Yariv, Phys. Rev. Lett. **73**, 3211 (1994); D. N. Christodoulides and M. I. Carvalho, J. Opt. Soc. Am. B **12**, 1628 (1995).
9. S. R. Singh, M. I. Carvalho, D. N. Christodoulides, Opt. Lett. **20**, 2177 (1996).
10. Y. S. Kivshar, Opt. Lett **14**, 1147 (1993).

The action of linear modes on the evolution and on the decay of discrete solitons

U.Peschel and F.Lederer
Friedrich-Schiller-Universität Jena, Max-Wien-Platz 1, 07743 Jena, Germany
phone: +(49) 3641 947176, fax: +(49) 3641 94717, e-mail: p6peul@rz.uni-jena.de

R. Morandotti and J. S. Aitchison
University of Toronto, 10 King's College Road, Toronto, Ontario, Canada M5S 3G4

H. S. Eisenberg and Y. Silberberg
The Weizmann Institute of Science, 76100 Rehovot, Israel

Abstract: We experimentally investigate how linear modes evolve around the soliton state. In the presence of nonlinear absorption they induce collapse and subsequent splitting of the soliton, or a transverse motion opposite to initial beam tilts.
©2000 Optical Society of America
OCIS codes: (190.4420) Nonlinear optics, transverse effects in, (130.4310) Integrated optics, nonlinear

Stationary solitary waves, usually termed solitons, define fixed-points of the nonlinear evolution in otherwise non-integrable systems. However, arbitrary input field profiles usually do not match the soliton shape. Hence, in most cases the initial state is already perturbed. If energy conservation holds, or losses are small these perturbations may persist for a long time. They evolve as internal modes of the respective soliton, and can influence the dynamics of this ground state considerably. Here we theoretically predict and experimentally demonstrate that the joint action of quasi-linear modes and nonlinear losses can result in the virtual destruction of a discrete soliton, propagating in an array of optical waveguides. However, the now diffracting field still carries an imprint of the evolution prior to the collapse,, which leads to unexpected steering phenomena.

To investigate discrete optical solitons we produced waveguide arrays from AlGaAs. The final sample consisted of 41 guides with a spacing center to center of 9 μm and an overall length of 6 mm. To reduce losses photon energies well below half the band gap of the material were chosen. At λ=1.53 μm the material has an almost ideal Kerr like nonlinearity, no two-photon absorption and only mimimal three-photon absorption Details of the experimental set-up are given in ref [1]). The amplitude, width and angle of the input excitation could be. The intensity distribution at the output facet was recorded on an infrared camera. To gain some insight into the field evolution within the sample we performed numerical simulations on the basis of the Discrete Nonlinear Schrödinger Equation (DNLS) with three-photon absorption included:

$$i\frac{da_n}{dz} + \gamma|a_n|^2 a_n + i\alpha_3|a_n|^4 a_n + C(a_{n+1} + a_{n-1}) = 0.$$

Here a_n is the field amplitude in guide number n, which evolves in the z-direction. Energy transport between adjacent guides is mediated by a linear coupling of strength $C=1.0mm^{-1}$. While $\gamma=3.6m^{-1}W^{-1}$ and $\alpha_3=10^{-4}m^{-1}W^{-1}$ account for the Kerr nonlinearity and the three photon absorption, respectively.

Although three-photon absorption can influence the evolution of the fields during propagation, it is still a weak perturbation. Therefore, we first study solutions of Eq.(1) in the absence of losses ($\alpha_3=0$). The DNLS is known to be non-integrabal, though it does possess stable bright solitary wave solutions of the form $a_n(z) = a_n^0 \exp(i\beta z)$, which have a stationary field distribution and a flat phase. Their total power increases, while their width decreases with growing wavenumber β. Hence, higher powers are required to generate narrower solitons. In contrast to its continuous counterpart, the nonlinear Schrödinger equation, the DNLS is not Galilean invariant and all stationary solutions travel parallel to the array. An arbitrary excitation can be decomposed into the soliton state and a respective perturbation $\delta a_n(z)$ as $a_n(z) = |a_n^0 + \delta a_n(z)|\exp(i\beta z)$. Parts of this excess energy are shed away, however, most of the energy remains attached to the soliton, which forms an effective waveguide. It is useful to decompose this quasi-linear radiation into modes or eigenstates of a linearized version of Eq.(1). In general stable discrete solitons have up to two non-trivial bound states [2], a symmetric and an asymmetric one. For the soliton powers which we are interested in both bound states have converged towards the continuous spectrum. Strictly speaking they are transformed into weakly radiating modes with an eigenvalue at the edge of the continuous

spectrum. For experimentally accessible propagation distances the resulting radiative damping is negligible. More importantly: Both modes have almost the same internal frequency $\lambda = \pm(\beta - 2C)$ and oscillate in phase. However, their influence on the total field dynamics is different. The symmetric mode induces breathing, where the antisymmetric mode mainly causes a wobbling around the center of gravity of the whole field distribution.
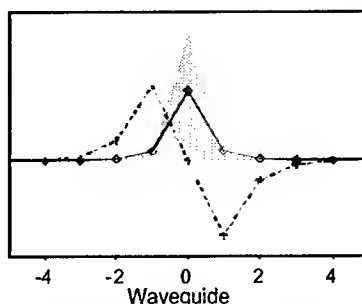
Fig.1 Linear modes of a discrete soliton with a total power of about 1200W (shadowed: discrete soliton, full line: symmetric breathing mode, dashed line: asymmetric quasi-translational mode. For both linear modes only the localized field component is shown)

By varying the three parameters: beam amplitude, width and tilt we can basically excite an arbitrary soliton with a chosen power distribution between symmetric and antisymmetric modes. Let us first discuss an excitation with an untilted beam, which is centered on the input guide (see Fig.2a). For symmetry reasons only a discrete soliton and the respective breathing mode are excited. Changes of the total power arise mainly from the presence of three-photon absorption, which is the dominant loss mechanism. Because it is highly nonlinear it influences the field propagation when self-focusing occurs. Here we choose a broad beam (13μm), with an incoupled peak power of about 2000W. We note that for this particular width, the power injected is much higher that the value required to generate a soliton. A narrower soliton with higher energy is chosen to minimize the energy stored in linear modes. For symmetry reasons only the symmetric mode is excited besides the soliton. It destructively interferes with the center of the soliton. In this way the field in the array adapts to the broader and less intense initial beam. However, the excited mode oscillates around the soliton. Hence, after propagation distance of ≈1.6mm a phase shift of π has accumulated and the interference with the soliton has reversed. Now the total intensity is increased in the center. Consequently the overall power distribution is narrowed and collapses almost into the central guide (see Fig.2a and 2b). For the pure lossless DNLSE this kind of self-focusing would appear periodically (see Fig.2a). However, nonlinear losses growth tremendously in the focal point due to three-photon absorption and a lot of energy is lost. As a result the basic soliton state ceases to exist. It is virtually eliminated by the action of the linear mode (see Fig.2b).

In contrast the internal mode is less affected by the three-photon absorption. In particular, the field stored in the wings of the internal mode is well conserved. However, the decay of the basic soliton state also has a dramatic effect on the internal mode. It has lost the effective waveguide, where it propagated and. therefore it radiates away. The field distribution emerging from the collapse point has two pronounced wings, which originate from the internal mode, however, it lacks power in its center, where the nonlinear absorption had its greatest effect. At the output facet we observe two well-separated maxima of the light distribution (see Fig.2b).

We have now the unique opportunity to vary the power distribution between symmetric and antisymmetric linear modes by changing the tilt of the exciting beam. If we incline the beam, the incident field is no longer symmetric. Therefore, the amount of power stored in the antisymmetric quasi-translational mode increases. An excitation of this mode induces oscillations of the soliton around its stationary state. Note that the symmetric mode is still present and induces breathing (see Fig.2c). Consequently we observe an asymmetry of the output field due to the growing contribution of the quasi-translational mode. However, the observed shift of the output field is opposite to the direction of the tilt. This "antisteering" can be reproduced to a high degree by numerical simulations (see Fig.2d). The reason of this surprising behavior is related to the oscillation of the whole light distribution around the stationary state. Because both internal modes have about the same internal frequency, also the quasi-translational mode has accumulated a phase shift of approximately π, when the collapse and the subsequent decay take place. Hence, for this propagation distance any initial asymmetry is reversed. Therefore, the emerging radiation leaves the collapse region in a direction opposite to the initial tilt. We would like to emphasize that only the collapse makes the action of the internal modes visible.

In order to probe these features experimentally we have monitored the output field while varying the incoupled power of the tilted input beam (see Fig.3a). Above a certain threshold a soliton is formed, which is locked to the

input guide. Then in a wide power range only a slight narrowing of the beam is observed. However, if the threshold for collapse is reached the output field suddenly jumps to the side opposite to the initial tilt. For all power levels the quasi-translational mode is excited. However, only after the decay of the basic soliton state it is allowed to propagate away. To verify that the final shift of the output field is indeed due to the break-up of a collapsing field distribution we have varied the tilt of the exciting beam keeping the power constant (see Fig.3b). For normal incidence a symmetric splitting is observed. For an increasing tilt only the part of the output field remains, which is opposite to the initial tilt (compare also Fig.2b and 2d). For even higher initial angles too much power is transferred to the quasi-translational mode. No breathing, or locking occurs. Consequently no decay happens and the beam follows its initial tilt.
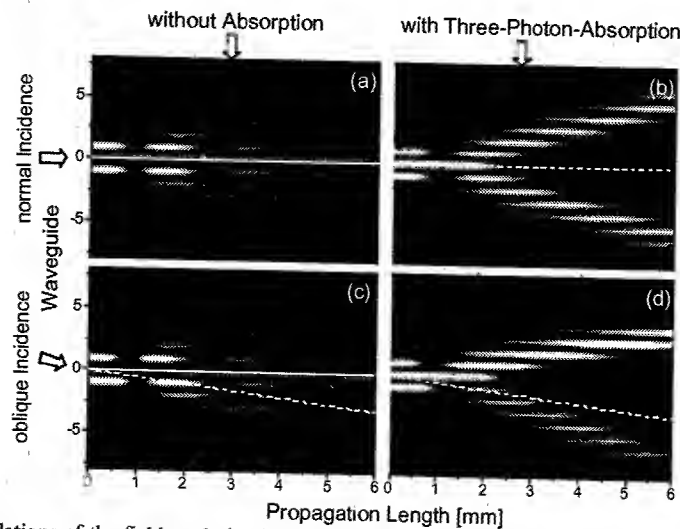
Fig. 2 Numerical simulations of the field evolution in a lossless (first column) and in an array with three-photon-absorption present (second column). Initial beams with normal (first row) and oblique (second row, angle in GaAs: 0.1°) incidence are used (A dashed line marks the direction of linear propagation).
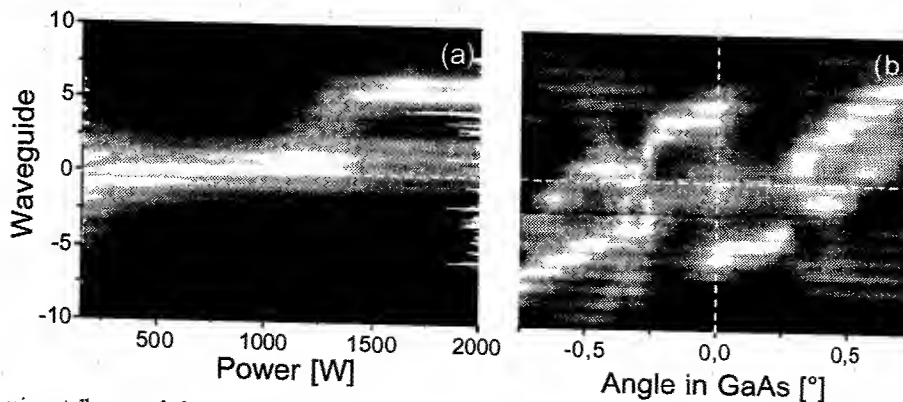
Fig.3 Experimentally recorded output field distributions for a) varying in-coupled peak power (fixed angular tilt of 0.1° in GaAs, dashed line: input guide) and b) varying tilt of the exciting beam (fixed in coupled peak power of 2000W, horizontal dashed line: input waveguide, vertical dashed line: untilted input beam)

In conclusion we have shown that linear modes, which originate from an imperfect excitation can have a major influence the evolution of the basic soliton state. Nonlinear losses induced by three-photon absorption amplify the action of linear modes. If constructive interference between a soliton state and its symmetric internal modes occurs the whole field distribution can collapse into a single guide, where nonlinear absorption eliminates the soliton. The residual field emerges in an almost linear fashion, but initial beam tilts are inversed giving rise to a nonlinearly induced anti-steering.

[1] R.Morandotti, U.Peschel, „J.S.Aitchison, H.S.Eisenberg, and Y.Silberberg, "Dynamics of discrete solitons in optical waveguide arrays," Phys.Rev.Lett.83, 2726 (1999).

[2] M.Johansson, et al, "Dynamics of breathers in discrete nonlinear Schrödinger models," Physica D 119, 115-124 (1998).

Strong Spatiotemporal Localization in an Array of Silica Waveguides

D. Cheskis and S. Bar-Ad
School of Physics and Astronomy, Tel Aviv University, Ramat Aviv
Tel Aviv, Israel, 69978

R. Morandotti and J. S. Aitchison
Department of Electrical and Computer Engineering, University of Toronto,
Toronto, Ontario, Canada, M5S 3G4
Tel: 001-416-9468088   E-mail: roberto.morandotti@utoronto.ca

D. Ross
Department of Electronics and Electrical Engineering, University of Glasgow, Glasgow, Scotland, G12 8QQ

H. S. Eisenberg and Y. Silberberg
Department of Physics of Complex Systems, Weizmann Institute of Science, Rehovot, Israel, 76100.

Abstract: We experimentally investigated beam propagation in an array of silica waveguides, under a regime of anomalous dispersion and for different input conditions. In all the cases, we succeeded in compressing most of the energy in a single waveguide.
©2002 Optical Society of America
OCIS codes: (190.4420) Nonlinear optics, transverse effects in, (190.5530) Pulse propagation and solitons

Strong Spatiotemporal Localization in an Array of Silica Waveguides

D. Cheskis and S. Bar-Ad
School of Physics and Astronomy, Tel Aviv University, Ramat Aviv
Tel Aviv, Israel, 69978

R. Morandotti and J. S. Aitchison
Department of Electrical and Computer Engineering, University of Toronto,
Toronto, Ontario, Canada, M5S 3G4
Tel: 001-416-9468088   E-mail: roberto.morandotti@utoronto.ca

D. Ross
Department of Electronics and Electrical Engineering, University of Glasgow, Glasgow, Scotland, G12 8QQ

H. S. Eisenberg and Y. Silberberg
Department of Physics of Complex Systems, Weizmann Institute of Science, Rehovot, Israel, 76100.

Nonlinear dynamics in discrete systems have recently attracted a significant amount of attention. This interest was stimulated by the fact that stable energy localizations, or *discrete solitons*, can propagate in discrete systems without broadening their distribution. Optical discrete solitons in arrays of nonlinear waveguides are examples of such localized states. First proposed by Christodoulides and Joseph [1], they have been recently demonstrated experimentally [2].

Discrete optical solitons are, in many aspects, similar to continuous solitons. Nevertheless, they present a number of novel and intriguing dynamical properties. For example, arrays of waveguides support both stable and unstable soliton solutions. In these systems, the difference in energy between these two types of solitons, called Peierls-Nabarro potential, accounts for the tendency of discrete solitons to lock to the waveguide direction at high powers, or to acquire transverse momentum and shift sideways when excited in specific ways. The sign and magnitude of diffraction in waveguide arrays can be engineered, with important consequences on the linear and nonlinear properties of such discrete systems.

All experiments in discrete solitons to date have been performed with AlGaAs waveguides. Here we discuss experiments with arrays of silica waveguides, which have anomalous dispersion at wavelengths above 1.3 µm. In these arrays we expect novel spatio-temporal effects, similar to the formation of light bullets in continuous systems [3].

Let us consider first the case of a planar waveguide with a material exhibiting positive nonlinearity and anomalous dispersion. At low energy, dispersion and diffraction tend to spread light in space and time. However, when the intensity is increased, the Kerr nonlinearity tends to compensate for both effects, leading to spatio-temporal compression of the pulse. Since the slab mode is confined along the vertical direction, but it is free to spatially diffract along the horizontal direction and to temporally disperse along the propagation direction, this case is referred to as "1+2". Basic analysis of the propagation of a multidimensional pulse, involving the slowly varying envelope approximation, predicts instability of the pulse in this configuration. In other words, it is expected that the pulse contracts to a single point when the energy of the pulse is higher than a certain critical value. In a recent experiment [3], we showed that multiphoton absorption and intraband Raman scattering counterbalance dispersion and Kerr nonlinearity and are the key factors that prevent a pulse propagating in a glass slab waveguide from undergoing catastrophic self-focusing.

Consider now the case of a one-dimensional array of waveguides, where the spreading of a spatial beam due to continuous diffraction is replaced by discrete coupling between neighbor waveguides. Aceves et al. [4] showed that the main effect of discrete diffraction is to redistribute energy among the waveguides in the array along with the evolution of the pulse in a single waveguide. The discrete nature of the structure effectively acts as a saturable nonlinearity, which prevents the singular growth, in clear contrast with the case of a continuous waveguide. In the limit of very high power, all the light concentrates in a single guide, forming a 1+1 temporal soliton. This process of reducing the dimensionality of the process at high powers should make spatio-temporal focusing in discrete geometry more controllable than in the continuous system.

In this paper we present experimental evidence of such pulse compression in a nonlinear array of optical waveguides. The sample we used in our experiment consisted of 101 weakly coupled buried waveguides, fabricated in flame hydrolysis deposited silica. The core of the waveguides was made of germanium-boron doped silica.

We used a Spectra Physics OPA 800 laser system; generating transform limited pulses with duration of 60 fs, at a wavelength of 1500 nm, resulting in peak powers of up to 20 MW inside the sample. The input spatial profile was varied in order to excite just one or several waveguides, and hence study different initial conditions. Results are presented here for both a narrow and a broad excitation. Let us consider the evolution of the spatial distribution first (Fig.1). The respective low power profiles, recorded at the output facet of the sample, are shown in Fig. 1a) and Fig. 1c). In particular, we note that for a single waveguide excitation, the field is spread to some 60 waveguides at low energy, but collapse almost entirely to a single waveguide at higher powers. When we inject a broader beam, the diffraction is much smaller at low intensity (Fig. 1c)), but again, the field exhibit the same single waveguide compression for higher energies (Fig. 1d)). We recorded the autocorrelation of the temporal profile in both configurations. In contrast to the case of a slab waveguide [3], were the temporal profile was compressed by almost a factor of two, we observed only a small degree of temporal compression in the case of broad excitation (Fig. 2)), suggesting that the discrete structure of our sample counterbalances the tendency to spatio-temporal collapse. In particular, these discrete localizations appear more stable in time and space when compared to their continuous counterpart.

In conclusion, we have experimentally investigated the spatio-temporal propagation of light pulses in arrays of nonlinear waveguides. The arrays, fabricated in glass, exhibit anomalous dispersion together with a positive Kerr nonlinearity. The spatial, temporal and spectral profiles were measured for different input conditions. In all cases, a significant spatial compression of the pulse was observed.
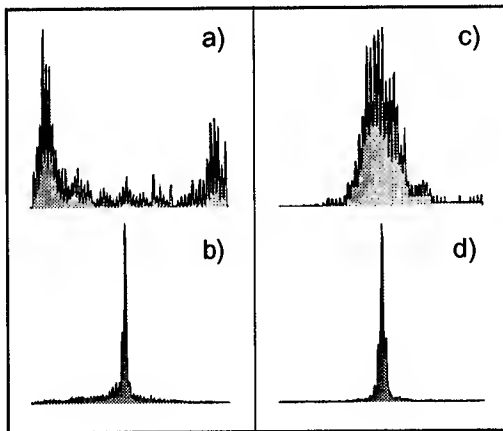
Fig. 1 Output profiles of the field intensity: a) narrow beam excitation, low power; b) narrow beam excitation, high power; c) broad beam excitation, low power ; b) broad beam excitation, high power
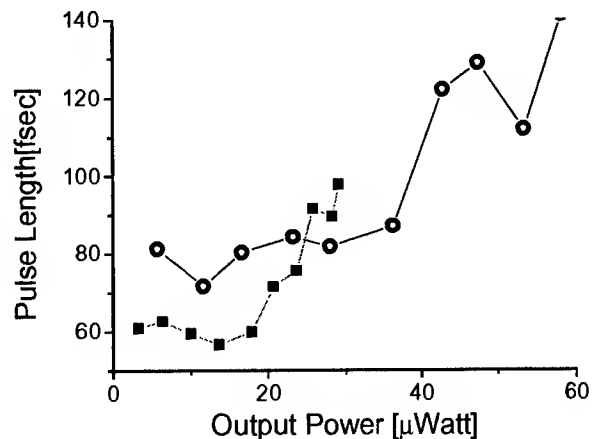
Fig. 2 Autocorrelation width of the output pulse in function of the average output power, for a narrow input excitation (empty circles) and for a broad one (solid squares)

References.

[1] D. N. Christodoulides and R. I. Joseph, "Discrete Self-Focusing in Nonlinear Arrays of Coupled Wave-Guides", Optics Letters, D13, 794-796 (1988).
[2] H. S. Eisenberg, Y. Silberberg, R. Morandotti, A. R. Boyd and J. S. Aitchison, "Discrete Spatial Optical Solitons in Waveguide Arrays", PRL, 81, 3383-3386 (1998).
[3] H. S. Eisenberg, R. Morandotti, Y. Silberberg, S. Bar-Ad , D. Ross and J. S. Aitchison, "Kerr Spatiotemporal Self-Focusing in a Planar Glass Waveguide", PRL, 87, art. no. 043902 (2001).
[4] A. B. Aceves, G. G. Luther, C. De Angelis, A. M. Rubenchik and S. K. Turitsyn , "Energy Localization in Nonlinear Fiber Arrays - Collapse-Effect Compressor", PRL, 75, 73-76 (1995).

Optically-controlled photorefractive soliton arrays

Jürgen Petter

Institute of Applied Physics, Darmstadt University of Technology,
Hochschulstr. 6, D-64289 Darmstadt, Germany
Tel. +49 6151 163122 Fax: +49 6151 164123
juergen.petter@physik.tu-darmstadt.de

Denis Träger, Cornelia Denz

Institut für Angewandte Physik, Westfälische Wilhelms-Universität Münster,
Corrensstr. 2/4, D-48149 Münster, Germany
Tel. +49 251 8333517 Fax: +49 251 8333513
dtraeger@uni-muenster.de denz@uni-muenster.de

Abstract: We present the creation of an optically-controlled array of photorefractive spatial screening solitons in a SBN crystal. Investigating the waveguide properties of each channel by a beam of different wavelength we find them to guide the probe beam independently. A supplementary beam is used to influence the paths of the array-solitons and to effectively combine two channels using mutual attraction of solitons.

OCIS codes: (190.5330) Photorefractive nonlinear optics; (230.7370) Waveguides

1 Introduction

During the last decade it was shown that spatial optical solitons in photorefractive media can easily be exploited for waveguide properties and that they may have a great potential in providing a solution to the problem of all-optical routing and switching. Their properties of mutual interaction and their possible influence on their own paths make all-optical switching feasible. The creation of photorefractive solitons and their characteristics has been and still is studied thoroughly (see e.g. [1, 2, 3]). Their waveguide properties were shown [4] as well as their capability to route or split paths of optical beams [5, 6]. While only few works studied the parallel propagation of several spatial solitons [7, 8], to our knowledge, none of these were performed for the special case of a photorefractive nonlinearity so far.

In this paper we present the creation of an array of coherent solitons propagating in parallel through a photorefractive SBN-crystal [9]. A crucial point in such a parallel propagation is the anisotropic structure of the refractive index and therefore the asymmetric mutual interaction of the solitons. Because of the nonlocality of the electrostatic potential, the refractive index modulation induced by each single soliton reaches beyond its effective waveguide [10]. Therefore, depending on their mutual distance in the incoherent case, solitons may repel, attract or even fuse, as shown in [11]. In the case of mutual coherent solitons their interaction becomes even more complex as their mutual phase may cause exchange of energy between them and annihilation or the creation of solitons my appear [12]. Beside the parallel propagation of several solitons we exploit the mutual attractive force between coherent solitons for the control of the channels in an array. By the use of a separate beam located between two channels of the array we let two solitons fuse to a single output at the back face of the crystal. This demonstrates the potential of an all-optical control of single channels in a large photorefractive soliton array. Furthermore we tested the waveguide properties of such an array using a separate beam of a wavelength that is not influencing the refractive index of the material. Here we find that each channel guides the red probe beam with a high efficiency.

2 Realization of a soliton array

To create an array of solitons in the photorefractive crystal we used a setup similar to the one used in [10]. In our case the beam of an frequency-doubled Nd:YAG-laser emitting at $\lambda = 532\,nm$ is not focused to the front face of a photoreferactive $Sr_{0.60}Ba_{0.40}Nb_2O_6$ (SBN60:Ce) crystal. Instead, the image of a spot array, which is imprinted onto the beam by a spatial light modulator, is imaged to the front face of the crystal. The crystal has dimensions of $5\,mm \times 5\,mm \times 20\,mm$, while the propagation always is along the 20 mm side.

In a first step we examined the creation of the soliton array. A regular pattern of 25 spots with a diameter

Fig. 1. 5 × 5 waveguide array induced by photorefractive solitons. a) Front face of the crystal where the spot-array is imaged. b) Interference patter due to linear propagation of the 25 beams. c) Array of 25 focused solitons.

of 15 μm and an intensity of $\approx 20\,mW/cm^2$ each was imaged onto the front face of the crystal (1a). In the linear case - without an applied electric field - the 25 beams diffract on their way through the crystal and interfere at the back face of the crystal, as depicted in 1b. Applying the electric field of $E_0 = 2\,kV/cm$, the 25 solitons, each with a diameter of about 12 μm (FWHM), form from the interference pattern within several seconds. Due to self-focusing in this nonlinear material every beam caused by one spot of the imaged array forms it's own waveguide. This situation can be seen in fig. 1c. To obtain a propagation without initial mutual interaction we took care of the initial distance between the single channels to be just large enough to let the solitons not interact.

To test for the waveguide properties of the channels of such a soliton array we used a seperate beam of a HeNe-laser to probe the single channels of a 3 × 3 soliton array. Since the photorefractive material is less sensitive to light in the red wavelength region, the induced refractive index modulation could be scanned with an even more intense probe beam without actually being influenced or erased. Positioning the red probe beam successively to the positions of the previously induced solitons on the crystals front face, we found the probe beam to be guided in each of the channels solely.

3   Control of separate channels

In a next step, we performed a controlled interaction between two channels of the array. To exploit the mutual attractive interaction between spatial solitons a third coherent beam causing another soliton is positioned between two adjoining channels. This third beam increases the refractive index between the two existing channels and causes all three solitons to fuse during their propagation through the crystal. To perform this control a separate beam of the Nd:YAG-laser was focused onto the front face of the crystal. This beam in function of a steering beam had an intensity of $\approx 160\ mW/cm^2$ and was positioned between two spots of the array imaged on the crystals front face (see inset of figure 2b). Figure 2a shows the back face of the crystal with the focused, but uncontrolled array. When the control beam was positioned between the central lower two solitons and the electric field was applied, the new soliton array formed. Due to the additional beam between the two lower central channels, the refractive index in between these channels is increased causing the solitons to attract and eventually fuse. Figure 2b shows the red probe beam guided in each channel of the controlled array separately. To obtain a picture of the complete array, every single channel was scanned
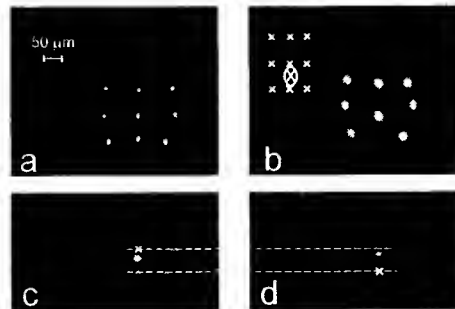
Fig. 2. Optical control of a soliton array. a) The uncontrolled soliton array. b) The controlled array probed by a read beam. c) and d) The probe beam coupled into the central and the lower middle channel of the controlled array, respectively. The probe beam leaves the crystal at the same position.

separately. Afterwards, the nine individual pictures were added electronically. In this figure the fusion of the two lower middle channels is obvious. Therefore, the case of coupling the probe beam into the central or the lower middle channel on the front face of the crystal leads to guiding it into the same output. This also can be seen in figures 2c and d. Here the probe beam was coupled into either of the two channels alternatively, but leaves the crystal at the same spot on its back face (the crosses mark the position of the exit of the channels in the uncontrolled array). This shows to our knowledge for the first time the control of single channels of an waveguide array just by a beam of light.

As shown in [7] for a Kerr-type material, also in our case the formation of larger soliton-patterns is not limited to symmetric figures or arrays. As an example, we imaged the pattern of the letters A and P as a spot array onto the front face of the crystal (figure 3a). Once the external electric field was applied, the solitons formed out of the interference pattern and clearly reproduced the image of the two letters (figure 3c).
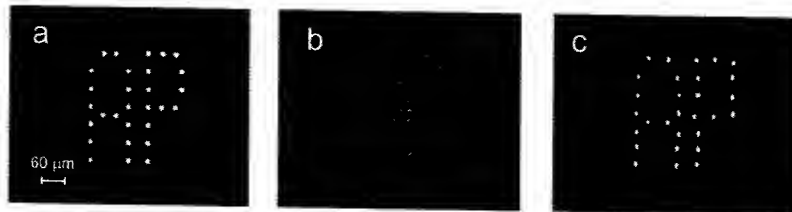
Fig. 3. Image processing with photorefractive solitons. a) Spot pattern at the front face of the crystal. b) Diffraction pattern of the beams at the back face of the crystal. c) Reconstruction of the image with focused soliton beams.

4 Conclusion

We presented to our knowledge the first control of an array of photorefractive solitons by a separate beam of light. We were able to show that a stable propagation of several parallel solitons and therefore the formation of a waveguide array is possible. Additionally we show that the all-optical control of single channels of such an array is possible by inducing a determined fusion of two channels, creating a Y-coupler within the waveguide array. Up to now all experiments were realized with mutually coherent beams. In the case of mutually incoherent beams a more stable propagation of the beams can be expected.

References

1. M. Segev, B. Crosignani, A. Yariv, B. Fischer, "Spatial solitons in photorefractive media", Phys. Rev. Lett. **68**, 923-6 (1992)
2. M. Mitchell, M. Segev, T. H. Coskun, D. N. Christodoulides, "Theory of self-trapped spatially incohrerent light beams", Phys. Rev. Lett. **79**, 4990-4993 (1997)
3. C. Weilnau, W. Królikowski, E. A. Ostrovskaya, M. Ahles, M. Geisser, G. McCarthy, C. Denz, Y. S. Kivshar, B. Luther-Davies, "Composite spatial solitons in a saturable nonlinear bulk medium", Appl. Phys. B DOI 10.1007/s003400100546 (2001)
4. M. Shih, Z. Chen, M. Mitchell, M. Segev, H. Lee, R. Feigelson, J. P. Wilde, "Waveguides induced by photorefractive screening solitons", J. Opt. Soc. Am. B **14**, 3091-3101 (1997)
5. S. Lan, E. DelRe, Z. Chen, M. Shih, M. Segev, "Directional coupler with soliton-induced waveguides", Opt. Lett. **24**, 475-478 (1999)
6. J. Petter, C. Denz, "Guiding and dividing waves with photorefractive solitons" Opt. Comm. **188**, 55-61 (2001)
7. A. Bramati, W. Chinaglia, S. Minardi, P. Di Trapani, "Reconstruction of blurred images by controlled formation of spatial solitons" Opt. Lett. **26**, 1409-1411 (2001)
8. M. Soljacić, S. Sears, M. Segev, "Self-trapping of "Necklace" beams in self-focusing Kerr media", Phys. Rev. Lett. **81**, 4851-4854 (1998)
9. J. Petter, D. Träger, C. Denz, "Optical control of arrays of photorefractive screening solitons", Opt. Lett. (submitted)
10. J. Petter, C. Denz A. Stepken, F. Kaiser, "Anisotropic waveguides induced by photorefractive (2+1)D-solitons", J. Opt. Soc. Am. B, **19** (2002), accepted for publication.
11. W. Królikowski, M. Saffman B. Luther-Davies, C. Denz, "Anomalous interaction of spatial solitons in photorefractive media", Phys. Rev. Lett. **80**, 3240-3 (1998)
12. W. Królikowski, C. Denz, A. Stepken, M. Saffman, B. Luther-Davies, "Interaction of spatial photorefractive solitons", Quantum Semiclass. Opt. **10**, 823-837 (1998)
13. W. Królikowski, S. Holstrom "Fusion and birth of spatial solitons upon collision", Opt. Lett. **22**, 369 (1997)

Discrete solitons in optically-induced real-time waveguide arrays

J. W. Fleischer[(1,2)], T. Carmon[(1)], M. Segev[(1,2)], N. K. Efremidis[(3)], and D. N. Christodoulides[(3)]

[1]*Physics Department, Technion –Israel Institute of Technology, Haifa 32000, Israel*
[2]*Electrical Engineering Department, Princeton University, New Jersey 08544*
[3]*School of Optics/CREOL, University of Central Florida, Florida 32816-2700*

Wave propagation in nonlinear periodic systems has recently been the focus of considerable attention. In these systems, the underlying dynamics are dominated by the interplay between the linear coupling between lattice points and the on-site nonlinearity. Indeed, a balance between these effects results in a self-localized state, better known as a discrete soliton [1-4]. Such examples occur in abundance, in all branches of science, such as biological [1] and solid-state physics [2], Bose-Einstein condensates [3], and nonlinear optics [4]. In general, the dynamical behavior of these discrete systems differs substantially from that of their continuous counterparts. For example, in the optical case, a periodic array of waveguides is associated with a Brillouin zone that significantly alters its collective diffraction properties. This, in turn, leads to a host of interesting properties, e.g. anomalous ("negative") diffraction and diffraction management [5], and to in-phase and out-of-phase (staggered) [6] soliton solutions. Thus far, 1D discrete linear diffraction and in-phase discrete solitons have been observed in semiconductor waveguide arrays [8]. Here, we report the first experimental observation of discrete solitons in an array of optically-induced waveguides. The waveguide arrays are induced in photorefractive crystals by interfering pairs of plane waves, and the solitons form when the screening nonlinearity is employed. We demonstrate both in-phase and staggered bright solitons in 1-D arrays and discuss recent experiments in 2D waveguide lattices. More specifically, the experiments with out-of-phase solitons constitute the first experimental observation of bright staggered solitons.

In optical waveguide arrays [4-8], when light propagation is linear, a beam focused in one waveguide will spread to its neighbors (via discrete diffraction, or tunneling), with the intensity mainly concentrated in the outer lobes. When the nonlinearity is sufficiently high (e.g., at high intensities if the nonlinearity is Kerr-type), the nonlinearity suppresses the coupling between adjacent waveguides. The combined effects of discrete diffraction and nonlinearity lead to discrete solitons, as predicted more than a decade ago [4], and observed in 1998 [8] in a fabricated 1-D array of AlGaAs waveguides. In a recent theoretical work [9], we have shown that optical discrete solitons are possible in biased photorefractive crystals. In this scenario, the photorefractive nonlinearity is utilized to optically-induce in real time waveguide arrays (either in 1D or 2D) by interfering pairs of plane waves. Note that similar techniques have been suggested in Bose-Einstein condensates [10], but, as of yet, the nonlinearity of the Gross-Pitaevskii system (in BEC) has not manifested itself in discrete soliton formation. In constructing the optically-induced waveguide arrays in photorefractives, it is essential that the waveguides are as uniform as possible. Therefore, the coupling between the interfering plane waves (forming the waveguide arrays) must be eliminated, so that the interference pattern does not vary in the propagation direction. The "signal" soliton-forming beam, on the other hand, must experience the highest possible nonlinearity. To achieve these two, seemingly conflicting, objectives, we choose a photorefractive crystal with a strong electro-optic anisotropy, polarize the interfering waves in a non-electro-optic direction, and at the same time polarize the signal beam in the crystalline orientation that yields the highest possible nonlinearity. In this arrangement, two (or more) interfering plane waves polarized perpendicular to the crystalline c-axis will propagate mostly linearly, while a signal beam polarized along the c-axis will experience both a periodic potential and a significant (screening) nonlinearity.

In our experiments, we use a 6mm long SBN-75 crystal, where $r_{33} \sim 1340$ pm/V and $r_{13} \sim 67$ pm/V. The 1D array is created by interfering ordinarily polarized light through a Mach-Zehnder interferometer. The signal beam is an extraordinary polarized beam that is coupled into a single waveguide. Voltage applied against the c-axis sets the photorefractive screening nonlinearity: it increases (with a nonlinear intensity dependence) the index contrast and creates a waveguide array, and also leads to localization of the signal beam. At the same time, the nonzero

electro-optic coefficient for the interfering waves allows a sufficiently high applied field to create a 2D waveguide array through the break-up of the 1D interference pattern (by transverse modulational instability).

Figures 1-3 show results from our 1D experiments. Figure 1 depicts the transition of the signal beam from discrete diffraction to discrete soliton for on-axis input as a function of increasing self-focusing nonlinearity (applied voltage). The array has a waveguide spacing of 8.8 μm, and the laser power of 200mW is divided between the array beam and the signal with an intensity ratio of 5:1. At low intensities, the signal beam experiences linear discrete diffraction: when the signal beam initially excites a single waveguide, two intensity lobes (separated by 3 waveguides) appear at the output (Figures 1A-B). On the other hand, in the nonlinear regime, a highly localized discrete soliton is formed (Figures 1E-F).

Figure 2 shows similar results when the signal beam is incident at an angle of 0.57^0 with respect to the crystal and is focused into a single waveguide of a 9.3 μm grating or waveguide array. In this case, the applied bias has been reversed (defocusing nonlinearity) and the "Bloch momentum" of the signal lies in the vicinity of the first Brillouin zone edge (~0.62°). As a result, because of anomalous diffraction, a staggered (π out-of-phase) bright soliton (as predicted in [6]) is observed (Figures 2E-F). For these results, the laser power was 300mW and was divided into a 10:1 ratio between the array and the signal.

Figure 3 shows in-phase and staggered bright solitons for a grating spacing of 7.8 μm. Figure 2A shows a discrete soliton created on-axis (in-phase), as in Figure 1, while Figure 2B is the corresponding interferogram (created via interference with a co-propagating plane wave) showing that all the lobes are in-phase with each other. Figure 2C shows a staggered discrete soliton produced at the edge of the first Brillouin zone, while the interferogram in Figure 2D shows that the central lobe is out of phase with its neighbors (constructive interference in the center and destructive interference at the outer lobes). There are two critical features to note: 1) the Brillouin edge *is defined by* $k_x D = \pi$, where D is the lattice spacing, guaranteeing that the signals in neighboring waveguides are π out of phase, and 2) the edge is in an **anomalous diffraction** region of the dispersion curve, so that an **attractive nonlinearity is created by applying a negative voltage to the crystal** (out-of-phase beams repel in a region of positive focus). **This exciting prospect of reversing both diffraction and nonlinearity can only be achieved in dynamical systems such as photorefractive crystals or Bose-Einstein condensates.**

Figure 4 shows results from a 2D experiment. In this case, the applied field was raised to 2.0 kV/cm to induce transverse (modulational) instability along the 1D waveguides. The resulting interference pattern generated an ordered 2D lattice of 2D waveguides (Figure 2A). The waveguides are elliptically-shaped (major and minor axes of 25 μm and 9.4 μm, respectively) with separation distances of 40 μm and 13.5 μm, respectively. Illuminating the central portion of the 2D array (Figure 2B) by a broad beam ("plane wave") shows clear evidence of 2D guidance (Figure 2C). Similar 2D waveguide structures can also be induced using four interfering plane waves. In the near future, using such a scheme, we anticipate the experimental observation of 2D optically-induced discrete solitons.

In conclusion, we have reported the first observation of discrete solitons in a 1D array of optically-induced waveguides. These experiments are also the first observations staggered discrete solitons in any medium. This work paves the way for the first experimental observation of 2D discrete solitons.

References

[1] A.S. Davydov, J. Theor. Biol. **38**, 559 (1973).
[2] W.P. Su, J.R. Schieffer, and A.J. Heeger, Phys. Rev. Lett. **42**, 1968 (1979); A.J. Sievers and S. Takeno, Phys. Rev. Lett. **61**, 970 (1988).
[3] A. Trombettoni and A. Smerzi, Phys. Rev. Lett. **86**, 2353 (2001).
[4] D.N. Christodoulides and R.1. Joseph, Opt. Lett. **13**, 794 (1988).
[5] H.S. Eisenberg, Y. Silberberg, R. Morandotti, and J. Aitchison, Phys. Rev. Lett. **85**, 1863 (2000).
[6] Y.S. Kivshar, Opt. Lett. **18**, 1147 (1993.)
[7] A. Aceves, D. De Angelis, T. Peschel, R. Muschall, F. Lederer, S. Trillo, S. Wabnitz, Phys. Rev. E **53**, 1172 (1996).
[8] H. S. Eisenberg, Y. Silberberg, R. Morandotti, A. R. Boyd, and J. S. Aitchison, Phys. Rev. Lett. **81**, 3383 (1998).
[9] N. K. Efremidis, J. Hudock, D. N. Christodoulides, J.W. Fleischer, S. M. Sears, and M. Segev, Discrete solitons in photorefractive optically-induced photonic lattices, **submitted to PRL.**
[10] C. Orzel, A.K. Tuchman, M.L. Fenselau, M. Yasuda, and M.A. Kasevich, Science **291**, 2386 (2001); M. Greiner, O. Mandel, T. Esslinger, T.W. Hansch, and I. Bloch, Nature **415**, 39 (2002).

Increasing Positive Voltage

Increasing Negative Voltage
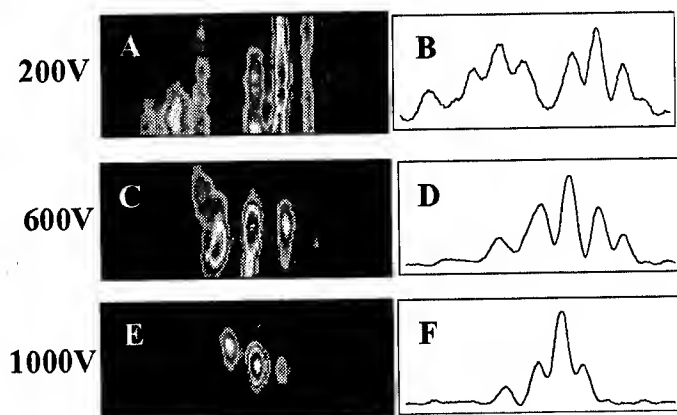
Figure 1. On-axis behavior as a function of increasing focusing nonlinearity (positive voltage) through an 8.8 μm grating. Crystal output and intensity profile for 200V (A,B), 600V (C,D), and 1000V (E,F).
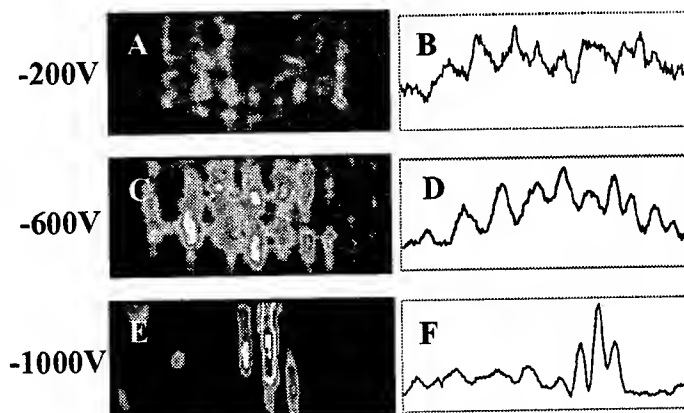
Figure 2. Angled probe (0.57°) behavior with increasing defocusing nonlinearity (negative voltage) through a 9.3 μm grating. Crystal output and intensity profile for –200V (A,B), -600V (C,D), and –1000V (E,F).

+800V   -1000V
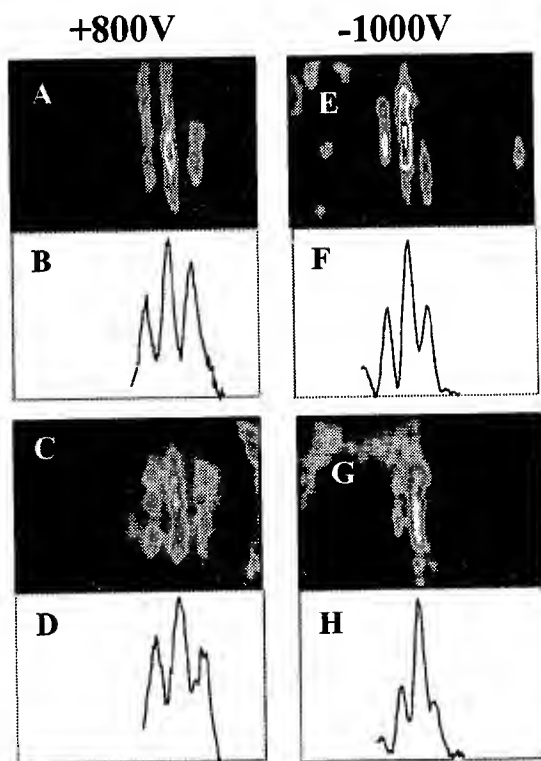
Figure 3. On-axis and staggered solitons through a 7.8 μm waveguide array. Crystal output and intensity profile for on-axis soliton at +800V (A,B) and staggered soliton at –1000V (E,F). Interferograms for the respective cases, showing in-phase behavior for the on-axis input (C,D) and out-of-phase behavior at the edge of the first Brillouin zone (G,H).
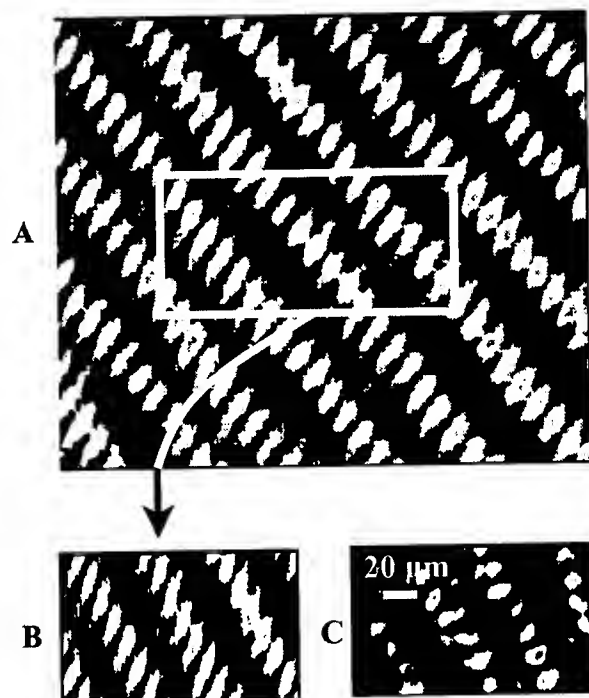
Figure 4. Waveguiding in optically-induced two-dimensional array. (A) Induced array with major and minor separation distances of 40 μm and 13.5 μm, respectively. (B) Close-up of central waveguide region. (C) Waveguiding of plane wave input into central region.

Dissipative Spatial Structures

Tuesday, September 3, 2002

Luigi Alberto Lugiato, Univ. Degli Studi Dell'Insubria, Italy
Presider

NLTuB
10:30am – 12:30pm
Auditorium

Interaction of dissipative localized structures in nonlinear optics

Dmitry V. Skryabin

Department of Physics, University of Bath, Bath BA2 7AY, United Kingdom
d.v.skryabin@bath.ac.uk; fax: 44 (1225) 386110

Localized structures of light in optical cavities – cavity solitons – have attracted significant attention in recent years. This is largely due to some striking experimental observations [1-4] and the variety of complex and interesting nonlinear phenomena involved in their stability [5,6], interaction [7-10] and control [2,3,5,11]. The last aspect also gives some hope for potential application of these structures for optical processing of information.

Problems related to cavity solitons can be naturally divided into two subcategories. One is related to the solitons in coherently pumped cavities, where phase of the intracavity field is locked to the phase of the external pump and the other is the solitons in the lasers with saturable absorbtion. Both systems exhibit phenomenon of optical bistability, which can be considered as one of the essential prerequisites for existence of the cavity solitons.

Cavity solitons are typically excited by a localized address pulse of light [2,3,5] and therefore independent solitons can be created at arbitrary non-overlapping address locations. If, however, they are excited sufficiently close one to another, then they exert mutual forces due to overlap of their tails. Through these forces, cavity solitons can group themselves into geometrical configurations, which we will refer below as *clusters*.

In this work we will report series of recent results on existence and stability of two dimensional clusters of cavity solitons. Focusing our analysis on the most interesting cases the $2D$ clusters which do not have analogs in the $1D$ geometry, e.g. triangles and squares. This type of structure has been previously observed in optical cavities both experimentally [3] and numerically [13-15].

We develop a technique for calculation of the expression for the interaction potential, which has applicability going beyond the models under consideration. Considering clusters in the coherently pumped cavities, where the phase degree of freedom is eliminated, we, among other problems, discuss the qualitative differences between stability properties of triangular and square clusters, which emphasize the role of diagonal interactions in the latter. In the lasers, where, cavity solitons have the phase degree of freedom we have found variety of dynamical clusters, which can, e.g., move or rotate with strictly fixed velocities, and transform one to another and the influence of different instabilities. We also propose a theory, which can qualitatively explain recent experimental observations of the circular arrangement of dissipative solitons in the presence of the gaussian pump field [12].

---

[1] M. Saffman, D. Montgomery, and D.Z. Anderson, Opt. Lett. **19**, 518 (1994).
[2] V.B. Taranenko, K. Staliunas, and C.O. Weiss, Phys. Rev. A **56**, 1582 (1997); K. Staliunas, V. B. Taranenko, G. Slekys, R. Viselga, and C. O. Weiss, Phys. Rev. A **57**, 599 (1998).
[3] V.B. Taranenko, I. Ganne, R.J. Kuszelewicz, and C.O. Weiss, Phys. Rev. A **61**, 063818 (2000).
[4] S. Barland, M. Giudici, J.R. Tredicce, L. Spinelli, G. Tissoni, L.A. Lugiato, and M. Brambilla, "Cavity solitons in one-dimensional semiconductor amplifiers: Experiment and theory agree", in *Nonlinear Guided Waves and Their Applications*, OSA Technical Digest (Optical Society of America, Washington DC, 2001), pp. 2-4.
[5] W.J. Firth and A.J. Scroggie, Phys. Rev. Lett. **76**, 1623 (1996);
[6] D.V. Skryabin, Phys. Rev. E **60**, R3508 (1999).
[7] S. Longhi, Phys. Rev. E **53**, 5520 (1996); *ibid.* **55**, 1060 (1997).
[8] I.V. Barashenkov, Y.S. Smirnov, and N.V. Alexeeva, Phys. Rev. E **57**, 2350 (1998).
[9] D.V. Skryabin and W.J. Firth, Opt. Lett. **24**, 1056 (1999).
[10] T. Maggipinto, M. Brambilla, G.K. Harkness, and W.J. Firth, Phys. Rev. E **62**, 8726 (2000).
[11] M. Brambilla, L.A. Lugiato, and M. Stefani, Europhys. Lett. **34**, 109 (1996).
[12] B. Schäpers, M. Feldmann, T. Ackemann, and W. Lange, Phys. Rev. Lett. **85**, 748 (2000).
[13] N.N. Rosanov and G.V. Khodova, J. Opt. Soc. Am. B **7**, 1057 (1990); N.N. Rosanov, Prog. Opt. **35**, 1 (1996).
[14] N.N. Rozanov, *'Optical bistability and hysteresis in distributed nonlinear systems'* (Moscow, Nauka, Fizmatlit, 1997).
[15] M. Tlidi, P. Mandel, and R. Lefever, Phys. Rev. Lett. **73**, 640 (1994).

Cavity Pattern Formation with Incoherent Light

Tal Carmon and Mordechai Segev

Physics Department, Technion - Israel Institute of Technology, Haifa 32000, Israel

Marin Soljačić

Physics Department, Massachusetts Institute of Technology, Cambridge, MA

We present the **first observation of cavity modulation instability and pattern formation with incoherent light**. In addition, we also study, theoretically and experimentally, the evolution of patterns in a nonlinear **cavity without resonant frequencies**: a passive cavity for which beams from different cycles are mutually-incoherent with one another.

Cavity Pattern Formation with Incoherent Light

T. Carmon,[1] M. Segev[1] and M. Soljačić[2]

(1) Physics Department, Technion - Israel Institute of Technology, Haifa 32000, Israel

(2) Physics Department, Massachusetts Institute of Technology, Cambridge, MA, USA

Pattern formation in optical cavities has been studied since lasers were discovered [1]. Patterns start when particular frequencies are selected from noise, because they experience higher gain, and, through the cavity feedback, stabilize to form a pattern. Examples include the formation of stripes, hexagons, spirals, vortices, shock waves, complex ring, and lattice-like features [for a review see Ref.[2]]. These phenomena were observed in a variety of materials: laser gain media, photorefractive crystals, thermal nonlinearities, quadratic nonlinearities, and more [3]. What signifies cavity effects from one-way propagation, is the existence of a threshold for pattern formation and the existence of resonant frequencies. In cavities, pattern formation exhibits different features below and above the threshold. The patterns are also highly affected by the detuning between the frequency of the light beam and the nearest resonant frequency of the cavity. However, for all of the resonators studied previously, pattern formation is a fully coherent process, that is, the coherence length of the light is much larger than the cavity length.

Here we present the **first experimental observation of cavity modulation instability and pattern formation with incoherent light**. In addition, we also study, theoretically and experimentally, the evolution of patterns in a nonlinear **cavity without resonant frequencies**. This is passive cavity for which beams from different cycles are mutually-incoherent with one another.

Starting with the most interesting result, we construct a partially spatially-incoherent cavity by passing a laser beam through a rotating diffuser, and then circulating it in a ring cavity. The characteristic speckle size of the diffuser sets the spatial correlation distance of the beam. The nonlinearity in our cavity is an SBN:60 photorefractive crystal displaying the screening nonlinearity, in which, in contradistinction with previous studies in photorefractive cavities (see some of the references in [3]), there is no energy exchange between beams from different cycles in the cavity. In this cavity, beams from different cycles interact with one another through a nonlinear index change, Δn, that is a function of the sum of the intensities of the circulating beams, but does not depend on interference terms between beams of different cycles. Our cavity is passive, i.e., the coherence properties of the light cannot be altered by amplification (keeping in mind the Law of Brightness), although the local correlation properties highly depend on the evolving pattern. As found previously [4], at zero feedback the beam undergoes a breakup due to modulation instability. However, the modulation instability (MI) occurs only if the nonlinearity is above a certain sharp threshold. Physically, this threshold occurs when the nonlinear attractive tendencies become just large enough to counteract the diffusive tendencies of the spatially incoherent beam. Note that such a threshold at zero feedback does not exist in the usual coherent-beam MI; for a coherent beam, modulation instability (albeit small) is present even for arbitrarily small nonlinearities [5]. This MI threshold is of a very different nature than any cavity threshold, including in an incoherent cavity. Consequently, once we turn on the feedback, we expect to have two very different thresholds occurring in our system simultaneously: the first threshold comes about from the MI threshold, above which the self-focusing tendencies overcome the diffusive tendencies of the incoherent light and a pattern forms. The second threshold results from the cavity threshold, which is set by the cavity losses. Because the origin of these two thresholds is of so different nature, their interplay offers an interesting new physical regime to explore.
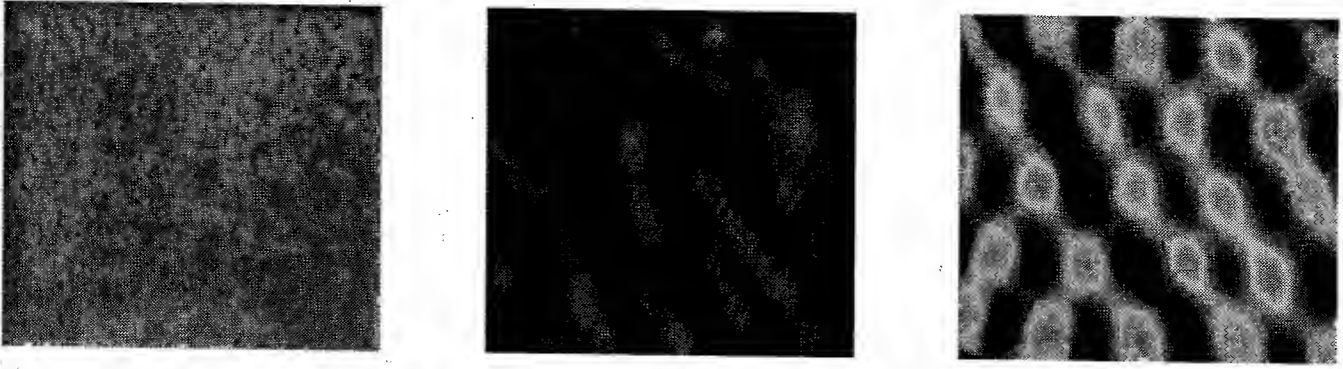
Figure 1: Intensity at the output face of the nonlinear crystal. The panel on the left shows the output when nonlinearity is off. The middle panel shows the output when nonlinearity is on, and above the modulation instability threshold, but the feedback is zero. The panel on the right shows the output when both the nonlinearity, and the feedback are on, and we operate in the regime above both the modulation instability threshold, and cavity threshold.

Typical results of our preliminary experiments are shown in Fig. 1. The left panel of that figure shows that there are no patterns observable at the output when the non-linearity is turned off. The middle panel shows the observation of the output when non-linearity is on, and above the modulation instability threshold, but there is no feedback; as we explained above, the output beam does show features, but their visibility is very small (because the nonlinearity is considerably weaker than that in the experiments presented in [4]). The right panel shows the result once we also turn on a significant amount of feedback. The features of the middle panel become much more pronounced. More significantly, these features become much more uniform in their distribution of sizes; this is a clear sign of the **line-narrowing (of the spatial spectrum)** which one expects to occur close to, and above, the cavity threshold. We are currently working on the theory describing spatially-incoherent cavities, and it is already obvious that it will greatly differ from all known theories of pattern formation in coherent feedback systems, including those in single-mirror feedback, because for spatially-incoherent light the spatial correlation statistics plays a key role.

Next we study a cavity which circulates a spatially-coherent light beam but in which beams from different cycles are mutually-incoherent with one another. We find, theoretically and experimentally, that the patterns emerging in our incoherent cavity exhibit line-narrowing in the spatial frequency domain as feedback is increased. Theoretically, we analyze the interaction between an input wave Ψ, with a wave Φ that went around the cavity loop once (Fig 2a). The governing equations in nonlinear Kerr medium are

$$i\frac{\partial \Psi}{\partial z} + \frac{\partial^2 \Psi}{2 \partial^2 x} + I\Psi = 0; \quad i\frac{\partial \Phi}{\partial z} + \frac{\partial^2 \Phi}{2 \partial^2 x} + I\Phi = 0 \quad , \tag{1}$$

where I (the total intensity) is $|\Psi|^2 + |\Phi|^2$. Assuming a weak feedback, and after some algebra, we find the field distribution in the spatial frequency domain (q) at the output of the nonlinear medium, to be

$$\hat{\psi}_1(q, z = L) \approx \hat{\psi}_1(q, z = 0) \exp(|g|L)/(1 - \varepsilon^2 \exp(|g|L)) \quad . \tag{2}$$

Where ε^2 is the intensity fraction that is recycled in the cavity, and g, the growth rate, is equal $|q|\sqrt{q^2/4 - |\Psi(z=0)|^2}$. For $\varepsilon = 0$, this relation converges to the known result of modulation instability in a system without feedback [5]. Notice that increasing the feedback ε leads to line-narrowing of the periodic pattern in the spatial frequency domain. As the feedback is increased and reaches a specific (threshold) value, there is a particular transverse wavelength q for which Eq. 2 diverges. As the feedback approaches the threshold value, the linewidth becomes very narrow as the particular q dominates. These

features are apparent in Fig. 2b, which shows the calculated bandwidth of $|\psi_1|^2$ as a function of the feedback.

Experimentally, we use a 488nm laser beam with a coherence length much smaller than the ring cavity length. The beam is launched into the 5.5 mm long crystal, and covers its entire input face uniformly. Taking the beam exiting the crystal, we recycle a measured fraction of its intensity in feedback loop of the ring cavity. We use lenses in the cavity pass to image the output face of the crystal on the input face (1:1 imaging). The lens diameter is large enough to pass all the spatial frequencies in the system. We monitor the patterns at the output face of the crystal (using a camera) while increasing the feedback (starting from zero feedback) and keeping all other parameters fixed (especially those which influence the nonlinearity). The results are shown in Fig.3. The linewidth narrowing is very obvious in these pictures, as feedback increases.

We compare the theoretical prediction and the experiments by plotting the measured spatial linewidth as a function of feedback intensity, as shown in Fig. 2b. Comparing the prediction to the experimental results proves that theory truly describes the behavior of the experimental system all the way from zero feedback to the threshold limit. Very close to the threshold and above it, the assumptions made in the theory are no longer valid. Experimentally, however, we obtain the functional line-narrowing behavior above the threshold value as well, all the way to the narrowest linewidth possible in our system.

Our present work on patterns in a nonlinear cavity which has no resonant frequencies, can bridge the gap between pattern formation in cavities and in single-mirror systems. The characteristic behavior resembles the linewidth narrowing in laser systems. In general, this behavior characterizes systems undergoing a phase transition. We expect that other phase transition phenomena should exist in our cavity with no resonant frequencies, and that they will have intriguing implications in a way that is very different than in coherent cavities. For example, critical slowing down near the threshold should offer new and exciting features that are different than those observed before with coherent cavities. Furthermore, in the case of incoherent beams, the beams from different cycles are incoherent with one another both in space and in time. Yet, from such a perfectly disordered system, clear order emerges in nonlinear non-instantaneous cavities. The interplay of the two physically very different thresholds that are both present in the system at the same time presents a new exciting regime to explore. We are not aware of any other systems in nature that have this characteristic.

References

[1] W. W. Rigrod, Appl. Phys. Lett. **2**, 51 (1963)

[2] F. T. Arecchi, S. Boccaletti and P.L. Ramazza, Phys. Rep. **318**, 1 (1999)

[3] W.J. Firth, A.J. Scroggie, Europhys. Lett. **26**, 521 (1994); Phys. Rev. Lett. 76, 1623 (1996); S. R. Liu and G. Indebetouw, J. Opt. Soc. Am. B 9, 1507 (1992); K. Staliunas, M. F. H. Tarroja, G. Slekys, and C. O. Weiss, Phys. Rev. A 51, 4140 (1995); Phys. Rev. Lett. 79, 2658, (1997); Z. Chen, D. McGee, and N. B. Abraham, JOSAB, **13**, 1482 (1996); T. Honda, Opt. Lett. **18**, 598 (1993); S. J. Bentley, R. W. Boyd, W. E. Butler and A. C. Melissinos, Opt. Lett. 26, 1084 (2001).

[4] M. Soljačić, M. Segev, T. Coskun, D. N. Christodoulides, and A. Vishwanath, Phys. Rev. Lett. **84**, 467 (2000); D. Kip, M. Soljacic, M. Segev, E. Eugenieva, and D. N. Christodoulides. Science, **20**, 290 (2000)

[5] G. Agrawal, Nonlinear Fiber Optics, Academic Press, 134, (1995)

Figure Captions

Figure 2: (a) The incoherent ring resonator (schematic). (b) Bandwidth of the spatial frequency power spectrum (FWHM) as a function of feedback intensity, for spatially coherent light. The experimental results below and above threshold are shown by the crosses. The theoretical results below threshold (solid curve) are based on Eq. 2 and the actual experimental parameters. The dashed curve above threshold is a guide to the eye.

Figure 3: Experimental results, bandwidth narrowing while increasing feedback intensity, for spatially coherent beams. Shown are photographs of the intensity distribution in a specific region at the crystal output (left), along with the calculated spatial power spectrum (right), at various feedback values. All measurements are taken without moving the crystal and without changing the nonlinearity. Bandwidth narrowing is obvious: the stripes become more sharp and regular with increasing feedback, and the spatial power spectrum goes from multiple peaks (at no feedback) to two isolated narrow peaks at high feedback.
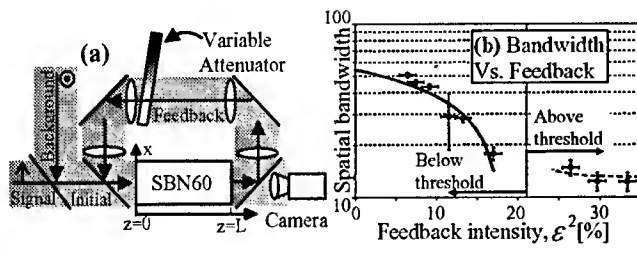
Figure 2
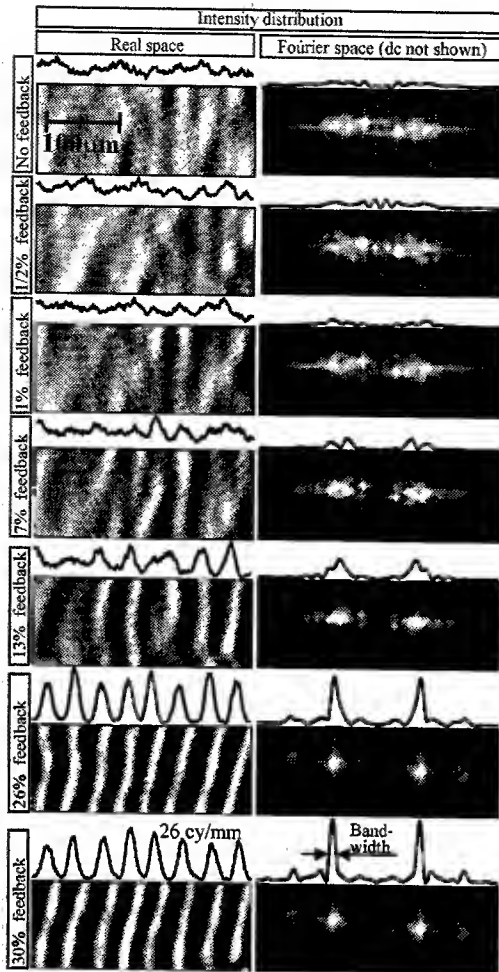
Figure 3

Self-propelled solitons and moving patterns in a nonlinear resonator

A. J. Scroggie, J. M. McSloy and W. J. Firth

Department of Physics and Applied Physics, University of Strathclyde
Glasgow G4 0NG, Scotland.

Phone (+44)141 5483269 ; FAX (+44)141 5522891
`email:willie@phys.strath.ac.uk`

Abstract: Spontaneously moving bright and dark spatial solitons and patterns are shown to exist in a nonlinear resonator. The motion is caused by thermal effects and arises through an instability of the stationary soliton.

Self-propelled solitons and moving patterns in a nonlinear resonator

A. J. Scroggie, J. M. McSloy and W. J. Firth

Department of Physics and Applied Physics, University of Strathclyde
Glasgow G4 0NG, Scotland.

Phone (+44)141 5483269 ; FAX (+44)141 5522891
email:willie@phys.strath.ac.uk

Stationary spatial solitons are a common feature of nonlinear optical cavity systems [1, 2, 3]. As localised, addressable spots of light these "cavity" solitons suggest themselves as natural elements in all–optical information processing and storage. It is known [4, 5] that parameter gradients, whether externally imposed or due to device inhomogeneities, induce soliton motion characterised by a purely position–dependent velocity. This is important for the manipulation and control of the solitons.

Here we demonstrate the existence of cavity solitons (both bright and dark) which undergo *spontaneous* motion. These are investigated in an alternative model to that presented in [6, 7] which gives a resonable approximation of spatio-temporal dynamics within a semiconductor microcavity. Our model of this nonlinear cavity describes the evolution of the optical field, the temperature of the nonlinear medium and the carriers which give rise to the nonlinearity. Localised, field-induced temperature changes create natural parameter gradients along which the soliton moves. In turn, translation of the soliton changes the temperature profile, in a self-consistent process which produces uniform translation (Figure 1). Moving solitons appear through an instability of the stationary solitons, when the thermal coupling exceeds a threshold value. Using both numerical and semi–analytical approaches we derive an equation of motion and determine that the moving solitons emerge from the stationary soliton through a supercritical bifurcation. We find that this leads to a position dependent acceleration of the structure and we note that this bifurcation has similarities to the Ising-Bloch transition of References [8, 9]. The same temperature–induced gradients can give rise to spontaneously translating *patterns* as well as isolated moving solitons.
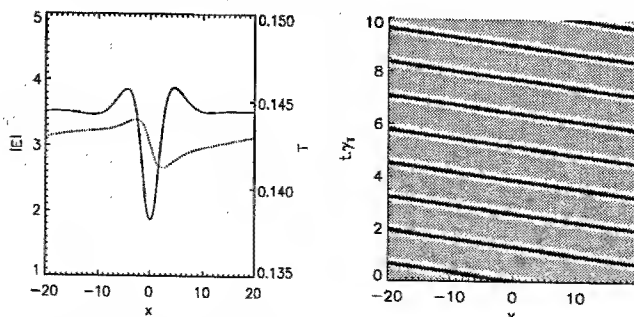
Fig. 1. Left: Electric field (solid) and thermal profile (dashed) of a moving, dark soliton. Right: Space-time plot of such a moving dark soliton.

We demonstrate interactions of moving solitons, an example of which is shown in Figure 2. Two moving solitons approach each other, form a metastable bound state, undergo some complicated dynamics and are subsequently ejected. We also show the effects on the motion of solitons of device inhomogeneities, where solitons move in modulated landscapes. Finally we highlight novel applications arising from these effects such as a *soliton factory* where moving solitons are spontaneously

generated within an engineered defect, and move out onto the homogeneous background. A novel form of *pattern disassembly* can also be achieved when a spontaneously moving roll or hexagon pattern travels over a "bump" which splits the pattern into its constituent building blocks.
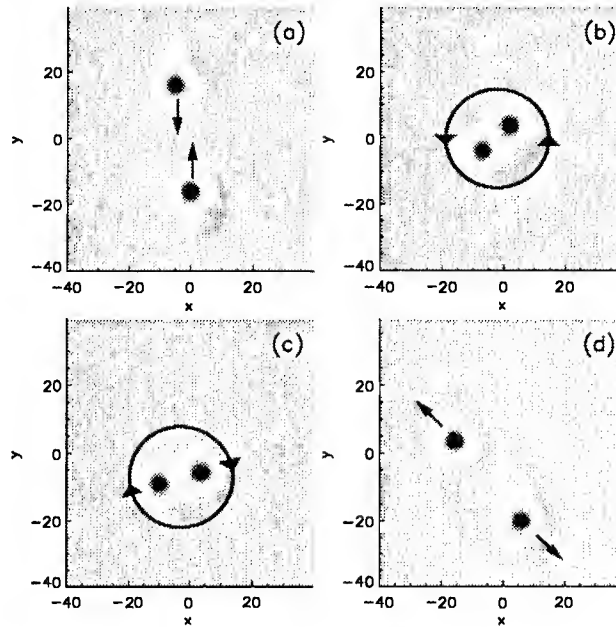
Fig. 2. Dynamical evolution of two colliding dark cavity solitons in 2D, with arrows indicating directions of motion.

We refine the model further by adiabatically eliminating the dynamics of the carrier field. This "two-field" model is shown to yield the same phenomena as the more detailed model.

References

1. W. J. Firth, "Theory of Cavity Solitons" in A. D. Boardman and A. P. Sukhorukov (eds.),"Soliton-Driven Photonics", Kluwer Academic Publishers, London, 459-485 (2001).
2. W. J. Firth and C. O. Weiss, "Cavity and Feedback Solitons", Optics and Photonics News, 26, 54-58 (2002).
3. A. Schreiber, B. Thüring, M. Kreuzer and T. Tshudi,"Experimental investigation of solitary structures in a nonlinear optical feedback system", Optics Communications, 136, 415-418 (1997).
4. W. J. Firth and A. J. Scroggie, "Optical Bullet Holes: Robust Controllable Localized States of a Nonlinear Cavity", Physical Review Letters, 76, 1623-1626 (1996).
5. T. Maggipinto, M. Brambilla, G. K. Harkness and W. J. Firth, "Cavity Solitons in Semiconductor Microresonators: Existence stability and dynamical properties", Physical Review, E62, 8726-8739 (2000).
6. L. Spinelli, G. Tissoni, M. Tarenghi and M. Brambilla, "First principle theory for cavity solitons in semiconductor microresonators", European Physical Journal, D15, 257-266, 2001.
7. L. Spinelli, G. Tissoni, L. Lugiato and M. Brambilla, "Thermal effects and transverse structures in semiconductor microcavities with population inversion", submitted to PRA.
8. P. Coullet, J. Lega, B. Houchmanzadeh and J. Lajzerowicz, "Breaking chirality in nonequilibrium systems", Physical Review Letters, 65, 1352-1355 (1990).
9. D. Michaelis, U. Peschel, F. Lederer, D. V. Skryabin and W. J. Firth, "Universal criterion and amplitude equation for a nonequilibrium Ising-Bloch transition", Physical Review, E63, 066602 (2001).

Cavity solitons work as pixels in semiconductors

S. Barland[1], M. Giudici[1], J. R. Tredicce[1], S. Balle[2], M. Brambilla[3], T. Maggipinto[3], L. A. Lugiato[4], L. Spinelli[4], G. Tissoni[4]*, T. Knödl[5], M. Miller[5] & R. Jäger[5]

[1]Institut Non Lineaire de Nice, 1361 Route des Lucioles, F-06560 Valbonne, France

[2]IMEDEA, Carrer Miguel Marques 21, 07190 Esporles, Islas Baleares, Spain

[3]Dipartimento Interateneo di Fisica, Università di Bari, Via Orabona 4, 70126 Bari, Italy

[4]Dipartimento di Scienze, Università dell'Insubria, Via Valleggio 11, 22100 Como, Italy

[5]Department of Optoelectronics, University of Ulm, D-89069 Ulm, Germany

* giovanna.tissoni@mi.infn.it

The investigations in the field of spatial pattern formation in nonlinear optical systems[1] offer an approach to parallel optical information processing, by encoding information in the transverse structure of the field.

The idea is of considering the transverse planes as a blackboard on which light spots can be written and erased in any desired location and in a controlled way. Optical patterns may display an array of light spots, but are unsuitable for this task because the intensity peaks are usually strongly correlated with one another, so that they cannot be manipulated as independent objects. This task becomes possible, instead, using cavity solitons (CSs)[2,3], a peculiar type of spatial solitons which arise in a dissipative environment.

CS are generated in optical resonators containing nonlinear materials and driven by a broad area, coherent and stationary holding beam. The device is operated under parametric conditions such that the output is basically uniform over an extended region. However, by injecting a localised laser pulse one can write a CS where the pulse passes and the CS persists after the pulse, thanks to the feedback exerted by the cavity. The CSs written in this way can be erased by injecting again pulses in the locations where they lie; in most cases, these pulses must be coherent and out of phase with respect to the holding beam[4].

Experimental observation of CSs in semiconductor microresonators is an important issue not only for fundamental physics but also for developing application-oriented devices. Soliton-like structures have been reported[5], but a demonstration of objects that can be manipulated independently of each other has not been achieved yet. In this presentation we provide such a demonstration using broad area, vertical cavity, driven semiconductor lasers slightly below threshold[6].
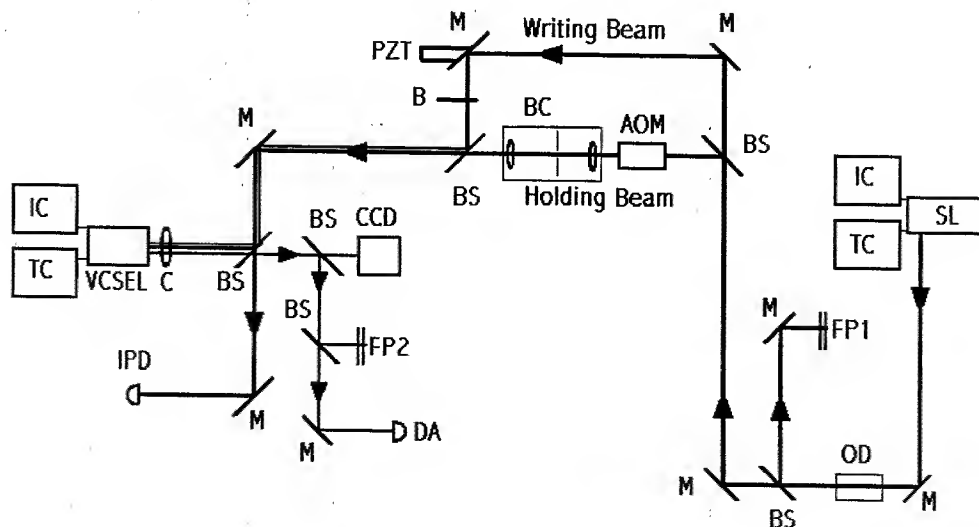
Figure 1 Schematic experimental setup

Our experimental set-up is schematically shown in Fig.1. It consists in a large area Vertical Cavity Surface Emitting Laser (VCSEL, 150 µm diameter), operated as an amplifier, injected by a coherent field (wavelength 970 nm), generated by a high power edge emitting laser with an external cavity grating. Its wavelength can be continuously tuned in the range 960-980 nm. The intensity of the external field can be varied by using an acousto-optic modulator or a polariser. The VCSEL is a bottom emitter, fabricated in Ulm, as described in ref. 6. One of the electrodes is deposited on the top covering the whole transverse size of the laser. A full area n-type contact with a circular emission window is deposited at the backside of the GaAs substrate. The large distance between this ring and the active medium insures a better uniformity of the current than in the case of top emitter lasers.

The demonstration of CS existence consists in generating at least two such structures at various locations in the transverse plane by injecting a control beam in different points and, subsequently, in erasing them independently of one another.

Because of the gradient of the cavity length along the transverse section, on the left-hand side of the sample there is a patterned region (created by a modulational spatial instability), whereas on the right there is a homogeneous region (fig2a). As suggested by theory, we inject the control beam to the right of the line which separates the two regions and write the two spots (figs. 2b-g) which are subsequently erased by applying again the control beam with a changed phase (figs. 2h-k). The power of the holding beam is 8 mW, that of the writing/erasing beam is 50 µW. CSs persist throughout the observation time (> 1 min.).
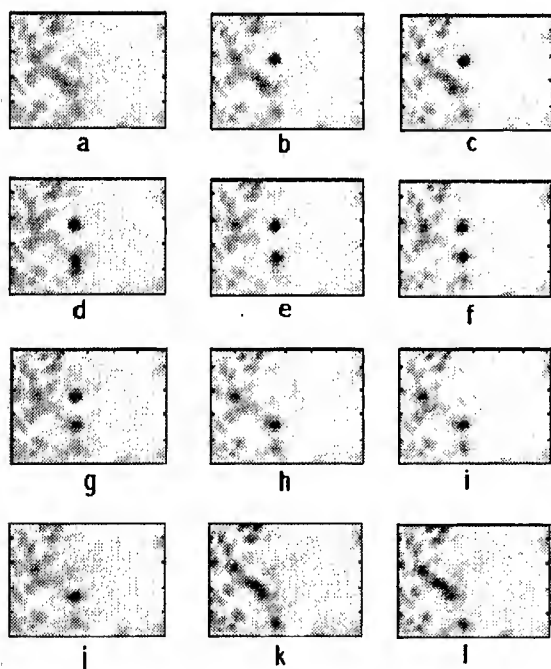
Figure 2 Intensity distribution of the output field over a 60 µm x 60 µm region of the sample. The holding beam is always on, and all parameters are kept constant a) the writing beam (WB) is blocked; b) the 15 µm focused WB is switched on into the homogeneous region; it induces the appearance of a single high intensity spot (dark in the figure) in a limited region of space; c) the WB is blocked again, a 10 µm spot remains and it is stable; d) the WB is displaced in position and switched-on again. It generates a second spot; e, f) the WB is blocked again and the two bright spots coexist; g) the WB is positioned again on the first spot; h) the relative phase of the WB with respect to the holding is changed by π, and the upper spot disappears; i) the WB is blocked again, the lower spot continues to exist while the upper spot disappeared; j) the WB is switched on again at the position of the lower spot; k) the phase of the WB with respect to the holding beam is again brought to π and the second spot disappeared; l) the WB is blocked, and the intensity distribution is identical to a).

We performed numerical simulations based on a model especially developed to describe the microresonators under investigations, which not only showed an excellent qualitative agreement with the experimental findings (see Fig.3) but, especially, they were functional in providing interpretation and guidelines to the experimental search. The main element of guide was the indication of the region where the writing beam has to be injected to form CSs, that is the part of the homogeneous domain close to the patterned region. The most important interpretation was the trapping role played by the thickness fluctuations in the sample.

This work represents a clear advance in several scientific aspects. We developed a novel type of VCSEL with a broad area, small frequency gradient and good current homogeneity. We developed a model containing the most relevant ingredients capable to describe the spatio-temporal behaviour of the VCSEL

resonator. Using CSs we realised the first monolithic 2-bits all-optical information processor. These results open a new frontier on the possibility of developing a practical device.
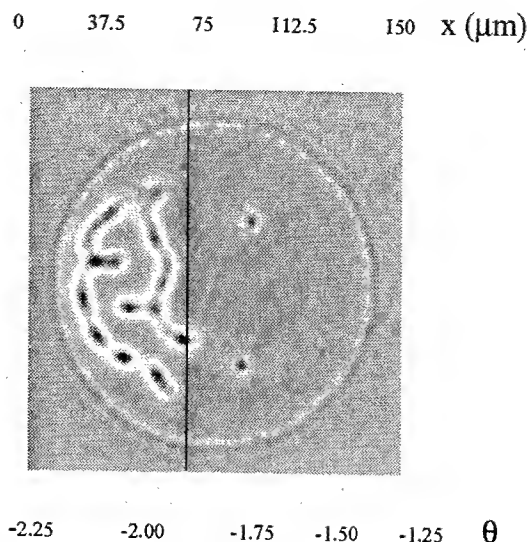
Figure 3 Numerical transverse field intensity profile at regime showing two CSs in the homogeneous region

The future development of these results requires to further increase the number of CSs which can be simultaneously present, and to attain the possibility of inducing the motion of CSs in a controlled way. To achieve these goals, it will be necessary to introduce appropriate spatial modulations in the holding beam and to further improve the homogeneity of the sample in the transverse plane.

References

[1] L.A. Lugiato, M. Brambilla & A. Gatti, Optical Pattern Formation. In *Advances in Atomic, Molecular and Optical Physics*, Vol. 40, eds. Bederson, B. & Walther, H. (Academic Press, 1998) pp. 229-306.

[2] W.J. Firth & A.J. Scroggie, Optical bullet holes: robust controllable localized states of a nonlinear cavity. *Phys. Rev. Lett.* 76, 1623-1626 (1996).

[3] M. Brambilla, L.A. Lugiato, F. Prati, L. Spinelli, & W. J. Firth, Spatial soliton pixels in semiconductor devices. *Phys. Rev. Lett.* 79, 2042-2045 (1997).

[4] M. Brambilla, L.A. Lugiato, & M. Stefani, Interaction and control of optical localized structures. *Europhys. Lett.* 34, 109-114 (1996).

[5] V.B. Taranenko, I. Ganne, R. Kuszelewicz, & C.O. Weiss, Spatial solitons in a semiconductor microresonator. *Appl. Phys. B* 72, 377-380 (2001).

[6] S. Barland, J.R. Tredicce, M. Brambilla, L.A. Lugiato, S. Balle, M. Giudici, T. Maggipinto, L. Spinelli, G. Tissoni, T. Knoedl, M. Miller and R. Jaeger, Cavity solitons work as pixels in semiconductors, submitted for publication.

The origin of motion of solitary waves near Hopf-bifurcations

D. Michaelis
Fraunhofer Institut für Angewandte Optik und Feinmechanik, 07745 Jena, Germany
tel.:+49 3641 807 750, fax:+49 3641 807 600, e-mail: dirk@pinet.uni.jena.de

U. Peschel and F. Lederer
Friedrich-Schiller-Universität Jena, Max-Wien-Platz 1, 07743 Jena, Germany

D.V. Skraybin
University of Bath, Bath BA2 7AY, UK

W.J. Firth
University of Strathclyde, Galsgow G4 0NG, UK

Abstract: We show that the coupling between oscillating eigenstates and the translational mode causes solitary waves to move steadily, oscillatory or with irregular jumps. Theoretical results are compared with numerical simulations for different dissipative systems.
©2000 Optical Society of America
OCIS codes: (190.4420) Transverse effects in nonlinear optics, (190.5530) Pulse propagation and solitons

Solitary waves (SWs) appear as localized excitations in most nonlinear environments. If translational symmetry exists in a Hamiltonian system or if Galilian invariance is present each resting SW is embedded in a family of moving ones. But, in general resting SWs are not trivially connected with moving ones. However, at particular points in parameter space moving SW can bifurcate from resting solutions via a nonequilibrium Ising-Bloch (NIB) transition [1]. In that case a symmetric SW destabilizes due to an eigenvector, which just passes the translational mode [1] and stable asymmetric moving SWs emerge. In this paper we identify a new kind of NIB transition, where motion is induced by the nontrivial coupling of the oscillating linear eigenstates of the SW with its translational mode. We apply our theory on two different nonlinear systems, namely polarization fronts in intracavity vectorial second harmonic generation (VSHG) and double hump solitons in the parametric driven Ginzburg-Landau equation (PGLE).

In the case of VSHG the normalized equations for the two orthogonally polarized fundamental harmonic fields $F_{1,2}$ (FH1, FH2) and the second harmonic field B (SH) read in the mean field limit as:

$$\left(i\partial_T + \partial_X^2 + \Delta_F + i\right)F_{1,2} + F_{2,1}^* B = E, \qquad \left(i\partial_T + 1/2\,\partial_X^2 + \Delta_B + i\gamma\right)B + F_1 F_2 = 0, \quad (1)$$

where ∂_x^2 describes diffraction and t is the dimensionless time. $\Delta_{F,B}$ denote the detunings of the Fabry-Perot cavity from the resonance condition at FH and SH frequencies. γ is the ratio of the photon life times at the two frequencies and E is the constant input field. Besides conventional CSs VSHG also allows for stationary fronts solutions, which are symmetric with respect to a spatial inversion together with a mutual exchange of the two FH components (see inset of Fig.1a). The PGLE

$$\partial_T F = (\mu + i\nu)F + (\delta + i\alpha)\partial_X^2 F - (\varepsilon + i\beta)|F|^2 F + \gamma F^* \qquad (2)$$

is a widely used model in nonlinear science. In optics it is used to describe the action of an optical parametric oscillator. It is well known that single hump SWs of the PGLE may form bound states or double hump SWs [4] (see inset of Fig.2a). In order to develop a general theory we describe the two above models by means of the equation

$$\partial_T \vec{u} = \vec{w}\big|_{\vec{u},\vec{p}}, \qquad (3)$$

where $\vec{u}$ is a real vector, which defines the solutions of the system. $\vec{w}$ is a nonlinear vector function, which depends on $\vec{u}$ and on a parameter set $\vec{p}$. It also contains the spatial operator ∂_X^2. In what follows we assume that Eq.(3) allows for a stationary SW solution $\vec{u}_0$ ($\vec{w}\big|_{\vec{u}_0,\vec{p}} = 0$). Additionally the system shell be invariant with respect to arbitrary translations ($\hat{T}_a[\vec{u}_0(x)] = \vec{u}_0(x+a)$) and a parity transformation ($\hat{P}$ with $\hat{P}^2 = \hat{I}$). For the PGLE $\hat{P}$ is the inversion $\hat{P}[\vec{u}_0(x)] = \vec{u}_0(-x)$ [1]. For VSHG $\hat{P}$ includes the inversion but also a permutation of the FH field

components [1]. Our starting point is a symmetric SW $\vec{u}_0(x)$, which obeys $\hat{P}[\vec{u}_0(x)] = \vec{u}_0(x)$. Here we focus on symmetry breaking due to an oscillatory instability. We presume that the SW bears linear bound eigenstates $\vec{e}$ with complex eigenvalues λ, with $\partial_u \vec{w}|_{\vec{u}_0,\vec{p}}(\vec{e}) = \lambda \vec{e}$, where $\partial_u \vec{w}|_{\vec{u}_0,\vec{p}}(.)$ is the Jacobian of eq. (3). Eigenvectors are either symmetric ($\hat{P}[\vec{s}] = \vec{s}$) or antisymmetric ($\hat{P}[\vec{a}] = -\vec{a}$). We consider the rather common situation that two eigenvectors with opposite symmetry are least damped and have almost the same eigenvalue.

If the homogenous background of VSHG is close to a Hopf bifurcation (Fig. 1a), a continuous band of unbound eigenvectors with complex valued eigenvalues exists. Due to the potential induced by the SW bound oscillatory eigenvectors split off from that continuous band in an alternating sequence of symmetric and antisymmetric states. The least damped eigenvector is typically symmetric and the next one antisymmetric. The eigenvalues of such a pair of eigenstates of opposite symmetry are almost equal (Fig. 1a).
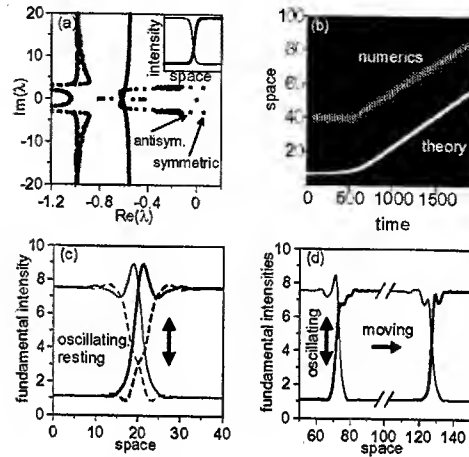
Fig.1. Spatial bifurcation of polarization fronts in VSHG, $\Delta_F = -1.5$, $\Delta_B = 1.5$, $\gamma = 0.55$, $E = 6.8$) (a) Linear spectrum of a stationary, symmetric polarization front, inset: intensity profile of the fundamental fields F_1, F_2, (b) Contour plot of the intensity of the second harmonic B - full numerics of Eq.(1), full white line: position dynamics of the SW determined by Eq.(4,5), (c) symmetrically oscillating and resting front (initial dynamics), (d) asymmetrically oscillating and moving front (final dynamics).

Another example is a double hump solution of the PGLE (Fig. 3a). If the isolated solitons are already close to a Hopf bifurcation, the double hump solution owns two oscillating modes. They correspond to symmetric $\vec{s}$ and antisymmetric $\vec{a}$ linear combinations of the eigenstates of the initial single hump SW. If the two humps are well separated the eigenvalues of the bound state are rather close to each other (Fig. 2a).

To investigate the evolution of the SW we perform a multiscale analysis around a critical point where $\text{Re}[\lambda_s] = \text{Re}[\lambda_a] = 0$. The solution up to first order oscillates as expected. It reads as $\vec{u} = \vec{u}_0 + S\,\vec{s}\,\exp(i\omega T) + A\,\vec{a}\,\exp(i\omega T) + c.c.$, where $\omega = \text{Im}[\lambda_s] = \text{Im}[\lambda_a]$ and S and A are the amplitudes of the symmetric $\vec{s}$ and antisymmetric $\vec{a}$ Hopf modes. In second order a surprising result is obtained. Due to the coupling between the oscillations and the translational mode the SW starts to move with a velocity v as

$$v = -S\,A^* \frac{\langle \vec{a}_0 | \partial_u^2 \vec{w}(\vec{a}^*, \vec{s}) \rangle}{\langle \vec{a}_0 | \vec{e}_0 \rangle} + c.c.. \tag{4}$$

Here $\langle .|. \rangle$ denotes the conventional scalar product, where $\vec{e}_0$ and $\vec{a}_0$ are the translational and the adjoint translational modes ($\partial_u \vec{w}|_{\vec{u}_0,\vec{p}}(\vec{e}_0) = 0$, $\partial_u \vec{w}^+|_{\vec{u}_0,\vec{p}}(\vec{a}_0) = 0$).

In third order we get two coupled ordinary differential equations for the amplitudes of the symmetric (S) and antisymmetric Hopf oscillations (A) as

$$\partial_T S = c_s S + \left[d_s |S|^2 + f_s |A|^2 \right] S + g_s A^2 S^* + v\,h_s A \tag{5}$$

$$\partial_T A = c_a A + \left[d_a |A|^2 + f_a |S|^2 \right] A + g_a S^2 A^* + v h_a S ,$$

where $c_{s,a}$, $d_{s,a}$, $f_{s,a}$, $g_{s,a}$, $h_{s,a}$ are complex constants. According of the actual values of these parameters the system can evolve in very different ways. According to Eq.(4) the dynamics of A and S is transferred into a motion of the SW. Here we discuss some particular examples, which appear in the two model systems.
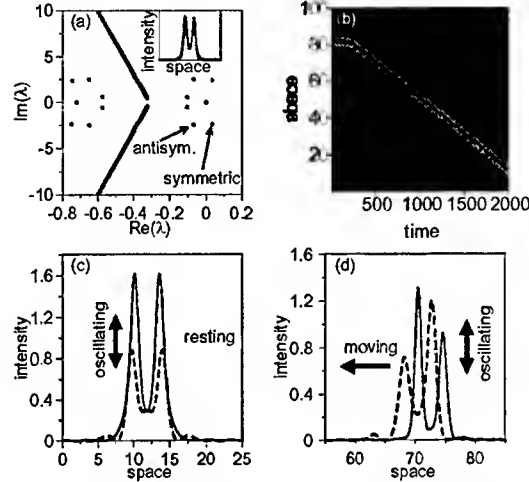
Fig.2. Spatial bifurcation of a double hump SW in PGLE (2), $\mu=-0.32$, $v=-1$, $\alpha=1$, $\delta=0.03$, $\varepsilon=0$, $\beta=-2.5$, $\gamma=0.88$), (a) Linear spectrum of a stationary, symmetric SW, inset: intensity profile, (b) Contour plot of the intensity, (c) symmetrically oscillating and resting SW (initial dynamics), (d) asymmetrically oscillating and moving SW (final dynamics).

First we start with a symmetric resting front of the VSHG system (Eq. (1)). Here the symmetric Hopf mode is unstable ($\mathrm{Re}(c_s) > 0$) and the front destabilize supercritically ($\mathrm{Re}(d_s) < 0$). In contrast the asymmetric mode is still linearly damped ($\mathrm{Re}(c_a) < 0$). Therefore the front starts to oscillate symmetrically ($\left(S, A \right) = \left(\pm \sqrt{-c_s / \mathrm{Re}(d_s)}, 0 \right)$, see Fig. 1c). But, if the amplitude of the symmetric oscillations exceeds a certain value it excites the other mode and the SW oscillates asymmetrically too. According to Eq. (4) the SW starts to propagate with a constant velocity v in either direction (see Fig.1b and d). A similar behaviour is found for double hump solitons of the PGLE. They initially oscillate symmetrically and are at rest (see Fig. 2c). After destabilization an asymmetric (Fig.2d) and moving (Fig.2b) localized structure is formed.
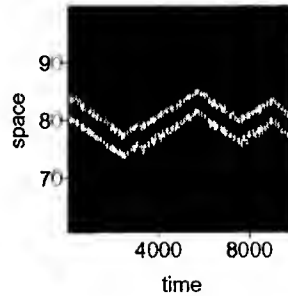
Fig.3. Contour plot of an irregular jumping SW in PGLE (2) ($\mu=-0.32$, $v=-1$, $\alpha=1$, $\delta=0.03$, $\varepsilon=0$, $\beta=-2.5$, $\gamma=0.83$).

However, the interaction between the two Hopf-modes need not result in a regular motion (see Fig.3). If the growth of the unstable symmetric Hopfmode is not intrisically saturated ($\mathrm{Re}[d_s] \geq 0$) the amplitude S increases exponentially fast. A large enough S excites the antisymmetric mode. Therefore the SW undergoes a position jump.

After this both amplitudes (S, A) are brought down to zero due to nonlinear damping induced by the asymmetric mode ($\mathrm{Re}(f_s) < 0$). This process can repeat in an irregular sequence. Hence, subsequent position shifts are weakly or not correlated and can have both signs (see Fig. 3).

[1] P. Coullet et al., "Breaking chirality in nonequilibrium systems." Phys. Rev. Lett. 65, 1352 (1990), D. Michaelis et al., "Universal criterion and amplitude equation for a nonequilibrium Ising-Bloch transition." Phys. Rev. E 63,066602, (2001).

Effects of nonlinear guiding on spontaneous pattern formation: Formation of spirals and target patterns

F. Huneus, T. Ackemann, B. Schäpers, and W. Lange

Institut für Angewandte Physik, Universität Münster, Corrensstraße 2/4,
D-48149 Münster, Germany
Tel.: +49-251-83-33553, Fax: +49-251-83-33513, E-mail:
huneus@uni-muenster.de, t.ackemann@uni-muenster.de, b.schaepers@web.de,
w.lange@uni-muenster.de

Abstract: Nonlinear guiding induced by gradients of the pump beam intensity can drastically affect optical pattern formation. A specific example is the emergence of spiral and target patterns in a single-mirror scheme with sodium vapor.
© 2002 Optical Society of America
OCIS codes: 270.3100, 190.4420, 190.3100

Phenomena of spontaneous optical pattern formation are usually discussed in a homogeneous environment even if it is common that the finite extent of the pump beam might lead to pronounced effects [1, 2]. It is also known that phase inhomogeneities and/or gradients may play an important role. They lead e. g. to a drift motion [3, 4, 5]. However, in most of these works only the phase profiles due to external optics are taken into account. We demonstrate here that the spatially inhomogeneous nonlinear refractive index distribution created by the Gaussian envelope of the pump beam used in experiments can induce a significant guidance effect which totally alters pattern formation. In the specific example under study target and spiral patterns appear in a situation in which oscillating hexagons are expected for a plane wave input.

The experimental scheme is a realization of the single-mirror feedback scheme analyzed in [6] utilizing sodium vapor as the nonlinear medium. An expanded and spatially filtered cw dye laser beam tuned several GHz above the sodium D_1–line is injected into a cell containing sodium vapor in a nitrogen buffer gas atmosphere. More than 90% of the transmitted power is fed back into the sodium cell by a plane mirror at distance d behind the vapor. By means of a CCD camera we observe the near field intensity distribution of the transmitted light (Fig. 1). The technique of video sampling enables us to obtain slow-motion movies of the dynamics of structures as long as the time dependence is regular [7]. The nonlinearity of the sodium vapor originates from optical pumping between the Zeeman sublevels of the sodium ground state by circularly polarized light. The magnetization induced by the pumping process interacts with an oblique dc magnetic field.
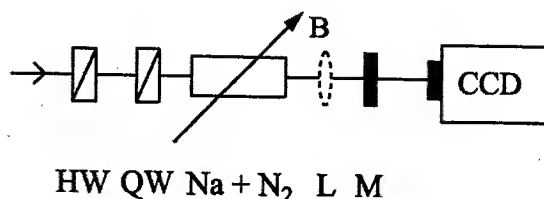
Fig. 1. Schematic view of setup. HW: half–wave plate, QW: quarter–wave plate, L: lens (optionally), M: mirror, B: magnetic field. The beam radius of the laser beam is $w_0 \approx 1.5$ mm.

For suitable chosen parameters we observe patterns consisting of several rings which are called *target patterns* (Fig. 2a). The rings move towards the center with a well defined speed and disappear there. At the same time new rings are constantly born at the boundary. For the same parameters *rotating spiral patterns* are observed, too (Fig. 2b). They also show an *inward* motion (Fig. 2c). The fact that the movement in the observed patterns is directed towards the center is intriguing since the movement of the well-known targets and spirals in chemistry and biology – with one very recent exception [8] – is directed outwardly [9].

A linear stability analysis of a microscopic model of the light-matter interaction yields the possibility of a Hopf bifurcation at a finite wave vector [10] which is related to a Larmor precession of the magnetization. For parameters close to the experimental ones, the predicted spatial wave length agrees well with the pitch between the arms of the spirals. In addition the dependence of the oscillation frequency on the strength of

a) b) c)
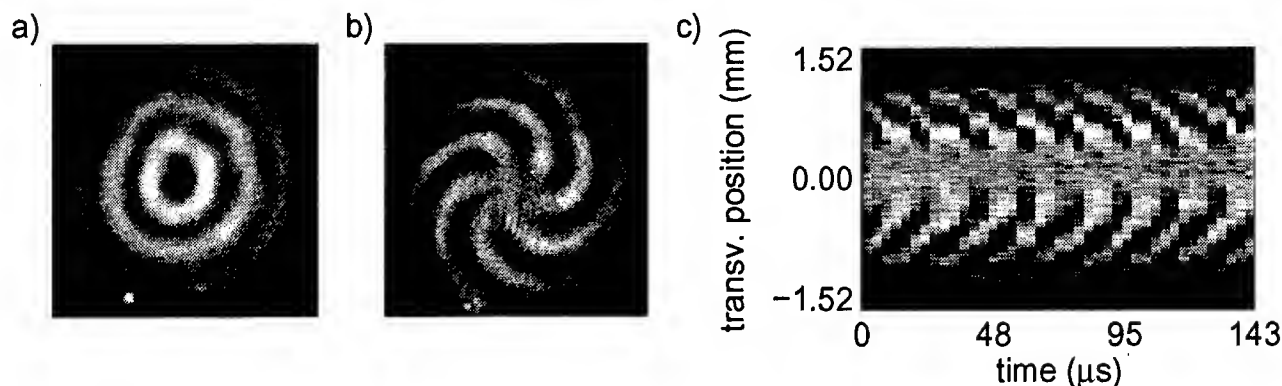
Fig. 2. Typical examples for the observed structures: a) target pattern , b) spiral pattern. c) Space-time-diagram illustrating radial motion in the patterns.

the magnetic field is in good agreement with theoretical expectation. This gives a strong indication that the appearance of the spirals is related to this Hopf bifurcation.

Simulations with a plane input beam indeed yield time-dependent patterns in this parameter region but these are not targets or spirals but oscillating hexagons or states with an irregular, possibly turbulent, space dependence (see also [10]). In particular, these patterns show no directed drift movement.

Hence we investigated the experimentally realistic situation with an inhomogeneous pump profile by numerical simulations. Fig. 3 shows the phase distribution of the transmitted beam after the sodium cell. The overall behavior is quite complex (cf. [11]). However, in the central region of the beam, in which pattern formation takes place, the distribution can approximately be described by a parabola, i.e. one expects a lens-like action of the medium. The drift direction induced by such a profile can be determined by a linear stability analysis if one assumes that the phase variation is linear in space. It turns out that the drift is indeed directed parallel to the gradient of phase. Furthermore, the appearance of inwardly drifting targets and spirals can be reproduced in numerical simulations using a Gaussian input beam. We remark that the spirals we observe bear some resemblance to the ones obtained in a liquid-crystal light-valve with field rotation [3], however, our system possesses rotational symmetry, i.e. the symmetry breaking from targets to spirals happens spontaneously.
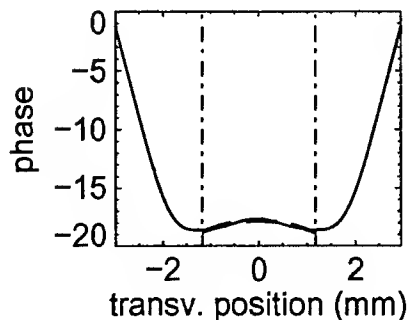
Fig. 3. Phase distribution of the transmitted beam after sodium cell. Dashed: parabola approximating phase distribution in the central region of the beam.

For an experimental demonstration of the importance of the phase profile a focusing lens is inserted in the feedback arm (Fig. 1). The focal power is chosen to be stronger than the focal power of the defocusing medium so that the phase profile of the beam has opposite curvature now. Again spiral patterns form (Fig. 4a). As the space-time plot in Fig. 4b shows the motion is directed to the perimeter in accordance with expectations.

Summarizing we demonstrated that the nonlinear guiding due to a radial dependence of the pump field

a)

b)
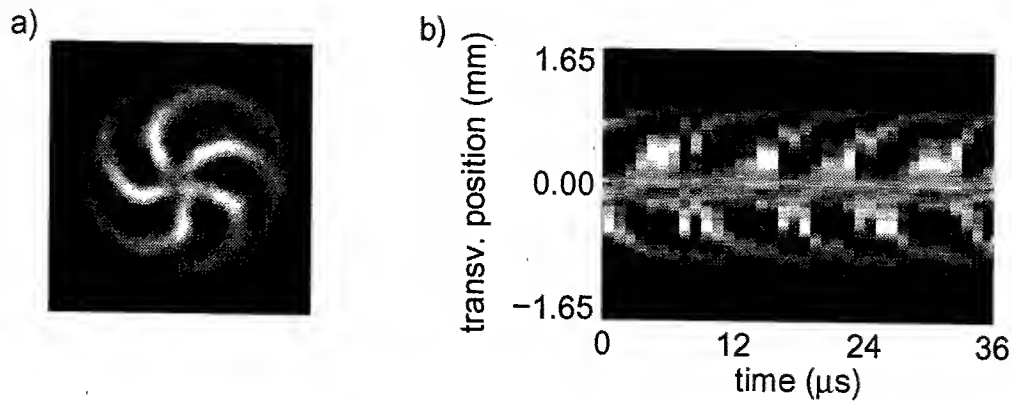
Fig. 4. a) Outwardly moving spiral pattern in presence of a focusing phase distribution; b) according space-time-diagram.

can qualitatively alter optical pattern formation leading to structures not expected in a plane input wave. Control of the drift motion was implemented. We remark that localized states and stationary patterns – existing in parameter region nearby – are also affected by the guiding, but drift in a direction *opposite* to the oscillating structures.

References

1. J. P. Seipenbusch *et al.*, Phys. Rev. A **56**, R4401 (1997).
2. E. Louvergneaux, Phys. Rev. Lett. **87**, 244501 (2001).
3. S. A. Akhmanov *et al.*, J. Opt. Soc. Am. B **9**, 78 (1992).
4. G. Grynberg, Opt. Commun. **109**, 483 (1994).
5. V. B. Taranenko, K. Staliunas, and C. O. Weiss, Phys. Rev. A **56**, 1582 (1997).
6. G. D'Alessandro and W. J. Firth, Phys. Rev. Lett. **66**, 2597 (1991).
7. M. Möller and H. J. Bruns, Rev. Sci. Instrum. **66**, 4535 (1995).
8. V. K. Vanag and I. E. Epstein, Science **294**, 835 (2001).
9. M. C. Cross and P. C. Hohenberg, Rev. Mod. Phys. **65**, 851 (1993).
10. Y. A. Logvin and T. Ackemann, Phys. Rev. E **58**, 1654 (1998).
11. T. Ackemann, A. Heuer, Y. A. Logvin, and W. Lange, Phys. Rev. A **56**, 2321 (1997).

Dark ring cavity solitons and stable droplets in models of nonlinear optical cavities

Damià Gomila[1], Pere Colet[1], Gian-Luca Oppo[2], Maxi San Miguel[1], and Andrew Scroggie[2]

[1] *Instituto Mediterráneo de Estudios Avanzados, IMEDEA (CSIC-UIB), Campus Universitat Illes Balears, E-07071 Palma de Mallorca, Spain. Phone: +34 971 173382, fax: +34 971 173248, e-mail: pere@imedea.uib.es http://www.imedea.uib.es/PhysDept*

[2] *Department of Physics and Applied Physics, University of Strathclyde, 107 Rottenrow, Glasgow G4 0NG, Scotland, UK.*

Spatially localized structures in nonlinear optical cavities, including Kerr resonators, optical parametric oscillators, saturable media and second harmonic generation, have attracted a large amount of attention in the last years. In particular, the existence of localized structures (LS) in nonlinear optical cavities have been recently shown [1, 2, 3]. These narrow soliton-like structures exist for a quite broad range of values of the pump for which there is bistability between two equivalent homogeneous solutions. Here we show the existence of a novel kind of stable localized structures, the stable droplets (SD) which have a much larger size and which are in fact large stable circular domain walls connecting the two homogeneous solutions.

The dynamics of formation of such localized structures is closely linked to the problem of the growth of spatial domains of different phases. Asymptotic domain growth laws have been established in the context of equilibrium phase transitions [4], where it is found that in systems with no conservation law domains made of equivalent phases grow as $R(t) \sim t^{1/2}$, while for systems with conserved order parameter $R(t) \sim t^{1/3}$. In non-equilibrium nonlinear optical systems the problem of domain growth has been addressed only very recently [1, 2]. For the systems considered here a growth law of the form $R(t) \sim t^{1/2}$ is found in a regime where labyrinthine patterns are form while in the regime of existence of the soliton-like structures, a large initial circular domain of one homogeneous solution embedded in the other shrinks following $R(t) \sim \sqrt{R(0) - \gamma t^{1/2}}$ with $\gamma > 0$ [1, 2]. Here we will show that between these two regimes there is a new regime in which an initially small (very large) circular domain grows (shrinks) following the law $\dot{R} \sim -1/R + R_0^2/R^3$ until a SD of radius R_0 is formed.

We consider here two different models of nonlinear optical cavities: a vectorial Kerr cavity and a doubly resonant degenerate optical parametric oscillator. The mean field equations for a self-defocusing vectorial Kerr cavity are [6, 7]:

$$\partial_t E_\pm = -(1 - i\theta)E_\pm + i\nabla^2 E_\pm + E_0 - \frac{1}{4}i[|E_\pm|^2 + \beta|E_\mp|^2]E_\pm \qquad (1)$$

where, $E_\pm$ are the circularly polarized field components, E_0 the pump (x-polarized), θ is the cavity detuning ($\theta = 1$), ∇^2 is the transverse Laplacian and β is related to the susceptibility tensor ($\beta = 7$). For $E_0 < E_{th} \approx 0.95$ the homogeneous symmetric solution $I_+ = I_-$ ($I_\pm = |E_\pm|^2$) is stable [7]. At this threshold value a y-polarized stripe pattern is formed. For pump values above a second threshold, $E_0 \approx 1.5$, there is bistability between two homogeneous asymmetric (elliptically polarized) solutions.

The mean field equations for a phase matched degenerated OPO where both pump A_0 and signal A_1 fields are resonant are [2]:

$$\begin{aligned}
\partial_t A_0 &= \Gamma[-A_0 + E_0 - A_1^2] + \frac{ia}{2}\nabla^2 A_0 \\
\partial_t A_1 &= -A_1 - \Delta_1 A_1 + A_0 A_1^* + ia\nabla^2 A_1,
\end{aligned} \qquad (2)$$

where Γ is the ratio between the pump and signal cavity decay rates ($\Gamma = 6$), E_0 is the amplitude of the external pump field, Δ_1 is the signal detuning ($\Delta_1 = -1$) and a is the diffraction parameter ($a = 0.5$). For $E_0 < 1$ the zero homogeneous solution is stable. Above threshold a stripe pattern is formed. For pump values above a second threshold, $E_0 \approx 1.56$, there is bistability between two nonzero homogeneous solutions.

FIG. 1. Growth rate γ for the vectorial Kerr (left) and DRDOPO (right). Vertical lines indicate from left to right $E_{0,1}$ and $E_{0,2}$. The upper figures show, from left to right, snapshots of typical configurations in the labyrinthine, localized structures and coarsening regimes.
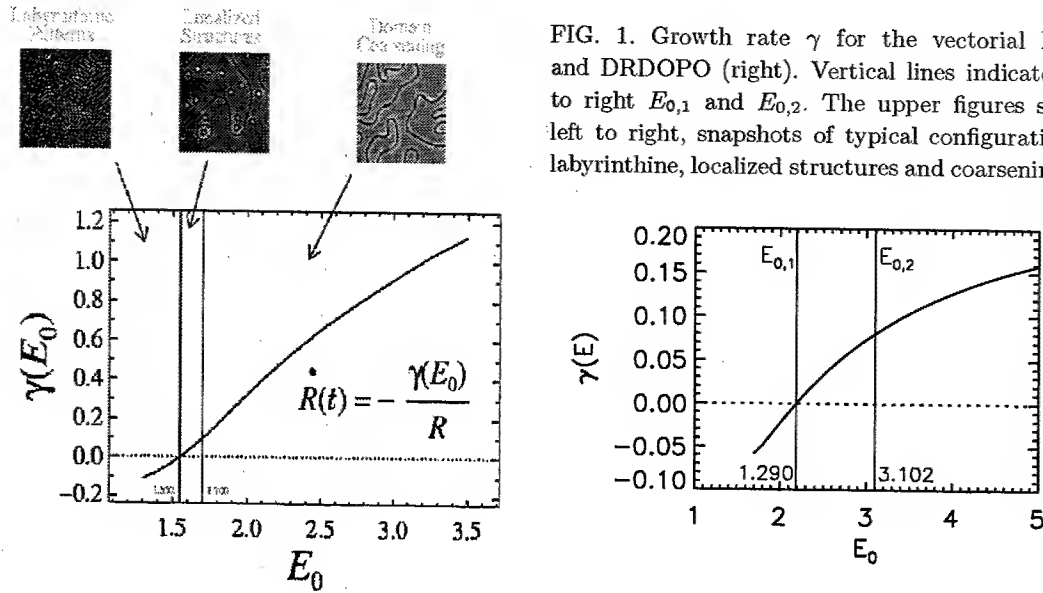
For both systems, there are three dynamical regimes in the bistability region depending on the value of the pump E_0 (Fig. 1) [1]. A regime of labyrinthine pattern formation for $E_0 < E_{0,1}$, a regime of formation of localized structures for $E_{0,1} < E_0 < E_{0,2}$ and a regime of domain coarsening for $E_{0,2} < E_0$ (see fig. 1). A growth rate for a droplet (a circular domain of one homogeneous solution surrounded by the other) of the form

$$\dot{R}(t) = -\gamma(E_0)/R \tag{3}$$

was proposed in [1] and demonstrated later in [8].

In the regime of labyrinthine pattern formation ($E_0 < E_{0,1}$) $\gamma < 0$, so a polarization droplet grows without limit as $R(t) \approx t^{1/2}$. $E_{0,1}$ can be identified with the modulational instability threshold of a flat wall connecting the two asymmetric homogeneous state [1, 8]. Both the modulational instability and the droplet growth indicate that the system prefers to have the longest possible domain walls, or equivalently the largest possible curvature.

For $E_0 > E_{0,1}$, $\gamma > 0$, so an initial droplet shrinks until it stops at a well defined value of the radius forming a LS called dark ring cavity soliton (DRCS) [2]. The existence of the DRCS can be understood as a delicate balance between the repulsive effect of the oscillatory tails of the 1D walls and the curvature effect that tends to reduce the circular domain walls. At $E_0 = E_{0,2}$, the threshold for the domain coarsening regime, the oscillatory tails interaction became too weak to counterbalance the curvature effect. The radius of the LS calculated following Ref. [2] is shown in Fig. 2. For the Kerr, LS exist from $E_0 = E_{0,1} = 1.5498$ to $E_0 = E_{0,2} = 1.7030$, where the stable LS collides with an unstable LS in a saddle node bifurcation. For the OPO there are two stable DRCS with different radius corresponding to locking at the first or the second tail oscillation.

Close to the point $E_{0,1}$ where γ vanishes nonlinear corrections to Eq. (3) must be considered [8]

$$\dot{R}(t) = -c_1(E - E_{0,1})/R - c_3/R^3, \tag{4}$$

where $c_1 > 0$ and $c_3 < 0$ are obtained from the nonlinear analysis.

We find that the LS branch has a change of behavior at $E_0 = E_{0,3}$ (Fig. 2). This particular point correspond to the value of the pump for which the interaction of the tails become of the same order than the nonlinear correction of Eq. 4. For $E_{0,3} < E_0 < E_{0,2}$ the oscillatory tails interaction is dominant and the DRCS is characterized by having a larger intensity at the center than in the surrounding background (Fig. 3 right). For $E_{0,1} < E_0 < E_{0,3}$ the nonlinear curvature effects dominate over the oscillatory tails interaction
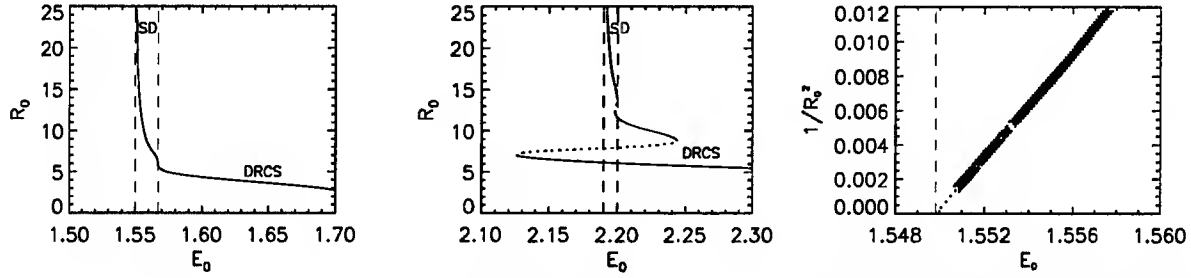
FIG. 2. Radius of the localized structures as function of the pump for the vectorial Kerr cavity (left) and OPO (center). Vertical dotted lines indicate from left to right $E_{0,1}$ and $E_{0,3}$. The figure on the right shows the linear dependence of $1/R_0^2$ with E_0 close to the point $E_{0,1}$ predicted analytically.
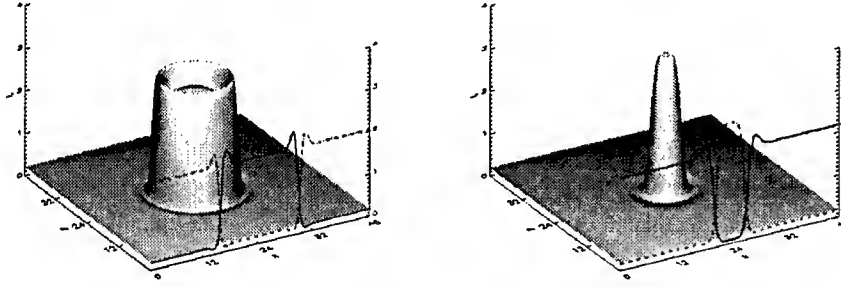
FIG. 3. Spatial dependence and transverse section of a vectorial Kerr SD for $E_0 = 1.5524$ (left) and of a vectorial Kerr LS* for $E_0 = 1.6$ (right).

leading to the formation of a stable stationary circular domain wall (SD) with a very large radius $R_0 = \sqrt{-c_3/c_1}/\sqrt{E - E_{0,1}}$. At the center the field takes the value of one of the homogeneous solutions (Fig. 3 left). Depending on the value of the pump, the radius of the SD can be extremely large. In fact, the radius diverges at $E_{0,1}$ as $R_0 \approx 1/\sqrt{E_0 - E_{0,1}}$ (Fig. 2 right).

When analyzing the dynamical evolution of a polarization droplet we find that the growth law (3), although accurate for $E_{0,3} < E_0 < E_{0,2}$ fails to describe the regime $E_{0,1} < E_0 < E_{0,3}$. From (4) we find that the growth law of the form

$$\dot{R}(t) \sim -1/R + R_0^2/R^3 \tag{5}$$

where R_0 is the radius of the stable LS, is suitable to describe the dynamics in both regimes. An initially small (very large) polarization droplet grows (shrinks) following (5). Finally the growth (shrinkage) stops and the droplet becomes a LS of radius R_0. For the DRCS R_0 is small, so if the initial droplet is relatively large, the term R_0^2/R^3 is a minor correction which can be neglected and we recover the growth law (3). But in the regime of existence of the SD, R_0 is large and the term R_0^2/R^3 can not be neglected anymore. In fact, as E_0 approaches $E_{0,1}$, the term R_0^2/R^3 becomes dominant so that $\dot{R}(t) \approx 1/R^3$ which implies that the radius of an initially relatively small polarization droplet increases with time as $R(t) \approx t^{1/4}$.

References

1. R. Gallego, M. San Miguel and R. Toral, Phys. Rev. E **61**, 2241 (2000).
2. G.-L. Oppo, A.J. Scroggie and W.J. Firth, Phys. Rev. E **63**, 066209 (2001).
3. V.B. Taranenko, K. Staliunas, and C.O. Weiss, Phys. Rev. Lett. **81** 2236 (1998).
4. J.D. Gunton, M. San Miguel and P. Sahni in *Phase Transitions and Critical Phenomena* **8**, 269, ed. C. Domb and J. Lebowitz (Academic Press, 1983); M. San Miguel, A. Amengual, E. Hernández-García, Phase Transitions **48**, 65 (1994).
5. G.L. Oppo, A.J. Scrogie and W.J. Firth, J. Opt. B **1**, 133 (1999); M. Tlidi, P. Mandel and R. Lefever, Phys. Rev. Lett. **81**, 979 (1998); U. Peschel et al, Phys. Rev. E **58**, R2745 (1998).
6. J.B. Geddes, J.V. Moloney, E.M. Wright and W.J. Firth, Opt. Comm. **111**, 623 (1994).
7. M. Hoyuelos, P. Colet, M. San Miguel, and D. Walgraef, Phys. Rev. E **58**, 2292 (1998).
8. D. Gomila, P. Colet, G.-L. Oppo and M. San Miguel, Phys. Rev. Lett., **87**, 194101 (2001).

Fiber Nonlinearity Applications

Tuesday, September 3, 2002

Nail N. Akhmediev, Australian Natl. Univ., Australia
Presider

NLTuC
2:00pm – 4:00pm
Auditorium

Ultrafast Optical TDM Transmission with the use of Novel Nonlinear Optical Fiber Devices

Masataka NAKAZAWA

Research Institute of Electrical Communication, Tohoku University
2-1-1 Katahira, Aoba-ku, Sendai-shi 980-8577, Japan
Tel. 81-22-217-5522, Fax: 81-22-217-5523, E-mail:nakazawa@riec.tohoku.ac.jp

Abstract *We have recently succeeded in transmitting an ultrafast OTDM signal which exceeds 1 Tbit/s over 70 km with the adoption of nonlinear optical fiber devices such as soliton compressor, DI-NOLM for pulse shaping, and NOLM for Terabit/s demultiplexing. In this talk, key technologies for ultrahigh-speed OTDM transmission are described.*

1. Introduction

With the recent maturity of WDM technology, high-speed OTDM (Optical TDM) techniques are becoming increasingly important for handling ultrashort pulse trains for high-speed signal processing and for investigating the ultimate transmission capability of a single channel [1]-[3]. In this paper we describe progress on OTDM single-channel terabit/s transmission using nonlinear optical fiber devices.

Figure 1 shows the progress in large capacity optical transmission experiments. Here N is the number of channels corresponding to the number of wavelengths. Recently, many multi-terabit/s transmission experiments have been successfully demonstrated by using WDM techniques as shown in the left of Fig. 1. Another interesting way of realizing such high capacity transmission, which is our target, is to undertake a single-channel ultrahigh speed TDM transmission using a femtosecond pulse train, as shown on the right side of Fig. 1 (N=1 line). Recently we reported 1.28 Tbit/s transmission which is the highest speed to date for a TDM scheme [4]. In order to realize a 1 terabit/s OTDM transmission, the pulse-to-pulse separation is 1 ps, therefore, the pulse width must be shorter than 1 ps. More exactly, 200–400 fs is ideal depending on the transmission distance, which is the reason why femtosecond technology is so important for terabit/s OTDM transmission.

2. Key Fiber Technologies for Ultrafast OTDM Transmission

In table 1, we list the key technologies for ultrahigh speed OTDM transmission using femtosecond pulses. We have developed several novel fiber devices which operate in the pico-femtosecond region. The first key technology is the generation of femtosecond pulses, in which we employed the following three techniques. We used pulse generation using a regeneratively mode-locked fiber laser, adiabatic soliton compression using a dispersion-flattened dispersion decreasing fiber, and pedestal reduction of compressed pulses using a dispersion-imbalanced nonlinear optical loop mirror (DI-NOLM). Since it is difficult to generate a femtosecond pulse train directly from a mode-locked laser, external pulse compression is commonly used. In addition, the electrical modulation speed of digital signals is currently limited to 40 Gbit/s, so it is impractical to prepare optical sources which have a

Fig. 1 Recent Progress In large capacity optical transmission experiments

repetition rate that exceeds 40 Gbit/s. Hence it is important to generate a 10-40 GHz low jitter pulse train with a pulse width of 100-400 fs. Our approach is to use a regeneratively mode-locked fiber laser which can emit a 3 ps, 10 GHz pulse train. The 3 ps pulse is compressed to 100-200 fs using adiabatic soliton compression in a dispersion decreasing fiber. The unwanted dispersive waves (pedestal components) are removed with the DI-NOLM.

The second is compensation of the total dispersion

(1) Generation of femtosecond pulses
• Pulse generation using regeneratively mode-locked fiber laser
• •Pulse compression using Dispersion-Flattened, Dispersion-Decreasing Fiber (DF-DDF)
• Pedestal-reduction of compressed pulses using Dispersion-Imbalanced Nonlinear Optical Loop Mirror (DI-NOLM)
(2) Compensation of the total dispersion of transmission line
• Third- and fourth-order simultaneous dispersion compensation using a phase modulator
(3) Ultrafast demultiplexing
• Ultrafast NOLM in which walk-off between the signal and control pulses is reduced

Table 1 Key fiber technologies for ultrafast OTDM transmission using femtosecond pulses (Opitcal fiber devices play very important roles for high speed communication.)

Setup for the generation of 10 GHz clock light

Setup for the generation of 1.28 Tbit/s signal

70 km transmission line

Setup for the demultiplexing of 1.28Tbit/s OTDM signal to 10 Gbit/s

Fig. 2 Experimental setup for 1.28 Tbit/s-70 km OTDM transmission with the use of novel nonlinear fiber devices

of the transmission line. A dispersion compensation and dispersion slope compensation fiber are commonly used to compensate for second and third order dispersions. It is also important to minimize the fourth order dispersion since the spectral width of the transmitted pulse is very wide. For this, we adopted an active dispersion compensation technique

1.28 Tbit/s - 0 km (Pre-Chirped)

1.28 Tbit/s - 70 km

Time   1.6 ps / div

Time   1.6 ps / div

(a)

(b)

After Polarization Demultiplexing

Time   1.6 ps / div

Time   1.6 ps / div

(c)

(d)

Fig. 3 Input and output waveforms

that uses a phase modulator.

The third key technology is ultrafast demultiplexing using a walk-off free nonlinear optical loop mirror. Since the transmitted OTDM terabit/s signal is too fast to detect directly with a photo detector, down-conversion of the signal via demultiplexing with a NOLM, four-wave mixing, or electro-absorption (EA) modulator is required. We used a NOLM to demultiplex the 1.28 Tbit/s signal to 10 Gbit/s.

3. 1.28 Tbit/s OTDM transmission

The terabit/s OTDM experimental setup is shown in Fig. 2. A 3 ps, 10 GHz regeneratively and harmonically mode-locked fiber laser at 1.544 μm was used as the original pulse source [5]. The advantage of this laser is its low jitter of approximately 100 fs, which is very important to realize ultrafast multiplexing in the OTDM. The output laser pulse is intensity-modulated at 10 Gbit/s with a PRBS of $2^{15}-1$ and the pulse train was coupled into a dispersion-flattened dispersion decreasing fiber (DF-DDF) [6] and the DI-NOLM [7]. The pulse width at the DI-NOLM output of was 200 fs and the peak-to-pedestal ratio was larger than 30 dB [6].

We incorporated a phase modulation technique that enabled us to compensate for third- and fourth-order dispersion [8]. This pre-chirping unit is shown in Fig. 2(a). In this scheme, we deliberately introduce a certain amount of second-order dispersion, in which the sum of the second-and fourth-order dispersion can be compensated for by a cosine phase modulation. The small third-order dispersion is compensated for by a sine phase modulation. This tech-

Fig. 4 Received power (@ BER=1x10⁻⁹) vs channel number

nique allows us to compensate for all the dispersion from the EDFAs and transmission fibers.

Then, the pre-chirped 10 GHz pulse train was optically multiplexed up to 1.28 Tbit/s by using a planar lightwave circuit (PLC) and polarization multiplexing. It is important to note that due to the pre-chirping, the data signal at the input end was no longer in the femtosecond regime, but a short pulse was recovered after transmission.

The transmission line was a 70 km-long single span fibre consisting of a 39.7 km-long SMF, a 4.6 km-long dispersion-shifted fibre (DSF), and a 25.1 km-long RDF[9]. The fibre loss was 17.6 dB. The dispersion and dispersion slope of the RDF had opposite signs and nearly the same magnitudes as these of SMF. The DSF was included to compensate for the residual dispersion slope of the whole transmission line. The third-order dispersion (dispersion slope) was as small as -0.0023 ps/nm². The total third-order dispersion including three wideband EDFAs was $+0.015$ ps/nm². The PMD of the RDF was 0.02 ps/$\sqrt{}$ km and the total PMD was 0.05 ps/$\sqrt{}$ km. It is important to note that the accumulated fourth-order dispersion became as large as -0.028 ps/nm³, which is no longer negligible for the long distance transmission of a femtosecond pulse train. The second-order dispersion, which we deliberately introduced, was -0.42 ps/nm. To compensate for all these dispersions, we use the pre-chirping technique that we previously described.

The transmitted 1.28 Tbit/s signal was converted into two 640 Gbit/s signals with a PBS, and then demultiplexed into 10 Gbit/s signals using a walk-off free, dispersion-flattened nonlinear optical loop mirror (DF-NOLM) [10]. The control pulse was generated from a phase-locked loop (PLL) operated mode-locked fibre laser at 1533 nm. To obtain a 10 GHz clock to drive the PLL fibre laser, we co-transmitted a clock light at a different wavelength, which was synchronized to the original 10 Gbit/s signal. The setup for generating the clock light is shown in Fig. 1(a). The same10 GHz clock that was used for the pre-chirping unit. A 1542 nm cw light from an external cavity laser diode was modulated at 10 GHz

with a LiNbO₃ modulator which was driven by the extracted 10 GHz clock. The 10 GHz clock and 1.28 Tbit/s signal light were combined in front of the transmission fibre by using a fibre coupler. After transmission, the clock was optically separated using two 1 nm optical filters, and was injected into the clock extraction circuit. The recovered 10 GHz clock was used to drive the PLL fibre laser. We set the oscillation wavelength of the PLL fibre laser at 1533 nm and the pulse width at 1.1 ps.

Figure 3 (a)-(d) shows the input and output data patterns. (a) is the input waveform. Due to the pre-chirped dispersion compensation the 1.28 Tbit/s signal is broadened. This signal changed into a clear 1.28 Tbit/s signal after a 70 km transmission, as shown in (b). This 1.28 Tbit/s signal is separated into two 640 Gbit/s signals with a PBS, as shown in (c) and (d). We successfully obtained very clean 640 Gbit/s signals. The pulse broadening after the transmission was as small as 20 fs. These 640 Gbit/s signals were demultiplexed into 10 Gbit/s signals and each BER was measured.

Figure 4 shows the received power at a BER of 1x10⁻⁹ for the 128 channels after a 70 km transmission. A BER of 1x10⁻⁹ was achieved for all of the channels at a received power of more than -21 dBm. The fluctuation in the received power for each channel is attributed to the residual amplitude difference between the signal channels, which were caused by imperfections in the PLC.

This work has been done with T. Yamamoto and K. R. Tamura when the author was with NTT Network Innovation Laboratories.

References

[1] S. Kawanishi, H. Takara, T. Morioka, O. Kamatani, K. Takiiguchi, T. Kitoh, and M. Saruwatari, Electron. Lett., vol. 32, pp. 916-917, 1996.

[2] G. Raybon, B. Mikkelsen, R-J. Essianbre, A. J. Stentz, T. N. Nielsen, D. W. Peckham, L. Hsu, L. Gruner-Nielsen, K. Dreyer, J. E. Johnson, OFC' 2000, Baltimore, U. S., PD29, 2000.

[3] S. Diez, R. Ludwig, and H. G. Weber,Electron. Lett., vol. 34, pp. 803-805, 1998.

[4] M. Nakazawa, T. Yamamoto, and K. R. Tamura, Electron. Lett, vol. 36, pp. 2027-2029, 2000.

[5] M. Nakazawa, E. Yoshida, and Y. Kimura, Electron. Lett., vol. 30, pp. 1603-1604, 1994

[6] K. R. Tamura, and M. Nakazawa, IEEE Photon. Technol. Lett., vol. 11, pp. 230-232, 1999.

[7] W. S. Wong, S. Namiki,, M. Margalit, H. A. Haus, and E. P. Ippen, Opt. Lett., vol. 22, pp. 1150-1152, 1997.

[8] M. D. Pelusi, Y. Matsui, A. Suzuki, Opt. Lett., vol. 25, pp. 296-298, 2000.

[9] K. Mukasa, Y. Akasaka, Y. Suzuki, and T. Kamiya, ECOC'97, Edinburgh, U. K., Sept. 1997, vol. 1, pp. 127-130.

[10] T. Yamamoto, E. Yoshida and M. Nakazawa, Electron. Lett., vol. 34, pp. 1013-1014, 1998.

Raman gain efficiencies of modern terrestrial transmission fibers in S-, C- and L-band

Erwan Pincemin, Didier Grot, Laurence Bathany, Stéphane Gosselin, Michel Joindot

France Telecom R&D, Technopôle Anticipa, 2 Avenue Pierre Marzin, 22307 Lannion Cedex, France
Tel : (33) 2 96 05 06 59   Fax : (33) 2 96 05 10 08   Email : erwan.pincemin@francetelecom.com

Sylvain Bordais, Yves Jaouen, Jean-Marc Delavaux

Keopsys, 21 Rue Louis De Broglie, 22300 Lannion, France
Tel : (33) 2 96 05 08 00   Fax : (33) 2 96 05 08 01   Email : sbordais@keopsys.com

Abstract : We report the most complete measurements presented to date of Raman gain efficiency and noise figure for current G.652 and G.655 fibers in all three transmission windows (S-, C- and L-band). Such fiber characterization is paramount to the engineering and deployment of future terrestrial 40 Gbit/s-based WDM transmission systems.
©2002 Optical Society of America
OCIS codes: 060.0060, 060.2320

Introduction

The continuous increase in capacity of long-haul transmission networks has resulted in a renewed interest for distributed Raman amplification (DRA), which offers both wide-band amplification and significant improvement of optical signal-to-noise ratio compared to lumped amplification [1,2]. Stimulated Raman scattering (SRS) is a privileged way to produce DRA in a fiber because it is intrinsic to any silica-based glass. Although SRS has been known for nearly 30 years [3], the DRA implementation in the field is now rendered possible by the availability of cost effective and reliable high-power pumps.

A detailed Raman gain profile of transmission fibers is required for an accurate modeling of broadband DRA generated by single or multiple pump wavelengths in long-haul DWDM systems [2]. The Raman gain efficiency (C_R) is principally determined by the fiber effective area (A_{eff}). GeO_2 and SiO_2 concentration ratio influences also both magnitude and profile of Raman gain spectrum [4]. In addition, the equivalent noise figure (NF_{eq}) is dependent on the pump loss, which determines in turn the distributed gain along the transmission fiber.

In order to predict the differences in the generation of SRS in the various commercially available fibers, we have performed the complete characterization of SRS produced in G.652-type (SMF, Allwave[TM]) and G.655-type (Teralight[TM], Truewave-RS[TM], LEAF[TM]) fibers in the three wavelength transmission windows (i.e. S-, C- and L-band). In particular, we have measured and compared these fibers in term of Raman gain efficiency and noise figure. Our choice represents a comprehensive set of modern fibers already deployed worldwide in the carriers' long-haul transmission networks.

Raman gain spectra measurements

The experimental setup is depicted in figure 1. In our test bed, we duplicated a realistic distributed terrestrial DRA scheme as follows. A constant 100-km fiber length was used for each fiber under test. The fiber was counter-pumped with a 300 mW CW Raman Fiber Laser (RFL) at either λ_{S-band} = 1395 nm, λ_{C-band} = 1455 nm and λ_{L-band} = 1480 nm. The residue of the pump at the span end is deflected via a circulator. The random polarized RFL pump light provides a polarization independent DRA. A tunable ECL laser set at P_s= 0 dBm was used as the input signal to measure the Raman small signal gain dependence on wavelength. The RFL power was limited to 300 mW in order to avoid the detrimental effects due to the generation of excess ASE and noise from double Rayleigh scattering (DRS). Splices were precisely calibrated by the cutback method to measure accurately the pump power injected into each fiber under test.
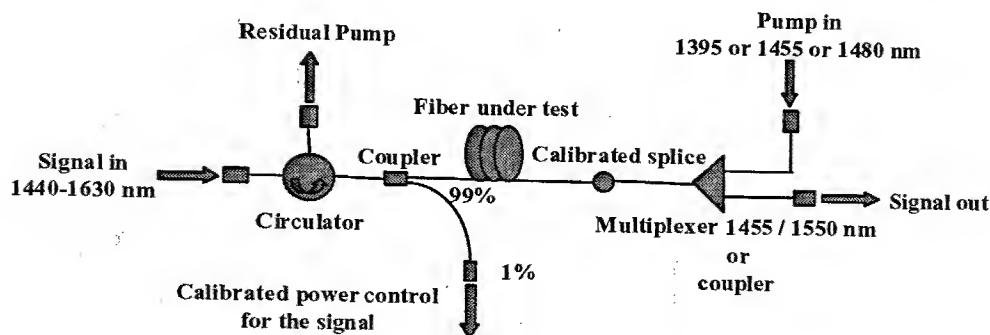
Figure 1: Experimental set-up

The $G_{on/off}$ measurements method [5,6] is chosen to cancel out any inaccuracy related to spectrally dependent attenuation of components, connectors, splices and fiber itself. For each fiber, a reference spectrum is acquired at the "signal out" port, with the pump turned "off", and a second spectrum with the pump turned "on", all other conditions being unchanged. The difference between these two spectrums gives $G_{on/off}$. The measurement accuracy was limited only by the power stability of the RFL (i.e. < 1%) and by the relative accuracy of the used OSA and power-meters. The fiber Raman efficiency C_R was derived from $G_{on/off}$ using the relation:

$$C_R = \frac{G_{on/off}}{P_{pump} \, L_{eff}} \quad with \quad L_{eff} = \frac{1 - e^{-\alpha_{pump} L_{span}}}{\alpha_{pump}} \quad (1)$$

P_{pump}, α_{pump}, L_{eff} and L_{span} are the injected pump power, the fiber loss at the pump wavelength, the effective length of the fiber under test, and the length of the amplification span (here 100 km), respectively.

Results and discussion

Figure 2 shows the Raman efficiency spectra over the S-, C- and L-band for the fibers under test. Table 1 summarizes the corresponding C_R and $G_{on/off}$ peak values as well as NF_{eq} measurements.
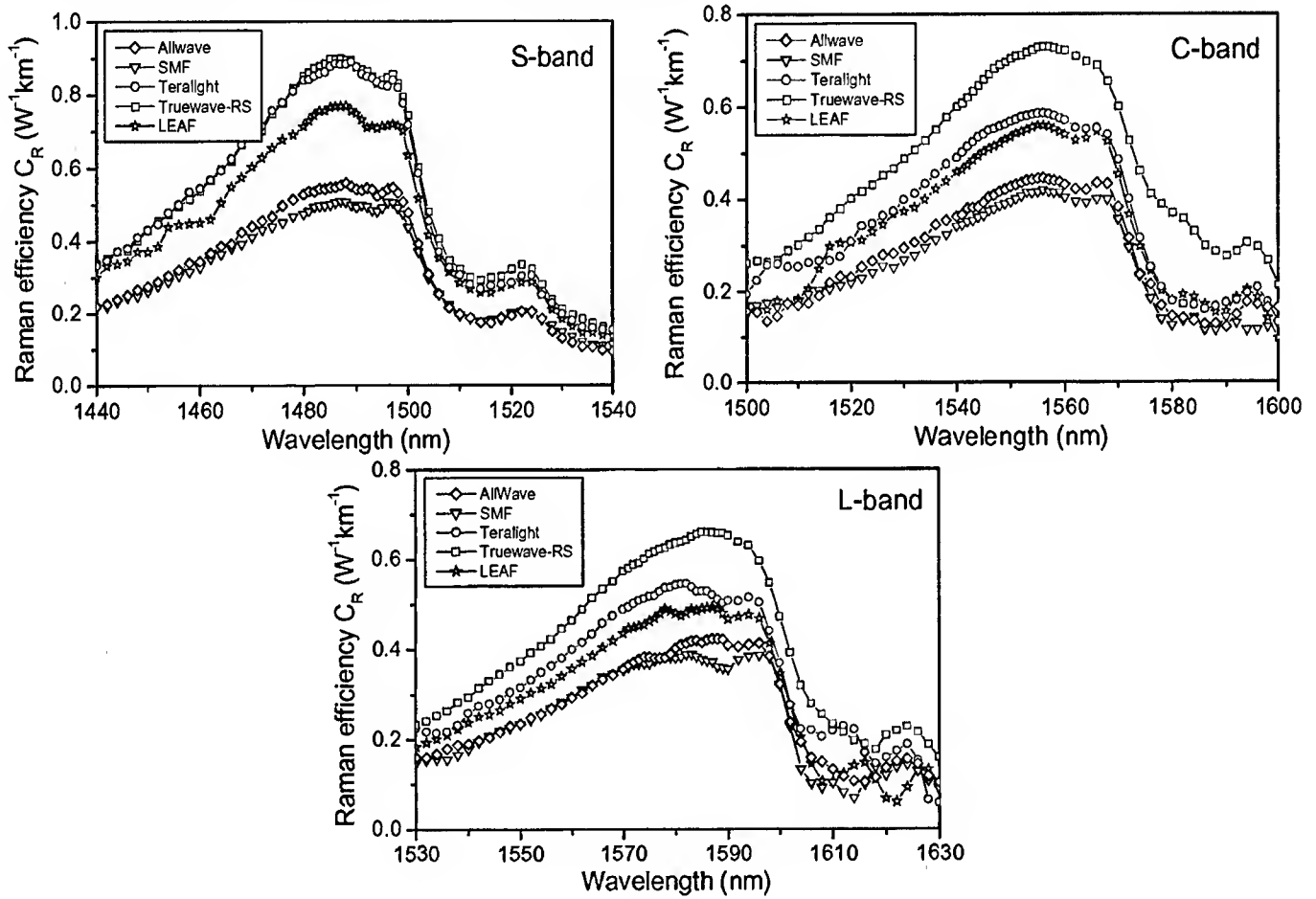
Figure 2: Raman gain efficiency of Allwave[TM], SMF, Teralight[TM], Truewave-RS[TM], and LEAF[TM] fibers in S-, C- and L-band.

The fiber presenting the highest Raman efficiency is Truewave-RS[TM] (0.90 $W^{-1}km^{-1}$ in S-band, 0.73 $W^{-1}km^{-1}$ in C-band, 0.66 $W^{-1}km^{-1}$ in L-band) because of it has the lowest A_{eff}. Then comes Teralight[TM] (0.89 $W^{-1}km^{-1}$ in S-band, 0.59 $W^{-1}km^{-1}$ in C-band, 0.54 $W^{-1}km^{-1}$ in L-band) and LEAF[TM] (0.77 $W^{-1}km^{-1}$ in S-band, 0.56 $W^{-1}km^{-1}$ in C-band, 0.49 $W^{-1}km^{-1}$ in L-band) which have larger effective area (A_{eff} =65 μm^2 and A_{eff} =72 μm^2 for Teralight[TM] and LEAF[TM], respectively) than Truewave-RS (A_{eff} =55 μm^2). The Raman cross section of material constituting the fiber has also a large influence on SRS efficiency. The germanium (GeO$_2$), used for increasing index of the fiber core, has a Raman gain coefficient substantially greater than that of silica (SiO$_2$) [4]. Consequently, fibers weakly doped in GeO$_2$ such as SMF and Allwave[TM] have the lowest Raman efficiencies: 0.51 $W^{-1}km^{-1}$ in S-band, 0.42 $W^{-1}km^{-1}$ in C-band, 0.39 $W^{-1}km^{-1}$ in L-band for SMF and 0.56 $W^{-1}km^{-1}$ in S-band, 0.44 $W^{-1}km^{-1}$ in C-band, 0.42 $W^{-1}km^{-1}$ in L-band for Allwave[TM]. The increase of GeO$_2$ doping results also in both growth and broadening of the principal Raman efficiency peak (located at 13.3 THz of the frequency pump) to the detriment of the secondary peak (placed at 14.5 THz of the frequency pump). Considering the results obtained over the

C-band, G.652 fibers (SMF and Allwave[TM]) have a particularly pronounced secondary peak compared to G.655 fibers (Teralight[TM] and Truewave-RS[TM]). The more highly GeO_2 doped fibers exhibit both clearly broader main and smoother secondary peaks. Moreover, it can be observed that the G.652 fibers present a much larger and flatter Raman gain profile over all S-, C- and L-band.

Table 1: S-, C- and L-band Raman gain efficiency and noise figure comparison for P_{pump} = 300 mW and P_s = 0 dBm.

Fiber type	1550 nm Fiber parameters			S-band			C-band			L-band		
	A_{eff} μm^2	D ps/nm/km	D' ps/nm²/km	α_{pump} dB/km	C_R W⁻¹km⁻¹	NF_{eq} dB	α_{pump} dB/km	C_R W⁻¹km⁻¹	NF_{eq} dB	α_{pump} dB/km	C_R W⁻¹km⁻¹	NF_{eq} dB
Allwave[TM]	80	17	0.07	0.27	0.56	-2.1	0.24	0.44	-3.2	0.22	0.42	-3.6
SMF	80	17	0.07	0.51	0.51	1.8	0.26	0.42	-1.0	0.24	0.39	-1.0
TeraLight[TM]	65	8	0.058	0.40	0.89	-0.7	0.27	0.59	-2.2	0.25	0.54	-2.0
Truewave-RS[TM]	55	4.4	0.045	0.36	0.90	0.0	0.25	0.73	-2.2	0.23	0.66	-2.2
LEAF[TM]	72	4.5	0.08	0.47	0.77	0.4	0.25	0.56	-1.6	0.24	0.49	-1.8

Comparison of overall Raman efficiencies values shows an increase trend from the L- to the S-band. The peak efficiencies obtained with 1395-nm pump are 0.90, 0.89, 0.77,, 0.56 and 0.51 W⁻¹km⁻¹ for respectively Truewave-RS[TM], Teralight[TM], LEAF[TM], Allwave[TM] and SMF whereas they are only 0.66, 0.54, 0.49, 0.42 and 0.39 W⁻¹km⁻¹ when pumped at 1480 nm. This trend is explained by the better confinement of signal and pump modes in the fiber core at shorter wavelength, resulting in a better pump-to-signal mode overlap in the S- than in the L-band.

As far as the noise figure results are concerned, it can be noticed first that higher NF_{eq} are measured in the S-band than in the C- and L-band. This situation is mainly due to increased pump losses when passing from the L- to the S-band. Indeed, higher pump loss induces smaller distributed gain, which results in higher NF_{eq}. As an example, for the Truewave-RS[TM], the NF_{eq} is improved by 2.2 dB from the S- to the L-band. The best overall NF_{eq} performances have been obtained for the Allwave[TM] due to the lower pump loss values for all three wavelength windows. The NF_{eq} improvement is especially notable in the S-band resulting from the removal of the OH⁻ attenuation peak (α_{pump}=0.27 dB/km for the Allwave[TM] instead of 0.51 dB/km for the SMF at λ_{S-band}). Correspondingly, the $G_{on/off}$ available in the S-band is 11.8 dB for the Allwave[TM] and only 5.8 dB for the SMF (for P_{pump}=300 mW).

Moreover, depending on the fiber physical properties, the DRS effect and ASE accumulation can limit the maximum Raman gain available. In that respect, the maximum pump power in the S-band was only about 300 mW and 400 mW for Truewave-RS[TM] and Teralight[TM], respectively. In the C- and L-band, pump power can be increased up to 500 mW without degradation for any fibers.

Conclusion

Raman gain efficiencies of recent G.652 and G.655 fibers over S-, C- and L-band have been measured and compared. We observed that Truewave-RS[TM] fiber presents the best Raman gain efficiency. However, in the S-band, the gain really available is severely limited by DRS effect and ASE noise accumulation. On the other hand, the Allwave[TM] fiber is particularly advantageous for DRA in the S-band when compared to standard SMF (in terms of $G_{on/off}$ and NF_{eq}). These complete Raman gain profiles, efficiencies and noise measurements could be applied for modeling the future DRA-based terrestrial 40 Gbit/s WDM transmission systems.

References

1. N. Takachio, H. Suzuki, H. Masuda, and M. Koga, "32x10 Gbit/s distributed Raman amplification transmission with 50 GHz channel spacing in the zero-dispersion region over 640 km of 1.55-μm dispersion-shifted-fiber", OFC'99, San Diego, OSA (Optical Society of the America), paper PD9 (1999).

2. S. Namiki and Y. Emori, "Ultrabroad-band Raman amplifiers pumped and gain-equalized by wavelength division multiplexed high power laser diodes", IEEE Journal On Selected Topics In Quantum Electronics, Vol.7, n°1, pp. 3-16 (2001).

3. R.H. Stolen and E.P. Ippen, "Raman gain in glass optical waveguides", Applied Physics letters, Vol.22, n°6, pp. 276-278 (1973).

4. J. Bromage, K. Rottwitt, and M.E. Lines, , "A method to predict the Raman gain spectra of germanosilicate fibers with arbitrary index profiles"

5. C. Fludger, A. Maroney, N. Jolley, R. Mears, "An analysis of the improvements in OSNR from distributed Raman amplifiers using modern transmission fibers", OFC'00, Baltimore, OSA (Optical Society of the America), paper FF2, pp.100-102 (2000).

6. D. Hamoir, N. Torabi, A. Bergonzo, S. Borne and D. Bayart, "Raman spectra of line fibers measured over 30THz"", Symposium on optical fiber measurements, Boulder, NIST (National Institute of Standards and Technology), paper 019 (2000).

160-GHz picosecond pulse train generation through multiwave mixing compression of a dual frequency beat signal

J. Fatome, S. Pitois and G. Millot

Laboratoire de Physique de l'Université de Bourgogne, Unité Mixte de Recherches CNRS n° 5027
9 Avenue A. Savary, BP 47 870, 21078 Dijon Cedex, France
Tel.: +33 (0)3 80 39 59 26, Fax: +33 (0)3 80 39 59 71, e-mail : jfatome@u-bourgogne.fr

Abstract : We report the experimental generation and characterization of a 160-GHz picosecond pulse train using multiple four-wave mixing temporal compression of an initial dual frequency beat signal in the anomalous-dispersion regime of a non-zero dispersion shifted fiber.

OCIS codes : (190.4370) Nonlinear optics, fibers; (190.7110) Ultrafast nonlinear optics

Multigigabit-compatible transform-limited (TL) optical pulse generators are expected to play a key role for increasing the transmission capacity in advanced optical fiber communication network, as well as for optical signal processing. In this context, the nonlinear transformation of a dual frequency optical beat signal propagating in an optical fiber is an attractive method for applications in high-speed optical communications. The reshaping of the beat signal into well separated short pulses was previously demonstrated by several methods based on dispersion decreasing along the fiber length [1], soliton Raman self-scattering effect in dispersion decreasing fiber [2] or switching in a nonlinear fiber loop mirror [3]. Alternative approachs of step-like [4] and comb-like [5] dispersion profiled fibers, using segments of conventional fibers with different dispersion, have been proposed for the generation of high repetition rate sub-picosecond pulse trains.

On the other hand, the propagation of a dual frequency signal in an optical fiber with constant anomalous dispersion may lead to a strong transfer of energy from the pumps into a relatively large set of sidebands generated by multiple four-wave mixing (FWM) [6]. The creation of high-order sidebands along the fiber is then accompagnied by a strong temporal compression of the initial sinusoidal beat signal [6]. Our objective is to present the first experimental demonstration of generation and characterization of high repetition rate train of TL pulses thanks to the technique of temporal compression via multiwave mixing process in the strong-interaction regime. In particular, in our experiments a 160-GHz train of 1.27 ps TL pulses has been obtained at 1550 nm using a single piece of 1-km-long non-zero dispersion-shifted fiber (NZ-DSF). The technique of frequency-resolved optical gating (FROG), adapted for high-repetition rate periodic pulse trains [7], was used to characterize directly the intensity and phase of the 160-GHz train generated from multiwave mixing interaction.

The initial beat signal is obtained by simultaneous injection in NZ-DSF of two incident continuous waves of different frequencies, with parallel linear polarizations and equal power. The nonlinear propagation of such a beat signal was numerically analyzed using the split-step Fourier method for the extended nonlinear Schrödinger (NLS) equation [8], including higher-order effects such as third-order fiber dispersion (TOD), self-steepening and intrapulse Raman scattering. Figure 1(a2) shows the 160-GHz sinusoidal input signal at 24 dBm average power evolving into compressed pulse train with 1.3 ps full width at half maximum (FWHM) pulses. The fiber length, where maximum compression occurs with minimum pedestal, is L = 2375 m. This length is relatively closed to the length for which the maximum conversion from the two initial waves into the first sidebands occurs (L = 2400 m), in good agreement with the prediction of Ref. 6. At the central wavelength of the initial sinusoidal beat signal, *i.e.* λ = 1550.35 nm, the fiber is assumed to have 0.21 dB/km loss, an anomalous dispersion of 1 ps/nm.km, a nonlinear coefficient of 1.7 $W^{-1}km^{-1}$, a Raman response time of 3 fs and a TOD of 0.07 ps/nm^2.km.

These parameters are those of the NZ-DSF used in our experiments. Figure 1(a1) shows that the phase across the pulses is constant, which implies TL pulses. The phase difference between the neighboring pulses is π. The output spectrum, shown in Fig. 1(a3), consisted of the two input frequencies that were used to generate the initial beating, as well as a cascade of equally spaced spectral lines, that is characteristic of the reshaping of the input beat signal into a train of well-separated pulses. At this power level, the multiwave mixing only slightly compressed the pulse from 3.125 ps to 1.3 ps to ensure no pedestal and TL pulses. On the other hand, as shown by Fig. 1(b2), as the average input power is increased up to 30 dBm, the compression factor increases (FWHM = 364 fs) and the required fiber length decreases to L = 977 m, while the pulse quality is degraded due to appearance of a broad low-intensity pedestal component and a non-uniform phase across the pulses [see Fig. 1(b1)]. The corresponding spectrum of Fig. 1(b3) exhibits a slight asymmetry due to the effect of TOD. Therefore, numerical solutions of the extended NLS equation show that there exist a trade-off between pulse quality, average power, pulsewidth, and fiber length.
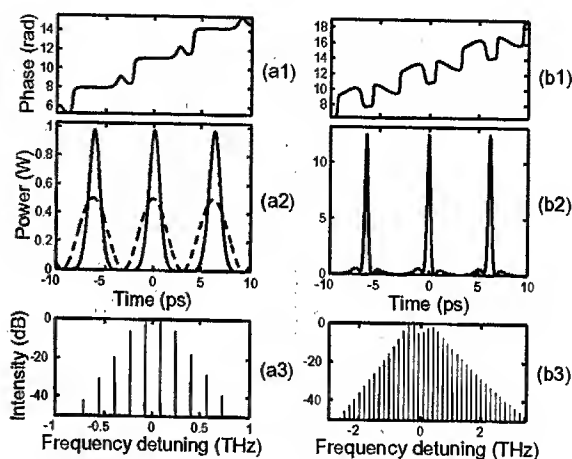
Fig. 1. Results of numerical simulation of a beat signal transformation into a train of short pulses for an input average total power of (a) 24 dBm and (b) 30 dBm.
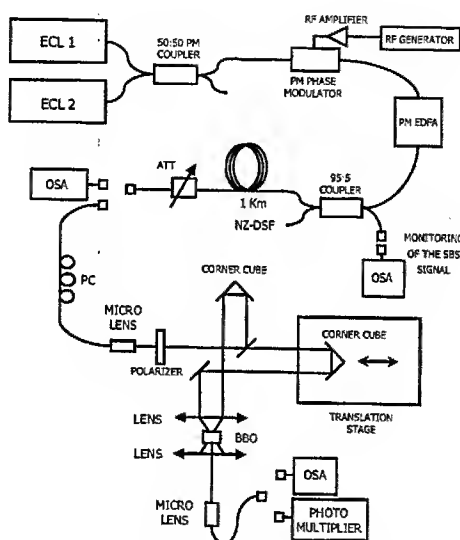
Fig. 2. Schematic of the experimental setup.

For the experimental demonstration of this technique, we have focused our attention on the case of generation of TL pulses. Figure 2 shows the design of the experimental setup. A dual frequency beat signal was synthesized from two cw 150-kHz-linewidth external cavity lasers (ECL1 and ECL2). The wavelength space between the two waves was set at 1.3 nm in order to generate pulse train at a near 160 GHz repetition rate. The center wavelength was fixed at $\lambda = 1550.35$ nm, while the zero-dispersion wavelength (ZDW) of the NZ-DSF is $\lambda_{ZD} = 1536.5$ nm. Both waves were combined by a fiber fused 50:50 coupler. The beat signal was then amplified to the desired average power level by an Erbium-doped fiber amplifier (EDFA). A phase modulator was used to suppress stimulated Brillouin scattering (SBS). The launched beat signal power into the 1-km-long NZ-DSF was set to 27.2 dBm. The output field after nonlinear reshaping in the NZ-DSF, was characterized with an optical spectrum analyzer (OSA), a background-free second-harmonic autocorrelator and a FROG setup.

Figures 3(a) and (b) show, respectively, the measured and retrieved SHG-FROG traces (128 x 128 grid) of the field after propagation through the 1-km NZ-DSF. The retrieval error was G = 0.0035. The corresponding retrieved intensity and phase are shown in Fig. 3(c). The intensity profile shows reshaped pulse train with remarkably no pedestal. The phase variation over the compressed pulses forming the train is also negligibly small, indicating that the pulses are nearly transform limited. The phase difference

between the neighboring pulses is π, in good agreement with theoretical predictions of Fig. 1. As shown in Fig. 3(d) the intensity profile corresponds very well to a gaussian function with 1.27-ps FWHM and 2.4-W peak power. The extinction ratio between peak power and interpulse background is in excess of 20 dB. As shown in Figs. 4(a) and 4(b) respectively, the spectrum and the autocorrelation that were derived from the retrieved pulse train (circles) are in excellent agreement with the independent direct experimental measurements (solid lines), confirming the reliability of the experimental setup.
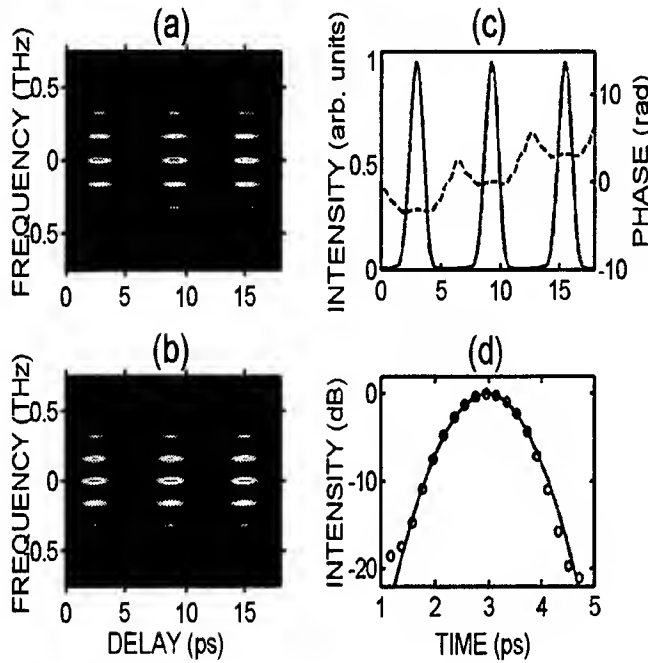
Fig. 3. (a) Measured and (b) retrieved SHG-FROG traces of the generated pulse train at 160 GHz. (c) The solid line shows the retrieved intensity (left-hand axis), whilst the dashed line shows the retrieved phase (right-hand axis). (d) Least squares fit of the retrieved pulse shape (solid line) by a gaussian function (open circles).
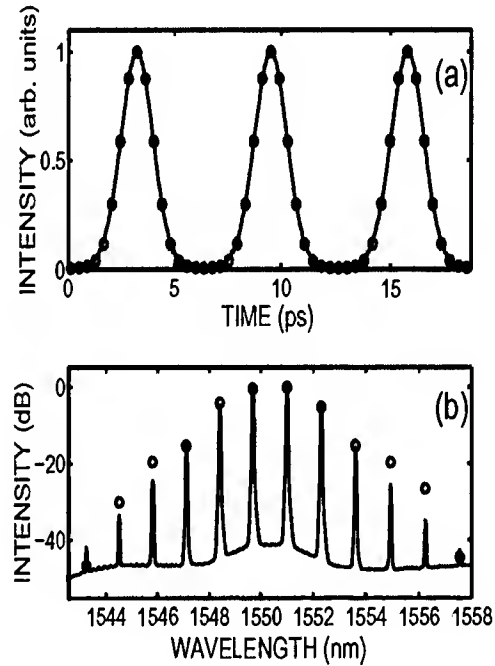
Fig. 4. (a) Measured autocorrelation and (b) spectrum of the 160-GHz pulse train at fiber output (solid curves). The open circles show the autocorrelation and spectrum calculated from the retrieved intensity and phase, respectively.

In conclusion, we have presented the experimental demonstration of multiwave mixing compression for reshaping of a beat signal into a high-quality train of picosecond TL pulses at 160-GHz repetition rate. We believe that this very simple technique has great potential as a high-quality source of TL pulses for dispersion-managed DWDM systems in future telecommunication networks.

References
1. P.V. Mamyshev, S.V. Chernikov, and E.M. Dianov, IEEE J. Quantum Electron. **27**, 2347 (1991); S.V. Chernikov, J..R. Taylor, P.V. Mamyshev, and E.M. Dianov, Electron. Lett. **28**, 931 (1992).
2. S.V. Chernikov, D.J. Richardson, R.I. Laming, E.M. Dianov, and D.N. Payne, Appl. Phys. Lett. **63**, 293 (1993).
3. S.V. Chernikov and J.R. Taylor, Electron. Lett. **29**, 658 (1993).
4. S.V. Chernikov, J..R. Taylor, and R. Kashyap, Electron. Lett. **30**, 433 (1994).
5. S.V. Chernikov, J..R. Taylor, and R. Kashyap, Electron. Lett. **29**, 1788 (1993); Opt. Lett. **19**, 539 (1994).
6. S. Trillo, S. Wabnitz, and T.A.B. Kennedy, Phys. Rev. A **50**, 1732 (1994).
7. F. Gutty, S. Pitois, P. Grelu, G. Millot, M.D. Thomson, and J.M. Dudley, Opt. Lett. **24**, 1389 (1999); J.M. Dudley, M.D. Thomson, F. Gutty, S. Pitois, P. Grelu, and G. Millot, Electron. Lett. **35**, 2042 (1999).
8. G.P. Agrawal, Nonlinear Fiber Optics, 3rd ed. New York: Academic (2001).

Cross correlation frequency-resolved optical gating characterization of supercontinuum generation in microstructure fiber: simulation and experiment

John M. Dudley
Laboratoire d'Optique P. M. Duffieux, Université de Franche-Comté, 25030 Besançon Cedex, FRANCE
Tel: +33 3 81 66 64 16, Fax: +33 3 81 66 64 23, Email: john.dudley@univ-fcomte.fr

Xun Gu, Lin Xu, Mark Kimmel, Erik Zeek, Patrick O'Shea, Aparna P. Shreenath, Rick Trebino
School of Physics, Georgia Institute of Technology, Atlanta, GA 30332-0430, USA

Stéphane Coen
Service d'Optique et Acoustique, Université Libre de Bruxelles, Av. F. D. Roosevelt 50, CP 194/5, B-1050 Brussels, BELGIUM

Abstract: Cross-correlation frequency resolved optical gating (XFROG) characterization of supercontinuum generation in microstructure fiber is studied using numerical simulations and experiments. The XFROG trace clearly reveals the signatures of dispersive wave and Raman soliton generation.
©2002 Optical Society of America
OCIS codes: (320.7100) Ultrafast measurements, (060.4370) Nonlinear optics, fibers.

1. Introduction

The generation of ultrabroadband supercontinuum (SC) spectra has been experimentally demonstrated by a number of research groups by injecting high power near-infrared femtosecond pulses into tapered or microstructure fibers [1–2]. Although some numerical modeling of SC generation has also been reported [3–4], a comparison between numerical simulations and experiments has not been possible because of difficulties in accurately characterizing the complex temporal and spectral structure of the SC. Recently, however, cross-correlation frequency resolved optical gating (XFROG) has allowed the first intensity and phase measurements of the generated SC to be carried out [5, 6] and, in this paper, we compare these XFROG measurements with the results of numerical simulations using an extended nonlinear Schrödinger equation (NLSE). The simulations allow several important physical processes responsible for SC generation to be identified and, moreover, illustrate how the XFROG trace itself provides an intuitive and powerful means of interpreting correlated temporal and spectral features of the SC.

2. Numerical Simulations

The extended NLSE is valid down to the three optical cycle regime, and includes quantum noise, higher order nonlinearity, and stimulated Raman scattering [7]. The fiber dispersion was modeled over the range 300–1600 nm. Pulse propagation was simulated for a 15 cm length of large air-fill fraction microstructure fiber with a zero dispersion wavelength (ZDW) at 780 nm [1]. Fig. 1(a) presents simulation results showing the spectral and temporal evolution as a function of propagation distance for 30 fs FWHM, 10 kW peak power input pulses injected at 800 nm. The initial propagation is dominated by approximately symmetrical spectral broadening and strong temporal compression, but after around 2 cm, the broadening becomes strongly asymmetric and is associated with the development of complex temporal features. In particular, the figure shows temporal pulse break-up, the development of ultrafast temporal oscillations on portions of the temporal intensity profile, as well as the generation of Raman soliton pulses which separate from the residual input pulse due to group velocity walkoff [8]. The spectral broadening increases with further propagation, extending over an octave from 550–1100 nm at the output. Fig. 1(b) shows the output characteristics in more detail, with numerical filtering used to correlate the distinct Raman solitons labeled A and B with the corresponding peaks in the output SC spectrum. The figure also shows several other interesting features. For example, a portion of the output temporal intensity profile is shown on an expanded timebase in order to highlight the ultrafast oscillations which have developed during propagation. The oscillation frequency varies slightly across the profile, with the mean frequency estimated at 115 THz. Another feature of interest is the strong normal dispersion-regime peak DW around 600 nm on the spectrum. This peak arises from the resonant transfer of energy from the Raman solitons via dispersive wave generation [9], and is manifested in the time-domain as a broad low-amplitude pulse on the Raman soliton trailing edge.
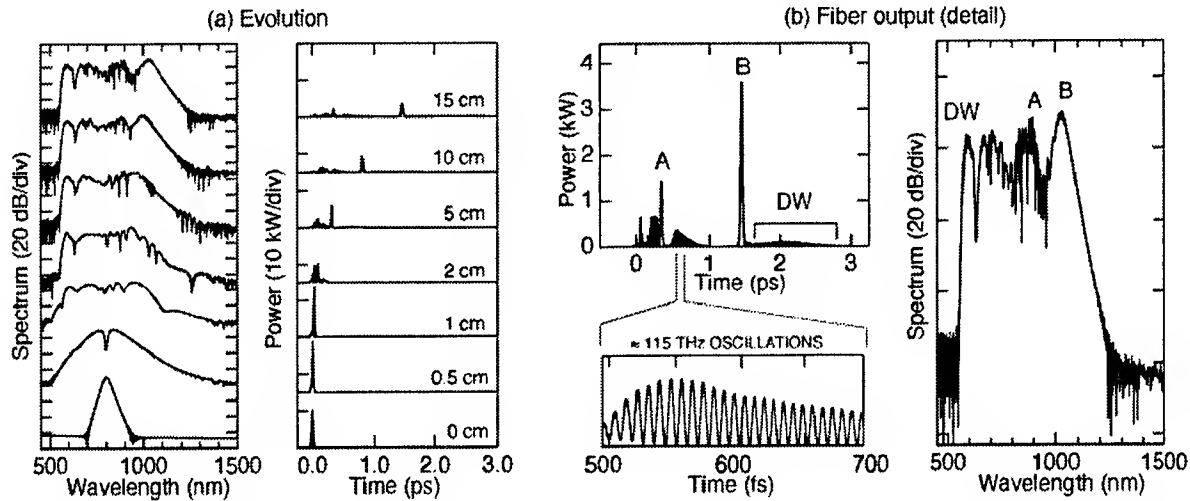
Fig. 1 (a) Spectral and temporal evolution in microstructure fiber of a 10kW peak power 30 fs input pulse injected at 800 nm. (b) Output intensity and spectrum shown in detail.

These predicted spectral and temporal characteristics are in good agreement with previous experiments which have observed strong normal dispersion regime peaks [2] and distinct Raman soliton formation [10, 11] during SC generation. However, it is of more interest to consider how these features are manifested in the XFROG trace of the fiber output, as this permits a direct comparison with the results of more recent experiments. To this end, Fig. 2 plots the calculated XFROG trace obtained from the spectral resolution of the sum-frequency generation (SFG) intensity cross-correlation between the generated SC and the 30 fs input pulse at 800 nm. The structure of the XFROG trace is compared with the SC temporal intensity (bottom) and spectrum (right) and we note that the spectral plot uses a nonlinear wavelength axis so that structure in the XFROG trace at a particular SFG wavelength can be directly related to the corresponding SC spectral component.
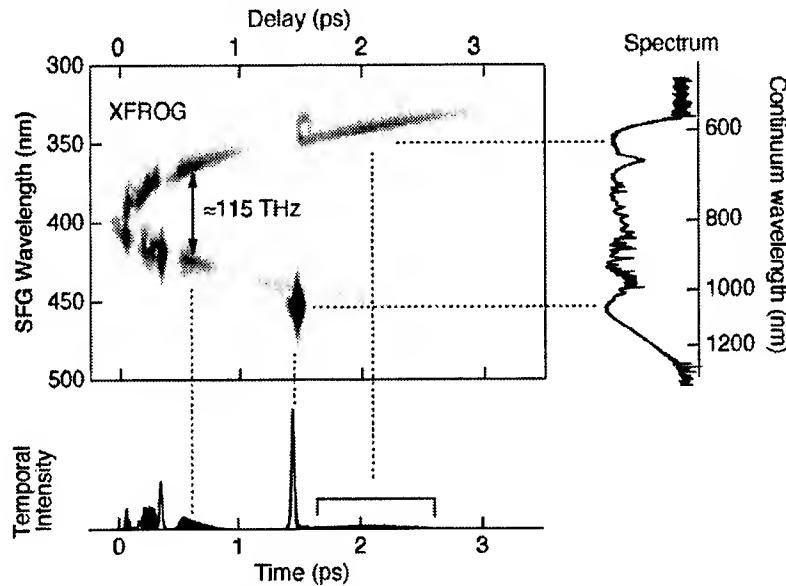
Fig. 2 Calculated XFROG trace with its structure correlated with the intensity and spectrum. Note the nonlinear wavelength axis used in the plot of the fundamental SC spectrum.

The advantages of using a time-frequency XFROG measurement for interpreting the different SC features can be clearly seen from this figure. For example, the simple visual inspection of the XFROG trace allows the particular time and frequency domain signatures of the dispersive wave and Raman soliton components to be immediately identified and correlated. In addition, the parabolic group delay variation with wavelength (which reflects the linear dispersive characteristics of the fiber) is immediately apparent. Even more significantly, since the portion of the

temporal intensity profile which has developed ultrafast oscillations is seen to be associated with two distinct XFROG wavelength components separated by 115 THz, the origin of the ultrafast modulation can be physically interpreted as a result of the beating between these components. Moreover, the fact that the corresponding components in the fundamental spectrum (at 679 nm and 917 nm) are distributed symmetrically (in frequency) about a wavelength of 780 nm, allows this modulation to be identified as a consequence of four wave mixing about the fiber ZDW [12]. The XFROG trace allows the origin of this modulation to be identified in a way which is not possible from examining the separate intensity and spectral measurements.

3. Comparison with Experiments

Several experiments have now reported preliminary XFROG measurements to characterize the intensity and phase of ultrabroadband SC spectra [5, 6]. Although uncertainties in the injected power and the fiber parameters used in these experiments preclude a detailed quantitative comparison with simulations, the numerical results above nonetheless allow several distinct features seen in the experimental XFROG traces to be physically interpreted. For example, Fig. 3(a) (taken from Ref. 6) and Fig. 3 (b) (taken from Ref. 5) show the measured XFROG traces obtained from two different experiments. Both XFROG traces exhibit the expected parabolic variation of group delay with wavelength and, in addition, trace (a) clearly shows both the development of pulse breakup near zero delay, and the development of a short-wavelength dispersive wave on the pulse trailing edge. These effects can also be seen on the retrieved profile intensity shown in Fig. 3(c). Trace (b) shows similar characteristics and, in addition, shows strong evidence for a Raman soliton component which has walked off from the zero delay position.
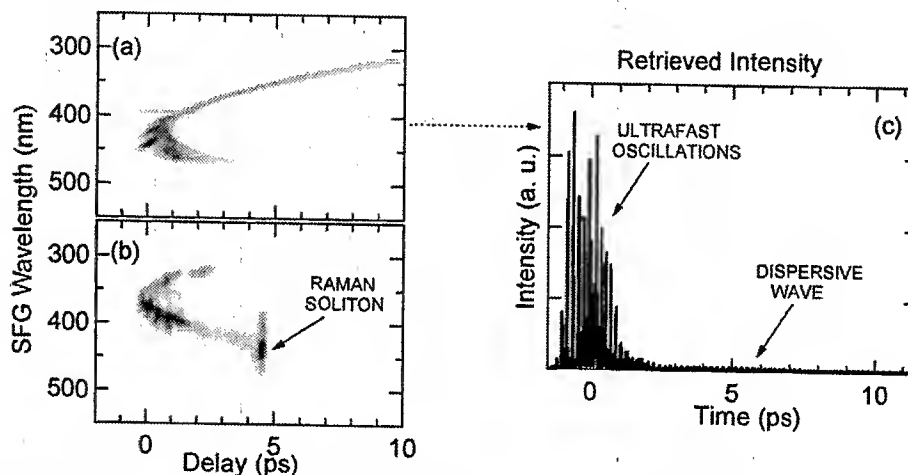
Fig. 3 (a) and (b): two different measured XFROG traces. (c) the retrieved intensity for trace (a).

4. Conclusions

Analyzing SC generation via the XFROG trace allows related spectral and temporal features to be intuitively correlated and permits their physical origin to be readily identified. Our simulations using a generalized NLSE predict distinct features in the XFROG trace which have been observed in several experiments. We anticipate that these simulations will find wide use in designing optimized SC generation experiments.

References

1. J. K. Ranka, R. S. Windeler, A. J. Stentz, Opt. Lett. **25**, 25 (2000).
2. T. A. Birks, W. J. Wadsworth, P. St. J. Russell, Opt. Lett. **25**, 1415 (2000).
3. A. Gaeta, Paper CMK3 in Conference on Lasers and Electro-optics (CLEO), OSA Technical Digest, 48 (2001).
4. A. V. Husakou and J. Herrmann, Phys. Rev. Lett. **87**, 203901 (2001).
5. L. Xu, M. W. Kimmel, P. O'Shea, R. Trebino, J. K. Ranka, R. S. Windeler, A. J. Stentz, Paper TuC6 in Conference on Ultrafast Phenomena (2000).
6. M. W. Kimmel, R. Trebino. J. K. Ranka, R. S. Windeler, A. J. Stentz, Paper CFL7 in Conference on Lasers and Electro-Optics (CLEO), OSA Technical Digest, 622 (2000)
7. K. J. Blow, D. Wood, IEEE J. Quant. Electron. **25**, 2665 (1989).
8. M. N. Islam, G. Sucha, l. Bar-Joseph, M. Wegener, J. P. Gordon, D. S. Chemla, J. Opt. Soc. Am. B **6**, 1149 (1989).
9. P. K. A. Wai, C. R. Menyuk, Y. C. Lee, H. H. Chen, Opt. Lett. **11**, 464 (1986).
10. B. R. Washburn, S. E. Ralph, P. A. Lacourt, J. M. Dudley, W. T. Rhodes, R. S. Windeler, S. Coen, Electron. Lett. **37**, 1510 (2001).
11. I. G. Cormack, D. T. Reid, W. J. Wadsworth, J. C. Knight, P. St. J. Russell, Electron. Lett. **38**, 167 (2002).
12. J. M. Dudley, L. Provino, N. Grossard, H. Maillotte, R. Windeler, B. J. Eggleton, S. Coen, J. Opt. Soc. Am. B. **19**, 765 (2002).

Broadband 60 % energy conversion of a two-pump fiber optical parametric amplifier

J.M. Chávez Boggio, W. Margulis[*], and H.L. Fragnito.

Optics and Photonics Research Center, Unicamp-IFGW, 13083-970, CP 6165 Campinas, SP Brazil. Fax:+ 55 19 788 5427, E-mail: jmchavez@ifi.unicamp.br

*ACREO, Electrum 236, Stockholm, 16440, Sweden.

Abstract. We demonstrate over 60 % energy conversion on 20 nm bandwidth centered at 1568 nm in a two-pump fiber optical parametric amplifier.

OCIS codes: 060.2320, 190.4380.

1. Introduction

Parametric amplification or wavelength conversion can be obtained from $\chi^{(2)}$ or $\chi^{(3)}$ nonlinear susceptibility. The mix of a strong pump wave with a weak signal wave into the nonlinear medium, amplify the signal and generates a strong idler at the output. Most attention have been focused on $\chi^{(2)}$ based devices, where the pump energy that is transferred to the signal and the idler waves can be in excess of 90 %. Devices based on the $\chi^{(3)}$ nonlinear susceptibility have been less investigated. In a one-pump fiber optical parametric amplifier (OP-FOPA) [1] Marhic et al. obtained ~90 % pump energy transfer in an 11 km dispersion shifted fiber pumped with 200 mW cw power. The main limitation of OP-FOPAs is that high energy conversion cannot be obtained over broad bandwidth, i.e., the efficiency is maximum for a particular signal wavelength where phase matching is most perfect [2] and reduces strongly for other wavelengths. In comparison, the two-pump FOPA (TP-FOPA) exhibits flatter and broader gain spectrum. The bandwidth in these devices is maximized when the two pumps are tuned nearly symmetrically to the zero dispersion wavelength of the fiber [2]. We demonstrate here efficient (65 %) energy conversion from the pumps to the signal and idler in a TP-FOPA. From our measurements we verified that high-energy conversion is obtained over 20 nm bandwidth with weak dependence on the signal wavelength.
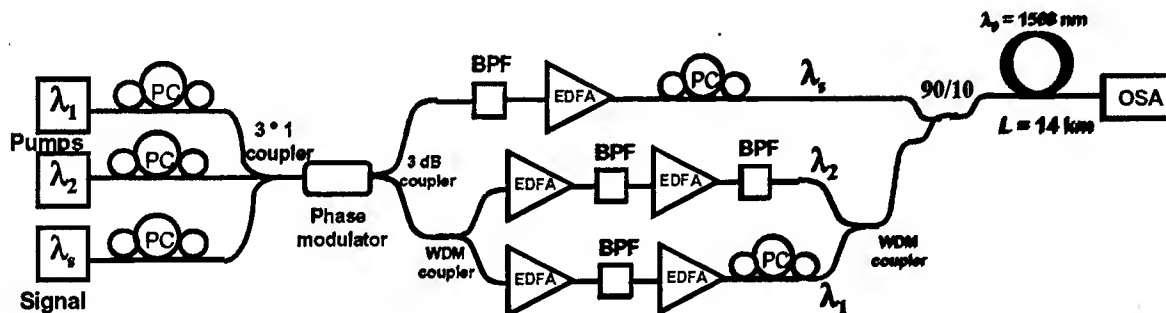
Figure 1. Two-pump FOPA configuration. PC: Polarization controller. BPF: Optical bandpass filter.

2. Experimental setup

The configuration of the two-pump FOPA is shown in figure 1. We used a 14 km Corning LS fiber with measured average zero dispersion wavelength λ_0 = 1567.9 nm, attenuation coefficient α = 0.053 km^{-1}, and nonlinear coefficient γ = 2.1 (W-km)$^{-1}$. The cw pumps lasers, at wavelengths λ_1 = 1558.4 and λ_2 = 1577 nm, and the tunable signal at λ_s were spectrally broadened by phase modulation at 840 MHz to prevent stimulated Brillouin backscattering. Usually, only the pump lasers are phase modulated. However, since we are interested in maximizing the energy conversion, the signal would eventually become as strong as the pumps. For this reason we also passed the signal through the phase modulator. Our phase modulator has an insertion loss of 12 dB. To compensate for this excessive loss we used three EDFAs to amplify independently the three lasers. The band-pass filters were used to remove most of the ASE from the EDFAs that is also amplified in the TP-FOPA and would eventually drive this last into saturation. The two WDM couplers (each with 0.21 dB insertion loss) are of the type generally used to couple or decouple L and C bands. The 90/10 coupler combined the signal and pumps. The three lasers were linearly polarized

with parallel polarizations. Spectra were measured with an optical spectrum analyzer (OSA) with 0.07 nm resolution.

4. Results and Discussion

Figure 2(a) shows the spectrum at the input fiber with a signal at 1561.75 nm. The input powers were P_1^{in} = 21.5 dBm (=141.2 mW), P_2^{in} = 19 dBm (= 79.5 mW), and P_s^{in} = 7.5 dBm (5.0 mW). Following ref. [1] we calculated the conversion efficiency as $\eta = (P_1^{out} + P_2^{out})_{signal\,on} / (P_1^{out} + P_2^{out})_{signal\,off}$. This definition, which is actually the pump depletion factor, is a good measure of conversion efficiency if the power diverted into the amplified noise and spurious FWM products can be neglected. Figure 2(b) shows the output spectra for the cases when the signal was turned off (dashed line) and turned on (solid line). With the signal off the output pumps powers were P_1^{out} = 17.4 dBm (= 54.95 mW), P_2^{out} = 16.85 dBm (48.4 mW), i.e. $(P_1^{out} + P_2^{out})_{signal\,off}$ = 103.15 mW, while in the presence of the signal we obtained and P_1^{out} = 13 dBm, P_2^{out} = 13.25 dBm, giving $(P_1^{out} + P_2^{out})_{signal\,on}$ = 40.85 mW. This represents a conversion of 60 %. Note in fig. 2b that the signal and the idler (P_s^{out} = 15.2 dBm and P_i^{out} = 14.7 dBm) are ~3 dB higher than the pumps, indicating the high efficiency of conversion of our TP-FOPA. Note also that the amplified noise and spurious FWM power is less than 1% of the pump lasers or the signal and idler, thus validating the procedure to calculate the conversion efficiency from the pump depletion factor. Finally note that the signal gain is only ~8 dB; high energy conversion is achieved for high input signals, when the FOPA operates in the gain saturation regime. This is clearly demonstrated in fig. 3 where we plot the conversion efficiency as a function of input signal power. As shown in fig.3, within the range of powers available in our experiment, the efficiency increases monotonically with P_s^{in}. The maximum achieved efficiency was limited in our experiment by the large insertion loss of the components in our setup.
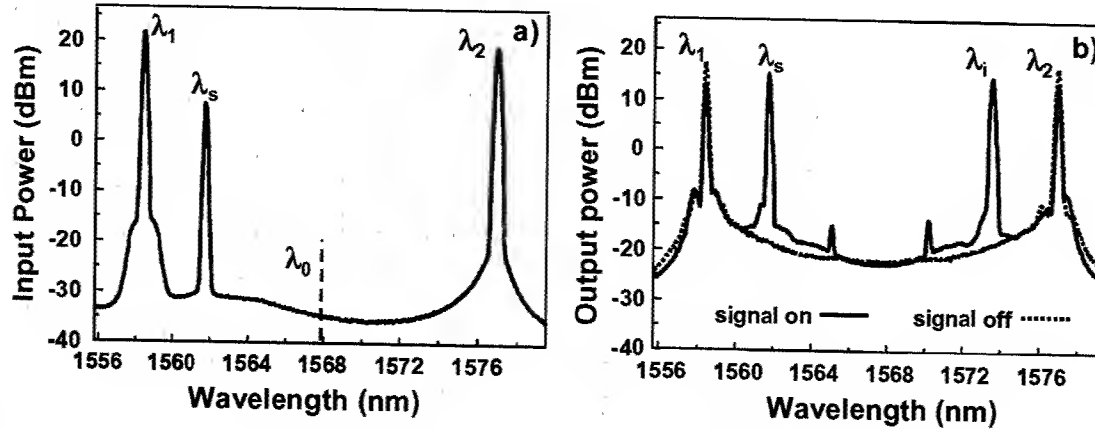
Figure 2. (a) Input spectrum. (b) Output spectra for λ_s = 1561.75 nm.
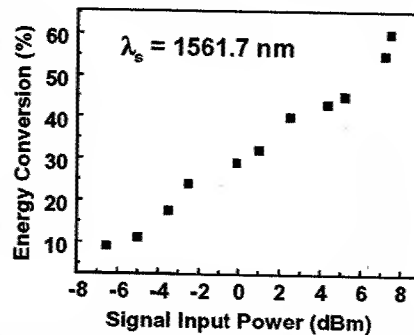
Figure 3. Measured energy conversion as a function of the signal input power for λ_s = 1561.7nm.

We measured the conversion efficiency for several signal wavelengths between λ_1 and λ_2 (18.5 nm bandwidth) and we always observed $\eta \sim 60$ %. Figures 4(a) and 4(b) show two typical output spectra when for $\lambda_s = 1560$ nm (65 % energy conversion) and $\lambda_s = 1566.5$ nm (60 % conversion), respectively. In all cases we verified that amplified noise and spurious FWM products did not contribute appreciably to pump depletion.
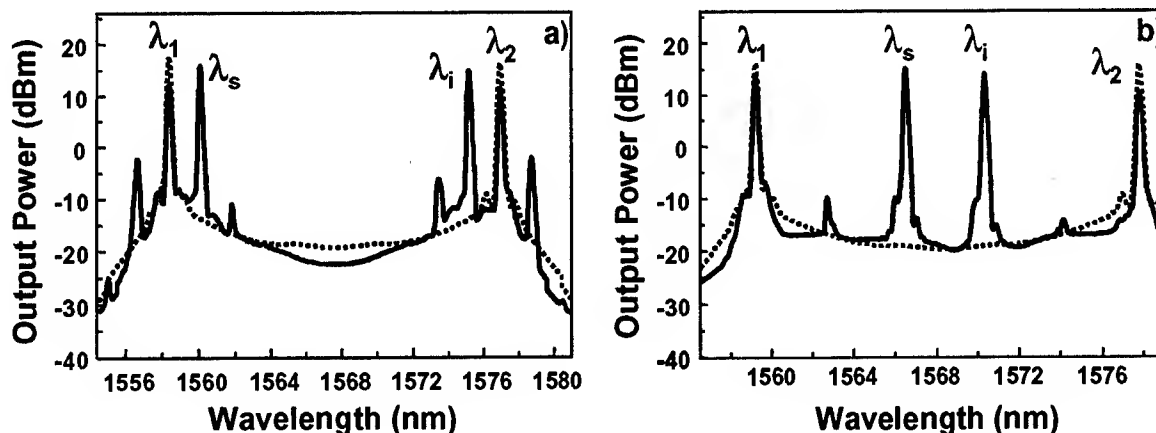
Figure 4. Measured output spectra for (a) $\lambda_s = 1560$ nm, and (b) $\lambda_s = 1566.5$ nm.

5. Conclusions

We experimentally demonstrated, for the first time, to the best of our knowledge, a two-pump fiber optical parametric amplifier having 60 % energy conversion over 20 nm bandwidth. The bandwidth and input signal power in our experiments were limited by the characteristics of the optical devices. On the basis of previous work [3] and the observed monotonic growth of efficiency with input signal power, we believe that even larger efficiencies and over broader bandwidths can be obtained with TP-FOPAs.

6. References

[1] M.E. Marhic, K.K.Y. Wong, M.C. Ho, L.G. Kazovsky, "92 % pump depletion in a continous-wave one-pump fiber-optical parametric amplifier," Opt. Lett., **26**, 620-622 (2001).

[2] G. Cappellini and S. Trillo, "Three-wave mixingmetric amplifiers and wavelength converters with low-ripple Chebyshev gain spectra," J. Opt. Soc. Am. B., **8**, 824-831 (1991).

[3] J.M. Chavez Boggio, F.A. Callegari, S. Tenenbaum, J.B. Rosolem, M.R.X. Barros, and H.L. Fragnito, "Demonstration of 26 dB on-off gain in a two-pump fiber optical parametric amplifier," in Optical Fiber Communication Conference, OFC'2002, OSA Technical Digest (Optical Society of America, Washington, DC, 2002), paper WGG-18.

Spectral phase fluctuations and coherence degradation in supercontinuum generation in photonic crystal fibers

John M. Dudley and Remo Giust

Laboratoire d'Optique P. M. Duffieux, Université de Franche-Comté, 25030 Besançon Cedex, FRANCE

john.dudley@univ-fcomte.fr

Stéphane Coen

Service d'Optique et Acoustique, Université Libre de Bruxelles, Av. F. D. Roosevelt 50, CP 194/5, B-1050 Brussels, BELGIUM

Abstract:. Numerical simulations are used to study spectral phase fluctuations and coherence degradation in supercontinuum generation in photonic crystal fibers. The spectral coherence is shown to depend strongly on the input pulse duration and wavelength.

©2002 Optical Society of America

OCIS codes: 190.4370, 190.4380

1. Introduction

Recent numerical modelling of supercontinuum (SC) generation in photonic crystal fibers (PCF) has provided an improved understanding of the important physical mechanisms underlying the observed extreme spectral broadening [1-3]. However, an aspect of SC generation in PCF which has not yet been the subject of detailed theoretical study is the sensitivity of these spectral broadening processes to input pulse noise. This is, nonetheless, a subject of much importance, as key optical metrology applications require highly coherent SC with low pulse-to-pulse fluctuations [4,5]. On the other hand, the noise properties of broadband spectra generated in standard optical fiber have previously been studied extensively in a telecommunications context, where spectrally-sliced SC have been proposed as dense wavelength division multiplexing sources. Significantly, this previous work has shown that SC generation using femtosecond pulse pumping in the presence of noise can, in fact, be associated with significant temporal jitter and a poorly defined spectral phase across the generated spectrum [6, 7]. In this paper, we present results of numerical simulations of SC generation in PCF which show that, for femtosecond pulse pumping in the anomalous dispersion regime, input pulse noise leads to large fluctuations in the spectral phase across the SC. By quantifying the phase fluctuations via the mutual degree of coherence, the influence of the input pulse wavelength and duration on the coherence is conveniently studied and the optimal experimental conditions for coherent SC generation are identified.

2. Numerical Model

Our simulations use a scalar generalized nonlinear Schrödinger equation (NLSE) [8] to model SC generation in a 10 cm length of PCF with a zero dispersion wavelength at 780 nm and an effective area of 2 μm^2. The NLSE included the fiber dispersion over 300–1700 nm, as well as self-steepening, Raman scattering and a phenomenological model for input pulse quantum noise based on a one photon per mode noise seed with random phase. Fig. 1(a) shows the output spectral and temporal profiles for 5 different simulations performed under identical conditions except for the initial quantum noise. The input field here was an 10 kW peak power 850 nm 150 fs $sech^2$ pulse. The output spectra exhibit 20dB spectral widths spanning over an octave from 550–1100 nm, in agreement with experiments. Several other important features are also highlighted. Nonlinear and dispersive interactions lead to rapid temporal oscillations from modulational instability (MI) which seeds Raman soliton formation associated with the temporal and spectral peaks A, B and C. As shown previously [6], SC generation in the presence of MI and Raman scattering can be very sensitive to noise, and significant spectral and temporal jitter from run to run is clearly seen in the figure. Figure 1(b) shows the average temporal and spectral profiles calculated from a large ensemble of simulations, clearly showing how the jitter leads to significant averaging of the fine structure observed in Fig. 1(a). In terms of the coherence properties, this jitter is also associated with shot-to-shot fluctuations in the spectral phase at each wavelength in the SC, and this quantified in the bottom plot in Fig. 1(b). Here, we plot as a function of wavelength, the standard deviation of the spectral phase calculated from the ensemble, and the figure illustrates the greater stability in the center relative to the edges of the spectrum
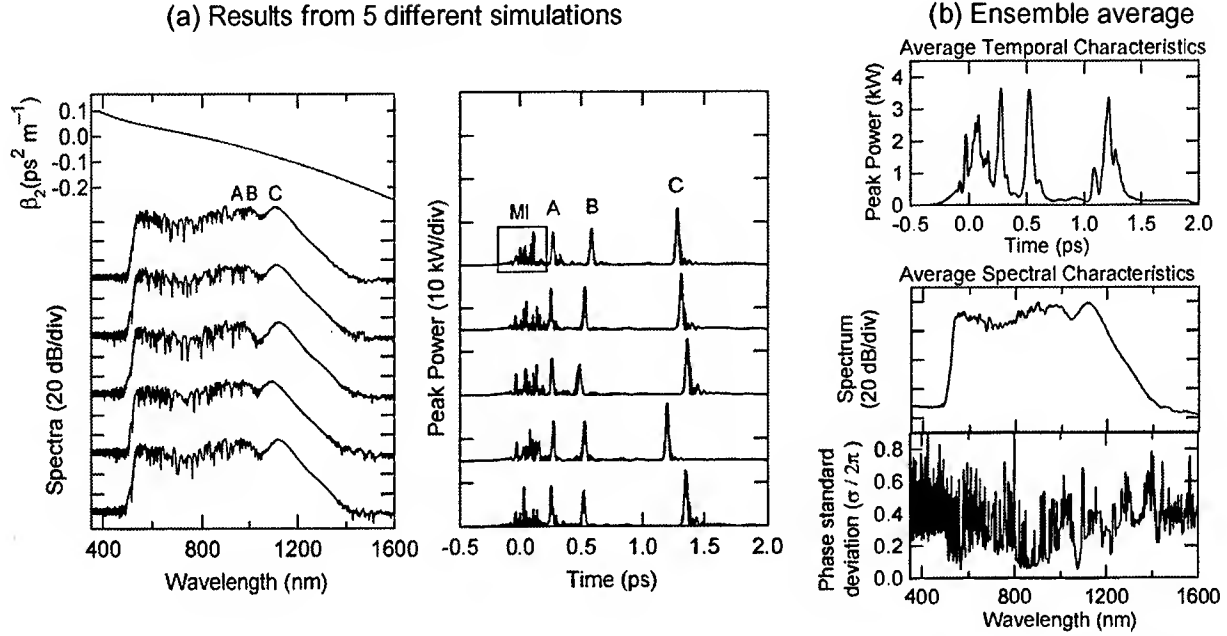
Fig.1 (a) Spectra (left) and temporal intensity profiles (right) from 5 different simulations. The spectral plot also includes the fiber group velocity dispersion variation (top). (b) Results from ensemble average showing the average temporal intensity (top) and the average spectrum and the standard deviation of the spectral phase (bottom).

The coherence degradation can be examined more quantitatively by using a modified Young's double slit set-up, adapted from recent experiments quantifying SC coherence in bulk media [9]. Here, two SC generated from successive pulses in a pulse train from a femtosecond modelocked pump laser separately illuminate two slits. A spectral filter (or a grating) placed after the slits is used to examine the interference fringes generated at each wavelength in the spectrum. Since the position of the fringe pattern is determined by the phase difference between the two SC, variations in this phase difference due to jitter between successively-generated SC is manifested in the shot-to-shot translation of the interference pattern and a consequent reduction in the fringe visibility. In fact, this visibility provides a rigorous measure of the local SC coherence properties since it is directly related to the modulus of the complex degree of (mutual) coherence between the independent SC sources $|g_{12}|$ defined as:

$$\left| g_{12}^{(1)}(\lambda, t_1 - t_2) \right| = \left| \frac{\left\langle E_1^*(\lambda, t_1) E_2(\lambda, t_2) \right\rangle}{\sqrt{\left\langle \left| E_1(\lambda, t_1) \right|^2 \right\rangle \left\langle \left| E_2(\lambda, t_2) \right|^2 \right\rangle}} \right|$$

We have calculated the degree of coherence $|g_{12}|$ from an ensemble of 200 pairs of independently-generated SC obtained from input pulses with different random quantum noise. The top curves in Fig. 2 present results which show the output spectra and the degree of coherence for pulse injected at 850 nm, with duration ranging from 150–50 fs. Although the spectral broadening in all cases is comparable, it is clear that the mutual coherence $|g_{12}| \ll 1$ over a large range of wavelengths for the 150 fs input pulse, whereas $|g_{12}| \approx 1$ across the entire spectrum for the shortest 50 fs input pulse.

The fact that improved coherence properties are observed with shorter pulses suggests that the decoherence is associated with MI-induced spectral broadening processes which are more significant for longer input pulses where the broadening due to self-phase modulation is reduced. Further support for this interpretation comes from simulations studying the variation of the coherence properties over a range of different wavelengths. These results are shown as the bottom curves in Fig. 2. Here we see clearly that for an input wavelength of 740 nm in the normal dispersion regime where MI is completely inhibited, there is negligible coherence degradation. The generated spectral width of 350 nm at the 20 dB level is, however, significantly less than that obtained with the anomalous dispersion regime pump at 850 nm.
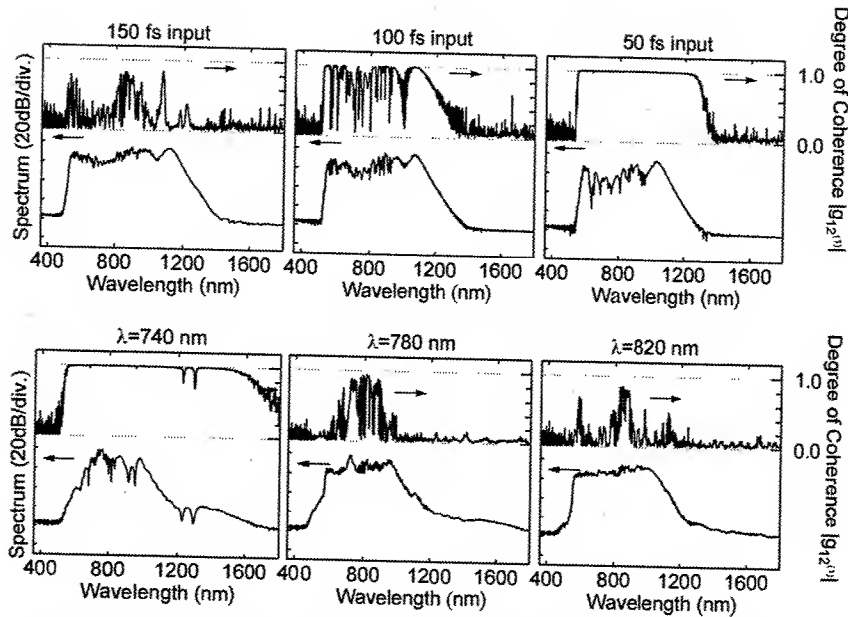
Fig. 2 Top: Output spectra and degree of coherence as a function of input pulse duration for a pulse at 850 nm. Bottom: Output spectra and degree of coherence as a function of input wavelength for a 150 fs input pulse.

3. Conclusions

The results above have several important implications. For frequency metrology, where coherent SC spanning more than an octave are required, our results suggest that this requires pulses of duration 50 fs or less. Further simulations which we have carried out also show that the presence of additional intensity noise (>0.1%) on the pump pulses increases the timing jitter and coherence degradation, illustrating the importance of using stabilized pump lasers in SC generation experiments. Finally we note that the temporal and spectral fluctuations which induce coherence degradation can also be manifested in the form of intensity fluctuations across the SC spectrum. This intensity noise exhibits frequency-dependence similar to that of the complex degree of coherence, and is minimized under the same conditions.

References

1. A. L. Gaeta, Paper CMK3 in Conference on Lasers and Electro-optics (CLEO 2001), OSA Technical Digest, 48 (2001).
2. S. Coen, A. H. L. Chau, R. Leonhardt, J. D. Harvey, J. C. Knight, W. J. Wadsworth, and P. St. J. Russell, Opt. Lett. **26**, 1356 (2001).
3. A. V. Husakou and J. Herrmann, Phys. Rev. Lett. **87**, 203901 (2001).
4. R. Holzwarth, M. Zimmermann, Th. Udem, T. W. Hänsch, P. Russbüldt, K. Gäbel, R. Poprawe, J. C. Knight, W. J. Wadsworth, P. St. J. Russell, Opt. Lett. **26**, 1376 (2001).
5. T. M. Fortier, J. Ye, S. T. Cundiff, R. Windeler, Opt. Lett. **27**, 445 (2002).
6. M. N. Islam, G. Sucha, I. Bar-Joseph, M. Wegener, J. P. Gordon, D. S. Chemla, J. Opt. Soc. Am. B, **6**, 1149 (1989).
7. H. Kubota, K. R. Tamura, and M. Nakazawa, J. Opt. Soc. Am. B **16**, 2223 (1999).
8. K. J. Blow and D. Wood, IEEE J. Quant. Electron. **25**, 2665 (1989).
9. M. Bellini and T. W. Hänsch, Opt. Lett. **25**, 1049 (2000).

Single-mode supercontinuum generation in a standard dispersion-shifted fiber using a nanosecond microchip laser

A. Mussot, L. Provino, T. Sylvestre and H. Maillotte

Laboratoire d'Optique P.M. Duffieux, UMR-6603 CNRS/Université de Franche-Comté,

16 route de Gray. 25030 Besançon cedex, France

arnaud.mussot@etudes.univ-fcomte.fr

Abstract: We have generated a single-mode supercontinuum of more than 1100-nm simply using a nanosecond microchip laser and an usual dispersion-shifted fiber in a regime in which both self-phase modulation and parametric generation near the zero-dispersion wavelength cannot be involved in the continuum formation.

In view of their potential for many applications such as optical metrology and high-bit rate communications, supercontinua (SC) have been the object of growing attention these last few years. In particular, several techniques have been recently demonstrated in specially-designed optical fibers that exhibit large nonlinearities and particular dispersion profiles [1–3,5,6]. For instance, SC with spectral extent of more than 1200-nm have been generated in photonic-crystal fibers (PCF) [2] and in tapered fibers [5]. It has been shown that the resulting spectral broadening was mainly due to the effect of self-phase modulation of powerful femtosecond pulses. Provino *et al.* and Coen *et al.* showed later that picosecond or nanosecond pulses can also generate broadband continua in a case where self-phase modulation is negligible [1,3]. Basically, the build-up of SC with femtosecond or longer pulses appears as an intriguing and complex frequency-conversion process and the physical mechanisms that are at play have been well understood only very recently by means of numerical simulations of an extended nonlinear Schrödinger equation including the Raman scattering [1,4]. In the picosecond and nanosecond regimes, the SC essentially results from a preliminary Raman-induced energy transfer from the pump to higher-wavelengths up to the vicinity of the zero-dispersion wavelength (ZDW) of PCF's, and a further merging of the wideband continuum through multiple four-wave mixing (FWM) processes. These techniques offer impressive results but they have the drawback of requiring special optical fibers and a bulky laser source in most cases. In this communication, we would like to emphasize that special optical fibers are not needed for ultra-broadband SC generation. To this end, we present experimental results performed in a standard long dispersion-shifted fiber (DSF) that demonstrate the generation of a spatially single-mode supercontinuum of more than 1100-nm with a spectral power density about 5 μW/nm. We used 0.4-ns pulses at 532 nm from a compact passively Q-switched Nd:YAG microchip laser in a regime in which self-phase modulation and FWM near the ZDW cannot be involved in the SC generation. Instead, we show that the SC in our experiment results from an interplay between parametric processes with multimode phase-matching and double cascade Raman scattering that further evolves in a spatially single-mode SC. It is worth noting that attempts have been made to generate continua in standard telecommunication fibers in the past [7–9], but it is significant that there has been no experimental results showing a spectral extent equivalent to that obtained in PCF or in tapered fibers.

The fiber used in our experiment was a 650-m-long DSF with ZDW at 1550 nm and cutoff at 1020 nm. The pump pulses were produced by a frequency-doubled, passively Q-switched Nd:YAG microchip laser at a repetition rate of 6.7 kHz. The mean power at 532-nm and pulse duration were 15 mW and 0.4 ns, respectively. The linearly-polarized single-mode output beam was focused into the DSF using a 10× microscope objective with a coupling efficiency exceeding 70 %. Finally, the continuum was recorded at the fiber output by means of an optical spectrum analyser and its dynamics was analyzed by tuning the launched power.

Figure 1 shows the different steps of the continuum formation for increasing input powers. In Fig. 1(a), the pump power was raised above the Raman threshold and we can clearly see a strong first-order Raman Stokes band (S_1) at 546 nm (Ω_R=13.2 THz). Additionally, another strong Stokes wave called (P_P) and shifted by
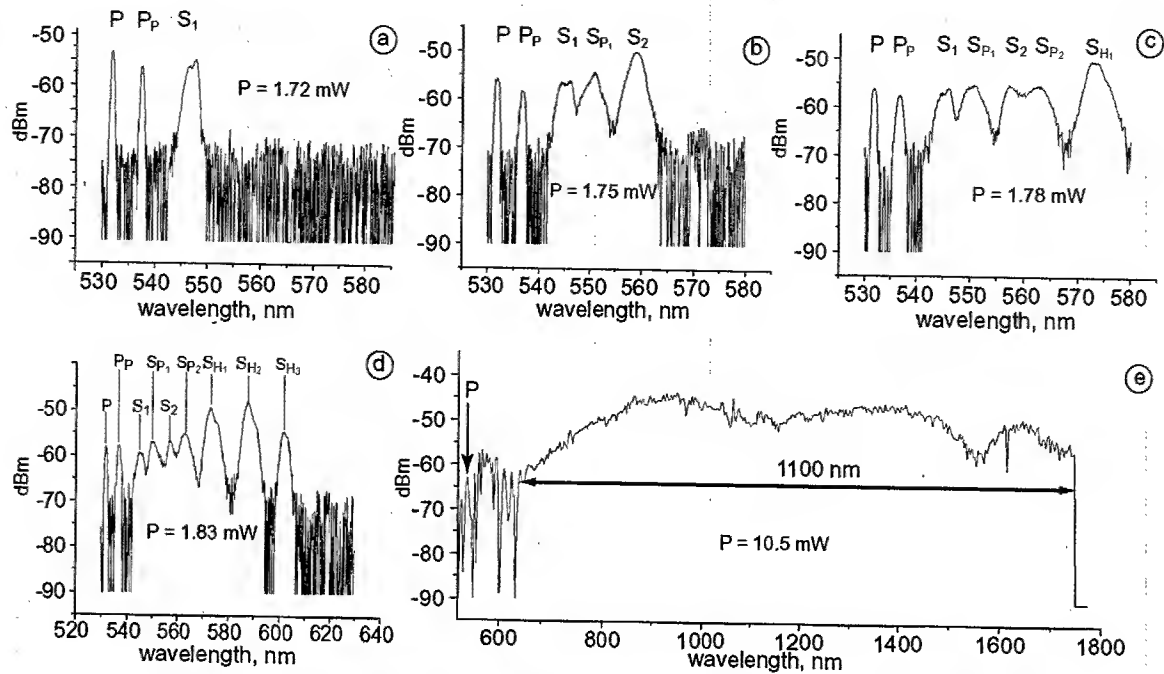
Fig. 1. SC formation for increasing mean powers from a (P=1.72 mW) to e (P=10.5 mW).
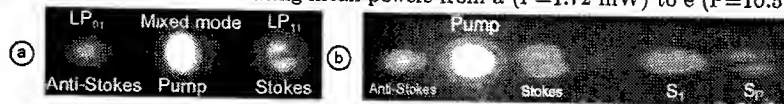
Fig. 2. Modal distribution of the FWM spectrum for the pump P (a) and for the Raman Stokes wave S_1 (b)).

5-nm from the pump was spontaneously generated through a multimode phase-matched parametric process, which will be detailed below. This parametric wave P_P acts as a second pump and generates its own first-order Raman Stokes band S_{P_1}, as illustrated in Fig. 1-(b). This interpretation can be easily verified in Fig. 1-(c) that shows the occurrence of a second-order Stokes wave S_{P_2} at 563 nm generated from S_{P_1}, which is close to the second-order Stokes wave S_2 associated with S_1.

Because of the multimode nature of the DSF in the visible, the wave S_{P_1} is further assisted by FWM gain with a multimode phase-matching involving the first-order Raman Stokes S_1 as a parametric pump. The initial pump pulse at 532 nm (P) and the parametric pump (P_P) at 537 nm are thereby responsible for the generation of two simultaneous Raman cascades. In Fig. 1-(d) in which the pump power was still increased, the double Raman cascade merge by creating a wider hybrid Raman Stokes wave S_{H_1} that in turn generates higher-order bands $S_{H_{2,3}}$, thus leading to an ultra-broadband continuum of more than 1100-nm (see Fig. 1-e).

Let us examine in details the different steps of the continuum formation in our experiment. First, because of the multimode nature of the DSF and its strong group-velocity dispersion at λ=532 nm, the generation of the wave (P_P) results from a well-known multimode phase-matched FWM process [10]. To identify the modal composition of this parametric process, a cut back experiment in a 1-m long fiber has revealed that the interacting modes in the FWM process are the LP_{11} and LP_{01}. As illustrated in Fig. 2-(a), the pump is distributed in these two modes, giving rise to a LP_{01} anti-Stokes wave and a LP_{11} Stokes wave. This same modal distribution appears in Fig. 2-(b) for the second FWM process involving S_1. Hence, S_{P_1} that is generated in the LP_{11} mode results from the combination of parametric generation from S_1 and Raman gain from P_P. Note that we did not observe the anti-Stokes waves associated with P and S_1 in Figs. 1-(a-d) because they are absorbed by Raman effect. Starting from the usual phase-matching relation [10] and by simply modelling the DSF as a step-index fiber, we calculated a frequency-shift of 5.7 nm for the Stokes wave in agreement with measurements (the parameters are 2.8 μm core radius, a core-cladding index difference of 0.0054, β_2=6.6.10^{-26}s^{2}m^{-1}).
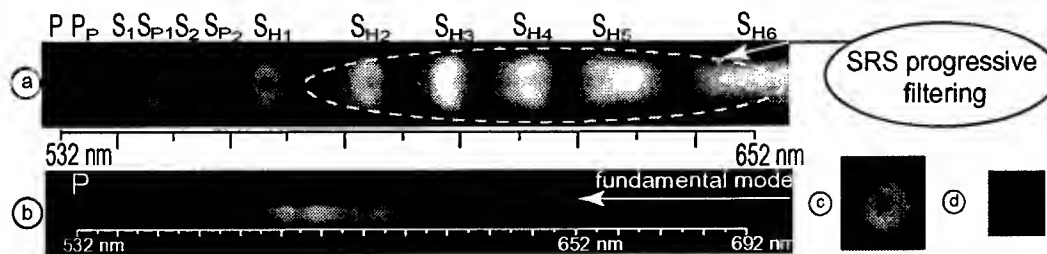
Fig. 3. Modal distribution of the SC in the spectral domain. (a) Recorded with a CCD camera, (b) recorded with a classical camera. Far-field intensity distribution of the output spot without (c) and with (d) chromatic filtering.

Then, the interplay of SRS and multimode FWM leads to the double Raman cascade. In the case of a simple Raman cascade, it has been shown in Ref. [8] that the spectral extent of a given higher-order Raman component S_N is typically two times that of the preceding Raman component S_{N-1}. Since two simultaneous Raman cascades initially appear in our case, we can except that this broadening process does account for the evolution from discrete Raman Stokes orders towards hybrid orders and subsequently towards the continuum generation.

Besides, the spatially single-mode character of the SC is an important issue for applications. Figures 3 (a-b) depict the modal composition (along vertical axis) of the SC spectrum recorded after dispersion on a diffraction grating. The mixed-mode distribution shown in Fig. 3(a) for the discrete components P to S_{H_5} is characteristic of mode coupling in long optical fibers [11]. Fig. 3(a) demonstrates that from S_{H_6} (λ=652 nm) the distribution evolves towards the fundamental LP_{01} mode. Indeed, the SC which is formed from λ=652 nm up to 1750 nm is exclusively generated in the fundamental mode, as shown in Fig. 3(b). To verify this property, the fiber output spot has been filtered by means of a low-pass chromatic filter at 650 nm. Figure 3-(c-d) shows the far-field spatial intensity distribution with and without the filter. The spot size reduction of the filtered mode as well as its homogeneous intensity distribution (Fig. 3-d) confirm that the SC is indeed single-mode. This interesting feature is due to a progressive modal filtering by the Raman gain and the transverse mode overlapping during propagation (see Fig. 3-a).

To conclude, a spatially single-mode visible-IR supercontinuum exceeding 1100-nm has been generated in an usual dispersion-shifted fiber using a microchip nanosecond laser. To our knowledge, this is the simplest setup that allows one to generate such supercontinua in optical fibers. The SC features, the compactness and attractive cost of the setup present many advantages for applications such as spectroscopy, interferometry, optical coherence tomography, and microscopy. Also, as the SC dynamics relies on an original combination of various nonlinear processes different from those involved in photonic-crystal fibers, these results contribute to a further understanding of the complexity of continuum generation in fibers.

References

1. S. Coen, A. H. Lun Chau, R. Leonhardt, J. D. Harvey, J. C. Knight, W. J. Wadsworth and P. St. J. Russell, J. Opt. Soc. Am. B, **19**, 4, 753 (2002).
2. J. K. Ranka, S. Windeler and A. J. Stenz, Opt. Lett. **25**, 25 (2000).
3. L. Provino, J.M. Dudley, H. Maillotte, N. Grossard, R. S. Windeler et B. J. Eggleton, Electron. Lett., **37**, 9, 558 (2001)
4. J.M. Dudley, L. Provino, H. Maillotte, N. Grossard, R. S. Windeler et B. J. Eggleton, and S. Coen, J. Opt. Soc. Am. B, **19**, 766 (2001).
5. KT. A. Birks, J. Wadsworth and P. St. J. Russel, Opt. Lett. **25**, 1415 (2000).
6. K. Mori , H. Takara and S. Kawanashi, J. Opt. Soc. Am. B, **12**, 1780 (2001).
7. C. Lin, and R. H. Stolen, Appl. Phys. Lett., **28**, 216 (1976).
8. I. Ilev, H. Kumagau, K. Tyoda and I. Koprinkov, Appl. Opt. **35**, 2548 (1996).
9. G. A. Nowak, J. Kim, and M. Islam, Appl. Opt. **38**, 7364 (1999).
10. G. P. Agrawal, *Nonlinear fiber optics*, Accademic Press, Optics and Photonics series, third edition, San Diego (2001).
11. King S. Chiang, Opt. Lett. **17**, 352 (1992).

Nonlinear Guided Waves

Poster Session: 2

Tuesday, September 3, 2002

NLTuD
4:00pm – 6:00pm
Lower Level Foyer

Thermal effects and spontaneous motion of cavity solitons in semiconductor microcavities

T. Maggipinto[1]*, I. M. Perrini[1], M. Brambilla[1], L. Spinelli[2], G. Tissoni[2] & L. A. Lugiato[2]

[1] *INFM, Dipartimento Interateneo di Fisica, Università di Bari, Via Orabona 4, 70126 Bari, Italy*

[2] *INFM, Dipartimento di Scienze, Università dell'Insubria, Via Valleggio 11, 22100 Como, Italy*

* t.maggipinto@fisica.uniba.it

One of the goals of the extensive work in the field of transverse pattern formation in nonlinear optical systems[1] is the investigation of possible applications to optical information technology. A major result is that the problem of correlation among different parts of a global structure, which eventually would destroy stored information, can be overcome by generating spatial structures that are localised in space, individually addressable and independent one from the other. These structures, called Cavity Solitons (CSs)[2,3], have been theoretically predicted in nonlinear materials inside a cavity driven by a coherent holding beam acting as an external input.

Most interesting from the practical viewpoint, for miniaturization purposes, is the case in which the active medium is a semiconductor. In recent works[3,4,5] a number of phenomenological models have been proposed in order to describe the semiconductor material. More accurate models including a microscopic description of the optical nonlinearity have also been reported[6,7]. For such models, existence and stability of CS have been theoretically predicted, both in active and passive configuration. The first clear and unequivocal experimental demonstration of CS in semiconductor devices has been recently achieved in[8].

Here, we want to study the role of thermal effects on semiconductor microcavities driven by an external coherent field. We evaluate their influence on the transverse spatio-temporal dynamics of the system and on the stability of CS, by studying thermally induced instabilities due to a combined effect of field diffraction, carrier diffusion, heating and thermal diffusion. We consider both the case of a bulk medium in a passive configuration, and the case of a MQW medium in an active configuration (that is, the device is electrically pumped, behaving as an amplifier).

The most striking result of our analysis has been obtained in the active case. It is the discovery that, for extended parametric domains, the slow thermal dynamics induces a spontaneous travelling-wave motion of both spatial patterns and cavity solitons[9]. This result has been later substantiated by Firth and collaborators[10] using a simplified model, which indicates the robustness of this phenomenon with respect to the details of the electronic nonlinearity. The analysis of [10] shows that the same phenomenon occurs, in restricted parametric domains, also for dark cavity solitons in passive systems.

We included the thermal dependence in the material susceptibility by considering a nonlinear red shift of the semiconductor band-gap when increasing temperature. We also introduced a linear thermal shift of the cavity resonance which accounts for the linear refractive index change. A simple rate equation for the lattice temperature has also been introduced under the assumption, reasonable in the regimes of our interest (sub lasing), that the plasma temperature has a much faster dynamics than the lattice temperature, so that it can be adiabatically eliminated. In the frame of paraxial and slowly varying envelope approximation, and in the mean field limit, the system equations reduce to three nonlinear PDEs, describing the dynamics of the intracavity field, of the carrier density and of the temperature field. These dynamical variables evolve on very different timescales: microseconds for the temperature, nanoseconds for the carriers and picoseconds for the field . The presence of three very different time scales requires a heavy computational effort.

In the passive case, we preliminarily decided to approach the problem by successive steps, the first of which was the reproduction of global, purely dynamical phenomena related to the role of heating, such as the Regenerative Oscillations (RO)[11] and the phenomena of switching point inversion.

By considering only the coupling between carrier and temperature field we could show the occurrence of a dominant Hopf instability giving rise to RO. We could also conclude that, as opposed to what has been shown in fluid dynamical models, carrier and thermal diffusions are unable, alone, to cause pattern formation or structure localisation.

As for the active case, we performed numerical simulations for both one and two transverse dimensions, but the figures shown in this summary concern only the 1D case, a physical situation appropriate to model the experiments on diode amplifiers carried out in Nice by Tredicce et. al. We consider a sample in which the active material consists of few GaAs/AlGaAs Quantum Wells. The device is pumped by an electrical current that causes a population inversion in the active material, so that the device becomes an amplifier, kept a few percent below lasing threshold.

We have performed the usual linear stability analysis of the homogeneous steady state; both Turing and Hopf instabilities are present, one or the other being dominant depending on the parameter choice. We show by direct numerical integration of the dynamical equations that, for particular choices of parameters, travelling spatial patterns arise. The existence of a travelling pattern is related to the presence of the Hopf instability with respect to spatially modulated perturbations (MI).

For the same values of parameters travelling CS can be obtained. We observe that a CS rapidly forms in the location of the address beam on the fast carrier time-scale (nanoseconds). Then, it persists there, for a time on the order of the thermal time-scale (microseconds), and then it starts to drift. This new CS behaviour is a feature of the thermal effects.

With the help of Fig. 1 we can thus interpret this evidence: after the CS formation, it starts to dig a minimum in the temperature spatial profile, because at the CS location there are less carriers and thus heating is reduced. When the temperature in the minimum reaches a value such that the CS would be no longer stable, it starts moving, following the temperature gradient, i.e. towards larger values of temperature.

Intensity profile   temperature profile
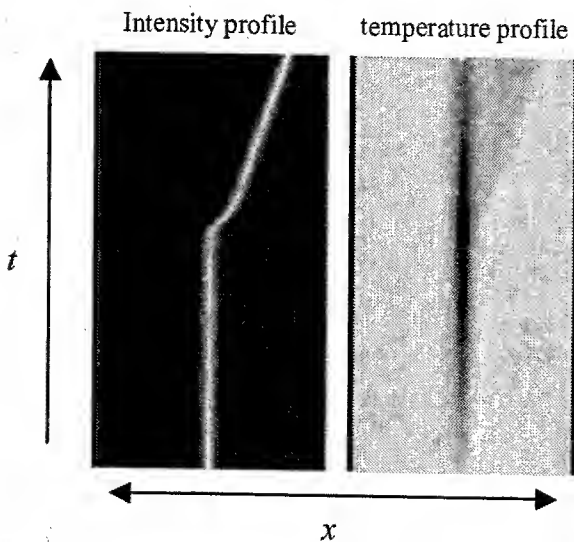
Fig 1 Grayscale plot of the time evolution of the intensity CS profile (left) and the temperature field profile (right) after the switch on of a CS. White corresponds to intensity and temperature maxima. On the vertical axis, time ranges from 0 to 1 μs. Sample width is 200 μm.

The time scale of CS drifting is of several microseconds. This means that if we can operate faster than this timescale, thermal effects have no influence. In particular this is true for applications such as information processing and commutation. For static optical encoding instead, this drift could in principle be a problem. However, despite this thermally induced instability, by proper use of a phase modulation in the holding beam[2,5] CS can be pinned in fixed locations. In Fig. 2 it is shown that progressively larger gradients in the phase of the holding beam confine the CS motion and eventually bring it back to a stationary behaviour where it remains fixed in the location where it has been switched on.
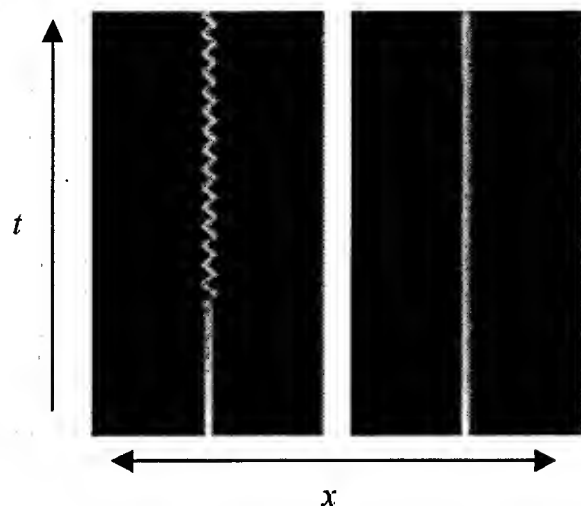
Fig 2 Grayscale plot of the time evolution of the intensity CS profile in presence of a phase modulation in the holding beam. White corresponds to intensity maxima. Starting from left, progressively larger phase gradients in the holding beam are considered.
The total integration time is of 12 μs.
Sample width is as Fig. 1

References

[1] L. A. Lugiato, M. Brambilla and A. Gatti, Optical Pattern Formation. In *Advances in Atomic, Molecular and Optical Physics*, Vol. 40, eds. Bederson, B. & Walther, H. (Academic Press, 1998) pp. 229-306.

[2] W.J. Firth and A.J. Scroggie, Optical bullet holes: robust controllable localized states of a nonlinear cavity. *Phys. Rev. Lett.* 76, 1623-1626 (1996).

[3] M. Brambilla, L.A. Lugiato, F. Prati, L. Spinelli and W.J. Firth, Spatial soliton pixels in semiconductor devices. *Phys. Rev. Lett.* 79, 2042-2045 (1997).

[4] D. Michaelis, U. Peschel and F. Lederer, Multistable localized structures and superlattices in semiconductor optical resonators. *Phys. Rev. A* 56, R3366-R3369 (1997).

[5] L. Spinelli, G. Tissoni, M. Brambilla, F. Prati and L. A. Lugiato, Spatial solitons in semiconductor microcavities. *Phys. Rev. A* 58, 2542-2559 (1997).

[6] G. Tissoni, L. Spinelli, M. Brambilla, T. Maggipinto, I.M. Perrini and L. A. Lugiato, Cavity solitons in passive bulk semiconductor microcavities. I. Microscopic model and instabilities. *J. Opt. Soc. Am.* B 16, 2083-2094 (1999).

[7] L. Spinelli, G. Tissoni, M. Tarenghi and M. Brambilla, First principle theory for cavity solitons in semiconductor microresonators, *Eur. Phys. J. D* 15, 257-266 (2001).

[8] S. Barland, J.R. Tredicce, M. Brambilla, L.A. Lugiato, S. Balle, M. Giudici, T. Maggipinto, L. Spinelli, G. Tissoni, T. Knoedl, M. Miller and R. Jaeger, Cavity solitons work as pixels in semiconductors, submitted for publication.

[9] L. Spinelli, G. Tissoni, L.A. Lugiato and M. Brambilla, Thermal effects and transverse structures in semiconductor microcavities with population inversion, submitted to *Phys. Rev. A* (2002).

[10] A. J. Scroggie, J. M. McSloy and W. J. Firth Self-propelled cavity solitons in semiconductor microcavities. Preprint 2002.

[11] E. Abraham, Modelling of regenerative pulsation in an InSb etalon, *Opt. Comm.* 61, 282-286 (1987) and references quoted therein.

Image processing with cavity type-II Second Harmonic Generation

Pierre Scotto, Pere Colet and Maxi San Miguel

Instituto Mediterráneo de Estudios Avanzados, IMEDEA (CSIC-UIB),
Campus Universitat Illes Balears, E-07071 Palma de Mallorca, Spain.
Phone: +34 971 173382, fax: +34 971 173248, e-mail: pere@imedea.uib.es
http://www.imedea.uib.es/PhysDept

Nonlinear optical effects may provide a way to perform all-optical parallel processing of images. Here, we investigate the possibilities offered by Type II intracavity second harmonic generation. We show that injecting an image in one polarization and a homogeneous field in the other, we obtain, according to the value of the latter, either the frequency and polarization transfer of the image or the possibility to enhance its contrast.

Intracavity SHG

The system we are considering is sketched in Fig. 1. A crystal with a $\chi^{(2)}$ nonlinearity is placed in a cavity, formed by a perfectly reflecting mirror (right mirror) and a highly reflecting coupling mirror (left mirror). The quadratic nonlinearity of the crystal allows photons of a given frequency 2ω to decay into pairs of photons ω_1 and ω_2 with $2\omega = \omega_1 + \omega_2$, as well as the reverse process of second harmonic generation. The efficiency of such a process depends crucially on the phase matching condition given by the longitudinal momentum conservation. Here, we consider a degenerate type II phase matching, for which the two fundamental photons have different polarisations, but the same frequency.

In the SHG-setup, the cavity is pumped at the fundamental frequency, which means that there are here two pump fields E_1 and E_2 associated with the two orthogonal linear polarization states, which can be chosen independently. This freedom gives a unique opportunity for designing optical devices with very various functions, as will be illustrated in the following.

The temporal evolution of the intracavity fields, obtained by means of a standard mean field model is governed by the following nonlinearly coupled equations:

$$\partial_t B = (-\gamma_0 + i\Delta_0)B + ia_0\nabla_\perp^2 B + i\chi A_1 A_2 \tag{1}$$

$$\partial_t A_1 = (-\gamma_1 + i\Delta_1)A_1 + ia_1\nabla_\perp^2 A_1 + i\chi A_2^* B + E_1 \tag{2}$$

$$\partial_t A_2 = (-\gamma_2 + i\Delta_2)A_2 + ia_2\nabla_\perp^2 A_2 + i\chi A_1^* B + E_2 \tag{3}$$

in which A_1 and A_2 are the fundamental field envelopes associated with polarization x and y respectively, and B is the envelope of the second harmonic field. $\gamma_0, \gamma_1, \gamma_2$ are the cavity decay rate for the three fields, Δ_0, Δ_1, Δ_2 the detunings and a_0, a_1, a_2 the diffraction parameters. The effects of diffraction come in through the differencial operator $\nabla_\perp^2$ acting in the transverse plane. E_1 and E_2 represent the pump field amplitude in each linear polarization state.
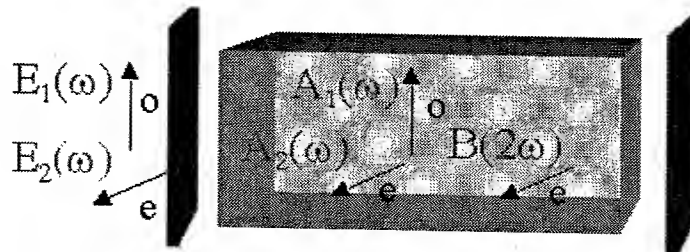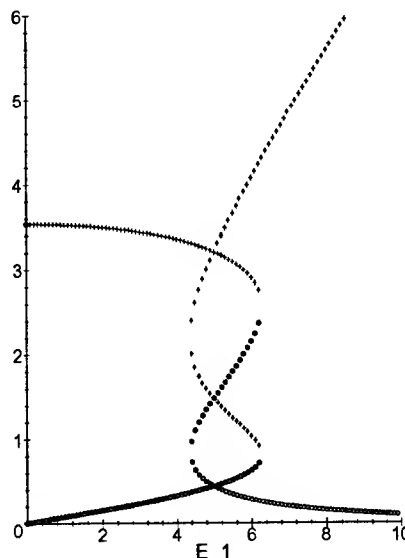
Fig. 2. Second-Harmonic-Generation for an asymmetric pumping. The two intracavity field amplitudes (A_1 (crosses) A_2 (circles)), corresponding to the steady state solution, are plotted as a function of the pump field E_1 for a fixed value of $E_2 = 5$. The other parameters of the system have been fixed as follows: $\Delta_0 = 0$, $\Delta_1 = \Delta_2 = 1.0$, $\gamma_0 = \gamma_1 = \gamma_2 = 1.0$.

Whereas the properties of this system have been mainly studied in the case of a symmetric pumping $E_1 = E_2$ (see [1, 2]), we will focuss here on a different situation: we will assume that the signal to be processed, an optical image described by a spatially dependent field $E_1(x)$, will be injected into the system in one polarization (say, the x polarization), whereas in the other polarization the pumping will be homogeneous in the transverse plane. We will show that the system presents different types of behaviour, depending on the relative value of $E_1(x)$ with respect to E_2.

Steady state solution
The study of the steady state solution of Eqs. (1) for an asymmetric pumping provides a valuable insight into the properties of the system under consideration. The values of the intracavity fields A_1 and A_2 in each polarization state are shown in Fig. 2 as a function of E_1 for a fixed value of E_2. For small E_1, the function $A_1(E_1)$ is single-valued and takes small values while $A_2(E_1)$ is large. For E_1 close to E_2, both functions $A_1(E_1)$ and $A_2(E_1)$ become S-shaped, therefore the system displays bistability. For E_1 much larger than E_2, $A_1(E_1)$ and $A_2(E_1)$ are again single-valued but now $A_1(E_1) >> A_2(E_1)$. The S-shape is in fact connected with the polarization instability well known to occure in this system for a symmetrical pumping [1]. It gives raise to interesting properties of the system, which can be exploited from the point of view of signal processing.

Image transfer (polarization and frequency)
If the intensity of the signal in x-polarization remains always below the value of the y-polarized pump field (i.e. if $E_1(x) < E_2$), the steady state intracavity field $A_1(x)$ never leaves the lower branch of the curve $A_1(E_1)$ shown in Fig. 2, and follows in a quasi linear way the spatial dependence of the input signal. The interesting feature of this operating regime appears when the output at SH frequency is considered: as a matter of facts, the output at frequency 2ω turns out to reproduce the spatial distribution of the input signal, as represented in Fig. 3. In this case, therefore, the device allows to transfer an input signal to an other frequency and polarization.

Image regeneration and contrast enhancement
If, on the contrary, the intensity of the signal in x-polarization is increased so that it locally exceeds the
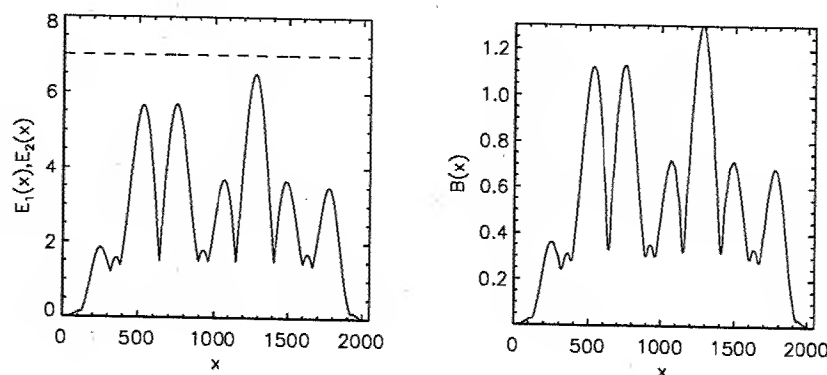
Fig. 3. On the left: The injected signal, in the one dimensional case, with, as a dotted line, the value of the pump E_2 for the orthogonal polarization. On the right: The field distribution at Second Harmonic Frequency, which reproduces the input signal.
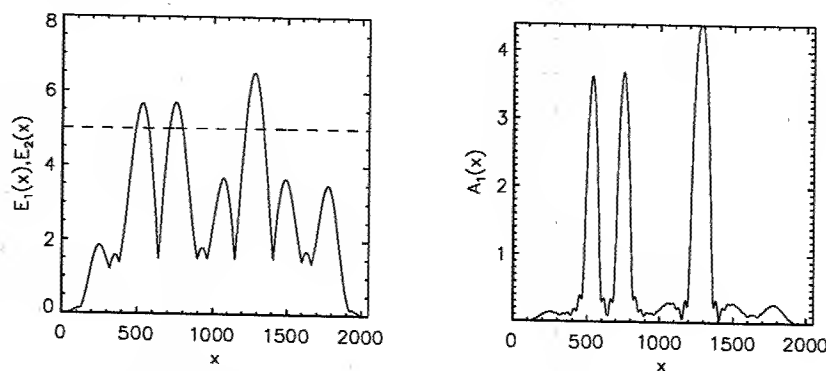
Fig. 4. On the left: The injected signal, in the one dimensional case, with, as a dotted line, the value of the pump E_2 for the orthogonal polarization. On the right: The field distribution in the same polarization state, which reproduces the input signal only in the regions, in which the signal is above the reference value E_2.

pump E_2, the S-shaped dependence of $A_1(E_1)$ comes into play: an immediate consequence is that above a certain value of E_1, $A_1(E_1)$ will be obliged to "jump" to the upper branch, leading to a sudden change in the value of the field A_1. This is precisely illustrated in Fig. 4, in which the spatial dependence of $A_1(x)$ reproduces the input signal in the regions where $E_1(x) > E_2$, whereas elsewhere, a suppression of the signal transmission is observed.

The threshold value, above which the jump to the upper branch takes place, occurs before the turning point $E_1 = 6.3$. For example, in Fig. 4, the first two peaks that cross $E_1 = E_2$ do not cross the turning point but nevertheless are amplified. In fact, it is found to occure close to the point, where $E_1(x) = E_2$. This device could be useful to regenerate an image deteriorated by a noisy backgroung or to enhance the contrast in an optical image.

References

1. U. Peschel, C. Etrich and F. Lederer, Opt. Lett. **23** (1998) 500; Phys. Rev. E **58** (1998) 4005
2. S. Longhi, Phys. Rev. A **59** (1999) 4021.

Noise-induced growth of arrays of spatial solitons in optical parametric oscillators

Ivan Rabbiosi, Andrew J. Scroggie, and Gian-Luca Oppo

Department of Physics and Applied Physics, University of Strathclyde,
107 Rottenrow, Glasgow G4 0NG, Scotland, UK.
Phone: +44-141-548-3761. Fax: +44-141-552-2891.
E-mail: gianluca@phys.strath.ac.uk

The stochastic dynamics of domain walls (DW) with oscillatory tails connecting two symmetric phases is analysed. In particular, we focus here on a stochastic model of an optical parametric oscillator (OPO) given by [1]:

$$\partial_t A_0 = \Gamma[-A_0 + E - A_1^2] + ia\partial_{xx}A_0 \tag{1}$$
$$\partial_t A_1 = -A_1 + A_0 A_1^* + i2a\partial_{xx}A_1 + \xi(x,t)$$

where A_0 and A_1 are the pump and signal complex fields respectively; Γ is the ratio of the pump and signal cavity decay rates; E is the amplitude of the external pump field; a is the diffraction coefficient. The stochastic term ξ represents local white noise, delta correlated and with zero mean value and variance $\langle|\xi|^2\rangle = 2D$, where D denotes the noise strength. For simplicity, noise appears in the equation for A_1 only. The addition of pump noise and detunings in (1) does not modify our results.

Above the threshold for signal generation ($E > 1$) and for $D = 0$, equations (1) admit the stable homogeneous steady state solutions $A_0^s = 1$, $A_{1\pm}^s = \pm\sqrt{E-1}$ and the unstable one $A_0^s = E$, $A_1^s = 0$. It is possible to demonstrate [1] that there are no modulational instabilities for any value of E and Γ. In the OPO model (1) DW correspond to heteroclinic trajectories with oscillatory tails. These trajectories connect the two stable homogeneous states asymptotically for $x \to \pm\infty$ by passing through the unstable solution $A_1^s = 0$, which defines the core of the defect (Ising walls).

In the absence of noise pairs of DW lock at given equilibrium distances $s = s_j$ ($j = 0, 1, 2, ...$) with $s_j < s_{j+1}$. A rich variety of stable locked states including cavity solitons at $s = s_0$ is then obtained. Coexisting with these spatially localized objects there are stable multiple-DW solutions (see Figure 1a) with a flat spectrum in Fourier space (see shaded curve in Figure 1b), typical of spatial disorder [2].
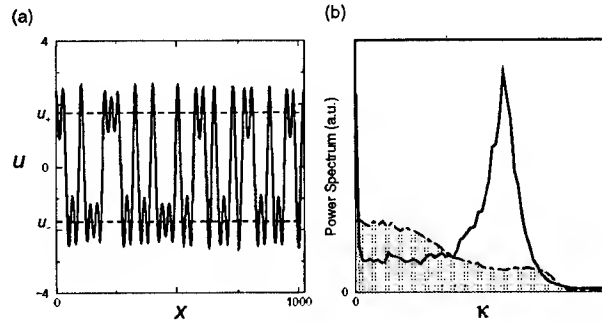
Fig. 1. a) *Real part of the signal stationary solution showing a disordered distribution of defects. b) Power spectra of the signal field in the deterministic case (D = 0) averaged over 10^3 random initial conditions (gray shading) and spectra of the field for D = 0.282 averaged over $8 \cdot 10^4$ time steps (solid line).*

In the presence of noise defects are created in pairs and subsequently their dynamics follows a discrete random motion between the equilibrium distances s_j which terminate with the annihilation of the defects. We consider the stochastic dynamics in the 1D transverse profile of the signal field by using Γ as control parameter. For small Γ the activation $\mathcal{E}_a$ and deactivation $\mathcal{E}_d$ energies required to create and erase a defect pairs at the distance s_0 are such that $D \leq \mathcal{E}_a \ll \mathcal{E}_d$, where D is the noise intensity.

We integrate (1) numerically for the parameter values $E = 4$, and $a = 0.5$. On reducing the decay rate Γ we are able to increase the ratio between the frequency and damping coefficient of the spatial oscillations [1]. Without loss of generality we start from a random initial condition. When a balance between pair-production and annihilation processes is achieved the density of defects along the lattice reaches an equilibrium value independent of the initial condition. In our simulations this is achieved after a long transient which depends on the noise strength, and is larger for smaller D. The defect dynamics is characterized by a discrete-like random walk among adjacent equilibrium distances s_j, which for small distance s may be represented by the transition $s_j \rightarrow s_{j\pm1}$ whilst for large s it becomes a continuous brownian motion as the interaction between DW becomes weaker. A typical evolution of the real part of A_1 is plotted in Figure 2 for $\Gamma = 0.2$ and $D = 0.282$. At equilibrium, arrays of spatial solitons of variable length replace the spatial chaos observed at $D = 0$. The spectrum of the transverse field in Fourier space averaged over a long time-series shows a pronounced peak at the wavenumber $k = 2\pi/s_0$ (see solid line in Figure 1b). We also provide the characterization of the stochastic process in terms of correlation lengths.
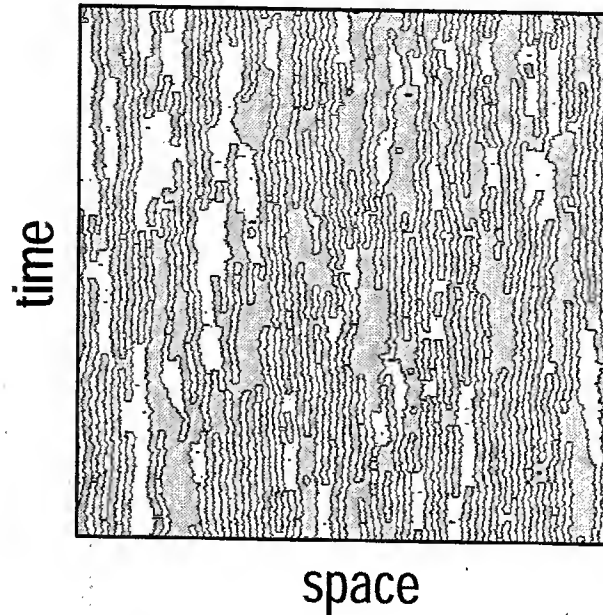
Fig. 2. *Stochastic time evolution of the real part of the signal field A_1 for $E = 4$, $a = 1$, $\Gamma = 0.2$ and $D = 0.282$ after transients have been discarded.*

In conclusion, we have shown that noise can suppress spatial chaos in a stochastic model of an OPO. We stress the importance of the parameter Γ, the ratio of the pump and signal decay rates in the cavity. For low values of Γ spatial chaos is replaced by long arrays of spatial solitons which display a high degree of correlation. It is interesting to note that at difference from temporal chaos where noise enhances disorder by, for example, lowering the threshold for the onset of chaos, noise leads here to the formation of highly ordered structures.

References
[1] G.-L. Oppo, A.J. Scroggie, W.J. Firth *Phys. Rev. E* **6** , 6209 (2001)
[2] P. Coullet, C. Elphick, D. Repaux, *Phys. Rev. Lett.* , **58**, 431 (1987)

Unconditional instability of the degenerate backward optical parametric oscillator

Carlos Montes[(1)], Céline Durniak[(2)], Majid Taki[(2)], and Antonio Picozzi[(1)]

Centre National de la Recherche Scientifique

[(1)]*Laboratoire de Physique de la Matière Condensée, Université de Nice*
- Sophia Antipolis, Parc Valrose, F-06108 Nice Cedex 2, France

[(2)]*Laboratoire de Physique des Lasers, Atomes et Molécules, Université des Sciences*
et Technologies de Lille, F-59655 Villeneuve d'Ascq Cedex, France

Generation of ultra-short optical pulses in CW-pumped cavities are mostly associated with mode locking in active media, such as doped fibers or solid-state lasers. The cavity contains not only a gain element (atoms or ions) but also a nonlinear element permitting self-phase modulation (SPM) or intensity dependent absorption. Spontaneous generation of a pulse in CW-pumped optical cavities without population inversion may also take place through the nonlinear three-wave counter-streaming interaction. It has been shown that the same mechanism, responsible for symbiotic solitary wave morphogenesis in the Brillouin-fiber-ring laser [1], may act for picosecond pulse generation in a quadratic optical parametric oscillator [2]. The resonant condition is automatically satisfied in stimulated Brillouin backscattering. However, in order to achieve quasi-phase matching (QPM) between the three optical counter-streaming waves in the $\chi^{(2)}$ medium, so that both signal and idler waves propagate backward with respect to the pump wave, a polarization inverted grating of sub-μm period is required. QPM second-harmonic (SH) generation for copropagating waves, in which the wave mismatch between the fundamental and SH waves is compensated with the assistance of spatial gratings of nonlinear or linear material constants, has been extensively studied [3]. If a grating with a sufficient short period is available, both waves traveling in opposite directions can be phase matched and the SH wave is generated in reflections [4]-[8]. Recent experiments of backward SH generation in periodically-poled LiNbO$_3$ [8][9] and KTP [10] avoid the technical difficulty of a sub-μm QPM by using higher-order gratings. Studies of QPM SH generation by backward propagating interaction have been done and the stability analysis of the counter-propagating interaction in the cavity has been performed, showing complex temporal pattern formation and self-pulsing [11].

Here we investigate the opposite mechanism, *i.e.* parametric down conversion, with the pump at 2ω, and where the backward signal wave at ω can spontaneously build up from quantum noise and is then amplified in the degenerate counter-streaming OPO. We perform the stability analysis of the CW-pumped degenerate backwad OPO by starting from the stationary solutions and following the procedure of Ref.[1]. The equations governing the QPM backward parametric down conversion without optical damping and dispersion, in dimensionless units are :

$$(\partial_t + \partial_x)\, P = -S^2 \tag{1a}$$

$$(\partial_t - \partial_x)\, S = PS^* \tag{1b}$$

with the boundary conditions for the singly resonant cavity

$$P(x=0,t) = 1 \;\; ; \;\;\; S(x=L,t) = \sqrt{R}\, S(x=0,t) \tag{2}$$

where P stands for the pump amplitude A_p at 2ω, S for the signal A_s (or idler A_i) amplitude at ω, L for the cavity length, and R for the intensity feedback parameter of the singly resonant OPO for S. At zero phase mismatch and in the absence of dispersion we can look for the stability of the real problem ($S^* = S$). The stationary equations admit two inhomogeneous solutions above OPO threshold $R_{thd} = \exp(-2L)$:

(a) for $P^2 - S^2 = D^2 = \text{const}$; $P_{st}(x) = D\coth(Dx + \phi_0)$; $S_{st}(x) = D/\sinh(Dx + \phi_0)$ (3)

(b) for $S^2 - P^2 = D^2 = \text{const}$; $P_{st}(x) = -D\tan(Dx + \phi_0)$; $S_{st}(x) = D/\cos(Dx + \phi_0)$ (4)

Let us look for the stability of such solutions by considering the time perturbative problem like in [1],

$$P(x,t) = P_{st}(x) + \delta P(x,t) = P_{st}(x) + X(x)\,\exp(-i\omega t) \tag{5}$$

$$S(x,t) = S_{st}(x) + \delta S(x,t) = S_{st}(x) + Y(x)\,\exp(-i\omega t) \tag{6}$$

where $X(x)$ and $Y(x)$ are the space dependent perturbations and $\omega = \omega_r + i\omega_i$ the complex eigenvalue frequency yielding instability when $\operatorname{Im}\omega \equiv \omega_i > 0$. From now on we will call $P \equiv P_{st}(x)$ and $S \equiv S_{st}(x)$. Linearizing Eqs.(1a,b) and introducing the pertinent variable $U = Y/S$, we obtain

$$U'' + (\omega^2 - 2S^2)U = 0 \quad ; \quad X = -i\omega U - U' \tag{7}$$

with the respective boundary conditions

$$U(L) = U(0) \quad ; \quad X(0) = -U'(0) - i\omega U(0) = 0. \tag{8}$$

Introducing in (7) the respective stationary solutions (3) or (4) for S we may integrate this linear inhomogeneous equation, and conditions (8) determine the eigenvalue problem for $\omega = \omega_r + i\omega_i$. For $(Dx)^2 \ll 1$ the inhomogeneous potential S has the simple form $S^2 = (1 \mp D^2)/(1 + x)^2$ (where $P^2 - S^2 = \pm D^2$) and Eq.(7) admit solutions in terms of Bessel functions [12], since it takes the form

$$y^2 U'' + [\omega^2 y^2 - 2(1 \pm D^2)]U = 0 \tag{9}$$

with $y = 1 + x$, which solution is

$$U = \sqrt{y}\,\left[C_1 J_\nu(\omega y) + C_2 Y_\nu(\omega y) \right] \quad ; \quad \nu^2 - 1/4 = 2(1 \pm D^2). \tag{10}$$

We have performed the analysis for case $D = 0$ ($\nu = 3/2$), for any x, and for $D \neq 0$ in the limit $|\omega y| \gg 1$, where an asymptotic expansion of Bessel functions (10) in terms of trigonometric angular functions is available [12]. It allows to analitically treat the interesting problem of the stability of the cavity modes $\operatorname{Re}\omega \simeq 2\pi N/L$ (N integer). From (10), boundary conditions (8) and imposing solvability for any couple (C_1, C_2), we obtain the complex dispersion relation for $\omega = \omega_r + i\omega_i$:

$$A + B\,\sin(\omega L) + C\,\cos(\omega L) = 0$$

$$A = (1 + L)(\omega^3 + a(a - 1)\omega)$$
$$B = i(1 + L)\omega^3 - aL\omega^2 + a^2(i\omega - 1)$$
$$C = -(1 + L)\omega^3 - iaL\omega^2 - a\omega(a - 1 - L)$$

where $a = (4\nu^2 - 1)/8 = 1 \pm D^2$. One obtains a couple of equations for (ω_r, ω_i) which is solved by a two variable Newton method; its solution always presents *instabilty* ($\operatorname{Im}\omega > 0$). The omnipresent instability is confirmed in the general case, beyond the asymptotic limit, by numerically solving Eqs.(1a,b). Fig.1 shows the growth rate $\operatorname{Im}\omega$ of the first cavity mode ($N = 1$) *vs.* the feedback rate R of the backward signal intensity for different OPO length L (and same pump input).

This striking result about the unconditional instability of the degenerate backward OPO is not so surprising, since the solitary wave which is generated exhibits unlimited amplification and compression above threshold, and therefore it is able to collapse whatever the cavity length. Moreover, starting from the stationary solutions, the time amplification rate γ_t of the generated signal wave modulation (corresponding to one pulse per round-trip, *i.e.* $N = 1$) is accurately given by the *analytical* value $\operatorname{Im}\omega$ of Fig.1, even for DL values not necessarily small. *E.g.* for $L = 0.3$, $D = 0.8185$ ($DL = 0.2455$), and $R = 0.56$ we obtain $\gamma_t = 1.92 \times 10^{-4}$ and $\operatorname{Im}\omega = 1.68 \times 10^{-4}$.

We know that the same equations governing the unbounded problem of a dissipative signal wave, backward propagating with respect to a CW pump wave do not have a stable attractor solution. Indeed, we may perform an asymptotic Kolmogorov-Petrovskii-Piskunov (KPP) analysis of the undepleted linear problem [13] [14] in order to prove the non existence of such attractor. Therefore it is necessary to stop this singular behavior by taking into account an additional physical mechanism. Since the solitary wave generated becomes extremely steep and narrow when its amplitude increases, a linear saturation effect is played by chromatic dispersion. The numerical behavior shows that the amplification of the solitary pulses is dynamically saturated by temporal modulation of the envelopes, yielding the dynamic solitary structure described in Ref.[14]. The saturation dynamics has been obtained for a set of different pump intensities and cavity lengths. Dispersion corresponds to actual (e-e) polarization interaction in

Instability growth rate for Re $\omega = 2\pi/L$
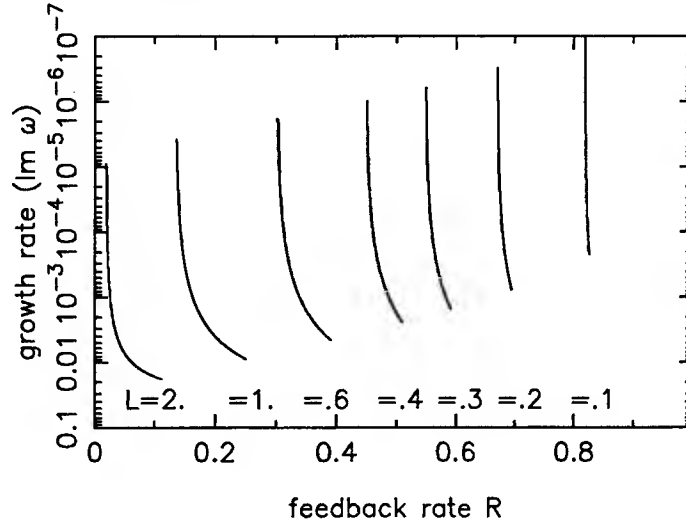
Figure 1: Instability growth rate Im ω of the first mode Re $\omega = 2\pi/L$ vs. the signal feedback rate R of the degenerate backward OPO, for different cavity length L.

LiNbO$_3$ at 100°C, namely 0.1131 ps^2/m for the pump P at $\lambda_p = 0.775$ μm, and 0.8930 ps^2/m for the backward signal wave S at $\lambda_s = 1.55$ μm. The power requirement for backward OPO operation depends on the ability to achieve low-order QPM over centimeter lengths. Thus,$e.g.$, for a first order QPM in LiNbO$_3$ the grating pitch is as small as $\Lambda_{QPM} = 2\pi/K = 0.179$ μm. For a CW-pump field $E_p = 0.725$ MV/m ($i.e.$, a pump intensity of $I_p = 100$ kW/cm^2) propagating in the quadratic $\chi^{(2)}$ material with the following values of the parameters: $d = 20$ pm/V, $n_p = 2.179$, $n_s = 2.141$, $v_p = 1.323 \times 10^8$m/s, $v_s = 1.371 \times 10^8$m/s, $v_i = 1.359 \times 10^8$m/s, the nonlinear characteristic time yields $\tau_0 = (\sigma_p E_p/2)^{-1} \simeq 0.37$ ns, where $\sigma_p = 2\pi d v_p/\lambda_p n_p$ is the coupling coefficient, and the nonlinear characteristic length of the cavity is $\Lambda = v_p \tau_0 = 5$ cm. For $L = \ell/\Lambda = 1$ the solitary pulses are compressed until 7.5 ps before dispersion begins the saturation process. The dynamic solitary structure being deeply modulated, the central peak has about 5 ps width, while the whole pulse spreads over some tens of picoseconds.

The analytical stability analysis of the degenerate backward quasi-phase-matching parametric decay interaction in a singly OPO cavity above threshold shows that the inhomogeneous stationary solutions are *unconditionally unstable*, whatever the cavity length and pump power. Starting from any initial condition the backward signal wave evolves to an unlimited pulse collapse. Taking into account dispersion we may saturate this singular behavior and obtain a new type of dynamic solitary wave.

[1] C. Montes, A. Mamhoud, and E. Picholle, *Phys. Rev. A* **49**, 1344 (1994).
[2] A. Picozzi and M. Hælterman, *Opt. Lett.* **23**, 1808 (1998).
[3] J.A. Armstrong, N. Bloembergen, J. Ducuing, and P.S. Perhan, *Phys. Rev.* **127**, 1918 (1992).
[4] P.St.J. Russell, IEEE J. Quantum Electron. **27**, 830 (1991).
[5] M.M. Fejer, G.A. Magel, D.H. Jundt, and R.L. Byer, *IEEE J. Quantum Electron.* **28**, 2631 (1992).
[6] M. Matsumoto and K. Tanaka, *IEEE J. Quantum Electron.* **31**, 700 (1995).
[7] Y.J. Ding and J.B. Khurgin, *IEEE J. Quantum Electron.* **32**, 1574 (1996).
[8] J.U. Kang, Y.J. Ding, W.K. Burns, and J.S. Melinger, *Opt. Lett.* **22**, 862 (1997).
[9] X. Gu, R.Y. Korotkov, Y.J. Ding, J.U. Kang, and J.B. Khurgin, *J.Opt.Soc.Am. B* **15**, 1561 (1998).
[10] X. Gu, M. Makarov, Y.J. Ding, J.B. Khurgin, and W.P. Risk, Opt. Lett. **24**, 127 (1999).
[11] G. D'Alessandro, P.St.J. Russell, and A.A. Wheeler, *Phys. Rev. A* **55**, 3211 (1997).
[12] M. Abramowitz and I.A. Stegun, *Hand. Math. Funct.*, 8th ed. Dover, New-York, p.451 (1972).
[13] C. Montes, A. Picozzi, and D. Bahloul, *Phys. Rev. E* **55**, 1092 (1997).
[14] A. Picozzi and M. Haælterman, *Phys. Rev. Lett.* **84**, 5760 (2000).

Spatial solitons in an optically pumped semiconductor microresonator

V. B. Taranenko, C. O. Weiss
Physikalisch-Technische Bundesanstalt 38116 Braunschweig/Germany
Telephone: +49-531-5924407, fax: +49-531-5924423, e-mail address: victor.taranenko@ptb.de

Abstract: We show experimentally and numerically the existence of stable spatial solitons in an optically pumped semiconductor microresonator. We demonstrate that the pump substantially reduces the light intensity necessary to sustain the solitons and thereby reduces destabilizing thermal effects. We demonstrate coherent switching on and off of bright solitons. We discuss differences between pumped and unpumped below bandgap-solitons.
©2000 Optical Society of America
OCIS codes: 190.4420, 210.4680

1. Introduction

Spatial solitons in semiconductor microresonators [1,2] are self-trapped light beams which can form due to both transverse (e.g., self-focusing) and longitudinal (nonlinear resonance [3]) nonlinear effects. These nonlinear effects can act in the same sense or oppositely, with the consequence of reduced soliton stability in the later case. Thus choice of nonlinear resonator parameters suited best for sustaining stable solitons is important. The best-suited schemes are unpumped microresonator excited above bandgap [4] and optically pumped microresonator excited below bandgap [5].

Here we pump a semiconductor microresonator optically in a range up to the lasing threshold and study formation of switched structures. We show experimentally and numerically the existence of the resonator solitons in the pumped microresonators. We demonstrate that the pumping substantially reduces the light intensity necessary to sustain and switch the solitons (diminishing thermal problems as a side effect) so that semiconductor laser diodes are sufficient for sustaining solitons. We discuss differences between pumped and unpumped solitons below bandgap.

2. Experiment

We pump a bistable quantum-well (GaAs/GaAlAs) microresonator using either a tunable Ti:sapphire laser or a high power multimode laser diode. The pumped area of the resonator is illuminated additionally by a focused beam from a single-mode laser diode that provides quite large Fresnel number (~100) and near resonant illumination of the resonator. The main control parameters in the experiment are the resonator detuning and intensities of the illumination and pump.
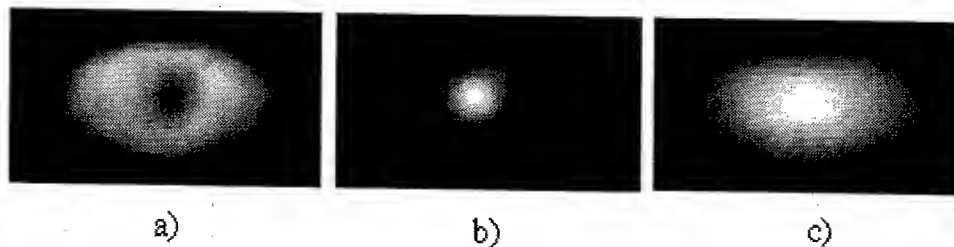
Fig. 1. Intensity snapshots of typical structures observed in reflection from pumped (below transparency) semiconductor microresonator illuminated near resonance showing bright (a) and dark (b) soliton. The illuminating beam from the laser diode has an elliptical shape (c).

Observations are done in reflection since the substrate of the microresonator structure is opaque at the working wavelengths: dark switched structures in reflection correspond to bright ones in transmission and vice versa. Switched structures formed in the illuminated beam cross section were monitored in the plane of

the microresonator in two ways: (i) A CCD camera with electro-optical shutter recorded 2D snapshots of switched structures. (ii) A fast and small aperture photo detector monitored local dynamics.

3. Results and discussions

Switched structures observed (Fig. 1 a,b) manifest themselves as resonator solitons: 1) they are of the size(~10 μm) expected for such solitons [1]; 2) they are round spots whose size and shape are independent on the intensity and shape of the illuminating beam (e.g., elliptical beam shape as shown in Fig. 1c); 3) they are robust against perturbations of the illuminating light intensity; 4) they are bistable, i.e. thay can be switched on (Fig. 2a) and off (Fig. 2b) by sharply focused address pulses.

This soliton nature of the observed switched structures is supported by numerical simulations of the intracavity field structures (in 2D) using the model equations for the pumped semiconductor microresonator
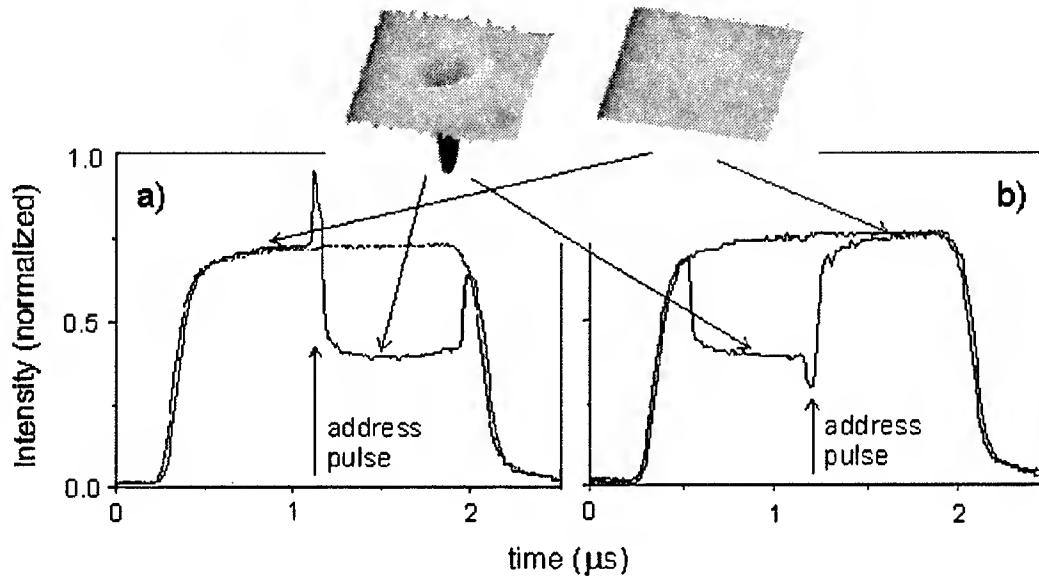
Fig. 2. Recording of switching-on (a) and switching-off (b) of a bright soliton. Vertical arrows mark the application of address pulses. Dotted traces: incident intensity. The insets show soliton and unswitched state in 3D representation.
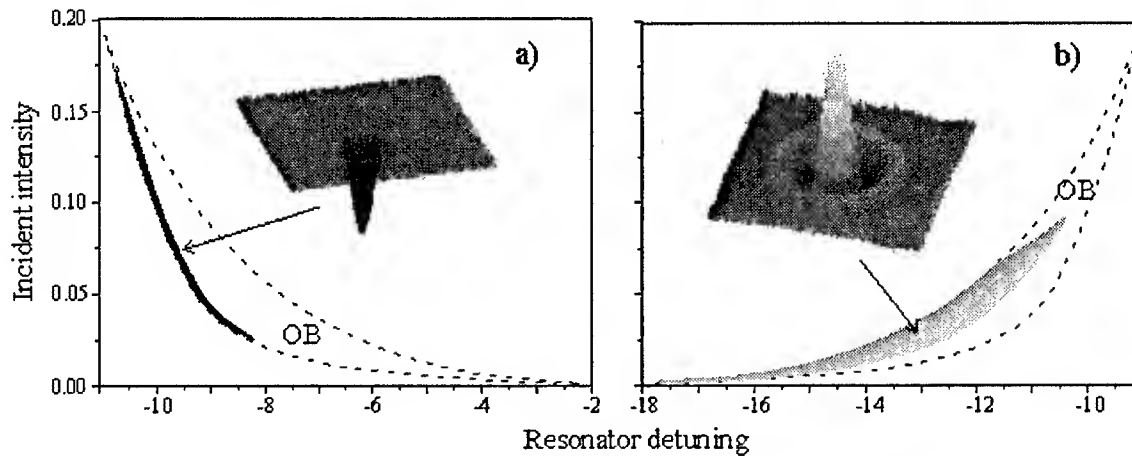
Fig. 3. Results of numerical simulations of below bandgap (purely dispersive) solitons using the model equations [4] for unpumped (a) and pumped above "transparency" point (b) microresonator. Insets are dark (a) and bright (b) solitons. Shaded areas are domains of existence of resonator solitons. Areas limited by dashed lines are optical bistability domains for plane waves.

driven by a plane wave [4]. Fig. 3 shows typical examples of calculated resonator solitons below bandgap. Bright solitons have a large existence range in the pumped case (Fig. 3b), dark solitons exist, though with smaller range of stability, in the unpumped case (Fig. 3a). Parameter domains of existence of resonator solitons are related to those of optical bistability for plane waves, are shown in Fig. 3.

Analysis shows that increase of the pump intensity leads to shrinking of the resonator solitons' existence domain and shifting towards low intensity of the light sustaining the solitons (Such reduction of the sustaining light intensity was observed experimentally in [4]).

When the pump intensity approaches the transparency point of the semiconductor material, the resonator solitons' domain of existence disappears. It reappears above the transparency point. In the experiment we have quite strong contribution of the imaginary part (absorption/gain) of the complex nonlinearity at the working wavelength (854 nm). Therefore the transparency point is very close to the lasing threshold so that inversion without lasing is difficult to realize.

Slightly above threshold we observe in presence of illumination structures (Fig. 4) reminiscent of the solitons in electrically pumped resonators [6].

a)   b)   c)
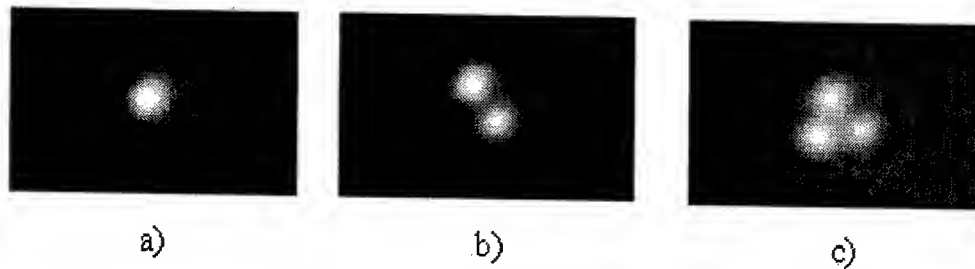
Fig. 4. Intensity snapshots of typical beam structures at optical pump intensities slightly above lasing threshold (pump increases from (a) to (c)).

4. Conclusion

In summary, optically pumped semiconductor resonators are well suited for sustaining solitons below bandgap: (i) background light intensity necessary to sustain and switch resonator solitons is substantially reduced by the pumping and therefore destabilizing thermal effects are minimized, (ii) above the transparency point only the dispersive part of semiconductor nonlinearity stabilizes a soliton, therefore the domain of existence of "below bandgap" (purely dispersive) bright solitons can be quite large. Moreover optical as opposed to electrical pumping allows more homogeneous pumping conditions [7]. This suggests that optically pumped resonators lend themselves more readily for localization and motion control of solitons then electrically pumped ones.

5. References

1.   L. Spinelli, G. Tissoni, M. Brambilla, F. Prati, L. A. Lugiato, "Spatial solitons in semiconductor microcavities," Phys. Rev. A **58**, 2542-2559 (1998); D. Michaelis, U. Peschel, F. Lederer, "Multistable localized structures and superlattices in semiconductor optical resonators," Phys. Rev. A **56**, R3366-3369 (1997).

2.   V. B. Taranenko, 1. Ganne, R. Kuszelewicz, C. O. Weiss, "Patterns and localized structures in bistable semiconductor resonators," Phys. Rev. A **61**, 063818-1-5 (2000); V. B. Taranenko, I. Ganne, R. Kuszelewicz, C. O. Weiss, "Spatial solitons in a semiconductor microresonator," Appl. Phys. B, **72**, 377-380 (2001); V. B. Taranenko, C. O. Weiss, B. Schaepers, "From coherent to incoherent hexagonal patterns in semiconductor resonators", Phys. Rev. A **65**, 013812/1-4 (2002).

3.   G. J. de Valcarcel, K. Staliunas, V. J. Sanchez-Morcillo, E. Roldan, "Transverse patterns in degenerate optical parametric oscillation and four-wave mixing," Phys. Rev. A **54**, 1609-1615 (1996).

4.   V. B. Taranenko, C. O. Weiss, W. Stolz, "Semiconductor resonator solitons above band gap", JOSA B, **19**, 684-688 (2002).

5.   V. B. Taranenko, C. O. Weiss, W. Stolz, "Spatial solitons in a pumped semiconductor resonator," Opt. Lett., **26**, 1574-1576 (2001).

6.   Report as given in www.pianos-int.org.

7.   W. J. Alford, T. D. Raymond, A. A. Allerman, "High power and good beam quality at 980 nm from a vertical external-cavity surface-emitting laser," J. Opt. Soc. Am. B **19**, 663-666 (2002).

Spectral control of solitons under periodical dispersion-slope compensation

Joji Maeda and Ichiro Matsuda

Faculty of Science and Technology, Tokyo University of Science,
2641 Yamazaki, Noda, Chiba 2788510 Japan
TEL: +81-4-7124-1501 ext.3705, FAX: +81-4-7124-7380
e-mail: jiji@ee.noda.sut.ac.jp

Abstract: Effects of guiding filters on solitons in fiber links with periodical dispersion-slope compensation are numerically studied with regard to 160Gbit/s transmission. It is predicted that slope compensating links require narrower filter bandwidth and higher transmission power than do slope-free fiber links.
© 2002 Optical Society of America
OCIS codes: (060.0060)Fiber optics and optical communications: (060.5530)Pulse propagation and solitons: (190.0190)Nonlinear optics; (190.4370)Nonlinear optics, fibers:

Soliton transmission control in frequency domain using narrow band filters is a well known technique to stabilize soliton pulse trains[1, 2, 3, 4]. The filters not only eliminate noisy dispersive wave outside the signal bandwidth but reshape the pulse spectrum. Stability of the spectrum reduces Gordon-Haus jitter[5], the jitter of the pulse position induced by the amplifier noise through self-phase modulation.

In ultra-high bit rate transmission systems of 100Gbps or above, group velocity dispersion (GVD) of fibers must be negligibly small to avoid pulse broadening. In such systems, the third order dispersion (TOD), or dispersion slope, becomes one of main factors that limit transmission distance.

Elimination of dispersion slope can be achieved by several methods. One solution is the use of dispersion flattened fiber all along the link. However, propagation parameter of a fiber varies with its environment, hence precise control of accumulated slope can only be achieved by compensating devices periodically inserted in the transmission line.

A question then arises whether the same guiding scheme as that of the ideal slope-free fiber link could be applied to the periodically slope-compensating fiber link. It has been known that the spectrum of a short pulse, whose central frequency is near zero dispersion frequency, can be split into two parts, one in the normal dispersion regime, and the other in the anomalous dispersion regime, and these two develop independently[6]. To avoid this spectral splitting, the bandwidth of filters must be narrower than the ideal case. Another consideration is that the accumulation of TOD and its cancellation in the compensating devices could automatically limit bandwidth of the transmitted spectrum as in dispersion managed links[7]. Then the spectral filtering must be more modest than the ideal case. The purpose of this paper is to numerically investigate optimal specification of guiding filters in a fiber link with periodical dispersion-slope compensation.

Fig 1 shows a schematic of a transmission system assumed in the simulation. Bit rate is 160Gbps using 1.25ps FWHM sech^2 formed initial pulses. Wavelength dispersion D and dispersion slope D' in a transmission fiber
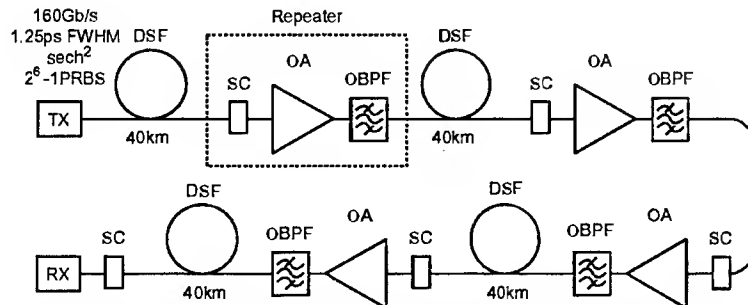
Fig. 1. System schematic. TX: optical transmitter, RX: optical receiver, SC: dispersion-slope compensator, OBPF: optical band pass filter, OA: optical amplifier.

(DSF) are 0.005ps/km/nm and 0.07ps/km/nm/nm, respectively. The dispersion slope accumulated within one repeater spacing is completely compensated at the next repeater. Each repeater consists of a slope compensator (SC), an inline amplifier (OA), and a Lorentzian bandpass filter (OBPF). Slope compensators are assumed to be ideal; loss less, without nonlinearity, and no dispersion other than TOD. The gain of each amplifier is automatically controlled so that the average power launching into the following transmission fiber is retained to the average power of the transmitter output.

In what follows, polarization mode dispersion, intrapulse Raman scattering, and the fourth or higher order dispersion are all neglected. Then, spatial evolution of pulse envelope $u(z,t)$ in a moving frame at a transmission distance z and a time t is described by the following generalized nonlinear Schrödinger equation,

$$i\frac{\partial u}{\partial z} = -i\frac{\Gamma}{2}u + \frac{\beta_2}{2}\frac{\partial^2 u}{\partial t^2} + i\frac{\beta_3}{6}\frac{\partial^3 u}{\partial t^3} - \gamma|u|^2 u, \tag{1}$$

where Γ is fiber loss, β_2 and β_3 are GVD and TOD, respectively, and γ is nonlinear parameter. The parameters β_2, β_3, and γ are related with conventional parameters by

$$\beta_2 = -\frac{\lambda^2}{2\pi c}D, \quad \beta_3 = \left(\frac{\lambda^2}{2\pi c}\right)^2 D' + \frac{\lambda^3}{2\pi^2 c^2}D, \quad \gamma = \frac{2\pi n_2}{\lambda A_{\text{eff}}}, \tag{2}$$

where λ is signal wavelength, c is speed of light in vacuum, A_{eff} is effective beam crosssection, and n_2 is nonlinear refractive index.

In the present analysis, eq.(1) is numerically solved by means of split-step-fourier method with an initial pulse pattern of $2^6 - 1$ PRBS. Transmission characteristics are estimated by eye diagrams, from which Q values at the maximum eye opening are calculated. Available transmission distance is defined by the maximum transmission distance that keeps Q larger than 7.

Inline amplifiers are assumed to be phase-insensitive[8], and are modeled by a lumped gain plus a spontaneous emission noise. The amplitude and phase components of the spontaneous emission noise are assumed to be white gaussian, and separately generated by using pseudo random numbers.

Peak power of initial pulses is assumed 12.5mW, 15.8mW, 19.6mW, and 23.7mW, each of which corresponds to soliton order n of 1.6, 1.8, 2.0, and 2.2, respectively. Note that path average power of the system under consideration is 0.39 times transmitter output power. This means soliton order n of the input pulse should be 1.6 if the path averaged power is made equal to the power of the fundamental soliton. Other parameters are summarized in Table 1.

Table 1. Parameters used in simulation.

Effective beam crosssection	$50\mu\text{m}^2$
Nonlinear refractive index	3.2×10^{-16} cm^2/W
Signal wavelength	1550nm
Noise figure of inline amplifiers	6dB
Repeater spacing	40km

Fig.2 shows the available transmission distance as a function of the filter bandwidth. Fig.2(a) is the result for a system utilizing dispersion flattened fibers ($\beta_3 = 0$), whereas Fig.2(b) is for the periodically slope-compensating system.

In all cases, we can find optimum bandwidth of filters. Smaller bandwidth results in cutting-off of signal sidebands, while larger bandwidth results in increase of Gordon-Haus jitter induced by larger spontaneous noise of amplifiers.

Comparing two figures, we find little difference in the maximum transmission distance, but clear difference in filter bandwidth and transmission power that gives the maximum, i.e., the slope-compensating system requires narrower filter bandwidth and higher transmission power.
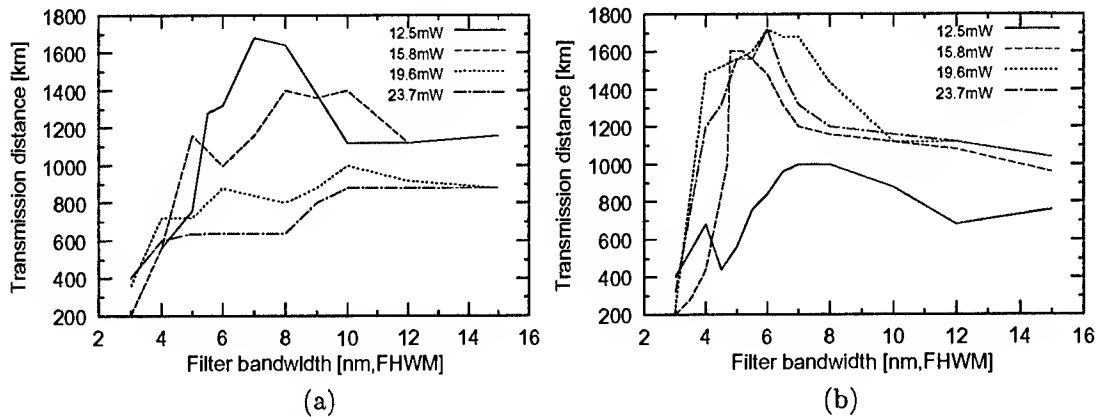
Fig. 2. Available transmission distance as a function of filter bandwidth. (a)system using slope-free fibers, (b)slope-compensating system. Parameters are peak power of initial pulses.

This result can be explained by the following discussion. During transmission of one compensation period, pulse shape is heavily unsymmetrized because of large TOD (note that TOD length of our system is only 3.1km). One of two edges becomes steep or pedestal-associated with large chirp imposed, whereas chirp on the other edge is much smaller because of rather modest intensity variation. This unbalance of chirp is preserved even after the slope-compensation, which is essentially a linear operation without dissipation. In expectation of cutting-off high frequency component and of restoring symmetricity of the pulse spectrum, the filter bandwidth suitable for slope-compensating systems must be narrower than that for slope-free systems. Since the energy cut-off by the filter becomes larger, the required transmission power becomes higher.

In summary, we have numerically investigated optimal specification of guiding filters in a fiber link with periodical dispersion-slope compensation. It has been predicted that the maximum transmission distance can be as long as that of slope-free fiber links but with narrower filter bandwidth and higher transmission power.

References

1. A. Mecozzi, J. Moores, H. A. Haus, and Y. Lai, "Soliton transmission control", Opt. Lett. **16**, 1841 (1991).
2. L. F. Mollenauer, J. P. Gordon, and S. G. Evangelides, "The sliding-frequency guiding filter: an improved form of soliton jitter control", Opt. Lett. **17**, 1575 (1992).
3. Y. Kodama and A. Hasegawa, "Generation of asymptotically stable optical solitons and suppression of the Gordon-Haus effect", Opt. Lett. **17**, 31 (1992).
4. M. Nakazawa, K. Kurokawa, H. Kubota, and E. Yamada, "Observation of the trapping of an optical soliton by adiabatic gain narrowing and its escape", Phys. Rev. Lett. **65**, 1881 (1990).
5. J. P. Gordon and H. A. Haus, "Random walk of coherently amplified solitons in optical fiber transmission", Opt. Lett. **11**, 665 (1986).
6. P. K. A. Wai, H. H. Chen, and Y. C. Lee, "Radiation by "Solitons" at the zero group-diepsersion wavelength of single-mode optical fibers", Phys. Rev. A 426 (1990).
7. I. Morita, M. Suzuki, N. Edagawa, S. Yamamoto. H. Taga, and S. Akiba, "20-Gb/s single-channel soliton tansmission over 9000km without inline filters", IEEE Photonics Technol. Lett. **8**, 1573 (1996).
8. C. M. Caves, K. S. Thorne, R. W. P. Drever, V. D. Sandberg. and M.Zimmermann, "On the measurement of a weak classical force coupled to a quantum- mechanical oscillator.I. Issues of principle", Rev. Mod. Phys **52**, 341 (1980).

Stability criterion for solitons in passively mode-locked fiber lasers

J. M. Soto-Crespo

Instituto de Óptica, C.S.I.C., Serrano 121, 28006 Madrid, Spain
Tf.:34915616800, Fax: 34915645557 E-mail:iodsc09@io.cfmac.csic.es

Nail Akhmediev

Optical Sciences Centre, RSPhysSE, IAS, Australian National University, ACT
0200, Australia
ph: (+612) 62490191, fax: (+612) 62495184, e-mail:
nna124@rsphysse.anu.edu.au

Graham Town

School of Electrical and Information Engineering (J03), University of Sydney.
NSW 2006, Australia
phone: 61-2-9351-2110, fax: 61-2-9351-3847, e-mail: towng@ee.usyd.edu.au

Abstract: The complex cubic-quintic Ginzburg-Landau equation (CGLE) has a multiplicity of soliton solutions for the same set of equation parameters. Based on their analysis, we propose a conjecture for a stability criterion for solitons in dissipative systems.
© 2002 Optical Society of America
OCIS codes: (060.5530) Pulse propagation and solitons; (140.3510) Lasers, fiber

Passively mode-locked fiber lasers can be modeled by the complex Ginzburg-Landau equation (CGLE). These devices generate ultra-short pulses which can be considered as solitons. The shape of these solitons are fixed for any given set of parameters of the system. However, more than one solution can exist for the same set of parameters. In fact, it is known [1] that, even in one dimension, solitons in dissipative systems appear in multiplicity. For each solution, the shape, amplitude and the width are all fixed and depend on the parameters of the CGLE. In some cases, we can observe up to five stable solutions in a given system [1]. Each type of solution may be stable in a certain region of the space of parameters. The existence of multiplicity of solitons for the CGLE raises an important issue: are those solitons stable? When we change the parameters of the equation, is it possible that a transition from stable to unstable soliton occurs? In other words, what is the stability criterion for solitons in dissipative systems? Up till now, we are not aware of any work which answers the above question.

In the situation where a single transverse (or temporal) coordinate is retained in the analysis, the cubic-quintic CGLE reads as [2]

$$\psi_z + \frac{D}{2}\psi_{tt} + |\psi|^2\psi = i\delta\psi + i\epsilon|\psi|^2\psi + i\beta\psi_{tt} + i\mu|\psi|^4\psi - \nu|\psi|^4\psi, \qquad (1)$$

where D, δ, β, ϵ, μ, and ν are real constants (we do not require them to be small). The CGLE applies, as we mentioned, to the problem of ultra-short pulse generation in passively mode-locked lasers. In this case, t is a retarded time, z is the number of round trips, ψ is the complex envelope of the optical field, D is the dispersion coefficient, δ gives account of the linear gain, β describes spectral filtering or parabolic gain ($\beta > 0$), ϵ accounts for nonlinear gain/absorption processes, μ represents a higher order correction to the nonlinear amplification/absorption, and ν is a possible higher order correction term to the intensity-dependent refractive index.

The numerical results for soliton solutions are presented in Fig.1. Fig.1(a) shows the peak amplitude of the single pulse (SP) soliton branch versus ϵ. This is the branch of solitons with the "plain" or bell-shape profile which resembles usual *sech*-profile solitons. The shape of the soliton continuously changes when we change ϵ. As a result we have a "branch" of solitons. It extends from the threshold both up and down in amplitude. For every value of ϵ above the threshold we have two SP soliton solutions. An interesting feature of the upper branch is its spiraling, shown more clearly in Fig.1(b) and 1(c). We have studied the stability of the SP solitons at every point of the solid curve in Fig.1 with the main attention concentrated on the spiraling part of the curve. In numerics, we used the linear stability analysis, described in detail in Ref. [3] and verified its results through direct numerical solution of the CGLE when the initial input is one of the SP solitons.
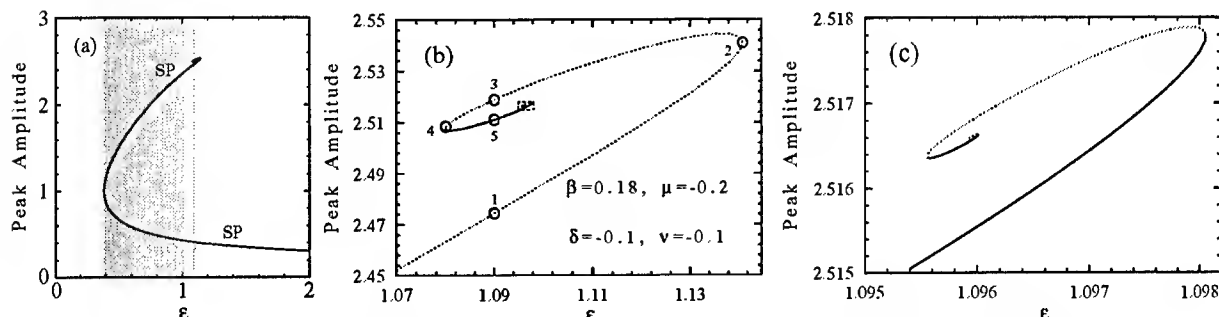
Fig. 1. (a) Maximum SP soliton amplitude (solid curve) versus ϵ. The shadow represents the values of the parameter ϵ where SP solitons of the upper branch are stable. (b) Maximum soliton amplitude versus ϵ for SP solitons at the top of the branch shown in (a). (c) Magnification of the curve shown in (b) inside the small rectangle.

The stability analysis allows us to calculate the growth rates (g) for the unstable solitons. The zeros of the growth rate g versus ϵ curves give us the boundaries of instability. This way we were able to find which parts of the spiral correspond to stable solitons and which parts do not. In particular, we found that the lower branch of the SP solitons is unstable up to the threshold point in Fig.1(a). The SP solitons are stable above this point.

The growth rate curves calculated for SP solitons in the spiraling part of the curve in Figs.1 are shown in Fig.2(a). The curve with the larger growth rate corresponds to the outer part of the spiral which is shown in magnified version in Fig.1(b). The arc of the growth rate curve from $\epsilon = 1.08$ to 1.14 corresponds to the part of the spiral from point 4 to point 2. The lower part of the growth rate which gradually goes to zero at smaller ϵ corresponds to the spiral from point 2 to point 1 and further away from the spiral. Between the different portions of the growth rate curve with the points $g = 0$, SP solitons are stable. We have eigenvalue transformations from being purely real to imaginary at the edges of soliton existence where g turns to zero.

The two bifurcations in the stability of solitons located at points numbered 4 and 2 are qualitatively different. At point 4, the growth rate goes to zero and the next part of the spiral corresponds to stable solitons. On the other hand, at point 2 the mode of instability changes but the solitons remain unstable. Moving to the left along the branch for SP solitons, the value of the growth rate monotonically decreases and below $\epsilon = 1.02$ the SP solitons become stable up to $\epsilon = 0.4$ which is the absolute minimum point of the SP soliton existence. Turning down beyond this point, SP solitons, which now become low amplitude ones, are everywhere unstable. This turning point is qualitatively similar to the point 4.

The point 2 in the spiral is a special one. Although this is the point of bifurcation, the SP soliton is unstable at both sides of this point. What changes at this point is the mode of instability. Namely, using the standard stability analysis for solitons we can write the solution in the form $\Psi(t,z) = [\psi_0(t) + \alpha f(t) \exp(gz)] \exp(-i\omega z)$ where $\psi_0(t)$ is a stationary soliton solution, α is a small parameter, $f(t)$ is the perturbation function and g is its growth rate. Substituting this equation into Eq.(1), assuming that α is small and linearizing around the soliton solution we will get an equation for eigenfunctions $f(t)$ and eigenvalues g. For details see e.g. section 13.7 of [4]. This equation can be solved numerically. This way we can find the perturbation function $f(t)$. We have a bifurcation at point 2 where the mode of perturbation changes. Moreover, the eigenvalue of the perturbation transforms from being complex with imaginary part different of zero below the point 2 to be purely real above the point 2. Its real part is the growth rate g. The instability has purely exponential growth above the point 2 and it is oscillatory below the point 2. The oscillatory instability is related to the birth of pulsating solitons [5] rather than to radiation phenomena.

The points of local minima and maxima of the range of soliton existence in the spiral are the points of bifurcation. Depending on the nature of the modes of perturbation these points might be the turning points of stability. This conjecture is confirmed with further investigation. The small curve in the dashed rectangle in Fig.2(a) corresponds to the inner part of the spiral which is shown in Fig.1(c). This small portion surrounded in dashed line is magnified in Fig.2(b). The smaller loop in Fig.2(b) corresponds to the innermost part of the spiral in Fig.1c. To establish the correspondence between the stationary solutions and its stability deduced
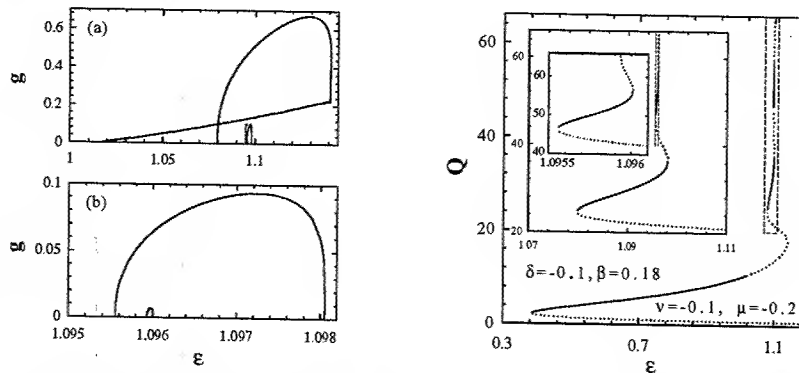
Fig. 2. (Left) (a) Perturbation growth rates versus ϵ for SP solitons around the spiral. (b) Magnification of the portion in (a) enclosed in a dashed rectangle.

Fig. 3. (Right) Energy of the soliton Q versus ϵ for SP solitons. Stable solitons are shown by solid line and unstable solitons by dotted line. The parameters of the equation (except ϵ) are the same as in Fig.1. Two consecutive magnifications of the small parts of the curve enclosed in dashed rectangles are shown in the insets.

from this analysis, the stable soliton branches are shown in Fig.1(b) and 1(c) by solid line. These curves confirm our conjecture that local maxima and minima of ϵ (i.e. the local edges in region of soliton existence) are the points where stability changes. The results of the stability analysis are illustrated in Figure 1(a). The shadowed area in this figure shows the values of ϵ where SP solitons of the higher amplitude are stable. The edges of stability are related to the local minima or maxima of ϵ on the curve for the SP solitons. An exception is the right hand side edge of the wide stripe around $\epsilon = 1$ where stability changes gradually. In between both shadowed areas, any input tends to give place to a pulsating solution in agreement with the above results on oscillatory instability.

The conjecture for soliton stability can be further refined if we plot as one of the parameters a measurable quantity, namely the soliton energy versus ϵ. The energy, $Q = \int_{-\infty}^{\infty} |\psi_o(t)|^2 dt$, has been calculated numerically for each point of the SP soliton branch. The value of Q versus ϵ for the SP solitons is shown in Fig.3. Energy increases to infinity while we move in along the spiral in Fig.1. The reason is that the width of the soliton increases indefinitely. The soliton becomes a composite structure consisting of the central peak and two fronts attached to it from both sides.

Comparison with the above stability results shows that the parts of the curve in Fig.3 with negative slope are all unstable. More accurately, the solid parts of the curve in Fig.3 correspond to stable solitons and the dotted parts to unstable solitons. As we can see, the stability change happens at the local minima and maxima of ϵ vs. Q, i.e. at the local edges of soliton existence in ϵ parameter. The point 2 is not an exception. It represents a point of bifurcation as discussed above but the modes of perturbation on each side of this maximum are different. As a result, the soliton has different type of instability on each side of this point.

Summarizing, we can formulate our conjecture for the stability criterion as follows. The local edges of soliton existence in ϵ-parameter are the points of bifurcation where stability of solitons changes. Between the points of bifurcation, the solitons are unstable if the slope of energy versus ϵ curve is negative. The opposite is not necessarily true, i.e. solitons might be unstable even if the slope is positive.

References

1. N. Akhmediev and J. M. Soto-Crespo, "Composite solitons in optical systems with fast and slow saturable absorbers", pp.307-316. Proceedings of SPIE, Vol. 3666 (1999).
2. J. D. Moores, Opt. Commun. **96**, 65 (1993).
3. J. M. Soto-Crespo, N. N. Akhmediev and V. V. Afanasjev, J. Opt. Soc. Am. B **13**, 1439 (1996).
4. N. N. Akhmediev and A. Ankiewicz. *Solitons: Nonlinear Pulses and beams*, (Chapman & Hall, London), 1997.
5. J. M. Soto-Crespo, N. Akhmediev and A. Ankiewicz. *Phys. Rev. Lett.* **85**, 2937 (2000).

Compound state of dark and bright solitons in dispersion-managed fibers

M. Stratmann and F. Mitschke

Universität Rostock, Fachbereich Physik, 18051 Rostock, Germany
phone +49-381 498 1648, fax +49-381 498 1650, email
martin.stratmann@physik.uni-rostock.de

Abstract: We report of a bright-dark-bright soliton compound state in dispersion managed fibers with either sign of path-average dispersion.

OCIS codes: (190.5530) Pulse propagation and solitons; (190.4370) Nonlinear optics, fibers

Compound state of dark and bright solitons in dispersion-managed fibers

M. Stratmann and F. Mitschke

Universität Rostock, Fachbereich Physik, 18051 Rostock, Germany
phone +49-381 498 1648, fax +49-381 498 1650, email
martin.stratmann@physik.uni-rostock.de

It is well know that in optical fibers with homogenous (i.e. constant) dispersion, stability ranges of bright and dark solitons are limited to anomalous and normal dispersion regime, respectively [1]. This statement needs to be modified, however, in fibers with alternating dispersion. Bright solitons are stable even in a small parameter range with normal path-average dispersion [2, 3, 4, 5, 6]. Very recently we showed that the corresponding statement holds for dark solitons [7]: Their range of existence extends somewhat into the anomalous path-average dispersion regime. As a consequence, dispersion maps with low path-average dispersion can support either flavor of solitons only depending on which is launched. One wonders then whether there can be coexistence of both kinds, and if so, what kinds of interaction will take place and whether there can be bound states. We here report that we found a stable bound state of bright and dark solitons in a dispersion-managed fiber for either sign of path-average dispersion.

While bound states between *spatial* bright and dark solitons have been reported before, the same for temporal solitons of the same frequency and polarization is a novelty. It is known that all two-soliton bound states in homogeneous fiber that are described by the Nonlinear Schrödinger Equation or the Complex Ginzburg-Landau Equation are unstable under perturbations [8]. As for bound states between bright and dark solitons, Buryak et al. [9] considered a birefringent fiber where the two solitons propagate in orthogonally polarized modes. Ania-Castañón et al. [10] considers bound pairs of bright solitons in a dispersion compensation scheme with fiber Bragg gratings but does not discuss dark solitons. In fibers with alternating dispersion, an antisymmetric [11] and a symmetric bi-soliton solution [12] were reported. Here we will present a different interpretation of the antisymmetric solution as a bound state of a dark soliton centered between two bright solitons.

Here is the core of our idea: In numerical simulation work on dark solitons one usually makes the pseudo-cw background of dark solitons as wide as possible, so that effects of its outer slopes do not perturb the dark soliton [13]. This creates considerable computational cost since the computational time window must be even wider. Here we turn this game around and make the background pulse so narrow that both its halves (on either side of the dark soliton) act as bright solitons in their own right.

We start with a pair of Gaussian pulses, with the optical power dipping to zero in the middle between them. At the zero, we let the electrical field undergo a phase jump of π. We then launch this structure down a dispersion-managed fiber. The value of dispersion alternates between normal ($\beta_+ > 0$) for length L_+ and anomalous ($\beta_- < 0$) for length L_-. The path-average dispersion is $\bar{\beta}_2 = (L_- \beta_+ + L_- \beta_-)/(L_+ + L_-)$, and the map strength is $s = (|\beta_+ - \bar{\beta}_2| L_+ + |\beta_- - \bar{\beta}_2| L_-)/\tau_0^2$. τ_0 is the initial full width at half maximum of the individual bright pulses. Propagation is calculated by the well know split step Fourier method.

Looking for a stable solution we speed up convergence by applying the averaging scheme described by Nijhof et al. [2]. We find that after some mild initial rearrangement, the structure propagates stably with both constant pulse separation and overall shape. The relative phase between the pulses remains stable at a value of π. In Fig. 1 one can clearly see dips in the outer pulse wings which are typical for bright DM solitons. The inner part of this structure evolves like a dark DM soliton, the bright pulses behave like bright DM solitons. Let us emphasize that in a homogenous fiber the bright pulses of opposite phase would reject each other.

We have repeated the simulation for various parameters and find that this structure is quite stable. To further test the stability and to find out what exactly causes it, we varied the input power of the pulse pair (see Fig. 2 trace a). For very low power, the bright pulse pair splits quite rapidly due to dispersion. When the power is increased, soon the velocity of separation is reduced, and at some critical value it reaches zero. Upon further increase of power, the pulses keep hanging together. Quite obviously, nonlinear effects stabilize this
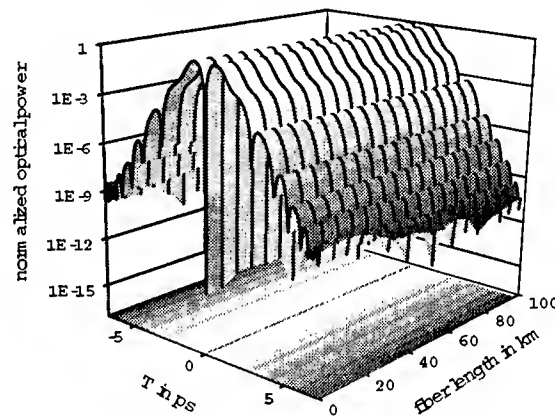
Fig. 1. Propagation of the compound soliton state displayed stroboscopically, shown for 260 nonlinear and 31 dispersion lengths. The parameters of the map are $\bar{\beta}_2 = -0.05\,\text{ps}^2/\text{km}$ and $s = 7.2$ with respect to the half width of the bright pulses. The log power scale reveals characteristic intensity dips in the outer pulse wings. Due to the π phase jump of the dark soliton the intensity vanishes between the two bright pulses.

structure against both dispersive effects and the tendency of opposite-phase pulses to separate. Remarkably, the dark soliton in the center seems to "glue" both bright pulses together.

If this interpretation is correct, the compound state should of course also exist in the normal path-average dispersion regime. For trace b in Fig. 2 all dispersion signs are reversed. For peak power below 0.3 W the structure is totally unstable, and there is no well defined peak position. In the power range between 0.3 W and 0.7 W there are two distinct peaks rejecting each other. Above a threshold of 0.75 W the same stabilization as above is observed. Of course the peak powers of either the bright or the dark solitons are different compared to the case of isolated noninteracting solitons.
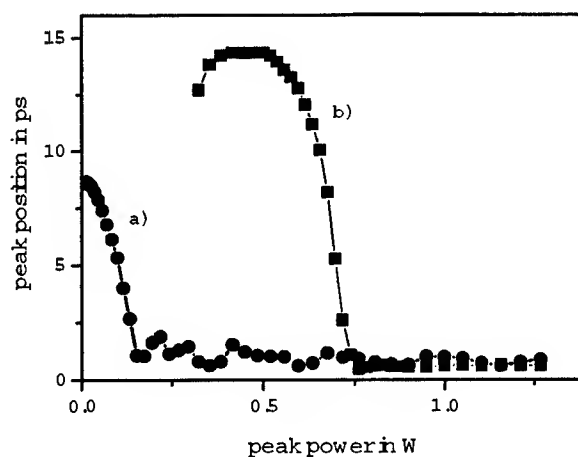
Fig. 2. Half separation of the bright pulses after a given fiber length of 506 km, corresponding to 36 dispersion lengths, as a function of input energy. The path-average dispersion of the map is $|\bar{\beta}_2| = 0.01\,\text{ps}^2/\text{km}$ with a map strength of $s = 12.9$ and a nonlinearity parameter $\gamma = 3.5\,10^{-3}\,(\text{mW})^{-1}$. The peak power of the fundamental soliton in a homogeneous fiber with the same dispersion is 0.018 W. Trace a: anomalous dispersion $\beta_+ = 9.99\,\text{ps}^2/\text{km}$, $\beta_- = -10.01\,\text{ps}^2/\text{km}$. Trace b: normal dispersion, all dispersion signs reversed.

Further research will show whether these soliton composites have a finite binding energy (so that one might speak of "soliton molecules"), and how they respond to various perturbations. We point out that stable bound states of solitons may play an important role in possible future non-binary data formats.

References

1. G. P. Agrawal, "Nonlinear Fiber Optics", Academic Press, (1995).
2. J. H. B. Nijhof, N. J. Doran, W. Forysiak, and F. M. Knox, "Stable soliton-like propagation in dispersion managed systems with net anomalous, zero and normal dispersion", Electron. Lett. **33**, 1726-1727 (1997).
3. Y. Chen and H. A. Haus, "Dispersion-managed solitons with net positive dispersion", Opt. Lett. **23**, 1013-1015 (1998).
4. S. K. Turytsin and E. G. Shapiro, "Dispersion-managed solitons in optical amplifier transmission systems with zero average dispersion", Opt. Lett. **23**, 682-684 (1998).
5. J. N. Kutz and S. G. Evangelides, "Dispersion-managed breathers with average normal dispersion", Opt. Lett. **23**, 685-687 (1998).
6. V. S. Grigoryan, C. R. Menyuk, "Dispersion-managed solitons at normal average dispersion", Opt. Lett. **23**, 609-611 (1998).
7. M. Stratmann, M. Böhm, and F. Mitschke, "Stable propagation of dark solitons in dispersion maps of either sign of path-average dispersion", Electron. Lett. **37**, 1182-1183 (2001).
8. N.N. Akhmediev, A. Ankiewicz, "Solitons: Nonlinear pulses and beams", Chapman & Hall, (1997).
9. A. V. Buryak, Y. S. Kivshar, and D. F. Parker, "Coupling between dark and bright solitons", Phys. Lett. A **27**, 57-62 (1996).
10. J. D. Ania-Castañón, P. Garcia-Fernández, and J. M. Soto-Crespo, "Stable multisoliton pulses in dispersion management with fiber Bragg gratings", Opt. Lett. **25**, 159-161 (2000).
11. C. Paré and P.-A. Bélanger, "Antisymmetric soliton in a dispersion-managed system", Opt. Comm. **168**, 103-109 (1999).
12. A. Maruta, Y. Nonaka and, T. Inoue, "Symmetric bi-soliton solution in dispersion-managed system", Electron. Lett. **37**, 1357-1358 (2001).
13. W. J. Tomlinson, R. J. Hawkins, A. M. Weiner, J. P. Heritage, and R. N. Thurston, "Dark optical solitons with finite-width background pulses", J. Opt. Soc. Am. B **6**, 329-334 (1989).

Cross-phase-modulation induced Modulation Instability in Raman fiber amplifiers.

I. Velchev, R. Pattnaik, J.Toulouse

Lehigh University, Department of Physics,
16 Memorial Drive East, Bethlehem PA 18015, U.S.A.
Tel: +1 610-758-3960; Fax: +1 610-758-5730; E-mail: jt02@lehigh.edu

Abstract: Modulation instability in forward-pumped Raman amplifiers is investigated in detail. The frequency dependence of the instability is explained in terms of a two-beam coupling process due to a finite relaxation time of the Kerr nonlinearity.
© 2002 Optical Society of America
OCIS codes: (060.4370) Nonlinear optics, fibers; (190.3100) Instabilities and chaos; (190.5650) Raman effect

Modulation instability (MI), due to the interplay between self-phase modulation (SPM) and anomalous group velocity dispersion (GVD) is a well known nonlinear effect, responsible for the break up of a CW beam into a train of ultrashort pulses and underlying the process of soliton formation in optical fibers. When two waves are simultaneously present, cross-phase modulation (XPM) can also lead to MI in both normal and anomalous dispersion regimes [1, 2]. The signature of MI is the development of symmetrical sidebands around the central peak in the spectrum of the optical wave. Because this effect is not easily observed in the CW regime, the first experiments were conducted with pulsed lasers [3]. However, the weak sidebands can be made detectable even in CW regime if amplified. In Raman fiber amplifiers, the Raman gain at frequency differences ~ 440 cm^{-1} can provide the necessary amplification source. The presence of both powerful pump and a signal wave in non-zero group velocity dispersion, provides the conditions for development of MI induced by XPM. In this study we have investigated the characteristics of MI in the presence of both Raman gain and two-wave coupling [4].
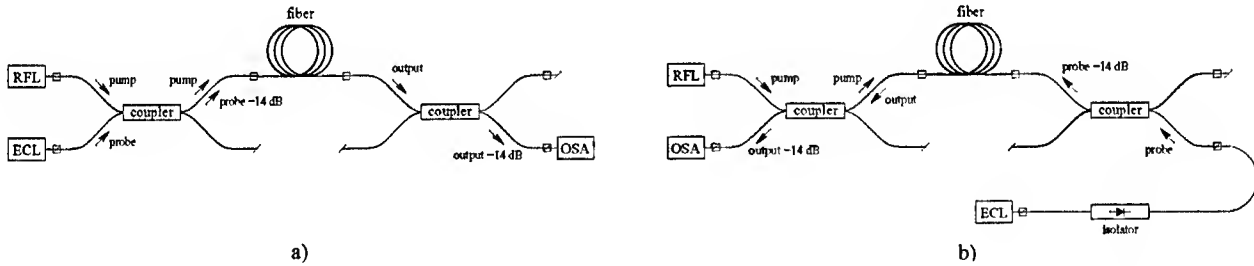
Fig. 1. Experimental setup for spectral characterization of fiber Raman amplifier; a) - forward-pumped scheme, b) - backward-pumped scheme.

The experimental setups for the spectral characterization of the output of the Raman amplifier in both forward- and backward-pumped geometry. are shown in Fig. 1. The pump source used is a commercial Raman fiber laser (RFL) operating at 1497 nm, with a spectral bandwidth $\Delta\lambda \approx 1$ nm at 1.5 W maximum power. The signal source is a set of narrow-band external cavity diode lasers (ECLs), continuously tunable over a broad wavelength range (1450 - 1650) nm and delivering powers up to 5 dBm. The schematics of a forward-pumped Raman fiber amplifier is presented in Fig. 1a. The pump and signal waves are launched into a single-mode fiber by means of a fiber coupler; both AllWave (25 km) and TrueWave (20 km) fibers were investigated in our experiment. The output spectrum is recorded by an optical spectrum analyzer (OSA) with a resolution of 0.1 nm. In the backward-pumped configuration, presented in Fig. 1b, the signal is launched through the fiber's far end, while the OSA was situated on the pump side. The fibers used in this study both have attenuation of ≈ 0.22 dB/km and the mode-field diameters are $A_{\text{eff}} = 87$ μm (AllWave) and $A_{\text{eff}} = 55$ μm (TrueWave). The attenuation in each coupler is shown in Fig. 1 along with the optical field to which the value pertains.

For the forward-pumped scheme in the AllWave fiber, the MI-broadened spectra of the probe are shown in Fig. 2(a-c) with solid lines. They correspond to three different offsets from the pump frequency, respectively on the red side (Fig. 2a), the peak (Fig. 2b) and the blue side (Fig. 2c) of the Raman gain curve. In the
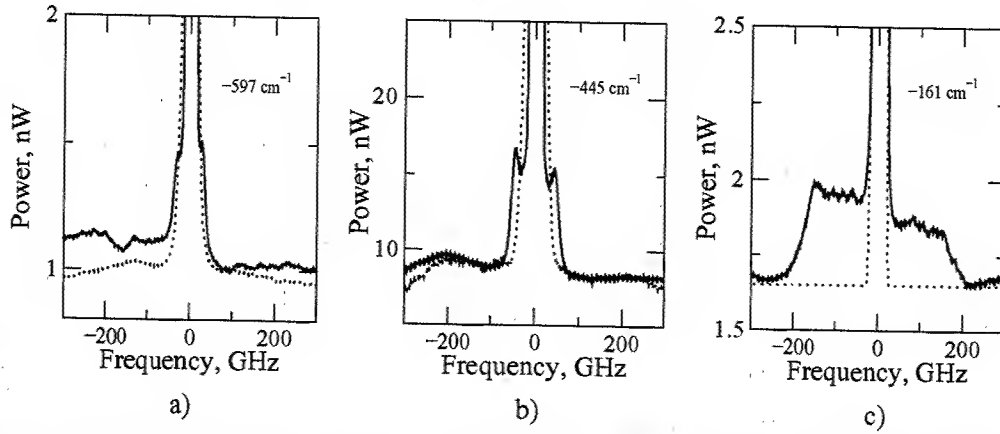
Fig. 2. Modulation instability-broadened spectra after Raman amplification in 25 km of AllWave fiber (solid line) for three probe frequency offsets: a) -597 cm^{-1}; b) -445 cm^{-1}; c) -161 cm^{-1}. The dotted lines represent the spectra from 20 km TrueWave fiber under the same conditions.

following, the sideband with the lower frequency is referred to as the red sideband and the higher frequency one as the blue sideband. The frequency difference between a sideband and the center probe frequency is referred to as the *sideband frequency shift*. For comparison, the results from the same experiment in the TrueWave fiber are shown with dotted lines in Fig. 2(a-c). In this case, no modulation instability is observed, which is to be expected when considering the dispersion properties of the TrueWave fiber [5]. The AllWave fiber exhibits anomalous dispersion at both pump and signal wavelengths, hence both SPM- and XPM-induced MI can develop. On the other hand, because the TrueWave fiber exhibits zero-dispersion for the pump and anomalous dispersion at the signal wavelength, XPM-induced MI is inhibited [1]. The same experiment with counter-propagating pump and signal beams (*see* Fig. 1b) shows no sidebands for both fibers.

It is clearly seen from Fig. 2(a-c), that the sideband frequency shift Δ grows when the signal frequency approaches that of the pump. This frequency dependence of the MI strength cannot simply be explained by the instantaneous interplay between GVD and XPM and can only be explained by the finite response time τ of the Kerr nonlinearity. When taken into account, this time dependence modifies the well known coupled nonlinear evolution equations [6] for the slowly varying amplitudes of the two plane waves with frequencies ω_1 (pump) and $\omega_2 = \omega_1 - \delta$ (signal) co-propagating in a Kerr-type nonlinear medium:

$$\frac{\partial A_1}{\partial z} + \frac{1}{v_{g1}}\frac{\partial A_1}{\partial t} + \frac{i}{2}\beta_{21}\frac{\partial^2 A_1}{\partial t^2} = -\frac{\alpha_1}{2}A_1 + i\gamma_1\left(|A_1|^2 + \kappa|A_2|^2\right)A_1 - \frac{\gamma_1}{2}\eta|A_2|^2 A_1, \tag{1 a}$$

$$\frac{\partial A_2}{\partial z} + \frac{1}{v_{g2}}\frac{\partial A_2}{\partial t} + \frac{i}{2}\beta_{22}\frac{\partial^2 A_2}{\partial t^2} = -\frac{\alpha_2}{2}A_2 + i\gamma_2\left(|A_2|^2 + \kappa|A_1|^2\right)A_2 + \frac{\gamma_2}{2}\eta|A_1|^2 A_2, \tag{1 b}$$

$$\kappa = \frac{2+\delta^2\tau^2}{1+\delta^2\tau^2}, \quad \eta = \frac{2\delta\tau}{1+\delta^2\tau^2}. \tag{1 c}$$

In Eqs.(1 a - 1 b) v_{gj} is the group velocity, β_{2j} - GVD coefficient, α_j - linear loss, and $\gamma_j = n_2\omega_j/(cA_{\text{eff}})$ - the nonlinear coefficient for the pump ($j = 1$) and the signal ($j = 2$) waves. The two parameters κ and η, defined in Eq.(1 c), are referred to as the XPM coupling coefficient and the two-beam coupling gain, respectively [4]. It is worth noting that, in the case of an infinitely fast nonlinear response ($\tau \to 0$) and finite pump-probe frequency difference δ, the XPM coupling approaches the symmetry determined value $\kappa = 2$, while the two-beam coupling gain vanishes. In the case of a finite response time, the XPM coupling has a frequency dependence of *Lorentzian* type with an offset, which determines the behavior of the sideband frequency shift Δ.

The measured blue sideband frequency shifts are shown with full squares in Fig. 3a for different values of δ. The best Lorentzian fit $\Delta(\delta) = a+b/(1+\delta^2\tau^2)$ through the data points converges with a value $\tau = 27$ fs for the relaxation time of the nonlinearity. Fitting the results from several independent measurements reproducibly yields the same value for τ. Our measurements also showed, that the red and blue sidebands are always symmetrically positioned around the central signal frequency. Therefore, the presence of Raman gain does
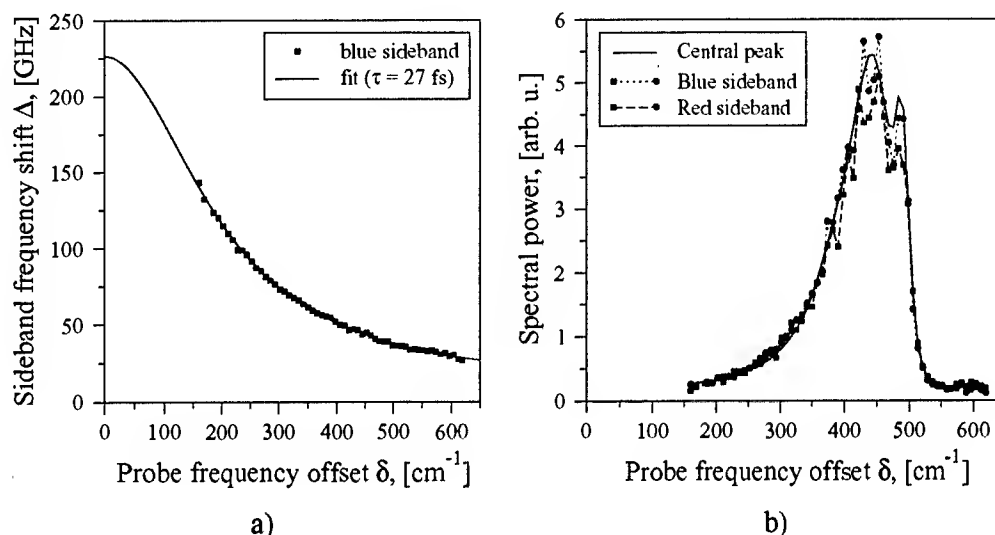
Fig. 3. Spectral characterization of MI: a) - blue sideband frequency shift $vs.$ probe frequency offset δ (the solid line represents the best fit, which yields value $\tau = 27$ fs for the relaxation time of the nonlinearity); b) - spectral power of the probe and sidebands showing the effect of the Raman gain on MI.

not appear to influence the trend in the frequency dependence of the MI strength. Its effect simply manifests itself in amplification of the weak sidebands, which otherwise might not be observable. This last point is clearly illustrated in Fig3b. Actually, when plotting the spectral power of the sidebands and central signal as a function of pump power (not shown), the sidebands are found to experience greater gain than the typical Raman gain measured for the central signal frequency, thus providing evidence for the presence of MI gain.

In the present experimental study we have shown that under specific conditions MI can develop in forward-pumped Raman amplifiers. The experimental evidence obtained enables us to conclude that the observed instability is not simply due to the instantaneous interplay between XPM and GVD, but also involves the two-beam coupling gain resulting from the finite relaxation time of the Kerr nonlinearity in silica. A more detailed theoretical analysis is being developed, which aims at bringing much needed clarity into the subtle dynamics of the processes qualitatively described in this work.

References

1. G. P. Agrawal, "Modulation instability induced by cross-phase modulation", Phys. Rev. Lett. **59**, 880 (1987).
2. G. P. Agrawal, P. L. Baldek, and R. R. Alfano, "Modulation instability induced by cross-phase modulation in optical fibers", Phys. Rev. A **39**, 3406 (1989).
3. K. Tai, A. Hasegawa, and A. Tomita, "Observation of modulation instability in optical fibers", Phys. Rev. Lett. **56**, 135 (1986).
4. Y. Silberberg and I. Bar-Joseph, "Optical instabilities in Kerr medium", J. Opt. Soc. Am. B **1**, 662 (1984).
5. J. J. Refi, Bell Labs Technical Journal, pp. 246-261, January-March 1999.
6. G. P. Agrawal, *Nonlinear fiber optics*, (Academic Press, Boston, 1989).

Numerical study of Parabolic Pulse Generation in Microstructured Fibre Raman Amplifiers

A. C. Peacock, N. G. R. Broderick and T. M. Monro

Optoelectronics Research Centre, University of Southampton, Southampton, SO17 1BJ, UK

Phone: +44 (0)23 80593172, Fax: +44 (0)23 80593149

email: acp@orc.soton.ac.uk

Abstract: Numerical simulations are used to demonstrate parabolic pulse generation in a highly nonlinear, normally dispersive microstructured fibre Raman amplifier. The results show that the output pulse shape depends on the sign of the third order dispersion.

© 2002 Optical Society of America

OCIS codes: (060.553) Pulse propagation and solitons; (190.5650) Raman effects; (190.4370) Nonlinear optics, fibres.

1 Introduction

In recent years self-similar parabolic pulses have generated considerable interest due to their ability to propagate in highly nonlinear media without suffering the usual deleterious pulse distortions whilst maintaining their linear chirp [1, 2]. Parabolic pulses thus offer themselves to a wide range of applications in many areas of optical technology and particularly, as their linear chirp facilitates efficient pulse compression, to the field of high-powered short pulse generation. Initial studies of parabolic pulse generation only considered their formation in optical fibre amplifiers with normal dispersion [3, 2, 4], and recently this work has been extended to examine the effects of the finite width of the gain spectrum [5]. This work has shown that the most efficient parabolic pulse generation occurs when the nonlinear effects are large enough so that the nonlinear propagation dominates over the dispersive propagation which requires a gain medium with a large gain bandwidth to support their growing spectral width.

In this paper we revisit the problem of parabolic pulse generation but this time employing a fibre Raman amplifier in order to exploit the broad Raman gain bandwidth [6]. Furthermore, as these amplifiers are not confined to any particular wavelength, this opens up the possibility for the use of parabolic pulses in optical communication systems which operate around 1.5 μm. Commercial Raman amplifiers based on standard fibre are available and are typically pumped via continuous wave sources operating at several watt power levels. In such a regime we expect that propagation lengths of the order of kilometers would be required for the pulse to become parabolic due to the small gain. As a result, it is questionable whether the nonlinear effects will be sufficiently large, and the dispersive effects sufficiently small, to generate parabolic pulses efficiently. To over come this problem here we consider using a high power pulsed pump source and, to further enhance the nonlinear effects, a microstructured fibre with a large effective nonlinearity [7]. This has the added advantage that the dispersion properties of microstructured fibres can be tailored such that they operate in the normal dispersion regime, necessary for parabolic pulse propagation, at 1.5 μm. The results of our numerical simulations presented here show that parabolic pulse generation is indeed possible via Raman amplification and that these pulses can be efficiently compressed to the sub picosecond regime.

2 Numerical Model and Simulations

The refractive index profile of the microstructured fibre we used is shown in Fig. 1(a) in which the core diameter is 1.1 μm, leading to an effective mode area of 2.5 μm² and the dispersion profile shown in Fig. 1(b). Such a fibre is similar to that used previously as a Raman amplifier [7] and although no-one has yet demonstrated microstructured fibres with normal dispersion at 1.5 μm it should be possible to fabricate such fibres in the near future. Given the modal properties of the microstructured fibre, pulse propagation can be described by the standard NLSE. Including the effects of Raman amplification the evolution of the pulses in our system
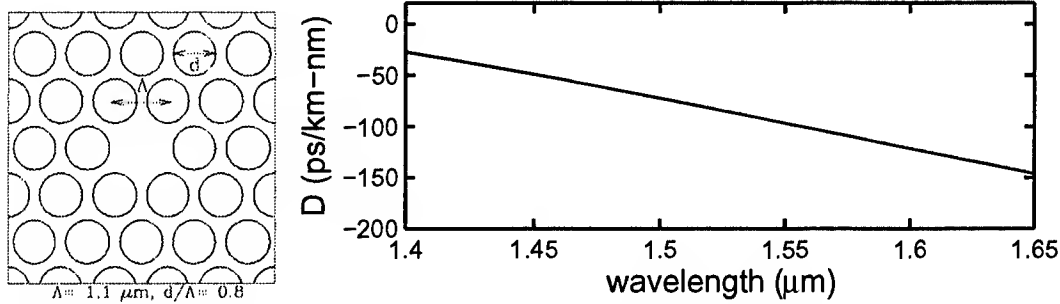
Fig. 1. (a) Fibre profile used in the simulations and (b) associated dispersion parameter D as a function of wavelength.

can then be described by a modified form of the NLSE [8]:

$$i\frac{\partial \Psi}{\partial z} = \frac{\beta_2}{2}\frac{\partial^2 \Psi}{\partial T^2} + i\frac{\beta_3}{6}\frac{\partial^3 \Psi}{\partial T^3} - \gamma\left(1 + \frac{i}{\omega_0}\frac{\partial}{\partial T}\right)\Psi \int_0^\infty R(T')\left|\Psi\left(z, T - T'\right)\right|^2 \mathrm{d}T', \qquad (1)$$

where β_2 is the GVD parameter, β_3 is the third order dispersion parameter and γ is the effective nonlinearity of the microstructured fibre. We write the nonlinear response function as $R\left(T\right) = \left(1 - f_R\right)\delta\left(T\right) + f_R h_R\left(T\right)$, assuming that the electronic contribution $\delta\left(T\right)$ is nearly instantaneous and that the relative size of the vibrational (Raman) contribution $h_R\left(T\right)$ is determined by f_R [6]. The field Ψ, in comoving coordinates, can be expressed in terms of the amplitude A_j and the phase Φ_j, $j = p, s$, of the pump and the signal beams as:

$$\Psi\left(z, T\right) = A_p\left(z, T\right)\exp\left[i\Phi_p\left(z, T\right)\right] + A_s\left(z, T\right)\exp\left[i\Phi_s\left(z, T\right)\right]. \qquad (2)$$

where the signal field is downshifted in frequency by 13.2 THz from the pump beam corresponding to the peak of the Raman gain spectrum. An important feature of Eq. (1) is the inclusion of the time-derivative operator in the nonlinear term which is necessary to ensure that the photon number is conserved, and not the optical energy, so that the Raman interaction is described correctly.

Our simulations consider the injection of a Gaussian signal pulse at 1.55 μm with a 1 ps duration (fwhm) and a peak power of 5 W together with a 315 ps (fwhm), 20 W super-Gaussian pump pulse at 1.45 μm. The fibre parameters which were calculated from the refractive index profile shown in Fig. 1 are: $\beta_2 = 0.126\,\mathrm{ps^2 m^{-1}}$, $\beta_3 = -0.001\,\mathrm{ps^3 m^{-1}}$, $\gamma = 0.041\,\mathrm{W^{-1} m^{-1}}$, and the fractional contribution of the delayed Raman response $f_R = 0.18$ [6]. The output signal pulse and spectrum are plotted in Fig. 2(a) after 20 m of propagation corresponding to a total pulse gain of $\sim 25\,\mathrm{dB}$. The top curves show the intensity profile, plotted on a log scale, together with the chirp, plotted on a linear scale, (solid lines), whilst the bottom curve shows the pulse spectrum. Despite the asymmetry in the output pulse, it is clear that this pulse displays the characteristic features of a parabolic pulse with a linear chirp including both the low intensity exponentially decaying wings and the oscillations on the spectrum [9]. Further confirmation is provided by the good agreement between the output pulse and the parabolic and linear fits to the intensity profile and the chirp, respectively (circles).

Although some of the asymmetry in the output pulse can be attributed to the shape of the gain spectrum [6] it is, in fact, primarily due to pump depletion where the leading edge of the pulse experiences more gain than the trailing edge. This effect is significant because the signal intensity eventually exceeds that of the pump intensity and, due to the large gains necessary to amplify a pulse to the parabolic regime, it is a difficult problem to avoid. An important consequence of the effects of the pump depletion is that the formation of a parabolic pulse is highly dependent on the sign of the third order dispersion. We have found that when $\beta_3 < 0$ then the asymmetry induced by the third order dispersion acts in the opposite direction to that induced by the pump depletion and thus can actually improve the quality of the output pulse. However, when $\beta_3 > 0$ the effects of the asymmetries combine which destroy the linearity of the chirp and can lead to the pulse developing oscillations on a long sloping training edge. Such effects can be seen in Fig. 2(b) where the top curves show the intensity profile and chirp, plotted on linear scales, and the bottom curve shows the spectrum of the output pulse generated under the same conditions as that in Fig. 2(a) but this time with
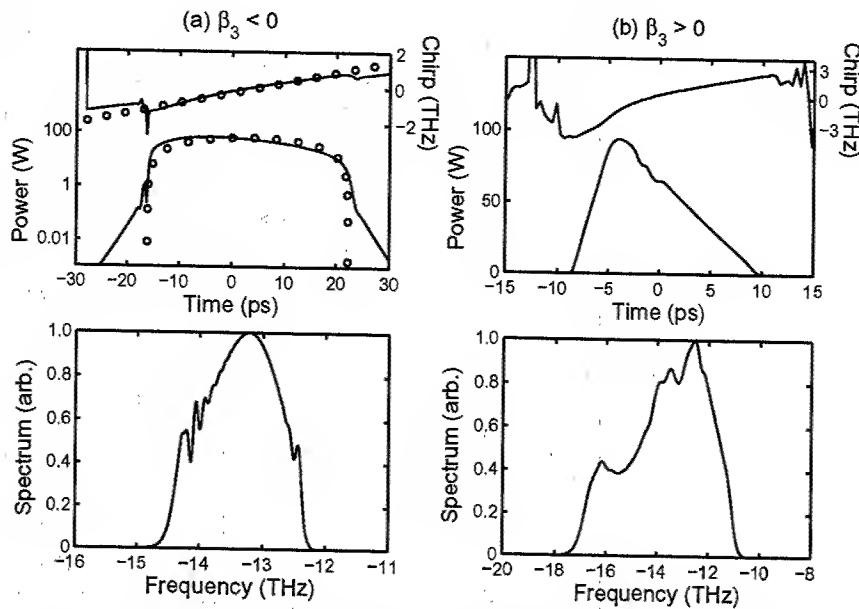
Fig. 2. Top, intensity (left axis) and chirp (right axis) of the fibre output obtained from simulations (solid lines), where (a) is compared with fitted curves (circles). Bottom, the corresponding spectra.

$\beta_3 = 0.001 \, \text{ps}^3 \text{m}^{-1}$. Although in standard single-mode fibres β_3 is typically positive this is not necessarily the case in microstructured fibres. Fig. 1(b) shows a plot of $D (= d\beta_1/d\lambda)$ as a function of wavelength and clearly both the condition that $\beta_2 > 0$ (necessary for parabolic pulse formation) and $\beta_3 < 0$ are satisfied.

To demonstrate the potential use of Raman amplified parabolic pulses for high-powered short pulse generation we considered the compression of the pulse in Fig. 2(a) via a simple linear grating pair. As a result of the asymmetry in the pulse we found that the compressed pulse develops a long pedestal on the trailing edge. Nonetheless, this still yields a pulse with a fwhm of 700 fs and a peak power of 1.4 kW and we expect that these results can be improved with the inclusion of third order dispersion compensation in the compression stage.

3   Conclusions

In conclusion, we have used numerical simulations to demonstrate parabolic pulse formation in a microstructured fibre Raman amplifier. The results have shown that the effects of pump depletion can be reduced with the appropriate sign of the third order dispersion and that such values of β_3 are currently available in microstructured fibres. The ease with which these pulses can be compressed suggests that Raman amplified parabolic pulses offer an efficient source of high-powered short pulses unrestricted by wavelength. We expect that they will find wide application in many areas of optical technology.

References

1. D. Anderson, et al. J. Opt. Soc. Am. B **10** 1185-1190 (1993).
2. M. E. Fermann, et al. Phys. Rev. Lett. **84** 6010-6013 (2000).
3. K. Tamura and M. Nakazawa, Opt. Lett. **21** 68-70 (1996).
4. V. I. Kruglov, et al. Opt. Lett. **25** 1753-1755 (2000).
5. A. C. Peacock, et al. Opt. Commun., (In press).
6. G. P. Agrawal, "Nonlinear fiber optics," Academic Press, 2001.
7. Z.Yusoff, et al. Opt. Lett. **27**(6), 424-426, 2002
8. K. J. Blow and D. Wood, IEEE J. Quantum. Electron. **25** 2665-2673 (1989).
9. V. I. Kruglov, et al. J. Opt. Soc. Am. B **19** 461-469 (2002).

Improving efficiency of supercontinuum generation in photonic crystal fibers by direct degenerate four-wave-mixing

N. Nikolov[1,2], O. Bang[1]

[1] *Informatics and Mathematical Modelling, Technical University of Denmark,*
DK-2800 Kongens Lyngby, Denmark
phone:+45 45 25 31 09, fax:+45 45 93 12 35, e-mail:nin@imm.dtu.dk

[2] *Risø National Laboratory, Optics and Fluid Dynamics Deptartment, OFD-128*
P.O. Box 49, DK-4000 Roskilde, Denmark

A. Bjarklev[3]

[3] *Research center COM, Technical University of Denmark, DK-2800 Kongens*
Lyngby, Denmark

Abstract: The efficiency of supercontinuum generation in photonic crystal fibers is significantly improved by designing the dispersion to allow widely separated spectral lines generated by degenerate four-wave-mixing directly from the pump to broaden and merge.

Photonic crystal fibers (PCFs) [1] and tapered fibers [2] are promising sources for efficient supercontinuum generation (SCG) due to their unusual dispersion properties and high effective nonlinearities. These fibers have similar dispersion and nonlinearity characteristics and they have the advantage that their dispersion may bemodified by a proper design of the cladding structure [3], and by changing the degree of tapering [2], respectively. Using femtosecond pulses a supercontinuum (SC) spanning one octave has been generated in a PCF, whereas impressive two octave SC has been obtained in a tapered fiber. The latter two octave wide SC was later explained to be a result of self-phase modulation (SPM) and direct degenerate four-wave-mixing (FWM) [4].

However complex high power femtosecond lasers are not necessary, - SCG may be achieved with picosecond and even nanosecond pulses. Thus Coen et al. generated a one octave SC in a PCF using sub-kilowatt picosecond pulses and showed that the primary mechanism was the combined effect of stimulated Raman scattering (SRS) and parametric FWM, allowing the Raman shifted components to interact efficiently with the pump [5]. Here we show how direct degenerate FWM can be used to significantly improve the efficiency of SCG with sub-kilowatt picosecond pulses in PCFs, if the dispersion is properly designed.

Improving efficiency of SCG with picosecond pulses in PCFs using degenerate FWM. We study the SCG process numerically using the well known coupled nonlinear Schrödinger equations that describe the evolution of the x- and y-polarization components of the field for pulses with a spectral width up to 1/3 of the pump frequency [5]. This model accounts for SPM, cross-phase-modulation, FWM, and SRS. An initial random phase noise seeding of one photon per mode is included.

We consider the same PCF and numerical and experimental data as in [5], kindly provided by S. Coen. Thus we pump along the slow axis with 30ps pulses of $I_p = 400W$ peak power and pump wavelength $\lambda_p = 647$nm. Our PCF has core area $A_{core} = 1.94m^2$, dispersion $D(\lambda_p) = -30ps/(nmkm)$, zero dispersion wavelength $z_1 = 675$nm, $n_2 = 3 \cdot 10^{-20}m^2/W$, and birefringence $n_x - n_y = 1.9 \cdot 10^{-6}$. The dispersion is expanded around the pump to include $\beta_2 = 7.0ps^2/km$, $\beta_3 = 5.1 \cdot 10^2 ps^3/km$, $\beta_4 = -4.9 \cdot 10^5 ps^4/km$, $\beta_5 = 1.2 \cdot 10^7 ps^5/km$, $\beta_6 = -1.8 \cdot 10^{10} ps^6/km$, and $\beta_7 = 1.2 \cdot 10^{13} ps^7/km$. A uniform loss of $0.1dB/m$ is used and the effective area is approximated with the core area, giving the nonlinearity parameter $\gamma = 2n_2/(\lambda_p A_{core}) = 0.15(Wm)^{-1}$. We use the standard split-step Fourier method with 217 points in a time window of $T = 236ps$. In our longest simulation out to $L = 3.7m$ the photon number is conservedto within 5% of its initial value. Due to our large spectral window (405nm 1613nm) we see in Fig.1(a) the emergence of FWM stokes and anti-stokes waves at the wavelengths $\lambda_s = 1100$nm and $\lambda_{as} = 458$nm for which the phase matching condition $\Delta\beta = \beta_s + \beta_{as} - 2\beta_p + \gamma I_p = 0$ is satisfied. The spectral window presented in [5] was narrower and thus λ_s and λ_{as} were not observed. From the standard expressions given in [6] we find the maximum FWM parametric

gain to be twice the maximum SRS gain, which explains why the FWM stokes and anti-stokes components appear before the SRS components. The loss and walk-off of the PCF gives the maximum distance L_{max} over
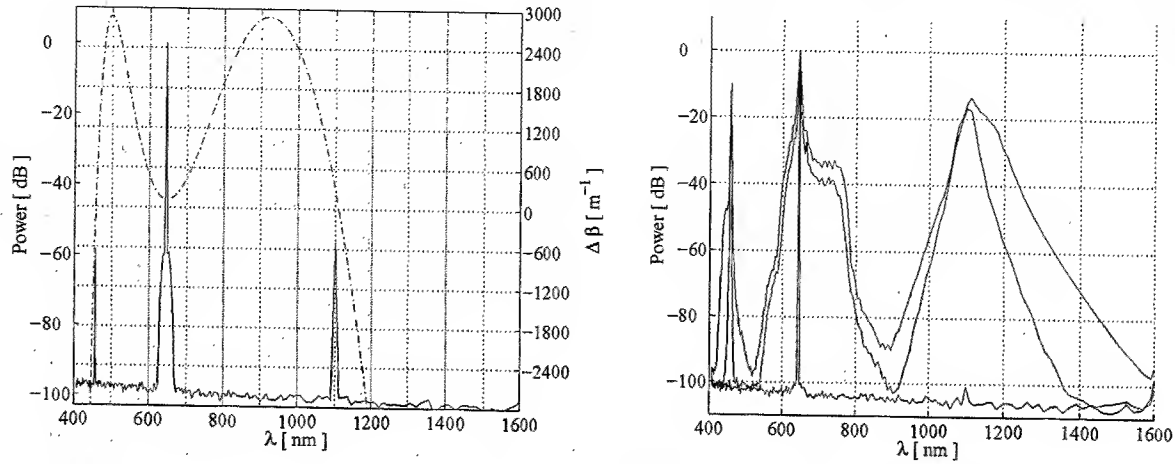
Fig. 1. a) Phase-mismatch $\Delta\beta$ and spectrum of the slow axis polarization component at $L = 17.4cm$. b) Same spectrum at $L = 4.3cm$, $2.6m$, and $3.7m$.

which nonlinear processes, and thus the SCG process, are efficient. From Fig.1(b) we see that after the FWM stokes and anti-stokes components are generated they broaden much in the same way as the central part of the spectrum around the pump. The merging of the spectral parts around λ_{as}, λ_p, and λ_s would create an ultra broad spectrum as observed in tapered fibers with femtosecond pulses [2,4]. However, in this particular case the FWM stokes and anti-stokes lines are too far away for a merging to take place within the maximum length L_{max}, i.e., before nonlinear effects become negligible. The wavelengths λ_s and λ_{as} can be adjusted to
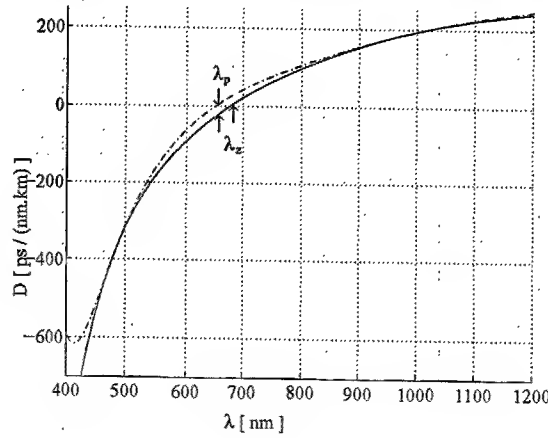
Fig. 2. Original dispersion [5] (solid line) and our modified dispersion (dashed line).

be closer to the pump wavelength λ_p by a proper design of the dispersion. This will enable the FWM stokes and anti-stokes lines to broaden enough to allow a final merging. To show the effect we modify β_2, β_4, and β_6 to $\beta_2 = 1.0ps^2/km$, $\beta_4 = -2.5 \cdot 10^5 ps^4/km$, and $\beta_6 = -3.25 \cdot 10^{10} ps^6/km$. The phase-matching condition $\Delta\beta = 0$ then gives $\lambda_s = 850nm$ and $\lambda_{as} = 530nm$. The effect on the dispersion profile is to down-shift the zero dispersion wavelength to $\lambda_p = 660nm$ and reduce the normal dispersion to $D(\lambda_p) = -4.35ps/(nmkm)$, as shown in Fig.2. The numerical results shown in Fig.3 confirm our hypothesis. The FWM stokes and
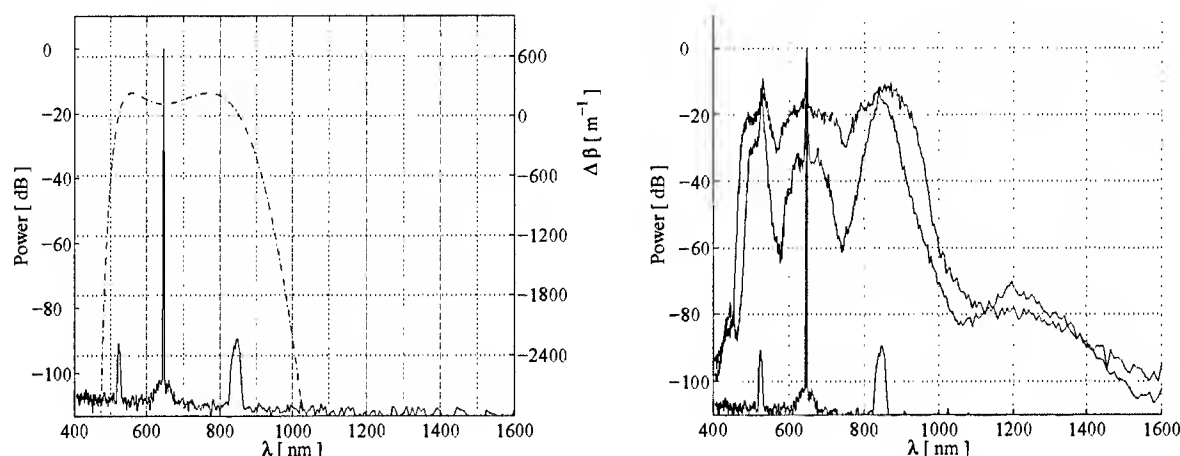
Fig. 3. a) Phase-mismatch $\Delta\beta$ and spectrum of the slow axis polarization component at $L = 17.4cm$. b) Same spectrum at $L = 8.7cm$, $43cm$, and $2.154m$.

anti-stokes lines are still widely separated, but now generated close enough to the pump to broaden and merge. The resulting ultrabroad SC is flat within 20dB and spans 510nm (at -40dB from the flat part) in contrast to the original 230nm observed in [5].

1   Conclusion

We have numerically considered SCG in birefringent PCFs using sub-kilowatt picosecond pulses. Our results show that by properly designing the dispersion properties and using the simultaneous broadening and final merging of widely separated pump and FWM stokes and anti-stokes lines the SCG efficiency can be significantly improved. Further investigations will involve the robustness of the process towards variations in the birefringence along the PCF. This work was supported by the Danish Technical Research Council (Grant no. 26-00-0355) and the Graduate School in Nonlinear Science (The Danish Research Agency).

References

1. J. K. Ranka, R. S. Windler, and A. J. Stentz, " Visible continuum generation in air-silica microstructure optical fibers with anomalous dispersion at 800 nm," Opt. Lett. **25**, 25 (2000).
2. T. A. Birks, W. J. Wadsworth, and P. St. J. Russell, "Superconyinuum generation in tapered fibers," Opt. Lett. **25**, 1415 (2000).
3. A. Ferrando, E. Silvestre, J. J. Miret, and P. Andres, "Nearly zero ultraflattened dispersion in photonic crystal fibers," Opt. Lett. **25**, 790 (2000).
4. A. V. Gusakov, V. P. Kalosha, and J. Herrmann, "Ultrawide spectral broadening and pulse compression in tapered and photonic fibers," QELS, pp. 29 (2001).
5. S. Coen, A. Chao, R. Leonardt, and J. Harvey, "Supercontinuum generation via stimulated Raman scattering and parametric four-wave-mixing in photonic crystal fibers," J. Opt. Soc. Am. B **26**, 1356 (2001)
6. G.P. Agrawal, *Nonlinear Fibre Optics*, 2nd ed. Academic, San Diego, Calif., (2000).

Carrier frequency hopping for optical pulse transmission in dispersion-managed fiber links

Alessandro Tonello
*Istituto Nazionale per la Fisica della Materia, Dept. of Information and Communication Technologies,
via Sommarive 14, 38050 Povo (TN), Italy*

Fabrizio Carbone, Luciano Socci and Marco Romagnoli
*Pirelli Labs Optical Innovation, viale Sarca 222, 20126 Milano, Italy
phone: +39 02 64423369, fax: +39 02 64423455, e-mail: fabrizio.carbone@pirelli.com*

Abstract: We propose a chirped return-to-zero transmission format, combining wavelength conversion with dispersion management. Periodically varying the pulse's carrier frequency at optimal points, we reduce the impairments of third-order dispersion and we mitigate the timing jitter.

OCIS codes: (060.4510) Optical Communications, (190.5530) Pulse propagation and solitons.

1. Introduction

 The study of fiber transmission systems with highly spectral efficiency represents an hotly debated topic nowadays. A particular attention is dedicated to dispersion-managed solitons, and more generally to chirped return-to zero (RZ) transmission formats, owing to their intrinsic robustness to noise and distortions induced by fiber nonlinearity [1]. Appropriate design of dispersion map will be probably one of the fundamental issues for the incoming generation of optical systems; specifically the basic principle of dispersion compensation is presently enriched of more sophisticated design requirements and challenges. Practical key rules that enable for limiting pulse interactions or collisions consequences in wavelength-division multiplexing (WDM) [2] have been recently translated into specific map structures, pointing out the possible combination of time, and frequency domain multiplexing to increase the overall spectral efficiency. Similarly, in the context of high-speed optical networks, the promising perspectives of all-optical wavelength converters (OWCs) envisage new potentialities for multi-channel transmissions [3-4]. For instance (see Ref.5), mid-span spectral inversion has been successfully applied for reducing the asymmetrical inter-channel Raman gain in a densely WDM optical link. However, the combination of OWCs and chirped pulses like DM solitons [6] may incur in severe limitations, whenever the shifting of carrier wavelength includes the inversion of the pulse's chirp, in presence of additional noise and losses [3].

 In this paper we optimize the compatibility of DM-solitons with periodical OWCs, exploiting their potential contribute for third-order dispersion compensation and jitter reduction.

2. Single pulse transmission

The pulse propagation $q(t,z)$ in a DM based fiber link can be studied by solving the so-called Nonlinear Schrödinger equation; we assume periodic coefficients both for the chromatic dispersion $D(z)$ and for fiber nonlinearity $\gamma(z)$, which accounts for distributed losses, periodical amplification and difference among fiber cross sections:

$$i\frac{\partial q}{\partial z}+\frac{D(z)}{2}\frac{\partial^2 q}{\partial t^2}+\gamma(z)\,|\,q\,|^2\,q=0 \qquad (1)$$

We have taken advantage of a variational method [6] under the assumption of chirped Gaussian solutions as $q(t,z)=A(z)\exp[-p(z)t^2+iC(z)t^2]$, obtaining   a preliminary indication of the pulse dynamics. OWCs are here assumed as black boxes of full spectral inversion, where the optical conjugation (OC) of signals $q_{out}(t,z)=q_{in}(t,z)^*$ represents an ideal limit, setting to zero the frequency shift. OCs have been assessed in the variational equations by mirroring the chirp as $C_{out}=-C_{in}$. Despite the presence of such chirp reversal condition, one can find that, for optimized system setups, OCs can be included in a dispersion map, leading again to a periodic evolution for the pulse parameters. For ease of discussion, let us suppose to refer, at the beginning, to an ideal lossless case, where the chirp-free conditions can be easily localized exploiting map symmetries. The dispersion map is composed by 10.1km of fiber with D=1ps/(km nm), γ=2.2km^{-1}W^{-1}, combined with 19.8km of a compensating span
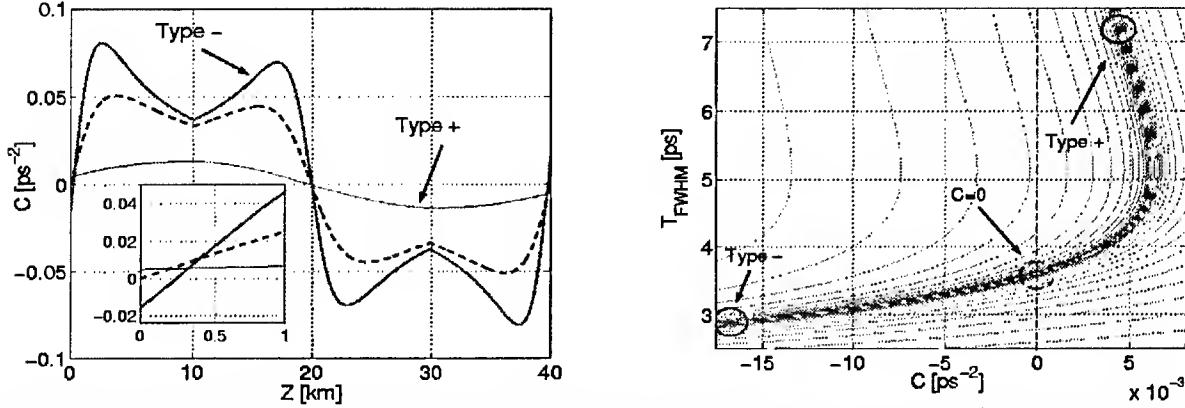
Fig.1. Left: chirp evolution: (dashed) reference case with C(z=0)=0; (thicker solid curve) a type- trajectory, (thin solid curve) a type+ trajectory. The periodicity C(z=0)=-C(z=40km) is ensured by OC at z=40km. Inset: detail of the initial evolutions. Right: peaks, input conditions close to periodical solutions with OCs. Chirp sign distinguishes between type- and type+ ; circles highlight the three input conditions shown in fig. 1,left.

[D=-1ps/(km nm), γ=3.6km^{-1}W^{-1}]; the dispersion map is symmetrically completed by including again a fiber span of 10.1km [D=1ps/(km nm), γ=2.2 km^{-1}W^{-1}]. We assume a pulse power of 3dBm, and OCs are placed at the end of each map. Owing to the map symmetry, the input soliton chirp, without OCs, verifies C(z=0)=0. However, the application of chirp reversal elements allows the presence of periodical solutions, even for input chirps weakly negative (type – trajectory) or positive (type + trajectory). These additional solutions are sustained by the periodical effect of OCs, and examples of three different periodical trajectories are shown in fig. 1,left. To focus a more precise discussion on this specific context, we represent in the width-chirp plane, the input conditions (z=0) of the variational equations that reproduce a closed orbit within a single dispersion map of given length L. An example of this input-map is shown in fig.1, right, where peaks identify input conditions close to periodical evolutions, and the chirp sign distinguishes between type – and type + solutions. However, when the lumped optical conjugation is repeatedly applied in the transmission link and the full NLS eq.1 is numerically solved, the optical pulses may visibly undergo a progressive disruption. Indeed small fluctuations of chirp with respect to stationary solution, either caused by pulse interactions or non optimal input conditions, may be converted by OCs into a weak but cumulative pulse spreading. We find numerically that such decay of the pulse peak power may be limited when OCs are localized as close as possible to the chirp-free points, that is when the chirp inversion leads to the lowest pulse's distortion; similarly one can improve the system entailing a dispersion map that intrinsically minimizes the chirp perturbations induced by pulse interactions.

3. System simulations

Let us combine now dispersion management with the OWCs in presence of third order dispersion (TOD). We can develop in principle a macro-cell composed of several sub-blocks of fibers and OWCs (see fig.2, left). Within each sub-block, the compensation ratio is mainly managed interchanging different fiber types, while the action of OWCs, coupling wavelength conversion with TOD, may adjust the macro-cell average dispersion. The resulting macro-element can then be periodically repeated within the optical link. Consequently, a periodical hopping of the carrier wavelengths takes place when the optical signal crosses a sequence of macro-cells. In presence of TOD, the average dispersion D_{avg} of a classical dispersion map at some specific wavelength may be incompatible with DM-solitons at high bit-rate (either because D_{avg} is too large or because it represents a normal dispersion regime [7]); in contrast, the average dispersion of a macro-cell can be redirected to a more convenient value with OWCs, and above all, can be potentially equalized at all wavelengths. The further presence of signal conjugation may lead to a reduction of timing jitter, without pulse distortions, owing to the special localization nearly at chirp free for OWCs.

Interesting results can be found whenever TOD is partially compensated with special fibers [1]. We exemplify in fig.3 (left), a periodical evolution obtained from the variational method for a dispersion map whose details at 1553.2nm are summarized in the tabular of fig2 (right). Here TOD is partially equalized employing dispersion compensating fibers (DCF) with reversed TOD [1], and the moderate bit-rate permits for low interaction forces and low chirp perturbations. The average power was of –0.96dBm, the amplifier spacing of 56.4km and the dispersion map design has been entailed for an input chirp-free condition. We show in the right side of fig.3, the numerical estimation of a 6 channels transmission at 20Gbit/s up to 60 maps (3384km) in presence of a weak amount of TOD (see the dashed line representing average dispersion). The different channels are here identified through their relative detuning $\Delta\lambda$ from the reference wavelength of λ=1553.2nm.
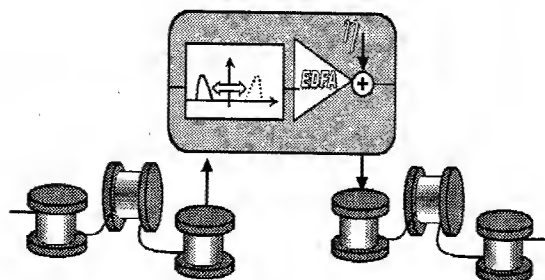
Fiber	D	TOD	loss	Aeff	L$_S$
SMF	17.2	0.062	0.2	80	10
DCF	-117.5	-0.78	0.6	20	2.2
NZD	3.772	0.085	0.25	50	28
DCF	-117.5	-0.78	0.6	20	2.2
SMF	17.2	0.062	0.2	80	14

Fig.2. Left: Schematic view of a macro-element composed of a two-blocks dispersion maps and an OWC that swaps the channel wavelengths. Right: map description, dispersion D [ps/(km nm)], TOD [ps/(km nm^2)], loss [dB/km], effective core area A [μm^2], segment length L$_S$ [km].
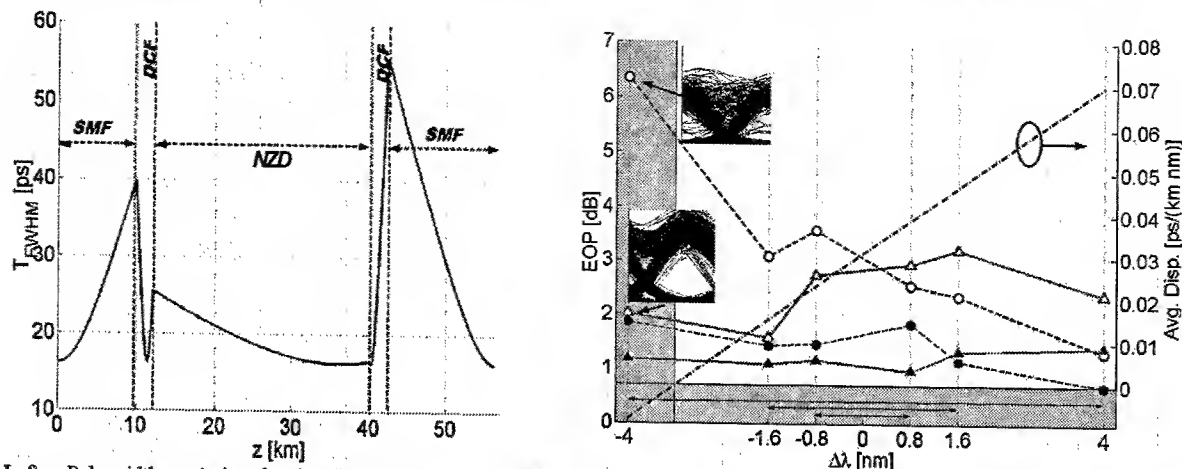
Fig.3. Left: Pulsewidth evolution for the dispersion map exemplified in fig.2, right. The soliton-like behavior is traced with the variational method in absence of OWCs. Right: Eye opening penalties versus channel displacement for 6 channels transmission at 20Gbit/s. The system with OWCs is in solid line, without OWCs in dashed lines. The transmission distance of 2256km (filled markers) and 3384km (empty markers).

We have assumed all equal input pulsewidths and prechirps; note however that the closest matching for a DM soliton would be satisfied at λ, and more strikingly, that at Δλ=−4nm the system crosses the average normal dispersion regime (shaded region) with consistent transmission penalties (see also Ref. 7). A reduction of penalties for channels with unsuitable average dispersion can be found by imposing a periodical hopping of the carrier wavelengths from λ−Δλ to λ+Δλ with OWCs spaced of 1128km (see the doubled arrows of fig.3 right). In our numerical simulations each OWC combines an ideal OC stage and a lumped loss of 10dB that is compensated by an Erbium amplifier. Despite such additional noise (the amplifiers have a common noise figure of 4.5dB) the comparison of the two eye diagrams of fig.3 (see the two insets), confirms the benefits of frequency hopping in the net normal average dispersion. Differently, when the average dispersion naturally enables for robust DM solitons, the propagation may be negatively influenced by the introduction of OWCs (see the channels with Δλ>0).

In conclusion we found that periodically hopping the carrier wavelength at chirp-free positions, one may equalize the impairments of third order dispersion, leading to a net improvement of the channels that naturally exhibit an unsuitable average dispersion for soliton-like transmissions. Additionally, the spectral inversion of OWCs may result effective in limiting the timing jitter, when the chirp distortion is controlled with an optimized system setup.

References

[1] L. F. Mollenauer, P. V. Mamyshev, J. Gripp, M. J. Neubelt, N. Mamysheva, Lars Grner-Nielsen, Torben Veng, " Demonstration of massive wavelength-division multiplexing over transoceanic distances by use of dispersion-managed solitons ", Opt. Lett. , 25 , 704, (2000).

[2] F. Neddam and S. Wabnitz,"Role of Intra and Interchannel Cross-Phase Modulation in Higher Order Fiber Dispersion Management", IEEE Phot. Tech. Lett., 12, 798, (2000).

[3] S.J.B Yoo, "Wavelength conversion technologies for WDM network applications", IEEE Journ. Light. Tech., 14, 955, (1996).

[4] H. Suche, G. Schreiber, Y. L. Lee, V. Quiring, R. Ricken, W. Sohler, A. Paoletti, F. Carbone, D. Caccioli, and A. Schiffini, "Efficient Ti:PPLN multi-wavelength converter for high bit rate WDM-transmission systems", Proc. ECOC 2001, Amsterdam, Sept. 30- Oct.4, 2001.

[5] A.G. Grandpierre, D. N. Christodulides, J. Toulouse, "Theory of Stimulated Raman Scattering Cancellation in Wavelength-Division-Multiplexed Systems via Spectral Inversion", IEEE Phot. Tech. Lett., 11, 1271, (1999).

[6] Y. Kodama, "Nonlinear pulse propagation in dispersion managed system", Physica D, 123, 255, (1998).

[7] M. Nakazawa, A. Sahara, H. Kubota, "Propagation of a solitonlike nonlinear pulse in average normal group-velocity dispersion and its unsuitability for high-speed, long-distance optical transmission", Journ. Opt. Soc. Am. B, 18, 409, (2001).

Eigenvalues of the Zakharov-Shabat scattering problem for real symmetric pulses

M. Desaix

Dept. of Engineering Sciences, University College of Borås, SE–501 90 Borås, Sweden

Tel.: +46 33 174652, Fax: +46 33 164008 , E-mail: Mats.Desaix@hb.se

D. Anderson, L. Helczynski, M. Lisak

Dept. of Electromagnetics, Chalmers University of Technology, SE–412 96 Göteborg, Sweden

Abstract: The problem of determining the solitons generated from symmetric real initial conditions in the Nonlinear Schrödinger equation is revisited. The corresponding Zakharov-Shabat scattering problem is solved for an example of a real double-humped rectangular initial pulse form. It is found that this real symmetric pulse generates moving soliton pulse pairs corresponding to eigenvalues with non-zero real parts.

The nonlinear Schrödinger (NLS) equation is one of the most fundamental nonlinear evolution equations in physics. For the case of a focusing nonlinearity, it can be written in the standard form:

$$i\frac{\partial\psi}{\partial t} + \frac{1}{2}\frac{\partial^2\psi}{\partial x^2} + |\psi|^2\psi = 0, \qquad \psi(0,x) = q(x) \tag{1}$$

The NLS equation belongs to the important class of equations which are integrable using the inverse scattering technique, cf e. g. Ref. [1]. A particularly important result of this solution procedure is that the discreet eigenvalues of the corresponding eigenvalue problem determine the soliton content of the initial pulse. The soliton content of different pulse forms has been investigated in many previous studies and in general it has been found that the eigenvalues of symmetric and real pulses are purely imaginary (i. e. the soliton pulses have no velocity), cf Ref. [2], and that the number of soliton pulses in a given initial condition is directly related to the integral of the pulse. As will be demonstrated in the present work, this general picture is not complete. In fact, by analyzing the Zakharov-Shabat eigenvalue problem for a real double-humped symmetric box profile we show that the conventional expression for the number of solitons is correct, provided it is interpreted as the number of solitons corresponding to purely imaginary eigenvalues. However, in addition to these eigenvalues, there may also exist a number of eigenvalues, which contain both real and imaginary parts corresponding to symmetrically separating solitons.

In the inverse scattering transform method for the NLS equation, a crucial step in the analysis is the Zakharov-Shabat scattering problem, where the initial pulse, $q(x)$, plays the role of a scattering potential. The characteristic equation reads

$$\begin{cases} \dfrac{dv_1}{dx} = -i\zeta v_1 + q(x)v_2 \\ \dfrac{dv_2}{dx} = -q^*(x)v_1 + i\zeta v_2 \end{cases}, \qquad \left.\begin{matrix} v_1 \to \exp(-i\zeta x) \\ v_2 \to 0 \end{matrix}\right\} \text{ as } x \to -\infty \tag{2}$$

The asymptotic behavior of the solution as $x \to \infty$ is given by $v_1 \to a(\zeta)\exp(-i\zeta x)$ and $v_2 \to b(\zeta)\exp(i\zeta x)$. The discrete eigenvalues ζ_n are solutions of the equation $a(\zeta) = 0$ in the upper complex plane. The eigenvalues determine the soliton energy according to ($\eta_k = Im\zeta_k$)

$$E_s = 2i\sum_{k=1}^{N}\zeta_k^* - \zeta_k = 4\sum_{k=1}^{N}\eta_k \tag{3}$$

whereas the total energy of the initial pulse, E_t, is

$$E_t = \int_{-\infty}^{\infty}|q(x)|^2 dx. \tag{4}$$

The conventional picture is that the number of solitons in a real pulse is given by

$$N = \left\lfloor \frac{1}{2} + \frac{1}{\pi} \int_{-\infty}^{\infty} q(x)dx \right\rfloor \tag{5}$$

where $\lfloor x \rfloor$ denotes the integer part of the argument x. Moreover, for most real symmetric initial pulses considered so far, the eigenvalues are found to be purely imaginary. However, in the numerical studies of the influence of pulse shape and frequency chirp on optical solitons carried out in Ref. [3], there were indications that this picture is not complete. In the present work we will consider this problem in more detail and show that indeed the situation is more complicated than the generally accepted picture.

Consider the case of a real double-humped initial pulse, which has constant amplitude A in the intervals $x_1 < |x| < x_2$. The corresponding Zakharov-Shabat scattering problem for this pulse can be solved by finding the appropriate solutions in the different regions where the potential is piece wise constant and then using the appropriate continuity conditions at the boundaries. This results in the following transcendental equation determining the eigenvalues ($\Delta \equiv x_2 - x_1$)

$$\cos^2[\Delta\sqrt{A^2 + \zeta^2}] - \frac{A^2 e^{i4\zeta x_1} + \zeta^2}{A^2 + \zeta^2} \sin^2[\Delta\sqrt{A^2 + \zeta^2}] - \frac{i\zeta}{\sqrt{A^2 + \zeta^2}} \sin[2\Delta\sqrt{A^2 + \zeta^2}] = 0 \tag{6}$$

We emphasize that for $x_1 = 0$, Eq. (6) reduces to the standard eigenvalue equation for a rectangular pulse. For easy comparison with results obtained in Ref. [3], we use the amplitude $A = 145.85$. If $x_2 = 0.01$ and $x_1 = 0$, the initial condition corresponds to a single humped pulse. The corresponding transcendental equation has one purely imaginary root in the upper complex plane, viz. $\zeta \approx i92.40$. The total energy of this particular single-humped rectangular pulse is $E_t = 425.44$ and the energy in the soliton part is $E_s = 4Im(\zeta) = 369.6$. The remaining part of the initial energy is contained in the continuous spectrum, which propagates in the form of dispersive waves. The number of solitons, according to Eq. (5) is $N = \lfloor 1/2 + 2\Delta A/\pi \rfloor \approx \lfloor 1.43 \rfloor = 1$. Thus, for this case, the result is in accordance with the classical picture. On the other hand, if we consider a double-humped pulse with $x_1 = 1.06$ and $x_2 = 1.07$, the condition (5) persists and indeed only one purely imaginary eigenvalue is obtained ($\zeta \approx i1.00$). Nevertheless, the eigenvalue equation (6) has a large number of eigenvalues with non-zero real part, compare figure 1.
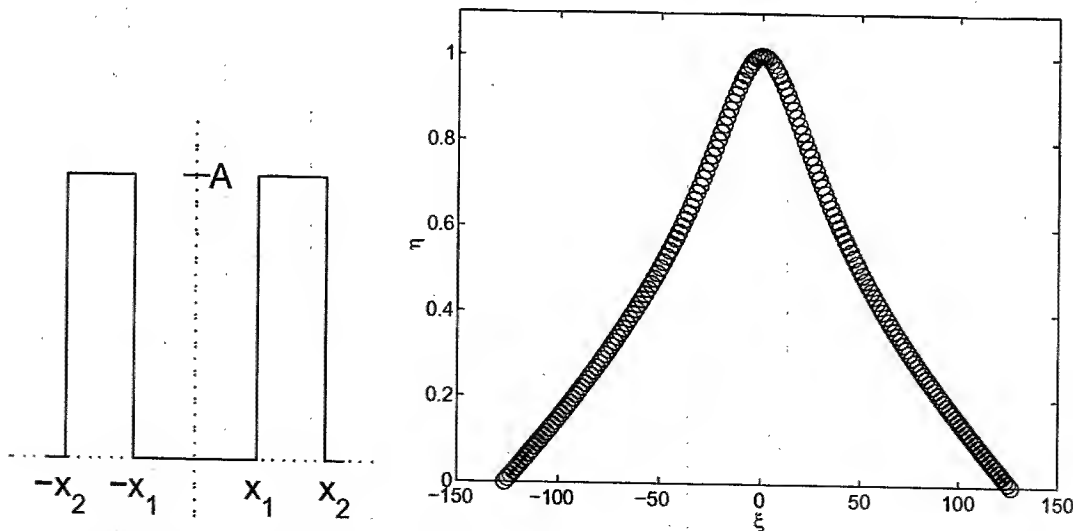
Fig. 1. Double-humped rectangular pulse and its corresponding eigenvalue distribution in the complex plane ($A = 145.85, x_1 = 1.06$ and $x_2 = 1.07$).

It is interesting to note that in the case of the double humped profile, neither of the humps has enough energy to create a soliton on its own and consequently should start to decay as dispersive radiation. However, during the collision between the decaying radiation from the two humps, nonlinear effects are strong enough to create a large number of small solitons, one of them stationary, but all the others with symmetric and increasing

velocities. The eigenvalues form an inverted V-structure in the complex ζ- plane, with the apex determined by the (single) imaginary eigenvalue, which also has the largest imaginary part. When the amplitude, A, of the box profile decreases, the number of eigenvalues decreases and for $A = A_{crit} \approx 78.54$, the last (purely imaginary) eigenvalue disappears. We emphasize that this agrees with the threshold condition for soliton generation as predicted by Eq. (5).

Since the eigenvalues in the double-humped case analyzed here have real and imaginary parts that are much smaller than the initial amplitude A, Eq. (6) can easily be solved approximately for the lowest order eigenvalues. When $|\zeta| \ll A$, the purely imaginary root, $\zeta = i\eta_0$ can be determined from

$$\cos^2(A\Delta) - \exp(-4x_1\eta_0)\sin^2(A\Delta) \approx 0 \qquad (7)$$

This directly implies that $\eta_0 \approx \ln(\tan(A\Delta))/(2x_1)$, which for the considered example yields $\eta \approx 1.03$, in good agreement with the numerical solution. For the neighbouring pairs of complex eigenvalues, we can assume that the imaginary parts are close to that of the first purely imaginary eigenvalue i. e. $\zeta \approx \xi + i\eta_0$. Using this fact and neglecting terms proportional to η/A, the eigenvalue equation reduces to simply

$$\exp(4ix_1\xi) \approx 1 \qquad (8)$$

i. e. $\xi \approx \pm n\pi/(2x_1)$. The first pairs of complex eigenvalues ($\zeta_n = \xi_n + i\eta_0$) are $\xi_1 \approx \pm 1.48$ (1.44), $\xi_2 \approx \pm 2.96$ (2.89) and $\xi_3 \approx \pm 4.45$ (4.33), again in good agreement with the numerical solution (given in parenthesis).

In conclusion, we have analyzed an example of a real and symmetric initial pulse which gives rise to soliton splitting. In other words, the corresponding Zakharov-Shabat scattering problem has solutions for which the eigenvalues have real as well as imaginary parts.

References

1. V. E. Zakharov and A. B. Shabat, "Exact theory of two-dimensional self-focusing and one-dimensional self-modulation of waves in nonlinear media", Sov. Phys. JETP **34**, 62 (1974)
2. J. Satsuma and N. Yajima, "Initial value problems of one-dimensional self-modulation of nonlinear waves in dispersive media", Prog. Theor. Phys. Suppl, **55**, 284 (1974)
3. M. Klaus and J. K. Shaw, "Influence of pulse shape and frequency chirp on stability of optical solitons", Optics Communication, **197**, 491-500 (2001).

Interaction of pulses in optical fibers

E. N. Tsoy and F. Kh. Abdullaev

Physical-Technical Institute of Uzbek Academy of Sciences, G. Mavlyanov street,
2-B, Tashkent, 700084, Uzbekistan
Tel: +998-712-354338, Fax: +998-712-354291, e-mail: etsoy@physic.uzsci.net

Abstract: Interaction of pulses in optical fibers is analyzed by solving the scattering problem associated with the nonlinear Schrödinger equation. It is shown that two pulses without initial phase modulation can generate *moving* daughter solitons.
© 2002 Optical Society of America
OCIS codes: (060.4370) Nonlinear optics, fibers; (190.5530) Pulse propagation and solitons

Interaction of solitons in optical fibers results in a variation of a separation distance and even in a formation of additional solitons with small amplitudes ("daughter pulses"). Both these factors constrict the repetition rate, which is an important characteristics of optical communication systems.

We consider the influence of different initial parameters to the soliton interaction. We show that nonlinear interference between pulses results in non-trivial dynamics. For example, depending on the separation distance, two pulses without initial phase modulation can generate a number of moving solitons. It is also shown that the relative constant phase is also important for the interaction dynamics.

The propagation of solitons in ideal optical fibers is described by the nonlinear Schrödinger (NLS) equation [1, 2]:

$$iu_z + u_{tt}/2 + |u|^2 u = 0, \tag{1}$$

where $u(t, z)$ is a slowly varying envelope of the electric field, z is the propagation distance, and t is the retarded time. As an initial condition the following profiles are considered: (i) two rectangular pulses $u(t, 0) = Q_1 B(t, -w_1 - L/2, -L/2) + Q_2 B(t, L/2, w_2 + L/2)$, and (ii) two sech-pulses $u(t, 0) = Q_1 \text{sech}[(t + L/2)/w_1] + Q_2 \text{sech}[(t - L/2)/w_2]$. Here Q_1 and Q_2 are constant complex amplitudes, L is a separation distance, w_1 and w_2 are the pulse widths, $B(t, t_1, t_2) \equiv [\theta(t - t_1) - \theta(t - t_2)]$, and $\theta(t)$ is the Heaviside step function.

It is known that NLS equation is integrated by the inverse scattering transform method [1]. The number N and parameters of solitons are found from the associated scattering problem [1]. The number N is equal to the number of poles $\lambda_n \equiv \nu_n + i\eta_n$, $\text{Im}(\lambda_n) > 0$, of the transmission coefficient $1/a(\lambda)$, while the amplitude and the speed of the n-th soliton are related to η_n and ν_n, respectively, and $n = 1, \dots, N$.

We solve analytically and numerically the Zakharov-Shabat scattering problem with the initial conditions mentioned. We study how the difference between the parameters of pulses ($w_1 \neq w_2$ or $Q_1 \neq Q_2$) affects to the interaction dynamics. The evolution of two pulses with the same width and intensity for the Manakov system, which is a vector generalization of the NLS equation, is considered in paper [3].

In the case of rectangular pulses the scattering problem is solved exactly, so that the parameters of emerging solitons are found from the following equation:

$$a(\lambda) = e^{i\lambda(w_1 + w_2)} \left[f(\lambda, k_1, w_1) f(\lambda, k_2, w_2) - Q_1^* Q_2 \sin(k_1 w_1) \sin(k_2 w_2) e^{2i\lambda L}/(k_1 k_2) \right] = 0, \tag{2}$$

where $f(\lambda, k, w) \equiv \cos(k w) - i\lambda \sin(k w)/k$, $k_j = (\lambda^2 + |Q_j|^2)^{1/2}$, and $j = 1, 2$.

Recall that zeros, which are pure imaginary, of $f(\lambda, k, w)$ determine the number N_{SR} and parameters of solitons emerging from a single rectangular pulse of width w and amplitude Q [4]. As known, $N_{SR} = \text{int}(|Q|w/\pi + 1/2)$, where $\text{int}(x)$ gives an integer part of x.

The last term in Eq. (2) is due to the nonlinear interference. The role of this term can be seen studying a simple case, when two rectangular pulses produce one soliton at $L = 0$ and two solitons at $L \to \infty$, e.g. $Q_1 = Q_2$, $w_1 = w_2$, and $\pi/2 < Q_1 w_1 < 3\pi/2$. The analysis of Eq. (2) shows that at intermediate L an appearance of λ_n with $\text{Re}(\lambda_n) \neq 0$, or an existence of moving solitons, is possible. The dependence $\lambda_n(L)$, $n = 1, \dots, 5$, corresponding to such a case, is presented in Fig. 1a. There exists one static soliton at $L \leq 0.6$, one static and two or four moving solitons at $0.6 < L \leq 4.1$, three-soliton state and two moving solitons at
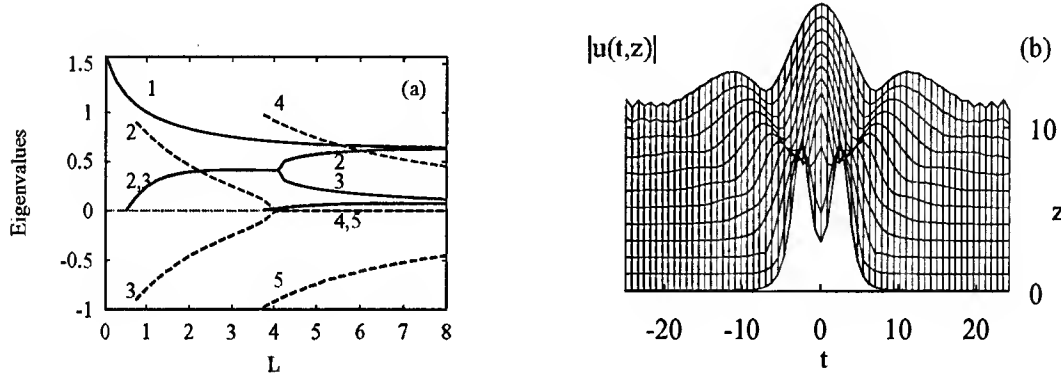
Fig. 1. (a) - The dependence of λ_n on the separation distance for two rectangular pulses, $Q_1 = Q_2 = 2, w_1 = w_2 = 1$. Solid (dashed) lines correspond to imaginary (real) part of λ_n. Numbers near lines corresponds to n; (b) - Evolution of the initial condition $0.7 [\operatorname{sech}(t + 2.5) + \operatorname{sech}(t - 2.5)]$.

$4.1 < L \leq 7$, and even more moving solitons at $L > 7$. The results of the scattering problem were checked by numerical simulation of NLS equation (1).

Similar dynamics is found for different forms of initial pulses. The possibility to generate moving solitons by a pure real initial profile in the form of two sech-pulses is shown in Fig. 1b. The parameters of the initial condition in Fig. 1b are chosen such that it generates at $z \to \infty$ one soliton, if $L = 0$, and two solitons, if $L \to \infty$. For $u(t, 0) = Q\operatorname{sech}t$ an exact result of the scattering problem was obtained in paper [5]. In the case of two sech-pulses we solve Eq. (2) numerically. We should mention that interaction of pulses with frequency and time separations in wavelength-division multiplexing systems was considered in paper [6].

Thresholds for bifurcations of the eigenvalue distribution are found from the analysis of Eq. (2). Since new λ_n penetrate to upper half-plane of λ, crossing the real axes, Eq. (2) with real λ is a set of equations for penetration points and threshold parameters. We analyse this set of equations in details for different pulse widths, amplitudes and a relative constant phase and find the corresponding thresholds.

Therefore, we have shown that the interaction of pulses without phase modulation may result in a formation of static and moving solitons, and multi-soliton complexes. For moderate amplitudes, the nonlinear interference is important, when pulses are close ($L/w \sim 1$ to 10) to each other.

References

1. V. E. Zakharov and A. B. Shabat, Sov. Phys. JETP, **34**, 62 (1972).
2. F. Kh. Abdullaev, S. A. Darmanyan, and P. K. Khabibullaev, *Optical Solitons* (Springer, Heidelberg, 1995).
3. F. Kh. Abdullaev and E. N. Tsoy, "The evolution of optical beams in self-focusing media", Physica D, **161**, 67-78 (2002).
4. S. V. Manakov, "Nonlinear Fraunhofer diffraction", Sov. Phys. JETP, **38**, 693, (1974).
5. J. Satsuma and N. Yajima, "Initial value problems of one-dimensional self-modulation of nonlinear waves in dispersive media", Suppl. of the Progr. of Theor. Phys., **55**, 285-306, (1974).
6. C. Etrich, N.- C. Panoiu, D. Mihalache, and F. Lederer, "Limits for interchannel frequency separation in a soliton wavelength-division multiplexing system", Phys. Rev. E, **63**, 6609, (2001).

Suppression of soliton self-frequency shift by up-shifted filtering

P. Tchofo Dinda[1], A. Labruyère[1], and K. Nakkeeran[2],

[1]*Laboratoire de Physique de l'Université de Bourgogne, Avenue Alain Savary, B.P. 47 870, 21078 Dijon, France*
Fax : (33) 3 80 39 59 71, phone : (33) 3 80 39 60 77, e-mail: Patrice.Tchofo-Dinda@u-bourgogne.fr
[2]*Photonics Research Center and Department of Elcctronic and Information Engineering, The Hong Kong*
Polytechnic University, Hung Hom, Kowloon, Hong Kong

Abstract

We propose an efficient method for suppressing the soliton self-frequency shift in high-speed transmission lines by means of up-shifted filters.

Suppression of soliton self-frequency shift by up-shifted filtering

P. Tchofo Dinda[1], A. Labruyère[1], and K. Nakkeeran[2],

[1]*Laboratoire de Physique de l'Université de Bourgogne, Avenue Alain Savary, B.P. 47 870, 21078 Dijon, France
Fax : (33) 3 80 39 59 71, phone : (33) 3 80 39 60 77, e-mail: Patrice.Tchofo-Dinda@u-bourgogne.fr*

[2]*Photonics Research Center and Department of Electronic and Information Engineering, The Hong Kong
Polytechnic University, Hung Hom, Kowloon, Hong Kong*

In 1986, Mitschke and Mollenauer [1] discovered an important phenomenon in the context of optical communications, called soliton self-frequency shift (SSFS), in which the stimulated Raman scattering (SRS) causes a continuous downshift of the mean frequency of short pulses propagating in optical fibers. The combined effects of SSFS and noise may lead to a loss of synchronism in a soliton bit pattern, and cause a strong transmission penalty in high-speed optical communication systems. In this research, we show that the impact of SRS can be effectively suppressed by use of filters whose peak frequency is appropriately up-shifted with respect to the transmission frequency. Very recently, we have demonstrated the effectiveness of up-shifted Gaussian filters for suppressing the SSFS [2]. Here we explain the working principle of both the Gaussian and super-Gaussian up-shifted filters. The pulse evolution in optical fiber links may be described by the nonlinear Schrödinger equation (NLSE) with the Raman effect and filters as

$$\psi_z = -[i\beta_2(z)/2]\psi_{tt} + i\gamma|\psi|^2\psi - (\alpha/2)\psi + F[\psi] + i\gamma\rho f_1\psi(|\psi|^2)_t, \tag{1}$$

where ψ is the pulse field at position z in the fiber and at time t; α, $\beta_2(z)$ and γ represent the loss, group-velocity dispersion (GVD) and self-phase modulation (SPM) parameters, respectively. The last term in Eq.(1) represents the SRS, with $\rho = 0.18$ and $f_1 = 7.06 \times 10^{-3}$, as typical values. We consider a lumped filtering characterized by a super-Gaussian transfer function $T(\omega) = \exp[-(2^m \ln 2)(\omega - \omega_f)^{2m}/B_f^{2m}]$, where B_f is the filter's bandwidth (BW). The parameter m is the filter's order ($m = 1$ corresponds to a Gaussian filter). The central frequency of the filter, ω_f, is up-shifted by $\Delta\omega = \omega_f - \omega_0$ with respect to the transmission frequency ω_0. One can obtain a more precise qualitative picture of the filter action by adopting the usual practice of approximating the lumped filtering by an equivalent continuous distributed filtering action along the line, defined by:

$$F[\psi] = \xi_m \sum_{k=0}^{2m} \left[C_{2m}^k \Delta\omega^{2m-k} (-i)^k \partial^k\psi/\partial t^k \right], \tag{2}$$

where $C_n^p = n!/(p!(n-p)!)$ and $\xi_m = 2^m \ln 2/(z_f B_f^{2m})$ represents the filter strength parameter. z_f is the filtering period, which we have chosen to be the same as the amplification period (z_A). The term corresponding to $k = 2m$ in Eq.(2), which does not depend on $\Delta\omega$, represents the non-shifted filtering action. To obtain a qualitative idea of the evolution of the pulse parameters we assume a Gaussian ansatz: $\psi = x_1 \exp[-\zeta^2/x_3^2 + ix_4\zeta^2/2 + ix_5\zeta + ix_6]$, where $\zeta = t - x_2$, and $x_1, x_2, \sqrt{2\ln 2}\,x_3$, $x_4/(2\pi), x_5/(2\pi)$ and x_6 represent the pulse amplitude, temporal position, width, chirp, frequency and phase respectively. For instance, in the presence of filters of order $m = 3$, we get the equation for the SSFS rate:

$$dx_5/dz = \mathcal{R} + \mathcal{F}_0 + \mathcal{F}(\Delta\omega), \tag{3}$$

where $\mathcal{R} = \sqrt{2}\gamma_r x_1^2 x_3^{-2}$, represents the SSFS rate. The term $\mathcal{F}_0$, which does not depend on $\Delta\omega$, represents the non-shifted filtering action. Here, $\mathcal{F}_0 = -\xi_3[\frac{45}{16}C_6^6 P^3 x_5 + \frac{15}{2}C_6^5 P^2 x_5^3 + 3C_6^4 P x_5^5]$, where $P = (x_3^4 x_4^2 + 4)/x_3^2$. The last term in the r.h.s. of Eq.(3), which arises only when up-shifted filters (USFs) are used, is given by $\mathcal{F} = \xi_3\{ P^3 \left[\frac{15}{32}C_6^5 \Delta\omega \right] + P^2 \left[\frac{3}{8}C_6^3\Delta\omega^3 - \frac{3}{2}C_6^4 x_5\Delta\omega^2 + \frac{15}{4}C_6^5 x_5^2\Delta\omega \right] + P[\frac{1}{2}C_6^1\Delta\omega^5 - C_6^2 x_5\Delta\omega^4 + \frac{3}{2}C_6^3 x_5^2\Delta\omega^3 - 2C_6^4 x_5^3\Delta\omega^2 + \frac{5}{2}C_6^5 x_5^4\Delta\omega]\}$.

Thus if non-shifted filters (NSFs) are used, the term $\mathcal{F}_0$, which acts in the opposite direction to the SSFS rate $\mathcal{R}$, will cause the pulse spectrum to be trapped near the carrier frequency ω_0. However NSFs will not completely cancel the average SSFS without a strong filter strength (i.e., a large ξ_m, or a small filter's BW) that can destroy the desired dynamics. When USFs are used, the additional term $\mathcal{F}$ acts in the direction opposite to the Raman-induced SSFS. The presence of $\mathcal{F}$ makes it possible to completely cancel the SSFS by simply tuning the central frequency of the filter, even with a moderate filter strength. Here lies the basic principle of SSFS suppression by up shifted filtering. The value of $\Delta\omega$ for suppressing the SSFS can be obtained by integrating Eq.(3) with the approximation $P(z) \simeq P(0)$. We obtain the following equation for any filter's order m [3]:

$$z_f \xi_m \sum_{k=1}^{m} \left\{ [(2k-1)!/(2^{3k-2}(k-1)!)]P(0)^k C_{2m}^{2k-1} \Delta\omega^{2m-2k+1} \right\} + \Delta x_{5R} = 0, \qquad (4)$$

where $\Delta x_{5R} = \int_0^{z_f} \mathcal{R}dz$ is the SSFS between two consecutive filters. For $m = 1$ (Gaussian filter), $\Delta\omega = -N_f^2 \Delta x_{5R}$, where $N_f \equiv B_f/B_p$ represents the ratio between the filter's BW and the spectral BW of the input pulse, defined by $B_p = \sqrt{2P(0)\ln 2}$. In short, we achieve SSFS suppression in fiber links as follows: First, we evaluate Δx_{5R} by simply letting the pulse propagate without filtering over the distance z_f, and we deduce Δx_{5R}. Then we choose the desired value for N_f (or equivalently B_f), and solve Eq.(4) to finally calculate the value of $\Delta\omega$ for suppressing the SSFS.

Figs.1, which represent the pulse parameters after each amplifier, illustrate the action of NSFs and USFs in a dispersion-managed (DM) fiber line with 36 maps in one amplification period of $z_A = z_f = 25\,km$, and GVD: $d_\pm = \pm 3.5\,ps/nm/km$. SPM: $\gamma_\pm = 0.002\,m^{-1}\,W^{-1}$. Losses: $\alpha_\pm = 0.22\,dB/km$. Here, the subscript $+(-)$ refers to normal (anomalous) fiber sections. The input pulse (fixed point) corresponds to unchirped Gaussian pulses of duration $1.39\,ps$ (FWHM) and energy $0.0526\,pJ$. As Fig.1 (a1) shows, NSFs cause the soliton ultimately to be trapped near a frequency $\omega_1(N_f) < \omega_0$. This permanent frequency shift $\omega_1 - \omega_0$, which appears clearly in Fig.1 (a1) for $N_f = 2$ (squares) and $N_f = 3$ (circles), can be reduced by a further decrease in the value of N_f, but it cannot be canceled completely without destabilizing the pulse propagation. Indeed, Fig.1 (c) shows that for narrow filters (i.e., small N_f) the slow dynamics move toward increasingly broadened and chirped pulses that do not necessarily correspond to the desired dynamics. Figures 2, which illustrate the action of super-Gaussian filters (with $m = 3$) in the same system as in Figs.1, exhibit the same general features as for the Gaussian filters (Figs.1) except that super-Gaussian filters lead to substantially reduced slow dynamics, even for relatively small filter BWs. Note that Figs.1 (c) and 2 (c) are the phase diagrams of USFs, which we found to be same as for NSFs.

We can also clearly illustrate the effectiveness of USFs with the simulation of a bit pattern $\langle 011110101100100 \rangle$ propagation at 160 Gb/s, in the above mentioned line with an amplifier noise figure of $4.5\,dB$, input unchirped Gaussian pulses of duration $1.39\,ps$ (FWHM) and energy $0.0526\,pJ$. After solving the NLSE, we have evaluated the transmission performance by means of the Q factor. Figures 3 (a) and 3(b), which we obtained with Gaussian and super-Gaussian ($m = 3$) filters, respectively, demonstrate the effectiveness of USFs in high-speed long-distance transmissions, with excellent performance of stability of the pulse bit pattern over several thousands of kilometers. A comparison between Figs.3 (a) and 3 (b) clearly indicates a better quality of transmission with super-Gaussian filters. This is due to the fact that the filters with flat top (such as super-Gaussian filters) will have the tendency to extract energy mainly from the wings of the pulse spectrum, which may be favorable for the pulse stability, when compared to filters with non flat top (such as Gaussian filters) which extract energy mainly from the central part of the pulse spectrum [3].

To conclude, we have demonstrated that the disastrous impact of SRS can be effectively suppressed in high-speed long-distance transmission lines by utilizing appropriate USFs.
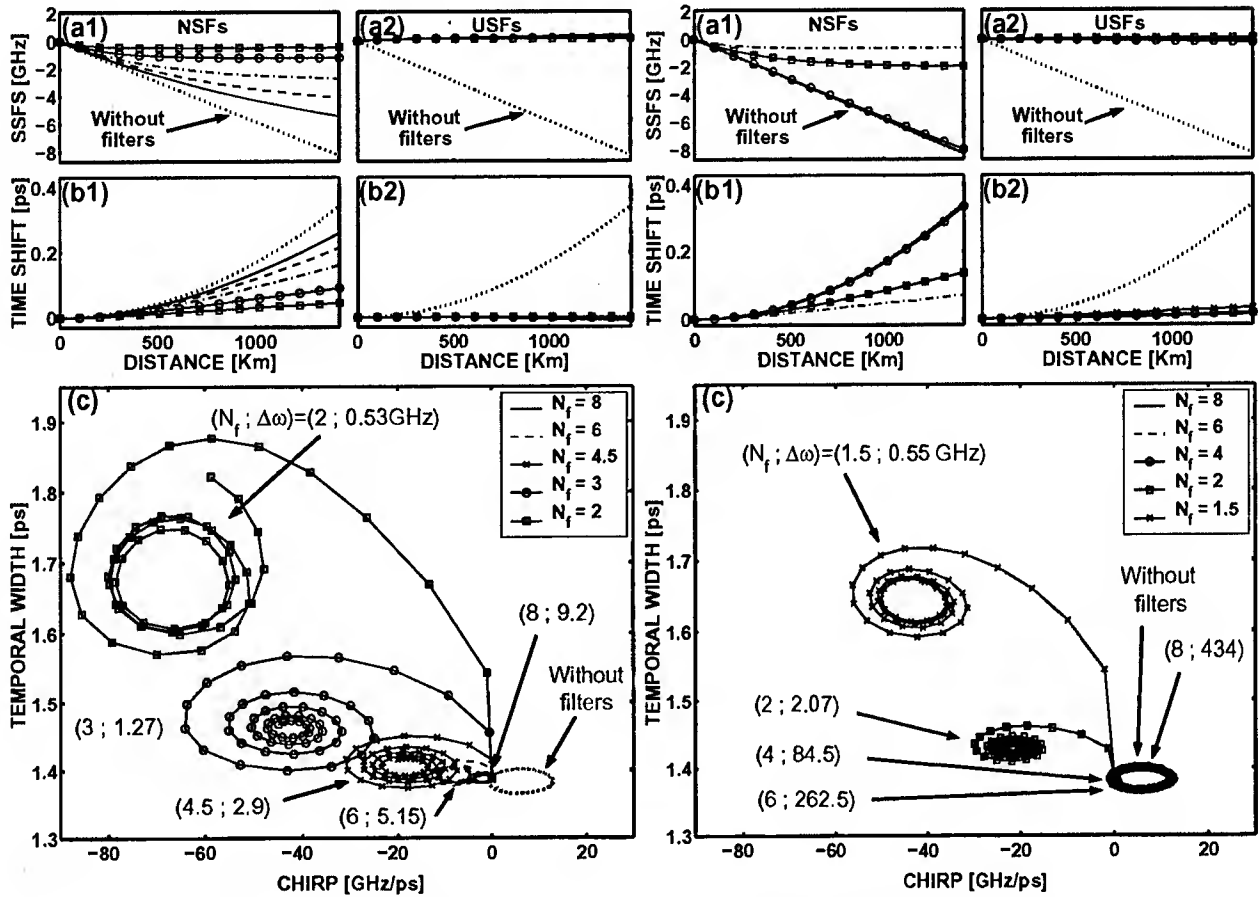
FIGURE 1 – Gaussian filters.

FIGURE 2 – Super-Gaussian filters.
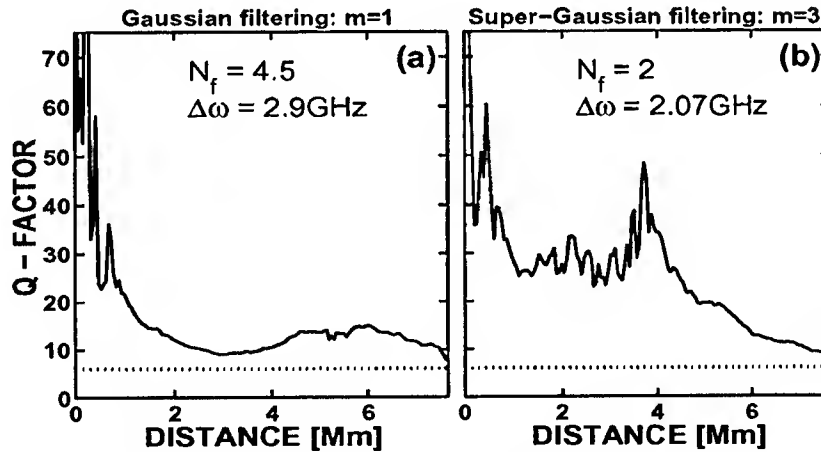
FIGURE 3 – Q factor vs distance for the line with (a) Gaussian filters, and (b) super-Gaussian filters.

References

[1] F. M. Mitschke and L. F. Mollenauer, *Opt. Lett.*, **11**, 659 (1986).

[2] P. Tchofo Dinda, K. Nakkeeran and A. Labruyère, *Opt. Lett.*, **27**, 382 (2002).

[3] P. Tchofo Dinda, A. Labruyère and K. Nakkeeran, *Phys. Rev. E*, (submitted) (2002).

Analytical design of dispersion-managed fiber systems with $S \approx 1.65$

K. Nakkeeran[1], A. B. Moubissi[2] and P. Tchofo Dinda[2]

[1] *Photonics Research Center and Department of Electronic and Information Engineering, The Hong Kong Polytechnic University, Hung Hom, Kowloon, Hong Kong*
Fax : (852) 2362 8439, phone : (852) 2766 4094, e-mail: ennaks@polyu.edu.hk

[2] *Laboratoire de Physique de l'Université de Bourgogne, Avenue Alain Savary, B.P. 47 870, 21078 Dijon, France*

Abstract

We present an easy analytical method for designing dispersion-managed fiber systems with map strength of 1.65, where the transmission lines have minimal pulse-pulse interactions.

Analytical design of dispersion-managed fiber system with $S \approx 1.65$

K. Nakkeeran[1], A. B. Moubissi[2] and P. Tchofo Dinda[2]

[1] *Photonics Research Center and Department of Electronic and Information Engineering, The Hong Kong Polytechnic University, Hung Hom, Kowloon, Hong Kong*
Fax : (852) 2362 8439, phone : (852) 2766 4094, e-mail: ennaks@polyu.edu.hk

[2] *Laboratoire de Physique de l'Université de Bourgogne, Avenue Alain Savary, B.P. 47 870, 21078 Dijon, France*

Dispersion-managed (DM) fiber system is one of the promising techniques that can be utilized for high-speed communications. The first step in the design of any DM line is to derive the fixed point. Nijhof et al [1] averaging method is the commonly used technique for finding the fixed point. Recently, we have reported an analytical method for designing the dispersion map for any desired input pulse width and energy [2], which is based on the analytical solution of the variational equations derived using a Gaussian ansatz. In DM systems, average dispersion and map strength are the parameters that define the stability of DM soliton. Map strength is defined by a S parameter:

$$S = (L_+\beta_+ - L_-\beta_-)/\tau_0^2, \tag{1}$$

where τ_0 is the FWHM pulse width at free-chirp point, β_+ (β_-) and L_+ (L_-) respectively represent the normal (anomalous) fiber dispersion parameter and length. Nakazawa et al [3], proved that the DM soliton propagating in average normal dispersion regime is unsuitable for high-speed long-distance communication. Malomed and Berntson [4] showed that DM solitons have stable propagation when $S \leq 4.79$ for anomalous average dispersion, $S \approx 4.79$ for zero average dispersion and $4.79 \leq S \leq 9.75$ for normal average dispersion and no stable DM solitons for $S \geq 9.75$. Yu et al [5], have numerically found that DM solitons propagating in DM fiber lines with map strength $S \approx 1.65$ will have weaker pulse-pulse interactions. Hence, we like to investigate the effectiveness of our analytical method [2] for designing DM lines in practically useful S parameter range $(0 \approx S < 4)$. In this work, we present an easy way to analytically design the DM fiber system with map strength $S \approx 1.65$ where the transmission lines have minimal interactions [5].

To investigate the effectiveness of our analytical method, we use the following parameters: dispersions $\mp 12.5\,ps/nm/km$ ($\beta_\pm$), initial pulse width (FWHM) varying from $12\,ps$ to $30\,ps$ to achieve different S values, energy $0.05 \times \sqrt{\pi/2}\,pJ$ and nonlinear coefficient $0.002\,W^{-1}m^{-1}$. The other required input parameter is the maximum pulse width, for which we respectively considered different values for different input pulse widths in such a way that the final design will always have the same total map length $L_T = L_- + L_+ = 41.2\,km$. Keeping the same total length for all maps is not a constraint, but it is very much useful for deriving an important feature of the DM solitons propagating in map with $S \approx 1.65$, as we show below. Using these parameters we have analytically calculated the fiber lengths for various maps with different S values [2]. Then using the initially assumed respective Gaussian pulses in the averaging method [1], we derived the numerical fixed points. Figures 1 (a) and (b) respectively show the plot of the energy and initial width of various fixed points. In Figs.1 (a) and (b), dashed curves represent the initial Gaussian energy and width used for the analytical design and the solid curves represent the energy and width of the numerical fixed points. From Figs.1 (a) and (b), it is clear that the parameters of the numerical fixed points are very close to the initially assumed Gaussian pulse around the S value 1.65. This reflects the fact that the DM soliton profile is very close to the Gaussian profile when $S \approx 1.65$. Figure 1 (c) shows the plot between the maximum width and S value. In Fig.1 (c) the solid and dashed curves represent the numerical and analytical results, respectively. Hence, the results presented in Figs.1, clearly prove that our analytical design procedure is very effective in designing the DM fiber line, and that the DM soliton propagating in dispersion map with $S \approx 1.65$ is very close to a Gaussian profile. From Fig.1 (c), we find that the maximum pulse width (x_{3m}) is minimum for $S \approx 1.65$.
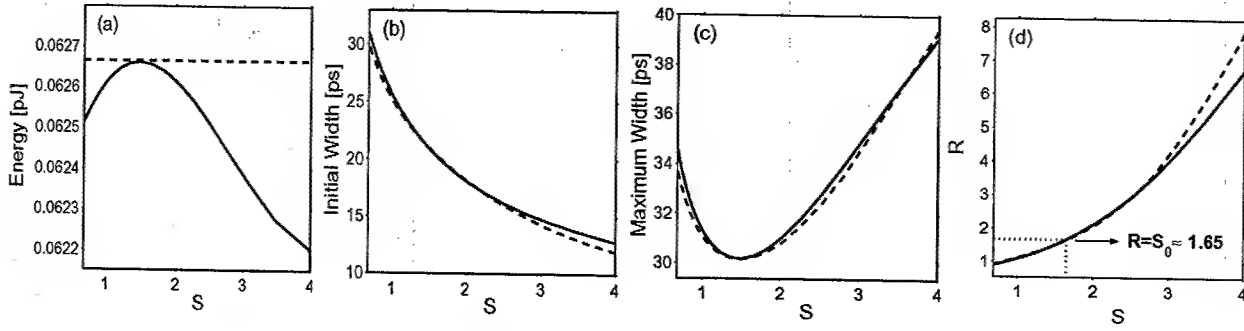
Fig.1: Pulse parameters Vs S parameter.

To get more insight into the minimum of x_{3m}, we introduce a breathing parameter:

$$R = x_{3m}^2/\tau_0^2. \tag{2}$$

Figure 1 (d) shows the variation of the breathing parameter R for different DM lines. In Fig.1 (d) the solid and the dashed curves respectively represent the numerical and analytical results. Substituting τ_0 expressed from Eq.(1) in Eq.(2), and then from the resulting equation, x_{3m} can be written as

$$x_{3m} = \sqrt{R(L_+\beta_+ - L_-\beta_-)/S}. \tag{3}$$

For a given DM line $L_+\beta_+ - L_-\beta_-$ is a constant [this is also true for the x_{3m} curve in Fig.1 (c) as $\beta_- = -\beta_+$ and L_T is same for all maps]. Under this condition from Eq.(3), we can see that $x_{3m} \propto \sqrt{R/S}$. Minimizing x_{3m} with respect to S (i.e., $dx_{3m}/dS = 0$) we derive

$$R = S_0, \tag{4}$$

where S_0 is the value of the S parameter for which x_{3m} is minimum [≈ 1.65, as Fig.1 (c) shows]. This is also clearly pointed out in Fig.1 (d) as the intersection of dotted horizontal and vertical lines. From Eqs.(1), (3) and (4), we get $x_{3mm} = \sqrt{L_+\beta_+ - L_-\beta_-}$, where x_{3mm} is the maximum width when $R = S_0 \approx 1.65$. For a Gaussian pulse, the FWHM τ_0 is related to x_{3-} (width at $1/e$ - intensity point) as $\tau_0 = \sqrt{2\ln 2}\, x_{3-}$. Note that x_{3-} is one of the input data required for our analytical design [2]. At $S = S_0 \approx 1.65$, substituting Eq.(4) into Eq.(3), we get

$$x_{3mm} = \sqrt{1.65}\,\tau_0 = \sqrt{1.65 \times 2\ln 2}\, x_{3-}. \tag{5}$$

Hence for analytically designing DM line with $S \approx 1.65$, we need only the minimum width (x_{3-}) and energy (E_0). The maximum width (x_{3m}) has to be calculated from Eq.(5). Also if we need to design a dispersion map with map strength $S < 1.65$ ($S > 1.65$), then we have to consider $x_{3m} < \sqrt{1.65 \times 2\ln 2}\, x_{3-}$ ($x_{3m} > \sqrt{1.65 \times 2\ln 2}\, x_{3-}$).

To illustrate the usefulness of our analytical design of dispersion map with strength $S \approx 1.65$, we have used the same fiber and pulse parameter values as in Fig.1, except the maximum pulse width, which we calculated from Eq.(5) and analytically calculated the fiber lengths. We have derived the numerical fixed points with the help of the averaging method [1] and we essentially find that the fixed points energies, minimum and maximum pulse widths are exactly same as the one used for the analytical design. Figure 2 shows the plot between the S parameter and average dispersion for various maps, which proves that our analytical method for designing DM line with map strength $S \approx 1.65$ is very effective.
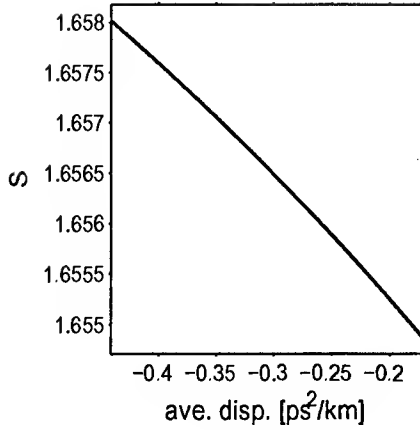
Fig.2: S parameter Vs Ave. Disp.
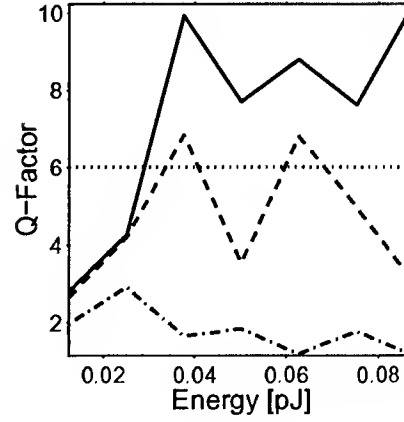
Fig.3: Q-factor Vs Energy

We can also show the effectiveness of our analytical design of dispersion map with $S \approx 1.65$, $S < 1.65$ and $S > 1.65$, using the simulation of a bit pattern ⟨011110101100100⟩ propagation in a single-channel transmission line operating at 40 Gb/s, with a periodic dispersion management using two types of fiber, with dispersions: $\pm 1\, ps/nm/km$ (for $S \approx 1.65$), $\pm 0.595\, ps/nm/km$ (for $S < 1.65$) and $\pm 2.5\, ps/nm/km$ (for $S > 1.65$), nonlinear coefficient: $0.002\, m^{-1}W^{-1}$, fiber loss: $0.22\, dB/km$, coupling loss: $0.1\, dB$. With these input data we have analytically designed different DM lines for input pulse width: $x_{3-} = 5.3\, ps$, energy ranging from $0.0125\, pJ$ to $0.0877\, pJ$, and amplification length of $50\, km$ (the individual values of the fiber lengths are not reported here and will be published elsewhere). In the simulations we have also included amplifier noise figure of $4.5\, dB$ and a Gaussian filter of bandwidth $80\, GHz$ to reduce the timing jitter. After solving the nonlinear schrödinger equation, we have evaluated the transmission performance by means of the Q-factor. Figure 3 shows the Q-factor after a propagation distance of $\sim 7000\, km$. In Fig.3 solid, dashed and dot-dashed curves represent respectively the performance of DM lines with map strengths $S \approx 1.65$, 0.976 and 4.15, which correspond to the breathing parameters: $R = 1.65$, 0.64 and 4. The horizontal dotted line represents Q=6, which corresponds to a bit-error rate of 10^{-9}. The results represented in Fig.3, clearly show that transmission performance in DM line with map strength $S \approx 1.65$ is superior than other map strengths for various input energies.

To conclude, we have presented a very easy and efficient way for analytically designing DM fiber lines with map strength around $S \approx 1.65$. Hence we believe that our analytical method will be very useful for designing DM fiber lines with $S \approx 1.65$ without the help of any numerical procedure.

References

[1] J.H.B. Nijhof, N.J. Doran, W. Forysiak and F.M. Knox, *Electron. Lett.*, **33**, 1726 (1997).
[2] K. Nakkeeran, A.B. Moubissi, P. Tchofo Dinda and S. Wabnitz, *Opt. Lett.*, **26**, 1544 (2001).
[3] M. Nakazawa, A. Sahara and H. Kubota, *J. Opt. Soc. Am. B*, **18**, 409 (2001).
[4] B.A. Malomed, A. Berntson, *J. Opt. Soc. Am. B*, **18**, 1243 (2001).
[5] T. Yu, E.A. Golovchenko, A.N. Pilipetskii and C.R. Menyuk, *Opt. Lett.*, **22**, 793 (1997).

Suppression of nonlinear effects by phase alternation in strongly dispersion-managed optical transmission

P. Johannisson, D. Anderson, M. Marklund

Dept. of Electromagnetics, Chalmers University of Technology, SE–412 96 Göteborg, Sweden
Tel.: +46 31 772 17 29, Fax: +46 31 772 15 73, E-mail: pontus.johannisson@elmagn.chalmers.se

A. Berntson, M. Forzati, J. Mårtensson

Optical Networks Research Laboratory, Ericsson Telecom AB, SE–126 25 Stockholm, Sweden

Abstract: The nonlinear effects amplitude jitter and ghost pulse generation can be suppressed by alternating the phase of the bits. This is due to destructive interference between different contributions to the total nonlinear effect.
OCIS codes: (060.2330) Fiber optics communications; (190.4370) Nonlinear optics, fibers;

Introduction

The properties of the return-to-zero (RZ) modulation format in dispersion-managed (DM) communication systems have been thoroughly examined since this scheme is believed to be one of the cornerstones of future systems. The large pulse overlaps occurring in these systems give rise to nonlinear effects via the Kerr nonlinearity in the fibre, a process which perturbatively can be viewed as if every combination of two or three pulses give rise to timing jitter, amplitude jitter or ghost pulses [1, 2]. These effects will transfer energy either from the signal pulses to the empty bit slots or between the signal pulses. All bit slots are affected by many such processes driven by different combinations of signal pulses. We here show that the nonlinear effects can be reduced by applying a phase shift, $\Delta\phi$, to every second bit slot, Fig. 1. This affects the phase in the nonlinear processes, and the total nonlinear effect can be minimised by a suitable choice of $\Delta\phi$. It is also found that the dependence on $\Delta\phi$ is periodic with a period π and symmetric about any multiple of $\pi/2$. A discussion, based on a perturbation analysis, is given of the physical background to this. The analysis has also been supported by numerical simulations.
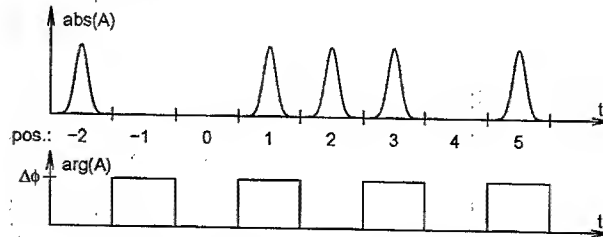
Fig. 1. Initial amplitude and phase modulation of a bit stream. The signal pulses are modelled as chirp-free Gaussian pulses.

Theory

The nonlinear effects in strongly DM systems have been examined by the means of a perturbation analysis [3, 4, 5]. The analysis is based on the nonlinear Schrödinger equation

$$i\frac{\partial A}{\partial z} = \frac{\beta_2}{2}\frac{\partial^2 A}{\partial t^2} - \gamma|A|^2 A - i\frac{\alpha}{2}A, \tag{1}$$

which includes the effects from the second order dispersion, the Kerr nonlinearity and the attenuation in the fibre. In a strongly DM system the nonlinear effects are weak and the envelope, A, can be split $A = A_l + A_p$, where A_l is the linear solution corresponding to $\gamma = 0$ and A_p is the nonlinear perturbation. Inserting this into Eq. (1) we obtain to the lowest order for the perturbation

$$i\frac{\partial A_p}{\partial z} - \frac{\beta_2}{2}\frac{\partial^2 A_p}{\partial t^2} + i\frac{\alpha}{2}A_p = -\gamma|A_l|^2 A_l. \tag{2}$$

For a pulse train $A_l = \sum_k A_k(z,t) = \sum_k A(z, t - kT_0)$, where $A(z,t)$ is a linearly propagating Gaussian pulse, T_0 is the bit slot and k runs over the bit slots containing signal pulses. Inserting this expression into $|A_l|^2 A_l$ and expanding we get source terms of the type $A_r A_s A_t^*$, where $A_r = A(z, t - rT_0)$ etc., and the linearity of Eq. (2) guarantees that A_p is the sum of the individual contributions from these source terms. There are four types of source terms. The first type, $|A_r|^2 A_r$, gives self-phase modulation of the signal pulse A_r. Terms of the type $|A_s|^2 A_r$, $r \neq s$, give cross-phase modulation of A_r and cause timing jitter [6]. In the present analysis we consider terms of the types $A_r^2 A_s^*$, $r \neq s$, and $A_r A_s A_t^*$, r, s and t all different. Depending on whether their contribution add to a signal pulse or not, they cause amplitude jitter and ghost pulses respectively, effects known to degrade DM systems.

The contribution from $A_r A_s A_t^*$ will end up in bit slot number $r + s - t$ [4]. Thus it can be predicted which source terms that contribute to the perturbation in a specified bit slot. We choose to study bit slot number zero which, for the time being, we suppose to be without phase shift. The condition that makes a contribution appear there is $r + s - t = 0$. Phase shifting of the signal pulses is equivalent to multiplying the different source terms by complex constants. By assuming that all odd bit slots are phase shifted $\Delta\phi$ the contributions acquire the phase shifts listed in Tab. 1 relative to their phases when $\Delta\phi = 0$. All contributions in the zeroth bit slot are shifted either 0 or $2\Delta\phi$, which explains why the dependence on $\Delta\phi$ is periodic with a period π. It also means that we can sum the contributions into two phasors. The first consists of the contributions that are not affected by a phase shift and the second is the sum of those that are rotated $2\Delta\phi$, see Fig. 2a and 2b. By optimising $\Delta\phi$ destructive interference can be obtained and the nonlinear effects can be minimised.

r	s	$t = r + s$	φ
even	even	even	0
even	odd	odd	0
odd	even	odd	0
odd	odd	even	$2\Delta\phi$

Table 1. The phase shift, φ, of the contribution to the perturbation from a specific source term depends on whether r, s and t are odd or even. It is assumed that all odd bit slots are phase shifted.

The amounts of amplitude jitter and ghost pulses are symmetric about any multiple of $\pi/2$, i.e., the phase shifts $n\pi/2 \pm \Delta\phi$, where n is an arbitrary integer, give the same results. To explain this the phase dependence of the contributions in a phase shifted bit slot is examined. By assuming that all even bit slots are phase shifted the results listed in Tab. 2 are found for bit slot zero. The contributions unaffected by a phase shift in Tab. 1 are now shifted $\Delta\phi$. However, the phase shift relative to the signal is still zero. The rotating phasor is shifted $-\Delta\phi$, or $-2\Delta\phi$ relative to the signal, Fig. 2c. Thus the rotating phasor rotates in the opposite direction as compared to a non-phase shifted bit slot. When $\Delta\phi$ is a multiple of $\pi/2$ the rotating phasors in phase shifted and non-phase shifted bit slots are identical. The two cases $\Delta\phi = 0$ and $\Delta\phi = \pi/2$ are seen in Fig. 2a and Fig. 2d. Starting from a multiple of $\pi/2$ and adding a phase shift means that the rotating phasors will rotate in different directions in the two bit slots. However, when comparing adding a phase shift to subtracting the same phase shift the only difference is that the situation in the phase shifted bit slot has changed places with that in the non-phase shifted bit slot, and this will not change the average amplitude jitter or ghost power. This gives rise to the symmetry.
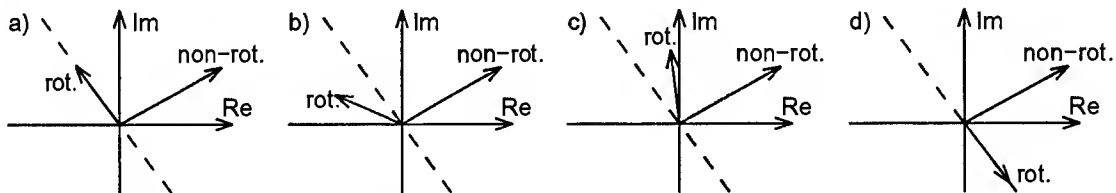
Fig. 2. a) The rotating and non-rotating phasors when $\Delta\phi = 0$. b) A phase shift $\Delta\phi$ gives a rotation $2\Delta\phi$. c) The situation in a phase shifted bit slot. The direction of rotation is changed. d) $\Delta\phi = \pi/2$. All bit slots are identical.

r	s	$t = r + s$	φ
even	even	even	$\Delta\phi$
even	odd	odd	$\Delta\phi$
odd	even	odd	$\Delta\phi$
odd	odd	even	$-\Delta\phi$

Table 2. The phase shift, φ, of the contributions in bit slot zero if all even bit slots are phase shifted.

The rotating and non-rotating phasors are not identical in all bit slots. They depend on which contributions that give rise to them, and this in turn depends on where the signal pulses are located around the bit slot. The above symmetry argument can be applied to all pairs of bit slots, one phase shifted and one non-phase shifted, interacting with identical surrounding bit patterns. The range of the interaction is approximately equal to the maximum pulse width and this determines how many bit slots we have to account for. It will always be possible to group the bit slots into pairs provided that the sequence is long enough. With large pulse breathing the interaction range is longer and a longer random bit stream is needed to find matching pairs and see the mentioned symmetries.

To verify the results stated here we have carried out a number of numerical simulations. We have found that the phase shifting can suppress the nonlinear effects and that a long pulse train is needed to see the symmetries [7]. We have also carried out system simulations checking the dependence on different system parameters, which also have confirmed the results stated here and shown that an increase of the Q-value is possible [8].

Conclusions

In conclusion the phase alternation technique has been shown to be able to reduce the nonlinear effects in transmission links. The reason for this is that different contributions to the nonlinear effects can be made to counteract each other. It has also been clarified why $Q(\Delta\phi)$ is symmetric around points where the phase modulation is a multiple of $\pi/2$.

References

1. P. V. Mamyshev and N. A. Mamysheva, "Pulse-overlapped dispersion-managed data transmission and intrachannel four-wave mixing", Opt. Lett. **24**, 1454 (1999).
2. R.-J. Essiambre, B. Mikkelsen, and G. Raybon, "Intra-channel cross-phase modulation and four-wave mixing in high-speed TDM system", Electron. Lett. **35**, 1576 (1999).
3. A. Mecozzi, C. B. Clausen, and M. Shtaif, "Analysis of Intrachannel Nonlinear Effects in Highly Dispered Optical Pulse Transmission", IEEE Photon. Technol. Lett. **12**, 392 (2000).
4. M. J. Ablowitz, and T. Hirooka, "Resonant nonlinear intrachannel interactions in strongly dispersion-managed transmission systems", Opt. Lett. **25**, 1750 (2000).
5. P. Johannisson, D. Anderson, A. Berntson, and J. Mårtensson, "Generation and dynamics of ghost pulses in strongly dispersion-managed fiber-optic communication systems", Opt. Lett. **26**, 1227 (2001).
6. J. Mårtensson, A. Berntson, M. Westlund, A. Danielsson, P. Johannisson, D. Anderson, M. Lisak, "Timing jitter owing to intrachannel pulse interactions in dispersion-managed transmission systems", Opt. Lett. **26**, 55 (2001).
7. P. Johannisson, D. Anderson, M. Marklund, A. Berntson, M. Forzati, and J. Mårtensson, "Suppression of nonlinear effects by phase alternation in strongly dispersion-managed optical transmission", Opt. Lett., to be published.
8. M. Forzati, J. Mårtensson, A. Berntson, A. Djupsjöbacka, and P. Johannisson, "Reduction of intra-channel four-wave mixing using the alternate-phase RZ modulation format", submitted to IEEE Photon. Technol. Lett.

Optical solitons in the femtosecond regime

J. Wyller

Department of Mathematical Sciences,

Agricultural University of Norway,

P.O.Box 5065, N-1432 Ås, NORWAY.

Tel +47 6494 8861   Fax: +47 6494 8810

E-mail: john.wyller@imf.nlh.no

J. S.Hesthaven

Division of Applied Mathematics

Brown University

Box F, Providence, RI 02912, USA

Tel: +1(401) 863 2671   Fax: +1(401) 8631 355

E-mail: jan.hesthaven@brown.edu

J.J. Rasmussen

Optics and Fluid Dynamics Department,

Risø National Laboratory,

P.O.Box 49, Dk-4000 Roskilde, DENMARK

Tel: +45 4677 4537   Fax: +45 4677 4565

E-mail: jens.juul.rasmussen@risoe.dk

Abstract

The evolution of optical solitons in the presence of amplification effects and nonlocal Raman response is investigated using perturbational analysis. The analysis reveals the existence of a soliton which acts as a global attractor in certain regimes of the amplification parameters.

When entering the femtosecond regime in the context of nonlinear wave packets one has to account for both instantaneous and time-delayed Raman nonlinearities, due to the short duration of the optical pulses. In such cases one ends up with nonlinear Schrödinger (NLS-) equations extended with nonlocal terms. This has been done by several authors (see the references in [1]).

In [1] topics like dynamical evolution of localized solution, the existence of travelling and stationary waves and modulational instability within the framework of nonlocal NLS model extended with amplification effects have been studied. The model equation can be written as

$$\partial_z q = gq + \left(b + \frac{1}{2}i\right)\partial_t^2 q + \beta \partial_t^3 q + (i + S\partial_t)\left[|q|^2 q + \varepsilon\left(H * |q|^2\right)q\right] \tag{1}$$

in this case. Here $H * |q|^2$ denotes the convolution integral

$$\left(H * |q|^2\right)(t) \equiv \int_{-\infty}^{\infty} H(t-x)|q|^2(x)\,dx$$

where the response kernel $H(t)$ assumes the form [3]

$$H(t) = \begin{cases} \frac{t_1^2 + t_2^2}{t_1 t_2^2}\exp\left[-\frac{t}{t_2}\right]\sin\left[\frac{t}{t_1}\right], & t > 0 \\ 0, & t \le 0 \end{cases}$$

The inverse timescale $1/t_1$ denotes the phonon frequency and $1/t_2$ the bandwidth of the Lorentzian line. Moreover, from [3] we have that these two timescales are related to the typical pulse duration time T_0 through $t_1 = \frac{12.2\ fs}{T_0}$ and $t_2 = \frac{32\ fs}{T_0}$. The parameter ε is defined as $\varepsilon \equiv \frac{1-f}{f}$, $0 < f \le 1$ and it measures the relative strength of the nonlocal delay effect versus the instantaneous response. The quantities involved are normalized and related to the physical quantities in the following way: The third order dispersion coefficient is given by $\beta \equiv \frac{k_0'''}{6T_0|k_0''|}$ and the nonlinear parameters N^2 and S as $N^2 \equiv \frac{\omega_0^2 P_0 T_0^2}{2k_0 c^2 |k_0''|}$ and $S \equiv -\frac{2}{\omega_0 T_0} < 0$,

respectively. Here k_0 is the carrier wavenumber evaluated at the carrier wavefrequency ω_0 through the linear dispersion relation, k_0'' and k_0''' the second and third derivative with respect to the carrier wavefrequency, respectively and c the velocity of light. q is equal to the envelope of the electric field normalized against the square root of the typical power density scale P_0, N and $\sqrt{f}$. The temporal coordinate t is equal to the retarded time divided by the typical timescale T_0 for the pulse duration, while the coordinate z appears as the longitudinal coordinate normalized against the dispersion length $T_0^2/\left|k_0''\right|$. The optical amplification effects are introduced by using a parabolic approximation to the gain - curve, represented by the two terms gq and $b\partial_t^2 q$, where $b = 0$ ($b > 0$) corresponds to infinite (finite) bandwidth of the amplifier.

The power P given as

$$P = \int_{-\infty}^{\infty} |q|^2 (t)\, dt \tag{2}$$

satisfies [1]

$$\frac{dP}{dz} = 2gP - 2b \int_{-\infty}^{\infty} |\partial_t q|^2\, dt - \frac{|S|}{\pi}\varepsilon \int_0^{\infty} \psi(k)\, |F(k)|^2\, dk \tag{3}$$

Here $F(k)$ and $\psi(k)$ are the Fourier transforms

$$F(k) = \int_{-\infty}^{\infty} |q|^2 (t) \exp[ikt]\, dt \quad,\quad \psi(k) = \frac{2t_1^2 t_2 \left(t_1^2 + t_2^2\right) k^2}{\left(t_1^2 + t_2^2 - t_1^2 t_2^2 k^2\right)^2 + 4t_1^4 t_2^2 k^2} \tag{4}$$

When omitting the nonlocal terms and the optical amplification effect in (1), the resulting equation possesses a 1 - parameter family of travelling wavepacket solutions termed Potasek-Tabor (PT-) solitons. They can be written on the form [2]

$$q_s(t, z) = \frac{A}{\cosh[B(t - v_s z)]} \exp[i(\kappa t - \omega z)] \tag{5}$$

when the parameter identifying the solitons is chosen to be the inverse soliton width B. Here the amplitude A, the velocity v_s, the frequency ω and the wave number κ is given as

$$A^2 \equiv -\frac{2\beta}{|S|}B^2 \quad,\quad v_s \equiv \kappa + 3\beta\kappa^2 - \beta B^2, \quad \omega \equiv \frac{1}{2}\kappa^2 + \beta\kappa^3 - \frac{1 + 6\beta\kappa}{2}B^2 \quad,\quad \kappa \equiv -\frac{|S| + 2\beta}{4|S|\beta} \tag{6}$$

The PT - solitons appear as an exact balance between the third order linear dispersion and the nonlinear terms, and it should be noticed that they cease to exist in the singular limit $\beta \to 0$. Notice that it is presupposed in the formulas (6) that $\beta < 0$

Next, we study the evolution of the PT - solitons in the presence of weak amplification effects and Raman response by means of a perturbational approach. The starting point of this analysis is the power equation (3). Following the ideas of soliton perturbation theory, we insert $q = q_s$ where q_s is the expression for the PT - soliton (5) - (6) into the power equation. Doing this, we have also tacitly assumed that the dominant part of the solution consists of the soliton component, and that the non-soliton part is of order the perturbation parameters.

We obtain

$$\frac{d\eta}{dz} = 4 \cdot \Delta g \cdot \eta + \varepsilon_b + \varepsilon_r \cdot \eta \cdot I[\eta; \theta] \tag{7}$$

for η and $I[\eta, \theta]$ given as

$$\eta \equiv \frac{\left(t_1^2 + t_2^2\right)\pi^2}{4t_1^2 t_2^2 B^2} = \frac{\left(t_1^2 + t_2^2\right)\pi^2 |\beta|}{2t_1^2 t_2^2 |S| A^2} \quad,\quad I[\eta; \theta] \equiv \int_0^{\infty} \frac{x^4}{\sinh^2(x)} \cdot \frac{1}{\left(x^2 - \eta\right)^2 + \eta\theta x^2}\, dx \tag{8}$$

respectively, with θ as the numerical factor

$$\theta \equiv \frac{4}{1 + \left(\frac{t_2}{t_1}\right)^2}$$

Moreover, we have introduced the perturbation parameters Δg, ε_b and ε_r as

$$\Delta g \equiv \kappa^2 b - g \quad , \quad \varepsilon_b \equiv \frac{\left(t_1^2 + t_2^2\right)\pi^2}{3t_1^2 t_2^2} b \quad , \quad \varepsilon_r \equiv 8\frac{\left(t_1^2 + t_2^2\right)}{t_1^2 t_2}\varepsilon\left|\beta\right|. \tag{9}$$

The parameters Δg and ε_b measure the optical amplification effects while the parameter ε_r accounts for the nonlocal Raman response. Notice also that ε_b, $\varepsilon_r \geq 0$ since $f \leq 1$ and b by assumption is positive, while the parameter Δg may change sign. Hereafter we will refer to Δg as *the shifted optical amplification parameter*.

The system (7) - (9) constitutes the basis for our further discussion. First, let us neglect the Raman - response, i.e. put $\varepsilon_r = 0$. Then one can find closed form expressions for the modulated soliton amplitude A and the inverse width B of the PT - soliton by means of (6) and (8). The following features are apparent: For $\Delta g \geq 0$, the soliton width (amplitude) increases (decreases) monotonically with time, while in the complementary regime $\Delta g < 0$ the initial pulse relaxates towards a soliton state with width $1/B_*$ and amplitude A_* as

$$A_* = \sqrt{\frac{6\left|\beta\right|}{\left|S\right|}\frac{\left|\Delta g\right|}{b}} \quad , \quad B_*^{-1} = \sqrt{\frac{b}{3\left|\Delta g\right|}} \tag{10}$$

Next, let us include the Raman response effect. Also in this case we can characterize the dynamical evolution of the PT - solitons completely in terms of the shifted optical amplification parameter Δg: For $\Delta g \geq 0$ the soliton width will grow without bound, i.e., the pulse becomes broader and consequently the amplitude will decrease. For the complementary parameter regime $\Delta g < 0$ one can prove that there is a soliton acting as a global attractor for all PT - solitons. The amplitude A_{st} and inverse width B_{st} of this attractor satisfy the bounds

$$A_* \geq A_{st} \geq A_+ \quad , \quad B_* \geq B_{st} \geq B_+$$

where A_* and B_* are given by (10) and A_+ and B_+ as

$$A_+ \equiv \sqrt{\frac{12\left|\beta\right|}{\left|S\right|}\frac{\left|\Delta g\right|}{b}\frac{1}{1+\sqrt{1+\epsilon}}} \quad , \quad B_+ \equiv \sqrt{\frac{6\left|\Delta g\right|}{b}\frac{1}{1+\sqrt{1+\epsilon}}}$$

with

$$\epsilon \equiv V\left(\theta\right)\frac{t_1^2 t_2 \varepsilon}{t_1^2 + t_2^2} \cdot \frac{\left|\beta\right|\left|\Delta g\right|}{b^2}$$

where

$$V\left(\theta\right) \equiv \begin{cases} \frac{192}{5} \cdot \frac{1}{\left(1-\frac{1}{4}\theta\right)\theta} & \text{for } 0 < \theta < 2 \\ \frac{192}{5} & \text{for } \theta \geq 2 \end{cases}$$

In addition, for broad pulses it can be inferred from the bound

$$0 < I\left[\eta;\theta\right] \leq \frac{\pi^4}{1152} \cdot \frac{V\left(\theta\right)}{\eta^2}$$

for (8) that the Raman response has negligible influence on the wave evolution as compared with the optical amplification effects. We have initiated a direct numerical solution of the model equation (1). Preliminary results of this study confirm the results from the perturbational analysis.

References

[1] J.Wyller. Physica D 157, 9, 2001.

[2] V. I. Karpman, J. J. Rasmussen and A. G. Shagalov. Phys. Rev. E (2001) 64 , 026614.1-026614.13..

[3] I.R.Gabitov, M.Romagnoli and S.Wabnitz. Appl. Phys. Lett., 59(15): 1811, 1991.

Stability of dissipative solitons in transmission lines beyond the average concept

C. Knöll, D. Michaelis, Z. Bakonyi, G. Onishchukov and F. Lederer

Friedrich Schiller Universität Jena, Institut für Festkörpertheorie und Optik
Max-Wien-Platz 1, D-07743 Jena Germany, tel:+(49)3641947174, fax: +(49)03641 947177 e-mail: knoell@pinet.uni-jena.de

Abstract: We investigate existence and stability of dissipative solitons in a transmission line with lumped amplification/absorption introducing a matrix algorithm. Parts of the domain in parameter space where the background is stable exhibit Hopf instabilities.

OCIS 190.5530;230.4320

The concept of balancing the fiber nonlinearity with dispersion in an optical transmission line directly leads to the soliton concept. Although solitons are very robust and stable structures, they are an idealized model belonging to an integrable, conservative system. In reality fiber losses and amplification, which can be highly nonlinear and noisy if semiconductor amplifiers are used, have to be taken into account. Hence the whole system is highly dissipative and has to be described with models well beyond the Nonlinear Schrödinger equation.

The system under consideration is driven by a semiconductor optical amplifier (SOA), which regenerates the signal energy. A saturable absorber (SA) has been incorporated for noise reduction, as reported in [1,2]. The fiber exhibits losses, nonlinearity and dispersion, the effect of the latter we minimized by operating at the zero dispersion wavelength. Given that the amplifier as well as the absorber imply a frequency shift and a spectral deformation of the signal, we use a bandwidth-limiting filter to stabilise the pulse. The experimental setup is configured as a recirculating fiber loop, thus one round trip corresponds to one passage of amplifier, absorber, fiber and filter.

In recent papers we have shown that in such a system stable structures, so-called dissipative solitons, can emerge [3] being appropriate for transmitting signals over long distances. They are stroboscopically stationary and, in contrast to the canonical conservative solitons, their properties are fixed by systems parameters. To identify the solutions and to probe their stability we used an algorithm based on a simple rate equation model [4], which takes into account the order of elements as well as the lumped nature (discreteness) of our system. Thus we did not make use of the very common ansatz of averaging the element effects over one amplifier spacing (round trip) but rather described each element in the loop individually. We restricted ourselves to a parameter space of the energy and the mean frequency of the dissipative soliton, neglecting changes in pulse shape and spectral width.

$$\begin{pmatrix} \varepsilon \\ \omega \end{pmatrix}_{z+1} = \underbrace{\hat{\mathbf{M}}^{B} \times \hat{\mathbf{M}}^{F} \times \hat{\mathbf{M}}^{-} \times \hat{\mathbf{M}}^{+}}_{\hat{\mathbf{P}}(\varepsilon, \omega)} \begin{pmatrix} \varepsilon \\ \omega \end{pmatrix}_{z}$$

Having a two-dimensional vector characterizing the soliton it is straightforward to use matrices as representatives of the various elements. The superscripts "B","F","-" and "+" mark the filter, the fiber, the absorber and the amplifier respectively. The multiplication of the matrices does not only allow for a proper representation of the lumped structure of the system but also for the specific order of the elements. In order to reduce the equations of the elements to the energy-frequency parameter space and to arrive at an analytic description we have to impose certain simplifications, which are justified by the experimental conditions, on our model. For the filter we assume Gaussian pulse - and filter shape. The system is supposed to be operated at the zero dispersion point and thus we can neglect any dispersive effects in the fiber compared to dispersion introduced by SOA/SA. Also, the fiber Kerr nonlinearity falls short behind the SOA/SA nonlinearities. Thus a single damping term may be used to characterize the fiber. The SOA/SA energy gain/loss is independent of the pulse shape, but we do have to make the assumption of a symmetric pulse shape to establish an energy dependent frequency

shift of both elements. The change of the pulse shape is neglected too. The matrices of the absorber and the amplifier have the same structure since they stem from the same set of equations [3] and are nonlinear in their energy and frequency dependence.
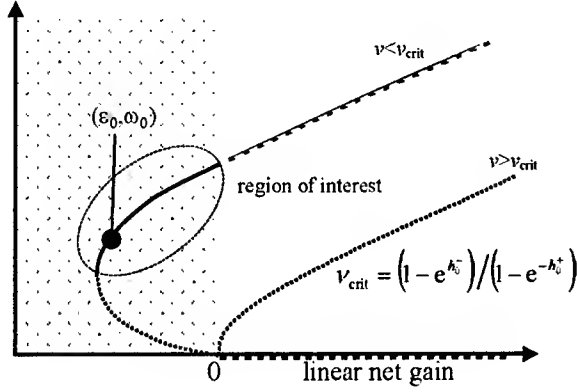
Fig. 1 Energy of solutions of the systems depending on the small signal net gain for two different ratios v of saturation energies
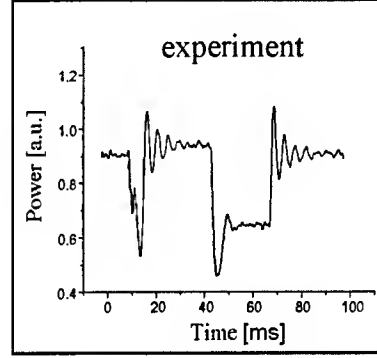
Fig. 2 : Average power of a soliton vs. propagation time. Abrupt changes of fiber loss during the propagation act as perturbations.

As a main control parameter we use the linear, unsaturated net gain covering also the case of net losses, a region where noise accumulation is suppressed. We found that the pulses bifurcate from the point of zero net gain. The ratio of saturation energies of absorber and amplifier has been found to govern the behaviour of the solution. For low saturation energies of the absorber there are solutions in the regime of net losses (subcritical bifurcation). On the contrary for high saturation energy of the absorber solutions to exist require positive net gain (supercritical bifurcation), where amplified noise destabilizes the solution. We have introduced an analytical criterion, which determines the bifurcation scenario for a given ratio $v = E_{SAT}^- / E_{SAT}^+$ of saturation energies of amplifier and absorber. The critical value depends on the small signal gain h_0 of amplifier (plus) and absorber (minus). As depicted in Fig.1 for positive net gain the background is unstable which leads to a degradation of the pulse during propagation.

The solutions in the region of net losses, shown in Fig.1 as solid line, is of special interest and therefore the subject of our stability analysis. As our experiments have shown (Fig.2) there are relaxation oscillations if the system is perturbed. This was a hint to Hopf oscillations and instabilities which have been verified by BPM-simulation.

Developing a linear stability analysis for lumped systems we have performed a systematic study of this destabilization scenario by using the Jacobian $\hat{\mathbf{J}}$ of the propagation matrix $\hat{\mathbf{P}}$, linearizing the matrices around a solution $(\varepsilon_0, \omega_0)$ and looking for the growth rate of a weak perturbation in energy and frequency $(\delta\varepsilon, \delta\omega)$. This leads to an eigenvalue equation :

$$\begin{pmatrix} \varepsilon_0 + \delta\varepsilon \\ \omega_0 + \delta\omega \end{pmatrix} = \hat{\mathbf{P}} \begin{pmatrix} \varepsilon_0 \\ \omega_0 \end{pmatrix} + \hat{\mathbf{J}} \begin{pmatrix} \delta\varepsilon \\ \delta\omega \end{pmatrix}$$

$$\hat{\mathbf{J}} \begin{pmatrix} \delta\varepsilon \\ \delta\omega \end{pmatrix} = \lambda \begin{pmatrix} \delta\varepsilon \\ \delta\omega \end{pmatrix}; \quad \hat{\mathbf{J}} = \frac{\partial \hat{\mathbf{P}}(\varepsilon, \omega) \begin{pmatrix} \varepsilon \\ \omega \end{pmatrix}}{\partial \begin{pmatrix} \varepsilon \\ \omega \end{pmatrix}} \Bigg|_{\begin{pmatrix} \varepsilon_0 \\ \omega_0 \end{pmatrix}}$$

In fact we have found that the respective eigenvalues in the domain of interest can attain complex values indicating oscillations. Their magnitude can even exceed unity evoking a growing instability

(Fig.3). This was found to take place near the turning point where net losses are highest. This is essential since here the noise suppression is strongest and the conditions are most suitable for pulse transmission.

In Fig.3 a situation is depicted where a section of the upper branch, starting from the turning point, is unstable (growth rate > 1, point c). The energy-frequency vector rotates a few times around the solution with increasing radius and finally converges to zero. Each point on the curve represents one round trip. For linear losses below the crossing point (point b) the oscillations of the perturbed system relax. Because the damping rate is small many round trips are required to achieve relaxation (compare with the experiment in Fig.2). If the growth rate is close to unity (point b) critical slowing down can be observed. The number of round trips is the same for every curve.
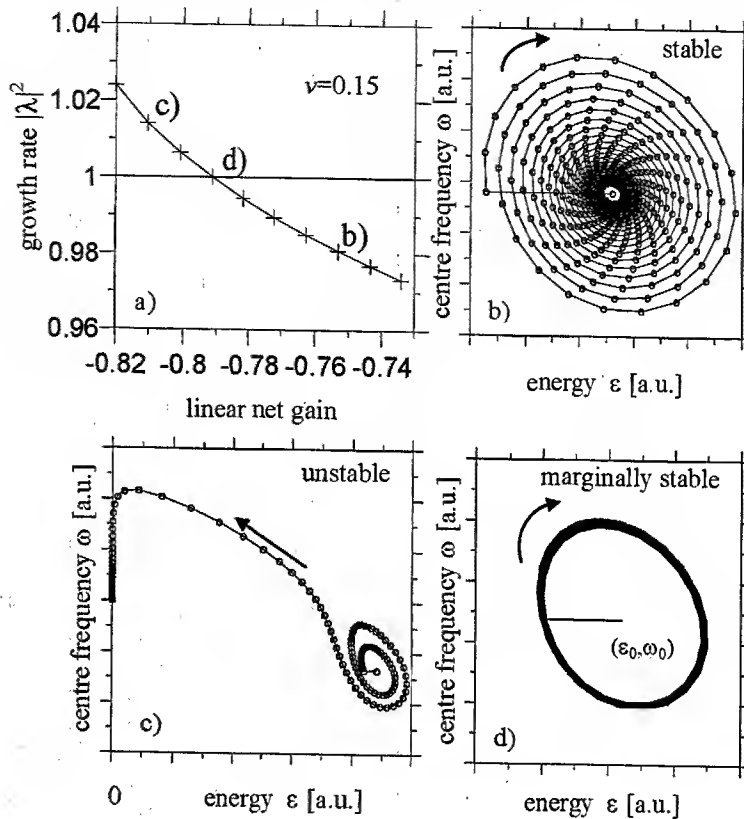
The mechanism behind these oscillations was found to be the interplay of energy depependent frequency shift caused by the amplifier / absorber and a frequency dependent damping in the filter.

The dependence of the region of Hopf instability on the ratio of saturation energies is shown in Fig.4. One can see that approaching the critical value for v the section of the branches become larger. This implies the necessity of low saturation energies for the absorber. The dependence on other parameters like filter bandwidth or pulse bandwidth has been investigated and led to the conclusion that strong filtering can prevent instabilites effectively.

In conclusion we found that in a recirculating fiber loop with lumped elements stable soliton solutions on a stable background may exist for net losses. In a domain of this very region Hopf instabilities have been found leading to signal degradation. The instabilities can be prevented by strong filtering and small saturation energies of the saturable absorber.

Fig.3 Growth rate $|\lambda|^2$ vs. linear net gain (a). b)-d) Evolution of soliton parameters after perturbation. Each point marks a round trip in the line, the arrows give the direction of time.

Fig.4 Domains of Hopf instability for different ratios of saturation energies v.

[1] C. Knoell et al., Opt. Commun. 187 (2001) 141
[2] Z. Bakonyi et al., IEEE Photon. Technol. Lett. 12 (2000) 570
[3] G. Agrawal et al., IEEE J. Quant. Electron. 25 (1989) 2297
[4] V. Grigoryan, Opt. Lett. 21 (1996) 1882

Dynamical evolution of weak perturbations superposed to dispersion-managed soliton transmission

Alessandro Tonello

Istituto Nazionale per la Fisica della Materia, Dept. of Information and Communication Technologies,
via Sommarive 14, 38050 Povo (TN), Italy

Antonio-D. Capobianco and Gianfranco Nalesso

Istituto Nazionale per la Fisica della Materia, Dip. di Elettronica e Informatica,
via Gradenigo 6/A, 35131 Padova (PD), Italy
ph: +39 049 8277723 fax: +39 049 8277699 email:adc@unipd.it

Costantino De Angelis and Francesco Consolandi

Istituto Nazionale per la Fisica della Materia, Dip. di Elettronica per l'Automazione,
via Branze 38, 25123 Brescia (BS), Italy

Abstract: We analyze numerically and analytically the evolution of weak perturbations in fiber systems with dispersion management. Linearizing the governing equation around a dispersion-managed soliton, we discuss the role of average dispersion and of nearby pulses.
© 2002 Optical Society of America
OCIS codes: (190.5530) Pulse propagation and solitons; (190.4410) Nonlinear optics, parametric processes

1 Introduction

Whatever the future structure of in-line optical amplifiers, as lumped, distributed or hybrid configurations, the unavoidable nonlinear interaction of optical noise and transmitted signal, with distortion or squeezing of the noise spectral density, represents an important issue in dispersion managed systems [1]. Such dynamical interplay, ruled by the nonlinearity of optical propagation in fiber, has been initially studied by Carter [2] explicitly discerning whether the squeezing effect is induced by a continuous wave (CW) or by a single classical soliton. Indeed CWs may represent unstable solutions of the Nonlinear Schrödinger equation (NLSE), and exponential growth of weak perturbations in the spectral domain may arise in presence of modulation instability (MI). Differently, small perturbations superposed to classical solitons may undergo a squeezing effect in absence of MI, owing to the intrinsic stability of solitons. However MI in the soliton regime was reported in presence of soliton trains [3], and previously in Ref. 4, for special waveguiding structures. For periodically dispersion-managed (DM) systems, again the CWs may exhibit MI with peculiar dynamics [5], whereas for the single DM soliton regime, a linear stability analysis (LSA) has been presented in Ref. 6, with specific attention to the soliton disruption in the average normal dispersion regime; an application of the LSA technique has been recently presented in Ref. 1 in the evaluation of the bit-error rate of noisy transmissions. In this work we apply the LSA technique to DM solitons, pointing out the role of average anomalous dispersion and the effect of neighboring pulses in the time domain, when elementary perturbations, that are superposed to DM solitons, undergo squeezing phenomena during their propagation.

2 Analytical description

Our starting point is the so called dispersion-managed nonlinear Schrödinger (DMNLS) equation, that has been derived through a multiscale approach by Ablowitz and Biondini [7], and with a different method by Medvedev and Turitsyn [8]. The DMNLS equation in the frequency domain, referring to normalized units like in Ref. 7, reads as:

$$i\frac{dU(z,\omega)}{dz} - \delta\frac{\omega^2}{2}U(z,\omega) + \int_{-\infty}^{+\infty}\int_{-\infty}^{+\infty} r(\omega_1\omega_2)U(z,\omega+\omega_1)U(z,\omega+\omega_2)U^*(z,\omega+\omega_1+\omega_2)d\omega_1 d\omega_2 = 0 \quad (1)$$

$$\text{where} \quad r(x) = \frac{1}{(2\pi)^2}\int_{-\frac{1}{2}}^{\frac{1}{2}} e^{iC(\zeta)x}d\zeta \quad \text{and} \quad C(\zeta) = \int_{-\frac{1}{2}}^{\zeta}[D(\zeta')-\delta]d\zeta'.$$

$U(z,\omega)$, according to Ref. 7, evolves with a scale that is much longer than the single dispersion map length L (normalized to $L=1$ in eq. 1), and more specifically, for DM solitons, $U(z,\omega) = F(\omega)\exp[iz\lambda^2/2]$; $r(x)$

accounts for the dispersion map periodicity [7], and $D(\zeta')$, δ represent the local and path average dispersion respectively. Following Refs. 2,3,4,6, one can assume $U(z,\omega) = [F(\omega) + u(z,\omega) + iv(z,\omega)]\exp[iz\lambda^2/2]$, where u and v are small perturbations, often called in-phase and quadrature components. At the numerical level [1], the dynamics of $u(z,\omega)$ and $v(z,\omega)$ can be calculated simply solving two times eq. 1 with different input conditions, the former with $U(z=0,\omega) = F(\omega) + u(z=0,\omega) + iv(z=0,\omega)$ and the latter with $U(z=0,\omega) = F(\omega)$, and finally applying a subtraction [1]. In our example we manage the local dispersion holding $D = 2ps/(km \cdot nm)$ for a span of $10.25km$, then $D = -2ps/(km \cdot nm)$ for $19.5km$ and then again $D = 2ps/(km \cdot nm)$ for $10.25km$, conceiving a dispersion map of $\delta = 0.05ps/(km \cdot nm)$. Assuming a common fiber cross section of $50\mu m^2$ and a soliton energy of $50fJ$ (initial pulse width of $6.85ps$), we show in fig. 1 $G_R = 20Log_{10}[|u(z,\omega)|/|u(0,\omega)|]$ and $G_I = 20Log_{10}[|v(z,\omega)|/|v(0,\omega)|]$. We neglect here the fiber losses and we assume $u(z=0,\omega)$, $v(z=0,\omega)$ of constant value, as a reference initial elementary perturbation.
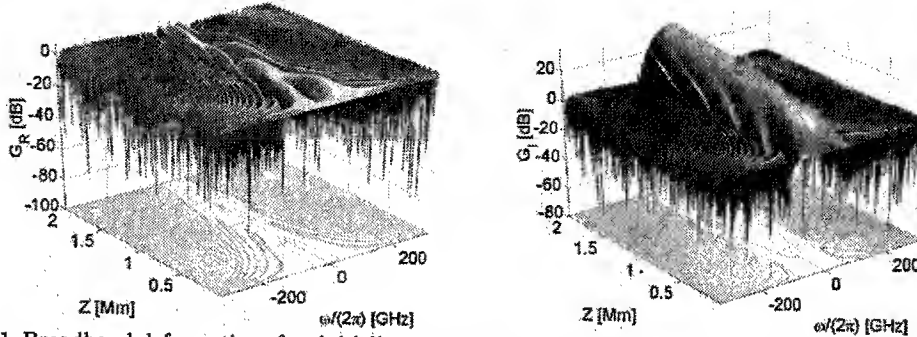
Fig. 1. Broadband deformation of an initially constant perturbation induced by a DM soliton in the frequency domain: G_R (left) and G_I (right); results have been calculated through the numerical solution of eq. 1.

3 Linearization of the DMNLS equation

Let us try now to exploit the solitonic nature of the stationary solution $F(\omega)$ to clarify analytically the squeezing effect. Linearizing eq. 1 around a soliton solution $F(\omega)$ we derive a consistent set of coupled equations for u, v as follows:

$$\frac{du}{dz} = \frac{\lambda^2}{2}v + \frac{\delta}{2}\omega^2 v + \int_{-\infty}^{+\infty}[M_\omega(\xi) - 2N_\omega(\xi)]v(\omega + \xi)d\xi, \quad \frac{dv}{dz} = -\frac{\lambda^2}{2}u - \frac{\delta}{2}\omega^2 u + \int_{-\infty}^{+\infty}[M_\omega(\xi) + 2N_\omega(\xi)]u(\omega + \xi)d\xi \quad (2)$$

$$M_\omega(\xi) = \int_{-\infty}^{+\infty}r[\omega_1(\xi - \omega_1)]F(\omega + \omega_1)F(\omega + \xi - \omega_1)d\omega_1, \quad N_\omega(\xi) = \int_{-\infty}^{+\infty}r(\omega_1\xi)F(\omega + \omega_1)F(\omega + \xi + \omega_1)d\omega_1.$$

Note that the nonlinear Kerr effect, now tailored by the stationary solution $F(\omega)$, may induce a significant frequency-dependent coupling in eqs. 2, that is represented by the functions $M_\omega(\xi)$, $N_\omega(\xi)$. Observe that these functions are invariant in z and can be computed just one time before solving the linear system of eqs. 2, owing to the spatial invariance of the DM soliton envelope. Examples of numerical solutions of eqs. 2, still in optimum agreement after $1000km$ with the results directly achieved applying the subtraction method in eq. 1, are shown in fig. 2; note the different distortion when we change $\delta = 0.1ps/(km \cdot nm)$, in case A, to $\delta = 0.025ps/(km \cdot nm)$ in case B. The direct numerical evaluation of eqs. 2 and of $M_\omega(\xi)$, $N_\omega(\xi)$ results extremely time consuming whenever the frequency domain is numerically resolved into a refined discrete grid. In the attempt to reduce the computation effort, for small energy pulses the DM soliton spectrum can be approximated with a gaussian function as $F(\omega) \simeq A\exp[-\omega^2/B^2]$; consequently one may express new coupling functions $\overline{M}_\omega(\xi)$ and $\overline{N}_\omega(\xi)$ as

$$\overline{M}_\omega(\xi) = A^2 \int_{-\frac{1}{2}}^{+\frac{1}{2}} \sqrt{\frac{\pi}{2/B^2 + iC(x)}} \exp\left[-\frac{8\omega^2 + 8\omega\xi + \xi^2(2 - iB^2C(x))}{4B^2}\right]dx$$

$$\overline{N}_\omega(\xi) = A^2 \int_{-\frac{1}{2}}^{+\frac{1}{2}} B\sqrt{\frac{\pi}{2}} \exp\left\{-\frac{\xi[4\xi + B^4C^2(x)\xi + i4B^2(2\omega + \xi)C(x)]}{8B^2}\right\}dx.$$

(3)

Eqs. 3 may be useful in solving eqs. 2, replacing $M_\omega(\xi)$ and $N_\omega(\xi)$, under a further warning: in addition to the perturbative limit, which was previously discussed, now we have explicitly assumed a Gaussian waveform

for $F(\omega)$ (Gaussian LSA, GLSA) limiting our analysis to low-power solitons. Nevertheless, for pulse's energy of $30fJ$ we found that the GLSA agrees with numerical results obtained solving twice eq. 1 (see dashed curves and filled dots in fig. 3), even for long distances. Finally the same elementary perturbation may result differently modified when DM solitons are closely packed. Indeed, if we reduce the bit slot from $T = 25ps$ ($40Gbit/s$ systems) down to $T = 20ps$, when transmitting a sequence 111, we notice in G_R and G_I an evident difference from the single pulse case (we retain a moderate propagation distance so that the jitter is still negligible). We have applied the GLSA assuming $U(z,\omega) = F(\omega)(1 + 2\cos[\omega T])\exp[iz\lambda^2/2]$ and we have calculated similar expressions for $\overline{M}_\omega(\xi)$, $\overline{N}_\omega(\xi)$, now dependent on the bit slot T. We present our results in fig.3 comparing the full numerical solutions of eq.1 with the GLSA both for a single pulse transmission and for a sequence 111 with T=20ps.

In conclusion, we calculated the dynamical evolution of small perturbations superposed to DM solitons applying a linear stability analysis to the DMNLS equation. We have improved the computational efficiency through the Gaussian assumption for the DM soliton and we have pointed out the eventual additional role of the patterning effect induced by closely adjacent pulses.
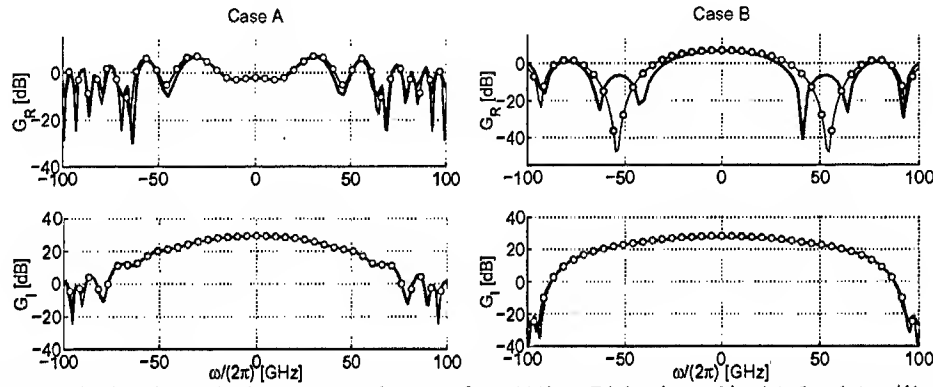
Fig. 2. Perturbation dynamics in phase, quadrature after 1000km. Right: (case A) with $\delta = 0.1ps/(km \cdot nm)$. Left: (case B) with $\delta = 0.025ps/(km \cdot nm)$. Solid line for the numerical results of eq. 1, dots for LSA solving eqs. 2.
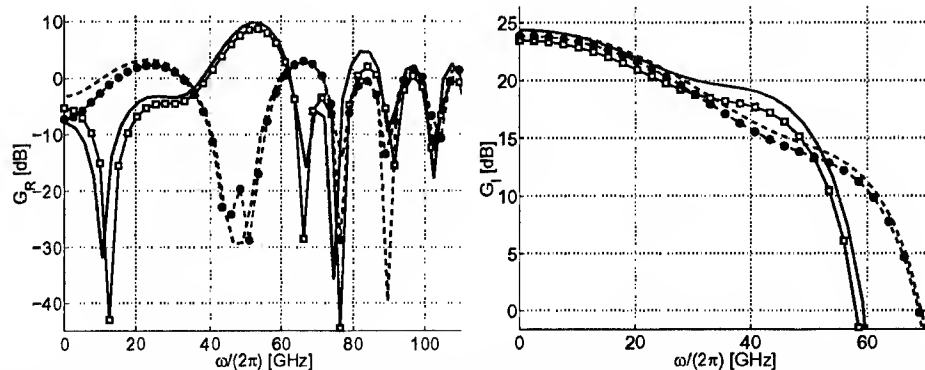
Fig. 3. Left: $G_R(\omega)$ after 950km. Effect of a sinlge pulse (dashed curve for numerics through eq. 1, filled dots for GLSA) and for a sequence 111 (solid curve for numerics through eq. 1, empty dots for GLSA). Right: $G_I(\omega)$ after 950km. Effect of a sinlge pulse (dashed curve for numerics through eq. 1, filled dots for GLSA) and for a sequence 111 (solid curve for numerics through eq. 1, empty dots for GLSA).

References

[1] R. Holzlöhner, V. S. Grigoryan, C. R. Menyuk, W. L. Kath, IEEE Journ. of Lightwave Tech., **20**, 389, (2002).
[2] S. J. Carter, P. D. Drummond, M. D. Reid, R. M. Shelby, Phys. Rev. Lett., **58**, 1841, (1987).
[3] E. A. Kuznetsov, M. D. Spector, Theoretical and Mathematical Physics, **120**, 997, (1999).
[4] A. B. Aceves, C. De Angelis, G. Luther, A. M. Rubenchik, Opt. Lett., **19**, 1186, (1994).
[5] N. J. Smith and N. J. Doran, Opt. Lett., **21**, 570, (1996).
[6] D. E. Pelinovsky, Phys. Rev. E, **62**, 4283, (2000).
[7] M. J. Ablowitz and G. Biondini, Opt. Lett., **23**, 1668, (1998).
[8] S. B. Medvedev, S. K. Turitsyn, JETP Letters, **69**, 499, (1999).

Dependence of Spectral Width and Gain of Stimulated Brillouin Scattering on Numerical Aperture in Optical Fibre

Valeri I. Kovalev* and Robert G. Harrison

Nonlinear Dynamics and Optics Group, Department of Physics, Heriot-Watt University, Edinburgh EH14 4AS, UK.
Tel: (44)131 451 3024, Fax: (44)131 451 3136, E-mail: V.Kovalev@hw.ac.uk
*Also with P.N.Lebedev Physics Institute of the Russian Academy of Sciences

Abstract: We give theoretical interpretation for the recently observed phenomenon of inhomogeneous spectral broadening of Brillouin scattering in optical fibres. SBS spectral width and gain dependencies on numerical aperture and are shown to be in good agreement with experiments for both single- and multi-mode fibres.

OCIS codes: (060.4370) Nonlinear optics, fibers; (290.5900) Scattering, stimulated Brillouin; (300.6170) Spectra

The key parameter of a medium for SBS is the width of the Brillouin scattering spectral line Γ. It determines SBS gain g ($g \propto \Gamma^{-1}$) and so SBS threshold power/intensity ($P_{th} \propto \Gamma$), it defines the buid-up time of scattering and the duration of transient processes, etc. Usually Γ is defined by damping of the acoustic wave due to viscosity. This is normally uniform in bulk media, resulting in homogeneous broadening of the Brillouin scattering spectrum /1/.

In optical fibres, however, it is known that the Brillouin line is broader than the classical homogeneous width /2/. Recently we provided first experimental evidence showing this excess broadening to be inhomogeneous and a generic feature of waveguiding systems /3/. We have shown in /3/ that this phenomenon arises from the ability of a fibre (even single-mode) to guide a fan of beam directions within an acceptance angle $2\theta_c$, where $\theta_c = \arcsin[(NA)/n_{co}]$ is the complement of the critical angle, n_{co} is a refractive index of the core and NA is the numerical aperture of a fibre. Since the Brillouin frequency shift, $F_B(\varphi)$, depends on the angle, φ, between the momentum vectors of the pump and scattered radiation ($F_B(\varphi) = 2nvsin(\varphi/2)/\lambda$ /2/, where v is the velocity of sound and λ is the radiation wavelength) there is a range of F_B's within angle $2\theta_c$. For every $F_B(\varphi)$ corresponds a homogeneously broadened line. The Stokes spectrum, broadened by the waveguiding, is then the convolution of these lines over all frequency components.

Here we show the dependence of FWHM linewidth of this inhomogeneously broadened spectrum (Γ) and the corresponding SBS gain (g) at maximum of the gain profile on the NA of a fibre are given by the expressions,

$$\Gamma \cong \sqrt{\Gamma_0^2 + F_B^2 \frac{(NA)^4}{4n_{co}^4}} \quad \text{and} \quad g \cong g_0 \frac{2CF_B n_{co}^2}{(NA)^2} \tan^{-1}\left[\frac{(NA)^2}{2CF_B n_{co}^2}\right],$$

where g_0 is the SBS gain for bulk silica, $\Gamma_0 = CF_B^2$ is the homogeneous width of the Brillouin line, C is the constant of a material.

Experimentally measured Γ in five fibre samples (three single-mode, one two-mode and one multi-mode) with different NA (from 0.12 to 0.24) are shown to be in good agreement with our theoretical expression given above (see Fig.1). In Fig.2 we show the dependencies of g and $P_{th} = G_{th}S/gL$ on NA, where G_{th} is the SBS threshold exponential gain, and S is the cross section area of the fibre core and L is the fibre length. P_{th} in this Figure is normalised to P_{th0}, which is the SBS threshold power in a fibre, taking the SBS gain coefficient as that for bulk silica.
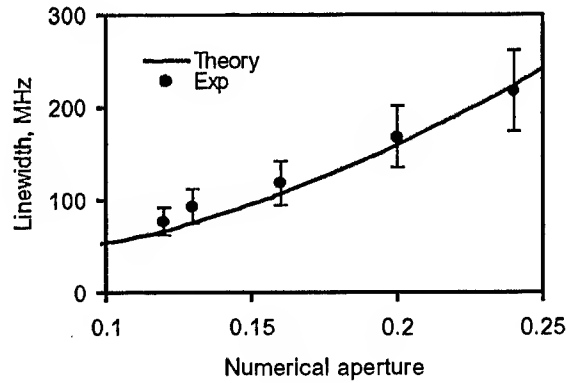
Fig.1
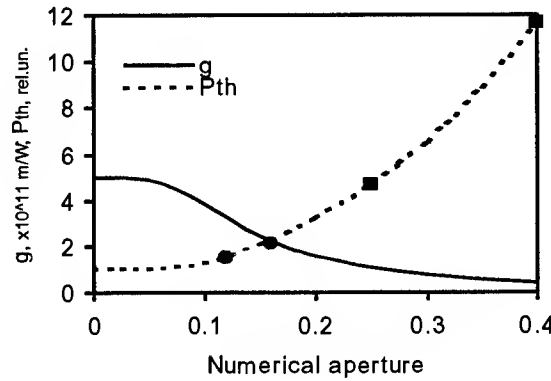
Fig.2

Figs 1 and 2. Dependencies of Γ (1), g and P_{th} (2) on NA for a fibre with $n_{co} \cong 1.46$ and C = $1.4 \cdot 10^{-7}$ (MHz)$^{-1}$.

The experimental data presented (dots and squares) are the relative values of SBS thresholds at appropriate values of NA in single-mode (dots, our measurements) and in multi-mode (squares, data from /4/) fibres. As seen there is good agreement between calculated and measured dependence of SBS threshold on NA. Figs 1 and 2 show in the limit that the NA approaches zero, corresponding to the case of the bulk media, the values for linewidth, gain and threshold power for SBS asymptotically approach the values expected, those for which the SBS gain is homogeneous.

References

1. V.S.Starunov and I.L.Fabelinskii. Sov. Phys.-Usp., **12**, 463 (1970).

2. G.P.Agrawal, *Nonlinear Fiber Optics*, 3^d ed. Academic Press Inc., Boston, 2001.

3. V.I.Kovalev and R.G.Harrison. Phys. Rev. Lett., **85**, 1879 (2000).

4. K.Tei, Y.Tsuruoka, T.Uchiyama, and T.Fujioka, Jpn. J. Appl. Phys. **40**, 3191 (2001).

Pulse broadening in dispersion-managed optical fiber links with random dispersion

T. Schäfer, R. O. Moore, and C. K. R. T. Jones

Division of Applied Mathematics, Brown University, 182 George St., P.O. Box F,
Providence, RI 02912
Phone: (401) 863-2049, Fax: (401) 863-2722, Email: tobias@cfm.brown.edu

Abstract: Random dispersion variations lead to pulse degradation in fiber lines. We discuss the validity of a finite-dimensional reduction of the nonlinear Schrödinger equation and derive an analytical formula describing pulse broadening induced by randomness.
© 2002 Optical Society of America

OCIS codes: (060.4370) Nonlinear optics, fibers ; (060.5530) Pulse propagation and solitons

Even though fibers can currently be manufactured to within very precise dispersion tolerances, small variations of the dispersion are always present [1]. If optimized return-to-zero (RZ) pulses such as solitons or dispersion-managed solitons are used as bit carriers, these deviations from the nominal dispersion degrade the performance of the network and can lead to pulse disintegration [2]. It is therefore important to understand how these random variations influence pulse evolution and to be able to characterize this effect.

The basic equation for studying pulses in optical communication lines is the cubic nonlinear Schrödinger equation

$$iA_z + d(z)A_{tt} + c(z)|A|^2A = 0. \tag{1}$$

The slowly varying electric field amplitude A is a complex-valued function that depends on the propagation distance z and retarded time t. Loss and amplification are included by allowing the nonlinear coefficient c to vary with propagation distance. Here, the dispersion $d(z) = d_{\det}(z) + d_r(z)$ consists of a deterministic part $d_{\det}(z)$ and a small random part $d_r(z)$. For the random part, we assume white noise of strength D, so that its correlation function is given by

$$\langle d_r(z)d_r(z')\rangle = D\delta(z - z'). \tag{2}$$

It has been shown [4, 5] that the core evolution of a dispersion-managed soliton is very accurately described by the first mode of an appropriately transformed Gauss-Hermite eigenfunction expansion, given by

$$A(z,t) = \frac{2^{3/4}N}{\sqrt{T(z)}}\exp\left(-\frac{t^2}{2T(z)^2}\right)\exp\left(i\frac{M(z)}{T(z)}t^2\right), \tag{3}$$

where the $1/e$ width $T(z)$ and the chirp $M(z)$ are governed by coupled nonlinear ordinary differential equations (ODEs):

$$\frac{dT}{dz} = 4d(z)M, \qquad \frac{dM}{dz} = \frac{d(z)}{T^3} - \frac{c(z)N^2}{T^2}. \tag{4}$$

This system of ODEs can also be obtained from Eqn. 1 though a variational approach and a consideration of certain moments of the pulse [5]. In the case considered here, these ODEs are stochastic because of the random component of $d(z)$.

We first demonstrate that the solution of Eqns. 4 stays close to the solution of Eqn. 1 in the presence of random dispersion. We consider a typical deterministic two-step map $d_{\det}$ for dispersion-managed systems consisting of two fibers of the same length having highly varying local dispersion $\pm d_{\text{loc}}$ and a small average dispersion d_{av}. We take a dispersion-managed soliton $A_s(t)$ as the initial condition for our PDE simulations, and the corresponding values of T and M of Eqns. 4 as the initial condition for the ordinary differential equations. For the PDE simulations, changes in pulse width can be described by the quantity

$$\Delta T \equiv \int t^2|A|^2dt - \int t^2|A_s|^2dt, \tag{5}$$

where we make use of the fact that $|A_s(z,t)|^2$ is strictly periodic in z with the dispersion map period. In the deterministic case, obviously $A = A_s$ and $\Delta T = 0$. Making use of Eqn. 3, we find the corresponding
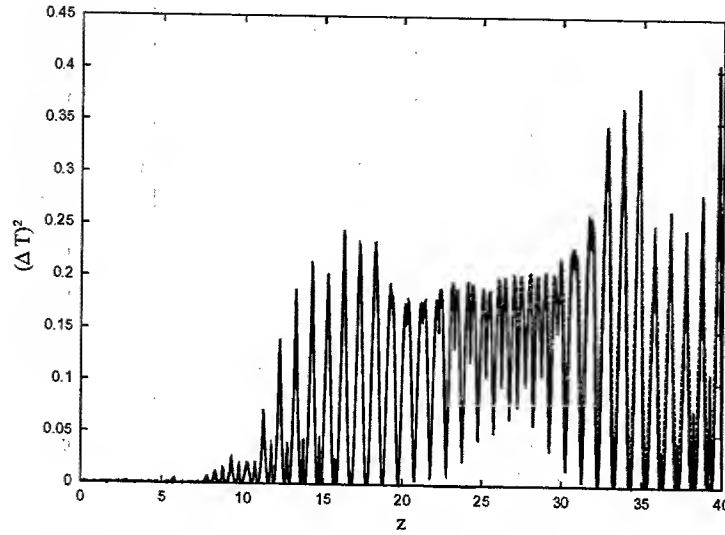
Fig. 1. Numerical comparison of the ODE simulations (solid line) and the PDE simulations (dashed line) in the distributed-gain limit (c constant). The amplitude of the noise is 0.05. The other parameters are $d_{\mathrm{loc}} = 5$, $d_{\mathrm{av}} = 0.15$, $N^2 = 0.117$.

expression for the ODEs:

$$\Delta T = \sqrt{2\pi} N^2 \left(T^2(z) - T_{\det}^2(z) \right). \tag{6}$$

We have compared values of ΔT obtained by numerically integrating Eqn. 1 with Eqn. 5 and Eqns. 4 with Eqn. 6 for various dispersion maps. Figure 1 shows very good agreement between these solutions for a typical map. This confirms that the ODE model given in Eqns. 4 represents a reasonable reduction of Eqn. 1 for studying the influence of random dispersion on pulse dynamics.

In order to obtain analytical results, we make use of the fact that nonlinearity is weak in physically realistic dispersion-managed fiber links. Whereas the fast dynamics is governed by the local variations of the dispersion, the slow evolution is determined by this weak nonlinearity and a correspondingly small residual dispersion. The random fluctuations introduce a third small quantity, and we can exploit these small quantities to obtain approximate expressions for the perturbed evolution of the pulse width.

To carry out these calculations, we write

$$d(z) = \tilde{d}(z) + \epsilon d_{\mathrm{av}} + \nu d_r(z) \tag{7}$$

where $\tilde{d}(z)$ is $\pm d_{\mathrm{loc}}$ in the different fiber spans, and ϵ and ν are small parameters. We can then write T and M in expansions

$$T = T_G + \mu T_{\mathrm{res}} + \nu T_1, \qquad M = M_G + \mu M_{\mathrm{res}} + \nu M_1, \tag{8}$$

where T_G and M_G represent the Gaussian core of the dispersion-managed soliton, satisfying

$$T_{Gz} = 4\tilde{d}(z)M_G, \qquad M_{Gz} = \frac{\tilde{d}(z)}{T_G^3}. \tag{9}$$

The evolution of T_{res} and M_{res} is then described at leading order by the corrections to this Gaussian caused by a small average dispersion and weak nonlinearity, leaving T_1 and M_1 to account for the influence of random dispersion, with

$$T_{1z} = 4d_r(z)M_G + 4\tilde{d}(z)M_1, \qquad M_{1z} = \frac{d_r(z)}{T_G^3} - \frac{3\tilde{d}(z)T_1}{T_G^4}. \tag{10}$$

This system of equations can be solved easily as it is equivalent (to the leading and first order) to

$$\tau(z) = T_G + \nu T_1, \qquad \gamma(z) = M_G + \nu M_1 \tag{11}$$
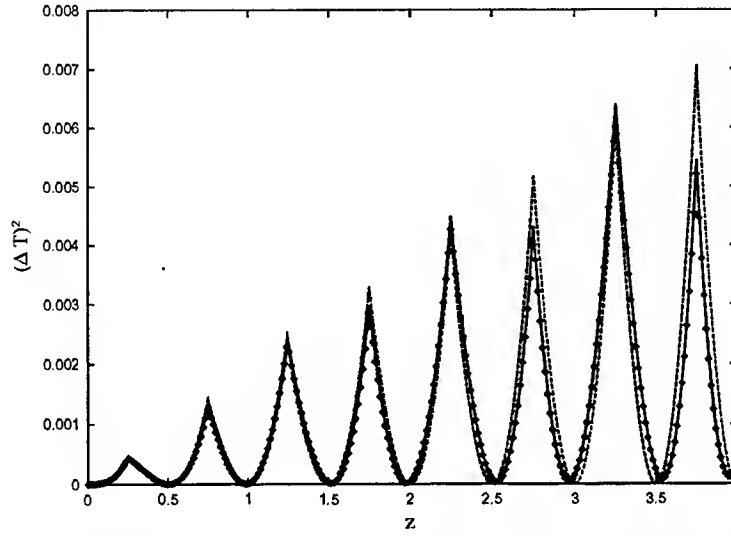
Fig. 2. Numerical comparison of the numerical simulations (solid line) of the ODE with the PDE simulations (dots) and with the analytical model (dashed line). The amplitude of the noise is 0.05. The figure shows an average over 5000 realizations.

$$\tau_z = 4(\tilde{d} + \nu d_r)\gamma, \qquad \gamma_z = \frac{\tilde{d} + \nu d_r}{\tau^3}, \tag{12}$$

with the solution

$$\tau^2(\rho) = \tau_0^2 + \frac{4\rho^2}{\tau_0^2}, \qquad \rho' = \tilde{d}(z) + \nu d_r(z). \tag{13}$$

From this formula we can directly obtain the pulse broadening:

$$\Delta T = \frac{8W_r(z)\tilde{R}(z)N^2\sqrt{2\pi}}{T_0^2}, \qquad \tilde{R}(z)' = \tilde{d}(z). \tag{14}$$

Here, $W_r(z)$ is a Wiener process derived from integrating white noise of strength D, and $\tilde{R}(z)$ is the accumulated dispersion (made periodic by the zero mean of $\tilde{d}(z)$). We can compare this analytical prediction to numerical simulations. Figure 2 shows clearly that, for z not too large, the analytical results describe very well the behavior governed by Eqns. 4. Given the long range of agreement demonstrated previously between this system of ODEs and Eqn. 1, the influence of random dispersion on pulse width is accurately represented by Eqn. 14.

In summary, we have successfully captured the effect of random dispersion on the propagation of dispersion-managed solitons through optical fiber by reducing the original partial differential equation to a simple pair of stochastic ODEs. Not only are these ODEs much faster to simulate in computations, but we have also demonstrated that a quasi-linear analysis of these ODEs accurately describes the effect of randomness for reasonably short evolution scales.

References

1. L. F. Moellenauer, P. V. Mamyshev, and M. J. Neubelt, "Method for facile and accurate measurement of optical fiber dispersion maps," Opt. Lett. **21**, 1724-1726 (1996).
2. F. Kh. Abdullaev and B. B. Baizakov, "Disintegration of a soliton in a dispersion-managed optical communication line with random parameters", Opt. Lett. **25**, 93-95 (2000).
3. G. P. Agrawal, "Nonlinear Fiber Optics", (Academic Press, Boston, 1989).
4. T. I. Lakoba and D. J. Kaup, "Hermite-Gaussian expansion for pulse propagation in strongly dispersion managed fibers", Phys. Rev. E **58**, 6728-6741 (1998).
5. S. K. Turitsyn, T. Schäfer, K. H. Spatschek and V. K. Mezentsev, "Path-averaged chirped optical soliton in dispersion-managed fiber communication lines", Opt. Comm. **163**, 122-158 (1999).
6. F. Kh. Abdullaev, J. C. Bronski, and G. Papanicolaou, "Soliton perturbations and the random Kepler problem", Physica D **135**, 369-386 (2000).

The role of dispersion of nonlinearity in supercontinuum generation with photonic crystal fibers

R. Iliew and F. Lederer
Institut für Festkörpertheorie und Theoretische Optik,
Friedrich-Schiller-Universiät Jena, Max-Wien-Platz 1, 07743 Jena, Germany
telephone +49-3641-947175, fax +49-3641-947177,
e-mail Rumen.Iliew@uni-jena.de

Abstract: We derive field equations in frequency domain for describing spectrally broad pulses in nonlinear waveguides. Applying this model to supercontinuum generation in photonic-crystal fibers we investigate the influence of a frequency-dependent nonlinear term for realistic fibers.
© 2002 Optical Society of America

With the emergence of photonic-crystal fibers (PCFs) [1] with tailorable optical properties there has been an appreciable progress in supercontinuum light generation experiments [2, 3, 4]. Different regimes of operation have been applied to generate a white-light continuum in the visible spectrum, so short pulses in the solitonic regime [4, 5] and longer pulses of moderate peak power where the interplay between Raman effect and four-wave mixing rules dynamics [2, 3]. These experiments rely on the modified dispersion properties, on the singlemode operation and on small effective areas of PCFs. The theoretical description has to take into account nonlinearity, the exact dispersion relation [2, 3], a frequency-dependent effective area (up to now only considered in a different context) [6] as well as the frequency dependent nonlinear refractive index, because of the expected extreme spectral width.
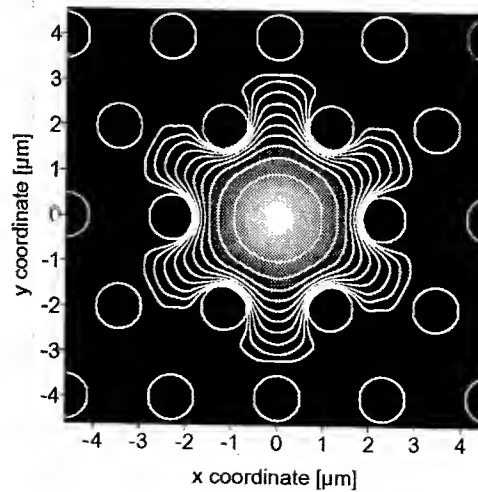
Fig. 1. Image plot of one component of the magnetic field and intensity contours of the mode of the PCF at a wavelength of 400 nm. The contour spacing is 3 dB.

The aim of this paper is to derive a model that takes these effects into account consistently. Evidently, the frequency domain is the natural choice to describe such highly dispersive systems. Starting from a total field formulation [7] we derive evolution equations with a general dispersive nonlinear term describing a frequency-dependent effective area as well as a third-order nonlinear coefficient. We include the exact dispersion relation, four-wave mixing, and stimulated Raman scattering (SRS). For a symmetric fiber only one mode in the expansion of the electric field has to be accounted for because of monomode operation of PCFs over a wide wavelength range. The normalized equation for the modal amplitude a then reads

$$\frac{\partial a(Z,u)}{\partial Z} = [i\delta(u) - \varepsilon(u)]a(Z,u)$$

$$+i\mu(1+u)\int_{-\Delta}^{+\Delta}du_1\int_{-\Delta}^{+\Delta}du_2\gamma(-u,u_1,u_2,u-u_1-u_2)a(Z,u_1)a(Z,u_2)a^*(Z,u_1+u_2-u) \qquad (1)$$

$$+i\mu_R(1+u)\int_{-\Delta}^{+\Delta}du_1 S(u_1)a(Z,u-u_1)\int_{-\Delta}^{+\Delta}du_2\gamma_R(-u,u-u_1,u_2,u_1-u_2)a(Z,u_2)a^*(Z,u_2-u_1).$$

Here Z is the normalized propagation distance, ε describes linear losses, u_i are the normalized frequencies relative to the reference frequency ω_0, μ and μ_R are the nonresonant (four-wave mixing) and the resonant (SRS) contribution to the third order nonlinearity, respectively, 2Δ the total bandwidth of the optical field, S the Raman susceptibility and $\delta = \beta(\omega) - \beta(\omega_0) - (\omega - \omega_0)/v_g$ represents the quadratic and higher order corrections to the propagation constant of the linear fiber mode around the reference frequency ω_0. The dispersive properties of the nonresonant and resonant nonlinear term are described by γ and γ_R, respectively. To make the equations numerically tractable we introduce a physically motivated model for the parameter γ dependent on four frequencies to describe also nondegenerate nonlinear processes. We put into this model the results from simulations of different PCFs. Also the exact dispersion relation $\beta(\omega)$ is taken from here.
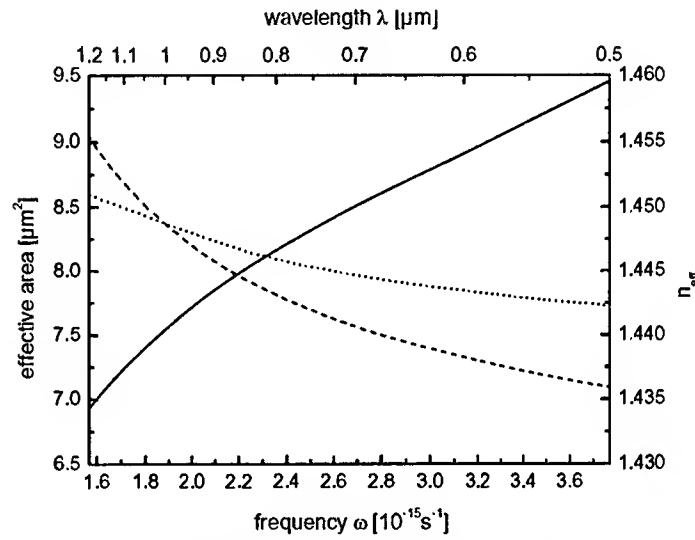
Fig. 2. Wavelength dependence of effective area for self-phase modulation (dashed) and cross-phase modulation of $\lambda = 1\,\mu$m (dotted) and effective index (solid) of the mode shown in Fig. 1. The Raman shift in silica is $\omega_R = 0.083 \times 10^{15}\text{s}^{-1}$.

Fig. 1 shows the field profile of a fiber similar to those used in recent experiments [3]. Fig. 2 shows the contribution of the fiber mode effective area to γ and the variation of the effective index of the mode as a measure for $\delta(\omega)$. We can recognize that for a 700 nm wide continuum the effective area of our sample fiber is altered by a factor of 1.4. Moreover, it is obvious that we have different effective areas for self-phase and cross-phase modulation, so for two phase-matched processes generating even the same wavelength (e.g. here $\lambda = 1\,\mu$m) we have different areas. The nonlinear optical coefficient of silica changes by a factor of 1.4 within the visible wavelength range [8]. This change adds constructively to the dispersive change of the effective area. At the same time the self-steepening factor $(1 + u)$ changes by a factor of 2.4 into the opposite direction. So at a first glance γ seems to reduce the self-steepening and shock effect. Due to photon number conservation γ is only effective when the sum of it's four arguments vanishes. We investigated this behavior by calculating the modal profiles at different wavlengths and by looking at γ at different frequency combinations in order to confirm the model.

As a simple example Fig. 3 compares the spectrum of a propagation simulation of an injected fifth order soliton after half a soliton period. Here the inverse soliton temporal width was in the order of the Raman shift and Raman-induced pulse splitting occurs. Already after half a period we can clearly see that for the case of dispersive effective area the separated wing travels slower. We will show results of propagation simulations investigating the influence of these corrections in different parameter ranges and we will compare to the models without frequency dependence.
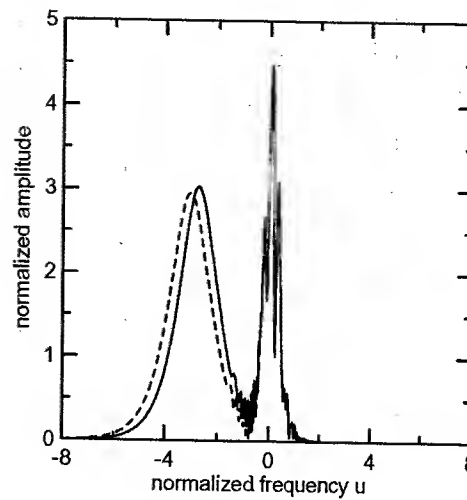
Fig. 3. Spectrum of the output after propagation of half a soliton period of an initial fifth order soliton calculated with constant effective area (dashed) and with a frequency dependent one (solid). The normalized Raman shift is $u = 3$.

References

1. D. Mogilevtsev, T. A. Birks, and P. St. J. Russell, "Group-velocity dispersion in photonic crystal fibers," Opt. Lett. **23**, 1662 (1998).

2. S. Coen, A. H. L. Chau, R. Leonhardt, J. D. Harvey, J. C. Knight, W. J. Wadsworth, and Philip St. J. Russell, "Supercontinuum generation by stimulated Raman scattering and parametric four-wave mixing in photonic crystal fibers," J. Opt. Soc. Am. B **19**, 753 (2002).

3. J. M. Dudley, L. Provino, N. Grossard, H. Maillotte, R. S. Windeler, B. J. Eggleton, and S. Coen, "Supercontinuum generation in air-silica microstructured fibers with nanosecond and femtosecond pulse pumping," J. Opt. Soc. Am. B **19**, 765 (2002).

4. J. Herrmann, U. Griebner, N. Zhavoronkov, A. Husakou, D. Nickel, J. C. Knight, W. J. Wadsworth, P. St. J. Russell, and G. Korn, "Experimental Evidence for Supercontinuum Generation by Fission of Higher-Order Solitons in Photonic Fibers," Phys. Rev. Lett. **88**, 173901 (2002).

5. A. V. Husakou and J. Herrmann, "Supercontinuum Generation of Higher-Order Solitons by Fission in Photonic Crystal Fibers," Phys. Rev. Lett. **87**, 203901 (2001).

6. S. V. Chernikov and P. V. Mamyshev, "Femtosecond soliton propagation in fibers with slowly decreasing dispersion," J. Opt. Soc. Am. B **8**, 1633 (1991).

7. P. L. François, "Nonlinear propagation of ultrashort pulses in optical fibers: total field formulation in the frequency domain," J. Opt. Soc. Am. B **8**, 276, (1991).

8. David Milam, "Review and assessment of measured values of the nonlinear refractive-index coefficient of fused silica," Appl. Opt. **37**, 546 (1998).

Pulse Train Dynamics in Actively Modelocked Lasers

J. Nathan Kutz and Jennifer J. O'Neil

Department of Applied Mathematics, University of Washington
Box 352420, Seattle, WA 98195-2420 USA
email: kutz@amath.washington.edu, phone: (206) 685-3029, fax: (206) 685-1440

Abstract

A new model for the active modulation of a modelocked laser cavity shows pulsetrains can
be stabilized only if adjacent pulses are out-of-phase, whereas instabilities destroy the pulsetrain
or give Q-switching.

Compact sources of optical pulses near wavelengths of 1.55 microns are key enabling technologies
for high speed fiber optic communication systems and interconnection networks. The primary focus
of this paper is the development of an analytic model describing active modelocking. Significant
strides have been made toward a complete description of femtosecond modelocking in solid state
lasers [1]. Additionally, passive modelocking in a fiber laser has been described with Haus' master
modelocking equation [2], as a soliton system under perturbation [3], or with a variety of other
specialized models. In contrast to the various descriptions developed, the model considered here
characterizes the entire actively modelocked pulse train. This allows for the exploration of the
stability and dynamics of the modelocked pulse stream which can exhibit instabilities not captured
by the isolated pulse approaches of previous works. Thus, phenomena such as Q-switching in active
modelocking can be observed and investigated within this framework.

The nonlinear Schrödinger equation (NLS) governs the underlying wave behavior of an optical
laser cavity exhibiting both chromatic dispersion and a weak Kerr nonlinearity. For active mode-
locking, the physical effects of dispersion and nonlinearity are accompanied by a bandwidth limited
gain and a periodic attenuation from the active modelocking element. The pulse evolution in the
actively modelocked laser system is governed by the equation [3, 4]:

$$i\frac{\partial Q}{\partial Z} + \frac{1}{2}\frac{\partial^2 Q}{\partial T^2} + |Q|^2 Q - i\left[g(Z)\left(1+\tau\frac{\partial^2}{\partial T^2}\right) - M(\Gamma - \mathrm{cn}^2(\omega T, k))\right]Q = 0. \tag{1}$$

where the gain is given by $g(Z) = 2g_0/(1 + \|Q\|^2/e_0)$ and all quantities have been normalized.

The active modulation model of modelocking is fundamentally different from passive techniques
whose nonlinear responses generate pulse shaping. Here it is the linear, time-dependent, periodic
forcing $M(\Gamma - \mathrm{cn}^2(T, k))$ which results in stabilized pulses. This periodic forcing generates peaks
and troughs in the gain as a function of the time T. Thus cavity energy will accumulate at the
local peaks of gain whereas cavity energy will be attenuated at the local troughs in the gain.
Similar to saturable absorption, this preferential localization of cavity energy gives the necessary
pulse shaping required to form and stabilize localized pulses in a periodic wavetrain. To proceed
analytically, we have generalized the normal periodic forcing given by $\cos^2 \omega T$ [3, 4] to the Jacobian
elliptic [5] cosine function $\mathrm{cn}^2(\omega T, k)$. Here $0 \leq k \leq 1$ is the elliptic modulus. In the limit $k = 0$,
the modulation reduces to a purely sinusoidal forcing as given previously [3, 4]. For values of
$k < 0.9$ the potential is virtually indistinguishable from the sinusoidal modulation. However, as
$k \to 1^-$, the forcing becomes a series of well separated hyperbolic secant shaped modulations. This
modulation is introduced not only for its mathematical generality and ease, but also because we
can find exact analytic solutions to (1) with a constant gain parameter $g(Z) = g =$ constant.
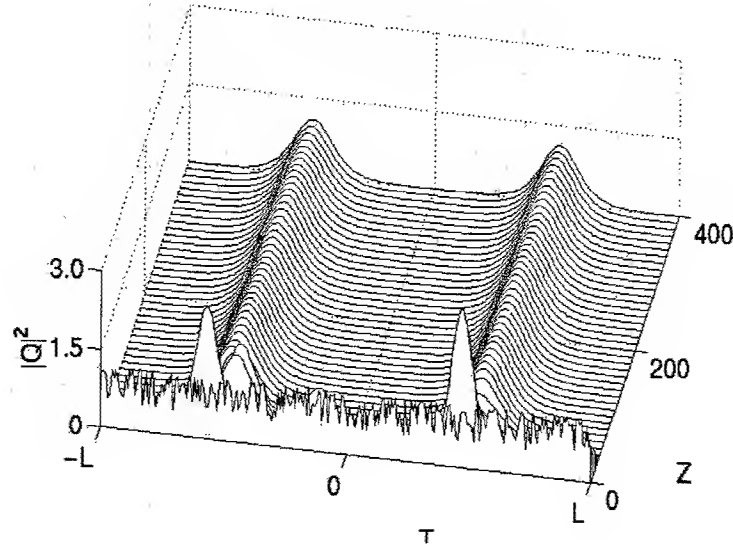
Figure 1: Stable evolution of the modelocking pulse train starting with initial noise. One period is considered with the parameters used being $k = 0.999$, $g = 0.3$ and $\tau = 0.1$. Note the formation of two pulses from this noise realization.

Unstable in-phase pulsetrain solutions are characterized by the absence of a node between neighboring pulses. Such solutions can be reprensented by the $dn(T, k)$ Jacobi elliptic functions [5]. In particular, the in-phase solution is found to be of the form

$$Q(Z, T) = dn(T, k) \exp\left[-i\left(\frac{k^2}{2} - 1\right)Z\right], \tag{2}$$

where $M = -2k^2 g\tau$ and $\Gamma = 2k^2\tau\left(1 - 1/k^2\right) + 1/k^2 + \tau(2 - k^2/k^2)/2$. The lack of a node will result in an unstable pulse train.

An out-of-phase pulsetrain is characterized by the presence of a node between neighboring pulses. Such solutions can be reprensented by the $cn(T, k)$ Jacobi elliptic functions [5]. In particular, the out-of-phase solution is found to be of the form

$$Q(Z, T) = k\,cn(T, k) \exp\left[-i\left(\frac{1}{2} - k^2\right)Z\right], \tag{3}$$

where $M = -2k^2 g\tau$ and $\Gamma = 1/2k^2(2k^2 - 1/\tau - 1)$. The nodal separation is critical to the stability of the pulse trains, i.e. adjacent pulses need to be out-of-phase in order to have the possibility of being stabilized.

Figure 1 shows the evolution over $T = 400$ given a set of random initial conditions. The pulse quickly settles to two modelocked pulses of the form (3) which are stable under further perturbation. The value of the elliptic modulus in this case is taken to be $k = 0.999$ which results in well-separated peaks in the actively modulated gain element. Thus the governing equations are capable of modeling the start up dynamics of the laser from a noisy initial state. In addition to this stable evolution, Fig. 2 considers the same solution with $k = 0.5$. The smaller value of the elliptic modulus forces the neighboring pulses to have significant overlap. As is observed, this overlap leads to a destabilization of the exact solution. However, the evolution quickly settles to a quasi-periodic dynamics where energy is exchanged periodically between neighboring peaks of the gain.
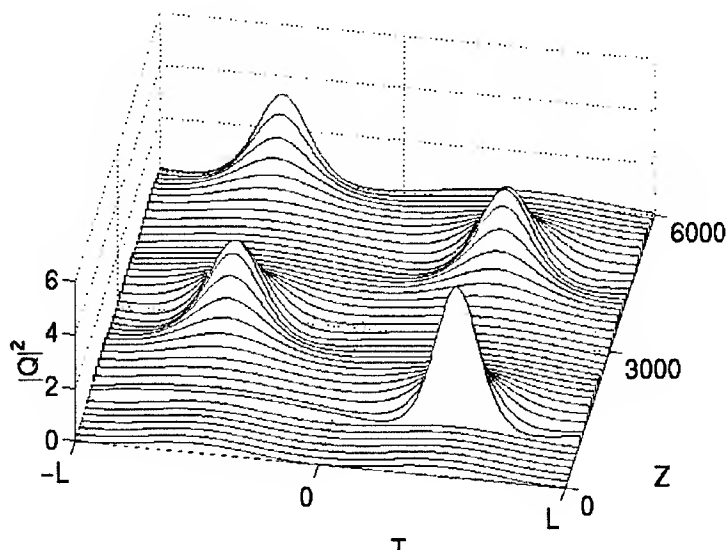
Figure 2: Unstable evolution of the modelocking pulse train starting near the exact solution given by (3). One period is considered with the parameters used being $k = 0.5$, $g = 0.3$ and $\tau = 0.1$.

This behavior is robust and persists under perturbation. Since the cavity is periodic, an output coupler produces a pulse stream for these quasi-periodic interactions which has the characteristic of Q-switching. In contrast to the out-of-phase solutions given by (3), the in-phase solutions of (2) all result in unstable solutions which decay to zero.

The model predicts that only out-of-phase pulse train solutions can be stabilized. Under large perturbation, the pulse train is often stabilized to a two-pulse per round trip configuration. All in-phase solutions are unstable and are destroyed. Further, for the out-of-phase solutions, if the pulse spacing is not sufficiently far, then the nearest neighbor interactions can dominate and lead to Q-switching behavior. For short cavities, this Q-switching can result in quasi-periodic behavior of the pulse train. For long cavities, the resulting Q-switching is chaotic in nature. For specific pulse separations where $k \approx 0.98$, the out-of-phase pulse train is destabilized and attenuated to zero. These results are consistent with experimental observations of laser cavities modelocked by active modulation [3].

References

[1] I. N. Duling, III and M. L. Dennis, *Compact sources of ultrashort pulses*, (Cambridge University Press, Cambridge, 1995).

[2] H. A. Haus, J. G. Fujimoto, and E. P. Ippen, "Structures for additive pulse mode locking," J. Opt. Soc. Am. B **8**, 2068-2076 (1991).

[3] F. X. Kärtner, D. Kopf, and U. Keller, "Solitary-pulse stabilization and shortening in actively mode-locked lasers," J. Opt. Soc. Am. B **12**, 486-496 (1995).

[4] H. A. Haus, "A theory of forced mode locking," IEEE J. Quant. Elec. **11**, 323-330 (1975).

[5] "Handbook of Mathematical Functions," edited by M. Abramowitz and I. A. Stegun (National Bureau of Standards, Washington, DC, 1964).

On the theory of self-similar parabolic optical solitary waves

Sonia Boscolo and **Sergei K. Turitsyn**

Photonics Research Group, School of Engineering and Applied Science,
Aston University, Birmingham B4 7ET, UK
Tel: +44 (0)121 359 3621 ext 4961, Fax: +44 (0)121 359 0156,
Email: boscolsa@aston.ac.uk

Victor Yu. Novokshenov

Institute of Mathematics RAS, 450000 Ufa, Russia

Jeroen H.B. Nijhof

Marconi Solstis, Stratford Technology Park, Stratford-Upon-Avon CV37 7GY, UK

Abstract: Solutions of the nonlinear Schrödinger equation with gain, describing optical pulse propagation in an amplifying medium, are examined. A self-similar parabolic solution in the energy-containing core of the pulse is matched to the linear low-amplitude tails. The theoretical analysis reproduces accurately the numerically calculated solution.
© 2002 Optical Society of America
OCIS codes: (060.2330) Fiber optics communications; (190.5530) Pulse propagation and solitons

Self-similarity techniques have been applied to study high-power pulse propagation in normal-dispersion fibres and fibre amplifiers. It has been shown that linearly chirped parabolic pulses are approximate self-similar solutions of the nonlinear Schrödinger equation (NLSE) in the high-intensity limit [1, 2]. Theoretical results have been confirmed experimentally [3]. The derivation of parabolically-shaped solutions in [1, 2] is based on the assumption that the linear dispersive term in the equation for the field amplitude is negligible as compared to the nonlinear term, similar to the quasi-classical approximation in quantum mechanics. Though the central core of the solution has already been described in the literature for some physical problems [1, 2], a comprehensive theory that includes matching with the linear tails has not been presented yet. In this paper we present the results of a detailed analysis of the solutions of the NLSE with gain. We construct a quasi-classical self-similar solution with parabolic temporal variation, that corresponds to the energy-containing core of the asymptotically propagating pulse in the amplifying medium. We match the self-similar core through Painlevé functions to the solution of the linearized equation, that corresponds to the low-amplitude tails of the pulse. The analytical solution proves to reproduce accurately the numerically calculated solution of the NLSE.

Localized optical pulse evolution in an amplifying medium in the absence of gain saturation and for incident pulses with spectral bandwidths less than the amplification bandwidth can be described by the well-known NLSE with gain term [4]:

$$i\psi_z - \frac{\beta_2}{2}\psi_{tt} + \sigma|\psi|^2\psi = i\frac{g(z)}{2}\psi. \tag{1}$$

We are looking for a solution of the form

$$\psi(z,t) = a(z)F(\eta,\xi)e^{iC(z)t^2}, \tag{2}$$

where new self-similar variables are introduced as $\xi = t/\tau(z)$, $\mathrm{d}\eta/\mathrm{d}z = \sigma a^2(z)$. These transformations yield coupled equations for a, τ, C, and F:

$$\frac{a_z}{a} = \beta_2 C + \frac{g}{2}, \qquad \frac{\tau_z}{\tau} = -2\beta_2 C, \qquad \left(C_z - 2\beta_2 C^2\right)\tau^2 = -\lambda\sigma a^2, \tag{3}$$

$$iF_\eta + (|F|^2 + \lambda\xi^2)F - \frac{1}{c(\eta)}F_{\xi\xi} = 0, \qquad c = \frac{2\sigma a^2\tau^2}{\beta_2}, \tag{4}$$

where λ is an arbitrary parameter, related to the pulse power. We separate F into a real amplitude A and a phase Φ, according to $F(\eta,\xi) = A(\eta,\xi)e^{i\Phi(\eta,\xi)}$, to obtain from Eq. (4) the "hydrodynamical" system of equations:

$$(A^2)_\eta - \frac{2}{c(\eta)}(A^2\Phi_\xi)_\xi = 0, \qquad \Phi_\eta + \frac{1}{c(\eta)}\left[\frac{A_{\xi\xi}}{A} - (\Phi_\xi)^2\right] - (A^2 + \lambda\xi^2) = 0. \tag{5}$$

First, we consider a possibility of an approximate description of the energy-containing core. Let us define a parameter ϵ as the ratio of the linear dispersive term to the nonlinear term in the second of Eqs. (5):

$$\epsilon(\eta, \xi) = \left| \frac{A_{\xi\xi}}{c(\eta)A^3} \right|. \tag{6}$$

High-intensity pulses are solutions for which the condition $\epsilon \ll 1$ is satisfied. This condition corresponds to the so-called quasi-classical limit of Eq. (1). When such a condition is met, the linear dispersive term in the second of Eqs. (5) can be neglected, and so it is easy to find a self-similar solution with a parabolic distribution of the intensity:

$$A(\xi) = [\lambda(1 - \xi^2)]^{1/2}, \qquad |\xi| \le 1, \qquad \Phi(\eta) = \lambda\eta. \tag{7}$$
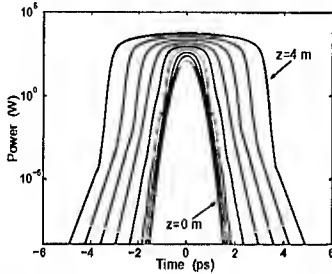
Fig. 1. Pulse evolution in the amplifier. Intensity profiles plotted on a logarithmic scale in 0.5 m increments.
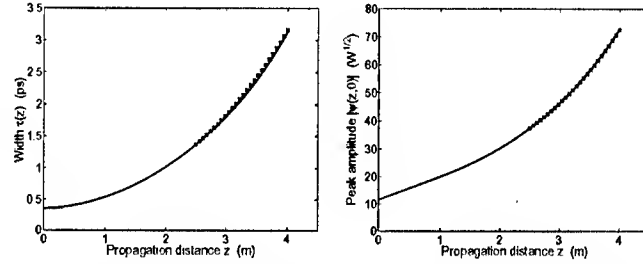
Fig. 2. Evolution of effective pulse width $\tau(z)$ and peak amplitude $|\Psi(z,0)|$. Solid curves, simulation results; x-marks, theoretical predictions for $z \ge 2.5\,\mathrm{m}$.

Figure 1 shows an example of pulse evolution in the amplifier obtained from numerical simulation of Eq. (1). In this example we have modeled the propagation of a Gaussian pulse with a FWHM pulse width of 0.5 ps and an energy of 70 pJ in a fibre amplifier with length of 4 m, an integrated gain of 25 dB, $\sigma = 6 \times 10^{-3}\,\mathrm{W^{-1}\,m^{-1}}$, and $\beta_2 = 35 \times 10^{-3}\,\mathrm{ps^2\,m^{-1}}$ [3], and we have considered a constant gain profile, $g(z) = g_a$ with $g_a = 1.44\,\mathrm{m^{-1}}$. We can see that, as the incident Gaussian pulse is amplified to high intensity, it evolves into a parabolic pulse in the second half of the amplifier. The interesting feature emerging from Fig. 1 is that the asymptotic pulse presents a self-similar energy-containing parabolic core sourrounded by low-amplitude wings. These tails start developing on the pulse near the points $t = \pm\tau$, i.e. in the region where the linear term neglected in the theory becomes important. Therefore the description of these tails requires a more detailed analysis of the pulse shape. Considering the asymptotic parabolic regime that occurs after some initial transition stage, here after a propagation distance of 2.5 m, we have compared the evolution of the pulse parameters from simulations with theory. Figure 2 shows the evolution of the effective width $\tau(z)$ and the peak amplitude $|\psi(z,0)|$ obtained from simulations (solid curves) and from the solutions of Eqs.(3) and (7), calculated for $z \ge 2.5\,\mathrm{m}$ (x-marks).
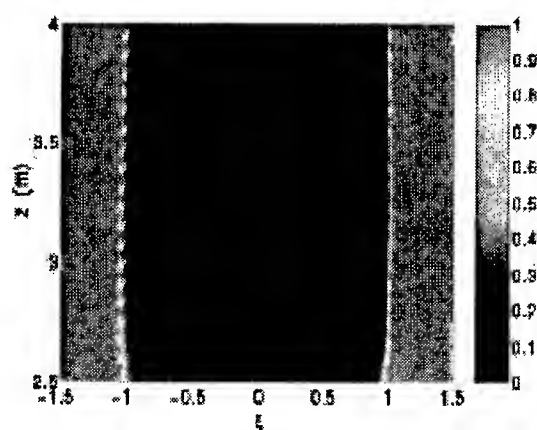
Fig. 3. Evolution of ϵ as a function of distance z and normalized time ξ, for $-1.5 \le \xi \le 1.5$ and $z \ge 2.5\,\mathrm{m}$.

These results, similar to those in [2], show that the parabolic approximation for the pulse shape can describe the central part of the asymptotically propagating pulse in the amplifying medium. Our aim now is to include

in the description the pulse tails. For this purpose, first of all we have studied the evolution in the plane time-distance of the parameter ϵ defined in Eq. (6). Figure 3 shows the evolution of ϵ as a function of propagation distance z and normalized time ξ calculated from numerical simulation of Eq. (1). The variation of ϵ is shown in the asymptotic regime, starting from 2.5 m propagation distance. The entire colormap is used for values ranging from 0 to 1, with values greater than 1 rendered with the same color associated to 1. It is clear from Fig. 3 that the transition of ϵ from values < 1 to values > 1 occurs in a narrow region around the points $\xi = \pm 1$, and this is in agreement with our intuitive expectations. One may also see that in the asymptotic regime the transition region does not move with distance (being presented in self-similar variables). On the basis of these results we define three regions on the ξ-axis. As the problem is symmetric in ξ we can limit our considerations to the semiaxis $\xi \geq 0$. Region (I), $0 \leq \xi \leq 1 - \Delta_1$, corresponds to the central part of the asymptotic pulse, where $\epsilon \ll 1$. Region (III), $\xi \geq 1 + \Delta_2$, corresponds to the pulse tails, where $\epsilon \gg 1$. Finally region (II), $1 - \Delta_1 \leq \xi \leq 1 + \Delta_2$, is a transition zone, where $\epsilon \approx 1$. The size of the transition zone is parametrized by $\Delta_1, \Delta_2 \ll 1$. We introduce two different Δ-intervals for the (left and right) regions around the point $\xi = 1$ because of an obvious asymmetry of the solutions relative to this point. In each of the regions we construct an approximate solution of Eq. (4), or equivalently of the system (5), at fixed η. We then match the solutions at the boundaries. Here, we only outline the procedure and we present the main results of the analysis. In region (I) we consider the quasi-classical solution specified by Eqs. (7). In region (III) we neglect the nonlinear term in the second of Eqs. (5) and solve the corresponding linearized system. The quasi-classical parabolic solution in the central part is then matched to the linear one through the small intermediate transition region. Following [5], the equation for the field amplitude in the transition region can be reduced to the second Painlevé equation (P_{II}). The asymptotic behaviours of the Painlevé transcendents and the connection problems for the Painlevé equations have been considered in many works (see e.g. [6]). Here, by using the asymptotic results for P_{II} we solve the amplitude matching problem. The construction of the solutions is completed by matching the phase of the field.
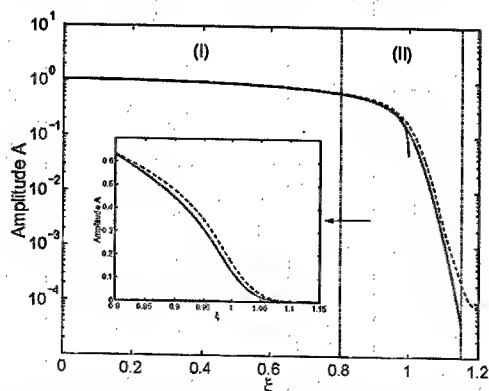
Fig. 4. Variation of the amplitude A as a function of ξ at the amplifier output. Dashed curve, numerical solution; solid curve, solution of the matching problem for $\Delta_1 = 0.2$ and $\Delta_2 = 0.15$; dotted curve, parabolic solution for $\Delta_1 = 0$. Inset: numerical solution and solution of the matching problem shown on a linear scale.

The solution of the matching problem has been compared with the numerical solution of Eq. (1). An example is given in Fig. 4, that shows the amplitude A of F as a function of ξ, for $0 \leq \xi \leq 1 + \Delta_2$, at the final distance in the amplifier. The dashed curve represents the numerical solution, while the solid curve represents the solution of the matching problem. The parabolic solution (7) is also plotted for $\Delta_1 = 0$ (dotted curve). The values of $\Delta_{1,2}$ used in Fig. 4 are $\Delta_1 = 0.2$ and $\Delta_2 = 0.15$. It can be seen that there is a good agreement between the analytical and the numerical results. As the inset clearly shows, the difference between the analytical and the numerical curves is, in fact, of order of $\Delta_{1,2}^2$, and this is consistent with our expectations, since the lowest order terms neglected in the analytical treatment are $O(\Delta_{1,2}^2)$.

In conclusion, we have examined solutions of the NLSE with gain, that governs optical pulse propagation in a fibre amplifying medium. Quasi-classical solutions with a parabolic temporal profile in the energy-containing core have been analysed theoretically and numerically. We have presented matching of the parabolic solution to the linear low-amplitude tails of the pulse. The theoretical analysis has been shown to reproduce accurately the solution obtained from numerical simulation of the NLSE.

References

1. D. Anderson, M. Desaix, M. Karlsson, M. Lisak, and M.L. Quiroga-Teixeiro, J. Opt. Soc. Am. B **10**, 1185 (1993).
2. V.I. Kruglov, A.C. Peacock, J.M. Dudley, and J.D. Harvey, Opt. Lett. **25**, 1753 (2000).
3. M.E. Fermann, V.I. Kruglov, B.C. Thomsen, J.M. Dudley, and J.D. Harvey, Phys. Rev. Lett. **84**, 6010 (2000).
4. E. Desurvire, *Erbium-Doped Fiber Amplifiers: Principles and Applications* (Wiley, New York, 1994).
5. V.E. Zakharov and E.A. Kuznetsov, Sov. Phys. JETP **64**, 773 (1986).
6. A.R. Its and V. Yu. Novokshenov, *The Isomonodromic Deformation Method in the Theory of Painlevé Equations*, Lecture Notes in Math. **1191** (Springer-Verlag, Berlin, 1986).

Error preventable line-coding schemes using bi-soliton to suppress intra-channel interactions in dispersion-managed system

Akihiro Maruta, Yasumichi Nonaka, and Takashi Inoue

Graduate School of Engineering, Osaka University
2-1 Yamada-oka, Suita, Osaka, 565-0871, JAPAN
Phone : +81-6-6879-7728, Fax : +81-6-6879-7688,
E-mail : maruta@comm.eng.osaka-u.ac.jp

Abstract: Bi-soliton is a periodically stationary pulse propagating in a dispersion-managed (DM) transmission system. We propose novel transmission line coding schemes in which binary data are assigned to single DM solitons and bi-solitons to reduce impairments arising from intra-channel interactions.

© 2002 Optical Society of America
OCIS codes: (190.4370) Nonlinear Optics, fibers ; (190.5530) Pulse propagation and solitons

Dispersion management is an essential technique to achieve long haul and high speed optical fiber transmission system. For a high speed system in which the bit rate is more than 40Gbit/s, intra-channel interactions play an detrimental role to extend the transmissible distance even in a single channel case. Bi-soliton[1] which is a periodically stationary pulse propagating in a dispersion-managed (DM) transmission system has a preferable feature for high bit-rate system because it is not affected with time position shift due to intra-channel interactions. In this paper, we propose novel transmission line coding schemes in which binary data are assigned to single DM solitons and bi-solitons. By using these schemes, impairments arising from intra-channel interactions can be drastically reduced. We also show that anti-phase (antisymmetric) bi-soliton[2] can be more densely packed in time than in-phase (symmetric) bi-soliton[1].

The optical pulse propagation in a DM system can be described by

$$i\frac{\partial u}{\partial z} - \frac{\beta(z)}{2}\frac{\partial^2 u}{\partial t^2} + s(z)|u|^2 u = 0 , \tag{1}$$

where $u(z,t)$ represents the complex envelope of electric field. $\beta(z)$ is fiber's group velocity dispersion and $s(z)$ is fiber's nonlinearity including the variation of optical power due to fiber's loss. z is the transmission distance and t is the retarded time. Here we consider a system in which both $\beta_2(z)$ and $s(z)$ are periodic functions of z with their period L. Only for simplicity, we consider a system in which $\beta(z) = \beta_1$ and $s(z) = s_1$ for $|z - nL| < L_1/2 \; (< L/2)$ and $\beta(z) = \beta_2$ and $s(z) = s_2$ for $L_1/2 < |z - nL|(< L/2)$ where $L = L_1 + L_2$ and n is an integer. We introduce the following three system parameters, the path-averaged dispersion B, the map strength S, and the ratio of accumulated nonlinearity in the fiber of s_1 to the total accumulated nonlinearity R, which characterize the dispersion map completely[1].

$$B = (\beta_1 L_1 + \beta_2 L_2)/\tau_m^2 , \qquad S = (|\beta_1|L_1 + |\beta_2|L_2)/\tau_m^2 , \qquad R = s_1 L_1/(s_1 L_1 + s_2 L_2) . \tag{2}$$

where τ_m represents the pulse's minimum FWHM in the period L. In the symmetric dispersion map, τ_m is observed at $z = nL$.

As we have shown in Ref.[1], in-phase bi-soliton can exist around $2 < S < 2.7$ and $0.75 < R < 1$ for $B = -0.1$ and the pulses spacing $t_s = 3\tau_m$. Figure 1 shows the evolution of waveform along the transmission line when the amount of input consecutive gaussian pulses are changed from 1 to 4. System parameters, $S = 2.3$, $B = -0.1$, and $R = 0.8$, under which both DM soliton and in-phase bi-soliton can exist are used. As one can see, 3 or 4 cosecutive pulses are affected with time position shifts and finally collide. Transmission line

coding schemes in which consecutive pulses more than 3 are excluded therefore should be designed to apply the bi-soliton to high bit-rate transmission system. We define the code I in which binary data, '1' and '0' are directly assigned to a pulse and a space respectively. In the code II, the binary data are firstly converted to one of three symbols, '00', '01', and '10', and then '0' and '1' in each symbol are converted into a pulse and a space respectively By using the code II, the amount of consective pulses is 2 at most.

For the width of time slot $t_s = 4\tau_m$[s] with the code I, the bit rate is $0.25/\tau_m$[bit/s]. Since the amount of symbols is 3 in the code II, the information content per symbol is $\log_2 3 = 1.585$[bit/symbol]. Adopting in-phase bi-soliton of $t_s = 3\tau_m$ in the code II, the symbol rate is $1/6\tau_m$[symbol/s] and the bit rate is then $0.264/\tau_m$[bit/s]. This fact means that the bit rate of the proposed code II is 1.05-fold larger than that of the code I. Let us compare these coding schemes with a concrete coding table shown in Table 1. Binary data of three figures are assigned to two symbols of the code II and the information content per symbol is 1.5bit/symbol. For the width of the time slot $t_s = 4\tau_m$ in the code I and $3\tau_m$ in the code II, both of the bit rates are the same. Figure 2(a) shows the evolution of the waveform using the code I for the system parameters, $S = 1.65$, $B = -0.1$, and $R = 0.5$, with which in-phase bi-soliton does not exist. For the initial input, binary data of 15 bits, '010110010001111', are directly converted to chirp-free gaussian pulses and spaces. Pulses' time position shifts induce the bit error after 200 periods transmission. Figure 2(b) shows the case using the code II for $S = 2.3$, $B = -0.1$, and $R = 0.8$. In this case, the same binary data are replaced to the symbols, '001010000010000011001', according to Table 1, the symbols are then converted to chirp-free gaussian pulses and spaces. Any time shift does not observed and stable pulse transmission is achieved for long distance. Generally speaking, the strength of interactions between neighborng solitons increase exponentially for narrower pulse spacing[3]. While the interactions occur between neighboring pulses of $t_s = 4\tau_m$ for the code I, $6\tau_m$ for the code II because the interaction induced time shift does not occur in bi-soliton. This is the reason why the interactions can be drastically reduced by using the proposed code II. To reducing the interactions in the code I, B and/or the peak power of input pulse should be reduced. In the code II, B and the peak power of input pulse can be kept large value and the signal-to-noise ratio can be improved. For packing the data more densely in time, anti-phase bi-soliton can be used because it exists for the system parameters, $S = 1.9$, $B = -0.1$, $R = 0.5$, and $t_s = 2\tau_m$. Figure 3(a) shows the evolution of the waveform using the code III whose phases are modulated as 'ss0s0sssss0ssssπ0ssπ'. In the sequence, 's' means a space. This is corresponding to carrier suppressed return-to-zero (CS-RZ) signal format. Interactions between neighboring in-phase pulses of $t_s = 4\tau_m$ induce the collision in this case. Figure 3(b) shows the case using the improved code IV whose phases are 'ss0sπsssss0ssssπ0ssπ'. In this code, not only the neighboring pulses of $t_s = 2\tau_m$ but also pulses of $t_s = 4\tau_m$ are anti-phase. Any time shift does not observed and densely packed transmission is achieved for long distance because the neighboring pulses of $t_s = 4\tau_m$ also form an anti-phase bi-soliton.

In conclusion, we have proposed novel transmission line coding schemes using the advantage of bi-soliton. It is effective for the system whose bit rate is over 40 Gbit/s in which the intra-channel interaction play the detrimental role to extend the transmissible distance.

References

1. A. Maruta, Y. Nonaka, and T. Inoue, 'Symmetric bi-soliton solution in a dispersion-managed system', Tech. Digest of NLGW2001, Clearwater, FL, Paper PD-4, and Electron. Lett., **37**, 1357-1358 (2001).

2. C. Paré and P. -A. Bélanger, 'Antisymmetric soliton in a dispersion-managed system', Opt. Commun., **168**, 103-109 (1999).

3. A. Hasegawa and Y. Kodama, Solitons in optical communications, p.153, Oxford University Press, Oxford, 1995.
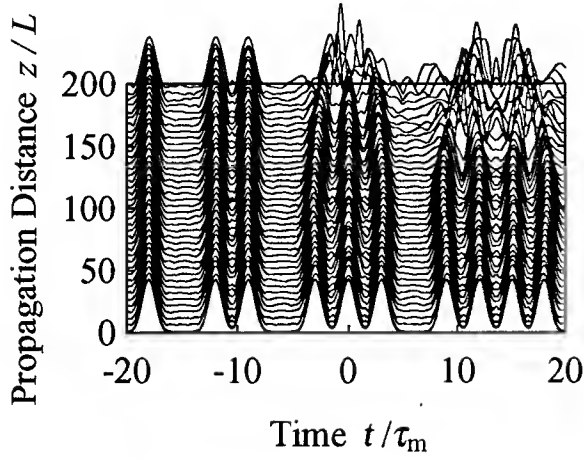
Fig. 1. Evolution of consecutive pulses.

Binary data	Code I	Code II
000	'0' '0' '0'	'00' '00'
001	'0' '0' '1'	'00' '01'
010	'0' '1' '0'	'00' '10'
011	'0' '1' '1'	'01' '00'
100	'1' '0' '0'	'01' '01'
101	'1' '0' '1'	'01' '10'
110	'1' '1' '0'	'10' '00'
111	'1' '1' '1'	'10' '01'
————	————	'10' '10'

Table 1. Symbol assignment for binary data of three figures.
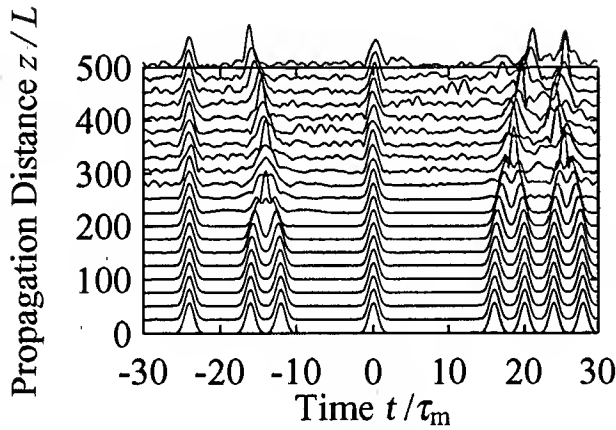
(a) using the code I.
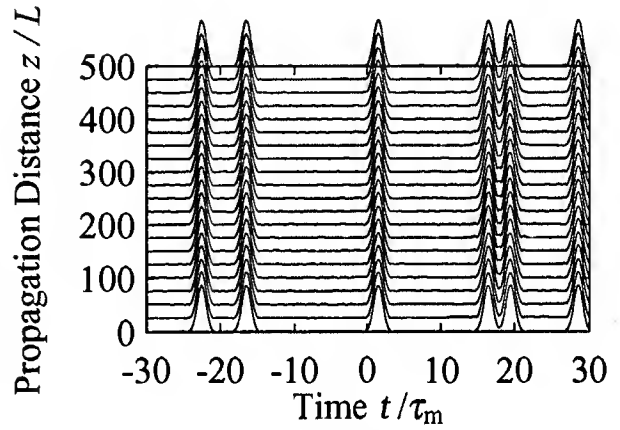
(b) using the code II.

Fig. 2. Evolution of bit sequence in a long haul transmission.
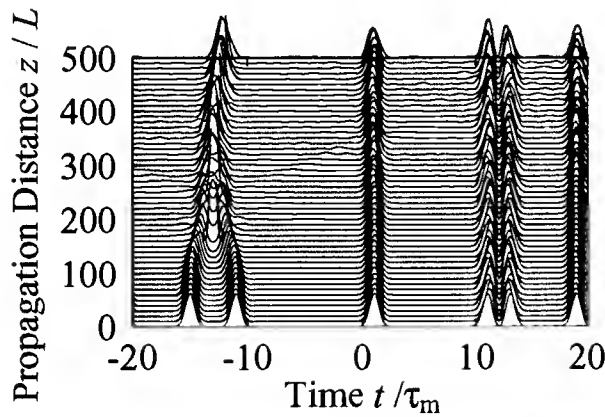
(a) using the phase modulated code III.
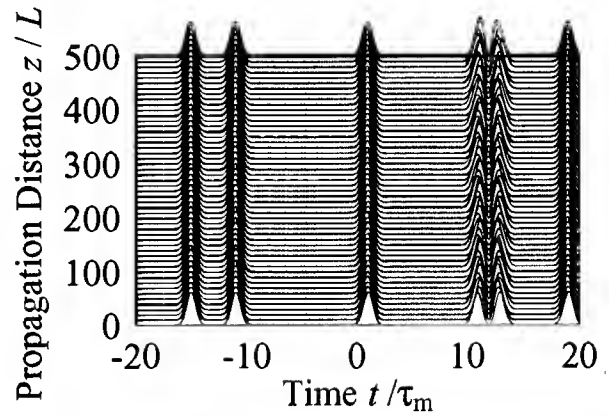
(b) using the phase modulated code IV.

Fig. 3. Evolution of bit sequence using anti-phase bi-soliton.

EXPERIMENTAL INVESTIGATIONS AND THEORETICAL DESCRIPTION OF THE SPECTRAL BROADENING OF A FEMTOSECOND PULSE TRAIN IN TAPERED FIBER

S.N.Bagayev[1], S.V.Chepurov[1], V.I.Denisov[1], A.K. Dmitriyev[1], A.S. Dychkov[1], V.M.Klementyev[1], D.B.Kolker[1], I.I.Korel[1], S.A.Kuznetsov[1], Yu.A.Matyugin[1], M.V. Okhapkin[1], V.S.Pivtsov[1], M.N. Skvortsov[1], V.F.Zakharyash[1], T.A.Birks[2], W.J.Wadsworth[2], P.St.J.Russell[2]

[1]Institute of Laser Physics, Siberian Branch of RAS, Lavrentyeva 13/3, 630090 Novosibirsk, Russia
[2] Department of Physics, University of Bath, Bath BA2 7AY, United Kingdom

INTRODUCTION

The radiation of continuous mode-locked lasers in the time domain is a sequence of short light pulses. The radiation spectrum of such lasers is a set of equidistant modes. This property is given by the condition of existence of the mode locking regime. It has been found experimentally that Δv (distance between the neighboring modes) is the same in all parts of the spectrum with an accuracy not worse than 10^{-16} [1]. Recently a separate direction on the applications of broadened by use of optical fiber discrete femtosecond laser radiation spectrum was formed in high-precision spectroscopy. This effect is especially important considering frequency synthesis processes and absolute frequency measurements in all wavelength ranges [1-4]. Special interest in tapered fibers is due to the high transformation effectiveness along with relatively low laser power required for spectral broadening and general experimental simplicity [5].

In spite of the fact that microstructure (or holey) and tapered fibers are widely used now to broaden the spectrum of femtosecond lasers, they have been poorly investigated. The broadening takes place owing to nonlinear interaction between radiation modes. There exist several nonlinearities in the fiber. Their contribution to the process of interaction of modes has also been little investigated. Optimal relations in the fiber configuration are not clear. The influence of the fiber on the increase of noise in the spectrum of passing radiation has not been investigated. It is not clear with what accuracy the equidistant character of frequency components after the fiber is preserved. This can take place because laser modes have finite width, and after transformation in the fiber their shape changes non-symmetrically. These factors determine the maximal achievable accuracy of measurements of schemes with the use of fibers. We experimentally investigated the shape of the envelope of the spectrum of output radiation for tapered fibers versus the waist diameter (Fig.1). We investigated fibers with waist diameters of 2 μm, 2,5 μm, and 3 μm. The parameters of input radiation are as follows: the central wavelength is 810 nm, the spectrum width is 20 nm, the pulse duration is 40 fs, and the average power is 200 mW. Typical characteristics of the spectrum envelope – long-wave maximum for all fibers, 2.5 μ m fibers have no central maximum but a number of short-wave maximums can be observed in contrast to 2 μ m and 3 μ m fibers that have an intensive maximum on the laser radiation wavelength and practically no short-wave maximums. Thus, for the 2.5 μ m fibers unlike 2 μ m and 3 μ m fibers a strong energy pumping from the laser radiation frequencies to the broadened spectrum edges was detected. Figures with double curves show dependencies for two different tunings of the input radiation relative to the fiber axis.

There are two general approaches to the ultrashort pulse train spectra theoretical investigations. First considers the ultrashort pulse train in fiber as a multi-mode field. This approach assumes the solution of a self-consistent system for propagation of the discrete spectral components in fiber. While it permits to get some important qualitative understanding, exact analytical solution is impossible and thorough numerical analysis needs a tremendous calculation efforts and resources. The second approach considers a pulse train spectrum as a result of the pulse train Fourier transform. This approach usually is the most effective because it permits to perform a numerical calculations in accordance with statistical methods.
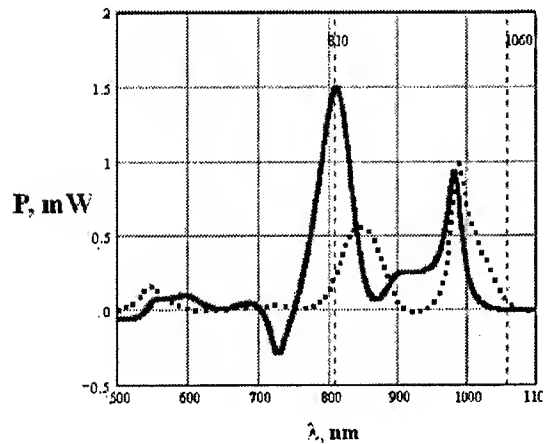
2 µm waist fiber
dots —max power at 1 mkm adjustment,
solid —max integral output power
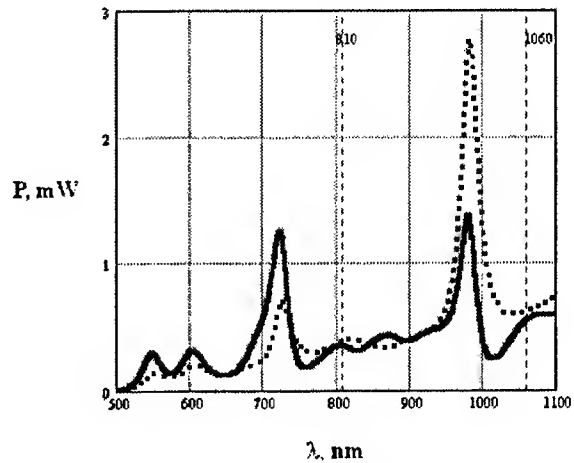
2,5 µm waist fiber
dots —max power at 1 mkm adjustment,
solid —max integral output power

Fig. 1. Power distribution at the output of tapered fibers

Our investigation based on the compilation of both approaches. We consider theoretical models, which describe self-phase modulation, dispersion, phase cross-modulation etc. with experimental results on given pulse train and fiber parameters processes of pulse train spectrum formation along with spectral distortions.

Spectral broadening in optical fibers is associated with an influence of the self-phase modulation (SPM) [6]. While SPM is a nonlinear effect and its significance can be estimated by comparison of the nonlinear length L_{NL} with the length of fiber, spectral broadening is proportional to the relation L/L_{NL}. For the the experimental tapered fiber (L ≈ 60mm) and pulse train of 500 mW average power, this relation is about 10^2, thus, the measured broadened spectrum was about 90 THz. Dispersion parameters were small in comparison with nonlinear characteristics and condition L_{NL}/L_D << 1 was true, (here L_D - dispersion length), thus for the general consideration of the single pulse propagation, dispersion effects could be neglected, however considering a pulse train with amplitude and phase fluctuations, it is important to solve a general pulse propagation problem. Figure 2 shows the result energy spectrum obtained by numerical solution of propagation problem for a sequence of 10^3 femtosecond pulses with experimental parameters and intensity fluctuations of 10^{-2} level along with experimental results. The typical feature of SPM effect is an oscillation structure with high peaks on the edges and number of peaks is close to the broadening coefficient. However, intensity and phase fluctuations along with the influence of dispersion effects smooth over the oscillation structure as it can be seen on figure.

Investigation of the tapered fiber influence on the noise pedestal of intermode beats was made for the 1st and 10th harmonics for different broadened spectrum ranges and for the full spectrum with different resolution and power of the input radiation. Processing of the spectrum permitted to divide phase and amplitude noises and to estimate the transformation level of the amplitude noise into phase noise in various conditions. For experimental conditions it was shown that tapered fiber increases insignificantly noise pedestal and transforms the amplitude noise into the phase noise.
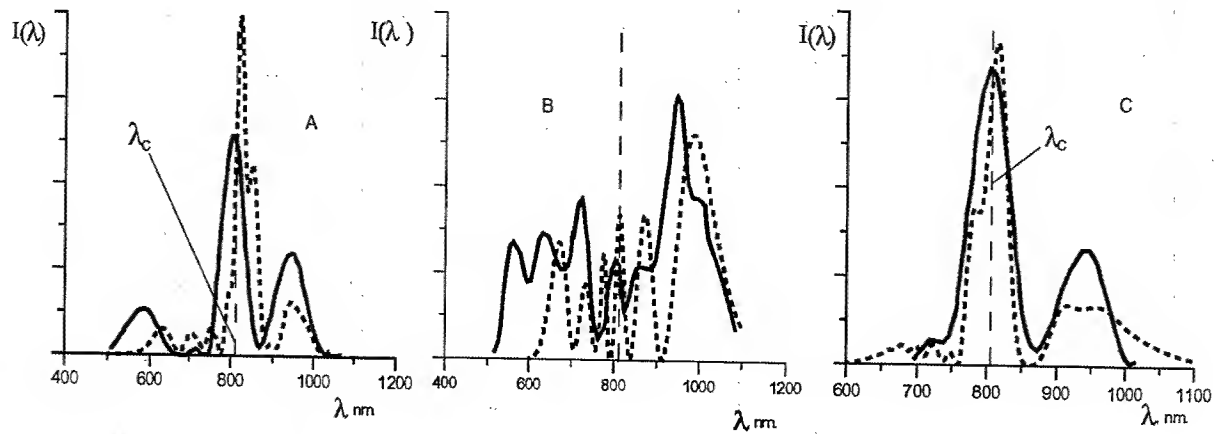
Fig. 2. Energy spectra of the femtosecond pulse train.
Solid line - experiment, dash line – theory, the nonlinear length $L_{NL} \approx 0.6$ mm, A – taper diameter d = 2 μm, zero-GVD wavelength λ_D = 680 nm; B - d = 2.5 μm, λ_D = 790 nm; C - d = 3 μm, λ_D = 900 nm

Investigations of the intermode frequency stability at different averaging times were carried out at the input and output of the tapered fiber. The experiments has shown that after the passage of the fiber the intermode frequency stability decreased slightly due to increase in the phase fluctuations. The short term stability (averaging time of 10 s) at the fiber output was two times less than that at the input. The long term stability (averaging time of 1000 s) practically did not change. Series of experiments in order to find out a possible influence of the spectral interval of measurement on the stability was carried out in the following way: the broadened spectral range was divided by use of light filters into two subregions and for each subregion an average value of measuring frequency on the fiber output was obtained. The experiments has shown that the intermode frequency stability does not depend on the broadened spectrum range.

Thus, a perspective of tapered fiber usage in precise optical frequency synthesizers and femtosecond optical clocks was demonstrated.

ACKNOWLEDGEMENT

REFERENCES

1. Th. Udem, J. Reichert, R. Holzwarth, T.W.Haensch, "Accurate measurement of large optical frequency differences with a mode-locked laser", Opt. Lett., v.24, 991-993 (1999).
2. S.A.Diddams, D.J.Jones, J.Ye, S.T.Cundiff, J.L.Hall, J.K.Ranka, R.S.Windeler, R.Holzwarth, T.Udem, T.W.Haensch, "Direct Link Microwave and Optical Frequencies with a 300 THz Femtosecond Laser Comb", Phys. Rev. Lett., v. 84, 5102 – 5105 (2000).
3. H.R.Telle, G.Steinmeyer, A.E.Dunlop, J.Stenger, D.H.Sutter, U.Keller, "Carrier-envelope offset phase control: A novel concept for absolute optical frequency measurement and ultrashort pulse generation", Appl.Phys. v.B69, 327-332 (1999).
4. S.N.Bagayev, S.V.Chepurov, V.M.Klementyev, S.A.Kuznetsov, V.S.Pivtsov, V.V.Pokasov, V.F.Zakharyash, "A Femtosecond Self-Mode-Locked Ti:Sapphire Laser with High Stability of Pulse-Repetition Frequency and its Applications", Appl.Phys. v.B70, 375 - 378 (2000).
5. T.A.Birks, W.J.Wadsworth, and P.St.J.Russell, "Supercontinuum generation in tapered fibers", Opt. Lett., v. 25, 1415 - 1417 (2000).
6. G.P. Agrawal, Noninear fiber optics, New York, Academic Press, Ch. 4, pp. 93, 1989.

Wavelength conversion of femtosecond pulses by cross-phase modulation in single-mode fibers

Gilbert Boyer

Laboratoire d'Optique Appliquée, Ecole Polytechnique-ENSTA, Centre de l'Yvette, Chemin de la Hunière 91761 Palaiseau, France
Tel :+33 1 69 31 97 31
Fax : +33 1 69 31 99 96
e-mail : boyer@enstay.ensta.fr

The optical fiber is an ideal tool for studying the dynamics of nonlinear interaction between pulses, and here in particular the wavelength-shift induced by cross-phase modulation (XPM) in an ultrashort pulses pump-probe configuration. So far, significant wavelength shifts in the visible and near-infrared have been demonstrated and modeled [1]. To demonstrate further the potentiality for all-optical switching and mux/demux applications, it is relevant to quantify the importance of the probe time-profile reshaping. To the best of my knowledge the present contribution is the first to present and discuss the autocorrelation traces of blue- and red-shifted femtosecond probes. In comparison to the picosecond regime, some particularities of the variations of the wavelength conversion as a function of the initial relative time-delay are depicted and interpreted in terms of pulse trapping across the fiber zero-dispersion wavelength (ZDW) [2].

Experimentally, the pulse pair was synthesized by filtering the spectrum of a Kerr-lens mode-locked Cr^{4+}:forsterite laser delivering pulses 110 fs full width at half maximum (FWHM) at the central wavelength of 1256 nm, 84 MHz in repetition rate [1]. Filtering was performed with two slits mounted as to allow for varying the pulses spectra in position and width. The pulse synthesizer consisted of a diffraction grating 600 rules/mm and a reflector. These two elements were positioned on both sides and in the focus planes of an achromatic doublet of a focal length of 250 mm [1]. The reflector was constituted by two parallel mirrors, one of which could be moved along the optic-axis to vary the pump-probe relative delay without any significant misalignment of the synthesizer. Careful alignment was found to be critical for the maximization of the wavelength-conversion amplitude. The pump central wavelength was λ_P =1256 nm, with an energy of 280 pJ per pulse and a duration of 340 fs. A generally occurring feature of solid-state lasers is the existence of sidebands of the emission spectrum. One of which was used as a probe. Its spectrum was centered on λ_T =1307 nm (see fig. 1a) with a spectral width of 4.49 nm FWHM, a width of 460 fs FWHM, and a pulse energy of about 550 nJ. The laser

beam was injected into a 9.8 m-long standard single-mode fiber with a ZDW of 1293 nm and an effective cross-section of 2.26×10^{-11} m². A background-free second-harmonic generation (SHG) autocorrelator was used for the observation of temporal reshaping. Careful optimization of that instrument was necessary to detect low peak power pulses. A high-pass high-slope filter at 1293 nm was used to block the pump radiation.
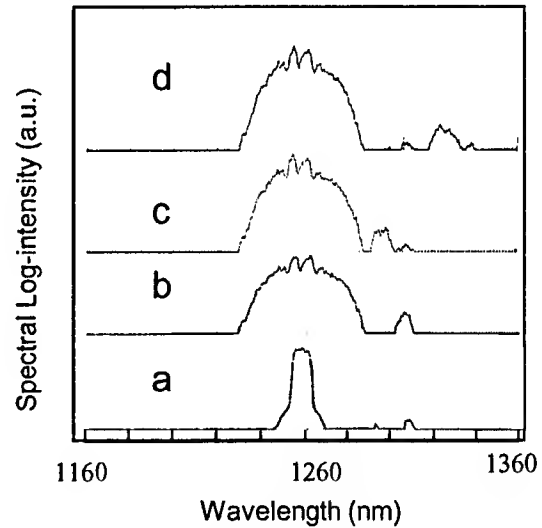
Fig. 1 : Spectra of the pulse pair before (a) and after propagation without non-linear interaction (b), with a blue-shift (c), and with a red-shift (d) of the probe pulse. The structure on top of the propagated pump is due to the spectral filtering with a slit.

The fiber GVD parameter $D(\lambda)$ was measured by synchronously injecting a pair of slightly detuned pulses, of equal peak power and width, and satisfying the condition $L_{NL} \gg L_D$, where L_{NL} and L_D are the nonlinear and dispersion lengths, respectively. The group-time mismatch was plotted after the autocorrelation trace as the two wavelengths were varied across the laser spectrum. $D(\lambda_P)$ and $D(\lambda_T)$ were found to be -0.76 ps/km/nm and 1.9 ps/km/nm, respectively, and to vary linearly between these two points.

The initial pulse-pair spectrum is in fig. 1a. Fig. 1b depicts the propagated pulse-pair for a complete time mismatch where pump appears spectrally broadened by the interplay between self-phase modulation (SPM) and GVD. According to the initial relative-delay setting, a blue or red shift is observed, as shown on figs. 1c and 1d, respectively, producing well-contrasted spectra and a wavelength-conversion range as large as 26 nm.
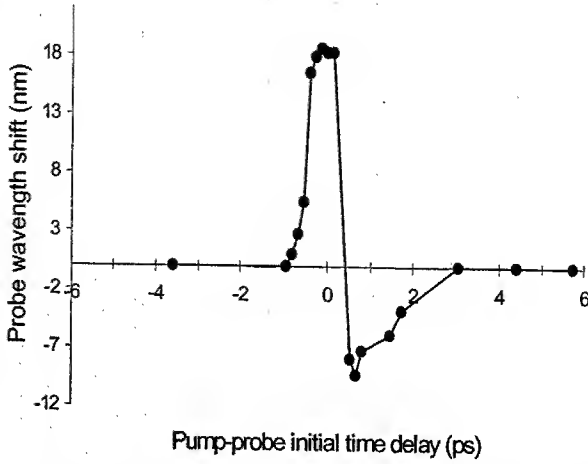
Fig. 2: Probe wavelength conversion as a function of the initial relative initial delay, which is positive when the probe lags the pump.

This wavelength shift was observed to increase with the injected pump power. The structures on the pump spectra of figs. 1b, c and d are due to the filtering with the slit of the synthesizer. Figs. 1c and 1d exhibit a probe residue that accompanies the shifted spectrum. This is can be explained by the different initial time widths of the pulse pair not allowing complete overlap and thereby leaving a small part of the probe remaining unshifted. This feature has been found to disappear when the two pulses were set to the same initial width. XPM-induced spectral broadening is visible on figs. 1c and 1d.

The variations of the wavelength conversion with respect to the initial relative delay are shown in fig. 2 and deserve further attention. In the present experiment the probe travels faster than the pump, and hence a maximum blue shift should be obtained when the probe just catches up with the pump trailing edge at the fiber end. Neglecting the pump broadening for the sake of simplicity, the corresponding relative delay for a maximum blue shift is approximated by $\delta T + T_{oP}/2$, where δT is the group-time mismatch over the fiber length l and T_{oP} is the pump half-width at 1/e-intensity point. Conversely, the maximum red shift occurs when the probe interacts with the pump leading edge, which is for a relative delay

$-T_{0P}/2$. Therefore the relative time-delay difference for a complete red-to-blue shift is $\delta T - T_{0P}$.

The group-time mismatch can be expressed as

$$\delta T = l \int_{\lambda_P}^{\lambda_T} D(\lambda)\, d\lambda$$

yielding $\delta T = 1.42$ ps and 1.23 ps for the GVD values indicated above for a complete blue-to-red relative-delay difference.

By contrast, fig. 2 shows a full flip from blue to red for a relative-delay variation of only 0.79 ps. This small but significant discrepancy can be explained by the recently demonstrated pulse trapping mechanism across the ZDW that reduces the group-velocity mismatch by XPM [2]. In ref [2], however, the probe is significantly reshaped, in opposition to the results presented below.

In the picosecond regime, the wavelength-shift variations have been predicted and demonstrated to be symmetrical with respect to the zero-delay point [3]. The curve of fig. 2 shows some asymmetry with a lower, longer negative lobe on the blue-shift side. This is so XPM is affected by the pump SPM-GVD broadening that also expands the walk-off length. The pump and probe dispersion lengths are L_{DP}=5.9 m L_{DT}=40.2 m, respectively, and the pump nonlinear dispersion length is L_{NL}=0.17 m. Furthermore the blue-shift amplitude might be affected by the pump-probe polarization mismatch arising from the pump self-induced nonlinear birefringence.

The previous evaluation of the group-time mismatch δT allows computing the walk-off length according to the prescription

$$L_W = l \frac{T_{0T}}{\delta T},$$

where T_{0T} is the half-width of the longest pulse, namely the probe. With the present parameters one obtains $L_W = 1.8$ m.

A set of autocorrelation traces is presented on fig. 3. The time width of the outgoing non shifted probe is 640 fs FWHM (fig. 3a), assuming a deconvolution factor of 1.55. The ratio of the time-bandwidth product to the Fourier limit is 1.6, indicating a non-soliton propagation regime, despite the anomalous GVD. The blue-shifted pulse trace reveals a small time expansion to 660 fs (fig. 3b), probably due to nonlinear interaction, but no significant reshaping is observed. The trace of the red-shifted probe represented in fig. 3c indicates a small but perceptible reshaping. The lower part of the autocorrelation trace is broadened, as a sign of time-profile reshaping. The width is increased to 720 fs.

Thus the probe is more perturbed on a red shift than a blue shift. One explanation to this is that the red shift

takes place just after the fiber input. As a result, the probe travels almost all along the fiber length under a comparatively higher GVD, whereas the blue shifted probe gets through the waveguide under a comparatively lower GVD.

In conclusion, the autocorrelation traces evolution of low-energy, ultrafast probe pulses has been observed after nonlinear interaction with a copropagating pump pulse along a standard single-mode fiber. The probe pulse is shown to undergo a small reshaping, even for spectral shifts that allow complete, well contrasted femtosecond

and acoustic unbalances and does not rely upon polarization effects.

Because of their superior nonlinear index and low dispersion parameter, air-silica fibers optimized for the 1300 nm spectral region would allow expanding the frequency-conversion amplitude and reducing the switching pump power, thus opening access to the laser-diode power range.

References
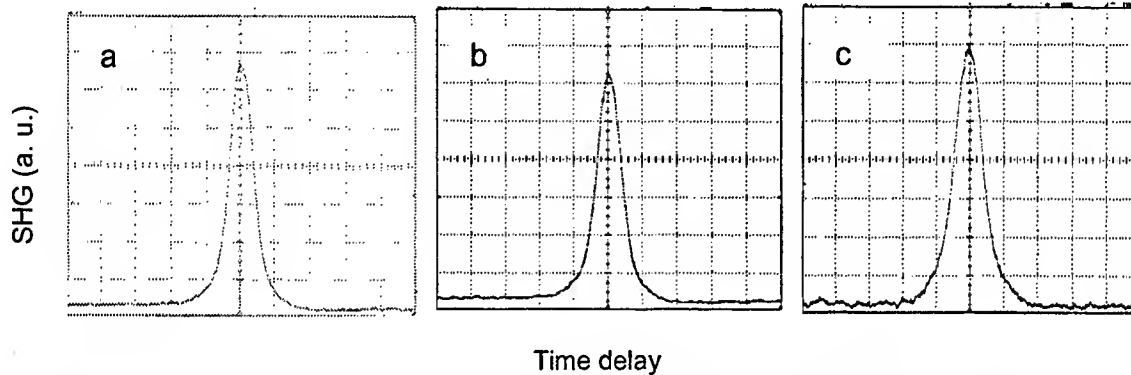
Fig. 3: Auto-correlation of the propagated but unshifted probe 640 fs FWHM (a). The width of the same probe after up-conversion is 660 fs (b) and 720 fs after down-conversion, (c). 1 div=1.2 ps.

switching. The variations of the wavelength shift with respect to the pump-probe time-delay are influenced by pulse trapping across ZDW.

The simplest way to increase the shift amplitude is to increase the pump power. But the SPM-GVD-induced broadening of the pump represents a limit beyond which the two spectra would merge. This limitation is of course stronger for a blue shift than for a red shift. When the pump power is increased further, other effects such as the so-called frequency-jump would appear [4].

The features presented here obviously demonstrate the suitability of the colliding pulses scheme to wavelength-based ultrahigh bit-rate all-optical switching systems. In opposition to interferometers often used for XPM switching, this scheme is non resonant, free of thermal

1-G. R. Boyer, M. A. Franco, B. Grèzes-Besset, M. Lachgar and A. Alexandrou : "Femtosecond pulse shaping scheme for cross-phase-modulation in single-mode optical fibers" JOSA B, **11**, 8, 1451 (1994)

2-N. Nishizawa and T. Goto : "Pulse trapping by ultrashort soliton pulses in optical fibers across zero-dispersion wavelength", Opt. Lett. **27**, 3, 152 (2002)

3-G. P. Agrawal, "Nonlinear fiber optics," 3rd ed. Academic Press, New York (2001)

4-Björn Hall, Gilbert Boyer, Dan Anderson, Mietek Lisak, Magnus Karlsson, Anders Bernston : "Pump-probe collision in optical fibers : Four-Wave-Mixing-induced frequency-jump", J. Opt. Soc. Am. B, **18**, 11, 1652-1658 (2001)

Anti-Guide Assisted Spatial Soliton Logic Gate

Balakishore Yellampalle, and Kelvin Wagner
Department of ECE, University of Colorado, Boulder, CO-80309, USA
kelvin@optics.colorado.edu

Steve Blair
Electrical Engineering Dept., University of Utah, Salt Lake City, UT-84112, USA
blair@ee.utah.edu

Abstract: An anti-guiding structure is shown to assist spatial soliton dragging logic gate. A weak beam easily breaks the balanced symmetry of a pump propagating in an anti-guide, allowing very efficient optical switching. More than an order of magnitude improvement over previous spatial dragging gates is possible.
© 2002 Optical Society of America
OCIS codes: Pulse propagation and solitons; (190.5530), Optical computing; (200.0200)

Spatial soliton dragging logic gates were studied extensively in the past [1]. These gate were shown to satisfy nearly all the requirements [2] necessary for building a logic gate including: gain (or fan-out) greater than 2, cascadability, logical completeness, phase insensitivity, and level restoration. These properties are necessary for optical logic gates, although not sufficient to make a practical gate technology. For example, a practical gate should have low switching energy and low average operational power (sum of average pump and signal powers) per device so that a number of devices can be operated simultaneously. Increasing the device length typically decreases the switching energy for optical switches. In this article an anti-guiding scheme is presented which allows low switching energy without requiring a long device length. The key idea of symmetry breaking in an anti-guide was recently investigated [3] [4], but is here advantageously combined with the spatial soliton dragging geometry. Most optical switching schemes require a phase change of the order of π. By using symmetry breaking, the anti-guide switch allows an order of magnitude smaller nonlinear phase change in order to produce a logic gate with comparable performance to the conventional spatial dragging gate.

Figure. 1(a) shows a schematic of a conventional soliton dragging logic gate (left) in comparison with an anti-guide assisted logic gate (right). These gates are based on self-phase and cross-phase interaction in a Kerr material. In the conventional dragging gate, in the absence of the signal, the pump travels straight through the spatial aperture, resulting in logic "high". In the presence of an orthogonally polarized signal beam traveling at an angle to the pump, because of cross-phase modulation, the two beams interact and form a bound pair that travels at an angle to the original pump direction. In this case the two beams miss the aperture which results in a "low" logic level output. In order to have high intensities, the signal and pump are confined linearly by a slab waveguide in the orthogonal y-direction. The switching energy is minimized by using short pulses for the pump and signal and operating near the zero dispersion wavelength so that within the device length, propagation dose not modify the pulse width noticeably. Alternatively operation in the anomalous dispersion regime would allow spatio-temporal soliton switching [1].

The anti-guide assisted spatial soliton dragging gate uses the same geometry as a conventional gate, and in addition, a smooth symmetric index profile is incorporated in the core of the waveguide. Figure 1(b) shows an example refractive index profile along the x-direction. This index gradient is tailored so that it is anti-guiding at low intensities and weakly anti-guiding for high intensity narrow soliton-like beam. Linear propagation at low intensity results in beam spreading out from the center of the index channel. When an intense nonlinear pump beam is closely centered (within about 1% of beamwidth for the gate presented here) in the anti-guide channel, it can overcome the anti-guide, resulting in longer confined propagation than a linear beam. However, if the pump beam has a small angle then it drifts away from the center of the channel and refracts away into the cladding. Switching in the anti-guide assisted soliton dragging gate utilizes this marginal stability of the pump beam inside the channel. Logical "high" operation corresponds to the pump beam traveling in the channel and out through the pinhole, in the absence of a signal. However, due to the anti-guiding, a small fraction of the pump beam is lost. In the presence of a tilted, overlapping signal beam, a small sideways shift of the pump is sufficient for the structure to assist the dragging thereby refracting both the beams away, resulting in a logic "low" output. This gate requires, for the same performance as a
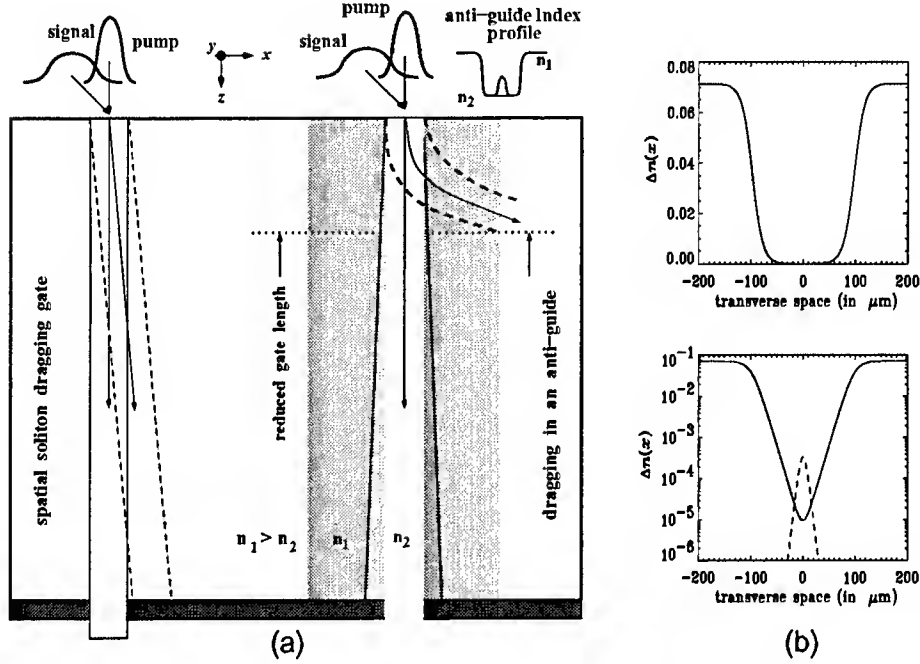
Fig. 1. (a) Comparison of spatial soliton dragging logic with a logic gate based on an anti-guide enhanced symmetry breaking dragging interaction. The solid lines show the trajectories of the pump beam in absence of the signal beam. The dashed lines represent trajectories during interaction. The refractive index structure (shown in (b)) allows the signal to break the pump symmetry thus aiding the dragging interaction.

conventional dragging gate, a smaller device length or lower switching power. Or alternatively for the same device length, substantially larger gain is possible.

The 3-D structure is guiding along y and weakly anti-guiding along x. The propagation of the slowly varying envelopes for the orthogonally-polarized pump and signal, is given in the dimensionless coordinates ($\xi = k_0 x$, $\zeta = k_0 z$) by the coupled evolution equation,

$$2i A_{1\zeta} + A_{1\xi\xi} + \left[\frac{2\Delta n(\xi)}{n_o} + \frac{2n(\xi)}{n_o} \left(\mid A_1(\xi) \mid^2 + \Delta \mid A_2(\xi,\zeta) \mid^2 \right) \right] A_1 = 0,$$

$$2i A_{2\zeta} + A_{2\xi\xi} + \left[\frac{2\Delta n(\xi)}{n_o} + \frac{2n(\xi)}{n_o} \left(\mid A_2(\xi) \mid^2 + \Delta \mid A_1(\xi,\zeta) \mid^2 \right) \right] A_2 = 0. \tag{1}$$

Where the pump (A_1) and signal (A_2) are dimensionless and normalized by $\sqrt{\frac{n_o}{n_2}}$. Here, n_2 is the nonlinear refractive index, n_0 is refractive index at channel center, and $\Delta n(\xi) = n(\xi) - n_0$. The ratio of cross-phase to self-phase modulation Δ is $\frac{2}{3}$ for linear polarizations in an isotropic media. Split-step Fourier beam propagation is used to study nonlinear propagation with this equations. Although they are not actually eigenmodes of the anti-guide sech profiles are used for the numerical simulations.

$$A_i(\xi) = \frac{1}{\sqrt{r_i}} \frac{1}{\xi_w} \mathrm{sech} \left(\frac{\xi}{\xi_w} \right) e^{i \sin(\theta_i)\xi} \tag{2}$$

The pump is chosen as a symmetric homogeneous soliton ($\theta_1 = 0$ and $r_1 = 1$), while the signal has same width but lower power ($r = \frac{r_2}{r_1}$, is device gain) and travels at an angle $\theta_2 = 1.5^o$. The refractive index variation used is,

$$n(\xi) = \Delta N \left[\frac{1}{1 + \exp\left(-(\xi - \xi_0)/\xi_E\right)} + \frac{1}{1 + \exp\left((\xi + \xi_0)/\xi_E\right)} \right] + n_o. \tag{3}$$

The parameters ΔN, ξ_0 ξ_E are the index change, edge position (half-width) of the anti-guide, and the steepness parameter respectively. Regions in parameter space (ξ_0, ξ_E, ξ_w and device length L_s) that allow
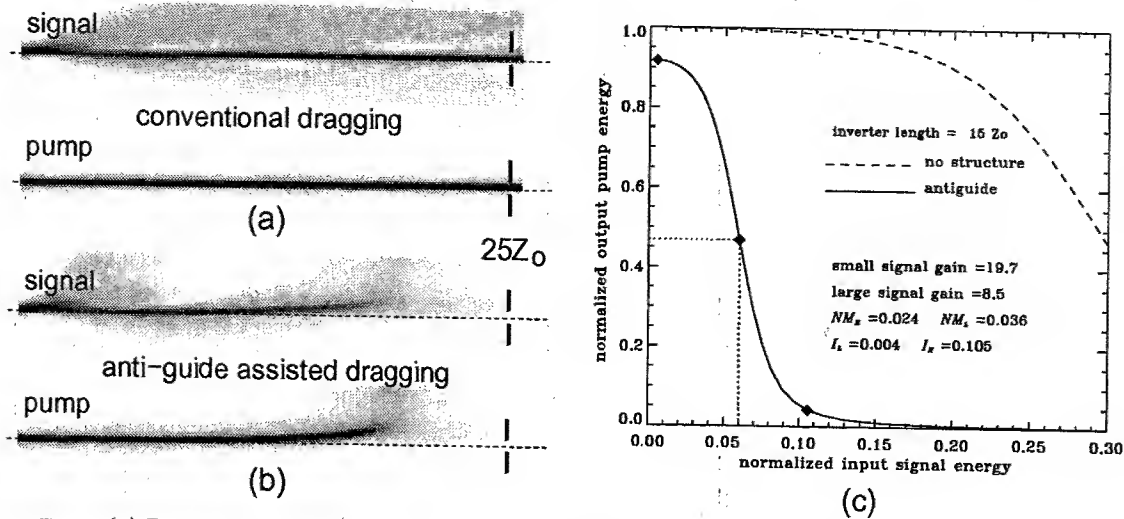
Fig. 2. (a) Dragging in absence of anti-guide. Pump-to-signal ratio of $r = 16$ requires approximately $16^2(2Z_0)$ for resolvable dragging. (b) For the same ratio r, a clearly resolvable spatial shift of the pump is seen within $16Z_0$, for the anti-guide. (c) Transfer characteristics of a high gain inverter with a gate length of $15Z_0$ ($r = 10$ for an anti-guide, $r = 2$ for a conventional gate).

90%, pump transmission through an aperture of width $2.4\xi_w$ are identified, and the maximum pumpwidth is used for gate simulations. For smaller pump widths lower gain is obtained and for larger pump widths, the "on" state transmission is lowered. For other kinds of smooth edged index profiles or pump shapes qualitatively simillar results were obtained. For the simulations results presented here, the parameters used were: $\Delta N = 0.08$, $\xi_E = 1.25\xi_w$, $\xi_0 = 12\xi_w$, $\xi_w \equiv 8.75\mu m$, $\lambda_0 = 1.3\mu m$, FWHM = $15.7\mu m$, and $Z_0 = \frac{\pi \xi_w^2}{2} \equiv 0.747$mm.

Figure 2(a) and (b) shows simulation of switching of a strong pump beam by a weak signal ($r = 16$). The conventional homogeneous dragging gate results in a negligible beam shift in $25Z_0$ of propagation. Whereas, for the same parameters, in the presence of an anti-guide, the new gate results in complete switching within $\approx 16Z_0$. As the pump approaches the index gradient, linear inhomogeneous propagation assists and shifts both the signal and the pump to the higher index cladding. The dynamics of the signal beam are similar to the pump, after some initial dissipation, due to mutual trapping. In the absence of the signal beam, the pump is undeviated but is seen to slowly dissipate energy to the sides and approximately 90% of pump is transmitted in the "on" state. When the tilted signal alone is present, since it is not a soliton, it diffracts within about $2Z_0$ and negligible output is produced.

The transfer characteristics of the two inverter devices [5] are compared for a gate length (L_s) of $15Z_0$, in Figure 2(c). The anti-guide assisted gate yields a transfer curve with a very low switching threshold of only $\frac{1}{10}$ of a soliton power for the same device parameters yielding an order of magnitude improvement. Alternatively devices with fixed gain and variable length can be compared. For a gain of 16, the conventional gate length is approximately $16^2(2Z_0)$ [1], which is approximately 20 times the gate length when an anti-guide is present giving an order of magnitude improvement in gate length. Smaller gate length requirement implies smaller phase change needed for switching which allows additional material optimization in the presence of absorption. Thus, more than an order of magnitude improvement in the device performance is expected using an anti-guiding structure in a spatial soliton dragging gate.

References

1. S. Blair, *Optical Soliton-Based Logic Gates*. PhD thesis, University of Colorado, 1998.
2. D. A. B. Miller, "Device requirements for digital optical processing," *SPIE Critical Reviews: Digital Optical Computing*, vol. CR35, pp. 68–76, 1990.
3. B. Gisin, A. Kaplan, and B. Malomed, "Spontaneous symmetry breaking and switching in planar nonlinear optical anti-waveguides," *Physical Review E* , vol. 62, p. 2804, 2000.
4. B. Gisin, A. Kaplan, and B. Malomed, "All-optical switching in an antiwaveguiding structure," *Optical and Quantum Electronics*, vol. 33, p. 201, 2001.
5. S. Blair and K. Wagner, "Cascadable spatial-soliton logic gates," *Applied Optics*, vol. 39, p. 6006, 2000.

Competition of gain–guided modes in stimulated Raman scattering with Bessel beams

T. Manz, J. Baier, J. Zeitler, U. T. Schwarz, and Max Maier

Fakultät für Physik, Universität Regensburg,

D-93040 Regensburg, Germany *

(Dated: April 22, 2002)

Abstract

Stimulated Raman scattering with a Bessel pump beam in hydrogen gas shows conical or axial Stokes emission. Selection of the gain–guided Stokes modes is due to gain suppression in phase–matched Stokes–anti–Stokes coupling.

OCIS codes: 190.4380, 190.4420, 290.5910.

---
*Electronic address: `uli.schwarz@physik.uni-regensburg.de`;

URL: `www.physik.uni-regensburg.de/forschung/maier/index.html`

Bessel beams are quasi non–diffracting beams which have been used for the investigation of stimulated Raman scattering. The radial field distribution of a Bessel beam corresponds to a Bessel function and is propagation invariant[1,2]. The intensity distribution of a J_0 Bessel beam has a central maximum which is surrounded by dark and bright rings. Bessel beams can be considered as a superposition of plane waves, the wave vectors of which lie on the surface of a cone with half–angle ϑ_P[1,2]. This property allows the generation of anti-Stokes light under very broad experimental phase matching conditions where the wave vectors of the pump, Stokes and anti–Stokes light are non–collinear and do not necessarily lie on a plane[3]. It has been demonstrated that depending on the experimental conditions the Raman Stokes light is emitted either as a conical mode[4,5] or an axial spot–like mode[6,7]. We did show that for small cone angles of the Bessel pump beam the Stokes mode is a gain–guided mode of the central maximum of the Bessel beam[4].

In order to clarify the origin of the different types of Raman Stokes emission we now investigate experimentally and theoretically stimulated Raman scattering with a J_0 Bessel pump beam with cone angles between 0.7 and 4.5 mrad in hydrogen gas over a wide range of pressure between 5 and 50 bar. Numerical solutions of the non–linear wave equation for the Stokes field show, in addition to the guided modes of the central maximum, the existence of further sets of modes which are gain–guided modes of the outer rings of the Bessel pump beam. Similar modes are observed as analytical solutions to the simplified model of a flat–top intensity distribution for the central spot and first ring of the Bessel beam, similar to a concentric arrangement

2

of a regular fiber within a hollow fiber.

We demonstrate that the selection in the competition of the different gain–guided modes is not due to the cut–off of a mode, but due to gain suppression by Stokes–anti–Stokes coupling. In the region of exact phase matching of the conical Stokes and anti–Stokes modes, i. e. where simultaneous longitudinal and transverse phase matching occurs, the Raman gain of the conical mode is substantially reduced, allowing the spot–like mode to dominate. As a consequence, a guided mode of the first Bessel beam ring and central peak is observed experimentally when the ratio p/ϑ_P^2 of the hydrogen pressure p and and the cone angle ϑ_P of the Bessel pump beam is smaller than a certain critical value.

References

[1] J. Durnin, J. J. Miceli, Jr. and J. E. Eberly, Phys. Rev. Lett. **58**, 1499 (1987).

[2] A. Vasara, J. Turunen, and A. T. Friberg, J. Opt. Soc. Am. **A 6**, 1748 (1989).

[3] S. Sogomonian, L. Niggl, and Max Maier, Opt. Comm. **162**, 261 (1999).

[4] L. Niggl and Max Maier, Opt. Comm. **154**, 65 (1998).

[5] U. T. Schwarz, L. Niggl, and Max Maier, Opt. Comm. **181**, 413 (2000).

[6] I. Golub, Opt. Lett. **20**, 910 (1995).

[7] S. Klewitz, P. Leiderer, S. Sogomonian, and S. Herminghaus, Opt. Lett. **21**, 248 (1996).

Spatial trapping in PPLN waveguides with picosecond pulsed excitation at 1548 nm

Fabio Baronio, Costantino De Angelis
Istituto Nazionale per la Fisica della Materia, Dipartimento di Elettronica per l'Automazione, Università di Brescia, via Branze 38, 25123 Brescia, Italy. Tel: +39 030 3715437, Fax: +39 030 380014, deangeli@ing.unibs.it
Paul Pioger, Vincent Couderc, Laurent Lefort, Alain Barthelemy
I.R.C.O.M., Faculté des Sciences Université de Limoges/CNRS,
123 ave. A. Thomas, 87060 Limoges, France. Tel : +33 555457256, Fax : +33 555457514, abarth@ircom.unilim.fr
Yoohong Min, Victor Quiring, Wolfgang Sohler
Universität-GH Paderborn, Angewandte Physik,
33095 Paderborn, Germany. Tel: +49-5251-60-2714, Fax: +49-5252-60-3422, sol_ws@physik.uni-paderborn.de

Abstract: Numerical simulations and experiments have shown the possibility of exciting spatially trapped beams in PPLN slab waveguides with pulses significantly shorter than the temporal walk off between FF and SH, with only FF at input.

1 Introduction

Cascaded $\chi^{(2)}$: $\chi^{(2)}$-parametric interactions of intense light signals in materials with quadratic nonlinearities offer a rich variety of phenomena [1]. Among other things, $\chi^{(2)}$ cascading processes have received considerable attention because they can yield strong nonlinear refraction effects at relatively low power levels [2, 3, 4]. In order to fully exploit the possibilities offered by $\chi^{(2)}$ nonlinear optics, the research has been driven in seeking new materials with high second order nonlinear coefficient and/or towards phase–matching techniques to efficiently use high nonlinearities of available materials. In the latter framework, Quasi Phase Matching (QPM) in lithium niobate is a major, well established, alternative to conventional phase matching in many applications based on parametric wave interaction in quadratic nonlinear media, since it allows to exploit the highest second order nonlinear coefficient of lithium niobate [5, 6].

In this paper we consider the interaction of a fundamental wave (FF) and a second harmonic one (SH), at frequency ω_0 and $2\omega_0$ respectively. We investigate, through numerical simulations and experiments, the possibility of exciting spatially trapped beams in periodically poled lithium niobate (PPLN) slab waveguides with pulses of few ps, with only the FF ($\lambda = 1548$ nm) at input. We present a detailed analysis of the spatial and temporal behaviours of these self-trapped optical signals.

2 Numerical modeling and experimental Set-Up

In a slab waveguide the electric fields E_1 and E_2, at ω_0 and $2\omega_0$ respectively, propagating in the z direction, can be written as $E_1(x,y,z,t) = \frac{1}{2}(W(y)w(x,z,t)\,e^{-j(\beta(\omega_0)z+\omega_0 t)} + c.c.)$ and $E_2(x,y,z,t) = \frac{1}{2}(V(y)v(x,z,t)\,e^{-j(\beta(2\omega_0)z+2\omega_0 t)} + c.c.)$, with W(y) and V(y) the mode profiles at ω_0 and $2\omega_0$ in the guided dimension, w and v the slowly varying envelopes. Averaging over the QPM periods, at the lowest order $w(x,z,t)$ and $v(x,z,t)$ obey the non-linear coupled equations:

$$j\frac{\partial w}{\partial z} - j\beta'_{\omega_0}\frac{\partial w}{\partial t} - \frac{\beta''_{\omega_0}}{2}\frac{\partial^2 w}{\partial t^2} + \frac{1}{2\beta_{\omega_0}}\frac{\partial^2 w}{\partial x^2} + \frac{\chi^{(2)}\omega_0}{2cn_{\omega_0}}\frac{\int V|W|^2 dy}{\int |W|^2 dy}vw^*e^{-j\Delta kz} = 0 \tag{1}$$

$$j\frac{\partial v}{\partial z} - j\beta'_{2\omega_0}\frac{\partial v}{\partial t} - \frac{\beta''_{2\omega_0}}{2}\frac{\partial^2 v}{\partial t^2} + \frac{1}{2\beta_{2\omega_0}}\frac{\partial^2 v}{\partial x^2} + \frac{\chi^{(2)}\omega_0}{2cn_{2\omega_0}}\frac{\int V|W|^2 dy}{\int |V|^2 dy}w^2 e^{j\Delta kz} = 0$$

where β represents the propagation constant, β' the inverse group velocity, β'' the inverse group–velocity dispersion; n is the refractive index, $\Delta k = 2\beta_{\omega_0} - \beta_{2\omega_0} + K_S$, where $K_S = 2\pi/\Lambda$, $\chi^{(2)} = 2/\pi\chi^{(2)}_{z'z'z'}$ is the nonlinear coefficient. By means of a finite difference vectorial mode solver the linear propagation properties of the slab waveguide are obtained, once the fabrication parameters of the specific waveguide are provided. We thus determine the mode profiles, β_{ω_0}, $\beta_{2\omega_0}$, β'_{ω_0}, $\beta'_{2\omega_0}$, β''_{ω_0} and $\beta''_{2\omega_0}$. Finally, using a finite difference beam

propagation technique, we solve the coupled nonlinear wave equations. Experiments have been performed in a 58 mm long Ti:PPLN z–cut waveguide with a poling period of 16.92μm. An all–fiber laser system delivered 4 ps pulses (FWHMI) at 1548 nm with a spectral width of 1.7 nm with up to 6 kW peak power at a repetition rate of 20 MHz. The laser beam has been shaped in a highly elliptical spot for an efficient coupling in the waveguide sample; we obtained a gaussian beam with a spot of $w_{ox} = 76\mu$m along the non guided direction and of $w_{oy} = 3.9\mu$m along the guided dimension. Under these conditions the crystal length corresponds to 3.2 times the FF diffraction length and 4.8 times the walk–off length between FF and SH. Spatial profiles of the output at FF were recorded with an IR camera and also scanning a magnified image of the output with an InGaAs photodiode for a better accuracy.

3 Results

We investigate the possibility of exciting spatially trapped beams in one transverse spatial dimension, with pulses that are significant shorter than the temporal walk off between FF and SH waves. Experiments and numerical simulations were carried out varying the phase–mismatch conditions (in particular the temperature T of the crystal) and the input pulse power, keeping fixed the temporal and spatial widths of the FF injected pulse. We measured the spatial profiles of the FF output beam versus the input intensity at different phase mismatches. In fig. 1 we compare typical measured and calculated normalized output profiles in the linear and the nonlinear regimes. In the linear regime the output beam profile had a width $w_x = 246\mu$m which corresponds to the diffracted input beam ($w_{ox} = 76\mu$m) after 58 mm of propagation along the waveguide. By increasing the incident intensity the nonlinear self focusing balances the effect of diffraction. In fig. 2 we report the spatial output profile width versus the injected intensity, for a fixed phase-mismatch. Qualitatively similar trends are observed over a wide range of phase–mismatch ($13\pi < \Delta kL < 70\pi$). Appreciable self trapping could be achieved for sufficiently large phase–mismatch and for input intensities that are the lower ever reported in $\chi^{(2)}$ nonlinear optics.

Typical FF and SH pulse temporal envelopes, when nonlinear self focusing balances the effect of diffraction, are shown in Fig. 3 (on the left). Despite a strong walk–off, the pulse at FF and a consistent contribution at SH overlap in time and lock together; condition that is necessary to guarantee an appreciable cascading self focusing effect. On the contrary, when the nonlinear effect does not balance the spatial diffraction, we note that the pulses do not overlap in time and lock together. This property has also been revealed experimentally by means of cross-correlator traces. The calculated output FF temporal profile envelope remains nearly gaussian: we reveal that a small self-steepening effect, due to the locking with the SH, occurs. In figure 3 (on the right) we report the measured intensity autocorrelation FF trace and in the inset the numerical simulated autocorrelation trace that agree with the measured one.

4 Conclusions

In conclusion we have proved the possibility of exciting spatially trapped beams in PPLN slab waveguide with pulses of few ps, significantly shorter than the temporal walk off between FF and SH waves, with only FF at input at 1548 nm. A numerical and experimental study has been carried out to determine the influence of the phase–mismatch and of the pulse power on the trapping effect. It is shown that, for short pulse excitation, beam trapping requires a sufficient large phase–mismatch. The temporal effects accompanying the self trapped propagation have been presented.

References

1. G. I. Stegeman, D. J. Hagan, L. Torner, *Optical and Quantum Electronics*, **28**, pp. 1691-1740, 1996.
2. Y. N. Karamzin, A. P. Sukhorukov, *Sov. Phys. JETP*, **41**, pp. 414-420, 1976.
3. W. E. Torruellas, Z. Wang, D. J. Hagan, E. W. Van Stryland, G. I. Stegeman, L. Torner, and C. R. Menyuk. *Phys. Rev. Lett.*, **74**, pp. 5036-5039,1995.
4. S. Kim, Z. Wang, D. J. Hagan, E. W. VanStryland, A. Kobyakov, F. Lederer, G. Assanto, *IEEE Journal of Quantum Electronics*, **34**, pp. 666–672, 1998.
5. V. Dierlof, A. B. Kutsenko, A. Ostendorf, W. von der Osten, W. Sohler, H. Suche, *Applied Physics B*, **B72**, pp. 803–810, 2001.
6. B. Bourliaguet, V. Couderc, A. Barthelemy, G. W. Ross, P. G. R. Smith, D. C. Hanna, C. De Angelis, *Optics Lett.*, **24**, 1410 (1999).
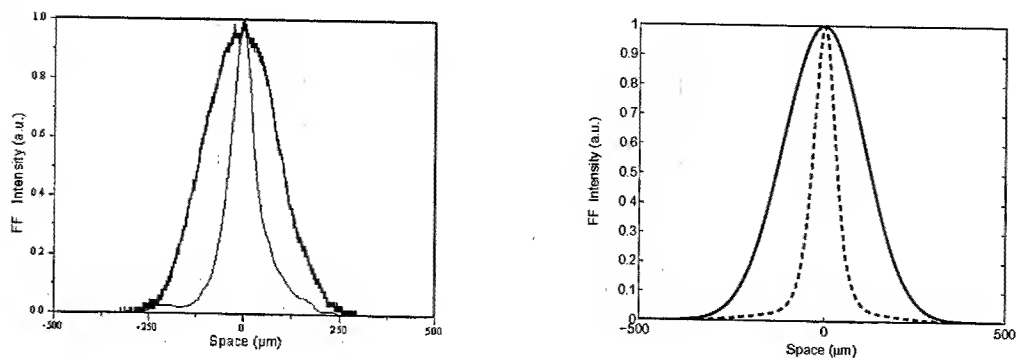
Fig. 1. Measured (left) and calculated (right) normalized output profiles in the linear (continuous line) and the nonlinear (dashed line) regimes. Here $\Delta k = 1200 m^{-1}$ and the input intensities at FF are $1\,\mathrm{MW/cm^2}$ and $0.12\,\mathrm{GW/cm^2}$.
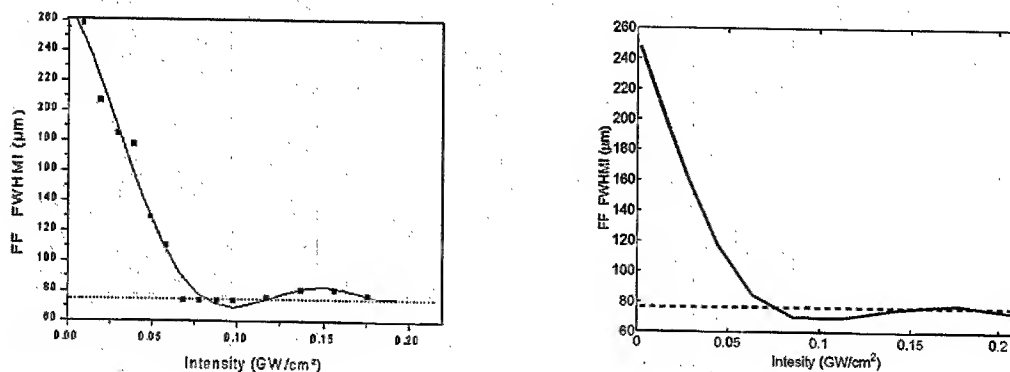
Fig. 2. Measured (left) and calculated (right) FF full width at half maximum intensity versus input intensity for $\Delta k = 1200 m^{-1}$. Dashed line stands for input beam width.
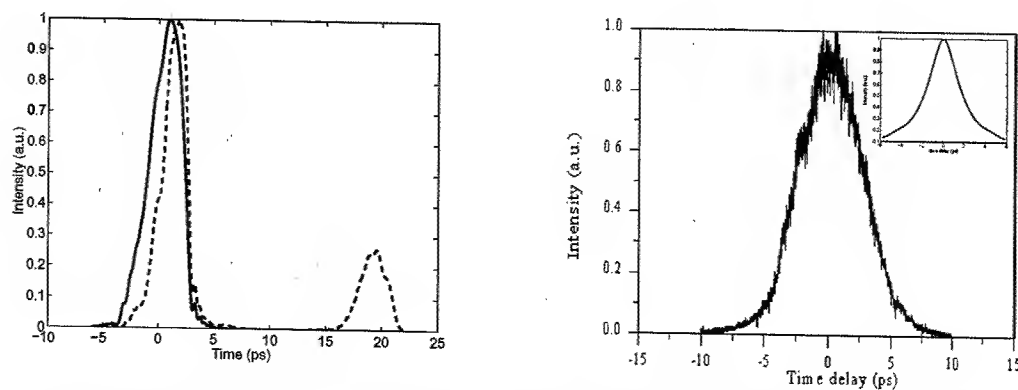
Fig. 3. FF (solid line) and SH (dashed line) pulse temporal envelopes for a trapped beam (on the left). Measured and numerically obtained (in the inset) autocorrelation trace of the FF (on the right). Here $\Delta k = 2400 m^{-1}$ and the input intensity at FF is $0.12\,\mathrm{GW/cm^2}$.

Ultrafast temporal reshaping of picosecond pulses based on quadratic spatial soliton generation

C. Simos, V. Couderc and A. Barthélémy
Institut de Recherche en Communications Optiques et Microondes, UMR 6615
Faculté des sciences de Limoges, 123 Avenue Albert Tomas, 87060 Limoges Cedex, France
Phone:+33 555 45 75 30 Fax: +33 555 45 72 53
E-mail: couderev@ireom.unilim.fr

Abstract: We propose and demonstrate the use of quadratic spatial soliton generation together with a spatial filtering of the optical beam, as an efficient mean for the realization of ultrafast temporal reshaping of optical pulses. We show that the device has an intensity-dependent transmission similar to the one of a saturable absorber and we numerically investigate the parameters for optimum temporal filtering.
©2000 Optical Society of America
OCIS codes: (190.4420) Nonlinear optics, transverse effects in

1. Introduction

Quadratic spatial solitons have been observed experimentally in various crystals (KTP, LiNbO$_3$, LBO), in conditions for second harmonic generation or parametric generation/amplification, in bulk crystals as well as in planar waveguides [1-4]. They consist of strongly coupled fundamental and second harmonic fields that propagate locked together in a single beam without experiencing the usual diffraction effects. The extensive theoretical and experimental research of their basic properties during the last years opened new fascinating perspectives for realizing elementary logical operations and ultra fast all-optical switching. By using soliton interaction, or soliton fusion and dragging, many types of all-optical processing devices have been proposed [5-7].

In this communication we propose and demonstrate the use of the most standard quadratic spatial soliton generation for performing a temporal reshaping of laser pulses. By means of spatial soliton generation combined with a spatial filtering of the output beam, pulses can be cleaned up from pedestal of low intensity and may be shortened in time. This kind of processing is particularly interesting for high bit rate optical communication links where it could achieve all-optical reshaping of distorted pulses at very high speeds (exceeding 100 Gbits/sec).

2. Principle of operation

Generation of spatial solitons with feasible crystal lengths in existing bulk quadratic (or cubic) nonlinear materials, requires the use of pulsed lasers because of the high intensity threshold (at the GW/cm^2 scale) of the soliton regime. To avoid crystal damage and thermal effects, mode locked laser sources delivering picosecond pulses are used. Typically, these pulses have gaussian or hyperbolic secant temporal profiles.
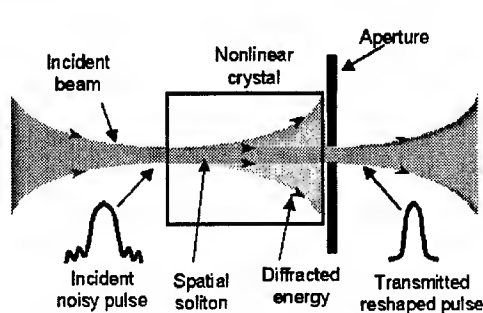
Fig. 1: (Left) Schematic drawing illustrating the spatial filtering implemented to select the spatial soliton beam at the output of a quadratic nonlinear medium. (Right) Intensity-dependent transmission and temporal selection of the device.
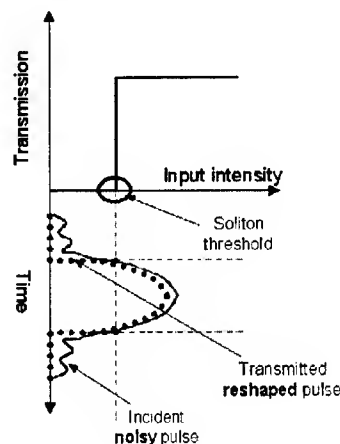
Therefore, only the fraction of power of each incident pulse that is higher than the power threshold for self-guided propagation is actually trapped and propagates as a spatial soliton. The low power parts of the pulse, both in time and space, behave linearly and undergo diffraction inside the crystal. Let as now consider a circular aperture of diameter approximately equal to the one of the soliton that is properly positioned at the output face of the crystal so as to transmit the output field energy confined in the spatial soliton and to block all the non trapped energy which is spread around (see Fig. 1). Therefore the transmitted pulse contains only the high power temporal part of the input pulse and the overall system (nonlinear propagation medium and aperture) acts as a saturable absorber with an ultrafast time response (Fig.1).

3. Experimental demonstration of the temporal selection of the device

We carried out experiments to demonstrate the above proposed principle. We used a Q-switched, mode-locked Nd:YAG laser which delivered 63 ps pulses (FWHMI: full width at half maximum in intensity) at 1064 nm. Laser beam was focused to a circular spot of 26μm diameter (FWHM) onto the entrance face of a 2cm long KTP crystal, cut for type II SHG and oriented close to phase matching. Crystal length represented here 7.8 times the diffraction length of the input wave. A magnified image (18.5X) of the output face of the crystal was displayed on a screen with a circular aperture, centered on the output soliton image, so as to transmit only the energy trapped in the solitary wave. After purging the beam from its SH component with an RG820 filter, the transmitted pulse was characterized using background free autocorrelation. At low intensity free diffraction of the input beam was observed. For peak input intensities higher than about 8.5GW/cm², the soliton regime was reached and self-guided propagation occurred. The circular points in Fig. 2a show the experimental evolution of the diameter of the output beam versus the input intensity. The output solitary wave had a width of 27 μm (FWHMI), very close to the one of the input beam. Figure 3 shows a typical autocorrelation of the output pulse recorded for an input peak intensity of 12 GW/cm² that is higher than the soliton threshold. The diameter of the circular aperture was set to be equal to the soliton diameter $2w_s$ (at $1/e^2$ of the maximum intensity) in the magnified image. The noise in the experimental points is due to the beam pointing instability of our laser. For comparison we plot on the same graph the autocorrelation trace of the input laser pulse. The autocorrelation of the pulse narrowed from 90ps at input to 50ps after spatial filtering of the soliton, thanks to the rejection of the low intensity parts of each pulse.
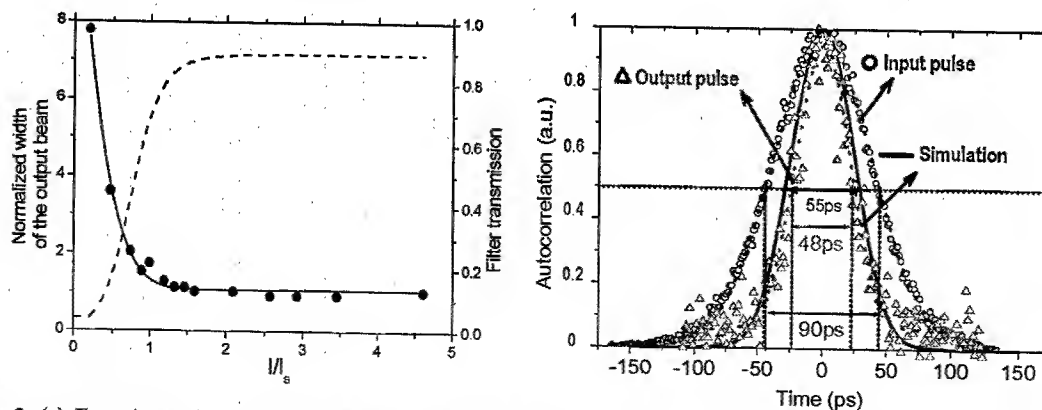
Fig. 2: (a) Experimental evolution of the output beam width (dots) versus the peak input intensity. Beam width and intensity are normalized to the soliton diameter and soliton threshold respectively. Solid line is a numerical fit of the experimental curve. Dotted line represents the numerically calculated intensity-dependent transmission of the device after spatial filtering of the spatial soliton. (b) Background free autocorrelation traces of the laser pulses (circles) and of pulses measured after nonlinear propagation and filtering of the soliton part (triangles). The numerical curve of the autocorrelation of the filtered pulse (solid line) is in good agreement with the experimental data.

4. Numerical simulation: determination of the parameters leading to optimal filtering

In order to verify the validity of the experimental results we numerically simulated the behavior of the entire device (nonlinear crystal + aperture). We calculated the intensity-dependent transmission by the overlap integral between the circular aperture and the incoming beam pattern supposing that the beam always kept a gaussian transverse distribution even in the soliton regime. The transmission computed in that way is plotted with dashed line in Fig. 2a and is similar to the one of a saturable absorber material. For the given peak intensity of 12 GW/cm² corresponding to our experimental conditions, we calculated the

filtered pulse profile as the product between the input pulse (assuming a gaussian temporal profile) and the nonlinear device intensity-dependent transmission. In order to compare numerical and experimental results we plotted in Fig. 2b (solid line) the autocorrelation of the calculated output pulse. There is a good agreement between the simulation and the experiment and it shows that our model gives a satisfactory description of the behavior of the quadratic spatial soliton based device.

The model has been used further to derive the condition for a stronger shortening and therefore for a more efficient filtering. The results are reported in Fig. 4 as a set of curves showing the evolution in width of the autocorrelation of the output pulse with respect to the input pulse peak intensity. In the situation considered here, a shortening as large as about 50% can be obtained for an optimized aperturing. It is worth to note that the minimum pulse width is obtained for an input intensity slightly lower than the intensity threshold for soliton trapping. Further increase of the intensity leads to enlarge the output pulse whose width asymptotically tends to the one of the input pulse.

Fig. 1: Width of the filtered pulses autocorrelation, after normalization to the laser pulse autocorrelation, versus their peak input intensity, normalized to the intensity threshold for soliton propagation, for various diameters d of the spatial filter. w_s denotes the soliton beam radius at $1/e^2$ of the peak intensity..

5. Conclusion

We proposed and demonstrated the use of spatial soliton propagation in a quadratic nonlinear material as a mean for achieving temporal filtering of the most powerful part of an optical pulse. In contrast to other kinds of saturable absorbers, the proposed scheme offers a broad flexibility. Changing the input beam width w, permits to adjust the intensity threshold for self-trapping which scales as w^{-4} [8] and corresponds to the maximum transparency of the device. The transmittance variation can be adjusted by changing the ratio L/L_D, i.e. propagation distance L divided by the diffraction length $L_D = \pi w^2 / \lambda^2$, with a transmittance at low power scaling approximately as $(L/L_D)^{-2}$. So the device can perform either a weak or a strong filtering with a high contrast ratio. In addition, it has the advantage of a very fast response time, limited only by the group velocity mismatch between fundamental and second harmonic radiation, which is independent from the power threshold for bleaching (in contrast to other kinds of saturable absorbers, where the intensity threshold for a high transmittance scales as the inverse of lifetime of the upper level and thus a fast response time thus leads to a high intensity threshold). In the present scheme based on a 2cm-KTP crystal, pulse widths as short as 10ps can be used. Finally it must be pointed out that the proposed device should not be considered as a pulse compressor, because other techniques might be found more efficient for that. The investigated device is better suited to perform reshaping of short pulses and background noise suppression. Beyond its potential use as a reshaping device for long distance communication links, the same set-up could be used in high power laser chain for increasing the contrast ratio of short laser pulses after the amplification stages.

References

[1] W. E. TORRUELLAS, Z. WANG, D. J. HAGAN, E. W. VANSTRYLAND, G. 1. STEGEMAN, L. TORNER, C. R. MENYUK: "Observation of two-dimensional spatial solitary waves in a quadratic medium", Phys. Rev. Lett., 74, pp.5036-5038, (1995).

[2] R. SCHIEK, Y. BAEK, G. I. STEGEMAN: "One-dimensional spatial solitary waves due to cascaded second order non-linerities in planar waveguides", Phys. Rev. E, 53, pp.1138-1140, (1996).

[3] P. DI TRAPPANI, G. VALIULIS, W. CHINAGLIA, A. ANDREONI: "Two-dimensional spatial solitary waves from traveling-wave parametric amplification of the quantum noise", Phys. Rev. Lett., 80, pp.265-267, (1998)

[4] B. BOURLIAGUET, A. BARTHELEMY, V. COUDERC, G. W. ROSS, D. C. HANNA, C. DE ANGELIS: "Observation of quadratic spatial solitons in periodically poled lithium niobate", Opt Lett., 24, pp.1410-1412, (1999)

[5] W. TORRUELLAS, G. ASSANTO, B. LAWRENCE, R. FUERST, G. 1. STEGEMAN: "All-optical switching by spatial walkoff compensation and solitary-wave locking", Appl. Phys. Lett., 68, pp.11-13, 1996

[6] A. V. BURYAK, V.V STEBLINA: "Soliton collisions in bulk quadratic media: comprehensive analytical and numerical study", J. Opt. Soc. Am. B, 16, no 2, pp. 245-255, 1999.

[7] V. COUDERC, E. LOPEZ-LAGO, C. SIMOS, A. BARTHELEMY: "Experiments on quadratic spatial soliton excitation and steering in non-collinear geometry", Opt. Lett., 26, no 12, pp. 905-907, 2001.

[8] L. TORNER: "Spatial solitons in quadratic nonlinear media", in Beam Shaping and Control with Nonlinear Optics, F. Kazjar and R. Reinisch Edit., Plenum Press, New York, 1998. pp.229-258

Collisions Between Optical Spatial Solitons

Propagating in Opposite Directions

Oren Cohen,[1] Raam Uzdin,[1] Tal Carmon,[1] Jason W. Fleischer,[1,2]

Mordechai Segev,[1,2] and Serguey Odouov,[3]

(1) Physics Department and Solid State Institute, Technion, Haifa 32000, Israel

(2) Electrical Engineering Department, Princeton University, Princeton, NJ 08544

(3) Institute of Physics, Kiev, Ukraine

Collisions between solitons are perhaps the most fascinating features of soliton phenomena because the interacting self-trapped wavepackets exhibit many particle-like features [1]. Solitons collisions have been extensively studied theoretically, both for the integrable (1+1)D Kerr case [2] and for the more general case in saturable nonlinearities (see [1] and references therein). Soliton collisions can be classified into two categories: coherent and incoherent interactions. Coherent interactions occur when the nonlinear medium responds to interference effects taking place where the beams overlap. Such collisions occur for all nonlinearities with an extremely fast time response (the optical Kerr effect and the quadratic nonlinearity). In materials with a long response time τ (e.g., photorefractives, liquid crystals, and thermal nonlinearity), coherent collisions occur only if the relative phase between the beams is stationary for a time longer than τ [3]. In such media, if the relative phase between the beams varies much faster than τ, then the contribution of the interference terms is averaged out and the surviving terms (in the nonlinear change of the refractive index, Δn) depend only on the sum of the intensities of the beams [4]. This latter case is generally referred to as incoherent collisions [1,4]. The interaction between two solitons can be described through the "Newtonian forces" they exert on one another. For coherent interactions, this force depends on the relative phase between the solitons. For example, two solitons launched in parallel attract (repel) each other if the relative phase between them is zero (π) [1,2,5]. For incoherent interactions, on the other hand, the interference terms do not contribute to Δn (as the relative phase between solitons varies much faster than τ). Thus, the incoherent force between bright solitons in self-focusing media is always attractive, is independent of the relative phase between the solitons, and is weaker than the force in a coherent interaction [4,6]. Thus far, all studies on optical soliton collisions have dealt with solitons propagating in the same general direction.

Here, we study theoretically the interactions between solitons that propagate in **opposite** directions (Fig. 1). Such collisions display new features, among them (i) the interactions are insensitive to the relative phase between the solitons, and (ii) the collision involves radiation loss even in ideal Kerr media.
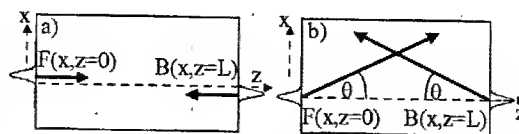
Figure 1: Interactions between spatial solitons that propagate in opposite directions.

The basic difference between this new scheme and the traditional "co-propagation configuration" is the relative propagation directions of the carrier waves. Consider a coherent interaction between two solitons in both schemes. The solitons interfere and give rise to a grating in Δn. For co-propagating solitons, the Δn grating is periodic in the transverse direction (x) with a period much greater the optical wavelength λ, thus the interacting solitons go through very few (~3) grating periods. On the other hand, for counter-propagating collision the Δn grating is in the propagation direction (z) and its period is $\sim \lambda/2$; hence the interacting solitons go through many (~10^6) periods. Consequently, the interaction in the counter-propagation scheme is strongly affected by the grating: Bragg scattering and grating effects play a dominant role. Second, in the new scheme, the relative phase between the solitons, and hence the dominant term in the soliton-soliton force varies periodically along the propagation axis on a scale much shorter than the soliton propagation scale (the soliton period). Thus, all the effects depending on the relative phase between solitons oscillate many (~10^3) times over one soliton period. Hence, the effective force between the solitons is independent of their relative phase.

Consider two counter-propagating beams in one transverse dimension (Fig. 1). Within the paraxial approximation, the envelope amplitudes of the two stationary counterpropagating beams, F and B, obey the following set of coupled NLS equations [7].

$$\frac{\partial^2 F}{\partial \xi^2} + i\frac{\partial F}{\partial \zeta} + \left[|F|^2 + |B|^2(1+h)\right]F = 0$$

$$\frac{\partial^2 B}{\partial \xi^2} - i\frac{\partial B}{\partial \zeta} + \left[|B|^2 + |F|^2(1+h)\right]B = 0$$

(1)

where ξ and ζ represent, in dimensionless units, the transverse and longitudinal coordinates, respectively, and the parameter h equal to one (zero) for coherent (incoherent) interaction. The extra nonlinearity term in coherent interaction is a consequence of the induced index grating due to the interference patterns.

Consider first the interactions in a configuration where two such beams are launched from two opposite planes $\zeta=0$ and $\zeta=1$ [Fig 1(a)]. The beams are launched parallel to each other with a transverse spacing (between peaks) of $\xi=7.5$. Simulation of the coherent interaction between these parallel counterpropagating beams is shown in Figs. 2(a-c). For clarity, we present the forward beam (Fig 2a and 2c) and the backward beam (Fig 2b) in separate plots. Figures 2(d-f) show an incoherent interaction between the same beams. For comparison, we simulate the same beams in co-propagating scheme (Fig 2(g-i)). Figures 2(g) [2(h)] shows a coherent interaction in which the relative phase between the launched beam is 0 [π]. Figure 2(i) shows an incoherent interaction. Clearly, the outcome of the

Figure 2: (a-c) Coherent interactions between the counterpropagating (a,c) forward and (b) backward solitons. (d-f) Incoherent interactions between the counterpropagating (d,f) forward and (e) backward solitons. For comparison, interactions between coherent [in-phase (g) and π out of phase (h)], and incoherent (i) copropagating solitons.

interaction between the beams in the counter-propagating scheme is very different than that in the co-propagating scheme, in both the coherent and incoherent cases. First, in the co-propagating scheme, the mutual force between the solitons is proportion to $-\cos(\Delta\Phi)$ [5], where $\Delta\Phi$ is the relative phase between the solitons, hence the interaction can be attractive (Fig. 2(g)) or repulsive (Fig. 2(h)). In contrast, in the counter-propagating case the relative phase oscillates on a scale much shorter than the soliton period, thus the relative phase does not play any role. Specifically, varying the initial relative phase between the launched solitons does not affect the interaction. Moreover, since the dominant coherent term in the mutual force, which is proportion to $-\cos(\Delta\Phi)$, is averaged out, the force between the counter-propagating beams is dominantly the incoherent term [6], which is always attractive and weaker than the coherent term. The second major difference between the counter- and co-propagating cases has to do with radiation. The coherent interaction in the counter-propagating scheme radiates (Fig. 2(a,b)), which implies that this system is nonintegrable. On the other hand, the incoherent interaction between the counter-propagating solitons does not radiate [Figs. 2(d-f)]. Finally, we notice that a portion of the forward beam couples into the region where the backward beam is propagating. In the incoherent interaction, the forward beam gradually tunnels into the backward soliton region, hence the forward intensity at the backward soliton region increases monotonically (Fig 2(f)). This behavior represents directional coupling (resonant tunneling). For coherent interactions the dynamics are more complex, as the intensity coupled from the forward beam to the region "under" the backward beam oscillates [see the sidebands in Figs. 2(c)], and, in contradistinction to the incoherent case, light does not accumulate in the "sidebands". The explanation is as
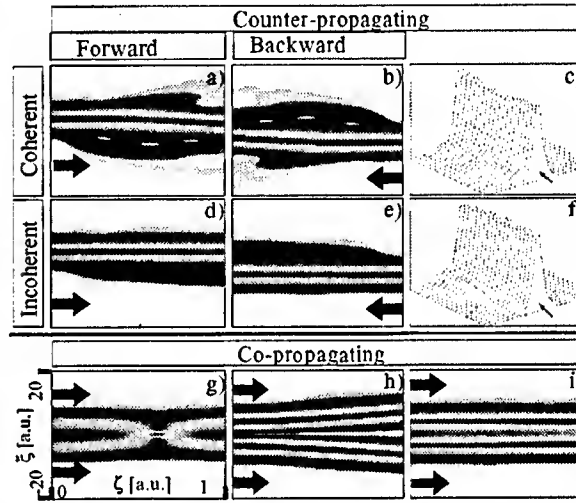
follows. The Bragg reflections of the backward beam serves as an extra source to the forward beam propagating at the backward soliton region. But, the forward beam under the backward soliton region is propagating slower than the original forward beam. Hence, the relative phase between the original beam and its sideband is alternating, and subsequently, the energy transfer (through tunneling) between these beams is alternating as well.

Finally, we investigate collisions at angles close (but not equal) to 180° [Fig. 1(b)]. We launch two beams from planes $\zeta=0$ and $\zeta=48$ that initially propagate at a (dimensionless) angle of $\theta=26.5^{0}$. The coherent and incoherent interactions are shown in Figs. 3(a,b), 3(c,d), respectively. The incoherent collision is fully elastic, and merely leads to a lateral displacement, resembling collisions of co-propagating solitons. Coherent collisions [Fig. 3(a,b)], on the other hand, are different, and lead to radiation.
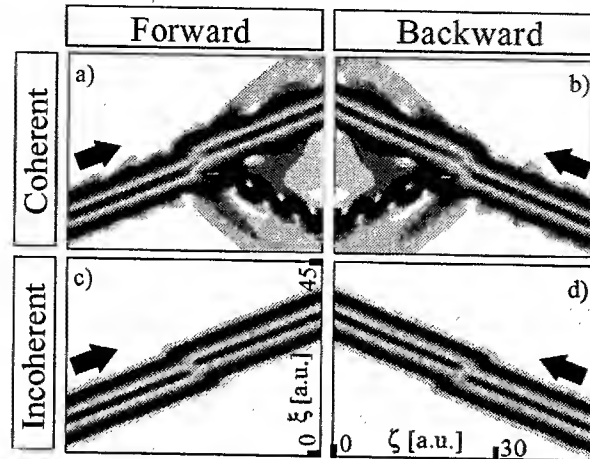
Figure 3: Coherent (a,b) and incoherent (c,d) interactions between almost-counter-propagating solitons.

References
1. For a review on spatial solitons interactions, see G. I. Stegman and M. Segev, Science **286**, 1518 (1999).
2. V. E. Zakharov and A. B. Shabat, Sov. Phys. JETP **34**, 62 (1972).
3. H. Meng et al., Opt. Lett. **22**, 448 (1997).
4. M. Shih and M. Segev, Opt. Lett. **21**, 1538 (1996).
5. J. P. Gordon, Opt. Lett. **8**, 596 (1983).
6. D. Anderson and M. Lisak, Phys. Rev. A **32**, 2270 (1995).
7. W. J. Firth and C. Pare, Opt. Lett. **13**, 1096 (1988).

High-order vortices and multi-hump rotating laser solitons

Sergey V. Fedorov, Nikolay N. Rosanov, Anatoliy N. Shatsev,

*Research Institute for Laser Physics, Theoretical Department, Birzhevaya liniya, 12, 199034 St. Petersburg, Russia.
Tel.7 812 328 10 93, Fax 7 812 328 58 91, E-mail:* sfedorov@sf3997.spb.edu, rosanov@ilph.spb.su

Nikolay A. Veretenov and Andrei G. Vladimirov

*St. Petersburg State University, Physics Faculty, 1 Ulianovskaya st, 198904 St. Petersburg, Russia.
Tel. 7 812 428 44 67, Fax 7 812 428 72 40, E-mail:* andrei@sp1254.spb.edu

Abstract: We present results of semianalytical and numerical study of transversely two-dimensional spatial and spatio-temporal solitons in a laser with a saturable absorber. We demonstrate axially symmetric and asymmetric rotating solitons with wavefront dislocations of different order.
©2002 Optical Society of America
OCIS codes: (140.3430) Laser theory: (190.4420) Nonlinear optics, transverse effects in

1. Introduction

Localized structures of coherent light in passive (driven nonlinear interferometers) and active (laser schemes with a saturable absorber) systems present an interesting class of dissipative solitons promising for applications in optical data processing (see [1] and references therein). Solitons in both passive and active systems have a discrete spectrum of their parameters. Nevertheless, there are important differences between these two types of solitons connected with the absence of holding radiation in laser schemes. Recently detailed study of laser solitons was performed for various scheme dimensionality, especially for one- and three-dimensional schemes [1].

The two-dimensional schemes are of the most interest for real laser experiments, on the other hand, are much simpler for the analysis and numerical simulations as compared with the three-dimensional case. The goal of this report is to give a systematic presentation of types and features of two-dimensional laser solitons in the case of fast nonlinearity of both gain and absorption. We study vortex solitons characterized by cylindrically symmetric intensity distribution and different topological charge. We analyse their linear stability and scenarios of their destabilization, and demonstrate the appearance of asymmetric multihump rotating solitons.

2. Initial equations

We consider a wide-aperture class A laser with a saturable absorber. The equation for the dimensionless electric field slowly varying envelope E in the mean-field approximation has the form [1,2]

$$\frac{\partial E}{\partial t} = (i+d)\Delta_{\perp}E + Ef(|E|^2)\cdot \tag{1}$$

Here t is the time normalized by the cavity relaxation time, $\Delta_{\perp} = \nabla_{\perp}^2 = \partial^2/\partial x^2 + \partial^2/\partial y^2$ is the transverse Laplacian, x and y are transverse coordinates normalized by the width of the effective Fresnel zone. The diffusion coefficient d depends on relaxation parameters of the active and passive media and is assumed to be small enough. The nonlinear function $f(I)$ of the field intensity $I = |E|^2$ describes fast saturation of gain and absorption. After neglecting frequency detunings, this function becomes real and takes the form

$$f(|E|^2) = -1 + \frac{g_0}{1+b|E|^2} - \frac{a_0}{1+|E|^2}, \tag{2}$$

where g_0 and a_0 are small-signal (linear) resonance gain and absorption, b is the ratio of saturation intensities for gain and absorption. In our numerical simulations we fix the following values of the parameters: $a_0 = 2$, $b = 10$.

3. Solitons with cylindrically symmetric intensity distribution

Solitons with such a symmetry are characterized by an integer value of azimuthal index, or topological charge m:

$$E = A(r)\exp(im\varphi - i\alpha t), \qquad r = \sqrt{x^2 + y^2}, \qquad (3)$$

where α is the frequency shift with respect to the frequency of transversely homogeneous lasing. The amplitude $A(r)$ is determined by ordinary differential equation

$$\frac{d^2 A}{dr^2} + \frac{1}{r}\frac{dA}{dr} + \frac{m^2}{r^2}A + \frac{1}{i+d}[i\alpha + f(|A|^2)]A = 0, \qquad (4)$$

with natural boundary conditions $A(r) \sim r^m$ for $r \to 0$ and $A(r) \to 0$ for $r \to \infty$. The frequency shift α plays the role of a spectral parameter (eigenvalue) and has a discrete spectrum. This shift and corresponding amplitude radial profiles $A(r)$ have been found numerically for different m and g_0 (a control parameter). In order the solution (3) be stable it is necessary that the total linear absorption be greater than the linear gain for a weak field

$$f(0) = -1 + g_0 + a_0 < 0. \qquad (5)$$

Sufficient stability conditions have been found by linear stability analysis. To this end we introduce small perturbations δA by the relation

$$E = [A(r) + \delta A(r, \varphi, t)]\exp(im\varphi - i\alpha t), \qquad (6)$$

where (r, φ) are the polar coordinates, and seek the solution of linearized Eq. (1) in the form

$$\delta A(r, \varphi, t) = a(r)\exp(i\delta m\varphi + \gamma t) + b^*(r)\exp(-i\delta m\varphi + \gamma^* t), \quad \delta m = 0,1,2,\ldots \qquad (7)$$

The growth rate of perturbations is determined by the real parts of the eigenvalues γ. If $\operatorname{Re}\gamma < 0$ for all the eigenvalues, except for those corresponding to the so-called "neutral modes", the localized structure is stable. We have found the eigenvalues γ numerically taking into account the symmetry properties of Eq. (1) and the existence of a number of "neutral modes" with zero eigenvalue $\gamma = 0$.

4. Semianalytical calculations

Laser soliton with regular wavefront ($m=0$) is stable even without diffusion ($d=0$) in a the interval $2.094 < g_0 < 2.1162$. However, vortex solitons are stable only for $d > 0$. For $d \to 0$ all these solitons are unstable with respect to perturbation harmonics with $\delta m = 2$. This leads to the appearance of two maxima of the field intensity distribution. For $d > 0$ and fixed m, there are several types of stable solitons differing by the number of oscillations in their intensity profile (Fig. 1).
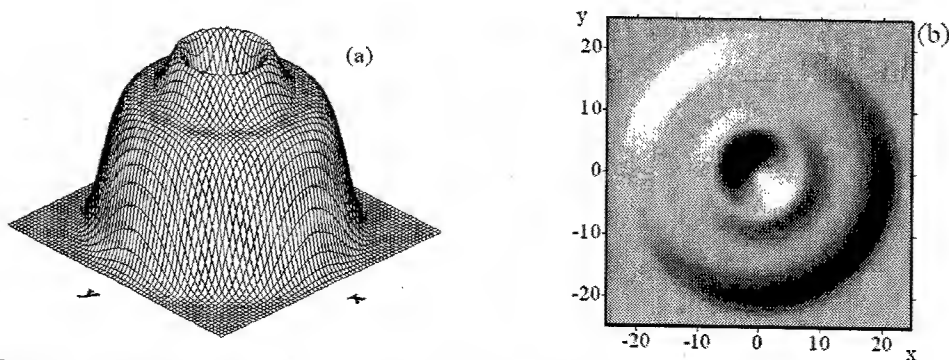
Fig. 1. Transverse distribution of intensity $I(x, y)$ (wired surface (a) and surface relief (b)) of an excited vortex soliton with $m = 1$; diffusion coefficient $d = 0.06$, gain $g_0 = 2.129776$, and frequency shift $\alpha = 0.06576$

For the "ground-state" solitons with $m = 1, 2$, the stability intervals are given in Fig. 2. With the increase of gain, solitons are destabilized by the growth of perturbations with $\delta m = 0$. Since the imaginary parts of the critical eigenvalues are nonzero, this instability corresponds to the Andronov-Hopf bifurcation. With the decrease of gain,

solitons lose their stability due to the growth of perturbations with $\delta m = 2$ for $m = 1$ and with $\delta m = 3$ for $m = 2$. In the latter case the field intensity has three maxima.
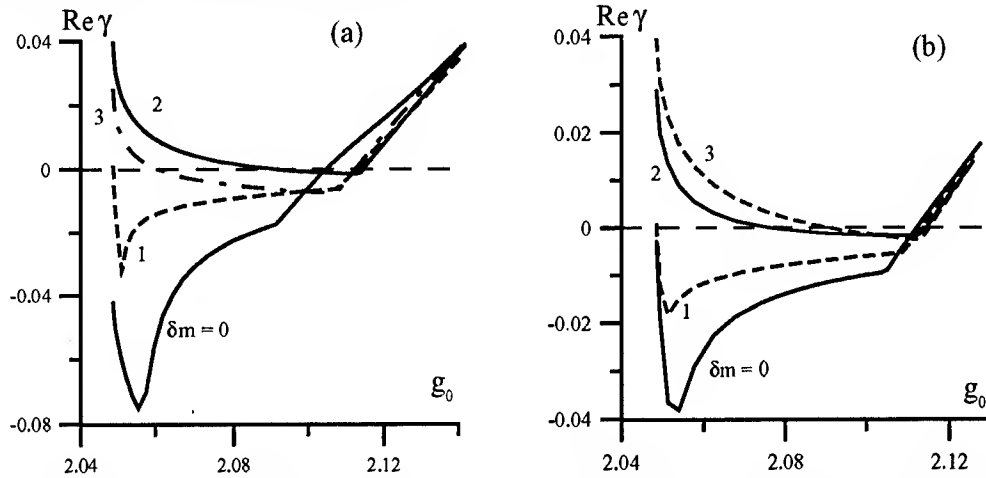
Fig. 2. Dependencies of the growth rate $\text{Re } \gamma$ on the small signal gain coefficient g_0 for perturbation's azimuthal harmonics $\delta m = 0,1,2,3$ (given near the curves) for ground-state vortex solitons with $m = 2$ (a) and 3 (b); $d = 0.1$

5. Numerical simulations

Direct solution of Eq. (1) by splitting method using the fast Fourier transform algorithm provides the information on the nonlinear stage of perturbation growth, scenarios of solitons' destabilization and on the resulting structures. The scenario of soliton destabilization depends on the soliton topological charge m. For solitons with $m = 0$ saddle-node bifurcation takes place with the decrease of gain. This instability leads to the decay of the field ($E \to 0$ at with time). Subcritical Andronov-Hopf bifurcation appears with the increase of gain and results in the growth of perturbations with $\delta m = 2$. At the first stage of the growth process the soliton exibits temporal oscillations, but finally cylindrically asymmetric two-hump (with two nearly equal intensity maxima) soliton is formed that rotates with a constant angular velocity. There are hysteresis jumps with variation of gain between symmetric and asymmetric solitons.

For solitons with $m > 0$ the scenarios of destabilization are different. In the case of $m = 1$, the symmetric soliton coexists with the two-hump soliton near the lower gain stability boundary. At higher gain the symmetric soliton is transformed into a rotating soliton with a single pronounced intensity maximum. For $m = 2$, the symmetric soliton is transformed into a two-hump soliton with the decrease of gain. At another boundary of its stability interval, i.e. at higher gain, the stationary symmetric soliton is transformed into an oscillating symmetric soliton that starts to rotate when the gain is further increased. An example of a stable three-hump soliton arising after destabilization of the symmetric soliton with $m = 3$ (low-gain domain) is given in Fig. 3. Some other localized structures and scenarios of their destabilization can be generated by varying parameters values.
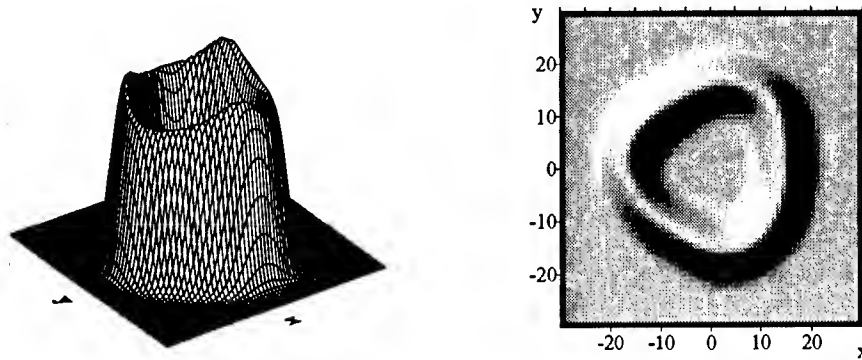
Fig. 3. Transverse intensity distribution for rotating triple-humped laser vortex: $g_0 = 2.0869$, $d = 0.1$

6. References

[1] N.N. Rosanov, *Spatial hysteresis and optical patterns* (Springer, Berlin, 2002).

[2] S.V. Fedorov, A.G. Vladimirov, G.V. Khodova, N.N. Rosanov, "Effect of frequency detunings and finite relaxation rates on laser localized structures," Phys. Rev. E **61**, 5814-5824 (2000).

Blocking and routing discrete solitons in two-dimensional networks of nonlinear waveguide arrays

Nikos K. Efremidis, Jared Hudock, and Demetrios N. Christodoulides
School of Optics/CREOL, University of Central Florida, Orlando, FL 32816
Eugenia D. Eugenieva
Intel Corporation, 300 Enzo Drive, San Jose CA 95138

Abstract: We show that discrete solitons can be navigated in two–dimensional nonlinear waveguide arrays. This can be accomplished by using vector interactions between two classes of solitons – signals and blockers. Disrete solitons in such two dimensional array networks exhibit a rich variety of functional operations, e.g. blocking, routing, logic functions, and time-gating.
©2001 Optical Society of America
OCIS codes: 190.5530, 200.4560

Discrete solitons are possible in several physical settings such as for example biological systems [1], nonlinear optics [2], solid-state physics, and Bose-Einstein condensates [3]. In optics discrete solitons (DS) were first predicted in nonlinear coupled waveguide arrays [2] and subsequently observed in AlGaAs systems [4]. In this latter case, discrete solitons exist due to the balance between the effects of discrete diffraction (that results from the coupling between successive waveguides) with that of material nonlinearity. Optical DS differ from their bulk counterparts in several important ways. For example, a unique property that arises from the discrete nature of waveguide-arrays, is that of reversed diffraction that allows dark DS in self-focusing media [5].

In this work we show that DS propagating in two-dimensional waveguide array networks can provide a rich environment for all-optical data processing applications. We demonstrate that such arrays can effectively act like *"soliton wires"* along which these self-trapped beams can travel. In addition, by using vector/incoherent interactions at the network junctions, these soliton signals can be routed at will along specific pathways. Therefore, this family of solitons can be *navigated anywhere* within a two-dimensional network of nonlinear waveguides. We begin our analysis by assuming that all waveguides are identical, regularly spaced, and separated from each other by distance D. To illustrate our results, let us assume that the cladding refractive index is $n_0 = 1.5$, the linear index difference between core and cladding is $\delta = 3 \times 10^{-3}$ and that the wavelength used is $\lambda_0 = 1.5 \ \mu m$. The effective core radius of each waveguide is $5.3 \ \mu m$ and the distance between them is $D = 15.9 \ \mu m$. These parameters result in a linear coupling constant of $c = 0.279 \ mm^{-1}$ between nearest neighbors. In addition we assume that the material is Kerr-nonlinear and supports vector interactions between two fields. In this case the two fields (propagating along z) evolve according to:

$$i\frac{\partial U}{\partial z} + \frac{1}{2k}\left(\frac{\partial^2 U}{\partial x^2} + \frac{\partial^2 U}{\partial y^2}\right) + \frac{k\delta f(x,y)}{n_0}U + \frac{kn_2 I_0}{n_0}\left(|U|^2 + |V|^2\right)U = 0 \qquad (1a)$$

$$i\frac{\partial V}{\partial z} + \frac{1}{2k}\left(\frac{\partial^2 V}{\partial x^2} + \frac{\partial^2 V}{\partial y^2}\right) + \frac{k\delta f(x,y)}{n_0}V + \frac{kn_2 I_0}{n_0}\left(|V|^2 + |U|^2\right)V = 0 \qquad (1b),$$

where U and V are the normalized field envelopes of the two optical fields, $k = 2\pi n_0 / \lambda_0$, and the scaled function $f(x,y)$ represents the linear refractive index distribution of this waveguide array. The term $n_2 I_0$ represents the maximum nonlinear contribution to the refractive index at the origin.

Using numerical relaxation methods we obtain discrete soliton solutions for a single row of waveguides. As an initial trial function we use the discrete soliton solution obtained from coupled mode theory [2]. We isolate two classes of solitons: (i) moderately confined solitons, or what we here call *signals*, and (ii) strongly confined beams or *blockers*. A signal beam is shown in Fig. 1(b). The maximum nonlinear change, required to support this self-trapped state is $\Delta n_{NL} = 4.6 \times 10^{-5}$. For signals, the maximum field amplitude at each lattice site follows a

hyperbolic secant function. The blocker beams used here are described approximately by a defect-like state of the form $\Psi(n) = \Psi_0 \exp(-|n| D / x_0)$ and require a nonlinear refractive index change of $\Delta n_{NL} = 1 \times 10^{-3}$. A simple 2D network along with a signal DS are shown in Fig1.
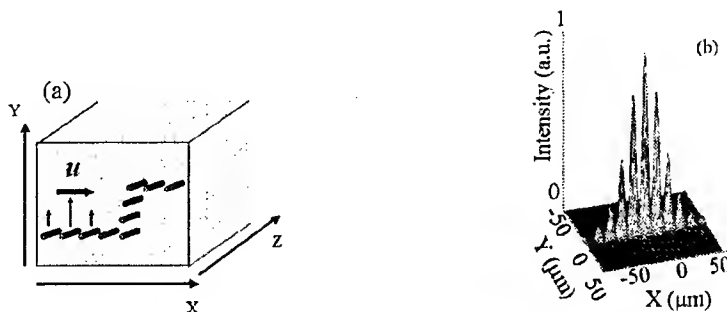
Fig1. (a) A simple 2-D network of waveguide arrays. (b) A signal discrete soliton.

Next, we set a signal DS in motion in a network involving two array branches intersecting at an angle of $120°$ or $90°$. This is done by initially imposing a linear chirp on the beam profile, i.e. $\Psi_n = \Psi_0 \mathrm{sech}(nD / x_0) \exp(i\gamma n)$, where in our example $\gamma = 0.6 \, \mathrm{rad}$. As a result the soliton slides along the waveguides with a speed of 1 lattice site per 4.2 mm of propagation. After passing the intersection the soliton moves to the upper branch. This motion occurs with almost no change in the soliton intensity and shape, i.e. the array behaves like a *soliton wire*. The loss after traversing the intersection is of the order of 1% and 5 %, for a $120°$ and a $90°$ bend, respectively.

Next we investigate how discrete solitons can be routed or blocked at network junctions using vector interactions. Fig. 2(a) shows a $Y - 120°$ degree junction involving three array branches. A DS of the blocking type is positioned at site A, right at the entrance of the lower branch. A signal soliton is then set in motion from left to right with $\gamma = 0.6 \, \mathrm{rad}$, starting from position B. The two solitons are mutually incoherent. Our simulations show that the signal is routed along the upper branch in an elastic fashion. Fig. 2(b) depicts the intensity of the signal at $z = 5.68 \, \mathrm{cm}$ (after passing the intersection). In all cases, the blocker always remains in its pre-assigned position. The transmission loss (after the junction) is in this case 2 % and is due to minor reflection and leakage losses to the lower branch. Our results show that a signal DS can also be routed at an X-junction with a 96% efficiency provided that two blocking beams are used at the pathway entries.
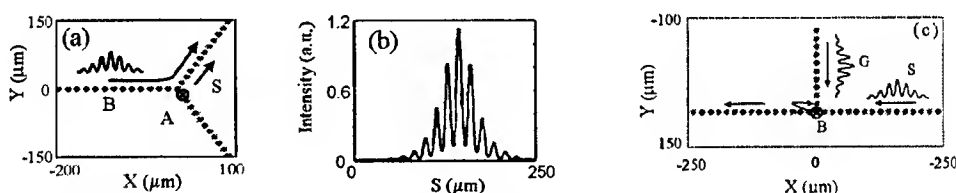
Fig2. (a) A 120 degree Y-junction, (b) a DS signal after passing the intersection, (c) a time-gating arrangement.

Finally, we have found that time-gating functions are also possible in such networks. Fig. 2(c) shows a T-junction with a blocker placed at the intersection. A signal DS (S), which is incoherent with the blocker travels from right to left. In this case, another signal DS (G) arrives before S and pulls up (by one slot) the blocker discrete soliton, just in time to allow S to pass through the gate.

Animations of the processes described in Figs. 1 and 2, as obtained numerically after solving Eqs.(1), can be viewed at www.lehigh.edu/~edc2/ .

References:

1. A.S.Davydov, *Biology and Quantum Mechanics* (Pergamon, Oxford, 1982).
2. D.N. Christodoulides and R.I. Joseph, "Discrete self-focusing in nonlinear arrays of coupled waveguides", Opt. Lett. **13**, pp. 794 - 796 (1988).

3.   A. Trombettoni and A. Smerzi, "Discrete solitons and breathers with dilute Bose-Einstein condensates", Phys. Rev. Lett. **86**, pp. 2353 -2356 (2001).

4.   H. S. Eisenberg, Y. Silberberg, R. Morandotti, A.R. Boyd, and J.S. Aithchison, "Discrete spatial optical solitons in waveguide arrays", Phys. Rev. Lett. **81**, pp. 3383 - 3386 (1998).

5.   R. Morandotti, H. S. Eisenberg, Y. Silberberg, M. Sorel, and J. S. Aitchison, "Self-focusing and defocusing in waveguide arrays", Phys. Rev. Lett. **86**, pp. 3296 – 3299 (2001).

Minimizing bending losses in two-dimensional discrete soliton networks

Jared Hudock, Nikos K. Efremidis, and Demetrios N. Christodoulides
School of Optics/CREOL, University of Central Florida, Orlando, FL 32816
Eugenia D. Eugenieva
Intel Corporation, 300 Enzo Drive, San Jose, CA 95138

Abstract: We show that reflection losses suffered by discrete solitons along sharp bends in two-dimensional waveguide-array networks can be almost eliminated. Analysis indicates that this can be accomplished by appropriately engineering the corner site of the bend. Our analytical results are verified using numerical simulations.
©2001 Optical Society of America
OCIS codes: 190.5530, 200.4560

In recent years, discrete solitons in nonlinear lattices have received considerable attention in many branches of science [1]. In optics, nonlinear waveguide arrays provide an excellent system where these entities can be experimentally studied and possibly used for all-optical applications [2,3]. In this latter context, discrete solitons (DS) are self-localized states that exist due to the balance between linear coupling effects and material nonlinearity. As previously noted in several works, the discrete nature of these systems can lead to a host of new effects that have no counterpart whatsoever in the continuous/bulk regime [2-4].

In a recent study we have shown that DS in two-dimensional networks can be used to realize *intelligent functional operations* such as blocking, routing, logic functions and time gating [5]. More specifically, this class of solitons can be all-optically navigated in 2-D array networks - a property highly desirable for optical routers. In this case, a DS can move transversely along any pre-assigned path and thus the array behaves like a *soliton wire*. Bends (like that of Fig. 1(a)) are essential elements of such DS networks. In general a soliton tends to loose power when it encounters a bend due to reflections. This becomes particularly problematic when bends are used in cascade. Thus reducing bending losses in such array networks is an issue of importance.

In this work we show that reflection losses occurring along sharp bends can be minimized by appropriate design. Analysis indicates that this can be accomplished by modifying the properties of the corner waveguide.

Let us consider a moderately confined DS (extending over 5 to 7 lattice sites) in a regularly spaced nonlinear waveguide array. In this regime, its envelope profile is described by $\Psi_n = \Psi_0 \operatorname{sec} h(nD / x_0) \exp(i\alpha nD)$, where D is the distance between successive waveguides, $n = 0, \pm 1, \ldots$ is the number of the waveguide site, x_0 is related to the DS spatial width, and α describes the phase tilt required to make the soliton travel along the array. We also assume single-mode, step-index-like waveguides of core radius $5.3 \,\mu m$. For demonstration purposes, let the cladding refractive index be $n_0 = 1.5$, that differs from that of the core by an amount $\delta = 3 \times 10^{-3}$. In this example, the wavelength is $\lambda_0 = 1.5 \,\mu m$ and the distance between waveguides is $D = 15.9 \,\mu m$. For this set of parameters, the linear coupling constant between adjacent waveguides is $c = 0.272 \, mm^{-1}$. In this case, the evolution of a discrete soliton in this Kerr nonlinear array is governed by:

$$i\frac{\partial U}{\partial z} + \frac{1}{2k_0 n_2}\left(\frac{\partial^2 U}{\partial x^2} + \frac{\partial^2 U}{\partial y^2}\right) + k_0 \delta f(x,y)U + k_0 \gamma I_0 |U|^2 U = 0 \qquad , \qquad (1)$$

where U is the normalized DS field envelope, γI_0 is the maximum nonlinear index change induced by the soliton at the origin, and $f(x, y)$ represents the two-dimensional index distribution of the waveguide array. A DS is obtained numerically using relaxation methods with $\gamma I_0 = 4.6 \times 10^{-5}$. When we launch such a soliton along a $70°$ bend (like that shown in Fig. 1(a)) with a phase tilt of $\alpha D = 0.6 \, rad$, the DS looses 38% of its energy after traversing the bend (after 7.4 cm of propagation).

To identify the source of these losses we employ the formalism of coupled mode theory. To do so we use the equivalent photonic circuit of the bend, shown in Fig.1(b). For the sake of generality, we assume that the waveguide at the corner is different from the rest, i.e. there is a defect at the site n = 0. The propagation constant for this site differs from the other waveguides by $\Delta\beta$. Let us also assume that the coupling constant between the waveguides n = -1 and n = 1 is κ. It follows from coupled mode theory that the field amplitudes at every site (except n = -1, 0, 1), are described by $i(da_n / dz) + c(a_{n+1} + a_{n-1}) = 0$. On the other hand, for n = -1,0,1, the optical fields evolve according to:

$$i\frac{da_{-1}}{dz} + \kappa a_1 + c(a_0 + a_{-2}) = 0 \tag{2a}$$

$$i\frac{da_0}{dz} + \Delta\beta\, a_0 + c(a_1 + a_{-1}) = 0 \tag{2b}$$

$$i\frac{da_1}{dz} + \kappa a_{-1} + c(a_0 + a_2) = 0 \tag{2c}$$
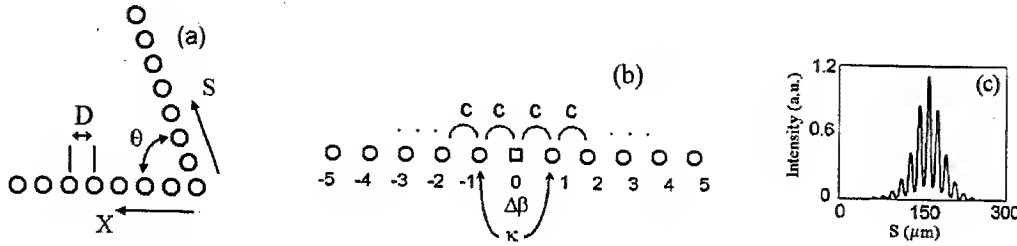
Fig1. (a) A waveguide array bend consisting of identical elements, (b) the unfolded photonic equivalent circuit, (c) the intensity profile of a discrete soliton after traversing a 70° bend when the corner site has been appropriately engineered.

By considering a forward, backward, and a transmitted wave, we can then obtain the field reflection and transmission coefficients. Analysis indicates that the bend reflection losses can be totally eliminated when:

$$\frac{\Delta\beta}{c} = -\frac{\left(\frac{2\kappa}{c}\right)\left[1 + \frac{\kappa}{c}\cos(\alpha D)\right]}{\left[1 - \left(\frac{\kappa}{c}\right)^2\right]} \tag{3}$$

For example, for the set of values used in the simulation and for $\theta = 70°$ and $\alpha D = 0.6\,\text{rad}$, Eq.(3) suggests that the reflection losses can be eliminated when $\Delta\beta/c = -1.91$. This required change $\Delta\beta$ at the corner site can be achieved by either modifying the core refractive index or by altering its radius. By keeping in mind that $\Delta\beta = k_0\Delta n_L$, the core refractive index at the corner site must be modified by an amount $\Delta n_L = \Delta\beta / k_0$ so as to minimize reflections. In this example, the required index change happens to be $\Delta n_L = -1.27\times10^{-4}$. In this case we find that a discrete soliton can traverse the bend with less than 1.1% losses (as opposed to 38% before the bend was engineered). The output intensity profile of the DS beam (shown in Fig1(c)), indicates that the DS has remained practically invariant after the bend. Similar results were also obtained for a 90° bend, where this time the required linear index change at $n = 0$ is $\Delta n_L = -2.24\times10^{-5}$. In this case the reflection losses were found to be below 0.65%.

In conclusion, we have demonstrated that by appropriate design, reflection losses suffered by DS along sharp bends in two-dimensional waveguide-array networks can be almost eliminated. This can be achieved by introducing a defect site at the bend corner.

Animations of the processes described in Fig. 1, as obtained numerically after solving Eq.(1), can be viewed at www.lehigh.edu/~nie2/ .

References:

1. A. C. Scott, Philos. Trans. R. Soc. London Ser. A **315**, 423 (1985).
2. D. N. Christodoulides and R. I. Joseph, "Discrete self-focusing in nonlinear arrays of coupled waveguides", Opt. Lett. **13**, pp. 794 - 796 (1988).
3. H. S. Eisenberg, Y. Silberberg. R. Morandotti, A. R. Boyd, and J. S. Aitchison. "Discrete spatial optical solitons in waveguide arrays", Phys. Rev. Lett. **81**, pp. 3383-3386 (1998).
4. R. Morandotti, H. S. Eisenberg, Y. Silberberg, M. Sorel, and J. S. Aitchinson. "Self-focusing and defocusing in waveguide arrays", Phys. Rev. Lett. **86**, pp. 3296 - 3299 (2001).
5. D. N. Christodoulides, and E.D. Eugenieva, " Blocking and routing discrete solitons in two-dimensional networks of nonlinear waveguide arrays", Phys. Rev. Lett., November 29, (2001).

Self-focusing of light mediated by cubic nonlinearities in potassium titanyl phosphate

Silvia Carrasco, Hongki Kim, and George Stegeman
CREOL/School of Optics, University of Central Florida, Orlando, Florida, 32816

Lluis Torner
Universitat Politecnica de Catalunya, Dept. of Signal Theory and Communications, 08034 Barcelona, Spain

Abstract: We report our observations of the self-narrowing of light beams mediated by dominant dissipative Kerr nonlinearities in a bulk KTP crystal. Observations agree with comprehensive numerical investigations. Drastic differences between up and down-conversion processes are uncovered.

1. Introduction

The impact of competing quadratic and cubic nonlinearities on optical soliton has been extensively studied (see, for example, [1]-[2]). In the usual case of second harmonic (SH) generation at or near phase matching between the fundamental frequency (FF) and second-harmonic (SH) interacting waves, the quadratic nonlinearity is dominant in the known materials that are transparent at optical wavelengths, and thus the cubic effects are very small and correspondingly difficult to observe experimentally. In contrast to this case, we report here observations conducted in a physical setting where the Kerr effect becomes dominant versus the quadratic one, modifying strongly the well-known beam evolution in media where only quadratic nonlinearities are significant. Two-photon absorption (TPA) was also present, and its effect on the solitons was analyzed numerically (see [3]-[4] for the impact of TPA on one dimensional solitons supported by pure Kerr nonlinearities in planar waveguides).

A suitable configuration for our purposes occurs when the quadratic effects are made small, for example in a crystal with a large Poynting-vector walk-off, or when the quadratic effects are reduced by operating at large wave vector mismatch between the FF and the SH. Such conditions occur, for example in potassium titanyl phosphate (KTP) cut for a Type II *oeo* interaction in the YZ plane. In such configurations, the walk-off angle between the two, orthogonally-polarized FF waves amounts to a large 1.8°. In addition, the quadratic nonlinear coefficient involved is small, i.e. d_{eff}=1.8 pm/V. These effects combined permit an unambiguous study of the importance of cubic effects in KTP. Notice that because of the huge existing walk-off, the FF(e) diverges rapidly from the FF(o), making quadratic soliton generation, even the "walking" type, impossible at powers below the damage threshold.

2. Numerical Simulations

To perform the simulations, we have considered standard cw (2+1) equations for a Type II oeo interaction, including quadratic nonlinearities, Poynting-vector walk-off, TPA, self-phase and cross-phase modulation, and diffraction all acting on the three interacting waves.

On physical grounds, it is very important to note that from Maxwell equations, the SH beam diffracts two times slower than the FF beams, while at the same time the strength of the effective cubic nonlinearities is two times larger at the SH wavelength than at the FF, even if the material's Kerr nonlinearity is the same at both frequencies. This is an indication that the impact of the cubic terms is expected to be much stronger in down-conversion than in up-conversion processes, an expectation fully confirmed by the experimental observations discussed below. In the simulations shown here we took the values of the Kerr and TPA coefficients reported in [5-6]. Simulations performed with different values of these coefficients show that the precise value of these coefficients does affect the evolution of the optical beams, but we verified that the main results discussed here hold for judicious variations of the coefficients around the values reported in [5-6]. The cross phase modulation coefficients in KTP are not known, and hence we also studied the impact of the assumed value for this coefficient. Fully (3+1) simulations for the long pulses used in the experiments (~20 ps) were also carried out.

Fig. 1 summarizes the outcome of our numerical findings. In down-conversion processes, the SH beam self-narrows due to the large cubic nonlinearity. The FF(o) beam which is co-directional with it narrows too, presumably by cross-phase modulation. Both beams feature a clean shape for reasonable values of the input power. On the contrary, in up-conversion processes, the SH breaks up due to TPA, and the FF(o) only narrows a bit. In either case a weak FF(e) beam is generated, that walks off the FF(o) (and SH) and diffracts.
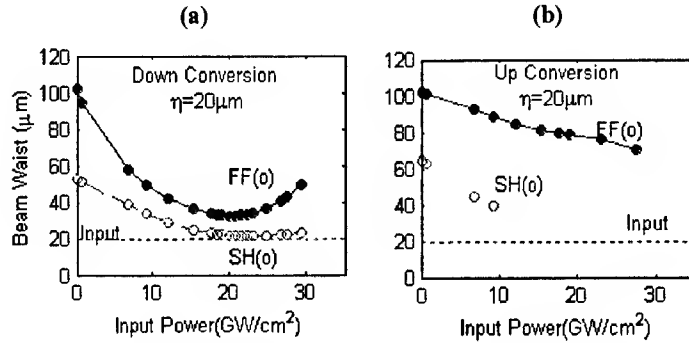
Figure 1: Simulations: Output beam waist of the FF(o) (filled circles) and SH (open circles) beams as a function of input intensity of the SH (a), and of the FF (b). Dotted line: input beam waist.

Figure 2 illustrates the typical output beams that are obtained in the simulations for up and down-conversion processes at a given input intensity. Notice that the FF(e) and FF(o) in down-conversion, and the SH in up conversion, are very weak because of the low efficiency of the frequency generation processes.
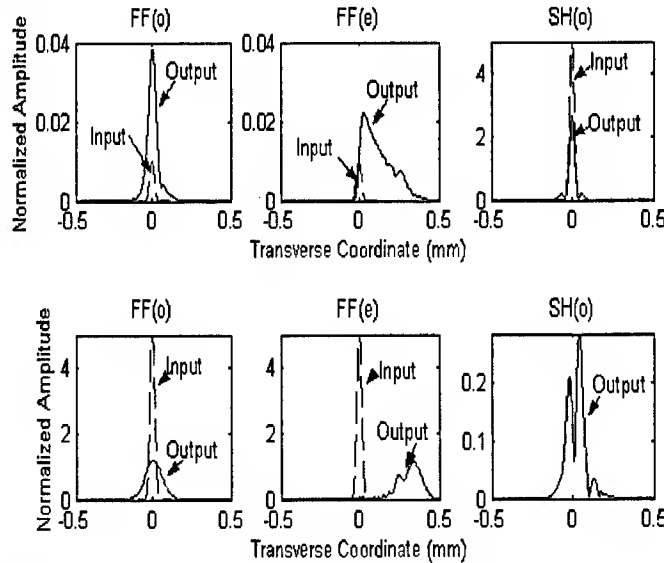
Figure 2: Simulations: Slices of the input(dashed lines) and typical output beams (solid lines) of the FF(o), FF(e) and SH beams in down (top) and up (bottom) conversion.

A key point to be addressed is whether the self-focusing of the SH and FF(o) beams predicted by the above simulations in down conversion processes is a purely Kerr-TPA effect, or the quadratic nonlinearity plays also a role. This question is answered by Fig. 3: One concludes than the self-focusing experienced by the SH beam does not depend on the phase-mismatch existing between the interacting waves; thus, it is to be attributed solely to the cubic nonlinearity. However, the simulations suggest that the self-narrowing of the FF(o) beam is a combination of quadratic nonlinearity and cubic cross-phase modulation. To be concrete, simulations suggest that when the strength of the cross-phase-modulation factors is assumed to be large enough, the quadratic nonlinearity does not play any relevant role; however, for weak cross-phase-modulation, self-narrowing of the FF(o) is only predicted to occur near phase- matching, an indication that the effects is due to competing cubic and quadratic effects.

(a)
(b)
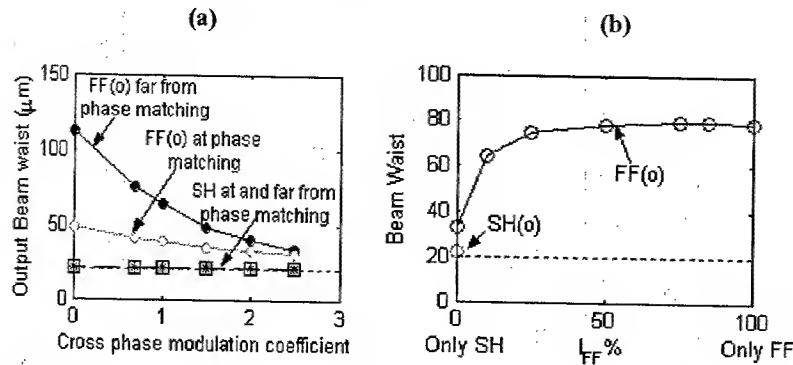
Figure 3: Simulations: (a) Output beam waist for down-conversion at and far from phase-matching. (b) Output beam waist of the beams for a fixed total intensity but different fractions of power on the FF(o) input signal.

3. Experimental Results

The experiments were conducted with input Gaussian beams (beam quality factor $M^2 \sim 1.1$-1.2) at 1064 nm from an EKSMA Nd:YAG laser delivering 25 ps pulses at a 10 Hz repetition rate. The input beam profile was focused into the input face of the 10 mm KTP bulk crystal cut for phase-matching in the YZ plane. Figure 4 summarizes the salient points of the observations. A very good agreement with numerical expectations is clear. For example, when only SH light was present at the entrance of the crystal, we observed a strong focusing of both SH and FF(o) beams at and outside phase-matching. In contrast, when only FF(o) was input, the output SH broke-up and the FF(o) beam diffracted. A comprehensive summary of the observations will be presented at the conference.

(a)
(b)
(c)
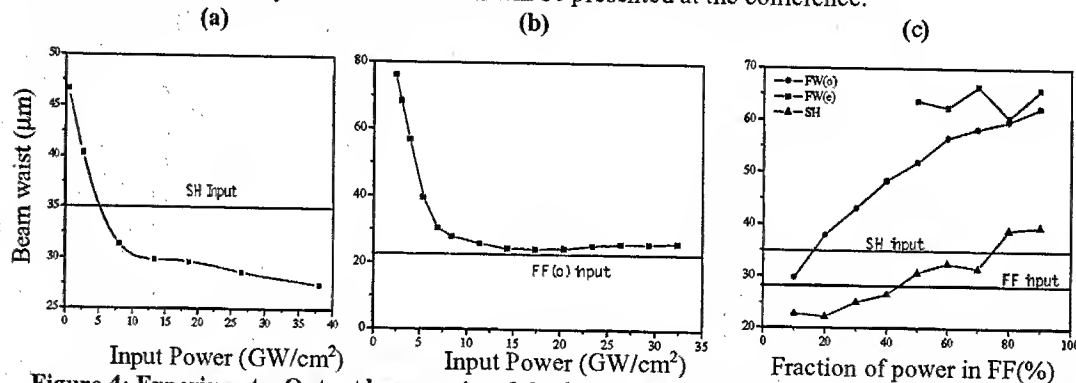
Figure 4: Experiments: Output beam waist of the SH, (a), and the FF(o), (b), versus input power on the SH in a down conversion configuration; (c) Output beam waist versus fraction of power in the input FF(o) for a fixed total input intensity of $33 GW/cm^2$.

4. Conclusions

We report our observations of the self-narrowing of the FF(o) and SH beams in down-conversion processes in a bulk crystal of KTP cut for phase-matching in the YZ plane. We attribute the narrowing of the SH beam to the dominant Kerr nonlinearity. The competition between the existing quadratic nonlinearity and the cubic cross-phase modulation effects are responsible for the narrowing of the FF(o) beam. Break-up of the SH was observed in up-conversion schemes, consistent with simulations.

This research was supported by an ARO MURI, and the Commission for Scientific Exchange between the USA and Spain.

5. References

[1] A.V.Buryak, Yu.S. Kivshar, S. Trillo, Opt. Lett. **20**, 1961 (1995).

[2] O. Bang, J. Opt. Soc. Am. B **14**, 51 (1997).

[3] J. S. Aitchison, Y. Silberberg, A. M. Weiner, D. E. Leaird, M. K. Oliver, J. L. Jackel, E. M. Vogel, and P.W. E. Smith, JOSA B, **8**, 1290 (1991).

[4] Y. Silberberg, Opt. Lett., **15**, 1005 (1990).

[5] R.DeSalvo, A.A. Said, D.J. Hagan, E. W. Van Stryland, and M.Sheik-Bahae, IEEE JQE, **32**, 1324 (1996).

[6] H. Li, F. Zhou, X. Zhang, W. Ji, Opt. Commun. **144**, 75 (1997).

Inverse transverse modulational instability

C. McCormick, R. Y. Chiao
Department of Physics
University of California
Berkeley, California 94720-7300
phone: 15106427166, fax: 15106438497
e-mail: chiao@physics.berkeley.edu

J. M. Hickmann
Departamento de Física
Universidade Federal de Alagoas
Cidade Universitária, 57072-970
Maceió, AL, Brazil
phone:+55822141424, fax:+55822141645
e-mail: hickmann@loqnl.ufal.br

Abstract: We investigate the inverse of a spatial modulational instability process which results from cross-phase modulation in a mediated four-wave interaction between two noncolinear beams crossing in a self-defocusing Kerr media.

Modulational instability (MI) is a common and important nonlinear effect in which a continuous wave breaks up into periodic, localized wave packets. Its long-term dynamics can lead to Fermi-Pasta-Ulam (FPU) recurrence, in which a nonlinear system returns to its initial energy configuration rather than thermalizing[1]. Interest in MI has increased since the recent experimental observation of FPU recurrence of nonlinear optical pulses in optical fibers[2]. MI in the spatial domain is known as beam filamentation and is a four-wave mixing process in which the phase matching is provided by cross-phase modulation[3, 4].

Recent experimental work has demonstrated the existence of a connected spatial effect, photon-photon scattering in the presence of a Kerr nonlinearity[5]. In this experiment, two counter-propagating beams "collide" in a rubidium vapor cell and photons scattered at ±90° from the beam axis are observed to be correlated in time, while photons are other angles are not. These results suggest a momentum-conserving photon-photon scattering process mediated by the Kerr nonlinearity.

In this paper we discuss a related process, in which the two "colliding" beams are in a frequency-degenerate, nearly-collinear configuration. Normally this configuration generates high-order diffracted beams, used for dephasing time measurements. We predict that a different kind of four-wave mixing process should be possible with this geometry, in which two photons of the noncollinear pump beams are absorbed and two collinear signal photons are generated in the direction of a bisector line between the pump beams. We will demonstrate that through a phenomenon similar to *weak-wave retardation* [6], phase matching is possible even if all four waves have the same frequency. We conclude by identifying this process as the inverse of the process that generates standard beam filamentation.

We begin by calculating the nonlinear polarization component in the direction of the signal beam, P_4. For simplicity we assume that this process will be stimulated, introducing a small seed field E_3 in the direction of the bisector line (see Fig. 1). The polarization of the signal field is

$$
\begin{aligned}
P_4 \;=\; & 3\chi^{(3)}_{xxxx}\{|E_4|^2 E_4 + 2(|E_1|^2 + |E_2|^2 + |E_3|^2|)E_4 \\
& + E_1 E_2 E_4^* exp(i((\vec{k}_1 + \vec{k}_2 - \vec{k}_3 - \vec{k}_4) \cdot \vec{z}) - (\omega_1 - \omega_2 + \omega_3 + \omega_4)t\}
\end{aligned}
\tag{1}
$$

where $\chi^{(3)}_{xxxx}$ is a component of the third order nonlinear susceptibility tensor and E_j are the fields associated with the pump ($j = 1, 2$) and signal ($j = 3, 4$) beams. The first term in this equation represents self-phase modulation (SPM), the second cross-phase modulation (XPM) and the third four-wave mixing. For a weak signal beam, SPM is negligible. The XPM terms from the pump beams are large and play an important part in the four-wave mixing process, while the XPM term from the signal beam may be neglected. The
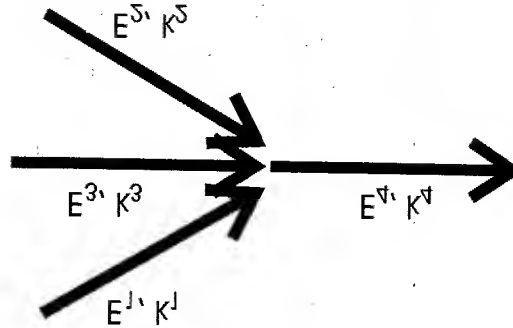
Fig. 1. Wave-vector configuration for weak-wave advancement.

exponential four-wave mixing term indicates that in order for this polarization to efficiently transfer energy into the signal field E_4, there must be energy conservation and phase matching between the different wave-vectors associated with each field.

In the degenerate case of equal frequencies, this phase matching appears difficult to achieve. However, the signal waves experience a decrease in the refractive index generated by the XPM term associated with the pump beams, assuming a negative nonlinear Kerr coefficient (the self-defocusing case). This difference in the refractive index is given by:

$$\Delta n = -\frac{3}{4n_0}|Re[\chi^{(3)}_{xxxx}]|(|E_1|^2 + |E_2|^2)$$

(2)

where n_0 is the linear index of refraction. Consequently, there exists a shortening of the weak-wave momentum vector by $\Delta k = -|\Delta n|\omega_0/c$, an effect which we call *weak-wave advancement* in analogy with "weak-wave retardation" in the case of the self-focusing sign of the Kerr nonlinearity[6]. For a certain parameter range, weak-wave advancement allows phase matching between the four wave vectors. In this range, this four-wave mixing process should transfer energy to the weak signal beam as efficiently as its counterpart.

Using Eq. 1 we calculate the evolution equation for the signal field E_4 in the paraxial and plane wave limits, finding

$$\frac{\partial E_4}{\partial z} = i4\gamma P(E_4 + 0.5E_4^* e^{i(6\gamma P - \Delta k)z})$$

(3)

where $\gamma = 6\pi|\vec{k}_4||\chi^{(3)}_{xxxx}/n_0^2$, P is the pump beam power and $\Delta k = |\vec{k}_1 + \vec{k}_2 - \vec{k}_3 - \vec{k}_4|$. In the self-defocusing case this equation has an exponentially growing solution for the parameter range

$$0 \le \Delta k \le 6\gamma P$$

(4)

with an exponential gain of

$$g = \sqrt{3(\gamma P)^2 - (\gamma P)\Delta k - 0.25(\Delta k)^2}$$

(5)

The signal beam gain is plotted against the collision half-angle in Fig. 2 for several values of γP.

We recall that weak-wave retardation in degenerate four-wave mixing is responsible for transverse modulational instability and resulting laser beam filamentation in the spatial domain[4]. This behavior is also in agreement with the idea that time domain modulational instability may be thought of as a four-wave mixing process where the fiber nonlinearity provides phase matching between the different fields[7]. In modulational instability in the time domain, a CW beam breaks up into a periodic pulse train with the simultaneous appearance of associated spectral side bands[8]. We conjecture that a time-domain version of the weak-wave
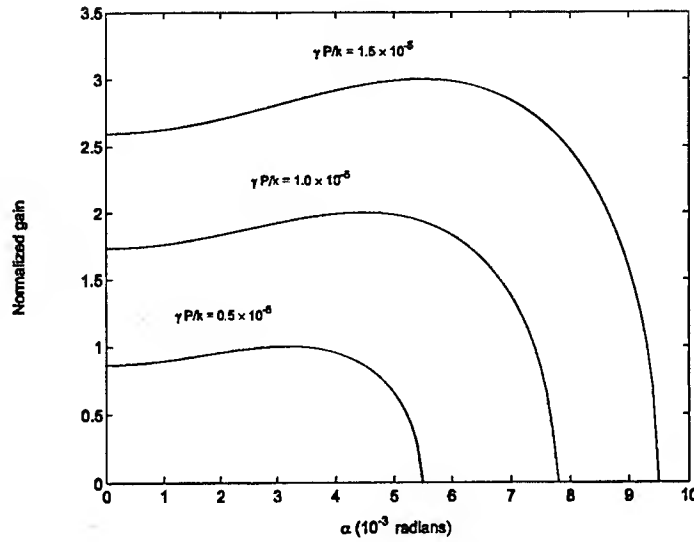
Fig. 2. Normalized signal beam gain as a function of collision half-angle.

advancement Kerr-mediated four-wave mixing effect described here should also exist. This time analogue effect should occur in the propagation of light at two different frequencies $\omega_0 + \Omega$ and $\omega_0 - \Omega$ through an optical fiber in the normal dispersion regime. These two optical frequency components correspond to the noncollinear pump beams in the spatial case discussed here. As a result, a stationary signal at the frequency ω_0 should be obtained, corresponding to the bisecting signal beam in the spatial case.

In conclusion, we have discussed a new four-wave mixing process mediated by the Kerr nonlinearity, and related this process to a different, inverse kind of modulational instability. We believe that this nonlinear scattering process could be at the heart of an experimental realization of a photonic Bose-Einstein condensate[9].

References

1. E. Fermi, J. Pasta, and H. C. Ulam, in *Collected Papers of Enrico Fermi*, edited by E. Segrè (The University of Chicago, Chicago, 1965), vol. 2 pp. 977-988.
2. G. Van Simaeys, Ph. Emplit, and M. Haelterman, Phys. Rev. Lett. **87**, 033902 (2001); G. Van Simaeys, P. Emplit, M. Haelterman, J. Opt. Soc. Am. **19**, 477 (2002); N. N. Akhmediev, Nature **413**, 267 (2001).
3. G. P. Agrawal, J. Opt. Soc. Am. B **7**, 1072 (1990).
4. R. W. Boyd, G. S. Agarwal, Phys. Rev. A **59**, R2587 (1999).
5. M. W. Mitchell, C. J. Hancox, and R. Y. Chiao, Phys. Rev. A **62**, 043819 (2000).
6. R. Y. Chiao, P. L. Kelley, and E. Garmire, Phys. Rev. Lett. **17**, 1158 (1966).
7. G. P. Agrawal, *Nonlinear Fiber Optics*, 2nd ed. (Academic, San Diego, 1995).
8. K. Tai. A. Hasegawa, and A. Tomita, Phys. Rev. Lett. **56**, 135 (1986).
9. R. Y. Chiao, Opt. Comm. **179**, 157 (2000).

Nonlocal mean-field theory in N-body quantum mechanics for Bose-Einstein condensation

Bernard Deconinck

Department of Mathematics, Colorado State University, Fort Collins, CO 80523-1874

J. Nathan Kutz

Department of Applied Mathematics, University of Washington
Box 352420, Seattle, WA 98195-2420 USA
email: kutz@amath.washington.edu, phone: (206) 685-3029, fax: (206) 685-1440

Abstract

Nonlocal interactions in the mean-field theory for Bose-Einstein condensation can destabilize nonlinear wavetrain solutions for a condensate trapped in standing light waves. The dynamics and stability are considered for arbitrary interaction potential.

The inherent complexity of the dynamics of N pairwise interacting particles in quantum mechanics often leads to the consideration of simplified mean-field descriptions. However, the simplified models can often neglect important physical effects which are present in the N particle description. Our specific interest is in the pairwise interaction potential between atoms in a Bose-Einstein condensate (BEC). So although we impose symmetry restrictions on the particle wave function [1], we do not impose any functional form assumptions on the pairwise interaction potential in our mean-field description [1, 2, 3]. We consider the trapping of a BEC in a standing-light wave. For this case we can construct exact solutions for the mean-field particle wave function for arbitrary interaction potential, which is an improvement on the canonical Gross-Pitaevskii description [2, 3].

The dynamics of N identical pairwise interacting quantum particles is governed by the time-dependent, N-body Schrödinger equation

$$i\hbar \frac{\partial \Psi}{\partial t} = -\frac{\hbar^2}{2m}\Delta^N \Psi + \sum_{i=1}^{N} W(\boldsymbol{x}_i - \boldsymbol{x}_j)\Psi + \sum_{i=1}^{N} V(\boldsymbol{x}_i)\Psi, \tag{1}$$

where $\boldsymbol{x}_i = (x_{i1}, x_{i2}, x_{i3})$, $\Psi = \Psi(\boldsymbol{x}_1, \boldsymbol{x}_2, \boldsymbol{x}_3, ..., \boldsymbol{x}_N, t)$ is the wave function of the N-particle system, $\Delta^N = \sum_{i=1}^{N}\left(\partial_{x_{i1}}^2 + \partial_{x_{i2}}^2 + \partial_{x_{i3}}^2\right)$ is the kinetic energy or Laplacian operator for N-particles, $W(\boldsymbol{x}_i - \boldsymbol{x}_j)$ is the symmetric interaction potential between the i-th and j-th particle, and $V(\boldsymbol{x}_i)$ is an external potential acting on the i-th particle.

The Hartree-Fock approximation (as used in [1]) for bosonic particles uses the separated wave function ansatz

$$\Psi = \psi_1(\boldsymbol{x}_1, t)\psi_2(\boldsymbol{x}_2, t)\cdots\psi_N(\boldsymbol{x}_N, t) \tag{2}$$

where each one-particle wave function $\psi(\boldsymbol{x}_i)$ is assumed to be normalized so that $\langle\psi(\boldsymbol{x}_i)|\psi(\boldsymbol{x}_i)\rangle^2 = 1$. Since identical particles are being considered,

$$\psi_1 = \psi_2 = \ldots = \psi_N = \psi, \tag{3}$$

enforcing total symmetry of the wavefunction. Using a Lagrangian reduction with the above assumed ansatz allows us to take the variational derivative with respect to $\psi(\boldsymbol{x}_i)$ which results in the Euler-Lagrange equation

$$i\hbar \frac{\partial \psi(\boldsymbol{x}, t)}{\partial t} = -\frac{\hbar^2}{2m}\Delta\psi(\boldsymbol{x}, t) + V(\boldsymbol{x})\psi(\boldsymbol{x}, t) + (N-1)\psi(\boldsymbol{x}, t)\int_{-\infty}^{\infty} W(\boldsymbol{x} - \boldsymbol{y})|\psi(\boldsymbol{y}, t)|^2 d\boldsymbol{y}. \tag{4}$$

NLTuD40-2

Kutz et al. "BECs in standing light waves"   2

Here, $x = x_i$, and Δ is the one-particle Laplacian in three dimensions. Note that the Euler-Lagrange equation (4) is identical for all $\psi(x_i, t)$. Equation (4) describes the nonlinear, non-local, mean-field dynamics of the wave function $\psi(x, t)$ under the standard assumptions (Eqs. (2) and (3)) of Hartree-Fock theory [1]. The coefficient of $\psi(x, t)$ in the last term in Eq. (4) represents the effective potential acting on $\psi(x, t)$ due to the presence of the other particles.

At this point, it is common to make an assumption on the functional form of the interaction potential $W(x - y)$. This is done so as to render Eq. (4) analytically and numerically tractable. Although the qualitative features of this functional form may be available, for instance from experiment, its quantitative details are rarely known. One convenient assumption in the case of short-range potential interactions is $W(x - y) = \kappa\delta(x - y)$. This leads to the Gross-Pitaevskii (GP) [2, 3] mean-field description:

$$i\hbar\frac{\partial\psi}{\partial t} = -\frac{\hbar^2}{2m}\Delta\psi + \beta|\psi|^2\psi + V(x)\psi, \qquad (5)$$

where $\beta = (N - 1)\kappa$ reflects whether the interaction is repulsive ($\beta > 0$) or attractive ($\beta < 0$). Although the Gross-Pitaevskii description is commonly accepted as the mean-field description for BECs, the assumption on the interaction potential $W(x - y)$ is difficult to justify physically and restricts the validity of Eq. (5). The considerations leading to Eqs. (4) and (5) are well known. They are included here since one of our aims is to emphasize the differences between two mean-field theories: one for which the interaction potential is given by a delta function, and one for which we assume arbitrary pairwise interactions. The limited validity of the GP equation leads us to reconsider Eq. (4), without imposing conditions on $W(x - y)$.

Although many BEC experiments rely solely on harmonic confinement to trap the condensate, we consider the situation of an external standing-light wave potential within a confining potential [4, 5]. This standing-light wave pattern is generated by the interference of two quasi-monochromatic lasers in a quasi-one-dimensional configuration. The rescaled governing mean-field evolution (4) in the quasi-one-dimensional regime is given by

$$i\frac{\partial\psi}{\partial t} = -\frac{1}{2}\frac{\partial^2\psi}{\partial x^2} + \alpha\psi\int_{-\infty}^{\infty}R(x - y)|\psi(y, t)|^2 dy + V(x)\psi. \qquad (6)$$

Here $\alpha = \pm 1$ is the sign of the interaction potential $W(x - y)$ at close range. Thus, α determines whether the close-range interaction is repulsive ($\alpha = 1$), or attractive ($\alpha = -1$). In other words, $\alpha = \text{sign}(a)$, where a is the s-wave scattering length of the atomic species. Depending on the species, a is either positive or negative, so that both signs of $\alpha = \text{sign}(a)$ are relevant for BEC applications. With these definitions, $R(x - y)$ is the rescaled interaction potential, which is positive at close range and $\int_{-\infty}^{\infty}R(z)\,dz = 1$. The external potential which models the standing light wave is given by

$$V(x) = V_0\sin^2(kx) \qquad (7)$$

where k determines the wavelength of the periodic potential.

The nonlocal, nonlinear equation (6) with the periodic potential (7) admits a one-parameter family of exact solutions. These solutions are found using an amplitude-phase decomposition of the form

$$\psi(x, t) = r(x)\exp\left[i\theta(x) - i\omega t\right]. \qquad (8)$$

Then $r(x)^2 = A\sin^2 x + B$ where B is a free parameter, $A = -V_0/\alpha\beta_1$, $\tan(\theta) = \sqrt{1 - V_0/\alpha B\beta_1}\,\tan(kx)$, $\omega = (V_0 + k^2)/2 + \alpha B - V_0/2\beta_1$, and $\beta_1 = \int_{-\infty}^{\infty}R(z)\cos(2kz)\,dz$. This can be verified by direct substitution, using the addition formula for $\cos(2(y - x) + 2x)$ and the fact that $R(x - y)$ is even.

NLTuD40-3

Kutz et al. "BECs in standing light waves"

3
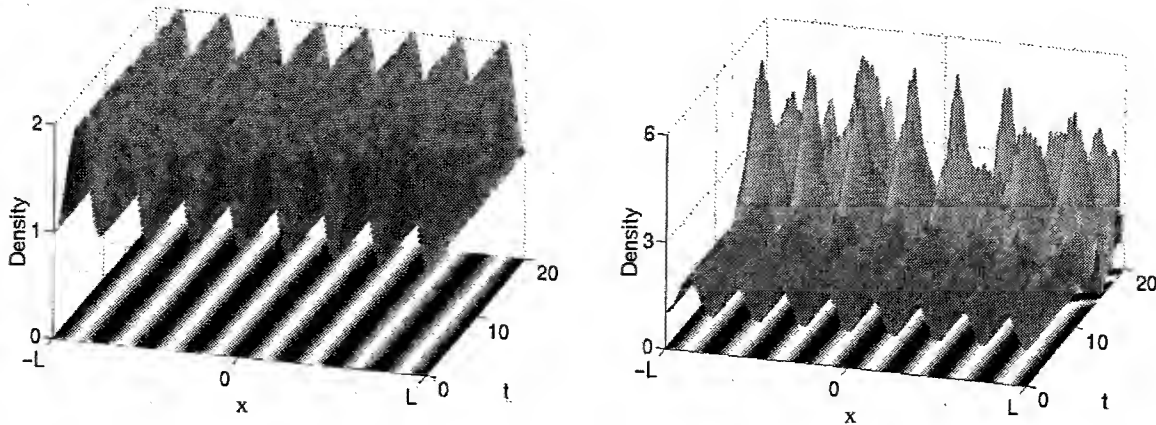
Figure 1: Evolution of the exact solution for (a) local ($\sigma = 0$) stable dynamics and (b) nonlocal ($\sigma = 0.005$) unstable dynamics.

Note again that aside from evenness, no mathematical assumptions on the interaction potential $R(x - y)$ were made in obtaining this family of exact solutions. The solutions to GP theory are easily recovered by letting $R(z) = \delta(z)$ [5].

In experiments, only stable solutions are expected to be observable. Likewise, unstable solutions whose onset of instability occurs on a timescale beyond the lifetime of the experiment may be observed. Of primary concern in this work is the stability of the condensate under the influence of nonlocality. To explore this, we consider the simple interaction potential

$$R(x - y) = \frac{1}{\sqrt{2\pi\sigma^2}} \exp\left(-\frac{(x - y)^2}{2\sigma^2}\right) \tag{9}$$

where σ determines the localization strength of the potential. In the limit $\sigma \to 0$, this interaction potential reduces to the Dirac delta function leading to the GP equation. Thus the parameter σ allows us to perturbatively explore the effects of localization.

Localization has a critical effect on the stability of exact solutions. In particular, the nonlocal contribution destabilizes an otherwise stable local solution. Figure 1 illustrates this phenomena by considering exact, repulsive solutions to Eq. (6) for both local ($\sigma = 0$) and nonlocal ($\sigma \neq 0$) evolutions. The local evolution is observed to be stable under perturbation whereas the nonlocal evolution quickly destabilizes. This suggests that the nonlocal contribution in the repulsive condensate results in a destabilization mechanism. Thus the simple GP mean-field approximation fails to capture a crucial aspect of the physical dynamics. Within the context of our model we explore the stability and dynamics of the condensate with the nonlocal contribution which is critical in determining the experimentally realizable behavior of the condensate.

References

[1] G. Baym, *Lectures on Quantum Mechanics*, (Addison-Wesley, Redwood City, CA, 1990).

[2] E. P. Gross, Nuovo Cimento **20**, 454 (1961).

[3] L. P. Pitaevskii, Sov. Phys. JETP **13**, 451 (1961).

[4] B. P. Anderson and M. A. Kasevich, Science **282**, 1686 (1998).

[5] J. C. Bronski, L. D. Carr, B. Deconinck, and J. N. Kutz, Phys. Rev. Lett. **86**, 1402 (2001).

All-optical AND and XOR logic gates in a single device

Marco A. Magaña Cervantes, J. Stewart Aitchison
Department of Electronics and Electrical Engineering
University of Glasgow, Glasgow G12 8QQ, UK
marcomag@elec.gla.ac.uk, jsa@elec.gla.ac.uk

Abstract: We simulate an all-optical device which performs the AND and XOR logic operations. The device is based on the Kerr-like nonlinear effect present in AlGaAs optimised to operate at 1.55 micrometers.
© 2002 Optical Society of America

OCISC codes: (130.0130) Integrated optics; (190.0190) Nonlinear optics

With the growing demand generated by the Internet there has been a growing interest in the use of all-optical switching and logic elements [1]. In this paper all-optical AND and XOR gates have been designed in a single device based on the Kerr-like non-linear effect in AlGaAs. The device is comprised of two different elements, a Y-junction and a nonlinear directional coupler connected as is shown in fig. 1.
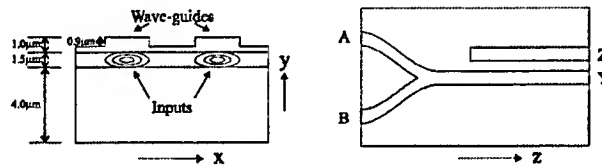
Figure 1. Left: Wafer structure. Right: Optical Device.

The device is based on an AlGaAs wafer with three layers with different concentrations of aluminium. The lower cladding has 24% of Al, which gives a refractive index of 3.3123 according to the Adachi method [2]. The guiding region has a concentration of 18% of Al and a refractive index of 3.3426. The upper cladding has the same composition as the first layer. These provide a light waveguide that confines the light in the 'y' direction. The physical thickness of the layers is 4.0 μm, 1.5 μm and 1.0 μm respectively from bottom to top. This configuration gives a mono-mode waveguide for a wavelength of 1.55 μm. The top layer presents rib waveguides to create the boundaries that give shape to the Y-junction and the directional coupler. In order to determine the core and cladding refractive indices ($n_c = 3.3298$, $n_o = 3.3255$) the rib waveguide is analysed by the effective-index method [3]. The width of the rib (4.0 μm) is selected for a mono- mode waveguide for a TE polarisation. The Y-junction is used as a two input port device and the nonlinear directional coupler as a switching element.

Non-linear directional couplers have been demonstrated to be good elements for switching [4]; this is a two parallel waveguide device with the same refractive index surrounded by lower refractive index material. It works as a coupled system in which a single light beam launched into one of its waveguides, called 'bar', is transferred to the second waveguide, called 'cross', at the coupling distance (Lc). When the power of the input beam is high enough to change the refractive index of the waveguide, (this due to the third order nonlinear effect $n = n_o + n_2I$), the system is decoupled and the light transition is reduced or completely cancelled, consequently the light goes straight through the bar waveguide. In this way the switching operation is achieved [5].

In order to control the light intensity of the input beam, we use the Y-junction to combine two light beams in phase to create a beam of high intensity. In this way, the absence or presence of light in either one of the inputs or both, produce different outputs which are interpreted as the AND, (bar waveguide or port Y), and the XOR, (cross waveguide or port Z) logic operations.

The whole device was simulated by the Beam Propagation Method (BPM) [6] and proved that the device makes two different logic operations. Figure 2 shows the device operation.

(a) Simulation of A = 1, B = 0, outputs Y = 0, Z = 1

(b) Simulation of A = 0, B = 1, outputs Y = 0, Z = 1

(c) Simulation of A = 1, B = 1, outputs Y = 1, Z = 0
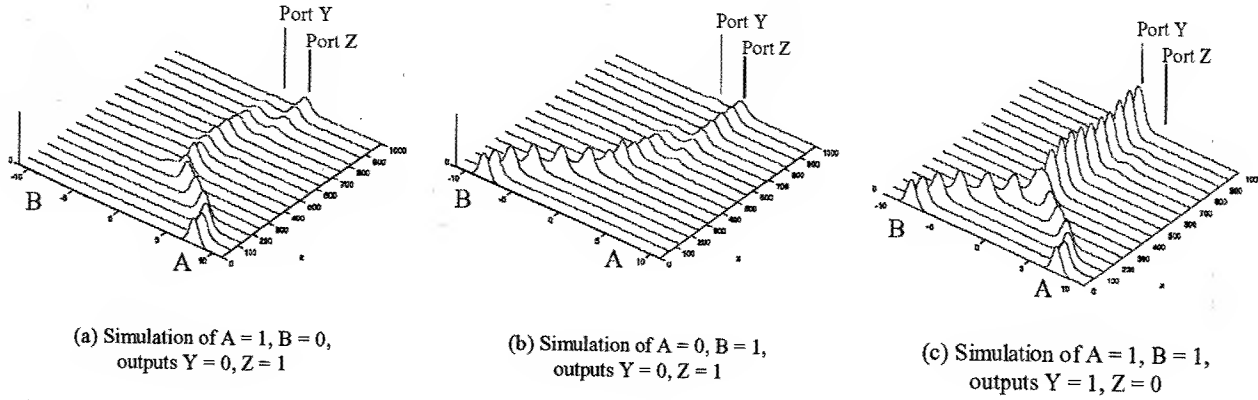
Figure 2.

The device behaviour shown on figure 2 shows that the device executes the logic operations presented in table 1. As the XOR gate is commonly used, as a programmable NOT gate, it is possible to invert any of the input signals if the second is set to a 'high' level.

Table 1. Logic operations made by the device.

A	B	Y	Z		A	B	Y	Z
0	0	0	0		1	0	0	1
0	1	0	1		1	1	1	0
1	0	0	1					
1	1	1	0					

Y = A AND B   Y = B
Z = A XOR B   Z = NOT B

On figures 2 (a) and (b) it is possible to observe that the coupling length is not the same due to the initial phase induced inherently by the Y-junction.

The Y-junction has been used as a combining element mainly in Mach-Zehnder Interferometers. In this both branches contain light beams of the same amplitude and combine them with the same or different phase to modulate the amplitude of the output beam. In the all-optical logic gate it is different because the Y-junction operates with light in only one of the input arm in two of the four possible input combinations. In these cases, the light experiments an abrupt change where the two branches join together and the width is doubled, as there is no light in the other branch to compensate the phase shift, it suffers a dramatic change in its phase and a new mode appears. As the waveguide width decreases the second mode spreads out of the waveguide, and the first mode bounces on the lateral boundaries causing a beating in the light beam as shown in fig 3.
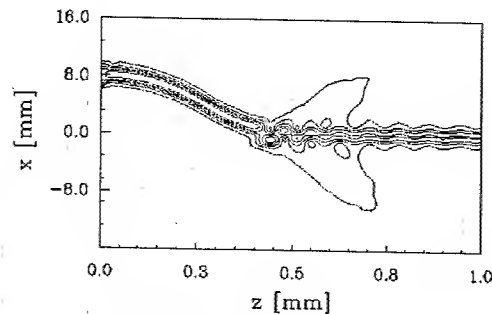
Figure 3. Light beating in the Y-junction.

This light bouncing affects the coupling distance of the coupler, preventing the achievement of an optimum design and performance. We will describe, in the future, different phase compensation techniques. One of those is to introduce a microprism in each one of the Y-junction arms just before the taper [7].

Conclusions: Although a light beating is introduced by the Y-junction, producing a slight shift in the coupling starting point, we have demonstrated the possibility of designing all-optical AND & XOR logic gates in a single device and also the possibility of using this as a NOT gate.

References:
[1]. C.K. Kim, J.M. Jeong, H. Chang, Japan. Journal of Applied Physics. **37**, 832, (1998)
[2]. S. Adachi, Journal of Applied Physics **58**, R1, (1985), S. Adachi, Journal of Applied Physics **66**, 6030, (1989)
[3]. K.S. Chaing, Optics Letters **16**-10, 714, (1991)
[4]. A. Villeneuve, C.C. Yang, P.G.W. Wigley, G.l. Stegeman, J.S. Aitchison, C.N. lronside, Applied Physics Letters **61**, 147, (1992)
[5]. J.S. Aitchison, A. Villeneuve, G.I. Stegeman, Journal of Nonlinear Optical Physics and Materials, **4**, 871, (1995)
[6]. J. Van Roey, J. Van Der Donk, P.E. Lagasse, Journal of the Optical Society of America, **71**, 803, (1981)
[7]. H. Jui-Ming, L. Ching-Ting, Applied Optics Letters, **38**-15, 3234, (1999)

Nonlinear beam shaping in an ensemble of cold rubidium atoms

T. Ackemann, M. Pesch

Institut für Angewandte Physik, Universität Münster, Corrensstraße 2/4,
D-48149 Münster, Germany
Tel.: +49-251-83-33553, Fax: +49-251-83-33513, E-mail:
t.ackemann@uni-muenster.de, pematze@uni-muenster.de

G. L. Lippi

Institut Non Linéaire de Nice, UMR 6618 CNRS, 1361 Route des Lucioles,
F-06560 Valbonne, France
lippi@inln.cnrs.fr

G. Labeyrie, B. Klappauf, R. Kaiser

Laboratoire Ondes et Désordre, FRE2302, 1361 Route des Lucioles, F-06560
Valbonne, France
labeyrie@inln.cnrs.fr, kaiser@inln.cnrs.fr

Abstract: Nonlinear beam shaping is observed in the far field of an intense resonant beam traversing a sample of cold rubidium atoms. Numerical simulations indicate the significance of the dispersive action of neighboring lines.
© 2002 Optical Society of America
OCIS codes: 190.4420, 190.3100

The tremendous success of optical cooling and trapping technology make samples of cold atoms of fairly high optical density readily available. First experiments indicate that huge optical nonlinearities might exist in these samples [1]. However, apparently not much work was done on effects of the optical nonlinearities on the spatial shape of the transmitted beam. Investigations on this subject appear to be particularly interesting since the atoms might be forced to move in an altered spatial profile of an intense beam if they are cold enough (see e.g. to [2]). This might yield new self-organized states of the coupled light-matter system. As a starting point we are investigating in this contribution beam shaping due to nonlinear beam propagation in a sample of cold rubidium atoms.

In our experiment, the nonlinear medium is a laser-cooled gas of Rubidium atoms (resonance wavelength $\lambda = 780$ nm, linewidth FWHM $\Gamma = 6$ MHz). The experimental setup has been described previously [3]. We prepare our atomic sample by loading a magneto-optical trap (MOT) from a dilute vapor of Rubidium 85 atom (magnetic gradient $\nabla B \approx 7$ G/cm, loading time $t_{load} \approx 0.7$ sec). Six independent trapping beams are obtained by splitting an initial laser beam slightly detuned to the red of the trapping transition (power per beam 30 mW, beam FWHM diameter 2.8 cm, Rubidium saturation intensity $I_{sat} \approx 1.6$ mW/cm^2, $\delta \approx -3\Gamma$). The repumper is obtained by two counterpropagating beams from a free running diode laser tuned to the $F = 3 \rightarrow F' = 3$ transition of the D2 line. Fluorescence measurements yield $N \approx 10^9$ atoms corresponding to a spatial density $n_{at} \approx 2 \times 10^9$ cm^{-3} at the center of the cloud (gaussian profile, FWHM diameter ≈ 7 mm). The velocity distribution of the atoms in the trap has been measured by a time-of-flight technique to be $v_{rms} \approx 10$ cm/s.

To observe the transmission of the intense probe beam (linear polarization) we alternate a transmission measurement phase with a MOT preparation phase. During the transmission phase, the magnetic gradient, the repumper and trapping beams of the MOT are switched off (residual power per trapping beam $0.2\mu W$). The resonant optical thickness of the sample, measured by transmission of a very weak probe beam is 18.
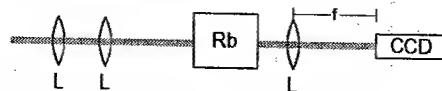
Fig. 1. Schematic view of setup. L lenses for adjusting beam parameters of input beam and far field imaging.

The injected beam has a Gaussian profile and is focused in the cloud (beam radius 74μm). The observation is done in far field in the focal plane of a $f = 300$ mm lens by means of a charge-coupled device camera with a dynamic range of 14 bit. Data taking starts at 2 ms after the switch off of the trapping beams and the

CCD image is integrated over 100 μs.

Fig. 2 shows a sequence of images obtained for increasing input power if the input beam is tuned to the F=3→F'=4 transition of ^{85}Rb. The difference between the transmitted beam after interaction with the cloud and the input beam without the cloud present is displayed. For low input power the beam is strongly absorbed. Correspondingly the transmission is reduced for small wave numbers (Fig. 2A). In the wings, at higher wave number there is already some indication for an enhancement of transmission indicating the onset of beam shaping effects. Increasing the power the areas with an enhancement of transmission move closer to the center (Fig. 2B) until there is actually an enhancement of transmission around zero wave number (Fig. 2C) For a saturation value of a few hundred the spatial Fourier spectrum of the transmitted beam is characterized by an enhancement in the center surrounded by a ring with reduced transmission. For the highest investigated power the ring starts to break up again (Fig. 2D). The origin of the intermediate symmetry breaking is not clear but is probably due to some astigmatism in the input beam.
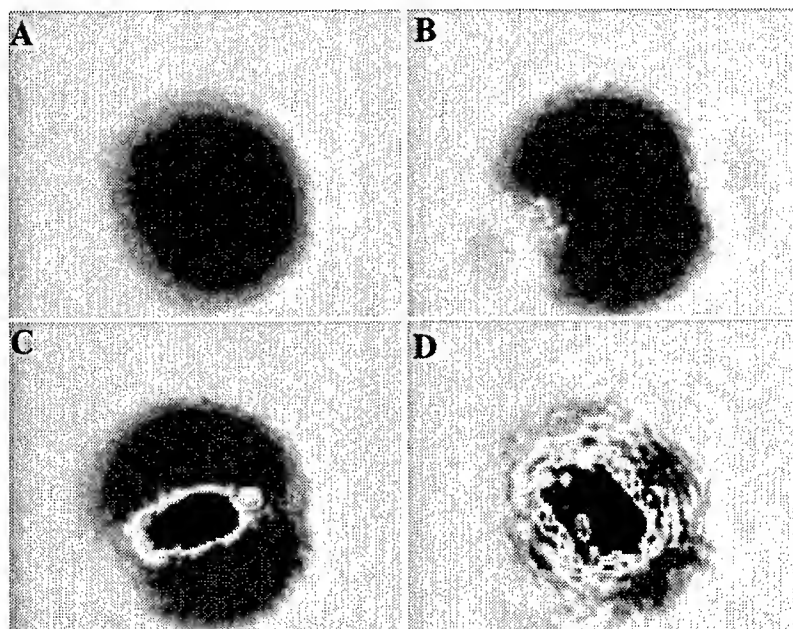
Fig. 2. Sequence of patterns obtained for increasing input power. Light grey denotes that the transmitted beam is less intense than the input beam, dark grey the opposite (denoting an enhancement via green to blue. Power levels: A) 6.9 μW, B) 23 μW, C) 92 μW, D) 460 μW.

For the sequence of images displayed in Fig. 2 the total (i.e. the spatially integrated) transmission of the sample increases from 0.2 to nearly 1 (Fig. 3). If the enhancement of transmission occurs for zero wave number the transmission if greater than 0.9, i.e. the sample is strongly saturated.
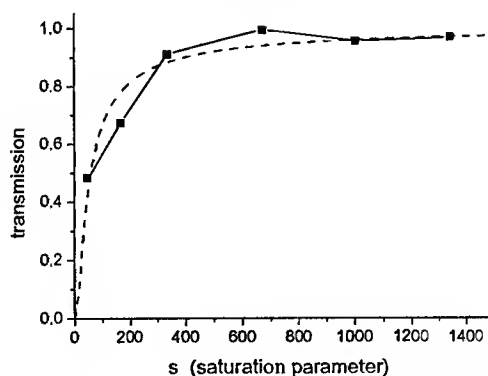
Fig. 3. Total transmission of the Rb sample in dependence of the saturation parameter s. s is calculated for the electronic transition. The dashed line is the theoretical prediction.

Under the experimental conditions the optical nonlinearity is a complicated mixture of contributions arising from electronic saturation, optical Zeeman pumping and hyperfine pumping and the strength of the respective contributions are not clear, yet. Hence, for a first treatment, we restrict modeling to a rate equation describing a generic saturable nonlinearity. The stationary solution is given by

$$w = \frac{P}{\gamma + P},$$

(1)

where P denotes the pump rate proportional to the intensity of the light field, γ the relevant relaxation rate and w denotes a normalized population difference. The stationary solution is used to determine the complex dielectric susceptibility $\chi = \chi_{lin}(1 - w)$ which enters into the beam propagation code.

For resonant excitation, i.e. allowing only for absorptive effects, numerical simulations yield beam shaping phenomena and the possibility of some small enhancement of transmission for some high wave numbers but no enhancement for the zero wave number. These results motivate the consideration of dispersive effects from neighboring lines as possible origin of the observed beam shaping.

The closest line is the F=3→F'=3 transition, which is 120 MHz (about 20 homogeneous linewidth, FWHM) at the low frequency side of the F=3→F'=4-transition. Since the F=3→F'=4 is driven resonantly and is essentially saturated we neglect it in a first approximation and perform numerical simulations assuming a strong blue detuning of 20 linewidths. It turns out that already for $P \approx \gamma$ one obtains an enhancement of transmission for zero wave number. This maximum is surrounded by a ring with a reduction of transmission. Since the saturation parameter for the resonant and the nonresonant transition should differ by a factor of about $40^2 = 1600$ also the absolute power scaling is not unreasonable.

To summarize we reported nonlinear beam shaping in a sample of called Rb atoms. The results indicate that one has to consider the contributions of several hyperfine transitions due the high light levels involved.

References

1. L. V. Hau, S. E. Harris, Z. Dutton, and C. H. Behroozi, Nature 397, 594 (1999).
2. M. Saffman, Phys. Rev. Lett. 81, 68 (1998).
3. G. Labeyrie, F. de Tomasi, J.-C. Bernard, C.A. Müller, Ch. Miniatura and R. Kaiser Phys. Rev. Lett., 83, 5266 (1999)

Soliton interaction in weakly nonlocal nonlinear media

N.I. Nikolov[1,2], **O. Bang**[1] and **P.L. Christiansen**[1]

[1]*Informatics and Mathematical Modelling, Technical University of Denmark,*
DK-2800 Kongens Lyngby, Denmark
phone:+45 45 25 31 09, fax:+45 45 93 12 35, e-mail:nin@imm.dtu.dk

J.J. Rasmussen[2]

[2]*Risø National Laboratory, Optics and Fluid Dynamics Deptartment, OFD-128*
P.O. Box 49, DK-4000 Roskilde, Denmark

Wiesław Królikowski[3]

[3]*Australian Photonics Cooperative Research Centre, Laser Physics Centre,*
Research School of Physical Science and Engineering,
The Australian National University, Canberra ACT 0200, Australia

Abstract: We study the interaction between spatial solitons in weakly nonlocal Kerr materials. The weak nonlocality may reduce the interaction and cause in-phase solitons to separate and out-of-phase solitons to attract.
© 2002 Optical Society of America
OCIS codes: (260.5950) Self-focusing ; (190.4420) Nonlinear optics, transverse effects in

Let us consider a phenomenological model of nonlocal nonlinear Kerr type media, in which the refractive index change Δn induced by a beam with intensity $I(x,z)$ can be represented in general form as

$$\Delta n(I) = \pm \int_{-\infty}^{\infty} R(x' - x)I(x',z)dx',\tag{1}$$

where the positive (negative) sign corresponds to a focusing (defocusing) nonlinearity and x and z denote transverse and propagation coordinates, respectively. The real, localized, and symmetric function $.(x)$ is the response function of the nonlocal medium, whose width determines the degree of nonlocality. For a singular response, $R(x) = \delta(x)$, the refractive index change becomes a local function of the light intensity, $\Delta n(I) = \pm I(x,z)$, i.e. the refractive index change at a given point is solely determined by the light intensity at that very point. With increasing width of $R(x)$ the light intensity in the vicinity of the point x also contributes the index change at that point. In the limit of a highly nonlocal response Snyder and Mitchell showed that the beam evolution was described by the simple equation for a linear harmonic oscillator [1]. The influence of nonlocality of the nonlinear response on the dynamics of beams was illustrated for the special logarithmic nonlinearity, which allows exact analytical treatment [2].

While Eq. (1) is a phenomenological model, it nevertheless describes several real physical situations. Possible physical mechanisms responsible for this type of nonlinear response includes various transport effects, such as heat conduction in materials with thermal nonlinearity [3, 4, 5], diffusion of molecules or atoms accompanying nonlinear light propagation in atomic vapours [6], and drift and/or diffusion of photoexcited charges in photorefractive materials [7, 8]. Nonlocal effects have been considered in discrete nonlinear lattices where the excitation extended over few sites results in appearance of higher order dispersion terms in the continuum limit [14, 15]. A highly nonlocal nonlinearity of the form (1) has also been identified in plasmas [9, 10, 11, 12] and of many body interaction processes in the description of Bose-Einstein condensates [13].

Even though it is quite apparent in some physical situations that the nonlinear response in general is nonlocal (as in the case of thermal lensing), the nonlocal contribution to the refractive index change was often neglected [16, 17]. This is justified if the spatial scale of the beam is large compared to the characteristic response length of the medium (given by the width of the response function). However, for very narrow beams the nonlocality can be of crucial importance and has to be taken into account. For instance, it has been shown theoretically that a weak nonlocal contribution arrests collapse (catastrophic self-focusing) of high power optical beams in a self-focusing medium and leads to the formation of stable 2D (diffracting in two transverse dimensions) solitons [11, 12, 18, 19]. On the other hand, a purely nonlocal nonlinearity leads to formation of so-called cusp solitons, which, however, are unstable [9].

Some of the consequences of nonlocality in the nonlinear response have been observed experimentally. Suter and Blasberg reported stabilization of 2D solitary beams in atomic vapors due to atomic diffusion, which

carries excitation away from the interaction region [6]. Also, the discrepancy between the theoretical model of dark solitons and that observed experimentally in a medium with thermal nonlinearity has been associated with nonlocality of the nonlinearity [16, 17]. We investigate the interaction of 1D beams in a weakly nonlocal nonlinear media with response of the general form (1). We start with the paraxial wave equation describing propagation of a 1D beam with envelope function $\psi = \psi(x, z)$ and intensity $I = I(x, z) = |\psi(x, z)|^2$,

$$i\partial_z\psi + \frac{1}{2}\partial_x^2\psi + \Delta n(I)\psi = 0. \tag{2}$$

For weak nonlocality, Fig. 1 (b), the response function $R(x)$ is narrow compared to the extent of the beam,
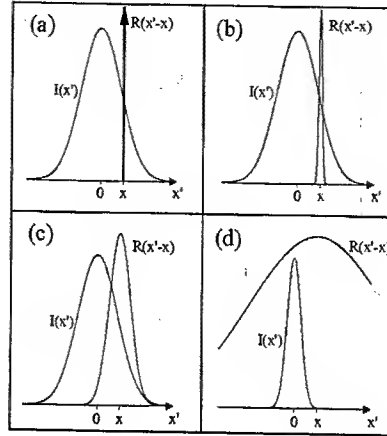
Fig. 1. Different degrees of nonlocality.

so we can expand $I(x', z)$ around the point $x' = x$ to obtain

$$\Delta n(I) = \pm(I + \gamma\partial_x^2 I), \tag{3}$$

where the nonlocality parameter $\gamma > 0$ is given by

$$\gamma = \frac{1}{2}\int_{-\infty}^{\infty} R(x)x^2 dx, \tag{4}$$

and where we have assumed that the response function is normalized, $\int_{-\infty}^{\infty} R(x)dx = 1$. Note that for $R(x) = \delta(x)$, $\gamma = 0$ and Eq. (3) describes the local Kerr nonlinearity. For weakly nonlocal meda $\gamma \ll 1$ is a small parameter. Substituting $\Delta n(I)$, given by Eq. (3), into Eq. (2) gives the modified nonlinear Schrödinger equation

$$i\partial_z\psi + \frac{1}{2}\partial_x^2\psi \pm (|\psi|^2 + \gamma\partial_x^2|\psi|^2)\psi = 0. \tag{5}$$

The weak nonlocality appears thus as a perturbation to the local nonlinear refractive index change. This perturbation is of negative sign in the central part of a beam, where it serves to decrease the refractive index change. Hence, even for very narrow and sharp intensity distributions, the resulting self-induced waveguide will be wide and a smooth function of the transverse coordinates.

The soliton interaction behavior for local nonlinear responce is well known to lead to attraction of in-phase solitons and repelling of solitons with phase difference equal to π- out-of-phase solitons. This behavior can be explained in terms of changes of the nonlinear refractive index. As it is seen from Fig. 2, in the case of fully local nonlinearity, the nonlinear refractive index, (1) is directly proportional to the total intensity of the two overlapping solitons. This leads to bigger Fig.2 (a) or lower Fig. 2 (b) values of the refractive index for the region between the two solitons, than in the case if a single soliton propagation is assumed. This can explain why in-phase solitons attract, and out-of-phase repell. In order to change this by weak nonlocality, the sign of the nonlocal parameter γ, should be properly chosen. The sign of the nonlocal contribution to the nonlinear refractive index, is determined by the sign of γ and the sign of the derivative of the total field. Aming compensation of the attraction or repelling, γ has to be negative for in-phase-soliton interactions and

positive for out-of-phase. In this way the nonlocality can compensate the increased or decreased nonlinear refractive index due to the soliton overlap. Fig. 2 reveals a possibility by chosing proper sign and value of the weak nonlocality to find interesting properties of soliton interaction in nonlocal media. Reduced interaction due to thermal nonlocality was recently reported in [25]. In this case the decrease of interaction due to loss, should be carefully distinguished from the nonlocal nonlinear effect.
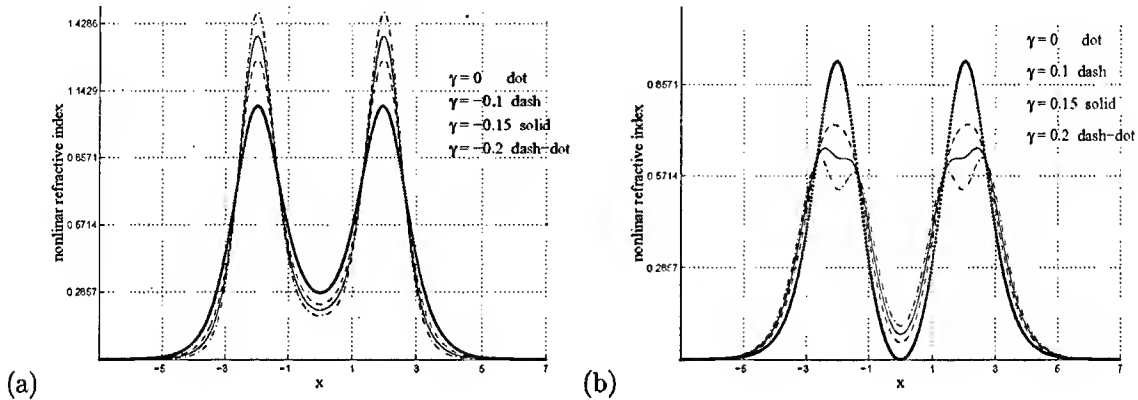
Fig. 2. The total nonlinear refractive index (3) for different values of γ and in-phase (a) and out-of-phase solitons (b).

1   Conclusion

We have shown that due to weak nonlocality, one can change the nonlinear refractive index aming reduction of Kerr type soliton interaction. Further investigations will involve variational and numerical investigations. This work was supported by the Danish Technical Research Council (Grant no. 26-00-0355) and the Graduate School in Nonlinear Science (The Danish Research Agency).

References

1. A. Snyder and J. Mitchell, Science **276**, 1538 (1997).
2. A. Snyder and J. Mitchell, J. Opt. Soc. Am. **16**, 236 (1999).
3. J.P. Gordon, R.C. Leite, R.S. Moore, S.P. Porto, and J.R. Whinnery, J. Appl. Phys. **36**, 3 (1965).
4. S. Akhmanov, D.P. Krindach, A.V. Migulin, A.P. Sukhorukov, and R.V. Khokhlov, IEEE J. Quant. Electron. QE-4, 568 (1968).
5. M. Horovitz, R. Daisy, O. Werner, and B. Fischer, Opt. Lett. **17**, 475 (1992); M.D. Iturbe-Castillo, J.J. Sanchez-Mondragon, and S. Stepanov, Opt. Lett. **21**, 1622 (1996); D. Kip, E. Krätzig, V. Shandarov, and P. Moretti, Opt. Lett. **23**, 343 (1998).
6. D. Suter and T. Blasberg, Phys. Rev. A **48**, 4583 (1993).
7. S. Gatz and J. Herrmann, Opt. Lett. **23**, 1176 (1998).
8. B. Crosignani, A. Degasperis, E. DelRe, P.Di Porto, and A.J. Agranat, Phys. Rev. Lett. **82**, 1664 (1999).
9. M.V. Porkolab and M.V. Goldman, Phys. Fluids, **19**, 872 (1976).
10. A.G. Litvak and A.M. Sergeev, JETP Lett. **27** 517 (1978).
11. H.L. Pecseli and J.J. Rasmussen, Plasma Phys. **22**, 421 (1980).
12. T.A. Davydova and A.I. Fishchuk, Ukr. J. Phys. **40**, 487 (1995).
13. F. Dalfovo, S. Giorgini, L.P. Pitaevskii, and S.Stringari, Rev. Mod. Phys. **71**, 463 (1999).
14. X. Wang, D. W.Brown, K. Lindenberg, and B.J. West, Phys. Rev. A **37**, 3557 (1988).
15. A. Nakamura, J. Phys. Soc. Japan **42**, 1824 (1977).
16. G.A. Swartzlander, Jr., and C.T. Law, Phys. Rev. Lett. **69**, 2503 (1992).
17. B. Luther-Davies and X. Yang, Opt. Lett. **17**, 1755 (1992); A. Dreschuh, G.G. Paulus, F. Zacher, F. Grasbon, and H. Walther, Phys. Rev. E **60**, 6111 (1999).
18. S.K. Turitsyn, Teoreticheskaya i Matematicheskaya Fizika, **64**, 226 (1985).
19. S. Abe and A. Ogura, Phys. Rev. E **57**, 6066 (1998).
20. E.W. Ladtke, K.H. Spatschek, and L. Stenflo, J. Math. Phys. **24**, 2764 (1983).
21. W. Krolikowski and O. Bang, *Modulation instability in nonlocal nonlinear media*, unpublished.
22. W. Krolikowski, N. Akhmediev, and B. Luther-Davies, Phys. Rev. E **48** 3980 (1993).
23. Y. Kivshar and W. Krolikowski, Opt. Lett. **20**, 1527 (1995).
24. I. Bialynicki-Birula and J. Mycielski, Phys. Scripta **20**, 539 (1979).
25. M. Bertolotti, R. Li Voti, S. Marchetti, C. Sibilia, Opt.. Comm. **133**, 578 (1997).

Dark spatial solitons in photorefractive planar waveguide LiNbO₃:Ti:Fe

Marina N. Frolova, Maxim V. Borodin, Stanislav M. Shandarov, Vladimir M. Shandarov
Department of Electronic Devices, State University of Control Systems and Radioelectronics, 40 Lenin Avenue, Tomsk 634050, Russia
frolova@phys.tsu.ru

Abstract: We study the processes of formation of dark photovoltaic spatial soliton in photorefractive LiNbO₃:Ti:Fe waveguide. The 2-D distribution of the optical field is considered to define the nonlinear change of the refractive index.
© 2002 Optical Society of America
OCIS codes: (190.5330) Photorefractive nonlinear optics

1. Introduction

Self-action of light beams in photorefractive nonlinear waveguides can be observed at very small light power. In LiNbO₃ photovoltaic defocusing nonlinearity leads to existence of dark spatial solitons which were observed both in bulk crystal and planar waveguide [2]. To determine the conditions of the soliton formation for different waveguide modes it is nessesery to take into account 2- dimentional distribution of optical field in guided layer. In this report we define the parameters of input beams to propagate of solitons for different modes of the waveguide formed by sequential diffusion of titanium and iron in Z-cut of LiNbO₃.

2. Theory

To analyze a nonlinear propagation of light beams along coordinate x in planar waveguide, we assume the optical field of TM mode as follows:

$$E(x,y,z,t) = E_{mz}(z)A(x,y)\exp(ikn_m x - i\omega t) + c.c. \ , \tag{1}$$

where $c.c.$ denotes the complex conjugate value, $k = 2\pi/\lambda$ is a wave number, λ is the wavelength for the free space, ω is the light frequency, n_m is the effective refractive index, $A(x,y)$ and $E_m(z)$ are the amplitude shape of a light beam and the normalized cross distribution of an optical field in waveguide mode, respectively. We assume that ordinary and extraordinary refractive indexes are dependent on transverse coordinate z, caused by impurity in-diffusion in the waveguide substrate, and the nonlinear changes of ones have two components caused by electro-optical effect:

$$n_o(x,y,z) = n_{so} + \Delta n_{wo}(z) + \Delta n_o(x,y,z) \tag{2}$$

$$n_e(x,y,z) = n_{se} + \Delta n_{we}(z) + \Delta n_e(x,y,z), \tag{3}$$

where n_{so} and n_{se} are the refractive indexes of the substrate.

The wave equation in paraxial approximation is described by:

$$\left(\frac{\partial}{\partial x} - \frac{i}{2kn_m}\frac{\partial^2}{\partial y^2}\right)A(x,y) = -ik\,\Delta\tilde{n}_e^m(x,y)\,A(x,y) \ , \tag{4}$$

where space-average nonlinear change of refractive index is

$$\Delta \tilde{n}_e^m (x,y) = \frac{\int\limits_0^\infty E_{mz}^2(z)\Delta n_e(x,y,z)dz}{\int\limits_0^\infty E_{mz}^2(z)dz} \,. \tag{5}$$

In the waveguides formed by diffusion of titanium and iron in LiNbO$_3$ the photovoltaic mechanism of photorefractive effect is predominant and photovoltaic current has only z component:

$$j_z^{ph} = \beta_{33}(z)\left|A(x,y)\right|^2 E_{mz}(z), \tag{6}$$

where E_{mz} is real function. The fact that the function $A(x,y)$ is more smooth then $E_{mz}(z)$ leads to charge distributes only along z-axis. So the x- and y- components of electric field are negligible, and the space charge field is:

$$E_{sc}^{TM}(x,y,z) = -\frac{\beta_{33}(z)E_{mz}^2(z)\left|A(x,y)\right|^2}{\sigma_d(z) + B_{ph}(z)E_{mz}^2(z)\left|A(x,y)\right|^2} \,, \tag{7}$$

in the case of TM modes. Here β_{33} are the components of photovoltaic tensor, σ_d is the dark conductivity, and B_{ph} is the photoconductivity coefficient.

The charge carriers excited by light field are redistributed in a space due to the photovoltaic effect, and then they are trapped in dark regions by deep traps, that forms a space charge electric field E_{sc}. This field modulates in Z-cut of LiNbO$_3$ crystal the extraordinary refractive indices $n_{o,e}$ via the electro-optic effect:

$$\Delta n_e = -\frac{1}{2}n_e^3 r_{33}E_{sc} \,, \tag{8}$$

where r_{33} are the components of the electro-optic tensor.

We calculate the distribution $E_{mz}(z)$ for different modes, modeling the waveguide refractive index profile by dependence of $n(z) = n_s + \Delta n \cdot ch^{-2}(z)$.

3. Results

In the numerical calculations we have used the inequality $\sigma_d \gg B_{ph}\left|A(x,y)\right|^2$ and the parameters of our LiNbO$_3$:Ti:Fe waveguide: $\beta_{33} / \sigma_d = 3.1$ m/A for TM$_6$ mode. It is found that the necessary conditions for dark
soliton formation are not only the width of a dark notch but also the forms and the width of input beam. Best results are for Gaussian or rectangular form of the input beam with half-intense width about 120 μm. The half-intense width dark notch is 10 μm. In Fig.1 the propagation of Gaussian beam of half-intense width 120 μm and width of dark notch 8 μm in crystal of 5 mm length is presented.
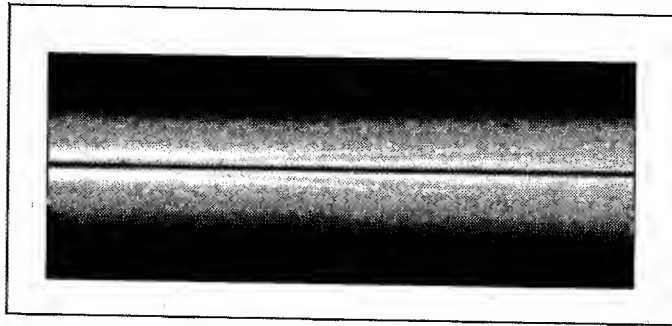
Fig. 1. Gaussian beam of width 120 μm with dark notch of width 8μm.

In the experiments the planar waveguide formed in Z-cut of $LiNbO_3$ sample was used. The dimensions of the wafer were $16 \times 20 \times 3$ mm^3 along the X, Y and Z axes of the crystal, respectively. The waveguide was produced by diffusion of a 40-nm-thick vacuum-deposited titanium layer at 1000°C during 6h in an air atmosphere. The photorefractive properties of this waveguide were enhanced using the additional Fe-diffusion from a film with thickness of ~50 nm at the same diffusion conditions. This planar structure supports 7 TM modes at the wavelength $\lambda = 0.63$ μm that was used in the experiment.

In conclusion, we have considered the necessary conditions for formation dark solution in the waveguide formed by sequential diffusion of titanium and iron in Z-cut of $LiNbO_3$.

References

1. V. Shandarov, D. Kip, M. Wesner, and J. Hukriede, "Observation of dark spatial photovoltaic solitons in planar waveguides in litium niobate", J. Opt. A Pure Appl. Opt., 2, 500-503 (2000).

Thermally Induced Spatial Soliton in Dye Doped Nematic Liquid Crystal

J.F. Henninot, F. Derrien, M. Debailleul, M. Warenghem
LPCIA, Université d'Artois, Faculté J. Perrin, SP 18, 62307 Lens   FRANCE
Tel : 00 33 3 21 79 17 80, Fax : 00 33 3 21 79 17 55
email : henninot@univ-artois.fr

Abstract : We have observed the self-trapping of a laser beam in a liquid crystal thick sample. This propagation mode, which can be assimilated to a spatial soliton, is due to a thermally induced index change, especially strong for nematics. We show here that the non-locality of the thermal effect insures the stability of the soliton.

Summary:

A few years ago, we have described the self-trapping of a narrow laser beam escaping from a single-mode fiber into a dye doped nematic liquid crystal (DDNLC) sample. We have shown that it was possible to obtain a stable 2D+1 spatial soliton on 4 to 5 diffraction lengths in this medium. We have explained this effect by considering the strong thermal non-linearity exhibited by the LC when a small part of the laser beam was convert to heat by absorption by the dye (0.1% in weight in the LC)[1].

In the case of laser-heating induced refractive index change, the process may not be exactly described by an intensity-dependant refractive index change of the form $\Delta n = n_2 I$. This non-locality, commonly connected to the thermal diffusion process, has been predicted to stabilize spatial solitons [2].   We report here on **experiments** performed to estimate the non-locality of the photo-thermal non-linearity and to establish the link between this non-locality and the stability of the soliton.
In order to measure the shape and the width of the thermally induced index profile by a laser beam, we have studied the interaction of two self-focused counter-propagating spatial solitons, parallel to each other (figure 1). We have obtained **an experimental index profile, allowing to quantify the non-locality of the thermal effect giving rise to a spatial soliton.**

Figure 1:   Mutual interaction between
counter-propagating self-trapped beams
in nematic liquid crystal

In a second part, we report on experimental results concerning **the tuning of the non-locality of the thermal effect**. When the laser light is chopped (pulses about 1 ms), the spatial soliton becomes unstable. In this case, we have also measured the index profile by the method of mutual deflexion of beams described previously and we have checked that this profile was narrower than in the CW case, revealing experimentally the link between non-locality and stability. We discuss then the possibility to use tunable non-locality to induce strong self-waveguiding in DDNLC samples.

Keywords: Spatial soliton, nematic liquid crystals, non-locality

References:
[1] F. Derrien, J.F. Henninot, M. Warenghem, G. Abbate, J. Opt. A: Pure Appl. Opt. 2, pp 332-337 (2000)
[2] W. Krolikowsky, O. Bang, Phys. Rev. E, **63**, 016610 (2000)

Instabilities of multicomponent spatial solitons in photorefractive media

Kristian Motzek and Friedemann Kaiser

Institute of Applied Physics, Technische Universität Darmstadt,
Hochschulstr. 4A, 64289 Darmstadt, Germany
e-mail: kmotzek@physik.tu-darmstadt.de

Wieslaw Krolikowski and Glen McCarthy

Laser Physics Centre, The Australian National University, Canberra, ACT 0200,
Australia

Carsten Weilnau and Cornelia Denz

Institute of Applied Physics, Westfälische Wilhelms-Universität Münster,
Corrensstr. 2/4, 48149 Münster, Germany

Anton Desyatnikov and Yuri S. Kivshar

Nonlinear Physics Group, The Australian National University, Canberra,
ACT 0200, Australia

Abstract: We investigate numerically the dynamics associated with the instabilities of multi-component spatial solitons in photorefractive media. The instabilities can lead to the formation of swinging structures, giving evidence of the oscillatory nature of the instabilities.
© 2002 Optical Society of America
OCIS codes: (190.4420),(190.5330)

In the field of spatial optical solitons, vector solitons have recently attracted great interest [1]. Vector solitons consist of several mutually incoherent light beams - or components - that jointly induce a waveguide in a nonlinear medium, such that each of the light beams is an eigenmode of the waveguide. Thus the beams self-trap and propagate without changing their intensity profile.

The main reason that makes vector solitons interesting is the fact that, in contrast to scalar solitons consisting only of a single light beam, some or even all of the components can be higher modes of the waveguide. Thus the structure of vector solitons can be quite complex, eventually exhibiting several maxima or points of zero intensity [2]. As a consequence of this complexity it is difficult to predict whether a given vector soliton is stable or unstable [3], and in many cases it can only be determined by using numerical methods.

In this paper we will be concerned with the instabilities of vector solitons consisting of a groundmode and two perpendicularly aligned dipole-modes. In order to obtain results that are suitable for an eventual experimental verification, we use a numerical model for our calculations, that describes the nonlinear properties of electrically biased photorefractive crystals very accurately. The propagation of the envelopes $E_j(x,y,z)$ of the light beams is given in paraxial and slowly varying amplitunde approximation by:

$$\partial_z E_j - \frac{i}{2}\nabla_\perp^2 E_j = i\gamma\partial_x\Phi E_j, \tag{1}$$

where γ is a material constant giving the strength of the nonlinear effect of the crystal.

The nonlinearity of the crystal is contained in the term $\partial_x\Phi$ on the right hand side, where Φ is the electric potential inside the crystal, which is found to solve the equation [4]:

$$\nabla^2\Phi + \nabla\ln(1+I)\nabla\Phi = E_{ext}\,\partial_x\ln(1+I) \tag{2}$$

Here $I(x,y,z) = \Sigma_j|E_j(x,y,z)|^2$ is the total light intensity and E_{ext} is the strength of the electric field applied to the crystal. Furthermore we have chosen the coordinate system such that the x-axis is parallel to the externally applied electric field, and the z-axis points in the direction of propagation of the light beams. Equation (2) is both anisotropic and nonlocal. This has some important consequences on the propagation behaviour of light, that are confirmed by experiment [5].

To obtain solitary solutions to the propagation equation we make the ansatz: $E_j(x,y,z) = a_j(x,y)\exp(i\lambda_j z)$. The λ_j are the propagation constants of the single components. With the above ansatz the set of equations (1)

and (2) can be solved numerically by using a relaxation technique. The values chosen for the λ_j's determine the powers P_j of the single light beams. Fig. 1 shows the power of the single components as a function of the propagation constant λ_3 of the dipole in x-direction, while keeping the other two propagation constants fixed. In Fig. 1(a) and (b) we also show two examples of the investigated vector solitons in a contour plot. For all the pictures $\lambda_1 = 0.20$ and $\lambda_2 = 0.13$. In (a) $\lambda_3 = 0.03$ and in (b) $\lambda_3 = 0.14$.
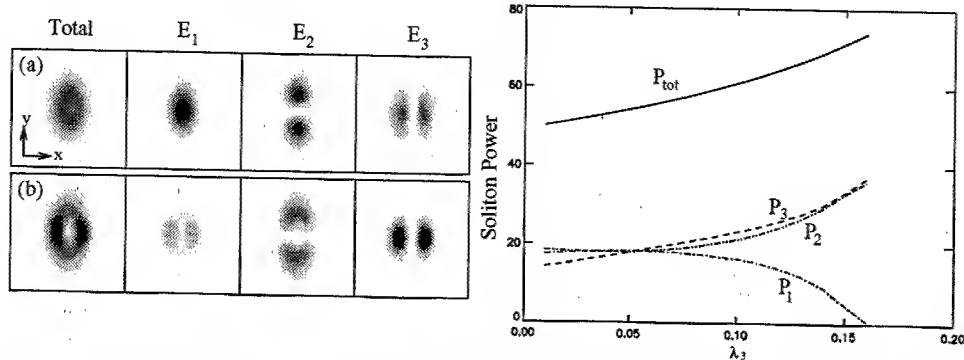
Fig. 1. Two examples of the investigated solitons and the dependence of the power of the single components on the propagation constants. P_1 stands for the power of the groundmode-beam, P_2 for the dipole in y-direction and P_3 for the dipole in x-direction.

It appears that stability properties of the soliton family depicted in Fig.1 vary with the value of the propagation constant λ_3. Under numerical propagation the solitons with $\lambda_3 < 0.06$ were shown to be stable, whereas they become unstable for higher λ_3. The effect of a weakly excited unstable mode on the propagation of a vector soliton can be described by the expression

$$E_j(x, y, z) = (a_j(x, y) + s(x, y) \exp(\beta z)) \exp(i\lambda_j z), \tag{3}$$

where the (positive) real part of β is the growth rate of the unstable mode. If the imaginary part of $\beta \neq 0$ one speaks of an oscillatory instability.

For a λ_3 slightly above the onset of instability, we expect that the real part of $\beta << 1$ for all unstable modes, which makes it easier to control the decay of the soliton by exciting one of the modes. In Fig. 2 we show the propagation of a soliton with the propagation constants $\lambda_1 = 0.2$, $\lambda_2 = 0.13$ and $\lambda_3 = 0.1$. In order to see the effect of the unstable modes breaking the symmetry of the soliton with respect to the y-axis, we initially perturb the numerically obtained soliton solution by making the right beamlet of the horizontal dipole 1% stronger and the left beamlet 1% weaker. In the pictures it can be seen that in the early stages of the propagation energy is transferred from one beamlet to the other and then back again, thus giving clear evidence of the oscillatory nature of the instability. It is remarkable that the oscillations persist even in the later stages of the propagation, when the structure consisting of the groundmode and the two dipoles has disappeared and evolved into an elongated structure consisting of a triple-humped, a double-humped and a nodeless beam, where the triple-humped beam has developed out of the horizontal dipole, one beamlet of which splits in half. The motion of the elongated structure as it propagates reminds roughly of the swinging dynamics of a linear 3-atom molecule, thus manifesting the particle-like properties of solitons. We could observe two full oscillations of these swinging dynamics before the structure decays further. Recently a very similar scenario could be observed in numerical calculations using a mathematical model representing a local and isotropic saturable nonlinearity [6].

One factor, that might make it difficult to observe the above described instability and subsequent dynamics experimentally is the fact, that it is not the only unstable mode of the soliton. In our calculations we observed the instability breaking the symmetry of the horizontal dipole always in combination with another instability breaking the symmetry of the vertical dipole.

For a slightly different kind of unstable propagation behaviour a very good agreement between theory and experiment can be observed. In Fig. 3(a-b) we demonstrate numerically found unstable propagation of the three-component soliton with $\lambda_1 = 0.25$ and $\lambda_2 = \lambda_3 = 0.16$. Fig.3(a) shows the stationary soliton solution while Fig.3(b) shows its structure after propagation over 5 diffraction lengths. It is evident that the instability
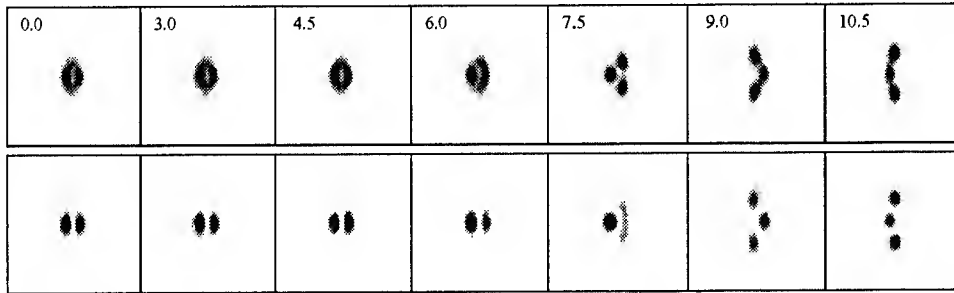
Fig. 2. The dynamics of the decay of a soliton with propagation constants $\lambda_1 = 0.20$, $\lambda_2 = 0.13$ and $\lambda_3 = 0.10$, that has been initially perturbed in the component of the x-dipole. The upper row shows the total intensity, the lower row the intensity of the x-dipole. The number indicate the propagation distance in diffraction lengths.

breaks the symmetry of the soliton and leads to its disintegration into a set of three beamlets that fly apart. Fig.3(c) shows experimental results obtained in a 20mm long electrically biased SBN-crystal. The upper row of (c) shows the result of the single components propagating through the crystal, the bottom row the result of a simultaneous propagation. It can be seen here as well that one of the beamlets of the horizontal dipole splits in half. But in contrast to the case of the solitons that evolve into an elongated swinging structure as described above, here the groundmode-beam isn't strong enough to hold the developing triple-humped structure together. Instead the groundmode-beam gets split as well and each of the three beamlets moving apart takes a bit of intensity of the groundmode.
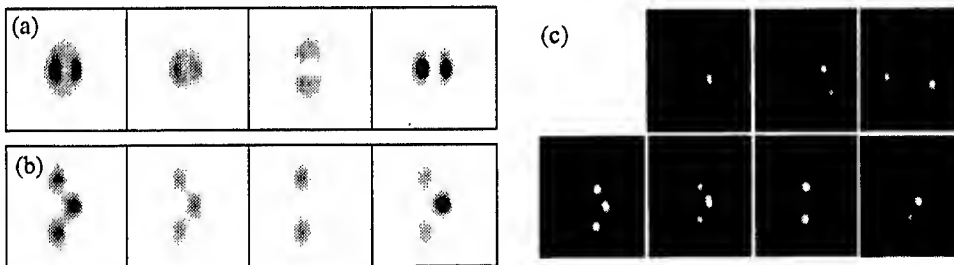
Fig. 3. The decay of a solitons into three beamlets that move away from each other: (a) shows a soliton with $\lambda_1 = 0.25$ and $\lambda_2 = \lambda_3 = 0.16$, (b) shows the result that is obtained when numerically propagating this soliton for 5 diffraction lengths. (c) experimental pictures: The upper row shows the result of the single components propagating through the crystal, the lower row shows the result of a simultaneous propagation of the three components.

As the power of the fundamental mode (component) is rather weak, this instability scenario is very similar to that of a vector soliton consisting of only two orthogonal dipoles, discussed in Ref.[2]. In that case the instability also leads to a breakup of the soliton into a set of three beamlets flying apart..

In conclusion, we studied theoretically and experimentally the stability properties of three-component photorefractive spatial solitons. We found that although these solitons are rather robust they may develop symmetry breaking instabilities for parameters outside the stability domain. This instability often exhibits oscillatory behavior. Our numerical simulations showed that increasing the power of the fundamental component of the vector soliton can stabilize the solitons.

References

1. M. Mitchell, M. Segev and D. N. Christodoulides, Phys. Rev. Lett. **80**, 4657 (1998).
2. M. Ahles, K. Motzek, A.Stepken, F. Kaiser, C. Weilnau and C. Denz, J. Opt. Soc. Am. B **19**, 557 (2002).
3. D. E. Pelinovsky and Yu. S. Kivshar, Phys. Rev. E **62**, 8668 (2000).
4. A. A. Zozulya and D. Z. Anderson, Phys. Rev. A **51**, 1520 (1995).
5. D. Neshev, G. McCarthy, W. Krolikowski, E. A. Ostrovskaya, Yu. S. Kivshar, G. F. Calvo and F. Agullo-Lopez, Opt. Lett. **26**, 1185 (2001).
6. A. S. Desyatnikov, Yu. S. Kivshar, K. Motzek, F. Kaiser, C. Weilnau and C. Denz, Opt. Lett. **27**, 634 (2002).

Distortion and improvement of the formation of quadratic spatial solitons by temporal walk-off and wave-vector-mismatch non-uniformities

Roland Schiek
University of Applied Sciences Regensburg, Prüfeninger Str. 58, D-93049 Regensburg, Germany
roland.schiek@e-technik.fh-regensburg.de

Robert Iwanow, George I. Stegeman
CREOL / School of Optics, University of Central Florida, 4000 Central Florida Blvd., Orlando FL-32816-2700, USA

Gerhard Schreiber, Wolfgang Sohler
University of Paderborn, Warburger Str. 100, D-33098 Paderborn, Germany

Abstract: The influence of temporal walk-off and wave-vector mismatch non-uniformities on the formation of quadratic spatial solitons in lithium niobate film waveguides with a specially engineered non-uniform QPM grating is experimentally investigated.
©2002 Optical Society of America
OCIS codes: (190.4410) Nonlinear Optics, parametric processes; (260.5950) Self-focusing

1. Introduction

For a given wave-vector mismatch value a whole family of quadratic spatial solitons exists. Each soliton family member has its unique spatial intensity profile for both, the fundamental (FD) and the second-harmonic (SH) part [1,2]. For a positive wave-vector mismatch value one specific member of the corresponding soliton family is evolving from each input condition. However, the soliton formation is an increasing oscillatory process for input conditions with fields that do not match the finally formed soliton fields. The oscillatory soliton formation process is not directly correlated to the diffraction length of the input beam and it may take tens, hundreds or even thousands of diffraction lengths for the soliton to settle down, at least for 1D solitons. Therefore, in order to characterize quadratic spatial solitons experimentally in samples of finite lengths it is advisable to prevent the transient oscillations of the beam by launching the soliton with the correct power, beam width and phase of both of its components, the FD and the SH. This is especially important when the beam evolution inside the sample is not observable (low scattering or sample housed in an oven) and the soliton observation is restricted to a measurement of the input and output beams at the sample's ends. In the case of beam width oscillations inside the sample, not every narrow output spot is a soliton!

Here we report on the excitation of different wide 1D quadratic solitons for different positive phase-mismatch values in 5-cm-long QPM lithium niobate slab waveguides and the quantitative measurement of the intensity profiles of their FD and SH part. The SH part of the soliton was generated in a specially designed 1-cm-long QPM region with a non-uniform distribution of the QPM period at the waveguide beginning. This SH seeder works well for a large range of positive wave-vector mismatch values and powers. With a laser pulse-duration for which the SHG walk-off length is comparable to the sample length the interpretation of FD and SH intensity patterns measured at the waveguide output only may mislead. Spatially resolved measurements of the spectra of the FD and the SH output help to identify walked-off non-soliton SH radiation and the soliton-part SH. Within the 20% measurement accuracy of the intensity profiles good agreement between experimental observation and theoretical description was observed.

2. Samples and experimental conditions

On a 5-cm-long Z-cut lithium niobate crystal a planar waveguide was fabricated by in-diffusion of a 70-nm-thick titanium layer for 8.5 hours at a temperature of 1060°C. For phase-matching SHG between the FD and the SH TM_0 modes a QPM grating was written in the sample by electric field poling with an effective periodicity growing smoothly in the first cm of the sample from 17.4800 μm to 17.6333 μm and keeping its value constant over the last 4 cm of the sample. The corresponding calculated phase-matching wavelength distribution along the sample is shown in Fig. 1. With non-colinear SHG in two crossed beams the local phase-matching wavelength was measured with a

cw wavelength-tunable laser diode. The comparison of results of these measurements with the theoretically expected values in Fig. 1 is evidence for a very well fabricated QPM grating. The decreasing phase-matching wavelength at the sample end is due to a temperature drop of a few degree at the oven end. The measured tuning curves are very well reproduced by theory with the actual measured phase-mismatch profile taken into account. Because measurements even at mW excitation power level were not reproducible at room temperature in every detail the sample was heated in an oven to prevent index inhomogeneities due to the photorefractive and pyroelectric effects. Above sample temperatures of 150°C neither photorefractivity nor pyroelectricity was observed.
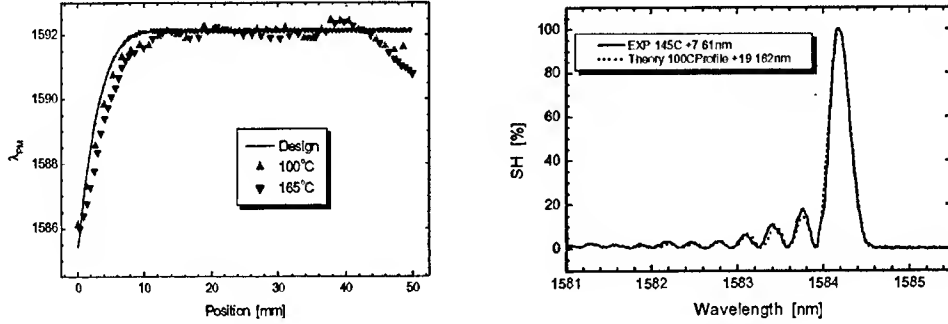
Fig. 1. Left: Phase-matching wavelength in a non-uniform QPM grating. Experimental values are measured at a sample temperatures of 100 and 165°C. Theoretical values are corrected for +4.5 nm due to uncertainties in temperature-dependent Sellmeier equations and waveguide characteristics. Right: Measured and calculated SHG tuning curve with measured phase-mismatch profile.

The high-power measurements were performed with a NaCl color center laser with 8.5-ps-long transform limited pulses with a repetition rate of 76 MHz and up to 200 mW average power. The wavelength is tunable between 1400 and 1650 nm. For a further reduction of the average power a 1:20 chopper was used. The input beam was shaped with cylindrical lenses and focused with a 10X microscope objective onto the input surface of the waveguide. The output surface was imaged with a 5X microscope objective onto a vidicon camera. The video camera was carefully linearized and scaled for absolute power measurements. Additionally FD input and FD and SH output powers were measured with power meters. The wave-vector mismatch was adjusted with temperature varying between 180 and 235°C. All high-power measurements were done at a fixed wavelength of 1587.8 nm.

3. Output beam width versus power

For different wave-vector mismatch values at temperatures between 180 and 235°C we launched gaussian beams with beam waists between 60 and 150 μm with the waist position exactly at the waveguide input. The output beam was monitored and its full width at half maximum (FWHM) is plotted versus the pulse peak input power.
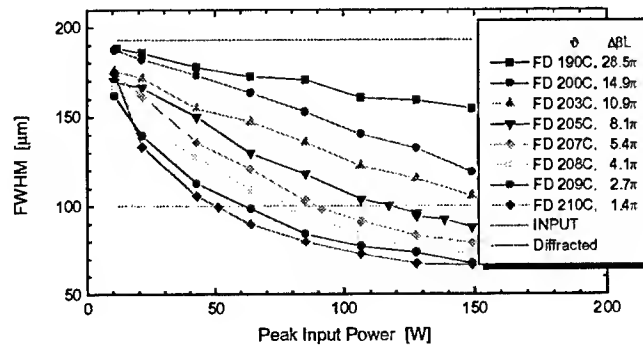
Fig.2. Output beam width versus power for different wave-vector mismatch $\Delta\beta L$ in units of π. The vertical lines show the input beam width and the low power diffracted output beam width.

We verified that the output beam width narrows smoothly from its low power diffracted beam width to a value that is equal to the input beam width for higher power. Fig. 2 shows typical results for a 100 μm wide input beam. The power for which the width of the output beam becomes for the first time equal to that of the input beam is the correct power for the propagation of a soliton with this width. Numerical simulations confirm that the beam at this power is indeed the beam with the minimum changes of its intensity profile along the propagation and therefore the one that closest resembles a soliton. For higher power the output may narrow even more (dependent on the input beam width) but the beam is strongly oscillatory and does not settle down to a narrower soliton in the 5-cm-sample length. The simulation also confirms that the SHG generator in the chirped QPM region works well.

4. Soliton families

Fig.3 shows FD and SH intensity profiles of those members with a 100 μm wide FD beam of 3 different soliton families. For the relatively large wave-vector mismatch of 8.1π the soliton evolves from an input beam with 115 W peak power. The SH beam profile is proportional to the square of the FD beam profile and the power ratio between FD and SH component is 99:1. The soliton at 205°C is therefore clearly a quadratic soliton in the "Kerr limit" of the cascaded nonlinearity. Closer to phase-matching at 208°C ($\Delta\beta L=4.1\pi$) the soliton evolves at the lower peak power of 85 W. The FD to SH power ratio is 97:3. This is still a "Kerr-like" soliton with only ~3% of the power in the SH. However, the SH profile is already slightly wider than the square of the FD profile indicating a small deviation from the "Kerr-limit". Very close to phase-matching 210°C a soliton-like beam forms at only 55 W peak input power with a power ratio of FD to SH of 73:27. The SH carries already ~27% of the total power. The SH and the FD components have similar widths indicating a quadratic soliton with its unique properties which cannot be studied in the "Kerr-limit".
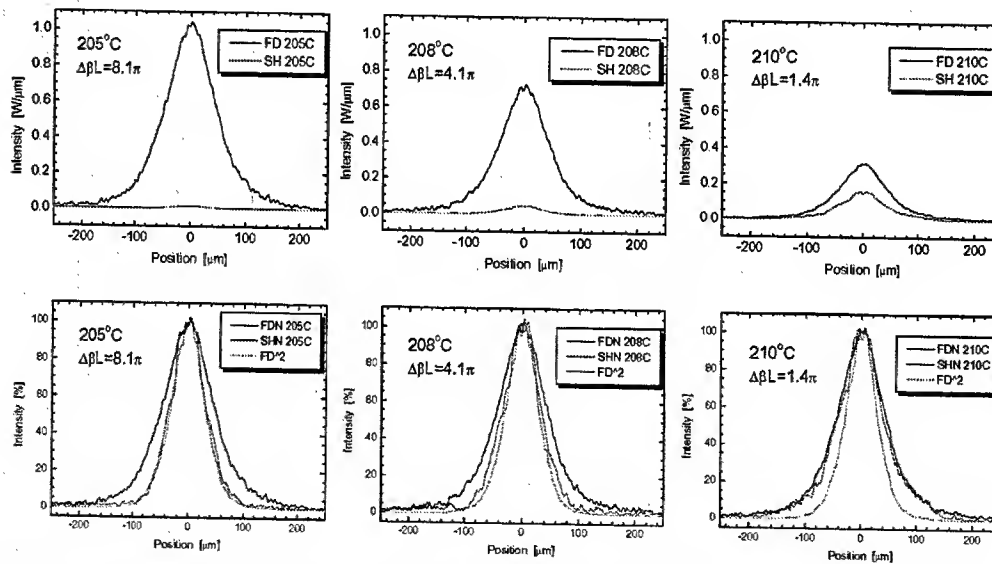
Fig. 3. FD and SH intensity profiles of different soliton members with the same width of 100 μm for the FD part. In the second row the normalized FD and the SH are compared, the square of the FD is also shown.

The measured widths and peak powers of both the FD and the SH are finally compared with cw-calculations of solitons of different families. For large phase-mismatch values the agreement is very good while for smaller phase-mismatch some SH walks-off. This non-soliton SH and the SH soliton part are not distinguishable in the camera picture which disturbs the SH profile measurement. Measurements of the FD and SH spectra of the output beams help to separate the two SH parts. For large wave-vector mismatch values the SH spectrum corresponds to the FD spectrum and walk-off is negligible. Closer to phase-matching new SH spectral components which do not belong to the quadratic soliton arise due to intra-spectral SHG and the SH output beam is a mixture of soliton and radiation SH.

5. References

A. V. Buryak and Y. S. Kivshar, "Solitons due to second harmonic generation," Physics Lett. A **197**, 407-412 (1995).
L. Torner, "Stationary solitary waves with second-order nonlinearities," Optics Comm. **114**, 136-140 (1995).

Internal oscillations of (2+1) dimensional solitons in a saturable nonlinear medium

Jianke Yang

Department of Mathematics and Statistics, University of Vermont, Burlington, VT 05401
Tel: 802-656-4314; fax: 802-656-2552; email: jyang@emba.uvm.edu

Internal oscillations of (2+1) dimensional fundamental solitons in a saturable nonlinear medium is studied. Internal modes both with and without angular dependence are discovered. The effect of angle-dependent internal modes on the soliton visually appears as a rotation of the perturbed soliton. OCIS codes: 190.0190, 190.5530

Spatial solitons are under intensive study these days due to their novel physics as well as application potentials. In a saturable nonlinear medium, fundamental solitons are linearly stable in any spatial dimension[1]. Interaction and collision of fundamental solitons in a saturable medium have also been studied to some extent[2]. There is also a large body of work on vector solitons in saturable media.

Internal oscillations of stable solitons are important for at least two reasons. The first reason is to understand long-time dynamics of solution behaviors. It is known that the solution generally relaxes onto fundamental solitons with oscillations plus some radiation. Thus this oscillating fundamental-soliton state needs detailed examination. The second reason is to understand collision dynamics of fundamental solitons. If robust internal oscillations exist, solitons during collision can temporarily store some of the translational energy in these internal oscillations, and retrieve this energy after the collision. This energy exchange mechanism can induce very complex collision structures such as window sequences and even fractal structures[3]. So far, the only piece of work on internal oscillations of solitons in a saturable medium is by Rosanov, et al.[4] for (3+1) dimensions. Even that work is not complete as only radially-symmetric internal modes were examined in detail. In fact, radially-asymmetric internal modes also abound, and they can induce more interesting evolution dynamics to the underlying soliton, as we will see later in this paper.

Here we comprehensively study internal oscillations of (2+1) dimensional fundamental solitons in a saturable medium. We show that both radially-symmetric and angle-dependent internal modes exist at high soliton powers. Internal oscillations induced by these internal modes are very robust. Furthermore, when angle-dependent internal modes are excited, the visual effect is that the perturbed soliton is rotating.

The model for (2+1) dimensional solitons in an isotropic saturable nonlinear medium is

$$iU_z + \Delta_\perp U - \frac{U}{1 + |U|^2} = 0, \qquad (1)$$

where U is the complex amplitude of the light beam, z is the propagation distance, and $\Delta_\perp$ is the transverse Laplacian (all quantities are non-dimensionalized). Fundamental solitons in this system are of the form

$$U(r, \theta, z) = u(r)e^{i\omega z}, \qquad (2)$$

where (r, θ) are the polar coordinates in the transverse plane, ω is the soliton frequency, and function $u(r)$ is single-humped (bell-shaped). The equation for $u(r)$ is

$$u_{rr} + \frac{1}{r}u_r - \omega u - \frac{u}{1 + u^2} = 0, \qquad (3)$$

with the vanishing boundary condition $u \to 0$ as $r \to \infty$. It is also obvious from Eq. (3) that u_r at $r = 0$ must be 0. These fundamental solitons are very easy to determine by numerical methods (such as shooting). It turns out that physically meaningful solutions (with finite mass) exist only when $-1 < \omega < 0$. The solution at $\omega = -0.1$ is shown in Fig. 1.

Next, we investigate the internal modes of fundamental solitons. Internal modes are discrete eigenfunctions of the linearization operator linearized around the soliton. To determine these modes, we write the perturbed soliton solution as

$$U(r, \theta, z) = e^{i\omega z}\left\{u(r) + \phi_n(r)e^{i(\lambda z + n\theta)} + \psi_n^*(r)e^{-i(\lambda^* z + n\theta)}\right\}, \qquad (4)$$

where $u(r)$ is a fundamental soliton, (ϕ_n, ψ_n) are small perturbations, λ is the eigenvalue, n is an integer representing the angle dependence of the disturbance, and "*" represents complex conjugation. When Eq. (4) is substituted into (1) and higher order terms in ϕ_n and ψ_n dropped, the eigenvalue problem is

$$\phi_{nrr} + \frac{1}{r}\phi_{nr} - \left(\omega + \lambda + \frac{n^2}{r^2} + \frac{1}{(1 + u^2)^2}\right)\phi_n + \frac{u^2}{(1 + u^2)^2}\psi_n = 0, \qquad (5)$$

$$\psi_{nrr} + \frac{1}{r}\psi_{nr} - \left(\omega - \lambda + \frac{n^2}{r^2} + \frac{1}{(1 + u^2)^2}\right)\psi_n + \frac{u^2}{(1 + u^2)^2}\phi_n = 0. \qquad (6)$$

It is easy to check that the square of the above linearization operator is self-adjoint, thus the discrete eigenvalue λ is either purely real (internal mode), or purely imaginary (unstable mode). As fundamental solitons are stable, purely imaginary eigenvalues of this operator can not exist, but internal modes do.

In the following, we exhaustively search for *all* internal modes (purely real eigenvalues λ) of fundamental solitons. In such cases, eigenfunctions ψ_n and ϕ_n are both real. The boundary conditions for these internal modes are

$$\phi_{0r}(r = 0) = \psi_{0r}(r = 0) = 0, \quad n = 0, \tag{7}$$

$$\phi_n(r = 0) = \psi_n(r = 0) = 0, \quad n \neq 0, \tag{8}$$

and $\psi_n \to 0$, $\phi_n \to 0$, $r \to \infty$. When $-1 < \omega < 0$ and $r \gg 1$, both equations (5) and (6) become a modified Bessel equation whose solutions are

$$\phi_n(r) = K_n(\sqrt{1 + \omega + \lambda}\, r), \tag{9}$$

$$\psi_n(r) = h K_n(\sqrt{1 + \omega + \lambda}\, r), \tag{10}$$

where h is a real parameter. Our strategy for finding all internal modes is the following. At each integer n, we make a large parameter mesh in the two-dimensional h and λ plane. At each (h, λ) mesh point, we numerically integrate Eqs. (5) and (6) starting from a large r value to zero. Due to the boundary conditions (7) and (8), at each n, we check if the target functions $\phi_{0r}(r = 0)$ and $\psi_{0r}(r = 0)$ (for $n = 0$) or $\phi_n(r = 0)$ and $\psi_n(r = 0)$ (for $n \neq 0$)'s zero-level curves in the (h, λ) plane intersect or not. If they do, then the intersection gives an internal mode. If not, then no internal modes at that ω and n values exist. After an intersection for internal modes is found, we then use the shooting method to determine this internal mode to very high accuracy.

Carrying out this strategy, we have discovered that both radially-symmetric ($n = 0$) and angle-dependent ($n \neq 0$) internal modes exist. For example, at $\omega = -0.1$, internal modes with $n = 0$ and 2 are shown in Fig. 2. Internal modes with $n = 1$ and 3 are also found but not shown. We have also traced the entire families of internal modes by varying frequency ω. The eigenvalues of these internal-mode families with $n = 0, 1, 2$ and 3 are summarized in Fig. 3. Internal modes at higher n values were also discovered, but they are very close to the continuous spectrum, thus will not be considered. Three features of internal modes in Fig. 3 are noted below. The first one is that internal modes with $n = 0$ and 2 are farthest from the continuous spectrum. Thus radiation damping of such modes should be the slowest. In other words, internal oscillations caused by such modes should be most robust. The second feature is that internal-mode eigenvalues go to zero when ω approaches 0^-. Note that the power of fundamental solitons increases with ω, we see that internal oscillations of high-power solitons are more robust. The third feature is that these internal modes disappear when the soliton power is low.

Next, we numerically study the dynamics of fundamental solitons under the perturbation of these internal modes. We just consider internal oscillations induced by modes $n = 0$ and 2, as those oscillations are most robust (see text above). First, we examine internal oscillations caused by the $n = 0$ mode which is radially symmetric. For simplicity, we take our initial condition as

$$U(r, \theta, z = 0) = (1 + \epsilon) u(r, \omega), \tag{11}$$

which is radially symmetric. Here $\epsilon \ll 1$ is a constant perturbation parameter. Obviously, this initial condition will only excite the radially-symmetric internal mode of $n = 0$ (and some radiation). Starting from this initial condition, we have simulated the original equation (1). The simulation results with $\epsilon = 0.2$ are displayed in Fig. 4. We see that indeed, a very robust amplitude oscillation is excited. This oscillation frequency is approximately 0.2, which is close to the $n = 0$ internal-mode frequency (which is 0.2187). To examine radiation damping of these oscillations, we show the radial solution profile $|U(r)|$ at three distances in the right panel of Fig. 4. Remarkably, the radiation emission from these internal oscillations is extremely small (almost invisible). Thus, we can expect these oscillations to last for a very long distance. This finding is consistent with that for (3+1)D solitons[4].

Below, we examine internal oscillations caused by the $n = 2$ mode. Here we take the initial condition as a superposition of the fundamental soliton and the $n = 2$ internal-mode perturbation, i.e.,

$$U(r, \theta, z = 0) = u(r, \omega) + \epsilon \left\{ \phi_2(r) e^{2i\theta} + \psi_2(r) e^{-2i\theta} \right\} \tag{12}$$

according to equation (4). In this case, the solution is angle-dependent. Simulation of Eq. (1) starting from the above initial condition shows that the internal oscillation induced by the $n = 2$ mode is also very robust. In addition, the effect of this internal-mode perturbation is to prolong the fundamental soliton in one direction, and the evolution of this internal oscillation visually appears as a *rotation* of the perturbed state. To illustrate, we select $\omega = -0.1$ and $\epsilon = 2$ in the initial condition (12). The fundamental soliton and the internal-mode eigenfunctions can be seen in Fig. 1 and Fig. 2(b). Note that since the amplitude of the fundamental soliton at $\omega = -0.1$ is about 10, thus $\epsilon = 2$ in Eq. (12) is still a small perturbation to the fundamental soliton. With this initial condition, the simulation results at five distances are displayed in Fig. 5. As we can see, the fundamental soliton under this $n = 2$ internal-mode perturbations appears to rotate counter-clockwise. This is an interesting and distinctive visual feature of internal oscillations of solitons in (2+1) dimensions.

In conclusion, we have investigated internal oscillations of scalar (2+1) dimensional fundamental solitons in a saturable nonlinear medium. Internal modes both with and without angular dependence have been found.

Internal oscillations caused by these modes are very robust. In addition, the internal oscillation caused by angle-dependent internal modes visually looks like the perturbed soliton is rotating.
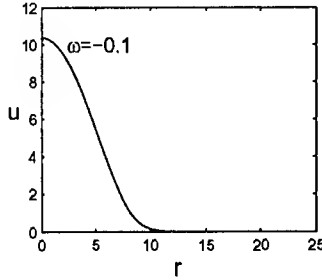
Fig. 1.   The fundamental soliton $u(r)$ with $\omega = -0.1$.
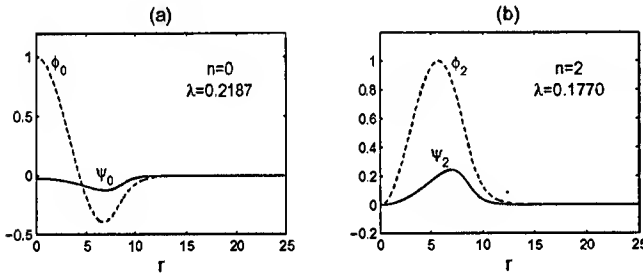
Fig. 2.   Internal modes of the $\omega = -0.1$ fundamental soliton at $n = 0$ and 2.
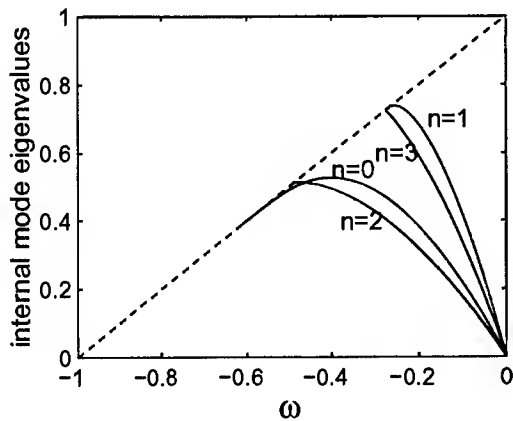
Fig. 3.   Internal-mode eigenvalues of fundamental solitons versus frequency ω. Here the dashed line is the edge of the continuous spectrum.
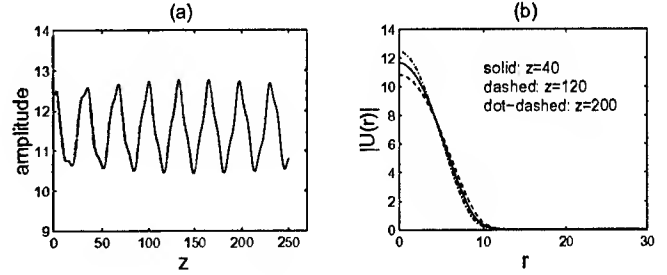
Fig. 4.   Evolution of the fundamental soliton with $\omega = -0.1$ under radially-symmetric perturbations. The initial perturbed state is given by Eq. (11) where $\epsilon = 0.2$.
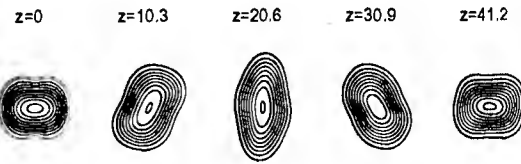
Fig. 5.   Evolution of the fundamental soliton with $\omega = -0.1$ under $n = 2$ internal-mode perturbations. The initial perturbed state is given by Eq. (12) where $\epsilon = 2$. Here contour levels 1:1:10 of the solution $|U(x, y, t)|$ at five distances are shown.

References

1. M. Mitchell, Z. Chen, M. Shih and M. Segev, Phys. Rev. Lett. **77**, 490-493 (1996); D. E. Edmundson, Phys. Rev. E **55**, 7636-44 (1997); N.G. Vakhitiov and A.A. Kolokolov, Sov. Radio. Phys. **16**, 783 (1973).

2. D.E. Edmundson and R.H. Enns, Phys. Rev. A **51**, 2491-98 (1995); J. Schjodt-Eriksen, M.R. Schmidt, J.J. rasmussen, P.L. CHristiansen, Y.B. Gaididei and L. Berge, Phys. Lett. A **246**, 423 (1998); Z.H. Musslimani, M. Soljacic, M. Segev and D.N. Christodoulides, Phys. Rev. E **63**, 066608 (2001); A.V. Buryak, Y.S. Kivshar, M. Shih and M. Segev, Phys. Rev. Lett. **82**, 81-84 (1999).

3. D.K. Campbell, J.F. Schonfeld, and C.A. Wingate, Physica D **9**, 1 (1983); P. Anninos, S. Oliveira and R. A. Matzner, Phys. Rev. D **44**, 1147-1160 (1991); J. Yang and Y. Tan, Phys. Rev. Lett. **85**, 3624 (2000).

4. N.N. Rosanov, S.V. Fedorov, N.A. Kaliteevskii, D.A. Kirsanov, P.I. Krepostnov and V.O. Popov, Nonlinear Optics, **23**, 21-238 (2000).

Single-component higher-order mode solitons in liquid crystals

X. Hutsebaut,[1] M. Haelterman,[1] A. Adamski,[2] K. Neyts,[2]

[1]*Service d'Optique et d'Acoustique, Université Libre de Bruxelles, CP 194/5*
Av. F. D. Roosevelt 50, B-1050 Brussels, Belgium
[2]*Electronics and Information Systems, Ghent University.*
St. Pietersnieuwstraat 41, B-9000 Gent, Belgium
Tel : +32-2-650.44.94, Fax : +32-2-650.44.96, e-mail : Marc.Haelterman@ulb.ac.be

Abstract: We demonstrate experimentally the existence of single-component multihump spatial solitons in a dye-doped nematic liquid crystal planar cell. The low absorption obtained at the working wavelength of 890 nm allows us to observe soliton propagation over lengths in the centimeter range.
© 2002 Optical Society of America

Laser soliton beams have already been studied in a large variety of configurations and materials for both their fundamental interest and their potential applications in light-controlled devices and, more particularly, in reconfigurable optical interconnects. Among the nonlinear materials considered in the literature, liquid crystals have attracted only little attention in spite of their huge nonlinearities (10^6 to 10^{11} times the nonlinearity of glass). The nonlinearity in liquid crystals (beside thermal effects) is of reorientational nature, non local and strongly polarization dependent, which leads to a rich phenomenology that has yet to be investigated experimentally. After the pioneering work of Braun *et al.* in which strong beam self-focusing has been demonstrated in nematic liquid crystals [1], several authors have investigated the possibility to propagate soliton beams in this material either in cylindrical (capilaries) [2] or in planar geometry [3]. In these studies attention has been devoted to the reduction of the thermal contribution to the nonlinearity and to the reduction of the required optical powers. Dye doping was used in Refs. [2] to enhance the reorientational nonlinearity while the authors of Ref. [3] resorted to a hybrid field polarization technique. In both these works however, soliton propagation was observed only over short distances of the order of hundreds of micrometers. The situation has been improved significantly in the work of Ref. [4] by applying an external static electric field to the liquid crystal cell to eliminate the Fréedericks threshold. This threshold is the light power necessary to initiate the reorientational motion of the molecules from the light field in the nematic phase of the crystal (i.e., to traverse the Fréedericks transition). Elimination of the Fréedericks threshold therefore leads to a significant increase of the effective nonlinearity of the liquid crystal. In this way soliton beams were observed with milliwatt powers over propagation distances of the order of the millimeter, which makes liquid crystal solitons closer to applications. As regards applications, the authors of Ref. [4] have demonstrated the possibility to guide a weak signal beam (at 633 nm) in the light-induced waveguide that constitutes the soliton.

In our communication we present the study of soliton propagation in nematic liquid crystals at near infrared wavelengths, closer to the spectral regions of relevance to optical telecommunications. Our purpose is two-fold. On the one hand, considering an applied viewpoint we show that soliton propagation lengths can be further increased at near infrared wavelengths and, on the other hand, considering fundamental aspects of soliton research, we demonstrate the existence of a new kind of optical soliton. The new soliton is composed of a self-guided higher-order mode in a way analog to the multimode (or multihump) vector solitons studied in Kerr-like materials. For their fundamental interest, multimode vector solitons have attracted a great deal of attention these last few years [5, 6]. In their standard form these solitons are composed of two components which is the reason why they are called vector solitons. They consist of a superposition of the fundamental mode and a higher-order mode of the waveguide induced by these modes themselves through self- and cross-phase modulations. It is the confining effect of the fundamental mode that allows for the confinement of the higher-order mode that in isolation can by no means be self-guided because of the natural repulsion existing between its lobes of opposite phase. This phenomenology is due to the locality of the nonlinearity considered up to now for the study of higher-order mode solitons (in general, theory is developed for Kerr-like nonlinearities, saturating or not) [5]. In liquid crystals, however, the nonlinearity is fundamentally different from the usual Kerr-like nonlinearity and, in particular, it is inherently non local. McLaughlin *et al.* have predicted that, owing to the non-locality of their nonlinearity, liquid crystals can sustain single-component higher-order mode solitons [7]. The existence of such solitons can be easily explained from the fact that, thanks to the nonlocality of the nonlinearity, the multihump intensity distribution of a higher-order mode induces a smooth guiding potential that is able to guide the mode itself. We present in our communication an experimental demonstration of the existence of such solitons.
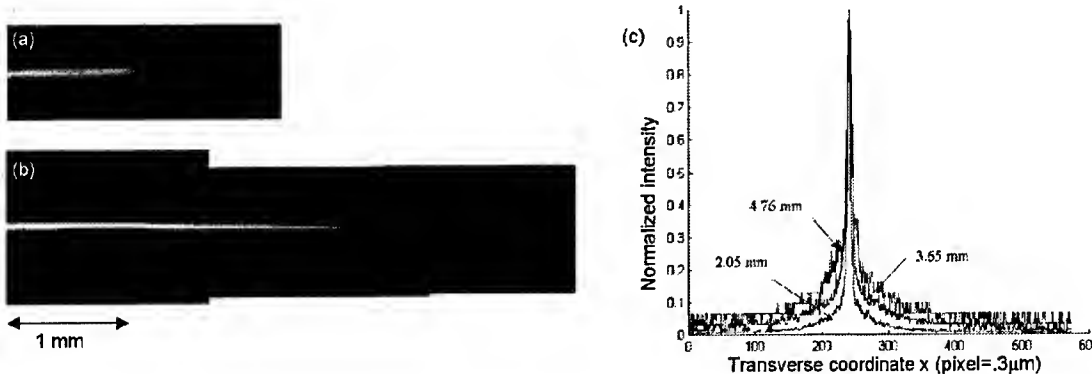
Fig. 1. CCD camera images of (a) the diffracting beam and (b) the corresponding fundamental soliton beam obtained at a power of 3 mW with an initial width of 3 μm and with an applied voltage of (a) 0 V and (b) 1.25 V. In (c) we plotted the intensity beam profiles extracted from image (b) at 0.205 cm, 0.365 cm and 0.476 cm.

We study soliton beam propagation in a planar cell of nematic liquid crystal in experimental conditions similar to those of Ref. [4] with some improvement. The E7 nematic liquid crystal is doped with methyl-red dye at a weight concentration of 0.8%. The doped liquid crystal is inserted by capillarity in a 75μm-thick planar cell made of two glass plates stuck together on the edges by ultra-violet hardening glue containing calibrated glass spacer balls. The inner faces of the glass plates are coated with indium-tin-oxyde layers that can be used as electrodes to apply the static electric field necessary to overcome the Fréedericks threshold (Note that in practice the applied electric field is not static but oscillating at low frequency in order to avoid charge accumulation). The indium-tin-oxyde layer is covered by a thin layer of rubbed polyimide whose purpose is to align the molecules along the desirable (rubbed) direction. Additionally, this layer gives a pre-tilt angle of 2 degrees to favor homogenous molecular orientation and, in this way, to avoid crystal dislocations. Along one of its edges the cell is not closed by glue but by a thin glass plate placed and glued perpendicularly to the liquid crystal layer in order to provide a polarization preserving input window for the laser beam. A rubbed polyimide layer covers the inner face of the input window to reduce at best the inhomogeneities (dislocations) at the beginning of the laser beam propagation. These conditions provide us with a very high quality liquid crystal exhibiting a very strong non-thermal nonlinearity, which is ideal for the study of soliton propagation.

Another significant improvement has been obtained by working in the near-infrared region where the absorption loss of the dye-doped liquid crystal is lower than in the visible wavelength range. Our laser source is a Ti:Sapphire laser operating at 890 nm. Our measurements showed that the absorption coefficient at this wavelength is of 0.5 cm^{-1}, which is half as large as its value measured at 633 nm (He-Ne laser). This improvement allows us to consider soliton propagation lengths in the centimeter range with milliwatt powers.

The Ti:Sapphire laser beam is collimated by a 20× microscope objective to a waist of $x_0 = 3$ μm corresponding to a diffraction length of $L_D = kx_0^2 = 90$ μm. A 10× microscope objective and a CCD camera are used to visualize the laser beam inside the cell thanks to the light scattered by the liquid crystal. Fig. 1 shows typical examples of beam propagation. Fig. 1(a) illustrates beam diffraction obtained at zero bias voltage (no self-guiding) while Fig. 1(b) shows soliton propagation with the same initial conditions, i.e, a power of 3 mW but with a 1 kHz ac bias voltage of 1.25 V. As can be seen, due to the reorientational nonlinearity the beam keeps its width up to half a centimeter of propagation. Such a long range self-confinement is possible, in spite of the loss, owing to the nonlinearity saturation. At high power, at the beginning of the propagation, the nonlinearity is saturated and the induced waveguide profile is almost insensitive to power variations. In this way, the induced waveguide keeps its shape unchanged until the power decreases and reaches to non-saturated regime of nonlinearity. This process is clearly illustrated in Fig. 1(c) that shows the beam intensity profiles measured at propagation distances of 0.205 cm, 0.365 cm and 0.476 cm. These profiles have been normalized so that their full-width-at-half-maximum (FWHM) can be easily compared, which allowed us to check that the beam FWHM is conserved over a distance in excess of half a centimeter. However, one can see in the long range profiles, the appearance of large noisy wings due to the progressive slackening of the nonlinearity saturation that induces gradual modifications of the induced waveguide profile. Note that a propagation distance of half a centimeter represents no fewer than 50 diffraction lengths. In the absence of bias voltage, this low-power self-guiding process does not occur because the Fréedericks transition is not reached (Fig. 1(a)). This result is an indication of the
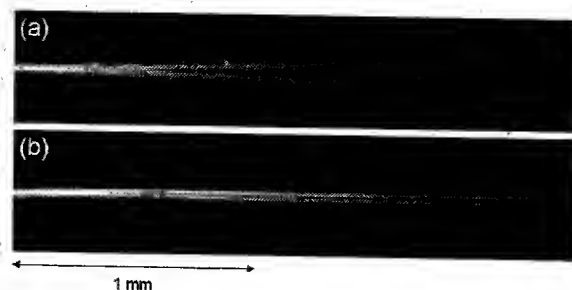
Fig. 2. CCD camera images of (a) the diffracting beam and (b) the corresponding higher-order mode soliton beam obtained at a power of 2.25 mW and with an applied voltage of (a) 0 V and (b) 1.25 V.

negligible role of thermal nonlinearity in our experiment.

Due to the quality of the liquid crystal cell, the effect of the inhomogeneous region close to the input window is minimized and the transient propagation regime is strongly limited, as can be seen in Fig. 1. This provides us with ideal conditions for the study of higher-order mode solitons. We studied the first-order mode soliton by generating the corresponding one-node antisymmetric transverse field distribution by means of a simple π-phase step plate placed before the collimating microscope objective. Fig. 2(a) shows the linear propagation of the antisymmetric field distribution. Due to its antisymmetric nature the beam undergoes a strong diffraction. As can be seen in Fig. 2(b), this diffraction can be compensated for by the reorientational nonlinearity of the liquid crystal to form a single-component first-order mode soliton. In this example the beam power is 2.25 mW and the applied voltage is 1.25 V. The rather long transient observed before the formation reveals that we did not optimize the initial condition as regards the beam width. However, after the transient, the double-hump beam propagates almost unchanged over more than 2 mm, which confirms the existence of higher-order mode soliton in liquid crystals predicted in Ref. [7].

In summary, by means of a high-quality liquid crystal cell based on several improvements (such as the inclusion of a pre-tilt angle at the cell boundaries to avoid dislocations at best) and by operating in the near-infrared spectral region for which liquid crystal losses are weaker, we have demonstrated soliton propagation over distances in the centimeter range with powers less than 3 milliwatts. These favorable experimental conditions allowed us to propagate single-component higher-order mode solitons. As for multimode vector solitons in photorefractive media [8], this result could be easily generalized to the simultaneous self-guided propagation of several superimposed higher-order modes in order to pave the way towards the experimental realization of soliton beams made of incoherent light in liquid crystals.

References

1. E. Braun, L. Faucheux, and A. Libchaber, Phys. Rev. A **48**, 611 (1993).
2. M. Warenghem, J. F. Henniot, and G. Abbate, Opt. Express **2**, 483 (1998).
3. M. A. Karpierz, M. Sierakowski, M. Swillo, and T. Wolinsky, Mol. Cryst. Liq. Cryst **320**, 157 (1998).
4. M. Peccianti, A. De Rossi, and G. Assanto, Appl. Phys. Lett. A **77**, 7 (2000).
5. Yu. Kivshar and G. Stegeman, Opt. Phot. News, **13**, 59 (2002).
6. See, e.g., the communication by C. Cambournac *et al.* on *Vector solitons in Kerr media* at the present meeting (NLGW'02).
7. D. W. McLaughlin, D. J. Muraki, and M. J. Shelley, Physica D **97**, 471 (1996).
8. M. Mitchell, Z. Chen, M. Shih, and M. Segev, Phys. Rev. Lett. **77**, 490 (1996).

Optical Solitons in Twisted Nematics

Mirosław A. Karpierz, Katarzyna Brzdąkiewicz, and Quang V. Nguyen

Faculty of Physics, Warsaw University of Technology,
Koszykowa 75, 00-662 Warszawa, Poland
tel.:(48 22)6607660; fax:(48 22)6282171; e-mail: karpierz@if.pw.edu.pl

Abstract: Light beam propagation in twisted nematic liquid crystal layer is analyzed theoretically. Reorientation nonlinearity induces self-focusing and moreover changes the direction of light beam propagation. It is worth to underline that creation of solitons and switching of their direction requires milliwats of light power.

Nematic liquid crystal is an excellent medium for nonlinear optics with nonlinear phenomena arising from molecular reorientation or/and thermal effects [1,2]. Nematic liquid crystals are also very interesting media for optical spatial solitons creation. Experimental results demonstrated that light beams of only milliwats could be self-trapped at distances of a few millimeters [3]. Usually the planar or homeotropic texture in layer structures [4-5] and axial in capillaries [6-8] were used. In this paper twisted nematics configuration is analyzed. Light beam propagating in such medium diffracts and due to the structural anisotropy propagates at some angle to the direction of the input light [9-10].

Optical nonlinearity due to the reorientation process causes that for higher light intensities the light beam is self-focused and additionally changes the direction of propagation. The light beam propagating in a layer filled with twisted nematic liquid crystal (see Fig.1) is taken into consideration. The electromagnetic field with dominating E_y component of the electric field is assumed. In nonlinear case the liquid crystal molecules are forced to reorient in the yz plane. This case is described by electrical permittivity tensor:
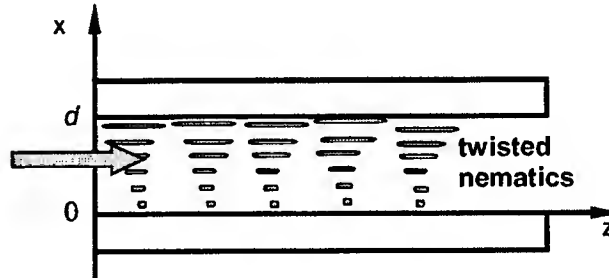
Fig.1 Schematic drawing of twisted nematic liquid crystal layer

$$\varepsilon = \begin{pmatrix} \varepsilon_\perp & 0 & 0 \\ 0 & \varepsilon_\perp + \Delta\varepsilon\cos^2\theta & \Delta\varepsilon\sin\theta\cos\theta \\ 0 & \Delta\varepsilon\sin\theta\cos\theta & \varepsilon_\perp + \Delta\varepsilon\sin^2\theta \end{pmatrix}, \qquad (1)$$

where $\Delta\varepsilon=\varepsilon_\parallel-\varepsilon_\perp$ is an optical anisotropy, $\varepsilon_\perp=n_o^2$ is an ordinary and $\varepsilon_\parallel=n_e^2$ is an extraordinary electric permittivity, and θ is an orientation angle measured as an angle between the liquid crystal molecules axis and the y-axis. In this medium the Maxwell's equations for monochromatic electromagnetic waves have the form:

$$\left[k_0^2\varepsilon_{yy}+\frac{\partial^2}{\partial x^2}+\frac{\partial^2}{\partial y^2}\frac{\varepsilon_{yy}}{\varepsilon_{xx}}+\frac{\partial^2}{\partial z^2}+\frac{\partial^2}{\partial y\partial z}\frac{\varepsilon_{yz}}{\varepsilon_{xx}}\right]E_y=\left[-k_0^2\varepsilon_{yz}-\frac{\partial^2}{\partial y^2}\frac{\varepsilon_{yz}}{\varepsilon_{xx}}-\frac{\partial^2}{\partial y\partial z}\left(\frac{\varepsilon_{zz}}{\varepsilon_{xx}}-1\right)\right]E_z, \quad (2)$$

$$\left[k_0^2\varepsilon_{zz}+\frac{\partial^2}{\partial x^2}+\frac{\partial^2}{\partial y^2}+\frac{\partial^2}{\partial z^2}\frac{\varepsilon_{zz}}{\varepsilon_{xx}}+\frac{\partial^2}{\partial y\partial z}\frac{\varepsilon_{yz}}{\varepsilon_{xx}}\right]E_z=\left[-k_0^2\varepsilon_{yz}-\frac{\partial^2}{\partial z^2}\frac{\varepsilon_{yz}}{\varepsilon_{xx}}-\frac{\partial^2}{\partial y\partial z}\left(\frac{\varepsilon_{yy}}{\varepsilon_{xx}}-1\right)\right]E_y, \quad (3)$$

where ε_{ab} are the components of the permittivity tensor (1) and $k_0=\omega/c$ is the wave vector.

The distribution of the orientation angle θ is calculated from the Euler-Lagrange equation in the form considered for the twisted nematic liquid crystals [2]:

$$\frac{d^2\theta}{dx^2}+\frac{d^2\theta}{dy^2}+\frac{\varepsilon_0\Delta\varepsilon}{4K_{22}}\left[2E_yE_z\cos 2\theta-\left(|E_y|^2-|E_z|^2\right)\sin 2\theta\right]=0, \quad (12)$$

where K_{22} is an elastic constant corresponding to the twist deformation. In the absence of the electrical field, the orientation angle in twisted nematics is a linear function of x co-ordinate: $\theta(x)=\theta(0)+\Delta\theta\,x/d$, where $\Delta\theta\leq\pi/2$. In this work we assumed $\Delta\theta=\pi/2$ and two different boundary conditions: symmetrical with $\theta(0)=-\pi/4$ and $\theta(d)=\pi/4$, and asymmetrical with $\theta(0)=0$ and $\theta(d)=\pi/2$.
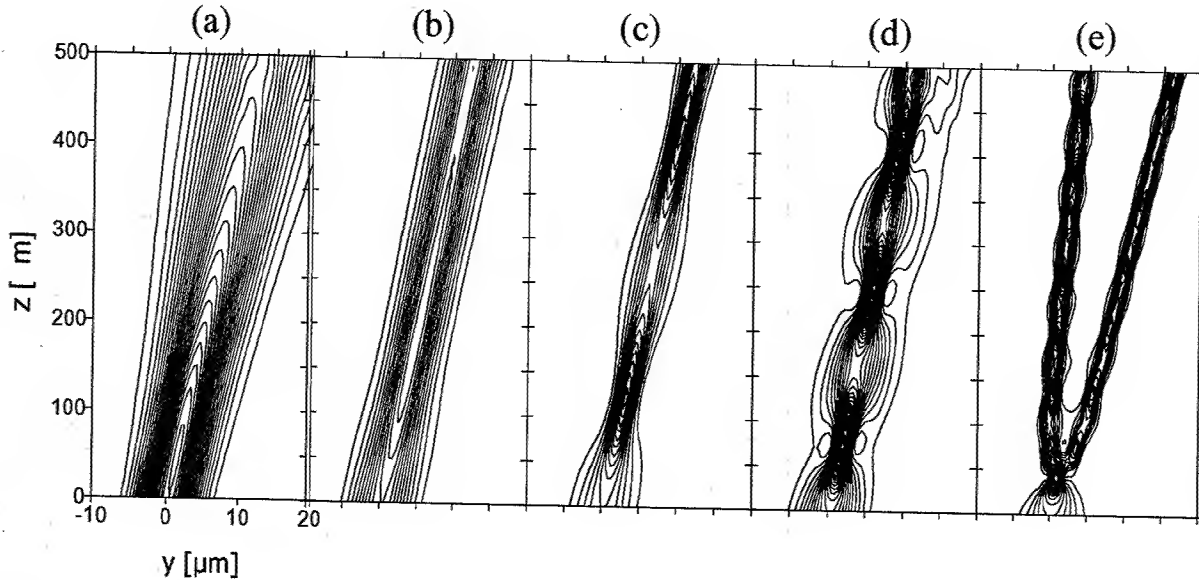
Fig.2. Light beam propagation in asymmetrical configuration of twisted nematics waveguide: (a) for the linear case; (b)-(e) for increasing light power in the presence of nonlinear reorientation.

Propagation of light beam in twisted nematics was investigated by using the numerical Beam Propagation Method with the TE-polarized Gaussian beam in the input plane. Numerical results were calculated for liquid crystal layer with refractive indices n_o=1.52 and n_e=1.69 surrounded by glass plates with refractive index n_c=1.45 and for the wavelength λ=842 nm.

In the symmetrical configuration light beam propagates in the center of the nematics layer because in this region the initial orientation creates the largest value of the refractive index. Reorientation of liquid crystals increases refractive index in the middle of the layer and the light beam is self-focused. Light propagates along z-axis and its direction is not modified by reorientation nonlinearity. Different behavior is obtained in asymmetrical configuration. In the linear case the light beam propagates down in the xz plane (going to the larger value of the refractive index), and walk off in the yz plane (due to the structural anisotropy). Nonlinear reorientation changes the direction of beam propagation and induces self-focusing (of the beam). However, the nonlinearity in thick samples can lead to the unstable propagation. Stable self-trapped beams exist in the waveguide structure. Results presented in Fig.2 were obtained for waveguide of thickness d=5µm. The reorientation nonlinearity supports self-focusing and changes the direction of light beam but also can induce splitting the beam into two or more components propagating in different directions (as in Fig. 2e).

References

[1] I.C. Khoo and S.T. Wu, *Optics and Nonlinear Optics of Liquid Crystals*, World Scientific Publishing Co Ltd., Singapore, New Jersey, London, Hongkong (1993).

[2] N.V.Tabiryan, A.V.Sukhov, B.Ya.Zel'dovich, *Mol. Cryst. Liq. Cryst.* **136**, 1-139 (1986).

[3] M.A. Karpierz, in *Soliton-driven Photonics*, ed. A.D. Boardman and A.P. Sukhorukov, Kluwer Academic Publishers, 41-57 (2001)

[4] M.A. Karpierz, M. Sierakowski, M. Świłło, T.R. Woliński, *Mol. Cryst. Liq. Cryst.* **320**, 157-164 (1998).

[5] M. Peccianti, A. De Rossi, G. Assanto, A. De Luca, C. Umeton, I.C. Khoo, *Appl. Phys. Lett.* **77**, 7-9 (2000); M. Peccianti and G. Assanto, Opt. Lett. **26**, 1690(2001); **26**, 1791 (2001); Phys. Rev. E **65**, 035603 (2002).

[6] E. Braun, L.P. Faucheux, A. Libchaber, *Phys. Rev. A* **48**, 611-622 (1993).

[7] D.W. McLaughlin, D.J. Muraki, M.J. Shelley, X. Wang, *Physica D* **88**, 55-81 (1995).

[8] M. Warenghem, J.F. Henninot, G. Abbate, *Mol. Cryst. Liq. Cryst.* **320**, 207-230 (1998); F. Derrien, J.F. Henninot, M. Warenghem, G. Abbate, *J. Opt. A - Pure Appl. Optics* **2**, 332-337 (2000).

[9] M.A. Karpierz, *Acta Phys. Polonica A* **99**, 161-173 (2001).

[10] M. A. Karpierz, M. Sierakowski, and T.R. Woliński, *Mol. Cryst. Liq. Cryst.* **375**, 313-320 (2002).

Formation of Photorefractive Solitons in Barium-Calcium Titanate: From Dark and Bright Solitons to Self-Trapped Bright Rings

Detlef Kip [(1)], **Monika Wesner** [(1)], **Vladymir M. Shandarov** [(2)], **Jingjun Xu** [(3)]

[(1)] Physics Department, University of Osnabrück, 49069 Osnabrück, Germany
Phone: (+49) 541 9692654, FAX (+49) 541 9693510, Email dkip@uos.de

[(2)] State University of Control Systems and Radioelectronics, Tomsk 634050, Russia

[(3)] Physics Department, Nankai University, Tianjin 300071, China

Abstract. We investigate photorefractive spatial soliton formation in iron-doped barium-calcium titanate. In this material with both photovoltaic and screening nonlinearity, we observe bright and dark spatial solitons, as well as the propagation of self-trapped bright rings.

Since the discovery of photorefractive spatial solitons [1,2], these non-diffracting beams have often been considered as components for the buildup of all-optical networks. Furthermore, in the last years the forefront of general soliton research has shifted to optics, in particular to various forms of spatial solitons. Until now steady-state bright spatial solitons have been observed in BTO [3], SBN [4], InP:Fe [5], $KNbO_3$ [6], KLTN [7], and $BaTiO_3$ [8] crystals. Barium-calcium titanate (BCT) [9,10] is a new promising photorefractive crystal and an alternative to $BaTiO_3$. It is much easier to grow and does not have any phase transition within the temperature range from $-120\ °C$ to $100\ °C$. This crystal also has slightly larger electrooptic coefficients $r_{13} \sim 20$ pm/V and $r_{33} \sim 130$ pm/V compared to $BaTiO_3$. In this contribution, we investigate photorefractive spatial soliton formation in iron-doped BCT. We observe, for the first time to our knowledge, the formation of bright and dark spatial solitons as well as the propagation of self-trapped bright rings in this material.

Samples of the congruently melting composition $Ba_{0.23}Ca_{0.77}TiO_3$ have been grown in the crystal-growth laboratory in Osnabrück. The dimension of our sample that is doped with 290 ppm Fe is $5×5×5$ mm^3. On both faces normal to the c-axis of the crystal, electrodes are prepared with silver paste. The light propagates along the a-axis in our experiment. Depending on external parameters, in our BCT crystals self-focusing as well as self-defocusing can be achieved. This may furhter enable us to study the coupling between coupled of dark and bright solitons in the same parameter range.

BCT crystals show a significant photovoltaic effect which leads to self-defocusing of light beams. The strength of the photovoltaic nonlinearity can be scaled by changing the intensity of the input beam. In a recent series of experiments we have shown that this mechanism leads to the formation of dark solitons in BCT, see the figure below. Here a dark spot evolves in the center of the Gaussian input beam and propagates without spatial diffraction through the sample.
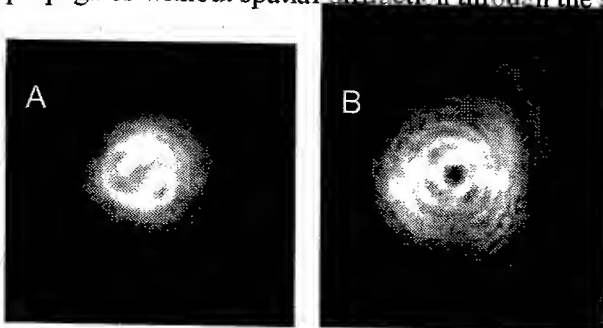
Dark soliton formation in a BCT crystal. A: output beam on the crystal's endface directly after switching on the light beam (t = 0). B: output beam on the endface in the steady-state (t = 80 s). In the center of the beam a dark spot evolves that does not change its shape during propagation. No external electric field is applied to the sample.

At the same time self-focusing of a bright beam can be achieved in BCT by applying an external electric field parallel to the ferroelectric c-axis. Therefore, in this material both, bright and dark spatial solitons, can coexist in the same parameter range. An example is given in the figure below. For low intensity of the input beam (A), the drift of electrons in the external field ('screening') dominates while photovoltaic effects are small. Thus a single self-trapped beam (B) is observed at the output face of the sample. However, when the intensity is increased, self-defocusing dominates in the center part of the beam, and the Gaussian input profile evolves to a donut-like beam (C) of similar transverse dimension. By using samples of different length we proved that, after some distance from the input face with its purely Gaussian intensity profile, this beam propagates stable in the sample as a self-trapped beam. Such a beam might be regarded as a stationary state of coupled dark and bright spatial solitons. Furthermore, for slightly different experimental parameters also more complex beam shapes form spontaneously, e.g., the trefoil-like structure in (D), where one dark spot is surrounded by four bright spots.
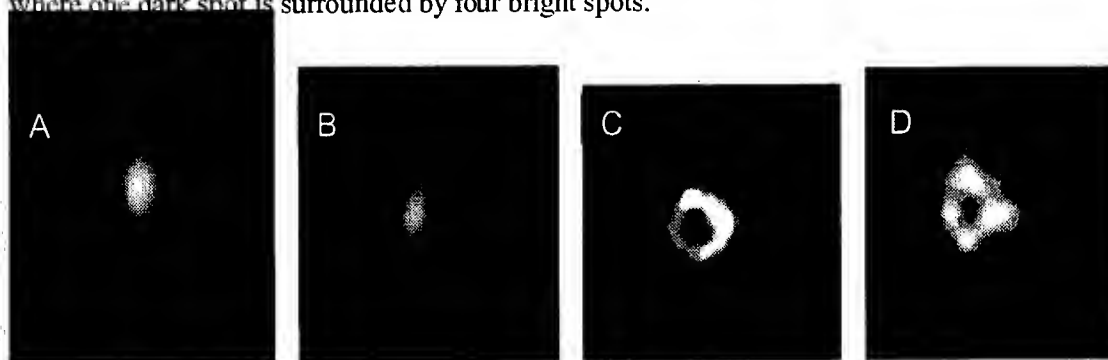
Soliton formation in a biased BCT crystal. A: input beam profile on the entrance face of the 5 mm-long sample. The beam width (FWHM) is about 12 μm. B: output beam profile for low input intensity (30 mW/cm^2) with an appropriate electric field applied along the ferroelectric c-axis. C: output beam profile for higher input intensity. A donut-like beam with a dark spot in the center appears. D: For slightly different parameters than in C the donut breaks into a trefoil-like structure.

These first results indicate that the coexistence of dark and bright solitons is due to a different intensity dependence of the two involved mechanisms. Therefore, this effect may be used to create ensembles of dark and bright solitons in the same parameter range. Theoretical modelling of this type of combined photovoltaic and screening nonlinearity is currently in progress.

[1]   M. Segev, B. Crosignani, A. Yariv, Phys. Rev. Lett. **68**, 923 (1992).
[2]   For a recent review on photorefractive solitons, see G. I. Stegeman and M. Segev, Science **280**, 889 (1998).
[3]   M. D. Iturbe-Castillo, P. A. Marquez-Aguilar, J. J. Sanchez-Mondragon, S. Stepanov, V. Vysloukh, Appl. Phys. Lett. **64**, 408 (1994).
[4]   G. Duree, J. L. Schultz, G. Salamo, M. Segev, A. Yariv, B. Crosignani, P. DiPorto, E. Sharp, R. R. Neurgaonkar, Phys. Rev. Lett. **71**, 535 (1993).
[5]   M. Chauvet, S. A. Hawkings, G. Salamo, M. Segev, D. F. Bliss, G. Bryant, Opt. Lett. **21**, 1333 (1996).
[6]   S. Lan, M. F. Shih, M. Segev, Opt. Lett. **22**, 1467 (1997).
[7]   E. DelRe, M. Tamburrini, M. Segev, M. Mitchell, E. Refaeli, A. Agranat, Appl. Phys. Lett. **73**, 16 (1998).
[8]   J. A. Andrade-Lucio, M. D. Iturbe-Castillo, P. A. Marquez-Aguilar, R. Ramos-Garcia, Opt. and Quant. Electron.
       30, 829 (1998).
[9]   H. Veenhuis, T. Börger, K. Buse, C. Kuper, H. Hesse, E. Krätzig, J. Appl. Phys. **88**, 1042 (2000).
[10] C. Kuper, K. Buse, U. van Stevendaal, M. Weber, T. Leidlo, H. Hesse, E. Krätzig, Ferroelectrics **208**, 213 (1998).

New Materials and New Directions

Wednesday, September 4, 2002

TBA *Presider*

NLWA
8:00am – 10:00am
Auditorium

Nonlinear phenomena in Bose-Einstein Condensates

L. Santos
Institut für Theoretische Physik, Universität Hannover,
Appelstr. 2, D-30167 Hannover, Germany
Telephone: 0049-511-7625891, Fax: 0049-511-7624945
e-mail: santos@itp.uni-hannover.de

For sufficiently low temperatures, a Bose gas experiences a transition into a Bose-Einstein condensate, characterized by a macroscopic occupation of the ground state of the system. The development of efficient cooling and trapping techniques for neutral atoms led in 1995, to the first observation of BEC in dilute alkali gases in ^{87}Rb [1]. This remarkable achievement has been followed by BEC experiments in various other elements. The BEC has become during the last years, one of the most active and fruitful research areas of modern atomic physics, constituting an interdisciplinary field, which links atomic physics with various other research areas, like quantum optics, condensed-matter physics, and very especially nonlinear physics.

The BEC constitutes a macroscopically occupied matter wave, but contrary to the traditional atom optics phenomena [2], which are basically single-particle, the BEC optics is, due to the atom-atom interactions, inherently nonlinear, being called nonlinear atom optics (NLAO). In particular, the BEC dynamics at very low temperatures is provided by a nonlinear Schrödinger equation (NLSE) with cubic nonlinearity:

$$i\hbar\frac{\partial}{\partial t}\psi(\vec{r},t) = \left\{ -\frac{\hbar^2}{2m}\nabla^2 + V(\vec{r}) + \frac{4\pi\hbar^2 a}{m}|\psi(\vec{r},t)|^2 \right\}\psi(\vec{r},t), \qquad (1)$$

also called Gross-Pitaevskii equation, where ψ is the BEC wavefunction, V denotes an external potential, and m is the atomic mass. The interparticle interactions are described by the s-wave scattering length a. If $a > 0$ the interactions are repulsive and condensates with an arbitrary number of particles may in principle be stable, resembling the case of defocusing nonlinear media in nonlinear optics (NLO). On the contrary spatially homogeneous condensates with $a < 0$ are absolutely unstable with regard to local collapses. The situation changes in the presence of a trapping potential, since for a number of particles below a critical value, the condensate is stabilized if the negative pressure caused by the interparticle attraction is compensated by the quantum pressure imposed by the trapping potential [3].

Several remarkable experiments have been reported in NLAO, as four-wave mixing [4] of matter waves, the generation of dark-solitons in media with $a > 0$, and the observation of the condensate collapse in gases with $a < 0$. A dark soliton in BEC is a macroscopic excitation of the condensate, which is characterized by a local density minimum and a sharp phase gradient of the wavefunction at the position of the minimum. The shape of the dip does not change due to the balance between kinetic energy and repulsive atom-atom collisions. These solitons have been created in very elongated condensates by means of the so-called phase-imprinting method [5], which consists of applying a given phase to one part of the condensate, by shining an appropriate laser pulse on it. Apart from their creation, several other aspects of the soliton physics in BEC have been recently investigated, in particular the dynamics, stability and dissipation of solitons in very elongated but not 1D geometries, and at finite temperature [6]. Additionally, in the recent years, the development of trapping techniques has allowed the creation of multi-component condensates, formed by trapping atoms in different internal (electronic) states. The physics of multicomponent solitons in BEC has been also recently discussed [8], and resembles recently observed phenomena in NLO [9].

The equivalent of the wave collapse studied in nonlinear physics, is produced for gases with $a < 0$ with sufficiently large number of particles. Recently, new techniques have been developed to modify the value and sign of a by means of Feshbach resonances [10]. In particular, condensates with $a > 0$ are created, and then the sign of a is reversed. After this change of a, the condensate undergoes an implosion (collapse) followed by the ejection of relatively hot atoms ("bose-nova"). This process can be understood by means of a NLSE with a quintic damping term [11], and resembles the analysis already performed in homogeneous systems in nonlinear physics [12].

There are other scenarios in which the nonlinearity could lead to interesting phenomena in BEC. The recent success in creating ultra-cold molecular clouds opens fascinating prospects to achieve BEC in trapped gases of heteronuclear molecules. In a sufficiently high electric field, these molecules interact via dipole-dipole interaction, and the equation which governs those systems is a NLSE as above, but with a nonlocal nonlinearity [13]. Another system which attracts a growing interest concerns the mixtures between atomic and molecular condensates, where the equivalent of second harmonic generation can be obtained [14].

References

[1] M. H. Anderson *et al.*, Science **269**, 198 (1995).

[2] C.S. Adams, M. Sigel, J. Mlynek, Phys. Rep. **240**, 145 (1994).

[3] See, e.g., F. Dalfovo *et al.*, Rev. Mod. Phys. **71**, 463 (1999).

[4] L. Deng *et al.*, , Nature **398**, 218 (1999).

[5] J. Denschlag *et al.*, Science **287**, 97 (2000); S. Burger *et al.*, Phys. Rev. Lett. **83**, 5198 (1999).

[6] Th. Busch, and J. R. Anglin, Phys. Rev. Lett. **84**, 2298 (2000); P. O. Fedichev, A. E. Muryshev, G. V. Shlyapnikov, Phys. Rev. A **60**, 3220 (1999); D. L. Feder *et al.*, Phys. Rev. A **62**, 053606 (2000); A. Muryshev *et al.*, XXXXXXX.

[7] C. J. Myatt *et al.*, Phys. Rev. Lett. **78**, 586 (1997); J. Stenger *et al.*, Nature **396**, 345 (1998).

[8] P. Öhberg and L. Santos, Phys. Rev. Lett. **86**, 2918 (2001); Th. Busch and J. R. Anglin, Phys. Rev. Lett. **87**, 010401 (2001)

[9] E. A. Ostrovskaya *et al.*, Opt. Lett. **24**, 327 (1999).

[10] S. Inouye *et al.*, Nature (London) **392**, 151 (1998); E. A. Donley *et al.*, Nature **412**, 295 (2001).

[11] H. Saito and M. Ueda, Phys. Rev. Lett. **86**, 1406 (2001); H. Saito and M. Ueda, cond-mat/0107248; L. Santos and G. V. Shlyapnikov, cond-mat/0112410.

[12] V. E. Zakharov and E. A. Kuznetsov, Zh. Eksp. Teor. Fiz. **91**, 1310 (1986) [Sov. Phys. JETP **64** 773 (1986)]; S. N. Vlasov *et al.*, Zh. Eksp. Teor. Fiz. **95**, 1945 (1989) [Sov. Phys. JETP **68**, 1125 (1125)]; M. E. Kosmatov *et al.*, Physica D (Amsterdam) **52**, 16 (1991).

[13] S. Yi and L. You, Phys. Rev. A **63**, 053607 (2001); K. Góral, K. Rzążewski and T. Pfau, Phys. Rev. A**61**, 051601 (2000); L. Santos *et al.*, Phys. Rev. Lett. **85**, 1791 (2000).

[14] T. J. Alexander, *et al.*, cond-mat/0112176.

Single-Photon and Two-Photon Photopolymerization
for Micro-Nano Fabrication

Satoshi Kawata

Graduate School of Information Science and Technology,

Osaka University

Yamadaoka 2-1, Suita 565-0871 Japan

TEL : +81-6-6879-7845

FAX : +81-6-6879-7330

e-mail : kawata@ap.eng.osaka-u.ac.jp

Photopolymerizable resin is lately one of the most attractive materials for manufacturing optical microdevices and complex three-dimensional(3D) structures. We have been studying the photofabrication of 3D micro-nano structures with photopolymerizable resin for micro-nano photonic devices and micro-electromechanical systems(MEMS). In this presentation, I will show several photopolymerization processes and micro-nano fabrication methods based on single-photon and two-photon absorptions.

First, a nonlinear process of single-photon photopolymerization is introduced. Figure 1(a) shows a polymerized micro-fiber structure, which is "self-grown" automatically when a laser beam is focused in photopolymerizable resin[1]. The photopolymerizable resin used here is SCR-500, which is polymerized with single-photon absorption by the irradiation of UV or blue light. In the experiment, we used a He-Cd laser ($\lambda = 441.6$ nm) to polymerize the resin. In the case of Fig. 1(a), the average power of the input laser beam and the numerical aperture (NA) of focusing objective lens were 0.15 mW and 0.5, respectively. The length of the fiber increased in proportion to the exposure time and reached several hundred μm after 2 s, however, the diameter of the fiber kept a constant value of 3 μm. This self-growing phenomenon is caused by the increase of the refractive index of the resin by photopolymerization. In the case of SCR-500 resin, the initial refractive index of 1.53 increases to 1.55 with the polymerization reaction. Higher refractive index of polymerized resin formed locally from the focal point produces the self-focusing effect, and then, incident laser light propagates in form of spatial optical soliton, which gives rise to the micro-fiber structure. When two laser beams are launched simultaneously in the resin and

two self-growing fibers are collided each other, the two fibers can merge to form a single fiber[2]. The merging occurs under the collision angle between the two fibers smaller than 9°. We also observed the growth of multiple-fibers by choosing high NA and high power of incident laser beam [Fig. 1(b)]. These phenomena are applicable to microfabrication of optical waveguides and optical components[3].
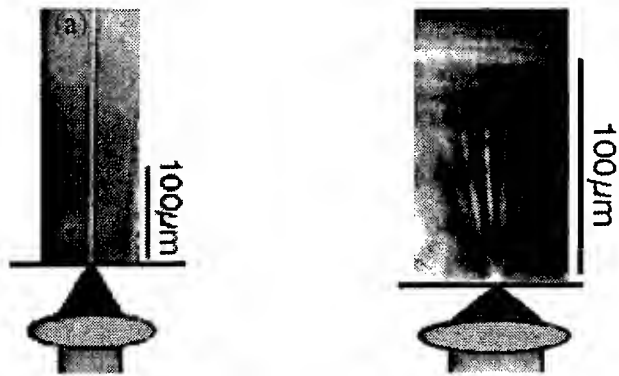
Figure 1   Self-grown micro-fiber structure in photopolymerizable resin.
(a)single fiber structure and (b)multiple fibers.

Photopolymerization by two-photon absorption shows different property from that of single-photon photopolymerization. In the experiment for two-photon photopolymerization, laser beam of a Ti:Sapphire laser, whose wavelength and pulse width are 780 nm and 150 fs respectively, was tightly focused in the same resin used in the previous experiment[4,5]. The resin absorbs the UV and blue light, as mentioned before, but does not absorb the infrared light by single-photon absorption. Only in a small volume at the center of the focus spot, the resin can be polymerized by two-photon absorption. As a result, the shape of the polymerized structure is a small 3D "dot" as shown in Fig. 2(a). The size of the polymerized volume can be smaller than the diffraction limit due to the quadratic dependence of two-photon absorption probability on the photon density[7]. Moreover, there is a threshold-type nonlinearity in photopolymerization reaction caused by reactive oxygen molecules and some other radical quenchers contained in the resin, which kill photo-induced radicals. So the photopolymerization occurs only at the light intensity exceeds a certain threshold. By tuning the input light intensity slightly above the threshold, a nano-dot of 120 nm diameter can be produced even though the wavelength of the laser light is 780 nm.

By scanning the focus spot in the photopolymerizable resin in three dimensions, 3D complex micro-nano structures can be fabricated. After scanning the focus spot,

non-polymerized resin is removed by ethanol to get the 3D structures. Figure2(b) is a statue of a bull[4], and Fig. 2(c) is a micro-spring of 150 nm thick polymer wire[4,6]. The spring constant of the micro-spring is about 10^{-8} N/m, and the spring works in solution. Because of the capability of subwavelength and 3D fabrication, we have also been studying any other application of two-photon process in opto-electronics[8] or biological field, such as 3D data storage, micro-nano surgery of biological cells, and so on.
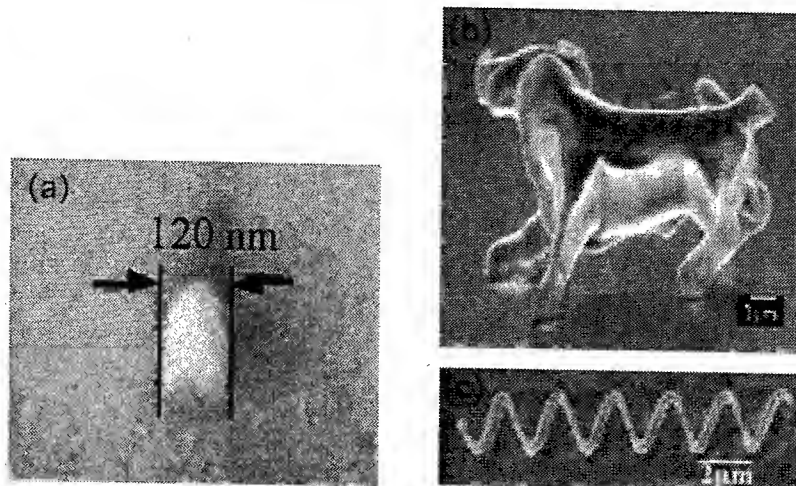
Figure 2   SEM images of (a) a 3D dot with the size of 120 nm obtained with two-photon photopolymerization, and (b)a statue of a bull and (c)micro spring, fabricated by scanning the focus spot in three dimensions.

REFERENCES

[1]   S. Shoji and S. Kawata, Appl. Phys. Lett., **75**, 737(1999).

[2]   S. Shoji and S. Kawata, Opt. Lett., **27**, 185 (2002).

[3]   S. Shoji and S. Kawata, Appl. Phys. Lett., **76**, 2668 (2000).

[4]   S. Kawata, H.-B. Sun, T. Tanaka, and K. Takada, Nature, **412**, 697(2001).

[5]   S. Maruo, O. Nakamura, and S. Kawata, Opt. Lett., **22**, 132(1997).

[6]   H.-B. Sun, T. Tanaka, K. Takada, S. Kawata, Appl. Phys. Lett., **79**, 1411(2001).

[7]   H.-B. Sun, K. Takada, and S. Kawata, Appl. Phys. Lett., **79**, 3173(2001).

[8]   B. H. Cumpston, et al., Nature, **398**, 51(1999).

Abstract

Self-growth of micro-fiber structures and spatial optical soliton propagation based on single-photon photopolymerization, and nonlinear property of two-photon photopolymerizaiton which gives rise to three-dimensional microfabrication with sub-diffraction limit spatial resolution are introduced.

Ultrahigh-speed All-optical Wavelength Conversion

Byoung S. Ham

Center for Quantum Coherence and Communications, ETRI, 161 Gajeong-dong, Yusung-gu, Daejon 305-350 S. Korea
+82-42-860-1309, +82-42-860-3815, bham@etri.re.kr

Philip R. Hemmer

Electrical Engineering Department, Texas A&M University, College Station, Texas 77843 USA
+1-979-845-8932, +1-979-845-6259, prhemmer@ee.tamu.edu

Abstract: Ultrahigh-speed all-optical wavelength conversion has been demonstrated using a rare-earth doped crystal as a proof of principle. The observed switching time is two orders of magnitude shorter than the carrier lifetime for on-resonance transitions. This demonstration shows a breakthrough in the T_1 limitation of current switching technologies.

1. Introduction

The increasing demand of information communications has been attracted in the study and development of ultrahigh-speed optical devices in fiber-optic communications networks. To process mass data traffic in fiber-optic communications, optical wavelength converters are extremely important under the environmental condition of wavelength division multiplexing. Of the most widely used methods in wavelength conversions are four-wave mixing, cross-phase modulation, and difference frequency generation.[1,2,3] These methods, however, simply rely on nonlinear coefficient to generate new wavelength. In general the nonlinear coefficient for off-resonance transitions are low so that high driving source is needed. Another method of optical switching is using resonance frequency. However, the switching speed in the resonant transitions is limited by the carrier lifetime or population relaxation time. To increase the switching speed, intersubband transitions are also applied.[4] In the experimental demonstration of optical switching using intersubband transitions, however, the extinction ratio is not high, and the output power level is low.

In this paper we present a new method based on dark resonance.[5] The dark resonance is well known phenomenon in which absorption is cancelled at line center due to destructive quantum interference. This absorption cancellation is called electromagnetically induced transparency (EIT) in optically dense media.[6] Recently similar on-resonance wavelength conversion method was proposed by using EIT.[7] The EIT based wavelength conversion is based on absorption cancellation so that the medium must be highly absorptive to generate high extinction ratio. However, because of using transparency and absorption difference, the input power must be low far below the saturation level. In our method, nondegenerate four-wave mixing processes are used to enhance dark resonance coherence. The conversion efficiency is highly efficient when the signal is weak owing to high pumping power.[8] Unlike the ref. 7, the wavelength converted signal can be amplified.[9] This amplification of the input signal gives a great advantage to practical applications.

2. Dark resonance based all-optical wavelength conversion

Figure 1 shows a basic energy level diagram of an optical medium for dark resonance based all-optical wavelength conversion. In Fig. I, ω_2 is an input signal to be switched and the ω_D is a switched signal through wavelength conversion processes. The ω_1 is needed to create dark resonance with ω_2, and ω_P is a probe to detect the dark resonance. The energy between input and output signal is ΔE. This type of nondegenerate four-wave mixing processes with dark resonance has been well studied theoretically and experimentally.[8,9,10,11] A unique characteristic of the dark resonance based nondegenerate four-wave mixing processes is the fact that the four-wave mixing generation in Fig. 1 can be amplified owing to the energy transfer from the probe to the switched signal. The dark resonance basically forms a moving grating, two-photon coherence, when the lights are incident into the optical medium with an angle. This grating formation is as fast as Rabi frequency applied. The decay time of the dark resonance is also as fast as the two-photon coherence decay time, which is the phase decay time between the energy levels $|1>$ and $|2>$. Here, it should be noted that the decay time of the moving grating is a major factor to determine

the switching time in the four-wave mixing processes. Moreover, the phase decay time between |1> and |2> is independent of optical transition properties of |1>-|3> or |2>-|3>. Therefore, optical wavelength conversion based on dark resonance is independent of the optical population decay time.
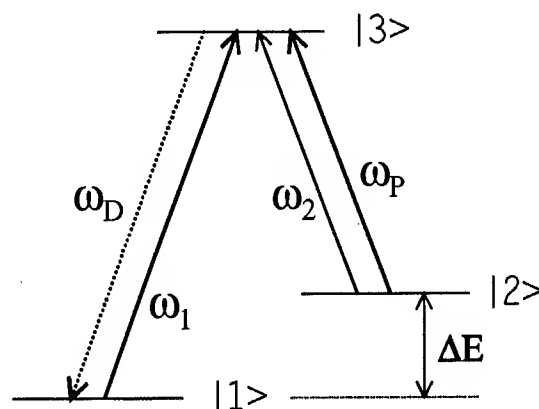
FIG. 1. Energy level diagram for wavelength conversion based on dark resonance enhanced nondegenerate four-wave mixing processes.

3. Results

Figure 2 shows an experimental results of the proposed idea based on Fig. 1 for three consecutive pulses. The obtained data in Fig. 2 is for wavelength converted signal ω_D by using dark resonance enhanced nondegenerate four-wave mixing processes. Here, ω_2 is an incoming signal to be switched. Each optical pulse width of the laser beams is 10 μs. As seen in Fig. 2, the switched signal follows the incoming modulation frequency of 100 kHz with modulation depth of 50%. The optical medium used in Fig. 2 is a rare-earth Pr^{3+} doped Y_2SiO_5 (Pr:YSO). The optical transition frequency of Pr:YSO is ~606 nm, and the lifetime for that transition is ~200 μs (relaxation rate Γ (=$1/2\pi T_1$) is ~1 kHz).[12] The switching bandwidth of the wavelength conversion processes in Fig. 2 is two orders of magnitude wider than the population relaxation rate of the optical medium of Pr:YSO. Therefore, the repetition rate of the optical switching for the wavelength conversion in Fig. 2 is a breakthrough in the T_1 limitation of current on-resonance optical switching technologies that can never be shorter than the lifetime.
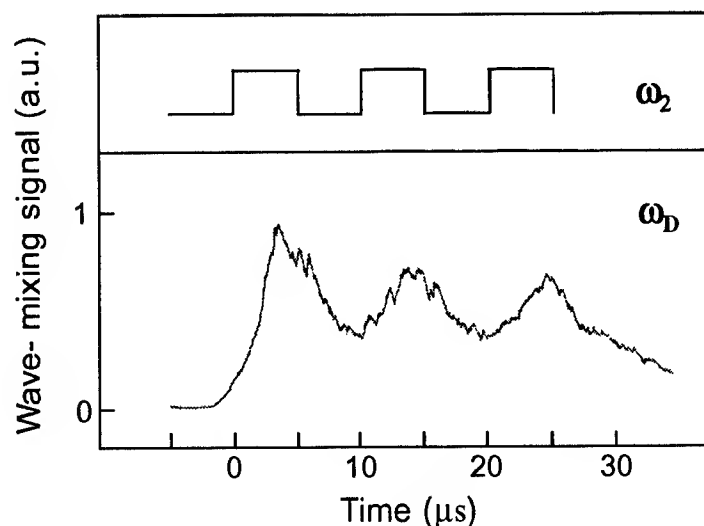
FIG. 2. All-optical switching: wavelength conversion.

For potential applications of the present demonstration, III-V semiconductor quantum wells such as GaAs/AlGaAs are considered. In GaAs/AlGaAs multiple quantum wells, coherence between heavy holes (hh) and light holes (lh) can be created by two resonant light fields.[13] Even though the optical decay time from the conduction lowest energy level to the valence hh or lh is subnanosecond, the coherence decay time between hh-lh mainly depends upon the photon interaction, so that the proposed all-optical switching method could be as fast as ~THz. Owing to the small size of the quantum wells and advanced fabrication technologies, this new type of all-optical devices may be integrated using moderate laser diodes via optical waveguides.

Acknowledgement

Reference

[1] D. Nesset et al., IEEE Commun. Mag. **36**, 56 (1998).

[2] S. nakamura et al., Appl. Phys. Lett. **67**, 2445 (1995).

[3] S. nakamura et al., IEEE Photon. Tech. Lett. **10**, 1575 (1998).

[4] H. Yoshida et al., IEEE Photon. Tech. Lett. **11**, 632 (1999).

[5] G. Alzetta et al., Nuovo Cimento Soc. Ital. Fis. **36B**, 5 (1976); E. Arimondo and G. Orriols, Nuovo Cimento Lett. **17**, 333 (1976).

[6] S. E. Harris, Physics Today **50** (7), 36 (1997).

[7] H. Schmidt and R. J. Ram, Appl. Phys. Lett. **76**, 3173 (2000).

[8] M. Jain et al., Phys. Rev .Lett. **77**, 4326 (1996).

[9] P. Hemmer et al., Opt. Lett. **20**, 982 (1995).

[10] B. S. Ham et al., Opt. Lett. **22**, 1138 (1997).

[11] Y. Li et al., Opt. Lett. **21**, 1064 (1996).

[12] R. W. Equall et al., Phys. Rev. B **52**, 3963 (1995).

[13] M. E. Donovan et al., Phys. Rev. Lett. **87**, 237402 (2001).

Place saver for invited speaker

Spatial Solitons

Wednesday, September 4, 2002

Demetrios N. Christodoulides, Univ. of Central Florida, USA
Presider

NLWB
10:30am – 12:30pm
Auditorium

Spatial solitons and their interactions via Nonlocality and Reorientation in nematic liquid crystals

Marco Peccianti, Claudio Conti and Gaetano Assanto

National Institute for the Physics of Matter (INFM)
Terza University of Rome, Via della Vasca Navale 84, 00146 Rome, Italy
Phone +39-0655177028, Fax +39-065579078, assanto@ele.uniroma3.it

Abstract

A reorientational nonlocal nonlinearity governs 3D-spatial solitons in undoped nematic liquid crystals. We demonstrate solitons, their attraction and interlacing, outlining the role of nonlocality in time and in space, in agreement with a simple model.

Spatial Solitons and their interactions via Nonlocality and Reorientation in nematic liquid crystals

Marco Peccianti, Claudio Conti and Gaetano Assanto

National Institute for the Physics of Matter (INFM)
Terza University of Rome, Via della Vasca Navale 84, 00146 Rome, Italy
Phone +39-0655177028, Fax +39-065579078, assanto@ele.uniroma3.it

Spatial solitons have been demonstrated in a variety of media exhibiting different kinds of nonlinearity, including Kerr, parametric and photorefractive responses.[1] Using planar cells with a voltage bias, we have recently demonstrated the generation and propagation of (2+1) dimensional optical spatial solitons in undoped nematic liquid crystals, taking advantage of their reorientational nonlinearity in the principal plane of a positive uniaxial.[2] Such solitons correspond to light trapping in actual bell-shaped refractive waveguides, both in the cases of coherent and partially incoherent excitations.[3] Therefore they are able to trap and guide co-polarized signals at different wavelengths and low powers, paving the way to all-optical interconnects and their reconfiguration.[4]

Because of the spatially nonlocal response characteristic of the liquid-crystalline medium, these 3D solitons are stable and can undergo long-range interactions, i. e., they can interact even at separations exceeding their transverse extension. In fact, the refractive index perturbation -due to an intense beam and corresponding to a soliton- can diffuse from the excitation region and overlap with the index well of another soliton in its proximity, causing the two solitons to perturb and attract each other.

Using the standard Frank's formalism and Maxwell equations, the initial stage of the interaction of two identical solitons propagating along z is simply described by:

$$m\frac{d^2\Delta}{dz^2} = -\frac{\partial}{\partial\Delta}U(\Delta)$$

where m is a form parameter (the effective mass) depending on the power of the solitons, and Δ is the normalized distance between them. The interaction can be described by an attractive potential $U(\Delta)=-e^{-\Delta^2}$ irrespective of the solitons' relative

phase, as expected on the basis of an intuitive understanding of the nonlocality and its role.[5]

A typical set of stationary results with Ar+ laser light at 514nm is reproduced in Fig. 1.
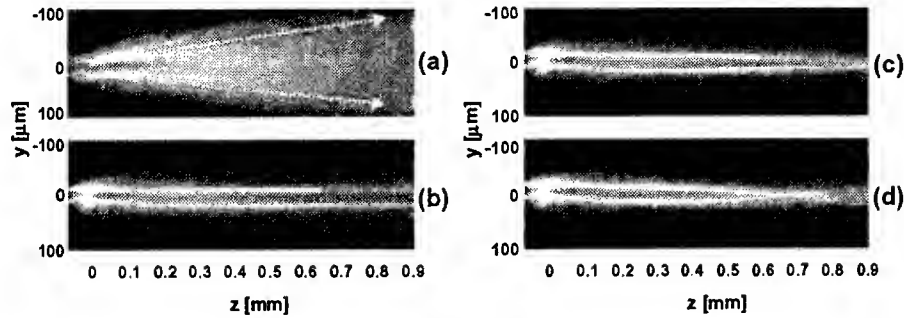
Figure 1 Attraction of two identical beams in a biased liquid crystal cell. The photos show green light propagating in the plane (y, z), after launching two Gaussian beams (10µm waist) in z=0 with a 28µm y-separation and a 5° relative angle: (a) linear behavior; (b) weak attraction between solitons each of power 2.8mW; (c) stronger attraction at 3.6mW; (d) crossing and interlacing at input powers of 4.5mW.

A case of soliton-soliton attraction leading to complete interlacing is shown in Fig. 2, obtained for 3mW Gaussian beams launched in parallel and separated by 11µm at the input interface. Notice that the longitudinal period decreases as the solitons keep reducing their transverse momenta.

Figure 2 Interlacing of 3mW solitons launched parallel to one another at 11µm separation in z=0.

Furthermore, since the nonlinearity of the liquid crystal is relatively slow, this temporal nonlocality results into the evolution of pairs of solitons as they progress towards a steady-state. Snapshots of the real-time evolution of a typical interaction between identical solitons are displayed in Fig. 3. The two Gaussian inputs, initially diverging and diffracting (Fig. 3a), turn into diverging spatial solitons (Fig. 3b) and, after a few seconds, attract and fuse due to the collapse of the interlacing behavior (Fig. 3c).

In conclusion, the specific nonlinear response of nematic liquid crystals features incoherent soliton interactions through nonlocality and reorientation, paving the way to

the realization of light controlled logic gates and all-optical guided-wave devices for signal processing/readdressing.
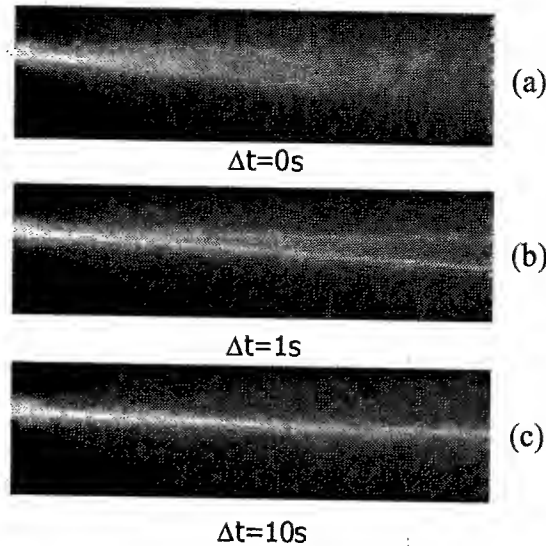
Figure 3 Interaction of two 3mW-spatial solitons launched in z=y=x=0 with a relative angle of 2.7° in the plane (y,z): from top to bottom, temporal sequence at Δt=0s (a), 1s (b) and 10s (c) after excitation. In (c) the solitons, established in (b), collapse and merge for z > 0.6mm.

References

[1] *Spatial Solitons*, S. Trillo and W. E. Torruellas eds., Springer-Verlag, Berlin (2001)
[2] M. Peccianti, A. Derossi, G. Assanto, A. de Luca, C.Umeton, and I.C.Khoo, Appl. Phys. Lett. **77**, 7(2000)
[3] M. Peccianti and G. Assanto, Opt. Lett. **26**, 1791 (2001)
[4] M. Peccianti and G. Assanto, Opt. Lett. **26**, 1690 (2001)
[5] D. Mitchell and A. Snyder, J. Opt. Soc. Am. B **16**, 236 (1999)

Experimental observation of phase controlled three-dimensional interactions between two quadratic spatial solitons: scattering, fusion and spiraling

C. Simos, V. Couderc and A. Barthélémy
Institut de Recherche en Communications Optiques et Microondes. UMR 6615
Faculté des sciences de Limoges. 123 Avenue Albert Tomas. 87060 Limoges Cedex. France
Phone:+33 555 45 75 30 Fax: +33 555 45 72 53
E-mail: coudercv@ircom.unilim.fr

Abstract: We experimentally investigated the non-planar interaction of two quadratic spatial solitary waves in a bulk crystal. We have obtained repulsion, fusion and spiraling by controlling the phase relationship between the input fields at the fundamental frequency and/or their direction. Influence of polarization imbalance, intensity and phase mismatch was observed.

OCIS codes: (190.4420) Nonlinear optics, transverse effects in

1. Introduction

In 1995 W. Torruellas et al. demonstrated experimentally the generation of a spatial soliton in a second order nonlinear media [1]. Interactions of multicolor spatial solitons have already been numerically and experimentally studied [2-8]. B. Bourliaguet et al. reported in 1998 experimental results on the interaction between two two-dimensional quadratic spatial solitary waves with type II phase matching in a KTP crystal. They proved that solitons interact either in a quasi-elastic or in an inelastic fashion, depending on the velocity of the collision [2]. Later on, G. Leo et al. investigated and demonstrated numerically the control of spatial solitary waves interactions in a collision sense, including the case of parallel input directions, through power imbalance. They obtained coalescence, steering, crossing or repulsion effects [7]. All the above results applied only to planar collisions (2D case). Actually, three-dimensional interactions between quadratic spatial solitons have been only theoretically studied either by numerical simulations or by analytical models [4-6]. In the most characteristic work V.V. Steblina et al. analyzed the three-dimensional interaction between two parametric solitons and predicted phase controlled non-planar beam switching in a bulk $\chi^{(2)}$ medium, leading to soliton scattering, spiraling and fusion [5-6]. Analysis was based on an analytical model derived from a mechanical approach that provides a physical description of soliton collisions in terms of interacting effective particles. This behavior was in accordance with the one predicted by direct numerical resolution of the equations of propagation.

In this communication we present, for the first time to our knowledge, experimental observations on non-planar interactions leading to scattering, fusion and spiraling of two solitary waves in a type II KTP crystal. All the phenomena were phase-controlled and repetitively observed. Moreover, we discuss the influence on the interaction of several experimental parameters such as phase mismatch, total input power and intensity imbalance between the ordinary and extraordinary components in each input beam.

2. Experimental layout

The experiments (Fig. 1) were performed with a Q-switched, mode-locked Nd:YAG laser which delivered 45ps pulses at 1064 nm. A Michelson-type interferometer with a polarization beam splitter cube as an input/output element split the fundamental beam in two separate beams with perpendicular polarizations. The distance between the beams and the relative orientation can be modified by the misalignment of one of the interferometer arms. Polarizing components served to adjust the total power as well as the intensity sharing between the two output beams which are then focused by means of a telescope
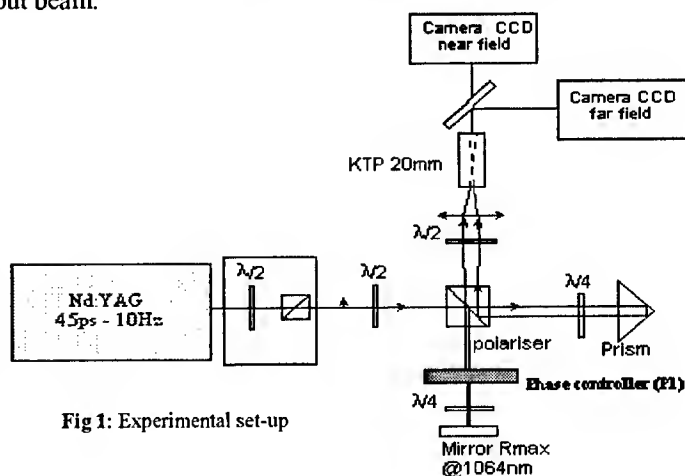
Fig 1: Experimental set-up

to 28 μm spots onto the entrance face of a 2cm long KTP crystal cut for type II SHG. A half wave plate adjusted the polarization of the incident fields in order to satisfy the type II phase matching and generate two independent solitons which propagate in the directions of the incident beams. So the two quadratic spatial solitary waves were excited with only the fundamental frequency components at the input of the crystal. Two CCD cameras connected to an image acquisition system were used to record simultaneously and to analyze the near- and far-field patterns of the beams after their propagation through the nonlinear crystal. A glass plate (P1) introduced in the trajectory of one of the beams allowed to changing the phase difference between the two input waves. Phase mismatch was controlled by the crystal orientation. Special attention must be given in the fact that in all the experiments presented here, the two solitary waves crossed the nonlinear crystal without overlapping. This clearly proves a three dimensional interaction.

3. Phase controlled interactions between quadratic spatial solitons

The first experiment was performed with the crystal oriented at exact phase matching for one of the two beams. The angle between the two incident waves at the input face of the nonlinear medium was set to 0.24° in the xOz plane and 0.81° in the yOz plane. This orientation corresponds to a phase mismatch of 0.75π for the second beam. The separation distance between the two beams on the input face of the crystal was equal to 43μm in the Ox and Oy directions.

Under the above-mentioned conditions, we have observed both attractive and repulsive effects according to the phase relationship between the two input beams. In the case of a repulsive interaction (Fig. 2(a)), the angular deviation of the solitons due to the mutual scattering was 0.22° (xOz plane) and 0.2° (yOz plane) for the soliton S1 and 0.1° (xOz plane) and 0.006° (yOz plane) for the soliton S2. The increase of the total relative angular separation between the two solitons was of 133% and 23% of the input angles in the xOz and yOz planes respectively. A tilt of the plate P1 modified the phase relationship between the two input beams

Fig. 2: Output near field patterns (output face of the crystal) corresponding to the combination of 3 recordings: one with S1 alone, one with S2 alone, one with S1+S2 simultaneously launched into the crystal; (a) scattering, (b) fusion.

and permitted to establish an attractive interaction, leading to the fusion of the two solitons in an intermediate position (Fig. 2(b)). A continuous tilt of the plate P1 permits the repetitive transition between a repulsive interaction (scattering) and an attractive one (fusion). Once the phase difference was fixed, both phenomena (scattering or fusion depending on the phase difference) were repetitively reproduced being stable on shot to shot. Moreover, it appeared that the barycentre of the two solitons moved during the interaction, breaking the collision symmetry. A similar phenomenon has been previously observed by G. Leo and G. Assanto during numerical simulations of 2D collisions [8] and was attributed to the intensity imbalance and the presence of spatial walk-off.

In a second step we have looked for the observation of spiraling interactions by slightly modifying the relative orientation of the incident beams. After adjustments, the angle between the two beams was equal to 0.24° in the xOz plane and 0.78° in the yOz plane. The separation distance of the two beams on the input face of the crystal was equal to 39μm (xOz plane) and 25μm (yOz plane). The separation distance between the two solitons at the cross points in the nonlinear crystal was 105μm in the Ox direction and 31μm in the Oy direction. It is worthy of note that this new configuration is extremely close to the one reported above. Similarly to the previous case, we observed both repulsive and attractive behavior owing to the phase relationship between the two input waves. The repulsive interaction gave birth to a scattering effect that created an angular deflection of 0.098° in the

Fig.3: Output near field patterns (output face of the crystal) corresponding to the combination of 3 recordings: one with S1 alone, one with S2 alone, one with S1+S2 simultaneously launched into the crystal; (a) scattering, (b) spiraling.

xOz plane and 0.14° in the yOz plane for the soliton S1 and of 0.33° in the xOz plane and 0.16° in the yOz plane for the soliton S2 (Fig. 3(a)). On the other hand and in contrast with the previous configuration, the attractive interaction that was established when appropriately adjusting the phase difference between the input beams, gave birth to a spiraling between the two solitary waves (Fig. 3(b)). The deflection angles were two times larger than for the scattering effect (S1: 0.18° (xOz) and 0.58° (yOz); S2: 0.94°(xOz) and 1.2° (yOz)). The spiraling behavior was reproducible and stable on shot to shot. It is important to notice that the initial conditions leading to fusion or spiraling were very close to each other and the relative orientation between the two input beams was extremely critical. Few microns of translation of one of the two beams led to fusion between the solitons. Like previously, the collision symmetry was, in each case (spiraling and scattering), not conserved.

Finally, we note that presented data concerning the modification of the soliton trajectories have been extracted from far-field recordings. These recordings confirm that beyond the change in output position of the two self-trapped beams, there were an actual change in propagation direction.

4. Influence of several experimental parameters: Intensity, phase mismatch and polarization imbalance

In a first step, we investigated the influence of the total input intensity on the collision. The input conditions (transverse positions and orientations of the two beams) were close to the previous situation. The relative phase was adjusted so as a repulsive interaction between the solitons was established. A simultaneous and equal increase of the input intensities of the two beams did not modify the nature of the interaction, which remained repulsive. Nevertheless, the deflection angles of the solitons were reduced in both planes. A similar dependence of the interaction strength on the total intensity of the beams has been numerically observed by G. Leo and G. Assanto [8] for the case of a 2D collision. They showed that the increase of input intensity led to a self confinement of each soliton and a modification of the fusion position in the non linear crystal. The case of repulsive or attractive 3D collision has not been dealt with.

In a second step, we studied the behavior of the interaction when an intensity imbalance is introduced between the (e) and (o) components of each input fundamental beam. The total intensity, the direction and the position of each incident beam were unchanged. We recorded the positions of the two solitary waves on the output face of the crystal versus the polarization imbalance ($\delta 1 = -\delta 2$), which is defined by $\delta = (Ie-Io)/(Ie+Io)$, Ie and Io being the intensity of the ordinary and extraordinary components in each incident fundamental frequency beam. We observed a continuous change of the positions of the two solitons in both planes. It was possible to change the nature of the interaction and to see the transition between repulsion and attraction. A similar behavior has previously been numerically predicted by G. Leo et al. in 1997 [7] in a bulk crystal for the case of a 2D collision. Finally, by modifying the overall phase mismatch we observed a transition between repulsive and attractive regimes.

5. Conclusion

We have experimentally investigated 3D interactions between two quadratic solitons generated by a type II SHG in KTP crystal. We showed that the nature of the collision can be attractive or repulsive according to the phase difference between the input fundamental beams. We determined the initial conditions, leading to fusion or spiralling of the solitons in the case of an attractive regime. The amplitude of spatial switching was measured in each case. We observed the non-conservation of the input symmetry in all experiments due to the presence of spatial walk off. The impact of soliton intensity, polarization imbalance and total phase mismatch was also investigated.

References
[1] W. Torruellas, Z.Wang. D.J. Hagan. E. W. Van Stryland, G.I. Stegeman, L. Torner. C. R. Menyuk. "Observation of two-dimensional Spatial Solitary Waves in a Quadratic Medium", Phys. Rev. Lett. 74, 5036 (1995).
[2] B. Costantini, C. De Angelis, A. Barthelemy, B. Bourliaguet and V. Kermene: "Collisions between type II two-dimensional quadratic solitons",Opt. Lett., 23, n°6, 424, 1998.
[3] E. Lopez-Lago, C. Simos, V. Couderc, A. Barthelemy, "Experiments on quadratic spatial soliton generation and steering in non-collinear geometry", Opt. Lett., 26, 805-807, (2001).
[4] G. Kälbermann, "Soliton interacting as a particle", Phys. Lett. A, 252 37-42, (1999).
[5] V.V. Steblina, Yu. S. Kivshar, A.V. Buryak: "Scattering and spiraling of solitons in a bulk quadratic medium", Opt. Lett. 23, 3 ,156-158 (1998).
[6] A.V. Buryak, V.V. Steblina,"Soliton collision in bulk quadratic media: Comprehensive analytical and numerical study"; J. Opt. Soc. Am. B. 16, 2 (1999).
[7] G. Leo, G. Assanto, W. E. Torruellas, "Intensity-controlled interactions between vectorial spatial solitary waves in a quadratic nonlinear media", Opt. Lett. 22, 1 ,7-9 (1997).
[8] G. Leo, G. Assanto, "Collisional interactions of vectorial spatial solitary waves in type II frequency-doubling media", J. Opt. Soc. Am. B. 14, 11 (1997).

Collisions of (2+1)D Dipole-mode vector solitons in an anisotropic nonlinear medium

Carsten Weilnau, and Cornelia Denz

Institute of Applied Physics, Westfälische Wilhelms-Universität Münster,
Correnstr. 2/4, D-48149 Münster, Germany
FAX:+49 251 83 33513, e-mail:weilnau@uni-muenster.de

Marcus Ahles, Kristian Motzek, and Friedemann Kaiser

Institute of Applied Physics, Darmstadt Technical University,
Hochschulstr. 6, D-64289 Darmstadt, Germany

Wieslaw Królikowski, and Glen McCarthy

Laser Physics Centre, Research School of Physical Sciences and Engineering, The
Australian National University, Canberra, ACT 0200, Australia

Abstract: We investigate the specific influence of anisotropy on generation, stability and dynamic properties of spatial dipole-mode vector solitons in a photorefractive medium, experimentally and numerically. Further, we demonstrate collision-induced transformation of transverse to angular momentum.

1 Introduction

The theoretical prediction and experimental observation of the dipole-mode vector soliton (DMVS) in a saturable nonlinear medium [1, 2] has stimulated further investigations in the field of self-focusing of multi-component optical beams. Vector- or multi-component solitary waves consist of mutually incoherent optical beams of different geometries that jointly induce a multi-mode waveguide structure in which they propagate self-consistently as eigenmodes.

Among various possible configurations of beams with different geometries it is particularly the dipole-mode vector soliton that displays a surprising robustness. It consists of a bell-shaped Gaussian beam and a double-humped beam with a π-phase shift across its transverse plane. It has been predicted on the basis of a model for an isotropic saturable nonlinearity [3]. However, the experimental investigations were carried out with a DC electric field-biased photorefractive Strontium Barium Niobate (SBN) crystal that exhibits an anisotropic and non-local refractive index modulation [1, 2]. This anisotropy is of crucial importance for the generation of optical spatial solitons since it breaks the symmetry of the system. As a consequence, all self-trapped optical beams exhibit no circular symmetric shape but an elliptical one in this particular medium. Recent investigations [4, 5] have revealed that even in case of the anisotropic photorefractive model [6] DMVS can exist. Whereas in the isotropic model stable solutions exist for any arbitrary orientation of the dipole-mode beam, the anisotropic model allows only one specific kind of DMVS to be stable. This class of solutions is characterized by the orientation of the dipole-mode beam. In order to be stable the dipole axis has to point in the vertical direction, perpendicular to the applied electric field. A second class of solutions exists with the dipole axis pointing in the direction parallel to the electric field, but this was already shown to be of quasi-stationary type [4].

2 Dipole-mode vector solitons displaying angular momentum

Here, we investigate the dynamics of the DMVS in a more general way. With the help of the split-step Fourier method we solve the appropriate equations [5, 6] numerically and demonstrate the evolution of the DMVS during propagation through the nonlinear material. When the dipole beam is launched at a certain angle with respect to the vector soliton's *stable* orientation, it starts to wobble around the vertical axis. Here we give an experimental proof of this behaviour by recording the exit face of the the photorefractive crystal while changing the dipole beam's initial orientation. Figure 1 illustrates the result of our experimental investigations, a sketch and detailed description of the setup can be seen elsewhere [1]. The top row depicts the input intensity distribution of the dipole component and the bottom row displays its corresponding intensity distribution after propagating simultaneously for 20 mm with a mutually incoherent Gaussian beam in the biased photorefractive crystal. As depicted in the frames (a)-(h) we successively rotate the
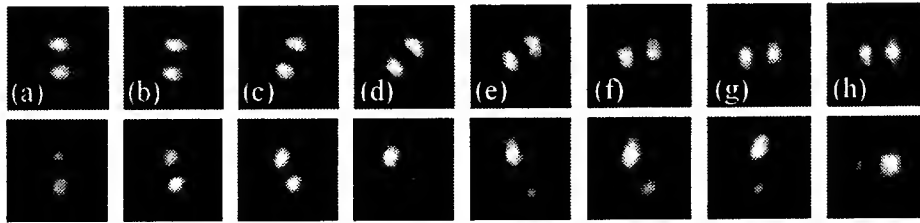
Fig. 1. Experimental results of the propagation (bottom row) of a DMVS for different initial orientations (top row). Frames (a)-(h) illustrate the scenarios for different input angles of the dipole-component. In all cases, the Gaussian component is present but not shown here.

axis of the dipole clockwise at the input face of the crystal. When the crystal is not biased, its nonlinear effect almost vanishes, the two lobes diffract linearly, and no change in the dipole's orientation is detectable. In the nonlinear regime, when the external voltage is turned on (bottom row), the dipole beam becomes the constituent of a DMVS and rotates towards it's stable orientation along the vertical axis. The induced *'angular momentum'* is so large that the dipole lobes even overshoot their stable vertical orientation while propagating and end up in a counterclockwise orientation at the exit face of the crystal. The effect becomes most distinct in Fig. 1(d) where the angle of rotation can be determined to almost 90°. As the dipole is turned further, the two lobes of the dipole align along the stable vertical axis which was referred to as a global minimum in [4]. In Fig. 1(h) finally, the two lobes are exactly horizontally aligned and represent a class of quasi-stationary solitary solutions. Nevertheless this state is unstable with respect to small perturbations, as can be seen from Fig. 1(g) where the initial orientation is tilted by an angle smaller than 2° (upper row). The dipole clearly rotates and ends up in its prefered vertical position (bottom row). Our experimental pictures underline clearly our numerical results. We would like to emphasize here, that this rotation occurs solely due to the anisotropic properties of the photorefractive nonlinearity. The two dipole lobes are π-out-of-phase and possess no initial *'transverse angular momentum'* that could stem from a screw-like phase distribution like the recently observed *'propeller soliton'* [7]. The wobbling motion is somehow characteristic for soliton interaction in anisotropic medium and has been observed earlier for the case of a multi-humped optical beam derived from the decay of an optical vortex [8].

3   Vector soliton collisions

The outstanding robustness of the DMVS motivates further investigations towards soliton collisions. In fact we will show that a DMVS even remains self-trapped when interacting strongly with a mutually coherent Gaussian beam. Since the composed light-structure remains in its entity it could be referred to as a *molecule of light*, a composite state of two simple beams, atoms of light. Again, we investigate this interaction numerically and experimentally. A typical experimental behavior is illustrated in Fig. 2. The frames (a)-(c) show
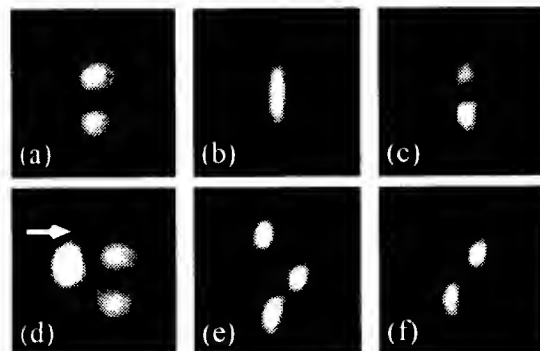
Fig. 2. A Gaussian beam colliding non-centro symmetrically with a dipole-mode vector soliton, that starts to rotate in the transverse plane. Top row: formation of a dipole-mode vector soliton, bottom row: interaction with Gaussian beam.(a),(d): input profiles; (b),(e): output profiles after 10 mm of propagation when all beams are present, and the contribution of the dipole-mode to the total intensity (c),(f).

the formation process of an ordinary dipole-mode vector soliton. The incident dipole structure is shown in Fig. 2(a), and the total intensity distribution after 10 mm of simultaneous propagation of both, the stabilizing Gaussian and the dipole-mode beam forming the DMVS is given in Fig. 2(b). Fig. 2(c) depicts the

contribution of the dipole component to the total light intensity given in (b). Comparing Figs. 2(a) and (c) it is obvious that the dipole beam does not spread in the vertical direction but remains trapped in the presence of the Gaussian beam. The dipole and the Gaussian component have a total power of $1.5\mu W$ and $0.9\mu W$ respectively. In a second step, in Fig. 2(d) we have an additional Gaussian beam of $1.6\mu W$ incident on the crystal's front face while keeping all other parameters constant. This beam is coherent to the dipole beam and in the linear regime (when the voltage is turned off) its trajectory points towards the upper dipole lobe at a very small angle ($< 1°$) as indicated by the arrow. The third, mutually incoherent stabilizing Gaussian component with a total power of $0.9\mu W$ that traps the dipole is not shown here. When the external electric field is raised to $V = 2.6kV/cm$, the DMVS forms as in the upper row, but the relatively intense additional beam forms a solitary light structure as well and collides non-centrosymmetrically with the dipole component. This collision causes the DMVS to rotate clockwise. Fig. 2(e) depicts the total light intensity at the exit face of the crystal. The uppermost peak is the scalar soliton that induces a rotational transverse motion on the dipole-mode vector soliton shown in the bottom section of Fig. 2(e). The dipole component of the DMVS is resolved in Fig. 2(f). Comparing Figs. 2(f) and (c) one can easily detect a rotation angle of 30°. The Gaussian component that traps the dipole beam in order to prevent a separation of the two lobes is not shown here but a remarkable change in its orientation as also clearly visible, as it always adapts to the shape and orientation of the dipole mode beam. Our experimental results are confirmed with corresponding numerical simulations based on the anisotropic model.

We were able to demonstrate that a linear momentum of a scalar soliton can be transfered into angular momentum of a vector soliton through an inelastic collision process. Since our experimental system and the theoretical model are inherently anisotropic we do not expect that the dipole-mode soliton continues to rotate in a clockwise direction when propagating further in the nonlinear material. According to numerical simulations for much larger propagation distances we reveal that the dipole component merely propagates in its typical twisting motion through the crystal [8]. As already mentioned above, dipole-mode solitons can exist for every abitrary orientation in an isotropic medium and therefore a collision with a scalar soliton can induce much larger rotation angles that exceed even 90°. Since a horizontal orientation of the dipole lobes is unstable in our anisotropic system the illustrated rotation angle of 30° is a clear evidence of the momentum transfer process taking place in the crystal.

4 Conclusion

In conclusion, we demonstrate rotational effects of dipole-mode vector solitons in an anisotropic medium that exhibits a non-local and self-focusing nonlinearity. We give an experimental evidence that these specific solitons are only stable when the dipole axis points in the direction perpendicular to the externally applied electric field. Deviations from this orientation lead to a rotational and twisting motion of these robust type of vector soliton. Further on we show that this kind of motion can also be induced by a non-centrosymmetrical collision with a scalar soliton. This new phenomenon in the field of (2+1)-dimensional spatial optical solitons underlines the particle character of self-trapped light structures that may now be interpreted as 'molecules of light'.

References

1. W. Królikowski, E. A. Ostrovskaya, C. Weilnau, M. Geisser, G. McCarthy, Yu. S. Kivshar, C. Denz, and B. Luther-Davies, "Observation of Dipole-Mode Vector Solitons," Phys. Rev. Lett. **84**, 1424-1427 (2000).
2. T. Carmon, Ch. Anastassiou, S. Lan, D. Kip, Z. H. Musslimani, and M. Segev, "Observation of two-dimensional multimode solitons" Opt. Lett. **25**, 1113-1115 (2000).
3. J. J. García-Ripoll, V. Pérez-García, E. A. Ostrovskaya, and Yu. S. Kivshar, "Dipole-Mode Vector Solitons," Phys. Rev. Lett. **85**, 82-85 (2000).
4. D. Neshev, G. McCarthy, W. Królikowski, E. A. Ostrovskaya, Yu. S. Kivshar, G. Fernandez Calvo, and F. Agullo-Lopez, "Dipole-mode vector solitons in anisotropic nonlocal self-focusing media," Opt. Lett. **26**, 1185-1187 (2001).
5. K. Motzek, A. Stepken, F. Kaiser, M. R. Belic, M. Ahles, C. Weilnau, and C. Denz, "Dipole-mode vector solitons in anisotropic photorefractic media," Opt. Comm. **197**, 161-167 (2001).
6. A. A. Zozulya, and D. Z. Anderson, "Propagation of an optical beam in a photorefractive medium in the presence of a photogalvanic nonlinearity or externally applied electric field," Phys. Rev. A **51**, 1520-1531 (1995).
7. T. Carmon, R. Uzdin, C. Pigier, Z. H. Musslimani, M. Segev, and A. Nepomnyashchy, "Rotating Propeller Solitons," Phys. Rev. Lett. **87**, 143901 (2001).
8. C. Weilnau, C. Denz, M. Ahles, A. Stepken, K. Motzek, and F. Kaiser, "Generation of higher-order (2+1)-dimensional spatial vector solitons in a nonlinear anisotropic medium," Phys. Rev. E **64**, 056601 (2001).

Multicomponent vector solitons: theory and experiment

Glen McCarthy, Wieslaw Krolikowski and Barry Luther-Davies
Laser Physics Centre. Research School of Physical Sciences and Engineering
Australian National University Canberra ACT 0200, Australia
Phone: +61-2-6125-3752 Fax: +61-2-6125-0029
Email: wzk111@rsphysse.anu.edu.au

Anton Desyatnikov and Yuri S. Kivshar
Nonlinear Physics Group, Research School of Physical Sciences and Engineering.
Australian National University, Canberra ACT 0200, Australia

Kristian Motzek and Friedemann Kaiser,
Institute of Applied Physics, Darmstadt University of Technology,
D-64285 Darmstadt, Germany

Carsten Weilnau and Cornelia Denz
Institute of Applied Physics, Westfalische Wilhelms-Universitat Muenster,
D-48149 Muenster, Germany

Abstract: We study, theoretically and experimentally, multicomponent spatial solitons in nonlinear saturable (isotropic and anisotropic photorefractive) bulk media. We find numerically a family of the three-component dipole-mode solitons and demonstrate their stability in a wide range of the input parameters. We also observe the formation and stability of these spatial solitons in experiment with photorefractive strontium barium niobate (SBN) crystals.

Introduction. Recent progress in the study of spatial optical solitons and their interaction, as well as the extensive experimental demonstrations of stable self-focusing of light in different types of nonlinear bulk media, has opened a road for the development of novel concepts for controlling optical beam diffraction and designing new all-optical devices for light switching, routing, and storage [1]. Many novel fundamental concepts in the physics of spatial optical solitons suggested recently are associated with the vectorial beam interaction and multicomponent optical beams that mutually self-trap in a nonlinear medium [2]. Such *composite multimode solitons* can have a complex structure and, in many cases, their total intensity profile exhibits multiple humps [2-4].

In a bulk medium, vector solitons exist in different forms and, as was recently shown for two-component self-trapped beams, many types of multipole vector solitons can be predicted and analyzed for an isotropic and anisotropic media with saturable nonlinearity [5]. Recently, an important generalization of this concept to the case of N-component two-dimensional vector solitons was suggested for an example of threshold nonlinearity [4]. In particular, Musslimani *et al.* [4] predicted the existence of multihump composite solitons that carry different topological charges (spins) and, therefore, can provide exciting possibilities for spin-dependent interaction of self-trapped optical beams. More recently, based on the concept of the dipole-mode solitons [6], we have described theoretically novel types of composite solitons consisting of dipole components [7].

Here, we study the formation and stability of several types of multicomponent spatial solitons. First, we show that spatial solitons carrying a nonzero total angular momentum described in Ref. [4] experience a symmetry-breaking instability. Then, following Ref. [7], we describe stable multicomponent solitons consisting of two orthogonal dipole components. We find the families of these solitons in the case of isotropic and anisotropic media and show their stability in a wide range of the parameter space.

Isotropic nonlinearity. First, we consider the propagation of N mutually temporally incoherent optical beams with the slowly varying amplitudes $E_j(x,y,z)$ (j=1,2,3...) in an isotropic saturable nonlinear medium, described by the normalized equations:

$$i\frac{\partial E_j}{\partial z} + \Delta_\perp E_j - \frac{E_j}{1 + \sum |E_j|^2} = 0$$

where $\sum|E_j|^2$ is the total light intensity. To describe multicomponent vector solitons, we will look for stationary solutions in the form $E_j(x,y,z)=u_j(x,y)\exp(-i\lambda_j z)$, where λ_j is the propagation constant of the j-th component, and $u_j(x,y)$ is its normalized envelope. First, following Ref. 4, we study multi-component *radially symmetric* solutions of Eq.(1) for which the fundamental (j=1) component has no nodes but other components carry different topological charges. We find numerically the whole family of these solitons and study their stability numerically. It appears that, provided that the total angular momentum is nonzero, all such multicomponent vortex-like solitons undergo a symmetry breaking instability and fragment into a number of fundamental solitons. This instability is similar to the instability of a two-component vortex-mode soliton which, after break-up, forms a dipole-mode vector soliton [6].
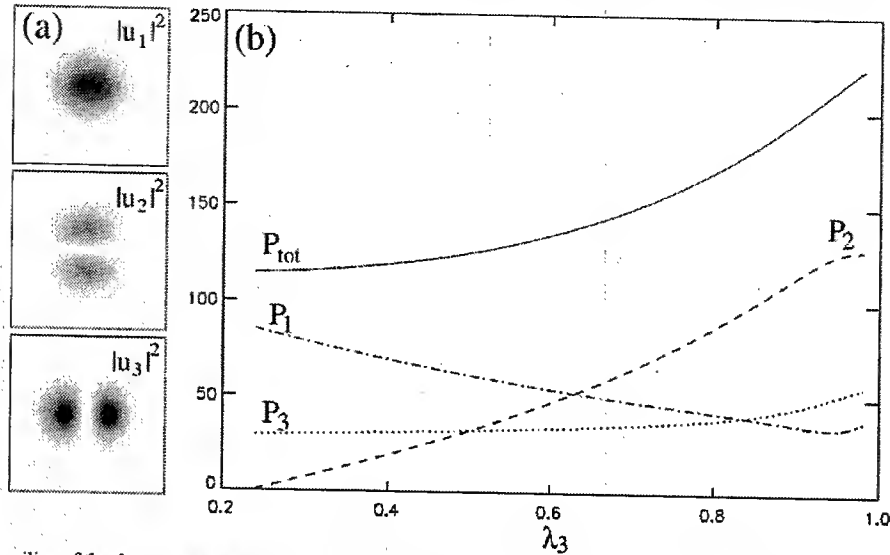
Fig. 1. Families of the three-component dipole-mode solitons in an isotropic medium. (a) an example of the soliton solution; (b) total and partial powers vs λ_3 at fixed $\lambda_1=1$ and $\lambda_2=0.5$.

On the contrary, we find that all radially symmetric solitons with *zero total angular momentum* are more robust and propagate over the distance of thousands diffraction lengths. However, being initially perturbed a (three-component) soliton displays instability for which the fundamental beam retains its ring-like structure but two vortex components (of the opposite charges) transform into a structure resembling two perpendicular dipoles. Although a composite soliton consisting of two orthogonal dipoles was shown to be unstable [8], it appears that the presence of the fundamental (nodeless) component can stabilize the structure. Indeed, this has been confirmed by our numerical simulations. The stabilization effect can be explained by the physics of the soliton-induced waveguides, since two crossed dipoles represent vectorial guided modes of a light induced waveguide. Using a relaxation technique, we were able to find the whole families of the three-component vector solitons consisting of a fundamental beam and two crossed dipoles. An example of this solution is shown in Fig. 1(a). The soliton family ranges from the solutions dominated by the fundamental mode to the solutions in which one mode dominates [see Fig. 1(b)].

Numerical propagation of these solitons revealed that they are stable over a wide range of their parameters. In particular, the solutions shown in Fig. 1(b) are stable for $\lambda_3 <0.7$ and unstable otherwise. A typical instability scenario involves breakup of the soliton into a fundamental soliton and the so-called *propeller soliton*, i.e., rotating dipole-mode vector soliton. We expect that the vibrational degrees of freedom of the composite soliton, which are usually associated with long-lived soliton internal modes, should manifest themselves in the rich dynamics of soliton collisions, as is known from the study of a two-component model.

Photorefractive nonlinearity. The theoretical analysis of the three-component solitons presented above is restricted to an isotropic model of nonlinear media. On the other hand, the photorefractive crystals which are frequently used to demonstrate the formation of various types of spatial solitons, exhibit strong anisotropy in their nonlinear response. This anisotropy has been shown to significantly affect properties of the solitons and their interaction [5]. To study the formation of the three-component solitons in photorefractive nonlinearity, we consider the Zozulya-Anderson model [9] which takes into account the most important properties of photorefractive nonlinearity and, in particular, its anisotropic nature. By solving the corresponding stationary propagation and material equations we

found classes of three-component localized solitons with two perpendicularly oriented dipoles and a co-propagating nodeless component. Our simulations show that these solitons are stable in a wide range of the soliton parameters. An example of such soliton is shown in Fig. 2(a). Because of the anisotropic nature of the PR medium nonlinearity, the stable stationary modes exist in such a geometry that their dipole components are oriented in two fixed directions - along and perpendicular to the biasing DC field.

Experimental results. We study the formation of three-component dipole-mode solitons experimentally using a SBN photorefractive crystal and an experimental setup similar to those described in Ref. 5. Two mutually incoherent light beams (wavelength of 532nm) derived from the Nd:YAG laser were transmitted through microscope glass slides to imprint desired π phase jumps across the beams. In this way two perpendicularly oriented dipole components were created. They were superimposed and combined with the Gaussian beam and subsequently focused onto the input facet of the 10 mm-long SBN crystal. The outgoing light intensity distribution was monitored by a CCD camera. In Fig. 2(b) we show an example of the experimentally generated three-component soliton. The initial powers in the fundamental, and both dipole beams were 2 mW, 2.2 mW and 1.8 mW, respectively. Top row of this figure shows the initial intensity distribution of the constituent components while the bottom row shows the intensities of each component after 10 mm of propagation through a biased photorefractive crystal. It can be clearly seen that the light beams self-trap and they form a stable vector soliton. The parameters of this experimentally observed soliton are very close to the numerical example shown in Fig. 2(a).
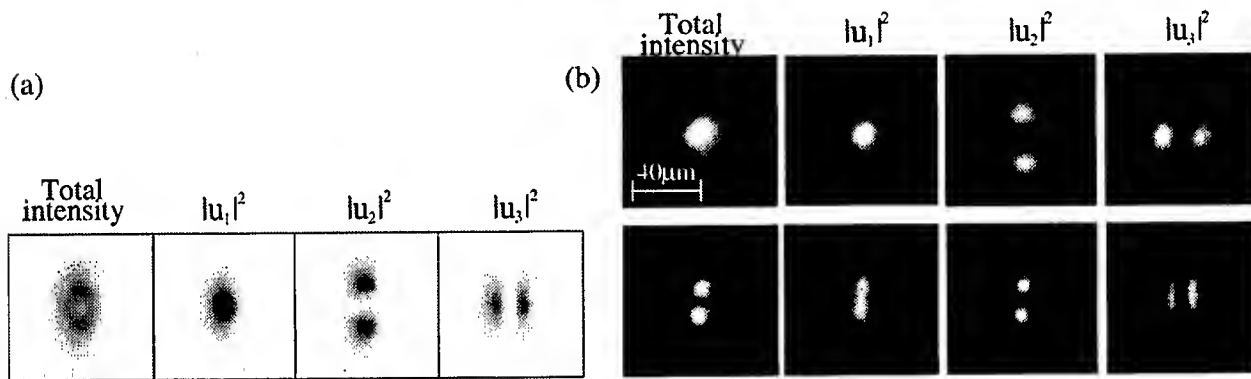
Fig. 2. Three-component spatial vector soliton in a photorefractive nonlinear medium. (a) numerically found soliton solution; (b) experimentally observed multicomponent soliton: top row – initial intensity distribution; bottom row-intensity after 10 mm of propagation in biased photorefractive SBN crystal.

Conclusions. We have shown that a self-focusing nonlinear medium supports novel types of composite spatial solitons. In the case of three components, such solitons consist of a fundamental and two orthogonal dipole components corresponding to the modes of a self-induced waveguide. The solitons are found to be stable in a wide range of their parameters. We have observed the formation of these novel solitons in experiment with photorefractive SBN crystal, with a good agreement with the theoretical predictions.

References:

1. S. Trillo and W. Toruellas, eds. *Spatial Solitons* (Springer-Verlag. Berlin, 2001).
2. Mitchell, M. Segev, and D.N. Christodoulides, "Observation of multihump multimode solitons", Phys. Rev. Lett. **80**, 4657-4560 (1998).
3. E. Ostrovskaya, Y.S. Kivshar, D. Skryabin, and W.J. Firth,. "Stability of multihump optical solitons", Phys. Rev. Lett. **83**, 296- 299 (1999).
4. Z. H. Musslimani, M. Segev, D. N. Christodoulides, and M. Soljacic, "Composite multihump vector solitons carrying topological charge", Phys. Rev. Lett. **84**, 1164-1167 (2000).
5. A. Desyatnikov et al, "Multipole composite spatial solitons: theory and experiment", J. Opt. Soc. Am. B **13**, 876-877 (2002).
6. W. Krolikowski, E. A. Ostrovskaya, C. Weilnau, M. Geisser, G. McCarthy, Y. S. Kivshar, C. Denz and B. Luther-Davies, ``Observation of dipole-mode vector solitons, "Phys. Rev. Lett. **85**, 1424-1427 (2000).
7. A. S. Desyatnikov, Y. S. Kivshar, K. Motzek, F. Kaiser, C. Weilnau, C. Denz, "Multicomponent dipole-mode vector solitons", Opt. Lett. **27**, 634-636 (2002).
8. A.S. Desyatnikov and Y..S. Kivshar, "Rotating optical soliton clusters", Phys. Rev. Lett, **88**, 053901-053904 (2002).
9. A. Zozulya and D.Z. Anderson, "Propagation of an optical beam in a photorefractive medium in the presence of a photogalvanic nonlinearity or an externally applied electric field", Phys. Rev. A **51**, 1520-1531 (1995).

Propagation of Spatially and Temporally Incoherent Light and Modulation Instability in Non-instantaneous Nonlinear Media

Hrvoje Buljan

Department of Physics, Faculty of Science, University of Zagreb, PP 332, 10000
Zagreb, Croatia
++385 1 460 5650, ++385 1 4680 336, hbuljan@phy.hr

Antonio Šiber

Institute of physics, Bijenička c. 46, 10000 Zagreb, Croatia
++ 385 1 469 8888, ++ 385 1 469 8889, asiber@ifs.hr

Marin Soljačić

Physics Department, Massachusetts Institute of Technology, Cambridge, MA
++1 617 253 2467, ++1 617 253 2562, soljacic@mit.edu

Mordechai Segev

Physics Department, Technion - Israel Institute of Technology, Haifa 32000, Israel
++972 4 829 3926, ++972 4 823 5107, msegev@techunix.technion.ac.il

Abstract: We present a theory describing propagation of spatially and temporally incoherent light in non-instantaneous nonlinear media, and demonstrate the existence of modulation instability of "white" light. We find that modulation instability of "white" light is fundamentally a collective effect, where all the temporal frequencies participate in the formation of a pattern, and self-adjust their respective contributions.

OCIS codes: (190.0190) Nonlinear optics; (030.0030) Coherence and statistical optics

Propagation of Spatially and Temporally Incoherent Light and Modulation Instability in Non-instantaneous Nonlinear Media

Hrvoje Buljan, Antonio Šiber, Marin Soljačić, and Mordechai Segev

Several years ago, Mitchell *et al.* [1] have experimentally demonstrated the existence of partially spatially incoherent solitons in non-instantaneous nonlinear medium. Subsequently, solitons made of light emitted from an incandescent bulb, i.e., solitons made of both spatially and temporally incoherent light were demonstrated by Mitchell and Segev [2]. These experimental results have started the avalanche of experimental and theoretical studies of incoherent light propagation, modulation instability, and the formation of solitons.

Several theories formulating the propagation of incoherent light in non-instantaneous nonlinear media have been proposed [3]. Three most accurate and formally equivalent theories: the coherent density function theory [4], the modal theory [5], and the mutual coherence function theory [6] have been developed. One of the key assumptions that was made in deriving these theories is that the light is quasi-monochromatic. Therefore, these theories are not capable of describing the experimental demonstration of "white" light solitons reported in Ref. [2]. Here we present a theory suitable for the description of "white" light self-trapping [2], and use it to predict the modulation instability of "white" light in non-instantaneous nonlinear medium, thereby extracting its most interesting features.

To develop the a theory, we make the following assumptions/approximations: (i) The light propagates in the dispersionless nonlinear medium that responds only to the time-averaged intensity I; the index of refraction is $n(I)^2 = n_0^2 + 2n_0\delta n(I)$. (ii) We study the propagation of light (in the z direction) in a temporal steady state, $\partial \delta n(I)/\partial t = 0$. (iii) The relative increment of the nonlinear change in the refractive index is small over a few wavelengths λ_0, leading to $\nabla(\nabla \cdot \mathbf{E}) \simeq 0$; λ_0 denotes the central wavelength within the power spectrum. (iv) The light is linearly polarized, and propagates paraxially along the z direction; the electric field is written as

$$\tilde{E}(x,y,z,t) = \frac{1}{2\pi}\int_0^\infty d\omega E_\omega(x,y,z)e^{ik_\omega z - i\omega t} \tag{1}$$

where $k_\omega = n_0\omega/c$, and approximately $|\partial^2 E_\omega/\partial z^2| \ll |k_\omega \partial E_\omega/\partial z|$. (v) The time response of the material $\tau_m \gg \omega_0^{-1}$, where ω_0 denotes the central frequency within the power spectrum.

The statistical properties of the light can be described by the mutual spectral density $B_\omega(\mathbf{r}_1,\mathbf{r}_2,z)$, evaluated at two points ($\mathbf{r}_a = x_a\,\mathbf{i} + y_a\,\mathbf{j}$, $a = 1,2$) from the same cross-section of the beam. Under the assumptions/approximations above, $B_\omega(\mathbf{r}_1,\mathbf{r}_2,z)$ is shown to evolve according to

$$\frac{\partial B_\omega}{\partial z} - \frac{i}{2k_\omega}[\nabla_{\perp1}^2 - \nabla_{\perp2}^2]B_\omega = \frac{ik_\omega}{n_0}\{\delta n(I(\mathbf{r}_1,z)) - \delta n(I(\mathbf{r}_2,z))\}B_\omega(\mathbf{r}_1,\mathbf{r}_2,z). \tag{2}$$

Equation (2) is an integro-differential equation since the time-averaged intensity is $I(\mathbf{r},z) = 1/2\pi \int_0^\infty d\omega B_\omega(\mathbf{r},\mathbf{r},z)$.

This theory is utilized to analytically describe MI of "white" light, and analyze its features in dependence of the statistical properties of the beam. We study one-dimensional system; the mutual spectral density of the uniform beam $B_\omega^{(0)}(\rho)$ is for each frequency ω a real-valued, bell-like shaped function of the coordinate $\rho = x_1 - x_2$ (e.g. Gaussian). The half width at half maximum of $B_\omega^{(0)}(\rho)$ is the spatial correlation distance for frequency ω: $l_s(\omega)$. The functional dependence $l_s(\omega)$ is modeled by $l_s(\omega) = 2\pi/K_0(\omega)$, where $K_0(\omega) = K_0[1 + s(\omega - \omega_0)/\omega_0]$; the parameter s determines whether $l_s(\omega)$ increases or decreases with ω.

Summary of the most interesting results is as follows: (i) We first recover the most important result from the temporally coherent MI analysis [7, 8]. For white light MI to occur, the nonlinearity must exceed a threshold imposed by the degree of spatial incoherence. The threshold increases with the decrease of the spatial correlation distance.
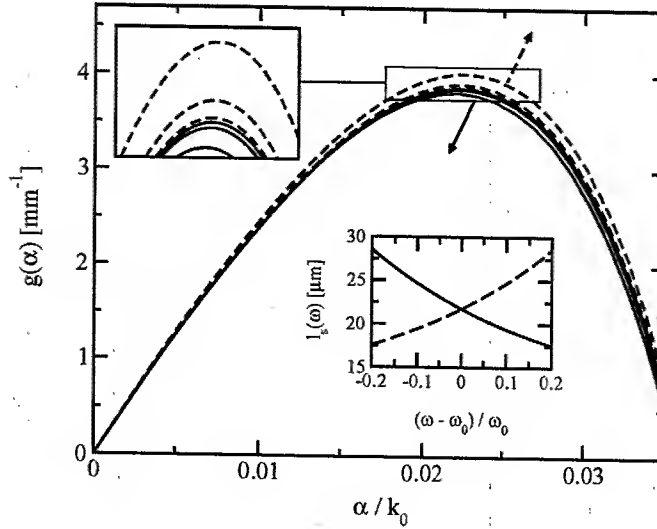
Fig. 1. The nonlinear gain coefficient g as a function of spatial wavenumber α. The plots correspond to widths of the power spectrum $\Delta\omega/\omega_0 = 2\%$, 5%, and 10%; The arrows indicate the increase of $\Delta\omega$. The lower insert shows the spatial correlation distance $l_s(\omega)$; the solid (dashed) curves correspond to $s = 1.2$ ($s = -1.2$), respectively.

(ii) Spectral density directly affects the stability of the beam, and can stabilize or destabilize the beam depending on the functional dependence of the spatial correlation distance on the temporal frequencies. This is significantly different from all previous studies of incoherent MI [7, 8], where the spectrum of the light had no effect on the MI process. In order to show this, small perturbations at the incident plane of the crystal are described as a superposition of modes. The modes are sinusoidal spatial modulations of transverse wavenumber α. The instability of a modulation is described by a gain coefficient $g(\alpha)$; the mode (and hence the whole beam) is unstable if Re $g(\alpha) > 0$. Figure 1 shows the gain coefficient $g(\alpha)$ as a function of transverse wavenumber α for $B_\omega^{(0)}(\rho)$ chosen to be a Gaussian in both ω and ρ variable, for three different spectral widths: $\Delta\omega/\omega_0 = 2\%$, 5%, and 10%, and for two different types of $l_s(\omega)$ dependencies. The insert in Fig. 1 shows the dependence of the spatial correlation distance l_s on the (temporal) frequency ω. For $s = 1.2$ ($s = -1.2$), l_s decreases (increases) with increasing spectral width, and the maximal gain g_{max} decreases (increases) with the increase of $\Delta\omega$. We find (numerically) that there exists a critical value $s_{crit} > 0$, such that for $s > s_{crit}$ ($s < s_{crit}$), the beam is stabilized (destabilized) by the increase of its spectral width $\Delta\omega$. Thus, the spectral width directly affects the MI threshold, although the influence of the temporal incoherence of the beam on the (in)stability is not as critical as the influence of the spatial incoherence.

(iii) From the studies on incoherent MI in temporally-coherent systems, we know that each temporal frequency has its own maximally destabilizing perturbation[7, 8]. But simply projecting this result to temporally and spatially incoherent MI may erroneously lead to the thought that in the linearized (low-visibility) regime, each frequency constituent of the beam would create its own pattern, with periodicity corresponding to its own maximally destabilizing spatial modulation. But the physical reality is different: MI in temporally and spatially incoherent wave systems is a fundamentally fully collective effect: *all* frequencies participate in *all* spatial modulations, thereby determining the growth rate $g(\alpha)$ corresponding to each spatial modulation α. Consequently, they collectively determine the perturbation with the highest gain, $g(\alpha_{max})$, and collectively participate in this perturbation, which prevails when z becomes sufficiently larger than $g(\alpha_{max})^{-1}$. Physically, this occurs because the propagation of all temporal frequency constituents of the light is entangled by the unique index of refraction "seen" by all of them. Mathematically, this follows from the integro-differential character of the evolution equation (2).

(iv) Closely connected to previous result, we point out another intriguing effect of white light MI: since different temporal frequencies tend to be modulated at different spatial periodic perturbations, the spectral
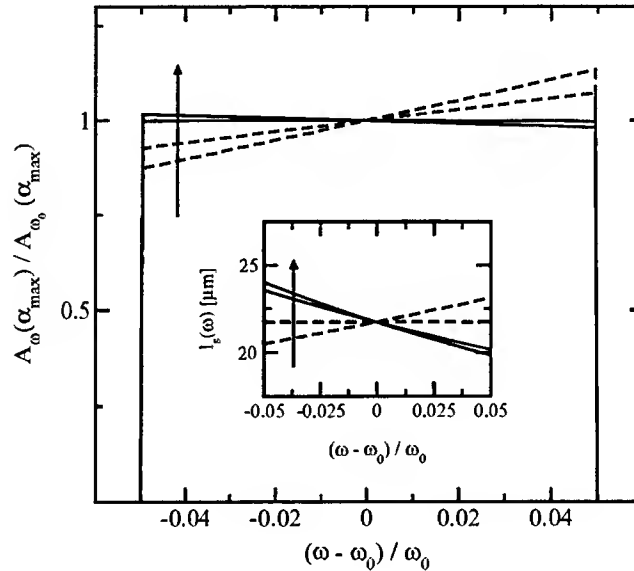
Fig. 2. Relative spectral density $A_\omega(\alpha_{max})/A_{\omega_0}(\alpha_{max})$ evaluated at the spatial wavenumber of highest gain, α_{max}. Different graphs correspond to different dependencies of the spatial correlation distance l_s on the frequency ω, shown in the insert. The parameter s that defines $l_s(\omega)$ is $s = -1.2$, 0.0, 1.55, and 1.9 (bottom to top).

density of a particular spatial modulation is *not* a simple replica of the spectral density of the incident beam, but is determined also by the dependence of the spatial correlation distance on the temporal frequency. To demonstrate this feature, consider a beam with spectral density constant in the frequency interval $[\omega_0 - \Delta\omega/2, \omega_0 + \Delta\omega/2]$, and zero otherwise. The width of the spectrum is $\frac{\Delta\omega}{\omega} = 10\%$. Fig. 2, displays the relative spectral density [call it $A_\omega(\alpha_{max})/A_{\omega_0}(\alpha_{max})$] corresponding to the maximally destabilizing spatial modulation α_{max}. Different plots correspond to different dependencies $l_s(\omega)$ (see the insert in Fig. 2). To summarize this important result, we find that the spectral density of any periodic perturbation adjusts itself in such a way that it is commensurate with the periodicity.

In summary, we have formulated the theory governing the propagation of spatially and temporally incoherent light in a non-instantaneous nonlinear media, predicted the existence of modulation instability of such a beam, and extracted its features. We have shown that the temporal power spectrum directly affects the strength of the instability (nonlinear gain), and that the increase of its width can destabilize or stabilize the beam. We have shown that MI of such a wave packet is fundamentally a collective effect in which all the temporal frequencies together participate in determining the spatial modulation of the highest gain. Consequently, the spectral density of the perturbation adjusts itself in a true collective fashion.

References

1. M. Mitchell, Z. Chen, M. Shih, and M. Segev, Phys. Rev. Lett. **77**, 490 (1996).
2. M. Mitchell and M. Segev, Nature (London) **387**, 880 (1997).
3. M. Segev and D. N. Christodoulides, *Incoherent Solitons*, in S. Trillo and W. Torruellas Eds., *Spatial Solitons*, Springer, Berlin 2001.
4. D. N. Christodoulides, T. H. Coskun, M. Mitchell, and M. Segev, Phys. Rev. Lett. **78**, 646 (1997).
5. M. Mitchell, M. Segev, T. H. Coskun, and D. N. Christodoulides, Phys. Rev. Lett. **79**, 4990 (1997).
6. V. V. Shkunov and D. Anderson, Phys. Rev, Lett. **81**, 2683 (1998); G. A. Pasmanik, Sov. Phys. JETP. **39**, 234 (1974).
7. M. Soljačić, M. Segev, T. Coscun, D.N. Christodoulides, and A. Wishwanath, Phys. Rev. Lett. **84**, 467 (2000).
8. D. Kip, M. Soljačić, M. Segev, E. E. Eugenieva, D. N. Christodoulides, Science **290** 495 (2000).

A solitonic all-optical switch based

on the fractional Talbot effect

Stefano Minardi, Gianluca Arrighi, Paolo Di Trapani

INFM and Dipartimento di Scienze CC.FF.MM. –Università degli Studi dell'Insubria –Via Valleggio, 11 –I 22100 COMO –Italy
Tel. +39 031 238 6257 Fax. +39 031 238 6209 e-mail: sminardi@fis.unico.it

Arunas Varanavičius, Algis Piskarskas

Department of Quantum Electronics –Vilnius University –Sauletekio g . 9 –r. III –LT 2040 VILNIUS –Lithuania
Tel. +370 2 366050 Fax. +370 2 366006 e-mail: arunas.varanavicius@ff.vu.lt

Abstract: In a parametric down-conversion scheme, a weak seeding can shift a periodic array of optical beams by half of its transverse period as the result of the spatial solitons excitation and the fractional Talbot effect.
©2002 Optical Society of America

OCIS Codes: 190.4410, 190.5530, 350.3950, 230.1150

Up to date, the possibility to use more than one parametric spatial soliton to perform all-optical logical or computational tasks was investigated in systems with less than a few tens of solitons. Two-soliton collisions could be used to build phase- and intensity- dependent optical switches [1,2], while focussed vortex beams wave mixing were shown to excite regular sets of solitons whose number is determined by simple algebraic rules [3]. Recently, blurred digital images with up to 15 pixels were reconstructed by means of the soliton excitation process as well [4].

However, the possibility to exploit the features of large periodical arrays of solitons (up to several hundreds) was not yet explored. One interesting point to investigate is the propagation symmetry break-up, which is expected to occur across the transition between the soliton (high-intensity) and the linear (low intensity) propagation regimes. In fact, once excited, the solitons are supposed to propagate inside the crystal with constant diameter and parallel to each other [4,5]. On the other hand, a periodic field propagating linearly experiences exact wave-front reconstruction only at discrete periodic propagation distances, a phenomenon known as self-imaging effect or Talbot effect [6]. The self-imaging propagation period is called the Talbot length (Z_T).

By keeping in mind this idea as a guideline, we developed a new all-optical switch, which exploit the features of both the Talbot effect and the soliton propagation regime. In particular, we focussed our attention on the fractional Talbot effect [7]. In linear propagation, after one Z_T the input pattern is reconstructed exactly, while a propagation distance of $Z_T/2$ leads to the same intensity profile of the input plane but shifted by the half of the transverse period of the pattern. The basic concept of the switch is to pump a non-linear quadratic crystal with a spatially periodic pump whose $Z_T/2$ coincides with the crystal length. By suitable conditions, it is possible to excite the solitons in first few mm of propagation thus providing at the output the same periodic structure of the input [4,5]. If that soliton excitation process is quenched (e.g. by reducing the pump intensity, or by stopping the seeder beam), the linear propagation regime of the pump is restored and the output pattern will be shifted by one half of the period respect to that of the input.

An example of the device operation is given in Fig. 1, where the results of a numerical simulation of degenerate parametric amplification with a periodic pump are presented. The used model is a spatial (2D+1) one and includes only the quadratic effects. The coupled wave equations are integrated by means of the split-step method with periodical boundary conditions. The soliton formation is achieved in the non-linear crystal pumped with an intense high frequency pump (ω_p) and seeded with a weaker sub-harmonic

beam ($\omega_s = \omega_p/2$). The crystal length was set to match exactly the $Z_T/2$ length for the chosen array period. The pump intensity was chosen such that its intensity is not high enough to trigger a soliton spontaneously from the quantum noise fluctuations. Both pump and seed beams are focussed at the entrance face of the crystal together. The seeding beam has a beam waist twice as large than that of the pump, thus providing the same divergence for both beams. The switch effect is clearly evident by comparing the pictures of the seeded and unseeded configurations.

(a)   (b)
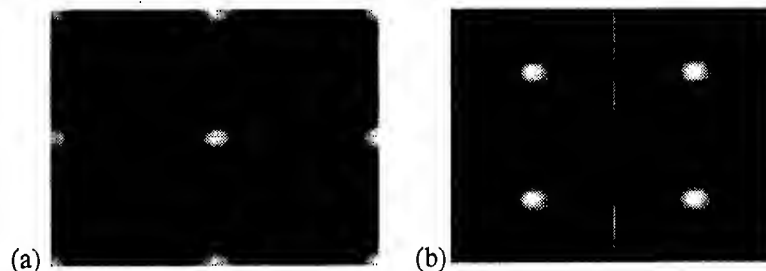
Fig.1 Output pump profiles as calculated by the numerical code. Output with no seed (a), and with injected seed. The area corresponding to two periods of the array is shown. Pump peak intensity at input: 75GW/cm^2. Seed peak-intensity: 0.75GW/cm^2. Simulated crystal length: 22 mm. The transverse spatial period of the array is 85 µm. All other parameters are similar to those employed in the experiment.

A sketch of the experimental implementation of the optical switch is depicted in Fig. 2. The millijoule infrared output of our 10 Hz, 1 ps, Nd:glass laser system (TWINKLE, Light Conversion) is split on two channels by means of a beam splitter. The second harmonic of the most intense channel, generated in a 1.5 cm long KDP crystal, is used as a pump for the parametric amplifier. The pulse energy in both pump and seed channels is regulated by means of a λ/2 and linear polarizer arrangement. A dichroic mirror is used to recombine the pump with the infrared channel, whose optical path length can be adjusted by means of a delay line. To transform efficiently the pump and seeder beams into a periodic pattern of several hundreds of narrow focussed beams we used a microlenses array. The focal plane of the array is imaged by means of a telescope onto the input face of a LBO crystal cut for type I non-critical phase-matching ($\theta=90°$, $\phi=0°$). We performed experiments with both a 22 and a 30-mm long non-linear crystal, the best results being achieved with the last one. The 30-mm long crystal is heated to a temperature of 158°C in order to ensure phase matching between the pump and the seeder beams (of 527.5 nm and 1055 nm wavelength, respectively). The imaging telescope has a magnification of 0.93, in order to have a transverse period of about 100 µm, which matches with the $Z_T/2$ equal to the crystal length. Finally, a CCD-based imaging system allows us to record the output face of the LBO crystal in either wavelength.
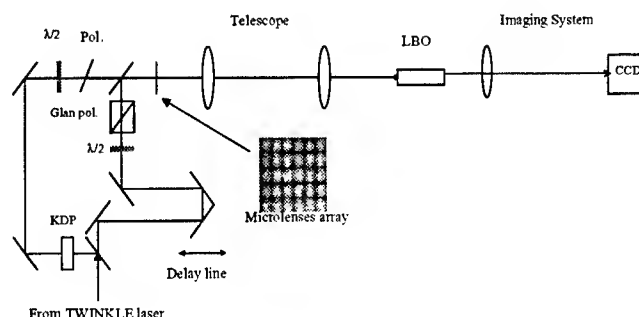
Fig. 2 A sketch of the experimental set-up.

In figure 3.a, a small portion of the output pattern of the pump beam in the unseeded case is shown. When the seed is allowed to mix with the pump (Fig.3.b), a soliton is formed in the position of the intensity minima of the unseed pattern (dashed reference frame). At the same time, the intensity of the local maxima of the unseeded pattern drops (continuos line reference frame). The achievement of the soliton regime is inferred from the observed mutual self-trapping between the harmonics, and the results of the numerical simulation. About the switch characteristics, the overall energy of the pump was fixed to 300 μJ while the seeding beam carried about 15μJ. At the center of the dashed line reference frame, the ratio between the switched-on and the switched-off beam peak intensities is 7. The same quantity was measured to be 3 at position corresponding to the continuos line reference frame. The switch can be still operated efficiently with variations of the pump intensities up to ±20% and with seed levels spanning from 5 to 230 μJ. Respect to simulation however there is some difference. In fact, the best contrast between the on and off states is achieved by focusing the input array 8 mm before the input face of the crystal, so that its output face is not exactly at the $Z_T/2$ distance from the best focus. As a result, the linear output is broadened and a consistent part of the energy is scattered in the interstitial points as well. We attribute this discrepancy to the non-optimal matching between the pump and seeder waist position, due to the chromatic aberration of the lenslet array and the reducing telescope. Work is in progress to improve the characteristics of the switch.
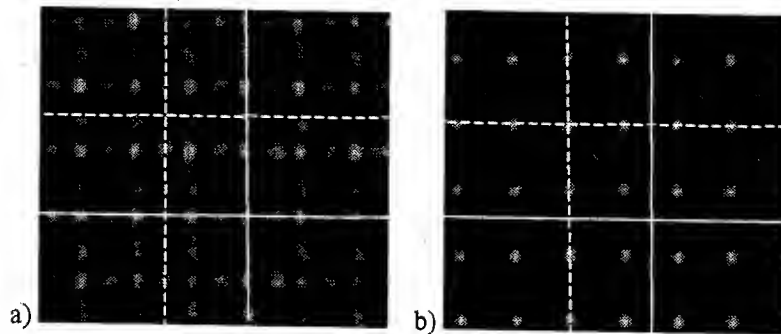
Fig. 3: The experimental output pump beam profile without (a) and with (b) injected seed. The filter set in front of the CCD camera is the same in both pictures. Overall input energy, pump 300 μJ and seed 15 μJ. The picture window dimensions are 540x505 μm.

In summary, we have demonstrated the possibility to combine the linear characteristics of a periodical light structure with the features of a multi-soliton array to arrange an all-optical switch, which could be operated at THz rates. We believe that could open new perspectives in the application of spatial solitons to photonics and in the physics of many-soliton environments.

[1] Y.Baek, R.Schiek, G.I.Stegeman, I.Bauman, and W.Sohler Opt. Lett. 22, 1550 (1997)

[2] H.Lopez-Lago, C.Simos, V.Couderc, and A.Barthelemy Opt.Lett. 26, 905 (2001)

[3] L.Torner, and D.V.Petrov Electron.Lett. 33, 608 (1997); S.Minardi, G.Molina-Terriza, P.Di Trapani, J.P.Torres, and L.Torner Opt.Lett. 26, 1004 (2001)

[4] A.Bramati, W.Chinaglia, S.Minardi, and P.Di Trapani Opt.Lett. 26, 1409 (2001)

[5] S.Minardi, S.Sapone, W.Chinaglia, P.Di Trapani, and A.Beržanskis Opt.Lett. 25, 326 (2000)

[6] F.Gori "Elementi di Ottica", Academica, Roma, 1997

[7] J.T. Wintrop, C.R. Worthington J.Opt.Soc.Am. 55, 373 (1965)

The Final State of Evolution of Incoherent Light Patterns in Nonlinear media

Raam Uzdin and Mordechai Segev*
Physics Department, Technion, Haifa 32000, Israel

Pattern formation and modulation instability in fully coherent systems have been investigated extensively in the past two decades. In the last few years, however, the observations of solitons made of spatially-incoherent (or weakly-correlated) light beams in several material systems[1-3] have led to the theoretical and experimental discovery of modulation instability and pattern formation in incoherent systems as well. In 2000, Soljacic et al.[4] predicted that a uniform distribution of spatially-incoherent light in a self-focusing medium will undergo Incoherent Modulation Instability (**IMI**, see fig. 1a), giving rise to intricate patterns. However, IMI occurs only if the strength of the nonlinearity is above a well-defined threshold; a threshold that is set by spatial coherence of the beam. If the nonlinearity is below the threshold (i.e., the beam is too incoherent), the intensity will remain uniform as all perturbations are suppressed. Shortly after, IMI and the presence of this threshold were indeed demonstrated experimentally[5].

A recent study[6] has investigated the long-term evolution of the pattern evolving from IMI and has shown that, in non-instantaneous nonlinearities the pattern evolving from IMI is actually an ensemble of soliton-like filaments, which interact with one another through long-range attractive forces. After a fairly short propagation distance, the IMI pattern forms an equally-spaced array of incoherent solitons. Following a long enough propagation distance, however, the pattern forms clusters (aggregates) of fine-scale filaments - clusters of solitons[6]. However, these facts are all that is known at this point on pattern formation in such nonlinear weakly-correlated systems, and many fundamental intriguing questions are still open. For example, there is no knowledge on whether (or not) the clusters of solitons are the final (equilibrium) stage in the evolution or just a transient and the system evolves into a different state. It is also not known whether an equilibrium state for this system actually exists, or perhaps this system continues to evolve. Furthermore, it is very difficult to even characterize these stages in the evolution of the system, as all its features are randomly distributed: the intensity structure exhibits random clustering of filaments, and the correlation statistics depends on the local coordinate. Unlike coherent pattern formation, for incoherent systems the phase "internal degrees of freedom" add much complexity. Unfortunately this extra feature of correlation statistics (incoherence) is hard to measure. Interferometry-based coherence measurements are difficult to perform, especially when the pattern feature size, and the coherence length are comparable, and indeed the correlation statics of incoherent solitons or of the IMI process have not been measured experimentally thus far.

Here we find the final equilibrium state of evolution of the patterns evolving from modulation instability in incoherent (weakly-correlated) nonlinear wave-systems. We develop a global measure of spatial coherence which can be easily measured without interferometry. Then, given the initial conditions we find analytically a relation between the pattern intensity profile and the average correlation distance.

We search for a global measure which characterizes the pattern as a whole and not a specific point in it. The conventional definition of the coherence length is given by[7]: $L_c(x_1) = \int |\mu(x_1, x_2)|^2 \, dx_2$ where $\mu(x_1, x_2)$ is the normalized (mutual) correlation function. Given a point x_1, point x whose distance to x_1 exceed L_c is no more phase correlated with x_1. There are several problems with this definition. For one, it is not local, but much worse than that it frequently diverge for many physical scenarios such as localized statistics ($\mu(x_1, x_2) \neq \mu(x_1 - x_2)$) or when the statistics is periodic in the $x_1 - x_2$ coordinate. For IMI, the statistics is typically both localized and periodic (see the second paper in[4]) .

We begin by defining a measure of coherence which is based on the diffraction angle of the incoherent beam. A beam of incoherent light diffracts not only due to the finite extent (width) of its envelope, but also due to its incoherence, that is, the phase fluctuations upon it. The diffraction angle of a coherent gaussian beam (width=w) is:

$$\theta = 2/(kw) \tag{1}$$

For a general coherent beam, the diffraction angle is the second moment in the transverse momentum space. Using either one of the methods commonly used now to describe incoherent solitons and IMI, namely, the coherent density[8] the modal theory[9], or the radiation transfer theory[10], incoherent light is described by a collection of coherent elements

*Electronic address: msegev@tx.technion.ac.il

(bundles or modes) which are mutually incoherent with one another. We therefore find the average diffraction angle following a logic similar to that of a general coherent beam:

$$< \theta^2 >_{tot} = \sum p_j \int \theta^2 \, |\Phi_j(\theta)|^2 \, d\theta \qquad (2)$$

where p_j is the relative power of each field ($\sum p_j = 1$) and $\Phi_j(\theta)$ is the normalized (like in Quantum Mechanichs) Fourier transform of the coherent beam $\Phi_j(x)$.

The diffraction angle of the total intensity holds information on both the envelope and the correlation statistics. To extract the contribution of the statistics, we subtract the diffraction angle of a totally coherent beam Ψ whose intensity profile is the same as that of the incoherent beam. We define:

$$< \theta^2 >_{stat} = < \theta^2 >_{tot} - < \theta^2 >_{env} \qquad (3)$$

where

$$< \theta^2 >_{env} = \int \theta^2 \, |\Psi(\theta)|^2 \, d\theta = \int \left| \frac{d}{dx} \sqrt{I_{norm}(x)} \right|^2 dx$$

(I_{norm} is the normalized **total** intensity!).

Next, In analogy with (1) we define the *average correlation distance*as:

$$< l_c > = 2/(k\sqrt{< \theta^2 >_{stat}}) \qquad (4)$$

This definition is free of the problem described earlier. In the same way we define the **feature size** as

$$< l_f > = 2/(k\sqrt{< \theta^2 >_{env}})$$

$< \theta^2 >_{stat}$ is an observable quantity. Even though it can be measured by calculating second moment of the far-field intensity ($=< \theta^2 >_{tot}$) and $< \theta^2 >_{env}$, we would like to relate it to the conventional notion of coherence in the coordinate space: $\mu(x_1, x_2)$. For delocalized statistics, $\mu(x_1, x_2) = \mu(x_2 - x_1) = \mu(\Delta x)$, it can be shown that:

$$< \theta^2 >_{stat} = -\mu(\Delta x) \partial_{xx} \mu(\Delta x) \, |_{\Delta x = 0} \qquad (5)$$

For the more general localized statistics we first calculate the effective delocalized statistics according to:

$$\mu_{eff}(\Delta x) = \int \mu(x_1, x_1 + \Delta x) I_{norm}(x_1) dx_1 \qquad (6)$$

and then use Eq (4) & (6) to get the correlation distance.

Next, we find the relation between the average correlation distance and the intensity profile of the evolving IMI pattern. For Hamiltonian systems, the Hamiltonian is conserved i.e. $H_i = H_f$ (i and f designate initial and final). For the Kerr case the Hamiltonian can be written as:

$$H = \frac{1}{2}Q < \theta^2 >_{tot} - \frac{1}{2} \int I^2 dx \qquad (7)$$

where $Q = \int I(x)dx$ is the total power of the beam which is conserved as well. Given the initial condition at the input face, H is easily calculated using Eq 7. $H_i = H_f \Rightarrow$

$$< l_c > = \frac{2}{k} \left[\frac{1}{Q}(2H_i + \int I_f^2 dx) - < \theta^2 >_{env}^f \right]^{-1/2} \qquad (8)$$

I_f is the intensity of the output pattern. We point out that all that is needed to evaluate $< l_c >$, is H and the intensity profile at the output face. In figure 1a we show evolution of a pattern through incoherent modulation instability (above), along with the ratio between the average correlation distance and the average feature size, as a function of propagation distance. The inserts in this figure show two very distinct stages: the formation of a quasi-periodic array of filaments (left), characterized by dominant harmonics of a specific spatial frequency (the frequency of the highest gain[4]), and the formation of clusters of solitons (right). As shown in this figure, we find that the clusters of solitons[6], which is characterized by the appearance of sub-harmonic spatial frequencies, is the final stage of evolution of this system. In principle, the spatial coherence can actually increase or decrease with z compared to

NLWB7-3

FIG. 1: The evolution of spatially incoherent wide beam above the pattern formation threshold is shown in (1a). First only the frequency of highest gain appears as seen in the Fourier Transform (1b), then, higher harmonics emerge and narrow filaments form (F.T. not shown here) and finally the clustering effect takes place with the appearance of sub harmonic frequencies (Fig 1c). Figure (1d) show that after long term evolution the ratio between the feature size and the average coherence length is roughly unity.

the input face. This effect is due to momentum exchange between the fields and the medium in the repeating collision processes. However the ratio between the average feature size and the average coherence length is roughly unity , and it remains unity (on average) throughout propagation.

In conclusion, have shown that the pattern evolving from modulation instability in nonlinear incoherent wave systems reaches an equilibrium "steady state" evolution when its average correlation distance equals its average feature size. To do that we have developed a new useful global measure of coherence which does not necessitate interferometric technics to be measured. Finally, we have shown that the average correlation distance can be found solely from the intensity profile, assuming only Hamiltonian conservation.

References

[1] M. Mitchell, Z. Chen, M. Shih, and M. Segev, Phys. Rev. Lett. **77**, 490 (1996).
[2] M. Mitchell and M. Segev, Nature (London) **387**, 880 (1997).
[3] M. Peccianti and G. Assanto, Opt. Lett. **26**, 1791 (2001).
[4] M. Soljacic, M. Segev, T. Coscun, D.N. Christodoulides, and A. Wishwanath, Phys. Rev. Lett. 84, 467 (2000); S. M. Sears, M. Soljacic, D.N. Christodoulides, and M. Segev, Phys. Rev. E **65** 36620 (2002).
[5] D. Kip, M. Soljacic, M. Segev, E. E. Eugenieva, D. N. Christodoulides, Science **290** 495 (2000); D. Kip, M. Soljacic, M. Segev, S. M. Sears, and D. N. Christodoulides, J. Opt. Soc. Am. B **19** 502 (2002).
[6] Z. Chen, S. M. Sears, H. Martin, D.N. Christodoulides, and M. Segev, Proc. Nat. Acad. Sci. of the USA (PNAS) 99, 5223 (2002)
[7] T. H. Coskun, D. N. Christodoulides, M. Mitchell, Z. Chen and M. Segev, Opt. Lett. **23**, 418 (1998).
[8] D. N. Christodoulides, T. H. Coskun, M. Mitchell, and M. Segev, Phys. Rev. Lett. **78**, 646 (1997).
[9] M. Mitchell, M. Segev, T. H. Coskun, and D. N. Christodoulides, Phys. Rev. Lett. **79**, 4990 (1997).
[10] V. V. Shkunov and D. Anderson, Phys. Rev, Lett. **81**, 2683 (1998).
[11] Solitons - Nonlinear pulses ans beams, N. N. Akhmediev and A. Ankiewicz, Chapman & Hall.

Nonlinear Beam Dynamics in $\chi^{(2)}$ Waveguides

G. Stegeman, R. Malendevich, R. Schiek, R. Iwanow, L. Jankovic and H. Fang

CREOL, Un. of Central Florida , 4000 Central Florida Blvd., Orlando, Florida 32816-2700

G. Schreiber and W. Sohler

Un. Paderborn, Fachbereich Physik, Angewandte Physik, D-33095 Paderborn, Germany

L. Torner

Un. Polit. de Catalunya, Dept. of Signal Theory and Commun., 08080 Barcelona, Spain

Address : CREOL, P.O. Box 162700,
4000 Central Florida Blvd.
Orlando, FL 32816-2700

Tel. 407-823-6915

Fax. 407-823-6955

E-mail : george@creol.ucf.edu

Abstract: The evolution from diffraction, to single and then multiple quadratic soliton generation, and finally the onset of modulational instability were observed for wide fundamental beams in both birefringence and quasi-phase matched $LiNbO_3$ slab waveguides.

Nonlinear Beam Dynamics in $\chi^{(2)}$ Waveguides

G. Stegeman, R. Malendevich, R. Schiek, R. Iwanow, L. Jankovic and H. Fang

CREOL, Un. of Central Florida , 4000 Central Florida Blvd., Orlando, Florida 32816

G. Schreiber and W. Sohler

Un. Paderborn, Fachbereich Physik, Angewandte Physik, D-33095 Paderborn, Germany

L. Torner
Un. Polit. de Catalunya, Dept. of Signal Theory and Commun., 08080 Barcelona, Spain

1. Introduction

The early work of Sukhorukov and colleagues showed that waves parametrically coupled via the second order nonlinearity $\chi^{(2)}$ can be mutually self-focused, and form quadratic solitons.[1]Subsequently, Trillo and co-authors showed that plane waves in quadratically nonlinear media are unstable and break-up into periodic structures.[2] Each of these regimes have been demonstrated experimentally in slab waveguides, soliton generation by inputting fundamental beams of the appropriate width and peak intensity for solitons, and beam break-up with very wide (mm width) input beams.[3-5] Furthermore, the spontaneous generation of multiple solitons has been predicted to occur at intensities higher than for single soliton generation and below those required for modulational instability (MI), but has not been observed experimentally yet.[6,7] In fact, all of these phenomena are caused by the same mutual self-focusing predicted originally by Sukhorukov and colleagues.[1] In this paper we report experimental evidence of some of these phenomena, and find smooth transitions between the different regimes.

2. Experimental Details
We have studied nonlinear beam evolution in two different LiNbO$_3$ slab waveguides. Five cm long, periodically poled slab waveguides were fabricated by Ti:indiffusion in a Z-cut X-propagating LiNbO$_3$ crystal with a quasi-phase-matched (QPM) period of 17.63 μm. Operating at the temperature of 180 ^{0}C to avoid photorefractive effects and a fundamental (FW) wavelength of 1580 nm resulted in a large positive phase mismatch. The 20 ps, TM$_0$ polarized, input beam with a waist ω_0 of ~74 μm (FWHM = 1.17ω_0) was obtained from an EKSMA Nd:YAG pumped BBO optical parametric generator-amplifier (OPG-OPA) system. The laser beam had a small asymmetry to one side of the peak (not in evidence in 1(a) below). Combinations of circular and cylindrical lenses were used to couple the highly elliptical beams into the waveguide. The output beam profiles were recorded with a camera.

The second waveguide was a 47 mm long, 8 μm thick Y-cut X-propagating, titanium-indiffused LiNbO$_3$ slab waveguide with > 50% coupling efficiency. A 180 μm wide elliptical beam, wavelength of 1.32 μm, was obtained from a home-made Nd:YAG-OPG-OPA laser system. This had an inherent asymmetric beam profile and much lower peak energy than the EKSMA system. The FW was a TM$_0$ waveguide mode and the second harmonic (SH) a TE$_1$ mode for the birefringent phase-matching used in this case, which required an operating temperature of $\approx$340^{0}C.

3. Experimental Results
Typical experimental results observed at the output facet of the QPM waveguide are shown below at three input power levels. The input beam diffracts to 220 μm at low powers, (a). (b) shows single soliton generation. At increasing intensities the output beam exhibited multiple soliton generation. For each case, multiple shots of the laser led to identically the same envelope, to within the laser power uncertainty. This reproducibility was observed for the data taken until high input power levels were reached. That

case, (c), exhibits the characteristics of modulational instability. The key point there is that the output pattern is not reproducible from shot-to-shot and the pattern is no longer centered on the input beam.
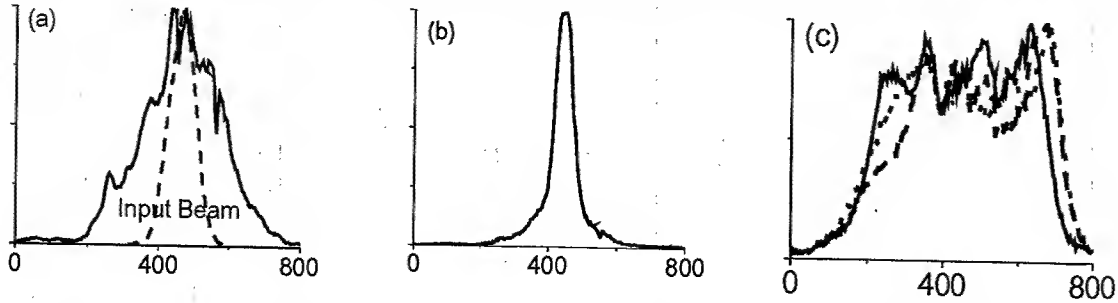
Figure 1   (a) The input (dashed line) and output (solid line) for a QPM slab waveguide at low powers. (b) Output just above the single soliton threshold. (c) Three output beam profiles at the same input power for high input powers.

The intensity region between (b) and (c) above was probed with a 180 μm wide elliptical beam in the birefringence phase-matched sample. This wide input beam made it easier to identify multiple soliton generation. Typical results are shown below. For multiple laser shots the reproducibility at the output was good, for example see (b). The input beam, (a), shows a small asymmetry. The input beam has generated two solitons in (b). This was verified by "propagating" the beams numerically over distances much longer than the samples and noting that indeed two solitons emerged from this pattern. Three solitons are generated in (c). Note that the cw simulations are in good agreement with the position of the experimental peaks although there is a background present in the experimental data due to the pulsed nature of the experiments. The key difference between these results and (c) shown above is that the centroid of the peaks tracks that of the input beam. Because the nonlinearity accessed here is $d_{31} \approx 5.1$ pm/V versus $d_{33} \approx 16$ pm/V for the QPM sample, the intensities needed for the onset of modulational instability would be much higher and were not attempted to avoid sample damage.
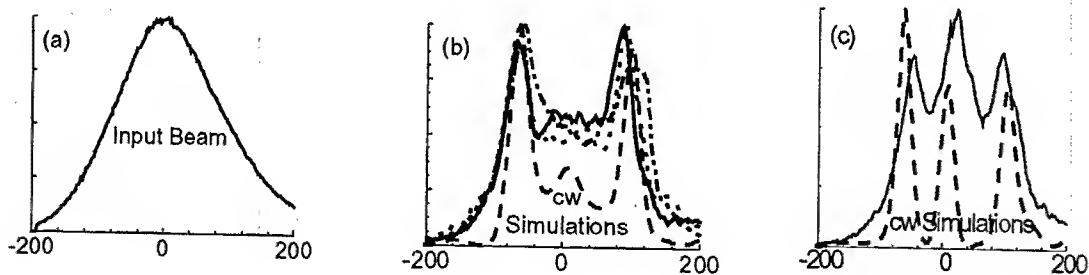
Figure 2   (a) Asymmetric input beam profile for the birefringence phase-matched waveguide. (b) Experimental two soliton generation (solid line) and cw simulations (dashed line). (c) Experimental three soliton generation and cw simulations (dashed line). (b) shows three experimental curves as well as the simulations (dashed line).

In summary, we have observed a variety of new beam distortion phenomena which occur when a high intensity beam is incident in a $\chi^{(2)}$-active medium near a phase-matching condition for second harmonic generation below and above the onset of MI.

4.   References

[1] Y. Karamzin, A. Sukhorukov, Zh. Eksp. Teor. Fiz. **68**, 834 (1975); Sov. Phys. JETP, **41**, 414 (1976).
[2] S. Trillo and P. Ferro, Opt. Lett. **20**, 438 (1995).
[3] R. Schiek, Y. Baek and G.I. Stegeman, Phys. Rev. E, **53**, 1138 (1996).
[4] H. Fang, R. Malendevich, R. Schiek and G. I. Stegeman, Opt. Lett., **25**, 1786 (2000)

[5] H. Fang, R. Malendevich, R. Schiek and G. I. Stegeman, Phys. Rev. Lett., **86**, 4528 (2001).

[6] L. Torner, J. P. Torres and C. R. Menyuk, Opt. Lett., **21**, 462 (1996).

[7] G. Leo and G. Assanto, Opt. Commun. **146**, 356 (1998).

Nonlinear Periodic Structures

Wednesday, September 4, 2002

Neil G. Broderick, Univ. of Southampton, UK
Presider

NLWC
2:00pm – 4:00pm
Auditorium

Tunable, switchable and nonlinear microstructured fiber devices

B.J. Eggleton
OFS Laboratories
19 Schoolhouse Road, Somerset, NJ 08873
egg@ofsoptics.com
¹also OFS, Specialty Photonics Division

Abstract

We review several applications of microstructured photonic crystal optical fibers that incorporate active materials infused into the air-holes. The tunable optical characteristics of the materials combined with the unique structure of the fiber enable a number of functionalities including reconfigurability, tunability and enhanced nonlinearities for various fiber device applications.

© 2002 Optical Society of America

OCIS codes: (060.2310) Fiber optics; (230.3990) Microstructure devices; (260.1560)

1. Introduction

Microstructured photonic crystal optical fibers (MOFs) have generated increased interest recently because they provide extra degrees of freedom in maniplating optical propeties of light such as dispersion, nonlinearity and birefingence of optical fibers [1-4]. For example, strong waveguide dispersion and enhanced nonlinearity can be obtained in a MOF that comprises a small silica core surrounded by closely spaced air-holes [4]. Similarly, enhanced birefringence can be achieved in such fibers, particularly in fiber designs that incorporate ellipitcal air-holes or asymmetrical distributions or air-holes [5].

In this paper we show that MOFs also provide a platform for a new class of optical devices. In particular, the air-holes allow for the infusion of active materials yielding novel hybrid all-fiber optical devices that exhibit desirable properties, such as enhanced tunability, dramatic nonlinear interactions, compactness, and intrinsic low insertion loss [6]. In these applications the active materials provide tunabilty, and enhanced nonlinear interactions, and the core region can incorporate a doped region allowing for the inscription of grating structures. These devices exploit index tunable materials as well as electrically driven microfluids to manipulate and switch mode propagation. We review several examples of such tunable devices including, tunable resonant filters, variable optical attenuators and an approach for introducing strong birefringence into MOF by infusing index tunable materials into specific air-holes.
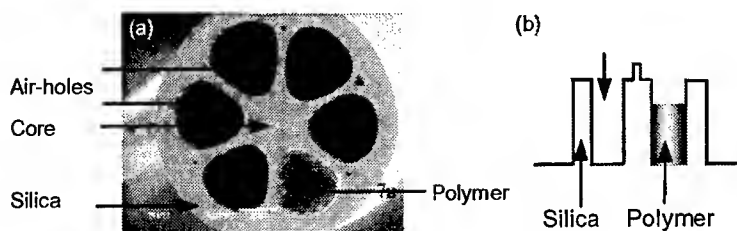
Fig. 1. (a) Scanning electron micrograph of the MOF with single layer of air-holes in the cladding and polymer infused in one of the holes. (b) Schematic cross-section of the asymmetric waveguide.

2. MOF waveguide design and characteristics

Fig. 1 summarizes the principle of the tunable MOF where selected air-holes can be infused with index tunable materials [6] and/or electrically driven microfluids [7]. The MOF has a photosensitive germanium (Ge) core with diameter ~8µm and $\Delta = (n_1 - n_2)/n_1$ ~0.35%, where n_1 and n_2 are the refractive indices of the Ge core and the silica respectively [8]. Fig. 1(a) shows a single layer of air-holes, each of diameter ~40µm, incorporated in the cladding of the MOF in a hexagonal geometric distribution. Interaction between the propagating mode and the tunable cladding region can be achieved in two different ways: excitation of a cladding mode by a long-period grating [9] or by tapering the MOF to a reduced outer diameter so that the fundamental mode leaves the core region and expands into the cladding [10,11]. The latter approach provides a robust device architecture for manipulating light propagation in the MOF and low splice loss to conventional fibers by collapsing the air-holes first and then fusing the fibers together.

Fig. 2 shows a schematic diagram of the tapered MOF. In the waist of the tapered MOF, the length is 1 cm, the outer diameter size is 30µm, the inner cladding region is ~8 µm and $\Delta = (n_2 - n_{air})/n_2$ (~30%) is large where n_2 and n_{air} are now the refractive indices of the silica-cladding and air, respectively. Light, which initially propagates in the Ge core, spreads into the cladding as it propagates into the taper region and is guided by total internal reflection at the silica/air-holes interface in the waist of the MOF. Infusion of tunable materials into the air-holes in the waist changes the boundary conditions at these interface.
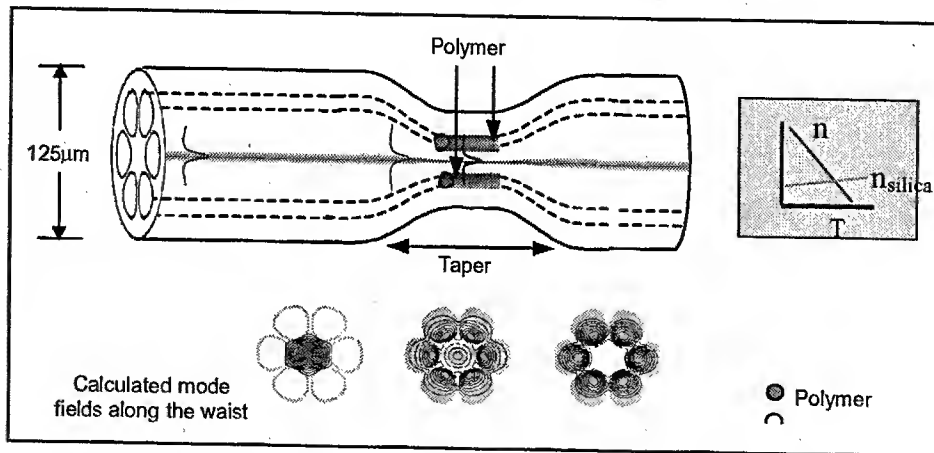
Fig. 2. Schematic of all-fiber variable attenuator based on tapered MOF with polymer infused in the waist, the inset shows refractive indices of the polymer and silica dependence on temperature. Also the mode field profiles are shown at different positions along the length of the waiste region of the MOF, with polymer (n_{pol}=1.434) at 0cm, 1cm, and 2cm along the waist.

3. Photonic Device Applications.

Active materials, such as polymers or fluids can be infused into the relatively large air-holes of the grapefruit MOF. Fig. 3(a) shows one end of the fiber immersed in a reservoir of material and sealed on the other end where vacuum is applied. The material then can be introduced into the air-holes of the fiber as shown in Fig. 3(b). The material can be liquid acrylate monomer mixture (viscosity ~30 centipoise), infused into the air-holes at a rate of 0.03 cm/sec and UV-cured for about 15 minutes to form a polymer with a desired refractive
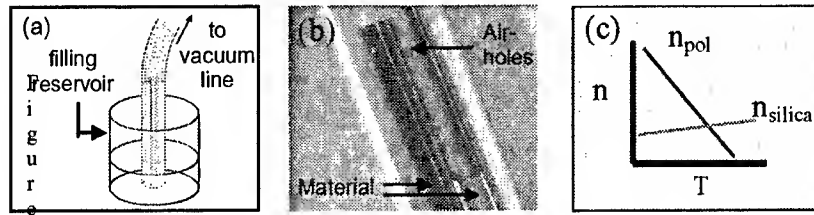
3. (a) Schematic drawing of material (polymer) infused in the air-holes of the MOF. (b) Picture showing material in the air-holes of the fiber. (c) Refractive indices of the polymer and silica.

index. Switching and modulating the index profile by displacing fluids to overlap with the modal field also allows for dramatic change in the optical properties [7]. To break the symmetry of this waveguide, we can selectively fill certain air-holes with index tunable materials, such as acrylate based polymer [12].

4. Enhanced nonlinear interactions

Tapered MOF provide an ideal structure for demonstrations of dramatic nonlinear effects. Laser pulses at 1.3 μm generated by a femtosecond Ti-sapphire pumped optical parametric oscillator were free-space coupled into the un-tapered portion of the MOF and then propagated through the taper. As shown in Fig. 4 tunable self-frequency shifting solitons can be generated over the important communications windows from 1.3μm to 1.65 μm with input pulse at 1.3μm [10]. As the light propagates through the MOF the light is continually shifted towards the red due to intrapulse Raman scattering, which transfers the energy of the high frequency part of the pulse spectrum to the low frequency part, we observe 60% of the input photons being self-frequency shifted. These dramatic results are possible because the fiber exhibits a large anomalous dispersion over a wide wavelength range.
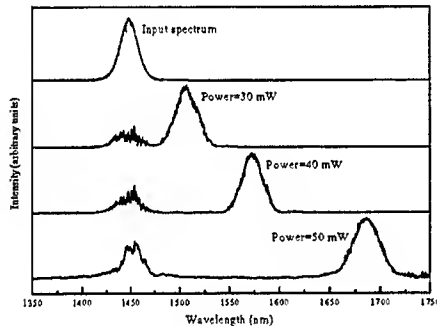
Fig. 4 Output spectra for different peak intensities

References

1. P.V. Kaiser and H.W. Astle, "Low-loss single-material fibers made from pure fused silica", The Bell System Technical Journal, 53, 1021-1039, (1974).
2. T.A. Birks et al., "Dispersion Compensation Using Single-Material Fibers," IEEE Phot. Tech. Lett, 11, 674-676, (1999).
3. T.P. Hansen, et al., "Highly birefringent index-guiding photonic crystal fibers," IEEE Phot. Tech. Lett, 13, 588-590, (2001).
4. J.K. Ranka et al., "Optical properties of high-delta air-silica microstructure optical fibers," Opt. Lett., 25, 796-798, (2000).
5. M.J. Steel et al., "Symmetry and degeneracy in microstructured optical fibers," Opt. Lett, 26, 488-490, (2001).
6. B.J. Eggleton et al., "Microstructured optical fiber devices," Opt. Express, 9, 698-713, (2002), http://www.opticsexpress.org/abstract.cfm?URI=OPEX-9-13-698 .
7. C. Kerbage et al., "Tunable devices based on dynamic positioning of micro-fluids in microstructure optical fiber," Optics Communications, April issue (2002).
8. B.J. Eggleton et al., "Cladding mode resonances in air-silica microstructure fiber," J. Lightwave Tech., 18, 1084-1100, (2000).
9. P. S. Westbrook et al., "Cladding mode loss in hybrid polymer-silica microstructured optical fiber gratings," IEEE Phot. Tech. Lett. 12, 495-497 (2000).
10. J.K. Chandalia et al., "Adiabatic Coupling in Tapered Air-Silica Microstructured Optical Fiber," IEEE Phot. Tech. Lett, 13, 52-54, (2001).
11. C. Kerbage et al., "Integrated all-fiber variable attenuator based on hybrid microstructure fiber," Appl. Phys. Lett., 79, 3191-3193, (2001).
12. C. Kerbage et al., "Microstructured optical fibre with tunable birefringence," Electronics Letters 38, 310-312 (2002).

Discrete temporal solitons along a chain of nonlinear coupled microcavities embedded in photonic crystals

Demetrios N. Christodoulides, Nikos K. Efremidis and Jared Hudock

School of Optics/CREOL, University of Central Florida,
Florida, 32816-2700

Abstract: We demonstrate that spatiotemporal discrete solitons are possible in nonlinear photonic crystal structures. Analysis indicates that these states can propagate undistorted along a series of coupled resonators or defects by balancing the effects of discrete lattice dispersion with material nonlinearity.
© 2002 Optical Society of America
OCIS codes: 130.4310, 190.4390, 190.5530

Photonic crystals are artificial microstructures in which the refractive index is periodically modulated at a length scale comparable to the wavelength of operation [1]. For specific crystal configurations, this index periodicity can lead to a complete photonic band-gap (in a certain range of frequencies), thus, inhibiting wave propagation in all three directions [1]. As it has been noted in several studies, the presence of gaps in the macroscopic dispersion relation of such periodic structures introduces a number of novel features that can be exploited to control the propagation of light. In this respect, photonic crystals are highly promising in terms of integrating useful optical components such as waveguides, couplers, cavities, filters, etc., on the same substrate. Recently, a new type of an optical waveguide that involves a periodic sequence of coupled high-Q resonators has been proposed [2, 3]. In these latter systems, waveguiding is accomplished via light hopping or tunneling among successive microcavities that effectively act like defects within the crystal.

In this paper, we show that spatiotemporal discrete solitons can propagate undistorted along a chain of coupled nonlinear high-Q cavities or defects that are embedded in a photonic crystal structure. Such states are possible as a result of the balance between the effect of discrete lattice dispersion with that of material nonlinearity. These self-localized entities are capable of exhibiting very low group velocities, depending on the coupling strength among successive microcavities and in principle they can remain immobile like *frozen bubbles of light*. In addition, this class of solitons can be effectively navigated along any pre-assigned path in a three-dimensional environment. Methods to optimize their transport efficiency when they encounter sharp bends will be also discussed.

We begin our analysis by considering a periodic sequence of identical coupled high- microcavities or defects, similar to that shown schematically in Fig. 1. In principle, these defects can confine light in either two- or three-dimensional geometries provided they are surrounded by an appropriate photonic band gap structure. The distance between successive resonators (or primitive cells) is D and the material is taken here to be Kerr nonlinear. Furthermore, we assume that each cavity/defect is single-moded, oscillating at an eigenfrequency ω_0. The electromagnetic mode of each resonator in isolation, is given by $\mathbf{E} = \mathbf{E}_0(\mathbf{r}) \exp(-i\omega_0 t)$ and $\mathbf{H} = \mathbf{H}_0(\mathbf{r}) \exp(-i\omega_0 t)$ where $\mathbf{E}_0(\mathbf{r})$ and $\mathbf{H}_0(\mathbf{r})$ represent the cavity eigenmodes. Evidently, because
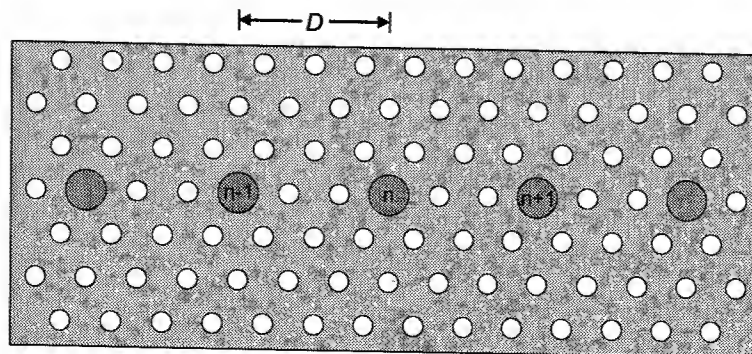
Fig. 1. Array of microcavities or defects embedded in a photonic crystal structure. The distance between elements is D.
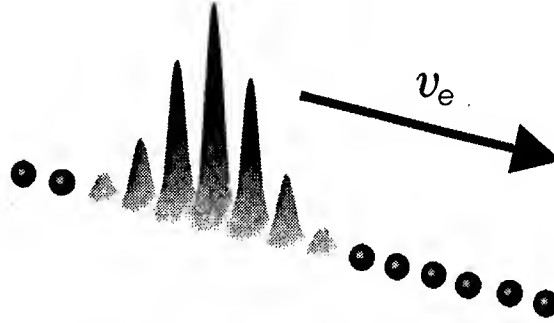
Fig. 2. Temporal discrete soliton propagating along a nonlinear chain of coupled resonators at a group speed v_e.

of proximity, a finite coupling exists between successive defects. Let us assume that the presence of the other cavities around a particular site perturbs the total permittivity from ε to ε'. In general, the perturbed fields $\mathbf{E}' = \mathbf{E}'_0(\mathbf{r}, t)\exp(-i\omega_0 t)$, $\mathbf{H}' = \mathbf{H}'_0(\mathbf{r}, t)\exp(-i\omega_0 t)$, obey $\nabla \times \mathbf{E}'_0 = \mu_0(i\omega_0 \mathbf{H}'_0 - \partial \mathbf{H}'_0/\partial t)$ and $\nabla \times \mathbf{H}'_0 = \varepsilon'(-i\omega_0 \mathbf{E}'_0 + \partial \mathbf{E}'_0/\partial t)$. By applying the divergence theorem on the quantity $\nabla \cdot (\mathbf{E}^*_0 \times \mathbf{H}'_0 + \mathbf{E}'_0 \times \mathbf{H}^*_0)$ and by using Maxwell's equations we obtain the Lorentz reciprocity relation:

$$\oiint ds \cdot (\mathbf{E}^*_0 \times \mathbf{H}'_0 + \mathbf{E}'_0 \times \mathbf{H}^*_0) = \iiint dv \left[i\omega_0(\varepsilon' - \varepsilon)\mathbf{E}'_0 \cdot \mathbf{E}^*_0 - \varepsilon\mathbf{E}^*_0 \cdot \frac{\partial \mathbf{E}'_0}{\partial t} - \mu_0\mathbf{H}^*_0 \cdot \frac{\partial \mathbf{H}'_0}{\partial t} \right]. \tag{1}$$

Since $\mathbf{E}_0$ and $\mathbf{H}_0$ represent bound modes that vanish at infinity, the surface integral of Eq. (1) is equal to zero. Next, we express the perturbed fields as a time-varying superposition of the cavities' bound states, e.g. $\mathbf{E}'_0(\mathbf{r}, t) = \sum a_m(t)\mathbf{E}_{0m}$ and $\mathbf{H}'_0(\mathbf{r}, t) = \sum a_m(t)\mathbf{H}_{0m}$ where the eigenfunctions $\mathbf{E}_{0m} = \mathbf{E}_0(\mathbf{r} - \mathbf{r}_m)$ and $\mathbf{H}_{0m} = \mathbf{H}_0(\mathbf{r} - \mathbf{r}_m)$ are localized at the lattice points. If we let in Eq. (1), $\mathbf{E}_0 = \mathbf{E}_{0n}$ and $\mathbf{H}_0 = \mathbf{H}_{0n}$, and by keeping in mind that the material is Kerr nonlinear ($n^2 = n_0^2 + 2n_0 n_2 |E|^2$), we then obtain the discrete nonlinear evolution equations:

$$i\frac{da_n}{dt} + \sum c_{mn} a_m + \gamma |a_n|^2 a_n = 0, \tag{2}$$

where the linear coupling coefficients c_{mn} and the self-phase modulation strength are given by

$$c_{mn} = \frac{\omega_0 \iiint dv(\varepsilon' - \varepsilon)\mathbf{E}^*_{0n} \cdot \mathbf{E}_{0m}}{\iiint dv\,(\mu_0|\mathbf{H}_{0n}|^2 + \varepsilon|\mathbf{E}_{0n}|^2)}, \qquad \gamma = \frac{2n_0 n_2 \varepsilon_0 \omega_0 \iiint dv|\mathbf{E}_{0n}|^4}{\iiint dv\,(\mu_0|\mathbf{H}_{0n}|^2 + \varepsilon|\mathbf{E}_{0n}|^2)}. \tag{3}$$

If we now consider only nearest-neighbor interactions (as for example in a straight chain of resonators), Eq. (2) takes the form:

$$i\frac{da_n}{dt} + \Delta\omega a_n c(a_{m+1} + a_{m-1}) + \gamma |a_n|^2 a_n = 0. \tag{4}$$

$\Delta\omega = c_{mm}$ represents a small shift in the eigenfrequency ω_0 arising from the presence of neighboring cavities. As a result, the effective eigenfrequency of each resonator in this chain is $\omega'_0 = \omega_0 - \Delta\omega$. In addition, $c = \pi/2\tau_c$ (measuring in inverse time units) stands for the coupling strength between successive sites where τ_c is the time required for one cavity to completely couple its energy to its neighbors (in the linear regime).

Equation (5) describes the evolution dynamics of the optical field in a nonlinear chain of resonators or microcavities. It has the form of a discrete nonlinear Schrödinger equation that is known to exhibit *discrete soliton* (DS) solutions. It is noteworthy pointing out that, so far, in nonlinear optics, the only other system that happens to support (spatial) DS states is that of nonlinear waveguide arrays [4]. However, unlike their spatial cousins [4, 5], the DS reported here are by nature *spatiotemporal* entities. The dispersive properties of this lattice become apparent if one considers the linear dispersion curve of Eq. (5). This can be obtained by using the discrete plane wave solution, $\exp[i(\Omega t - Kx_n)]$ at low amplitudes, where $x_n = nD$ and Ω, K are its angular frequency and wavenumber respectively. In this case one readily finds that $\Omega = 2c\cos(KD) + \Delta\omega$ which, in turn, describes the photonic band structure of this lattice within the Brillouin zone. In general, Eq. (5) does not exhibit closed form solutions. Yet, in two limiting cases (for broad and highly localized pulses), this equation can be accurately treated analytically. For example, for broad enough solitons, the
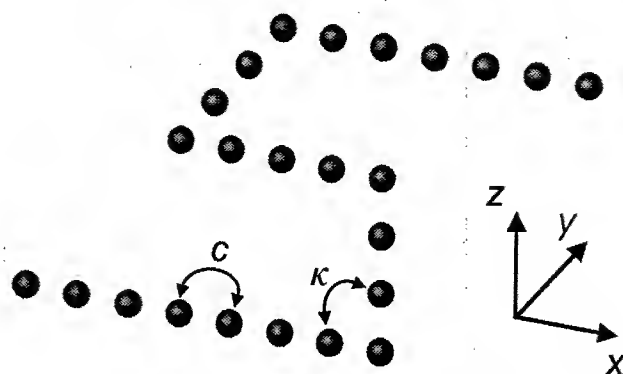
Fig. 3. Three-dimensional pathway of coupled resonators.

so-called long-wavelength approximation can be employed. The optical field profile of a moderately confined discrete soliton is shown schematically in Fig. 2. In principle, the soliton group velocity v_e can be very low for very small coupling coefficients or for $q = 0, \pi$. If the phase shift $q = 0$, the group velocity $v_e = 0$, and thus the DS becomes in essence immobile (frozen light). On the other hand for $0 \leq q \leq \pi/2$, when the lattice dispersion is anomalous, this discrete soliton propagates at $v_e = 2cD \sin(q)$. For $q = \pi$, the dispersion is normal (for $c > 0$) and thus immobile π-out-of-phase dark solitons are expected to exist. Similarly, when the nonlinearity of the chain is of the defocusing type, dark solitons are allowed at $q = 0$ and staggered bright solitons are expected to exist at the end of the Brillouin zone ($q = \pi$) when again $c > 0$. The regime close to $q \approx \pi/2$ is also of interest since to first order the dispersion is close to zero, thus allowing dispersion management as well as dispersion-free propagation in the linear regime [7]. In addition, to the weakly or moderately localized discrete soliton states, other considerably more confined solutions of Eq. (4) are also known to exist. This latter type of discrete solitons is associated with nonlinear defect states that have altogether different transport properties because of Peierls-Nabarro effects. In this case, the discrete field distribution (in self-focusing systems with $q = 0$) has approximately the form $a_n \approx a_0 \exp(-|n|D/x_0)$.

Finally, we would like to mention that this class of solitons can be navigated along any pre-assigned path in a three-dimensional environment. This for example could occur in a three-dimensional chain of nonlinear coupled resonators (completely surrounded by a photonic crystal), as depicted in Fig. 3. As it has been shown in Ref. [8], reflection losses in such a discrete system arise when the soliton traverses a sharp bend. This is because the finite coupling strength between the two sites around the corner plays an important role in this process. Yet, these bending losses can be essentially eliminated by appropriately engineering the corner site of the bend. Following the analysis of [8], this is accomplished by slightly detuning the corner site by an amount $\Delta\Omega$ in the effective eigenfrequency of the resonator according to

$$\frac{\Delta\Omega}{c} = -\frac{\left(\frac{2\kappa}{c}\right)\left[1 + \frac{\kappa}{c}\cos(q)\right]}{\left[1 - \left(\frac{\kappa}{c}\right)^2\right]}. \tag{5}$$

The required detuning $\Delta\Omega$ at the corner could be obtained by either changing the dimensions or the index composition of the microcavity. In conclusion, we have shown that temporal discrete solitons can propagate along a chain of nonlinear coupled resonators or defects that are embedded in a photonic crystal structure.

References

1. E. Yablonovitch, Phys. Rev. Lett. **58**, 2059 (1987).
2. N. Stefanou and A. Modinos, Phys. Rev. B **57**, 12127 (1998).
3. A. Yariv, Y. Xu, R. K. Lee, and A. Scherer, Opt. Lett. **24**, 711 (1999).
4. D. N. Christodoulides and R. I. Joseph, Opt. Lett. **13**, 794 (1988).
5. H. S. Eisenberg, Y. Silberberg, R. Morandotti, A. R. Boyd, and J. S. Aitchison, Phys. Rev. Lett. **81**, 3383 (1998).
6. R. Morandotti, H. S. Eisenberg, Y. Silberberg, M. Sorel, and J. S. Aitchison, Phys. Rev. Lett. **86**, 3296 (2001).
7. H. S. Eisenberg, Y. Silberberg, R. Morandotti, and J. S. Aitchison, Phys. Rev. Lett. **85**, 1863 (2000).
8. D. N. Christodoulides and E. D. Eugenieva, Opt. Lett. **26**, 1876 (2001).

Soliton engineering with two-period QPM gratings

Steffen Kjær Johansen[*1,2], Silvia Carrasco[*1], Lluis Torner[*1],
and Ole Bang[*2]

(*1) *Laboratory of Photonics, Department of Signal Theory and Communications,*
Universitat Politccnica de Catalunya,
Gran Capitan UPC-D3, Barcelona, ES 08034, Spain

(*2) *Department of Informatics and Mathematical Modelling,*
Technical University of Denmark,
DK-2800 Lyngby, Denmark
Tel: +45 45 25 30 95, fax: +45 45 93 12 35, email: skj@imm.dtu.dk

Abstract: *Two-period* quasi-phase-matching schemes might make it *practically* possible to engineer the averaged effective competing nonlinearities governing beams in quadratic materials. We show that the bandwidth for soliton generation is broader than in homogeneous structures.
©2002 Optical Society of America
OCIS codes: (190.0190) Nonlinear optics; (260.0260) Physical optics

We consider beam propagation under type-I second harmonic generation (SHG) conditions in a lossless quasi-phase-matching (QPM) $\chi^{(2)}$ slab waveguide. The slowly varying envelope of the fundamental wave (FW), $E_1 = E_1(x, z)$, and its second harmonic (SH), $E_2 = E_2(x, z)$, are[1]

$$i\frac{\partial E_1}{\partial z} + \frac{1}{2}\frac{\partial^2 E_1}{\partial x^2} + d(z)E_1^* E_2 e^{-i\beta z} = 0, \quad i\frac{\partial E_2}{\partial z} + \frac{1}{4}\frac{\partial^2 E_2}{\partial x^2} + d(z)E_1^2 e^{i\beta z} = 0. \quad (1)$$

The normalized wave-vector mismatch is introduced via the real parameter $\beta = k_1\omega_0^2 \Delta k$, where $\Delta k = 2k_1 - k_2$, and ω_0 is the beam width, and $k_{1,2}$ are the linear wave numbers of the FW and SH, respectively. The scaled transverse coordinate, x, is measured in units of ω_0 and the propagation coordinate, z, is measured in units of $2l_d$ where $l_d = k_1\omega_0^2/2$ is the diffraction length of the FW. As depicted in Fig. 1 the spatial periodic modulation of the nonlinearity $d(z)$ consists of a primary grating, $d^{(1)}(z)$, and a superimposed secondary grating, $d^{(2)}(z)$.
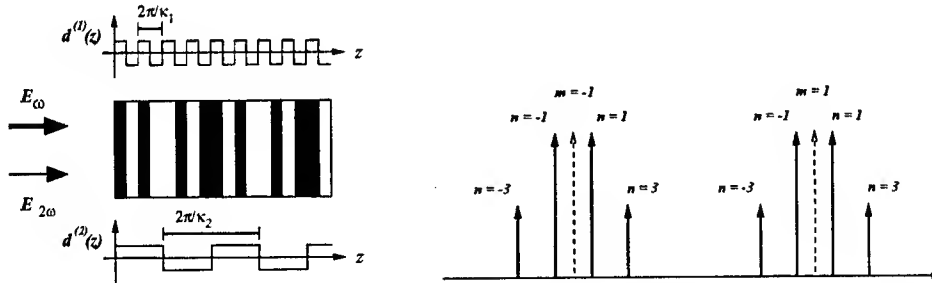
Fig. 1. Left figure: The square two-period QPM grating. Right figure: Peak splitting in the two-period QPM grating. Dashed peaks indicate the location of the 1'st order peaks in the one-period case.

We expand $d(z)$ in a Fourier series $d(z) = \sum d_k^{(1)} \exp(ik\kappa_1 z) \times \sum d_l^{(2)} \exp(il\kappa_2 z)$ where the summations are over all (k, l). If we assume the grating functions to be square, only the odd harmonics enter into the expansion, $d_{2l+1} = 2/i\pi(2l + 1)$ and $d_{2l} = 0$. κ_1 and κ_2 are the spatial grating frequencies pertaining to the primary and secondary grating, respectively. The effect of the superimposed period is to split each peak of the original one-period QPM grating into an infinite family of peaks[2]. As shown in Fig. 1 peaks appear at all spatial QPM frequencies $m\kappa_1 + n\kappa_2$, where m and n are the QPM orders related to the primary and secondary grating, respectively.

By applying the asymptotic expansion[3, 4] technique we have established a perturbation theory describing the propagation of the averaged fields in this two-period QPM system. We make the transformation $E_1(x, z) = w(x, z)$ and $E_2(x, z) = v(x, z)\exp(i\epsilon z)$, where $\epsilon = \beta - m\kappa_1 - n\kappa_2$, is the residual phase mismatch assumed to be small. The functions $w(x, z)$ and $v(x, z)$ are assumed to vary slowly on the scale given by the QPM periods and can be expanded in the Fourier series. For the averaged fields w_0 and v_0 of the Fourier

series we arrive at the following governing set of equations,

$$i\frac{\partial w_0}{\partial z} + \frac{1}{2}\frac{\partial^2 w_0}{\partial x^2} + \eta w_0^* v_0 + \gamma(|w_0|^2 - |v_0|^2)w_0 = 0, \tag{2}$$

$$i\frac{\partial v_0}{\partial z} + \frac{1}{4}\frac{\partial^2 v_0}{\partial x^2} - \epsilon v_0 + \eta w_0^2 - 2\gamma|w_0|^2 v_0 = 0. \tag{3}$$

In real crystals, the domain lengths $\Lambda_{1,2} = \pi/\kappa_{1,2}$ vary according to some statistical distribution. With this in mind we can show [5] that the averaged nonlinearities for 1'st order QPM, i.e. $m = \pm 1$ and $n = \pm 1$, and square grating functions are given by

$$\eta = -\text{sign}(mn)\frac{4}{\pi^2}, \quad \gamma = -\frac{4}{\pi^2}(1 - 8/\pi^2)(\text{sign}(m)/\kappa_1 + \text{sign}(n)/\kappa_2), \tag{4}$$

Equations (2-3) were first derived in [3]. They have the same form regardless of the specific type of grating, η and γ merely given as sums over the Fourier coefficients of the grating. Whole families of solitons exist, whose properties are by now well known [6, 7]. Engineering of the nonlinearities with QPM have been shown to be feasible in [8], although the grating considered was practically unrealizable. With two-period QPM we can bring the system close to phase matching by choosing one of the periods in the order of the intrinsic phase mismatch (in lithium niobate $|\beta| \sim 10^3$). The second period can the be exploited to tailor the residual phase mismatch to our needs. Hence, what two-period QPM offers is the extra degree of freedom necessary to engineer the averaged nonlinearities in real systems.
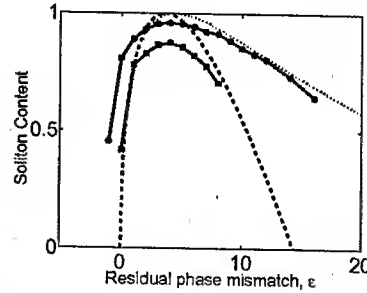
Fig. 2. Soliton content for sech input FW as a function of the residual phase mismatch $\epsilon = \beta - \kappa_1 - \kappa_2$ ($m = n = 1$). Input power is $P_{in} = 50$. $(\kappa_1, \kappa_2) = (195, 13)$ ($\eta \simeq -0.38, \tilde{\gamma} \simeq 0.050$). $\bullet$: SC for two-period QPM. $\blacksquare$: SC for purely quadratic model (see text). The discrete points are the outcome of numerical experiments; the full lines in between are only to help the eye. The dashed and dotted lines are estimates from the limiting NLSE for a pure quadratic model and for a model with cubic terms, respectively.

For the induced averaged nonlinearities addressed to be of potential practical importance, they have to impact the observable soliton properties, including their excitation conditions. In Fig. 2 we show the behavior found for the soliton content[9], SC, as a function of the residual phase mismatch in a two-period structure with QPM frequencies $(\kappa_1, \kappa_2) = (195, 13)$. We launch a FW signal, with a sech-shape, and no SH seeding and calculate how much of the initial power, P_{in}, is bound in the soliton which eventually forms. We propagate until a steady state has emerged and then we collect the power in a window wide enough to enclose substantially all the soliton. Typical values are propagation until $z = 10^3$ and collection of power in a window of $x = \pm 10$, but these values were adapted whenever needed in order to capture always all the soliton power. Simulations where carried out in the actual two-period QPM structure. The bandwidth of the SC for sech inputs can be estimated by using the Zakharov-Shabat scattering equations associated with the (1+1)-dimensional nonlinear Schrödinger equation, NLSE. With cubic terms, i.e. for system (2-3), one gets the estimate

$$\text{SC} \simeq \frac{2\sqrt{\frac{\eta^2\epsilon}{\eta^2+\gamma\epsilon}}}{\eta^2 P_{in}}\left(\sqrt{2\eta^2 P_{in}} - \sqrt{\frac{\eta^2\epsilon}{\eta^2 + \gamma\epsilon}}\right). \tag{5}$$

In the figure we compare the SC for the two-period structure with the SC for the corresponding homogeneous pure quadratic case, i.e. we launch the FW power $P_{in,hom} = \eta^2 P_{in}$ in a homogeneous crystal and plot SC as

a function of intrinsic phase mismatch (with no QPM the residual and the intrinsic phase mismatches are one and the same). The bandwidth for the two-period structure is found to be wider than the bandwidth in the homogeneous case. This effect is entirely due to the induced averaged cubic nonlinearity, which is easily seen from (5), i.e. $\eta^2\epsilon/(\eta^2 + \gamma\epsilon) < \epsilon$.

In Fig. 3 we plot the soliton content for the $(\kappa_1, \kappa_2) = (195, 13)$ case, but now we scan mismatches not only around the $(m = n = 1)$-peak but also around the $(m = 1, n = -1)$-peak.
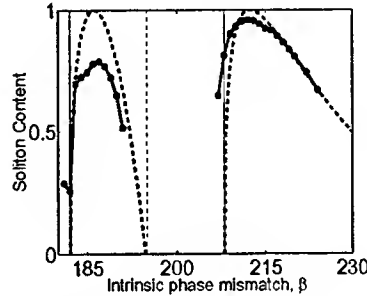
Fig. 3. Soliton content for sech Input FW as a function of intrinsic phase mismatch β with $(\kappa_1, \kappa_2) = (195, 13)$. Input power is $P_{in} = 50$. The discrete points are the outcome of numerical experiments; the full lines in between are only to help the eye. The dashed curves are estimates from the limiting NLSE. The vertical lines located at $\beta = 182$ and $\beta = 208$ indicate the $m = 1, n = -1$ and $m = n = 1$ peaks, respectively. The dashed vertical line at $\beta = 195$ indicates the location of the peak in the absence of a second period.

One observes that soliton generation around the $(m = 1, n = -1)$-peak takes place within a narrower band of mismatches and is less efficient than around the $(m = 1, n = 1)$-peak. This is because the average nonlinearities (4) are nonlinear functions of m and n and hence they change their relative strengths at the two peaks. We remark that one finds soliton generation around other peaks than the $(m = 1, n = \pm 1)$-peak. For example, in the $(\kappa_1, \kappa_2) = (195, 13)$ case we observe a band (not shown in the plot) around $\epsilon = 39$ corresponding to the $(m = 1, n = 3)$-peak. However, soliton formation in this band is much less efficient than in the $(m = 1, n = \pm 1)$-band and therefore we did not include it the plot. Similarly, other bands with higher QPM order also exist but one has to launch correspondingly high powers to excite solitons.

References

1. C. R. Menyuk, R. Schiek, and L. Torner, "Solitary waves due to $\chi^{(2)} : \chi^{(2)}$ cascading." J. Opt. Soc. Am. B **11**, 2434–2443 (1994).
2. M. H. Chou, K. R. Parameswaran, M. M. Fejer, and I. Brener, "Multiple-channel wavelength conversion by use of engineered quasi-phase-matching structures in LiNbO$_3$ waveguides," Opt. Lett. **24**, 1157–1159 (1999).
3. C. B. Clausen, O. Bang, and Y. S. Kivshar, "Spatial solitons and induced Kerr effects in QPM media," Phys. Rev. Lett. **78**, 4749–4752 (1997).
4. Y. S. Kivshar, N. Grønbech-Jensen, and R. D. Parmentier, "Kinks in the presence of rapidly varying perturbations," Phys. Rev. E **49**, 4542–4551 (1994).
5. S. K. Johansen, S. Carrasco, L. Torner, and O. Bang, "Engineering of spatial solitons in two-period QPM structures," Opt. Commun. **203**, 393–402 (2002).
6. O. Bang, T. W. Graversen, and J. F. Corney, "Accurate switching intensities and length scales in quasi-phase-matched materials," Opt. Lett. **26**, 1007–1009 (2001).
7. J. F. Corney and O. Bang, "Solitons in quadratic nonlinear photonic crystals," Phys. Rev. E **64**, 047601 (2001).
8. O. Bang, C. B. Clausen, P. L. Christiansen, and L. Torner, "Engineering competing nonlinearities," Opt. Lett. **24**, 1413–1415 (1999).
9. L. Torner, J. P. Torres, D. Artigas, D. Mihalache, and D. Mazilu, "Soliton content with quadratic nonlinearities," Opt. Commun. **164**, 153–159 (1999).

Quasi-phase-matched second harmonic generation in polymer rib waveguides

Jung-Jin Ju, Suntak Park, Seung Koo Park, Jung Yun Do, and Myung-Hyun Lee

Wideband Optical Devices Team, Electronics and Telecommunications Research Institute (ETRI),
161 Kajong-Dong Yusung-Gu, Taejon 305-350, Korea
Phone: +82 42 860 5186, Fax: +82 42 860 6836, E-mail: jjju@etri.re.kr

Abstract: Single-mode rib waveguides at both pump and second harmonic wavelengths were fabricated with low-loss polymers. We investigated the quasi-phase matching characteristics, and the second harmonic generation properties for wavelength conversions at the optical communication band.
©2002 Optical Society of America
OCIS codes: (190.2620) frequency conversion, optical design and fabrication

1. Introduction

Wavelength converter is one of the key devices to construct optical cross connects (OXC) in wavelength-division multiplexed (WDM) networks. Grouped multi-channels routing architecture has recently been proposed to simplify the OXC that handles the large number of WDM channels.[1,2] Cascading difference frequency generation (DFG) devices are well matched to the new architecture due to their novel features, multi-channels conversion, high-speed, low noise and good transparency. These have been demonstrated with periodically poled LiNbO$_3$ waveguides[3,4] and AlGaAs waveguides [5]. Polymer wavelength converters have promising features of a low cost and an easy fabrication. However, several issues such as conversion efficiency, fiber-to-fiber insertion loss, and photochemical stability have to be further improved for real applications

In the case of quasi-phase-matched (QPM) polymer waveguides, pump and second harmonic(SH) waves have to be guided with single-mode to maintain an enough field overlap between the two waves. A core thickness satisfying single-mode guiding conditions at the two waves is to be less than 1 □ because index differences between core and clad polymers are usually several times of 10^{-3}. A coupling loss between the optical fiber and the waveguide becomes very high due to the small vertical mode size in the thin waveguide. Thus, it is difficult to get high conversion efficiency with the waveguide of the small core thickness.

In this work, we proposed a rib waveguide structure to reduce the coupling loss of the pump beam, and fabricated the single-mode QPM waveguides through an alternative electric contact poling and a reactive ion beam etching. A side-chain polymer of polyetherimide backbone with DASS chromophores(PEI-DASS) and an UV curable polyacrylate polymer(UFC170) were used as low-loss core and clad, respectively. We measured the single-mode guiding modes for the pump(1.55 □, ps fiber laser) and the generated SH waves, the fiber-to fiber insertion loss of 9 dB at the pump wavelength for a periodically poled waveguide length of 1 cm, effective interaction length of 7.5 mm, and the normalized SHG conversion efficiency of about 1□10^{-2} %/(W·cm^2).

2. Waveguide design and fabrication

The several material properties were measured (Table 1) for waveguide design. In the core material development, we mainly considered the optical loss at the SH wavelength for conversion efficiency, and the glass transition temperature(T$_g$) for relaxations of the aligned chromophores during waveguide fabrication. In addition, the clad polymer was designed that have the same order of conductivity with the core polymer for efficient poling.

Table 1. The measured material properties for the QPM waveguide fabrication

Parameters	Refractive index™	d$_{33}$ (pm/V)	Absorption peak (nm)	Planar waveguide loss (dB/cm)	T$_g$(□)
PEI-DASS	1.593 (1.55 □) 1.615 (0.78 □)	9 (1.55 □)	380	1.80 (1.55 □) 3.80 (0.78 □)	165
UFC170	1.498 (1.55 □) 1.505 (0.78 □)	-	-	0.28 (1.55 □) 0.15 (0.78 □)	-

(a)   (b)

Fig. 1. (a) Rib waveguide structure. (b) A microscope image of the core layer after the QPM poling and thick straight line in the grating center is a photoresister pattern for the waveguide etching.

(a)   (b)   (c)
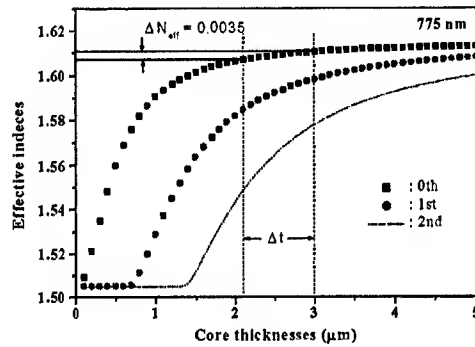
Fig. 2. (a) Effective index of the slab waveguide as a function of the core thickness. In the rib waveguide structure, the waveguide side is etched by Δt to get the effective index contrast of ΔN_{eff} for the SH wave. (b) Guided single-mode image of the pump beam. (c) Generated single-mode image of the SH beam by the pump beam.

The designed rib waveguide as shown in Fig.1(a) confines only one mode at both pump and SH waves by radiating higher order modes laterally into slab modes. In the type of rib structure, the single-mode condition does not require a thin core layer. For thicker core thickness, it is still possible to find one mode guiding condition by taking a proper etching depth. The etching depth in the structure was determined to get sufficient beam confinement in the lateral direction. As shown in Fig.2(a), the effective index contrast ΔN_{eff} (the difference between the effective index of the etched slab region(2.1 □) and that of the un-etched region((3 □)) of 0.0035 was required to keep the single-mode condition at the SHG wavelength. In the case of the pump wavelength, single-mode guiding condition was also satisfied with the effective index contrast of 0.0086. Although the 3-□ slab waveguide can support higher order modes these are difficult to propagate through the rib waveguide because the effective index of the first higher order mode in the 3-□ slab region is lower than that of the fundamental mode in the 2.1-□ slab region. It means that the higher order modes supported by the 3- □ slab region will be coupled into the fundamental mode of the 2.1-□ slab region.

The rib waveguides were fabricated by ion beam etching in oxygen. After the core coating, these were periodically poled with an electric field of 100V/□ for 5 min at 160 □. Several waveguides with the QPM periods from 20 □ to 30 □ with a step of 0.5 □ were made to find the phase matching period at the 1.55 □ pump wavelength. In order to investigate the core pattern of the periodically poled region, we took a microscopic image as shown in Fig.1(b). It shows a uniform grating period of 21 □ and small surface deformations. The scattering loss of 1dB due to the periodic poling was estimated by comparing the fiber-to fiber insertion losses between the periodically poled waveguide(9 dB) and the un-poled waveguide(8 dB) for the waveguide length of 1 cm. The guided mode profiles were shown in Fig.2 (b) and (c), which were taken by CCD camera through a lens imaging of the output beams of the waveguide. It shows that the pump and SHG beams are guided with the expected single-mode without the higher order modes excitation.

3. QPM SHG properties

The SHG experiments were performed with a ps fiber laser. It has the pulse width of 5 ps and the repetition rate of 20 MHz with the maximum average power of 2 mW. Figure 3 shows the phase matching curve by tuning the pump wavelengths. The QPM period of 22.5 □ was phase matched at the center wavelength of 1.5565 □ with the FWHM

of 1.5 nm. The center wavelengths of the phase matching were decreased about 9.8 nm by reducing the QPM period of 1 ⊐. The effective interaction length of 7.5 mm was estimated by fitting the measured data with the sinc^2 function. Since the $\Delta\alpha L=(\alpha_{2\omega}- \alpha_\omega)L$ <2 [6], the $\Delta\beta L$-dependence function can be approximated by the usual sinc$^2(\Delta\beta L/2)$ function of the lossless case. In the fit, $d(\Delta\beta)/d\lambda$ = -0.49 ⊏ ^{2} was calculated with the effective indexes dispersion of the rib waveguide.
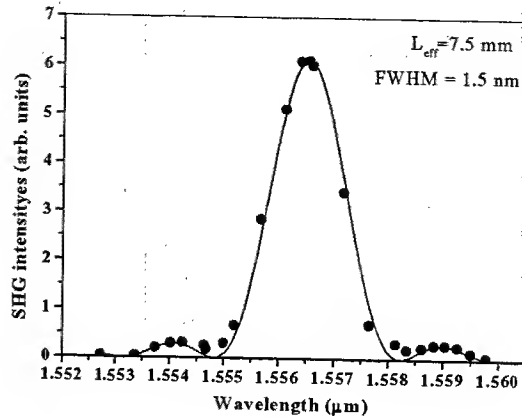
Fig. 3. SHG turning curve of the 1-cm-long waveguide with the QPM period of 22.5 ◻

The 22.5 ⊐ QPM waveguide records a normalized conversion efficiency(figure of merit) of 1◻10^{-2} %/(W·cm^2). The efficiency was not optimum because the waveguide faces of the input and the output were not polished, just sawed with a diamond blade (thickenss: 80 ◻). Thus, a significant scattering loss for the SHG will be produced at the output waveguide face, but it is negligible for the pump wavelength.

In conclusion, we proposed a rib waveguide structure that can reduce a coupling loss from the single-mode optical fiber to the periodically poled polymer waveguide by using a thick core thickness and a proper etching depth. The single-mode guidings at both the pump and the SH wavelengths were demonstrated with the rib waveguide that fabricated with low-loss core and clad polymers. The normalized SHG conversion efficiency is still very low, but it is in progress.

References

[1]. E. Ciaramella, "Introducing wavelength granularity to reduce the complexity of optical cross connects, " IEEE Photon. Technol. Lett. 12, 699-701(2000)

[2]. J. Yamawaku, W. Imajuku, A. Takada, and S. Okamoto, "Element number evaluation on the grouped wavelength path routing network," Proc. Of the 2001 IEICE General Conf. Vol. B2, B-10-110, 534(2001)

[3]. G. Schreiber, H. Suche, Y.L. Lee, W. Grundkotter, V. Quiring, R. Ricken, W. Sohler, " Efficient cascaded difference frequency conversion in periodically poled Ti:LiNbO₃ waveguides using pulsed and cw pumping," Appl. Phys. B 73, 501-504(2001)

[4]. M.H.Chou, B. Brener, M.M. Fejer, E.E.Chaban, S.B. Christman, "1.5-◻-band wavelength conversion based on cascaded second order nonlinearity in LiNbO₃ waveguides," IEEE Photon. Technol. Lett. 11, 653-655(1999)

[5]. S.J.B. Yoo, C. Caneau, R.Bhat, M.A. Koza, A.Rajhel, N. Antoniades, "Wavelength conversion by difference frequency generation in AlGaAs waveguides with periodic domain inversion achieved by wafer bonding," Appl. Phys. Lett. 68(19), 2609-2611(1996)

[6]. M. Jager, G.1. Stegeman, M.C. Flipse, M. Diemeer, G. Mohlmann, " Modal dispersion phase matching over 7 mm length in overdamped polymeric channel waveguides," Appl. Phys. Lett. 69(27), 4139-4141(1996)

Quadratic interactions
in an Hexagonally Poled Lithium Niobate buried waveguide

K. Gallo, R.T. Bratfalean, A. C. Peacock, Neil G. R. Broderick, C. B. E. Gawith, L. Ming, P. G. R. Smith and D. J. Richardson

Optoelectronics Research Centre, University of Southampton, Southampton, SO17 1BJ, United Kingdom
tel. 023 8059 2825, fax: 023 8059 3149, e-mail address: kag@orc.soton.ac.uk

Abstract: We demonstrate for the first time second harmonic generation from 1.536 μm in a buried planar waveguide fabricated by an annealed and reverse proton exchange in a two-dimensional (2D) nonlinear photonic LiNbO$_3$ crystal.
©2002 Optical Society of America
OCIS codes: (230.7390) Waveguides, planar, (190.4390) Nonlinear optics, integrated optics, (130.3730) Lithium niobate

1. Introduction

Nonlinear frequency conversion in 2D quadratic photonic crystals is significantly enriched with respect to the 1D case due to the possibility of phase-matching simultaneously several parametric interactions in the 2D plane [1].

The first example of a 2D nonlinear photonic crystal (NPC), with a constant refractive index and a spatially periodic nonlinear susceptibility, was demonstrated in Lithium Niobate by an extension of the electrical field poling technology used to fabricate 1D $\chi^{(2)}$ gratings [2], to two dimensional hexagonal patterns (HeXLN)[3]. Several bulk experiments have confirmed the potential of HeXLN crystals for multiple harmonic generation (red, green and blue) and Second Harmonic Generation (SHG) with an enhanced tuning range [3,4]. In addition other researchers have demonstrated simultaneous wavelength interchange using a NPC [5].

In these early experiments the conversion efficiency was relatively low (particularly in the case of high harmonic generation). Several approaches can be taken in order to increase the quadratic efficiency in 2D NPC. One consists in resorting to a planar guided-wave configuration to increase the field intensities and also to improve the modal overlap compared to the bulk case. Moving to a planar geometry at the same time preserves all the versatility and peculiarities of the 2D NPC structure associated with the availability of multiple reciprocal lattice vectors and the possibility of implementing non-collinear interactions.

In this paper, we present what we believe to be the first demonstration of quadratic interactions in a planar HeXLN waveguide fabricated using the technology of annealed and reverse proton exchange.

The waveguide generates simultaneously noncollinear second, third and fourth harmonic beams. Here we briefly discuss our first results concerning essentially the SHG response. Ultimately we hope to use the SHG response to characterize the waveguide parameters. For example, information about the effective index of the waveguide can be obtained by comparing the angles at which SHG is emitted in the waveguide compared to the bulk.

2. Fabrication

The 2D NPC was fabricated by periodically poling a *z*-cut 500-μm thick, congruent LiNbO$_3$ crystal with an hexagonal pattern in the *x-y* plane. First, we deposited a thin layer of photoresist onto the *-z* face on which we defined photolithographically the hexagonal array with a spatial period Λ = 18.05 μm. The pattern was then transferred to the sample by applying an electric field via liquid electrodes on the $\pm z$ faces at room temperature [3]. The HeXLN structure and its orientation with respect to the crystal axes (*x,y,z*) is sketched in Fig. 1*a*.

The planar buried waveguide was fabricated after the poling, via the sequence of proton exchange, annealing and reverse proton exchange [6]. The initial proton exchange (PE), performed at 160°C for 31 hours, yielded a proton-rich layer on top of the crystal, corresponding to a high refractive index, low-nonlinearity surface planar waveguide for the extraordinary polarization. The PE waveguide was then annealed to let protons diffuse into the substrate, creating a deeper, graded-index waveguide. Finally, a Li$^+$ rich layer was re-created at the surface of the annealed PE waveguide by a reverse proton exchange (RPE) in a eutectic melt of LiNO$_3$, KNO$_3$ and NaNO$_3$.

The process conditions were chosen to allow the realization of a nonlinearity-preserving buried planar waveguide, which is designed to be single-moded (TM$_0$) at wavelengths around 1.53 μm. The buried waveguide structure is sketched in Fig. 1*b*.

Lastly, we polished the $\pm x$ faces of the HeXLN waveguide allowing a propagation length of 14 mm through the crystal in the *x* axis direction.
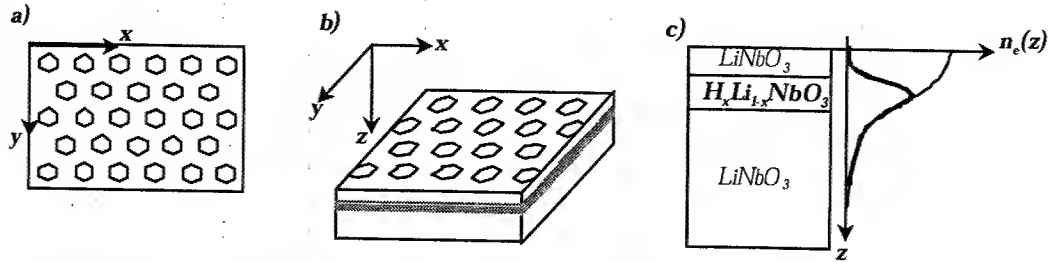
Fig.1: *a)* structure of the LiNbO$_3$ hexagonal domain pattern (HeXLN) in the *x-y* plane, *b)* sketch of the HeXLN and of the buried waveguide, *c)* typical structure in depth (z) of a buried waveguide made by PE + annealing + RPE: the guiding region corresponds to the proton-rich layer (H$_x$Li$_{1-x}$NbO$_3$). On the right, sketch of the extraordinary index profile of the buried waveguide (thick line), along with the profile of the surface waveguide before the last RPE step (thin line).

3. Experimental setup

The experimental setup used to characterize the response of our buried HeXLN waveguide is schematically shown in Fig. 2. The source for the experiments was an all-fiber amplifier chain seeded by an externally modulated laser diode, delivering 5 ns pulses at 1.536 µm, with adjustable repetition rates (1 – 500 kHz) and peak powers (up to 20 kW).

In order to avoid photorefractive effects, the HeXLN waveguide was placed in a computer controlled oven (maintained at temperatures beyond 100°C). The oven was mounted on a rotation stage, to allow adjusting of the pump incidence angle.

To couple the infrared light into the waveguide, we first shaped the laser beam into an ellipse with a cylindrical lens (focal length: f = 20 cm) and then focused the elliptical beam through a spherical lens (10X objective). The resulting spot size of the 1.536 µm pump at the waveguide input was 5.6 µm x 80 µm FWHM. We measured a 36 % coupling efficiency into the planar waveguide. The inset of Fig. 2 shows an image of the intensity profile of the TM$_0$ mode at 1.536 µm, collected at the waveguide output with an IR camera.

*λ$_\omega$ field profile
at the waveguide output*
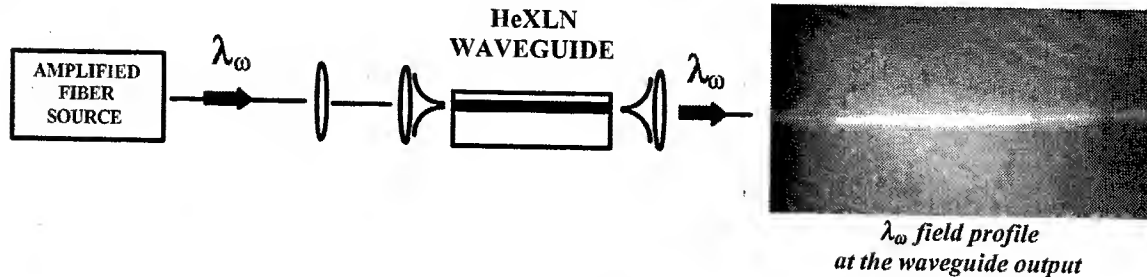
Fig. 2. Experimental setup used to measure the response of the HeXLN waveguide. The source consists of a CW diode laser the output of which is externally modulated and amplified by the cascade of several fiber amplifier stages. The inset shows an image of the intensity of the TM$_0$ mode at the pump wavelength (λ$_\omega$), taken at the waveguide output.

4. Quadratic response

The quadratic response of 2D nonlinear photonic crystals is very rich. Although our HeXLN waveguide generates simultaneously multiple beams at different wavelengths and at different angles with respect to the fundamental beam direction, the first measurements we made concern the SHG, which in itself can provide information on both the linear and the nonlinear properties of the device.

By moving the crystal vertically the light could be coupled either into the waveguide or into the bulk of the crystal. When moving from the waveguide to the bulk the angle that the SH was emitted at was observed to change and at the same time an increase in the generated red and green light was apparent.

It is worth mentioning that the HeXLN period we used in these preliminary experiments (18.05 µm) is meant to maximize the efficiency of SHG in the bulk with a pump at 1.536 µm propagating along the *x* axis. Therefore our experimental conditions do not correspond to the optimum for SHG in the buried waveguide, due to the fact that its dispersion properties differ from those of the bulk. Nevertheless, by letting the fundamental beam propagate slightly off the *x* axis, we could still exploit the same reciprocal lattice vector used in previous bulk experiments (i.e. G$_0$) to generate red and green light in the waveguide although at angles different from the bulk quadratic interaction.

The SHG response of the waveguide can be studied by varying several parameters such as the infrared pump power, the temperature, the incidence angle. As an example, Fig. 3a shows the internal SHG conversion efficiency ($\eta_{SHG}{}^{internal}$), calculated as the ratio of the *average* powers of the SH at the output ($P_{2\omega}{}^{OUT}$) and of the fundamental at the input of the waveguide ($P_\omega{}^{IN}$), as a function of $P_\omega{}^{IN}$, for a given pump incidence angle. Fig. 3b, on the other side, shows a typical SHG temperature tuning curve of our waveguide. Its asymmetry is to be attributed to the fact that, due to thermal expansion of the oven, the vertical position of the input beam changes with respect to the waveguide as the temperature is varied. Namely, in the case of fig. 3b, the peak at 138°C corresponds to SHG from the waveguide. The "shoulder" at lower temperatures corresponds to the beam getting into the bulk, while the rapid decay of the SHG signal at higher temperatures corresponds to the beam getting into the upper cladding (air).

A better insight into the properties of the waveguide would be provided by a systematic study of the SHG angular response and of the SHG temperature tuning curves. We are at present pursuing this objective to the aim of further optimizing the structure towards the realization of true "device".
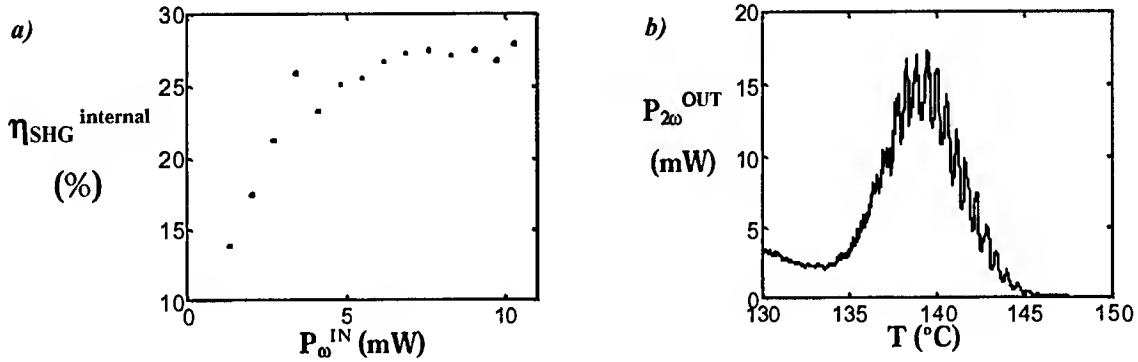
Fig. 3. $a)$ SHG internal efficiency ($\eta_{SHG}{}^{internal}$) as a function of the average power at λ_ω coupled in the waveguide ($P_\omega{}^{IN}$) measured for a given pump incidence angle at a 1 kHz pulse repetition rate and $b)$ generated SH average power at the output measured as a function of temperature.

7. Conclusions

In conclusion we have fabricated the first planar buried waveguide in a HeXLN crystal and explored its quadratic response, by studying experimentally the SHG from a 1.536 μm pulsed pump. The SHG response in itself is very rich and can provide useful information on the properties of both the 2D nonlinear grating and the waveguide, which would allow a further joint optimization of the waveguide and 2D NPC for maximum efficiency.

Although these are only preliminary results and margin is still left for optimization, the guided-wave configuration appears well suited to fully exploiting the capabilities of HeXLN for both telecommunication and fundamental physics.

8. References

[1]. V. Berger, "Nonlinear photonic crystals", *Phys. Rev. Lett.* 81, 4136-4139 (1998).

[2]. M. Yamada, N. Nada, M. Saitoh, and K. Watanabe, "First order quasi-phase-matched LiNbO₃ waveguide periodically poled by applying and external field for efficient blue second-harmonic generation", *Appl. Phys. Lett.* 62, 435-436 (1993).

[3]. N. G. R. Broderick, G. W. Ross, H. L. Offerhaus, D. J. Richardson, and D. C. Hanna, "Hexagonally poled lithium niobate: a two-dimensional nonlinear photonic crystal", *Phys. Rev. Lett.* 84, 4345-4348 (2000).

[4]. R. Bratfalean, N. G. R. Broderick, D. Richardson, "Observation of simultaneous generation of multiple harmonics in hexagonally poled lithium niobate", *CLEO 2002 Conf.*, Paper CWE3, May 19-24 2002, Long Beach, California.

[5]. A. Chowdhury et al. "Experimental demonstration of 1535-1555-nm simultaneous optical wavelength interchange with a nonlinear photonic crystal", *Opt. Lett.* 26, 1353-1355 (2001).

[6]. K. R. Parameswaran, R. K. Route, J. R. Kurz, R. V. Roussev, M. M. Fejer, and M. Fujimura, "Highly efficient second-harmonic generation in buried waveguides formed by annealed and reverse proton-exchange in periodically poled lithium niobate" *Opt. Lett.* 27, 179-181 (2002).

Bistability in Photonic Crystal Defects

Marin Soljačić[(&)], **Mihai Ibanescu**[(&)], **Steven G. Johnson**[(&)], **Shanhui Fan**[(·)], **Chiyan Luo**[(&)], **Yoel Fink**[(%)], and **J.D.Joannopoulos**[(&)]

(&) Physics department, MIT, USA
(·) Electrical Engineering department, Stanford University, USA
(%) Material Science department, MIT, USA

We present an analytical theory and computational experiments to demonstrate optical bistability in a class of non-linear photonic crystal devices. Lengths of our devices are smaller than the wavelength of light, they can operate with only a few mW of power, and can be faster than 1ps.

The promising ability of photonic crystals (PCs) to control light in novel ways makes them ideal to miniaturize optical components and devices for eventual large-scale integration. Non-linear PCs might ultimately lead to production of active all-optical devices at large-scale integration length-scales. In the current work, we use the flexibility offered by PCs to design systems that are effectively one-dimensional, although they are embedded in a higher-dimensional world. Because of this, we have optimal control over input and output; in particular we can achieve 100% peak theoretical transmission. Consequently, our systems are particularly suitable for large-scale all-optical integration. We solve the full non-linear Maxwell's equations numerically (with minimal physical approximations) to demonstrate optical bistability in our systems. We also develop an analytical model that excellently describes the behavior of the systems and is very useful in predicting optimal designs.

Our first design is shown in Figure 1. It resides in a square lattice 2D PC of high-ε dielectric rods embedded in a low-ε dielectric material; the electric field is always parallel to the rods. We create a resonant cavity (point defect) that supports a dipole-type localized resonant mode by increasing the radius of a single rod, surrounded by bulk crystal. We connect this cavity with the outside world by placing it 3 unperturbed rods away from two single mode waveguides. One of the waveguides serves as the input port to the cavity and the other serves as the output port. The cavity couples to the ports through tunneling processes. We consider a physical system where the high-index material has an instantaneous Kerr non-linearity (the index change is $n_2|E|^2$, where n_2 is the Kerr coefficient).
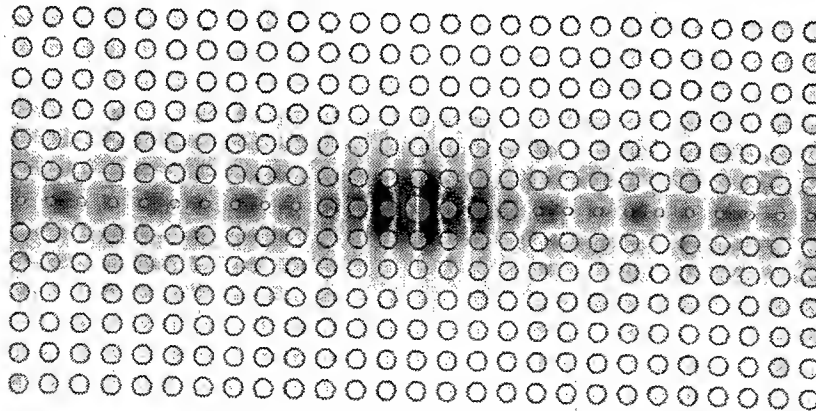
Figure 1: Electric field for a photonic crystal device that we use to demonstrate optical bistability, here exhibiting 100% resonant linear transmission.

The cavity has resonant frequency of $\omega_{RES}=0.2581(2\pi c)/a$ and a Lorentzian transmission spectrum: $T(\omega) \equiv P_{OUT}(\omega)/P_{IN}(\omega) \cdot \gamma^2/[\gamma^2+(\omega-\omega_{RES})^2]$, where P_{OUT} and P_{IN} are the outgoing and incoming powers respectively, and γ is the width of the resonance. We obtain a quality factor $Q=\omega_{RES}/2\gamma=557$.

For the case of CW signals, we achieve a precise analytical understanding of bistability in this system. Let us denote by $P_{IN}{}^S, P_{OUT}{}^S$ the steady-state values of P_{IN} and P_{OUT} respectively. We show [1] that there is a single additional fundamental physical quantity associated with this cavity (in addition to Q and ω_{RES}) that allows one to fully predict the $P_{OUT}{}^S(P_{IN}{}^S)$ behavior of the system. The quantity:

1

$$\kappa \equiv \frac{1}{Q} * \frac{1}{T * P_{IN}^{S}} * \frac{\int\limits_{AREA} d^2 x \sqrt{\varepsilon(x,y)} |E(x,y)|^4 n_2(x,y)}{\int\limits_{AREA} d^2 x \varepsilon(x,y) |E(x,y)|^2} , \tag{1}$$

which we call *the nonlinear feedback parameter* is roughly a constant of this non-linear system. Moreover, the value of κ does not change as we add more rods to the "walls" that separate the cavity from the waveguides, thereby increasing the Q of the cavity. κ is a measure of efficiency of the non-linear feedback of a given system: the larger the κ, the more efficient our system is.

We define two more useful quantities: $\delta = (\omega_{res} - \omega_0)/\gamma$ is the relative detuning of the carrier frequency from the resonance frequency, and $P_0 = 2/(3Q^2\kappa)$ is a "characteristic power" of the cavity. With these definitions the dependency between P_{OUT}^{S} and P_{IN}^{S} becomes:

$$\frac{P_{OUT}^{S}}{P_{IN}^{S}} = \frac{1}{1 + \left(P_{OUT}^{S} \middle/ P_0 - \delta \right)^2} . \tag{2}$$

This cubic equation can have either one or three real solutions for P_{OUT}^{S}, depending on the value of the detuning parameter δ. The bistable regime corresponds to three real solutions and requires a detuning parameter $\delta > \cdot 3$. By Eq.(2), this tells us the minimum power needed for bistability: $P_{b.min} = P_{100\%} = \cdot 3P_0$. The physical interpretation of the non-linear feedback parameter is now apparent; $1/(\kappa Q^2)$ is a measure of the characteristic power needed to observe bistability in the cavity in question.
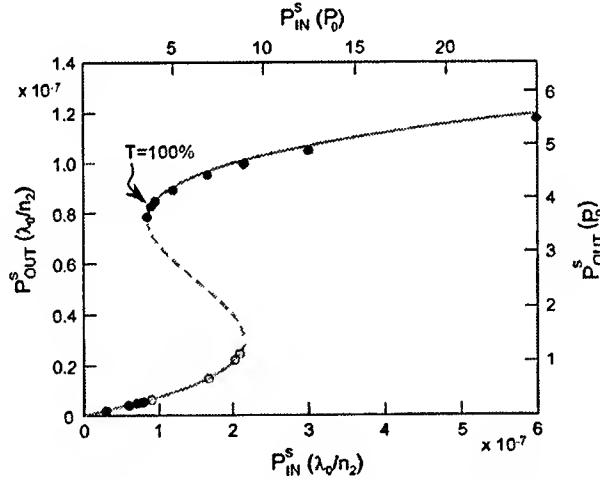
Figure 2: Plot of the observed P_{OUT}^{S} vs. P_{IN}^{S} for the device from Figure 1, when $\delta = 3.8$. The circles are points obtained from numerical experiments. The line is our analytical prediction, which clearly matches the numerical experiments.

To check our analytic theory, we obtain $\kappa = 99.9 n_2/\lambda_0$ from a single non-linear run, and together with the knowledge of Q and ω_{RES}, we obtain $P_{OUT}^{S}(P_{IN}^{S})$ for $\delta = 3.8$ which we plot as the green line in Figure 2. Our analytic theory is seen to be in an excellent agreement with the numerical experiments. The "middle" hysteresis branch (the dashed line in Figure 2) is unstable - any tiny perturbation makes a solution on that branch decay either to the upper or to the lower branch.

We can use our 2D simulations to immediately predict behavior of a similar system, implemented in 3D [2]. Assuming that the Kerr coefficient is $\check{n}_2 = 1.5 * 10^{-17} m^2/W$, (a value achievable in many nearly-instantaneous non-linear materials[*]), and that the carrier $\lambda_0 = 1.55\mu m$, the minimum power to observe bistability is $P_{b.min} = 119mW$. This value is many orders of magnitude lower than in other small all-optical ultra-fast switches; the reason for this is two-fold. First, the transverse area of the modes in the system of Figure 1 is only $\cdot (\lambda/3)^2$; consequently, to achieve the same-size non-linear effects, we need much less power than in some other systems that have larger transverse modal area. Second, since we are dealing with a highly confined, high-Q cavity, the field inside the cavity is much larger than the

---

[*] Please note that in our notation, $n_2 = cn_H\varepsilon_0\check{n}_2$, where n_H is n of our high-ε material.

field outside the cavity; this happens because of energy accumulation in the cavity. In fact, from the expression for the characteristic power P_0, one can see that the operating power falls as $1/Q^2$. Building a highly confined, high-Q cavity is very difficult in systems other than PCs, so we expect high-Q cavities in PCs to be nearly optimal systems for optical bistability.
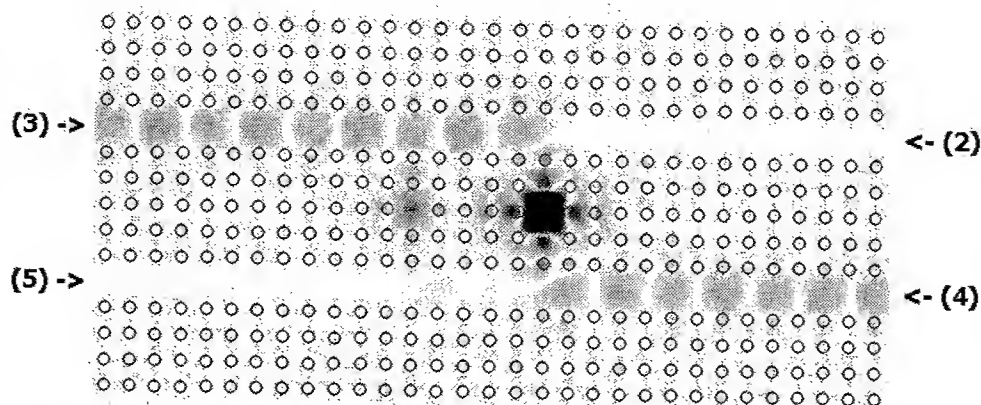
Figure 3: Electric field for a channel-drop photonic crystal device that we use to demonstrate optical bistability, here exhibiting 100% resonant linear transmission from port (3) to port (4). The details of the device are explained in Ref. 3. We model the high index rods as having an instantaneous Kerr non-linearity.

Another embodiment of the concept presented above is to observe optical bistability in non-linear channel drop filters from Ref. 3. A channel drop filter (shown in Figure 3) has 4 equivalent ports that are mutually coupled via two resonant cavities. However, the even, and the odd state supported by this 2-cavity system are degenerate both in their resonant frequencies, and in their decay times. Consequently, one effectively observes only a single resonant state in this system. Let's use the port (3) in that figure as the input to our device. If the carrier frequency is the same as the resonant frequency of the filter, 100% of the signal exits at port (4). If the carrier frequency is far away from the resonant frequency, most of the signal exits at port (2), while only a small amount exits at port (4). In fact, the transmission at port (4) has a lorentzian shape: $T_4(\omega) \equiv P_{OUT4}(\omega)/P_{IN3}(\omega) \cdot \gamma^2/[\gamma^2+(\omega-\omega_{RES})^2]$, where P_{OUT4} and P_{IN3} are the outgoing and incoming powers respectively, and γ is the width of the resonance. Consequently, this system can also be characterized solely in terms of its resonant frequency ω_{RES}, and its quality factor Q. Any power that does not go into port (4) exits through port (2): $T_2(\omega)=1-T_4(\omega)$; no power ever exists into port (5). Because of this, one can think of the systems from Figure 1, and Figure 3 being entirely equivalent, except for one point: in the system from Figure 1, what ever does not exit at the output is being reflected back towards the input. In contrast, in the system from Figure 3, all the power that does not get through to the port (4) gets channeled into the port (2), instead of being reflected back towards the input.

Non-linear analysis of the system of Figure 3 closely follows the non-linear analysis of the system of Figure 1 [4]. Since one effectively observes only a single resonant state, one can define a nonlinear feedback parameter κ, as given by the equation (1). By performing numerical experiments, we confirmed that the analytical theory presented above applies for this class of systems also. Bistability behavior is predicted, and closely mirrors the behavior of the system from Figure 1; the only difference is that the rejected part of the signal is always being redirected into port (2) from Figure 3, rather than being sent back towards the input.

Typically, one will be using the ports (3) and/or (5) as the inputs, and the ports (2) and/or (4) be used as the outputs. Having zero reflections towards the inputs is a great advantage in integrated optics; reflections can be detrimental when integrating non-linear or active devices on the same chip. Furthermore, having 4 ports offers much more design flexibility than in the system of Figure 1.

REFERENCES

1   Marin Soljačić, Mihai Ibanescu, Steven G. Johnson, Yoel Fink, and J.D.Joannopoulos, "*Optimal Bistable Switching in Non-Linear Photonic Crystals*", submitted for publication.
2   M.L.Povinelli, S.G.Johnson, S.Fan, and J.D.Joannopoulos, Phys. Rev. B **64**, 075313 (2001).
3   S.Fan, P.R.Villeneuve, J.D.Joannopoulos, and H.A.Haus, Phys. Rev. Lett. **80**, 960 (1998).
4   Marin Soljačić, Shanhui Fan, Chiyan Luo, and J.D.Joannopoulos, manuscript in preparation.

Notes

Key to Authors and Presiders

Nonlinear Guided Waves and Their Applications
Technical Program Committee

General Chairs
Alain Barthelemy, *Univ. de Limoges, France*
Yuri Kivshar, *Australian Natl. Univ, Canberra Australia*

Program Chairs
Marc Haelterman, *Univ. Libre de Bruxelles, Belgium*
Luigi A. Lugiato, *Univ. dell' Insubria a Como, Italy*
Richart Slusher, *Lucent Tech., USA*

Category 1: Nonlinear Fiber Effects and Temporal Solitons
Stefan Wabnitz, *Alcatel CIT, France,* Subcommittee Chair
Govind P. Agrawal, *Univ. of Rochester, USA*
Nail N. Akhmediev, *Australian Natl. Univ., Australia*
Peter A. Andrekson, *Cenix, USA*
Guy Millot, *Univ. de Bourgogne, France*

Category 2: Spatial Solitons and Transverse Effects
Demetrios N Christodoulides, *Lehigh Univ., USA,* Subcommittee Chair
Gaetano Assanto, *Univ. degli Studi Roma, Italy*
Allan Boardman, *Univ. of Salford, UK*
Paolo Di Trapani, *Univ. dell' Insubria a Como, Italy*
Lluis Torner, *Polytechnic Univ. of Catalonia, Spain*

Category 3: Nonlinear Periodic Structures and Frequency Conversion
Neil G. R. Broderick, *Univ. of Southampton, UK,* Subcommittee Chair
Ole Bang, *Univ. of Denmark, Denmark*
Martij de Sterke, *Univ of Sydney, Australia*
Benjamin J. Eggleton, *Lucent Tech., Bell Labs., USA*

Category 4: Solitons and Self - organized Spatial Structures in Cavities and Feedback Systems
William J. Firth, *Strathclyde Univ., UK,* Subcommitte Chair
Thorsten Ackermann, *Univ. Munster, Germany*
Nikolay Rosanov, *S.I Vavilov State Opt. Inst., Russia*
Mark Staffman, *Univ. of Wisconsin-Madison, USA*

Category 5: Materials and Fabrication
Joseph Zyss, *Ecole Normale Superieure de Cachan, France,* Subcommitte Chair
Alfred Drlessen, *Univ. of Twente, the Netherlands*
James Grote, *Air Force Research Lab., USA*
Peter Van Daele, *Optoelectronics/ Optoelectronics Tech., Belgium*
Sholmo Ruschin, *tel Aviv Univ., Israel*
Daniel Gauthier, *Duke Univ., USA**

*Denotes the OSA Technical Council Representative